ISSN 0288-4534
CODEN: KPPJAD

KONA Powder and Particle Journal

No.33 (2016)

Hosokawa Powder Technology Foundation

available online-www.kona.or.jp

About this Journal

KONA Powder and Particle Journal is a refereed scientific journal that publishes articles on powder and particle science and technology. This journal has been published annually since 1983 and is distributed free of charge to researchers, members of the scientific communities, universities and research libraries throughout the world, by Hosokawa Powder Technology Foundation (http://www.kona.or.jp/) established by Mr. Masuo Hosokawa in 1991.

The Chinese character "粉" in the cover is pronounced "KONA" in Japanese, and means "Powder". The hand written "  " is after the late Mr. Eiichi Hosokawa, founder of the Hosokawa Micron Corporation (http://www.hosokawa-micron.co.jp).

About the Cover:

Introduction of numerical simulation technologies is desired to optimize the design of industrial devices and/ or the operational conditions. The discrete element method (DEM) is often employed in the simulation of the granular flow. At present, the DEM has critical problems form a viewpoint of the industrial application. Specifically, modeling of arbitrary shaped wall boundary became problematic since solid particle-wall interaction algorithm was much complex. Signed distance function (SDF) based wall boundary model was newly developed to simulate the granular flow in an industrial system. The DEM/SDF method has been applied to actual industrial systems such as the die-filling, ribbon mixer and twin-screw kneader so far. For front cover, a new die-filling simulation was performed, where the die shape was "粉" (see the video at Doi:10.14356/kona.2016023). Please read the paper on pp.169–178.

Headquarters of Hosokawa Micron Corporation

Editorial Board

■ Publication Office

Hosokawa Powder Technology Foundation (http://www.kona.or.jp)
(in the headquarters building of Hosokawa Micron Corporation)
1-9, Shodaitajika, Hirakata-shi, Osaka 573-1132, Japan
E-mail: contact_zainq@hmc.hosokawa.com

<Original Research Papers>

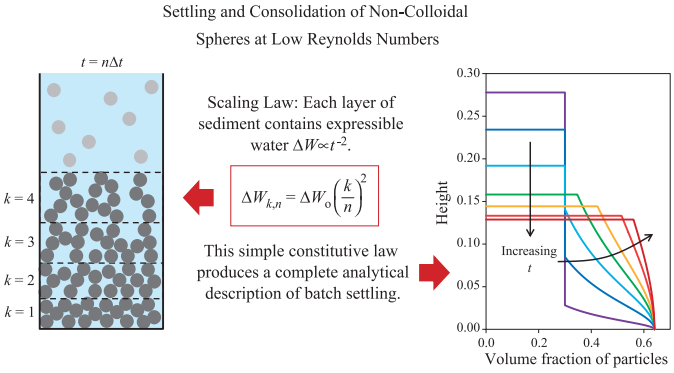

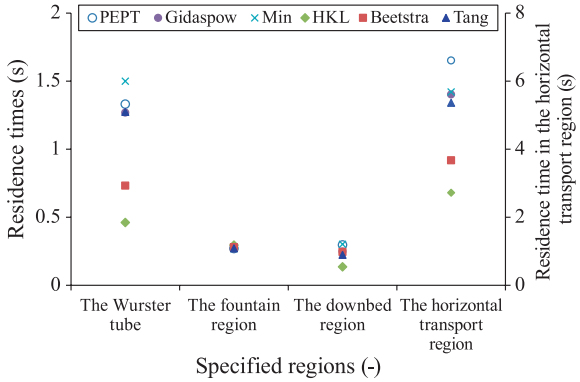

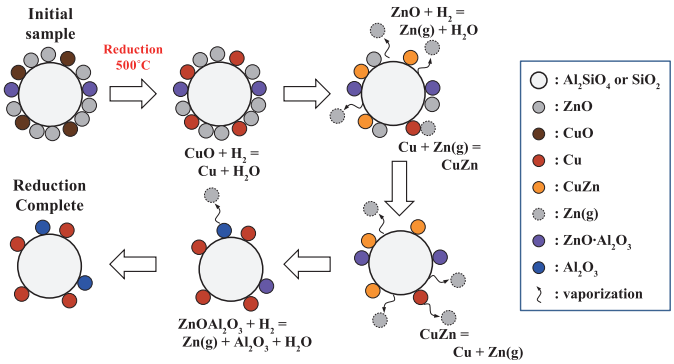

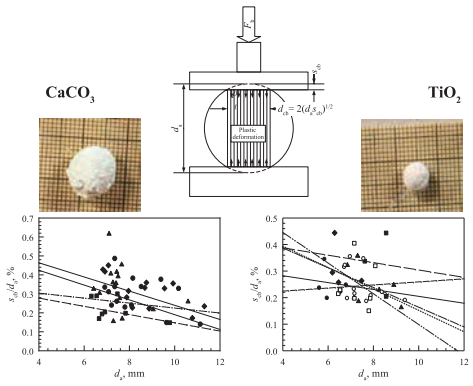

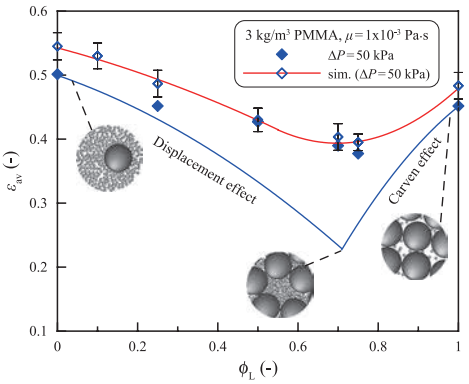

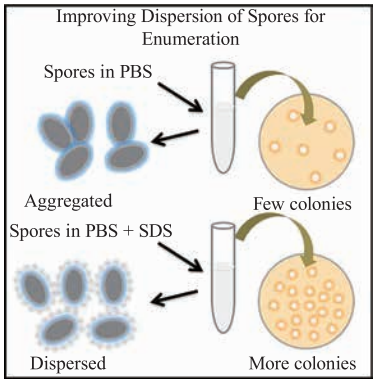

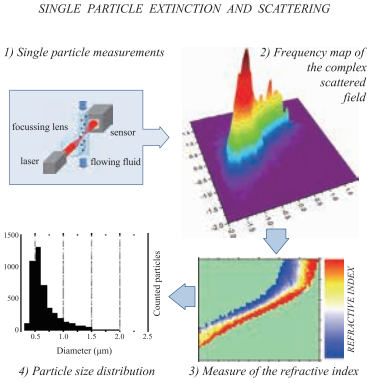

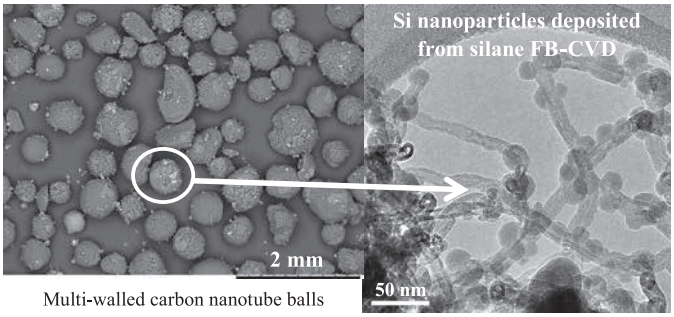

Multi-walled carbon nanotube balls

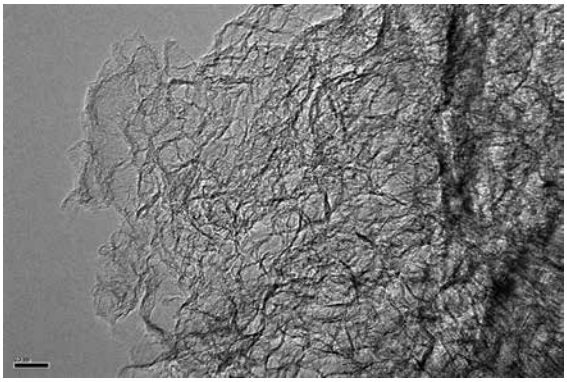

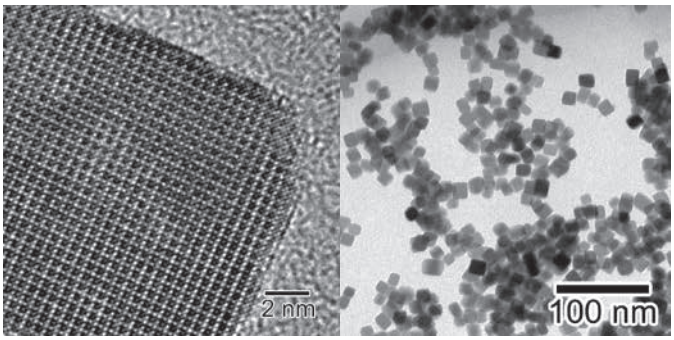

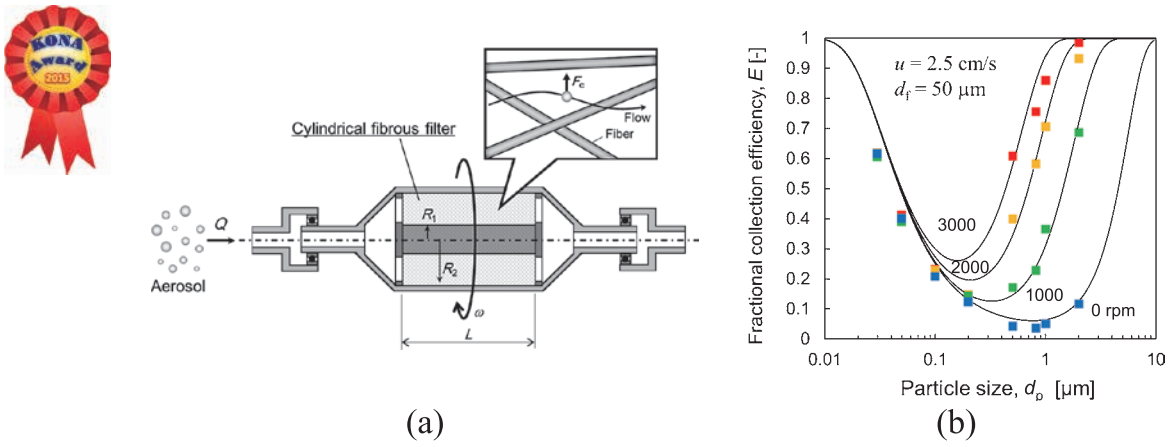

Some achievements of the research for the 22nd KONA Award: (a) Illustration of centrifugal filter. (b) Fractional collection efficiency of centrifugal filter at various rotation speed. (p.356)

Reviewer Appreciation

Jusuke Hidaka, Editor-in-Chief

Doshisha University, Japan

I express our gratitude to the reviewers for the publication of this KONA Powder and Particle Journal. Thanks to the generous contributions of the volunteer reviewers as well as the interest of researchers in our journal, the number of submission to this journal is increasing after the registration on the major international journal platforms and its level is further improving. Because of the limited space of this annual journal, the number of papers published there is regrettably rather restricted. Therefore the papers of good quality need to be selected for the journal and further improved and refined by the reviewing.

The editorial team of KONA Journal would like to take this opportunity to gratefully acknowledge the reviewers here and deeply appreciate their valuable time and professional contributions to the KONA Journal. We apologize to any reviewer who may have inadvertently been omitted from this list. We are sincerely grateful to all who have been of any assistance to the publication of this journal.

BISCANS, Béatrice
COPPENS, Marc-Olivier
DOBASHI, Ritsu
FUERSTENAU, Douglas
FUJI, Masayoshi
FUKUI, Kunihiro
FUKUMORI, Yoshinobu
GOTOH, Kuniaki
GRADOŃ, Leon
HICKEY, Anthony
HIDAKA, Jusuke
HIGASHITANI, Ko
HIROTA, Ken
HOGG, Richard
HUANG, Ching-Chung
ICHIKAWA, Hideki
IIMURA, Kenji
ITO, TAKEO
IWASAKI, Tomohiro
IWATA, Masashi
KAJISHIMA, Takeo
KAMIYA, Hidehiro
KANAOKA, Chikao
KANO, Junya
KAWASAKI, Akira
KIMATA, Mitsumasa
LENGGORO, Wuled
MAENOSONO, Shinya
MAKINO, Hisao
MASUDA, Hiroaki
MATSUSAKA, Shuji
MEESTERS, Gabriel
MIYAHARA, Minoru
MIYAMOTO, Yoshinari
MORI, Yasushige
MORIMOTO, Yasuo
MOUDGIL, Brij
MURAMATSU, Atsushi
NAITO, Makio
NAKAHIRA, Atsushi
NAKAZATO, Tsutomu
NOGI, Kiyoshi
NOMURA, Toshiyuki
OGI, Takashi
OKUYAMA, Kikuo
OTANI, Yoshio
PEUKERT, Wolfgang
PRATSINIS, Sotiris
PURI, Virendra
RAJAMANI, Raj
ROSATO, Anthony
SAITO, Fumio
SAKAI, Mikio
SATOH, Munetaka
SHARMA, Parvesh
SHINTO, Hiroyuki
SHIRAKAWA, Yoshiyuki
SUZUKI, Hisao
SUZUKI, Michitaka
TAKEDA, Shin-ichi
TAKEUCHI, Hirofumi
TAKEUCHI, Manabu
TANAKA, Satoshi
TATAMI, Junichi
TAVARES, Luis Marcelo
TOKORO, Chiharu
TOYODA, Masahiro
TOZUKA, Yuichi
TSUJI, Yutaka
TSUKAGOSHI, Kazuhiko
VALVERDE, José Manuel
WAKAI, Fumihiro
WATANO, Satoru
WINDOWS-YULE, Kit
YASUDA, Kouichi
YOKOYAMA, Toyokazu
YOSHIDA, Hideto
YUU, Shinichi

J. Hidaka

November 10, 2015

Editor's Preface

Brij M. Moudgil
Chairman of American Editorial Board
University of Florida, USA

As Chair of the American Editorial Board, I am pleased to introduce the KONA Powder & Particle Journal No. 33, and to also share my thoughts on powder and particle technology opportunities and challenges.

Globally, powder and particle technology remains strong, primarily because the quality of life improvements all across are leading to higher demand for powder and particle mediated products. Powder technology is recognized as an important business with great global opportunity.

Demand for nonrenewable resources continues to be the driver for powder and particle technology advances in Central and South America and Canada; whereas in the USA, nanotechnology applications in life sciences, health care, microelectronics, and food and agriculture are leading particle technology innovations. Advances in simulation and modeling at practical scales are on the horizon, and are expected to result in new powder and particle mediated products with enhanced performance. It is likely that more people are working in particle science and technology than before albeit without recognizing the field as such. Sustainable production and utilization of powders and particles with minimal environmental footprint is gaining attention as society becomes more appreciative of such products.

However, training the next generation of powder and particle industry professionals is becoming our most significant challenge and opportunity. Particle technology knowledge now seems to be spread across departments and disciplines, especially in the USA with a very limited number of single departments offering a comprehensive training in powder and particle production, characterization and processing. Expertise continues to be lost in industry due to mergers and reorganizations, whereas in academia, powder and particle technology champions have been lost to retirement. New leadership is stepping up to the plate but more champions in industry and academe are required to carry the subject forward. Additionally, students also have more majors to choose from as seemingly more glamorous and rewarding professional degree options become available.

Industry primarily hires scientists and engineers who have the depth and rigor in a traditional discipline, and in addition are willing to undertake interdisciplinary and collaborative team research endeavors. Additionally, young professionals with effective communication skills, and teamwork and leadership experience have competitive advantage over those who lack such skills.

Although existing academic structure would continue to provide education and training in the traditional fields, which are in demand by industry in a large number of graduates on a continuing basis; training a smaller and highly specialized field workforce requires new economic models at the university level. A number of options can be envisioned for providing customized training to a smaller number of graduates needed by a specific industry sector.

Establishing university based education program in close cooperation with industry (or professors of practice) in designing and delivery of the curriculum is one option. In this regard, a one year Master's degree program in particulate engineering at the University of Delaware was recently launched, and another master's degree program to meet pharmaceutical industry needs was designed by the University of Massachusetts, Amherst. Another option is to design a 5 (3 + 2) year MS degree program (post-high school) that requires 1 year internship in a company; or allows students to acquire business and/or finance skills. This model would be successful only if the financial and career growth opportunity benefits outweigh an additional year's investment of time and financial resources. These approaches can involve multiple departments across universities so that no single university has to offer all

the required courses.

Technology Bootcamps can be another option. In the IT industry sector, for profit organizations are offering technology boot camps for training in specific fields within a period of a few months. Although tuition for boot camps is reported to be in tens of thousands of dollars for a three month course, graduates are promised high paying jobs upon graduation. This model can be a valuable tool, especially for acquiring specific skills to avail new career opportunities.

At the same time, it is recognized that we cannot teach what we cannot understand, and acquiring deep understanding requires sustained research. Fortunately, as other economies grow, a lot of good research is being conducted around the globe. A golden opportunity exists to mine the new knowledge, and organize it in a fashion that enhances the existing curriculum and also develops new courses to train the next generation of powder and particle technology professionals.

Overall, I believe it is a time of unique opportunity for revitalizing powder and particle technology education for training a diverse workforce. International partnership opportunities in research and education are available to provide the platform for capitalizing on global teaching excellence, practice expertise and research facilities.

Current issue of KONA contains a number of excellent invited research and review articles from groups across the globe working on emerging powder and particle technology applications. I sincerely hope you enjoy this issue of KONA. I am certain KONA will continue to serve as an important and meaningful platform for dialog and knowledge dissemination in the years to come.

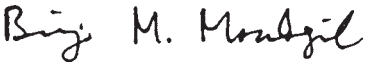

Brij M. Moudgil
Chairman of American Editorial Board
November 9, 2015

KONA Powder and Particle Journal No. 33 (2016) 3–16/Doi:10.14356/kona.2016005 Review Paper

Viscosity Reduction of Heavy Oil Using Nanocatalyst in Aquathermolysis Reaction †

Ferry Iskandar [1,2]*, Erlandy Dwinanto [1], Mikrajuddin Abdullah [1], Khairurrijal [1] and Oki Muraza [3]

[1] *Department of Physics, Faculty of Mathematics and Natural Sciences, Institut Teknologi Bandung, Indonesia*
[2] *National Research Center for Nanotechnology (NRCN), Institut Teknologi Bandung, Indonesia*
[3] *Chemical Engineering Department and Center of Excellence in Nanotechnology, King Fahd University of Petroleum and Minerals, Saudi Arabia*

Abstract

Enhanced oil recovery (EOR) in the last several years has become an important factor in oil production due to the shortfall in high quality crude oil. Heavy oil as one of the unconventional hydrocarbons is still vastly abundant in nature and is hence frequently explored with EOR. The viscous characteristic of heavy oil necessitates further in-situ upgrading processes to be executed before extraction. An interesting upgrading method is through aquathermolysis under the addition of catalyst. This review focuses on presenting nanoparticle catalysts, such as nickel-, iron- and cobalt-based nanocatalyst. The explanation covers topics from synthesis methods and characterization up to the effect of reducing the viscosity of heavy oil. Lastly, concluding remarks and future perspectives are highlighted regarding the visibility and available approaches of developing nanofluids for EOR.

Keywords: aquathermolysis, catalyst, enhanced oil recovery, heavy oil, nanoparticles

1. Introduction

Global energy demands increase quite considerably every year due to the ever-increasing population of mankind. Therefore, oil and gas acting as main sources of energy up until now (IEA, 2014), need to be explored even further to meet those demands. Recently, in its annual "Statistical Review of World Energy 2014", British Petroleum (BP) in 2014 reported that global oil consumption increased above the average, by 1.4 % or equivalent to 1.4 million barrels per day (b/d) (Petroleum B., 2014). However, since the predicted scarcity of high quality crude oil supply is starting to take effect, interest is shifting towards an abundant natural resource that has rarely been developed extensively before, which is unconventional hydrocarbon in the presence of heavy oil. As shown in **Fig. 1**, heavy oil and bitumen are predicted to account for about 70 % of the total remaining hydrocarbon resources (Alboudwarej H. et al., 2006). Several well-known fields of heavy oil are found scattered among many oil fields in different countries, such as Orinoco, Venezuela (Martinez A.R., 1987), Alberta, Canada (Semple K. and Westlake D., 1987), Liaohe and Shengli, China (Wen S. et al., 2007; Wu C. et al., 2010), Mariner, United Kingdom (Knudsen M.T. and Hill D., 2012), and Duri, Indonesia (Arfie M. et al., 2005).

The main characteristic of heavy oil is its density or specific gravity that is defined to be less than 20° API (Dusseault M., 2001) and its high viscosity due to the high average molecular weight of its structure, as stated by Hyne (Hyne J. et al., 1982). Therefore heavy oil has a poor

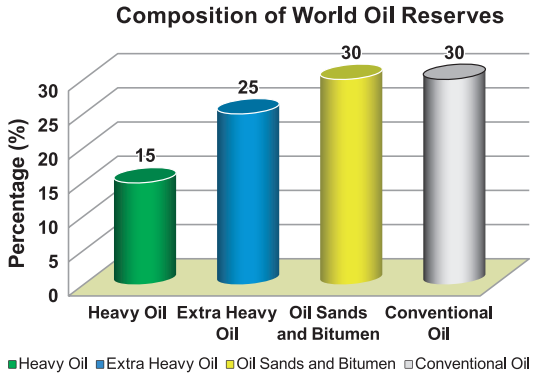

Fig. 1 Column chart of total world oil reserves where unconventional hydrocarbon resources hold 70 % of the total reserves.

† Received 17 April 2015; Accepted 10 June 2015
J-STAGE Advance published online 10 July 2015
[1,2] Jl. Ganesha 10, Bandung 40132, Indonesia
[3] Dhahran 31261, Saudi Arabia
* Corresponding author: Ferry Iskandar;
E-mail: ferry@fi.itb.ac.id
TEL: +62-22-2500834 FAX: +62-22-2506452

flow rate and hence is very difficult to transport. Heavy oil is also known for its low quality because of high amounts of asphaltenes and resin, whereas the saturated and aromatic hydrocarbon contents are relatively low. Moreover, higher contents of asphaltenes and resin, both of which have a high average molecular weight, will consequently cause difficulties in exploitation and induce high production costs. Another constituent of unconventional hydrocarbon is extra heavy oil, defined to have a gravity below 10° API and a viscosity of more than 100 Pa·s by the World Energy Council in 2010, with a contribution of around 25 % to total world oil reserves.

2. Aquathermolysis reaction

Several reaction methods have been developed and adopted in order to enhance heavy oil recovery and reduce its viscosity. A variety of methods exist, ranging from chemical flooding to water flooding and gas drive for non-thermal treatment, while steam injection, hot water flooding and in-situ combustion for thermal treatment are popular and frequently used (Owen J. and Floyd J., 1981). Hyne et al. have proposed another reaction, called aquathermolysis, which is a promising way to reduce the viscosity of heavy oil (Hyne J. et al., 1982). During the aquathermolysis reaction, heavy oil will be added with water or steam at 200–280 °C with the reaction time varied from a few hours up to several days.

Laboratory-scale aquathermolysis can be executed in a high-pressure reactor, usually an autoclave, which is capable to withstand pressures up to 3 MPa. Meanwhile in-situ aquathermolysis frequently uses the "Huff and Puff" process, which takes place deep inside the well and consist of three main steps, i.e. injection of steam, well shutdown, and finally production of oil as depicted in **Fig. 2** (Maity S.K. et al., 2010). Later, it was discovered that aquathermolysis reaction solely using water hydrolysis did not proceed as well as predicted since the hetero atoms S, N, and O in the heavy oil molecule can interact with each other by means of hydrogen bonding or Van der Waals forces, and polymerize to form larger molecules. Hence, this is not a very effective way to reduce heavy oil viscosity (Chen Y. et al., 2008).

Based on the problems described above, a better solution is needed to address the problems arising in the aquathermolysis reaction. Usage of catalyst, either a mineral, water-soluble, oil-soluble, or nanoparticle catalyst, is proposed to have the necessary effects to overcome the problems. This is due to the fact that a catalyst only acts as an intermediary substance between the reactant and the product in order to lower the activation energy of the reaction and therefore does not alter the general reaction during the process.

Clark et al. studied the addition of aqueous metal to further reduce the viscosity of heavy oil compared to the steam-only aquathermolysis method (Clark P. and Hyne J., 1984). The usage of catalyst in aquathermolysis proved to be a success, since it enables prevention of regression due to polymerization while also promoting pyrolysis to break larger molecules of the heavy oil into smaller ones and various other synergistic reactions like hydrogenation and ring opening as illustrated in **Fig. 3**. Below is the chemical reaction for aquathermolysis (Hyne J. et al., 1982):

$$RCH_2CH_2SCH_3 + 2H_2O \rightarrow RCH_3 + CO_2 + H_2 + H_2S + CH_4 \quad (1)$$

The cleavage of the C-S bonds results in a reduction of the average molecular weight, bringing along the reduction of viscosity, improvement of flow properties and simplifying the exploitation and transportation of heavy oil. Actually, not only the C-S bonds but also the C-N and C-O bonds are broken in a catalytic aquathermolysis reaction. However, due to the lower bond energy of C-S, the decrease of sulfur content in heavy oil after catalytic aquathermolysis is more significant. Overall, with the help of a catalyst in the aquathermolysis reaction, it is

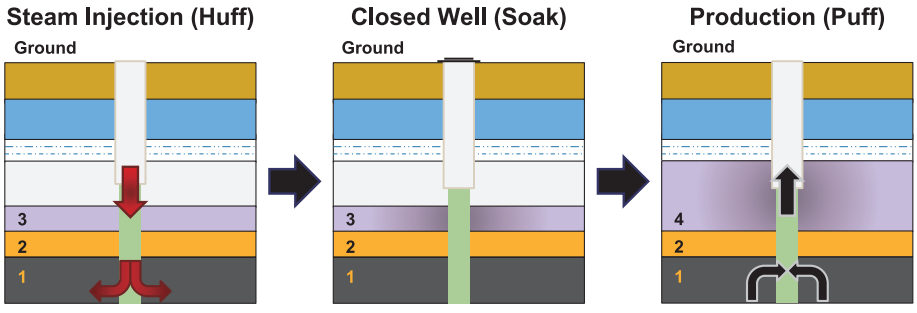

Fig. 2 A simplified flow diagram of "Huff and Puff" process used commercially for recovery of heavy crude oils. Reprinted with permission from Maity, S.K. et al. Copyright © 2010, American Chemical Society.

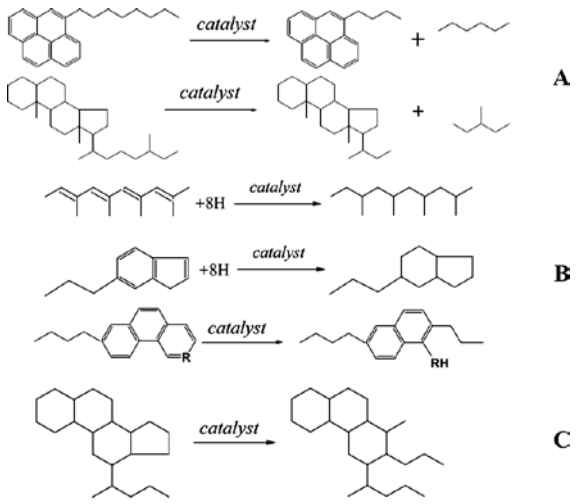

Fig. 3 Schematic representation of reactions that occur in catalytic aquathermolysis. A: pyrolysis, B: hydrogenation, and C: ring opening. Reprinted with permission from Wang, Y. et al. Copyright © 2010, American Chemical Society.

noticeable that the amount of asphaltenes and resins will decrease and, in contrast, the amount of aromatic hydrocarbon and saturated hydrocarbons will increase (Chao K. et al., 2012). The whole process of aquathermolysis with the introduction of a catalyst is called catalytic aquathermolysis.

The catalytic aquathermolysis process can also cause domino effects like increasing the H/C ratio of the oil due to hydrogenation during aquathermolysis reaction. In fact, Hamedi Shokrlu and Babadagli found that the presence of metal nanocatalyst improved the heat transfer capabilities during the process of steam injection (Hamedi Shokrlu Y. and Babadagli T., 2010). This thermal promotion effect occurs because metals known for high thermal conductivity can improve the thermal conductivity of hydrocarbon or the porous medium inside the reservoir.

The presence of hydrogen donor additives during the aquathermolysis process can have a favorable effect on the general reaction. As stated by Liu and Fan, a hydrogen donor, represented by tetralin in their work, can improve the stability of viscosity reduction of heavy oil (Liu Y. and Fan H., 2002). When the hydrogen donor was added, besides the additional viscosity reduction of the heavy oil, there was also the noticeable benefit of the diminution of viscosity regression after the reaction. The reason this regression occurs under the absence of a hydrogen donor is that active chains produced as a by-product of the aquathermolysis reaction can react with each other to create a high molecular weight chain. On the other hand, under a sufficient amount of active H_2, the active chain will instead react with the active H_2 to produce a low molecular weight chain.

Another source of hydrogen donor can be found in zeolite. Silicate and aluminate, both having the shape of a tetrahedral, are the main building units of zeolite. The main source of hydrogen donor inside zeolite is the presence of Brønsted acid site, usually located in the vicinity of Si-O-Al bonds. With the possibility of seed-assisted or organic structure-directing agent (OSDA)-free synthesis (Kamimura Y. et al., 2011; Purnomo C.W. et al., 2012), valuable synthetic zeolite is now easier to produce. Because of this, synthetic zeolite is often employed as catalyst in the field of oil processing (Degnan T.F. et al., 2000; Van Donk S. et al., 2003) with MFI, FAU, Beta and MOR-type zeolite being the most frequently used due to their larger pore size that is well fitted with the corresponding molecular size (Xu B. et al., 2006).

However, the percentage of viscosity reduction in static/laboratory experiments is usually higher compared with dynamic/in-situ experiments. This difference appears because in-situ conditions are more complicated and complex, such as the gradual drop of steam temperature with the increase of depth from the surface. This condition causes a decreasing amount of energy which is required for the reaction to take place and provides less momentum to make contact with the heavy oil. Another condition that contributes to reduced viscosity reduction in dynamic experiments is the adsorption of catalyst by rock or minerals inside the well. Accordingly, recent developments in the synthesis of catalyst are aimed at overcoming these problems by designing a low-temperature activated catalyst by using ultrasonic or elastic wave stimulation to assist the catalytic aquathermolysis reaction.

Wave stimulated aquathermolysis, started back in 1994, when Beresnev and Johnson noticed that elastic wave stimulation (by an earthquake for example) implies some changes, the most noticeable one being an increase of water level and oil production in the reservoir (Beresnev I.A. and Johnson P.A., 1994). This notion was later validated in a number of related works, such as Guo, et al. and Pride et al., based on high-frequency vibration and numerical simulation theory, respectively (Guo X. et al., 2004; Pride S.R. et al., 2008). Integration of either high-frequency or low-frequency vibration in catalytic aquathermolysis has recently been performed (Xu H. et al., 2012; Xu H.X. and Pu C.S., 2011). They reported that both types of vibration assisted catalytic aquathermolysis, producing synergistic effects on the performance of heavy oil viscosity reduction as well as the composition of saturated, aromatic, resin and asphaltenes (SARA) of the heavy oil. Compared to a catalytic aquathermolysis-only process, low-frequency vibration-assisted catalytic aquathermolysis produces better viscosity reduction, up to 6.6 %, with lower average molecular weight crude oil.

3. Nanocatalysts

Depending on the catalyst-reactant phase, catalysts can be grouped into two different kinds: homogeneous, if the catalyst and reactant are in the same phase (e.g. liquid-liquid), and heterogeneous, if the catalyst and reactant are in a different phase (e.g. solid-liquid). Meanwhile based on their solubility, catalysts can be grouped into mineral, water-soluble, oil-soluble, and dispersed catalyst. In this review, we will limit the discussion to catalyst based on dispersed nanoparticles in the form of powder.

One of the advantages of nanoparticle catalysts is their relatively high surface area, which makes them ideal for catalytic aquathermolysis, so as to increase the light fraction of crude oil and hence improve the overall quality of the heavy oil. In addition, nanocatalysts have the advantage of easier separation process in the catalytic aquathermolysis process and, after proper thermal treatment, they are available to be re-used in the process with adequate performance (Junaid A.S.M. et al., 2014).

3.1 Nickel-based nanocatalysts

Nickel (Ni) is a chemical element with atomic number 28, which belongs to the first row transition metals. Because of this, nickel has a partially filled 3d orbital electron band and is very reactive to chemical reactions, in particular when in the powder form, having a larger surface area. On the other hand, in an ambient air environment, nickel will slowly react with oxygen to form nickel oxide compound. Nickel is quite abundant on earth, but it is rarely found in pristine condition. It has been proposed that nickel-iron is one of the components that form the earth's core.

Lenggoro et al. reported their effort to synthesize nickel oxide via spray pyrolysis using several precursors, such as nickel chloride, nitrate and formate (Lenggoro I.W. et al., 2003). The resulting particles have a broad range of sizes, with only the nickel nitrate precursor resulting in the nanoparticle range, whereas the chloride and formate precursor result in submicron particles. In another attempt, Ai et al. studied the synthesis of nickel oxide nanoparticles via a wet chemical method using ethylene glycol (EG) as solvent (Ai D. et al., 2004). Apart from being the solvent, the role of ethylene glycol can be extended to agglomeration-preventing agent, forming a protective layer around the nickel particle, thus creating a well-dispersed nanoparticle.

Meneses et al. further developed nickel oxide nanoparticles using gelatin instead of EG as the organic precursor (Meneses C.T. et al., 2007). Although very small particles sizes (3.2 nm) were successfully obtained, the polydispersed characteristic of the nanoparticles still persisted as a major problem until Li, et al. (2007) found a better way to synthesize nano-nickel using the micro emulsion method. In the attempted method, oil phase (e.g. cyclohexane, methyl cyclohexane) was used to prepare nano-nickel catalyst that could act as hydrogen donor to further improve the heavy oil characteristics via some mechanisms already explained in the section about the aquathermolysis reaction. The nano-nickel particles obtained had a spherical shape and an average diameter of 6.3 nm. Li et al, further applied nano-nickel as catalyst in an aquathermolysis reaction of Liaohe extra heavy oil at 280 °C (Li W. et al., 2007). As predicted, the best viscosity reduction of heavy oil as measured at 50 °C, was achieved under the presence of nano-nickel catalyst, with up to 98 % viscosity reduction. Aside from the viscosity reduction, an increase in H/C ratio and reduced amount of asphaltenes, resin, and sulfur content was also noticed in the catalytic aquathermolysis-reacted heavy oil. The nano-nickel via microemulsion experiment was again attempted by Wu et al., this time under much lower reaction temperature of 200 °C, yet high catalytic performance with more than 90 % viscosity reduction was obtained (Wu C. et al., 2013).

It has been reported that there is the possibility of a metal catalytic reaction of heavy oil without the addition of water or steam or non-aquathermolysis reaction. However, the reduction of viscosity would be more significant after water or steams is added into a system (Hamedi Shokrlu Y. and Babadagli T., 2010).

The development of nano-nickel-based catalyst for use in aquathermolysis was further reported by Wu et al., who utilized San56-13-19 extra heavy oil as the subject of an aquathermolysis reaction at 200 °C (Wu C. et al., 2013). The nano-nickel catalyst was successfully prepared by the microemulsion methods according to (Wu Z. et al., 2008). Transmission electron microscopy (TEM) characterization indicated that the size of the nano-nickel catalyst was around 4.2 nm. Viscosity reduction was around 90.36 % as measured by Bruker Avance-500 NMR spectrometer, and group composition after reaction also changed, with a decrease in asphaltene and resin of 5.28 % and 6.48 %, whereas saturated and aromatic hydrocarbons increased by 6.73 % and 5.03 %.

Based on these findings, Noorlaily et al. have tried to synthesize nickel oxide nanoparticles employing microwave-assisted co-precipitation methods (Noorlaily P. et al., 2013). Using $NiCl_2 \cdot 6H_2O$ as nickel source, with NH_4HCO_3 and ethylene glycol as reductant and solvent respectively, spherical morphology, uniform size distribution around 65 nm, and a large surface area particle of 158.4 m^2/gram were obtainable. **Fig. 4** shows the x-ray diffraction patterns of the nickel oxide nanoparticles produced. Applying Scherrer's equation to the strongest peak, the crystal sizes of NiO were predicted to be 4.77 nm, 9.08 nm and 15.26 nm, respectively, at for

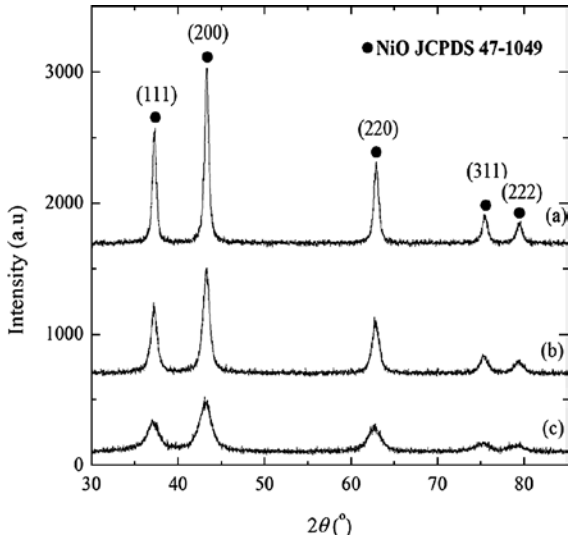

Fig. 4 X-ray diffraction patterns of prepared NiO at calcination temperature of (a) 500 °C, (b) 400 °C, (c) 300 °C. Reprinted with permission from Noorlaily, P. et al., copyright © 2013, Trans Tech Publications Inc.

300 °C, 400 °C and 500 °C calcination temperature. The effect of NiO nanoparticles on the viscosity reduction of heavy oil after catalytic aquathermolysis reaction was reported to be 22 %.

3.2 Iron-based nanocatalysts

Iron (Fe) is one of the metal elements that compose the earth's crust, therefore it is the fourth most abundant element in terms of weight, at around 5 wt%. Iron has an atomic number of 26 with electron configuration [Ar] $3d^6$ $4s^2$. In general, there are two forms of iron based-nanocatalyst, which are often encountered as specified by the oxidation states of the iron: hematite and magnetite (α-Fe_2O_3 and γ-Fe_2O_3) and magnetite (Fe_3O_4). Iron in general is classified as magnetic materials, with the relationship of magnetic properties of materials to their catalytic activity has been long investigated in the field of magneto-chemistry. As early as 1946, Selwood P.W. described the close relationship of magnetic properties to adsorption phenomena, whereas adsorption of several strongly paramagnetic compound is found to be more prominent due to the strong tendency in forming electron pairing arising from the unpaired electrons spin (Selwood P., 1946). Therefore, magnetic materials in general, indicated by magnetic moment, are good adsorbent and suitable to be used as catalyst, just like the one applied by Khamarui, et al. (Khamarui S. et al., 2015). Another advantage of having magnetic nano metal-oxides particles is their synergistic to be implemented in the electromagnetic-solvent heating. In an extensive review paper written by Bera and Babadagli, magnetic nanoparticles in the radio frequency electromagnetic heating will increase and improve the overall reaction rates since they will fluctuate and create more contact with the reactant molecules (Bera A. and Babadagli T., 2015). Because usually the optimum amount of additional Fe as catalyst range only around 0.1–1 wt% (Greff J.H. and Babadagli T., 2012), the amount of Fe ions could well be insignificant compared with the amount of other minerals inside the reservoir. Consequently, there is only slight chance of corrosion caused by the addition of Fe-based catalyst, although it does not completely rule out the possibility that there would arise some minor contributing factor.

3.2.1 Hematite (α-Fe_2O_3) and maghemite (γ-Fe_2O_3)

Fe_2O_3 is a polymorph material with two naturally occurring and hence commonly found substances of iron. The two naturally occurring forms are the α phase and the γ phase, with the difference between those two arising from the most fundamental crystal structure.

While α-Fe_2O_3 (hematite) has a rhombohedral crystal structure like corundum (α-Al_2O_3), γ-Fe_2O_3 (maghemite) has a cubic crystal structure. The magnetic characteristics of hematite and maghemite also show some distinction. Hematite is found to be weakly ferromagnetic in between 260 K and 950 K, while maghemite shows ferromagnetic properties, making it often being used for recording tape component. The characteristics described above are restricted to bulk form; there is a discrepancy between nanoparticle and bulk form, especially regarding magnetic properties. Magnetic nanoparticles usually show superparamagnetic phenomena due to the finite- size limit that is distinctive for every material. However, there is similarity between hematite and maghemite, with both consisting of Fe^{2+} divalent iron compound, usually known as ferrous ion. In contrast, Fe_3O_4 (magnetite) consists of both ferrous and ferric ion.

As a matter of fact, all three iron oxides—hematite, maghemite, and magnetite—are connected and therefore can be produced by transformation into each other. Fe_3O_4 can be produced by α-Fe_2O_3 reduction, while when appropriately annealed and re-oxidized, Fe_3O_4 will results in the formation of γ-Fe_2O_3 (Aharoni A. et al., 1962). Finally, to complete the cycle of transformation, γ-Fe_2O_3 can be heated to the required temperature to create hematite. Shimomura et al. have suggested that γ-Fe_2O_3 could also be formed directly as an intermediate phase during the reduction of α-Fe_2O_3 (Shimomura Y. et al., 1954). This was proven afterwards by Randrianantoandro, et al., as they succeeded to create γ-Fe_2O_3 directly from α-Fe_2O_3 employing high-energy ball milling with the aid of ethanol (Randrianantoandro N. et al., 2001). In another attempt to produce γ-Fe_2O_3 nanoparticles, some researchers are using a microemulsion method that utilizes a surfactant to stabilize the mixture as well as a precipitating agent (e.g. NH_3, NaOH)(Sahoo S. et al., 2010; Tueros M.J.

et al., 2003).

Hematite, meanwhile, reportedly can be synthesized using various methods, such as co-precipitation (Zhang H. et al., 2008), hydrothermal (Giri S. et al., 2005), sol-gel (Woo K. et al., 2003) and forced hydrolysis (Musić S. et al., 1997). In his work, Music used precursors such as $FeCl_3 \cdot 6H_2O$ and 10 % solution of tetramethylammonium hydroxide (TMAH). Later on, in 2003, Musić et al. published a paper explaining the factors influencing forced hydrolysis of $FeCl_3$solution (Musić S. et al., 2003). Another way to synthesize α-Fe_2O_3 is through hydrothermal methods. Giri et al. (2005) explained that hematite, with size and nature depending strongly on pH was successfully created under a complex microemulsion system. A narrow-distribution ultrafine dispersed Fe_2O_3 nanoparticle was reported by Zhang H., et al., where a co-precipitation method was employed with NaOH as the precipitating agent (Zhang H. et al., 2008). NaCl salts produced as a by-product of the reaction can help encapsulating the precursor, so that in the end the nanoparticle size varies only from 1.9 nm to 2.6 nm.

Wang et al., then tested the influence of Fe^{3+} ion catalyst under the synthesizing method of Chen et al. which utilizes Fe_2O_3 or Fe and aromatic sulfonic acid to prepare what is called amphiphilic metallic chelate catalyst (Chen Y. et al., 2008; Wang Y. et al., 2010). The catalytic aquathermolysis experiments were conducted using an oil/water ratio of 7:3 and 0.3 g of catalyst. The viscosity of the heavy oil after the reaction showed a decrease of around 95 % under a recorded ambient temperature of 50 °C. Apart from the viscosity reduction, Wang et al. also characterized the composition and content level of SARA before and after the reaction. All parameters showed improved quality of the heavy oil, since the level of saturated and aromatic hydrocarbons and the H/C ratio increased, while resin and asphaltenes decreased under a recorded ambient temperature of 50 °C.

Nurhayati et al., have reported the synthesis of α-Fe_2O_3 nanoparticles using a microwave-assisted calcination method (Nurhayati T. et al., 2013). They reported that the method could reduce the preparation time needed, while keeping the heat distributed evenly throughout the process because of resonance and relaxation from the electromagnetic radiation, as explained by Lagashetty, et al. (Lagashetty A. et al., 2007). The precursors used were $FeCl_3 \cdot 6H_2O$, with NaOH as a precipitating agent, which was later titrated into the $FeCl_3$ solution. The morphology and size of the nanoparticles characterized using SEM can be seen in **Fig. 5**. Firstly, the overall stoichiometric reactions that occurred during the course of this experiment can be represented by:

$$FeCl_3 \cdot 6H_2O(aq) + 3\ NaOH(aq) \rightarrow Fe(OH)_3(s) + 3\ NaCl(aq) + 6\ H_2O(l) \quad (2)$$

$$Fe(OH)_3(s) \rightarrow FeOOH(s) + H_2O(l) \quad (3)$$

$$2\ FeOOH(s)\ [heated] \rightarrow Fe_2O_3(s) + H_2O(l) \quad (4)$$

Furthermore, the microwave heating process would give the initial stage of crystal growth. The crystal growth mechanism may be a combination of O-R (Ostwald-ripening) and O-A (oriented-attachment) pathways, whereas the secondary crystal growth occurred during the calcination process.

The development of nanocomposites in order to combine the strength of two or more materials has gained popularity since a nanocomposite of hematite with silicon was studied thoroughly back in 1988, when Ishikawa and Matijevic attempted to synthesize it (Ishikawa T. and Matijević E., 1988). The goal of composing another material with hematite is to prevent agglomeration due to its magnetic surface interaction. As already studied by Vasquez-Mansilla et al. (Vasquez-Mansilla M. et al., 1999) and by Willis, et al. (Willis A.L. et al., 2005), magnetic interaction on the surface of antiferromagnetic hematite

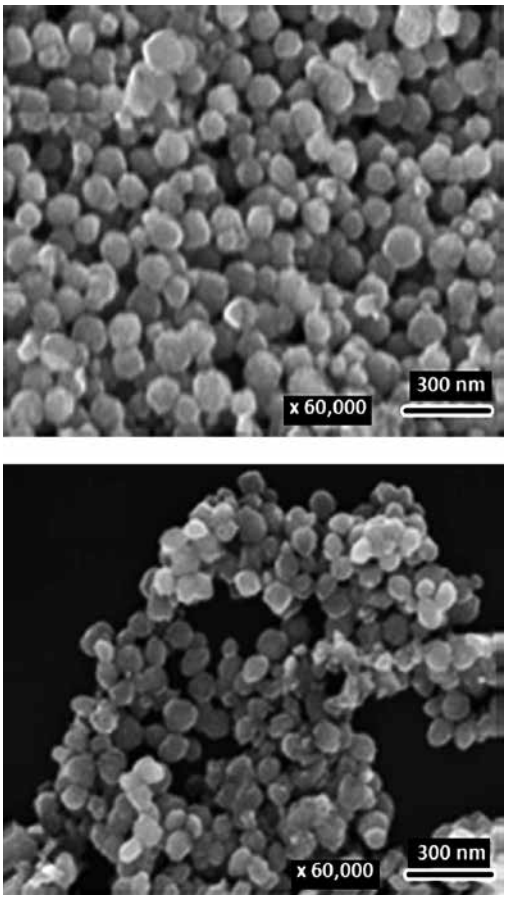

Fig. 5 Comparison between two SEM images of Fe_2O_3 nanoparticle catalyst. Top: sample calcined at 300 °C. Bottom: sample calcined at 350 °C. Reprinted with permission from Nurhayati, et al., copyright © 2013, Trans Tech Publications Inc.

arises because of magnetic moment as well as anisotropy energy originating within the surface. It is therefore necessary to passivate the surface by a ligand coating of oleic acid. However, problems emerge since oleic acid as a ligand coating suffers a structural change during high-temperature synthesis. Consequently, carbon coating like the one used by Zhang Y., et al. became imminent (Zhang Y. et al., 2011).

Swardhani et al. have reported a preparation of carbon-coated α-Fe_2O_3 nanoparticles using microwave-assisted calcination method (Swardhani A.P. et al., 2014). It resulted in creating nanoparticles with a mean size of 199 nm from scanning electron microscopy (SEM) characterization, with 33 % carbon content giving the optimum result. It is interesting to note that the presence of carbon will give a smaller internal crystal size of hematite and on the other hand an increase of the surface area, therefore increasing its effectiveness and making it more suitable to be used as catalyst. **Fig. 6** presented the SEM image of the resulting nanocomposite, indicating that the carbon coated around the shape of Fe_2O_3 nanorod. Another work in α-Fe_2O_3 nanocomposite synthesis was done using zeolite (Iskandar F. et al., 2014). Using the same methods as for the α-Fe_2O_3/C nanocomposite, it was observed that the nanoparticles size grows larger as the microwave heating time and calcination temperature increase, with optimum calcination temperature thus giving better α-Fe_2O_3/zeolite crystallinity, at 450 °C. This pattern of improving crystallinity with increasing temperature is something that has to do with the sintering process that comes from excessive thermal energy, as explained more comprehensively by Wang, et al. (Wang Y. et al., 2009).

3.2.2 Magnetite (Fe_3O_4)

Fe_3O_4, usually called magnetite, is another type of iron oxide that is commonly encountered. It consists of both Fe^{2+} and Fe^{3+} ions that form both the octahedral and tetrahedral of the inverse spinel crystal structure. Fe_3O_4 shows ferrimagnetic phenomena at room temperature, having some magnetic domains that oppose each other. However, there is net magnetization in the direction of the dominant domain with magnitude relatively the same as in ferromagnetic materials. Interest in studying Fe_3O_4 nanoparticles appear from the broad domains it can be applied in, such as magnetic recording, biomedics, etc (Ito A. et al., 2004; Mornet S. et al., 2004).

As usual, the number of variations of the method to synthesize Fe_3O_4 is incredibly vast. Jiang, et al. tried to synthesize nano-Fe_3O_4 particles using co-precipitation, a simple and relatively high-yield method. $FeSO_4 \cdot 7H_2O$ and $FeCl_3 \cdot 6H_2O$ were used as Fe source, while NH_4OH, produced by mixing ammonia with aqueous solution, was titrated until the pH of the mixture reached 10-11 (Jiang W. et al., 2004). Control of pH is very critical during the synthesis process, since it was proven to affect the size distribution of the nanoparticles created. In his work, Jiang successfully synthesized Fe_3O_4 nanoparticles with relatively small average size and narrow particle distribution, i.e. 25.3 nm and 5.9 nm, respectively. In other works, some researchers carried out hydrothermal methods in order to synthesize Fe_3O_4 nanoparticles (Daou T. et al., 2006; Mizutani N. et al., 2008). Although both discuss the same methods, the interesting point is having two authors using a different approach. Daou's report emphasized that magnetite nanoparticles with a mean size of 39 nm and good dispersity were correctly synthesized, as proven using XRD and other characterization techniques. Meanwhile, Mizutani emphasized the challenge of the effect of ferrous/ferric ions molar ratio, with a higher ions molar ratio resulting in more crystallinity and larger particle size. The full reaction regarding the transformation mechanism can be written as follow:

$$Fe(OH)_2 + 2FeOOH \rightarrow Fe_3O_4 + 2H_2O \quad (5)$$

with the FeOOH transformed from ferric hydroxide ($Fe(OH)_3$). Other methods performed to synthesize Fe_3O_4 are chemical vapor deposition (Chao L.T. et al., 2006), which resulted in Fe_3O_4 thin film deposited on Si substrate, and microemulsion (Koutzarova T. et al., 2006), by which nanopowder of polydispersed size was obtained.

Nugraha et al. have reported the synthesis of Fe_3O_4 nanoparticles (Nugraha M.I. et al., 2013). During the experiment, the co-precipitation approach to synthesize $Ni_xFe_{3-x}O_4$ was chosen due to its simplicity. The result showed that the average particle size was 43 nm and that the best composition for enhancing oil recovery is when there is no nickel impurity, with reduction of heavy oil viscosity approaching 30 % after the catalytic aquathermolysis reaction. Like Fe_2O_3, nanocomposite of Fe_3O_4

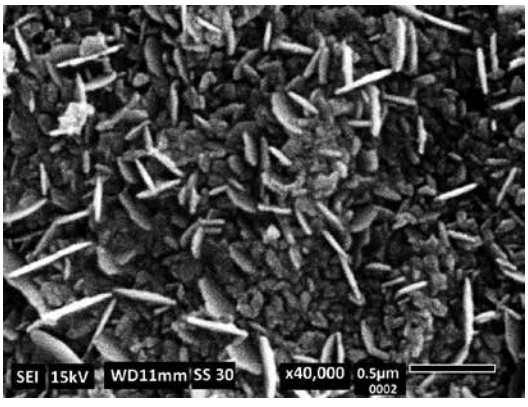

Fig. 6 SEM images of carbon-coated Fe_2O_3 nanoparticle with rod morphology, under carbon content of 33 %. Reprinted with permission from Swardhani, et al, copyright © 2013, Trans Tech Publications Inc.

was also studied in the hope of modifying the surface characteristics of the nanoparticles and stabilizing the nanoparticles dispersion so that catalytic performance could be improved. Lan, et al. tried to coat Fe_3O_4 nanoparticles with oleic acid (Lan Q. et al., 2007). Employing a co-precipitation method followed by hydrothermal synthesis, the resulting colloidal system indicated no precipitate that showed its stability. Recently, Haryono et al. have tried a modification of this method using a three-neck flask (Haryono A. et al., 2013). They obtained a smaller particle size, in the order of around 2 nm. However, as we already knew, oleic acid suffers from detrimental structural change in high temperature conditions, which is typical in hydrothermal synthesis methods. Thus, an alternative was given by Stjerndahl, et al. (Stjerndahl M. et al., 2008), making use of SiO_2 or silica instead of oleic acid. Under a water-in-oil microemulsion system, the loading of iron oxide crystals, thickness of silica shells and particle size are tunable. More detailed picture of phase influence is given in **Fig. 7**, with darker component indicating the superparamagnetic iron oxides (SPIOs).

Iskandar et al. have reported a first attempt of magnetite nanocomposite Fe_3O_4/Zeolite synthesis by employing simple microwave heating methods (Iskandar F. et al., 2014). The reason behind the selection of zeolite as a matrix phase in the nanocomposite was that zeolite is well-known for its ability to act as a hydrogen donor that is essential in improving the quality of the heavy oil during catalytic aquathermolysis and is also easy to find since it is abundant in quantity, either as heulandite or as clipnotilolite (Merissa S. et al., 2013). However, in order to be ready for use, natural zeolite requires thermal treatment to activate and reduce the amount of metal content while at the same time increasing the surface area as well as the ratio of Si/Al. In terms of catalytic performance, i.e. the rate of heavy oil viscosity reduction, the Fe_3O_4/zeolite nanocomposite we produced, with heulandite type of natural zeolite, reached levels of up to 92 % for a Fe_3O_4: zeolite ratio of 20:80.

3.3 Cobalt-based nanocatalysts

Cobalt oxide is composed of both Co^{2+} and Co^{3+} ions, just like Fe_3O_4. Co_3O_4 is an inorganic compound that has antiferromagnetic properties at room temperature. Approaches that have been used to synthesize Co_3O_4 are thermal decomposition (He T. et al., 2004), mechanochemical (Yang H. et al., 2004) and hydrothermal methods (Dong Y. et al., 2007). Using thermal decomposition, it has been detected that an intermediate product is produced, with the final Co_3O_4 nanocrystals created were later separated by centrifugation and washed with cyclohexane three times. In another study, Yang stated that via mechanochemical milling of $Co(NO_3)_2{\cdot}6H_2O$ with NH_4HCO_3 and continued by thermal treatment, approximately 38 nm crystal size was obtained. The reaction stoichiometry of both the milling and calcination process is given by:

$$2Co(NO_3)_2{\cdot}6H_2O + 5\ NH_4HCO_3 \rightarrow Co_2(OH)_2CO_3 + 4\ NH_4NO_3 + NH_3 + 4\ CO_2 + 14\ H_2O \quad (6)$$

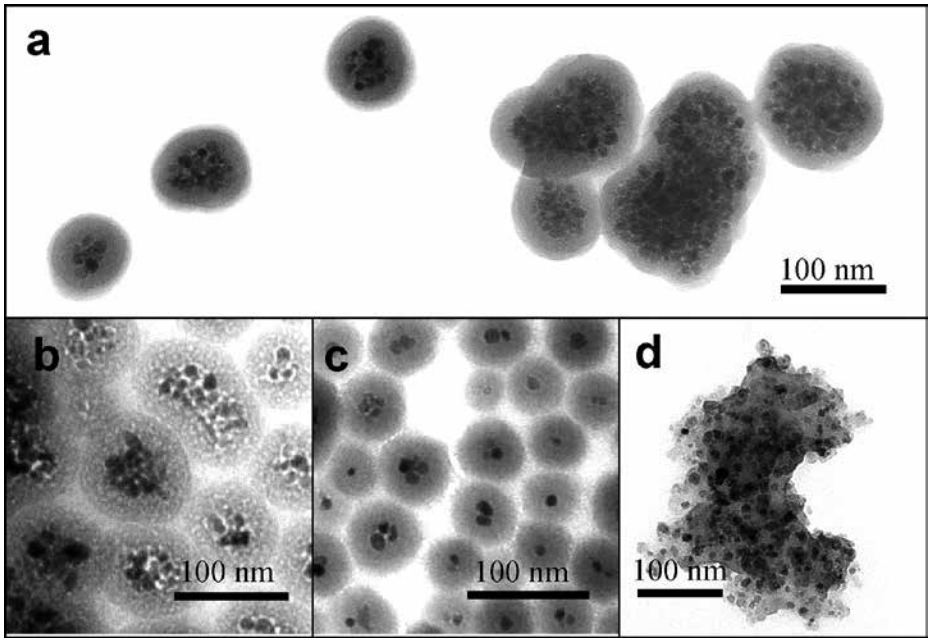

Fig. 7 TEM micrographs of shell-coated Fe_3O_4/SiO_2 nanocomposites under different synthesis conditions, (a–c) within microemulsion region, (d) in the two-phase region. Reprinted with permission from Stjerndahl, et al. Copyright © 2008, American Chemical Society.

$$3\ Co_2(OH)_2CO_3 + O_2 \rightarrow 2\ Co_3O_4 + 3\ H_2O + 3\ CO_2 \quad (7)$$

Nassar, et al. reported that using Co_3O_4 nanoparticles with a surface area of 41 m^2 based on BET characterization, the reduction of asphaltenes content of heavy oil could reach 32 % at 300 °C (Nassar N.N. et al., 2011). Further analysis on asphaltenes cracking activation energy, based on the Coats—Redfern method, indicated a significant decrease of the activation energy in the presence of nanoparticles catalyst, making the reaction possible to undergo at lower temperature.

4. Concluding remarks and future perspective

Based on the above reviews, all discussed materials are found to have synergistic effects when used as catalyst during catalytic aquathermolysis and hence are able to greatly improve the reduction of heavy oil viscosity and enhance the heavy crude oil recovery and quality. **Table 1** summarizes several characteristic features of nanoparticles and their catalytic performance during enhanced oil recovery through aquathermolysis. Although no specific report regarding the optimum size of catalyst to be used in catalytic aquathermolysis, small nanoparticles and porous materials are certainly ideal and becoming the main subject of interest as they inherited high surface area which indicate excellent catalytic performance. As for porous materials, pores in the range of mesopores (2–50 nm) is more suitable in heavy oil conversion as reported by Van Donk, et al. due to better accessibility of large molecules (Van Donk S. et al., 2003). There are many other nanoparticles, including their variations and derivatives, that have not yet been synthesized due to the enormous amount of methods and complexities in this field, therefore further study in exploring new discoveries is still very much wide open.

In the future, we expect to see that the development of nanocatalysts in enhanced oil recovery will be heading towards colloidal mixtures of nanoparticles with base fluid, known as nanofluids, as first described comprehensively by Wang et al. for the purpose of increasing the heat transfer (Wang Y. et al., 2009). The superiority of using nano-sized particles in base fluids is due to the fact that they would increase the contact between the reactant molecule and the catalyst, such as the water-oil-catalyst surface in the aquathermolysis reaction, which leads to a more progressive reaction. Moreover, nanofluids offer

Table 1 Summary of various nanoparticles used in enhanced oil recovery

Nanoparticle	Synthesis Method	Particle Size	Catalytic performance	Ref.
Ni	microemulsion	6.3 nm	viscosity reduction: 98.2 % H/C: 1.46; M_W = 422	Li, et al. (2007)
		4.2 nm	viscosity reduction: 90.36 % H/C: 2.09; 28.06 % decreased of asphaltene M_W	Wu, et al. (2013)
NiO	co-precipitation	60–70 nm	viscosity reduction: 22 %	Noorlaily, et al. (2013)
NiO	unknown (purchased)	12 nm (crystal size)	% conversion of asphaltene at 300 °C: 37 %	Nassar, et al. (2011)
α-Fe_2O_3	mixing Fe_2O_3 with aromatic sulfonic acid	—	(1) maximum viscosity reduction up to 93.3 %.	Chen, et al. (2008)
		—	(2) viscosity reduction: 95.6 %; decrease in asphaltene and resin, increase in saturated and aromatic.	Wang Y., et al. (2010)
α-Fe_2O_3/zeolite	microwave assisted co-precipitation + calcination	135 nm	viscosity reduction: 89 % (for α-Fe_2O_3:zeolite composition of 1:3)	Nurhayati, et al. (2013)
Fe_3O_4	microwave assisted co-precipitation	43 nm	viscosity reduction: 30 %	Nugraha, et al. (2013)
Fe_3O_4	obtained from nanostructured and amorphous materials	22 nm (crystal size)	% conversion of asphaltene at 300 °C: 33 %	Nassar, et al. (2011)
Fe_3O_4/zeolite	microwave assisted co-precipitation	96 nm	viscosity reduction: 92 % (for Fe_3O_4:zeolite composition of 1:4)	Iskandar, et al. (2014)
Co_3O_4	unknown (purchased)	22 nm (crystal size)	% conversion of asphaltene at 300 °C: 20 %	Nassar, et al. (2011)

more stability compared to the use of micron- or millimeter-dimension particles, which can cause severe abrasion and clogging problems. Another prospect of nanofluids, observed by Eastman, et al., is that nanofluids consisting of nano-copper particles dispersed in ethylene glycol have up to 40 % better thermal conductivity properties compared to those of pure fluid (Eastman J.A. et al., 2001). Based on this fact, nanofluids show great potential for various industries, one of which is the oil and gas industry where in-situ steam flooding is customarily used to enhance oil recovery. To find out what causes the increase in thermal conductivity, Keblinski, et al. proposed four possible mechanisms of heat flow in nanofluids, i.e. Brownian motion of the particles, molecular layering of the liquid at the liquid-particles interface, the nature of heat transport in nanoparticles, and effects of nanoparticle clustering (Keblinski P. et al., 2001).

Related to the preparation method, simple liquid-solid interfusion will not work towards achieving good nanofluids. Special methods, for example using surface activators and dispersants, or ultrasonic vibration, are available to create stable nanofluids that produce no precipitate over longer times (Xuan Y. and Li Q., 2000). Zeta potential analysis is one of the most effective ways to predict nanofluids stability. Generally, nanofluids preparation methods can be divided into two groups: single-step methods and two-step methods, as discussed comprehensively in the review paper by Li et al. and Haddad et al. (Haddad Z. et al., 2014; Li W. et al., 2007). One important aspect to note is the necessity to compromise the optimum value of nanoparticles inside the base fluid so as to get the best thermal conductivity, yet still a very stable colloidal suspension.

Another way to achieve this objective is to use beads milling, with which a stable colloidal nanoparticle suspension can be prepared. An illustration of the beads mill apparatus can be seen in Inkyo et al., which used bead particles with a diameter of only 15 μm, the smallest at the time, and employed centrifugal force in the upper part of the apparatus to separate the beads from the nanoparticle suspension (Inkyo M. et al., 2006). As a result, nanoparticles with a size of only 15 nm dominated the composition after 180 minutes of milling and low contamination from zirconia (ZrO_2), the beads' constituent material, was achieved.

Our preliminary work of water-based Fe_3O_4 nanofluids preparation showed initial success in increasing the viscosity reduction of heavy oil compared to the use of nanoparticles (Iskandar F. et al., 2015). The result also reflected that the presence of surfactant under the addition of 20 wt% ethylene glycol had a negligible effect on catalytic performance degradation.

Acknowledgements

This scientific work was partly financed from *"Dana Riset Inovasi ITB 2015"* and was also supported by *"TWAS Research Grants Programme in Basic Sciences 2014–2015" No. 14-236 RG/PHYS/AS_I.*

References

Aharoni A., Frei E.H., Schieber M., Some properties of γ-Fe_2O_3 obtained by hydrogen reduction of α-Fe_2O_3, Journal of Physics and Chemistry of Solids, 23 (1962) 545–554.

Ai D., Dai X., Li Q., Deng C., Kang S., Synthesis of NiO nanoparticles in ethylene glycol, China Particuology, 2 (2004) 157–159, DOI:http://dx.doi.org/10.1016/S1672-2515(07)60047-5.

Alboudwarej H., Felix J., Taylor S., Badry R., Bremner C., Brough B., Skeates C., Baker A., Palmer D., Pattison K., Beshry M., Krawchuk P., Brown G., Calvo R., Triana J. A.C., Hathcock R., Koerner K., Hughes T., Kundu D., De Cárdenas J.L., West C., Highlighting heavy oil, Oilfield Review, 18 (2006) 34–53.

Arfie M., Marika E., Woodard H.A., Purbodiningrat E.S., Implementation of slurry fracture injection technology for E&P wastes at duri oilfield, Society of Petroleum Engineers, 2005, DOI:10.2118/96543-MS.

Bera A., Babadagli T., Status of electromagnetic heating for enhanced heavy oil/bitumen recovery and future prospects: A review, Applied Energy, 151 (2015) 206–226, DOI:http://dx.doi.org/10.1016/j.apenergy.2015.04.031.

Beresnev I.A., Johnson P.A., Elastic-wave stimulation of oil production: a review of methods and results, Geophysics, 59 (1994) 1000–1017.

Chao K., Chen Y., Li J., Zhang X., Dong B., Upgrading and visbreaking of super-heavy oil by catalytic aquathermolysis with aromatic sulfonic copper, Fuel Processing Technology, 104 (2012) 174–180, DOI:http://dx.doi.org/10.1016/j.fuproc.2012.05.010.

Chao L.T., Wei M., MacManus-Driscoll J.L., Synthesis and characterisation of nanocrystalline iron oxides via ultrasonic spray assisted chemical vapour deposition, Journal of Physics: Conference Series, 26 (2006) 304–307, DOI:10.1088/1742-6596/26/1/073.

Chen Y., Wang Y., Wu C., Xia F., Laboratory experiments and field tests of an amphiphilic metallic chelate for catalytic aquathermolysis of heavy oil, Energy and Fuels, 22 (2008) 1502–1508, DOI:10.1021/ef8000136.

Clark P., Hyne J., Steam-oil chemical reactions: mechanisms for the aquathermolysis of heavy oils, AOSTRA Journal of research, 1 (1984) 15–20.

Daou T., Pourroy G., Begin-Colin S., Greneche J., Ulhaq-Bouillet C., Legare P., Bernhardt P., Leuvrey C., Rogez G., Hydrothermal synthesis of monodisperse magnetite nanoparticles, Chemistry of Materials, 18 (2006) 4399–4404.

Degnan T.F., Chitnis G.K., Schipper P.H., History of ZSM-5 fluid catalytic cracking additive development at Mobil, Microporous and Mesoporous Materials, 35–36 (2000)

245–252, DOI:10.1016/S1387-1811(99)00225-5.

Dong Y., He K., Yin L., Zhang A., A facile route to controlled synthesis of Co_3O_4 nanoparticles and their environmental catalytic properties, Nanotechnology, 18 (2007) 1–6, DOI:10.1088/0957-4484/18/43/435602.

Dusseault M., Comparing Venezuelan and Canadian heavy oil and tar sands. Paper presented at the Canadian International Petroleum Conference, Calgary, Alberta, Canada, (2001) 061.

Eastman J.A., Choi S.U.S., Li S., Yu W., Thompson L.J., Anomalously increased effective thermal conductivities of ethylene glycol-based nanofluids containing copper nanoparticles, Applied Physics Letters, 78 (2001) 718–720, DOI:10.1063/1.1341218.

Giri S., Samanta S., Maji S., Ganguli S., Bhaumik A., Magnetic properties of α-Fe_2O_3 nanoparticle synthesized by a new hydrothermal method, Journal of Magnetism and Magnetic Materials, 285 (2005) 296–302, DOI:10.1016/j.jmmm.2004.08.007.

Greff J.H., Babadagli T., Use of nano-metal particles as catalyst under electromagnetic heating for viscosity reduction of heavy oil. Paper presented at the Society of Petroleum Engineers—International Petroleum Technology Conference 2012, IPTC 2012.

Guo X., Du Z., Li G., Shu Z., High frequency vibration recovery enhancement technology in the heavy oil fields of China, Society of Petroleum Engineers, 2014, DOI:10.2118/86956-MS.

Haddad Z., Abid C., Oztop H.F., Mataoui A., A review on how the researchers prepare their nanofluids, International Journal of Thermal Sciences, 76 (2014) 168–189, DOI:10.1016/j.ijthermalsci.2013.08.010.

Hamedi Shokrlu Y., Babadagli T., Effects of nano-sized metals on viscosity reduction of heavy oil/bitumen during thermal applications, Society of Petroleum Engineers, 2010, DOI:10.2118/137540-MS.

Haryono A., Harmami B., Sondari D., Preparation of magnetite nanoparticles by thermal decomposition of iron (III) acetylacetonate with oleic acid as capping agent, Materials Science Forum, 737 (2013) 153–158, DOI:10.4028/www.scientific.net/MSF.737.153.

He T., Chen D., Jiao X., Controlled Synthesis of Co_3O_4 Nanoparticles through Oriented Aggregation, Chemistry of Materials, 16 (2004) 737–743, DOI:10.1021/ cm0303033.

Houbiers M., Wiarda E., Mispel J., Nikolenko D., Vigh D., Knudsen B.-E., Thompson M., Hill D., 3D full-waveform inversion at mariner — a shallow north sea reservoir, (Eds.), SEG technical program expanded abstracts (2012) 1–5, DOI:10.1190/segam2012-0242.1

Hyne J., Clark P., Clarke R., Koo J., Greidanus J., Tyrer J., Verona D., Aquathermolysis of heavy oils, Revista Tecnica Intevep, 2 (1982) 87–94.

IEA (International Energy Agency), 2014, World Energy Outlook 2014—Executive Summary <www.iea.org> accessed 29.06.2015.

Inkyo M., Tahara T., Iwaki T., Iskandar F., Hogan Jr C.J., Okuyama K., Experimental investigation of nanoparticle dispersion by beads milling with centrifugal bead separation, Journal of Colloid and Interface Science, 304 (2006) 535–540, DOI:10.1016/j.jcis.2006.09.021.

Ishikawa T., Matijević E., Formation of monodispersed pure and coated spindle-type iron particles, Langmuir, 4 (1988) 26–31.

Iskandar F., Asbahri A., Dwinanto E., Abdullah M., Khairurrijal K., Synthesis of Fe_3O_4 Nanoparticles Using Co-Precipitation Method and Its Development into Nanofluids as Catalyst in Aquathermolysis Reaction, Advanced Materials Research, 1112 (2015) 205–208.

Iskandar F., Fitriani P., Merissa S., Mukti R.R., Khairurrijal, Abdullah M., Fe_3O_4/zeolite nanocomposites synthesized by microwave assisted coprecipitation and its performance in reducing viscosity of heavy oil, AIP Conference Proceedings, 1586 (2014) 132-135.

Ito A., Takizawa Y., Honda H., Hata K.I., Kagami H., Ueda M., Kobayashi T., Tissue engineering using magnetite nanoparticles and magnetic force: Heterotypic layers of cocultured hepatocytes and endothelial cells, Tissue Engineering, 10 (2004) 833–840, DOI:10.1089/ 1076327041348301.

Jiang W., Yang H.C., Yang S.Y., Horng H.E., Hung J.C., Chen Y.C., Hong C.Y., Preparation and properties of superparamagnetic nanoparticles with narrow size distribution and biocompatible, Journal of Magnetism and Magnetic Materials, 283 (2004) 210–214, DOI:10.1016/j.jmmm.2004.05.022.

Junaid A.S.M., Rahman M.M., Rocha G., Wang W., Kuznicki T., McCaffrey W.C., Kuznicki S.M., On the role of water in natural-zeolite-catalyzed cracking of athabasca oilsands bitumen, Energy and Fuels, 28 (2014) 3367–3376, DOI:10.1021/ef500532w.

Kamimura Y., Tanahashi S., Itabashi K., Sugawara A., Wakihara T., Shimojima A., Okubo T., Crystallization behavior of zeolite beta in OSDA-free, seed-assisted synthesis, Journal of Physical Chemistry C, 115 (2011) 744–750, DOI:10.1021/jp1098975.

Keblinski P., Phillpot S.R., Choi S.U.S., Eastman J.A., Mechanisms of heat flow in suspensions of nano-sized particles (nanofluids), International Journal of Heat and Mass Transfer, 45 (2001) 855–863, DOI:10.1016/S0017-9310(01)00175-2.

Khamarui S., Saima Y., Laha R.M., Ghosh S., Maiti D.K., Functionalised MnVI-nanoparticles: An advanced high-valent magnetic catalyst, Scientific Reports, 5 (2015) 8636, DOI:10.1038/srep08636.

Koutzarova T., Kolev S., Ghelev C., Paneva D., Nedkov I., Microstructural study and size control of iron oxide nanoparticles produced by microemulsion technique, Physica Status Solidi C: Conferences, 3 (2006) 1302–1307, DOI:10.1002/pssc.200563115.

Lagashetty A., Havanoor V., Basavaraja S., Balaji S.D., Venkataraman A., Microwave-assisted route for synthesis of nanosized metal oxides, Science and Technology of Advanced Materials, 8 (2007) 484–493, DOI:10.1016/j.stam.2007.07.001.

Lan Q., Liu C., Yang F., Liu S., Xu J., Sun D., Synthesis of bilayer oleic acid-coated Fe_3O_4 nanoparticles and their application in pH-responsive Pickering emulsions, Journal of Colloid and Interface Science, 310 (2007) 260–269,

DOI:10.1016/j.jcis.2007.01.081.

Lenggoro I.W., Itoh Y., Iida N., Okuyama K., Control of size and morphology in NiO particles prepared by a low-pressure spray pyrolysis, Materials Research Bulletin, 38 (2003) 1819–1827, DOI:10.1016/j.materresbull.2003.08. 005.

Li W., Zhu J.h., Qi J.h., Application of nano-nickel catalyst in the viscosity reduction of Liaohe extra-heavy oil by aqua-thermolysis, Ranliao Huaxue Xuebao/Journal of Fuel Chemistry and Technology, 35 (2007) 176–180, DOI: 10.1016/S1872-5813(07)60016-4.

Liu Y., Fan H., The effect of hydrogen donor additive on the viscosity of heavy oil during steam stimulation, Energy and Fuels, 16 (2002) 842–846, DOI:10.1021/ef010247x.

Maity S.K., Ancheyta J., Marroquín G., Catalytic aquathermolysis used for viscosity reduction of heavy crude oils: A review, Energy and Fuels, 24 (2010) 2809–2816, DOI: 10.1021/ef100230k.

Martinez A.R., The Orinoco Oil Belt, Venezuela, Journal of Petroleum Geology, 10 (1987) 125–134.

Meneses C.T., Flores W.H., Garcia F., Sasaki J.M., A simple route to the synthesis of high-quality NiO nanoparticles, Journal of Nanoparticle Research, 9 (2007) 501–505, DOI:10.1007/s11051-006-9109-2.

Merissa S., Fitriani P., Iskandar F., Abdullah M., Khairurrijal, Preliminary study of natural zeolite as catalyst for decreasing the viscosity of heavy oil, AIP Conference Proceedings, 1554 (2013) 131–134.

Mizutani N., Iwasaki T., Watano S., Yanagida T., Tanaka H., Kawai T., Effect of ferrous/ferric ions molar ratio on reaction mechanism for hydrothermal synthesis of magnetite nanoparticles, Bulletin of Materials Science, 31 (2008) 713–717.

Mornet S., Vasseur S., Grasset F., Duguet E., Magnetic nanoparticle design for medical diagnosis and therapy, Journal of Materials Chemistry, 14 (2004) 2161–2175, DOI:10.1039/b402025a.

Musić S., Czakó-Nagy I., Salaj-Obelić I., Ljubešić N., Formation of α-Fe_2O_3 particles in aqueous medium and their properties, Materials Letters, 32 (1997) 301–305.

Musić S., Krehula S., Popović S., Skoko Ž., Some factors influencing forced hydrolysis of FeCl3 solutions, Materials Letters, 57 (2003) 1096–1102.

Nassar N.N., Hassan A., Pereira-Almao P., Application of nanotechnology for heavy oil upgrading: Catalytic steam gasification/cracking of asphaltenes, Energy & Fuels, 25 (2011) 1566–1570.

Noorlaily P., Nugraha M.I, Khairurrijal, Abdullah M., Iskandar F., Ethylene glycol route synthesis of nickel oxide nanoparticles as a catalyst in aquathermolysis, Materials Science Forum, 737 (2013) 93–97, DOI:10.4028/www.scientific.net/MSF.737.93.

Nugraha M.I., Noorlaily P., Abdullah M., Khairurrijal, Iskandara F., Synthesis of $Ni_xFe_{3-x}O_4$ nanoparticles by microwave-assisted coprecipitation and their application on viscosity reduction of heavy oil, Materials Science Forum, 737 (2013) 204–208, DOI:10.4028/www. scientific.net/MSF.737.204.

Nurhayati T., Iskandar F., Abdullah M., Khairurrijal, Syntheses of hematite (α-Fe_2O_3) nanoparticles using microwave-assisted calcination method, Materials Science Forum, 737 (2013) 197–203, DOI:10.4028/ www.scientific.net/MSF.737.197.

Owen J., Floyd J., Enhanced oil recovery methods, Oil Gas Petrochem Equip, 27 (1981) 11.

Petroleum B. (2014). BP Statistical Review of World Energy 2014, 1 June 2014.

Pride S.R., Flekkøy E.G., Aursjø O., Seismic stimulation for enhanced oil recovery, Geophysics, 73 (2008) O23–O35.

Purnomo C.W., Salim C., Hinode H., Synthesis of pure Na-X and Na-A zeolite from bagasse fly ash, Microporous and Mesoporous Materials, 162 (2012) 6–13, DOI: 10.1016/j.micromeso.2012.06.007.

Randrianantoandro N., Mercier A.M., Hervieu M., Grenèche J.M., Direct phase transformation from hematite to maghemite during high energy ball milling, Materials Letters, 47 (2001) 150–158, DOI:10.1016/S0167-577X(00)00227-5.

Sahoo S., Agarwal K., Singh A., Polke B., Raha K., Characterization of γ- and α-Fe_2O_3 nano powders synthesized by emulsion precipitation-calcination route and rheological behaviour of α-Fe_2O_3, International Journal of Engineering, Science and Technology, 2 (2010) 118–126.

Selwood P., Magnetism and catalysis, Chemical reviews, 38 (1946) 41–82.

Semple K., Westlake D., Characterization of iron-reducing Alteromonas putrefaciens strains from oil field fluids, Canadian journal of microbiology, 33 (1987) 366–371.

Shimomura Y., Tsubokawa I., Kojima M., On Nickel Oxides of High Oxygen Content, Journal of the Physical Society of Japan, 9 (1954) 521–524.

Stjerndahl M., Andersson M., Hall H.E., Pajerowski D.M., Meisel M.W., Duran R.S., Superparamagnetic Fe_3O_4/SiO_2 nanocomposites: enabling the tuning of both the iron oxide load and the size of the nanoparticles, Langmuir, 24 (2008) 3532–3536.

Swardhani A.P., Iskandar F., Abdullah M., Khairurrijal, Synthesis of Fe_2O_3/C Nanocomposite Using Microwave Assisted Calcination Method, Advanced Materials Research, 896 (2014) 100–103.

Tueros M.J., Baum L.A., Borzi R.A., Stewart S.J., Mercader R.C., Marchetti S.G., Bengoa J.F., Mogni L.V., Characterization of Nanosized Maghemite Particles Prepared by Microemulsion Using an Ionic Surfactant, Hyperfine Interactions, 148–149 (2003) 103–108, DOI:10.1023/B:HYPE.0000003770.22742.e7.

Van Donk S., Janssen A.H., Bitter J.H., De Jong K.P., Generation, characterization, and impact of mesopores in zeolite catalysts, Catalysis Reviews—Science and Engineering, 45 (2003) 297–319, DOI:10.1081/CR-120023908.

Vasquez-Mansilla M., Zysler R.D., Arciprete C., Dimitrijewits M.I., Saragovi C., Greneche J.M., Magnetic interaction evidence in α-Fe_2O_3 nanoparticles by magnetization and Mossbauer measurements, Journal of Magnetism and Magnetic Materials, 204 (1999) 29–35, DOI:10.1016/S0304-8853(99)00404-7.

Wang Y., Chen Y., He J., Li P., Yang C., Mechanism of catalytic aquathermolysis: Influences on heavy oil by two types of

efficient catalytic ions: Fe^{3+} and Mo^{6+}, Energy and Fuels, 24 (2010) 1502–1510, DOI:10.1021/ ef901339k.

Wang Y., Du W., Xu Y., Effect of sintering temperature on the photocatalytic activities and stabilities of hematite and silica-dispersed hematite particles for organic degradation in aqueous suspensions, Langmuir, 25 (2009) 2895–2899, DOI:10.1021/la803714m.

Wen S., Zhao Y., Liu Y., Hu S., A study on catalytic aquathermolysis of heavy crude oil during steam stimulation, Society of Petroleum Engineers, DOI:10.2118/106180-MS.

Willis A.L., Turro N.J., O'Brien S., Spectroscopic characterization of the surface of iron oxide nanocrystals, Chemistry of Materials, 17 (2005) 5970–5975, DOI:10.1021/cm051370v.

Woo K., Lee H.J., Ahn J.P., Park Y.S., Sol-Gel Mediated Synthesis of Fe2O3 Nanorods, Advanced Materials, 15 (2003) 1761–1764, DOI:10.1002/adma.200305561.

Wu C., Lei G., Yao C., Jia X., In situ upgrading extra-heavy oil by catalytic aquathermolysis treatment using a new catalyst based anamphiphilic molybdenum chelate, Society of Petroleum Engineers, DOI:10.2118/130333-MS.

Wu C., Su J., Zhang R., Lei G., Cao Y., The use of a nano-nickel catalyst for upgrading extra-heavy oil by an aquathermolysis treatment under steam injection conditions, Petroleum Science and Technology, 31 (2013) 2211–2218, DOI:10.1080 /10916466.2011.644016.

Wu Z., Zhang M., Zhao Z., Li W., Tao K., Synthesis of a Pd on Ni-B nanoparticle catalyst by the replacement reaction method for hydrodechlorination, Journal of Catalysis, 256 (2008) 323–330, DOI:10.1016/j.jcat.2008.03.026.

Xu B., Sievers C., Hong S.B., Prins R., van Bokhoven J.A., Catalytic activity of Brønsted acid sites in zeolites: Intrinsic activity, rate-limiting step, and influence of the local structure of the acid sites, Journal of Catalysis, 244 (2006) 163–168, DOI:10.1016/j.jcat.2006.08.022.

Xu H., Pu C., Wu F., Low frequency vibration assisted catalytic aquathermolysis of heavy crude oil, Energy and Fuels, 26 (2012) 5655–5662, DOI:10.1021/ef301057t.

Xu H.X., Pu C.S., Experimental study of heavy oil underground aquathermolysis using catalyst and ultrasonic, Ranliao Huaxue Xuebao/Journal of Fuel Chemistry and Technology, 39 (2011) 606–610.

Xuan Y., Li Q., Heat transfer enhancement of nanofluids, International Journal of Heat and Fluid Flow, 21 (2000) 58–64, DOI:http://dx.doi.org/10.1016/S0142-727X(99)00067-3.

Yang H., Hu Y., Zhang X., Qiu G., Mechanochemical synthesis of cobalt oxide nanoparticles, Materials Letters, 58 (2004) 387–389, DOI:http://dx.doi.org/10.1016/S0167-577X(03)00507-X.

Zhang H., Wang W., Li H., Meng S., Li D., A strategy to prepare ultrafine dispersed Fe_2O_3 nanoparticles, Materials Letters, 62 (2008) 1230–1233, DOI:http://dx.doi.org/10.1016/j.matlet.2007.08.026.

Zhang Y., Liu X., Nie J., Yu L., Zhong Y., Huang C., Improve the catalytic activity of α-Fe_2O_3 particles in decomposition of ammonium perchlorate by coating amorphous carbon on their surface, Journal of Solid State Chemistry, 184 (2011) 387–390, DOI:http://dx.doi.org/10.1016/j.jssc.2010.12.004.

Author's short biography

Ferry Iskandar

Dr. Ferry Iskandar is a researcher and lecturer in Department of Physics, Institut Teknologi Bandung (ITB). He received his Bachelor and Master Degree at Kanazawa University, Japan before completing his Doctoral Degree at Hiroshima University, Japan. He began his teaching career as Assistant Professor in Chemical Engineering Department, Graduate School of Engineering, Hiroshima University before joined Department of Physics, Institut Teknologi Bandung (ITB) in 2010. His research and interest include Material Physics, Filtration and Separation Engineering (Aerosol and Colloids), Powder and Nanomaterials, Chemical Reaction Engineering and Advanced Materials. He has published more than 130 research papers and 14 patents.

Author's short biography

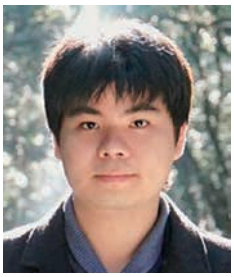

Erlandy Dwinanto

Erlandy Dwinanto holds his Bachelor Degree from Department of Physics, Institut Teknologi Bandung (ITB). He began his research in Energy and Environmental Materials Laboratory ITB on topics regarding nanoparticles synthesis and application in the field of enhanced oil recovery (EOR) of heavy crude oil, under the supervision of Dr. Ferry Iskandar. His research interests include catalysts, adsorbents and related materials. He is currently preparing for his Master course at Graduate School of Engineering, Tokyo Institute of Technology on International Graduate Program.

Mikrajuddin Abdullah

Prof. Mikrajuddin Abdullah is a Professor at the Faculty of Mathematics and Natural Sciences Institut Teknology Bandung (ITB). He received his Bachelor Degree and Master Degree at Institut Teknologi Bandung (ITB), Indonesia and Doctoral Degree at Hiroshima University, Japan. His research interests are related to synthesis of nanomaterials (nanoparticles, carbon nanotubes, nanocomposites), applications of nanostructured materials (display, luminescent nano-ink, nanocatalyst, cosmetics, etc.), and other interests in Physical Education.

Khairurrijal

Prof. Khairurrijal is a Professor from Departement of Physics, Institut Teknologi Bandung, Indonesia. He is a member of Physics of Electronic Materials Research Division, Faculty of Mathematics and Natural Sciences, ITB. He received his Bachelor Degree and Master Degree at Institut Teknologi Bandung (ITB), Indonesia and Doctoral Degree at Hiroshima University, Japan. He is working on research topics in Physics, Materials Science and Engineering, Instrumentation and Measurement Science, Automatic Control, Educational Technology, and Science Education.

Oki Muraza

Dr. Oki Muraza is a researcher at Center of Research Excellence in Nano Technology (CENT) and a faculty in the Chemical Engineering Department at King Fahd University of Petroleum & Minerals. He received his PhD in Chemical Engineering at Technische Universiteit Eindhoven (TU Eindhoven). His research interest mainly are nanostructured catalysts and nanoparticles such as nanostructured catalytic thin films in (micro) structured reactors, zeolite nanocrystals in catalysis, and nanoparticles for heavy oil upgrading.

KONA Powder and Particle Journal No. 33 (2016) 17–32/Doi:10.14356/kona.2016007 Review Paper

Surface Chemistry and Rheology of Slurries of Kaolinite and Montmorillonite from Different Sources †

Pek-Ing Au and Yee-Kwong Leong *

[1] *School of Mechanical and Chemical Engineering, The University of Western Australian, Australia*

Abstract

Zeta potential (ζ)-pH and yield stress (τ_y)-pH behaviour of a number of kaolinite and montmorillonite slurries, including CMS-sourced materials, were compared. The CMS KGa-2 and Crown kaolin with very similar elemental composition displayed almost identical ζ-pH and τ_y-pH behaviour. Both displayed a $pH_{\zeta=0}$ at 3–4 where the maximum τ_y was located. This $pH_{\zeta=0}$ was higher at higher ionic strength as the pH-dependent charge increased with ionic strength and the permanent structural charge being invariant. The other kaolinite slurries (Reidel and Unimin) with different composition showed different behaviour. The surface chemistry and rheological properties of CMS-sourced SWy-2 (Na-) and STx-1b (Ca-) montmorillonite and bentonite slurries were also compared. They all displayed a negative zeta potential that was insensitive to pH. STx-1b slurries required a much higher solid concentration to form a gel. Maximum τ_y occurred over a broad range of pH. This pH is ~5 for SWy-2, 8 for STx-1b, <2 for bentonite and 12 for API bentonite. Their difference in clay mineral composition such as impurities and exchangeable cations were highlighted. The point of zero charge (pzc) of kaolinite and montmorillonite slurries obtained via Mular-Roberts pH-salt addition method did not correlate well with the $pH_{\zeta=0}$ except for the KGa-2 and Crown kaolin.

Keywords: drilling fluids, yield stress-volume fraction, zeta potential, clay mineralogy, fractal dimension, Mular-Roberts, KGa-2, SWy-2, STx-1b

1. Introduction

Kaolin mineral slurries from different sources or deposits display different rheological and surface chemical properties (Au P. and Leong Y., 2013; Au P. et al., 2014; Lagaly G., 1989; Rand B. and Melton I.E., 1977; Teh E. et al., 2009). Kaolin is a very important commodity mined all over the world. The ability to use its mineral and elemental composition to predict its slurry rheological behaviour from its surface properties would be extremely useful and beneficial when processing this clay mineral. However not all of the important factors responsible for the variation in rheological behaviour have been identified and their effects understood. Attempts have been made to identify these factors (Rand B. and Melton I.E., 1977; Teh E. et al., 2009). Factors such as Ca(II) or CaO content or Ca/Na ratio (Avadiar L. et al., 2014; Avadiar L. et al., 2015; Lagaly G., 1989) have been identified. The presence of a relatively small amount of smectite content can also have a very significant effect on the rheological behaviour of kaolinite slurries (Au P. and Leong Y., 2013).

Bentonite composed of mainly sodium montmorillonite (Na^+Mt) is another important commercial clay mineral because of its many uses, for example in paper coating, catalysts, pharmaceutical products, drilling muds, as an impermeable slurry wall and nuclear waste storage barrier. Slurries of bentonite displayed highly complex time-dependent rheological properties. Na^+Mt in water swelled considerably. Factors affecting its rheological behaviour are thus more numerous such as impurities, exchangeable cations and salt concentration (Chang W. and Leong Y., 2014; Goh R. et al., 2011; van Olphen H., 1955). However, despite the numerous studies, the knowledge available in the open literature is still quite confusing. Gels of Na^+Mt from different sources displayed different rheological properties. According to Lagaly G. (1989), the important factors are particle structure and texture. Upon swelling different Na^+Mt will disintegrate to different extents giving rise to stack-layered particles of different thickness, different particle concentration and different shape flow units producing gels. A better evaluation of the difference would be to compare the rheological properties over a wide pH range. Like kaolinite, the comparison should also include zeta potential-pH behaviour. Such a comparison would allow for a more effective evaluation of the factors responsible for the rheological variation.

† Received 26 May 2015; Accepted 29 June 2015
J-STAGE Advance published online 25 July 2015
[1] 35 Stirling Highway, Crawley WA 6009, Perth, Australia
* Corresponding author: Yee-Kwong Leong;
E-mail: yeekwong.leong@uwa.edu.au
TEL: +61-8-6488 3602 FAX: +61-8-6488 1084

Rheological and surface properties data from slurries prepared from standard or well-characterised Na^{+}Mt and kaolinite are required for comparison and evaluation. Such clay minerals can be sourced from the Clay Mineral Society USA (CMS) and will have well-characterised compositional, physical and surface properties data (CMS, 2015). The surface chemistry and rheological property data obtained for these clay mineral slurries will form the baseline or benchmark data for other kaolin and montmorillonite slurries to compare in this search to identify the important factors and understand their effects. CMS-sourced kaolin KGa-2 and Na^{+}Mt SWy-2 and Ca^{2+}Mt STx-1b were used in this study.

The complete characterization of the surface properties of the clay minerals may require the value of several components: point of zero charge (pzc) or isoelectric point (IEP) (Pradip et al., 2015), point of zero net proton charge, zeta potential-pH-ionic strength behaviour, charges (layer, tetrahedral, octahedral, unbalanced and extra Si) and cation exchanged capacity or CEC. For CMS-sourced clay minerals, most of these parameters are known and listed on their database (CMS, 2015). For correlation with rheological properties, normally only the zeta potential, including pzc, is required because the magnitude of the rheological parameters such as yield stress and viscosity, is governed by the nature and strength of the predominant interparticle force. Zeta potential is a measure of the strength of the interparticle repulsive force and is often used to define the state of the slurries; flocculated or dispersed. A high magnitude is normally associated with no or a very low yield stress. This is often not the case with some clay mineral slurries (Leong Y. et al. 2012; Au P. and Leong Y. 2013). Many kaolin slurries do obey the yield stress-DLVO model (Hunter R. and Nicol S., 1968; Teh E. et al., 2009; Au P. and Leong Y, 2013).

Among the many yield stress τ_y-DLVO force or interaction energy models (Hunter R. and Nicol S., 1968; Leong Y. and Ong B., 2003; Teh E. et al., 2010) is one based on constant surface potential for interactions between spherical particles and is given by (Scales P., et al., 1998):

$$\tau_y \approx \frac{\phi_s^{\,2}}{a}\left(\frac{A_H}{12D_o^{\,2}} - 2\pi\varepsilon_o\varepsilon\xi^2\frac{\kappa e^{-\kappa D_o}}{1+e^{-\kappa D_o}}\right) \quad (1)$$

The number of particles per unit area is scaled to $\phi_s^{\,2}/a^2$. The model predicts a linear relationship between τ_y and zeta potential squared ξ^2 at a fixed ionic strength. The critical zeta potential ξ_{cri} characterizes the point of transition from flocculated to dispersed state where $\tau_y = 0$ (Leong Y.K. and Ong B.C., 2003). Thus Eqn. 1 is reduced to give

$$\xi_{cri} = \sqrt{\frac{A_H(1+e^{-\kappa D_o})}{24D_o^{\,2}\pi\varepsilon_o\varepsilon\kappa e^{-\kappa D_o}}} \quad (2)$$

ξ_{cri} is proportional to the square root of the Hamaker constant A_H and is independent of the particle size a and concentration of the dispersion. This equation has been used to determine the Hamaker constant of pristine oxide in water (Leong Y. and Ong B., 2003; Teh E. et al., 2010).

Laxton P. and Berg J. (2006), however, observed a positive slope for the linear relationship between τ_y and ξ^2 of kaolinite–bentonite composite slurries. They attributed this to positive–negative charge attraction between the clay platelets. In their study, the zeta potential was varied by ionic strength instead of pH.

Apart from zeta potential, there are several techniques for characterizing the pzc of a mineral powder. One such technique is the Mular–Roberts (MR) salt addition–pH method (Mular A. and Roberts R., 1966). This method has been shown to accurately determine the pzc of pure inorganic oxides such as, Fe_2O_3, Al_2O_3, SiO_2 and TiO_2 (Alvarez-Silva M. et al., 2010; Mular A.L. and Roberts R.B., 1966). Its accuracy with clay minerals such as serpentine and chlorite phyllosilicate minerals is still questionable (Alvarez-Silva M. et al., 2010). For a pristine inorganic oxide such as rutile TiO_2, the pzc is independent of the ionic strength of an indifferent electrolyte (Hunter R., 2003). The MR method exploited this property to determine the pzc. At pzc, the pH of the mineral suspended in 0.001 M sodium chloride concentration will remain unchanged when the salt concentration is increased to 0.01 M. At other pH levels, a difference in the pH between these two ionic strength states will be present. With pure oxides, such as alumina and silica, the surface charges are all pH-dependent. In contrast, clay minerals contain permanent structural negative charges which are pH-independent (Bolland M. et al., 1980).

Alvarez-Silva M. et al. (2010) found that the MR method for pzc determination was suitable for serpentine but not for chlorite phyllosilicate mineral. In this study, we extended their work to other clay minerals and included rheological data to correlate with the surface chemistry data. In addition, we also aim to develop an understanding of the applications and limitations of the MR method for kaolinite and montmorillonite.

2. Materials and methods

2.1 Materials and mineral characterisation

The CMS KGa-2 kaolin was sourced from a deposit located in Warren County, Georgia, USA. KGa-2 is a high defect or low crystallinity kaolin with a crystallinity index of only 0.16. It was composed of 96 % kaolinite (with 3 % anatase, 1 % crandallite + trace mica and/or illite) (Chipera S. and Bish D., 2001). It has a BET surface area of 23.5 ± 0.06 $m^2\ g^{-1}$ and a cation exchange capacity (CEC) of only 3.3 meq/100 g. The large BET area is an

Table 1 Elemental composition of kaolinite from different sources expressed in oxide content (wt%).

	KGa-2	Crown	Reidel	Unimin
SiO_2	43.9	45.1	48.5	46.8
Al_2O_3	38.5	37.7	38.2	36.6
TiO_2	2.08	1.9	0.06	0.8
Fe_2O_3	0.98	1.4	0.93	1.02
FeO	0.15			
Na_2O	< 0.005	0.03	n.d.	0.36
K_2O	0.065	0.05	2.064	0.22
CaO	n.d.	0.06	0.028	0.495
MgO	0.03	0.06	0.4	0.3
MnO	n.d.		0.007	0.01
F	0.02			
P_2O_5	0.045		0.147	0.011
S	0.02		0.04	<0.01

n.d.: not detectable

Table 2 Elemental composition of montmorillonite from different sources in terms of oxide content (wt%)

	Swy-2	Bent (B3378)	STx-1b	API bent
SiO_2	62.9	60.5	70.1	63
Al_2O_3	19.6	21	16	1.49
TiO_2	0.09	0.153	0.22	0.975
Fe_2O_3	3.35	3.88	0.65	0.76
FeO	0.32		0.15	
Na_2O	1.53	2.11	0.27	2.18
K_2O	0.53	0.318	0.078	0.737
CaO	1.68	1.02	1.59	1.78
MgO	3.05	2.76	3.69	1.6
MnO	0.006	0.009	0.009	0.54
F	0.11		0.084	
P_2O_5	0.049	0.04	0.026	0.08
SO_3	0.05 (S)	0.74	0.04 (S)	0.02

indication of its high fine particle content. The elemental compositions of KGa-2 and other kaolinites, expressed in oxide content, are contained in **Table 1** (CMS, 2015). The air-floated Crown kaolin (sourced from a deposit in Georgia) was provided by Active-Minerals Inc (USA) who indicated a median particle size of 0.3 μm and the crystallinity index of ~0.5. It composed 96–100 % kaolin, with 0–2 % quartz and 0–2 % TiO_2 (as anatase).

KGa-2 displayed a point of zero charge (pzc) at pH 3.5 and a point of zero net proton charge (pznpc) at 5.4 (Schroth B.K. and Sposito G., 1997). Zeta potential characterization of this kaolinite slurry produced a similar pzc at pH 3–4 (Du J. et al., 2010).

The other clay minerals used in this study were Unimin kaolin (Unimin Corp.), Riedel kaolin (Sigma-Aldrich), SWy-2 Na^+Mt and STx-1b Ca^{2+}Mt (both from CMS), bentonite from USA (B3378, Sigma-Aldrich) and an API bentonite (Rheochem Ltd). This API bentonite is used in the formulation of drilling fluids. The BET surface area of Unimin and Riedel kaolin were 19.9 and 9.9 $m^2\ g^{-1}$ respectively (Avadiar L. et al., 2014). The Reidel displayed a very low TiO_2 content. XRD data showed the presence of quartz (< 5 %) in the Unimin and—of both quartz and mica/illite (both < 5 %) in the Reidel (thus the high K_2O content).

The elemental composition of the montmorillonites used in this study is given in **Table 2**. The CEC of SWy-2 and STx-1b were 76.4 and 84.4 meq/100 g, and their specific areas were 31.82 and 83.79 $m^2\ g^{-1}$ respectively, The principal exchange cations were Na^+ and Ca^{2+} for SWy-2 and Ca^{2+} for STx-1b. The SWy-2 was from a deposit in Crook County, Wyoming, USA. It was composed of 75 % smectite, 8 % quartz, 16 % feldspar, 1 % gypsum, and traces of mica and/or illite and kaolinite and/or Chlorite (Chipera S.J. and Bish D.L., 2001). The STx-1b comprised 63 % smectite, 33 % opal-CT (SiO_2) and 3 % quartz (trace amount of feldspar and kaolinite) (Humphries S.D. et al., 2011).

Powder characterization included particle sizing and particle morphology examination. The particle size distribution was measured with a laser Malvern Mastersizer Microplus. The morphology of the particles was imaged with a Zeiss 1555 VP-FESEM scanning electron microscope (SEM). The median size of KGa-2, Unimin, Riedel kaolin, Swy-2 and bentonite were found to be 1.7, 3.26, 5.70, 2.09, and 2.77 μm respectively. The SEM images of the various clay mineral powders are shown in **Fig. 1(a)–(f)**.

All four kaolin tested were poorly crystalline. **Fig. 1(a)** shows that the KGa-2 possessed a complex surface structure on its basal surface, including micro-pits, the high frequency occurrence of micro-islands, and ragged and broken edges. This was also observed in the poorly crystallised Unimin, Riedel and Crown kaolin. The overall particle shape of these high defect kaolinites should lead to higher aspect ratios (Żbik M. and Smart R., 1998). The kaolinite crystals in SEM micrographs appear as rigid particles. However the particles of Swy-2 Na^+Mt and bentonite appeared as undulated flexible sheets, as seen in **Figs. 1(e)** and **1(f)**.The difference in microstructure between kaolinite and smectite is due to the relatively strong hydrogen bonding between hydroxyl groups on the 1:1 kaolinite sheets (Żbik M. et al., 2010).

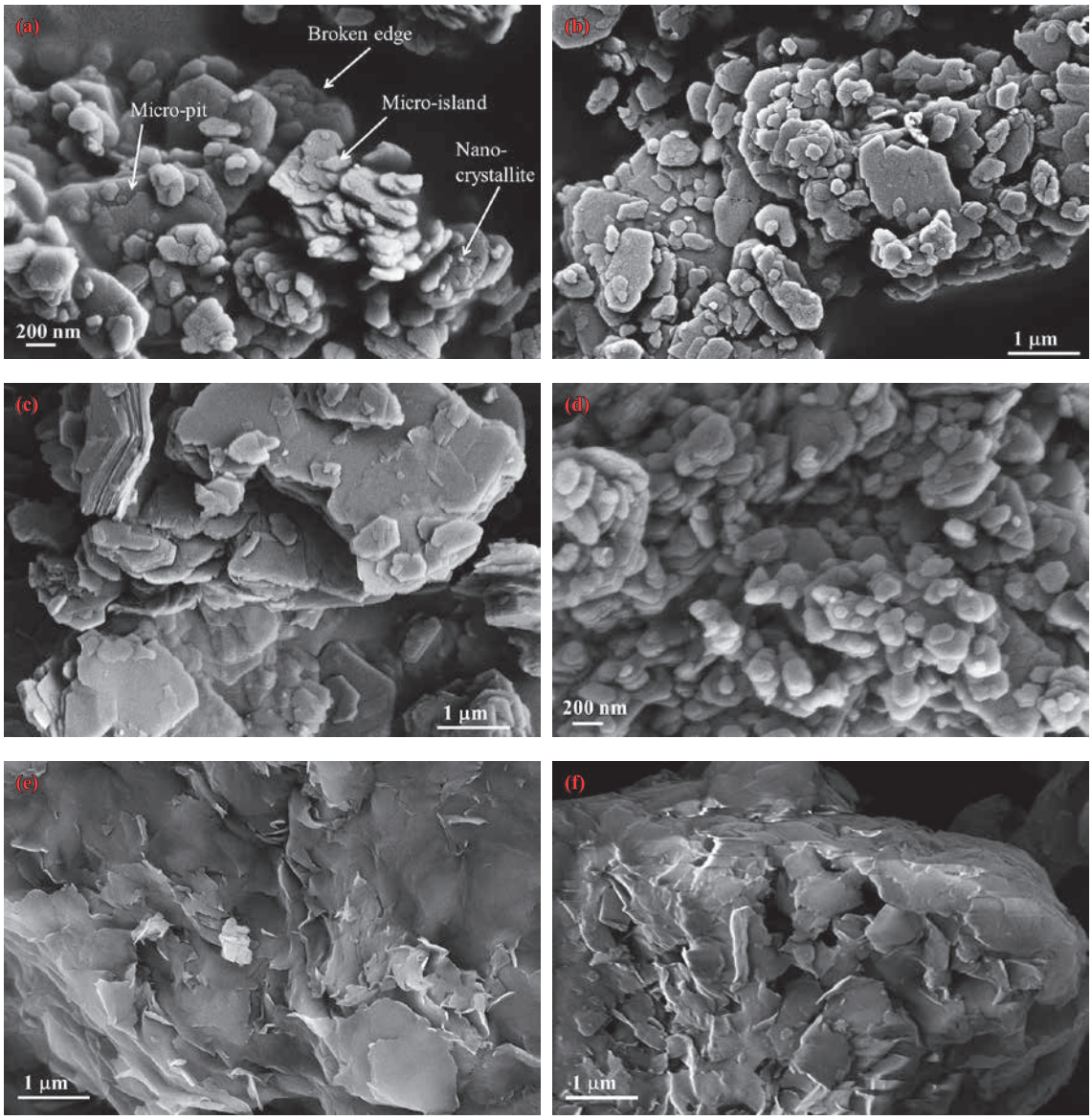

Fig. 1 SEM images of various kaolin (a) KGa-2, (b) Unimin, (c) Riedel and (d) crown. SEM images of (e) SWy-2 sodium montmorillonite and (f) bentonite.

2.2 Rheological charaterization

The rheological parameter used was the yield stress, which was measured directly using a vane technique (Nguyen Q. and Boger D., 1983). Clay suspensions were prepared at high pHs by homogenising a mixture of clay powder and solution with a Branson Sonifier which break ups the particle aggregates by sonic vibration. Dilute suspensions were prepared in the same manner for zeta potential measurement.

Brookfield vane viscometers with different spring constants, LVDV-II + Pro and RVDV-II + Pro, were used. A range of four-blade vanes were used to cover yield stress values ranging from < 1 Pa to 1000 Pa. The suspension pH was varied by using a 10 M potassium hydroxide and a 6.61 M nitric acid solution in order to avoid excessive dilution of sample during pH change in the experiment. Yield stress measurement was conducted in the direction from high to low pH so as to avoid the dissolution of clay minerals and the precipitation of the hydrolysis products of metal ions.

2.3 Zeta potential and pzc determination

Zeta potential was measured using a Colloidal Dynamics ZetaProbe (Appel C. et al., 2003). The pzc or IEP usually corresponded to the pH of zero zeta potential. The pzc determination via the MR method of pH-salt addition measurement required preparation of a 2 wt% slurry in a 0.001 M NaCl solution at a specific pH ranging from 3 to 11. In the case of kaolinite, 1 g of material was placed in a 50 mL of a 0.001 M NaCl solution prepared and the initial

pH (pH_{ini}) was measured. Dry NaCl solids was then added to increase the ionic strength from 0.001 to 0.1 M and the final pH (pH_{fin}) was recorded. When ΔpH (= $pH_{fin} - pH_{ini}$) is zero, the pH_{fin} is the pzc. The clay particle is positively charged when ΔpH is positive (Ndlovu B. et al., 2014). For smectite swelling clay, 0.5 g was added to a 50 ml 0.001 M NaCl solution. Measurement for swelling clay was performed 24 hours after preparation. Goh R. et al. (2011) reported that freshly prepared bentonite gels required about a day to reach surface chemical equilibrium.

3. Results and discussion

3.1 Kaolinite slurries

The zeta potential–pH behaviour of KGa-2 and Crown kaolin slurries was compared. They displayed almost identical zeta potential–pH behaviour at an ionic strength of 0.1 M NaCl (**Fig. 2**). An isoelectric point (IEP) or pzc at pH 3–4 was observed. Both contained a very low amount of CaO and other mineral impurities such as quartz, mica and the like.

The pzc of Crown kaolin at lower ionic strength of 0.001 M NaCl occurred at a lower pH of 3.0 as shown in **Fig. 2**. Kaolin possesses both permanent structural (negative) charge due to isomorphic substitution and pH-dependent charge. Unlike pH-dependent charge, the amount of permanent negative charge is not dependent upon the ionic strength. For pristine oxides such as TiO_2 with only pH-dependent charges, its surface charge density at a given pH increased with ionic strength—except at the pzc (Hunter R., 2003). At the pzc, the amount of positive charges must be equal to the negative charges. With kaolin slurries, at a given pH (below pznpc) away from pznpc, the positive pH-dependent positive charge density increased with ionic strength. At low ionic strength, the pH must be further away from the pznpc for the kaolin particles to acquire sufficient positive charge to balance the permanent negative charge (Tombácz E. and Szekeres M., 2006). Thus for Crown kaolin, a lower pH is required to acquire a sufficient amount of pH-dependent positive charge to balance the permanent negative charge at low ionic strength. This is the likely explanation for the lower pzc.

The yield stress–pH behaviour shown in **Fig. 3(a)** for KGa-2 and **3(b)** for Crown kaolin were also similar, namely, high yield stress at low pH and low yield stress at high pH. The maximum yield stress was observed to be located at or close to pzc or IEP.

The yield stress–solids volume fraction relationships shown in **Fig. 4** at low pH of ~3 were almost identical. A power law model described this relationship. An exponent value of ~3 was obtained. A similar exponent value was

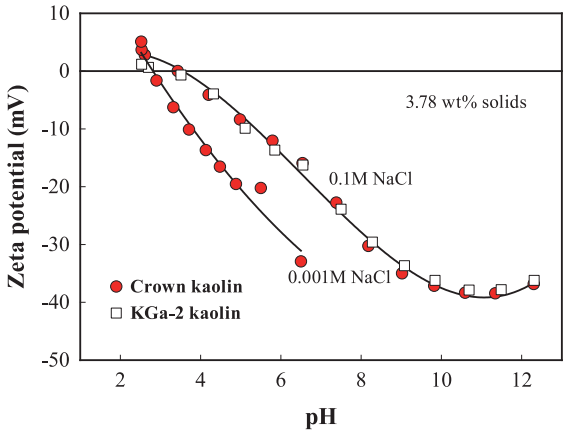

Fig. 2 Zeta potential–pH behaviour of 3.76 wt% KGa-2 and Crown kaolin slurries (pzc of 3.4) and the effect of ionic strength on Crown kaolin slurries.

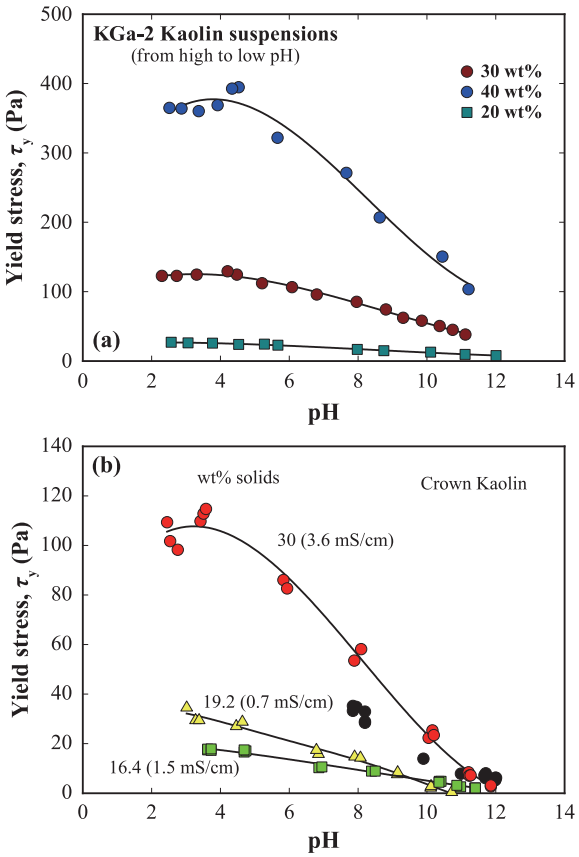

Fig. 3 Yield stress–pH behaviour of a) KGa-2 kaolin and (b) air-floated crown kaolin slurries.

observed at a higher pH of 7 for the Crown kaolin. The low CaO Reidel kaolin slurries also displayed a similar exponent value of 3.1 (Au P.I. et al., 2014). This exponent value was related to the fractal dimension of the microstructure in the slurries (Au P. and Leong Y., 2015; Au P.I. et al., 2015). Kranenburg C. (1994) derived the following relationship between yield stress τ_y and ϕ_s from scaling theory:

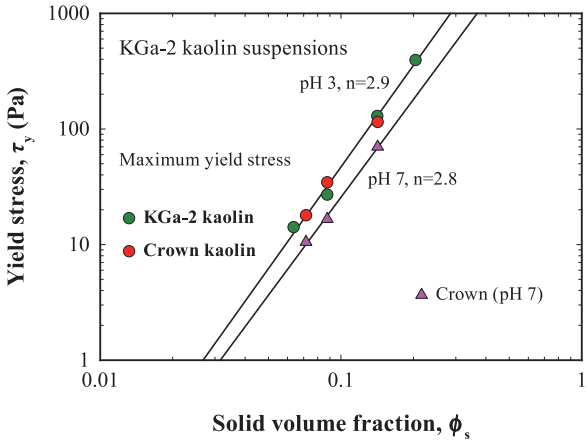

Fig. 4 The yield stress–solid volume fraction relationship of KGa-2 and Crown kaolin dispersions.

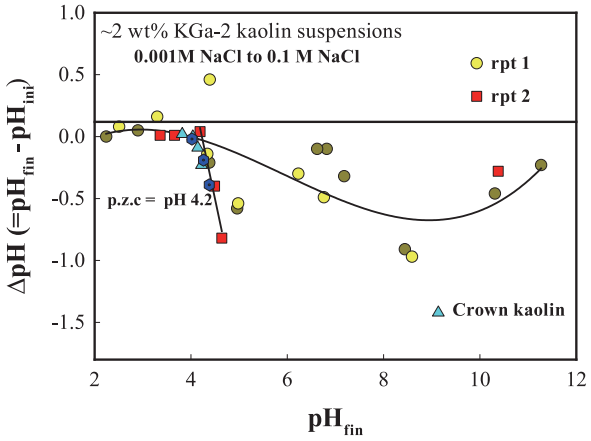

Fig. 6 The Mular–Roberts pH-salt addition results for ~2 wt% KGa-2 and Crown kaolin slurries.

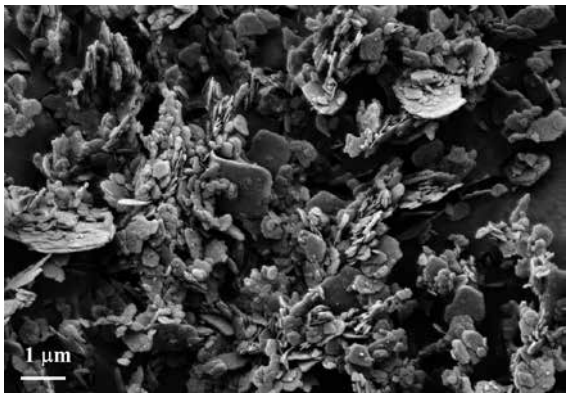

Fig. 5 The cyro-SEM image of 15 wt% KGa-2 slurries at the maximum yield stress of pH 4.2.

$$\tau_y \sim \phi_s^{2/(3-D_f)} \quad (3)$$

and applied it to clay sediment and suspensions. The same equation was derived earlier by Wessel R. and Ball R. (1992) for creeping shear flow of fractal aggregates and gels. Using Eqn (3), the fractal dimension D_f of these kaolin slurries was determined to have a value of 2.3. The predominant particle interaction configuration is face–face or stair–step (Au P. et al., 2014) with some face–face aggregates interacting via edge–face configurations (Gupta V. et al., 2011).

The cryo-SEM image of microstructure of KGa-2 slurries at the maximum yield stress with a fractal dimension of 2.3 is shown in **Fig. 5**. The image shows that dense aggregates formed predominantly by face–face and stair-step interactions participating in a mixture of interaction configurations—between aggregates such as edge–face, edge–edge and face–face. Many of the edge–face interactions involved a particle face resting on the edge of another particle at a very acute angle.

Fig. 6 shows the MR salt addition-pH result for KGa-2 and Crown kaolin. For KGa-2, the experiment was repeated with a fresh sample. The two sets of data fitted with a third order polynomimal. For both KGa-2 and Crown kaolin the ΔpH = 0 occurred at pH 4.2. This value is similar to the pH of zero zeta potential of 4 obtained for both at the same ionic strength of 0.1 M NaCl. It seemed that good agreement in value between the two methods was achieved. Different mixing methods—spatula mixing and sonication—were evaluated for their effect on the pzc value for Crown kaolin. No significant effect was observed.

The pzc of KGa-2 obtained here was in agreement with the value in the literature (Schroth B. and Sposito G., 1997; Du F. et al., 2010). Point of zero salt effect, point of zero net proton charge (pznpc) and point of zero net charge (pzc) of KGa-2 kaolin were reported to have a value of pH 2.8, 5.4 and ~4 respectively (Schroth B. and Sposito G., 1997). The good correlation between the maximum yield stress and IEP or pzc suggested that the surface chemistry–yield stress result can act as a good reference point for comparison by other kaolinites.

The low CaO Riedel kaolin also displayed similar yield stress–pH behaviour (**Fig. 7**), low yield stress at high pH and high yield stress at low pH. Complete dispersion ($\tau_y = 0$) of the slurries with 30 and 40 wt% solids was observed at pH 9. These slurries' maximum yield stress, τ_{ymax}, was located at pH 3. Its zeta potential–pH behaviour, however, did not display a pzc or IEP at low pH (**Fig. 8**). The trend of a decreasing negative zeta potential with decreasing pH was similar to others such as KGa-2 and Crown kaolin. The absence of pzc is probably due to the presence of mica/illite and quartz, as its main mineral impurities. Both these minerals have a very low IEP of ~2.0. The MR method, however, gave a pzc value of 4.0 for this kaolin (**Fig. 9**). Note that not all low CaO kaolin slurries displayed complete dispersion at high pH (Teh E. et al., 2009).

Unimin kaolin has a relatively high CaO content. Its

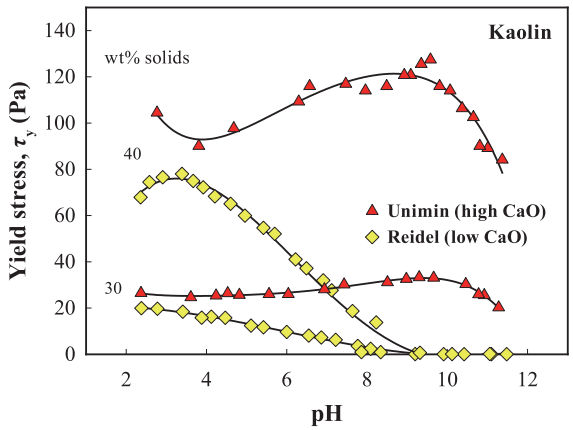

Fig. 7 Yield stress–pH behaviour of Riedel and Unimin kaolin slurries at 30 and 40 wt% solids.

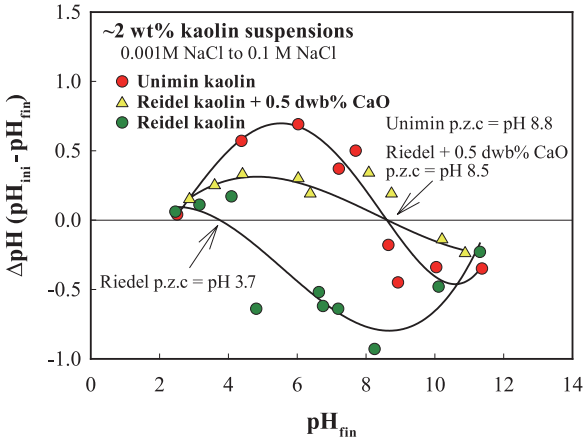

Fig. 9 The MR pH–salt titration curves of ~2 wt% Riedel and Unimin kaolin slurries showing the effect of calcium content in kaolinite.

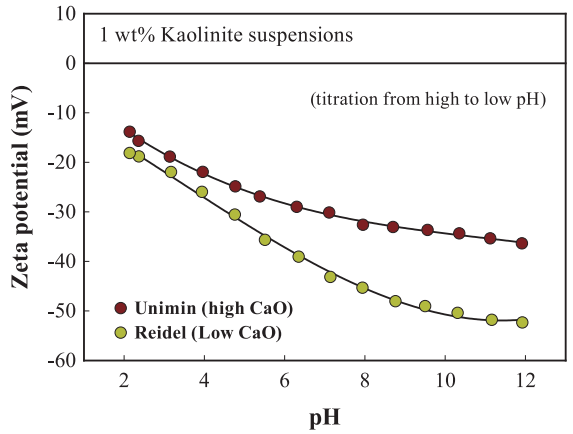

Fig. 8 Zeta potential–pH behaviour of 1 wt% low Ca(II) Riedel and high Ca(II) Unimin kaolin suspensions.

slurries displayed very different yield stress–pH behaviour (**Fig. 7**). The τ_{ymax} was located at pH 7–9 where the negative zeta potential is relatively large (**Fig. 8**). The addition of $CaSO_4$ was found to increase the Bingham yield stress of homoionic kaolinite slurries at alkaline pH (Lagaly G., 1989). The decreasing negative zeta potential with decreasing pH was similar to all others—Reidel, Fluka and Sigma kaolin (Teh E. et al., 2009). The magnitude of the zeta potential was smaller for the Unimin. No pH of zero zeta potential was observed. However the result of the MR method gave a high pzc value of pH 8.8 (see **Fig. 9**), which coincidentally was the location of the τ_{ymax}.

The value of the τ_{ymax} for the Unimin was much larger than that of Reidel at the same solid loading. At 30 wt% solids, the τ_{ymax} was 40 Pa for the Unimin compared to only 20 Pa for the Riedel. This is probably due to the smaller particle size of Unimin (3.26 μm) compared to Riedel (5.70 μm) which meant a higher particle concentration in the Unimin—which should result in more particles participating in attractive interaction forming a stronger network structure (Leong Y. et al., 1995).

From the elemental composition data in **Table 1**, it can be seen that all four kaolin—KGa-2, Crown, Reidel and Unimin—possessed similar iron content in terms of Fe_2O_3 and FeO. So, Fe content does not account for the differences in the yield stress–pH, zeta potential–pH and MR pzc results. The Ti content was very similar for KGa-2, Crown and Unimin. But it was very low in Reidel, 10 times smaller in concentration, and yet its yield stress-pH behaviour is very similar to that of KGa-2 and Crown kaolin. In addition, this Reidel kaolin has a very high content of K (from mica/illite impurities), at least 10 times larger than the other three kaolin. Only Unimin slurries displayed very different yield stress–pH behaviour. The only element significantly different to the others is the Ca(II) content quoted in terms of CaO. Avadiar L. et al. (2012; 2104; 2105) have conducted extensive studies on the effect of Ca(II) on the yield stress–pH and zeta potential–pH of kaolin, silica and alumina particles. They found that the addition of Ca(II) produced similar yield stress–pH behaviour in low CaO kaolin and that it also depressed the magnitude of the negative zeta potential. Their studies were quite conclusive in showing that CaO was the cause of the difference in yield stress–pH and zeta potential–pH behaviour.

Ca(II) shifts the maximum yield stress and pH of zero zeta potential to a higher pH (Avadiar L. et al. 2015). The adsorption of calcium ions on kaolinite surface increased in the high pH region in the form of positively charged of calcium complexes and precipitate in solution to provide positive charges to the negatively charged kaolinite surfaces (Atesok G. et al., 1988; Heidmann I. et al., 2005). Apart from that, the complex surface structure of poorly crystalline kaolinite produces a higher concentration of hydroxyl groups on the basal surfaces which provide ad-

ditional sites for the adsorption of Ca^{2+} ions. At low pH, Ca^{2+} ions adsorption has reduced as a result of increasing ionic strength and the competition with the dissolved Al^{3+}, Si^{4+}, Fe^{3+} and Cu^{2+} ions (Au P. et al. 2014; Heidmann I. et al., 2005; Zhou Z. and Gunter W., 1992). Therefore, Ca^{2+} is the cause of the shift in the location of the maximum yield stress and the increase in the yield strength of the kaolinite suspensions.

The excellent correlation between yield stress and zeta potential observed in KGa-2 and Crown kaolinite was not observed with Unimin. Although the zeta potential–pH behaviour does not explain the yield stress behaviour for the Unimin, it clearly demonstrated the effect of calcium content. The difference in magnitude of negative zeta potential between high Ca(II) Unimin and low Ca(II) Riedel kaolin was considerably larger at the high pH region. The smaller negative zeta potential of Unimin at high pH was attributed to the adsorption of calcium ions and its positively charged hydrolysis product (Avadiar L. et al., 2014; McFarlane A.J. et al., 2006). At low pH, and where calcium ions adsorption is not important, the zeta potential of both Riedel and Unimin kaolin was similar in value. This confirms the adsorption of calcium species affecting the properties and behaviour of kaolinites.

MR Salt–pH addition results in **Fig. 9** showed the $\Delta pH = 0$ was located at a particular pH (pzc for pure material) for both Riedel and Unimin kaolin. For Riedel kaolin, the $\Delta pH = 0$ was located at a much lower pH of 4, which was close to the location of the maximum yield stress. The addition of 0.5 dwb% CaO to Reidel shifted $\Delta pH = 0$ to a higher pH of 8.7, a value similar to that displayed by Unimin. This result showed that CaO was responsible for the high pH of $\Delta pH = 0$.

Kaolin slurries with low CaO content such as Reidel, Sigma and Fluka, obeyed the yield stress–DLVO model (Au P. and Leong Y., 2013; Teh E. et al., 2009). High CaO content Unimin slurries were found to obey this model only after treatment with phosphate-based additives (Leong Y. et al., 2012; Shankar P. et al., 2010). The linear decrease of τ_y with ζ^2 illustrated in **Fig. 10** showed that the Crown kaolin slurries also obeyed the model. The ζ^2_{cri} which characterises the state of transition from flocculated to disperse state (Leong Y.K. and Ong B.C., 2003; Teh E.J. et al., 2010) is very high, 6000–7000 mV^2. This does not mean its Hamaker constant in water is very high. Rather, positive edge-negative face interactions in kaolin slurries contributed to this high value.

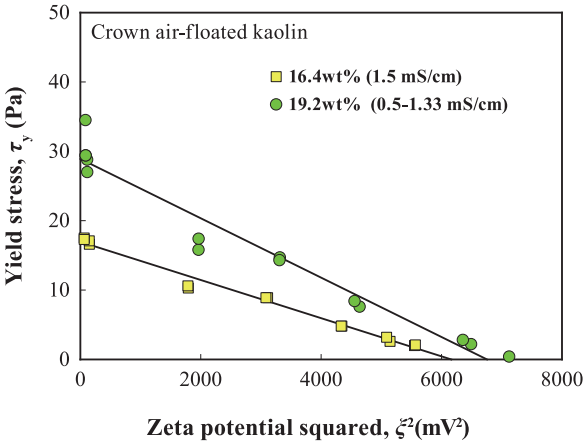

Fig. 10 The yield stress–DLVO model fit to the yield stress-zeta potential data of Crown kaolin.

3.2 Montmorillonite slurries

The complex rheological behaviour of Na^+Mt slurries is well-known and has been the subject of numerous studies with surface chemistry effects being the main focus (Lagaly G., 1989; Liang H. et al., 2010; Packter A., 1956; Paineau E. et al., 2011; Ramos-Tejada M. et al., 2001; Sakairi N. et al., 2005). The surface chemistry parameters evaluated were pH (Kelessidis V. and Maglione R., 2008; Lagaly G., 1989; Tombácz E. and Szekeres M., 2004), salt type and concentration (Abend S. and Lagaly G., 2000; Abu-Jdayil B., 2011; Brandenburg U. and Lagaly G., 1988; Yildiz N. et al., 1999), and a range of adsorbed additives such as pyro- and poly-phosphates (Goh R. et al., 2011; Lagaly G., 1989; Yoon J. and El Mohtar C., 2015), polymers (Dolz M. et al., 2007), and surfactants (Luckham P. and Rossi S., 1999; Permien T. and Lagaly G., 1994). The interpretation of the results was complicated by the pronounced swelling and thixotropic behaviour of these slurries (Abend S. and Lagaly G., 2000; Galindo-Rosales F. and Rubio-Hernández F., 2006; Lagaly G., 1989; Lee C. et al., 2012; van Olphen H., 1955, Yoon J. and El Mohtar C., 2013). Even the sequence of reagent addition such as KOH during gel preparation has a dramatic effect on the yield stress–pH behaviour (Au P. and Leong Y., 2013). Despite more 50 years of research on this material, there is still no consensus on the nature of the predominant interparticle forces operating in the Na^+Mt gels. Van Olphen H. (1951) suggested that the space-filling gel was due to attractive interaction between the positively charged edge and the negative face forming a card-house structure and many others agreed (Brandenburg U. and Lagaly G., 1988; Lockhart N., 1980). Norrish K. (1954) and others (Callaghan I. and Ottewill R., 1974; Paineau E. et al., 2011) believed that the electrostatic double layer (repulsive) force was responsible. Reliable information on the effect of surface chemistry such as pH and ionic strength on surface forces which could be evaluated in terms of rheological properties such as yield stress, shear modulus and viscosity, may help to settle this issue. However this was not helped by its (negative) zeta potential being quite pH-insensitive (Callaghan I. and Ottewill R., 1974; Goh R. et al., 2011) while its rheological properties such as yield

stress or intrinsic viscosity showing strong pH-dependence (Packter A., 1956; Goh R. et al., 2011). High concentrations (> 0.1 M) of common salts such as LiCl, NaCl, KCl and CsCl, were found to weaken the gel structure of the bentonite slurries which appeared to contradict the DLVO theory (Chang W. and Leong Y., 2014).

Like the kaolinite slurries, evaluation of the trend of the yield stress–pH behaviour should be included in establishing differences among the Na^+Mt slurries from difference sources rather than just comparing the rheological properties alone. Such evaluation should be accompanied by information on their zeta potential–pH behaviour. The evaluation of both the yield stress and zeta potential behaviour across a broad pH range was completed for bentonite and bentonite–kaolin composite slurries (Goh R. et al., 2011; Au P. and Leong Y., 2013). Past evaluations of rheological properties have been conducted at its natural pH, over a narrow pH range and at a small number of pH values. Packter A. (1956) evaluated the intrinsic viscosity of very dilute Na^+Mt sols over a very narrow pH range from 7 to 11.5. Here we present yield stress and zeta potential data across a wide pH range from 2 to 13 for a range of montmorillonite slurries. These slurries contained a significant amount of other mineral impurities and different exchangeable cations.

The time-dependent behaviour can complicate the comparison of the rheological properties of Na^+Mt gels from different sources. The ageing gels can have many rheological states. Comparison should be conducted at the same surface chemical and structural state (Chang W and Leong Y., 2014; Sehly K. et al., 2015). Ideally the rheological characterization should be conducted after the montmorillonite gels have attained surface chemical equilibrium and their flocculated network structure broken down to an equilibrium state. Doing this allowed the rheological data from different sources measured at this specific state which was easily attainable, to be quantitatively comparable.

The particle interaction configuration in the montmorillonite gel is crucial in understanding the relationship between surface forces and rheological behaviour. However, clear SEM/TEM images of distinct montmorillonite particles interacting are not possible to capture. According to Lagaly G. (2006) Na^+Mt particles are strictly not true crystals and the particles are an assemblage of disordered and bent silicate layers that do not have the regular shape of real crystals. In Ca^{2+}Mt particles, only a few silicate layers formed the coherent domains. These silicate layers are separated by two layers of water molecules.

The effect of mineral additives such as barite and kaolin on the ageing and rheological behaviour of bentonite slurries have been recently investigated (Yap J. et al., 2011; Au P. and Leong Y., 2015). Bentonite displayed a very large influence on the rheological and ageing behaviour of the composite slurries. To identify mineral impurities with a significant impact on rheological properties, more montmorillonite from various sources need to be evaluated. This paper will present surface chemistry and rheological results of well-characterised CMS source montmorillonite (Swy-2 and STx-1b) in terms of mineralogy, impurities and elemental compositions, and exchangeable cations in addition to surface properties such as BET area, CEC, layer and structural charges and others. In addition, similar types of results for other bentonite slurries with different mineral impurities are presented for comparison. One of these is an API bentonite containing a very high content of mineral impurities and having the following mineralogy: 24.5 % quartz (SiO_2), 1.3 % cristobalite (SiO_2), 1.5 % calcite ($CaCO_3$), 16.3 % kaolinite, 16.0 % sepiolite ($Mg_4Si_6O_{15}(OH)_2{\cdot}6H_2O$) and 40.4 % smectite (amorphous). **Table 2** lists its elemental composition which shows a relatively high content of iron compounds.

The yield stress–pH behaviour for (a) SWy-2 Na^+Mt and (b) for bentonite and API bentonite slurries is shown in **Fig. 11**. A characteristic feature of these clay mineral slurries is the very high yield stress of several hundred Pa at very low solid loading of a few wt%. The shape of the

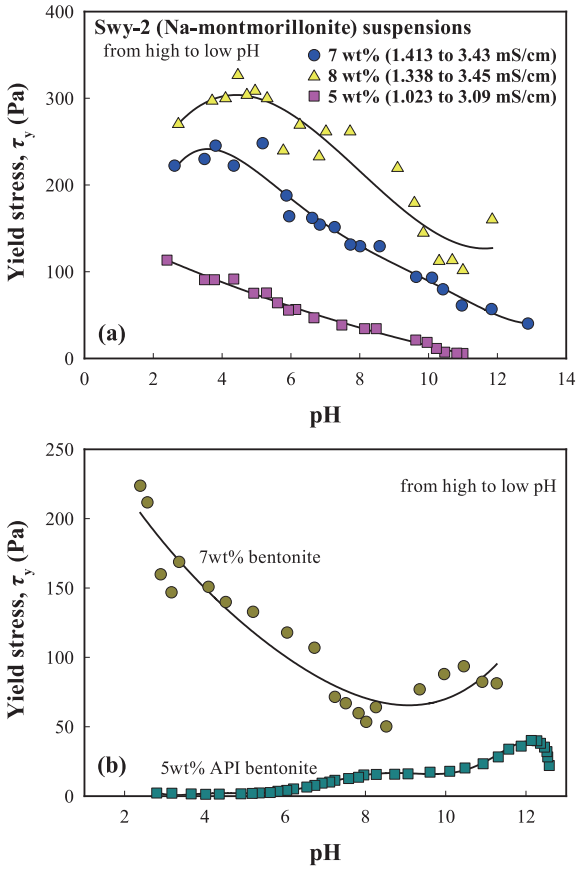

Fig. 11 The yield stress–pH behaviour of various a) montmorillonite and b) bentonite slurries.

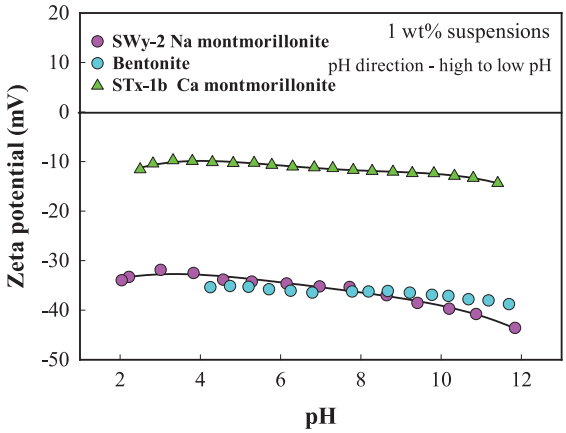

Fig. 12 Zeta potential–pH behaviour of montmorillonite and bentonite slurries.

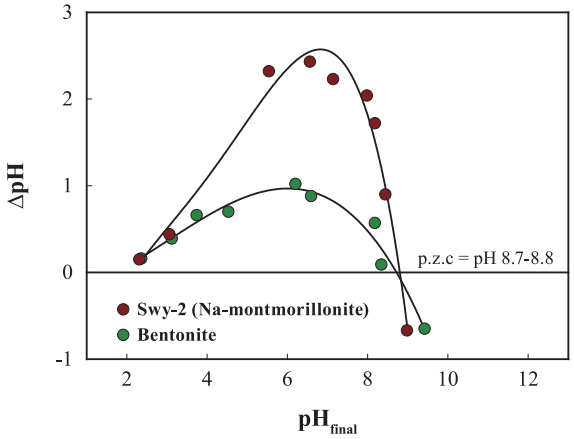

Fig. 13 MR results for Swy-2 and bentonite.

yield stress–pH curve of both the SWy-2 and bentonite slurries differed slightly. The Swy-2 displayed a yield stress decreasing with pH. At low pH the high yield stress showed a plateauing trend. The yield stress of the bentonite slurries displayed a minimum at pH 8 and an increasing yield stress that showed no plateau trend at low pH. Packter A. (1956) observed similar behaviour with Wyoming Na^{+}Mt sols with its intrinsic viscosity increasing with pH from pH 7 to 11.5. Similarly, Brandenburg U. and Lagaly G. (1988) observed a minimum shear stress at a fixed shear rate at pH ~ 8 for Wyoming bentonite and homoionic Na^{+}Mt slurries. The yield stress–pH behaviour of the API bentonite slurry is very different. It displayed almost no yield stress in the low pH region, between 3 to 6, and a maximum yield stress at pH 12. Its zeta potential was more pH–sensitive as shown in **Fig. 12**. The mineral composition showed that the montmorillonite content was relatively low at 40 % and the kaolinite and sepiolite content being relatively high, at 16.3 and 16 % respectively. Sepiolite is a magnesium silicate smectite with a fibrous morphology (Aznar A. et al., 1992). It formed stable thixotropic gel in water and was used as a rheological modifier. It is a common ingredient of drilling muds because of its rheological behaviour being insensitive to salt concentration and it also imparts high temperature stability to the muds (Galan E., 1996).

The dominant exchange cation in these clay minerals was Na^{+} which resided in the interlayer of the clay particles. In the presence of water molecules, hydration of the exchangeable Na^{+} ions occurred in the interlayer, bringing about surface charge development, which caused swelling and delamination of the particles. The delamination of smectite layered particles increased the number of primary particles and the concentration of these particles participating in attractive interactions. This is the likely cause of the much higher yield stress observed (Leong Y. et al., 1995).

The zeta potential–pH behaviour of SWy-2 Na^{+}Mt and bentonite slurries was very similar (**Fig. 12**). The insensitivity of the negative zeta potential to pH ranging from 2 to 12, was clearly displayed by these two clay minerals. This insensitivity is due to the pH–insensitive permanent negative charge accounting for 90–95 % of the total charges (Duc M. et al., 2005). There was no correlation between zeta potential and the yield stress for these clay mineral slurries. This gives the impression that the DLVO particle interaction theory is being violated. As can be seen in **Fig. 12**, the zeta potential–pH behaviour of STx-1b Ca^{2+} Mont also showed insensitivity to pH. The magnitude of the negative zeta potential is much lower than that of SWy-2 Na^{+}Mont slurries. Addition of Ca(II) ions does reduce the magnitude of the negative zeta potential of both smectite and kaolin slurries (McFarlane A. et al., 2006; Avadiar L. et al., 2014).

As **Fig. 13** illustrates, the MR method for SWy-2 and bentonite resulted in $\Delta pH = 0$ for both, at pH ~ 9.0. Both had a relatively high CaO content of 1.68 % (SWy-2) and 1.02 % (bentonite) as shown in **Table 2**. A similar pH value for $\Delta pH = 0$ was observed for kaolin with a high content of CaO (**Fig. 9**). Smectite (2:1) clay minerals normally possessed a higher SiO_2 content (**Table 2**). As the pzc of SiO_2 is located at a very low pH of 2.0, the smectite particles should also have a low pzc value. According to Reymond J. and Kolenda F. (1999) the pzc of mixed alumina and silica oxide would progress towards a lower pH as the silica content increases. For this SWy-2 slurry, Tombácz E. and Szekeres M. (2004) found no common pzc at different salt contents or no pzse (pH of zero salt effect). Even so, the edge pzc was attributed a pH value of ~ 7 (Tombácz E. and Szekeres M., 2004; Durán J. et.al., 2000; Heath D. and Tadros T., 1983)

Kosmulski M. (2011), however, attributed a pzc of pH 6.4–7.2 to Swy-2, which was obtained by potentiometric titration at different salt concentrations and a pzc of

pH 8.1, using the method of the common intersection point of potentiometric titration curves. He based these attributions on the data obtained by Tombácz E. and Szekeres M. (2004).

With Na^{+}Mt and bentonite suspensions, there is no obvious correlation between yield stress and zeta potential. Similarly, there is no correlation between the maximum yield stress and MR "pzc". This lack of correlation between surface properties and rheological properties is not uncommon with thixotropic swelling clay. This may be due to the rheological properties being determined by the swelling behaviour. The very high yield stress at low solid concentrations suggested a very high concentration of particles being released by the clay swelling participating in attractive particle interactions forming the very strong gel structure. Many studies have determined the particle interaction configurations (EE, FF and EF) of these smectite particles in water to be a function of pH, salt concentration and Ca(II) concentration (Stawinski J. et al., 1990; Żbik M. et al., 2008). However, clear SEM or TEM images of delaminated smectite particles interactions have not been available.

The trend of an increasing yield stress with decreasing pH of SWy-2 and bentonite is a reflection of a strengthening gel structure. This enhancement could be due to a stronger attractive interaction between particles or a stronger repulsion of the overlapping double layers. The enhancement at low pH was accompanied by 3 times the increase in the conductivity for the SWy-2 slurries. This meant a thinner double layer at this pH. The double layer repulsion responsible for the caging effect Norrish K., 1954; Callaghan I. and Ottewill R., 1974; Paineau E. et al., 2011) should be weaker and thus cannot be responsible for the yield stress enhancement. A stronger particle–particle attraction can come about by the following means:

i) the same particle interaction configuration but a stronger van der Waals or negative–positive charge attraction or both,

ii) a change to a stronger particle-particle interaction configuration—face–face to edge–face interactions; or

iii) more particles being release by the swelling and delamination process, increasing the number concentration of attractive interactions at lower pH.

The yield stress at high pH is due to the smectite particle–particle attraction being mediated by other positively charged particles and hydrolysis products of cations such as Mg(II) and Ca(II). These smectite particles are negatively charged since 90–95 % of the total charges being the permanent structural negative charge. A portion of Ca(II) content was locked in the less soluble minerals such as gypsum and plagioclase. At low acidic pH, these cations became hydrated and remained in solution, acting as an indifferent electrolyte. The pH–dependent charge density of the smectite particles increased at the same time. This could have changed the particle interaction configuration to a predominately EF interaction at low pH (van Olphen H., 1977; Heath D. and Tadros T., 1983).

The STx-1b montmorillonite suspension also displayed a pH insensitive zeta potential behaviour (**Fig. 12**). The magnitude of the negative zeta potential was much smaller. The predominant exchangeable cation of STx-1b was calcium (CMS, 2015). In contrast the main exchangeable cations of Swy-2 were sodium and calcium. A high proportion of these cations were the exchangeable interlayer cations. STx-1b can therefore be regarded as the Ca-form montmorillonite. The rheological behaviour of Ca^{2+}Mt was known to be very different to the Na^{+}Mt (van Olphen, H., 1955; 1957). The layered particle structure of Ca^{2+}Mt remained intact and the particles retained their aggregated behaviour (Lagaly, G., 1989; van Olphen H., 1957).

The yield stress–pH behaviour of the STx-1b Ca^{2+}Mt suspension is shown in **Fig. 14**. A much higher loading of solids was required to achieve a gel or yield stress material. The solid loading required was at least 20 wt%, ~ 4 times more concentrated than the lowest yield stress gel of SWy-2 Na^{+}Mt. The pH and magnitude of the τ_{ymax} increased with solid loading. The τ_{ymax} was 52, 190, 399 and 716 Pa located at pH 7.6, 8.3, 9.7 and 10.1 and for solid loadings of 20, 25, 30 and 40 wt% respectively. Unimin kaolin slurries with a relatively high CaO content also displayed a high pH of maximum yield stress of ~9. The yield stress of STx-1b slurries was smaller at low and high pH. The value was as low as zero for the 20 wt% slurries at pH 10.5 and ~17 Pa at pH 11 for the 25 wt% slurries. At pH 4 the yield stress was about 25 Pa for the 20 wt% slurry and 76 Pa for the 25 wt% slurry. This marked variation of the yield stress with pH bore no correlation with zeta potential-pH behaviour. Again the DLVO theory appeared not to explain the yield stress behaviour despite its lack of thixotropy. The higher solid loading required to form a gel is consistent with the earlier findings of H. van

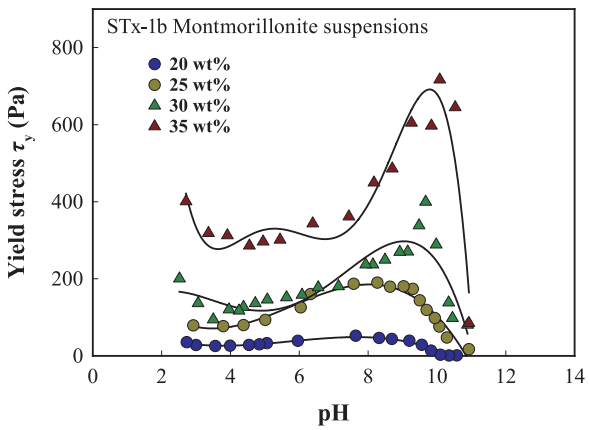

Fig. 14 Yield stress–pH behaviour of STx-1b (Ca^{2+}Mt) slurries.

Olphen (1955; 1957) research on Ca^{2+}Mt slurries.

The maximum yield stress–solids volume fraction relationships are shown in **Fig. 15** for the montmorillonite slurries. The value of the slope is 2.2 for SWy-2 and 3.8 for STx-1b. Hence the fractal dimension D_f of Na^{+}Mt slurries is 2.1 and that of Ca^{2+}Mt slurries is 2.5. The microstructure of STx-1b is thus more compact and more sphere-like in shape. A Cryo-SEM image of the STx-1b microstructure at the maximum yield stress prepared by plunged freezing of a slurry droplet is shown in **Fig. 16**. Connection of compacted domains in the microstructure was clearly seen. An image with such distinct particles was not available for SWy-2 slurries—a reflection of the delaminated silicate layers being in the nano-size dimension. For Unimin kaolin with more soluble Ca(II) minerals, the value of the slope was 3.6 to 3.9 (Au P. et al., 2014) similar to that obtained for the Ca^{2+}Mt slurries. It was found that 25 % of the CaO in the Unimin kaolin were soluble at pH 4.

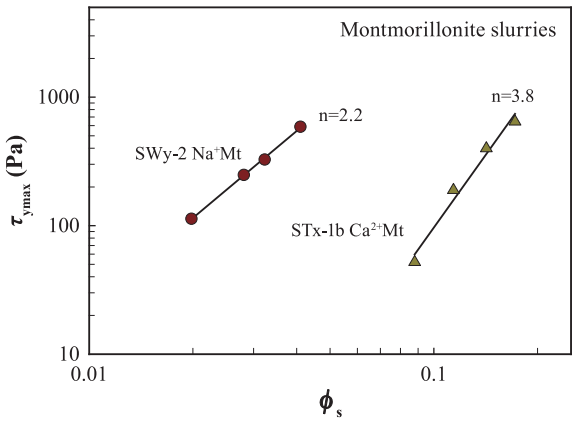

Fig. 15 The maximum yield stress–volume fraction relationship for Na^{+}Mt and Ca^{2+}Mt slurries.

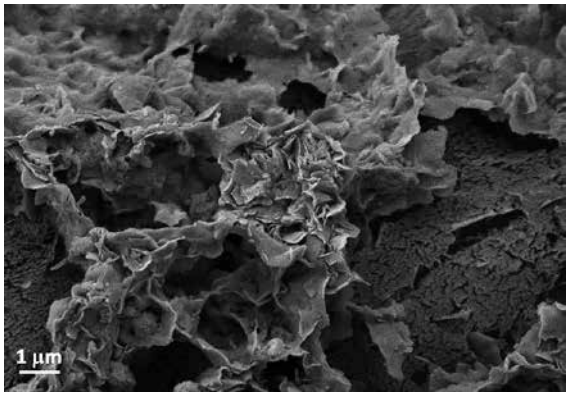

Fig. 16 Cryo-SEM of STx-1b slurries at the maximum yield stress (pH ~ 9.5).

4. Conclusion

All kaolinite slurries with a low CaO content displayed similar yield stress–pH behaviour: high yield stress at low pH and low yield stress at high pH. High CaO content kaolinite slurries displayed maximum yield stress at high pH of ~9. Many of the mineral impurities at the level in the as-received kaolinites played a small or insignificant role in determining this yield stress-pH behaviour. It was shown here that the difference in the trend of the yield stress–pH result could be used to identify factors in the kaolinite responsible for this difference.

For high purity Crown kaolinite, the pH of zero zeta potential or pzc showed a slight dependence on ionic strength. The pH-independent permanent structural charge required a lower pH for the clay mineral to acquire sufficient pH-dependent positive charge to neutralise it at lower ionic strength.

This study reviewed that the Mular–Roberts salt addition–pH method was not suitable for determining the point of zero charge (pzc) of clay minerals. This is particularly true for clay minerals containing a high content of basic impurities such as CaO. The addition of a small amount of CaO (0.5 %) to Reidel kaolin increased its pzc from 4 to 8. All clay minerals such as kaolin, bentonite and Na-montmorillonite, with high content of CaO, ranging from 0.5 to 1.7 %, displayed ΔpH sign reversal ("pzc") at pH 8–9.

For the two low CaO Crown and KGa-2 kaolin suspensions, the maximum yield stress is located at or near the point of zero zeta potential or zero charge of pH ~4. In addition to yield stress–pH behaviour both kaolinite slurries displayed similar zeta potential–pH behaviour and an identical maximum yield stress–solid volume fraction relationship. No point of zero zeta potential was detected for another low CaO Riedel kaolin slurry. The values of the power law exponent representing the yield stress-volume fraction relationship were similar: ~3 for all three low CaO kaolin slurries. In contrast high CaO Unimin kaolin displayed a maximum yield stress at pH ~9 and no point of zero zeta potential.

The negative zeta potential of SWy-2 Na^{+}Mt, STx-1b Ca^{2+}Mt and bentonite slurries was quite pH-insensitive. No clear correlation between the yield stress and zeta potential was observed for these slurries. Maximum yield stress was detected at a low pH < 3 for SWy-2 and bentonite and at a high pH > 9 for the STx-2b slurries. The swelling property of the SWy-2 and bentonite controlled its rheological behaviour to a greater extent than surface chemistry such as pH. The difficulty of imaging Na^{+}Mt particles via SEM or TEM suggests the swelling–liberated particles are nano-size in dimension. The high concentration of these nanoparticles can explain the demonstration of high yield stress at very low solid loading and the

time-dependent rheological behaviour displayed by Na^{+}Mt and bentonite slurries.

Unimin Kaolin and STx-1b Ca^{2+}Mt slurries displayed a larger power law exponent value of ~3.8. Both have a high content of soluble Ca(II) minerals or exchangeable Ca^{2+} .

Acknowledgment

The authors acknowledged the use of the facilities and the scientific and technical assistance of the Australian Microscopy & Microanalysis Research Facility at the Centre for Microscopy, Characterisation & Analysis, The University of Western Australia, a facility funded by the University, State and Commonwealth Governments. Visiting professor Weian Huang conducted the yield stress-zeta potential-pH characterization of the API bentonite during his stay at UWA.

Nomenclature

BET	Brunauer-Emmett-Teller
Ca^{2+}Mt	Calcium montomorillonite
CMS	Clay Mineral Society (USA)
CEC	Cation Exchange Capacity (meq.g^{-1})
DLVO	Deryaquin Landau Verwey Overbeek
MR	Mular-Roberts
Na^{+}Mt	Sodium montomorillonite
IEP	isoelectric point
pzc	point of zero charge
pzse	pH of zero salt effect
pznpc	point of zero net proton charge
pzse	point of zero salt effect
SEM	Scanning Electron Microscope
TEM	Transmission Electron Microscope
a	particle size (m)
A_H	particle Hamaker constant in water (J)
D_o	surface separation of interacting particles (m)
D_f	fractal dimension
ε	the relative dielectric constant of water (–)
ε_0	the permittivity of free space (C^2.J^{-1}.m^{-1})
ϕ_s	solid volume fraction (–)
κ	inverse of double layer thickness (m^{-1})
τ_y	yield stress (Pa)
τ_{ymax}	maximum yield stress (Pa)
ξ	zeta potential (mV)
ξ_{cri}	critical zeta potential (mV)

References

Abend S., Lagaly G., Sol–gel transitions of sodium montmorillonite dispersions, Applied Clay Science, 16 (2000) 201–227.

Abu-Jdayil B., Rheology of sodium and calcium bentonite–water dispersions: Effect of electrolytes and aging time, Int. J. Miner. Process., 98 (2011) 208–213.

Alvarez-Silva M., Uribe-Salas A., Mirnezami M., Finch J.A., The point of zero charge of phyllosilicate minerals using the Mular–Roberts titration technique, Minerals Engineering, 23 (2010) 383–389.

Appel C., Ma L.Q., Dean Rhue R., Kennelley E., Point of zero charge determination in soils and minerals via traditional methods and detection of electroacoustic mobility, Geoderma, 113 (2003) 77–93.

Atesok G., Somasundaran P., Morgan L.J., Adsorption properties of Ca^{2+} on Na-kaolinite and its effect on flocculation using polyacrylamides, Colloids and Surfaces, 32 (1988) 127–138.

Au P.I., Leong Y.K., Rheological and zeta potential behaviour of kaolin and bentonite composite slurries: Colloids Surfaces A: Physicochem. Eng. Aspects 436 (2013) 530–541.

Au P.I., Siow S.Y., Avadiar L., Lee E.M., Leong Y.K., Muscovite mica and koalin slurries: Yield stress–volume fraction and deflocculation point zeta potential comparison, Powder Technology, 262 (2014) 124–130.

Au P.I., Leong Y.K., Surface chemistry and rheology of laponite dispersions-zeta potential, yield stress, ageing, fractal dimension and pyrophosphate, Applied Clay Science, 107 (2015) 36–45.

Avadiar L., Leong Y.K., Fourie A., Nugraha T., Rheological Response to Ca(II) Concentration—The Source of Kaolin Slurry Rheological Variation, Chemeca 2012: The 42th Australasian Chemical Engineering Conference, Engineer Australia, (2012) 243.pdf.

Avadiar L., Leong Y.K., Fourie A., Nugraha T., Clode P.L., Source of Unimin kaolin rheological variation–Ca^{2+} concentration, Colloids and Surfaces A: Physicochemical and Engineering Aspects, 459 (2014) 90–99.

Avadiar L., Leong Y.K., Fourie A., Physicochemical behaviors of kaolin slurries with and without cations—Contributions of alumina and silica sheets, Colloids and Surfaces A: Physicochemical and Engineering Aspects 468 (2015) 103–113.

Aznar A.J., Casal B., Ruiz-Hitzky E., Lopez-Arbeloa I., Lopez-Arbeloa F., Santaren J., Alvarez A., Adsorption of methylene blue on sepiolite gels: spectroscopic and rheological studies, Clay Minerals, 27 (1992) 101–108.

Bolland M.D.A., Posner A.M., Quirk J.P., pH-Independent and pH-dependent surface charges on kaolinite, Clays and Clay minerals, 28 (1980) 412–418.

Brandenburg U., Lagaly G., Rheological properties of sodium montmorillonite dispersions, Applied Clay Science, 3 (1988) 263–279. Zbik, M.S., Smart R.S.C., Morris G.E., Kaolinite flocculation structure, Journal Colloid Interface Science, 328 (2008) 73–80.

Callaghan I.C., Ottewill R.H., Interparticle forces in montmo-

rillonite gels, Faraday Discussion, 57 (1974) 110–118.
Chang, W.Z., Leong, Y.K., Ageing and collapse of bentonite gels—effects of Li, Na, K and Cs ions, Rheological Acta, 53 (2014) 109–122.
Chipera S.J., Bish D.L., Baseline studies of the clay minerals society source clays: powder X-ray diffraction analyses. Clays and Clay Minerals, 49 (2001) 398–409.
CMS (Clay Mineral Society USA), 2015, SC Data <http://www.clays.org/SOURCE%20CLAYS/SCdata.html> accessed 1.04.2015.
Dolz M., Jiménez J., Hernández M.J., Delegido J., Casanovas A., Flow and thixotropy of non-contaminating oil drilling fluids formulated with bent and sodium carboxymethyl cellulose, Journal of Petroleum Science and Engineering, 57 (2007) 294–302.
Du J., Morris G., Pushkarova R.A., Smart R. St. C., Effect of Surface Structure of Kaolinite on Aggregation, Settling Rate, and Bed Density, Langmuir, 26 (2010) 13227–13235.
Duc M., Gaboriaud F., Thomas F., Sensitivity of the acid–base properties of clays to the methods of preparation and measurement: 1. Literature review, Journal of Colloid and Interface Science, 289 (2005) 139–147.
Durán J.D.G., Ramos-Tejada M.M., Arroyo F.J., González-Caballero F., Rheological and electrokinetic properties of sodium montmorillonite suspensions: I. rheological properties and interparticle energy of interaction, Journal of Colloid and Interface Science, 229 (2000) 107–117.
Galan E., Properties and application of palygorskite-sepiolite clays, Clay Minerals, 31 (1996) 443–453.
Galindo-Rosales F.J., Rubio-Hernández F.J., Structural breakdown and build-up in bentonite dispersions, Applied Clay Science, 33 (2006) 109–115.
Goh R., Leong Y.K., Lehane B., Bentonite slurries—zeta potential, yield stress, adsorbed additive and time-dependent behaviour, Rheologica Acta, 50 (2011) 29–38.
Gupta V., Hampton M.A., Stokes J.R., Nguyen A.V., Miller J.D., Particle interactions in kaolinite suspensions and corresponding aggregate structures, Journal Colloid Interface Science, 359 (2011) 95–103.
Heath D., Tadros T.F., Influence of pH, electrolyte, and poly (vinyl alcohol) addition on the rheological characteristics of aqueous dispersions of sodium montmorillonite, Journal of Colloid and Interface Science, 93 (1983) 307–319.
Heidmann I., Christl I., Leu C., Kretzschmar R., Competitive sorption of protons and metal cations onto kaolinite: experiments and modeling, Journal Colloid and Interface Science, 282 (2005) 270–282.
Humphries S.D., Vaniman D.T., Sharma S.K., Bates D.E., Misra A.K., Wiens R.C., McInroy R.E., Clegg S.M., Investigation of Mars clay analogs by remote Laser Induced Breakdown Spectroscopy (LIBS), 42nd Lunar and Planetary Science Conference (2011) 1851.pdf
Hunter R.J. Introduction to Modern Colloid Science, OUP, Oxford, p. 226 (2003).
Hunter R.J., Nicol S.K., The dependence of plastic flow behaviour of clay suspensions on surface properties: J. Colloid Interface Sci. 28 (1968) 250–259.
Kelessidis V.C. and Maglione R., Yield stress of water–bentonite dispersions, Colloids and Surfaces A: Physicochemical and Engineering Aspects, 318 (2008) 217–226.
Kosmulski M., The pH-dependent surface charging and points of zero charge: V. Update, Journal of Colloid and Interface Science, 353 (2011) 1–15.
Kranenburg C., On the fractal structure of cohesive sediment aggregates, Estuarine Coast Shelf Science, 39 (1994) 451–460.
Lagaly G., Principles of flow of kaolin and bentonite dispersions, Applied Clay Science, 4 (1989) 105–123.
Lagaly G., Colloid clay science, in: Bergaya F., Theng B.K.G., Lagaly G. (Eds.), Handbook of Clay Science, Elsevier, Amsterdam, 2006, pp.141–142.
Laxton P.B., Berg J.C., Relating clay yield stress to colloidal parameters, Journal of Colloid and Interface Science, 296 (2006) 749–755.
Lee C.E., Chandra S., Leong Y.K., Structural recovery behaviour of kaolin, bentonite and K-montmorillonite slurries. Powder Technology, 223 (2012) 105–109.
Leong Y.K., Ong B.C., Critical zeta potential and the Hamaker constant of oxides in water, Powder Technology, 134 (2003) 249–254
Leong Y.K., Scales P.J., Healy T.W., Boger D.V., Effect of Particle Size on Colloidal Zirconia Rheology at the Isoelectric Point, Journal of the American Ceramic Society, 78 (1995) 2209–2212.
Leong Y.K., Teo J., Teh E.J., Smith J., Widjaja J., Lee J.X., Fourie A., Fahey M., Chen R., Controlling attractive interparticle forces via small anionic and cationic additives in kaolin clay slurries, Chemical Engineering Research and Design, 90 (2012) 658–666.
Liang H.N., Long Z., Zhang H., Yang S.H., Rheological properties of acid-activated bentonite dispersions. Clays and Clay Minerals, 58 (2010) 311–317.
Lockhart N.C., Electrical properties and the surface characteristics and structure of clays I. swelling clays, Journal Colloid Interface Science, 74 (1980) 509–519.
Luckham P.F., Rossi S., The colloidal and rheological properties of bentonite dispersions. Advanced Colloid Interface Science, 82 (1999) 43–92.
McFarlane, A.J., Addai-Mensah, J., Bremmell, K.E., Improved dewatering behaviour of clay minerals dispersions via interfacial chemistry and particle interactions optimization. J. Colloid Interface Sci., 293(2006) 116–127.
Melton I.E., Rand B., Particle interactions in aqueous kaolin suspensions II. Comparison of some laboratory and commercial kaolin samples, Journal Colloid Interface Science, 60 (1977) 321–330.
Mular A.L., Roberts R.B., A simplified method to determine isoelectric points of oxides Transactions of the Canadian Institute of Mining and Metallurgy, 69 (1966) 438–439.
Ndlovu B., Forbes E., Farrokhpay S., Becker M., Bradshaw D., Deglon D., A preliminary rheological classification of phyllosilicate group minerals, Minerals Engineering, 55 (2014) 190–200.
Nguyen Q.D., Boger D.V., Yield stress measurement for concentrated suspensions, Journal of Rheology 27 (1983) 321–349.
Norrish K., The swelling of montmorillonite, Discussion Faraday

Society, 18 (1954) 120–134.
Packter A., Studies in the rheology of clay-water systems, Kolloid-Z, 149 (1956) 109–115.
Paineau E., Michot L.J., Bihannic I., Baravian C., Aqueous suspensions of natural swelling clay minerals. 2. rheological characterization, Langmuir, 27 (2011) 7806–7819.
Permien T., Lagaly G., The rheological and colloidal properties of bentonite dispersions in the presence of organic compounds IV. sodium montmorillonite and acids, Applied Clay Science 9 (1994) 251–263.
Pradip, Li C.C.H., Fuerstenau D.W., Surface chemical characterization of bastnaesite through electrokinetics, KONA Powder and Particle Journal, 32 (2015) 176–183.
Ramos-Tejada M.M., Arroyo F.J., Perea R., Duran J.D., Scaling behavior of the rheological properties of montmorillonite dispersions: correlation between interparticle interaction and degree of flocculation, Journal Colloid Interface Science, 235 (2001) 251–259.
Rand B., Melton I.E., Particle interactions in aqueous kaolinite suspensions: I. Effect of pH and electrolyte upon the mode of particle interaction in homoionic sodium kaolinite suspensions, Journal of Colloid Interface Science, 60 (1977) 308–320.
Reymond J.P., Kolenda F., Estimation of the point of zero charge of simple and mixed oxides by mass titration, Powder Technology, 103 (1999) 30–36.
Sakairi N., Kobayashi M., Adachi Y., Effects of salt concentration on the yield stress of sodium montmorillonite suspension, Journal Colloid Interface Science, 283 (2005) 245–250.
Scales P.J., Johnson S.B., Healy T.W., Kapur P.C., Shear yield stress of partially flocculated colloidal suspensions, American Institute Chemical Engineering Journal, 44 (1998) 538–544.
Schroth B.K., Sposito G., Surface charge properties of kaolinite, Clays and Clay minerals, 45 (1997) 85–91.
Sehly K., Chiew H.L., Li H., Song A., Leong Y.K., Huang W., Stability and ageing behaviour and the formulation of potassium-based drilling muds, Applied Clay Science, 104 (2015) 309–317.
Shankar P., Teo J., Leong Y.K., Fourie A., Fahey M., Adsorbed phosphate additives for interrogating the nature of interparticle forces in kaolin clay slurries via rheological yield stress, Advanced Powder Technology, 21 (2010) 380–385.
Stawinski J., Wierzchos J., Garcia-Gonzalez M.T., Influence of calcium and sodium concentration on the microstructure of bentonite and kaolin, Clays and Clay Minerals, 38 (1990) 617–622.
Teh E.J., Leong Y.K., Liu Y., Fourie A,B., Fahey M., Differences in the rheology and surface chemistry of kaolin clay slurries: the source of the variations, Chemical Engineering Science, 64 (2009) 3817–3825.
Teh E.J., Leong Y.K., Liu Y., Ong B.C., Berndt C.C., Chen S.B., Yield stress and zeta potential of washed and highly spherical oxide dispersions—critical zeta potential and Hamaker constant, Powder Technology, 198 (2010) 114–119.
Tombácz E., Szekeres M., Colloidal behavior of aqueous montmorillonite suspensions: the specific role of pH in the presence of indifferent electrolytes, Applied Clay Science, 27 (2004) 75–94.
Tombácz E., Szekeres M., Surface charge heterogeneity of kaolinite in aqueous suspension in comparison with montmorillonite, Applied Clay Science, 34 (2006) 105–124.
van Olphen H., Rheological phenomena of clay sols in connection with charge distribution on the micelles, Discussion Faraday Society, 11 (1951) 82–84.
van Olphen, H., Forces between suspended bentonite particles. Clays and Clay Minerals, 4 (1955) 204–224.
van Olphen, H., Forces between suspended bentonite particles part II—calcium bentonite. Clays and Clay Minerals, 6 (1957) 196–206.
van Olphen H., An Introduction to Clay Colloid Chemistry, Wiley, New York, 1977.
Wessel R., Ball R.C., Fractal aggregates and gels in shear flow, Physical Review A, 46 (1992) R3008–R3011.
Yap J., Leong Y.K., Liu J., Structural recovery behavior of barite-loaded bentonite drilling muds, Journal Petroleum Science and Engineering, 78 (2011) 552–558.
Yildiz N., Sarikaya Y., Çalimli A., The effect of the electrolyte concentration and pH on the rheological properties of the original and the Na2CO3-activated Kütahya bentonite, Applied Clay Science, 14 (1999) 319–327.
Yoon J., El Mohtar C., Dynamic rheological properties of sodium pyrophosphate modified bentonite dispersions for liquefaction mitigation, Clays and Clay Minerals 61 (2013) 319–327.
Yoon J., El Mohtar C., Constitutive model parameters of concentrated bentonite suspensions modified with sodium pyrophosphate, Journal of Material Science, (2015) DOI 10.1007/s10853-015-9073-2.
Żbik M.S., Smart R.S.C., Nanomorphology of kaolinites: comparative SEM and AFM studies, Clays and Clay minerals, 46 (1998) 153–160.
Żbik M.S., Smart R. St.C., Morris G.E., Kaolinite flocculation structure, Journal of Colloid Interface Science, 328 (2008) 73–80.
Żbik M.S., Raftery N.A., Smart R.S.C., Frost R.L., Kaolinite platelet orientation for XRD and AFM applications, Applied Clay Science, 50 (2010) 299–304.
Zhou Z., Gunter W.D., The nature of the surface charge of kaolinite, Clays and Clay minerals, 40 (1992) 365–368.

Author's short biography

Pek-Ing Au

Pek-Ing Au is a PhD student in the School of Mechanical and Chemical Engineering, The University of Western Australia. She obtained a first class honours in Chemical and Process Engineering from the same university in 2012. She has several journal and conference publications.

Yee-Kwong Leong

Yee-Kwong Leong employed rheological yield stress technique to study surface forces especially those arising from adsorbed additives, in colloidal suspensions. He has over 100 publications in this area. Some of his experimental results can be found in textbooks such as the "Structure and Rheology of Complex fluid" and "Suspension Rheology". An ageing or structural recovery model was named after him by his colleagues. He is a professor at the School of Mechanical and Chemical Engineering, The University of Western Australia. He obtained his PhD in 1989 from the University of Melbourne.

KONA Powder and Particle Journal No. 33 (2016) 33–47/Doi:10.14356/kona.2016010 Review Paper

Controlled Magnetic Properties of Iron Oxide-Based Nanoparticles for Smart Therapy †

Dung The Nguyen and Kyo-Seon Kim*

[1] *Department of Chemical Engineering, Kangwon National University, Republic of Korea*

Abstract

Magnetic nanoparticles provide a unique nanosystem for various smart therapy applications because of their biocompatibility, their nanostructures which can be prepared controllably to match with the interest of study and, specifically, their responses to an external magnetic field. Interests in utilizing magnetic nanoparticles for biomedical treatments originate from their external controllability of transportation and movement inside biological objects and magnetic heat generation which provide tremendous advantages for targeted drug delivery and controlled drug release as well as magnetic hyperthermia. Recent progress in synthesis and functionalization has led to the formation of various functional magnetic nanoparticles with controlled magnetic properties based on controlling their particle size, shape and composition. In this review, we focus on the synthesis, protection and functionalization of iron oxide-based magnetic nanoparticles in order to control magnetic properties of nanostructured systems. We also highlight the recent advances in the development of multifunctional therapeutic nanosystems combining magnetic nanoparticles and drugs as well as their superior efficacy in biomedical treatments with smart performance by including therapy and modulated drug delivery and release through magnetic heating.

Keywords: magnetic nanoparticles, magnetic properties, controlled synthesis, therapy, hyperthermia, drug delivery

1. Introduction

Over the last decades, interest in magnetic nanoparticles has increased enormously. The magnetic nanomaterials are unique because of their magnetic behaviors with magnetic fields and field gradients. Fundamental researches exploiting various nanostructures with corresponding magnetic characteristics have utilized magnetic nanoparticles for various applications. The magnetic nanoparticles with appropriate modifications have been extensively investigated for biomedical and pharmaceutical applications such as drug delivery, hyperthermia, magnetic resonance imaging, tissue engineering and repair, biosensing, biochemical separations, and bioanalysis as widely reported and reviewed (Hervault and Thanh, 2014; Kumar and Mohammad, Laurent et al., 2008; Lu et al., 2007; 2011; Nguyen and Kim, 2014; Reddy et al., 2012). In the field of disease therapy, advances in magnetic nanoparticle technology resulted in the development of theranostic nanoparticles which consist of therapeutic and diagnostic agents within a single particle. These magnetic nanoparticles should possess very uniform morphology with high magnetization values which ensure the external controllability. They also must have good dispersion, stability and biocompatibility to prevent endocytosis by macrophages as well as to extend their residence time in circulating blood. The developments and applications of these nanoparticles strongly require synthesis of magnetic nanoparticles of customized size and shape with appropriate surface engineering. Precise control over the synthetic conditions and surface functionalization of magnetic nanoparticles is crucial because it governs their magnetic characteristics, colloidal stability, physicochemical properties, and biological responses. However, the magnetic nanoparticles obtained under different synthetic conditions may display large differences regarding their magnetic properties due to formation of structural disorder and phase boundaries, or the existence of a magnetically dead layer at the particle surface. Therefore, to understand, exploit and improve applications of magnetic nanoparticles as well as to develop new ones, careful studies for controlled synthesis and surface modification are utmost important.

Herein, we briefly discuss the backgrounds on physical properties of magnetic nanoparticles and then introduce the design strategies for magnetic nanoparticles as a smart

† Received 30 June 2015; Accepted 21 July 2015
J-STAGE Advance published online 20 August 2015
[1] Chuncheon, Kangwon-do, 200-701, Republic of Korea
* Corresponding author: Kyo-Seon Kim;
E-mail: kkyoseon@kangwon.ac.kr
TEL: +82-33-250-6334

platform for controlled drug delivery and hyperthermia treatment. We will highlight the recent progress on the synthesis of magnetic nanostructures with growth mechanisms in order to control their magnetic behavior. We also introduce and discuss some typical developments of mechanical actuation and manipulation of drug release. Finally, we will highlight recent state-of-the-art uses of magnetic nanoparticles in hyperthermia treatment.

2. Magnetism and engineering of magnetic nanoparticles for smart therapies

The properties of magnetic materials are characterized by the alignment of atomic magnetic moments generated by the spinning of electrons. The atomic magnetic moments can be aligned in a parallel or antiparallel fashion with respect to the neighboring ones in the crystal lattice and this type of interaction gives rise to the macroscopic magnetic behaviors which are usually measured by magnetization, coercivity, and magnetocrystalline anisotropy constant (Leslie-Pelecky, 1996). A large-sized magnetic material usually consists of a number of domains in order to minimize its internal energy and exhibits ferromagnetic characteristics. When an external magnetic field of strength is applied to a multidomain magnetic particle, the magnetization increases with the increase of magnetic field until a saturation value is reached because the magnetic moments tend to align themselves in the same direction of applied field. When these particles are removed from the magnetic field, the magnetic domains do not return to their original orientations and cause a remnant magnetization. The remnant magnetization can only be removed by applying a coercive field in the opposite direction to the initially applied field. The coercivity is strictly related to the magnetocrystalline anisotropy constant which reflects the energy required to change the direction of magnetic moments.

When the particle size decreases to a certain level, the formation of a domain wall structure is not thermodynamically favored and thus the magnetic nanoparticles consist of all spins aligned in the same direction (Bean and Livingston, 1959). As the particle size decreases toward critical particle diameter for single domain structure, D_{sd}, the formation of domain walls becomes energetically unfavorable and the particles are called single domain. As the particle size continues to decrease and reaches a critical size where thermal energy exceeds the magnetic anisotropy energy barrier, the magnetization measured in a finite time interval or that in a removal of an external magnetic field is zero. This particle size represents the critical size for superparamagnetism behavior, D_{sp}, and such particles are superparamagnetic. The characteristic temperature which defines a transition from ferromagnetic to a thermally unstable or superparamagnetic behavior is called the blocking temperature, T_B. The corresponding magnetization curve of the superparamagnetic material exhibits a saturation of the magnetization and no hysteresis around the origin. The negligible remnant magnetization of superparamagnetic nanoparticles is advantageous because the nanoparticles can avoid their aggregation during preparation and storage and after administration. The magnetism of nanoparticles is mainly determined by the type of material, the crystallinity of the structures, and also the particle size. The critical size for single domain structure and that for superparamagnetic behavior could be predicted as shown in **Fig. 1** (Krishnan et al., 2006 and Krishnan, 2010) by using the physical theories for domain stability in crystalline particles (Kittel C., 1949) as well as the bulk properties available in the literature. Analysis and calculation for the critical sizes for magnetization behavior and that for single-domain behavior could be referred from Bean (1955) and Frei et al (1957), respectively.

The magnetic behavior of magnetic nanoparticles in a specific system is the results of both the intrinsic properties of the nanoparticles and the interactions between nanoparticles and surrounding materials. The biomedical applications of magnetic nanoparticles depend on a number of factors related to the size, shape and magnetism of the biocompatible nanoparticles as well as the physicochemical properties of the drug-loaded nanoparticles, field strength and geometry, depth of target tissue, rate of blood flow and so on. In order to maximize performance of magnetic nanoparticles in biomedical applications, it is

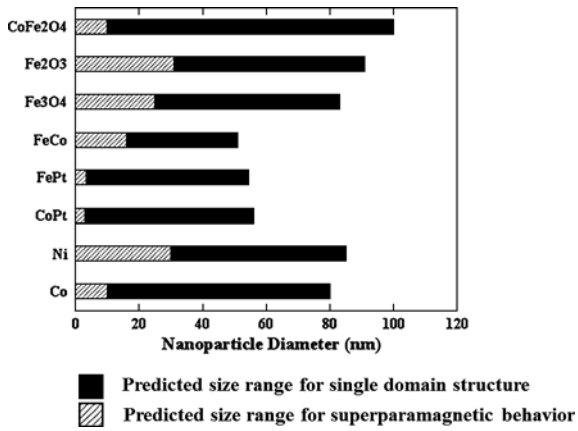

Fig. 1 Predicted size ranges for single domain structure and superparamagnetism behavior of common magnetic materials. For diameters (D) larger than maximum diameter for single domain structure (D_{sd}), $D > D_{sd}$, the magnetic materials split into multiple domains; for diameters (D) smaller than maximum diameter for superparamagnetism behavior (D_{sp}), $D < D_{sp}$, they exhibit superparamagnetism; and for diameters in between, $D_{sd} > D > D_{sp}$, they are single domain and ferromagnetic (Krishnan et al., 2006; Krishnan, 2010).

necessary to consider the change of magnetic characteristics in the presence of various biocompatible coating or suspension media. In fact, surface modification and functionalization of magnetic nanoparticles is required to protect particle agglomeration and to provide functional groups for the conjugation of other materials such as drugs, targeting ligands, proteins and DNA sequences (Cuyper et al., 2007; Gupta and Curtis, 2004; Liu et al., 2008; Ma et al., 2006). Such modification can be achieved by a diverse group of materials such as polymeric stabilizers/surfactants like dextran (Bulte et al., 1992), carboxydextran (Briley-Saebo et al., 2006), poly(ethylene glycol) (PEG) (Butterworth et al., 2001; Lutz et al., 2006) or poly(vinyl alcohol) (PVA) (Liu et al., 2008); or by a layer of oxide surfaces (SiO_2) (Chastellain, et al., 2004), or inorganic metals (gold) (Jeong et al., 2006).

When polymeric materials are employed as stabilizers, the adsorption of polymers onto the magnetic nanoparticles provides protective steric repulsion and acts as a barrier against the interaction between the particles and thus keeping the particles from aggregation (Duran et al., 2008). The polymeric coatings can also tailor the surface properties by introducing new chemical functionality and surface charge to the nanoparticles for further attachment of other materials. The key characteristics of polymeric materials should be considered including length and molecular weight, biodegradability and hydrophobic/hydrophilic nature, conformation, degree of surface coverage, and attachment mechanism to the particle surface. Several functional materials such as dimercaptosuccinic acid (Fauconnier et al., 1997), bisphosphonates (Portet et al., 2001) may be employed to facilitate the efficient attachment of the polymers onto the surface of magnetic nanoparticles.

Inorganic coatings such as gold and SiO_2 are other useful coating materials. For instance, Au-Fe_3O_4 nanoparticles could be synthesized by controlling growth of Au on the surface of Fe_3O_4 (Goon et al., 2009; Nguyen et al., 2011; Xu et al., 2007) and the Au could provide new surface to be functionalized with various ligands such as protein, oligonucleotide, DNA sequences through Au–S covalent bonding as reviewed (Nguyen et al., 2011). Robinson et al. (2010) reported that surface coating of Fe_3O_4 by Au nanoparticles and subsequent functionalization with thiolated DNA slightly reduced the magnetization saturation due to addition of nonmagnetic materials but helped particles to remain stable in aqueous solution. It was also discussed that gold coating could modify the magnetic properties by isolating the magnetic cores and thus could provide possibility of producing very efficient nanostructures (Banerjee et al., 2011; Wang et al., 2005). For example, a gold coating of approximately 0.4 to 0.5 nm thickness around superparamagnetic iron oxide nanoparticles resulted in a four- to five-fold increase in the amount of heat release in comparison with uncoated nanoparticles on application of low frequency oscillating magnetic fields (Mohammad et al., 2010).

It should be noted that, in most cases, the presence of polymers or other nonmagnetic materials may induce the imperfections in crystal structure that, consequently, may negatively influence the magnetic properties of the nanoparticles. However, it has also been observed that it is possible to maintain the magnetic properties by coating the magnetic nanoparticles with phosphonates (Daou et al., 2008) which are supposed to reduce the spin canting in the particle surface. In fact, since the magnetic response of a system to the surface modification is complex and system specific, no correlation between surface coating and magnetic response of a system has been clearly established.

3. Controlled properties of nanoparticles

Many publications have described the efficient synthetic procedures to size- and shape-controlled, highly stable, and monodisperse magnetic nanoparticles. High-quality magnetic nanoparticles have been synthesized with a number of different methods such as chemical co-precipitation (Massart, 1981; Wu et al., 2007), thermal decomposition and/or reduction (Kimata et al., 2003), microemulsion synthesis (Chin and Yaacob, 2007), hydrothermal/solvothermal synthesis (Chen et al., 2008; Khollam et al., 2002). Among these methods, the magnetic nanoparticles prepared from thermal decomposition and hydrothermal/solvothermal approaches exhibit high uniformity in both size, shape with excellent magnetic properties and the preparation processes show high potential on a large scale fabrication. Herein, we highlight several typical synthesis processes to control magnetic properties of nanoparticles with the corresponding particle formation mechanisms, focusing on the Fe_3O_4-based material.

Monodisperse and superparamagnetic iron oxide nanoparticles have been widely synthesized by thermal decomposition of organometallic compounds in high-boiling organic solvents containing stabilizing surfactants. Since the system temperature is high, the magnetic nanoparticles are formed with high crystallinity and magnetization. Sun et al. (2002 and 2004) reported a synthesis of 4 nm monodisperse magnetite nanoparticles by refluxing a reaction mixture containing the iron (III) acetylacetonate, $Fe(acac)_3$, 1,2-hexadecanediol, oleic acid, and oleylamine in diphenyl ether solvent (boiling point of 265 °C), while 6-nm monodisperse Fe_3O_4 nanoparticles were obtained in benzyl ether solvent (boiling point of 300 °C). The oleylamine acted as both reducing agent and stabilizer to obtain monodisperse nanoparticles. To make larger Fe_3O_4

nanoparticles, a seeded growth process was demonstrated for generating nanoparticles up to 16 nm by controlling the ratio of seed to additional precursor. The magnetic saturation values of 16 nm magnetite nanoparticles were experimentally determined to be excellent with a value of 83 emu g^{-1}. In another study, monodisperse magnetic nanoparticles were synthesized by mixing iron oleate with octadecane and oleic acid, followed by heating to 300 °C (Jana et al., 2004). The diameter of the Fe_3O_4 nanoparticles could be controlled between 6 and 50 nm by changing the ratio of ferric oleate to oleic acid from 0.1 to 10. Similar to that in the synthesis of Fe_3O_4 nanoparticles, the high temperature reaction of $Fe(acac)_3$ and $Mn(acac)_2$ gives monodisperse $MnFe_2O_4$ nanoparticles with their size, composition, and shape controlled by the reactant concentrations (Zeng et al., 2004). It was reported that triethylene glycol directly reacted with $Fe(acac)_3$ at an elevated temperature to prepare non-agglomerated Fe_3O_4 nanoparticles with uniform shape and narrow size distribution (Cai and Wan, 2007).

Hyeon's group prepared monodisperse iron oxide nanoparticles with sizes of 4, 8, and 11 nm by thermal decomposition of $[Fe(CO)_5]$ as iron precursor and oleic acid with different molar ratios, followed by controlled chemical oxidation with trimethylamine N-oxide as a mild oxidant (Hyeon et al., 2001). In this synthesis, monodisperse iron nanoparticles were initially generated, and these were further oxidized controllably by trimethylamine N-oxide to produce iron oxide nanoparticles. The particle size could be controlled by using different solvents with different boiling points. For instance, 5-, 9-, 12-, 16-, and 22-nm-sized iron oxide nanoparticles were synthesized by using 1-hexadecene, octyl ether, 1-octadecene, 1-eicosene, and trioctylamine which have the boiling point of 274 °C, 287 °C, 317 °C, 330 °C and 365 °C, respectively (Park et al., 2007). The current synthetic procedure is quite general, and nanoparticles of many transition-metal oxides, such as MnO, CoO, and ZnO, have been synthesized by using a similar procedure. Hyeon's group also reported that sequential decomposition of iron pentacarbonyl and the iron oleate complex at different temperatures results in the formation of monodisperse iron nanoparticles in the size range of 6–15 nm (Park et al., 2005). The overall synthetic procedure was similar to seed-mediated growth. The thermal decomposition of $[Fe(CO)_5]$ at relatively low temperature induced short burst of nucleation from a supersaturated solution, and the decomposition of the iron oleate complex at a higher temperature facilitated subsequent growth of particles without any significant additional nucleation (Kwon et al., 2007). They also developed an ultra-large-scale synthesis of 40-g monodisperse Fe_3O_4 nanoparticles using Fe-oleate complex prepared from hydrated iron chloride and sodium oleate as reactants as shown in **Fig. 2** (Park et al., 2004). The magnetic nanoparticles are dispersible in various organic solvents including hexane and toluene. The water-soluble magnetite nanoparticles could be prepared under similar reaction conditions with addition of α,ω-dicarboxyl-terminated poly(ethylene glycol) as a surface capping agent (Hu et al., 2006).

Zhao et al. (2008) reported the formation of nanoporous Fe_3O_4 particles with excellent magnetic properties and various specific morphologies by simply changing the solvent system and amount of KOH. In a typical process, the $FeSO_4$ was dissolved in ethylene glycol or glycerol to form a homogeneous solution, followed by a quick addition of KOH at room temperature. The mixture was then transferred into a Teflon lined stainless steel autoclave, sealed, and maintained at 200 °C for 24 h for the complete formation of product particles. The KOH concentration and solvent properties determined the growth of particles, leading to the evolution of different particle morphologies including cube, truncated octahedron, octahedron, sphere, truncated cube and equilateral octahedron. All particles exhibited magnetic saturation values of around 90 emu g^{-1} with negligible remnant magnetization and coercivity.

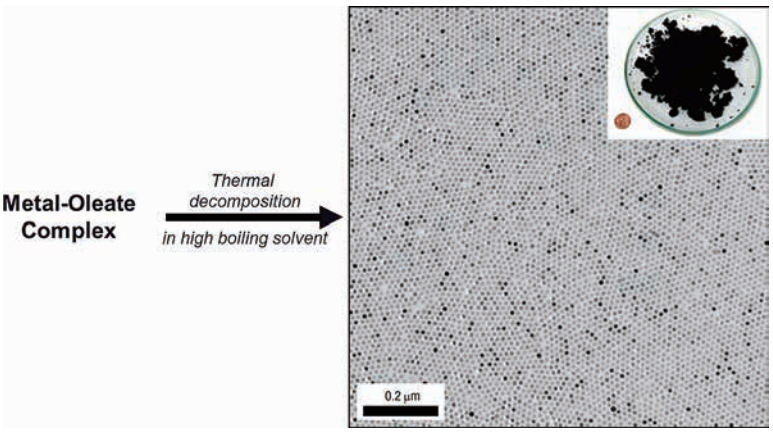

Fig. 2 The overall scheme for the ultra-large-scale synthesis of monodisperse magnetic nanoparticles (Park et al., 2004).

It is utmost important to synthesize monodisperse and superparamagnetic nanoparticles with high saturation magnetization values. A metal dopant of ferrite nanoparticles has been pursued to achieve high and tunable nanomagnetism (Beji et al., 2010; Hochepied and Pileni, 2000; Sun et al., 2004). Jang et al. (2009) synthesized Zn^{2+} doped ferrite nanoparticles ($(Zn_xMn_{1-x})Fe_2O_4$ and $(Zn_xFe_{1-x})Fe_2O_4$, with x = 0, 0.1, 0.2, 0.3, 0.4, and 0.8) by thermal decomposition of a metal chloride (MCl_2, M = Zn^{2+}, Mn^{2+}, and Fe^{2+}) with $Fe(acac)_3$. The Zn^{2+} doping level was carefully controlled by varying the initial molar ratio of the metal chloride precursors. The structure investigation and magnetization saturation measurement revealed that, in both cases, the magnetization saturation value reaches its maximum of 175 emu g^{-1} (Zn + Mn + Fe) and 161 emu g^{-1} (Zn + Fe) at x = 0.4, which far exceeds the value of 127 emu g^{-1} (Fe) observed for undoped bulk iron oxide (Fe_3O_4).

Formation of Fe_3O_4 nanoparticles with porous/hollow structures is expected to integrate the valuable characteristics of porous/hollow structure and unique magnetic property of Fe_3O_4 material in a single platform which can provide opportunities to tune their properties for specific applications. Porous hollow magnetic nanoparticles are expected to have similar magnetic, chemical, and biological properties as the solid nanoparticles and their structures offer the additional opportunity to store and release drugs at a target. Hollow nanocapsules of either haematite or magnetite were produced through a wrap-bake-peel process, depending on the heat treatment conditions (Piao et al., 2008; Wu et al., 2011). The spindle-shaped β-FeOOH nanoparticles were prepared and then coated with a thin layer of silica by esterification of tetraethoxysilane in a base solution. The silica coated spindle was subject to a thermal treatment at 500 °C in air, leading to the formation of porous hollow nanocapsule structure with a rhombohedral haematite (α-Fe_2O_3). The haematite α-Fe_2O_3 was converted to magnetite Fe_3O_4 under a flow of hydrogen. Interestingly, the β-FeOOH nanorods and α-Fe_2O_3 nanocapsules were paramagnetic while the Fe_3O_4 nanocapsules were superparamagnetic at room temperature.

Recently, one template-free method to prepare Fe_3O_4 hollow nanoparticles has been developed based on the inside-out Ostwald ripening (Cheng et al., 2011; Hu et al., 2009; Lin et al., 2012; Liu et al., 2009; Zhu et al., 2008). The plausible mechanism was supported by several experimental observations, considering the chemical conversion as an important factor for the hollowing process (Nguyen and Kim, 2013). The chemical conversions of solid material caused a little shrinkage of the grain size and thus made more voids between the grains inside the aggregates and led to the formation of loose package of aggregates. The inner grains would dissolve into the solution and then diffuse to the outer stable shell by the Ostwald ripening process, resulting in continuous expansion of cavity space inside the aggregates (**Fig. 3**). The Fe_3O_4 porous/hollow nanoparticles with tunable particle size and porosity were synthesized controllably by simply adjusting the initial concentrations of Fe precursor and additive or varying other process variables such as processing time and temperature (Nguyen and Kim, 2013; Nguyen et al., 2014 and 2015).

It has been reported that a magnetic coating on a magnetic nanoparticle leads to new magnetic nanocomposites containing exchange of anisotropy between core and shell materials which causes a specific magnetization (López-Ortega et al., 2015; Nogus et al., 2005). For example, Yoon et al. (2011) presented the formation of nanoparticles consisted of an elemental iron (Fe) core and a ferrite shell (Fe@MFe_2O_4, M = Fe, Mn, Co) by a seed-mediated growth approach. In the first step, the Fe cores were prepared by thermally decomposing iron complex [$Fe(CO)_5$] in the presence of oleylamine under air-free conditions. After that, by co-injecting Fe-oleate complexes with Mn-oleate or Co-oleate complexes into Fe nanoparticle suspension then annealing the mixture at elevated temperatures, the Fe@Fe_3O_4, Fe@$MnFe_2O_4$ or Fe@$CoFe_2O_4$ core-shell structures were obtained. The core-sell nanoparticles displayed a hysteresis loop with high saturation magnetization of about 150 emu g^{-1} but with negligible coercivity and remanence. Increasing the crystallinity of ferrite shells could further improve the magnetization of such core-shell nanoparticles. For example, highly crystalline Fe/Fe_3O_4 nanoparticles exhibit 50 % higher magnetization than amorphous Fe/Fe_3O_4 nanoparticles (Lacroix et al., 2011).

4. Application of magnetic nanoparticles for smart therapies

4.1 Magnetic nanoparticles for controlled drug release

Controlled drug delivery by nanostructured functional materials is attracting great attention because of the high opportunities in cancer therapy. The magnetic nanoparticles have been widely used for targeted delivery and controlled drug release due to their response to a magnetic field. Design of magnetic nanoparticles for biomedical applications required careful considerations for the physicochemical stability, targeting ability, drug loading and release. The functionalized magnetic nanoparticles could carry other active targeting moieties, drugs and imaging agents by both physical interactions and covalent linkages (Gupta and Gupta, 2005; Mahmoudia et al., 2011; Oh and Park, 2011). A controlled drug delivery system should be able to deliver drugs to a targeted location in the body,

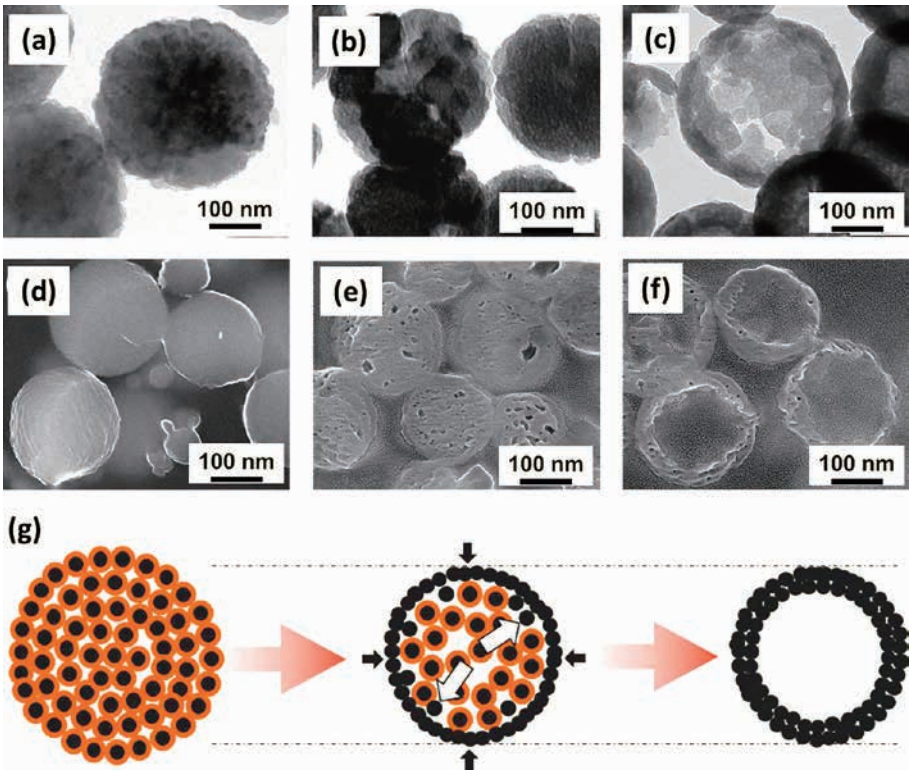

Fig. 3 (a, b, c) TEM images and (d, e, f) corresponding SEM images of cross-section of Fe_3O_4 nanoparticles prepared by solvothermal process for 6 h, 8 h and 12 h of processing times, respectively, showing the evolution of porous/hollow structures, and (g) schematic of the hollow structure development in solvothermal process (Nguyen and Kim, 2013).

and to maintain drug levels within the required concentration range for therapy. A high-gradient of external magnetic fields could be used to guide and concentrate the magnetic nanocarriers at targeted site in order to reduce the systemic distribution of cytotoxic compounds, and to enhance drug uptake, resulting in more effective treatment at lower doses (Chertok et al., 2011; Todd et al., 2014).

Magnetic nanoparticles embedded in a polymer matrix which could be mechanically deformed upon application of a static magnetic field or generate heat under an alternating current field was used to deliver drug and control drug release. For example, upon applying a static magnetic field, the magnetic particles in the polymer matrix aggregated instantly and produced a bulk magnetic moment, leading to a "close" configuration and resulted in a slower drug release than that when the static magnetic field was off (Hu et al., 2007; Liu et al., 2006). This magnetic-induced mechanical deformation of the polymer could be utilized to sustain drug levels within the desired therapeutic range for a long time. On the contrary with the static magnetic field, drug release could be enhanced under an alternating magnetic field. The thermal energy from magnetic nanoparticles could be used as an external and remotely controlled trigger for controlled drug release.

The magnetic nanoparticles conjugated with thermoresponsive polymers offered a class of "smart" nanocarriers which have ability to respond to a change in surrounding temperature. The poly(ethyleneoxide)-poly(propyleneoxide)-poly(ethylene-oxide) (PEO-PPO-PEO) block copolymers were used to squeeze out drugs with magnetic nanoparticles and then was investigated for drug release at different temperatures (Liu et al., 2009). The profiles of drug release rate were very favorable: very slow at 4 °C and 25 °C, modest at 37 °C, much faster at 45 °C and bursting upon magnetic heating. It has been revealed that, under magnetic heating, burst-like release was observed due to the irreversible and disruptive changes of the magnetic nanoparticle core (Liu et al., 2009).

Several systems have been developed to demonstrate the remotely controlled pulsatile drug release for a number of different drugs as well as for different "on–off" durations of an alternating magnetic fields. Hoare et al. (2009) developed nanocomposite membranes based on poly(N-isopropylacrylamide)-based nanogels and magnetite nanoparticles entrapped in ethyl cellulose to achieve "on-demand" drug delivery upon the application of an oscillating magnetic field as shown in **Fig. 4**. A small-scale device made by gluing two 1 cm diameter membrane disks to the ends of a 1cm length of silicone tubing filled with a sodium fluorescein solution was mounted inside a flow cell placed in a solenoid coil. Under an oscillating

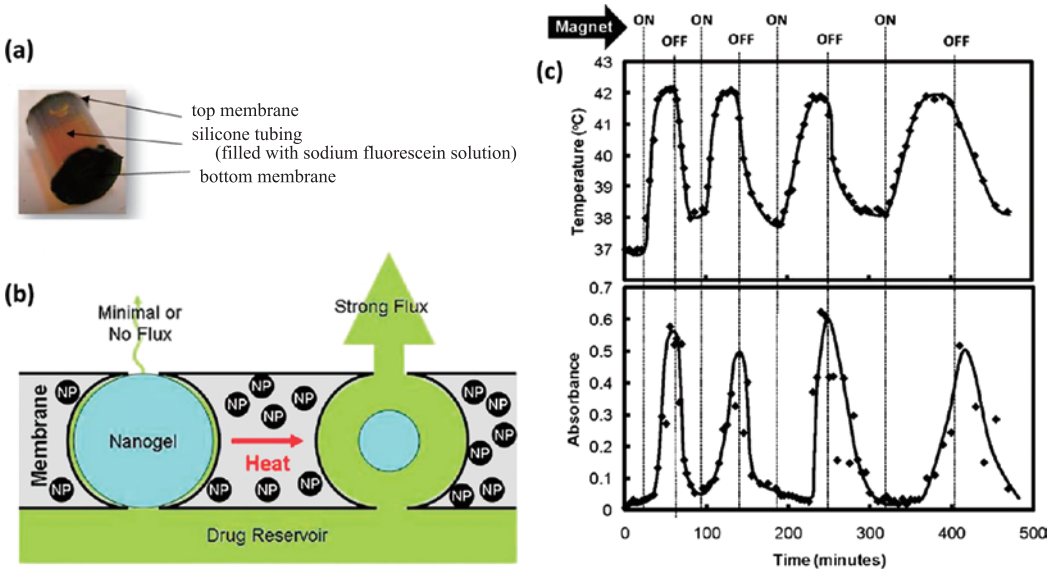

Fig. 4 (a) Picture of membrane capped capsules used for magnetic flux testing. (b) The concept of the "on-demand" drug delivery upon the application of an oscillating magnetic field. (c) Temperature profile in the sample chamber and differential flux of sodium fluorescein out of membrane-capped devices as a function of time over four successive on/off cycles of the external magnetic field (Hoare et al., 2009).

applied field, heat generated by magnetite nanoparticles caused the shrinkage of nanogels and permitted drug diffusion out of the device. When the magnetic field was turned off, the nanogels reswelled and refilled the membrane pores, resulting in the return to a near-zero value of drug flux. This study demonstrated new development of adaptable therapeutic tools which could provide smart control of drug release over real time drug dosing. In another study, poly(D,L-lactic-co-glycolic acid) (PLGA) microcapsules (1–3 mm in diameter) with a 250 nm thick membrane containing a high density of iron oxide nanoparticles loaded with doxorubicin were prepared and then used in cancer treatment (Chiang et al., 2012). It was demonstrated that, for magnetic nanoparticles loading of at least 25 wt%, an application of alternative magnetic field of 100 kHz and 2.5 kA m^{-1} could induce heating above the glass temperature of PLGA and thus could allow controlled pulsatile release of the drug.

The thermal energy from magnetic heating was utilized to open the gates of drug carriers which contain drugs for therapy as shown in **Fig. 5**. Thomas et al. (2010) synthesized 15 nm $(Zn_{0.4}Fe_{0.6})Fe_2O_4$ nanoparticles and then incorporated these nanoparticles inside porous drug carrier nanoparticles. The drug molecules were loaded and kept by nanovalves consisted of N-(6-N-Aminohexyl) aminomethyltriethoxysilane and cucurbit[6]uril capped onto the pores. When an external alternating magnetic field was applied, heat generation and subsequent pressure buildup inside the porous nanoparticles caused the rapid removal of molecular valves and rapid release of drug molecules. These magnetic nanoparticles were considered as effective actuators for controlled drug release from carriers.

4.2 Magnetic nanoparticles for hyperthermia treatment

The use of magnetic nanoparticles for hyperthermia has shown great promise in the field of disease treatment. By raising the temperature of tissues to between 42 °C and 46 °C, the viability of the disease tissues is reduced and their sensitivity to chemotherapy is increased (Chan et al.,1993; Jordan et al.,1993; Gilchrist et al.,1957; Overgaard and Overgaard, 1972). In addition to selectively killing tumor cells, a potential of developing antitumor immunity after hyperthermia treatment has been also suggested (Ito et al., 2003; Sivasai et al., 2010; Suzuki et al., 2003). In fact, it should be considered that the impact of the alternative magnetic field on human body is connected with heating effects due to eddy currents induced in the electrically conducting tissue. It has been suggested that the upper limit for the magnetic field (the product of amplitude, H, and frequency, f) should not exceed 5×10^9 A/m s^{-1} (Hergt and Dutz, 2007).

As shown in **Fig. 6** (Nguyen and Kim, 2014), when exposed magnetic nanoparticles to an alternating magnetic field, the external magnetic field is dissipated with the relaxation of the magnetic moment to its equilibrium orientation, or so-called Néel relaxation for superparamagnetic nanoparticles. A so-called hysteresis loss mechanism dominates heat generation of ferromagnetic materials whose sizes exceed the domain wall width. Under application of an alternative field, the magnetic moments oscillate and cause domain wall displacement which generates heat. The heat generation depends not only on the applied field but also on the magnetic pre-history of material. It

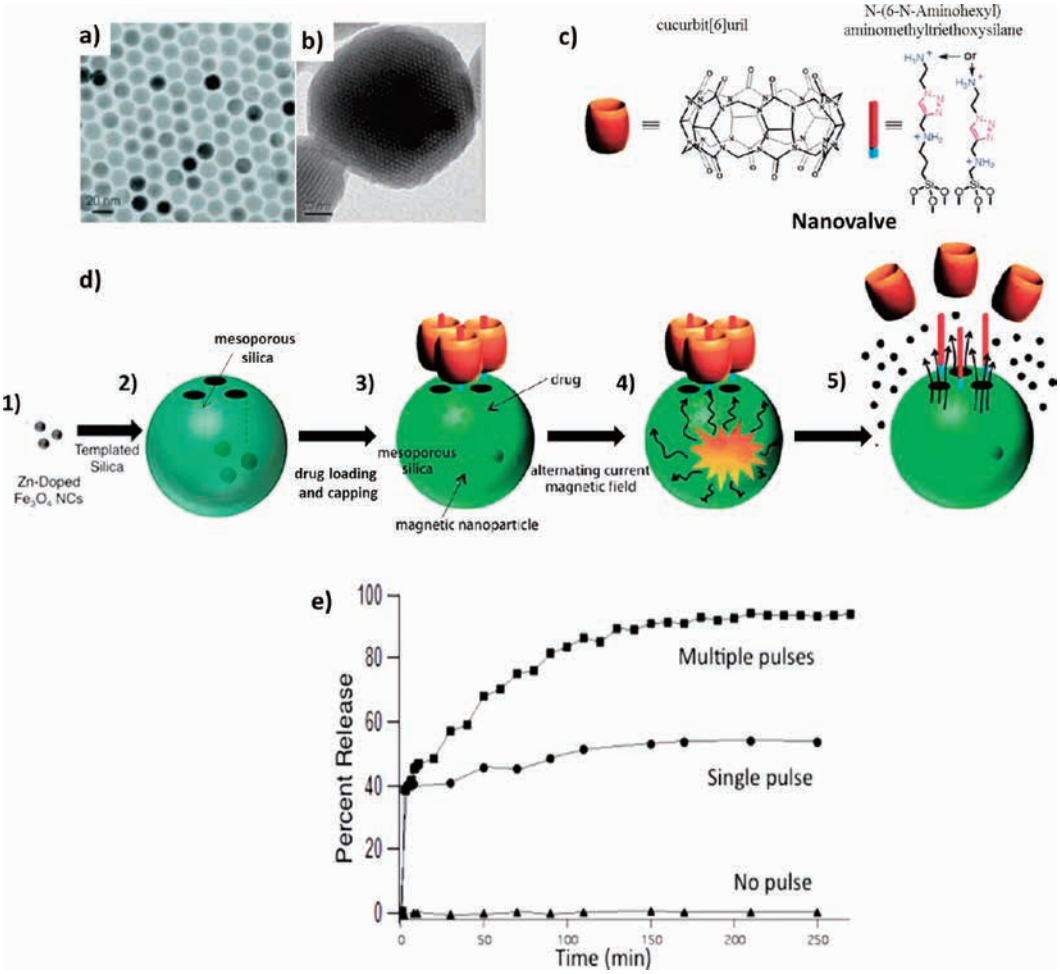

Fig. 5 a) TEM image of $(Zn_{0.4}Fe_{0.6})Fe_2O_4$ nanoparticles. b) TEM image of $(Zn_{0.4}Fe_{0.6})Fe_2O_4$ encapsulated silica nanoparticles. c) Chemical structure of nanovalve. d) Schematic of nanoparticles formation (1), ecapsulation (2), drug loading and nanovalve assembly (3), pore opening by the local internal heating (4), and drug release (5). e) Drug release profile monitored during the AC field application with multiple AC field pulses, single initial pulse, and no pulse. The sample was kept at 0 °C to determine whether internal heating alone causes the valve opening or not (Thomas et al., 2010).

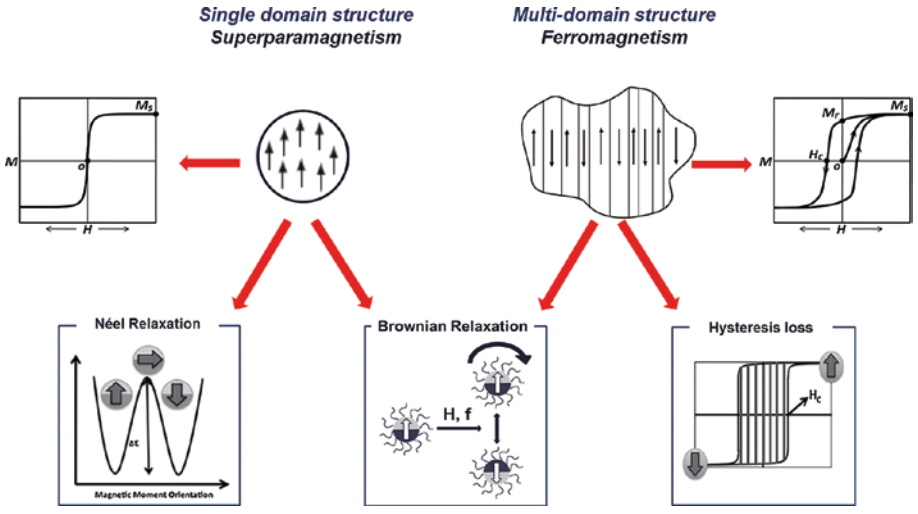

Fig. 6 General mechanisms for heat generation of magnetic nanoparticles (Nguyen and Kim, 2014).

has been found that, when the applied field is small, the hysteresis loops differ from full hysteresis loops in that they are minor loops having relatively smaller areas and the amount of heat generated is considered to be proportional to the frequency multiplied by the area of the loop (Kita et al., 2010; Vallejo-Fernandez et al., 2013). Considerable heat generation can be expected if we apply a magnetic field with appropriate frequency which is sufficient to saturate the magnetization of magnetic material. For all types of magnetic nanoparticles, heat generation is also caused by the rotational Brownian motion within a dispersed media because of the torque exerted on the magnetic moment by the external alternating magnetic field. In this condition, the thermal energy is characterized by the viscosity of medium and the global hydrodynamic diameter of particle. However, due to the high viscosity of the intracellular medium, the Brownian relaxation mechanisms could be significantly hindered and consequently the performance of the nanoparticles mainly depended on their primitive mechanisms (Fortin et al., 2008; Rivière et al., 2007; Wilhelm et al., 2007).

Magnetic particles in hyperthermia treatment have been focused on the magnetite Fe_3O_4 and also on the nanoparticles related with cobalt, nickel, or other substitutions in a size range from several nanometers to a few tenths of a micron. The magnetic iron oxide nanoparticles are still the most studied magnetic material for hyperthermia applications, due to their low toxicity, good biocompatibility, ease of synthesis and surface functionalization. The main parameter to determine the heating of tissue is the specific loss power (SLP) or specific absorption rate (SAR) which can be calculated based on the following equation.

$$SLP\ (SAR) = \frac{C}{m}\frac{\Delta T}{\Delta t} \tag{1}$$

where C represents the sample specific heat capacity, m is the amount of magnetic material per mass or volume of sample used in the experiment and ($\Delta T/\Delta t$) is the initial slope of the time-dependent heating curve.

The hyperthermia efficiency which could be reflected by heating rate or SLP values depended on various factors, including the intrinsic factors of material such as particle structure, magnetic properties and the external factors such as amplitude and frequency of applied magnetic field (Deatsch and Evans, 2014; Laurent et al., 2011; Mornet et al., 2004). Rosensweig (2002) formulated and computed heating rates for various magnetic samples and reported that the highest heating rates depended on the particle size. In this work, the very sharp maximum of the heating rate was observed for monodisperse Fe_3O_4 nanoparticles of about 14 nm diameter. An increase of the size distribution caused a very fast decrease of the heating rate. In another study, by using available data for domain

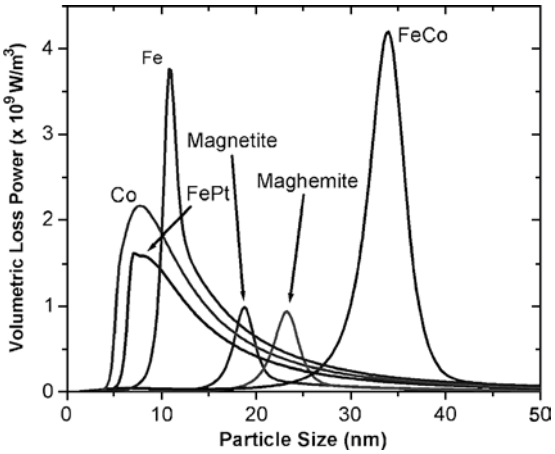

Fig. 7 Size-dependent volumetric SLP values for different magnetic nanoparticles in single domain regime (Habib et al., 2008).

magnetization and magnetic anisotropy constant, Habib et al. (2008) predicted the dependence of SLP values on particle size for various materials in single domain regime as shown in **Fig. 7** wherein the maximum heating rate of monodisperse Fe_3O_4 nanoparticles was achieved for particles of about 19 nm diameter.

Practically, effect of each significant parameter such as particle size and shape, functionalization, magnetic properties on the hyperthermia efficiency has been independently investigated from study to study with different particle synthesis methods and different magnetic-induced heating systems. Ma et al. (2004) reported that the SLP values depended on the particle size and the coercivity of Fe_3O_4 nanoparticles. A maximum SLP was recorded for sample containing 46 nm diameter of Fe_3O_4 nanoparticles which also has the highest coercivity under an applied field of 80 kHz frequency and 32.5 kA m^{-1} amplitude. Gonzales-Weimuller et al. (2009) demonstrated that the highest SLP was measured for 11.2 nm particles under an applied field of 400 kHz frequency and 24.5 kA m^{-1} amplitude while Gonzalez-Fernandez et al. (2009) showed a maximum of SLP for particles of around 30 nm diameter by applying an alternative magnetic field of 260 kHz frequency and 100 Oe (about 8 kA m^{-1}) amplitude to induce heat generation.

The choices of the ligand and thickness of coating are important because it can modify the magnetic properties of the magnetic nanoparticles. Larumbe et al. (2012) showed that silica coating on magnetite nanoparticles resulted in the decreases of the magnetic properties and the SLP values, due to an enhancement of spin disorder caused by the silica coating. In another recent study, the heating efficiency was observed to decrease with increasing polymer chain length. However, with a proper coating, a ferromagnetic nanoparticle could give a fast heating rate for disease treatment. For instance, chitosan

oligosaccharide-stabilized iron oxide nanocubes (Chito-FIONs) were developed for cancer hyperthermia (Bae et al., 2012). The magnetic heating revealed that Chito-FIONs encapsulated with multiple 30-nm-sized iron oxide nanocubes showed the higher hyperthermal efficiency than single nanocube and more than 30 times higher than that of the Feridex particles as reference. In this study, it should be noticed that an evolution of aggregation of the nanoparticles caused a modification of the SLP values due to the effect of dipolar interparticle coupling with Néel relaxation.

There are potential opportunities to enhance hyperthermia through manipulation of magnetic properties utilizing core-shell architecture. The combination of different magnetic nanoparticles such as $MnFe_2O_4/CoFe_2O_4$ or $CoFe_2O_4/MnFe_2O_4$ or $CoFe_2O_4/NiFe_2O_4$ has been developed to enhance hyperthermia efficiency compared to single phase nanoparticles (Lee et al., 2011). Remarkably, further enhancement of the SLP values has been obtained in cubic $Zn_{0.4}Fe_{2.6}O_4/CoFe_2O_4$ core/shell nanoparticles for achieving SLP values 14 times higher than the spherical single Fe_3O_4 nanoparticles (Noh et al., 2012).

The temperature control during heating is essential but still remains challenges because heat conduction and energy adsorption *in vivo* are widely unknown and local overheating may damage the healthy tissue and, therefore, the magnetic materials with a maximum self-heating temperature are very attractive for hyperthermia applications. Achieving self-controlled and self-regulated heating by developing materials with Curie temperature (T_C) slightly above the therapeutic temperature has been considered as an effective method to prevent such local overheating problem. The Curie temperature is the maximal temperature reachable by magnetic particles to maintain their magnetic properties. Above this temperature, the magnetic particles lose their magnetic properties, and thus they do not convert electromagnetic energy into heat. Syntheses of several materials including $M_{1-x}Zn_xFe_2O_4$ (with M = Ni, Cu, Co, Mn) and alloy such as $Ni_{1-x}Cr_x$ with adjustable T_C were reported. It has been also reported that the T_C of Gd-substituted Zn-ferrite ($ZnGd_xFe_{2-x}O_4$) increased with an increasing Gd content and was found to be around 45 °C at x = 0.02 (Yao et al., 2009) while the T_C of $Ni_{1-x}Cr_x$ increased with decreasing Cr content and was found equal to 44 °C at x = 5.63 (Akin et al., 2009). Other studies reported that the T_C of 46 °C could be achieved for $Mn_{1+x}Ti_xFe_2O_4$ with x = 0.55 (Barati et al., 2013) and for $Mg_{1+x}Fe_{2-2x}Ti_xO_4$ with x = 0.37 (Ferk et al., 2014). Certainly, an ideal material with optimal physical features for self-controlled and self-regulated magnetic heating has not been well developed yet but, indeed, this concept offers a smart way to control hyperthermia treatment.

The combination of hyperthermia and traditional chemotherapeutic functions in the same system could utilize the great potentials of individual hyperthermia and controlled drug delivery as well as could raise synergistic effects in the treatment of cancer. Kulshrestha et al. (2012) developed paclitaxel loaded magnetoliposomes and achieved a better cell killing efficacy than individual magnetoliposomes or paclitaxel loaded liposomes. The drug release behaviors were studied under an AC magnetic field at 37 °C and 43 °C. At 37 °C, only 1.2 % of paclitaxel were released compared to 55.6 % at 43 °C. The hyperthermia was performed on HeLa cells at 42.5 ± 1 °C for a duration of 30 min with magnetoliposomes containing 6 mg mL^{-1} of magnetic nanoparticles only or in combination with 100 nM paclitaxel. The cell viability was decreased by 37 % after the heat treatment with magnetic particle alone and by about 50 % and 89 % for paclitaxel loaded magnetoliposomes without and with application of an alternative magnetic field, respectively. This study demonstrated that the magnetoliposomes exhibit promising potential for combined thermo-chemotherapy due to its good biocompatibility, slow drug release at 37 °C, burst drug release at 43 °C and synergistic cancer cell killing effect.

5. Conclusion

Controlled drug delivery and hyperthermia treatment by magnetic nanoparticles exhibited high opportunities in biomedical treatments. High-gradient, external magnetic fields could be utilized to guide and concentrate the magnetic nanocarriers at target locations where the therapy has to act specifically. A combination of hyperthermia-based therapy and controlled drug release has strong potential to develop an intelligent therapy for cancer treatment. The hyperthermia and traditional chemotherapeutic functions combined in the same system could utilize the great potential of individual hyperthermia and controlled drug delivery as well as could raise the synergistic effects in the treatment of cancer. It is still a great challenge to develop a system that minimizes nanoparticle dose for actual treatment. In order to conquer this challenge, it is crucial to develop systematic strategies of controlled synthesis and surface modification of magnetic nanoparticles to obtain the nanoparticles of customized size and shape with high homogeneity as well as sufficient magnetization. However, the magnetic nanoparticles obtained under different synthetic conditions may display large differences due to formation of structural disorder and antiphase boundaries, or the existence of a magnetically dead layer at the particle surface and, thus, the synthesis and functionalization of high-quality magnetic nanoparticles in a controlled manner are still the critical challenges to be faced in the coming years. It will also be desirable to develop the large-scale synthesis of highly

functional magnetic nanoparticles with the requirement of reproducible and industrial processes without any laborious purification step to ensure cost effective synthetic procedures.

Acknowledgements

This research was supported by the Converging Research Center Program through the Ministry of Science, ICT and Future Planning (Grant number 2014048827).

References

Akin Y., Obaidat I.M., Issa B., Haik Y., $Ni_{1-x}Cr_x$ alloy for self controlled magnetic hyperthermia, Crystal Research and Technology, 44 (2009) 386–390.

Bae K.H., Park M., Do M.J., Lee N., Ryu J.H., Kim G.W., Kim C.G., Park T.G., Hyeon T., Chitosan oligosaccharide–stabilized ferrimagnetic iron oxide nanocubes for magnetically modulated cancer hyperthermia, ACS Nano, 6 (2012) 5266–5273.

Banerjee S., Raja S.O., Sardar M., Gayathri N., Ghosh B., Dasgupta A., Iron oxide nanoparticles coated with gold: Enhanced magnetic moment due to interfacial effects, Journal of Applied Physics,109 (2011) 123902.

Barati M.R., Suzuki K., Selomulya C., Garitaonandia J. S., New T_c–tuned manganese ferrite-based magnetic implant for hyperthermia therapy application, IEEE Transactions on Magnetics, 49 (2013) 3460–3463.

Bean C.P., Hysteresis loops of mixtures of ferromagnetic micropowders, Journal of Applied Physics, 26 (1955) 1381–1383.

Bean C.P., Livingston J.D., Superparamagnetism, Journal of Applied Physics, 30 (1959) 120S–129S.

Beji Z., Hanini A., Smiri L.S., Gavard J., Kacem K., Villain F., Greneche J.-M., Chau F., Ammar S., Magnetic properties of Zn-substituted $MnFe_2O_4$ nanoparticles synthesized in polyol as potential heating agents for hyperthermia. Evaluation of their toxicity on Endothelial cells, Chemistry of Materials, 22 (2010) 5420–5429.

Briley-Saebo K.C., Johansson L.O., Hustvedt S.O., Haldorsen A.G., Bjørnerud A., Fayad Z.A., Ahlstrom H.K., Clearance of iron oxide particles in rat liver: effect of hydrated particle size and coating material on liver metabolism, Investigative Radiology, 41 (2006) 560–571.

Bulte J.W., Hoekstra Y., Kamman R.L., Magin R.L., Webb A.G., Briggs R.W., Go, K.G., Hulstaert, C.E., Miltenyi S., The T.H., Leij L.D., Specific MR imaging of human lymphocytes by monoclonal antibody-guided dextran-magnetite particles, Magnetic Resonance in Medicine, 25 (1992) 148–157.

Butterworth M.D., Illum L., Davis S.S., Preparation of ultrafine silica- and PEG-coated magnetite particles, Colloids and Surfaces A: Physicochemical and Engineering Aspects, 179 (2001) 93–102.

Cai W., Wan J., Facile synthesis of superparamagnetic magnetite nanoparticles in liquid polyols, Journal of Colloid and Interface Science, 305 (2007) 366–370.

Chan D.C.F., Kirpotin D.B., Bunn P.A., Synthesis and evaluation of colloidal magnetic iron oxides for the site-specific radiofrequency-induced hyperthermia of cancer, Journal of Magnetism and Magnetic Materials, 122 (1993) 374–378.

Chastellain M., Petri A., Gupta A., Rao K.V., Hofmann H., Superparamagnetic silica-iron oxide nanocomposites for application in hyperthermia, Advanced Engineering Materials, 6 (2004) 235–241.

Chen F., Gao Q., Hong G., Ni J., Synthesis and characterization of magnetite dodecahedron nanostructure by hydrothermal method, Journal of Magnetism and Magnetic Materials, 320 (2008) 1775–1780.

Cheng C., Xu F., Gu H., Facile synthesis and morphology evolution of magnetic iron oxide nanoparticles in different polyol processes, New Journal Of Chemistry, 35 (2011) 1072–1079.

Chertok B., David A.E., Yang V.C., Brain tumor targeting of magnetic nanoparticles for potential drug delivery: Effect of administration route and magnetic field topography, Journal of Controlled Release, 155 (2011) 393–399.

Chiang W.-L., Ke C.-J., Liao Z.-X., Chen S.-Y., Chen F.-R., Tsai C.-Y., Xia Y., Sung H.-W., Pulsatile drug release from PLGA hollow microspheres by controlling the permeability of their walls with a magnetic field, Small, 8 (2012) 3584–3588.

Chin A.B., Yaacob I.I., Synthesis and characterization of magnetic iron oxide nanoparticles via w/o microemulsion and Massart's procedure, Journal of Materials Processing Technology, 191 (2007) 235–237.

Cuyper M., Soenen S.J.H., Coenegrachts K., Beek L.T., Surface functionalization of magnetoliposomes in view of improving iron oxide-based magnetic resonance imaging contrast agents: Anchoring of gadolinium ions to a lipophilic chelate, Analytical Biochemistry, 367 (2007) 266–273.

Daou T.J., Greneche J.M., Pourroy G., Buathong S., Derory A., Ulhaq-Bouillet C., Donnio B., Guillon D., Begin-Colin S., Coupling agent effect on magnetic properties of functionalized magnetite-based nanoparticles, Chemistry of Materials, 20 (2008) 5869–5875.

Deatsch A.E., Evans B.A., Heating efficiency in magnetic nanoparticle hyperthermia, Journal of Magnetism and Magnetic Materials, 354 (2014) 163–172.

Duran J.D.G., Arias J.L., Gallardo V., Delgado A.V.J., Magnetic colloids as drug vehicles, Pharmaceutical Sciences, 97 (2008) 2948–2983.

Fauconnier N., Pons J.N., Roger J., Bee A., Thiolation of Maghemite Nanoparticles by Dimercaptosuccinic Acid, Journal of Colloid and Interface Science, 194 (1997) 427–433.

Ferk G., Drofenik M., Lisjak D., Hamler A., Jaglicic Z., Makovec D., Synthesis and characterization of $Mg_{1+}xFe_{2-2}xTixO_4$ nanoparticles with an adjustable Curie point, Journal of Magnetism and Magnetic Materials, 350 (2014) 124–128.

Fortin J.P., Gazeau F., Wilhelm C., Intracellular heating of living cells through Néel relaxation of magnetic nanoparticles, European Biophysics Journal, 37 (2008) 223–228.

Frei E.H., Shtrikman S, Treves D., Critical size and nucleation

field of ideal ferromagnetic particles, Physical Review, 106 (1957) 446–455.

Gilchrist R.K., Medal R., Shorey W.D., Hanselman R.C., Parott J.C., Taylor C.B., Selective inductive heating of lymph nodes, Annals of Surgery, 146 (1957) 596–606.

Gonzalez-Fernandez M.A., Torres T.E., Andrés-Vergés M., Costo R., de la Presa P., Serna C.J., Moralesa M.P., Marquina C., Ibarra M.R., Goya G.F., Magnetic nanoparticles for power absorption: Optimizing size, shape and magnetic properties, Journal of Solid State Chemistry, 182 (2009) 2779–2784.

Gonzales-Weimuller M., Zeisberger M., Krishnan K.M., Size-depend ant heating rates of iron oxide nanoparticles for magnetic fluid hyperthermia, Journal of Magnetism and Magnetic Materials, 321 (2009) 1947–1950.

Goon I.Y., Lai L.M.H., Lim M., Munroe P., Gooding J.J., Amal R., Fabrication and dispersion of gold-shell-protected magnetite nanoparticles: systematic control using polyethyleneimine, Chemistry of Materials, 21 (2009) 673–681.

Gupta A.K., Curtis A.S.G., Surface modified superparamagnetic nanoparticles for drug delivery: interaction studies with human fibroblasts in culture, Journal of Materials Science: Materials in Medicine, 15 (2004) 493–496.

Gupta A.K., Gupta M., Synthesis and surface engineering of iron oxide nanoparticles for biomedical applications, Biomaterials, 26 (2005) 3995–4021.

Habib A.H., Ondeck C.L., Chaudhary P., Bockstaller M.R., McHenry M.E., Evaluation of iron-cobalt/ferrite core-shell nanoparticles for cancer thermotherapy, Journal of Applied Physics, 103 (2008) 07A307.

Hergt R., Dutz S.J., Magnetic particle hyperthermia—biophysical limitations of a visionary tumour therapy, Journal of Magnetism and Magnetic Materials, 311 (2007) 187–192.

Hervault A., Thanh N.T.K., Magnetic nanoparticle-based therapeutic agents for thermo-chemotherapy treatment of cancer, Nanoscale, 6, 2014, 11553–11573.

Hoare T., Santamaria J., Goya G.F., Irusta S., Lin D., Lau S., Padera R., Langer R., Kohane D.S., A magnetically triggered composite membrane for on-demand drug delivery, Nano Letters, 9 (2009) 3651–3657.

Hochepied J.F., Pileni M.P., Magnetic properties of mixed cobalt-zinc ferrite nanoparticles, Journal of Applied Physics, 87 (2000) 2472–2478.

Hu F.Q., Wei L., Zhou Z., Ran Y.L., Li Z., Gao M.Y., Preparation of biocompatible magnetite nanocrystals for in vivo magnetic resonance detection of cancer, Advanced Materials, 18 (2006) 2553–2556.

Hu S.-H., Liu T.-Y., Liu D.-M., Chen S.-Y., Nano-ferrosponges for controlled drug release, Journal of Controlled Release, 121 (2007) 181–189.

Hu P., Yu L., Zuo A., Guo C. Yuan F., Fabrication of monodisperse magnetite hollow spheres, Journal of Physical Chemistry C, 113 (2009) 900–906.

Hyeon T., Lee S.S., Park J., Chung Y., Na H.B., Synthesis of Highly Crystalline and Monodisperse Maghemite Nanocrystallites without a Size-Selection Process, Journal of the American Chemical Society, 123 (2001) 12798–12801.

Ito A., Shinkai M., Honda H., Yoshikawa K., S. Saga, Wakabayashi T., Yoshida J., Kobayashi T., Heat shock protein 70 expression induces antitumor immunity during intracellular hyperthermia using magnetite nanoparticles, Cancer Immunology Immunotherapy, 52 (2003) 80–88.

Jana N.R., Chen Y.F., Peng X.G., Size- and shape-controlled magnetic (Cr, Mn, Fe, Co, Ni) oxide nanocrystals via a simple and general approach, Chemistry of Materials, 16 (2004) 3931–3935.

Jang J.-T., Nah H., Lee J.-H., Moon S.H., Kim M.G., Cheon J., Critical Enhancements of MRI Contrast and Hyperthermic Effects by Dopant-Controlled Magnetic Nanoparticles, Angewandte Chemie International Edition, 48 (2009) 1234–1238.

Jeong J., Ha T.H., Chung B.H., Enhanced reusability of hexa-arginine-tagged esterase immobilized on gold-coated magnetic nanoparticles, Analytica Chimica Acta, 569 (2006) 203–209.

Jordan A., Wust P., Fahling H., John W., Hinz A., Felix R., Inductive heating of ferrimagnetic particles and magnetic fluids: physical evaluation of their potential for hyperthermia, International Journal of Hyperthermia, 9 (1993) 51–68.

Khollam Y.B., Dhage S.R., Potdar H.S., Deshpande S.B., Bakare P.P., Kulkarni S.D., Date S.K., Microwave hydrothermal preparation of submicron-sized spherical magnetite (Fe_3O_4) powders, Materials Letters, 56 (2002) 571–577.

Kimata M., Nakagawa D., Hasegawa M., Preparation of monodisperse magnetic particles by hydrolysis of iron alkoxide, Powder Technology, 132 (2003) 112–118.

Kita E., Oda T., Kayano T., Sato S., Minagawa M., Yanagihara H., Kishimoto M., Mitsumata C., Hashimoto S., Yamada K., Ohkohchi N., Ferromagnetic nanoparticles for magnetic hyperthermia and thermoablation therapy, Journal of Physics D Applied Physics, 43 (2010) 474011.

Krishnan K.M., Pakhomov A.B., Bao Y., Blomqvist P., Chun Y., Gonzales M., Griffin K., Ji X., Roberts B.K., Nanomagnetism and spin electronics: Materials, microstructure and novel properties, Journal of Materials Science, 41 (2006) 793–815.

Krishnan K.M., Biomedical nanomagnetics: a spin through possibilities in imaging, diagnostics, and therapy, IEEE Transactions on Magnetics, 46 (2010) 2523–2558.

Kulshrestha P., Gogoi M., Bahadur D., Banerjee R., In vitro application of paclitaxel loaded magnetoliposomes for combined chemotherapy and hyperthermia, Colloids and Surfaces B: Biointerfaces, 96 (2012) 1–7.

Kumar C.S.S.R., Mohammad F., Magnetic nanomaterials for hyperthermia-based therapy and controlled drug delivery, Advanced Drug Delivery Reviews, 63 (2011) 789–808.

Kwon S.G., Piao Y., Park J., Angappane S., Jo Y., Hwang N.-M., Park J.-G., Hyeon T., Kinetics of monodisperse iron oxide nanocrystal formation by "heating-up" process, Journal of the American Chemical Society, 129 (2007) 12571–12584.

Lacroix L.-M., Huls N.F., Ho D., Sun X., Cheng K., Sun S., Stable Single-Crystalline Body Centered Cubic Fe Nanoparticles, Nano Letters, 11 (2011) 1641–1645.

Larumbe S., Gomez-Polo C., Perez-Landazabal J.I., Pastor J.M., Effect of a SiO_2 coating on the magnetic properties of Fe_3O_4

nanoparticles, Journal of Physics: Condensed Matter, 24 (2012) 266007.

Laurent S., Forge D., Port M., Roch A., Robic C., Elst L.V., Muller R.N., Magnetic iron oxide nanoparticles: synthesis, stabilization, vectorization, physicochemical characterizations, and biological applications, Chemical Reviews, 108 (2008) 2064–2110.

Laurent S., Dutz S., Häfeli U.O., Mahmoudi M., Magnetic fluid hyperthermia: Focus on superparamagnetic iron oxide nanoparticles, Advances in Colloid and Interface Science, 166 (2011), 8.

Lee J.H., Jang J.T., Choi J.S., Moon S.H., Noh S.H., Kim J.W., Kim J.G., Kim I.S., Park K.I., Cheon J.W., Exchange-coupled magnetic nanoparticles for efficient heat induction, Nature Nanotechnology, 6 (2011) 418–422.

Leslie-Pelecky D.L., Magnetic properties of nanostructured materials, Chemistry of Materials, 8 (1996) 1770–1783.

Lin X., Ji G., Liu Y., Huang Q., Yang Z., Du Y., Formation mechanism and magnetic properties of hollow Fe_3O_4 nanospheres synthesized without any surfactant, CrystEngComm, 14 (2012) 8658–8663.

Liu H., Guo J., Jin L., Yang W., Wang C., Fabrication and functionalization of dendritic poly(amidoamine)-immobilized magnetic polymer composite microspheres, Journal of Physical Chemistry B 112 (2008) 3315–3321.

Liu S., Xing R., Lu F., Rana R.K., Zhu J.J., One-pot template-free fabrication of hollow magnetite nanospheres and their application as potential drug carriers, Journal of Physical Chemistry C, 113 (2009) 21042.

Liu T.Y., Hu S.H., Liu T.Y., Liu D.M., Chen S.Y., Magnetic-sensitive behavior of intelligent ferrogels for controlled release of drug, Langmuir, 22 (2006) 5974–5978.

Liu T.Y., Hu S.H., Liu K.H., Liu D.M., Chen S.Y., Study on controlled drug permeation of magnetic-sensitive ferrogels: effect of Fe_3O_4 and PVA, Journal of Controlled Release, 126 (2008) 228–236.

Liu T.Y., Hu S.H., Liu D.M., Chen S.Y., Chen I.W., Biomedical nanoparticle carriers with combined thermal and magnetic responses, Nano Today, 4 (2009) 52–65.

Liu T.Y., Liu K.H., Liu D.M., Chen S.Y., Chen I.W., Temperature-sensitive nanocapsules for controlled drug release caused by magnetically triggered structural disruption, Advanced Functional Materials, 19 (2009) 616–623.

López-Ortega A. Estrader M., Salazar-Alvarez G., Roca A.G., Nogués J., Applications of exchange coupled bi-magnetic hard/soft and soft/hard magnetic core/shell nanoparticles, Physics Reports, 553 (2015) 1–32.

Lu A.-H., Salabas E.L., Schüth F., Magnetic nanoparticles: synthesis, protection, functionalization, and application, Angewandte Chemie International Edition, 46 (2007) 1222–1244.

Lutz J.F., Stiller S., Hoth A., Kaufner L., Pison U., Cartier R., One-pot synthesis of pegylated ultrasmall iron-oxide nanoparticles and their in vivo evaluation as magnetic resonance imaging contrast agents, Biomacromolecules, 7 (2006) 3132–3138.

Ma D.L., Guan J.W., Normandin F., Denommee S., Enright G., Veres T., Simard B., Multifunctional Nano-Architecture for Biomedical Applications, Chemistry of Materials, 18 (2006) 1920–1927.

Ma M., Wu Y., Zhou J., Sun Y., Zhang Y., Gu N., Size dependence of specific power absorption of Fe_3O_4 particles in AC magnetic field, Journal of Magnetism and Magnetic Materials, 268 (2004) 33–39.

Mahmoudia M., Sant S., Wang B., Laurent S., Sen T., Superparamagnetic iron oxide nanoparticles (SPIONs): Development, surface modification and applications in chemotherapy, Advanced Drug Delivery Reviews, 63 (2011) 24–46.

Massart R., Preparation of aqueous magnetic liquids in alkaline and acidic media, IEEE Transactions on Magnetics, 17 (1981) 1247–1248.

Mohammad F., Balaji G., Weber A., Uppu R.M., Kumar C. S.S.R., Influence of gold nanoshell on hyperthermia of superparamagnetic iron oxide nanoparticles, Journal of Physical Chemistry C 114 (2010) 19194–19201.

Mornet S., Vasseur S., Grasset F., Duguet E., Magnetic nanoparticle design for medical diagnosis and therapy, Journal of Materials Chemistry, 14 (2004) 2161.

Nguyen D.T., Kim D.-J., Kim K.-S., Controlled synthesis and biomolecular probe application of gold nanoparticles, Micron, 42 (2011) 207–227.

Nguyen D.T., Park D.-W., Kim K.-S., Seed-mediated synthesis of iron oxide and gold/iron oxide nanoparticles, Journal for Nanoscience and Nanotechnology, 11 (2011) 7214–7217.

Nguyen D.T., Kim K.-S., Analysis on development of magnetite hollow spheres through one-pot solvothermal process, AIChE J., 59 (2013) 3594–3600.

Nguyen D.T., Kim K.-S., Template-free synthesis and characterization of monodisperse magnetite hollow nanoparticles through solvothermal process, Journal for Nanoscience and Nanotechnology 13 (2013) 5773–5776.

Nguyen D. T., Charinpanitkul T., Park D.-W., Kim K.-S., Preparation of magnetite hollow structure for drug delivery application, Journal for Nanoscience and Nanotechnology, 14 (2014) 7995–7999.

Nguyen D.T., Kim K.-S., Functionalization of magnetic nanoparticles for biomedical applications, Korean Journal of Chemical Engineering, 31 (2014) 1289–1305.

Nguyen D.T., Park D.-W., Kim T., Kim K.-S., Controlled synthesis of magnetite porous/hollow nanoparticles through a template-free solvothermal process, Journal for Nanoscience and Nanotechnology, 15 (2015) 591–594.

Nogus J., Sort J., Langlais V., Skumryev V., Surinach S., Munoz J.S., Baro M.D., Exchange bias in nanostructures, Physics Reports, 422 (2005) 65–117.

Noh S.H., Na W., Jang J.T., Lee J.H., Lee E.J., Moon S.H., Lim Y., Shin J.S., Cheon J., Nanoscale magnetism control via surface and exchange anisotropy for optimized ferrimagnetic hysteresis, Nano Letters, 12 (2012) 3716–3721.

Oh J.K., Park J.M., Iron oxide-based superparamagnetic polymeric nanomaterials: Design, preparation, and biomedical application, Progress in Polymer Science, 36 (2011) 168–189.

Overgaard K., Overgaard J., Investigations on the possibility of a thermic tumour therapy. I. Short-wave treatment of a

transplanted isologous mouse mammary carcinoma, European Journal of Cancer, 8 (1972) 65–78.

Park J., An K., Hwang Y., Park J.G., Noh H.J., Kim J.Y., Park J.H., Hwang N.M,, Hyeon T., Ultra-large-scale syntheses of monodisperse nanocrystals, Nature Materials, 3 (2004) 891–985.

Park J., Lee E., Hwang N.M., Kang M., Kim S.C., Hwang Y., Park J.G., Noh H.J., Kim J.Y., Park J.H., Hyeon T., One-nanometer-scale size-controlled synthesis of monodisperse magnetic iron oxide nanoparticles, Angewandte Chemie International Edition, 44 (2005) 2872–2877.

Park J., Joo J., Kwon S.G., Jang Y., Hyeon T., Synthesis of monodisperse spherical nanocrystals, Angewandte Chemie International Edition, 46 (2007) 4630–4660.

Piao Y., Kim J., Na H.B., Kim D., Baek J.S., Ko M.K., Lee J.H., Shokouhimehr M., Hyeon T., Wrap-bake-peel process for nanostructural transformation from β-FeOOH nanorods to biocompatible iron oxide nanocapsules, Nature Materials, 7 (2008) 242–247.

Portet D., Denizot B., Rump E., Lejeune J.-J., Jallet P., Nonpolymeric coatings of iron oxide colloids for biological use as magnetic resonance imaging contrast agents, Journal of Colloid and Interface Science, 238 (2001) 37–42.

Reddy L.H., Arias J.L., Nicolas J., Couvreur P., Magnetic nanoparticles: design and characterization, toxicity and biocompatibility, pharmaceutical and biomedical applications, Chemical Reviews, 112 (2012) 5818–5878.

Rivière C., Wilhelm C., Cousin F., Dupuis V., Gazeau F., Perzynski R., Internal structure of magnetic endosomes, European Physical Journal E, 22 (2007) 1–10.

Robinson I., Tung L.D., Maenosono S., Walti C., Thanh N.T.K, Synthesis of core-shell gold coated magnetic nanoparticles and their interaction with thiolated DNA, Nanoscale, 2 (2010) 2624–2630.

Rosensweig R.E., Heating magnetic fluid with alternating magnetic field, Journal of Magnetism and Magnetic Materials, 252 (2002) 370–374.

Sivasai B., Rajashekar R., Hongwang W., Thilani S.N., RajKumar D., Marla P., Franklin K.O., Brandon W., Xiaoxuan L., Olga K.B., Masaaki T., Viktor C., Stefan B.H., Deryl T.L., A/C magnetic hyperthermia of melanoma mediated by iron(0)/iron oxide core/shell magnetic nanoparticles: a mouse study, BMC Cancer, 10 (2010) 119.

Sun S., Zeng H., Size-controlled synthesis of magnetite nanoparticles, J. Am. Chem. Soc., 124 (2002) 8204–8205.

Sun S., Zeng H., Robinson D.B., Raoux S., Rice P.M., Wang S.X., Li G., Monodisperse MFe_2O_4 (M = Fe, Co, Mn) nanoparticles, Journal of the American Chemical Society, 126 (2004) 273–279.

Suzuki M., Shinkai M., Honda H., Kobayashi T., Anticancer effect and immune induction by hyperthermia of malignant melanoma using magnetite cationic liposomes, Melanoma Research, 13 (2003) 129–135.

Thomas C.R., Ferris D.P., Lee J.H., Choi E., Cho M.H., Kim E.S., Stoddart J.F., Shin J.S., Cheon J., Zink J.I., Noninvasive remote-controlled release of drug molecules in vitro using magnetic actuation of mechanized nanoparticles, Journal of the American Chemical Society, 132 (2010) 10623–10625.

Todd T., Zhen Z., Tang W., Chen H., Wang G., Chuang Y.-J., Deaton K., Pan Z., Xie J., Iron oxide nanoparticle encapsulated diatoms for magnetic delivery of small molecules to tumors, Nanoscale, 6 (2014) 2073–2076.

Vallejo-Fernandez G., Roca A.G., Hussain S., Timmis J., Patel V., O'Grady K., Mechanisms of hyperthermia in magnetic nanoparticles, Journal of Physics D: Applied Physics, 46 (2013) 312001.

Wang L.Y., Luo J., Fan Q., Suzuki M., Suzuki I.S., Engelhard M.H., Lin Y.H., Kim N., Wang J.Q., Zhong C.J., Monodispersed core−shell Fe_3O_4@Au nanoparticles, Journal of Physical Chemistry B, 109 (2005) 21593–21601.

Wilhelm C., Fortin J.P., Gazeau F., Tumour cell toxicity of intracellular hyperthermia mediated by magnetic nanoparticles, Journal for Nanoscience and Nanotechnology, 7 (2007) 2933–2937.

Wu J.H., Ko S.P., Liu H.L., Kim S., Ju J.S., Kim Y.K., Sub 5 nm magnetite nanoparticles: Synthesis, microstructure, and magnetic properties, Materials Letters, 61 (2007) 3124–3129.

Wu H., Zhang S., Zhang J., Liu G., Shi J., Zhang L., Cui X., Ruan M., He Q., Bu W., A hollow-core, magnetic, and mesoporous double-shell nanostructure: in situ decomposition/reduction synthesis, bioimaging, and drug-delivery properties, Advanced Functional Materials, 21 (2011) 1850–1862.

Xu Z., Hou Y., Sun S., Magnetic Core/Shell Fe_3O_4/Au and Fe_3O_4/Au/Ag Nanoparticles with Tunable Plasmonic Properties, Journal of the American Chemical Society, 129 (2007) 8698–8699.

Yao A.H., Ai F.R., Wang D.P., Huang W.H., Zhang X.C., Synthesis, characterization and in vitro cytotoxicity of self-regulating magnetic implant material for hyperthermia application, Materials Science and Engineering C: Materials for Biological Applications, 29 (2009) 2525–2529.

Yoon T.-J., Lee H., Shao H., Weissleder R., Highly magnetic core-shell nanoparticles with a unique magnetization mechanism, Angewandte Chemie International Edition, 50 (2011) 4663–4666.

Zeng, H., Rice, P. M., Wang, S. X., Sun, S. H. Shape-controlled synthesis and shape induced texture of $MnFe_2O_4$ nanoparticles. Journal of the American Chemical Society, 2004, 126 (37), 11458–11459.

Zhao L., Zhang H., Xing Y., Song S., Yu S., Shi W., Guo X., Yang J., Lei Y., Cao F., Morphology-controlled synthesis of magnetites with nanoporous structures and excellent magnetic properties, Chemistry of Materials, 20 (2008) 198–204.

Zhu L.P., Xiao H.M., Zhang W.D., Yang G., Fu S.Y., One-pot template-free synthesis of monodisperse and single-crystal magnetite hollow spheres by a simple solvothermal route, Crystal Growth & Design, 8 (2008) 957–963.

Author's short biography

Dung The Nguyen

Dung The Nguyen received his BS degree in chemical engineering from VNU University of Science, Vietnam National University, Vietnam in 2006 and then obtained the PhD degree in chemical engineering from Kangwon National University in 2014. He is now working as a full time researcher in Department of Chemical Engineering, Kangwon National University. His current research interests include controlled synthesis of multifunctional nanoparticles and engineering of chemical reactions and processes.

Kyo-Seon Kim

Kyo-Seon Kim is currently a Professor of Chemical Engineering Department at Kangwon National University, Chuncheon, Korea, where he has been working from 1989. He received the BS, MS and PhD degrees all in Chemical Engineering from Seoul National University, KAIST and University of Cincinnati, USA in 1979, 1981 and 1989, respectively. He worked at Korea Institute of Energy and Resources as a researcher for 1981–1985. On his sabbatical leaves, he was a Visiting Professor at Mechanical Engineering Research Laboratory, Hitachi, Ltd, Japan for 1993–1994 and at DuPont Central Research Laboratory, USA for 2003–2004. His research interests are mainly focused on preparation and modification of nanoparticles by the gas, liquid and plasma processes for the applications to medical devices, pollution control and energy harvest.

KONA Powder and Particle Journal No. 33 (2016) 48–62/Doi:10.14356/kona.2016012 Review Paper

Analysis of Particle Size Distributions of Quantum Dots: From Theory to Application †

Doris Segets

[1] *Institute of Particle Technology, Friedrich-Alexander-Universität Erlangen-Nürnberg (FAU), Germany*

Abstract

Small, quantum-confined semiconductor nanoparticles, known as quantum dots (QDs) are highly important material systems due to their unique optoelectronic properties and their pronounced structure-property relationships. QD applications are seen in the emerging fields of thin films and solar cells. In this review, different characterization techniques for particle size distributions (PSDs) will be summarized with special emphasis on strategies developed and suggested in the past to derive data on the dispersity of a sample from optical absorbance spectra. The latter use the assumption of superimposed individual optical contributions according to the relative abundance of different sizes of a colloidal dispersion. In the second part, the high potential of detailed PSD analysis to get deeper insights of typical QD processes such as classification by size selective precipitation (SSP) will be demonstrated. This is expected to lead to an improved understanding of colloidal surface properties which is of major importance for the development of assumption-free interaction models.

Keywords: particle size distribution, quantum dot, structure-property relationship, classification by size selective precipitation, solubility parameters

1. Introduction

Quantum dots (QDs) are semiconductor nanoparticles which are small enough that quantum confinement occurs in all three dimensions. The first systematic dynamic investigations of interfacial electron and hole processes as well as reports on the size-dependent optical properties of QDs in solution date back to the early 1980s (Duonghong D. et al., 1982; Kuczinski J. and Thomas J.K., 1982; Rossetti R. et al., 1984). Therefrom motivated, Brus was the first who developed a quantum mechanical model based on the effective mass approximation (EMA) of electrons and wholes to predict the evolution of the size-dependent band gap energy (Brus L.E., 1983, 1984; Steigerwald M.L. and Brus L.E., 1990).

Afterwards, as recently summarized by Tyrakowski and Snee (Tyrakowski C.M. and Snee P.T., 2014), more than two decades of intense research on QDs passed, covering various aspects from quantum mechanics and optical properties (Alivisatos A.P., 1996), particle synthesis (Park J. et al., 2007), functionalization and ligand exchange (Alvarado S.R. et al., 2014; Lin W. et al., 2015). Nowadays—although not yet an established mass product—QDs are commercially available via online shops and are highly relevant for the emerging fields of printed solar cells (Debnath R. et al., 2011) and thin-film electronics (Choi J.-H. et al., 2012; Moynihan T., 2015). Moreover, they become increasingly attractive for medical and biological applications (Cottingham K., 2005).

The fine-tuning of a PSD is decisive for any kind of later application. This is due to the aforementioned pronounced size-property relationships of those transient structures situated at the interface between dissolved molecules and solid particles. Thus, QDs are inherently related to interdisciplinary research. Whereas the molecular, rather than the chemical and physical approach is the point where investigations of QDs have originally been started, those nanoparticles provide many aspects that are of equal interest to the field of process engineering and particle technology. Usually, QDs with tailored optical properties in terms of defined absorption onset and emission features in combination with a narrow size distribution are required (Nightingale A.M. and De Mello J.C., 2010; Yen B.K. et al., 2005). This is not only a central issue related to scale-up but equally demanding in terms of characterization—especially when keeping in mind the small particle sizes of a few nanometers in maximum.

To quantitatively compare the narrowness of a PSD throughout different samples, the relative standard deviation (RSD) or coefficient of variation, defined as the stan-

† Received 15 May 2015; Accepted 26 June 2015
J-STAGE Advance published online 10 September 2015
1 Cauerstraße 4, 91058 Erlangen, Germany
E-mail: Doris.Segets@fau.de
TEL: +49-9131-85-29404 FAX: +49-9131-85-29402

dard deviation divided by the mean particle size (RSD = σ/x_{mean}), is usually applied. Following the convention, "monodispersity" is achieved if RSD < 0.05, whereas "narrow" PSDs are found for RSD < 0.1. This fundamental requirement of narrow distributions raises the following central questions:

i) How can QDs that cover particle sizes clearly below 10 nm, often even down to 1 nm, be accurately characterized with justifiable experimental effort?
ii) To what extent can narrow PSDs with RSDs below 0.1 or even below 0.05 be achieved?
iii) Can knowledge on i) and ii) be used to access particle-particle interactions of small colloids?

Whereas the second issue has already recently been discussed by Kowalczyk and Mori and the second issue at least partly addressed by Mori (Kowalczyk B. et al., 2011; Mori Y., 2015), the challenge of size characterization remains. Therefore, in the following sections, different strategies based on the deconvolution of absorbance measurements developed by different groups will be discussed and compared to standard and advanced methods of small particle characterization found in the field of QDs and/or particle technology. The latter will be done with respect to accuracy, availability, experimental effort and potential of the method to become a suitable online technique. In the last part of this work, the high potential of size analysis—aiming to make particle interactions accessible—will be demonstrated by a more recent example on QD classification by size selective precipitation (SSP) (Segets D. et al., 2015). The study shows how careful particle characterization on an Å-level is of paramount importance in order to access colloidal surface properties, and how those may be linked in the near future to permit calculation of assumption-free interaction potentials.

2. Size characterization of QDs

In the following sections, methods for QD size characterization will be introduced. First, standard methods such as (high-resolution (HR)) transmission electron microscopy (TEM) and dynamic light scattering (DLS) as well as advanced techniques such as small-angle X-ray scattering (SAXS), field-flow fractionation (FFF) and analytical ultracentrifugation (AUC) will be discussed briefly. Then, special emphasis will be placed on different approaches for the deconvolution of absorption data to derive a PSD beyond a mean particle size and a standard deviation.

(High-resolution) transmission electron microscopy

At first glance, the most obvious way to analyze QDs is (HR)TEM. It not only gives access to the primary particle size and shape—most of QDs are in good approximation spherical, however, other shapes such as cubes are reported as well (Pietryga J.M. et al., 2004)—but also allows a discrimination of isolated particles from aggregates or superstructures. Moreover, crystallinity and thus the inner structure of the particles can be derived directly from TEM data. Drawbacks are the necessity of an additional drying step and poor statistics that need to be carefully considered when conclusions based on a limited amount of particles (< 1000) are to be drawn for the ensemble (>> 10^{10}). Finally, side effects such as ripening on the TEM substrate induced by the electron beam need to be considered as well (Segets D. et al., 2013). Although over the past years, reports on liquid cell TEM (Nielsen M.H. et al., 2014; Zheng H. et al., 2009) and the evaluation of larger datasets due to automatized image analysis (Segets D. et al., 2012; Sun Y. et al., 2012) came more and more into the focus of interest, electron microscopy is demanding and not (yet) suitable for larger sample numbers and online analysis.

Dynamic light scattering

A frequently used technique for particle size analysis is DLS. It is commercially available, applicable in the liquid phase, and comparatively fast (~ min). It is based on the dynamic change in the scattering of coherent, monochromatic laser light due to the diffusion of small particles in a fluid. An autocorrelation function for the analysis of those fluctuations gives access to the diffusion coefficient D. With known temperature T and viscosity of the fluid η, the hydrodynamic particle diameter x_h (particle core + adsorbate/ligand shell) is available via the Stokes-Einstein equation:

$$D = \frac{k_B T}{3\pi\eta x_h} \tag{1}$$

If the extinction-weighted distribution of hydrodynamic particle sizes is to be transferred to a volume or number PSD, a Mie correction is necessary to consider the size-dependent extinction coefficient.

Regarding smallest nanoparticles such as QDs, it becomes obvious that a core size distribution is hardly accessible via DLS due to the fact that the ligand shell is no longer negligible (Marczak R. et al., 2010; Oshima H., 2009; Reindl A. and Peukert W., 2008). Additionally, the scattering intensity of particles below 10 nm is small, causing a low resolution of commercial devices in the size range of interest between 1 and 10 nm.

Small-Angle X-ray Scattering

In addition to the already mentioned standard techniques, other methods also exist to characterize PSDs with good or even outstanding accuracy. For instance, SAXS can be applied in situ to characterize colloids with

respect to primary particle size and, if required, gives access to agglomerates and even hierarchical structures such as mesocrystals (Seto J. et al., 2012; Sun Y. and Ren Y., 2013). The scattering signal correlates with the electron density distribution within the sample and is thus sensitive to concentration, size and shape (Keshari A.K. and Pandey A.C., 2008; Pauw B.R., 2013). As only one superimposed scattering curve is recorded, data interpretation is challenging and cross-validation against other, independent techniques is required. However, once established for a certain system, SAXS is a powerful technique for particle analysis (Abécassis B. et al., 2015; Caetano B.L. et al., 2010; Polte J. et al., 2010).

Field-Flow Fractionation

A versatile method for the size characterization of not only QDs but also of proteins, polymers, macromolecules, cells and colloids in general is field-flow fractionation (FFF) (Baalousha M. et al., 2011). It is a chromatographic technique, which means that it includes classification of the solute during the measurement. This is seen as a clear advantage with respect to resolution and also with respect to detection (Kowalczyk B. et al., 2011; Mori Y., 1994, 2015). Regarding the measurement principle, no column is needed but separation rather occurs in a laminar flow channel which is superimposed with an orthogonal second field. This second field is often a flow field, but also thermal, electric, magnetic and gravitational fields are possible (Baalousha M. et al., 2011; Williams S.K.R. et al., 2011). For nanoparticles, asymmetric flow FFF (AsFlFFF or A4F) is usually applied. A further advantage of FFF is the flexible detection that can be realized online (e.g. UV/Vis, organic carbon, fluorescence) or offline (e.g. TEM, atomic force microscopy, AUC). Thus, although the investment costs are comparatively high and solute concentrations are an issue, FFF is a promising technique, especially in combination with multiple detectors and with other, complementary analytical methods for size characterization (Dieckmann Y. et al., 2009; Hagendorfer H. et al., 2012).

Analytical Ultracentrifugation

Another outstanding characterization technique is AUC. Due to rotor speeds of up to 60 krpm, it has unrivaled resolution on an Å-level and can detect smallest particles even below 1 nm. The sedimentation of the particles in a centrifugal field is recorded and—usually based on extinction analysis over time—the sedimentation velocity is derived. From this, the particle size, shape and surface properties in terms of the ligand shell are accessible, which makes AUC an excellent technique for the characterization of smallest colloids (Lees E.E. et al., 2008). In parallel, special emphasis has been devoted to the development of advanced evaluation routines and algorithms (Brookes E.H. and Demeler B., 2008; Walter J. et al., 2015b). More recently, AUC has been developed further to allow not only for the detection of a single wavelength but to extend for multiwavelength (MWL) data analysis (Balbo A. et al., 2005; Bhattacharyya S.K. et al., 2006; Strauss H.M. et al., 2008; Walter J. et al., 2014). As a result, the optical properties of individual species in a mixture, such as the absorbance of discrete-sized QDs, will become accessible.

Although the availability of AUC is still limited and online analysis is not possible, it is expected to become the gold standard for particle characterization due to its unmatched resolution of multimodal size distributions and the possibility to extend towards multidimensional characterization. For instance, size and spectral properties, size and shape or size and density (Carney R.P. et al., 2011; Walter J. et al., 2014; Walter J. et al., 2015a; Walter J. et al., 2015b).

At this point it should be briefly mentioned that the same holds true for analytical centrifugation (AC) which works with lower gravitational fields but extends the measurement range to larger particle sizes (Detloff T. and Lerche D., 2008; Jafarzadeh S. et al., 2011; Krause B. et al., 2010; Walter J. et al., 2015c). Noteworthy, offline information from AUC, like for instance the optical properties of discrete QD fractions, could be implemented in evaluation routines based on UV/Vis spectroscopy. The latter is widely available and well-suited for fast online investigations which are needed for kinetic studies at high-time resolution (~ ms). Hence, the technique will be discussed in more detail in the following text with special emphasis on different approaches of data evaluation.

2.1 Deconvolution of absorbance spectra

A rather simple and straightforward strategy for the inline PSD analysis of QDs is the use of optical properties such as absorption and emission. This is possible due to the pronounced structure-property relationships of these materials such as—one of the most prominent examples—the size-dependent band gap energy $E_g(x)$. As exemplarily depicted in **Fig. 1** for Cd-based materials, both absorbance and emission can be tuned over a wide wavelength range by adjusting the particle size (Yu W.W. et al., 2003).

Knowledge of $E_g(x)$ allows correlation of different features of an absorbance spectrum such as i) wavelength of the absorption onset, ii) wavelength of the absorption maximum of the first peak or iii) point of inflexion with discrete particle diameters. This leads to a rough estimation of the particle sizes present in a sample. However, although QD size distributions are narrow, often with RSDs below 0.1 or even below 0.05, Mićić et al. pointed out more than 20 years ago that already small polydispersity

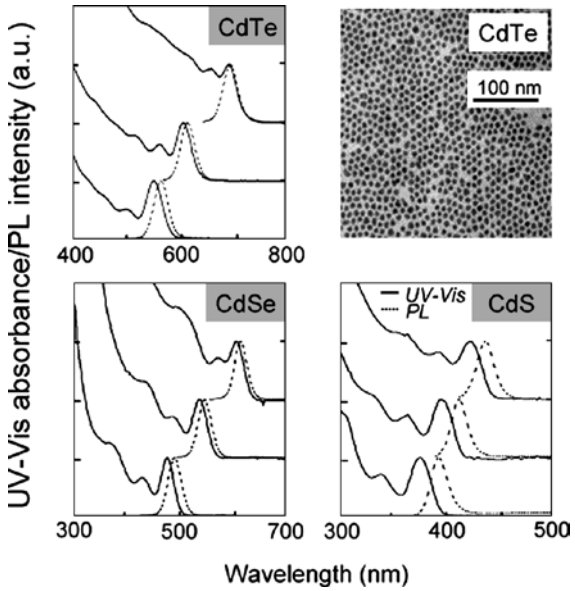

Fig. 1 UV/Vis and PL spectra of CdTe, CdSe and CdS nanocrystal samples. A typical TEM image of CdTe is shown in the upper right corner. Reprinted with permission from Yu et al., "Experimental Determination of the Extinction Coefficient of CdTe, CdSe, and CdS Nanocrystals" Chem. Mater. 2003 15(14), p. 2854–2860. Copyright 2003 American Chemical Society.

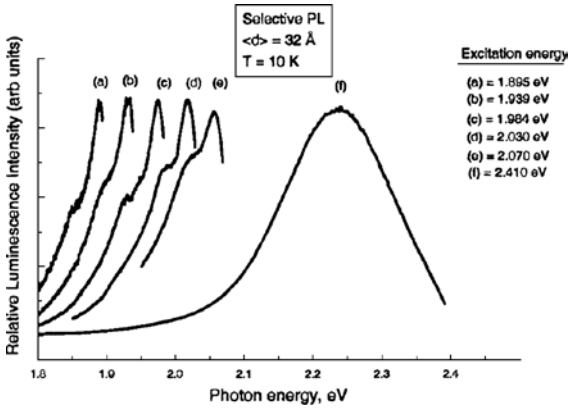

Fig. 2 PL spectra at 10 K for an ensemble of InP quantum dots with a mean diameter of 3.2 nm for different excitation energies. The first absorption peak of the QD ensemble is at 2.17 eV, so that the PL curves a–e result from excitation (1.895–2.070 eV) in the red tail of the onset region of the absorption spectrum and are fluorescence-line-narrowing (FLN) spectra; curve f is a global PL spectrum since its excitation was at 2.14 eV and is well into the blue end of the first absorption peak. Reprinted with permission from Mićić et al., "Size-Dependent Spectroscopy of InP Quantum Dots" J. Phys. Chem. B 1997 101(25), p. 4904–4912. Copyright 1997 American Chemical Society.

values of 0.1 noticeably affect the emission properties (Mićić O.I. et al., 1997). For instance, emission line width strongly depends on which particle sizes in a sample are excited. As can be seen from **Fig. 2**, if the excitation energy at 10 K is small, only electrons in large particles are excited and a small band width is monitored. If the excitation energy is gradually increased by using smaller wavelengths (spectra a–e), the emission blue shifts to larger photon energies and becomes broader. If a larger excitation energy (spectrum f) is used that is shifted to the blue end of the first absorption peak of the QD ensemble, a large fraction of all QDs in the sample is excited. Therefore, the global emission is substantially broader due to polydispersity.

With respect to applications such as displays, it is obvious that a narrow emission is required and that the development of synthesis protocols and theoretical models to decrease polydispersity has been strongly in the focus of interest (Embden J.V. et al., 2009; Rogach A.L. et al., 2002). However, on the one hand standard techniques for the derivation of PSDs such as DLS and TEM are not convincing with respect to size resolution and measurement time, whereas on the other hand, advanced techniques such as SAXS or AUC are either not directly available or are only suitable for offline analysis. Therefore, several approaches were developed to deconvolute the absorbance data of quantum-confined semiconductor nanoparticles with a direct band gap to PSDs. Although possibly not as accurate as SAXS, FFF and/or AUC, UV/Vis absorbance spectroscopy is a standard technology that is widely available and suitable for fast inline analysis (~ ms).

At this point it needs to be mentioned that photoluminescence (PL) spectroscopy is sometimes applied as well to get an impression of the dispersity of a sample (Peng X. et al., 1998). However, as already mentioned by the authors of this work, the assumptions of (i) a δ-function emission and (ii) a size-independent emission intensity lead to an overestimation of the width of the reported PSDs. Moreover, as later pointed out by Viswanatha and Sarma, the PL approach is restricted to fully passivated samples and thus would, e.g. fail in the case of ZnO QDs that do not show a band edge tuning (Viswanatha R. and Sarma D.D., 2006).

Therefore in the following text, only approaches based on absorbance analysis will be discussed (Mićić O.I. et al., 1994; Pesika N.S. et al., 2003a; Pesika N.S. et al., 2003b; Segets D. et al., 2009; Segets D. et al., 2012; Viswanatha R. and Sarma D.D., 2006). Despite differences in the exact deconvolution procedure, they all use the same basic assumptions and restrictions, namely

i) semiconductor nanoparticles with a direct band gap which are small enough that the scattering contribution to the total extinction is negligible and quantum confinement occurs,
ii) a monotone dependency between particle size and

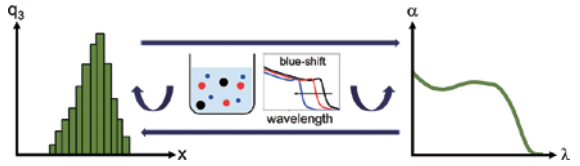

Fig. 3 Sketch of the correlation between polydispersity in particle size and absorbance that is finally accessible by UV/Vis/NIR analysis (Segets D. and Peukert W., 2014).

band gap energy,

iii) a linear superposition of the individual contributions of the different particle size fractions as illustrated in **Fig. 3**.

Within a polydisperse sample of quantum-confined particles, every size fraction has its specific absorption spectrum. According to the relative abundance of the differently sized QDs in the macroscopic sample, the global absorption is created. The challenge is to deduce from an absorbance measurement the size of the underlying species together with their relative abundance and therefrom to create a PSD.

Approach 1: Least squares fit and pre-assumption of PSD shape

Mićić et al. were the first who derived PSDs from absorbance data. In doing so, they already followed a highly innovative two-step approach (Mićić O.I. et al., 1994). First, they synthesized rather polydisperse InP QDs and determined the underlying PSD by HRTEM. Then, they derived by a fit to experimental data (Palik E.D., 1985) an analytical equation for the absorption coefficient α as a function of energy $h\nu$ (or wavelength, respectively) and band gap E_g. The latter included the particle size x (or strictly the particle radius $r = x/2$) and two fitting parameters n and p:

$$\alpha = f\left[h\nu, E_g(r,n,p)\right] \tag{2}$$

Now assuming a PSD following the frequently observed shape of a lognormal distribution, a least squares fit was performed to find a PSD that gives a best match with the measured absorption data (**Fig. 4**, dataset a). Noteworthy is that after having calibrated parameters n and p, they were kept constant throughout all further PSD calculations that matched the expectations well (**Fig. 4**, datasets b and c) (Mićić O.I. et al., 1994).

Disadvantages are the limited number of particles that were evaluated for the calibration PSD, the missing validation of $E_g(x)$ against literature data and the predefined shape of the PSD. However, the first two points can be clearly attributed to the time when the study was performed. In the early 90s, TEM capabilities were much lower than nowadays and reference data did not yet exist

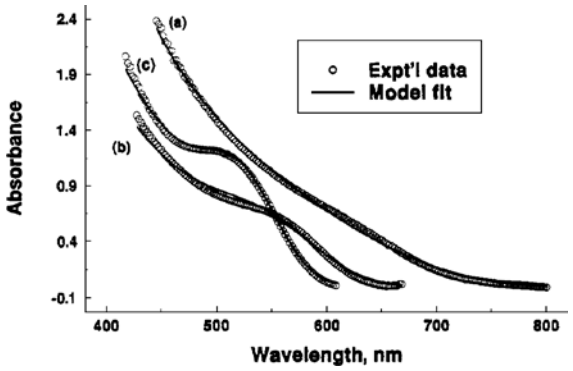

Fig. 4 Experimental absorption spectra (circles) for InP QD colloids with fit to model shown as a solid line: (a) fit made to yield the dependence of QD band gap on QD size; (b and c) fit made to yield the size distribution from the results of (a). Reprinted with permission from Mićić et al., "Synthesis and Characterization of InP Quantum Dots" J. Phys. Chem. 1994 98(19), p. 4966–4969. Copyright 1994 American Chemical Society.

as QDs and related research had just started to come into being. Thus, the work is pioneering in a way that it not only allows the calculation of non-symmetric lognormal PSDs, but even offers the possibility to derive $E_g(x)$ as a material property.

More than a decade later, Viswanatha and Sarma confirmed the applicability of this concept to other material systems by generalizing it to experimental data of ZnO, ZnS and CdSe QDs (Viswanatha R. and Sarma D.D., 2006). In contrast to the earlier work of Mićić, they used Gaussian instead of lognormal distributions and did not calibrate $E_g(x)$ but used fundamental literature data. For instance, in the case of ZnO, a carefully validated tight-binding model (TBM) was applied (Viswanatha R. et al., 2004). Moreover, they proved the assumption of the parallel-shifted bulk absorption spectrum to higher energies for decreasing particle sizes. Therefore they compared the results of the original approach to the outcome when a simple 0-1 step function was used for the shape of the absorption coefficient α. It was found that the difference in the calculated PSDs was negligible. Finally, the apparent width of the experimental and simulated absorbance data of various material systems (ZnO, ZnS(e), CdS(e), GaAs, InAs, InP) on a particle size scale (Δd_{app}) was compared to the true widths of the underlying PSDs (ΔD_{actual}). A material-independent, empiric relationship was thereby identified that allows a quick estimate of a sample's polydispersity from Δd_{app}. In addition to the absorption data, only knowledge of $E_g(x)$ is required:

$$\Delta D_{actual} = -0.0025 \times \frac{\Delta d_{app}^2}{nm} + 0.524 \times \Delta d_{app} - 1.41nm \tag{3}$$

However, for both approaches, the aforementioned is-

sue of a predefined shape of the underlying PSD remains. Therefore, in the following sections, two alternatives that are able to access multimodal distributions without any assumptions on the PSD shape(s) will be discussed.

Approach 2: Wavelength-based deconvolution for arbitrary shaped PSDs

In 2003, the first concept of deriving arbitrary shaped PSDs from absorbance data was developed by Pesika et al. (Pesika N.S. et al., 2003a; Pesika N.S. et al., 2003b). Although the first report of their method was rather restricted to ZnO QDs, they summarized the procedure in the same year again with a more general point of view.

Based on absorbance data of a (0001) ZnO single crystal (**Fig. 5**), they came up with a comparatively simple but useful assumption, namely that in the case of a direct band gap semiconductor, the absorption coefficient α in the vicinity of the onset is given by (Pesika N.S. et al., 2003a; Pesika N.S. et al., 2003b):

$$\alpha = \frac{C\left(h\nu - E_g^{bulk}\right)^{1/2}}{h\nu} \tag{4}$$

C is a constant, $h\nu$ is the photon energy and E_g^{bulk} is the bulk band gap.

Using an effective mass model according to Brus (Brus L., 1986) for the correlation between band gap energy and particle size and further assuming spherical particles and a size-independent absorption coefficient, the following connection between absorbance A, particle size x and relative abundance n was derived (Pesika N.S. et al., 2003a; Pesika N.S. et al., 2003b):

$$A(x) \propto \int_x^{\infty} \frac{\pi}{6} x^3 n(x) \mathrm{d}x \tag{5}$$

From **Eq. 5** it becomes clear that (i) the absorbance of QDs is a volume signal that (ii) can be used to calculate the relative abundance of distinct sizes from the local slope of the absorbance spectrum (boundary condition: $n(x) = 0$ for $x \rightarrow \infty$):

$$n(x) \propto -\frac{\frac{\mathrm{d}A}{\mathrm{d}x}}{\frac{\pi}{6}x^3} \tag{6}$$

As becomes clear from **Fig. 6**, validation of the calculation results revealed an excellent agreement with the size distributions determined by TEM. However, in contrast to the formerly discussed approaches, even bimodal distributions of arbitrary shape could be derived without any input parameters. This was proven by the evaluation of absorbance data of mixed suspensions containing controlled amounts of small and large particles. A nearly perfect match was found when the results from the bimodal absorbance spectrum were compared to the expected distributions obtained from the individually evaluated absorption data of small and large particles. Another advantage of the technique is its comparatively simple implementation as only a correlation for the size-dependent band gap energy $E_g(x)$ and the local slope of the absorbance spectrum are required. The only drawback, how-

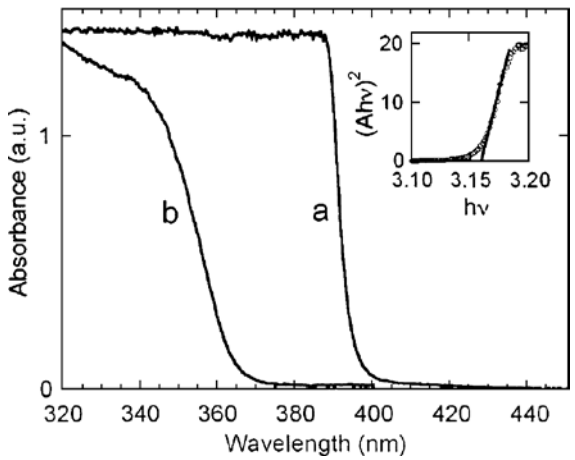

Fig. 5 (a) Absorbance spectrum for a (0001) ZnO single crystal and (b) absorbance spectrum for a suspension of ZnO quantum particles after 2 h of growth at 65 °C. The inset shows the spectrum for the ZnO single crystal plotted as $(Ahv)^2$ versus hv. Reprinted with permission from Pesika et al., "Relationship between Absorbance Spectra and Particle Size Distributions for Quantum-Sized Nanocrystals" J. Phys. Chem. B 2003 107(38), p. 10412–10415. Copyright 2003 American Chemical Society.

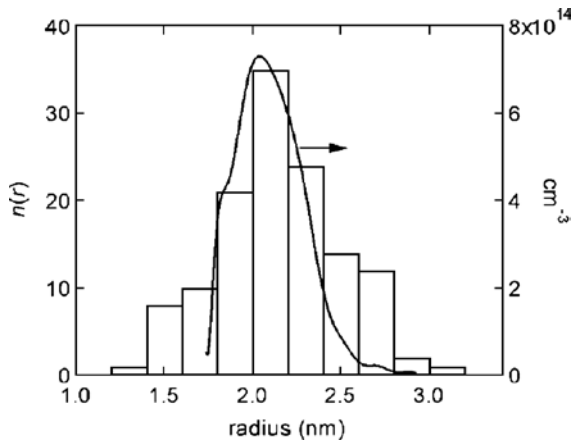

Fig. 6 Distribution results of ZnO QDs after 2 h of growth at 65 °C. The histogram was obtained from analysis of high-resolution transmission electron microscope images of 125 particles. The solid line was obtained from the absorbance spectrum. Reprinted with permission from Pesika et al., "Relationship between Absorbance Spectra and Particle Size Distributions for Quantum-Sized Nanocrystals" J. Phys. Chem. B 2003 107(38), p. 10412–10415. Copyright 2003 American Chemical Society.

ever, is the strong assumption of a step function for the absorbance of monodisperse particles. Simply trying to make a reconstruction of the original absorbance spectrum by using a known $n(x)$ and applying **Eq. 5**, the minimum observed after the first absorbance peak is never obtained—especially in the case of smaller nanoparticles.

To address this issue, Segets et al. developed a more flexible approach with respect to the shape evolution of the shifted absorption coefficient (Segets D. et al., 2009; Segets D. et al., 2012). Instead of using a step function, the bulk absorption coefficient was used as an assumption for the shape of the monodisperse QD absorption evolution. The size dependency was simply addressed by a parallel shift of the bulk absorption to smaller wavelengths according to $E_g(x)$. Regarding the deconvolution of a measured absorbance spectrum $A(\lambda)$ into partial spectra $A_i'(\lambda)$, each of these assumed to have the form of the bulk absorption $\alpha(\lambda)$, the algorithm is realized as follows (Segets D. et al., 2009; Segets D. et al., 2012):

(i) First, the bulk absorption α is parallel-shifted in a way that its peak position matches the largest wavelength under consideration (λ_i). The particle diameter that is related to this specific wavelength needs to be derived either from quantum mechanics or from a separate calibration by matching calculated $PSDs^{calc}$ against $PSDs^{TEM}$, as suggested by Mićić et al. In the following text, this shifted absorption coefficient will be denoted as $\alpha_{shift,i}(\lambda)$.

(ii) Then, $\alpha_{shift,i}(\lambda)$ is scaled in a way that it coincides with the measurement value $A(\lambda_i)$:

$$A_i'(\lambda) = \frac{\alpha_{shift,i}(\lambda)}{\alpha_{shift,i}(\lambda_i)} \times A_i(\lambda_i) \tag{7}$$

This leads to the first partial absorbance spectrum that exactly matches the measurement value at position λ_i.

(iii) Dividing $A_i(\lambda_i)$ by the value of the shifted absorption coefficient at this wavelength ($\alpha_{shift,i}(\lambda_i)$), the particle size interval $\Delta x = x_{i+1} - x_i$ under consideration and the optical path length d_c, the first value of a size distribution that is still related to the total mass of solid QD material is obtained (Segets D. et al., 2009). Worthy of note is that x_{i+1} is the particle size which is linked with the next smaller wavelength analyzed. Thus, Δx_i depends on the measurement settings.

(iv) Then, the absorbance contribution of this known, largest particle size fraction is subtracted from the measurement spectrum according to:

$$A(\lambda) = A(\lambda) - A_i'(\lambda) \tag{8}$$

Thus, a new spectrum is created and steps (i–iv) are repeated until all relevant wavelengths are analyzed.

(v) Finally, the concentration-related distribution is converted to a PSD that fulfills the requirement of a normalized density distribution:

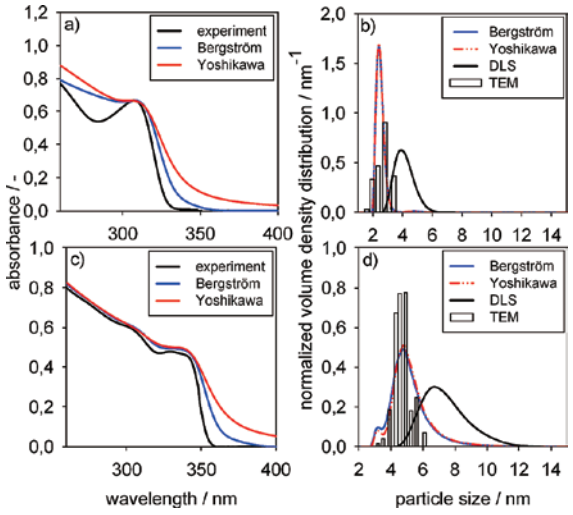

Fig. 7 Comparison between the calculated PSDs, DLS and optical image analysis of two different samples of b) small and d) large ZnO QDs and the related measured (black solid line) and reconstructed (blue and red solid lines) absorbance spectra for a) smaller and c) larger-sized samples. Reprinted with permission from Segets et al., "Analysis of Optical Absorbance Spectra for the Determination of ZnO Nanoparticle Size Distribution, Solubility, and Surface Energy" ACS Nano 2009 3(7), p. 1703–1710. Copyright 2009 American Chemical Society.

$$\sum_{x_{min}}^{x_{max}} [q_3(x) \cdot \Delta x] = 1 \tag{9}$$

As already expected from the analysis of Viswanatha and Sarma (Viswanatha R. and Sarma D.D., 2006) using Gaussian distributions, the final results are not strongly affected by the assumed shape of the parallel-shifted bulk absorption (Segets D. et al., 2012) also in the case of arbitrary PSDs. To illustrate this, **Fig. 7** shows the deconvolution results of absorbance data derived for small (a, b) and large (c, d) ZnO QDs using two different datasets for the bulk absorption coefficient (Bergström L. et al., 1996; Yoshikawa H. and Adachi S., 1997). For validation, TEM and DLS results are presented as well.

It becomes clear that while the calculated PSDs are not affected by the dataset used for the absorption coefficient, the reconstructed absorbance measurements do depend on the optical properties chosen. Noteworthy is that the shifted bulk absorption is not yet expected to be the correct absorption evolution of monodisperse QDs. However, as soon as discrete optical properties are accessible, for instance via AUC analysis, they are easily implemented to the existing code. A proof of the correct optical properties would be obtained as soon as not only the forward calculation of a PSD^{calc} is done correctly, but when also

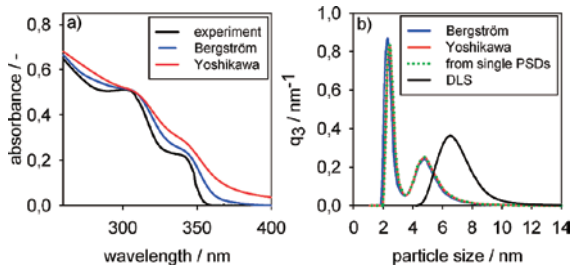

Fig. 8 a) Absorbance spectrum of the bimodal PSD after mixing the two suspensions in the same volume ratio (black line) and its corresponding reconstructions (blue and red lines); b) bimodal PSD calculated from the bimodal absorbance spectrum with the bulk properties from Bergström and Yoshikawa (blue and red lines), expected bimodal PSD calculated from the PSDs of the pure unmixed suspensions (green dotted line), and bimodal PSD measured with DLS (black line). Reprinted with permission from Segets et al., "Analysis of Optical Absorbance Spectra for the Determination of ZnO Nanoparticle Size Distribution, Solubility, and Surface Energy" ACS Nano 2009 3(7), p. 1703–1710. Copyright 2009 American Chemical Society.

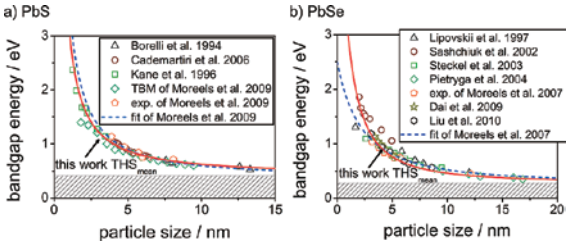

Fig. 9 Relationship between fundamental band gap energy and particle size as derived in this work along with comparison to literature data for a) PbS (Borrelli N.F. and Smith D.W., 1994; Cademartiri L. et al., 2006; Kane R.S. et al., 1996; Moreels I. et al., 2009) and b) PbSe (Dai Q. et al., 2009; Koole R. et al., 2008; Lipovskii A. et al., 1997; Liu Y. et al., 2010; Ma W. et al., 2011; Moreels I. et al., 2007; Pietryga J.M. et al., 2004; Sashchiuk A. et al., 2001; Steckel J.S. et al., 2003) as indicated. Reprinted with permission from Segets et al., "Determination of the Quantum Dot Band Gap Dependence on Particle Size from Optical Absorbance and Transmission Electron Microscopy Measurements" ACS Nano 2012 6(10), p. 9021–9032. Copyright 2012 American Chemical Society.

the reconstructed absorbance spectrum based on PSD^{calc} matches the measurement data. As already discussed, the analysis of bimodal distributions without any input parameters is possible as well using this approach. This is summarized in **Fig. 8**.

Additionally, in a subsequent work, the original idea of Mićić to derive $E_g(x)$ by careful calibration was picked up again (Segets D. et al., 2012). A study on PbS(e) was performed to demonstrate the general applicability of the method originally developed for ZnO by means of a completely different QD system. In addition, in the case of PbS(e) QDs that were chosen for this study, well-established and properly validated literature data on $E_g(x)$ is available. Small and large particles were synthesized and aberration-corrected TEM micrographs were analyzed by semi-automatized image analysis. In parallel, a power law with three empiric parameters a [nm], b [–] and c [nm] was used for description of the size-dependent band gap energy $\Delta E_i(x_i)$:

$$x_i = a\left(\frac{\Delta E_i}{eV}\right)^b + c \tag{10}$$

Finally, a, b and c were modified until a best match was obtained between $PSDs^{calc}$ derived by the algorithm and $PSDs^{TEM}$ derived by image analysis. It was found to be preferable to analyze two samples covering two different particle size regimes in order to arrive at compromise values for a, b and c. This leads to a function of $E_g(x)$ which is valid over a wide size range. The results are shown in **Fig. 9**.

It becomes clear that an excellent agreement exists with literature data collected over the past decades. This confirms the large potential of QD absorbance data analysis. Thus, the usefulness of PSD calculation from absorbance measurements by various approaches with all of them having their specific advantages and disadvantages is sufficiently proven. Future directions are seen in the combination of different characterization methods (e.g. SAXS, FFF, AUC and UV/Vis analysis) to increase accuracy and resolution even further.

Especially the latter is somewhat limited by the absorbance approach as i) information on small particles might be hidden in the tail of absorbance spectra of larger sizes and as ii) the resolution is somewhat limited by the requirement of a noticeable change of $E_g(x)$ for two different particle diameters. Therefore, AUC that provides a maximum knowledge gain with respect to a PSD with sub-nm resolution, composition and surface chemistry becomes one of the most important techniques for QD characterization (Carney R.P. et al., 2011; Lees E.E. et al., 2008). In combination with in-situ techniques such as UV/Vis or SAXS, it is expected to provide new, mechanistic insights of QD formation with unrivaled accuracy.

3. Application to classification

At this stage, some fundamental conclusions with respect to colloidal interactions are possible. This is demonstrated by applying the method to classification on a sub-10 nm scale. Worthy of note is that various approaches

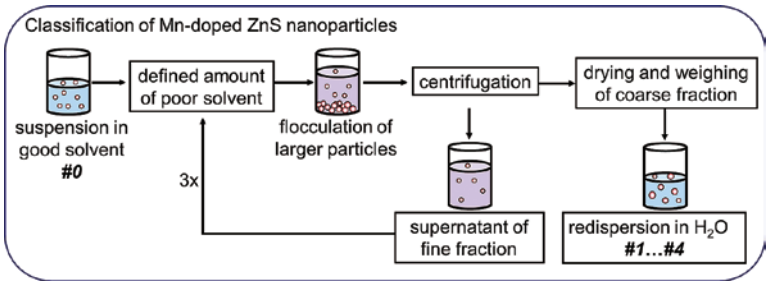

Fig. 10 Illustration of the experimental procedure of SSP. With kind permission from Springer Science+Business Media: Segets et al., "Quantitative evaluation of size selective precipitation of Mn-doped ZnS quantum dots by size distributions calculated from UV/Vis absorbance spectra" J. Nanopart. Res. 2013 15:1486, Scheme 1.

for nanoparticle classification and purification exist that are already described in excellent review papers (Kowalczyk B. et al., 2011; Mori Y., 2015; Sapsford K.E. et al., 2011). However, for QDs, size selective precipitation (SSP)—which is the preferred flocculation of larger particles in a non-solvent—is still the most important post-processing strategy.

In the following sections, first the working principle of SSP will be introduced. It will be discussed how SSP can be described theoretically based on results obtained from careful PSD and mass balance analysis. Finally, things are set into perspective by an outlook that shows how classification by SSP is linked to Hansen solubility parameters (HSP) which in turn give access to the Flory-Huggins interaction parameter χ. Knowledge of χ is decisive for derivation of the osmotic interactions between the ligand shells around QDs and thus represents an important parameter in the context of steric stabilization.

3.1 Size selective precipitation

The working principle of SSP first reported by the groups of Murray and Weller is as rational as it is simple (Murray C.B. et al., 1993; Vossmeyer T. et al., 1994). Starting from QDs dispersed in a good solvent, a non-solvent is added that induces the preferred, reversible flocculation of larger particles.

In the case of nanoparticles with polar surface termination, a non-solvent would be something non-polar such as toluene or heptane, in the case of nanoparticles with hydrophobic surface properties, a non-solvent would be hydrophilic, e.g. ethanol or acetone. Due to the fact that the flocculates are in the size range of µm to mm, a solid-liquid separation by centrifugation in a typical lab centrifuge with up to ~10 000 g is sufficient to separate the flocculated larger particles from small QDs in the supernatant. As illustrated in **Fig. 10**, the process can be repeated in several cycles and even redispersion of the QDs on a primary particle level after centrifugation is possible. In the past it was demonstrated in various works that SSP is a highly efficient procedure that is able to substantially narrow PSDs and improve the emission properties of a sample (Komada S. et al., 2012; Nag A. et al., 2007). For instance, Mastronardi et al. subdivided a starting suspension of Si nanoparticles into the impressive amount of 14 differently sized samples with all of them revealing substantial differences in their optical properties (Mastronardi M.L. et al., 2011).

However, in addition to the final outcome of SSP in terms of samples with small RSD as well as varying absorbance and emission properties, the classification process itself can be analyzed by means of well-known concepts from the field of process engineering and particle technology (Segets D. et al., 2013; Segets D. et al., 2015). This will be briefly summarized in the following section.

Knowing the relative masses of the coarse fraction g ($= m_{recovered}/m_{in}$) and the fine fraction f ($= m_{supernatant}/m_{in}$) after drying as well as the PSDs of the feed $q_F(x)$, the coarse $q_g(x)$ and the fines $q_f(x)$ from UV/Vis data, the following parameters are accessible (Segets D. et al., 2015):

(i) The cut size x_t at the intersection between the mass weighted density distribution of the coarse $g \cdot q_g(x)$ and the fines $f \cdot q_f(x)$.

(ii) The separation efficiency:

$$T(x) = \frac{g q_g(x)}{q_F(x)} \tag{11}$$

(iii) The separation sharpness κ to characterize the steepness of the cut with $x_{25,t}$ and $x_{75,t}$ being the particle sizes at which $T(x)$ is 0.25 or 0.75, respectively:

$$\kappa = \frac{x_{25,t}}{x_{75,t}} \tag{12}$$

(iv) The yields for coarse η_g and fines η_f to evaluate the efficiency of the process:

$$\eta_g = \frac{\int_{x_t}^{x_{max}} [g q_g(x)\,dx]}{\int_{x_t}^{x_{max}} [q_F(x)\,dx]} \quad (13)$$

$$\eta_f = \frac{\int_{x_{min}}^{x_t} [f q_f(x)\,dx]}{\int_{x_{min}}^{x_t} [q_F(x)\,dx]} \quad (14)$$

For more details the reader is referred to the literature (Leschonski K., 1977; Leschonski K. et al., 1974; Rhodes M.J., 1999; Rumpf H., 1990), however, two important aspects shall be stressed here: the intrinsic inclusion of the mass balance in $T(x)$ (note that $f + g = 1$ and $f \cdot q_f(x) + g \cdot q_g(x) = 1$) and its independency of the quantity (number, area, volume/mass) based on which the PSD is derived. Thus, $T(x)$ is a perfect measure for the classification process whereas RSD is a perfect measure for the classification result in terms of the derived product PSD.

Using **Eqs. 11–14** and performing classification studies on ZnS QDs with different feed distributions and various good solvent/poor solvent combinations, Segets et al. found the following analytical description of SSP that can be understood as a law of mass action (Segets D. et al., 2015) with dissociation constant K_{diss}:

$$K_{diss,i}(x_i) = \frac{f q_f(x_i)}{g q_g(x_i)} = \frac{q_F(x_i) - g q_g(x_i)}{g q_g(x_i)} = \frac{1 - T(x_i)}{T(x_i)} \quad (15)$$

Thus, the cut of an SSP experiment neither depends on the feed PSD nor on process parameters such as stirring, time of poor solvent exposure or dosing. Even the solids concentration of the feed does not have any influence as long as it does not clearly exceed a comparatively high, critical upper limit (e.g. >> 10 g L^{-1} in the case of ZnS). SSP is determined in terms of the steepness and position of the cut by the chemical structure of the good and the poor solvent as well as their volume ratio. Comparing the effect of different solvents, the relative permittivity of the final mixture—which is of major importance for the van der Waals interaction—is not the sole influencing factor on SSP. In fact, the specific chemistry of the applied solvents and their interaction with the stabilizing ligands adsorbed at the QD surface are significant as well. This represents the connection between classification results, solubility parameters and steric stabilization and will be described in the following section.

3.2 Link to Flory-Huggins interaction parameter

It was found that the best way of data representation is to plot the QD dispersibility of a specific size fraction in a 3-dimensional Hansen space normalized to the Hamaker constant of the core material in the solvent mixture (Segets D. et al., 2015). Further, it turned out that the HSP of decorated nanoparticles which are understood as the ensemble of QD core plus ligand shell need to be clearly distinguished from the HSP of the unbound, free ligands on a molecular level. The balance of van der Waals attraction and HSP is in agreement with works of the groups of Korgel and Roberts. They reported that in the case of SSP, a steric repulsive force comprised of an elastic and an osmotic interaction due to solvation of the ligand tail by the solvent—the latter being related to solubility parameters—needs to be balanced vs. van der Waals adhesion (Kitchens C.L. et al., 2003; Saunders S.R. and Roberts C.B., 2009; Shah P.S. et al., 2002a; Shah P.S. et al., 2002b; Vincent B. et al., 1986). As recently pointed out by Mori (Mori Y., 2015), this can be extended by electrostatic and Born repulsion, possibly entropic effects such as depletion might need to be considered as well (Mao Y. et al., 1995). However, in line with the findings of Segets et al. (Segets D. et al., 2015), especially the study of Mori revealed that van der Waals adhesion and osmotic interaction are the main contributors to the total interaction.

Analyzing the osmotic term in more detail, two quantities are decisive: the volume fraction of the ligand ϕ and the Flory-Huggins interaction parameter χ_{12} (with index 1 referring to the solvent and index 2 referring to the ligand). Whereas the former can be estimated by the surface coverage or is directly accessible via AUC or small-angle neutron scattering (SANS) (Whitell G.V. and Kitchens C.L., 2010), the latter is even more challenging. It relates to the Hildebrand solubility parameter δ_i (or the cohesive energy density $c_i = \delta_i^2$):

$$\chi_{12} = \frac{V_m}{RT}(\delta_1 - \delta_2)^2 \quad (16)$$

With V_m being the molar volume, R being the ideal gas constant and T being the temperature.

Hansen subdivided the energy of cohesion into a polar contribution δ_p, a disperse contribution δ_d and the ability to exchange electrons δ_h according to the concept of Lewis acids and bases (Hansen C.M., Hansen C.M. and Skaarup K.J., 1967). **Eq. 16** can be rewritten as (Hansen C.M., 2007):

$$\chi_{12} = \frac{V_m}{RT}\left[(\delta_{d2} - \delta_{d1})^2 + 0.25(\delta_{p2} - \delta_{p1})^2 + 0.25(\delta_{h2} - \delta_{h1})^2\right] \quad (17)$$

Thus, once having access to the HSP of small nanoparticles, χ_{12} can be derived. Together with additional knowledge of the surface coverage, the osmotic interaction potential is accessible and steric effects can be balanced vs. van der Waals adhesion.

By the careful analysis of PSDs established from absorbance spectra, the principal applicability of HSP to QDs

could already be demonstrated (Segets D. et al., 2015). Now suitable measurement techniques for HSP, for instance by using analytical centrifugation in the liquid phase (Lerche D. and Sobisch T., 2014), need to be established and validated against numeric data like it was already done in the case of polymers (Díaz I. et al., 2013) or gas-phase results, e.g. obtained by inverse gas chromatography (Liu Y. and Shi B., 2008). Thus, the careful evaluation of QD dispersity not only gives important insights into the classification process itself but can even make an important contribution to a better understanding of the steric stabilization of small colloids.

4. Conclusion and perspectives

Different methods for analyzing the particle size distribution (PSD) of quantum dots (QD) were discussed. In addition to standard techniques such as high-resolution (HR) transmission electron microscopy (TEM) and dynamic light scattering (DLS) as well as advanced techniques such as small-angle X-ray scattering (SAXS), Field-Flow Fractionation (FFF) and analytical ultracentrifugation (AUC), the focus was put on the conversion of absorbance spectra to PSDs. In this context four approaches were presented, with two of them (according to Mićić et al. and Viswanatha et al.) using predefined PSD shapes (lognormal and Gaussian) and two of them (according to Pesika et al. and Segets et al.) using a step-wise deconvolution approach. The two latter are seen to be preferred whenever the shape of the target PSD is not known. The technique of Pesika et al. uses the local slope of the absorbance spectrum. The approach of Segets et al. uses a shifted bulk absorption coefficient that brings the possibility to include the optical properties of discrete QD size fractions as soon as they are available. Worthy of note is that data of such monodisperse fractions is becoming more and more available, e.g. by using AUC equipped with multiwavelength (MWL) detection.

In the last part of this work, a clear perspective of exactly why precise PSD characterization on an Ångström level matters was presented. A colloidal classification technique that is widely applied in the field of QDs, the so-called size selective precipitation (SSP) was introduced. It is based on the precise tailoring of steric interactions vs. van der Waals adhesion and can be evaluated with established routines from the field of process engineering and particle technology. SSP is not only described well by the separation efficiency $T(x)$ following a law of mass action, but classification results can be illustrated in a 3D Hansen space normalized to van der Waals attraction.

Based on this finding, knowledge on PSDs potentially allows the determination of Hansen solubility parameters (HSP). The latter give access to the osmotic interaction potential originating from the ligand shells adsorbed at the QD surface and thus lead to a better description of steric stabilization. This is of major importance not only with respect to tailored classification processes but also with respect to formulation issues.

Acknowledgments

The support of the Deutsche Forschungsgemeinschaft (DFG) is gratefully acknowledged through the Cluster of Excellence “Engineering of Advanced Materials”. Moreover, I want to thank Johannes Walter and Wolfgang Peukert for fruitful discussion.

References

Abécassis B., Bouet C., Garnero C., Constantin D., Lequeux N., Ithurria S., Dubertret B., Pauw B.R., Pontoni D., Real-time in situ probing of high-temperature quantum dots solution synthesis, Nano Lett., 15 (2015) 2620–2626.

Alivisatos A.P., Semiconductor clusters, nanocrystals, and quantum dots, Science, 271 (1996) 933–937.

Alvarado S.R., Guo Y., Purnima T., Ruberu P.A., Tavasoli E., Vela J., Inorganic chemistry solutions to semiconductor nanocrystal problems, Coordin. Chem. Rev., 263–264 (2014) 182–196.

Baalousha M., Stolpe B., Lead J.R., Flow field-flow fractionation for the analysis and characterization of natural colloids and manufactured nanoparticles in environmental systems: A critical review, J. Chromatogr. A, 1218 (2011) 4078–4103.

Balbo A., Minor K.H., Velikovsky C.A., Mariuzza R.A., Peterson C.B., Schuck P., Studying multiprotein complexes by multisignal sedimentation velocity analytical ultracentrifugation, Proc. Natl. Acad. Sci. U.S.A., 102 (2005) 81–86.

Bergström L., Meurk A., Arwin H., Rowcliffe D.J., Estimation of Hamaker constants of ceramic materials from optical data using Lifshitz theory, J. Am. Ceram. Soc., 79 (1996) 339–348.

Bhattacharyya S.K., Maciejewska P., Börger L., Stadler M., Gülsün A.M., Cicek H.B., Cölfen H., Development of a fast fiber based UV-Vis multiwavelength detector for an ultracentrifuge, Prog. Coll. Pol. Sci. S, 131 (2006) 9–22.

Borrelli N.F., Smith D.W., Quantum confinement of PbS microcrystals in glass, J. Non.-Cryst. Solids, 180 (1994) 25–31.

Brookes E.H., Demeler B., Monte Carlo analysis of sedimentation experiments, Colloid Polym. Sci., 286 (2008) 138–148.

Brus L., Electronic wave functions in semiconductor clusters: Experiment and theory, J. Phys. Chem., 90 (1986) 2555–2560.

Brus L.E., A simple model for the ionization potential, electron affinity, and aqueous redox potentials of small semiconductor crystallites, J. Chem. Phys., 79 (1983) 5566–5571.

Brus L.E., Electron-electron and electron-hole interactions in small semiconductor crystallites: The size dependence of

the lowest excited electronic state, J. Chem. Phys., 80 (1984) 4403–4409.

Cademartiri L., Montanari E., Calestani G., Migliori A., Guagliardi A., Ozin G.A., Size-dependent extinction coefficient of PbS quantum dots, J. Am. Chem. Soc., 128 (2006) 10337–10346.

Caetano B.L., Santilli C.V., Meneau F., Briois V., Pulcinelli S.H., In situ and simultaneous UV-Vis/SAXS and UV-Vis/XAFS time-resolved monitoring of ZnO quantum dots formation and growth, J. Phys. Chem. C, 115 (2010) 4404–4412.

Carney R.P., Kim J.K., Qian H., Jin R., Mehenni H., Stellacci F., Bakr O.M., Determination of nanoparticle size distribution together with density or molecular weight by 2D analytical ultracentrifugation, Nat. Commun., 2 (2011) 1–8.

Choi J.-H., Fafarman A.T., Oh S.J., Ko D.-K., Kim D.K., Diroll B.T., Muramoto S., Gillen J.G., Murray C.B., Kagan C.R., Bandlike transport in strongly coupled and doped quantum dot solids: A route to high-performance thin-film electronics, Nano Lett., 12 (2012) 2631–2638.

Cottingham K., Quantum dots leave the light on, Anal. Chem., 77 (2005) 354A–357A.

Dai Q., Wang Y., Li X., Zhang Y., Pellegrino D.J., Zhao M., Zou B., Seo J.T., Wang Y., Yu W.W., Size-dependent composition and molar extinction coefficient of PbSe semiconductor nanocrystals, ACS Nano, 3 (2009) 1518–1524.

Debnath R., Bakr O.M., Sargent E.H., Solution-processed colloidal quantum dot photovoltaics: A perspective, Energy Environ. Sci., 4 (2011) 4870–4881.

Detloff T., Lerche D., Centrifugal separation in tube and disc geometries: Experiments and theoretical models, Acta Mech., 201 (2008) 83–94.

Díaz I., Díez E., Camacho J., León S., Ovejero G., Comparison between three predictive methods for the calculation of polymer solubility parameters, Fluid Phase Equilib., 337 (2013) 6–10.

Dieckmann Y., Cölfen H., Hofmann H., Petri-Fink A., Particle size distribution measurements of manganese-doped ZnS nanoparticles, Anal. Chem., 81 (2009) 3889–3895.

Duonghong D., Ramsden J., Grätzel M., Dynamics of interfacial electron-transfer processes in colloidal semiconductor systems, J. Am. Chem. Soc., 104 (1982) 2977–2985.

Embden J.V., Sader J.E., Davidson M., Mulvaney P., Evolution of colloidal nanocrystals: Theory and modeling of their nucleation and growth, J. Phys. Chem. C, 113 (2009) 16342–16355.

Hagendorfer H., Kaegi R., Parlinska M., Sinnet B., Ludwig C., Ulrich A., Characterization of silver nanoparticle products using asymmetric flow field flow fractionation with a multidetector approach—a comparison to transmission electron microscopy and batch dynamic light scattering, Anal. Chem., 84 (2012) 2678–2685.

Hansen C.M., The official Hansen solubility parameter site, <www.hansen-solubility.com> (accessed Aug 8, 2014).

Hansen C.M., Hansen solubility parameters: A user's handbook, 2nd edition, CRC Press, Boca Raton, FL, USA, 2007.

Hansen C.M., Skaarup K.J., The three dimensional solubility parameter—key to paint component affinities: III independent calculations of the parameter components, J. Paint Technol., 39 (1967) 511–520.

Jafarzadeh S., Thormann E., Rönnevall T., Adhikari A., Sundell P.-E., Pan J., Claesson P.M., Toward homogeneous nanostructured polyaniline/resin blends, ACS Appl. Mater. Interfaces, 3 (2011) 1681–1691.

Kane R.S., Cohen R.E., Silbey R., Theoretical study of the electronic structure of PbS nanoclusters, J. Phys. Chem., 100 (1996) 7928–7932.

Keshari A.K., Pandey A.C., Size and distribution: A comparison of XRD, SAXS and SANS study of II–VI semiconductor nanocrystals, J. Nanosci. Nanotech., 8 (2008) 1221–1227.

Kitchens C.L., McLeod M.C., Roberts C.B., Solvent effects on the growth and steric stabilization of copper metallic nanoparticles in AOT reverse micelle systems, J. Phys. Chem. B, 107 (2003) 11331–11338.

Komada S., Kobayashi T., Arao Y., Tsuchiya K., Mori Y., Optical properties of manganese-doped zinc sulfide nanoparticles classified by size using poor solvent, Adv. Powder Technol., 23 (2012) 872–877.

Koole R., Allan G., Delerue C., Meijerink A., Vanmaekelbergh D., Houtepen A.J., Optical investigation of quantum confinement in PbSe nanocrystals at different points in the Brillouin zone, Small, 4 (2008) 127–133.

Kowalczyk B., Lagzi I., Grzybowski B.A., Nanoseparations: Strategies for size and/or shape-selective purification, Curr. Op. Coll. Int. Sci., 16 (2011) 135–148.

Krause B., Mende M., Pötschke P., Petzold G., Dispersability and particle size distribution of CNTs in an aqueous surfactant dispersion as a function of ultrasonic treatment time, Carbon, 48 (2010) 2746–2754.

Kuczinski J., Thomas J.K., Photochemistry at the surface of colloidal cadmium sulfide, Chem. Phys. Lett., 88 (1982) 445–447.

Lees E.E., Gunzburg M.J., Nguyen T.-L., Howlett G.J., Rothacker J., Nice E.C., Clayton A.H.A., Mulvaney P., Experimental determination of quantum dot size distributions, ligand packing densities, and bioconjugation using analytical ultracentrifugation, Nano Lett., 8 (2008) 2883–2890.

Lerche D., Sobisch T., Evaluation of particle interactions by in situ visualization of separation behaviour Coll. Surf. A: Physicochem. Aspects, 440 (2014) 122–130.

Leschonski K., Das Klassieren disperser Feststoffe in gasförmigen Medien, Chem.-Ing.-Tech., 49 (1977) 708–719.

Leschonski K., Alex. W., Koglin B., Teilchengrößenanalyse, Chem.-Ing.-Tech., 46 (1974) 23–26.

Lin W., Walter J., Burger A., Maid H., Hirsch A., Peukert W., Segets D., A general approach to study the thermodynamics of ligand adsorption to colloidal surfaces demonstrated by means of catechols binding to zinc oxide quantum dots, Chem. Mater., 27 (2015) 358–369.

Lipovskii A., Kolobkova E., Petrikov V., Kang I., Olkhovets A., Krauss T., Thomas M., Silcox J., Wise F., Shen Q., Kycia S., Synthesis and characterization of PbSe quantum dots in phosphate glass, Appl. Phys. Lett., 71 (1997) 3406–3408.

Liu Y., Gibbs M., Puthussery J., Gaik S., Ihly R., Hillhouse H.W., Law M., Dependence of carrier mobility on nanocrystal size and ligand length in PbSe nanocrystal solids,

Nano Lett., 10 (2010) 1960–1969.
Liu Y., Shi B., Determination of Flory interaction parameters between polyimide and organic solvents by HSP theory and IGC, Polym. Bull., 61 (2008) 501–509.
Ma W., Swisher S.L., Ewers T., Engel J., Ferry V.E., Atwater H.A., Alivisatos A.P., Photovoltaic performance of ultrasmall PbSe quantum dots, ACS Nano, 5 (2011) 8140–8147.
Mao Y., Cates M.E., Lekkerkerker H.N.W., Depletion force in colloidal systems, Physica A, 222 (1995) 10–24.
Marczak R., Segets D., Voigt M., Peukert W., Optimum between purification and colloidal stability of ZnO nanoparticles, Adv. Powder Technol., 21 (2010) 41–49.
Mastronardi M.L., Maier-Flaig F., Faulkner D., Henderson E.J., Kübel C., Lemmer U., Ozin G.A., Size-dependent absolute quantum yields for size-separated colloidally-stable silicon nanocrystals, Nano Lett., 12 (2011) 337–342.
Mićić O.I., Cheong H.M., Fu H., Zunger A., Sprague J.R., Mascarenhas A., Nozik A.J., Size-dependent spectroscopy of InP quantum dots, J. Phys. Chem. B, 101 (1997) 4904–4912.
Mićić O.I., Curtis C.J., Jones K.M., Sprague J.R., Nozik A.J., Synthesis and characterization of InP quantum dots, J. Phys. Chem., 98 (1994) 4966–4969.
Moreels I., Lambert K., De Muynck D., Vanhaecke F., Poelman D., Martins J.C., Allan G., Hens Z., Composition and size-dependent extinction coefficient of colloidal PbSe quantum dots, Chem. Mater., 19 (2007) 6101–6106.
Moreels I., Lambert K., Smeets D., De Muynck D., Nollet T., Martins J.C., Vanhaecke F., Vantomme A., Delerue C., Allan G., Hens Z., Size-dependent optical properties of colloidal PbS quantum dots, ACS Nano, 3 (2009) 3023–3030.
Mori Y., Retention behavior of colloidal dispersions in sedimentation field-flow fractionation, Adv. Colloid Interface Sci., 53 (1994) 129–140.
Mori Y., Size-selective separation techniques for nanoparticles in liquid, KONA Powder and Particle Journal, 32 (2015) 102–114.
Moynihan T., What are quantum dots, and why do I want them in my TV? <www.Wired.Com/2015/01/primer-quantum-dot/>, WIRED.com, 2015 (accessed April 8, 2015)
Murray C.B., Norris D.J., Bawendi M.G., Synthesis and characterization of nearly monodisperse CdE (E = S, Se, Te) semiconductor nanocrystallites, J. Am. Chem. Soc., 115 (1993) 8706–8715.
Nag A., Sapra S., Nagamani C., Sharma A., Pradhan N., Bhat S.V., Sarma D.D., A study of Mn^{2+} doping in CdS nanocrystals, Chem. Mater., 19 (2007) 3252–3259.
Nielsen M.H., Li D., Zhang H., Aloni S., Han T.Y.-J., Frandsen C., Seto J., Banfield J.F., Cölfen H., De Yoreo J.J., Investigating processes of nanocrystal formation and transformation via liquid cell TEM, Microsc. Microanal., 20 (2014) 425–436.
Nightingale A.M., de Mello J.C., Microscale synthesis of quantum dots, J. Mater. Chem., 20 (2010) 8454–8463.
Oshima H., Theory of electrostatics and electrokinetics of soft particles, Sci. Technol. Adv. Mater., 10 (2009) 063001.
Palik E.D., Handbook of optical constants of solids, Academic Press, London, 1985.
Park J., Joo J., Kwon S.G., Jang Y., Hyeon T., Synthesis of monodisperse spherical nanocrystals, Angew. Chem. Int. Ed., 46 (2007) 4630–4660.
Pauw B.R., Everything SAXS: Small-angle scattering pattern collection and correction, J. Phys.: Condens. Matter, 25 (2013) 383201.
Peng X., Wickham J., Alivisatos A.P., Kinetics of II–VI and III–V colloidal semiconductor nanocrystal growth: "Focusing" of size distributions, J. Am. Chem. Soc., 120 (1998) 5343–5344.
Pesika N.S., Stebe K.J., Searson P.C., Determination of the particle size distribution of quantum nanocrystals from absorbance spectra, Adv. Mater., 15 (2003a) 1289–1291.
Pesika N.S., Stebe K.J., Searson P.C., Relationship between absorbance spectra and particle size distributions for quantum-sized nanocrystals, J. Phys. Chem. B, 107 (2003b) 10412–10415.
Pietryga J.M., Schaller R.D., Werder D., Stewart M.H., Klimov V.I., Hollingsworth J.A., Pushing the band gap envelope: Mid-infrared emitting colloidal PbSe quantum dots, J. Am. Chem. Soc., 126 (2004) 11752–11753.
Polte J., Erler R., Thünemann A.F., Sokolov S., Ahner T.T., Rademann K., Emmerling S., Kraehnert R., Nucleation and growth of gold nanoparticles studied via in situ small angle X-ray scattering at millisecond time resolution, ACS Nano, 4 (2010) 1076–1082.
Reindl A., Peukert W., Intrinsically stable dispersions of silicon nanoparticles, J. Coll. Int. Sci., 325 (2008) 173–178.
Rhodes M.J., Introduction to particle technology, John Wiley & Sons Ltd., London, 1999.
Rogach A.L., Talapin D.V., Shevchenko E.V., Kornowski A., Haase M., Weller H., Organization of matter on different size scales: monodisperse nanocrystals and their superstructures, Adv. Funct. Mater., 12 (2002) 653–664.
Rossetti R., Ellison J.L., Gibson J.M., Brus L.E., Size effects in the excited states of small colloidal CdS crystallites, J. Chem. Phys., 80 (1984) 4464–4469.
Rumpf H., Particle technology, Chapmann and Hall, London, 1990.
Sapsford K.E., Tyner K.M., Dair B.J., Deschamps J.R., Medintz I.L., Analyzing material bioconjugates: A review of current and emerging purification and characterization techniques, Anal. Chem., 83 (2011) 4453–4488.
Sashchiuk A., Langof L., Chaim R., Lifshitz E., Synthesis and characterization of PbSe and PbSe/PbS core-shell colloidal nanocrystals, J. Cryst. Growth, 240 (2001) 431–438.
Saunders S.R., Roberts C.B., Size-selective fractionation of nanoparticles at an application scale using CO_2 gas-expanded liquids, Nanotechn., 20 (2009) 475605.
Segets D., Gradl J., Klupp Taylor R., Vassilev V., Peukert W., Analysis of optical absorbance spectra for the determination of ZnO nanoparticle size distribution, solubility and surface energy, ACS Nano, 3 (2009) 1703–1710.
Segets D., Komada S., Butz B., Spiecker E., Mori Y., Peukert W., Quantitative evaluation of the size selective precipitation of Mn-doped ZnS quantum dots by size distributions calculated from UV/Vis absorbance spectra, J. Nanopart. Res., 15 (2013) 1486.

Segets D., Lucas J.M., Klupp Taylor R.N., Scheele M., Zheng H., Alivisatos A.P., Peukert W., Determination of the quantum dot bandgap dependence on particle size from optical absorbance and transmission electron microscopical measurements, ACS Nano, 6 (2012) 9021–9032.

Segets D., Lutz C., Yamamoto K., Komada S., Süß S., Mori Y., Peukert W., Classification of zinc sulfide quantum dots by size: Insights into the particle surface-solvent interaction of colloids, J. Phys. Chem. C, 119 (2015) 4009–4022.

Segets D., Peukert W., UV/Vis-spektroskopie zur in-situ-teilchengrößenanalyse, Laborpraxis, (2014).

Seto J., Ma Y., Davis S.A., Meldrum F., Gourrier A., Kim Y.-Y., Schilde U., Sztucki M., Burghammer M., Maltsev S., Jäger C., Cölfen H., Structure-property relationships of a biological mesocrystal in the adult sea urchin spine, Proc. Natl. Acad. Sci. U.S.A., 109 (2012) 3699–3704.

Shah P.S., Holmes J.D., Johnston K.P., Korgel B.A., Size-selective dispersion of dodecanethiol-coated nanocrystals in liquid and supercritical ethane by density tuning, J. Phys. Chem. B, 106 (2002a) 2545–2551.

Shah P.S., Husain S., Johnston K.P., Korgel B.A., Role of steric stabilization on the arrested growth of silver nanocrystals in supercritical carbon dioxide, J. Phys. Chem. B, 106 (2002b) 12178–12185.

Steckel J.S., Coe-Sullivan S., Bulovic V., Bawendi M.G., 1.3 μm to 1.55 μm tunable electroluminescence from PbSe quantum dots embedded within an organic device, Adv. Mater., 15 (2003) 1862–1866.

Steigerwald M.L., Brus L.E., Semiconductor crystallites: A class of large molecules, Acc. Chem. Res., 23 (1990) 183–188.

Strauss H.M., Karabudak E., Bhattacharyya S., Kretzschmar A., Wohlleben W., Cölfen H., Performance of a fast fiber based UV/Vis multiwavelength detector for the analytical ultracentrifuge, Colloid Polym. Sci., 286 (2008) 121–128.

Sun Y., Ren Y., In situ synchrotron X-ray techniques for real-time probing of colloidal nanoparticle synthesis, Part. Part. Sys. Charact., 30 (2013) 399–419.

Sun Y., Welch G.C., Leong W.L., Takacs C.J., Bazan G.C., Heeger A.J., Solution-processed small-molecular solar cells with 6.7 % efficiency, Nature Mater., 11 (2012) 44–48.

Tyrakowski C.M., Snee P.T., A primer on the synthesis, water-solubilization, and functionalization of quantum dots, their use as biological sensing agents, and present status, Phys. Chem. Chem. Phys., 16 (2014) 837–855.

Vincent B., Edwards J., Emmett S., Jones A., Depletion flocculation in dispersions of sterically-stabilised particles ("soft spheres"), Colloid Surface, 18 (1986) 261–281.

Viswanatha R., Sapra S., Satpati B., Satyam P.V., Dev B.N., Sarma D.D., Understanding the quantum size effects in ZnO nanocrystals, J. Mater. Chem., 14 (2004) 661–668.

Viswanatha R., Sarma D.D., Study of the growth of capped ZnO nanocrystals: A route to rational synthesis, Chem. Eur. J., 12 (2006) 180–186.

Vossmeyer T., Katsikas L., Giersig M., Popovic I.G., Diesner K., Chemseddine A., Eychmüller A., Weller H., CdS nanoclusters: Synthesis, characterization, size dependent oscillator strength, temperature shift of the excitonic transition energy, and reversible absorbance shift, J. Phys. Chem., 98 (1994) 7665–7673.

Walter J., Löhr K., Karabudak E., Reis W., Mikhael J., Peukert W., Wohlleben W., Cölfen H., Multidimensional analysis of nanoparticles with highly disperse properties using multi-wavelength analytical ultracentrifugation, ACS Nano, 8 (2014) 8871–8886.

Walter J., Nacken T.J., Thajudeen T., Eigler S., Peukert W., Determination of the lateral dimension of graphene oxide nanosheets using analytical ultracentrifugation, Small, 11 (2015a) 814–825.

Walter J., Sherwood P.J., Lin W., Segets D., Stafford W.F., Peukert W., Simultaneous analysis of hydrodynamic and optical properties using analytical ultracentrifugation equipped with multiwavelength detection, Anal. Chem., 87 (2015b) 3396–3403.

Walter J., Thajudeen T., Süß S., Segets D., Peukert W., New possibilities of accurate particle characterisation by applying direct boundary models to analytical centrifugation, Nanoscale, 7 (2015c) 6574–6587.

Whitell G.V., Kitchens C.L., Small-angle neutron scattering of silver nanoparticles in gas-expanded hexane, J. Phys. Chem. C, 114 (2010) 16285–16291.

Williams S.K.R., Runyon J.R., Ashames A.A., Field-flow fractionation: Addressing the nano challenge, Anal. Chem., 83 (2011) 634–642.

Yen B.K., Günther A., Schmidt M.A., Jensen K.F., Bawendi M.G., A microfabricated gas-liquid segmented flow reactor for high-temperature synthesis: The case of CdSe quantum dots, Angew. Chem. Int. Ed., 44 (2005) 5447–5451.

Yoshikawa H., Adachi S., Optical constants of ZnO, Jpn. J. Appl. Phys., 36 (1997) 6237–6243.

Yu W.W., Qu L., Guo W., Peng X., Experimental determination of the extinction coefficient of CdTe, CdSe, and CdS nanocrystals, Chem. Mater., 15 (2003) 2854–2860.

Zheng H., Smith R.K., Jun Y.-W., Kisielowski C., Dahmen U., Alivisatos A.P., Observation of single colloidal platinum nanocrystal growth trajectories, Science, 324 (2009) 1309–1311.

Nomenclature

Abbreviations

AC	analytical centrifugation
AsFlFFF	asymmetric flow field-flow fractionation
AUC	analytical ultracentrifugation
A4F	asymmetric flow field-flow fractionation
DLS	dynamic light scattering
EMA	effective mass approximation
FFF	field-flow fractionation
FLN	fluorescence line narrowing
HR	high resolution
HSP	Hansen solubility parameters

MWL	multiwavelength
PL	photoluminescence
PSD	particle size distribution
QD	quantum dot
RSD	relative standard deviation
SANS	small angle neutron scattering
SAXS	small angle X-ray scattering
SSP	size selective precipitation
TEM	transmission electron microscopy

Greek Symbols

α	absorption coefficient (M^{-1} m^{-1})
$\alpha_{shift,i}(\lambda)$	shifted absorption coefficient (M^{-1} m^{-1})
χ	Flory Huggins parameter (–)
ΔD_{actual}	true width of PSD (m)
Δd_{app}	apparent width of absorbance data on a particle size scale (m)
δ_d	disperse contribution to HSP ($(J\ m^{-3})^{0.5}$)
δ_h	HSP for ability to exchange electrons ($(J\ m^{-3})^{0.5}$)
δ_i	Hildebrand solubility parameter ($(J\ m^{-3})^{0.5}$)
δ_p	polar contribution to HSP ($(J\ m^{-3})^{0.5}$)
ϕ	volume fraction of ligand (–)
σ	standard deviation (m)
η	dynamic viscosity (Pa s)
η_f	yield of fines (–)
η_g	yield of coarse (–)
κ	separation sharpness (–)
λ	wavelength (m)

Latin Symbols

A	absorbance (–)
$A(\lambda)$	measured absorbance (–)
$A_i'(\lambda)$	partial absorbance (–)
a	empiric parameter (m)
b	empiric parameter (–)
c	empiric parameter (m)
C	constant ($eV^{0.5}$ m^{-1})
c_i	cohesive energy density ($J\ m^{-3}$)
D	diffusion coefficient ($m^2\ s^{-1}$)
d_c	optical path length (m)
E_g	band gap energy (eV)
f	relative mass of fine fraction (–)
g	relative mass of coarse fraction (–)
hv	energy (J)
K_{diss}	dissociation constant (–)
m	mass (kg)
n	fitting parameter (–)
$n(x)$	relative abundance (–)
p	fitting parameter (–)
q_3	volume density (m^{-1})
R	ideal gas constant ($J\ mol^{-1}\ K^{-1}$)
r	particle radius (m)
T	temperature (K)
$T(x)$	separation efficiency (–)
V_m	molar volume ($m^3\ mol^{-1}$)
x	particle diameter (m)
x_h	hydrodynamic particle diameter (m)
x_t	cut size (m)

Author's short biography

Doris Segets

Dr. Segets is currently affiliated at the Institute of Particle Technology of the Friedrich-Alexander-Universität Erlangen-Nürnberg (FAU). She received her PhD in 2013 and her research interests include the characterization and tailoring of technically relevant colloidal interfaces, the development of new concepts for process engineering and the scale-up of colloidal nanoparticles, micro reaction technology and high-throughput experimentation (HTE) as well as the application of well-defined nanoparticles for ultra-filtration and chromatography.

KONA Powder and Particle Journal No. 33 (2016) 63–85/Doi:10.14356/kona.2016014 Review Paper

Aerosol Delivery of siRNA to the Lungs. Part 1: Rationale for Gene Delivery Systems †

Susanne R. Youngren-Ortiz [1], Nishant S. Gandhi [1], Laura España-Serrano [1] and Mahavir B. Chougule [1,2]*

[1] *Department of Pharmaceutical Sciences, The Daniel K. Inouye College of Pharmacy, University of Hawaii at Hilo, USA*
[2] *Natural Products and Experimental Therapeutics Program, University of Hawaii Cancer Center, University of Hawaii at Manoa, USA*

Abstract

This article reviews the pulmonary route of administration, aerosol delivery devices, characterization of pulmonary drug delivery systems, and discusses the rationale for inhaled delivery of siRNA. Diseases with known protein malfunctions may be mitigated through the use of siRNA therapeutics. The inhalation route of administration provides local delivery of siRNA therapeutics for the treatment of various pulmonary diseases, however barriers to pulmonary delivery and intracellular delivery of siRNA exists. siRNA loaded nanocarriers can be used to overcome the barriers associated with the pulmonary route, such as anatomical barriers, mucociliary clearance, and alveolar macrophage clearance. Apart from naked siRNA aerosol delivery, previously studied siRNA carrier systems comprise of lipidic, polymeric, peptide, or inorganic origin. Such siRNA delivery systems formulated as aerosols can be successfully delivered via an inhaler or nebulizer to the pulmonary region. Preclinical animal investigations of inhaled siRNA therapeutics rely on intratracheal and intranasal siRNA and siRNA nanocarrier delivery. Aerosolized siRNA delivery systems may be characterized using *in vitro* techniques, such as dissolution test, inertial cascade impaction, delivered dose uniformity assay, laser diffraction, and laser Doppler velocimetry. The *ex vivo* techniques used to characterize pulmonary administered formulations include the isolated perfused lung model. *In vivo* techniques like gamma scintigraphy, 3D SPECT, PET, MRI, fluorescence imaging and pharmacokinetic/pharmacodynamics analysis may be used for evaluation of aerosolized siRNA delivery systems. The use of inhalable siRNA delivery systems encounters barriers to their delivery, however overcoming the barriers while formulating a safe and effective delivery system will offer unique advances to the field of inhaled medicine.

Keywords: siRNA, nanocarrier, nanoparticle, aerosolization, pulmonary, lung

1. Introduction

RNA interference (RNAi) is a process in which RNA molecules inhibit gene expression by causing the destruction of specific messenger RNA (mRNA). Small interfering RNA (siRNA) are double stranded RNA molecules containing 20–25 nucleotides that are involved in the RNAi pathway and interfere with the expression of a specific gene with complementary nucleotide sequences (Agrawal N. et al., 2003). As shown in **Fig. 1**, siRNA degrades mRNA after transcription, thereby preventing translation, or plays a role in RNAi-related pathways (Agrawal N. et al., 2003). siRNA has potential therapeutic applications in treating 'undruggable' diseases by downregulating the expression of a target gene in a post-transcriptional manner. Since the discovery of siRNA in 1998 by Fire and Mello et al., the mechanisms of RNAi have been extensively reviewed (Fellmann C. and Lowe S.W., 2014; Fire A. et al., 1998; Hannon G.J., 2002; Kim D.H. and Rossi J.J., 2007). The siRNA possess a specific sequence that is complementary with its target mRNA that induces site-specific cleavage and subsequent inhibition of intracellular protein synthesis. The siRNA, once in the cytoplasm of the cell, can incorporate within the RNA-induced silencing complex (RISC) and activates this complex. The sense strand is then removed from the duplex and is degraded by nucleases in the activated RISC complex. At the same time, the antisense strand directs the RISC to the base-complementary sequence of the target mRNA located within the cell cytoplasm. Binding of mRNA to the antisense strand in the activated RISC eventually induces cleavage by the endonuclease Argonaute and post-transcriptional silencing of the target gene expression. Major advantages

† Received 16 July 2015; Accepted 21 August 2015
J-STAGE Advance published online 30 September 2015
1 200 West Kawili Street, Hilo, Hawaii 96720, USA
2 Honolulu, Hawaii 96813, USA
* Corresponding author: Mahavir B. Chougule;
E-mail: mahavir@hawaii.edu
TEL: +1-808-981-4519 FAX: +1-808-981-4520

of siRNA over small molecule drugs or protein therapeutics are that the sequences can be rapidly designed for highly specific inhibition of the target of interest and that the synthesis of siRNAs is relatively simple because it does not require a cellular expression system, complex protein purification, or refolding schemes (Amarzguioui M. et al., 2005).

Pulmonary diseases such as lung cancer, cystic fibrosis, pulmonary hypertension, asthma, and chronic obstructive pulmonary disorder (COPD) have potential siRNA therapeutic targets (Amarzguioui M. et al., 2005; Burnett J.C. and Rossi J.J., 2012; Kanasty R. et al., 2013). Nevertheless, siRNA delivery systems are likely to have instability issues that cause premature release of the nucleic acids, especially with systems that incorporate their cargo through electrostatic interactions. Due to the high negative charge density and relatively large size of the siRNA molecules, naked siRNA molecules are not able to enter cells efficiently (Reischl D. and Zimmer A., 2009). Pulmonary delivery of siRNA faces major challenges that involve a lack of correlation between *in vitro* and *in vivo* experiments, difficulty in translation from animal models to humans, and non-applicable administration routes used in animal studies for human use (Lam J.K.-W. et al., 2012).

In Part I, we review the modes of pulmonary delivery of siRNA, the evaluation of aerosol drug delivery systems, and the rationale for the use of nanocarriers to overcome the barriers of pulmonary delivery and cellular uptake of siRNA. Part II focuses on the siRNA loaded non-viral particulates for aerosolized delivery systems, and preparation and characterization techniques for siRNA loaded nanoparticles.

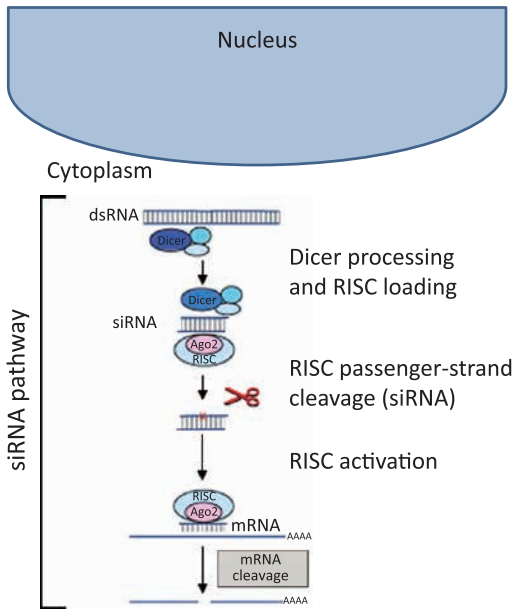

Fig. 1 siRNA pathway schematic. Reprinted with permission from Ref. (De Fougerolles A. and Novobrantseva T., 2008; De Fougerolles A. et al., 2007). Copyright: (2007) Nature Publishing Group.

2. Pulmonary route of administration

To achieve pulmonary delivery, inhalable aerosols generated by an inhaler or nebulizer are the preferred option. Before entering clinical trials, new therapeutic agents must demonstrate preclinical efficacy in appropriate animal models that are translatable to humans (Laube B.L., 2014). Pulmonary aerosols are usually administered via the inhalation, intratracheal, or intranasal routes. Intratracheal and intranasal routes of administration are commonly used to deliver therapeutic siRNA or other therapeutic agents to the lungs of animals due to ease of experimental setup and control (Driscoll K.E. et al., 2000). In preclinical studies, the very different lung anatomy of mice and humans needs to be considered while selecting the route of administration to assess delivery and efficacy. Formulations administered via the pulmonary route of administration are required to be nonirritating to reduce risk of pharyngeal edema, bronchial spasm, anaphylaxis, peracute death, and chronic pulmonary fibrosis (Turner P.V. et al., 2011). These factors are vital to the successful development of an orally or intranasally inhaled siRNA delivery system.

2.1 Inhalation route

The most non-invasive way to locally deliver therapeutics to the lungs is through inhalation. Four types of inhalation devices are currently available including pressurized metered dose inhalers (pMDIs), dry powder inhalers (DPIs), nebulizers, and soft mist inhalers (SMIs). With appropriate developmental optimization, these devices may deliver siRNA to the lungs. During development, key parameters should be considered for an optimum inhaler system, as shown in **Table 1**.

2.1.1 Inhalation aerosol delivery devices

pMDIs are currently the most commonly used inhalers. The therapeutic agents within a pMDI are in either a suspended particulate state or dissolved within propellants, such as chlorofluorocarbons (CFCs) and hydrofluoroalkanes (HFAs) (Lam J.K.-W. et al., 2012). The propellants are an indispensable part of pMDIs as they supply the energy required to aerosolize the drug for inhalation. siRNA or siRNA loaded nanocarriers may not be compatible with propellant vehicles which limit the formulation of siRNA into the pMDIs (Lam J.K.-W. et al., 2012). However, crosslinked chitosan-PEG1000 based nanocarriers with particle size of less than 230 nm were found to be physically stable within HFA-227, highly dispersible, and

Table 1 Parameters to consider in siRNA formulation design for inhalation

Property	Parameters
Aerosol properties	Mass median aerodynamic diameter
	Geometric standard deviation
	Fine particle fraction
	Air/particle velocity
Particle properties	Volume diameter
	Bulk density
	Tap density
	Shape
	Charge
Physiochemical properties	Solubility
	Hygroscopicity
Lung properties	Disease state on airway structure and breathing pattern
	Disease state on surfactant production
	Disease state on mucus production and mucociliary clearance
	Age of patient, pulmonary or nasal breathing
	Airway structure and diameter

successfully delivered to the deep lung airways using pMDIs (Sharma K. et al., 2012). Selecting a stable and appropriate formulation for use with the pMDI devices will allow for the development of siRNA containing pMDIs.

DPIs and their formulations allow for the inhalation of aerosol clouds of dry particles. DPI device design has a major impact on their performance. Advantages of DPIs are that they have improved sterility and chemical stability of biomolecules compared to liquid aerosols (Lam J. K.-W. et al., 2012). Drug deposition from inhaled DPIs is dependent on the inspiration flow rate of the patient, and often times the illness that warrants their use of the inhalation therapy causes their inspiration flow rates to be abnormally low (Feddah M.R. et al., 2000; Ross D.L. and Schultz R.K., 1996). The device must be designed to minimize these variation with respect to patient disease state (Shoyele S.A. and Slowey A., 2006). Spray drying techniques are often used to prepare protein and peptide inhalable DPI formulations that have demonstrated successful *in vivo* delivery of therapeutic macromolecules (Bai S. et al., 2010; Codrons V. et al., 2003; Mastrandrea L.D. and Quattrin T., 2006; Rawat A. et al., 2008). The DPIs formulation can be used for pulmonary delivery of siRNA. The issues and challenges that have risen from the formulation of biological macromolecules, such as flowability, dispersibility, and biochemical stability needs to be also considered for development of siRNA based DPIs (Chan H.-K., 2003). Considerations for formulation of proteins as powder aerosols have been reviewed previously (Chan H.-K., 2003). Maintaining biochemical stability of siRNA during formulation limits the processes that may be used to prepare siRNA based dry powder formulations.

Nebulizers generate liquid aerosols that can deliver saline-based solutions or suspensions of drug product at large volumes via inhalation (Sharma K. et al., 2013). Nebulizer treatments usually last over several minutes, rather than single inhalation. Generated droplets have aerodynamic diameters between 1–10 μm, depending on the formulation and the type of nebulizer device. The four major categories of nebulizers are jet (pneumatic), vibrating mesh/membrane, smart, and ultrasonic nebulizers (Ari A., 2014; Dailey L.A. et al., 2003).

A jet, or pneumatic nebulizer, can be used to deliver suspension formulation delivery suspension formulation, which makes them suitable for delivering siRNA or siRNA carrier delivery systems. Breath-enhanced jet nebulizers release more aerosol during inhalation, whereas breath-actuated jet nebulizers sense the patient's inspiratory flow and deliver aerosol only during inhalation (Arunthari V. et al., 2012; Haynes J.M., 2012; Ho S.L. et al., 2001). In an air jet nebulizer, compressed gas draws up bulk liquid to a jet by the Bernoulli effect and atomization takes place where the liquid emerging from the jet interacts with the shear force set up by the gas flow. Rayleigh dispersion of bulk liquid into droplets occurs and baffles remove the coarse droplets, which fall back into the reservoir, whereas droplets with aerodynamic diameters of < 10 μm are available for inhalation. It has been estimated that 99 % of the generated aerosols are recycled back to the reservoir, thus shear stress is exerted multiple times on the formulation and hence, the possible degradation of naked siRNA during this process needs to be evaluated (Agu R.U. et al., 2001).

Vibrating mesh nebulizers use micropumps to force liquid through a mesh or aperture plate for aerosol generation. Suspensions, nanocarriers, and nucleic acids have been successfully delivered via mesh nebulizers (Elhissi A. et al., 2006; Elhissi A. and Taylor K., 2005; Hibbitts A. et al., 2014; Lentz Y.K. et al., 2006; Luo Y. et al., 2012; Wagner A. et al., 2006; Yoshiyama Y. et al., 2002). Mesh nebulizers have consistent and improved aerosol generation efficiency, large fine-particle fraction, low residual volume, and the ability to nebulize low volumes (Ari A., 2014; Dhand R., 2002; Dolovich M.B. and Dhand R., 2011; Waldrep J. and Dhand R., 2008). Vibrating mesh/membrane nebulizers are more expensive than jet nebulizers because of the electronics involved with controlling the vibration process. In addition, mesh nebulizers are

difficult to clean. However, mesh nebulizers are more efficient than jet nebulizers at providing higher drug doses to patients (Ari A., 2014). The limitations of mesh nebulizers include the blocking of the mesh or apertures during the nebulization of viscous suspensions or the precipitation and crystallization of drug or excipients (Ari A., 2014; Najlah M. et al., 2014). This should be a consideration when formulating a siRNA nanocarrier suspension for nebulization.

There are two types of vibrating mesh nebulizers, termed active and passive. Active mesh nebulizers utilize a piezoelectrical element that expands and contracts upon application of electrical currents which then vibrates a mesh in contact with the medication to generate the aerosol. Passive mesh nebulizers use a transducer horn that induces passive vibrations on the mesh plate for aerosol generation (Ari A., 2014).

Smart nebulizers incorporate adaptive aerosol delivery (AAD®) technology that analyzes the patient's breathing pattern in order to determine the timing of aerosol drug delivery during inhalation (Denyer J. and Dyche T., 2010). The device is able to adapt to the patients breathing pattern, therefore it is able to reduce the aerosol losses and the variation in drug delivery. Smart nebulizers can provide effectiveness and end of dose feedback to the patient during therapy, which can increase patient compliance (Denyer J. and Dyche T., 2010; Denyer J. et al., 2004).

Ultrasonic nebulizers utilize a piezoelectric crystal vibrating at high frequencies of 1–3 MHz to produce aerosols. These types of nebulizers have the limitations of large residual volumes, inability to aerosolize viscous solutions, and degradation of heat sensitive materials (Ari A., 2014; Ari A. et al., 2009; Ari A. and Restrepo R.D., 2012). Therefore, ultrasonic nebulizers may not be useful for suspensions of naked siRNA or siRNA nanocarriers (Taylor K.M. and Mccallion O.N., 1997; Watts A.B. et al., 2008).

Chemical and physical stability of the naked siRNA during the nebulization process is of high concern. Therefore, delivery of siRNA using nebulizers should involve the development of a formulation which protects the siRNA from physical degradation, shear stress, and chemical degradation mediated via hydrolysis and endogenous enzymes (Lam J.K.-W. et al., 2012).

SMIs are a recently introduced category of inhaler delivery system marketed as Respimat® produced by Boehringer-Ingelhem (Dalby R. et al., 2004). This technology provides a metered dose to the user who activates the inhaler and energy from a spring imposes pressure on the liquid container. The SMI generates the aerosol by impinging opposing droplet streams emerging from a uniblock nozzle created using silicon wafer technology (Dalby R. et al., 2004). The advantages of the SMI are that it has high lung deposition due to the low velocity of the aerosol cloud and thus minimizing the deposition in the mouth and throat (Dalby R. et al., 2004; Hochrainer D. et al., 2005). In addition, the patient is not required to exert excessive inspiratory force in generating the aerosol clouds associated with DPIs. The effect on physical and chemical stability of siRNA must be considered while delivering a formulation via SMIs (Merkel O.M. et al., 2014; Sharma K. et al., 2013). The feasibility of SMIs as delivery devices for non-viral siRNA delivery has not been explored, but it may be a viable option.

2.2 Intratracheal route

The intratracheal route of administration is used most often in animal studies for assessing the inhalation delivery of various drugs. However, the clinical application of this route is limited due to its invasive setup and uncomfortable delivery technique (Driscoll K.E. et al., 2000; Sakagami M., 2006). The intratracheal route is not feasible for human clinical studies due to method invasiveness that involves inserting a tube to dispense the formulation within a surgical incision made within the tracheal rings (Lam J.K.-W. et al., 2012). The traditional method involves the animal to be anesthetized, undergo surgical tracheotomy, and after the trachea is exposed, an endotracheal tube or needle is inserted into the incision between the tracheal cartilaginous rings, with the tip projected at a defined position before the tracheal bifurcation, as shown in **Fig. 2**. The drug solution or suspension formulation is administered through the tube using a microsyringe and instilled into the airways. Bivas-Benita et al. described a non-invasive intratracheal instillation that did not involve surgical resection of the trachea that is also known as the oro-tracheal route (Bivas-Benita M. et al., 2005). Aerosol is delivered to the lungs by placing a microsprayer over the anesthetized animals tongue and down to the trachea or the animal is intubated and the drug is instilled in solution or suspension form. This method has the drawbacks of diffi-

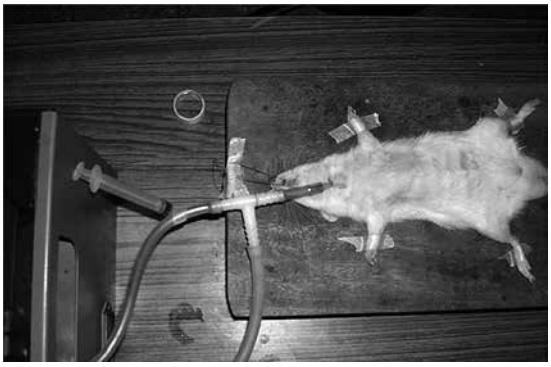

Fig. 2 Intratracheal instillation and bronchoalveolar lavage on rat. Reprinted with permission from Ref. (Patel G. et al., 2009).

culty in accurate placement of the microsprayer catheter and reduced mucociliary clearance due to anesthesia.

There have been a number of studies that utilized the intratracheal route for siRNA delivery to the lungs (Conde J. et al., 2013; Garbuzenko O.B. et al., 2009; Merkel O.M. et al., 2009; Moschos S.A. et al., 2007; Perl M. et al., 2005; Rosas-Taraco A.G. et al., 2009; Wang J.-C. et al., 2010). Drug deposition by this route is less uniform than by the inhalation route of administration (Sakagami M., 2006). Since this route avoids oropharynx deposition, the amount of drug loss is lower compared to the inhalation route. However, this route of delivery does not allow for determination of the effect of aerodynamic particle size on the lung deposition, therefore the *in vivo* intratracheal instillation studies in the animals do not reflect the intricacies of lung deposition. The intratracheal instillation route of delivery is suitable for providing proof-of-concept for local lung delivery studies in animal models.

2.2.1 Intratracheal aerosol delivery devices

Intratracheal aerosolization devices consists of an atomizer located in the distal tip of a long, narrow, stainless steel or plastic tube used to deliver an aerosol directly to the lungs when inserted down the trachea, above the carina or further down, in an anesthetized animal. Devices for preclinical studies include commercially available technologies for administration of solution and for dry powder aerosol formulations. Intratracheal delivery can be achieved through devices, such as the Penn-Century microsprayer (Gutbier B. et al., 2010; Rosas-Taraco A.G. et al., 2009), the Micro-Mist nebulizer (Zamora-Avila D. et al., 2009), or the Aeroprobe nebulizing catheter (Nielsen E.J. et al., 2010). The Penn-Century, Inc. (Wyndmoor, PA, USA) offers an air-free liquid device and an air-driven dry powder device for preclinical use (Bivas-Benita M. et al., 2005; Morello M. et al., 2009). The miniaturized nebulizing catheter system has shown success for targeted gene delivery to the lungs (Koping-Hoggard M. et al., 2005; Tronde A. et al., 2002). The nebulizing catheter device (NCD) was first adapted for the delivery of peptide therapeutics to the rat lungs (Aeroprobe^{TM}, Trudell Medical International, London, Ontario, Canada) (Tronde A. et al., 2002). This NCD delivers a liquid, which is transported down a tube through a central lumen and pressurized gas is pushed through the peripheral lumens from a compressed airway source at 50 psi. The close proximity of the liquid and gas lumens at the distal tip produces an aerosol in the particle size range of 20–40 μm (Tronde A. et al., 2002).

2.3 Intranasal route

The intranasal route provides a straight forward animal model experimental setup for delivery of siRNA to the lungs, therefore it is another common siRNA delivery route (Bitko V. et al., 2005; Fulton A. et al., 2009; Ghosn B. et al., 2010; Gutbier B. et al., 2010; Hosoya K. et al., 2011; Howard K.A. et al., 2006; Li B.-J. et al., 2005; Massaro D. et al., 2004; Senoo T. et al., 2010; Tompkins S.M. et al., 2004; Zhang X. et al., 2004). The animals must be anesthetized and siRNA formulations are then instilled into the nasal cavity to be breathed in. Although this route has shown success in siRNA delivery to the lungs in mouse animal models, the translation of these studies to humans has been limited. Humans are not obligate nose breathers and have a nasal cavity that filters out the majority of particulates, therefore human intranasal studies do not see such a high lung deposition (Hickey A.J. and Garcia-Contreras L., 2001). Additionally, anesthetics cause the animals to have reduced mucociliary action, therefore the reduced mucociliary clearance overestimates the transfection efficiency of the formulations (Hinchcliffe M. and Illum L., 1999). A study by Heyder et al. found that only 3 % of monodisperse powder particles with aerodynamic diameters of 1–5 μm were deposited within human bronchial airways after intranasal administration (Heyder J. et al., 1986). Since approximately 97 % of the monodisperse particles were deposited within the nasopharynx area, the intranasal route of delivery is ideal for targeting this site in humans. The ALN-RSV01 siRNA, which targets the mRNA encoding the N-protein of respiratory syncytial virus (RSV), developed by Alnylam Pharmaceuticals (Cambridge, MA, USA), has completed phase II clinical trials for the treatment of human RSB infections using the intranasal route of administration (Devincenzo J. et al., 2008; Devincenzo J. et al., 2010; Zamora M.R. et al., 2011). This naked siRNA was delivered via a nasal spray to the upper respiratory tract.

The intranasal route may also be used to allow for systemic or central nervous system (CNS) delivery of siRNA. Protein and peptide biological macromolecules have been previously administered via the intranasal route to access the systemic circulation (Hinchcliffe M. and Illum L., 1999). The nasal cavity has a relatively large surface area and vascularization for facilitating rapid absorption. The intranasal route can access the CNS by bypassing the blood-brain barrier (Hanson L.R. and Frey W.H., 2nd, 2008; Kamei N. and Takeda-Morishita M., 2015).

2.3.1 Intranasal aerosol delivery devices

Intranasal delivery devices for liquid solution or suspension include the rhinyle catheter and instillation tube. This simple method, often used on anesthetized or sedated animals, involves the intranasal insertion of a fine catheter or micropipette followed by instilling the liquid into the desired area to be aspirated into the airways during breathing (Fernandes C.A. and Vanbever R.,

2009). The use of small volumes of 5 µL per nostril or 10 µL total limited drug deposition to the nasal cavity, whereas larger volumes of 25 µL per nostril or 50 µL total allowed for deposition with the lung upper airways (Minne A. et al., 2007). Intranasal instillation is limited due to its hindered ability to reach the deep lung.

For the intranasal delivery of dry powders to the pulmonary route of administration, the Dry Powder Insufflator™ for mice can be used to aerosolize the powder dose (Sinsuebpol C. et al., 2013). This device is actuated using either an air syringe or a Penn-Century air pump, which generates 200 µL puffs of air that generates the powder dose and carries it into the deep lung.

2.4 Passive inhalation exposure chambers for animal studies

Aerosol exposure chambers may be classified as nose-only, head-only, and whole-body exposure chambers. These systems are commonly used to deliver nebulized formulations (Cryan S.-A. et al., 2007). An example of a nose-only exposure chamber is the InExpose™ (SCIREQ®) model as shown in **Fig. 3**. This device has been evaluated for use with inhalable drug carrier systems containing antisense oligonucleotides and siRNA for the treatment of lung cancer (Mainelis G. et al., 2013). Liposomes with particle size and mass median diameter of 130 nm and 270 nm respectively, aerosolized by a jet Collison nebulizer were found to be stable over the continuous aerosolization and a higher lung dose and retention time compared to intravenous route was observed (Mainelis G. et al., 2013). Other examples of nose-only exposure chambers include the Oro-Nasal and Respiratory Exposure Systems (CH Technologies, Westwood, NJ) and the In-Tox Products Small Animal Exposure System (Intox Products, Edgewood, NM). Nose-only and head-only exposure chambers avoid exposure of the aerosol to other parts of body. These set-ups can be stressful for the animal due to the restraint and exposure facemasks placed on the animals face and neck (Cryan S.-A. et al., 2007).

Fig. 3 InExpose™ (SCIREQ®) nose-only exposure system.

The whole-body exposure setup represents a less invasive exposure chamber because rodents are free to move during the passive aerosol delivery (Cryan S.-A. et al., 2007). Whole-body exposure can also simulate environmental exposures to aerosols (Mühlfeld C. et al., 2008). These exposure chambers are usually composed of a chamber where the animal resides during the aerosol therapy, and a port where aerosol can be delivered to the inside of the chamber (Adamcakova-Dodd A. et al., 2014; O'shaughnessy P.T. et al., 2003; Pettis R.J. et al., 2000). When delivering a therapeutic aerosol via a whole-body exposure chamber, there is possible administration of significant amount of formulation to other routes, such as the oral route (Cryan S.-A. et al., 2007). Parameters that impact the variation of the study may include the size of the chamber, the animals size, lung capacity, the inspiratory flow rate, and the formulation characteristics (Cryan S.-A. et al., 2007).

3. Evaluation of pulmonary drug delivery systems

Aerosolized siRNA formulations are characterized using various *in vitro*, *ex vivo*, and *in vivo* techniques that are

Table 2 Techniques for evaluating pulmonary drug delivery systems

Type	Technique	Measurement determined
In vitro	Dissolution test	Dissolution rate
	Inertial impaction using cascade impactor	Aerodynamic particle size distribution (APSD)
	Delivered dose assay	Total delivered dose uniformity
	Laser diffraction	Particle size and particle size distribution
	Laser Doppler velocimetry	Aerosol velocity
Ex vivo	Isolated perfused lung	Mechanisms of drug transport and deposition
In vivo	Scintigraphy	Visualization and quantification of aerosol deposition in respiratory tract
	Pharmacokinetic (PK)-animal model/clinical trial	PK parameters
	Pharmacodynamics (PD)	Biochemical and physiological effects of a drug

Table 3 USP and Ph.Eur. Cascade Impactors for orally inhaled dosage forms

Dosage Form	USP	Ph.Eur.
pMDI	- Andersen 8-stage non-viable cascade impactor configuration at 28.3 L/min flow rate - NGI	- Single Stage Twin Impinger - Andersen 8-stage non-viable cascade impactor configuration at 28.3 L/min flow rate - NGI
DPI	- Marple-Miller impactor (model 160, MMI) - Andersen 8-stage non-viable cascade impactor configuration at flow rates other than 28.3 L/min - Multi-stage liquid impinge - NGI	- Multi-stage liquid impinger - Andersen 8-stage non-viable cascade impactor configuration at 28.3 L/min flow rate - NGI
Nebulizer*	- Harmonized with Ph.Eur.	- Single-stage twin impinger - NGI

* operated at a flow rate of 15 L/min. Ph.Eur. 2.9.44 includes the NGI and is harmonized with <1601> of the USP

shown in **Table 2** (Mansour H.M. et al., 2009; Newman S.P. et al., 2000). The purpose of these performance tests is primarily to establish the efficacy of the drug product and device delivery platform have been addressed. These tests were elaborated in Chapter <601> of the USP (Chapters U.G., 2009).

3.1 *In vitro* characterization

Aerosolized siRNA formulation dissolution tests may be performed by adding the formulation within dissolution medium vessel under constant agitation (Shah V.P. et al., 2008; Son Y.J. and Mcconville J.T., 2009). The solution is then sampled at pre-determined time intervals to measure the amount of siRNA released from the nanoparticles. Since there is not a standard method developed for determining siRNA dissolution rate, various media, such as distilled water (Dickinson P.A. et al., 2001), phosphate buffer (Murata N. et al., 2008), simulated lung fluid (SLF) and modified SLF have been used. In addition, various apparatus, such as the flow-through cell (Davies N.M. and Feddah M.R., 2003), standard USP dissolution apparatus, and stirring vessels have been used. Test conditions, such as sink, and particle introduction into the medium being either direct or by aerosolization have been used to characterize the dissolution rate of inhaled drugs.

Inertial impaction is a standard *in vitro* technique used to predict aerosol deposition in the lungs (Padhi B.K. et al., 2009). The cascade impactor is the equipment of choice for particle size analysis of most inhaled aerosols because it allow assay for mass of drug, determined aerodynamic size directly, and provide size information that be indicative of lung deposition. The inertial size-separation and fractionation in a cascade or sequence of single stages within the cascade impactor apparatus measures aerodynamic particle size distribution (APSD) (Chapters U.G., 2009; Hickey A.J., 2003). The jet stream is aimed towards a flat impaction plate, upon which the flow of particles having high inertia is disrupted and impact on the plate. Meanwhile, particles with lower inertia remain within the streamline airflow and do not impact onto the plate (Chapters U.G., 2009; Hickey A.J., 2003; Merkus H.G., 2009). Several impactor plates separate aerosol particles into size ranges according to their aerodynamic size. The larger particles will impact on the plate, whereas the smaller ones will remain airborne. The Stokes number, which is defined as the ratio of the stopping distance to the orifice diameter, can be used to estimate the impaction efficiency (Mitchell J.P. and Nagel M.W., 2003).

The available cascade impactors accepted by the United States Pharmacopeia (USP) and the European Pharmacopeia (Ph.Eur.) are listed in **Table 3** (Mitchell J.P. et al., 2010; Nichols S.C. et al., 2013). The Andersen Cascade Impactor (ACI) is a pharmacopeial method for pMDIs and DPIs and is the most commonly used inertial impactor instrument (**Fig. 4A**). Other cascade impactors include the Marple-Miller model 160 (**Fig. 4B**) and the multistage liquid impinger (**Fig. 4C**) for DPIs. Nebulizers are suggested to be characterized by the USP <601>/ Ph.Eur. 2.9.44 using the Next-Generation Impactor (NGI) at 15 L/min or with a suitable validated cascade impactor that operates at ≤15 L/min (Nichols S.C. et al., 2013).

Cascade impactors are apparatuses for measuring APSD of inhaled aerosols and are not lung simulators or models (Mitchell J.P. and Nagel M.W., 2003). Since cascade impactors operate at a constant flow rate, they do not simulate the environment of the respiratory tract, such as temperature, relative humidity, and the size-selectivity of the various processes that govern the deposition in the human respiratory tract. The constant particle velocity within a cascade impactor contrasts with the decreasing air velocity with increasing airway generation number in the lung. The cascade impactor stage selectivity is much steeper than selectivity for regional deposition (Dunbar C. and Mitchell J., 2005).

Non-aerodynamic droplet or particle size distribution

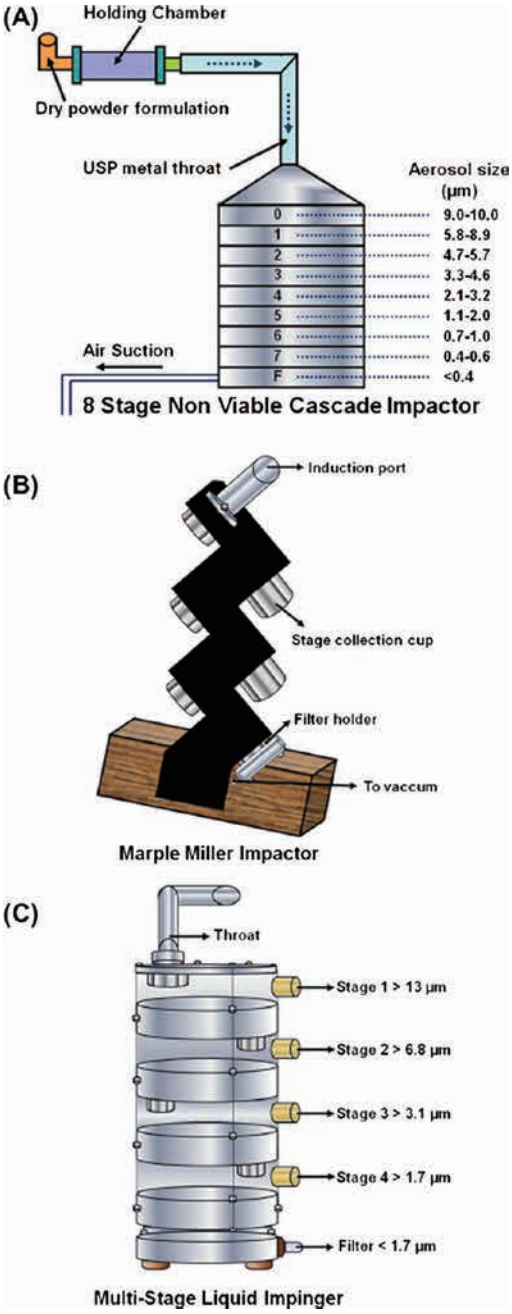

Fig. 4 Schematic representation of the (A) Andersen 8-stage cascade impactor, (B) Marple-Miller impactor, and (C) Multi-stage liquid impinger. Reprinted with permission from Ref. (Nahar K. et al., 2013). Copyright 2013.

was determined using laser diffraction (Chougule M. et al., 2008; De Boer A.H. et al., 2002; Padhi B.K. et al., 2009). This technique measures the low angle scattering of monochromatic coherent light from every particle in the measurement zone. These simultaneous measurements are combined to contribute to the angular scattered light intensity profile. Laser diffraction has the advantages of that it is non-invasive, rapid, has high resolution, wide-dynamic range, can measure volume weighted particle size distribution directly, and is an absolute technique that does not require calibration or verification using optical reticles (Lee Black D. et al., 1996). During a laser diffraction particle size determination measurement, particles of the same size scatter light to the same position in the detector array, where smaller particles scatter light to wider angles (De Boer A.H. et al., 2002). Efficient data inversion algorithms ensure rapid convergence to a valid solution. Laser diffraction method utilizes the interpretation of the relationship between scattered light intensity and scattering angle, which is the distance from the central axis of the photodetector. The Fraunhofer approximation is a simplified description assuming particles absorb light completely (Eshel G. et al., 2004). In this case, only scattering at contour is considered and the particle refractive index (Np) is not needed. The Fraunhofer model works best when particle size is much larger than the wavelength of light, and when the particles are opaque, spherical, and when Np is different to the refractive index of the surrounding medium (e.g. air) (Newman S.P. et al., 2001). The Lorenz-Mie theory is a complete description of angular light scattering process that requires a full description of complex particle refractive index, which at times is unknown (Eshel G. et al., 2004). The Lorenz-Mie model applies to all sizes of particles, but assumes that particles are homogeneous, isotropic, spherical, and has a known complex Np that incorporates both refraction and absorption components. A time-averaged data presentation mode is useful to capture overall performance of a pulmonary inhaled product. The size distribution can be presented in both differential and cumulative formats and the key metrics like particle size of the 10^{th}, 50^{th}, and 90^{th} volume percentiles can be obtained (De Boer A.H. et al., 2002). Laser diffraction equipment can either be an open bench or a close cell. Open bench is simple to perform and is widely used where the aerosol can be directed across the measurement zone. Closed sampling is necessary for DPI testing and may be needed to control evaporation for some measurements, especially with continuous nebulizers. The limitations for laser diffraction are that the method has no assay for drug mass, particles are assumed to be spherical, constant droplet density versus size, vignetting, beam splitting, and droplet evaporation (De Boer A.H. et al., 2002).

The delivered dose uniformity assay is used to quantitatively determine the delivered dose and dose uniformity using a dose uniformity sampling apparatus (DUSA) (Chapters U.G., 2009). The apparatus is connected to an aerosol delivery system through a mouthpiece adapter and a vacuum pump is connected at the other end to provide the desired air flow. The aerosol released into the sampling apparatus is captured onto a filter that is then assayed to quantify the delivered dose. The dose uniformity is determined from variability of the measured delivered dose by the collection of the total mass of contents for the

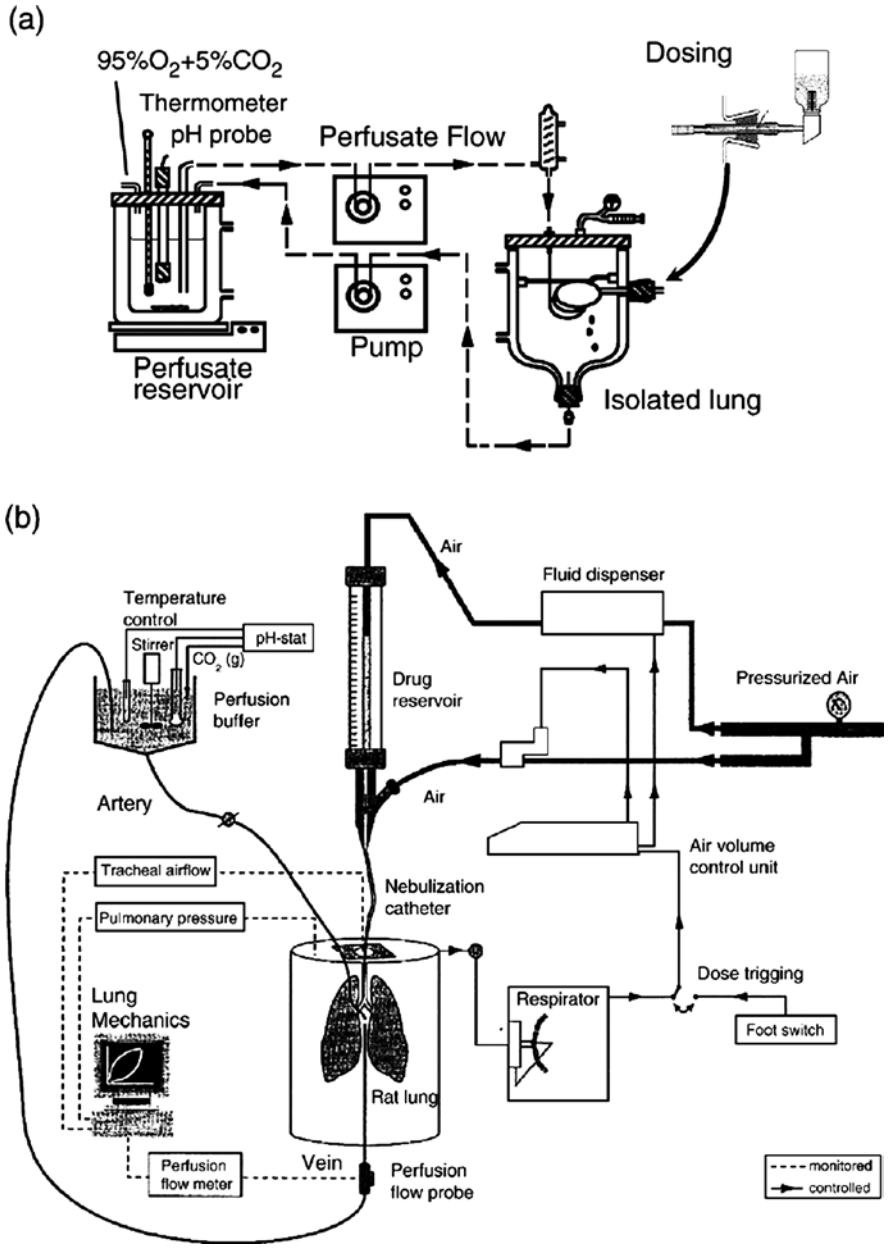

Fig. 5 Isolated perfused rat lung preparations: (a) horizontally positioned isolated perfused rat lung with a scheme of forced solution instillation, (b) vertically positioned isolated perfused rat lung with a scheme of nebulization catheter dosing. Reprinted with permission from Ref. (Sakagami M., 2006). Copyright 2003.

actuation of the clinical dose on the label, excluding volatile propellant and low-volatile species.

3.2 *Ex vivo* characterization

Ex vivo studies are used to identify lung-specific PK without interference from systemic absorption, distribution, metabolism, and excretion (ADME) that occur during *in vivo* studies (Sakagami M., 2006). The isolated perfused lung method includes the isolation of a lung from the body and keeping it within an artificial system under certain experimental conditions. These tests utilize isolated perfused lung models that maintain lung tissue functionality and architecture (Cryan S.-A. et al., 2007; Sakagami M., 2006). The isolated perfused lung model is often used to establish the mechanisms of drug absorption and deposition in the lungs. The shortcoming of *ex vivo* methods include relatively shortened timeframes for data collections due to the viability of the perfused lungs, complex experimental set up, and the absence of tracheo-bronchial circulation and mucociliary clearance (Cryan S.-A. et al., 2007).

The isolated perfused lung preparation has been used in rats, guinea pigs, rabbits, dogs, and monkeys (Sakagami M., 2006). The preparation, as shown in **Fig. 5A–B**, consists of peristaltic pumps and a tubing assembly to carry

the perfusate to and from the lung, and a double-jacketed artificial thorax to house the isolated perfused lung at 37 °C. Perfusate flow, which is normally at 12–15 mL/min in rat lungs, is pumped from the reservoir to the isolated perfused lung through a central porthole of the thorax lid. The bottom of the thorax has an opening, where the perfusate can return to the reservoir or be collected. The thorax is sealed, which enables negative or positive pressure ventilation or the maintenance of pressure (Sakagami M., 2006). While the animal is under anesthesia, the pulmonary circulation in cannulated via the pulmonary artery and the lung is perfused with autologous whole blood or a buffered artificial medium at pH 7.4 (Sakagami M., 2006). The surgical procedures involved in preparing the isolated perfused lung model was discussed previously (Sakagami M., 2006). Following perfusion, the formulations are administered via the tracheal port and the perfusate samples may be collected at predetermined time points to establish absorption profiles (Sakagami M., 2006).

3.3 *In vivo* characterization

Gamma scintigraphy is a non-invasive imaging technique that allows for visualization of drug deposition following pulmonary delivery in the respiratory tract, predicts *in vivo* efficacy, and estimates mucociliary clearance (Newman S. and Wilding I., 1998; Newman S.P. and Wilding I.R., 1999; Snell N. and Ganderton D., 1999). Prior to pulmonary delivery, the drug formulation is radio-labelled with gamma-ray-emitting radiotracer, such as Technetium 99m (99mTc). Alternatively, the radiolabel can be incorporated or attached to the microparticle or nanocarrier instead of the drug (Nahar K. et al., 2013). Radiolabeling could be simply achieved by mixing a radiotracer solution with the formulation (Newman S.P. et al., 2003). An appropriate *in vitro* validation is required to ensure distribution of the radiotracer across particle size range and that the radiotracer is not affecting the particle size distribution (Newman S. and Wilding I., 1998). A gamma camera is used to visualize and quantify the drug deposition in regions of interest within the respiratory tract following inhalation of the radiolabeled formulation. Scintigraphy data are considered an equivalency assessment tool since the data have been demonstrated to correlate well with clinical efficacy data (Bondesson E. et al., 2003; Newman S. and Wilding I., 1998). After pulmonary delivery of the formulation, a gamma camera scans the thorax and radioactive counts can be digitalized to get a 2D image of the lungs, oropharynx, stomach, the inhalation device, and the exhalation filter (Majoral C. et al., 2014; Nahar K. et al., 2013). The periphery of the lungs is imaged by ^{80m}Kr ventilation or transmission scans, and is superimposed to quantify the gamma-labelled particles to establish distribution and permeation (Conway J., 2012; Nahar K. et al., 2013). However, the two dimensional (2D) nature of gamma scintigraphy images make it difficult to differentiate the overlaid anatomical structures. The ratio of peripheral to central deposition, known as the penetration index (PI), measures the extent to which an aerosol reached the lower airways in the lung periphery (Conway J., 2012; Nahar K. et al., 2013).

Three dimensional (3D) imaging methods, such as single photon emission computed tomography (SPECT) overcome 2D imaging issues in distinguishing physiological landmarks (Perring S. et al., 1994). Radiolabeled formulations are tracked by a gamma camera that rotates completely around the subject to form a topographical image in all planes (Conway J., 2012; Fleming J. et al., 2011; Nahar K. et al., 2013). 3D images can be formed using computer software (Snell N. and Ganderton D., 1999). A limitation of SPECT is the possible occurrence of regional deposition, redistribution by mucociliary clearance, coughing, and absorption to the bloodstream during the 30 min method timeframe (Huchon G.J. et al., 1987; Nahar K. et al., 2013). Other limitations are the requirement of a high dose and the use of radiation. Other *in vivo* imaging methods have been applied to overcome these issues, nevertheless the relatively lower cost and technical skills required are much lower for planar gamma scintigraphy or SPECT imaging (Everard M.L., 1994; Nahar K. et al., 2013). SPECT 3D imaging is suitable for correlating *in vitro* and *in vivo* data (Chan H.-K. et al., 2007; Eberl S. et al., 2006; Snell N. and Ganderton D., 1999).

Positron emission tomography (PET) utilizes positron labeled drugs that emits two high-energy photons through electron annihilation (Cherry S.R. and Gambhir S.S., 2001; Dolovich M.B., 2009; Nahar K. et al., 2013; Phelps M.E., 2000). These photons are concurrently emitted at 180° from one another, then detected and counted as a single event (Nahar K. et al., 2013). Accurate delineation regions of interest are obtained by combining the 3D PET image with MRI or spiral CT scan of the thorax (Frauenfelder T. et al., 2015; Yoon S.H. et al., 2014). This allows for the calculation of the percentage of the inhaled dose deposited in these regions (Nahar K. et al., 2013). The advantage of PET is that the drug can act as the radioactive tracer by incorporating a positron emitting isotope (^{11}C, ^{15}O, ^{13}N, ^{18}F, ^{64}Cu, and ^{124}I) by isotopic substitution at trace amounts (Carvalho T.C. et al., 2011; Chakravarty R. et al., 2014; Conway J., 2012; Park C.-W. et al., 2012). PET has been employed to analyze lung pathology, biochemistry, inflammation, transgene expression, and cellular responses *in vivo* (Park C.-W. et al., 2012). The utility of the method is limited by the short half-life (^{11}C $t_{1/2}$ ~20 min) of radionuclides that necessitates the need to be close to a cyclotron during the study (Saha G.B. et al., 1992). PET has been suggested to have no advantage over planar

gamma scintigraphy and PK studies for the calculation of total lung deposition of pulmonary inhaled formulations (Nahar K. et al., 2013; Snell N. and Ganderton D., 1999).

Magnetic resonance imaging (MRI) does not require the radiolabeling of an aerosol to determine qualitative and quantitative deposition of particles in the lungs, but rather is based on the Nuclear Magnetic Resonance phenomenon. This method utilizes non-ionizable radiation to generate images that can be augmented through the use of soft tissue contrast mechanisms and orientations of 2D and 3D images (Nahar K. et al., 2013). The interaction of nuclear magnetic moments of the experimental sample tissue with an external magnetic and electromagnetic fields form spin density, T_1 and T_2 relaxation times, and motion which ranges from diffusion to rapid produce the signals the MRI equipment utilized to form images. T_1 and T_2 depend on the local nuclei environment which is subject to disease state of the tissues, where T_1 is the longitudinal relaxation time constant and T_2 is the transverse relaxation time constant (Nahar K. et al., 2013; Thompson R.B. and Finlay W.H., 2012). Signals measured from the nuclei are either full or half integer values of spin in proportion to the angular momentum that results from an odd number of protons or neutrons. The majority of MRIs measure the signal from the ubiquitous hydrogen (^{1}H) atom, however lung imaging performed using helium-based (^{3}He) methods is now well established because the non-lipid soluble properties of helium allow it to stay within the airspace (Komlosi P. et al., 2015; Kruger S.J. et al., 2014; Nahar K. et al., 2013). Hyperpolarized 3He or ^{129}Xe gas MRI produce more polarization, which leads to better imaging (Mosbah K. et al., 2008; Taratula O. and Dmochowski I.J., 2010; Thompson R.B. and Finlay W.H., 2012). MRI has been employed within *in vivo* animal studies and within *in vitro* human lung airway replicas (Martin A.R. et al., 2008; Sood B.G. et al., 2008; Sood B.G. et al., 2010; Thompson R.B. and Finlay W.H., 2012; Wang H. et al., 2015).

Fluorescence imaging tracks fluorescently tagged particles within an aerosol to monitor their deposition in the lungs (Nahar K. et al., 2013; Ntziachristos V. et al., 2008). This method is limited due to the issues of the excitation and emission fluorescence signals are scattered, reflected, and absorbed by the tissues (Nahar K. et al., 2013; Yi D. et al., 2010). This affects the light captured by the detector and the actual number of molecules. In addition, a heterogeneous background signal exists because biological tissue has the capability to auto-fluoresce (Yi D. et al., 2010). The autofluorescence background can be measured using untreated tissue and subtracted from the experimental background or the use of near-infrared wavelengths can be used to overcome this issue (Adams K.E. et al., 2007; Comsa D.C. et al., 2008; Kovar J.L. et al., 2007; Murata M. et al., 2014). Fluorescent dyes are aerosolized, delivered to the lungs via inhalation, intracheal, or intranasal routes, and imaged using an *in vivo* imaging system (IVIS). The particle deposition in the lobes of the lungs can be visualized and quantified using image analyzing software (Nahar K. et al., 2013). Fluorescence imaging eliminates the need for radioactive tags, therefore it may be used to image deposition patterns in live animals (Ntziachristos V. et al., 2008).

PK studies investigate ADME of drugs by collecting lung deposition and plasma concentration data from either animal or human test subjects to determine the PK parameters. These parameters include drug absorption parameters such as the peak drug concentration (C_{max}), the time C_{max} occurs (t_{max}), and the absorption rate constant (k_a) to determine the absorption rate and the area under curve (AUC) to estimate bioavailability. Also, drug distribution and elimination parameters such as clearance (CL), volume of distribution (Vd), and half-life of the drug ($t_{1/2}$) can be determined. Mice and rat animal models are commonly used in animal PK studies because of their development in modeling various respiratory diseases, smaller drug requirement, and low cost (Cryan S.-A. et al., 2007; Sakagami M., 2006). The drug can be administered through intranasal or intratracheal routes or by using passive inhalation (Cryan S.-A. et al., 2007; Sakagami M., 2006; Zhang J. et al., 2011). Intratracheal or intranasal direct administration avoids oropharyngeal deposition, enabling accurate and reproducible dosing (Chiang P.-C. et al., 2009).

4. siRNA delivery to the lungs

For clinical use, siRNA needs to be delivered to the target region of the lung and be released within the cytoplasm after entering the target cells as shown in **Fig. 6**. Successful gene therapy requires the effective levels of transgene expression in specific cell types to enhance the treatment efficacy and to avoid adverse side effects caused by the expression in inappropriate cell types.

siRNA is a highly negatively charged, hydrophilic, and large sized (approximately 13.3 kDa) macromolecule that cannot cross biological membranes to reach their target sites. Viral vectors have previously demonstrated cell uptake and siRNA efficacy, however, major limitations to human therapeutic delivery exist, such as uncontrolled viral replication, immunogenicity, tumorigenicity, and toxicity (Thomas C.E. et al., 2003). Due to these concerns, non-viral delivery systems have been developed and successfully used to deliver siRNA. An ideal siRNA delivery system should (1) condense siRNA into nano-sized particles, (2) protect siRNA from enzymatic degradation, (3) facilitate cellular uptake, (4) promote endosomal escape to release siRNA to the cytoplasm

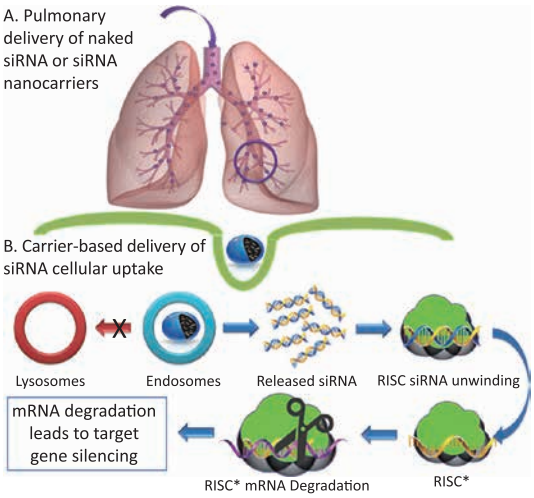

Fig. 6 Aerosol siRNA delivery to the lungs. (A) pulmonary delivery of naked or siRNA nanocarriers, (B) Carrier-based delivery of siRNA cellular uptake. The aerosolized formulation of siRNA and use of appropriate device delivers siRNA by inhalation, intratracheal, or intranasal delivery to the human or animal lung. Once the siRNA carriers reach the lower respiratory tract, they may reach target cells and become internalized through endocytosis. Carriers capable of endosomal escape avoid degradation in the lysosome and release free siRNA within the cytoplasm. The RNAi pathway may then be initiated, ultimately leading to mRNA degradation and gene silencing.

where the RISC is located, (5) have negligible effects on gene silencing activity or specificity and (6) have negligible toxicity (Lam J.K.-W. et al., 2012; Merkel O.M. et al., 2012). Non-viral delivery systems include naked siRNA delivery, and delivery vectors such as lipids, polymers, peptides, and inorganic materials.

4.1 Barriers of pulmonary delivery of siRNA

Delivering siRNA efficiently to the lungs via the pulmonary route requires understanding of the anatomical and physiological characteristics of the respiratory tract. The human respiratory tract has a highly efficient gas exchange capacity and to keep particulates out (**Table 4**) as discussed previously (Merkel O.M. et al., 2014). Therefore, the development of siRNA aerosol delivery systems should consider careful control of particle or droplet size to bypass the lungs natural defense mechanisms.

The respiratory tract is divided into two regions, (1) the conducting airways and (2) the respiratory region. The conducting airways encompass the nasal cavity, pharynx, trachea, bronchi, and bronchioles and the respiratory region consists of the respiratory bronchioles and alveoli (Lam J.K.-W. et al., 2012). The human respiratory tract has evolved to be a size selective fractionator that prevents particulates from reaching the deep lung. For example, the largest particles are removed at the naso- or oropharynx and progressively finer particles deposit in the proximal, intermediate, and distal airways. The main feature of the respiratory tract is the high degree of bifurcations that have been described according to Weibel's lung model to have 24 generation in total. These gradually narrowing airways from the carina to the alveolar sacs cause increased particle velocity, which causes particles to impact the walls of airways instead of reaching the lower regions of the lungs. Therefore, for a therapeutic agent to reach the target site of action, it must possess aerodynamic properties to allow it to pass through the branched airways to the deep lung.

Table 4 Pulmonary barriers to lung siRNA delivery (Merkel O.M. et al., 2014)

Airway Defenses	Alveoli Defenses
Upper airway (nose, throat, and trachea)	Degradative Enzymes e.g. proteases, RNase
Bifurcations	Neutrophils
Mucus	Opsonins
Mucociliary Clearance	Surfactant
Cough Clearance	Complement
Airway epithelium	Alveolar Macrophages

Aerodynamic particle size distribution is an important influence on the location of lung deposition of a formulation (Bisgaard H. et al., 2001). Three forces dominate particle motion within an aerosol cloud: gravitational sedimentation, inertial impaction, and Brownian diffusion. Gravitational sedimentation and inertial impaction are dominant when the aerodynamic diameter is > 2 μm. Large particles with aerodynamic particle size of > 6 μm deposit mostly on the airway walls at bifurcations in the upper airways due to their high momentum. Smaller particles of aerodynamic diameters of < 1 μm deposit due to Brownian diffusion (Morén F., 1993). If submicron sized particles are delivered without a larger carrier particle or droplet, then they would be mostly exhaled in the breath. A breath hold method may be used to increase deposition within the lower respiratory tract, however, it has lower efficiency. The most optimum aerodynamic particle sizes for deposition within the lower airways are between 1 to 5 μm (Agu R.U. et al., 2001; Sakagami M., 2006). As particle size decreases below 1 μm, lung deposition increases due to increased diffusional mobility (Yang W. et al., 2008). For particles less than 100 nm in size, approximately 50 % of the nanoparticles will deposit within the alveolar region of the lungs. These nanoparticles often enter the lungs as large agglomerates that break apart upon deposition.

The elimination pathways for nanoparticles within the

lungs involve coughing, dissolution, clearance via the mucociliary escalator, translocation from the airways, phagocytosis by macrophages and neuronal uptake (Roy I. and Vij N., 2010; Sanders N. et al., 2009; Zhang J. et al., 2011). Nanoparticle degradation is dependent on the composition of the delivery system and mediated through hydrolysis, oxidation, and reduction pathways (Roy I. and Vij N., 2010; Rytting E. et al., 2008). After deposition in the lower airways following inhalation, free siRNA will be susceptible to degradation from RNase, whose enzymatic activity is very high in the lungs (Amatngalim G.D. et al., 2015; Morita T. et al., 1986; Sorrentino S., 1998).

A major pulmonary delivery barrier is the mucociliary clearance driven by the physical action of the ciliated epithelial cells, which move the mucus and alveolar fluid towards the upper airways, and eventually, the throat. Mucociliary clearance also includes the alveolar macrophages along the airways, which phagocytose foreign particles and deposits their remains to be removed by the mucociliary escalator. Mucus is present on the respiratory epithelium from the nasal cavity to the terminal bronchioles (Knowles M.R. and Boucher R.C., 2002). Types of glycosylated protein, known as mucins, are the main component of mucus (Rose M.C. et al., 2001). Mucus is a physical barrier as it increases in viscosity of the moist surface of the lung epithelial cells, thereby reducing drug penetration and diffusion rate (Hill D.B. et al., 2014; Mellnik J. et al., 2014). Particles that are deposited on the mucosal layer above the ciliated epithelial cells are rapidly removed by mucociliary clearance and are eventually either coughed out or swallowed into the gastrointestinal tract (Knowles M.R. and Boucher R.C., 2002; Rubin B.K., 2002). The alveolar fluid is found on the surface of alveoli epithelium as a thin layer of pulmonary surfactant which is composed of phospholipids and surfactant-associated proteins known as SP-A, SP-B, SP-C and SP-D (Bastacky J. et al., 1995; Possmayer F. et al., 2001). Following delivery of foreign antigen or nanocarrier, pulmonary surfactant proteins SP-A and SP-D have been shown to play a role in macrophage uptake by acting as opsonins and scavenger molecules (Kishore U. et al., 2006). These pulmonary surfactants are located at the air-liquid interface of the alveoli, therefore they can interact with particulate aerosols that reach the lower airways (Seaton B.A. et al., 2010). Other major opsonins of the airways and alveoli of the lungs include immunoglobulins (IgG or IgM), complement fragments (C3, C4, C5), fibronectin, and laminin (Kuroki Y. et al., 2007; Patel B. et al., 2015). The alveolar macrophages located within the alveoli rapidly engulf foreign particles by phagocytosis as a defense mechanism (Patton J.S., 1996; Weinberger B. et al., 2014; Zhao F. et al., 2011).

In addition to macrophages, the other major phagocytes are the neutrophils, or polymorphonuclear neutrophilic leukocytes (PMNs or polys), that are abundant in the blood but are not present in normal healthy tissue (Kolaczkowska E. and Kubes P., 2013). Like macrophages, neutrophils are phagocytic cells that have a role in the innate immunity because they recognize, ingest, and destroy many pathogens without the adaptive immune response (Kolaczkowska E. and Kubes P., 2013). When macrophages first encounter a pathogen within the lung, their action is augmented by the recruitment of large number of neutrophils to the infection site (Burns A.R. et al., 2003; Kolaczkowska E. and Kubes P., 2013). Pulmonary administered naked siRNA is susceptible to alveolar macrophage or neutrophil uptake and are subsequently degraded within these cells, thus reducing their therapeutic efficacy.

Considering disease state is an important aspect of pulmonary clearance since the physiological conditions of the airways are altered and pose a threat on the efficiency of an aerosolized siRNA delivery system. During infection and inflammation, the airways become congested because there is increased mucus secretion and decreased mucociliary clearance (Groneberg D. et al., 2002; Patton J.S. et al., 2010). The thickness, viscosity, viscoelasticity, and the composition of the mucus layer depend on the pathological condition and have inter-patient variability (Sanders N. et al., 2009). For different therapeutic applications, disease state of the patient should be considered in order to design an effective aerosolized delivery system. In addition to using particles with small aerodynamic diameter suitable for deposition in the lower airways, it has been reported that the use of large porous particles can prolong retention time in the lungs by effectively avoiding alveolar macrophage phagocytosis (Arnold M.M. et al., 2007; Ben-Jebria A. et al., 2000; Edwards D.A. et al., 1997). Porous particles over 10 μm in geometric diameter have a smaller aerodynamic diameter due to their mass-inertia relationship. Their smaller aerodynamic diameters of 1–3 μm fall within the ideal aerodynamic size range for effective lung deposition, while their actual geometric size is larger than the size range of alveolar macrophage uptake and removal.

The mucus layer may be partially deteriorated using mucolytic agents that break down the three dimensional gel network of mucus. A mucus inhibitor, such as glycopyrrolate, may also be used to overcome the mucus barrier (Ferrari S. et al., 2001). In patients with bronchiectasis or cystic fibrosis, mannitol has been clinically proven to improve the hydration and viscoelastic surface properties of the sputum, which increased mucus clearance (Daviskas E. et al., 2010). The deposition site of nucleic acid delivery systems in the airways has been previously manipulated and directed through the use of ultrasound and magnetic field technologies (Dames P. et al., 2007; Xenariou S. et al., 2006; Xenariou S. et al., 2007). Another less-invasive option to enhance the transport across the mucus layer is

to coat the surface of nanoparticles with neutrally charged molecules, like polyethylene glycol (PEG) (Schuster B.S. et al., 2013).

Lung disease involving chronic lung inflammation, like cystic fibrosis, emphysema, or asthma, are characterized by increased levels of pulmonary proteases (Greene C.M. and Mcelvaney N.G., 2009). These proteases may degrade peptide conjugated siRNA or polymeric nanocarriers of siRNA before the carrier gets to target specific cells of interest.

4.2 Barriers of intracellular siRNA delivery

To exert their effects, the siRNA must cross the cellular membrane and be released within the cytoplasm of the target cells of the respiratory tract, and it must access the RISC, where their intracellular interaction takes place. Due to the size of 13 kDa and a negative charge, the siRNA do not readily cross biological membranes. Therefore, an appropriate delivery system should facilitate siRNA cellular uptake.

The major cellular uptake pathway for non-viral siRNA delivery systems that are under 150 nm in size is endocytosis (Khalil I.A. et al., 2006). Endocytosis is the mechanism by which cells engulf polar molecules or nanocarriers that cannot readily pass through the hydrophobic cellular membrane. The four endocytosis pathways are clathrin-mediated endocytosis, caveolae-mediated endocytosis, micropinocytosis, and phagocytosis (Marsh M., 2001). For the inhalation route of administration, a particle size of less than 150 nm also avoids macrophage uptake, thus slowing lung clearance (Lebhardt T. et al., 2010). Clathrin-mediated endocytosis is the major pathway that allows for particle uptake through enclosed clathrin-coated vesicles (Khalil I.A. et al., 2006). These vesicles then fuse with early endosomes to form late endosomes, which subsequently form into lysosomes. As this process progresses from early endosome to lysosome, the pH within the vesicles drop down to approximately pH 5.0 and degradative DNAse and RNase are present within the lysosome (Bally M.B. et al., 1999; Khalil I.A. et al., 2006; Maxfield F.R. and Mcgraw T.E., 2004). For a siRNA to elicit therapeutic effects within the cell, it must escape from the endosome and be released within the cytoplasm to avoid degradation by degradative enzymes. To promote endosomal escape, the "proton sponge hypothesis" can be practiced by using a high buffering capacity polymer with a large pH range, such as polyethylenimine (PEI), which will become protonated as the pH of the endosome drops (Boussif O. et al., 1995; Gunther M. et al., 2011). This protonation of the polymer causes an influx of chloride ions, protons and water into the endosomes. The building osmotic pressure causes the endosomes to burst, thus releasing its contents into the cytoplasm (Gunther M. et al., 2011). However, the use of PEI has been associated with toxicity issues (Seow W.Y. et al., 2013). An alternative strategy to promote endosomal escape is through the use of pH sensitive fusogenic peptides. These peptides undergo pH-dependent conformation changes at low pH which cause a membrane disrupting conformational change that destabilizes endosomal membranes (Choi S.W. et al., 2010; Kusumoto K. et al., 2013; Lee S.H. et al., 2007; Oliveira S. et al., 2007).

Another cellular uptake mechanism of siRNA delivery systems is the caveolae-mediated endocytosis pathway (Khalil I.A. et al., 2006). The delivery system is internalized through a caveolin-coated vesicle known as a caveosome. The caveosomes are void of nucleases, degradative enzymes, and have a non-acidic pH. The delivery systems avoid lysosomal degradation because the contents of the caveosomes are transported to the Golgi or endoplasmic reticulum. Caveolin is expressed within lung tissues, therefore it may be a more efficient route for inhalation siRNA delivery systems compared to clathrin-mediated endocytosis, especially if the delivery system doesn't possess endosomal escape properties (Lam J.K.-W. et al., 2012; Parton R.G. and Richards A.A., 2003; Yacobi N.R. et al., 2010).

Another cellular uptake mechanism of cells of the lungs is phagocytosis (Khalil I.A. et al., 2006). This route can only be performed by alveolar macrophages and other specialized cells. Unless the target cell type is alveolar macrophages, then uptake of delivery systems by this pathway should be avoided since siRNA molecules taken up are eventually degraded by the phagolysosomes of the cells.

5. Conclusion

Lower airway pulmonary delivery can be achieved through the inhalation of an aerosol from delivery devices such as pMDIs, DPIs, nebulizers, and SMIs. Preclinical safety and efficacy studies using animal models often deliver pulmonary aerosols via the inhalation, intratracheal, and intranasal routes. The lung physiological and anatomical differences between human and animals are an integral consideration when selecting the route of administration to assess the efficacy of an aerosol. Intratracheal administration involves an invasive surgical setup and anesthesia. The intranasal route of administration can be used to reach the airways in mouse models by instilling and aspirating the liquid solution or suspension into the nasal cavity of the animal. Dry powder formulations can be delivered using a microsprayer that when actuated, generates the aerosol and propels it into the airways. The nose-only exposure chamber used in preclinical studies has provided a robust means of delivering aerosols to the deep lung.

Aerosolized siRNA formulations are characterized using *in vitro*, *ex vivo*, and *in vivo* techniques. *In vitro* techniques measure the dissolution rate, aerodynamic particle size distribution, total delivery dose uniformity, particle size, and aerosol velocity. *Ex vivo* techniques analyze the mechanisms of drug transport, deposition, and absorption. *In vivo* techniques provide visualization and quantification of aerosol deposition in the respiratory tract, PK parameters, and biochemical and physiological effects of the pulmonary delivered drug. Barriers for pulmonary delivery of siRNA exist due to the natural defenses of the lungs to keep exogenous particulates and substances out. Delivering aerosolized siRNA effectively to the lungs and to their target site-of-action involves the understanding of the anatomical and physiological characteristics of the respiratory tract. The barriers for aerosolized delivery of siRNA include degradation by RNase and mucociliary clearance. Intracellular naked siRNA delivery is impeded due to their large size, negative charge, and susceptibility to degradation. These intracellular delivery constraints may be mitigated through the use of siRNA nanocarrier systems for aerosol delivery including those of lipidic, polymeric, peptide, or inorganic origin. Part II of this review article will discuss the preparation methods of various siRNA nanocarrier systems, accompanied by a series of examples.

Acknowledgements

The authors acknowledge the support of the National Institute of General Medical Science of the National Institutes of Health under award number SC3GM109873. The authors acknowledge Hawai'i Community Foundation, Honolulu, HI 96813, USA, for research support on lung cancer, mesothelioma, and asthma projects (Leahi Fund) in 2015, 2013, and 2011, respectively. The authors would like to acknowledge the 2013 George F. Straub Trust and Robert C. Perry Fund of the Hawai'i Community Foundation, Honolulu, HI 96813, USA, for research support on lung cancer. The authors also acknowledge a seed grant from the Research Corporation of the University of Hawai'i at Hilo, Hilo, HI 96720, USA, and The Daniel K. Inouye College of Pharmacy, University of Hawai'i at Hilo, Hilo, HI 96720, USA, for providing start-up financial support to their research group. The authors acknowledge the donation from Dr. Robert S. Shapiro, MD, Dermatologist, Hilo, HI, USA in support of development of nanotechnology based medicines.

References

Adamcakova-Dodd A., Stebounova L.V., Kim J.S., Vorrink S.U., Ault A.P., O'shaughnessy P.T., Grassian V.H., Thorne P.S., Toxicity assessment of zinc oxide nanoparticles using sub-acute and sub-chronic murine inhalation models, Part Fibre Toxicol, 11 (2014) b1.

Adams K.E., Ke S., Kwon S., Liang F., Fan Z., Lu Y., Hirschi K., Mawad M.E., Barry M.A., Sevick-Muraca E.M., Comparison of visible and near-infrared wavelength-excitable fluorescent dyes for molecular imaging of cancer, Journal of biomedical optics, 12 (2007) 024017-024017-024019.

Agrawal N., Dasaradhi P., Mohmmed A., Malhotra P., Bhatnagar R.K., Mukherjee S.K., RNA interference: Biology, mechanism, and applications, Microbiology and molecular biology reviews, 67 (2003) 657–685.

Agu R.U., Ugwoke M.I., Armand M., Kinget R., Verbeke N., The lung as a route for systemic delivery of therapeutic proteins and peptides, Respiratory research, 2 (2001) 198.

Amarzguioui M., Rossi J.J., Kim D., Approaches for chemically synthesized siRNA and vector-mediated RNAi, FEBS Letters, 579 (2005) 5974–5981.

Amatngalim G.D., Van Wijck Y., De Mooij-Eijk Y., Verhoosel R.M., Harder J., Lekkerkerker A.N., Janssen R.A., Hiemstra P.S., Basal cells contribute to innate immunity of the airway epithelium through production of the antimicrobial protein rnase 7, J Immunol, 194 (2015) 3340–3350.

Ari A., Jet, ultrasonic, and mesh nebulizers: An evaluation of nebulizers for better clinical outcomes (2014).

Ari A., Hess D., Myers T., Rau J., A guide to aerosol delivery devices for respiratory therapists, Dallas, Texas: American Association for Respiratory Care (2009).

Ari A., Restrepo R.D., Aerosol delivery device selection for spontaneously breathing patients: 2012, Respiratory care, 57 (2012) 613–626.

Arnold M.M., Gorman E.M., Schieber L.J., Munson E.J., Berkland C., NanoCipro encapsulation in monodisperse large porous PLGA microparticles, Journal of Controlled Release, 121 (2007) 100–109.

Arunthari V., Bruinsma R.S., Lee A.S., Johnson M.M., A prospective, comparative trial of standard and breath-actuated nebulizer: Efficacy, safety, and satisfaction, Respiratory care, 57 (2012) 1242–1247.

Bai S., Gupta V., Ahsan F., Inhalable lactose-based dry powder formulations of low molecular weight heparin, Journal of aerosol medicine and pulmonary drug delivery, 23 (2010) 97–104.

Bally M.B., Harvie P., Wong F.M., Kong S., Wasan E.K., Reimer D.L., Biological barriers to cellular delivery of lipid-based DNA carriers, Advanced drug delivery reviews, 38 (1999) 291–315.

Bastacky J., Lee C., Goerke J., Koushafar H., Yager D., Kenaga L., Speed T.P., Chen Y., Clements J.A., Alveolar lining layer is thin and continuous: Low-temperature scanning electron microscopy of rat lung, Journal of Applied Physiology, 79 (1995) 1615–1628.

Ben-Jebria A., Eskew M.L., Edwards D.A., Inhalation system for pulmonary aerosol drug delivery in rodents using large porous particles, Aerosol Science & Technology, 32 (2000) 421–433.

Bisgaard H., O'callaghan C., Smaldone G.C., Drug delivery to

the lung, CRC Press, 2001.
Bitko V., Musiyenko A., Shulyayeva O., Barik S., Inhibition of respiratory viruses by nasally administered siRNA, Nature medicine, 11 (2005) 50–55.
Bivas-Benita M., Zwier R., Junginger H.E., Borchard G., Non-invasive pulmonary aerosol delivery in mice by the endotracheal route, European Journal of Pharmaceutics and Biopharmaceutics, 61 (2005) 214–218.
Bondesson E., Bengtsson T., Borgström L., Nilsson L.-E., Norrgren K., Trofast E., Wollmer P., Planar gamma scintigraphy—points to consider when quantifying pulmonary dry powder aerosol deposition, International journal of pharmaceutics, 258 (2003) 227–240.
Boussif O., Lezoualc'h F., Zanta M.A., Mergny M.D., Scherman D., Demeneix B., Behr J.-P., A versatile vector for gene and oligonucleotide transfer into cells in culture and *in vivo*: Polyethylenimine, Proceedings of the National Academy of Sciences, 92 (1995) 7297–7301.
Burnett J.C., Rossi J.J., RNA-based therapeutics: Current progress and future prospects, Chemistry & biology, 19 (2012) 60–71.
Burns A.R., Smith C.W., Walker D.C., Unique structural features that influence neutrophil emigration into the lung, 2003.
Carvalho T.C., Peters J.I., Williams Iii R.O., Influence of particle size on regional lung deposition—what evidence is there?, International Journal of Pharmaceutics, 406 (2011) 1–10.
Chakravarty R., Hong H., Cai W., Positron emission tomography image-guided drug delivery: Current status and future perspectives, Molecular pharmaceutics, 11 (2014) 3777–3797.
Chan H.-K., Formulation challenges: Protein powders for inhalation, Drugs and the Pharmaceutical Sciences, 126 (2003) 879–890.
Chan H.-K., Eberl S., Glover W., Radiolabeling of pharmaceutical aerosols and gamma scintigraphic imaging for lung deposition, Encyclopedia of Pharmaceutical Technology, 3rd ed. Informa Healthcare, New York, (2007) 3094–3107.
Chapters U.G., USP <601> Aerosols, nasal sprays, metered-dose inhalers and dry powder inhalers, USP 32-NF (2009).
Cherry S.R., Gambhir S.S., Use of positron emission tomography in animal research, ILAR journal, 42 (2001) 219–232.
Chiang P.-C., Alsup J.W., Lai Y., Hu Y., Heyde B.R., Tung D., Evaluation of aerosol delivery of nanosuspension for pre-clinical pulmonary drug delivery, Nanoscale research letters, 4 (2009) 254–261.
Choi S.W., Lee S.H., Mok H., Park T.G., Multifunctional siRNA delivery system: Polyelectrolyte complex micelles of six-arm PEG conjugate of siRNA and cell penetrating peptide with crosslinked fusogenic peptide, Biotechnology progress, 26 (2010) 57–63.
Chougule M., Padhi B., Misra A., Development of spray dried liposomal dry powder inhaler of dapsone, AAPS PharmSciTech, 9 (2008) 47–53.
Codrons V., Vanderbist F., Verbeeck R.K., Arras M., Lison D., Préat V., Vanbever R., Systemic delivery of parathyroid hormone (1–34) using inhalation dry powders in rats, Journal of pharmaceutical sciences, 92 (2003) 938–950.
Comsa D.C., Farrell T.J., Patterson M.S., Quantitative fluorescence imaging of point-like sources in small animals, Physics in medicine and biology, 53 (2008) 5797.
Conde J., Tian F., Hernandez Y., Bao C., Cui D., Janssen K.P., Ibarra M.R., Baptista P.V., Stoeger T., De La Fuente J.M., *In vivo* tumor targeting via nanoparticle-mediated therapeutic siRNA coupled to inflammatory response in lung cancer mouse models, Biomaterials, 34 (2013) 7744–7753.
Conway J., Lung imaging—two dimensional gamma scintigraphy, SPECT, CT and PET, Advanced drug delivery reviews, 64 (2012) 357–368.
Cryan S.-A., Sivadas N., Garcia-Contreras L., *In vivo* animal models for drug delivery across the lung mucosal barrier, Advanced drug delivery reviews, 59 (2007) 1133–1151.
Dailey L.A., Schmehl T., Gessler T., Wittmar M., Grimminger F., Seeger W., Kissel T., Nebulization of biodegradable nanoparticles: Impact of nebulizer technology and nanoparticle characteristics on aerosol features, Journal of Controlled Release, 86 (2003) 131–144.
Dalby R., Spallek M., Voshaar T., A review of the development of respimat® soft mist™ inhaler, International journal of pharmaceutics, 283 (2004) 1–9.
Dames P., Gleich B., Flemmer A., Hajek K., Seidl N., Wiekhorst F., Eberbeck D., Bittmann I., Bergemann C., Weyh T., Trahms L., Rosenecker J., Rudolph C., Targeted delivery of magnetic aerosol droplets to the lung, Nat Nanotechnol, 2 (2007) 495–499.
Davies N.M., Feddah M.R., A novel method for assessing dissolution of aerosol inhaler products, International journal of pharmaceutics, 255 (2003) 175–187.
Daviskas E., Anderson S.D., Jaques A., Charlton B., Inhaled mannitol improves the hydration and surface properties of sputum in patients with cystic fibrosis, CHEST Journal, 137 (2010) 861–868.
De Boer A.H., Gjaltema D., Hagedoorn P., Frijlink H.W., Characterization of inhalation aerosols: A critical evaluation of cascade impactor analysis and laser diffraction technique, Int J Pharm, 249 (2002) 219–231.
De Fougerolles A., Novobrantseva T., SiRNA and the lung: Research tool or therapeutic drug?, Current opinion in pharmacology, 8 (2008) 280–285.
De Fougerolles A., Vornlocher H.-P., Maraganore J., Lieberman J., Interfering with disease: A progress report on siRNA-based therapeutics, Nat Rev Drug Discov, 6 (2007) 443–453.
Denyer J., Dyche T., The adaptive aerosol delivery (AAD) technology: Past, present, and future, Journal of aerosol medicine and pulmonary drug delivery, 23 (2010) S-1–S-10.
Denyer J., Nikander K., Smith N., Adaptive aerosol delivery (AAD®) technology, Expert opinion on drug delivery, 1 (2004) 165–176.
Devincenzo J., Cehelsky J.E., Alvarez R., Elbashir S., Harborth J., Toudjarska I., Nechev L., Murugaiah V., Van Vliet A., Vaishnaw A.K., Evaluation of the safety, tolerability and pharmacokinetics of ALN-RSV01, a novel RNAi antiviral therapeutic directed against respiratory syncytial virus (RSV), Antiviral research, 77 (2008) 225–231.

Devincenzo J., Lambkin-Williams R., Wilkinson T., Cehelsky J., Nochur S., Walsh E., Meyers R., Gollob J., Vaishnaw A., A randomized, double-blind, placebo-controlled study of an RNAi-based therapy directed against respiratory syncytial virus, Proceedings of the National Academy of Sciences, 107 (2010) 8800–8805.

Dhand R., Nebulizers that use a vibrating mesh or plate with multiple apertures to generate aerosol, Respiratory care, 47 (2002) 1406–1416; discussion 1416–1408.

Dickinson P.A., Howells S.W., Kellaway I.W., Novel nanoparticles for pulmonary drug administration, Journal of drug targeting, 9 (2001) 295–302.

Dolovich M.B., 18f-fluorodeoxyglucose positron emission tomographic imaging of pulmonary functions, pathology, and drug delivery, Proceedings of the American Thoracic Society, 6 (2009) 477–485.

Dolovich M.B., Dhand R., Aerosol drug delivery: Developments in device design and clinical use, The Lancet, 377 (2011) 1032–1045.

Driscoll K.E., Costa D.L., Hatch G., Henderson R., Oberdorster G., Salem H., Schlesinger R.B., Intratracheal instillation as an exposure technique for the evaluation of respiratory tract toxicity: Uses and limitations, Toxicological Sciences, 55 (2000) 24–35.

Dunbar C., Mitchell J., Analysis of cascade impactor mass distributions, Journal of Aerosol Medicine-Deposition Clearance and Effects in the Lung, 18 (2005) 439–451.

Eberl S., Chan H.-K., Daviskas E., SPECT imaging for radioaerosol deposition and clearance studies, Journal of aerosol medicine, 19 (2006) 8–20.

Edwards D.A., Hanes J., Caponetti G., Hrkach J., Ben-Jebria A., Eskew M.L., Mintzes J., Deaver D., Lotan N., Langer R., Large porous particles for pulmonary drug delivery, Science, 276 (1997) 1868–1872.

Elhissi A., Karnam K.K., Danesh-Azari M.R., Gill H.S., Taylor K.M., Formulations generated from ethanol-based proliposomes for delivery via medical nebulizers, Journal of pharmacy and pharmacology, 58 (2006) 887–894.

Elhissi A., Taylor K., Delivery of liposomes generated from proliposomes using air-jet, ultrasonic, and vibrating-mesh nebulisers, Journal of drug delivery science and technology, 15 (2005) 261–265.

Eshel G., Levy G., Mingelgrin U., Singer M., Critical evaluation of the use of laser diffraction for particle-size distribution analysis, Soil Science Society of America Journal, 68 (2004) 736–743.

Everard M.L., Studies using radiolabelled aerosols in children, Thorax, 49 (1994) 1259–1266.

Feddah M.R., Brown K.F., Gipps E.M., Davies N.M., In-vitro characterisation of metered dose inhaler versus dry powder inhaler glucocorticoid products: Influence of inspiratory flow rates, J Pharm Pharm Sci, 3 (2000) 318–324.

Fellmann C., Lowe S.W., Stable RNA interference rules for silencing, Nature cell biology, 16 (2014) 10–18.

Fernandes C.A., Vanbever R., Preclinical models for pulmonary drug delivery, Expert opinion on drug delivery, 6 (2009) 1231–1245.

Ferrari S., Kitson C., Farley R., Steel R., Marriott C., Parkins D., Scarpa M., Wainwright B., Evans M., Colledge W., Mucus altering agents as adjuncts for nonviral gene transfer to airway epithelium, Gene therapy, 8 (2001) 1380–1386.

Fire A., Xu S.Q., Montgomery M.K., Kostas S.A., Driver S.E., Mello C.C., Potent and specific genetic interference by double-stranded RNA in caenorhabditis elegans, Nature, 391 (1998) 806–811.

Fleming J., Conway J., Majoral C., Tossici-Bolt L., Katz I., Caillibotte G., Perchet D., Pichelin M., Muellinger B., Martonen T., The use of combined single photon emission computed tomography and X-ray computed tomography to assess the fate of inhaled aerosol, Journal of aerosol medicine and pulmonary drug delivery, 24 (2011) 49–60.

Frauenfelder T., Kestenholz P., Hunziker R., Nguyen T.D.L., Fries M., Veit-Haibach P., Husmann L., Stahel R., Weder W., Opitz I., Use of computed tomography and positron emission tomography/computed tomography for staging of local extent in patients with malignant pleural mesothelioma, Journal of computer assisted tomography, 39 (2015) 160–165.

Fulton A., Peters S.T., Perkins G.A., Jarosinski K.W., Damiani A., Brosnahan M., Buckles E.L., Osterrieder N., Van De Walle G.R., Effective treatment of respiratory alphaherpesvirus infection using RNA interference, PLoS One, 4 (2009) e4118.

Garbuzenko O.B., Saad M., Betigeri S., Zhang M., Vetcher A.A., Soldatenkov V.A., Reimer D.C., Pozharov V.P., Minko T., Intratracheal versus intravenous liposomal delivery of siRNA, antisense oligonucleotides and anticancer drug, Pharmaceutical Research, 26 (2009) 382–394.

Ghosn B., Singh A., Li M., Vlassov A.V., Burnett C., Puri N., Roy K., Efficient gene silencing in lungs and liver using imidazole-modified chitosan as a nanocarrier for small interfering RNA, Oligonucleotides, 20 (2010) 163–172.

Greene C.M., Mcelvaney N.G., Proteases and antiproteases in chronic neutrophilic lung disease-relevance to drug discovery, British journal of pharmacology, 158 (2009) 1048–1058.

Groneberg D., Eynott P., Lim S., Oates T., Wu R., Carlstedt I., Roberts P., Mccann B., Nicholson A., Harrison B., Expression of respiratory mucins in fatal status asthmaticus and mild asthma, Histopathology, 40 (2002) 367–373.

Gunther M., Lipka J., Malek A., Gutsch D., Kreyling W., Aigner A., Polyethylenimines for RNAi-mediated gene targeting *in vivo* and siRNA delivery to the lung, Eur J Pharm Biopharm, 77 (2011) 438–449.

Gutbier B., Kube S.M., Reppe K., Santel A., Lange C., Kaufmann J., Suttorp N., Witzenrath M., RNAi-mediated suppression of constitutive pulmonary gene expression by small interfering RNA in mice, Pulmonary pharmacology & therapeutics, 23 (2010) 334–344.

Hannon G.J., RNA interference, Nature, 418 (2002) 244–251.

Hanson L.R., Frey W.H., 2nd, Intranasal delivery bypasses the blood-brain barrier to target therapeutic agents to the central nervous system and treat neurodegenerative disease, BMC Neurosci, 9 Suppl 3 (2008) S5.

Haynes J.M., Randomized controlled trial of a breath-activated nebulizer in patients with exacerbation of COPD, Respira-

tory care, 57 (2012) 1385–1390.
Heyder J., Gebhart J., Rudolf G., Schiller C.F., Stahlhofen W., Deposition of particles in the human respiratory tract in the size range 0.005–15 μm, Journal of Aerosol Science, 17 (1986) 811–825.
Hibbitts A., O'mahony A.M., Forde E., Nolan L., Ogier J., Desgranges S., Darcy R., Macloughlin R., O'driscoll C.M., Cryan S.A., Early-stage development of novel cyclodextrin-siRNA nanocomplexes allows for successful postnebulization transfection of bronchial epithelial cells, J Aerosol Med Pulm Drug Deliv, 27 (2014) 466–477.
Hickey A.J., Pharmaceutical inhalation aerosol technology, CRC Press, 2003.
Hickey A.J., Garcia-Contreras L., Immunological and toxicological implications of short-term studies in animals of pharmaceutical aerosol delivery to the lungs: Relevance to humans, Critical Reviews™ in Therapeutic Drug Carrier Systems, 18 (2001).
Hill D.B., Vasquez P.A., Mellnik J., Mckinley S.A., Vose A., Mu F., Henderson A.G., Donaldson S.H., Alexis N.E., Boucher R.C., A biophysical basis for mucus solids concentration as a candidate biomarker for airways disease, PloS one, 9 (2014) e87681.
Hinchcliffe M., Illum L., Intranasal insulin delivery and therapy, Adv Drug Deliv Rev, 35 (1999) 199–234.
Ho S.L., Kwong W.J., O'drowsky L., Coates A.L., Evaluation of four breath-enhanced nebulizers for home use, Journal of aerosol medicine, 14 (2001) 467–475.
Hochrainer D., Hölz H., Kreher C., Scaffidi L., Spallek M., Wachtel H., Comparison of the aerosol velocity and spray duration of respimat® soft mist™ inhaler and pressurized metered dose inhalers, Journal of aerosol medicine, 18 (2005) 273–282.
Hosoya K., Satoh T., Yamamoto Y., Saeki K., Igawa K., Okano M., Moriya T., Imamura O., Nemoto Y., Yokozeki H., Gene silencing of STAT6 with siRNA ameliorates contact hypersensitivity and allergic rhinitis, Allergy, 66 (2011) 124–131.
Howard K.A., Rahbek U.L., Liu X., Damgaard C.K., Glud S.Z., Andersen M.O., Hovgaard M.B., Schmitz A., Nyengaard J.R., Besenbacher F., Kjems J., RNA interference *in vitro* and *in vivo* using a novel chitosan/siRNA nanoparticle system, Mol Ther, 14 (2006) 476–484.
Huchon G.J., Montgomery A.B., Lipavsky A., Hoeffel J.M., Murray J.F., Respiratory clearance of aerosolized radioactive solutes of varying molecular weight, Journal of nuclear medicine: official publication, Society of Nuclear Medicine, 28 (1987) 894–902.
Kamei N., Takeda-Morishita M., Brain delivery of insulin boosted by intranasal coadministration with cell-penetrating peptides, J Control Release, 197 (2015) 105–110.
Kanasty R., Dorkin J.R., Vegas A., Anderson D., Delivery materials for siRNA therapeutics, Nature materials, 12 (2013) 967–977.
Khalil I.A., Kogure K., Akita H., Harashima H., Uptake pathways and subsequent intracellular trafficking in nonviral gene delivery, Pharmacological reviews, 58 (2006) 32–45.
Kim D.H., Rossi J.J., Strategies for silencing human disease using RNA interference, Nature Reviews Genetics, 8 (2007) 173–184.
Kishore U., Greenhough T.J., Waters P., Shrive A.K., Ghai R., Kamran M.F., Bernal A.L., Reid K.B., Madan T., Chakraborty T., Surfactant proteins SP-A and SP-D: Structure, function and receptors, Mol Immunol, 43 (2006) 1293–1315.
Knowles M.R., Boucher R.C., Mucus clearance as a primary innate defense mechanism for mammalian airways, The Journal of clinical investigation, 109 (2002) 571–577.
Kolaczkowska E., Kubes P., Neutrophil recruitment and function in health and inflammation, Nat Rev Immunol, 13 (2013) 159–175.
Komlosi P., Altes T.A., Qing K., Mooney K.E., Miller G.W., Mata J.F., De Lange E.E., Tobias W.A., Cates G.D., Brookeman J.R., Regional anisotropy of airspace orientation in the lung as assessed with hyperpolarized helium-3 diffusion MRI, Journal of Magnetic Resonance Imaging (2015).
Koping-Hoggard M., Issa M.M., Kohler T., Tronde A., Varum K.M., Artursson P., A miniaturized nebulization catheter for improved gene delivery to the mouse lung, J Gene Med, 7 (2005) 1215–1222.
Kovar J.L., Simpson M.A., Schutz-Geschwender A., Olive D.M., A systematic approach to the development of fluorescent contrast agents for optical imaging of mouse cancer models, Analytical biochemistry, 367 (2007) 1–12.
Kruger S.J., Niles D.J., Dardzinski B., Harman A., Jarjour N.N., Ruddy M., Nagle S.K., Francois C.J., Sorkness R.L., Burton R.M., Hyperpolarized helium-3 MRI of exercise-induced bronchoconstriction during challenge and therapy, Journal of Magnetic Resonance Imaging, 39 (2014) 1230–1237.
Kuroki Y., Takahashi M., Nishitani C., Pulmonary collectins in innate immunity of the lung, Cellular microbiology, 9 (2007) 1871–1879.
Kusumoto K., Akita H., Ishitsuka T., Matsumoto Y., Nomoto T., Furukawa R., El-Sayed A., Hatakeyama H., Kajimoto K., Yamada Y., Kataoka K., Harashima H., Lipid envelope-type nanoparticle incorporating a multifunctional peptide for systemic siRNA delivery to the pulmonary endothelium, ACS Nano, 7 (2013) 7534–7541.
Lam J.K.-W., Liang W., Chan H.-K., Pulmonary delivery of therapeutic siRNA, Advanced drug delivery reviews, 64 (2012) 1–15.
Laube B.L., The expanding role of aerosols in systemic drug delivery, gene therapy and vaccination: An update, Translational Respiratory Medicine, 2 (2014) 1–12.
Lebhardt T., Roesler S., Beck-Broichsitter M., Kissel T., Polymeric nanocarriers for drug delivery to the lung, Journal of Drug Delivery Science and Technology, 20 (2010) 171–180.
Lee Black D., Mcquay M.Q., Bonin M.P., Laser-based techniques for particle-size measurement: A review of sizing methods and their industrial applications, Progress in Energy and Combustion Science, 22 (1996) 267–306.
Lee S.H., Kim S.H., Park T.G., Intracellular siRNA delivery system using polyelectrolyte complex micelles prepared from VEGF siRNA-PEG conjugate and cationic fusogenic peptide, Biochemical and biophysical research communications, 357 (2007) 511–516.
Lentz Y.K., Anchordoquy T.J., Lengsfeld C.S., Rationale for the

selection of an aerosol delivery system for gene delivery, Journal of aerosol medicine, 19 (2006) 372–384.

Li B.-J., Tang Q., Cheng D., Qin C., Xie F.Y., Wei Q., Xu J., Liu Y., Zheng B.-J., Woodle M.C., Using siRNA in prophylactic and therapeutic regimens against SARS coronavirus in rhesus macaque, Nature medicine, 11 (2005) 944–951.

Luo Y., Zhai X., Ma C., Sun P., Fu Z., Liu W., Xu J., An inhalable beta(2)-adrenoceptor ligand-directed guanidinylated chitosan carrier for targeted delivery of siRNA to lung, J Control Release, 162 (2012) 28–36.

Mainelis G., Seshadri S., Garbuzenko O., Han T., Wang Z., Minko T., Characterization and application of a nose-only exposure chamber for inhalation delivery of liposomal drugs and nucleic acids to mice, Journal of aerosol medicine and pulmonary drug delivery, 26 (2013) 345–354.

Majoral C., Fleming J., Conway J., Katz I., Tossici-Bolt L., Pichelin M., Montesantos S., Caillibotte G., Controlled, parametric, individualized, 2D and 3D imaging measurements of aerosol deposition in the respiratory tract of healthy human volunteers: *In vivo* data analysis, Journal of aerosol medicine and pulmonary drug delivery, 27 (2014) 349–362.

Mansour H.M., Rhee Y.-S., Wu X., Nanomedicine in pulmonary delivery, International Journal of Nanomedicine, 4 (2009) 299–319.

Marsh M., Endocytosis (2001).

Martin A.R., Thompson R.B., Finlay W.H., MRI measurement of regional lung deposition in mice exposed nose-only to nebulized superparamagnetic iron oxide nanoparticles, Journal of aerosol medicine and pulmonary drug delivery, 21 (2008) 335–342.

Massaro D., Massaro G.D., Clerch L.B., Noninvasive delivery of small inhibitory RNA and other reagents to pulmonary alveoli in mice, American Journal of Physiology-Lung Cellular and Molecular Physiology, 287 (2004) L1066–L1070.

Mastrandrea L.D., Quattrin T., Clinical evaluation of inhaled insulin, Advanced drug delivery reviews, 58 (2006) 1061–1075.

Maxfield F.R., Mcgraw T.E., Endocytic recycling, Nature reviews Molecular cell biology, 5 (2004) 121–132.

Mellnik J., Vasquez P.A., Mckinley S.A., Witten J., Hill D.B., Forest M.G., Micro-heterogeneity metrics for diffusion in soft matter, Soft matter, 10 (2014) 7781–7796.

Merkel O.M., Beyerle A., Librizzi D., Pfestroff A., Behr T.M., Sproat B., Barth P.J., Kissel T., Nonviral siRNA delivery to the lung: Investigation of PEG-PEI polyplexes and their *in vivo* performance, Molecular pharmaceutics, 6 (2009) 1246–1260.

Merkel O.M., Rubinstein I., Kissel T., SiRNA delivery to the lung: What's new?, Adv Drug Deliv Rev, 75 (2014) 112–128.

Merkel O.M., Zheng M., Debus H., Kissel T., Pulmonary gene delivery using polymeric nonviral vectors, Bioconjug Chem, 23 (2012) 3–20.

Merkus H.G., Particle size measurements: Fundamentals, practice, quality, Springer Science & Business Media, 2009.

Minne A., Louahed J., Mehauden S., Baras B., Renauld J.C., Vanbever R., The delivery site of a monovalent influenza vaccine within the respiratory tract impacts on the immune response, Immunology, 122 (2007) 316–325.

Mitchell J.P., Nagel M.W., Cascade impactors for the size characterization of aerosols from medical inhalers: Their uses and limitations, Journal of Aerosol Medicine-Deposition Clearance and Effects in the Lung, 16 (2003) 341–+.

Mitchell J.P., Nagel M.W., Doyle C.C., Ali R.S., Avvakoumova V.I., Christopher J.D., Quiroz J., Strickland H., Tougas T., Lyapustina S., Relative precision of inhaler aerodynamic particle size distribution (APSD) metrics by full resolution and abbreviated andersen cascade impactors (ACIs): Part 1, Aaps Pharmscitech, 11 (2010) 843–851.

Morello M., Krone C.L., Dickerson S., Howerth E., Germishuizen W.A., Wong Y.-L., Edwards D., Bloom B.R., Hondalus M.K., Dry-powder pulmonary insufflation in the mouse for application to vaccine or drug studies, Tuberculosis, 89 (2009) 371–377.

Morén F., Aerosols in medicine: Principles, diagnosis, and therapy, Elsevier Science Limited, 1993.

Morita T., Niwata Y., Ohgi K., Ogawa M., Irie M., Distribution of two urinary ribonuclease-like enzymes in human organs and body fluids, J Biochem, 99 (1986) 17–25.

Mosbah K., Ruiz-Cabello J., Berthezene Y., Cremillieux Y., Aerosols and gaseous contrast agents for magnetic resonance imaging of the lung, Contrast media & molecular imaging, 3 (2008) 173–190.

Moschos S.A., Jones S.W., Perry M.M., Williams A.E., Erjefalt J.S., Turner J.J., Barnes P.J., Sproat B.S., Gait M.J., Lindsay M.A., Lung delivery studies using siRNA conjugated to TAT (48–60) and penetratin reveal peptide induced reduction in gene expression and induction of innate immunity, Bioconjugate chemistry, 18 (2007) 1450–1459.

Mühlfeld C., Rothen-Rutishauser B., Blank F., Vanhecke D., Ochs M., Gehr P., Interactions of nanoparticles with pulmonary structures and cellular responses, American Journal of Physiology-Lung Cellular and Molecular Physiology, 294 (2008) L817–L829.

Murata M., Tahara K., Takeuchi H., Real-time *in vivo* imaging of surface-modified liposomes to evaluate their behavior after pulmonary administration, European Journal of Pharmaceutics and Biopharmaceutics, 86 (2014) 115–119.

Murata N., Takashima Y., Toyoshima K., Yamamoto M., Okada H., Anti-tumor effects of anti-VEGF siRNA encapsulated with PLGA microspheres in mice, Journal of Controlled Release, 126 (2008) 246–254.

Nahar K., Gupta N., Gauvin R., Absar S., Patel B., Gupta V., Khademhosseini A., Ahsan F., *In vitro*, *in vivo* and *ex vivo* models for studying particle deposition and drug absorption of inhaled pharmaceuticals, Eur J Pharm Sci, 49 (2013) 805–818.

Najlah M., Parveen I., Alhnan M.A., Ahmed W., Faheem A., Phoenix D.A., Taylor K.M., Elhissi A., The effects of suspension particle size on the performance of air-jet, ultrasonic and vibrating-mesh nebulisers, Int J Pharm, 461 (2014) 234–241.

Newman S., Wilding I., Gamma scintigraphy: An *in vivo* technique for assessing the equivalence of inhaled products, International journal of pharmaceutics, 170 (1998) 1–9.

Newman S.P., Pitcairn G.R., Hirst P.H., A brief history of gamma scintigraphy, Journal of Aerosol Medicine, 14 (2001) 139–145.

Newman S.P., Pitcairn G.R., Hirst P.H., Rankin L., Radionuclide imaging technologies and their use in evaluating asthma drug deposition in the lungs, Advanced drug delivery reviews, 55 (2003) 851–867.

Newman S.P., Wilding I.R., Imaging techniques for assessing drug delivery in man, Pharmaceutical science & technology today, 2 (1999) 181–189.

Newman S.P., Wilding I.R., Hirst P.H., Human lung deposition data: The bridge between *in vitro* and clinical evaluations for inhaled drug products?, International journal of pharmaceutics, 208 (2000) 49–60.

Nichols S.C., Mitchell J.P., Shelton C.M., Roberts D.L., Good cascade impactor practice (GCIP) and considerations for "in-use" specifications, Aaps Pharmscitech, 14 (2013) 375–390.

Nielsen E.J., Nielsen J.M., Becker D., Karlas A., Prakash H., Glud S.Z., Merrison J., Besenbacher F., Meyer T.F., Kjems J., Howard K.A., Pulmonary gene silencing in transgenic EGFP mice using aerosolised chitosan/siRNA nanoparticles, Pharm Res, 27 (2010) 2520–2527.

Ntziachristos V., Culver J.P., Rice B.W., Small-animal optical imaging, Journal of biomedical optics, 13 (2008) 011001-011001-011001.

O'shaughnessy P.T., Achutan C., O'neill M.E., Thorne P.S., A small whole-body exposure chamber for laboratory use, Inhalation toxicology, 15 (2003) 251–263.

Oliveira S., Van Rooy I., Kranenburg O., Storm G., Schiffelers R.M., Fusogenic peptides enhance endosomal escape improving siRNA-induced silencing of oncogenes, International journal of pharmaceutics, 331 (2007) 211–214.

Padhi B.K., Chougule M.B., Misra A., Aerosol performance of large respirable particles of amikacin sulfate produced by spray and freeze drying techniques, Curr Drug Deliv, 6 (2009) 8–16.

Park C.-W., Rhee Y.-S., Vogt F.G., Hayes D., Zwischenberger J.B., Deluca P.P., Mansour H.M., Advances in microscopy and complementary imaging techniques to assess the fate of drugs *ex vivo* in respiratory drug delivery: An invited paper, Advanced drug delivery reviews, 64 (2012) 344–356.

Parton R.G., Richards A.A., Lipid rafts and caveolae as portals for endocytosis: New insights and common mechanisms, Traffic, 4 (2003) 724–738.

Patel B., Gupta N., Ahsan F., Particle engineering to enhance or lessen particle uptake by alveolar macrophages and to influence the therapeutic outcome, European Journal of Pharmaceutics and Biopharmaceutics, 89 (2015) 163–174.

Patel G., Chougule M., Singh M., Misra A., Nanoliposomal dry powder formulations, Methods in enzymology, 464 (2009) 167–191.

Patton J.S., Mechanisms of macromolecule absorption by the lungs, Advanced Drug Delivery Reviews, 19 (1996) 3–36.

Patton J.S., Brain J.D., Davies L.A., Fiegel J., Gumbleton M., Kim K.J., Sakagami M., Vanbever R., Ehrhardt C., The particle has landed-characterizing the fate of inhaled pharmaceuticals, J Aerosol Med Pulm Drug Deliv, 23 Suppl 2 (2010) S71–87.

Perl M., Chung C.-S., Lomas-Neira J., Rachel T.-M., Biffl W.L., Cioffi W.G., Ayala A., Silencing of Fas, but not caspase-8, in lung epithelial cells ameliorates pulmonary apoptosis, inflammation, and neutrophil influx after hemorrhagic shock and sepsis, The American journal of pathology, 167 (2005) 1545–1559.

Perring S., Summers Q., Fleming J., Nassim M., Holgate S., A new method of quantification of the pulmonary regional distribution of aerosols using combined CT and SPECT and its application to nedocromil sodium administered by metered dose inhaler, The British journal of radiology, 67 (1994) 46–53.

Pettis R.J., Hall I., Costa D., Hickey A.J., Aerosol delivery of muramyl dipeptide to rodent lungs, AAPS PharmSci, 2 (2000) 53–61.

Phelps M.E., Positron emission tomography provides molecular imaging of biological processes, Proceedings of the National Academy of Sciences, 97 (2000) 9226–9233.

Possmayer F., Nag K., Rodriguez K., Qanbar R., Schürch S., Surface activity *in vitro*: Role of surfactant proteins, Comparative Biochemistry and Physiology Part A: Molecular & Integrative Physiology, 129 (2001) 209–220.

Rawat A., Majumder Q.H., Ahsan F., Inhalable large porous microspheres of low molecular weight heparin: *In vitro* and *in vivo* evaluation, Journal of Controlled Release, 128 (2008) 224–232.

Reischl D., Zimmer A., Drug delivery of siRNA therapeutics: Potentials and limits of nanosystems, Nanomedicine: Nanotechnology, Biology and Medicine, 5 (2009) 8–20.

Rosas-Taraco A.G., Higgins D.M., Sánchez-Campillo J., Lee E.J., Orme I.M., González-Juarrero M., Intrapulmonary delivery of XCL1-targeting small interfering RNA in mice chronically infected with mycobacterium tuberculosis, American journal of respiratory cell and molecular biology, 41 (2009) 136–145.

Rose M.C., Nickola T.J., Voynow J.A., Airway mucus obstruction: Mucin glycoproteins, MUC gene regulation and goblet cell hyperplasia, American Journal of Respiratory Cell and Molecular Biology, 25 (2001) 533–537.

Ross D.L., Schultz R.K., Effect of inhalation flow rate on the dosing characteristics of dry powder inhaler (DPI) and metered dose inhaler (MDI) products, Journal of aerosol medicine, 9 (1996) 215–226.

Roy I., Vij N., Nanodelivery in airway diseases: Challenges and therapeutic applications, Nanomedicine, 6 (2010) 237–244.

Rubin B.K., Physiology of airway mucus clearance, Respir Care, 47 (2002) 761–768.

Rytting E., Nguyen J., Wang X., Kissel T., Biodegradable polymeric nanocarriers for pulmonary drug delivery, Expert Opin Drug Deliv, 5 (2008) 629–639.

Saha G.B., Macintyre W.J., Go R.T., Cyclotrons and positron emission tomography radiopharmaceuticals for clinical imaging, Seminars in nuclear medicine, Elsevier, 1992.

Sakagami M., *In vivo*, *in vitro* and *ex vivo* models to assess pulmonary absorption and disposition of inhaled therapeutics for systemic delivery, Advanced drug delivery reviews, 58 (2006) 1030–1060.

Sanders N., Rudolph C., Braeckmans K., De Smedt S.C., Demeester J., Extracellular barriers in respiratory gene therapy, Advanced drug delivery reviews, 61 (2009) 115–127.

Schuster B.S., Suk J.S., Woodworth G.F., Hanes J., Nanoparticle diffusion in respiratory mucus from humans without lung disease, Biomaterials, 34 (2013) 3439–3446.

Seaton B.A., Crouch E.C., Mccormack F.X., Head J.F., Hartshorn K.L., Mendelsohn R., Structural determinants of pattern recognition by lung collectins, Innate Immunity (2010).

Senoo T., Hattori N., Tanimoto T., Furonaka M., Ishikawa N., Fujitaka K., Haruta Y., Murai H., Yokoyama A., Kohno N., Suppression of plasminogen activator inhibitor-1 by RNA interference attenuates pulmonary fibrosis, Thorax, 65 (2010) 334–340.

Seow W.Y., Liang K., Kurisawa M., Hauser C.A., Oxidation as a facile strategy to reduce the surface charge and toxicity of polyethyleneimine gene carriers, Biomacromolecules, 14 (2013) 2340–2346.

Shah V.P., Smurthwaite M.J., Veranth J.M., Zaidi K., The inhalation ad hoc advisory panel for the USP performance tests of inhalation dosage forms (2008).

Sharma K., Somavarapu S., Colombani A., Govind N., Taylor K.M., Nebulised siRNA encapsulated crosslinked chitosan nanoparticles for pulmonary delivery, Int J Pharm, 455 (2013) 241–247.

Sharma K., Somavarapu S., Colombani A., Govind N., Taylor K.M.G., Crosslinked chitosan nanoparticle formulations for delivery from pressurized metered dose inhalers, European Journal of Pharmaceutics and Biopharmaceutics, 81 (2012) 74–81.

Shoyele S.A., Slowey A., Prospects of formulating proteins/peptides as aerosols for pulmonary drug delivery, International journal of pharmaceutics, 314 (2006) 1–8.

Sinsuebpol C., Chatchawalsaisin J., Kulvanich P., Preparation and *in vivo* absorption evaluation of spray dried powders containing salmon calcitonin loaded chitosan nanoparticles for pulmonary delivery, Drug Design, Development and Therapy, 7 (2013) 861–873.

Snell N., Ganderton D., Assessing lung deposition of inhaled medications: Consensus statement from a workshop of the British Association for Lung Research, held at the Institute of Biology, London, U.K. on 17 April 1998, Respiratory medicine, 93 (1999) 123–133.

Son Y.J., Mcconville J.T., Development of a standardized dissolution test method for inhaled pharmaceutical formulations, Int J Pharm, 382 (2009) 15–22.

Sood B.G., Shen Y., Latif Z., Chen X., Sharp J., Neelavalli J., Joshi A., Slovis T.L., Haacke E., Aerosol delivery in ventilated newborn pigs: An MRI evaluation, Pediatric research, 64 (2008) 159–164.

Sood B.G., Shen Y., Latif Z., Galli B., Dawe E.J., Haacke E.M., Effective aerosol delivery during high-frequency ventilation in neonatal pigs, Respirology, 15 (2010) 551–555.

Sorrentino S., Human extracellular ribonucleases: Multiplicity, molecular diversity and catalytic properties of the major RNase types, Cell Mol Life Sci, 54 (1998) 785–794.

Taratula O., Dmochowski I.J., Functionalized ^{129}Xe contrast agents for magnetic resonance imaging, Current opinion in chemical biology, 14 (2010) 97–104.

Taylor K.M., Mccallion O.N., Ultrasonic nebulisers for pulmonary drug delivery, International journal of pharmaceutics, 153 (1997) 93–104.

Thomas C.E., Ehrhardt A., Kay M.A., Progress and problems with the use of viral vectors for gene therapy, Nature Reviews Genetics, 4 (2003) 346–358.

Thompson R.B., Finlay W.H., Using MRI to measure aerosol deposition, Journal of aerosol medicine and pulmonary drug delivery, 25 (2012) 55–62.

Tompkins S.M., Lo C.-Y., Tumpey T.M., Epstein S.L., Protection against lethal influenza virus challenge by RNA interference *in vivo*, Proceedings of the National Academy of Sciences of the United States of America, 101 (2004) 8682–8686.

Tronde A., Baran G., Eirefelt S., Lennernäs H., Bengtsson U.H., Miniaturized nebulization catheters: A new approach for delivery of defined aerosol doses to the rat lung, Journal of aerosol medicine, 15 (2002) 283–296.

Turner P.V., Brabb T., Pekow C., Vasbinder M.A., Administration of substances to laboratory animals: Routes of administration and factors to consider, Journal of the American Association for Laboratory Animal Science: JAALAS, 50 (2011) 600–613.

Wagner A., Vorauer-Uhl K., Katinger H., Nebulization of liposomal rh-Cu/Zn-SOD with a novel vibrating membrane nebulizer, Journal of liposome research, 16 (2006) 113–125.

Waldrep J., Dhand R., Advanced nebulizer designs employing vibrating mesh/aperture plate technologies for aerosol generation, Current Drug Delivery, 5 (2008) 114–119.

Wang H., Sebrié C., Ruaud J.P., Guillot G., Bouazizi-Verdier K., Willoquet G., Maître X., Darrasse L., De Rochefort L., Aerosol deposition in the lungs of spontaneously breathing rats using Gd-DOTA-based contrast agents and ultra-short echo time MRI at 1.5 tesla, Magnetic Resonance in Medicine, (2015).

Wang J.-C., Lai S., Guo X., Zhang X., De Crombrugghe B., Sonnylal S., Arnett F.C., Zhou X., Attenuation of fibrosis *in vitro* and *in vivo* with SPARC siRNA, Arthritis research & therapy, 12 (2010) R60.

Watts A.B., Mcconville J.T., Williams Iii R.O., Current therapies and technological advances in aqueous aerosol drug delivery, Drug development and industrial pharmacy, 34 (2008) 913–922.

Weinberger B., Sinko P.J., Laskin J.D., Laskin D.L., Interaction with lung macrophages, Nanoparticles in the Lung: Environmental Exposure and Drug Delivery, (2014) 85.

Xenariou S., Griesenbach U., Ferrari S., Dean P., Scheule R., Cheng S., Geddes D., Plank C., Alton E., Using magnetic forces to enhance non-viral gene transfer to airway epithelium *in vivo*, Gene therapy, 13 (2006) 1545–1552.

Xenariou S., Griesenbach U., Liang H., Zhu J., Farley R., Somerton L., Singh C., Jeffery P., Ferrari S., Scheule R., Use of ultrasound to enhance nonviral lung gene transfer *in vivo*, Gene therapy, 14 (2007) 768–774.

Yacobi N.R., Malmstadt N., Fazlollahi F., Demaio L., Marchelletta R., Hamm-Alvarez S.F., Borok Z., Kim K.-J.,

Crandall E.D., Mechanisms of alveolar epithelial translocation of a defined population of nanoparticles, American journal of respiratory cell and molecular biology, 42 (2010) 604–614.

Yang W., Peters J.I., Williams R.O., 3rd, Inhaled nanoparticles—a current review, Int J Pharm, 356 (2008) 239–247.

Yi D., Price A., Panoskaltsis-Mortari A., Naqwi A., Wiedmann T.S., Measurement of the distribution of aerosols among mouse lobes by fluorescent imaging, Analytical biochemistry, 403 (2010) 88–93.

Yoon S.H., Goo J.M., Lee S.M., Park C.M., Seo H.J., Cheon G.J., Positron emission tomography/magnetic resonance imaging evaluation of lung cancer: Current status and future prospects, Journal of thoracic imaging, 29 (2014) 4–16.

Yoshiyama Y., Yazaki T., Arai M., Asai K., Kanke M., The nebulization of budesonide suspensions by a newly designed mesh nebulizer, Respiratory drug delivery VIII. Raleigh: Davis Horwood, (2002) 487–489.

Zamora-Avila D., Zapata-Benavides P., Franco-Molina M., Saavedra-Alonso S., Trejo-Avila L., Resendez-Perez D., Mendez-Vazquez J., Isaias-Badillo J., Rodriguez-Padilla C., WT1 gene silencing by aerosol delivery of PEI–RNAi complexes inhibits B16-F10 lung metastases growth, Cancer gene therapy, 16 (2009) 892–899.

Zamora M.R., Budev M., Rolfe M., Gottlieb J., Humar A., Devincenzo J., Vaishnaw A., Cehelsky J., Albert G., Nochur S., Gollob J.A., Glanville A.R., RNA interference therapy in lung transplant patients infected with respiratory syncytial virus, Am J Respir Crit Care Med, 183 (2011) 531–538.

Zhang J., Wu L., Chan H.-K., Watanabe W., Formation, characterization, and fate of inhaled drug nanoparticles, Advanced drug delivery reviews, 63 (2011) 441–455.

Zhang X., Shan P., Jiang D., Noble P.W., Abraham N.G., Kappas A., Lee P.J., Small interfering RNA targeting heme oxygenase-1 enhances ischemia-reperfusion-induced lung apoptosis, Journal of Biological Chemistry, 279 (2004) 10677–10684.

Zhao F., Zhao Y., Liu Y., Chang X., Chen C., Zhao Y., Cellular uptake, intracellular trafficking, and cytotoxicity of nanomaterials, Small, 7 (2011) 1322–1337.

Author's short biography

Susanne R. Youngren-Ortiz

Susanne R. Youngren-Ortiz is a Ph.D. candidate the Daniel K. Inouye College of Pharmacy of the University of Hawai'i at Hilo. She obtained her Bachelor of Science Degree in Pharmaceutical Sciences with specialization in Industrial and Physical Pharmacy and minors in Chemistry and Statistics from Purdue University. Her dissertation research project investigates the optimal delivery and the evaluation of cellular effects of therapeutic nanocarriers for the treatment of asthma. She has authored original research and review articles. She is an active member of the American Association of Pharmaceutical Scientists and has chaired the University of Hawaii Student Chapter.

Nishant S. Gandhi

Nishant S. Gandhi is a Ph.D. candidate at the Daniel K. Inouye College of Pharmacy UH Hilo. He has completed his B.Pharm and M.Pharm from University of Pune in India. He has also worked as a chemist at Aristo Pharmaceuticals in Bhopal, India. He is currently working on developing novel nanotechnology based drug delivery systems for the treatment of lung cancer. He has authored publications including original research articles, review articles and book chapters. He is currently serving as chair of American Association of Pharmaceutical Scientists (DKICP chapter) and is currently a member of professional pharmacy fraternity "Phi Delta Chi".

Laura España-Serrano

Dr. Laura España-Serrano is a research associate in the Translational Drug Delivery Research laboratory in the department of Pharmaceutical Sciences of the Daniel K. Inouye College of Pharmacy at the UH Hilo. She obtained her PhD in Biochemistry and Molecular Biology from the *Complutense* University of Madrid, Spain. She has nine years of experience in the fields of Cellular and Molecular Biology of Cancer and Psychiatric diseases. She has authored original research publications and review articles, and she is a member of the National Postdoctoral Association and the American Association of Pharmaceutical Scientists.

Mahavir B. Chougule

Mahavir B. Chougule, Associate Professor of the Department of Pharmaceutical Sciences, investigates the use of therapeutic agent, siRNA, and targeted nanotechnology based formulations for treatment of lung cancer and asthma. Chougule has 25 publications, 8 patents, 3 review articles, and 5 book chapters. He delivered 16 invited talks and 63 scientific presentations at the international conferences. He served as a grant reviewer on the NIH, DOD, and international review panels. He is also serving as a member of editorial board on 5 international journals. Dr. Chougule is a recipient of several awards including recent American Association of Cancer Research Minority-Serving Institution Faculty Scholar in Cancer Research Award. He is an active member of American Association of Cancer Research and American Association of Pharmaceutical Scientists.

KONA Powder and Particle Journal No. 33 (2016) 86–108/Doi:10.14356/kona.2016017 Review Paper

Effect of Process Conditions on Fluidization †

Paola Lettieri * and Domenico Macrì

[1] *Department of Chemical Engineering, University College London, UK*

Abstract

The influence of process conditions such as temperature and the presence of fines on the fluidization behaviour of gas-fluidized beds is of major importance in industrial fluid bed processes, which are often operated at temperatures well above ambient and where it is common practice to add fine particles to improve the reactor performance. Several works have demonstrated that process conditions can influence the role of the interparticle forces in the fluidization behaviour of powders. In particular, the beneficial effect on fluidization of adding fines to the bulk of the material is well known.

The objective of this paper is to review experimental and theoretical studies of gas-solids fluidized beds operated at high temperature and the effect of fines and fines distribution within the bed. The survey begins with a review of the effect of temperature on fundamental fluidization parameters such as minimum fluidization, bed expansion and deaeration, and the role of hydrodynamic and interparticle forces at ambient conditions and high temperature is discussed. The effect of temperature and fines and fines size distribution on the dynamics of gas-fluidized beds is considered next, highlighting areas of current gaps in knowledge. Given the complexity of the phenomena involved, a direct quantification of the particle-particle interactions in fluidized beds and of their changes under process conditions is very difficult. The review concludes by touching upon powder rheology as a methodology to evaluate indirectly the effects of the IPFs on fluidization. This leads to a review of the work done at UCL on linking rheological measurements to fluidization tests in the attempt to quantify the effect of process conditions, i.e. high temperature and the effect of fines on fluidization.

Keywords: fluidization, high temperature, fines particle fraction, powder rheology

1. Introduction

Fluidization is the operation by which solid particles are transformed into a fluid-like state through suspension in a gas or liquid (Kunii and Levenspiel, 1991). Fluidized beds can be considered the most powerful method to handle a variety of solid particulate materials in industry (Horio, 2013).

Fluidized beds are widely applied in industry for their ability to provide a high heat transfer rate and rapid solids mixing which lead to isothermal conditions in the particle bed, and high heat and mass transfer rates between gas and particles. Whenever a chemical reaction employing a particulate solid as a reactant or as a catalyst requires reliable temperature control, a fluidized bed reactor is often the choice for ensuring nearly isothermal conditions by suitable selection of the operating conditions.

Fluidization was created as an industrial operation in the Winkler process for the gasification of lignite and the Ignifluid process for the combustion of coal, but it was only with introduction in the 1940s of the FCC process that its true potential became apparent.

It was in 1942 when a desperate need for aviation fuel during the Second World War brought together a group of oil companies which included Standard Oil Indiana (later Amoco and now BP Amoco), M.W. Kellogg, Shell and the Standard Oil Development Company (now Exxon) to design the first fluidized solids process for catalytic cracking. Fluidization started as an innovative and successful oil refining technology, revealing the potential of the technique for gas-solids reaction engineering. Since then it has been applied in many other areas, becoming a firmly established technique in the processing industries. The applications are spread throughout the chemicals, environmental, energy, nuclear, petrochemical, pharmaceuticals, and process industries. Some examples of industrial applications are presented in **Table 1**.

In addition to this, fluidized bed technology has witnessed a resurgence of interest particularly from the point of view of clean energy generation over the last two decades. Fluidized beds are employed for the combustion and gasification of solid fuels (coal, wastes and biomass),

† Received 8 June 2015; Accepted 4 August 2015
J-STAGE Advance Published date: 10 October 2015
[1] Torrington Place, London WC1E 7JE, UK
* Corresponding author: Paola Lettieri;
E-mail: p.lettieri@ucl.ac.uk
TEL: +44 20 7679-7867 FAX: +44-20-7679-7092

Table 1 Some industrial applications of fluidized beds

Process	Example	Process conditions		
		T [°C]	*P* [atm]	Fines Content [%]
Cracking of hydrocarbons	FCC[a]	480–550	1–3	10–30
	Ethylene and propylene[b]	750	~1	10–30
Chemical synthesis	Acrylonitrile[b]	400–500	1.5–3	20–40
	Melamine[a]	400	> 1	—
	Maleic anhydride (Mitsubishi Chem. Ind.)[c]	410–420	1–5	25–55
	Maleic anhydride (DuPont)[c]	360–420	< 5	—
	Ethylene dichloride[c]	220–245	2.5–6	30
	Phthalic anhydride[c]	345–385	2.7	28
	Polyethylene[c]	75–105	20–25	—
Metallurgical industry	Iron[a]	850	3.5	—
	AlF_3 synthesis[c]	530	1	—
	Alumina calcination[c,d]	800–1200	1	0–50
	Limestone calcination[d]	770	1	Variable
	Gold roasting[c]	650	1	—
	SO_2 from sulphide ore roasting[b]	650–700	1	—
	Pyrite roasting[b]	660–920	1	—
	FeS_2 from sulphide ore roasting[d]	650–1100	1	< 3
Drying of solids	Inorganic materials[d]	60–110	1	Variable
	Pharmaceuticals[d]	60	1	Variable
Semiconductor industry	$SiHCl_3$ production[b,d]	300	1	100
	Silicon production[c]	600–800	~1	—
Nuclear industry	Separation of U-235 from U-238[b]	450	—	—

[a] Winter and Schratzer (2013)
[b] Kunii and Levenspiel (1991)
[c] Jazayeri (2003)
[d] Bruni (2005)

to generate steam for boilers, syngas, chemicals or fuels (Newby, 2003; Arena, 2013; Basu, 2013), including the recent development of a dual-stage fluid-bed plasma gasification process in UK for the production of electricity and biosubstitute natural gas from waste gasification (Materazzi et al., 2013, 2015); fluidized beds are also employed in the waste incineration of solids and sludge (Horio, 2013). Another development gaining prominence in this area and aimed at new processes for clean energy production is the use of fluidized beds for chemical looping combustion, Fan (2010). A review of fluid bed industrial applications can be found in Kunii and Levenspiel, 1991; Jazayeri, 2003; Winter and Schratzer, 2013.

In parallel with industrial developments, fluidization also became the focus of a great deal of academic effort aimed at providing a theoretical framework to underpin the subject.

The first examples are the pioneering study of bubble motion in fluidized beds by Davidson (1961), later developed by Davidson and Harrison (1963), Jackson (1963) and Murray (1965), and Geldart's empirical classification (Geldart, 1973) of fluidizable powders into four groups, A, B, C and D, according to their particle size and density and gas density (see Yates, 1996).

It is important to note that both bubble motion theories and Geldart's classification are based on observations made under ambient conditions, hence it is not immediately obvious how accurate their predictions would be under process conditions such as high temperature and pressure.

For these reasons, fluid beds are commonly used when high thermal efficiency, excellent temperature control and

intimate gas-solids contact are desired. Despite this, the effects of process conditions on fluidization are still not entirely understood. Design criteria and performance predictions for fluid bed units working at high temperature have been largely based on fluid-dynamic models and correlations established from tests developed at ambient temperature. However, extrapolating the results and relationships available at ambient conditions to elevated temperatures can lead to misleading predictions of the fluid bed performance at high temperature. Drastic changes can occur in the fluidization behaviour between low and high temperatures, due to possible modifications induced by the temperature in the structure of the fluidized bed. In order to understand the factors responsible for such changes in fluidization behaviour, the role of the interparticle forces (IPFs) and hydrodynamic forces (HDFs) has been studied, but much controversy still remains to define their relative importance.

This work reviews experimental and theoretical research on the effect of process conditions such as high temperature, fines content and fines size distribution on fluidization. The review will begin by considering the influence of temperature on fundamental parameters of gas-solids fluidization such as minimum fluidization, bed expansion, bed voidage and deaeration rates.

The review will then address the effect of fines and fines size distribution on the dynamics of gas-fluidized beds. This will lead to a review of the main techniques used for the characterization and prediction of the flow properties of powders. These include the standard bed collapse test and rheological tests. The latter covering both stationary measurements (angle of repose, Hausner ratio, etc.) as well as dynamic tests (shear-cell-type tests and viscometer-type tests). The paper will conclude by reviewing the work done at the University College London on linking rheological measurements to fluidization tests, in the attempt to quantify the role of the interparticle forces on the fluidization behaviour of different industrial powders.

2. Effect of temperature on minimum fluidization conditions

Although several studies have been carried out on the influence of operating conditions on fluidization, the findings are still controversial and a satisfactory understanding of the phenomena which cause differences between ambient conditions and high temperature processes has not yet been achieved (Grewal and Gupta, 1989; Geldart, 1990; Fletcher et al., 1992; Knowlton, 1992; Yates, 1996; Lettieri et al., 2000, 2001, 2002; Coltters and Rivas, 2004).

The operating conditions influence the operation of fluid-particle systems because they affect gas density and viscosity. Increasing temperature causes the gas density to decrease and gas viscosity to increase. Most predictions of fluidization behaviour at high temperatures have been based solely on considering such changes in the gas properties. However, this approach is valid under the condition that only hydrodynamic forces control the fluidization behaviour. Temperature can have a considerable effect on particle adhesion, enhancing the role of the interparticle forces (IPFs) on the fluidization quality, if the system is operated at temperatures close to the minimum sintering temperature of the particles. In addition, the increase of temperature may enhance the Hamaker constant and therefore the van der Waals' attractive forces.

As reported by Lettieri et al. (2000), the effect of temperature on a fluidized bed is also strongly dependent on the particle size, which in turn defines the type of particle-particle and fluid-particle interaction, thus determining the stronger or weaker role of the IPFs. Much theoretical debate is reported in the literature on the role of the interparticle forces on the fluid-bed behaviour and a sound understanding of the phenomena which control changes in fluidization behaviour at high temperature has not yet been achieved.

In this section we report some of the most significant findings of the effect of temperature on the fluid-bed behaviour, outlining some of the most important aspects.

The minimum fluidization velocity, u_{mf}, is a fundamental parameter when designing fluidized-bed systems. The minimum fluidization velocity may be found by measuring the pressure drop across a bed of particles as a function of the gas velocity. At u_{mf}, the weight of the bed is fully supported by the flow and the pressure drop becomes constant. u_{mf} may also be calculated on the basis of the Ergun equation for the pressure drop through a packed bed.

Various correlations can be found in the literature to predict u_{mf} at high temperature (see **Table 2**), as for example the correlation given by Wu and Baeyens (1991). However, this approach is uncertain and not necessarily reliable, because it is often necessary to extrapolate results for the conditions of interest and, in addition, it overlooks possible changes induced by temperature on the structure of the fluidized bed that can in turn cause drastic alterations in the flow behaviour and powder stability (Yang et al., 1985; Lettieri et al., 2000).

Despite this, the Ergun equation (Eqn. 1) is one of the most frequently equations used in order to evaluate the effect of temperature on minimum fluidization conditions. Although the unknown voidage at minimum conditions may be a problem in applying this equation, numerous predictive correlations for u_{mf} are based on a modified Ergun equation, as developed by Wen and Yu (1966). Eqn. 1 can be rewritten using Archimedes dimensionless

Table 2 Selected equations for the calculation of minimum fluidization velocity

Authors	Equation	
Ergun (1952)	$150\frac{\mu_g u_{mf}}{(\phi d_p)^2}\frac{(1-\varepsilon_{mf})}{\varepsilon_{mf}^3}+1.75\frac{\rho_g u_{mf}^2}{\phi d_p}\frac{1}{\varepsilon_{mf}^3}=g(\rho_p-\rho_g)$	(1)
Carman (1937)	$u_{mf}=\frac{(\phi d_p)^2}{180}\frac{(\rho_p-\rho_g)}{\mu_g}g\left(\frac{\varepsilon_{mf}^3}{1-\varepsilon_{mf}}\right)$	(2)
Miller and Logwinuk (1951)	$u_{mf}=\frac{1.25\times10^{-3}d_p^2(\rho_p-\rho_g)^{0.9}\rho_g^{0.1}g}{\mu_g}$	(3)
Leva et al. (1956)	$u_{mf}=\frac{7.39\,d_p^{1.82}(\rho_p-\rho_g)^{0.94}}{\rho_g^{0.06}}$	(4)
Goroshko et al. (1958)	$u_{mf}=\frac{\mu_g}{\rho_g d_p}\left(\frac{Ar}{1400+5.2\sqrt{Ar}}\right)$	(5)
Leva (1959)	$u_{mf}=\frac{8.1\times10^{-3}d_p^2(\rho_p-\rho_g)g}{\mu_g}$	(6)
Broadhurst and Becker (1975)	$u_{mf}=\frac{\mu_g}{\rho_g d_p}\left(\frac{Ar}{2.42\times10^5 Ar^{0.85}\left(\frac{\rho_p}{\rho_g}\right)^{0.13}+37.7}\right)^{0.5}$	(7)
Riba et al. (1978)	$u_{mf}=\frac{\mu_g}{\rho_g d_p}\left(1.54\times10^{-2}\left(\frac{d_p^3\rho_g^2 g}{\mu_g^2}\right)^{0.66}\left(\frac{\rho_p-\rho_g}{\rho_g}\right)^{0.7}\right)$	(8)
Doichev and Akhmakov (1979)	$u_{mf}=\frac{\mu_g}{\rho_g d_p}(1.08\times10^{-3}Ar^{0.947})$	(9)
Wu and Baeyens (1991)	$u_{mf}=\frac{\mu_g}{\rho_g d_p}(7.33\times10^{-5}\times10^{\sqrt{8.24\log_{10}Ar-8.81}})$	(10)

number (Ar) and Reynolds number at minimum fluidization conditions as follows:

$$Ar=150\frac{(1-\varepsilon_{mf})}{\phi^2\varepsilon_{mf}^3}Re_{mf}+\frac{1.75}{\phi\varepsilon_{mf}^3}Re_{mf}^2 \tag{11}$$

Wen and Yu (1966) showed that the voidage and shape factor functions in both the viscous and inertial term of Eqn. 11 can be approximated as:

$$\frac{1-\varepsilon_{mf}}{\phi^2\varepsilon_{mf}^3}\approx 11 \tag{12}$$

$$\frac{1}{\phi\varepsilon_{mf}^3}\approx 14 \tag{13}$$

Leading to a modified form of Eqn. 11:

$$Ar=1650\,Re_{mf}+24.5\,Re_{mf}^2 \tag{14}$$

That can be rearranged to the general formulas:

$$Ar=A\,Re_{mf}+B\,Re_{mf}^2 \tag{15}$$

or

$$Re_{mf}=\sqrt{a^2+b(Ar)}-a \tag{16}$$

where $a=\frac{A}{2B}$ and $b=\frac{1}{B}$

Values reported in the literature for the constants a and b are listed in **Table 3**. However, predictions using Eqn. 14 do not take into account possible changes in the voidage which may occur with increasing temperature, as discussed later.

Pattipati and Wen (1981) reported that the Wen and Yu correlation is capable of predicting changes in u_{mf} when temperature increases for sand material. They did not observe important changes with temperature in the voidage at minimum fluidization and they found good matching between experimental and predicted u_{mf} values.

The effect of temperature on the minimum fluidization velocity has been reported by several other authors. At first, we review work that is specific to large particles falling within Geldart's Group B and D particles. Generally, the experimental findings confirmed the trend predicted by the Wen and Yu equation. Nevertheless,

Table 3 Values for the constants a and b in Eqn. 16.

Authors	$Re_{mf} = \sqrt{a^2 + b\,Ar} - a$	
	a	b
Wen and Yu (1966)	33.7	0.0408
Bourgeois and Grenier (1968)	25.46	0.03824
Saxena and Vogel (1977)	25.28	0.0571
Babu et al. (1978)	25.25	0.0651
Richardson and Jerónimo (1979)	25.7	0.0365
Grace and Hetsroni (1982)	27.2	0.0408
Chitester and Kornosky (1984)	28.7	0.0494
Thonglimp et al. (1984)	31.6	0.0425
Lucas and Arnaldos (1986)	25.2	0.0672
Bin (1993)	27.31	0.0386
Reina et al. (2000)	48	0.045

absolute values did not always match the experiments. Knowlton (1992) stated that one of the reasons lies in the evaluation of the correct mean particle size and shape factor. He suggested that this could be back-calculated from the Ergun equation using previously measured values of u_{mf}. Doing so, an effective value for the particle size and shape factor would be found.

Botterill et al. (1982) reported experimental verification of the temperature effect on u_{mf} for some Group B and D powders. They observed a decrease of u_{mf} with increasing temperature for Group B materials due to the consequent increase in gas viscosity. They compared their results with predictions from the Wen and Yu equation and noted that the decrease was less than that predicted since a change in ε_{mf} had occurred. This is not in agreement with the results of Pattipati and Wen (1981). For Group D powders, Botterill et al. (1982) observed an increase in u_{mf}, because of the decrease of gas density. They also found that ε_{mf} for the Group D materials did not change with temperature. Their experimental data matched predictions obtained from the Ergun equation, using the values of ε_{mf} measured at the corresponding operating temperatures, and using also an appropriate value of the shape factor, back-calculated from the Ergun equation for a given experiment (Lettieri, 1999).

Fletcher et al. (1992) reported that applying Eqn. 16 can introduce a significant error into the prediction of u_{mf}, mainly because the a and b constants are a function of the shape factor (ϕ) and voidage at minimum fluidization conditions, which are difficult to measure experimentally. They proposed different correlations for the prediction of Re_{mf} at ambient temperature on the basis of the shape of the particles, see **Table 4**.

A decade later, Coltters and Rivas (2004), proposed a

Table 4 Correlations for the prediction of Re_{mf} at ambient temperature (Fletcher et al., 1992).

Type of sands		
Round	$Re_{mf} = \dfrac{Ar}{1400+5\sqrt{Ar}}$ $(Ar \geq 1480)$	(17a)
	$Re_{mf} = \dfrac{Ar}{1400}$ $(Ar<1480)$	(17b)
Moderately sharp	$Re_{mf} = \dfrac{Ar}{1170+\sqrt{Ar}}$	(18)
Very angular, coked	$Re_{mf} = \dfrac{Ar}{790+7\sqrt{Ar}}$	(19)

new equation to estimate the minimum fluidization velocity without having to experimentally determine the bed voidage and shape factor:

$$u_{mf} = K\left[\frac{d_p^2(\rho_p - \rho_g)g}{\mu}\left(\frac{\rho_p}{\rho_g}\right)^{1.23}\right]^{\alpha} \tag{20}$$

where K and α are constants and are functions of the solids-gas system. They tested their correlation against 189 experiments reported in the literature on about 90 different materials, and their results showed good agreement with the experimental data. In parallel, Delebarre (2004), proposed the following revisited Wen and Yu equations for the prediction of u_{mf} without the dependency on the voidage and shape factor:

$$Ar = 24.5\,Re_{mf}^2 + 29400\,\varepsilon_{mf}^3(1-\varepsilon_{mf})\,Re_{mf} \tag{21}$$

The relative role of the hydrodynamic and interparticle forces on the minimum fluidization conditions at elevated temperature for Group A and C powders has been analysed by various authors. Lucas et al. (1986) reported that changes with temperature in ε_{mf} can be explained on a hydrodynamic basis, contrary to Raso et al. (1992) and Formisani et al. (1998) who later related such changes to a variation of IPFs with temperature.

Lucas et al. (1986) explained the variation of ε_{mf} with temperature in terms of a change in the flow pattern inside the bed. They analysed the variation of ε_{mf} as a function of Re_{mf} and observed that under flow regimes with Re_{mf}, less than 0.75, ε_{mf} remains constant while it decreases when this value is exceeded, becoming constant again at an Re_{mf} higher than 2. They explained that at low Re_{mf} a sucking effect is produced in the particle boundary layer which increases the closeness of the particles and causes ε_{mf} to decrease. At higher values of Re_{mf}, the attractive forces between the particles decrease and ε_{mf} gradually increases up to an approximately constant value. From this theory, a powder classification scheme based on the nature of the boundary layer around a parti-

cle was elaborated by Mathur and Saxena (1986), and validated with data on u_{mf} and ε_{mf} obtained by Botterill et al. (1982) and Lucas et al. (1986) at high temperatures.

In agreement with Raso et al. (1992), Yamazaki et al. (1995) reported that the role of the IPFs should not be ignored when trying to explain changes in ε_{mf} with temperature. They showed that variations in bed voidage depend both on the physical properties of the fluidizing fluid, i.e. density and viscosity, and on changes in the physicochemical properties of the particles. In particular, they studied the effect of water adsorbed onto the surface of silica particles with increasing temperature. At low temperatures, they observed a decrease in ε_{mf} as humidity increased, while at higher temperatures higher values of ε_{mf} were found for the same humidity. They explained such changes in terms of the amount of water adsorbed onto the surface of the silica, and concluded that variation of the ε_{mf} with temperature is caused by a change in the adhesion forces, which at velocities as low as u_{mf} can cause the formation of clusters, making the bed settle with a relatively looser structure.

Formisani et al. (1998) and Lettieri et al. (2000) also reported on the effect of temperature on minimum fluidization conditions, and they stated that the Ergun equation and Wen and Yu correlation are capable of predicting changes in the minimum fluidization velocity with temperature if, in addition to changes of gas density and viscosity, the dependence of ε_{mf} on temperature is also accounted for.

Formisani et al. (1998) observed a linear increase of ε_{mf} for various Group A, B and D powders and a linear increase of the voidage of the fixed bed with temperature (**Fig. 1–2**). Formisani et al. (1998) performed their experiments in a transparent quartz column equipped with a stainless steel porous plate able to provide a homogeneous gas distribution; a video camera was used to record the experiments. The total pressure drop across the particle bed was measured with a pressure tap located just above the gas distributor level; a graduated scale was used to determine the bed height at each temperature, and the average bed voidage was subsequently determined from the values of the bed height. The authors reported that bed height measurements were affected by a 0.5-mm approximation, which caused uncertainty in the bed voidage evaluations of around 1 %.

They attributed the increase of the fixed bed voidage to an increase of the interparticle forces which was thought to stabilize the structure of the fixed bed state, in the total absence of a gas flow. They found a close similarity between the slope of the fixed bed voidage and ε_{mf} and so they concluded that the increase of ε_{mf}, and in turn changes in u_{mf} with temperature, are not due only to changes in the properties of the fluidizing gas but also to changes in packing properties.

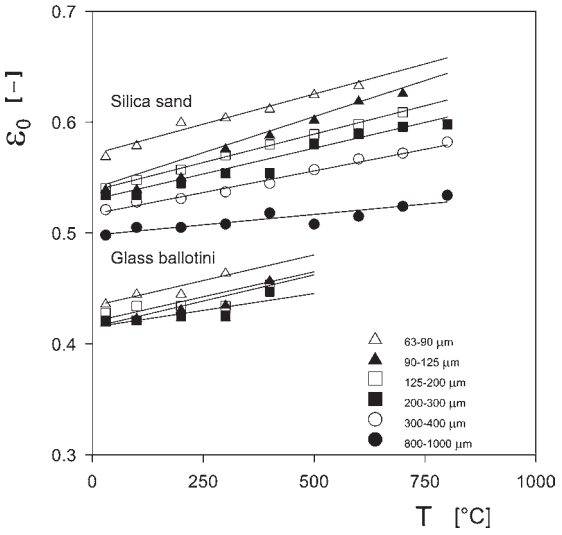

Fig. 1 Effect of temperature on the fixed bed voidage for glass ballotini and silica sand particles of different size. Reprinted with permission from Ref. (Formisani et al., 1998). Copyright: (1998) Elsevier Limited.

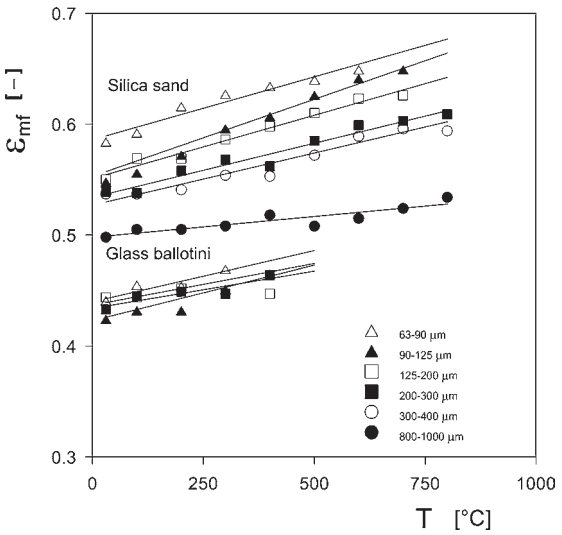

Fig. 2 Effect of temperature on the bed voidage at minimum fluidization for glass ballotini and silica sand particles of different size. Reprinted with permission from Ref. (Formisani et al., 1998). Copyright: (1998) Elsevier Limited.

They attributed the capability of the bed to form a looser structure to an increase of the Van der Waals' forces with temperature. The results of Formisani et al. (1998) confirmed findings reported by Raso et al. (1992) on a 2D fluidized-bed.

Lettieri et al. (2000, 2001) reported experimental observations on the effect of temperature on the fluidization of three fresh FCC catalysts and an equilibrium (E-cat) FCC tested at ambient pressure and at temperatures up to 650 °C. Where changes in fluidization at high temperature were observed, the factors responsible were investigated

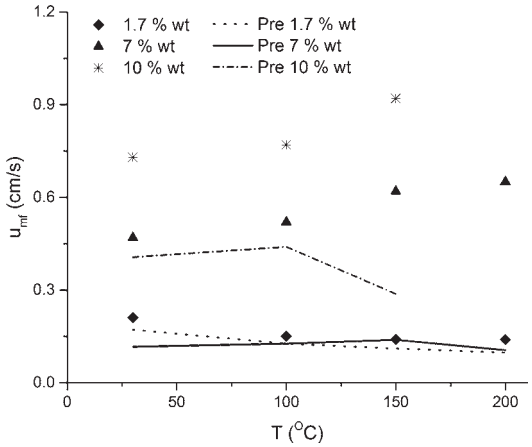

Fig. 3 u_{mf} vs temperature for a silica catalyst doped with increasing values of potassium acetate, comparison of experiment with prediction. Reprinted with permission from Ref. (Lettieri et al., 2000). Copyright: (2000) Elsevier Limited.

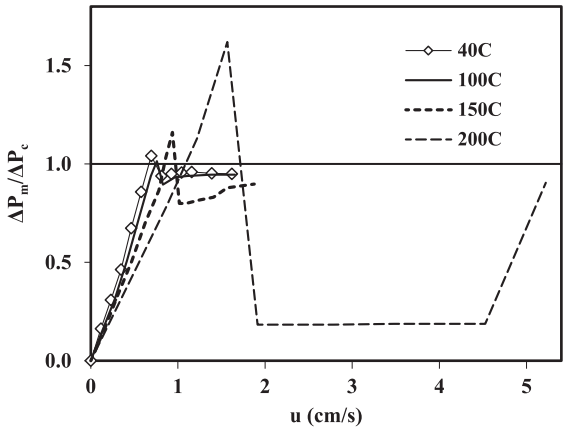

Fig. 4 $\Delta P_m/\Delta P_c$ vs bed velocity as a function of temperature for a silica catalyst doped with 10 %wt of potassium acetate. Reprinted with permission from Ref. (Lettieri et al., 2000). Copyright: (2000) Elsevier Limited.

via thermo-mechanical analyses. The physical properties of a porous Group A powder were changed deliberately in order to highlight under which conditions the fluidization behaviour is dominated by the IPFs.

These results demonstrated how temperature can increase the effect of IPFs, causing a Group A material to behave in a similar manner to a Group C material. **Fig. 3** shows the effect of temperature on the fluidization at minimum fluidization conditions for three silica catalysts doped with different amounts of potassium acetate (KOAc). **Fig. 3** shows that the prediction and experimental values of u_{mf} match only for the catalyst sample doped with 1.7 %wt of KOAc. Values of u_{mf} obtained for the doped samples with 7 % and 10 %wt of KOAc were found to be higher than the predicted ones at ambient temperatures. Lettieri et al. (2000) explained that during the drying process, some potassium acetate might have migrated to the mouth of the pores from within, making this responsible for the higher values of u_{mf}, hence reflecting the influence of the IPFs on the fluidization behaviour.

Significant changes in the fluidization quality of the sample with 10 %wt of potassium acetate occurred with increasing temperature. The ratio between the measured and calculated pressure drop across the bed of material is plotted against gas velocity in **Fig. 4**, as temperature is increased. The fluidization behaviour of this material significantly changed when the bed temperature was about 200 °C. A rapid decrease of the pressure drop was noted and channels were seen on the X-ray images. This material exhibited a typical cohesive Group C behaviour. Good fluidization at 200 °C could be achieved only when operating the system at a higher velocity, thus causing the channels and rat holes to be broken down. When the bed was cooled down to 150 °C, good fluidization was obtained again at low velocities.

Lettieri et al. (2000) explained that at increasing temperature, the potassium acetate contained within the catalyst pores became mobile and migrated to the surface of the particles due to decreases in the surface tension and viscosity. The presence of potassium acetate on the surface of the catalyst caused the material to become sticky and therefore to channel. On the other hand, as the bed temperature decreased, re-absorption of the potassium acetate into the catalyst pores may have occurred, thus allowing good fluidization of the material to be re-established.

Several authors have also investigated the combined effects of temperature and particle size and particle size distribution (PSD) on minimum fluidization velocity, Lin et al. (2002), Bruni et al. (2006), Subramani et al. (2007), Hartman et al. (2007), Goo et al. (2010), Chen et al. (2010) and Jiliang et al. (2013).

Hartman et al. (2007) performed experimental measurements on beds of ceramsite over a temperature range from 293 K to 1073 K, using very narrow fractions of ceramsite particles spanning a range of 0.13–2.25 mm. They reported that u_{mf} decreases with increasing bed temperature for all the particles, except for the largest ones (2.25 mm), which exhibited a non-monotonic dependence of u_{mf} on temperature.

Goo et al. (2010) investigated the effects of temperature and particle size on minimum fluidization velocity in a dual fluidized bed, using silica sands over a range of temperature between 298 K and 1073 K. They reported that u_{mf} decreases with increasing operating temperatures regardless of particle diameters or particle types, and they proposed a correlation to predict such a velocity at different temperature. Chen et al. (2010) have also observed similar behaviour.

Lin et al. (2002) and Jiliang et al. (2013) demonstrated that operating temperature and PSD can influence the

minimum fluidization velocity simultaneously, making variations of u_{mf} non-monotonic with temperature. In particular, Jiliang et al. (2013) investigated quartz sand and bottom ash in a bench-scale bubbling fluidized bed reactor at atmospheric pressure, with four PSDs between 30 and 600 °C. The PSDs evaluated included a narrow cut (as reference powder), a Gaussian-type powder, a binary mixture and a uniformly distributed powder. They concluded that the minimum fluidization velocity of the powders with wide PSD decreases with the increase in bed temperature and varies with the mass fraction of rough particles. In addition, they observed that the binary and uniform PSD behaved similarly to each other but generally they had higher values of u_{mf} than the Gaussian and narrow cut distributions. To predict the correct values of u_{mf} for wide-range-sized particles, Jiliang et al. (2013) proposed new correlations based on their experimental data.

Several correlations have been derived for the prediction on the minimum fluidization conditions at high temperature, these are, however, case-specific. The debate of the phenomena causing changes in behaviour with increasing temperature remains controversial with still much disagreement on the role of the hydrodynamic and interparticle forces.

3. Effect of temperature on bed expansion and minimum bubbling conditions

Many attempts have been made to describe the fluid dynamic properties of fluidized beds, with special attention paid to the transition between the particulate and bubbling regime of Geldart's (1973) Group A powders. These materials are those which exhibit a stable region of non-bubbling expansion between minimum fluidization velocity, u_{mf}, and minimum bubbling velocity, u_{mb}, with $u_{mb}/u_{mf} > 1$. The phenomenon of uniform expansion, or delayed bubbling, has been the subject of much research since it is significant to show differences between gas- and liquid-fluidized beds for the formation of gas bubbles in the former but not generally in the latter. The mechanism of bubble-free expansion in gas-fluidized beds has been assumed by some workers to be the same as the homogeneous expansion in a liquid-fluidized bed to which the Richardson and Zaki (1954) equation applies:

$$u = u_t \varepsilon^n \tag{22}$$

where u is the liquid velocity of the suspension, u_t is the terminal fall velocity and n is a parameter that depends on the free-fall particle Reynolds number and normally has values between 4.65 (viscous regime) and 2.4 (turbulent regime). However, the validity of this comparison has not always been accepted. Massimilla et al. (1972) and Donsi' and Massimilla (1973) made some experimental observations on the bubble-free expansion of gas-fluidized beds of fine particles and described the expansion mechanism as being due to the nucleation and growth of cavities which they assumed had occurred because of a broad distribution of interparticle forces. The phenomenon of delayed bubbling is not only limited to fine Geldart's Group A powders, it has also been observed with large particles fluidized under high pressure conditions, see Yates (1996), and also with magnetised large particles, as reported by Agbim et al. (1971) and later by Siegell (1989).

This phenomenon of delayed bubbling has been the subject of much research since it has a strong bearing on the difference between gas- and liquid-fluidized beds and on the reasons for the formation of bubbles in the one but not in the other.

The limiting condition for the stability of gas-fluidized beds is defined by the voidage at minimum bubbling, ε_{mb}, whose determination has been at the centre of much theoretical controversy due to the ill-defined role of the HDFs and IPFs. Mathematical models have been developed by various authors to predict the transition between particulate and bubbling regime. Two different approaches have been considered. On the one hand, criteria have been developed based on the assumption that hydrodynamic forces (HDFs) are the controlling factor. On the other hand, interparticle forces (IPFs) were considered to play the dominant role over the hydrodynamic forces. The first stability criterion based solely on hydrodynamic forces was proposed by Jackson (1963). His model failed to predict a stable region for the expansion of fluidized beds of fine materials. He found that the fluidized state was intrinsically unstable towards small concentration disturbances, regardless of the fluid-particle system considered. This conclusion is contrary to the experimental evidence obtained for Geldart's Group A powders.

Verloop and Heertjes (1970) re-formulated the hydrodynamic model applying the Wallis (1969) stability criterion, which compares the propagation of kinematic and dynamic wave velocities through the fluidized bed. According to this criterion, bubbles form when the propagation velocity of a voidage disturbance reaches the velocity of an elastic wave in the bed. Foscolo and Gibilaro (1984) adopted the approach of Verloop and Heertjes and developed a model (the "particle-bed model") to predict the onset of bubbling, ε_{mb}, in a fluidized bed. The key to application of their criterion lies in the formulation of the fluid-particle interaction model. This is discussed in Foscolo et al. (1983). A detailed formulation of the particle-bed model is reported in Foscolo and Gibilaro (1987) where reasonable agreement between predictions and experimental data available at ambient and high pressure conditions was found. Furthermore, Brandani and Foscolo (1994) mapped the various fluidization be-

haviours by analysing the discontinuities arising from the one-dimensional equations of change in the particle-bed model.

On the other hand, interparticle forces were considered to play the dominant role over the hydrodynamic forces (Mutsers and Rietema, 1977; Piepers et al., 1984; Cottaar and Rietema, 1986; Rietema et al., 1993).

Rietema and co-workers formulated a stability model which accounted for additional forces to the fluid-dynamic forces and gravitational weight. They assumed that the interparticle forces between cohering particles give rise to a powder structure with a certain mechanical strength even in the expanded state of homogeneous fluidization. This mechanical structure can be broken only with gas velocities sufficiently high so that the drag force exerted by the fluid becomes greater than the cohesive forces. Rietema and co-workers assumed that the mechanical strength of the powder structure controls the stability of a fluidized system. Similarly to Foscolo and Gibilaro (1984), Mutsers and Rietema (1977) followed the approach of Wallis to predict the stability of a fluidized system, and gave expressions for the kinematic and dynamic wave velocities. Their formulation for the bed elasticity and the theoretical concept behind it represents, however, the crucial difference between their model and the criteria developed solely on the basis of the hydrodynamic forces.

According to Mutsers and Rietema, the bed elasticity is the essential property which determines the dynamic behaviour of the bed, and whose origin is to be found in the Van der Waals' forces which the solid particles exert upon each other.

However, whereas models based on HDFs such as Foscolo and Gibilaro (1984) provide explicit formulations for the minimum bubbling condition, the formulation proposed by Rietema and co-workers cannot be used to make a-priori predictions.

The effect of temperature on the transition between particulate to bubbling fluidization was investigated by Rapagna' et al. (1994), who demonstrated the capability of the Foscolo and Gibilaro criterion to predict ε_{mb} for FCC powders of mean particle sizes of 65 and 103 μm in a 50-mm i.d. column from ambient conditions up to 900 °C. They used a fast responding pressure transducer connected to an oscilloscope to detect the passage of bubbles in the bed. They observed a decrease in the average bubble size and a delay of the onset of bubbling with increasing temperature for both FCC powders. This corresponded to an increase in the voidage at minimum bubbling with temperature. Also, a larger increase in ε_{mb} was observed for the finer materials, a comparison of their experimental values for ε_{mb} with those predicted by the Foscolo and Gibilaro fluid-bed model showed good agreement for both powders at ambient and high temperatures (**Fig. 5**). Xie and Geldart (1995) investigated the role of the IPFs on the bubbling conditions with increasing temperature by measurements of the voidage. They observed virtually no change in ε_{mb} as the temperature increased for any of the FCC catalysts investigated, in contrast to the results of Rapagna' et al. (1994). They also reported that predictions of ε_{mb} given by the Foscolo and Gibilaro (1984) and the modified particle-bed model by Jean and Fan (1992) matched experiments at ambient temperature for FCC powders larger than 60 μm. However, both models over-predicted ε_{mb} values at ambient temperatures for the finer powders, and they also predicted significant changes in ε_{mb} with temperature, in contrast to the experimental results reported.

The failure of the hydrodynamic models to correctly predict the transition between the particulate and bubbling regime was assumed to be the result of ignoring the

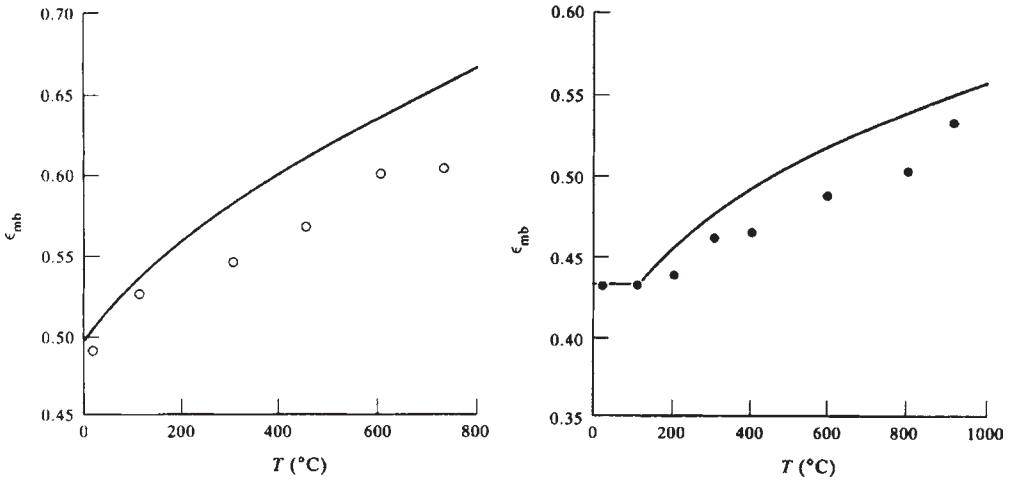

Fig. 5 Experimental and calculated values of bed voidage at minimum bubbling conditions as a function of temperature for sample I (on the left) and sample II (on the right), Reprinted with permission from Ref. (Rapagna et al., 1994). Copyright: (1994) Elsevier Limited.

interparticle forces.

The onset of bubbling was also studied by Formisani et al. (1998). They measured changes in the minimum bubbling velocity of FCC catalysts and silica sand with increasing temperature from ambient up to 800 °C in a 55-mm i.d. quartz column. They relied on visual observation to determine the commencement of bubbling. For all materials tested, they observed an increase of u_{mb} with increasing temperature with a trend very similar to the increase observed for u_{mf}. Unlike Rapagna' et al. (1994), they observed a very small bed expansion increase with increasing temperature.

Lettieri et al. (2001) investigated the fluid-bed stability of three fresh FCC catalysts both experimentally and theoretically as a function of increasing temperature. Values of the voidage at minimum bubbling conditions were obtained from 20 °C up to 650 °C, and compared with predictions given by the Foscolo and Gibilaro particle-bed model.

For all FCC catalysts, the experimental ε_{mb} values increased little with increasing temperature. At first, the values were compared with predictions obtained using the Foscolo and Gibilaro particle-bed model. This predicted changes in ε_{mb} much greater than found experimentally, see **Fig. 6**. The disagreement between predicted and experimental ε_{mb} values was related to the large discrepancy between the values of n and ut in the Richardson and Zaki equation, obtained from the experimental bed expansion profiles and the calculated ones.

For all FCC catalysts, the highest values of the experimental n and u_t were found at ambient conditions.

In order to correctly apply the particle-bed model to these particle systems, Lettieri et al. (2001) generalized the expression of the drag force given by Foscolo and Gibilaro for the viscous flow regime. Consequently, they re-examined the procedure followed to obtain the Foscolo and Gibilaro stability criterion and proposed a generalized expression of their criterion. Predicted ε_{mb} values obtained with the generalized expression of the Foscolo-Gibilaro criterion were within 5 % for all FCC catalysts. Although the particle-bed model was originally developed on the assumption that the hydrodynamic forces govern the fluid-bed stability, the results presented by Lettieri et al. (2001) suggested that the contribution of the interparticle forces to the bed stability of the materials studied cannot be ruled out.

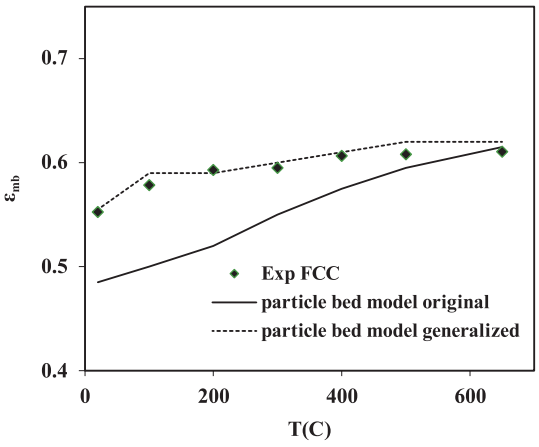

Fig. 6 Comparison between measured ε_{mb} values and predictions using the original and generalized Foscolo-Gibilaro particle-bed model for an FCC catalyst. Reprinted with permission from Ref. (Lettieri et al., 2001). Copyright: (2001) Elsevier Limited.

As a follow-up study, Lettieri and Mazzei (2008) analysed the effect of temperature on the fluid-bed stability of the same three FCC catalysts used in Lettieri's previous work, but this time through considerations on the fluid-bed elasticity.

They reported experimental findings on the effect of temperature on the elasticity modulus at minimum bubbling conditions, calculated according to the theory of Foscolo & Gibilaro (1984) and also adopting the criterion of Mutsers & Rietema (1977). In accordance with the theoretical postulation of Mutsers & Rietema, the results from bed expansion presented by Lettieri and Mazzei (2008) and previously by Lettieri at al. (2002) showed that the role played by the IPFs can affect the stability of Group A powders. However, the sensitive analysis carried out by Lettieri and Mazzei (2008) on the parameters which dominate the elasticity modulus revealed that the gas viscosity was the dominant factor which defined its variations with temperature, as shown in **Figs. 7** and **8**. This highlighted the importance of both HDFs and IPFs on the stability of Group A powders and the need for a correct and complete description of both contributions.

In line with Lettieri et al (2001), Valverde and co-workers (2001) emphasized the importance of the interparticle forces on the settling and particulate fluidization of fine powders. They proposed an extension of the Richardson and Zaki empirical correlation and the theoretical Mills-Snabre (1994) model, originally developed for the settling of non-cohesive spheres, to predict the settling of aggregates which may form when the interparticle forces exceed the particle weight by several orders of magnitude. Valverde et al. (2003) extended the previous study, investigating—from both macroscopic and local measurements—the transition between the solid-like, fluid-like and bubbling fluidization of gas-fluidized fine powders. They showed that the transition between the solid-like and the fluid-like regimes takes place along an interval of gas velocities in which transient active regions alternate with transient solid networks. Using optical probe local measurements, they showed the existence of meso-scale pseudo-turbulent structures and short-lived voids in the fluid-like state, which make the prediction of the transition between the different regimes a complex task.

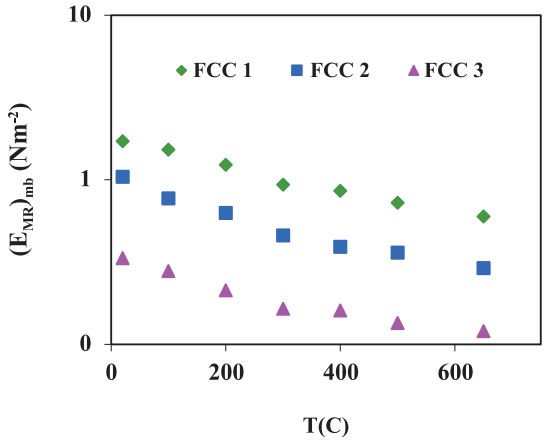

Fig. 7 Effect of temperature on the elasticity modulus at ε_{mb} according to the Mutsers & Rietema criterion, for all fresh FCCs. Reprinted with permission from Ref. (Lettieri and Mazzei, 2008). Copyright: (2008) Elsevier Limited.

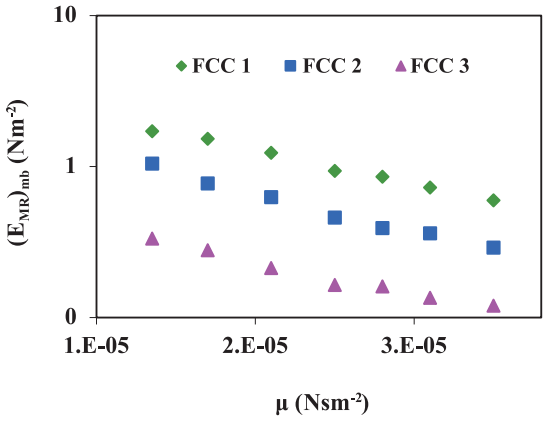

Fig. 8 Influence of gas viscosity on the elasticity modulus at ε_{mb} according to the Mutsers & Rietema criterion, for all fresh FCCs. Reprinted with permission from Ref. (Lettieri and Mazzei, 2008). Copyright: (2008) Elsevier Limited.

Castellanos (2005) observed that the onset of fluidization of fine and ultrafine powders was characterized by the presence of agglomerates which give place to a highly expanded state of uniform fluid-like fluidization. In an attempt to unify the above observations, Valverde and Castellanos (2008) proposed an extension of Geldart's classification of powders to predict the gas-fluidization behaviour of cohesive particles, which reconciles the role of the interparticle and hydrodynamic forces on the existence of a non-bubbling regime. In the new phase diagram proposed by Valverde and Castellanos, the boundaries between the different types of fluidization are defined as a function of fluid viscosity, particle density, the fractal dimension of the agglomerates and the powder's compaction history, as previously reported by Valverde and Castellanos (2006).

Girimonte and Formisani (2009) reported on the influence of operating temperature on the transition to the bubbling regime for samples of FCC, silica and corundum sands, at temperatures ranging from 30 to 500 °C. They determined the minimum bubbling velocity using four different methods and obtained different results for u_{mb} with increasing temperature. The first method was based on the direct observation of the velocity at which the first bubble erupted on the free surface of the bed. The second method was based on measurement of the pressure drop across the whole bed, and u_{mb} was taken as the point where a shallow minimum of the Δp versus u curve occurs. The last two methods were derived from analysis of the "fluidization map", namely examination of the expansion behaviour of the bed over a range of fluidization velocities from the fixed-bed state to the bubbling regime.

They demonstrated that the optical method and the method based on detection of the pressure drop minimum were unreliable for correctly determining the starting point of bubbling. They stated that only the analysis of bed expansion as a function of the fluidization velocity allows the succession of phenomena through which a stable flow of bubbles across the solid mass ensues to be reconstructed.

More recently, Girimonte and Formisani (2014) reported on new experiments carried out on the effect of temperature on the fluidization of FCC particles. They used a non-invasive optical technique for acquiring images of the bubbles' eruption at the free surface and results from bed collapse tests. Their experiments showed that high temperature influences the quality of bubbles and produces a smoother regime of bubbling, which they attributed to the thermal enhancement of IPFs that in turn leads to a higher porosity and lower interstitial flow in the emulsion phase.

In summary, high temperature clearly affects the stability of fluidized beds of Group A powders; well-established theories and models fail to predict correctly the voidage at minimum bubbling with increasing temperature. Models corrected on the basis of experimental data are capable of reproducing correct trends; however, a-priori predictions of the fluid-bed stability with increasing temperature are yet to be achieved. The challenge here is still in the ability to describe the forces that determine the transition from particulate to bubbling fluidization. Hence, some kind of quantification of the effects of the IPFs on fluidization is needed in order to advance the understanding of fluidization at high temperature.

4. Effect of fines content and fines size distribution on fluidization

The presence of fine particles is known to improve the

fluidization quality of fluidized beds (Rowe et al., 1978; Abrahamsen and Geldart, 1980; Newton, 1984). For this reason many industrial fluidized bed reactors operate with a high fines fraction ($d_p < 45$ μm) of between 10 and 50 wt% in order to improve the fluid bed performance and to achieve high product yields (Pell and Jordan, 1987; Lorences et al., 2003; Bruni et al., 2006). Furthermore, the fines increase the mass transfer rate between the dense and bubble phase, the minimum bubbling velocity, the interstitial gas velocity, the bed expansion and reduce bubble size (Werther, 1983; Rowe, 1984; Sun and Grace, 1992; Lorences et al., 2003). Fresh catalysts generally contain a higher proportion of fines and show less of a tendency to segregate or cluster (Avidan and Yerushalmi, 1982).

However, as pointed out by Lorences et al. (2003), there is an associated cost in maintaining a high level of fines. Plant investment may be higher because more cyclones and a larger reactor volume are required due to the lower solids suspension density. Catalyst make-up costs are also higher because of the increased attrition rate.

Many researchers have investigated the effect of fines on the fluidization quality in order to determine the optimal amount of fine particles to be added (Rowe et al., 1978; Barreto et al., 1983; Newton, 1984; Avidan and Edwards, 1986; Yates and Newton, 1986; Pell and Jordan, 1987; Sun and Grace, 1990; Lorences et al., 2003; Bruni et al., 2006).

Rowe et al. (1978) examined the dense phase voidage ε_d of freely bubbling fluidized beds containing different amounts of fines using the X-ray absorption technique. Voidage measurements were made by comparing the X-ray absorption of the dense phase of the freely bubbling bed with that of a calibration wedge containing the same material. They carried out experiments on a commercial silica-based catalyst of mean particle diameter 52 μm, but with three different percentages of fines: 2.7, 20 and 27.6 %. They found that both the dense phase voidage and the overall expansion of the bed increased with increasing fines content. Furthermore, they observed that the measured voidage of the dense phase was an order of magnitude greater than the voidage corresponding to the minimum fluidization condition. Accordingly, they deduced that the interstitial gas flow in a bubbling bed is greater than the minimum fluidization flow, hence questioning the validity of the "two-phase" theory of Toomey and Johnstone (1952) on beds of fine particles. This states that all gas in excess of that required to just fluidize the particles passes through the bed in the form of bubbles. Rowe et al. (1978) concluded that since the dense phase is much more effective in bringing about a chemical reaction than the bubble phase, the overall performance of a catalytic fluidized bed reactor can be enhanced by the addition of fines.

Later, Barreto et al. (1983) compared the Rowe et al. (1978) measurements with those obtained with a bed collapse test technique. They found good agreement between the dense phases properties obtained using the two techniques over the range of velocities studied.

In order to test the conclusions from the earlier study of Rowe et al. (1978), Newton (1984) and Yates and Newton (1986) also examined the influence of fines fractions on fluidization by monitoring the conversion in catalytic fluidized bed reactors containing different amounts of fines. They highlighted that an increase in the conversion measured for a given throughput of reactant can be obtained by increasing the fines content and that this is due to changes caused by fine particles in the gas distribution between the dense phase and the bubble phase. Newton (1984) carried out experiments on a commercial oxidation catalyst, and he used three batches containing 0, 16 and 27 % of fines with a mean particle diameter of 81, 58 and 52 μm, respectively. Results at each temperature showed an increase in conversion with increasing fines content and for the same fines content an increase in conversion with temperature, therefore confirming the hypothesis that increasing fines content causes more gas to flow through the emulsion phase and less through the bubble phase.

Abrahamsen and Geldart (1980) had also extensively investigated the effect of fines on the fluidization of Geldert's Group A powders and found that the dense phase voidage increases as the fraction of fines increases; they stressed, however, the need for studying the effects of fines fractions, mean diameter and size distribution independently.

Khoe et al. (1991) investigated the effect of changing the mean particle diameter independently of the PSD by modifying a sample of FCC catalyst and a sample of glass ballotini. They created three samples with a narrow size distribution and differing in mean particle diameter (83, 53 and 34 μm for the FCC and 113, 72 and 37 μm for the glass ballotini). Then they examined the effect of changing the PSD independently of the mean diameter by creating for each powder two more samples with the same mean particle diameter as the intermediate narrow sample (~53 μm for the FCC and ~72 μm for the glass), but with a wide and bimodal PSD, respectively.

They performed the bed collapse test on all samples and found that the effect of increasing the mean particle diameter for both FCC and glass powders was to increase the dense phase collapse rate and to decrease the voidage of the dense phase. These effects were enhanced when the samples with the same d_p and different PSD were compared. The most aeratable FCC sample was the one with a wide distribution, while the most aeratable glass sample was the one with a bimodal distribution.

Bruni et al. (2006) investigated the independent effect

on fluidization of adding different fine sub-cuts to a virtually fines-free starting material. The fluidization behaviour of an alumina powder was monitored at temperatures ranging from ambient to 400 °C and by adding two fine sub-cuts of nominal size 0–25 and 25–45 μm to the material previously deprived of fines. Results were obtained by performing fluidization tests such as bed collapse tests, pressure drop profiles and bed expansion profiles. Fines content and fines size distribution significantly affected the fluidization behaviour of the powders tested. The fluidization tests highlighted significant differences in the characteristics of the settled and expanded bed of the materials investigated. The results showed that the addition of fines made the materials more capable of retaining the aeration gas hence expanding more and taking longer to collapse when the gas was suddenly cut off than the bed deprived of fines. The effects of the IPFs become more evident for the powders containing the smaller fines cut than for powders containing the same amount of bigger fines. Bruni et al (2007a,b) subsequently developed a parallel fluidization-rheology approach (discussed in Section 7 of this paper) to establish the relative role between the interparticle and hydrodynamic forces on the aeratability of the powders with increasing temperature.

The literature reported to this point reveals the complexity of the phenomena involved, and the difficulty of a direct quantification of the particle-particle interactions in fluidized beds and of their changes at process conditions. Within this framework, powder rheology represents an appealing tool to evaluate indirectly the effects of the IPFs on fluidization. This is tackled in the next two sections of this paper.

5. Powder flowability measurement tests

A great deal of research has been carried out over the last sixty years in order by means of simple tests to define and measure parameters apt to characterize and predict the flow properties of solid materials. To this end, various approaches have been undertaken and are presented in this section. These include both stationary measurements and dynamic tests.

On one hand, stationary measurements (angle of repose, Hausner ratio, etc.) have been proposed as simple tests to predict the flowability of bulk powders (Carr, 1965). On the other hand, dynamic tests have been used as a means for determining the flow characteristic of powders. These dynamic tests can be classified into two distinct groups: the shear-cell-type tests, first introduced by Jenike in 1953, and the viscometer-type tests, whose study was initiated by Schugerl in the late sixties. The former is a test performed on the powder in a compressed state where the shear measurements are used to obtain a yield locus that represents the limiting shear stresses under any normal stress when failure, i.e. flow, occurs. The shape of the yield locus is related to the material cohesiveness. The latter is based on the analogy between fluidized beds and liquids and in particular on the idea that in a fluidized bed, a resistance against flow exists just as in liquids, and that this resistance is a kind of internal friction between the particles in the suspension forming the dense phase and resembles the concept of viscosity used in describing the rheology of liquids.

Carr (1965) developed a classification system to predict the flow characteristics of a bulk of particulate solids. In Carr's method, a numerical value is assigned to the results of several tests and it is summated to produce a relative flowability index for that particular bulk material. The method is further discussed in Carr (1970). Defined here are some of the main parameters used in Carr's method: the angle of repose, the angle of fall, the angle of difference, the angle of internal friction, the angle of spatula and cohesion. In addition, the Hausner Ratio (HR, i.e. the ratio between the loose and the packed bulk density) and the compressibility are also used to define the cohesiveness and thus the flowability of a material (Geldart and Wong, 1984, 1985; Bruni, 2005).

The *angle of repose* is defined as the constant angle to the horizontal assumed by a cone-like pile of the material. It is a direct indication of the potential flowability of a material: materials with good flowability are characterized by low angles of repose.

The *angle of fall* is determined by dropping a small weight onto the platform on which an angle of repose has been formed. The fall causes a decrease of the angle of repose that is called angle of fall. The more free-flowing the material, the lower the angle of fall.

The *angle of difference* is the difference between the angle of repose and the angle of fall. The greater this angle, the better the flow.

The *angle of internal friction* is defined (Carr, 1970) as the angle at which the dynamic equilibrium between the moving particles of a material and its bulk solid is achieved. This is of particular interest for flows in hoppers and bins.

The *angle of spatula* is a quick measurement of the angle of internal friction. It is the angle, measured from the horizontal, that a material assumes on a flat spatula that has been stuck into the dry material and then lifted up and out of it. A free-flowing material will have formed one angle of repose on the spatula's blade. A cohesive material will have formed several angles of repose on the blade; the average of these is taken. The higher the angle of spatula of a material, the less flowable it is.

Cohesion is defined as the apparent cohesive forces existing on the surface of fine particles or powders. The cohesion test consists of passing the material through three

vibrating sieves in series. The material left on each sieve is weighed and a cohesion index is determined from the relative amounts retained.

The *Hausner Ratio* (*HR*) is the ratio between the loose and the packed bulk density and is used as an indication of the cohesiveness of the materials, see Geldart and Wong (1984). The loose bulk density (ρ_{BDL}) is measured by gently pouring a sample of powder into a container through a screen, whereas the packed or tapped bulk density (ρ_{BDP}) is determined after settling and deaeration of the powder has occurred due to tapping of the sample. In addition to the *HR*, the powder compressibility is also used to define cohesiveness, this is expressed as 100 $(\rho_{BDP}-\rho_{BDL})/\rho_{BDP}$.

The main advantage of these tests is their simplicity that makes them an attractive tool to determine powder flowability and it explains their wide use in industry and academia. However, these tests are scarcely reproducible and their procedures are very difficult to standardise, as amply discussed by Santomaso et al. (2003) with special regard to the Hausner ratio. Furthermore, the link between the fluidization behaviour and the static properties is not at all straightforward, due to the uncertain relationship between the IPFs and the HDFs involved when gas is passed through a bed of particles. The use of static methods to predict the fluidization behaviour of powders, despite being widely employed, is therefore questionable, especially when the fluidization behaviour needs to be assessed under process conditions (Bruni, 2005).

5.1 Shear testers

Shear-cell-type tests, first introduced by Jenike in 1953, are performed on the powder in a compressed state where the shear measurements are used to obtain a yield locus that represents the limiting shear stresses under any normal stress when failure, or to be precise flow, occurs. The shape of the obtained yield locus is related to the material cohesiveness. Many conventional testers are available for measurement of the flowability and they can be distinguished between direct (translational and rotational) and indirect (uniaxial, biaxial and triaxial) shear testers (Schwedes, 2003). Some examples of translational direct testers are Jenike's shear cell and Casagrande's shear tester, while some of the most important rotational direct testers are the torsional and the ring shear testers.

Shear cell measurements are widely used to assess the flowability of powders for applications that involve powder discharge. Most of the principles of such tests have their origin in soil mechanics and in bunker designing, but they have become increasingly useful for the general characterisation of particulate materials. However, as for the static tests, a direct link between the failure properties of the material measured with a shear cell and the corresponding fluidization behaviour is not straightforward.

Shear testers are known to be very useful to predict the solids flow from a tall silo in which the relatively high loading pressure of the solids prevails. However, due to the very small or zero loads on the bulk of a fluidized powder, standard shear testers are unlikely to provide an accurate characterization of fluid bed behaviour, as values of the failure properties need to be extrapolated from data at higher loads. Barletta et al. (2005, 2007) overcame this problem in their modified Peshl shear cell by introducing a cinematic chain to counterbalance the weight of the lid of the cell and therefore allow measurements under low normal stresses. Such a modified Peschl shear cell was used by Bruni et al. (2007a, b), whose work is discussed in the next section.

Moreover, existing shear cells are not designed to operate at high temperature because applications involving powder discharge are run at ambient temperature. Therefore, shear cells are not capable of detecting possible changes in the settled bed packing with increasing temperature.

Few studies available in the literature have addressed the experimental evaluation of powder flow properties at high temperature. The first attempt was carried out by Smith et al. (1997), who preheated powder samples of $MgSO_4$ and $CaSO_4$ up to 750 °C and moved them into a Jenike shear cell and performed shear tests immediately without any control of the temperature. Experimental results for consolidation stresses in the range 40–200 kPa showed an increase of the unconfined yield strength with increasing temperature for all the analysed powders. This was explained with the aid of SEM observations and X-ray diffraction measurements which showed the formation of agglomerates during preheating of the sample.

The lack of proper measurement of the temperature during the shear tests was to some extent overcome by placing the shear cell inside a heated chamber with temperature control (Kanaoka et al., 2001; Tsukada et al., 2008).

Ripp and Ripperger (2010) designed a temperature-controlled annular shear cell for the Schulze shear tester operating from 80 °C to 220 °C. For this purpose, an electric heater was placed on the lid while the vertical walls and the bottom of the cell were provided with a double casing through which a heating or a cooling medium can flow.

Recently, Tomasetta et al. (2013) modified a Schulze shear cell to perform measurements of the powder flow properties of powders up to 500 °C. Electric heaters were introduced below the cell bottom and on the lid to heat the cell and the powder sample contained in it. A covering of insulating material was placed around the trough of the cell and above the lid in order to reduce the heat flux from the external surface of the cell and then to minimise the

temperature gradient within the sample. They evaluated the yield loci at room temperature and at 500 °C for different samples: FCC powder, fly ashes, glass beads, natural corundum and synthetic porous α-alumina. Furthermore, in order to simulate the formation of liquid bridges derived from the melting of one of the phases and to verify the role of capillary forces on the flow properties of bulk solids at high temperature, a sample of glass beads was mixed with some (1 % of the total weight) high-density polyethylene (HDPE) which has a relatively low melting point. The results showed that there was no significant effect of the temperature in the range 20–500 °C on the shear flow of the FCC powder, fly ashes, corundum powder and alumina. On the other hand, a small but significant increase of cohesion and, therefore, of the unconfined yield strength was observed with temperature for glass beads.

More recently, Chirone et al. (2015) used the high-temperature annular shear cell developed by Tomasetta et al (2013) to characterize the flow properties of five ceramic powder samples with different particle size distributions between ambient temperature and 500 °C. Moreover, a model based on the multiscale approach proposed by Rumpf (1970) and Molerus (1975) was used to predict the effect of temperature on the tensile strength of the powder samples. They observed a significant increase of powder cohesion at 500 °C for different cuts of the same powder with a particle size larger than 20 μm. This resulted in a lower flowability of the samples. Thermal analysis on the powder samples revealed that the temperature effect on the powder flow properties was only due to van der Waals' forces.

5.2 Fluid bed viscosity

Particles fluidized by a gas can be treated as a continuum at length scales much larger than the particle diameter. The rheology of such a continuum results from a cumulative effect of microscopic (at length scale of the particles) forces due to the interaction between particles, such as Van der Waals', capillary or electrostatic forces and hydrodynamic drag forces. Rheological properties, in the form of flow constitutive equations, are thus an essential component of the averaged continuum equations for determining the flow of fluidized particles.

Fluid bed viscosity represents an extremely attractive parameter to characterise fluid bed behaviour, but unfortunately the results obtained in many of the works available in literature are not consistent at all with each other, as reported by Newton et al. (1999). Newton et al. reviewed the results of the available studies and reported that different orders of magnitude for the bed viscosity were obtained using the various methods.

It should be noted that the viscosity is influenced by the shape of the particles, the voidage of the bed, the fluidizing velocity and the fluidizing gas viscosity.

Moreover, according to Rietema (1991), making measurements in a freely bubbling bed is pointless because when a bubble collides with the measuring device the shear stress will locally approach zero. Therefore, only the measurement of the viscosity of the dense phase seems to be meaningful.

Various measuring devices have been employed to determine the viscosity of powders. Conventional-type viscometers are those where the material is sheared by a rotating element (Stormer, Brookfield and Couette) and the resistance to the rotation is measured. Other methods are the floating and falling ball and the torsion pendulum. In the method developed by Grace (1970), measurement of the shape of rising bubbles is used to indirectly calculate the bed viscosity. All these methods are in some ways "intrusive", as an external object is immersed in the bed in all cases. An indirect method is the quasi-solid emulsion viscosity method developed by Kono et al. (2002), where the viscosity is measured indirectly through the measurement of fluidization parameters.

Whether a fluidized bed has to be considered a Newtonian or a non-Newtonian fluid is also a controversial question. In the early studies of gas-fluidized-bed rheology, an implicit assumption was that the fluidized beds behave as a Newtonian fluid (Matheson et al., 1949; Kramers, 1951; Diekman and Forsythe, 1953; Furukawa and Ohmae, 1958; Shuster and Haas, 1960; Daniels, 1965). Kai et al. (1991) also assumed Newtonian behaviour for the fluidized bed that they modelled. Others authors, however, described fluidized beds using a non-Newtonian visco-plastic model, in particular a Bingham fluid model (Anjaneyulu and Khakhar, 1995; Zhao and Wei, 2000).

Gibilaro et al. (2007) and Colafigli et al. (2009) also reported on the apparent viscosity of a fluidized bed and they proposed theoretical models and experimental analysis in order to evaluate such a property on the base of the analogy between fluidized beds and fluids.

In the next section, we discuss the relationship between the rheological properties of powders and the corresponding fluidization behaviour in the attempt to interpret and quantify the effect of the interparticle forces on fluidized powders.

6. Link between rheological measurements and fluidization

As shown in the previous section, a great deal of research work has been carried out towards understanding the powder rheology. Establishing a relationship between the rheological properties of powders and the correspond-

ing fluidization behaviour is reviewed in this section.

Reiling (1992) explored the link between the apparent viscosities of fine catalyst powders and the bubble size. In particular, he studied the effects on viscosity of adding ultrafine silica cuts to the bed of catalyst, using a Brookfield paddle viscometer. Reiling (1992) questioned the validity of the instability/wave perturbation theory, according to which low-viscosity and low-density fluid beds should promote the suppression or destruction of large bubbles and thus contain smaller bubbles than beds of high viscosity or high density (Rice and Wilhelm, 1958; Romero and Johanson, 1962). The experimental data reported by the author did not support this conclusion. The addition of ultrafine silica had a large effect on the dense-phase voidage but only a small effect on the viscosity of the fluidized bed. Therefore, Reiling (1992) concluded that the link between bubble size and apparent viscosity is not supported by a viscous mechanism.

Newton et al. (1999) also tried to relate the bubble size and bubble number to the bed viscosity. They used a ball dropping technique in order to measure the viscosity of a bed of Geldart group B polymer powder with increasing temperature (17–96 °C). The authors reported that the effect of increasing temperature on the polymer cohesiveness and stickiness was demonstrated by the significant changes observed on the mean bubble size and number of bubbles. However, the viscosities measured through the ball dropping technique did not show dramatic changes with increasing temperature. Newton et al. (1999), in line with the findings of Reiling (1992), concluded that viscosity effects do not explain bubble sizes in the case of the tested powder and that they could not assign a viscosity to the dense phase.

Kai et al. (1991) related the apparent bed viscosity to the bubble diameter and to pressure fluctuation measurements. The authors, in disagreement with Reiling (1992) and Newton et al. (1999), found that the bubble diameter increased with increasing viscosity. They also carried out experiments with increasing temperature, but they did not clearly state what trend they found for the apparent viscosity with such a parameter. However, they showed that the experimental data for the bubble diameter and the viscosity at high temperatures followed the same relationship found at ambient temperature. They obtained similar results by plotting experimental data obtained at high pressure by Weimer and Quarderer (1985). The authors also proposed an empirical correlation to predict the variation of apparent bed viscosity with operating temperature.

Khoe et al. (1991) analysed the fluidization and the rheological behaviour of sets of powders differing in PSD and fines content. According to the method described by Molerus (1975, 1978), they used shear tests measurements and experimental values of ε_{mf} and mean particle diameter d_{sv} to derive an expression for the average adhesive force per contact, F. The method assumes each powder to be a semi-continuum and derives the average tensile strength, from which the average F value at the contact points between monosized particles of diameter d_{sv} is calculated. Khoe et al. (1991) found that the adhesive force per contact, F, correlated very well with the ratio $(\varepsilon_{mb}-\varepsilon_{mf})/\varepsilon_{mf}$ obtained from experiments. In particular, they found that F increases when the maximum dense-phase expansion increases. The authors used the F values obtained from the shear cell measurements to also question the commonly accepted assumption that at the minimum bubbling velocity, the average adhesive forces counterbalance the overall hydrodynamic forces. They developed a model to calculate a theoretical ΔF which would be needed to reach the minimum bubbling without expanding the bed, and compared it with the measured values of F. They found that $\Delta F \ll F$ and thus they stated that the energy needed to reach minimum bubbling without expanding the bed is much smaller than the average interparticle bond strength. Khoe et al. (1991) also concluded that vertically elongated microcavities are responsible for a premature weakening of the bed structure, allowing bubbling to start at a much lower value of the hydrodynamic force than F. This result was in agreement with findings of Donsì and Massimilla (1973), who also observed cavities and microchannels in the homogeneous expansion of Geldart group A powders.

Kono et al. (1994) performed several fluidization tests on powders differing in size, shape, density, chemical properties and surface characteristics, but all fluidizable and free from any agglomeration or segregation phenomenon. They used spent FCC, glass beads, carbon black and various starch powders with sizes ranging from 15 to 70 μm. For each powder, the fracture strength σ_f and the plastic deformation Y were evaluated at ambient temperature and, for the FCC experiments, were calculated at temperatures up to 500 °C as well. The authors proposed a correlation between Y and σ_f:

$$\sigma_f = 0.11\, Y^{0.90} \tag{23}$$

which held true for all the experimental data, regardless of the type of powder, properties or operating temperature. Kono et al. (1994) interpreted this line as a flow characteristic line, where all powders characterized by smooth fluidization should fall. This idea was supported by the fact that when powders forming agglomerates were fluidized or wall effects were significant, the rheological parameters could not be related using Eqn. 23. Furthermore, a qualitative correspondence was found between the measured rheological parameters and the observed fluidization behaviour. The smaller the values of Y and/or $\sigma_{f,mb}$, the larger the expansion of the dense phase at u_{mb}, and the smaller the values of bubble size in freely fluidized beds observed in a 2D fluidized bed. Therefore,

moving along the linear relationship given by Eqn. 23, it was possible to predict different degrees of flowability among fluidizable powders. In particular, the points obtained with increasing temperature systematically shifted along the line towards the small values of the rheological parameters, which was in agreement with the widely reported positive effect of temperature on the fluidization behaviour of free-flowing materials (Lettieri, 1999).

Quintanilla et al. (2001) investigated the correlation between bulk stresses and adhesion forces in fine powders. They presented measurements of the tensile strength as a function of the consolidation stress for a set of fine cohesive powders (i.e. xerographic toners) of 12.7 μm particle size and with a range of concentration of submicron fumed silica as a flow control additive. Castellanos et al. (2002) investigated the dynamics of fine cohesive powders inside rotating drums with the aim of studying the transition from rigid-plastic flow to gas-fluidized regime. They performed experimental measurements on the bed expansion as a function of the rotation velocity, using drums of different diameters and fine powders of different cohesiveness. They demonstrated that the onset of fluidization in the rotating drum is determined by the ratio of the powder kinetic energy per unit volume to its tensile strength, and that once the powder is completely fluidized, the average interstitial gas velocity increases proportionally to the rotation velocity. Subsequently, Castellanos et al. (2004) presented the so-called Sevilla Powder Tester (SPT), a 4.45-cm diameter, 17-cm high cylinder placed on a shaker to help fluidization of cohesive materials. The SPT showed the interdependence between the consolidation stresses, the tensile yield stress and the particle volume fraction for powders with different levels of surface additives which were used to vary the powders' degree of flowability.

Bruni and co-workers (Bruni, 2005; Bruni et al., 2004, 2005, 2007a, 2007b) investigated the effects of adding different fines cuts on the fluidization and the rheological behaviour of an alumina powder. To this end, they followed a twofold approach to establish a link between the two aspects of the work. On the one hand, the fluidization behaviour of the alumina was studied at process temperatures ranging from ambient to 400 °C and by adding two fine sub-cuts of nominal size 0–25 and 26–45 μm, respectively (discussed in Section 5 of this paper), to the material previously deprived of fines. Fluidization experiments were carried out, changing the total fines content from 22 % to 30 % by weight. On the other hand, a new mechanically stirred fluid-bed rheometer (the msFBR, 15 cm in diameter and 30 cm tall) was designed, built and commissioned at ambient temperature to determine the rheological behaviour of the powders containing different fines sub-cuts (Bruni et al., 2005). The rheological experiments were carried out at different rates of aeration and impeller depths (**Figs. 9–10**).

In parallel, the failure properties of the materials were also determined using a modified Peschl shear cell (Bruni et al., 2007a). A model was developed based on the failure properties of the materials to determine the stress distribution corresponding to any given rate of aeration in the msFBR (Bruni et al., 2007b). This allowed a true comparison to be made between the rheological behaviour of different powders, aiding assessment of the effect of the fines size distribution on powder rheology. Moreover, the model allowed prediction of the torque measured with the msFBR and assessment of the effect of aeration on powder rheology.

The interpretation of the failure properties of the materials provided an indication of the capability of the powders to flow and underpinned the link between the fluidization and the rheological behaviour below the minimum fluidization conditions, interpreted as the capability of the powders to fail under a certain load and their capability to attain fluidization.

In particular, for all materials tested, measurements of the torque at different impeller depths and different levels of aeration showed that the torque reaches a plateau (see **Fig. 9**), similar to a normal stress profile in silos (Janssen, 1895).

The effect of increasing the aeration rate was to linearly decrease the torque needed to stir the materials. These trends were explained considering that the stress distribution in the bed changes with changing aeration, as shown in **Fig. 10**. Thus, at a constant impeller depth and when the aeration rate is increased, the normal load on the impeller will decrease due to the additional upward drag force exerted by the gas on the powder. This reduces the apparent gravity and reduces the local state of stress that is responsible for the measured torque. On the basis of the above results, Bruni et al. (2007b) developed a model to estimate the state of stress by varying the impeller depth, following Janssen's approach and Janssen's

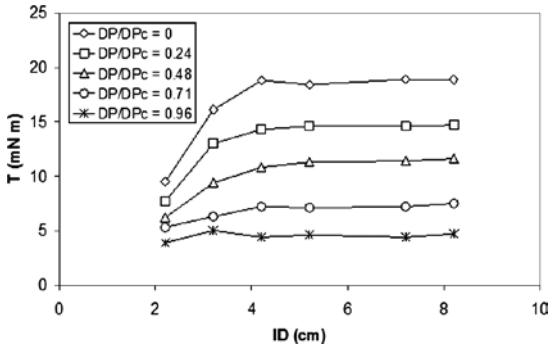

Fig. 9 Effect of impeller depth (ID) on torque—alumina containing fines sub-cut 26–45 μm. Reprinted with permission from Ref. (Bruni, 2005). Copyright: (2005) Ph.D. Thesis, University College London.

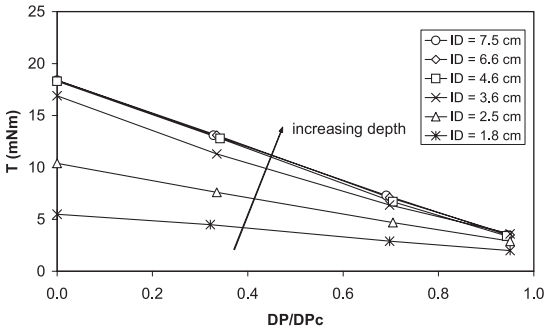

Fig. 10 Effect of aeration rate ($\Delta p/\Delta p_c$) on torque—alumina containing fines sub-cut 26–45 μm. Reprinted with permission from Ref. (Bruni, 2005). Copyright: (2005) Ph.D. Thesis, University College London.

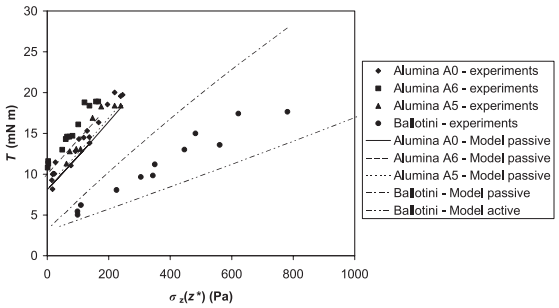

Fig. 11 Experimental torque vs calculated normal stress σ_z at impeller depth for all materials. Reprinted with permission from Ref. (Bruni et al., 2007b). Copyright: (2007) Elsevier Limited.

analysis for silo design, which was modified to take the aeration of the bed and the possible cohesiveness of the material into account.

The model uses properties such as the dynamic and the wall yield loci of the powders used, which were estimated with a Peschl shear cell modified for small loads. The comparison between the experimental and predicted values for the torque demonstrated that the torque is defined by the plastic deformation of the powders and can be explained within a simple Mohr-Coulomb approach to powder flow.

Bruni et al. (2007a) highlighted significant differences in the rheological behaviour of the alumina sample containing the small fines sub-cut (0–25 μm) compared to the sample containing the same amount of bigger fines (26–45 μm) or to the sample that was virtually free of fines.

Under the same normal load, the torque needed to stir the alumina sample containing the small fines sub-cut was found to be higher than the torque needed to stir the sample containing the larger fines sub-cut or the sample that was free of fines. In other words, the presence of small fines increases the powder's resistance to flow. In **Fig. 11**, a comparison is also shown with glass ballotini (fines-free) requiring the least torque. These results were found to be in agreement also with the results obtained for the voidage of the settled bed, the voidage of the bed at the minimum fluidization velocity, and the expansion and dearation tests. The alumina containing the smaller fines sub-cut was arranged in a more compacted packing when settled and at the minimum fluidization compared to the alumina sample containing the same amount of bigger fines.

It also exhibited a more pronounced change in slope during bed expansion, which was interpreted as a weakening of the bed structure before the onset of bubbling.

More recently, Tomasetta et al. (2012) re-examined the model developed by Bruni et al. (2007b) and performed a sensitivity analysis on the wall failure properties and on some of the original model assumptions regarding the active and passive state of stress in the fluid-bed rheometer. Tomasetta et al. (2012) also proposed a novel procedure for the inverse application of the model developed by Bruni et al. (2007b), such that the powder flow properties could be estimated starting from the torque measurements. The application of this procedure provided good results in terms of effective angle of internal friction and was deemed promising for the ability of the system to explore powder flow at very low consolidation states.

7. Conclusions

This review has demonstrated the important role that process conditions, namely temperature, fines and fines distribution, play on the fluidization behaviour of gas-solids fluidized beds.

Process conditions influence fundamental parameters describing the minimum fluidization conditions, bed expansion and contraction, and the transition from particulate to bubbling fluidization.

Analysis of the influence of elevated temperatures on fluidization highlights the enhanced role that the interparticle forces can play on the fluidization quality over the hydrodynamic forces.

The review on the influence of adding fines to the fluid bed and the role played by the particle size distribution and distribution of the fines emphasized the need for a quantification of the effects of the interparticle forces.

To this end, the multidisciplinary approach based on linking rheology and fluidization is encouraging. Further work is, however, needed; the challenge lies in the difficulty to relate the different rheological measurements to fluidization, mostly due to the variety of techniques employed, which makes standardisation of rheological tests very difficult.

A more systematic assessment of the independent and the combined effects of process conditions on fluid bed rheology and fluidization still needs to be accomplished.

Nomenclature

Ar	Archimedes number (—)
d_p	Particle diameter (m)
E_{MR}	Elasticity modulus (N m^{-2})
g	Gravitational acceleration (m s^{-2})
HDFs	Hydrodynamic forces
IPFs	Interparticle forces
n	Richardson-Zaki exponent
PSD	Particle size distribution
Re	Reynolds number (—)
Re_{mf}	Reynolds number at minimum fluidization (—)
T	Temperature (°C)
u	Superficial velocity (m s^{-1})
u_{mb}	Minimum bubbling velocity (m s^{-1})
u_{mf}	Minimum fluidization velocity (m s^{-1})
u_t	Terminal fall velocity (m s^{-1})
Y	Plastic deformation coefficient (Pa)
Δp	Pressure drop (Pa)
Δp_c	Calculated pressure drop (Pa)
Δp_m	Measured pressure drop (Pa)
ε	Bed voidage (—)
ε_0	Fixed bed voidage (—)
ε_d	Dense-phase voidage (—)
ε_{mb}	Minimum bubbling voidage (—)
ε_{mf}	Minimum fluidization voidage (—)
μ	Viscosity (Pa s)
μ_g	Gas Viscosity (Pa s)
ρ_{BDL}	Bulk density loose (kg m^{-3})
ρ_{BDP}	Bulk density packed (kg m^{-3})
ρ_g	Gas density (kg m^{-3})
ρ_p	Solids density (kg m^{-3})
σ_f	Fracture strength of powder structure (Pa)
σ_z	Calculated Normal stress (Pa)
ϕ	Shape factor (—)

References

Abrahamsen A., Geldart D., Behaviour of gas-fluidized beds of fine powders part II. Voidage of the dense phase in bubbling beds, Powder Technol., 26 (1980) 47–55.

Agbim J.A., Rowe P.N., Nienow A.W., Interparticle forces that suppress bubbling in gas fluidized beds, Chem. Eng. Sci., 26 (1971) 1293–1294.

Anjaneyulu P., Khakhar D., Rheology of a gas-fluidized bed, Powder Technol., 83 (1995) 29–34.

Arena U., Fluidized bed gasification, in: Scala F. (Ed.), Fluidized Bed Technologies for Near-Zero Emission Combustion and Gasification, Woodhead Publishing Limited, Cambridge (UK), 2013, pp. 765–812. doi: 10.1533/9780857098801.3.765

Avidan A., Yerushalmi J., Bed expansion in high velocity fluidization, Powder Technol., 32 (1982) 223–232.

Avidan A., Edwards M., Modeling and scale-up of Mobil's fluid-bed MTG process, Proceeding of Fluidization V, New York, 1986, pp. 457–464.

Babu S.P., Shah B., Talwalkar A., Fluidization correlations for coal gasification materials-minimum fluidization velocity and fluidized bed expansion ratio, AIChE Symp. Ser. (1978) 176–186.

Barletta D., Donsì G., Ferrari G., Poletto M., Aerated flow of fine cohesive powders in a Peschl shear cell, in: Powders and Grains 2005—Proceedings of the 5th International Conference on Micromechanics of Granular Media, Stuttgart, 2005, pp. 1033–1037.

Barletta D., Donsì G., Ferrari G., Poletto M., A Rotational Tester for the Characterization of Aerated Shear Flow of Powders, Part. Part. Syst. Charact., 24 (2007) 259–270. doi: 10.1002/ppsc.200701115

Barreto G., Yates J., Rowe P., The measurement of emulsion phase voidage in gas fluidized beds of fine powders, Chem. Eng. Sci., 38 (1983) 345.

Basu P., Biomass Gasification, Pyrolysis and Torrefaction: Practical Design and Theory, second ed., Academic Press – Elsevier, London, 2013.

Bin A.K., Prediction of the minimum fluidization velocity. Powder Technol., 81(1993) 197–199.

Botterill J.S.M., Teoman Y., Yüregir K.R., The effect of operating temperature on the velocity of minimum fluidization, bed voidage and general behaviour, Powder Technol., 31 (1982) 101–110.

Bourgeois P., Grenier P., The ratio of terminal velocity to minimum fluidising velocity for spherical particles, Can. J. Chem. Eng., 46 (1968) 325–328. doi: 10.1002/cjce.5450460508

Brandani S., Foscolo P.U., Analysis of discontinuities arising from the one-dimensional equations of change for fluidization, Chem. Eng. Sci., 49 (1994) 611–619.

Broadhurst T.E., Becker H.A., Onset of fluidization and slugging in beds of uniform particles, AIChE J., 21 (1975) 238–247. doi: 10.1002/aic.690210204

Bruni G., Lettieri P., Elson T., Yates J., The effect of process conditions on the fluidization behaviour of gas fluidized beds, AIChE Annual Meeting, 2004, pp. 2815–2820.

Bruni G., An investigation of the influence of fines size distribution and high temperature on the fluidization behaviour of gas fluidized beds linked with rheological studies, Ph.D. Thesis, University College London, 2005.

Bruni G., Colafigli A., Lettieri P., Elson T., Torque Measurements in Aerated Powders Using a Mechanically Stirred Fluidized Bed Rheometer (msFBR), Chem. Eng. Res. Des., 83 (2005) 1311–1318. doi: 10.1205/cherd.05092

Bruni G., Lettieri P., Newton D., Yates J.G., The influence of fines size distribution on the behaviour of gas fluidized beds at high temperature, Powder Technol., 163 (2006) 88–97. doi: 10.1016/j.powtec.2006.01.007

Bruni G., Barletta D., Poletto M., Lettieri P., A rheological model for the flowability of aerated fine powders, Chem. Eng. Sci., 62 (2007a) 397–407. doi: 10.1016/j.ces.2006.08.060

Bruni G., Lettieri P., Newton D., Barletta D., An investigation

of the effect of the interparticle forces on the fluidization behaviour of fine powders linked with rheological studies, Chem. Eng. Sci., 62 (2007b) 387–396. doi: 10.1016/j.ces.2006.08.059

Carman P.C., Fluid flow through granular beds, Trans. Inst. Chem. Eng., 15 (1937) 150. doi: 10.1016/S0263-8762(97)80003-2

Carr R.L., Evaluating flow properties of solids, Chem. Eng., 72 (1965) 163–168.

Carr R.L., Particle behaviour storage and flow, Bri Chem. Eng., 15 (1970) 1541–1549.

Castellanos A., The relationship between attractive interparticle forces and bulk behaviour in dry and uncharged fine powders, Adv. Phys., 54 (2005) 263–376.

Castellanos A., Valverde J. M., Quintanilla M., Fine cohesive powders in rotating drums: Transition from rigid-plastic flow to gas-fluidized regime, Phys. Rev. E-Stat. Nonlinear, Soft Matter Phys, 65 (2002) 1–7.

Castellanos A., Valverde J., Quintanilla M., The Sevilla powder tester: a tool for characterizing the physical properties of fine cohesive powders at very small consolidations, KONA Powder Part. J., 22 (2004) 66–81.

Chen Y.-M., Applications for Fluid Catalytic Cracking, in: Yang W.C. (Ed.), Handbook of Fluidization and Fluid-Particle Systems, Marcel Dekker Inc., New York, 2003, pp. 379–396.

Chen Z.D., Chen X.P., Wu Y., Chen R.C., Study on minimum fluidization velocity at elevated temperature, Proc. Chinese Soc. Electr. Eng., 30 (2010) 21–25.

Chirone R., Barletta D., Lettieri P., Poletto M., Measurement of high temperature powder flow properties to estimate interparticle forces in high temperature fluidization, in: The 8th International Conference for Conveying and Handling of Particulate Solids, 2015.

Chitester D., Kornosky R., Characteristics of fluidization at high pressure, Chem. Eng. Sci., 39 (1984) 253–261.

Colafigli A., Mazzei L., Lettieri P., Gibilaro L., Apparent viscosity measurements in a homogeneous gas-fluidized bed, Chem. Eng. Sci., 64 (2009) 144–152. doi: 10.1016/j.ces.2008.08.036

Coltters R., Rivas A.L., Minimum fluidization velocity correlations in particulate systems, Powder Technol., 147 (2004) 34–48. doi: 10.1016/j.powtec.2004.06.013

Cottaar E., Rietema K., A theoretical study on the influence of gas adsorption on interparticle forces in powders, J. Colloid Interface Sci., 109 (1986) 249–260.

Daniels T., Measurement of the drag on immersed bodies in fluidised beds. Rheol. Acta, 3(1965) 192–197.

Davidson J.F., Discussion following symposium on fluidization, Trans. Instn. Chem. Eng., 39 (1961) 230–232.

Davidson J.F., Harrison D., Fluidised Particles, Cambridge University Press, Cambridge (UK), 1963.

Delebarre A., Revisiting the Wen and Yu Equations for Minimum Fluidization Velocity Prediction, Chem. Eng. Res. Des., 82 (2004) 587–590. doi: 10.1205/026387604323142621

Diekman R., Forsythe W., Laboratory prediction of flow properties of fluidized solids, Ind. Eng. Chem., 45 (1953) 1174–1177.

Doichev K., Akhmakov N., Fluidisation of polydisperse systems, Chem. Eng. Sci., (1979) 2–4.

Donsì G., Massimilla L., Bubble-free expansion of gas-fluidized beds of fine particles, AIChE J., 19 (1973) 1104–1110. doi: 10.1002/aic.690190604

Ergun S., Fluid flow through packed columns. Chem. Eng. Prog., (1952) 48.

Fan L.S., Chemical looping systems for fossil energy conversions, Wiley-AIChE, New York, 2010.

Fletcher J., Deo M., Hanson F., Re-examination of minimum fluidization velocity correlations applied to Group B sands and coked sands, Powder Technol., 69 (1992) 147–155.

Formisani B., Girimonte R., Mancuso L., Analysis of the fluidization process of particle beds at high temperature, Chem. Eng. Sci., 53 (1998) 951–961.

Foscolo P.U., Gibilaro L.G., Waldram S.P., A unified model for particulate expansion of fluidized beds and flow in fixed porous media, Chem. Eng. Sci., 38 (1983) 1251–1260.

Foscolo P.U., Gibilaro L., A fully predictive criterion for the transition between particulate and aggregate fluidization, Chem. Eng. Sci., 39 (1984) 1667–1675.

Foscolo P.U., Gibilaro L., Fluid dynamic stability of fluidised suspensions: the particle bed model, Chem. Eng. Sci., 42 (1987) 1489–1500.

Furukawa J., Ohmae T., Liquid like properties of fluidized systems, Ind. Eng. Chem., 50 (1958) 821–828.

Geldart D., Types of gas fluidization, Powder Technol., 7 (1973) 285–292.

Geldart D., Wong A., Fluidization of powders showing degrees of cohesiveness—I. Bed expansion, Chem. Eng. Sci., 39 (1984) 1481–1488.

Geldart D., Wong A., Fluidization of powders showing degrees of cohesiveness—II. Experiments on rates of de-aeration, Chem. Eng. Sci., 40 (1985) 653–661.

Geldart D., Estimation of basic particle properties for use in fluid-particle process calculations, Powder Technol., 60 (1990) 1–13. doi: 10.1016/0032-5910(90)80099-K

Gibilaro L.G., Gallucci K., Di Felice R., Pagliai P., On the apparent viscosity of a fluidized bed, Chem. Eng. Sci., 62 (2007) 294–300. doi: 10.1016/j.ces.2006.08.030

Girimonte R., Formisani B., The minimum bubbling velocity of fluidized beds operating at high temperature, Powder Technol., 189 (2009) 74–81. doi: 10.1016/j.powtec.2008.06.006

Girimonte R., Formisani B., Effects of operating temperature on the bubble phase properties in fluidized beds of FCC particles, Powder Technol., 262 (2014) 14–21. doi: 10.1016/j.powtec.2014.04.041

Goo J.H., Seo M.W., Kim S.D., Song B.H., Effects of temperature and particle size on minimum fluidization and transport velocities in a dual fluidized bed, in: Proceedings of the 20th International Conference on Fluidized Bed Combustion, 2010, pp. 305–310.

Goroshko V.D., Rozembaum R.B., Toedes O.H., Approximate relationships for suspended beds and hindered fall, Izv. Vuzov, Neft. Gaz., 1 (1958) 125.

Grace J.R., The viscosity of fluidized beds, Can. J. Chem. Eng., 48 (1970) 30–33. doi: 10.1002/cjce.5450480106

Grace J.R., Hetsroni G., Handbook of multiphase systems, Hetsroni MG Edition, New York, 1982.

Grewal N.S., Gupta A., Total and gas convective heat transfer

from a vertical tube to a mixed particle gas-solid fluidized bed, Powder Technol., 57 (1989) 27–38. doi: 10.1016/0032-5910(89)80101-80109

Hartman M., Trnka O., Pohořelý M., Minimum and Terminal Velocities in Fluidization of Particulate Ceramsite at Ambient and Elevated Temperature, Ind. Eng. Chem. Res., 46 (2007) 7260–7266. doi: 10.1021/ie0615685

Horio M., Overview of fluidization science and fluidized bed technologies, in: Scala F. (Ed.), Fluidized Bed Technologies for Near-Zero Emission Combustion and Gasification, Woodhead Publishing Limited, Cambridge (UK), 2013, pp. 3–41. doi: 10.1533/9780857098801.1.3

Jackson R., The mechanics of fluidized beds, Trans. Instn. Chem. Engnr., 41 (1963) 22–48.

Jazayeri B., Applications for Chemical Production and processing, in: Yang W.C. (Ed.), Handbook of Fluidization and Fluid-Particle Systems, Marcel Dekker Inc., New York, 2003, pp. 421–444

Jean R., Fan L., On the model equations of Gibilaro and Foscolo with corrected buoyancy force, Powder Technol., 72 (1992) 201–205.

Jiliang M., Xiaoping C., Daoyin L., Minimum fluidization velocity of particles with wide size distribution at high temperatures, Powder Technol., 235 (2013) 271–278. doi: 10.1016/j.powtec.2012.10.016

Kai T., Murakami M., Yamasaki K., Takahashi T., Relationship between apparent bed viscosity and fluidization quality in a fluidized bed with fine particles, J. Chem. Eng. Japan, 24 (1991) 494–500.

Kanaoka C., Hata M., Makino H., Measurement of adhesive force of coal flyash particles at high temperatures and different gas compositions, Powder Technol., 118 (1991) 107–112. doi: 10.1016/S0032-5910(01)00300-X

Khoe G., Ip T., Grace J., Rheological and fluidization behaviour of powders of different particle size distribution, Powder Technol., 66 (1991) 127–141.

Knowlton T.M., Pressure and temperature effects in fluid-particle systems, in: Proceeding of Fluidization VII, New York, 1992, pp. 27–46.

Kono H., Aksoy E., Itani Y., Measurement and application of the rheological parameters of aerated fine powders—a novel characterization approach to powder flow properties, Powder Technol., 81 (1994) 177–187.

Kono H., Narasimhan S., Richman L.M., Ohtake T., Flow properties of homogeneously aerated, expanded emulsion phase of fine powders (quasi-solid emulsion phase viscosity), Powder Technol., 122 (2002) 168–176.

Kramers H., On the "viscosity" of a bed of fluidized solids, Chem. Eng. Sci., 1 (1951) 35–37.

Kunii D., Levenspiel, O., Fluidization Engineering, Butterworth-Heinemann, Newton (USA), 1991.

Lettieri P., A study on the influence of temperature on the flow behaviour of solid materials in a gas fluidized bed, Ph.D. Thesis, University College London, 1999.

Lettieri P., Yates J.G., Newton D., The influence of interparticle forces on the fluidization behaviour of some industrial materials at high temperature, Powder Technol., 110 (2000) 117–127. doi: 10.1016/S0032-5910(99)00274-0

Lettieri P., Newton D., Yates J.G., High temperature effects on the dense phase properties of gas fluidized beds, Powder Technol., 120 (2001) 34–40. doi: 10.1016/S0032-5910(01)00344-8

Lettieri P., Newton D., Yates J.G., Homogeneous bed expansion of FCC catalysts, influence of temperature on the parameters of the Richardson–Zaki equation, Powder Technol., 123 (2002) 221–231. doi: 10.1016/S0032-5910(01)00463-6

Lettieri P., Mazzei L., Analysis of the fluid-bed stability of FCC catalysts at high temperature in terms of bed elasticity, Particuology, 6 (2008) 30–37.

Leva M., Shirai T., Wen C.Y., Prediction of onset of fluidization in beds of granular solids, Genie Chim., 75 (1956) 33.

Leva M., Fluidization, McGraw-Hill Inc., New York, Toronto, London, 1959

Lin C.L., Wey M.Y., You S.D., The effect of particle size distribution on minimum fluidization velocity at high temperature, Powder Technol., 126 (2002) 297–301. doi: 10.1016/S0032-5910(02)00074-8

Lorences M.J., Patience G.S., Díez F. V, Coca J., Fines effects on collapsing fluidized beds, Powder Technol., 131 (2003) 234–240. doi: 10.1016/S0032-5910(03)00004-4

Lucas A., Arnaldos J., Improved equation for the calculation of minimum fluidization velocity, Ind. Eng. Chem. Process Des. Dev., 25 (1986) 426–429.

Lucas A., Arnaldos J., Casal J., Puigjaner L., High temperature incipient fluidization in mono and polydisperse systems, Chem. Eng. Commun., 41 (1986) 121–132. doi: 10.1080/00986448608911715

Massimilla L., Donsì G., Zucchini C., The structure of bubble-free gas fluidized beds of fine fluid cracking catalyst particles, Chem. Eng. Sci., 27 (1972) 2005–2015.

Materazzi M., Lettieri P., Mazzei L., Taylor R., Chapman C., Thermodynamic modelling and evaluation of a two-stage thermal process for waste gasification, Fuel, 108 (2013) 356–369.

Materazzi M., Lettieri P., Mazzei L., Taylor R., Chapman C., Fate and behavior of inorganic constituents of RDF in a two stage fluid bed-plasma gasification plant, Fuel, 150 (2015) 473–485.

Matheson G., Herbst W., Holt P., Characteristics of fluid-solid systems, Ind. Eng. Chem., 41 (1949) 1099–1104.

Mathur A., Saxena S., Particle classification scheme of saxena and ganzha and high-temperature bed voidage data at minimum fluidization, Powder Technol., 45 (1986) 287–289.

Miller C., Logwinuk A., Fluidization Studies of Solid Particles, Ind. Eng. Chem., (1951) 1220–1226.

Mills P., Snabre P., Settling of a Suspension of Hard Spheres, Europhys. Lett., 25 (1994) 651–656.

Molerus O., Theory of yield of cohesive powders, Powder Technol., 12 (1975) 259–275.

Molerus O., Effect of interparticle cohesive forces on the flow behaviour of powders, Powder Technol., 20 (1978) 161–175.

Murray J.D., On the mathematics of fluidization, J. Fluid Mech., 22 (1965) 57–63.

Mutsers S.M.P., Rietema K., The effect of interparticle forces on the expansion of a homogeneous gas-fluidized bed, Powder Technol., 18 (1977) 239–248. doi: 10.1016/0032-5910(77)80014-4

Newby R.A., Applications for Gasifiers and Combustors, in:

Yang W.C. (Ed.), Handbook of Fluidization and Fluid-Particle Systems, Marcel Dekker Inc., New York, 2003, pp. 397–420.

Newton D., PhD Dissertation, Department of Chemical Engineering, University College London, 1984.

Newton D., Smith G., Hird N., Comments on experimental data on the suitability of assigning a viscosity to the fluidized bed dense phase, in: Unpublished Paper Presented at the Fifth International Conference on Fluid Particle Interactions, 1999.

Pattipati R.R., Wen C.Y., Minimum fluidization velocity at high temperatures, Ind. Eng. Chem. Process Des. Dev. 20 (1981) 705–707. doi: 10.1021/i200015a022

Pell M., Jordan S.P., Effects of fines and velocity on fluid bed reactor performance, American Institute of Chemical Engineers, New York, 1987.

Piepers H., Cottaar E., Verkooijen A., Rietema K., Effects of pressure and type of gas on particle-particle interaction and the consequences for gas-solid fluidization behaviour. Powder Technol., 37 (1984) 55–70.

Quintanilla M., Castellanos A., Valverde J.M., Correlation between bulk stresses and interparticle contact forces in fine powders, Phys. Rev. E. Stat. Nonlin. Soft Matter Phys., 64, 031301 (2001).

Rapagna S., Foscolo P., Gibilaro L., The influence of temperature on the quality of gas fluidization, Int. J. Multiph. Flow, 20 (1994) 305–313.

Raso G., D'Amore M., Formisani B., Lignola P., The influence of temperature on the properties of the particulate phase at incipient fluidization, Powder Technol., 72 (1992) 71–76.

Reiling V.G., The effects of ultrafine particles on powder cohesion and fluidization, Ph.D. Thesis, Case Westner Reserve University, 1992.

Reina J., Velo E., Puigjaner L., Predicting the minimum fluidization velocity of polydisperse mixtures of scrap-wood particles, Powder Technol., 111 (2000) 245–251.

Riba J.P., Routie R., Couderc J.P., Conditions minimales de mise en fluidisation par un liquid, Can. J. Chem. Eng., 56 (1978) 26–30. doi: 10.1002/cjce.5450560104

Rice W.J., Wilhelm R.H., Surface dynamics of fluidized beds and quality of fluidization, AIChE J., 4 (1958) 423–429. doi: 10.1002/aic.690040409

Richardson J., Zaki W.N., Sedimentation and fluidisation: Part I, Trans. Inst. Chem. Eng., 32 (1954) 35–53

Richardson J., Jerónimo M., Velocity-voidage relations for sedimentation and fluidisation, Chem. Eng. Sci., 5 (1979) 1419–1422.

Rietema K., The Dynamics of Fine Powders, Springer Netherlands, Dordrecht, 1991. doi: 10.1007/978-94-011-3672-3

Rietema K., Cottaar E., Piepers H., The effects of interparticle forces on the stability of gas-fluidized beds—II. Theoretical derivation of bed elasticity on the basis of van der Waals forces between, Chem. Eng. Sci., 48 (1993) 1687–1697.

Ripp M., Ripperger S., Influence of temperature on the flow properties of bulk solids, Chem. Eng. Sci., 65 (2010) 4007–4013. doi: 10.1016/j.ces.2010.03.046

Romero J., Johanson L., Factors affecting fluidized bed quality, Chem. Eng. Prog. Symp. Ser., 58 (1962) 28–37.

Rowe P., Santoro L., Yates J., The division of gas between bubble and interstitial phases in fluidised beds of fine powders, Chem. Eng. Sci., 33 (1978) 133–140.

Rowe P., The effect of pressure on minimum fluidisation velocity, Chem. Eng. Sci., 39 (1984) 173–174.

Rumpf H., Zur theorie der zugfestigkeit von agglomeraten bei kraftuebertragung an kontaktpunkten, Chemie Ing. Tech., 42 (1970) 538–540.

Santomaso A., Lazzaro P., Canu P., Powder flowability and density ratios: the impact of granules packing, Chem. Eng. Sci., 58 (2003) 2857–2874. doi: 10.1016/S0009-2509(03)00137-4

Saxena S.C., Vogel G.L., The measurement of incipient fluidisation velocities in a bed of coarse dolomite at temperature and pressure, Chem. Eng. Res. Des., 55 (1977) 184.

Schwedes J., Review on testers for measuring flow properties of bulk solids, Granul. Matter, 5 (2003) 1–43. doi: 10.1007/s10035-002-0124-4

Siegell J.H., Early studies of magnetized fluidized beds, Powder Technol., 57 (1989) 213–220.

Shuster W., Haas F., Point Viscosity Measurements in a Fluidized Bed, J. Chem. Eng. Data, 5 (1960) 525–530.

Smith D., Haddad G., Ferer M., Shear strengths of heated and unheated mixtures of MgSO4 and CaSO4 powders. Model pressurized fluidized bed combustion filter cakes, Energy & fuels, 11 (1997) 1006–1011.

Subramani H.J., Mothivel Balaiyya M.B., Miranda L.R., Minimum fluidization velocity at elevated temperatures for Geldart's group-B powders, Exp. Therm. Fluid Sci., 32 (2007) 166–173. doi: 10.1016/j.expthermflusci.2007.03.003

Sun G., Grace J., The effect of particle size distribution on the performance of a catalytic fluidized bed reactor, Chem. Eng. Sci., 45 (1990) 2187–2194.

Sun G., Grace J.R., Effect of particle size distribution in different fluidization regimes, AIChE J., 38 (1992) 716–722. doi: 10.1002/aic.690380508

Thonglimp V., Hiquily N., Laguerie C., Vitesse minimale de fluidisation et expansion des couches fluidisées par un gaz, Powder Technol., 38 (1984) 233–253.

Tomasetta I., Barletta D., Lettieri P., Poletto M., The measurement of powder flow properties with a mechanically stirred aerated bed, Chem. Eng. Sci., 69 (2012) 373–381.

Tomasetta I., Barletta D., Poletto M., The High Temperature Annular Shear Cell: A modified ring shear tester to measure the flow properties of powders at high temperature, Adv. Powder Technol., 24 (2013) 609–617. doi: 10.1016/j.apt.2012.11.007

Toomey R. D., Johnstone H. F., Gaseous fluidization of solid particles. Chem. Eng. Progress, 48 (1952), 220–226.

Tsukada M., Kawashima K., Yamada H., Yao Y., Kamiya H., Analysis of adhesion behavior of waste combustion ash at high temperatures and its control by the addition of coarse particles, Powder Technol., 180 (2008) 259–264. doi: 10.1016/j.powtec.2007.04.005

Valverde J.M., Quintanilla M., Castellanos A., Mills P., The settling of fine cohesive powders, Europhys. Lett., 54 (2001) 329–334.

Valverde J.M., Castellanos A., Mills P., Quintanilla M., Effect of particle size and interparticle force on the fluidization behavior of gas-fluidized beds, Phys. Rev. E. Stat. Nonlin. Soft Matter Phys., 67, 051305 (2003).

Valverde J.M., Castellanos A., Effect of compaction history on the fluidization behavior of fine cohesive powders, Phys. Rev. E-Stat. Nonlinear, Soft Matter Phys., 73 (2006) 1–5.

Valverde J.M., Castellanos A., Bubbling Suppression in Fluidized Beds of Fine and Ultrafine Powders, Part. Sci. Technol., 26 (2008) 197–213.

Verloop J., Heertjes P., Shock waves as a criterion for the transition from homogeneous to heterogeneous fluidization, Chem. Eng. Sci., 25 (1970) 825–832.

Wallis G.B., One-dimensional two-phase flow, McGraw-Hill, New York, 1969.

Weimer A.W., Quarderer G.J., On dense phase voidage and bubble size in high pressure fluidized beds of fine powders, AIChE J., 31 (1985) 1019–1028. doi: 10.1002/aic.690310619

Wen C.Y., Yu Y.H., A generalized method for predicting the minimum fluidization velocity, AIChE J., 12 (1966) 610–612. doi: 10.1002/aic.690120343

Werther J., Hydrodynamics and mass transfer between the bubble and emulsion phases in fluidized beds of sand and cracking catalyst, in: Proc. 4th Int. Conf. On Fluidization, Edited by D. Kunii and R. Toei, AIChE., New York, 1983, pp. 93–101.

Winter F., Schratzer B., Applications of fluidized bed technology in processes other than combustion and gasification, in: in: Scala F., Fluidized Bed Technologies for Near-Zero Emission Combustion and Gasification, Woodhead Publishing Limited, Cambridge (UK), 2013, pp. 1005–1033. doi: 10.1533/9780857098801.5.1005

Wu S., Baeyens J., Effect of operating temperature on minimum fluidization velocity, Powder Technol., 67 (1991) 217–220.

Xie H.-Y., Geldart D., Fluidization of FCC powders in the bubble-free regime: effect of types of gases and temperature, Powder Technol., 82 (1995) 269–277. doi: 10.1016/0032-5910(94)02932-E

Yamazaki R., Han N., Sun Z., Jimbo G., Effect of chemisorbed water on bed voidage of high temperature fluidized bed, Powder Technol., 84 (1995) 15–22.

Yang W.C., Chitester D.C., Kornosky R.M., Keairrns D.L., A generalized methodology for estimating minimum fluidization velocity at elevated pressure and temperature, AIChE J., 31 (1985) 1086–1092.

Yates J., Newton D., Fine particle effects in a fluidized-bed reactor, Chem. Eng. Sci., 41 (1986) 801–806.

Yates J., Effects of temperature and pressure on gas-solid fluidization, Chem. Eng. Sci., 51 (1996) 168–205.

Zaki W.N., Richardson J.F., Sedimentation and fluidisation: Part I, Trans. Inst. Chem. Eng., 32 (1954) 35–53.

Zhao Y., Wei L., Rheology of gas–solid fluidized bed, Fuel Process. Technol., 68 (2000) 153–160. doi: 10.1016/S0378-3820(00)00122-3

Author's short biography

Paola Lettieri

Paola Lettieri FIChemE is a professor of chemical engineering at the University College London and head of the Fluidization Research Group. She has 20 years experience in particle technology and fluidization with applications spanning across the chemical, petrochemical, nuclear and energy-from-waste sectors. Her research focuses on the effect of process conditions on fluidization, encompassing experimental studies, mathematical modelling, rheology, X-ray imaging and reactor design. She has published 150 refereed articles and 6 book chapters, and has been awarded two prestigious fellowships from the Royal Academy of Engineering for her work in fluidization.

Domenico Macrí

Domenico Macrí is currently a PhD student in chemical engineering at the University College London. He received his Master's degree in chemical engineering from the University of Calabria in 2014. His main research interests focus on the effect of temperature on the defluidization of industrial reactive powders.

KONA Powder and Particle Journal No. 33 (2016) 109–126/Doi:10.14356/kona.2016020 Review Paper

Transport Properties and Segregation Phenomena in Vibrating Granular Beds †

Chun-Chung Liao [1] and Shu-San Hsiau [2]*

[1] *Department of Mold and Die Engineering, National Kauhsiung University of Applied Sciences, Taiwan*
[2] *Department of Mechanical Engineering, National Central University, Taiwan*

Abstract

Granular materials are common in daily life and in many industrial processes. Both fundamental research and industrial application studies are crucial for understanding the transport properties and segregation mechanisms of vibrating granular beds. One major related research topic is granular materials subjected to external vibration; such granular materials exhibit complex movement and Brazil nut segregation. Understanding the transport properties and the rising of an intruder immersed in granular materials is a challenge in granular flow research. This paper presents a review of transport properties and segregation phenomena in a vibrating granular bed, and discusses the relationship between transport properties and granular segregation. Furthermore, how the vibration conditions, liquid bridge force, bed height, surface roughness of granular materials, and a bumpy base of granular beds affect the transport properties, convection, and granular segregation are reported. The results indicate that the transport properties and segregation behavior are significantly influenced by the addition of small amounts of liquids and by the surface roughness and a bumpy base. Diffusive and convective motions are weakened as the base roughness increases, leading to a weaker Brazil nut effect.

Keywords: granular flows, vibrating granular beds, transport properties, convection, granular segregation, surface roughness

1. Introduction

Granular materials and powders are aggregates of discrete solid particles dispersed in an interstitial fluid. Granular materials (e.g., sand, salt, sugar, metal powders, glass beads, steel balls, coffee beans, pills, wheat, and rice) are commonly encountered in daily life and widely used in many industrial processes such as pharmaceutical manufacturing, gasification, pyrolysis, chemical manufacturing, mineral processing, metal powder injection molding, additive manufacturing, and powder metallurgy. The materials are also used for food transport and storage. Granular flows are also found in nature (e.g., avalanches, landslides, and debris flows) and can cause disasters. Understanding the transport properties and physical mechanism of granular flows is crucial; however, our understanding of granular materials is poor. Random particle motions resulting from interactive collisions between particles are the dominant mechanism influencing the flow behavior and transport properties of granular materials (Campbell, 1990). These materials do not flow homogeneously like a fluid when the external driving force is small. By contrast, they may behave like a gas if the granular system is relatively diluted and the external force is sufficiently large. Furthermore, the materials may behave like a solid when the external energy is insufficient. These three motion states may occur simultaneously or exist individually in granular systems (Jaeger, 1996). Although the rheological behavior of granular matter is complex, an understanding of granular matter is crucial in numerous industrial applications and for resolving various environmental problems.

Knowledge of granular segregation and transport properties has become crucial in many industrial processes (e.g., pharmaceutical manufacturing, foodstuff production, powder metallurgy, metal powder injection molding, and detergent, chemical, and plastic manufacturing) and in nature research (e.g., landslides, avalanches, and debris flows). In particular, granular segregation is a complex and poorly understood process. Therefore, numerous researchers have studied the transport properties and segregation mechanisms of granular materials (Bose et al., 2007; Breu et al., 2003; Bridgwater, 1976; Brito et al., 2008; Campbell,

† Received 9 July 2015; Accepted 4 September 2015
J-STAGE online 28 February 2016
[1] 415 Chien Kung Road, Kaohsiung 807, Taiwan
[2] No.300, Jhongda Rd. Jhongli City, Taoyuan County 32001, Taiwan
* Corresponding author: Shu-San Hsiau;
E-mail: sshsiau@cc.ncu.edu.tw
TEL: +886-3-426-7341 FAX: +886-3-425-4501

1997; Halsey and Levine, 1998; Herminghaus, 2005; Hsiau and Shieh, 1999; Hsiau and Yang, 2002; Hsiau and Yang, 2003; Hsiau et al., 2013; Khakhar et al., 1997; Kudrolli, 2004, 2008; Liao and Hsiau, 2009, 2010; Liao et al., 2010a, 2015; Liffman et al., 2011; Lozano et al., 2015; Lu and Hsiau, 2008; Natarajan et al., 1995; Saez et al., 2005; Shi et al., 2007; Tai and Hsiau, 2004; van der Vaart et al., 2015; Williams, 1976; Windows-Yule et al., 2015a). The segregation phenomenon in granular materials can be influenced by external driving conditions (Ciamarra et al., 2006; Hsiau and Yu, 1997; Hsiau et al., 2002), the interstitial fluid (Clement et al., 2010; Klein et al., 2006), the container geometry (Hsiau et al., 2002), and particle properties such as size (Cooke et al., 1996; Knight et al., 1993; Mobius et al., 2004; Zamankhan, 2013), density (Klein et al., 2006; Tai et al., 2010; Windows-Yule and Parker, 2015; Zeilstra et al., 2008), restitution coefficient (Brito and Soto, 2009), shape (Kudrolli, 2004; Williams, 1976), and friction coefficient (Kondic et al., 2006; Liao et al., 2012; Plantard et al., 2006). The segregation of granular materials also occurs in vibrating granular beds. The well-known Brazil nut problem associated with large particles (the so-called intruders) immersed in smaller granular materials has been studied extensively by using experiments, computer simulations, and theoretical models. Segregation has been demonstrated as occurring when grains vary in size, density, friction coefficient, and restitution coefficient. Segregation has also been observed in several configurations when an external driving force, in the form of a vibrating bed, shear cell, rotating drum, or chute flow, is applied to the system.

Granular temperature is defined as the specific fluctuation kinetic energy of particles, analogous to the thermodynamic temperature of a gas, and is a key parameter for describing the flow behavior of granular materials (Campbell, 1990; Hsiau et al., 2008; Liao et al., 2015; Ogawa, 1978; Wildman and Huntley, 2000; Zivkovic et al., 2011). Ogawa (1978) proposed the concept of granular temperature to quantify random motions of particles, and this concept has been widely used in related research. In the dense-gas kinetic theory for granular flows, granular temperature is assumed to be isotropically distributed. However, this key assumption is not observed in many practical scenarios, primarily because inelastic collisions and the frictional effect continually dissipate the energy of the granular materials. Thus, external energy must be continually introduced into the system to maintain the granular temperature. The granular temperature depends on the net energy between the energy generated by external vibration and the energy dissipated by the interstitial fluid, inelastic collisions, and frictional effect.

Understanding transport properties and segregation mechanisms is a challenge in granular material research. Studies have shown that granular materials may transition from a solid-like state to a liquid-like state when sufficient energy is supplied to the granular system (Hsiau and Yu, 1997; Liao et al., 2012). During the expansion of a granular bed, voids are formed between particles and they trigger particle reorganization; consequently, smaller particles fall through the voids to the bottom of the bed, resulting in size segregation (Hsiau and Yu, 1997; Rosato et al., 1987). Duran et al. (1993) showed that large disks rise upward continuously in small steps through the arching effect, in which an intruder is supported by the surrounding network of smaller particles. However, smaller particles may rise intermittently only when the excitation amplitude is sufficiently strong. Cooke et al. (1996) found that the segregation rate increased with the peak acceleration and size ratio. They also observed that convection cells play a crucial role in the segregation mechanism. Liao et al. (2012) demonstrated that the Brazil nut effect was reduced when the intruder surface roughness was high. Furthermore, they found that the penetration length of the intruder increased with a decrease in the intruder surface roughness and that the penetration length scaled exponentially with the vibration frequency. Segregation also occurs in a binary mixture system with various densities because of the buoyancy effect of denser particles sinking to lower levels of the granular bed while lighter particles rise. The granular temperature and convection also influence density-induced segregation in vibrating granular beds appreciably (Tai et al., 2010). When the number of filling layers is small, heavier beads with a low granular temperature migrate to the bottom regions. Thus, the granular temperature plays a significant role in density-induced segregation. For the higher filling layers, bulk convective motion is the main mechanism affecting segregation, and thus heavier beads cluster at the convection center. Tai and Hsiau (2004) determined the transport properties in vibrating granular beds and found that the convection strength increases when the dimensionless vibration velocity exceeds 2. van der Vaart et al., (2015) reported that large and small particles show an underlying asymmetry that is dependent on the local particle concentration, with small particles segregation faster in regions of many large particles and large particles segregation slower in regions of many small particles.

2. Vibrating granular bed equipment and transport property measurement technique

Vibrating granular beds are widely used in industrial processes for drying, transporting, mixing, and segregating granular materials. **Fig. 1** shows a schematic of the experimental apparatus used in the current study. A Techron VTS-100 electromagnetic vibration system driven by sinusoidal signals produced by a function gen-

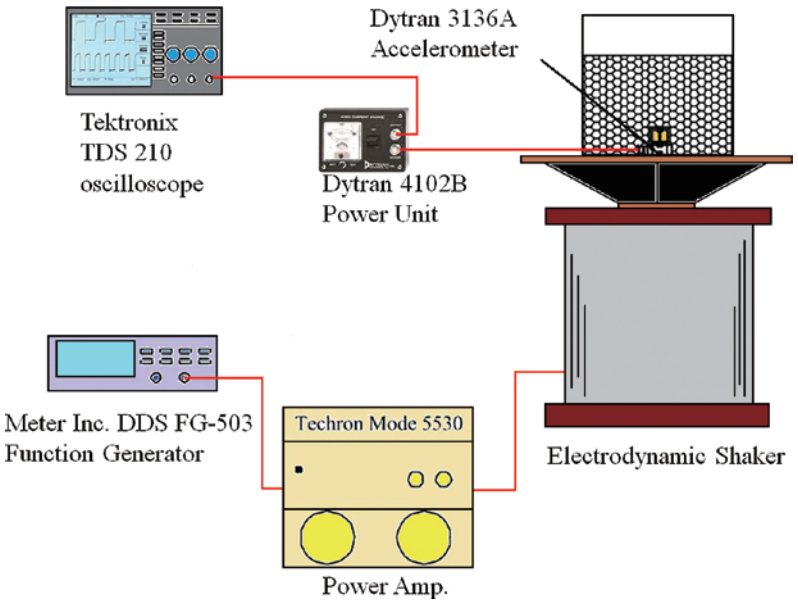

Fig. 1 Schematic drawing of the vibration granular bed apparatus.

erator (Meter Inc., DDS FG-503) and supplied through a power amplifier (Techron Model 5530) was used to vertically shake the assembly. The vibration frequency f and vibration acceleration a were measured using a Dytran 3136A accelerometer attached to the shaker and connected to an oscilloscope (Tektronix TDS 210). Given the radian frequency ($\omega = 2\pi f$), the amplitude A of the vibration was calculated using the relation $A = a/\omega^2$. The dimensionless vibration acceleration Γ is defined as $\Gamma = a/g$, where g is the gravitational acceleration.

The granular bed was vertically shaken. In a two-dimensional granular bed, rougher sidewalls induce stronger particle motions and convection cells (Hsiau et al., 2002). Therefore, a layer of glass beads with identical physical properties or a layer of emery paper was glued to the sidewalls of the container to induce a shear force sufficient for generating motions in the granular material. A high-speed charge-coupled device camera recorded the front view of the intruder motion. Using a particle-tracking method and image-processing system, the position of the intruder could be determined. All images were taken after the system had vibrated for at least 1 minute, to ensure that the flow field was in a steady state. The bed was divided into square bins, and an autocorrelation technique was employed to process the recorded images and determine the shift of each tracer particle between two consecutive images. The local velocities were then calculated from all the tracer velocities in the bin (Hsiau and Shieh, 1999; Hsiau et al., 2002; Liao et al., 2010b; Natarajan et al., 1995).

$$< u_i > = \frac{\sum_{k=1}^{N_i} u_{ki}}{N_i} \tag{1}$$

$$< v_i > = \frac{\sum_{k=1}^{N_i} v_{ki}}{N_i} \tag{2}$$

Here, $<u_i>$ and $<v_i>$ denote the ensemble average velocities in the horizontal and vertical directions, respectively, in the ith bin; the average velocities are obtained using the N_i tracer particles. The subscript k denotes the kth tracer particle in the ith bin.

The fluctuation velocities in the ith bin were defined as the root mean square value of the deviations between the local velocities and ensemble average velocities:

$$< u_i'^2 >^{1/2} = \sqrt{\frac{\sum_{k=1}^{N_i} (u_{ki} - < u_i >)^2}{N_i}} \tag{3}$$

$$< v_i'^2 >^{1/2} = \sqrt{\frac{\sum_{k=1}^{N_i} (v_{ki} - < v_i >)^2}{N_i}} \tag{4}$$

The granular temperature in the ith bin was then determined as

$$T_i = \frac{< u_i'^2 > + < v_i'^2 >}{2} \tag{5}$$

The average granular temperature of the entire bed was calculated as

$$T = \frac{\sum_i N_i \times T_i}{\sum_i N_i} \tag{6}$$

The granular temperature quantifies the fluctuation kinetic energy per unit mass associated with the random motions of the particles. The granular temperature was defined as the ensemble average of the fluctuation velocities of all the tracer particles in the vibrating granular bed. A higher granular temperature indicated a more energetic and fluidized vibrating bed.

Particle diffusion results from particle fluctuations. The concept of analyzing diffusive phenomena involving suspended particles undergoing Brownian motion in a liquid was first proposed by Einstein (1956). Campbell (1997) and Savage and Dai (1993) used the technique to investigate the self-diffusive behavior of granular flow systems through computer simulations. The self-diffusion coefficient D_{ij} is defined as

$$\lim_{t\to\infty} < \Delta x_i(t)\Delta x_j(t) > = 2D_{ij}t \tag{7}$$

where Δx_i and Δx_j are functions of t and represent the diffusive displacements in directions i and j, respectively, relative to their initial positions. Natarajan et al. (1995) and Liao and Hsiau (2009) employed a similar method in measuring self-diffusion in a vertical channel and in sheared granular flows, respectively.

Convection is also a crucial mechanism that affects particle motion and segregation in vibrating granular beds. Hsiau and Chen (2000) suggested that within each convection cell, the mass flow rates in the top, right, bottom, and left portions should be conserved. In the horizontal plane including the center of the convection cells, the horizontal velocity is zero and only a vertical velocity component $<v>_c$ exists. Hence, at this center location, the convection mass flow rate $\dot{m}$ (at the same horizontal level as the convection centers) can be defined as

$$\dot{m} = \int_{x=0}^{x=W} \frac{\rho_p \nu |< v >_c|}{2} dx \tag{8}$$

where ν is the solid fraction, ρ_p is the true bead density, and W is the half-width of the container measured in the aforementioned horizontal plane including the convection cell center. Assuming that the solid fraction is constant across each horizontal plane, the channel can be divided horizontally into experimental bins. Accordingly, J can be expressed as

$$J = \frac{\dot{m}}{\rho_p \nu 2W\sqrt{gd}} = \frac{\sum |< v >_c \Delta x|}{2W\sqrt{gd}} \tag{9}$$

where d is the bead diameter, Δx is the width of each bin. Hsiau and Chen (2000) detailed the definition and formation of bins.

3. Results and discussion

3.1 Transport properties in wet vibrating granular beds

Granular materials are common in many industries. In particular, the existence of a small amount of interstitial liquid in granular materials may complicate their handling or processing. Granular flow behavior changes considerably because of the formation and rupture of liquid bridges in wet granular materials (Grof et al., 2008; Liao et al., 2010c, 2013; Lim, 2014; Mason et al., 1999; Schulz et al., 2003). Some studies have investigated the forces generated by liquid bridges, both theoretically and experimentally (Ennis et al., 1990; Fisher, 1926; Mason and Clark, 1965; Mehrotra and Sastry, 1980; Mikami et al., 1998; Pitois et al., 2000). Fraysse et al. (1999) performed experiments to study how humidity affects the stability of sandpiles. They found that the maximal angle of stability increased with humidity. Hsiau and Yang (2003) used the discrete element method to study the effect of liquid content on the transport properties in a vertically vibrating wet granular bed. They observed that the liquid bridge force is a critical force influencing the particle motions and transport properties of wet granular systems. Liao and Hsiau (2010) found that the effect of the liquid bridge force on the dynamic behavior of wet granular matter was dependent on the kinetic energy of the granular system and liquid viscosity.

Many researchers have studied the dynamics of dry granular systems (Fortini and Huang, 2015; Hsiau et al., 2011; Knight et al., 1996; Tai and Hsiau, 2004). However, the flow behavior and dynamic properties of wet granular materials have received less attention. Most studies have focused on how liquid addition affects the flow behavior and dynamic properties of wet granular matter. Few experimental studies have examined how liquid surface tension affects the dynamic properties and convective behavior of granular matter.

The granular Bond number is somewhat reminiscent of the Bond number in fluid mechanics. Nase et al. (2001) defined the granular Bond number as follows:

$$Bo_g = \frac{F_c}{W_p} = \frac{2\pi R\gamma}{\frac{4}{3}\pi R^3 \rho_p g} = \frac{3\gamma}{2R^2\rho_p g} \tag{10}$$

where F_c is the capillary force, W_p is the particle weight, γ is the surface tension, g is the gravity and R is the sphere radius. The granular material becomes cohesive and the liquid bridge force becomes dominant when Bo_g exceeds 1. However, Nase et al. (2001) did not consider the effect of liquid content in their calculations. Some studies have reported that the number of liquid bridges and liquid bridge volume increase with liquid content, enhancing the

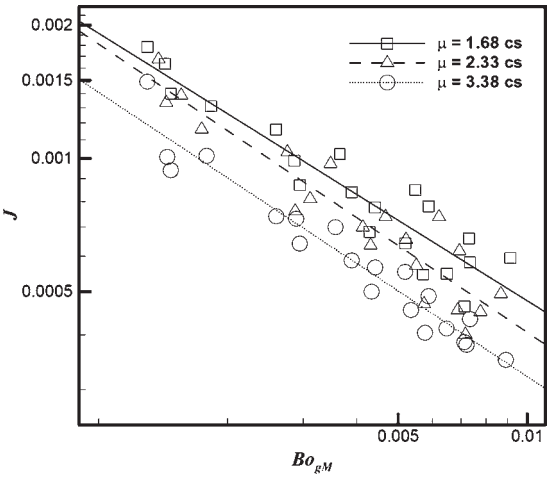

Fig. 2 The dimensionless convection flow rate plotted against the dimensionless modified granular Bond number (Bo_{gM}) in logarithmic scale (Hsiau S.S. et al., 2013).

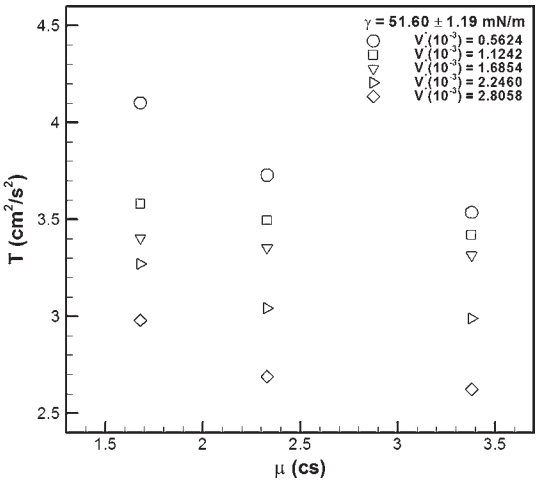

Fig. 3 The average granular temperatures plotted against with the added liquid viscosity μ with different liquid content at specific liquid surface tension (Hsiau S.S. et al., 2013).

strength of existing liquid bridges (Herminghaus, 2005; Kohonen et al., 2004; Liao et al., 2010c; Scheel et al., 2008). Herminghaus' research group (Herminghaus, 2005; Scheel et al., 2008) calculated the liquid content threshold for bridge formation to be approximately 7×10^{-4} and that capillary bridges were predominant when the liquid content was below 2.4×10^{-2}. Notably, the dimensionless liquid content V^* was defined as $V^* = V_w/(V_p + V_w)$, where V_w is the total volume of liquid added and V_p is the total volume of all beads in the bed. The number and strength of liquid bridges increase with the liquid content in the pendular state. Therefore, the granular Bond number should be modified by multiplying it with the dimensionless liquid content. The modified granular Bond number Bo_{gM} can be defined as

$$Bo_{gM} = Bo_g \times V^* = \frac{3\gamma}{2R^2\rho_p g} \times V^* \tag{11}$$

Fig. 2 shows the dimensionless convective flow rate plotted as a function of the modified granular Bond number on the logarithmic scale. The dimensionless convective flow rate decreases in a power decay with an increase in the modified granular Bond number for each specific liquid viscosity. The exponents for the different liquid viscosities (μ = 1.68, 2.33, and 3.38 cs) are –0.604, –0.651, and –0.642, respectively. This indicates that the convective flow rate decreases as the surface tension and added liquid content increase, resulting in stronger liquid bridge forces. A larger modified granular Bond number implies more and stronger liquid bridges and larger liquid bridge forces between particles; the larger liquid bridge forces result from the higher surface tension and liquid content. A stronger liquid bridge force reduces particle motion and interactive collisions. Energy dissipation caused by the formation and rupture of liquid bridges also increases with the liquid bridge force. Thus, because of the stronger liquid bridge forces, the convective flow rate decreases as the modified granular Bond number increases.

Fig. 3 shows the average granular temperature plotted as a function of the liquid viscosity for different V^* values at specific surface tensions. Clearly, the granular temperature decreases as the liquid viscosity increases (at a given liquid content). Adding more viscous liquid reduces particle motion and interactive collisions, thereby increasing the liquid bridge forces. A higher liquid viscosity leads to higher energy dissipation because of the formation and rupture of the liquid bridges between particles and the generation of a larger viscous force. Hence, an increase in the liquid viscosity reduces the strength of particle motion and interactive collisions, lowering the granular temperature. Sheared cell studies by Liao and Hsiau (2010) and Yang and Hsiau (2005) showed similar results, specifically that the presence of viscous and frictional force within a granular system causes high dissipation of the kinetic energy of particles. Therefore, the granular temperature decreases as the liquid viscosity and liquid content increase.

3.2 Segregation in wet vibrated granular beds

Adding liquid to granular materials creates liquid bridges among particles. The creation and disintegration of such bridges causes the behavior in a wet granular system to change substantially (Schulz et al., 2003). In recent years, although dry granular systems' segregation mechanism has been researched thoroughly, considerably few studies have researched the effect of adding small amounts of liquid on the segregation behavior of granular materials (Chou et al., 2010; Geromichalos et al., 2003; Li and McCarthy, 2003, 2006; McCarthy, 2009; Samadani

and Kudrolli, 2000, 2001). Geromichalos et al. (2003) found segregation behavior to increase as the liquid content was increased but began to drop after reaching a critical amount of liquid content. Hsiau and Yang (2003) researched the mixing and diffusion processes of a wet vibrating granular bed, finding that liquid content changed both processes. Samadani and Kudrolli (2000) discovered that segregation behavior decreased as more liquid was added and then reached a steady state once reaching a specific amount of liquid. The results of Chou et al. (2010) showed that the segregation condition can be determined from the repose angle of a granular mixture for wet granular systems, notwithstanding the addition of a liquid or viscosity.

The index used to calculate segregation degree is described below:

$$I = \sqrt{\frac{\sum_{i=1}^{n}(C_i - \overline{C})^2}{n-1}} \tag{12}$$

in which C_i represents the concentration of nylon beads in the ith cell, $\overline{C}$ represents the average concentration of nylon beads in the entire bed ($\overline{C}$ = 0.5), and n represents the number of sub-regions. The segregation index spans from 0.5 to 0; 0.5 signifies a totally segregated state while 0 signifies a consistently mixed state (Chou et al., 2010; Khakhar, 1997; Liao et al., 2010a).

In order to understand the effect of liquid bridges on the segregation of wet granular matter, some of the primary forces involved must first be discussed. The quasi-static force of the liquid bridge among particles can be estimated as $2\pi R\gamma$, in which γ is the surface tension of the liquid and R is the radius of the particle. When considering only capillary force, the viscosity of the added liquid is generally not considered in the assessment of the static properties of wet granular matter. However, the viscosity of the liquid present in the dynamic interactions among particles influences the bonding force. With regards to lubrication theory, the Reynolds Equation provides a measurement method for the viscous force, which is derived in this equation from two rigid spherical surfaces (Pitois et al., 2000; Samadani and Kudrolli, 2001). The equation suggests that the pressure P created within the liquid relies on the relative displacement of the two solid particles; the equation is written below:

$$\frac{\mathrm{d}}{\mathrm{d}r}\left[rH_{\mathrm{d}}^{3}(r)\frac{\mathrm{d}P(r)}{\mathrm{d}r}\right] = 12\eta r\frac{\mathrm{d}S}{\mathrm{d}t} \tag{13}$$

in which $H_{\mathrm{d}}(r) = S + r^2/R$ represents the distance between the two spherical surfaces at radial distance r from the center of the neck, S represents the distance between particles, and η represents liquid dynamic viscosity. Assuming that the particles are totally submerged into the liquid, the viscous force working on the particles can be expressed through integration of Eq. (13) two times:

$$F_{\mathrm{v}} = -\frac{3}{2}\pi\eta R^2\frac{1}{S}\frac{\mathrm{d}S}{\mathrm{d}t} \tag{14}$$

A liquid bridge requires a correction coefficient to be added to Eq. (14), which creates the following equation:

$$F_{\mathrm{v}} = -\frac{3}{2}\pi\eta R^2\left[1-\frac{D_{\mathrm{s}}}{H(b)}\right]^2\frac{1}{D_{\mathrm{s}}}\frac{\mathrm{d}D_{\mathrm{s}}}{\mathrm{d}t} \tag{15}$$

in which b represents the radius of the wet area, and D_{s} represents the length of the liquid bridge. The total dynamic force of the liquid bridge is found using the superposition of the capillary force and the viscous force. Samadani and Kudrolli (2001) applied Reynolds Equation and discovered that the viscous force is proportional to the liquid viscosity.

The segregation index was applied to measure the degree of granular segregation within a granular system. **Fig. 4** depicts variations to the final segregation index once a steady state is reached due to adding liquids of varying viscosities. In most cases, the segregation index decreased as the liquid content and viscosity increase. Increasing the quantity and viscosity of the liquid added to the granular materials results in both more and stronger liquid bridges created among the particles. Consequently, the energy that dissipates as a result of the creation and disintegration of said liquid bridges also increases, thus decreasing particle motion within the wet system. As has been found in prior studies, the particles' kinetic energy probably dissipates due to the creation of liquid bridge forces among the particles in the wet system (Geromichalos et al., 2003; Schulz et al., 2003). The liquid bridges generally pushed the small glass beads together to clump and form larger clusters, thereby decreasing the percolation

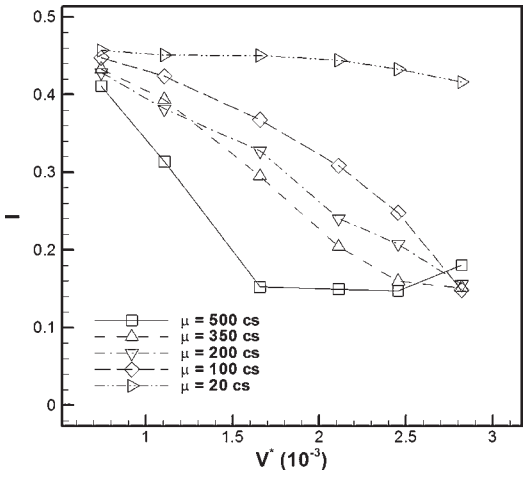

Fig. 4 The segregation index of the final state in the shaker with V^* with different viscosities of added silicon oil (Liao C.C. et al., 2010c).

effect on the segregation amount (Samadani and Kudrolli, 2000, 2001). The amount of segregation did not change much even when increasing the liquid content with a low liquid viscosity of 20 cs, as shown in **Fig. 4**, which suggests that the liquid bridge force is insignificant with no substantial effect on either the particles' motion or segregation. Furthermore, **Fig. 4** shows that the addition of a highly viscous liquid (500 cs) to the granular materials significantly decreases the final segregation index and increases the value of V^*. Nevertheless, the final segregation index remained constant as $V^* \geq 1.655 \times 10^{-3}$, which is similar to that the findings of Samadani and Kudrolli (2000). Remarkably, the final segregation index showed a small increase in the highest liquid content and viscosity ($V^* = 2.8137 \times 10^{-3}$ and $\mu = 500$ cs). This is the liquid content and viscosity that creates the strongest liquid bridge force, which leads to the most feeble particle motion, which subsequently results in a minor increase in the final segregation index (**Fig. 4**).

Figs. 5(a)–5(e) are photographs taken of the amount of segregation in the binary mixtures for varying liquid contents and viscosities. **Fig. 5(a)** depicts the initial amount of segregation, where the smaller glass beads are positioned above the larger nylon beads. Meanwhile, the last segregation amount of the dry system is revealed in **Fig. 5(b),** which shows that complete segregation was attained once the larger particles moved to the upper bed. As presented in the aforementioned material, the liquid that was added to the granular materials can be assumed to restrict the movement of particles, reducing segregation in many cases. However, the addition of extremely little liquid with a very low viscosity did not influence the final segregation amounts ($V^* = 0.7428 \times 10^{-3}$, $\mu = 20$ cs). This finding is depicted in **Fig. 5(c)** and suggests that the liquid bridge force was too weak to lessen particle motion or significantly affect the segregation index. **Fig. 5(d)** depicts the final condition (the consistently mixed state) of the binary mixtures for $V^* = 1.6550 \times 10^{-3}$ and $\mu = 500$ cs. The adequate liquid content and viscosity reduced the driving segregation force due to the creation of the liquid bridge force. As a result, the amount of segregation was converted into the final homogeneous mixing state illustrated in **Fig. 5(d)**. **Fig. 5(e)** shows the final nonhomogeneous mixing state for $V^* = 2.8137 \times 10^{-3}$ and $\mu = 500$ cs. A small portion of the upper part of the container, which is circled in **Fig. 5(e)**, clearly depicts the nonhomogeneous mixing state. The particle motions were not sufficiently adequate for obtaining the homogeneous mixing state with the addition of the largest liquid content and viscosity to the granular materials ($V^* = 2.8137 \times 10^{-3}$ and $\mu = 500$ cs). Therefore, this study has demonstrated that the amount of segregation can be managed by altering the liquid content and viscosity.

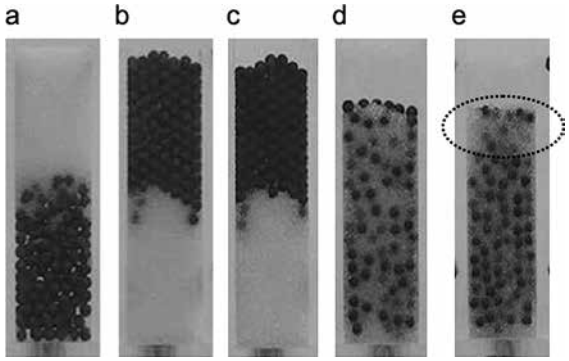

Fig. 5 Snapshots of the level of segregation of binary granular mixtures: (a) initial segregation level of the dry system, (b) steady segregation level of the dry system, (c) steady segregation level of the wet system, $\mu = 20$ cs and $V^* = 0.7428 \times 10^{-3}$, (d) steady homogeneous and mixed level of the wet system, $\mu = 500$ cs and $V^* = 1.6550 \times 10^{-3}$, (e) steady non-homogeneous mixing level of the wet system $\mu = 500$ cs and $V^* = 2.8137 \times 10^{-3}$, with the circled part depicting the non-homogeneous mixing region (Liao C.C. et al., 2010c).

3.3 Influence of bed height on convection cell formation

The convection of granular materials is vital to granular flow. Vibration acceleration, once it surpasses a specific threshold, causes convective flow patterns. In addition, convection is important to granular segregation behavior (Hsiau et al., 2002; Huerta and Ruiz-Suarez, 2004; Liao et al., 2014; Saez et al, 2005). The granular materials within a bed move in a circular pattern, from the top of the bed downward along the sidewalls toward the bottom and then toward the top through the center of the container. The occurrence of vertical vibration causes the granular system to become fluid, which thus transforms the granular bed from a consolidated state to a fluid-like state. In certain situations, the flow of granular materials between the top and bottom occurs as convection cells. In recent years, such convection has attracted many researchers (Chung et al., 2013; Gallas et al., 1992; Hsiau and Chen, 2000; Huerta and Ruiz-Suarez, 2004; Saez et al., 2005; Viswanathan, 2011). Inelastic collisions cause energy dissipation in a vibrofluidized granular system, which results in larger densities and temperature gradients. Once the temperature gradient becomes big enough, convection occurs (Wildman et al., 2001). Elperin and Golshtein (1997) applied a particle dynamics method to evaluate the influence of convection and friction on the level of segregation within a two-dimensional vibrating bed and discovered that the segregation rate significantly increased with convective roll. Furthermore, Majid and Walzel (2009) realized that convection cell patterns are contingent on the operating conditions. Hsiau et al. (2002) researched the effect of container geometry, wall friction, and vibration conditions on

convection cells in a two-dimensional vibrating bed and determined that reverse convection cells were created when the two sidewalls had an 8° incline. Klongboonjit and Campbell (2008) completed a soft-particle recreation, in which convection strength was usually augmented with particle stiffness, as well as upon reaching a maximum value, the convective strength then decreases even with the further increase of particle stiffness. Fortini and Huang (2015) discovered that wall-induced convection happens within the bouncing bed region of the parameter's space, within which the granular bed acts similarly to a bouncing ball.

The original bed height can be non-dimensionalized by dividing it by bead diameter d, resulting in $H = h/d$. H spans from 15 to 90 with intervals of 5, which is consistent with a range of h from 3 to 18 cm. **Fig. 6** depicts the variations of dimensionless convection strength J and overall average granular temperature T^* with the initial dimensionless bed height H for the fixed vibration conditions of $f = 40$ Hz and $\Gamma = 16$. The value of J has two distinct peak values, which are $H = H_{p1}$ (= 45) and H_{p2} (= 70), and a single minimum value, which is $H = H_v$ (= 75). Augmenting H from 15 to 45 causes the dimensionless convection strength to significantly increase (in an almost linear manner). A smaller amount of material (smaller H) in the bed fluidizes the bed materials more violently than if they had been in a thicker bed. When height of the initial bed surpasses the first critical (maximum) value H_{p1}, the convection strength starts decreasing as the bed height increases. Once the bed height surpasses a specific value, a "solid-like" flow region is created within the material at the bottom of the bed due to gravity. The beads in this solid-like region show weak relative movement and interactive collisions, which both dissipate the energy that comes from the shaker, thus resulting in less energy being transferred to the convection cells in the upper bed layers (the fluid-like region).

Increased convection strength as a result of increased bed height stops once H surpasses the second peak H_{p2}, at which point the whole solid-like region acts similar to a solid body. An increase in H signifies a thicker "solid." Said thicker solid can absorb more energy, thus transferring less energy to then be received by the upper convection region, ultimately resulting in weaker convection. **Fig. 6** shows the two peaks and one valley of the curve for T^*. The aforementioned variation of the initial bed height with T^* resembles the variations in the J values. A larger J value denotes that the granular bed becomes more active when the T^* value is higher.

The granular temperature of each individual horizontal layer can be determined by taking the average of the root-mean-square fluctuation velocity of each tracer particle that moves through the layer. **Fig. 7** depicts variations of the granular temperature with the dimensionless height y/d within a fixed vibration environment of $f = 40$ Hz, $\Gamma = 16$, and $H = 90$. The curve can best be described categorized into three regions. The granular temperatures of the lower bed have small values near 0 and can vary ($y/d < 60$), which suggests that the beads in this section have extremely weak motion, resulting in the lower bed acting like a solid. H_S indicates the thickness of this solid-like region. The beads located above the solid-like region have substantial convective motion ($60 < y/d < 85$) and significantly larger granular temperatures than those in the solid-like region. The so-called "liquid-like" region features convective rolling. H_C indicates the thickness of the convection rolls. The beads in certain layers (free surface, $y/d > 85$) have substantially higher granular temperatures.

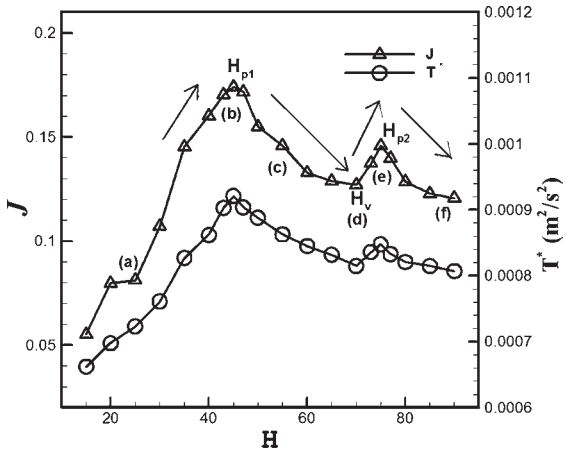

Fig. 6 Variations of the dimensionless convection strength J and the overall average granular temperature T^*, with changes to the initial dimensionless bed height H, with a fixed vibration environment of $f = 40$ Hz and $\Gamma = 16$ (Hsiau S.S. et al., 2011).

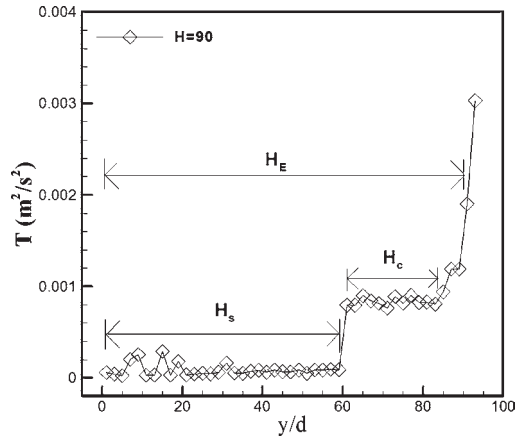

Fig. 7 The granular temperature varying with the dimensionless height with a fixed vibration environment of $f = 40$ Hz, $\Gamma = 16$, and $H = 90$. The inset plot depicts the total bed thickness in complete expansion state H_E, the thicknesses of "solid-like" region H_S and the thickness of convection region H_C (Hsiau S.S. et al., 2011).

The total bed thickness throughout the state of maximal expansion is written as H_E. The inset depicts the total bed thickness throughout complete expansion state H_E, the thickness of solid-like region H_S, and the thickness of convection region H_C.

Fig. 8 depicts the various values of H_E, H_C, and H_S, and of J with H in the fixed vibration environment of $f = 40$ Hz and $\Gamma = 16$. These three thicknesses' data were found through the analysis of the experimental plots of the granular temperature versus initial bed thickness, as shown in **Fig. 7**. The expansion height (open square symbols) goes up practically linearly as the initial bed height is increased, and $H_E > H$. The bed has two different flow regimes: a convection region with thickness H_C and a solid-like region with thickness H_S ($H_E \cong H_C + H_S$). With H values between 25 and 45, all of the bed material moves to create two symmetric convection cells, and the bed has no solid-like region ($H_S \cong 0$, $H_C \cong H$). Furthermore, convection cell height H_C maintains its increasing behavior as the initial bed height becomes larger. Once the initial bed height surpasses 47, the mass of the bed becomes too thick to be completely fluidized, and the solid-like region is forced to expand. The solid-like region's height begins to increase with an increasing H, as shown in **Fig. 8**. A thicker solid-like region shows that the beads within it utilize more input energy, thus leaving less energy for the upper material, which results in decreased H_C. This tendency reverses once $H = 70$. For $70 < H < 75$, the solid-like region appears to be a rigid, solid body, in which the "solid" beads dissipate less energy, which causes more energy to be transferred into the upper layers. While the thicknesses of the solid-like region remain similar in both situations, the thickness of the convection cells increases with a growing H. As the bed mass (H) further increases, H_C starts to decrease.

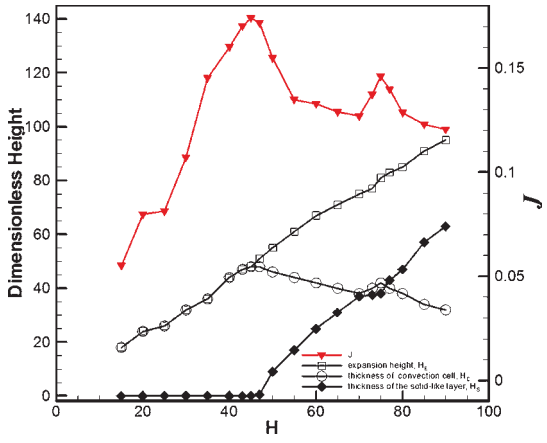

Fig. 8 The thicknesses of total expansion height H_E, convection cells H_C, "solid-like" region H_S, and dimensionless convection strength J, against initial bed height H, in a fixed vibration environment of $f = 40$ Hz, $\Gamma = 16$ (Hsiau S.S. et al., 2011).

The relationship between H_C and the initial bed height closely resembles the variation of J values with the initial bed height, both of which feature two peaks (H_{p1} and H_{p2}) and a valley (H_v). Although the initial bed height influences convection strength, these two parameters were not found to be monotonically related. The thickness of the convection rolls substantially influences dimensionless convection strength, and the thicker the convection roll is, then the more fluidized the granular bed in the container is. Therefore, J and H_C ought to present similar tendencies versus initial bed height. **Fig. 8** depicts the relationship between J and H_C.

3.4 Influence of intruder surface roughness on granular segregation in a vertically vibrated bed

Much research has already investigated friction-induced segregation, which is a serious problem in many industries (Kondic et al., 2006; Pohlman et al., 2006; Plantard et al., 2006; Liao et al., 2014). Srebro and Levine (2003) evaluated the effect of friction with regard to the segregation of binary granular mixtures by combining Edwards' thermodynamic hypothesis using a simple mechanical model and found that segregation took place with specific degrees of compactness within the binary mixtures of grains with varying frictional properties. Furthermore, Kondic et al. (2006) found that friction led to granular segregation in a horizontally shaken container with a mound centered at the bottom. Ulrich et al. (2007) performed experiments that resulted in a transition from the reverse Brazil nut effect to the Brazil nut effect when the particle friction coefficient became higher due to long periods of shaking, which was explained as the result of sidewall-driven convection and buoyancy. Liao et al. (2014) discovered that the internal friction did not significantly affect Brazil nut granular segregation when dealing with a small filling bed height. However, internal friction was vital for the rise dynamics of intruders when dealing with a large bed height in a granular system. Unac et al. (2014) further discovered that isolated intruders may sometimes rise when tapped based not only on the size ratio but also on the environment's degree of ordering.

Recently, research regarding the rise of an intruder in a granular fluid has garnered considerable attention. However, the influence of surface roughness on a rising intruder has not been studied as much but is worthy of further investigation. Understanding the influence of friction on segregation in vibrating granular systems may provide insights into unknown physical mechanisms.

Fig. 9 shows the time dependence curves of the intruder height of three degrees of surface roughness of intruders and three Γ values (3, 4.2, and 4.8) with a vibration frequency of 35 Hz. The slow rise of the intruder from just

above the bottom to the free surface occurs in all cases because of the Brazil nut effect. The rougher the intruder is, the longer the rise time is, and vice versa. Energy dissipation happens during the binary collision of particles due to friction and inelastic collisions. The friction that exists between the intruder and the beads is vital for the rise dynamics of the intruder. Furthermore, the restitution coefficient values of each intruder may affect the rise dynamics. In a considerably densely packed bed, the drag between the intruder and beads typically results in the dissipation of the rising intruder's kinetic energy. Rougher intruders experience greater degrees of dissipation due to their larger friction coefficient and smaller restitution coefficient, thus creating weaker upward motion and a longer rise time, as is shown in the curves in **Fig. 9**. Moreover, small Γ values cause the intruder dynamics to be divided into two stages during the rise of the intruder. The rise experienced is slower in the lower part of the granular bed and quicker in the upper part (convection region). In such a condition, the system has less external energy, and bead compactness is higher, which creates weaker motion in the bed's lower part. Therefore, the intruder rises more slowly as a consequence of the high friction between said intruder and the beads located in the lower part of the bed during the vibration cycle, thus causing weaker percolation. On the other hand, the convection cell increases in size and strength as the value of Γ increases. Thus, the intruder rises more easily and quickly and demonstrates a generally linear evolution with larger Γ values.

Furthermore, the slopes of the intruders' curves with three varying degrees of surface roughness all resembled one another in the bed's upper part. The convection mechanism in the bed's upper part controlled the rise dynamics, and convection strength was found to be similar within the studied vibration conditions. Moreover, intruders with a smooth surface had reduced friction, and the rise time variation was not significant with higher Γ values.

Nahmad-Molinari et al. (2003) defined penetration length P_l and discovered that the intruder penetrates the granular bed due to its inertia over a small distance during each cycle. This study further found that the intruder's kinetic energy dissipates because of friction as it enters the granular bed during each cycle. Based on the aforementioned findings, the researchers developed a model based on a simple energy balance during each cycle:

$$\frac{1}{2}m_i v_t^2 = \beta P_l \tag{16}$$

in which m_i signifies the intruder mass, v_t signifies the intruder take-off velocity upon the system reaching a negative acceleration, $a_i = -g$, β signifies the drag between the beads and intruder, and P_l signifies the penetration length. The parameter v_t is the value of $\dot{z}(t)$ when $\dot{z}(t) = -g$, and $z(t) = A\sin(\omega t)$. Therefore, the following can be derived:

$$v_t = \left[A^2\omega^2 - g^2/\omega^2\right]^{1/2} \tag{17}$$

The position of the intruder is graphed as a function of the vibration cycle ($t\omega/2\pi$) with the condition of $\Gamma = 3$ and $f = 35$ Hz (**Fig. 10**). Each curve's slope is the exact same as the penetration length of the corresponding intruder (Nahmad-Molinari et al., 2003). The lower parts of the curves have linear fits as a result of the convection's decrease. The linear fit of the data reveals the penetration length of each vibration cycle. The penetration length is graphed as a function of the vibration amplitude for varying intruders (**Fig. 11**), which shows that the penetration length decreases as the surface roughness of the intruder increases under the given vibration conditions, as well as that the penetration length increases as the vibration amplitude increases.

Eq. (16) shows that the penetration length is inversely proportional to drag β. Rougher intruders with larger β

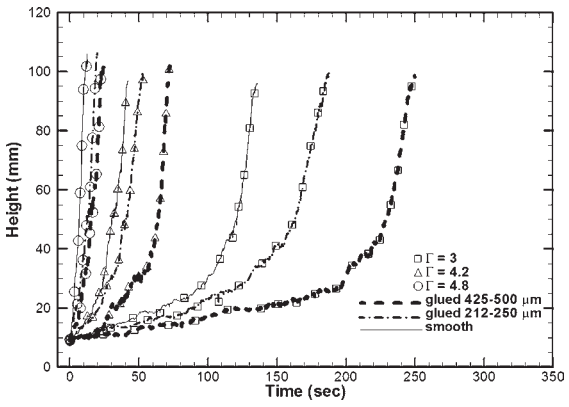

Fig. 9 Intruder height as a function of vibrating time with the conditions of $\Gamma = 3$, 4.2, 4.8 and $f = 35$ Hz (Liao C.C. et al., 2012).

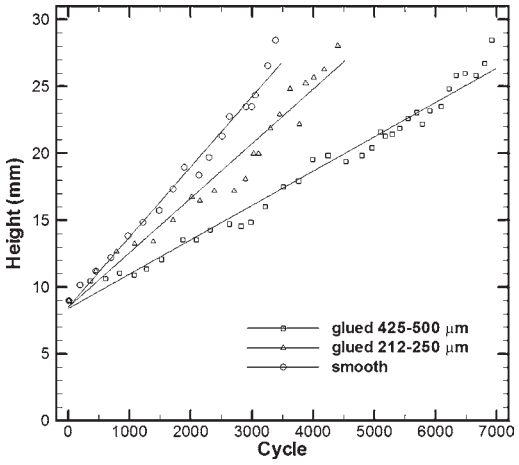

Fig. 10 Intruder height as a function of vibrating cycle ($t\omega/2\pi$) (Liao C.C. et al., 2012).

dissipate more kinetic energy and thus have shorter penetration lengths. To test this hypothesis, we calculated β using Eq. (16). By plotting β against the vibration amplitude (**Fig. 12**), the β value increased with the intruder friction coefficient under the condition of a given vibration amplitude. Higher drag causes higher intruder friction coefficients due to the increased friction between the beads and the intruder during its rise. The curves in **Fig. 12** show that β is reduced as the vibration amplitude becomes bigger. Both convection and fluidization increase along with the vibration amplitude within the system. The flow behavior of the granular materials further transforms from a quasistatic state into a dynamic state. The strength of both the particle motions and the collisions is enhanced when in the dynamic state. Consequently, friction has a less serious effect on the intruder's rise dynamics. Even with varying intruder friction coefficient values, increasing the vibration amplitude reduces both β and its variations.

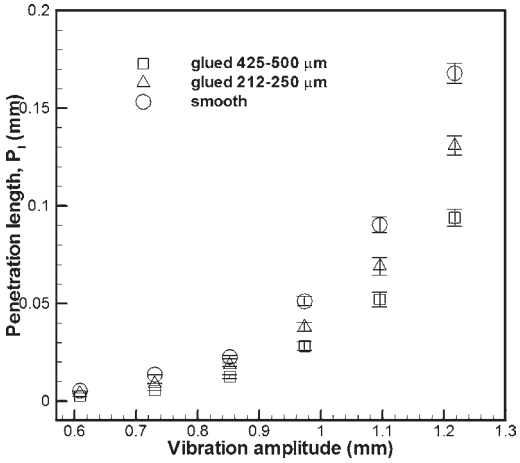

Fig. 11 Penetration length as a function of vibration amplitude for intruders with varying degrees of surface roughness (Liao C.C. et al., 2012).

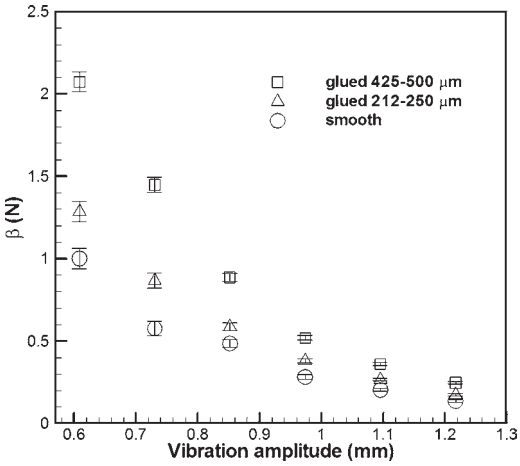

Fig. 12 Drag β as a function of vibration amplitude for intruders of varying degrees of surface roughness (Liao C.C. et al., 2012).

In **Fig. 13**, the penetration length is plotted as a function of vibration frequency on the logarithmic-normal scale for intruders with varying degrees of surface roughness. The straight lines, which are found with the least-squares method, reveal the exponential decay of the penetration length with the frequency. Vanel et al. (1997) found that the dimensionless rise time (the number of vibration cycles) is scaled exponentially when $f < 15$. Similarly, the current study's dimensionless rise time was proportional to $1/P_l$, even though the vibration frequency range does not match completely. The discrepancy is most likely due to the use of different experimental containers, in which would have undoubtedly affected particle motion and flow behavior. A two-dimensional container was used in our experiments, while a three-dimensional one was employed by Vanel et al. (1997). Nevertheless, both studies found convection to be vital to the rise dynamics of the intruder.

3.5 Effect of a bumpy base on granular segregation and transport properties for vertical vibration

In a real granular system, the wall conditions may also be bumpy or uneven. The effect of a bumpy base on the rise dynamics of an intruder and transport properties has not been previously examined, and it offers insights into the complexities of segregation. Farkas et al. (1999) performed experiments and simulations to study the horizontal transport of granular particles in a vertically vibrating bed with a sawtooth-shaped base. Levanon and Rapaport (2000) investigated the horizontal flow of granular materials in a vertically vibrating sawtooth-shaped base. Their simulation results showed that the induced flow rate varies with the bed height and that counterflow could occur

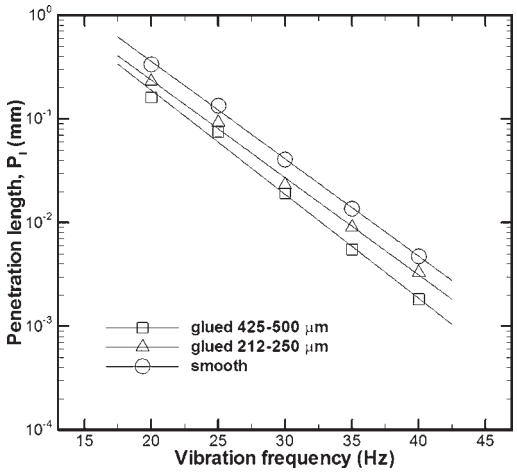

Fig. 13 Penetration length plotted against vibration frequency in logarithmic-normal scale for intruders with varying degrees of surface roughness. The straight lines represent fit data obtained using the least-square method (Liao C.C. et al., 2012).

at different levels. Hsiau et al. (2002) indicated that convection and segregation rates increase with the sidewall friction coefficient in a vertical shaker. Hsiau and Yang (2002) reported that for sheared granular flow, rougher wall conditions enhance the transport properties of granular materials. Hsiau et al. (2006) reported that the stress and self-diffusion coefficients of particles are inversely proportional to the internal friction coefficient. Lu and Hsiau (2008) investigated the mixing behavior in vibrating granular beds by using a discrete element method. They demonstrated that the mixing rates increase exponentially with the convection and vertical self-diffusion coefficient. Ma et al. (2014) found that even with the same size and density ratio of the intruder to the background particles, the intruder exhibits a distinct behavior at the given vibrational conditions. Windows-Yule et al. (2015b) demonstrated that even for a fixed input energy from the wall, energy conveyed to the granular system under excitation could vary significantly dependent on the amplitude and frequency of the driving oscillations.

In the current study, a layer of densely packed glass beads was glued to the base of a container to form a bumpy base surface. To quantify the relative size of the particles on the base, we defined a base factor R_f:

$$R_f = \frac{P_d}{d_b} \tag{18}$$

where P_d is the diameter of the glued beads and d_b is the diameter of immersed glass beads ($d_b = 2$ mm in this study). Four different base factors ($R_f = 0$, 0.5, 1, 2) were used; $R_f = 0$ corresponded to a flat base surface, and $R_f = 2$ represented the largest wall protrusions.

Fig. 14 shows the rise time plotted as a function of R_f for different Γ at $f = 25$ Hz. The rise time increases with R_f for each Γ because the strength of the particle motions is reduced for a large base factor. The rise times also decrease as the Γ for each container base condition increases. Previous research has shown that for higher Γ, the granular bed becomes more fluidized, enhancing the percolation effect and resulting in a faster rise time. Additionally, the influence of a bumpy base on the rise time is significant at smaller Γ and becomes less pronounced at higher Γ because more energy can be introduced in the system at higher Γ. Previous studies have shown that the rise time is similar if the granular bed is fluidized. Increased fluidization could be achieved with higher Γ. Hence, the rise time increases slightly at greater Γ in bumpy surface instances. By contrast, the particle motions are weakened and the granular bed becomes less fluidized for smaller Γ. Under these conditions, the base roughness has significantly influences the dynamic properties of the granular material and leads to a larger variation of the rise time for different base conditions.

The transport properties of the immersed glass beads play a crucial role in the Brazil nut mechanism. Here, we discuss the Brazil nut problem from the viewpoint of micromechanics by determining the transport properties of immersed glass beads. **Fig. 15** shows the average granular temperature and rise time as a function of R_f for $f = 25$ Hz and $\Gamma = 3$. The base condition significantly influences the granular temperature. The average granular temperature decreases and the rise time increases with an increase in the base factor. The total external energy is constant for fixed vibration conditions. More energy could be introduced into the bed to increase the granular temperature for a small base factor. The particle motions and interactive collisions become stronger and the bed shows greater fluidization as the granular temperature increases. Hence, the intruder experiences less resistance during the rise process, which leads to a shorter rise time for a larger granular temperature.

Particle diffusion is a crucial parameter in studying the mixing and segregation of granular materials. The self-diffusion coefficients are determined from the rela-

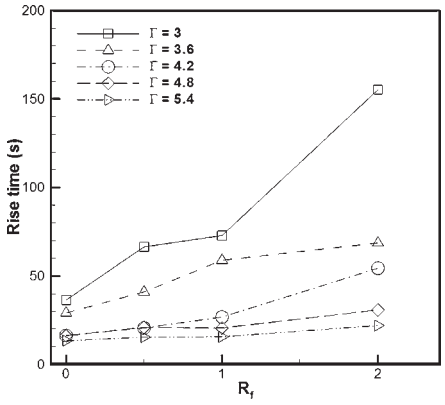

Fig. 14 Rise time as a function of R_f with different Γ for fixed $f = 25$ Hz (Liao C.C. et al., 2014).

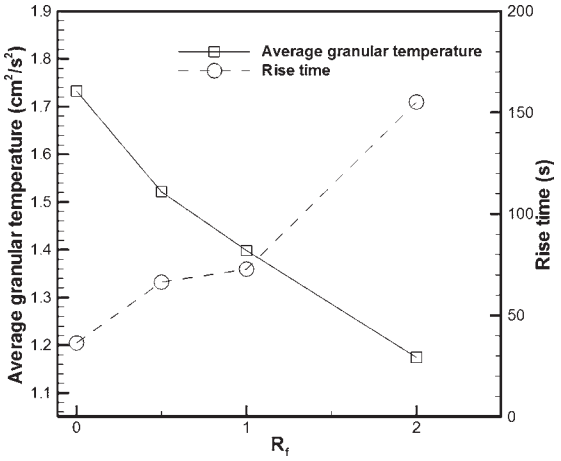

Fig. 15 Average granular temperature and rise time as a function of R_f for fixed $f = 25$ Hz and $\Gamma = 3$ (Liao C.C. et al., 2014).

tionship between mean-square diffusive displacements and time, as shown in Eq. (7), by conducting experimental procedures similar to those of previous studies (Hsiau and Yang, 2002; Liao and Hsiau, 2009; Tai and Hsiau, 2004). Self-diffusion coefficients and rise times are plotted as a function of R_f for $f = 25$ Hz and $\Gamma = 3$, as shown in **Fig. 16**. The self-diffusion coefficients are inversely proportional to the rise time of the base factor. Particle diffusion behavior results from particle fluctuations. Previous studies (Hsiau and Yang, 2002; Savage and Dai, 1993) have indicated that the self-diffusion coefficient is proportional to the square root of granular temperature. For a higher base factor, external energy could not be introduced into the system effectively, leading to weaker interactive collisions and a smaller granular temperature. Therefore, a decreasing self-diffusion coefficient increases the rise time for a large base factor, as shown in **Fig. 16**.

Fig. 17 shows the dimensionless convective flow rate J and rise time plotted as a function of R_f for the fixed conditions $f = 25$ Hz and $\Gamma = 3$. As the base factor decreases, J increases and the rise time decreases. The flow field is more fluidized, which strengthens the convection for a smaller base factor. Consequently, J increases and the rise time decreases as the base factor decreases. This result supports those of previous studies (Hsiau, 2002; Liao et al., 2012).

4. Conclusions

Granular materials are widely used in many industries and commonly encountered in daily life. To handle and control them, understanding the transport properties and segregation mechanisms in dry and wet granular systems is essential. Furthermore, controlling granular segregation is difficult. This paper presents the main results obtained by our research group; the results pertain to transport properties and segregation in a vibrating granular bed. The addition of a small amount of liquid to granular materials generally reduced the fluidization of the granular bed because liquid bridges formed between particles. The convective flow rate and granular temperature decreased as the added liquid content, surface tension, and viscosity increased. Increasing the added liquid content, surface tension, and viscosity also caused higher energy dissipation in a wet vibrating granular bed. Thus, higher liquid content, surface tension, and viscosity reduce the granular temperature and convection strength. The convective flow rate decreases according to a power law as the modified granular Bond number increases. The granular segregation can also be reduced by adding a small amount of liquid to the granular materials. Both the liquid content and viscosity considerably influence granular segregation. We demonstrated that the initial segregation state may change to a homogeneous mixing state when an appropriate amount of liquid with sufficient viscosity is added to the granular matter.

This paper also discusses how the bed height influences convection cells. The results of our study show that the convection strength and overall average granular temperature lead to a two-peak phenomenon with the increasing bed height. We demonstrated that this two-peak pattern occurs because a solid-like region forms in the granular bed.

The current results also indicated that intruder surface roughness has a significantly influence on the rise dynamics of intruder. The Brazil nut segregation effect is mitigated as the intruder surface roughness increases. The rise time for a rough intruder is longer than that for a smooth intruder because higher surface roughness results in more energy dissipation. The penetration length is enhanced as the intruder surface roughness is reduced, and

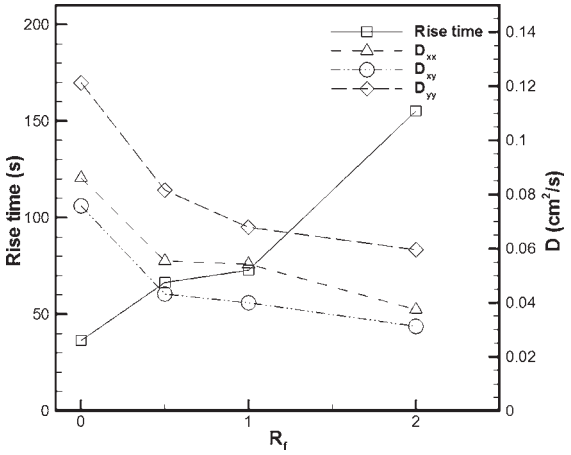

Fig. 16 Self-diffusion coefficients D and rise time as a function of R_f for fixed $f = 25$ Hz and $\Gamma = 3$ (Liao C.C. et al., 2014).

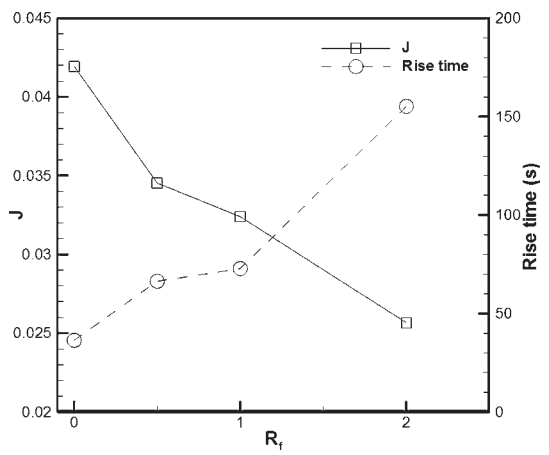

Fig. 17 Dimensionless convection flow rate J and rise time as a function of R_f for fixed $f = 25$ Hz and $\Gamma = 3$ (Liao C.C. et al., 2014).

is scaled exponentially with the vibration frequency. Additionally, the drag increases with the intruder surface roughness. We also observed that the intruder rise dynamics and transport properties of the immersed glass beads are influenced significantly by the base roughness. The penetration length is enhanced as the base factor is reduced. Additionally, the drag force increases with the base factor. The granular temperature, diffusion coefficients, and dimensionless convective flow rate decrease as the base factor increases and are inversely proportional to the rise time.

Acknowledgments

The authors acknowledge the financial support provided by the Ministry of Science and Technology, R.O.C., through grants MOST 103-2218-E-008-004-MY2 and MOST 103-2221-E-008-042-MY3.

Nomenclature

A	vibration amplitude, mm
a	vibration acceleration, m/s^2
a_i	negative gravitational acceleration
Bo_g	granular Bond number
Bo_{gM}	modified granular Bond number
b	radius of the wetted area, mm
C_i	concentration of nylon beads in the ith cell
$\overline{C}$	average concentration of nylon beads in the entire bed
D_s	separation distance of liquid bridge, mm
D_{ij}	self-diffusion coefficient
d	bead diameter
d_b	diameter of immersed glass beads
F_c	capillary force, N
F_v	viscous force, N
f	vibration frequency, Hz
g	gravitational acceleration, m/s^2
H	dimensionless initial bed height
h	initial bed height, cm
$H(b)$	distance between the two spherical surfaces at radius of the wetted area, mm
$H_d(r)$	distance between the two spherical surfaces, mm
H_E	total bed thickness in the full expansion state
H_S	solid-like region
H_C	convection region
H_{p1}	first critical (maximum) value
H_{p2}	second peak
H_v	the valley
I	segregation index
J	dimensionless convection strength
$\dot{m}$	convection mass flow rate
m_i	intruder mass
n	number of subregions
N_i	number of tracer particles in the ith bin
P	pressure generated in the liquid, N/m^2
P_d	diameter of glued beads
P_l	penetration length
r	radial distance
R	particle radius, mm
R_f	base factor
S	distance between particles, mm
t	time
T	average granular temperature
T_i	granular temperature in the ith bin
T^*	overall average granular temperature
$\langle u_i \rangle$	the ensemble average velocity in the horizontal direction in the ith bin
$\langle u_i'^2 \rangle^{1/2}$	fluctuation velocity in the horizontal direction in the ith bin
u_{ki}	the velocity of the kth tracer particle in the horizontal direction in the ith bin
V^*	dimensionless liquid content
V_w	total volume of silicon oil added, cm^3
V_p	total volume of whole beads in the bed, cm^3
$\langle v \rangle_c$	vertical velocity component
$\langle v_i \rangle$	ensemble average velocity in the vertical direction in the ith bin
$\langle v_i'^2 \rangle^{1/2}$	fluctuation velocity in the vertical direction in the ith bin
v_{ki}	the velocity of the kth tracer particle in the vertical direction in the ith bin
v_t	intruder take-off velocity
W	the half-width of the container
W_p	particle weight
Δx	the width of each bin
Δx_i	the diffusive displacement in direction i
Δx_j	the diffusive displacement in direction j

y	bed height
$z(t)$	Sine function

Greek letters

Γ	dimensionless vibration acceleration
γ	surface tension of the liquid, mN/m
β	drag between the beads and the intruder
μ	liquid kinematic viscosity, cs
v	solid fraction
η	liquid dynamic viscosity, cP
ρ_p	the true bead density, g/cm^3
ω	vibration radian frequency, rad/s

References

Bose M., Rhodes M., Dynamis of an intruder in a shaken granular bed, Powder Technology, 179 (2007) 25–30. DOI: 10.1016/j.powtec.2006.11.012

Bridgwater J., Fundamental powder mixing mechanisms, Powder Technology, 15 (1976) 215–236. DOI: 10.1016/0032-5910(76)80051-4

Breu A.P.J., Ensner H.M., Kruelle C.A., Rehberg I., Reversing the Brazil-nut effect: Competition between percolation and condensation, Physical Review Letters, 90 (2003) 014302. DOI: 10.1103/PhysRevLett.90.014302

Brito R., Enríquez H., Godoy S., Soto R., Segregation induced by inelasticity in a vibrofluidized granular mixture, Physical Review E, 77 (2008) 061301. DOI: 10.1103/PhysRevE.77.061301

Brito R., Soto R., Competition of Brazil nut effect, buoyancy, and inelasticity induced segregation in a granular mixture, European Physical Journal-Special Topics, 179 (2009) 207–219. DOI: 10.1140/epjst/e2010-01204-5

Campbell C.S., Rapid granular flows, Annual Review Fluid Mechanics, 22 (1990) 57–92. DOI: 10.1146/annurev.fl.22.010190.000421

Campbell C.S., Self-diffusion in granular shear flows, Journal of Fluid Mechanics, 348 (1997) 85–101. DOI: 10.1103/PhysRevE.69.031308

Chou S.H., Liao C.C., Hsiau S.S., An experimental study on the effect of liquid content and viscosity on particle segregation in a rotating drum, Powder Technology, 201 (2010) 266–272. DOI: 10.1016/j.powtec.2010.04.009

Chung Y.C., Liao H.H., Hsiau S.S., Convection behavior of non-spherical particles in a vibrating bed: Discrete element modelling and experimental validation, Powder Technology, 237 (2013) 53–66. DOI: 10.1016/j.powtec.2012.12.052

Ciamarra M.P., Vizia M.D.D., Fierro A., Tarzia M., Coniglio A., Nicodemi M., Granular species segregation under vertical tapping: effects of size, density, friction, and shaking amplitude, Physical Review Letters, 96 (2006) 058001. DOI: 10.1103/PhysRevLett.96.058001

Clement C.P., Pacheco-Martinez H.A., Swift M.R., King P.J., The water-enhanced Brazil nut effect, Europhysics Letters, 91 (2010) 54001. DOI: 10.1209/0295-5075/91/54001

Cooke W., Warr S., Huntley J.M., Ball R.C., Particle size segregation in a two-dimensional bed undergoing vertical vibration, Physical Review E, 53 (1996) 2812–2822. DOI: 10.1103/PhysRevE.53.2812

Duran J., Rajchenbach J., Clément E., Arching effect model for particle-size segregation, Physical Review Letters, 70 (1993) 2431–2434. DOI: 10.1103/PhysRevLett.70.2431

Einstein A., In R. Furth, Albert Einstein, Investigations on the theory of non-uniform gases, New York: Dover Publ. Co. Chap. 1, (1956) 12.

Elperin T., Golshtein E., Effects of convection and on size segregation in vibration in vibrated granular beds, Physica A, 247 (1997) 67–78. DOI: 10.1016/S0378-4371(97)00400-7

Ennis B.J., Li J., Tardos G.I., Pfeffer R., The influence of viscosity on the strength of an axially strained pendular liquid bridge, Chemical Engineering Science, 45 (1990) 3071–3088. DOI: 10.1016/0009-2509(90)80054-I

Farkas Z., Tegzes P., Vukics A., Vicsek T., Transitions in the horizontal transport of vertically vibrated granular layers, Physical Review E, 60 (1999) 7022. DOI: 10.1103/PhysRevE.60.7022

Fisher R.A., On the capillary forces in an ideal soil; correction of formulae given by WB Haines, Journal of Agricultural Science, 16 (1926) 492–505. DOI: 10.1017/S0021859600007838

Fortini A., Huang K., Role of defects in the onset of wall-induced granular convection, Physical Review E, 91 (2015) 032206. DOI: 10.1103/PhysRevE.91.032206

Fraysse N., Thomé H., Petit L., Humidity effects on the stability of a sandpile, The European Physical Journal B, 11 (1999) 615–619. DOI: 10.1007/s100510051189

Gallas J.A.C., Herrmann H.J., Sokolowski S., Convection cells in vibrating granular media. Physical Review Letters, 69 (1992) 1371–1374. DOI: 10.1103/PhysRevLett.69.1371

Geromichalos D., Kohonen M.M., Mugele F., Herminghaus S., Mixing and condensation in a wet granular medium, Physical Review Letters, 90 (2003) 168702. DOI: 10.1103/PhysRevLett.90.168702

Grof Z., Lawrence C.J., Štěpánek F., Computer simulation of evolving capillary bridges in granular media, Granular Matter, 10 (2008) 93–103. DOI: 10.1007/s10035-007-0071-1

Halsey T.C., Levine A.J., How sandcastles fall, Physical Review Letters, 80 (1998) 3141–3144. DOI: 10.1103/PhysRevLett.80.3141

Herminghaus S., Dynamics of wet granular matter, Advances in Physics, 54 (2005) 221–261. DOI: 10.1080/00018730500167855

Hsiau S.S., Chen C. H., Granular convection cells in a vertical shaker, Powder Technology, 111 (2000) 210–217. DOI: 10.1016/S0032-5910(99)00287-9

Hsiau S.S., Liao C.C., Sheng P.Y., Tai S.C., Experimental study the influence of bed height on convection cell formation, Experiments in Fluids, 51 (2011) 795–800. DOI: 10.1007/s00348-011-1099-x

Hsiau S.S., Liao C.C., Tai C.H., Wang C.Y., The dynamics of wet granular matter under a vertical vibration bed, Granular Matter, 15 (2013) 437–446. DOI: 10.1007/s10035-013-0412-1

Hsiau S.S., Lu L.S., Tai C.H., Experimental investigations of granular temperature in vertical vibrated beds, Powder Technology, 182 (2008) 202–210. DOI: 10.1016/j.powtec.2007.09.015

Hsiau S.S., Shieh Y.M., Fluctuations and self-diffusion of sheared granular material flows, Journal of Rheology, 43 (1999) 1049–1066. DOI: 10.1122/1.551027

Hsiau S.S., Shin J.Y., Yang W.L., Lu L.S., Influence of internal friction on transport properties in sheared granular flows, AIChE Journal, 52 (2006) 3592–3599. DOI: 10.1002/aic.10977

Hsiau S.S., Tai C.H., Chiang M.C., Effect of moisture content on the convection motion of powders in a vibrated bed, Advanced Powder Technology, 15 (2004) 673–686. DOI: 10.1163/1568552042456197

Hsiau S.S., Wang P.C., Tai C.H., Convection cells and segregation in a vibrated granular bed, AIChE Journal 48 (2002) 1430–1438. DOI: 10.1002/aic.690480707

Hsiau S.S., Yang S.C., Numerical simulation of self-diffusion and mixing in a vibrated granular bed with the cohesive effect of liquid bridges, Chemical Engineering Science, 58 (2003) 339–351. DOI: 10.1016/S0009-2509(02)00519-5

Hsiau S.S., Yang W.L., Stresses and transport phenomena in sheared granular flows, Physics of Fluids, 14 (2002) 612. DOI: 10.1063/1.1428324

Hsiau S.S., Yu H.Y., Segregation phenomena in a shaker, Powder Technology, 93 (1997) 83–88. DOI: 10.1016/S0032-5910(97)03263-4

Huerta D.A., Ruiz-Suarez J.C., Vibration-induced granular segregation: A phenomenon driven by three mechanisms, Physical Review Letters, 92 (2004) 114301. DOI: 10.1103/PhysRevLett.92.114301

Jaeger H.M., Nagel S.R., Behringer R.P., Granular solids, liquids and gases, Reviews of Modern Physics, 68 (1996) 1259–1273. DOI: 10.1103/RevModPhys.68.1259

Khakhar D.V., McCarthy J.J., Ottino J.M., Radial segregation of granular mixtures in rotating cylinders, Physics of Fluids, 9 (1997) 3600–3614. DOI: 10.1063/1.869498

Klein M., Tsai L.L., Rosen M.S., Pavlin T., Candela D., Walsworth R.L., Interstitial gas and density segregation of vertically vibrated granular media, Physical Review E, 74 (2006) 010301. DOI: 10.1103/PhysRevE.74.010301

Klongboonjit S., Campbell C.S, Convection in deep vertically shaken particle beds. I. General features, Physics of Fluids, 20 (2008) 103301-1-103301-6. DOI: 10.1063/1.2996136

Knight J.B., Jaeger H.M., Nagel S.R., Vibration-induced size separation in granular media-the convection connection, Physical Review Letters, 70 (1993) 3728–3731. DOI: 10.1103/PhysRevLett.70.3728

Knight J.B., Ehrichs E.E., Kuperman V.Y., Flint J.K., Jaeger H.M., Nagel S.R., An experimental study of granular convection, Physical Review E, 54 (1996) 5726-5738. DOI: 10.1103/PhysRevE.54.5726

Kohonen M.M., Geromichalos D., Scheel M., Schier C., Herminghaus S., On capillary bridges in wet granular materials, Physica A, 39 (2004) 7–15. DOI: 10.1016/j.physa.2004.03.047

Kondic L., Hartley R.R., Tennakoon S.G.K., Painter B., Behringer R.P., Segregation by friction, Europhysics Letters, 61 (2006) 742–748. DOI: 10.1209/epl/i2003-00291-y

Kudrolli A., Size separation in vibrated granular matter, Reports on progress in physics, 67 (2004) 209–247. DOI: 10.1.1.306.2695

Kudrolli A., Granular matter-sticky sand, Nature Materials 7 (2008) 174–175. DOI: 10.1038/nmat2131

Levanon M., Rapaport D.C., Stratified horizontal flow in vertically vibrated granular layers, Physical Review Letters, 60 (2001) 011304. DOI: 10.1103/PhysRevE.64.011304

Li H., McCarthy J.J., Controlling cohesive particle mixing and segregation, Physical Review Letters, 90 (2003) 184301. DOI: 10.1103/PhysRevLett.90.184301

Li H., McCarthy J.J., Cohesive particle mixing and segregation under shear, Powder Technology, 164 (2006) 58–64. DOI: 10.1016/j.powtec.2005.12.018

Liao C.C., Hsiau S.S., Influence of interstitial fluid viscosity on transport phenomenon in sheared granular materials, Chemical Engineering Science, 64 (2009) 2562. DOI: 10.1016/j.ces.2009.02.030

Liao C.C., Hsiau S.S., Experimental analysis of dynamic properties in wet sheared granular matter, Powder Technology, 197 (2010) 222–229. DOI: 10.1016/j.powtec.2009.09.017

Liao C.C., Hsiau S.S., Chang P.S., Bottom wall friction coefficients on the dynamics properties of sheared granular flows, Powder Technology, 270 (2015) 348–357. DOI: 10.1016/j.powtec.2014.10.043

Liao C.C., Hsiau S.S., Kiwing To, Granular dynamics of a slurry in a rotating drum, Physical Review E, 82 (2010a) 010302. DOI: 10.1103/PhysRevE.82.010302

Liao C.C., Hsiau S.S., Li J.S., Tai C.H., The influence of gravity on dynamic properties in sheared granular flows, Chemical Engineering Science, 65 (2010b) 2531–2540. DOI: 10.1016/j.ces.2009.12.034

Liao C.C., Hsiau S.S., Wu C.S., Experimental study on the effect of surface roughness on Brazil nut problem in a vertically vibrated bed, Physical Review E, 86 (2012) 061316. DOI: 10.1103/PhysRevE.86.061316

Liao C.C., Hsiau S.S., Wu C.S., Combined effects of internal friction and bed height on the Brazil-nut problem in a shaker, Powder Technology, 253 (2014) 561–567. DOI: 10.1016/j.powtec.2013.12.031

Liao C.C., Hsiau S.S., Tsai T.H., Tai C.H., Segregation to mixing in wet granular matter under vibration, Chemical Engineering Science, 65 (2010c) 1109–1116. DOI: 10.1016/j.ces.2009.09.065

Liao C.C., Hunt M.L., Hsiau S.S., Lu S.H., Investigation of the effect of a bumpy base on granular segregation and transport properties under vertical vibration, Physics of Fluids, 26 (2014) 073302. DOI: 10.1063/1.4890363

Liffman K., Muniandy K., Rhodes M., Gutteridge D., Metcalfe G., A segregation mechanism in a vertically shaken bed, Granular Matter, 3 (2011) 205–214. DOI: 10.1007/s100350100093

Lim E.W.C., Pattern formation in vibrated beds of dry and wet granular materials, Physics of Fluids, 26 (2014) 013301. DOI: 10.1063/1.4860115

Lozano C., Zuriguel I., Garcimartin A., Mullin T., Granular

segregation driven by particle interactions, Physical Review Letters, 114 (2015) 178002. DOI: 10.1103/PhysRevLett.114.178002

Lu L.S., Hsiau S.S., Mixing in a vibrated granular bed: Diffusive and convective effects, Powder Technology, 184 (2008) 31–43. DOI: 10.1016/j.powtec.2007.07.036

Ma H.P., Lv Y.J., Zheng N., Li L.S., Shi Q.F., Intruder motion in two-dimensional shaken granular beds, Chinese Physics Letters, 31 (2014) 114501. DOI: 10.1088/0256-307X/31/11/114501

Majid M., Walzel P., Convection and segregation in vertically vibrated granular beds, Powder Technology, 192 (2009) 311–317. DOI: 10.1016/j.powtec.2009.01.012

Mason G., Clark W.C., Liquid bridges between spheres, Chemical Engineering Science, 20 (1965) 859–866. DOI: 10.1016/0009-2509(65)80082-3

Mason T.G., Levine A.J., Ertaş D., Halsey T.C., Critical angle of wet sandpiles, Physical Review E, 60 (1999) 5044–5047. DOI: 10.1103/PhysRevE.60.R5044

McCarthy J.J., Turning the corner in segregation, Powder Technology, 192 (2009) 137–142. DOI: 10.1016/j.powtec.2008.12.008

Mehrotra V.P., Sastry K.V.S., Pendular bond strength between unequal sized spherical particles, Powder Technology, 25 (1980) 203–214. DOI: 10.1016/0032-5910(80)87031-8

Mikami T., Kamiya H., Horio M., Numerical simulation of cohesive powder behavior in a fluidized bed, Chemical Engineering Science, 53 (1998) 1927–1940. DOI: 10.1016/S0009-2509(97)00325-4

Mobius M.E., Cheng X., Karczmar G.S., Nagel S.R., Jaeger H.M., Intruders in the dust: Air-driven granular size separation, Physical Review Letters, 93 (2004) 198001. DOI: 10.1103/PhysRevLett.93.198001

Nahmad-Molinari Y., Canul-Chay G., Ruiz-Suarez J.C., Inertia in the Brazil nut problem, Physical Review E, 68 (2003) 041301. DOI: 10.1103/PhysRevE.68.041301

Nase S.T., Vargas W.L., Abatan A.A., McCarthy J.J., Discrete characterization tools for cohesive granular material, Powder Technology, 116 (2001) 214–223. DOI: 10.1016/S0032-5910(00)00398-3

Natarajan V.V.R., Hunt M.L., Taylor E.D., Local measurements of velocity fluctuations and diffusion coefficients for a granular material flow, Journal of Fluid Mechanics, 304 (1995) 1–25. DOI: 10.1017/S0022112095004320

Ogawa S., Multi-temperature theory of granular materials, in Proceedings of US-Japan Seminar on Continuum-Mechanical and Statistical Approaches in the Mechanics of Granular Materials, Tokyo 208 (1978).

Pitois O., Moucheront P., Chateau X., Liquid bridge between two moving spheres: an experimental study of viscosity effects, Journal of Colloid and Interface Science, 231 (2000) 26–31. DOI: 10.1006/jcis.2000.7096

Plantard G., Saadaoui H., Snabre P., Pouligny B., Surface-roughness-driven segregation in a granular slurry under shear, Europhysics Letters, 75 (2006) 335–341. DOI: 10.1209/epl/i2006-10088-6

Pohlman N.A., Severson B.L., Ottino J.M., Lueptow R.M., Surface roughness effects in granular matter: influence on angle of repose and the absence of segregation, Physical Review E, 73 (2006) 031304. DOI: 10.1103/PhysRevE.73.031304

Rosato A., Strandburg K.J., Prinz F., Swendsen R.H., Why the Brazil nuts are on top: size segregation of particulate matter by shaking, Physical Review Letters, 58 (1987) 1038–1040. DOI: 10.1103/PhysRevLett.58.1038

Saez A., Vivanco F., Melo F., Size segregation, convection, and arching effect, Physical Review E, 72 (2005) 021307. DOI: 10.1103/PhysRevE.72.021307

Samadani A., Kudrolli A., Segregation transitions in wet granular matter, Physical Review Letters, 85 (2000) 5102–5105. DOI: 10.1103/PhysRevLett.85.5102

Samadani A., Kudrolli A., Angle of repose and segregation in cohesive granular matter, Physical Review E, 64 (2001) 051301. DOI: 10.1103/PhysRevE.64.051301

Savage S.B., Dai R., Studies of granular shear flows: wall slip velocities, 'layering' and self-diffusion, Mechanics of Materials, 16 (1993) 225–238. DOI: 10.1016/0167-6636(93)90047-U

Scheel M., Seemann R., Brinkmann M., Michiel M.D., Herminghaus S., Liquid distribution and cohesion in wet granular assembiles beyond the capillary bridge regime, Journal of Physics-Condesend Matter, 20 (2008) 494236. DOI: 10.1088/0953-8984/20/49/494236

Schulz M., Schulz B.M., Herminghaus S., Shear-induced solid-fluid transition in a wet granular medium, Physical Review E, 67 (2003) 052301. DOI: 10.1103/PhysRevE.67.052301

Shi D., Abatan A.A., Vargas W.L., McCarthy J.J., Eliminating segregation in free-surface flows of particles, Physical Review Letters, 99 (2007) 148001. DOI: 10.1103/PhysRevLett.99.148001

Srebro Y., Levine D., Role of friction in compaction and segregation of granular materials, Physical Review E, 68 (2003) 061301. DOI: 10.1103/PhysRevE.68.061301

Tai C.H., Hsiau S.S., Dynamic behaviors of powders in a vibrating bed, Powder Technology, 139 (2004) 221–232. DOI: 10.1016/j.powtec.2003.12.004

Tai C.H., Hsiau S.S., Kruelle C.A., Density segregation in a vertically vibrated granular bed, Powder Technology, 204 (2010) 255–262. DOI: 10.1016/j.powtec.2010.08.010

Unac R.O., Benito J.G., Vidales A.M., Pugnaloni L.A., Arching during the segregation of two-dimensional tapped granular systems: Mixtures versus intruders, European Physcial Journal E, 37 (2014) 117. DOI: 10.1140/epje/i2014-14117-y

Ulrich S., Schröter M., Swinney H.L., Influence of friction on granular segregation, Physical Review E, 76 (2007) 042301. DOI: 10.1103/PhysRevE.76.042301

van der Vaart K., Gajjar P., Epely-Chauvin G., Andreini N., Gray J.M.N.T., Ancey C., Underlying asymmetry within particle size segregation, Physical Review letters, 114 (2015) 238001. DOI: 10.1103/PhysRevLett.114.238001

Vanel L., Rosato A.D., Dave R.N., Rise-time regimes of a large sphere in vibrated bulk solids, Physical Review Letters, 78 (1997) 1255. DOI: 10.1103/PhysRevLett.78.1255

Viswanathan H., Sheikh N.A., Wildman R.D., Huntley J.M., Convection in three-dimensional vibrofluidized granular

beds, Journal of Fluid Mechanics, 682 (2011) 185–212. DOI: 10.1017/jfm.2011.209

Wildman R.D., Huntley J.M., Novel method for measurement of granular temperature distributions in two-dimensional vibro-fluidised beds, Powder Technology, 113 (2000) 14–22. DOI: 10.1016/S0032-5910(99)00286-7

Wildman R.D., Huntley J.M., Parker D.J., Convection in highly fluidized three-dimensional granular beds, Physical Review Letters, 86 (2001) 3304–3307. DOI: 10.1103/PhysRevLett.86.3304

Williams J.C., Segregation of particulate materials—a review, Powder Technology, 15 (1976) 245–251. DOI: 10.1016/0032-5910(76)80053-8

Windows-Yule C.R.K., Douglas G.J.M., Parker D.J., Competition between geometrically induced and density-driven segregation mechanisms in vibrofluidized granular systems, Physical Review E, 91 (2015a) 032205. DOI: 10.1103/PhysRevE.91.032205

Windows-Yule C.R.K., Rosato A.D., Parker D.J., Thornton A.R., Maximizing energy transfer in vibrofluidized granular systems, Physical Review E, 91 (2015b) 052203. DOI: 10.1103/PhysRevE.91.052203

Windows-Yule K., Parker D., Density-driven segregation in binary and ternary granular systems, Kona Powder and Particle Journal, 32 (2015) 163–175. DOI: 10.14356/kona.2015004

Yang W.L., Hsiau S.S., Wet granular materials in sheared flows, Chemical Engineering Science, 60 (2005) 4265–4274. DOI: 10.1016/j.ces.2005.03.001

Zamankhan P., Sinking and recirculation of large intruders in vertically vibrated granular beds, Advanced Powder Technology, 24 (2013) 1070–1085. DOI: 10.1016/j.apt.2013.03.010

Zeilstra C., van der Hoef M.A., Kuipers J.A.M., Simulation of density segregation in vibrated beds, Physical Review E, 77 (2008) 031309. DOI: 10.1103/PhysRevE.77.031309

Zivkovic V., Biggs M.J., Glass D.H., Scaling of granular temperature in a vibrated granular bed, Physical Review E, 83 (2011) 031308. DOI: 10.1103/PhysRevE.83.031308

Author's short biography

Chun-Chung Liao

Dr. Chun-Chung Liao received his PhD degree from National Central University (Taiwan) in 2010, majored in Mechanical Engineering. After receiving the PhD degree, he started his academic career as a postdoctoral fellow at National Central University in Jhongli, Taiwan. He was a visiting scholar in Mechanical Engineering in Caltech from Oct. 2013–Jul. 2014. Currently, he is the assistant professor at Department of Mold and Die engineering in National Kaohsiung University of Applied Sciences from Feb. 2015. His research interests include powder technology, granular flows, fast pyrolysis of biomass.

Shu-San Hsiau

Dr. Shu-San Hsiau received his MS and PhD degrees from California Institute of Technology, majored in Mechanical Engineering in 1993, and started his professorship life in National Central University (NCU). Currently he is a Distinguished Professor of Mechanical Engineering, and also Institute of Energy Engineering of NCU. He received the Humboldt award and went to Darmstadt University of Technology (Germany) in 2003. His research area includes Powder Technology, Clean Coal Technology, Biomass (Pyrolysis, Gasification), Modeling and Design of MOCVD, Energy Technology, Hot-Gas Cleanup, Debris Flow and Avalanche, Powder Technology, Hydrogen Energy, Energy Education, Creative Engineering Education, Thermo-Fluids, Pharmaceutical Engineering. He served as the chairman of Mechanical Engineering (2010–2013) and also as the director of Institute of Energy Engineering (2008–2010). Currently he is the deputy dean of R&D office (NCU), and also the director of Clean Coal Research Center.

KONA Powder and Particle Journal No. 33 (2016) 127–149/Doi:10.14356/kona.2016021 Review Paper

Mixing and Fluid Dynamics Effects in Particle Precipitation Processes †

Jerzy Bałdyga

[1] *Faculty of Chemical and Process Engineering, Warsaw University of Technology, Poland*

Abstract

Precipitation defined as the rapid formation of moderately soluble crystalline or amorphous solid particles from a liquid solution under high supersaturation conditions is considered. It involves the simultaneous and fast occurrence of primary nucleation and growth of particles together with the secondary processes such as aggregation and breakage. It is shown how the effects of fluid flow and mixing affect the subprocesses forming the overall precipitation process. Examples are presented for reactive precipitation and antisolvent precipitation with supercritical fluids applied as the antisolvents.

The elementary subprocesses forming the overall precipitation process (i.e. macro-, meso-, micromixing, chemical reaction, nucleation and growth of particles, aggregation and breakage) are characterized by the related time constants and the application of time constants in the modeling and scale-up of precipitation processes is presented. The effects of turbulence on particle formation are simulated using mechanistic models, CFD and population balances (including the method of moments and the quadrature method of moments). The results of modeling are compared with experimental data.

Finally, it is shown in the context of practical applications to what extent the approaches discussed in this paper can be applied to "design" particles.

Keywords: aggregation, breakage, fluid dynamics, mixing, population balance, precipitation

1. Introduction

Precipitation refers to the rapid formation of moderately soluble crystalline or amorphous solid particles from a liquid solution, whereas particle formation occurs under high supersaturation conditions. Precipitation involves the simultaneous and fast occurrence of primary nucleation and growth together with the secondary processes such as Ostwald ripening, aggregation and breakage.

Precipitation processes are of importance in technology as they are employed in the production of bulk and fine chemicals including fertilizers, pigments, catalysts, magnetic materials, drugs, etc. The solid product usually has a wide crystal size distribution (CSD) which determines the filtration, washing and settling abilities of suspensions, and thus the quality of the product (crystal size homogeneity, surface area, etc.). Other factors which can strongly influence the product quality are the morphology and purity of the precipitating particles. It is well known that both the CSD and the morphology can strongly depend on mixing conditions during the process.

The high supersaturation is usually created either by performing chemical reactions or by mixing the solution with an antisolvent which decreases the solute solubility. Chemical reactions applied in so-called reactive crystallization processes are usually very fast, which means that their course depends on mixing as well. This also means that the role of mixing, including the effects of macro-, meso- and micromixing, can be very important for the creation and dilution of supersaturation. Very important are also effects of the fluid flow as they affect mixing and may affect phenomena of particle agglomeration and coagulation; agglomeration dominates the precipitation processes at high supersaturation, in the case of coagulation only physical forces are involved to hold particles together.

Another aspect of high supersaturation is its effect on the nucleation mechanism. Namely at high supersaturation, there is negligible secondary nucleation resulting from the presence of solute crystalline material but rather primary homogeneous or heterogeneous nucleation dominates the process. Due to the high sensitivity of primary nucleation to supersaturation, the number of primary particles is controlled by nucleation and affected by mixing, whereas crystal growth is less important, because after complete unloading of supersaturation, it is more the

† Received 25 June 2015; Accepted 17 August 2015
J-STAGE online 28 February 2016
[1] ul. Waryńskiego 1, Warsaw, Poland
E-mail: j.baldyga@ichip.pw.edu.pl
TEL: +48-22-234-6376 FAX: +48-22-825-6037

number of crystals than the rate of their growth that determines their final size. The growth rate can, however, affect their shape.

In this paper, the effects of mixing and fluid flow observed in reactive precipitation, and antisolvent precipitation with supercritical fluids applied as the antisolvents are considered. The material is organized as follows.

First, the elementary subprocesses forming the overall precipitation process (i.e. macro-, meso-, micromixing, chemical reaction, nucleation, and growth of particles) are characterized by the related time constants and length scales. The application of time constants for the modeling and scale-up of precipitation processes is then presented.

Second, because in most of the precipitation devices the flow and mixing are turbulent, it is shown how to predict interactions of turbulence with particle formation phenomena. In this context, the phenomenological models, mechanistic and based on CFD (including solution of the closure problem for chemical reaction and precipitation) and population balances (including method of moments and quadrature method of moments) are presented and the results of modeling are compared with experimental data.

Third, an attempt to classify aggregation, i.e. agglomeration and coagulation processes, is presented from the point of view of the characteristic length and time scales.

Fourth, suitable kernels for aggregation processes (from orthokinetic to perikinetic, including effects of fluid dynamics and colloidal forces) and breakage processes are presented, and the results of application of these kernels, implemented in some cases in a CFD environment, are presented and compared with experimental data.

This paper finishes with discussion on practical applications where the properties of precipitated particles are of key importance and thus great attention is paid to "particle design". It is also discussed to what extent the approaches presented in this paper can be applied to "design" particles and scale-up processes.

This is a review paper and the intention of the author is to review important problems, ideas and challenges related in the author's opinion to the most important aspects of precipitation. The approaches and examples of results presented are based on the author's own work, and supported by the ideas and results of other researchers who investigated this fascinating problem of precipitation.

Despite its practical importance and a long tradition of investigating precipitation, it still requires better understanding and development of theoretical approaches for process interpretation. This is, for example, depicted by a small number of books devoted to precipitation. There are some fundamental books on precipitation including Kinetics of Precipitation by Nielsen A.E. (1964), The Formation and Properties of Precipitates by Walton A.G. (1964) and Precipitation by Söhnel O. and Garside J. (1992); there are also chapters devoted to precipitation in the Crystallization Technology Handbook, edited by Mersmann A. (2001), Handbook of Industrial Crystallization edited by Myerson A.S. (2002), Turbulent Mixing and Chemical Reactions by Bałdyga J. and Bourne J.R. (1999), Supercritical Fluid Technology for Drug Product Development edited by York, P. et al. (2004), Handbook of Industrial Mixing, Science and Practice edited by Paul E.L. et al. (2003) and Formulating Poorly Water Soluble Drugs by Rowe, J.M. and Johnston, K.P. (2012); discussion on computational methods that can possibly be used to model precipitation can be found in Computational Models for Polydisperse Particulate and Multiphase Systems by Marchisio D.L. and Fox R.O. (2013).

1.1 Driving force for precipitation

Precipitation is a kinetic process and its rate depends on the appropriately defined driving force, called supersaturation in the case considered here. The supersaturation, σ, is defined as the dimensionless difference between the molar chemical potential (the molar Gibbs free energy) μ in supersaturated solution and μ_{eq} in the crystalline state (equal to the potential in saturated solution) that can be expressed using solute activities, a, (Davey R. and Garside J., 2000).

$$\sigma = \frac{\mu\text{-}\mu_{eq}}{RT} = \ln\frac{a}{a_{eq}} \tag{1}$$

where μ and a are the actual molar chemical potential and the actual activity of the solute in solution, respectively, whereas T is the absolute temperature.

The value $\mu - \mu_{eq} = 0$ defines equilibrium: for $\mu - \mu_{eq} > 0$ spontaneous crystallization may occur, and $\mu - \mu_{eq} < 0$ means that an opposite transformation, i.e. dissolution, becomes spontaneous. The sign of $\Delta\mu$ determines the direction of the possible phase transformation, whereas the absolute value of $\Delta\mu$ signifies the distance from the equilibrium. $\Delta\mu/RT$ represents the thermodynamic driving force for crystallization, and both the rate of nucleation and the rate of crystal growth depend on $\Delta\mu/RT$. The driving force is usually expressed in a simpler form than Eqn. (1):

$$\begin{aligned}\sigma &= \ln\left(\frac{a}{a_{eq}}\right) \approx S_a - 1 = \frac{a - a_{eq}}{a_{eq}} \\ &\approx S - 1 = \frac{x - x_{eq}}{x_{eq}}\end{aligned} \tag{2}$$

In chemical engineering, concentration is often expressed in the units appropriate for the specific application, e.g., molar concentration, c

$$S_a = \frac{a_c}{a_{c,eq}} \approx S = \frac{c}{c_{eq}} \tag{3}$$

where a_c represents the activity of dissolved component

of concentration c, c_{eq} is the equilibrium solubility and $S_a \approx S$ is the supersaturation ratio that is also known as relative supersaturation or saturation ratio. Supersaturation is also sometimes expressed as a concentration difference

$$\Delta c = c - c_{eq} \tag{4}$$

The solution is supersaturated when $S_a > 1$, $S > 1$, $\Delta c > 0$ or $\sigma > 0$. For electrolytes, which dissociate giving ν^+ cations and ν^- anions, $\nu = \nu^+ + \nu^-$, and

$$\sigma = \frac{\mu - \mu_{eq}}{\nu RT} = \ln\left[\frac{\left(a_+^{\nu^+} a_-^{\nu^-}\right)}{\left(a_+^{\nu^+} a_-^{\nu^-}\right)_{eq}}\right]^{1/\nu} = \ln S_a \tag{5}$$

which defines both the ionic activity product $\left(a_+^{\nu^+} a_-^{\nu^-}\right)$ and the thermodynamic solubility product $\left(a_+^{\nu^+} a_-^{\nu^-}\right)_{eq}$. For dilute solutions, activities can be replaced by concentrations yielding $\left(c_+^{\nu^+} c_-^{\nu^-}\right)$ and $\left(c_+^{\nu^+} c_-^{\nu^-}\right)_{eq}$ for both products. In practice, supersaturation is often expressed as $\sigma = S_a - 1$ or as a "concentration" difference

$$\Delta c = \left[\left(c_+^{\nu^+} c_-^{\nu^-}\right)^{1/\nu} - \left(c_+^{\nu^+} c_-^{\nu^-}\right)_{eq}^{1/\nu}\right] \tag{6}$$

where ν represents the number of moles of ions formed from one mole of electrolyte.

Notice that Eqns. (5) and (6) should be combined with the relations describing equilibrium in the solution to account for the effect of solution composition on both solubility and driving force.

1.2 Kinetics of precipitation

The formation rate of a new solid phase, i.e. nucleation, and the rate of crystal growth from solution as well as the secondary changes such as agglomeration and aging all depend on supersaturation. Nucleation proceeds by two mechanisms: primary nucleation, occurring without influencing the crystallizing material, and secondary nucleation that is induced by the presence of the solid phase being formed. There are two types of the primary nucleation: homogeneous nucleation, in which the solid phase formation is not caused by the presence of any solid phase, and heterogeneous nucleation, which is induced by the presence of the foreign solid phase.

An expression for the rate of homogeneous nucleation was developed by Nielsen A.E. (1964),

$$J = \Omega \exp\left(\frac{-\Delta G^*}{k_B T}\right) = \Omega \exp\left[\frac{-B}{(\ln S)^2}\right] \tag{7}$$

where $\Delta G^* = \dfrac{16\pi\sigma^3 v^2}{3k_B{}^2 T^2 (\ln S)^2}$ is the energy barrier for homogeneous nucleation and the pre-exponential term reads $\Omega = \dfrac{D}{d^5 N^*}\left(\dfrac{4\Delta G^*}{3\pi k_B T}\right)^{\frac{1}{2}}$, B is a constant defined as $B = \dfrac{16\pi\sigma^3 v^2}{3k_B{}^3 T^3}$ where D is the diffusion coefficient of the solute, k_B is Boltzmann's constant, d is the molecular diameter, N^* is the number of molecules or ions forming the critical embryo-nucleus, σ is the surface energy and v is the molecular volume. Nielsen A.E. (1964), Nývlt J. (1971), and Söhnel O. and Garside J. (1992) have shown that over limited ranges of supersaturation, Eqn. (7) may be simplified to

$$J = k_N S^n \tag{8}$$

where n, the kinetic 'order' of nucleation, varies between 1 and 10.

Heterogeneous nucleation results from presence of foreign substances that are always present in a solution and may act as 'catalysts' of nucleation. This catalytic effect results mainly from decrease the energy barrier to nucleation, $\Delta G^*_{het} < \Delta G^*$ thanks to smaller σ for nucleus forming on the surface of the foreign phase. Hence, rate of heterogeneous nucleation (Turnbull D. and Vonnegut B., 1952) can be presented in similar way as homogeneous nucleation, Eqn. (7).

$$J_{het} = \Omega_{het} \exp\left(\frac{-\Delta G^*_{het}}{k_B T}\right) \tag{9}$$

where $\Omega_{het} < \Omega$. Heterogeneous nucleation is observed much more frequently than homogeneous nucleation.

In true secondary nucleation, nuclei are either formed on the surface of the solid phase as dendrites that are subsequently broken off the crystal or in the surface proximity (adsorption layer, liquid adjacent to the crystal); in contact secondary nucleation, nuclei result from the effects of impact energy of the crystal-crystal and crystal-equipment collisions. In the case of precipitation of moderately soluble materials, the secondary nucleation is not an important mechanism of nuclei formation because the particles are too small for the high-impact collisions that would be able to produce secondary nuclei, and the effects of crystal-solution interactions are negligible (Söhnel O. and Garside J., 1992). It is only in the case of rapid agglomeration that the resultant particles can be large enough to induce a sufficiently high impact energy for the generation of nuclei.

Once nuclei are formed in a supersaturated solution, they start to grow into crystals. The rate of crystal growth can be presented as the rate of growth of each crystal face. In the case of precipitation, particles are small and thus a concept of the overall rate of growth, $G = dL/dt$ is used with the crystal volume expressed by $v_c = k_V L^3$, k_V being the volume shape factor. The rate of growth is affected by two processes: the mass transfer of growth units to the crystal-solution interface by bulk diffusion and the surface integration of growth units into the crystal lattice. This can be represented by

$$G = k_D(c - c_i) = k_R(c_i - c_{eq})^r \tag{10}$$

where $k_D = 2k_d/\rho_c$, k_d is the mass transfer coefficient, k_R is the surface integration constant that is independent of crystal size and r represents the "order" of the surface integration process. In Eqn. (10), c is the bulk solute concentration, the subscript i describes the concentration at the crystal-solution interface and the subscript eq indicates the concentration at equilibrium. When the resistance of mass transfer to the crystal k_D^{-1} is much lower than that of the subsequent surface integration step $k_R^{-1}(c - c_{eq})^{1-r}$, the surface integration process controls the overall rate of growth, $G = k_R(c - c_{eq})^r$. In the opposite case, the overall rate of growth is determined by the rate of mass transport from the solution to the crystal $G = k_D(c - c_{eq})$. When the growth is controlled by combined mechanisms, then the concentration at the crystal-solution interface c_i in Eqn. (10) has to be eliminated, in this way relating the rate of growth to the bulk and equilibrium solute concentrations.

A similar approach can be used in the case of more complex systems when there is, for example, a reaction between the constituent ions on the crystal surface before integration into the lattice. As an example, consider precipitation of the barium sulfate $BaSO_4$. Vicum L. et al. (2003) applied thermodynamic models for aqueous Ba^{2+}, SO_4^{2-}, Na^+, Cl^- solutions differing in composition.

The dependence of solubility on composition is then expressed using the thermodynamic solubility product

$$\begin{aligned} K_{SP} &= a_{Ba^{2+}(aq)}\, a_{SO_4^{2-}(aq)} \\ &= c_{Ba^{2+}}\, c_{SO_4^{2-}}\, \gamma_{Ba^{2+}}\, \gamma_{SO_4^{2-}} = c_{Ba^{2+}}\, c_{SO_4^{2-}}\, \gamma_{\pm}^2 \end{aligned} \tag{11}$$

where c_i represents the concentration of ions i with γ_i being the activity coefficient of the ionic species i, and $\gamma_\pm$ represents the mean ionic activity coefficient that depends on the ionic strength.

The mean ionic activity coefficient $\gamma_\pm$ can be calculated using semi-empirical forms of the Debye-Hückel law, either that proposed by Bromley L.A., (1973), applicable for the ionic strength up to 6M, or the Pitzer K. (1991) model, valid for higher values of the ionic strength. The equilibrium between ions and undissociated ion pairs is expressed by the dissociation equilibrium, with K_a being the dissociation constant

$$K_a = \frac{c_{Ba^{2+}}\, c_{SO_4^{2-}} \gamma_\pm^{\,2}}{c_{BaSO_4(aq)} \gamma_{BaSO_4(aq)}} \tag{12}$$

The driving force for precipitation, S, is then expressed by:

$$S = \left(\frac{c_{Ba^{2+}}\, c_{SO_4^{2-}}}{K_{SP}} \right)^{0.5} \gamma_\pm \tag{13}$$

The impact of the composition on the driving force, including its effect on complex formation, is presented in **Fig. 1**, and the rate of growth expressed by Eqn. (14).

$$\begin{aligned} G &= k_R \left[\left(\frac{c_{Ba^{2+},i}\; c_{SO_4^{2-},i}}{K_{SP}} \right)^{0.5} \gamma_{\pm,int} - 1 \right]^2 \\ &= k_D \left(c_{Ba^{2+}} - c_{Ba^{2+},i} \right) = k_D \left(c_{SO_4^{2-}} - c_{SO_4^{2-},i} \right) \end{aligned} \tag{14}$$

with $k_r = 9.1 \times 10^{-12}$ ms^{-1} (Vicum L. et al., 2003) and $k_D = 4.0 \times 10^{-5}$ m^{4}s^{-1}kmol^{-1} (Bałdyga J. et al., 1995).

2. Time constants for precipitation and mixing

It has been well known since years (Bałdyga J. and Bourne J.R., 1999) that the history of supersaturation and the history of supersaturation structure determine the PSD and the crystal morphology in precipitation.

Before starting scale-up or modeling the precipitation processes, it is good policy to assess the importance of mixing in these processes. One should consider the time constants for all mixing and precipitation phenomena that affect the distribution of supersaturation and compare the characteristic time constants for these processes (Bałdyga and Bourne, 1999).

2.1 Time scales for precipitation

A comparison of the characteristic time constants for precipitation and mixing should yield the rate of the controlling mechanism. In the following section, the time constants that can be used to characterize precipitation

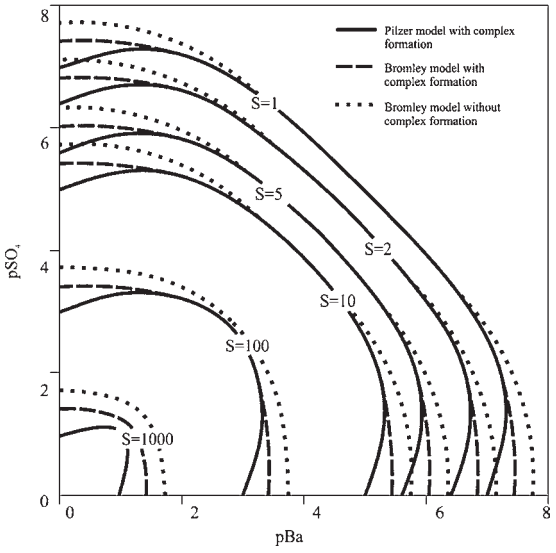

Fig. 1 Precipitation diagram for $BaCl_2$ and Na_2SO_4 in aqueous solution at 25 °C (constructed based on Vicum L. et al., 2003)

are presented. The first one is the time constant for the n^{th}-order chemical kinetics of homogeneous reaction,

$$\tau_R = \left[k_n\, c_{A0}^{n-1}\right]^{-1} \tag{15}$$

where k_n is the rate constant of the chemical reaction of order n and c_{A0} is the initial or feed concentration of reactant A. This time constant characterizes the rate of consumption of reactant A and thus the rate of creation of supersaturation provided that the chemical reaction controls this process. For a more general definition and more exact identification of τ_R, the method given by Bałdyga J. and Bourne J.R. (1999) is recommended; for example, for reaction of the type $A + \nu_B B \xrightarrow{k_2} C$, this method yields

$$\tau_R = \frac{1}{\nu_B k_2 \bar{c}_A + k_2 \bar{c}_B} \tag{16}$$

For the primary nucleation, the time constant can be approximated by the induction period, i.e. the time that elapsed between mixing on the molecular scale two reacting solutions and the appearance of the first crystals of precipitate; the induction period is considered to be inversely proportional to the rate of nucleation (Dirksen J.A. and Ring T.A., 1991).

$$\tau_N = \frac{6dN^*}{D \ln S} \simeq \frac{K}{J} \tag{17}$$

where K is a constant. The time constant τ_N represents a characteristic time that is necessary to form a characteristic, significant number of nuclei per unit volume.

The characteristic time for crystal growth can be expressed in relation to the rate of product concentration decrease caused by the crystal growth

$$\tau_{Gcr} = \left(\frac{\rho_c\, G}{M_c} A_g\right)^{-1} \left(c_c - c_c^*\right) \tag{18}$$

where c_c is the concentration of precipitating substance, and A_g is the specific surface area per unit volume of suspension.

Note the different role of processes characterized by the time constants presented above; the time constants τ_R and τ_{Gcr} characterize processes that in a similar way to mixing directly affect the distribution of supersaturation in the system, but only τ_{Gcr} depends on supersaturation itself. On the other hand, the nucleation process that is characterized by τ_N significantly depends on the supersaturation distribution but does not directly affect this distribution.

2.2 Time scales for mixing

The time constants for precipitation should be correlated with the process time and time constants for mixing.

The process time represents the batch time in the case of a batch precipitator and can be identified with the mean residence time τ in the case of the continuous flow systems.

Chemical reactions, nucleation and crystal growth are essentially the molecular-molecular-level process, which means that mixing on the molecular scale can directly influence the course of precipitation. However, the larger-scale mixing mechanisms often indirectly affect the precipitation process by changing the environment for local mixing. Hence the complete sequence of mixing processes, namely macromixing, mesomixing and micromixing, needs to be considered.

Macromixing can be identified as fluid blending on the scale of the precipitator. The characteristic length scale for this process is thus the size of the precipitator. Macromixing in the tank of volume V_t can be identified with the macroscopic flow pattern; e.g. the blending time τ_b or circulation time τ_C

$$\tau_b \propto \tau_C = const.\ \frac{V_t}{N D_S^3} \tag{19}$$

can be used as simple characteristics of macromixing in a stirred tank. In Eqn. (19), N represents the stirrer frequency and D_S is the stirrer diameter.

There are two mechanisms of mixing on a meso-scale.

The first mechanism of mixing on the meso-scale refers to the coarse-scale turbulent exchange between the fresh feed and its surroundings. The time constant τ_D for meso-scale mixing by turbulent diffusion can be expressed by

$$\tau_D = \frac{Q}{\bar{u}\, D_t} \tag{20}$$

where Q is the feeding rate, D_t represents turbulent diffusivity, and $\bar{u}$ is the local, average fluid velocity. The related length scale can be estimated either as $(Q/\bar{u})^{1/2}$ for high feeding rates or can be represented by the feed pipe diameter d_f for low feeding rates, when $(Q/\bar{u})^{1/2} < d_f$.

The second mechanism of mesomixing refers to disintegration of large eddies of a size larger than the Kolmogorov microscale, $\lambda_K = \nu^{3/4}/\varepsilon^{1/4}$, but smaller than the integral scale of concentration fluctuations, Λ_C. Inertial-convective disintegration proceeds without being influenced by molecular-scale mixing, however, it itself affects the micromixing by changing the local environment. The time scale τ_S for meso-scale mixing resulting from the inertial-convective disintegration of the large eddies reads

$$\tau_S = A \frac{\Lambda_C^{2/3}}{\varepsilon^{1/3}} \tag{21}$$

where A is the proportionality constant equal roughly to 1.2.

Micromixing processes are driven by the mechanism of the viscous-convective deformation of fluid elements, followed by molecular diffusion. A characteristic time constant for viscous convective mixing, i.e. for eddies smaller

than the Kolmogorov microscale scale, λ_K is known as the engulfment time constant (Bałdyga J. and Bourne J.R., 1989):

$$\tau_E = 17\left(\frac{\nu}{\varepsilon}\right)^{1/2} \tag{22}$$

that for a high Schmidt number can be replaced by the time constant for the viscous-convective and viscous-diffusive mixing

$$\tau_{VCVD} = 0.5\left(\frac{\nu}{\varepsilon}\right)^{1/2} \ln Sc \tag{23}$$

Based on these characteristic times, Bałdyga J. and Bourne J.R. (1999) proposed a classification of precipitation by comparing the characteristic times for mixing and reactive precipitation. Using τ_M to denote the characteristic mixing time (this can be any mixing time listed above), one can classify the precipitation subprocesses from the point of view of competition between precipitation and mixing. Therefore the reaction can be instantaneous ($\tau_M >> \tau_R$), fast ($\tau_M \approx \tau_R$) or slow ($\tau_M << \tau_R$). The effects of mixing should be observed in the first two cases.

It should be noted that the chemical reaction can be classified as slow compared to micromixing, but fast or instantaneous when compared to mesomixing or macromixing. For an instantaneous, mixing-controlled reaction (i.e. for τ_R much smaller than any mixing time scale) but with $\tau_N > \tau_{VCVD}$, the influence of molecular diffusion on nucleation can be neglected. However, when $\tau_N \approx \tau_E$, the viscous-convective micromixing (engulfment) affects precipitation. Usually, $\tau_N << \tau_{Gcr}$—thus mixing affects precipitation mainly through the nucleation step.

Note also that for a sufficiently slow feeding $\tau >> \tau_C$, one can assume a uniform concentration of the bulk and just model the reaction zone using meso- and/or micromixing modeling. If precipitation is slow compared to meso- and micromixing, the assumption of ideal mixing can be used. Considerations similar to the ones presented above can be helpful in choosing the model of mixing that is most suitable for the modeling and scaling up of precipitation processes.

2.3 Scale-up principles for precipitation

Scaling up industrial apparatus represents a fundamental step in the realization of industrial plants. The scale-up procedures are, however, not obvious in the case of complex processes, including precipitation. To scale up the process, one can use an empirical approach, i.e. carry out the process at a number of scales and gain enough information to make an empirical prediction of the system performance on a larger scale, i.e. extrapolate the process using principles of similarity. Dimensionless similarity criteria can be derived using the available governing equations for mass, momentum, species, energy, and population balances; when they are not available, the Buckingham's Pi Theorem can be used instead (Zlokarnik M., 2002).

In the geometrically similar systems, a complete similarity occurs if all necessary dimensionless criteria derived either from the differential equations or obtained using the Pi Theorem are equal. For example, to have a similar velocity distribution in a single-phase system, it is enough to apply the same Reynolds number in both systems. In complex precipitation processes, such complete similarity is impossible and in fact not necessary. We usually want to reproduce the product quality, for example, the particle size and morphology at the larger scale and obtain identical not similar products from the systems differing in scale. Thus, one should apply a partial similarity and in this way obtain a reduced number of the most important similarity criteria for the process.

A more fundamental approach to scale-up is based on modeling with the goal of predicting the effect of scale-up and of understanding the process in sufficient detail.

The strategy recommended here is to start by performing an analysis of time constants to identify which sub-processes are less important on the large scale, and gain information on which requirements related to such processes can be neglected. Afterwards, a physical model employing CFD should be applied to predict the scale-up effects more correctly and finally to optimize the process.

As an example of scaling up with a combined application of time scale analysis and CFD, let us consider an antisolvents precipitation method known as the solution-enhanced dispersion by supercritical fluids process (SEDS^{TM}) that has been proposed by York P. and Hanna M. (1996). In the SEDS^{TM} process, the supercritical fluid (SCF) acts as an antisolvent and the substrate solution is co-introduced into a nozzle and mixed intensively with the antisolvent in a nozzle chamber, from where they both flow into the precipitation vessel at high velocity as a turbulent jet, as schematically depicted in **Fig. 2**. The process is carried out above the mixture critical pressure, so the antisolvent (CO_2) is completely miscible with the solvent (ethanol). As mentioned earlier, the distribution of supersaturation and the supersaturation history of fluid elements determine the PSD and the crystal morphology in precipitation, which means that macro-, meso-, and micromixing processes can affect the particle size distribution.

To scale a process up or down, one needs invariability of all characteristic times: $\tau = idem$, and $\tau_i = idem$ from Eqn. (15) to (23), which is of course impossible.

Details on the scale-up of the SEDS process can be found in Bałdyga J. et al. (2010). Interpreting the precipitation vessel shown in **Fig. 2** as a pipe-in-pipe system, with the outer tube fluid velocity equal to zero, one can

characterize a similarity of the flow pattern using the Curtet number (Becker H.A., et al., 1963; Craya A. and Curtet R., 1955), which characterizes turbulent self-entrainment.

$$C_t = \frac{d_0/D_v}{\sqrt{1-0.5(d_0/D_v)^2}} \tag{24}$$

where d_0 is the nozzle orifice diameter and D_v is the diameter of the precipitation vessel. This means that under process conditions, there is a recirculation eddy induced as shown in **Fig. 3**, and the flow similarity requires $d_0/D_v = const$. The recirculation eddy causes the exhausted, residual fluids to dilute the fresh supersaturated solution, which significantly reduces the nucleation rate.

The supersaturation is then unloaded mainly due to the particle growth.

Using the jet nozzle diameter d_0 for the length scale, and the nozzle velocity u_0 for the velocity scale, we express the rate of energy dissipation by

$$\varepsilon(\vec{x}/d_0) = \frac{u_0^3}{d_0} f(\vec{x}/d_0) = \varepsilon_0 f(\vec{x}/d_0) \tag{25}$$

where function $f(\vec{x}/d_0)$ represents the dimensionless distributions of the rate of energy dissipation.

This means that both the mean residence time τ and the characteristic convection time τ_C can be expressed by

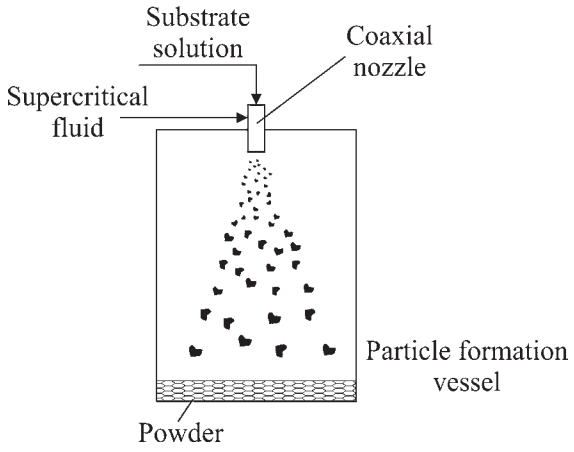

Fig. 2 Solution-Enhanced Dispersion by Supercritical Fluid Process (SEDS Process).

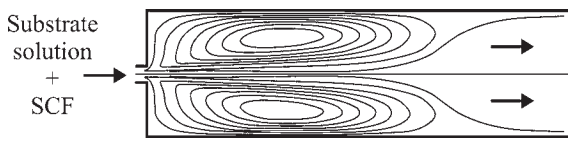

Fig. 3 The structure of the flow in the SEDS particle formation vessel, represented by the stream lines (Bałdyga J. et al., 2010, copyright 2010 Elsevier Ltd., reprinted with permission).

$$\tau \propto \tau_C = \frac{d_0}{u_0} \tag{26}$$

and the fluid elements should have the same dimensionless positions $\vec{x}/d_0$ after the same dimensionless time period t/τ_C.

The time constants for meso-scale mixing then read

$$\tau_D = \frac{Q}{\bar{u}D_t} \propto \frac{u_0 d_0^2}{u_0 \varepsilon_0^{1/3} d_0^{4/3}} = \frac{d_0}{u_0} \tag{27}$$

where $D_t \propto u'\Lambda_C \propto (\varepsilon d_0)^{1/3} \cdot d_0$, and

$$\tau_S \propto \frac{\Lambda_C^{2/3}}{\varepsilon^{1/3}} \propto \frac{d_0^{2/3}}{(u_0^3/d_0)^{1/3}} \propto \frac{d_0}{u_0} \tag{28}$$

The time constants for the viscous-convective and viscous-diffusive micromixing processes scale as $\varepsilon^{-1/2}$ see Eqns. (22) and (23), which means that $\tau_E = 1/E \propto d_0^{1/2}/u_0^{3/2}$ and $\tau_{VCVD} \propto d_0^{1/2}/u_0^{3/2}$ when the fluid properties are the same in both scales considered. Hence, the ratio of any mesomixing time constant and micromixing time constant scales as $Re_0^{1/2}$, where $Re_0 = u_0 d_0/\nu$, for example $\tau_S/\tau_E = Re_0^{1/2}$. This shows that at large Reynolds number values, $\tau_S >> \tau_E$, with mesomixing controlling the process and negligible micromixing effects. Based on this, Bałdyga J., et al. (2010) proposed the following:

(1) for developed turbulence, characterized by the high Re_0 values, micromixing effects are negligible, the scale-up criterion is then $(d_0/u_0)_1 = (d_0/u_0)_2$ and thus $(u_0)_2/(u_0)_1 = X^{1/3}$, $(d_0)_2/(d_0)_1 = X^{1/3}$ for the throughput ratio $X = Q_2/Q_1 = (u_0 d_0^2)_2/(u_0 d_0^2)_1$,

(2) for weakly turbulent flows micromixing dominates, and the scale-up criterion is then $\tau_{E1} = \tau_{E2}$ or $(u_0^3/d_0)_1 = (u_0^3/d_0)_2$ and thus $(u_0)_2/(u_0)_1 = X^{1/7}$ and $(d_0)_2/(d_0)_1 = X^{3/7}$. As a safe scale-up method, the criterion based on high Reynolds number flows has been recommended.

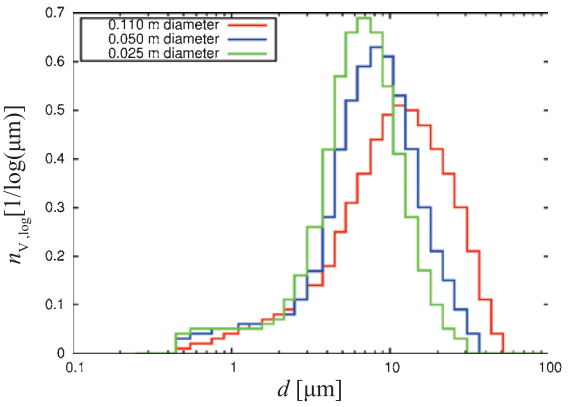

Fig. 4 Particle size distribution of the product obtained in vessels of different diameter D_v with a nozzle diameter $d_0 = 9 \times 10^{-4}$ m; $C_t = 0.036$ for $D_v = 0.025$ m, $C_t = 0.018$ for $D_v = 0.050$ m, $C_t = 0.0082$ for $D_v = 0.11$ m ($p = 120$ bar, $T = 323$ K). (Bałdyga J. et al., 2010, copyright 2010 Elsevier Ltd., reprinted with permission).

To validate this criterion, CFD simulations and experimental investigations for acetaminophen precipitation were carried out for three equipment scales: a laboratory scale with $d_0 = 2.0 \cdot 10^{-4}$ m, a pilot scale with $d_0 = 4.0 \cdot 10^{-4}$ m, and a small manufacturing plant (SMP) scale with $d_0 = 9.0 \cdot 10^{-4}$ m. **Fig. 4** shows the importance of the geometric similarity; the particle size distributions obtained for the same process conditions, but different vessel diameters and thus different C_t values, are shown in **Fig. 4**.

Fig. 5 shows the results of application of the scale-up criterion $(d_0/u_0)_1 = (d_0/u_0)_2$. The micromixing effects decrease with increasing system scale, following the relation $Re_{02}/Re_{01} = (d_{02}/d_{01})^2$, and are negligible in the case of both the pilot plant and the SMP results presented in **Fig. 5**.

Fig. 6 shows an example of the CFD prediction of the supersaturation distribution in the small manufacturing plant; a similar distribution was observed in the case of the pilot plant, whereas in the case of the laboratory scale, the supersaturation was about 7 % higher due to a too small Reynolds number.

The importance of the time constants, either for the direct modeling-based scaling up or for the formulation of scale-up rules, has been emphasized in several publications. For example, Zauner R. and Jones A.G. (2000) have shown that the calcium oxalate precipitation can be scaled up by using the time constants for micro- and mesomixing in combination with a simple segregated feed model. An interesting discussion on using time constants is presented by Gavi E. et al. (2007), in the context of the scale-up of Confined Impinging Jet Reactors (CIJR) based on the results of Marchisio D.L. et al. (2006).

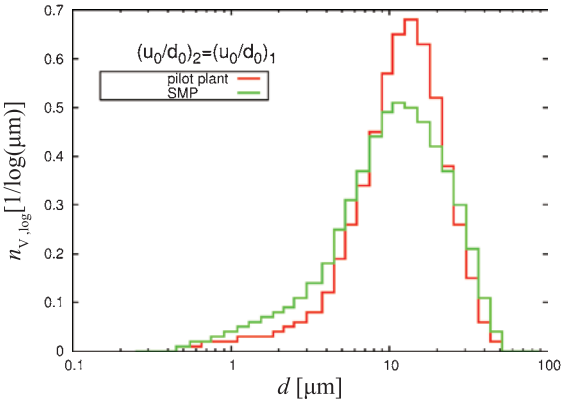

Fig. 5 Scale-up from pilot plant to small production scale: (log PSD, $p = 120$ bar, $T = 323$ K, $C_t \approx 0.015$). (Bałdyga J. et al., 2010, copyright 2010 Elsevier Ltd., reprinted with permission).

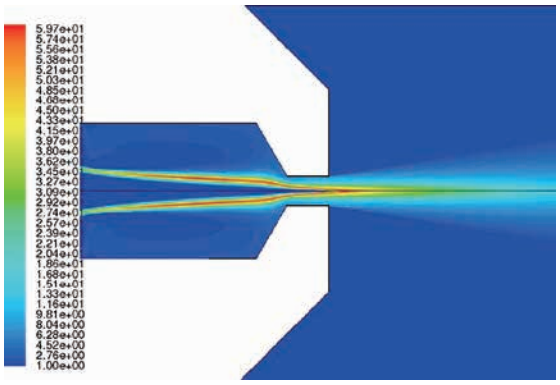

Fig. 6 Supersaturation ratio distribution in the nozzle and the jet of SMP. (Bałdyga J. et al., 2010, copyright 2010 Elsevier Ltd., reprinted with permission).

3. Modeling of precipitation

3.1 Concept of population balance

The balancing of populations is related to classic problems of statistical mechanics that were defined in the 19th century, whereas the fundamentals of the methods of treating populations of aggregating particles were introduced by Smoluchowski M. (1917). The present status of the population balance equation is a result of application of the Liouville equation to particulate processes by Hulburt H.M. and Katz S. (1964). Hulburt H.M. and Katz S. (1964) transformed the Liouville equation by replacing the momentum coordinates by other coordinates, equivalent to particle properties.

$$\frac{\partial n}{\partial t} + \sum_{i=1}^{3} \frac{\partial \left[u_{pi}(\vec{x},t) n \right]}{\partial x_i} + \sum_{j=1}^{m} \frac{\partial \left[w_{pj}(\vec{x},t) n \right]}{\partial x_j} = B(\vec{x},t) - D(\vec{x},t) \tag{29}$$

where x_i are the external coordinates representing positions in the physical space and x_j are the internal coordinates representing properties of particles, n is the population number density, u_{pi} refers to the component of the rate of change of particle position in the physical space, m is the number of particle properties, and w_{pj} refers to the component of the rate of change of the particle property, and B and D are the birth and death functions at the point in the phase space.

Very often, the property of the particle is identified with the particle size, L, and then Eqn. (29) takes the form

$$\frac{\partial n}{\partial t} + \sum_{i=1}^{3} \frac{\partial \left[u_{pi}(\vec{x},t) n \right]}{\partial x_i} + \frac{\partial \left[G(\vec{x},t) n \right]}{\partial L} = B(\vec{x},t) - D(\vec{x},t) \tag{30}$$

Eqn. (30) can be used under assumption that the shape of the particles remains unchanged during particle growth, and the concept of constant shape factors can be used, with the particle volume $v_p = k_v L^3$, the particle surface area $a_p = k_a L^2$, and the characteristic size L chosen so that the ratio of the shape factors $k_a/k_v = 6$. However, this

is not always the case. When, for example, the particle shape is determined by the growth of two faces, Eqn. (29) should be used as

$$\frac{\partial n}{\partial t}+\sum_{i=1}^{3}\frac{\partial\left[u_{\mathrm{p}i}(\vec{x},t)n\right]}{\partial x_i}+\frac{\partial(G_1 n)}{\partial L_1}+\frac{\partial(G_2 n)}{\partial L_2} = B(\vec{x},t)-D(\vec{x},t) \tag{31}$$

Eqn. (29) should be solved together with the mass, momentum, energy, and species balances to determine the particle velocity in the physical space as well as the rates of change of the particle properties. This creates numerical difficulties because the population balance equation should be solved in $(m + 3)$-dimensional space, whereas all other equations are defined in the 3-dimensional physical space.

To reduce the dimensionality, the volume-averaged population balance can be used by applying either a mechanistic model of micromixing, (Bałdyga J. et al., 1995) or another macroscopic domain including the entire equipment, e.g. the crystallizer (Randolph A.D. and Larson M.A., 1971). This reduces the number of coordinates to the number of particle properties, m.

In the literature, for $m > 1$, one can find mostly publications dealing with such volume-averaged populations. Ramkrishna D. and Mahoney A.W. (2002) considered the application of the multi-dimensional population balances to represent the dynamics of particle morphology. They discussed the possibility of finding precipitation kinetics from the dynamics of the particle size distribution by the inversion of the multidimensional population balances (i.e. by solving the inverse problem). Efficient numerical techniques to treat the problem numerically were considered by Qamar S. and Seidel-Morgenstein A. (2009). Briesen H. (2006) tried to simulate the crystal size and shape by means of the population balance model based on the crystal volume and the shape factor as internal coordinates. Ochsenbein, D.R. et al. (2015ab) considered the growth and agglomeration of particles including effects on their shape.

To reduce the problem to the 3-dimensional physical space, one can use the moment transformation of the population balance. For example, for particles described by one internal coordinate L, Eqn. (30) can be used, so for $m = 1$, one gets the set of equations represented by Eqn. (32)

$$\frac{\partial m_j}{\partial t}+\frac{\partial\left(u_{\mathrm{p}i}m_j\right)}{\partial x_i} = 0^j J + \mathrm{j}G\,m_{j\text{-}1}+B_{\mathrm{f}\,j}-D_{\mathrm{f}\,j} \tag{32}$$

for $i = 1, 2, 3$ and $j = 0, 1, 2, ...$

where $\vec{u}_{\mathrm{p}}=\left(u_{\mathrm{p}1},u_{\mathrm{p}2},u_{\mathrm{p}3}\right)$ is the vector of particle velocity, and the moments of order j are defined as

$$m_j(\vec{x},t)=\int_0^\infty n(\vec{x},t,L)\,L^j\,\mathrm{d}L \tag{33}$$

and $n(\vec{x},t,L)$ represents the crystal size distribution at the time t and position $\vec{x}$, and $B_{\mathrm{f}j}$ and $D_{\mathrm{f}j}$ are the birth and death terms for the moments of order j.

The averaged birth and death terms for the moments of the order j are not closed as the form of the CSD is not known in advance. This creates the first "closure problem" that can be solved using an idea of the presumed distribution. A good example here is the quadrature method of moments (McGraw R., 1997).

3.2 Application of CFD

Consider the process of precipitation of a solid product from two liquid ionic solutions A and B $A^{n+} + B^{n-} \rightarrow C\downarrow$ involving an instantaneous chemical reaction that produces a supersaturated solution of the product C, and its subsequent crystallization-precipitation, in the systems with turbulent flow.

A quantitative description of this process requires a complete knowledge of the spatial distribution of the instantaneous local concentration of ions A^{n+} and B^{n-}, product C, and other ions present in the system to properly express the driving force. Identification of these concentrations requires the solving of a system of partial differential equations describing the momentum, mass, species, and population balances in the system.

The Reynolds averaging procedure, typical for treating turbulent flows, produces more unknowns than the number of the balance equations, and the set of the partial differential equations becomes unclosed. We thus have the second "closure problem". This "closure problem" is usually solved by forming a "closure hypothesis". The "closure hypothesis" introduces additional information based on the experimental data, investigator's experience, or intuition. They are included in CFD models such as the k-ε model, Reynolds Stress Model or Large Eddy Simulation model. To simulate the course of precipitation, CFD should be combined with the averaged population balance equation. In the simplest case it can be the standard k-ε turbulence model (Launder B.E. and Spalding D.E., 1972) which employs the hypothesis of gradient diffusion for momentum and species transport.

Eqn. (32) employs the local, instantaneous values of the velocity and concentration. Application of Eqn. (32) to the case of turbulent flow by utilizing the Reynolds decomposition and the Reynolds averaging (denoted with overbar) was obtained by Bałdyga J. and Orciuch W. (2001).

$$\frac{\partial\overline{m_j}}{\partial t}+\frac{\partial\overline{u_{\mathrm{p}i}m_j}}{\partial x_i} = 0^j\overline{J}+j\overline{G\,m_{j-1}}+\overline{B_{\mathrm{f}}}-\overline{D_{\mathrm{f}}} \tag{34}$$

After introducing a concept of gradient diffusion for particles and employing a concept of mixture fraction f that can be interpreted as a volume fraction of the non-reacting fluid originating in the A stream when A and B solutions are mixed, one gets Eqn. (34) in the closed form

$$\frac{\partial \overline{m}_j}{\partial t} + \frac{\partial \left(\overline{m}_j \overline{u}_{\mathrm{p}i}\right)}{\partial x_i} = \frac{\partial}{\partial x_i}\left\{D_{\mathrm{pT}} \frac{\partial \overline{m_j}}{\partial x_i}\right\} + 0^j \overline{J} + j\int_0^1 G(f) m_{j-1} \Phi(f)\,\mathrm{d}f + \overline{B}_{\mathrm{f}} - \overline{D}_{\mathrm{f}} \tag{35}$$

where D_{pT} is the local value of the particle turbulent diffusivity coefficient.

The statistics of fluid elements is expressed using the probability density functions, PDF, $\Phi(f)$, for example the presumed beta distribution (Bałdyga J. and Bourne J.R., 1999). The distributions of the average concentrations $\overline{f}$ and the inert tracer concentration variance, $\sigma_{\mathrm{S}}^2 = \overline{\left(f - \overline{f}\right)^2}$ are necessary to define the presumed PDF and can be calculated using CFD and one of the mixing models: the multiple-time-scale model of the turbulent mixer (Bałdyga J., 1989) or the spectral relaxation model (Fox R.O., 1995). Eqn. (35) should be solved together with the partial differential equations describing the species balances.

$$\frac{\partial \overline{c_\alpha}}{\partial t} + \overline{u}_i \frac{\partial \overline{c_\alpha}}{\partial x_i} = \frac{\partial}{\partial x_i}\left[\left(D_\alpha + D_{\mathrm{t}}\right)\frac{\partial \overline{c_\alpha}}{\partial x_i}\right] - \frac{k_{\mathrm{a}}}{2}\frac{\rho_{\mathrm{p}}}{M_{\mathrm{C}}}\int_0^1 G(f)\, m_2(f)\, \Phi(f)\,\mathrm{d}f \tag{36}$$

The results of application to the SEDS process of the model presented above were already shown in **Fig. 6**. More results are presented in **Fig. 7**. The method of SEDS modeling is described in detail by (Bałdyga J. et al., 2004, 2008a) and (Henczka M. et al., 2005).

Fig. 7 explains how one can control the particle size by varying the flow rate (expressed here by *Re*); this effect resulting from the competition between the creation of supersaturation by mixing fresh fluids and its decrease by dilution with residual fluids was considered in Section 2.3 for scaling up precipitation processes. **Fig. 7** also illustrates the competition between meso- and micromixing. The comparison of CFD models, the first model neglecting and the second including micromixing effects shows that micromixing dominates the process at small Reynolds number turbulent flows, whereas mesomixing dominates at high *Re*. It is interesting that predictions of the mechanistic E-model (Shekunov B.Y. et al., 2001) are very good and illustrate very well the effects of creation and dilution of supersaturation due to mixing.

Other methods applying the presumed PDF are based on the application of groups of the Dirac delta functions

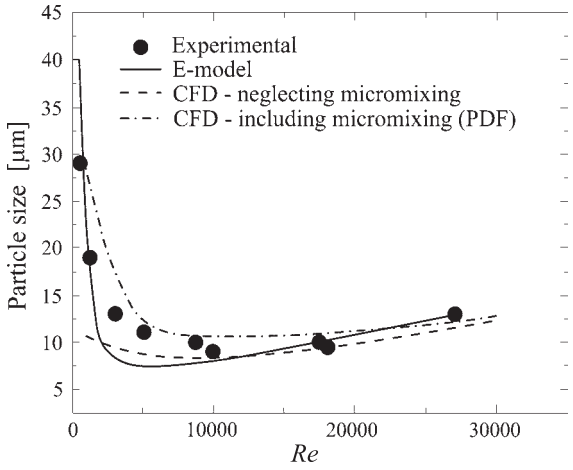

Fig. 7 Comparison of the model predictions with the experimental results for mean particle size of acetaminophen crystals obtained in the SEDS process—E-model from Shekunov B.Y. et al. (2001), CFD from Henczka M. et al. (2005)

representing different environments (Piton D. et al., 2000, Marchisio D.L. et al., 2001), or combining DQMOM with the IEM model of micromixing (Gavi E. et al., 2007). A full PDF method was applied by Di Veroli G. and Rigopoulos S. (2010). The comparison of these three approaches, based on the presumed beta-PDF, multienvironment, and the full PDF, was carried out by Fissore D. et al. (2002). The following examples present the effects of mixing on the precipitation of $BaSO_4$ in the single-feed and double-feed stirred tank reactors operating in semi-batch mode.

Fig. 8 presents a visualization of the mixing zone for the single-feed simulations, which is regarded as the zone of the intensity of segregation, $I_{\mathrm{S}} = \overline{(f')^2} \Big/ \left[\overline{f}\left(1-\overline{f}\right)\right]$ larger than 0.01. The intensity of segregation represents the normalized variance of concentration of the inert tracer. Clearly, the micromixing is not instantaneous and not localized at the feed point.

Fig. 9 compares the measured and predicted effects of the initial concentration on the particle size for the single-feed mode. The effect of concentration is predicted well, especially at the higher concentration values.

In the case of the double-feed precipitation, the effects of mixing are more significant. Segregation of the fresh feeds A and B prevents the creation of supersaturation, and thus micromixing decreases segregation, increases supersaturation and the nucleation rate close to the feed pipe.

At a further distance from the feed point, micromixing with the residual solution from the bulk decreases supersaturation and limits nucleation. The local intensity of the segregation of fresh fluids A and B is presented in **Fig. 10**, showing the zone where mixing affects the precipitation

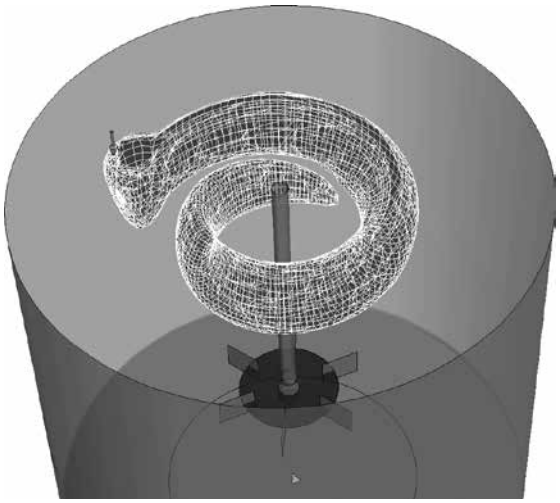

Fig. 8 Visualization of the mixing zone (Bałdyga J. et al. 2006) for the single-feed mode for $N = 5s^{-1}$ and $t_f = 1230$ s. (Bałdyga et al. 2006, reprinted with permission).

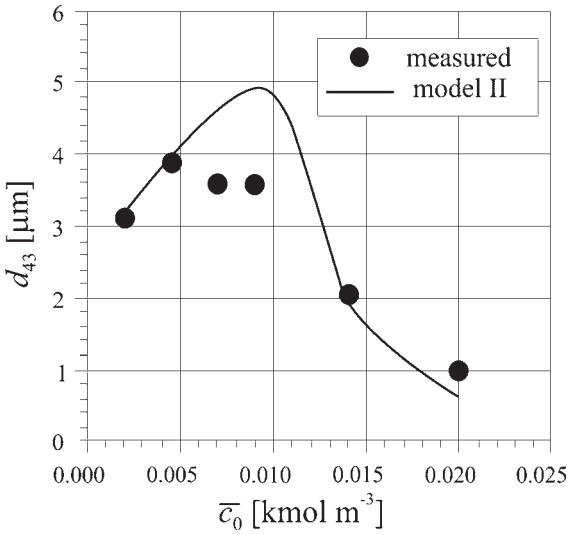

Fig. 9 Comparison of the model predictions with the experimental results for single-feed mode with the feed introduced above the impeller (Bałdyga J. et al., 2006, reprinted with permission). Model II accounts for the micromixing effect.

Fig. 10 Mixing in the feed zone of a double-feed precipitator operating at $N = 3s^{-1}$ and $q_f = 0.12 \times 10^{-6}m^3s^{-1}$ 3D representation of the feed zone for the intensity of segregation $I_S \geq 0.01$ (Bałdyga et al. 2006, reprinted with permission).

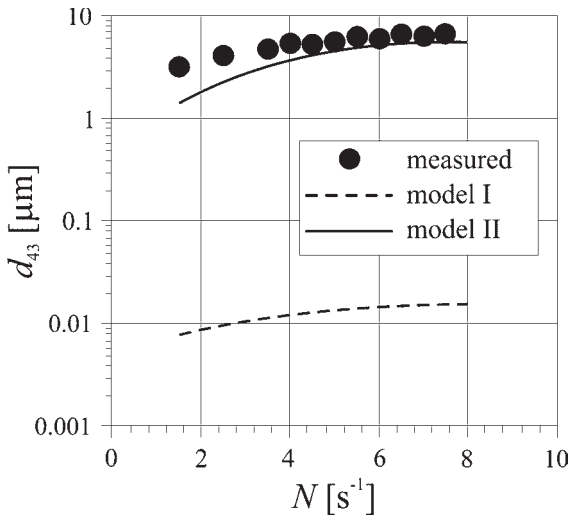

Fig. 11 The effect of the stirrer speed on the mean crystal size for $q_f = 0.12 \times 10^{-6}m^3s^{-1}$, $\overline{c}_0 = 0.0045$ kmolm^{-3}, feed concentrations $c_{A0} = c_{B0} = 0.234$ kmol m^{-3} and $\alpha_V = 50$. Solid line—predicted by Model II accounting for the micromixing effects; dashed line—predicted by Model I neglecting the micromixing effects (Bałdyga et al. 2006, reprinted with permission).

process.

Fig. 11 presents a comparison of two models: model I neglecting fluctuations of species concentrations, thus neglecting the effect of the inertial-convective and viscous-convective concentration fluctuations, and based on the local average concentrations, with complete model II including the effects of micromixing. There is a satisfactory agreement of the experimental data with the model predictions only in the case of model II.

Neglecting the micromixing (model I) results in a very large amount of very small particles, due to the fact that very high supersaturation values are created in the region of the impeller which—due to the strong nonlinearity of Eqn. (7)—results in a very large amount of small particles. The time constant for nucleation (about 10^{-5} s), is much smaller than the time constant for micromixing that—close to the impeller—is of the order of milliseconds. This clearly shows that at high supersaturation, the micromixing effects need to be included to match the simulation results with the experimental data.

4. Time and length scales for aggregation

According to Söhnel O. and Garside J. (1992), aggregation denotes all processes of clustering of separate particles to form larger particles, whereas in the agglomeration process, strong secondary particles are formed that are held together by crystalline bridges or physical forces. In the case of coagulation, only very small particles are involved and only physical forces hold them together. Let us now discuss what we mean by small particles, and let us try to classify them based on their size. In the case of solid-liquid particulate systems, particles of a size smaller than 1 μm are called colloidal, whereas the larger ones—suspended (Elimelech M. et al., 1995).

In the case of a dispersion subjected to turbulent flow, the classification should be based on the comparison of the particle size expressed by the particle radius a with the characteristic length scales for turbulence.

We apply two characteristic scales of turbulence: the Kolmogorov microscale $\lambda_K = \nu^{3/4}/\varepsilon^{1/4}$, the smallest scale of turbulent flow, and $L_e = (u')^3/\varepsilon$, the scale of the large, energy-containing eddies; here u' is the root-mean-square velocity fluctuation.

Particles of the size a, smaller than the Kolmogorov length microscale, λ_K, are classified as small. The very small particles are groups of the small particles for which $a << (D_B^\infty/E)^{1/2}$ or $Pe = Ea^2/D_B^\infty << 1$, so their movements are dominated by the Brownian motion, which leads to perikinetic collisions and perikinetic aggregation. The Péclet number is defined as the ratio of the diffusion time a^2/D_B^∞ to the convection time $1/E$. E represents the rate of deformation here and D_B^∞ is the coefficient of Brownian diffusion for a particle separated from other particles. In the group of large particles ($a > \lambda_K$), there are inertial-convective effects; aggregation of very large particles, $a > L_e$, is hardly possible in practice.

The time-scale analysis is also important to make the description more complete as it considers more mechanisms which affect aggregation. The time scales characterizing particles are: the diffusion time τ_B, and the relaxation time τ_p, respectively:

$$\tau_B = \frac{(a_1 + a_2)^2}{D_{12}^\infty} \tag{37}$$

$$\tau_p = \frac{16\rho_p\left(1 + \frac{1}{2}\frac{\rho}{\rho_p}\right)a^2}{3\mu C_D Re_p} \tag{38}$$

where D_{12}^∞ is the mutual Brownian diffusion coefficient for large particle separation, C_D is a friction factor (also known as a drag coefficient), ρ_p is the particle density, the Reynolds number, Re_p, is defined using the relative velocity fluid-particle and the equal volume sphere diameter. They can be compared with the time scales for turbulence: the Kolmogorov time microscale, τ_K,

$$\tau_K = \left(\frac{\nu}{\varepsilon}\right)^{1/2} \tag{39}$$

and the Lagrangian integral time scale, T_L that can be estimated using Eqn. (40) (Hinze J.O., 1975).

$$T_L = \beta\frac{\Lambda_f}{u'} = \frac{\beta(u')^2}{2\varepsilon} = 0.2\,\frac{(u')^2}{\varepsilon} \tag{40}$$

where Λ_f is the longitudinal integral scale of turbulence, u' is the r.m.s. (root-mean-square) velocity fluctuation, and $\beta \approx 0.4$.

For $\tau_p < \tau_K$, there is no correlation between particle motions if $\tau_B < \tau_K$ and the motions are correlated for $\tau_B > \tau_K$. For $\tau_K < \tau_p < T_L$ and $\tau_B > T_L$ there is a partial correlation of particle motions; for $\tau_p > T_L$ and $\tau_B > T_L$ there is no correlation between motions of the particles.

One can see that it is not enough that particles are small $a < \lambda_K$, to understand the mechanism of aggregation because either perikinetic or orthokinetic aggregation can be observed depending on the relation between time scales or related values of the Péclet number. Similarly in the case of large particles, $a > \lambda_K$, with partial or no correlation of particle motions, the appropriate kernels including inertial effects should be applied.

5. Modeling of aggregation and breakage of agglomerates

5.1 Aggregation

The aggregation rates can be considered either in the Lagrangian or the Eulerian frame of reference. The Lagrangian approach is based on the trajectory analysis of the particles and the Eulerian approach is based on the concept of the pair distribution function that mimics in a continuous way the particle concentration distribution. It enables identification of the probability of finding another particle (and its orientation if not spherical) in the vicinity of the considered particle.

In the Lagrangian approach, instantaneous values of the relative particle velocity are calculated from Newton's second law, including or not including Brownian motions. If they are included then the model takes the form of a stochastic Langevin-type differential equation with solutions representing stochastic trajectories. In practice, the concept of limiting trajectories is most often applied, which means that the random movements are neglected and the limiting trajectories define the collision cross-section. To include random movements, the methods of dynamic simulations can be used; a detailed description of these methods can be found in the book by Elimelech M. et al. (1995).

In the Eulerian approach, the Fokker-Planck equations are applied. Consider small particles with $\tau_p \ll \tau_K$. The particles are conveyed by the fluid, diffused by the Brownian motion, and are subjected to colloidal DLVO-type forces. They can be in the perikinetic $\tau_B < \tau_K$ or orthokinetic $\tau_B > \tau_K$ regime, or in the regime in between the two $\tau_B \approx \tau_K$.

The collision rate constant, β_c, can be calculated from the pair probability function, c_{pair}, distribution:

$$\beta_c = \int_{S_C} \left(\overline{\overline{D}}_B \cdot \vec{\nabla} c_{pair} - \vec{u}_f c_{pair} - \vec{u}_{int} c_{pair} \right) \cdot \vec{n} \, dS_C \tag{41}$$

where $\vec{u}_f$ is the relative particle velocity resulting from the fluid flow, $\vec{u}_{int}$ is the relative particle velocity resulting from the colloidal interactions, S_C is the entire collision surface and $\vec{n}$ is the normal to this surface (Melis S. et al., 1999). Eqn. (41) can be simplified (Bałdyga J. and Orciuch W., 2001) by taking an ensemble average of Eqn. (41) and using a concept of the gradient turbulent diffusion, expressed in terms of a generalized form of the stability ratio W.

$$\beta_c = 4\pi D_{12}^{\infty} (a_1 + a_2)/W \tag{42}$$

$$W = (a_1 + a_2) \int_{a_1+a_2}^{\infty} \frac{\exp \int_{\infty}^{r} \frac{1}{R_D k_B T} \left(\frac{dV}{ds} \right) ds}{R_D G(r,\lambda) r^2} dr \tag{43}$$

where V is the interaction potential, $G(r,\lambda)$ is the hydrodynamic function describing the squeezing of the liquid out of the space between particles, r is the center-to-center distance, λ is the particle size ratio, and R_D represents the overall (turbulent and Brownian) diffusivity ratio.

Fig. 12 shows the stability ratio values calculated using the DLM model to predict the surface potential.

The predicted values of the surface potential are shown in **Fig. 13**. They have been calculated using either the Double Layer Model, DLM, Löbbus M. et al. (1998), or the Gel Layer Model, GLM, (Löbbus M. et al., 1998; Adler J.J. et al., 2001). One can see strong repulsion effects for pH > 6, with strong effects on the stability ratio, and almost no repulsion below pH = 6.

Fig. 14 shows that at $Pe \to 0$ (because $\varepsilon \to 0$), we observe perikinetic aggregation with no effect of the rate of energy dissipation, whereas for large ε, the orthokinetic aggregation controlled by convection ($Pe >>> 1$) is observed. The effects of colloidal forces are observed at the perikinetic limit only and are negligible when the orthokinetic mechanism dominates.

When the relaxation time is large enough, $\tau_p \geq \tau_K$, the inertial effects cannot be neglected and then the rate of collision depends on fluctuations of the relative velocity of particles w, which depends on the fluid velocity fluctu-

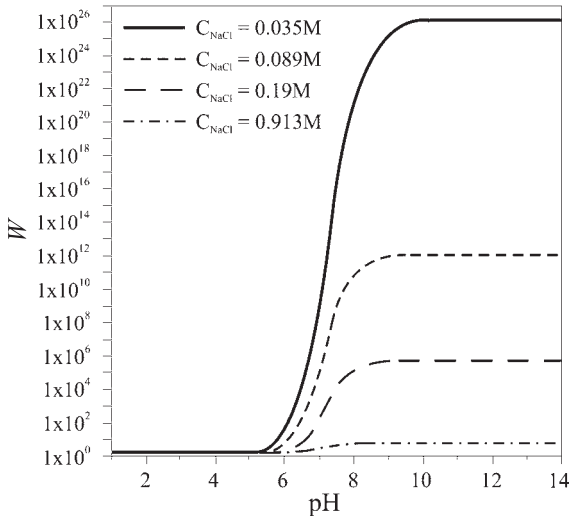

Fig. 12 The effect of the process conditions on the stability ratio, W, for 10 nm particles (Bałdyga J. et al., 2012, copyright 2012 Elsevier Ltd., reprinted with permission).

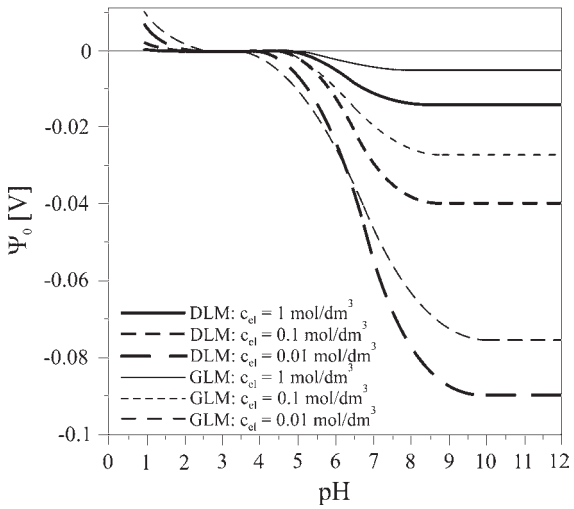

Fig. 13 The effect of the pH and ionic strength on the surface potential according to the DLM and GLM models.

ations and relaxation time (Kruis F.E. and Kusters K.A., 1996)

$$\beta = \sqrt{\frac{8\pi}{3}} (a_i + a_j)^2 \sqrt{w^2} \tag{44}$$

Because not every collision leads to agglomeration, the concept of the probability or efficiency of agglomeration, P_S, can be used (Bałdyga J. et al., 2003).

$$P_S = \exp\left(-\overline{t_c}/\overline{t_i} \right) \tag{45}$$

where $\overline{t_c}$ represents the average time necessary to build a strong enough bridge between the particles and $\overline{t_i}$ is the average interaction time.

The time period $\overline{t_c}$ can be interpreted as the time nec-

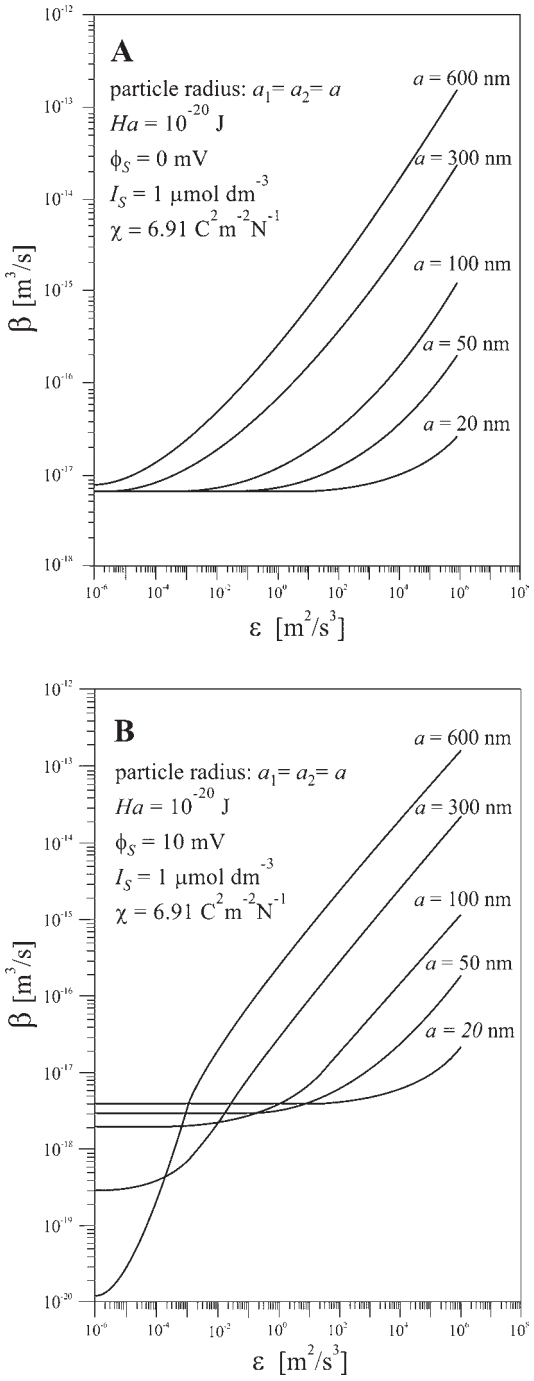

Fig. 14 Collision rate constant, β, as a function of the energy dissipation rate and particle size. A) no repulsion, B) weak repulsion. *Ha* is Hamaker constant, ϕ_s is surface potential and χ represents the dielectric permittivity.

essary to reach the bridge diameter D_b with the local rate of crystal growth G,

$$\bar{t}_c = \frac{D_b}{f(\lambda)G} \tag{46}$$

where $f(\lambda)$ represents the shape function as proposed by David R. et al. (1991). The results of the simulations show that at constant supersaturation, both an increase of the

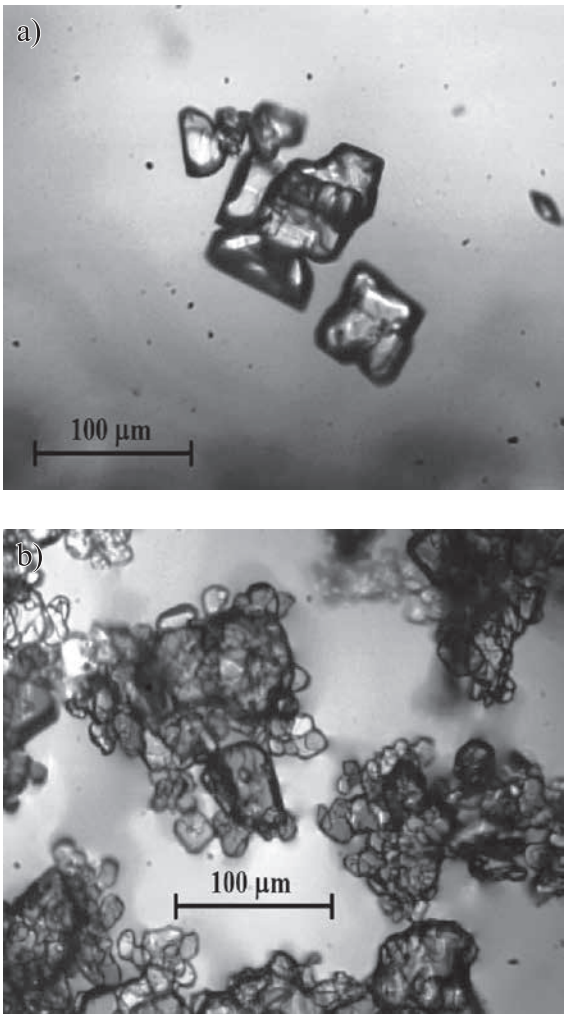

Fig. 15 Crystals of benzoic acid produced with the feeding tube tip positioned close to the impeller. $Q = 50$ cm^3/min
a) $c_{A0} = 0.5$ mol/dm^3, $c_{B0} = 0.5$ mol/dm^3, $N = 200$ rpm;
b) $c_{A0} = 2.0$ mol/dm^3, $c_{B0} = 2.0$ mol/dm^3, $N = 300$ rpm.
(based on Bałdyga J. and Krasiński A., 2005).

energy input and an increase of the particle size lower the probability of agglomeration during collisions. The agglomeration kernel $\beta(L_1,L_2)$ can then be expressed as the product of the collision kernel, denoted here by β_c, and the agglomeration probability, P_S:

$$\beta = \beta_c \cdot P_S \tag{47}$$

The results of Bałdyga J. and Krasiński A. (2005) illustrate this phenomenon for the reactive, agglomerative precipitation of benzoic acid in a semibatch, stirred tank reactor. Supersaturation was created in this case by the homogeneous chemical reaction between sodium benzoate and hydrochloric acid. **Figs. 15** and **16** illustrate main results.

The model correctly predicts the trends of the effect of the concentration and the stirrer revolutions observed in the experiments.

The microscopic pictures of the primary particles and

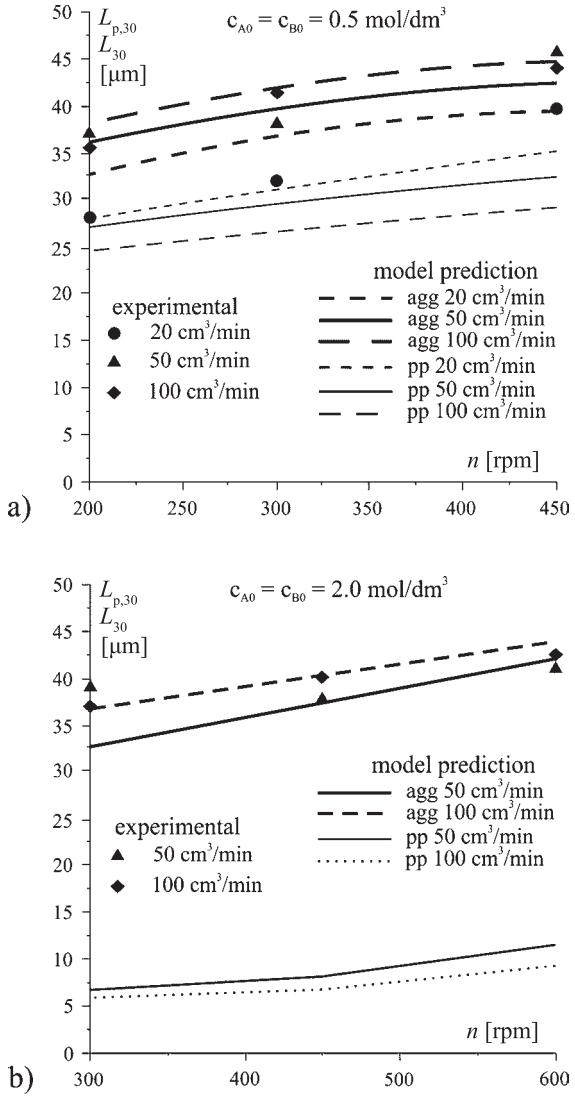

Fig. 16 Comparison of the experimental data with the model predictions for agglomerates (agg) L_{30}, and primary particles (pp) $L_{p,30}$. Feeding point close to the stirrer (based on Bałdyga J. and Krasiński A., 2005).

the aggregates confirm that the model correctly predicts both the size of the primary particles forming agglomerates and the size of non-agglomerated particles. Notice the effects of supersaturation on both:

size of primary particles due to particle growth and size of agglomerates due to building strong bridges between primary particles forming agglomerates.

5.2 Breakage

Disintegration processes play a significant role in the chemicals industry. There are many types of devices (e.g. rotor-stators, high-pressure nozzles, stirred tanks) that can be applied to generate stresses. There are of course different mechanisms involved in stress generation and thus different mechanisms of deagglomeration. For example in the case of high-pressure systems, disintegration

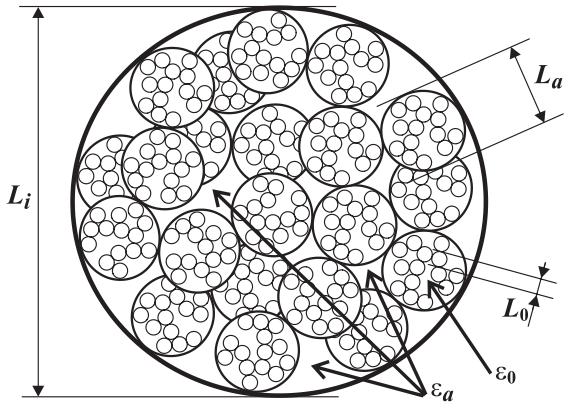

Fig. 17 Structure of large agglomerates (clusters).

results from hydrodynamic and cavitation stresses, whereas in the case of the rotor-stator system, only hydrodynamic stresses are active. To select the most suitable equipment for the desired parameters of the final product, one can use relatively simple mechanistic modeling in combination with CFD. The modeling presented in this paper includes the effects of agglomerate structure and suspension rheology on the disintegration processes.

The strength of the agglomerate depends on its structure, which in turn determines the mechanism of its breakage. A typical agglomerate structure of Aerosil fumed silica particles is represented by the cluster-fractal model as shown on **Fig. 17**. Large clusters of size L_i consist of smaller primary aggregates of a size L_a, which are composed of primary particles of size L_0. They are characterized by the fractal dimension D_f. The primary particles forming primary aggregates are connected by strong chemical bonds. Such aggregates are strong, stable and resistant against mechanical forces. They are characterized by an average fractal dimension D_{f0}. The clusters of size L_i, connected by adhesion forces, are relatively unstable, and they can be disintegrated by mechanical forces. Fractal geometry is used to estimate the tensile strength of agglomerates.

There is experimental evidence (Baldyga J. et al., 2008bc) that the break-up of Aerosil 200 V agglomerates occurs through erosion in a rotor-stator mixer, and through shattering and rupture in both a high-pressure nozzle disintegrator and the ultrasonic device. Break-up processes control the agglomerate size distribution; details of break-up depend on the agglomerate structure strength and the stresses generated in the fluid. On the other hand, the rheological properties of the suspension depend on the concentration of particles, their size distribution and morphology.

To describe all these phenomena and simulate the process, a model based on the population balance was developed. In the model, the population balance equations are supplemented with adequate breakage kinetics and solved

using the quadrature method of moments (McGraw, R., 1997) in the CFD environment. The commercial CFD code Fluent (the k-ε model of turbulence) is supplemented with UDFs for suspension rheology. Suspension rheology is described with the Buyevich Yu. A. and Kabpsov S.K. (1999) model. Models considered in this work were compared with experimental data in publications (Baldyga J. et al., 2008bc). In the simulations, two mechanisms of stress generation were considered: hydrodynamic stresses generated by the flow with frequency $\Gamma_h(L)$, and stresses generated by cavitation events with cavitation itself generated either by the flow or by the ultrasonic waves, at frequency $\Gamma_c(L)$ for agglomerates of size L. In the simulations, a superposition of breakage mechanisms is assumed.

$$\Gamma(L) = \Gamma_h(L) + \Gamma_c(L) \tag{48}$$

The related time constants can be defined as reciprocals of these frequencies: $\tau_{hydr} = 1/\Gamma_h(L)$, $\tau_{cav} = 1/\Gamma_c(L)$.

Comparison of these time constants with residence time values in the region of stresses higher than the tensile strength of agglomerates characterizes the extent of disintegration. Typical results for the rotor-stator, high-pressure nozzle and ultrasonic device are presented below.

The geometry of the rotor-stator device is shown in **Fig. 18**. **Fig. 19** shows the distribution of hydrodynamic stresses and particle size in the rotor-stator mixer.

The stresses are not strong enough to disperse agglomerates in one passage through the system, and thus to disperse agglomerates, the effective residence time should be increased and this is possible by multiplying the number of passages through the rotor-stator as shown in **Fig. 20**.

Much higher stresses (hydrodynamic and induced by cavitation) are generated in the high-pressure nozzle device (**Fig. 21**), and the system is so effective that one passage through the system results in effective dispersion of agglomerates (**Fig. 22**). Comparing the model with the experimental results, one can exclude the rupture mechanism; because the stresses are much higher than those in the rotor-stator mixer, one can expect that the breakage mechanism is shattering. More precisely this is represented by the fragmentation number defined in Rwei S.P. et al. (1990, 1991); for the stress τ, it can be expressed in a more general form (Bałdyga et al., 2008b) by:

$$Fa = \frac{48\tau\varepsilon_a L_a^2 H^2}{1.1(1-\varepsilon_a)HaL_0} \tag{49}$$

where τ is the stress, Ha is the effective Hamaker constant and H represents the surface-to-surface distance.

Fractal geometry is used to estimate the tensile strength of agglomerates applied in Eqn. (49). The number of bonds connecting aggregates in an agglomerate can be related to the agglomerate porosity by means of the following equation (Rumpf H., 1962; Tang S. et al., 2001):

$$\sigma_T = 1.1\frac{1-\varepsilon_a}{\varepsilon_a}\frac{F}{{L_a}^2} \tag{50}$$

where F represents the bonding force between aggregates

Fig. 18 Rotor-stator computational grid showing device geometry.

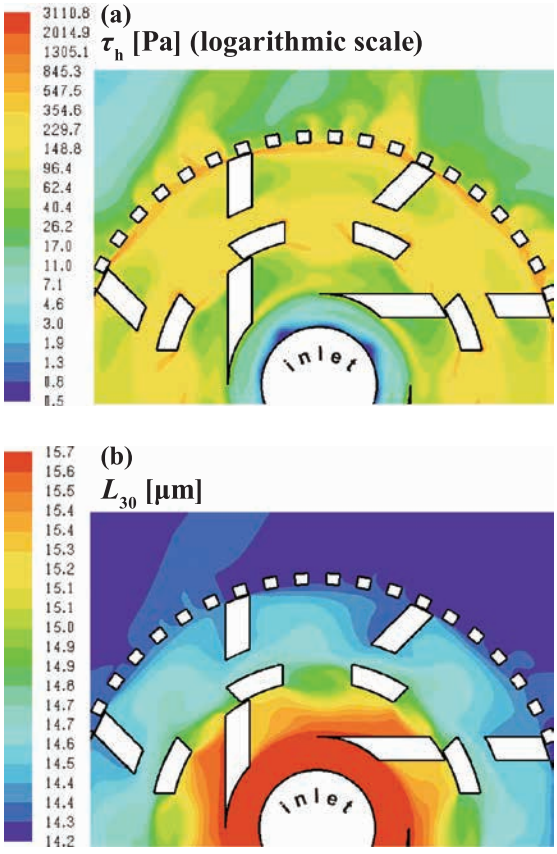

Fig. 19 Hydrodynamic stresses τ_h and mean particle size L_{30} distributions in the rotor-stator system for $Q = 0.6$ dm^3/s, $N = 9000$ rpm (150 s^{-1}) and 5 wt.% of Aerosil, for conditions applied by Bałdyga et al. (2008c).

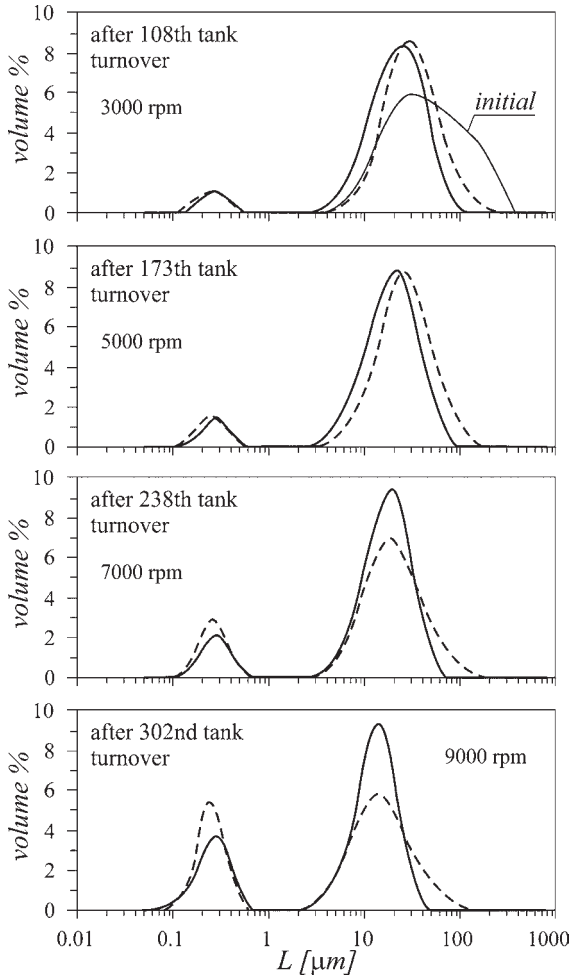

Fig. 20 Progress of deagglomeration in the rotor-stator system. Experimental results are marked by solid lines, and results of simulations by broken lines (Bałdyga et al., 2008c, copyright 2008 American Chemical Society, reprinted with permission)

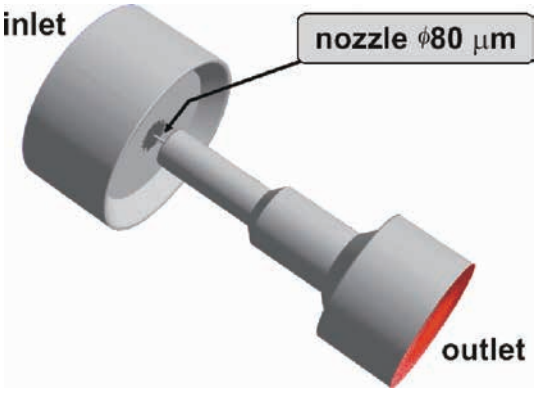

Fig. 21 Schematic of the high-pressure nozzle.

in the agglomerate that is calculated using the classic DLVO theory. In the present case, F is expressed by the van der Waals' attractive forces F_A that are calculated assuming that all primary particles have equal diameters,

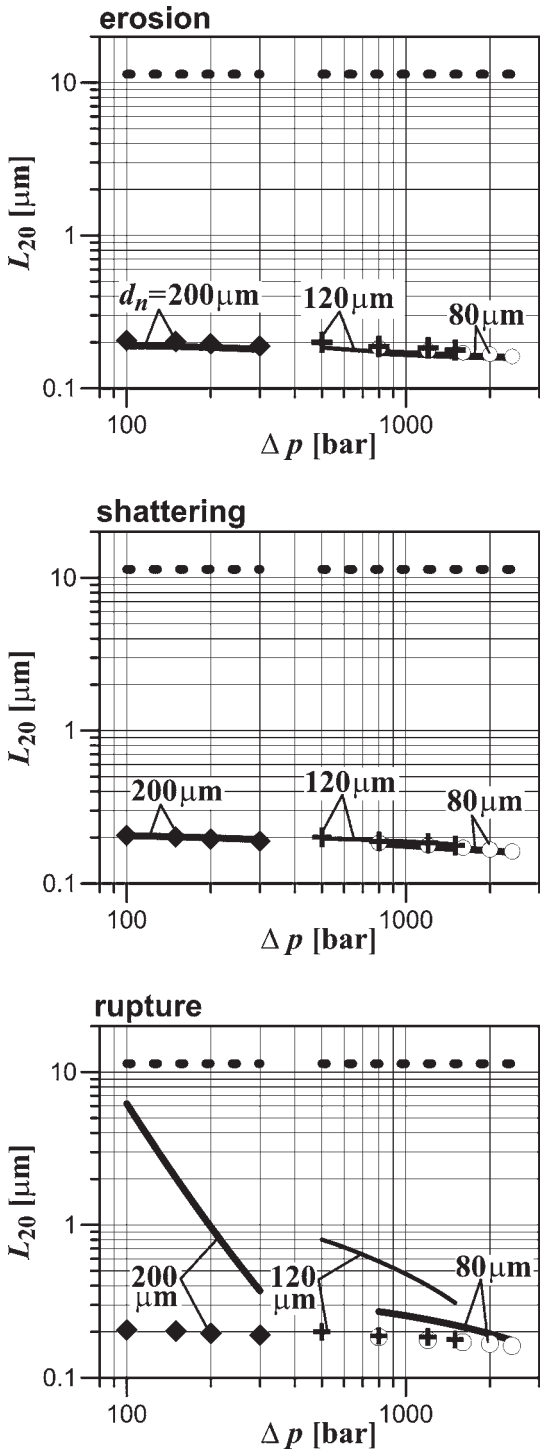

Fig. 22 Comparison of experimental data with model predictions based on: erosion, shattering and rupture mechanisms of deagglomeration for the nozzles of three different diameters d_n. Experimental results are marked by points, solid lines represent the results of simulations and dashed lines show the mean size of particles in pre-dispersion. (Bałdyga et al., 2009, copyright 2009 The Institution of Chemical Engineers, reprinted with permission)

L_0:

$$F_A = -\frac{Ha\, L_0}{48\, H^2} \tag{51}$$

To complete the description, one should define the stresses τ for each mechanism of generation.

In the case of turbulent flow for aggregates smaller than the Kolmogorov microscale, $\lambda_K = (\nu^3/\varepsilon)^{1/4}$, Eqn. (52) works for breakage kernel Γ with deformation rate defined by $\dot{\gamma} = (\varepsilon/\nu)^{0/5}$.

$$\begin{aligned} &\Gamma = C_b\,\dot{\gamma} \quad if \quad \mu\dot{\gamma} > \sigma_T \\ &\Gamma = 0 \quad\;\; if \quad \mu\dot{\gamma} \le \sigma_T \end{aligned} \tag{52}$$

For turbulent flows, and for aggregates larger than the Kolmogorov microscale, $L > \lambda_K$, one has

$$\begin{cases} \Gamma_h = C_b \dfrac{\varepsilon^{1/3}}{L^{2/3}} & if \quad \rho\varepsilon^{2/3}L^{2/3} > \sigma_T \\ \Gamma_h = 0 & if \quad \rho\varepsilon^{2/3}L^{2/3} \le \sigma_T \end{cases} \tag{53}$$

where C_b is a proportionality constant.

When cavitation is induced by the flow then the breakage kernel is recalculated from the condensation rate R_C using the model by (Singhal A.K. et al., 2002).

The rate of collapse of the bubbles serving as the breakage kernel is defined as a ratio of the mass condensation rate to the mass of a bubble:

$$\Gamma_C = C_{bc} \frac{R_C}{\frac{4}{3}\pi R_0^3 \rho_v} \tag{54}$$

with C_{bc} being an empirical constant and ρ_v the vapor density. The bubble radius value, R_0, is expressed using the Blake equation for the critical bubble diameter (Brennen, C.E., 2005).

The stresses generated by bubble implosion (generated by shock waves and high-velocity microjets) can be estimated using the semi-empirical equation (Crum, L., 1988)

$$\tau_c = \alpha\rho c V_j \tag{55}$$

where c is the velocity of compressional waves in the liquid, V_j is the microjet velocity and α is a constant that varies from 0.41 to 3.0.

The breakage kernel for ultrasonic-wave-induced cavitation and for ultrasonic frequency f, reads:

$$\begin{aligned} &\Gamma_c = C_{bc} f \quad \text{for} \;\; \tau_c = \alpha\,\rho c V_j > \sigma_T \\ &\Gamma_c = 0 \;\; \text{otherwise} \end{aligned} \tag{56}$$

for the ultrasonic wave propagation, we use the wave equation (Saez V. et al., 2005)

$$\nabla\left(\frac{1}{\rho}\nabla p\right) - \frac{1}{\rho c^2}\frac{\partial^2 p}{\partial t^2} = 0 \tag{57}$$

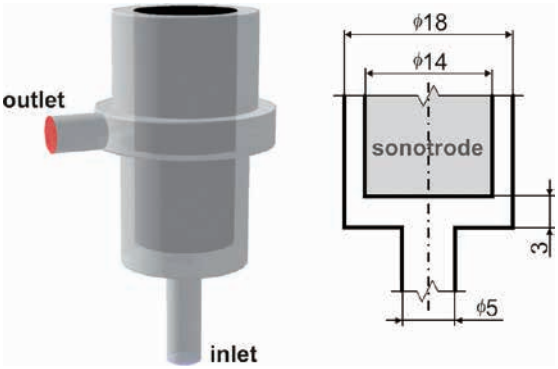

Fig. 23 Geometry of the ultrasonic device. (Bałdyga et al., 2008b, copyright 2008 The Institution of Chemical Engineers, reprinted with permission.)

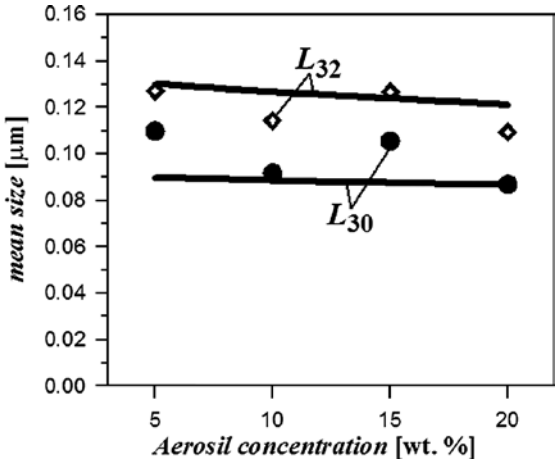

Fig. 24 Comparison of model predictions with experimental data for one passage through the ultrasonic cell. Effect of Aerosil concentration for energy density $E_v = 300$ GJm^{-3}. (Bałdyga et al., 2008b, copyright 2008 The Institution of Chemical Engineers, reprinted with permission.)

Fig. 23 shows the experimental system, whereas comparisons of model predictions with experimental data is given in **Fig. 24**. The model predicts well the small effect of Aerosil concentration on the average agglomerate size. **Fig. 25** shows the distribution of cavitation stresses generated in the ultrasonic cell. They are many orders of magnitude larger than the stresses generated in the rotor-stator (**Fig. 19a**), and the deagglomeration process has either a rupture or shattering mechanism.

Experimental results and model predictions for the deagglomeration of silica nanoparticle agglomerates (Aerosil 200 V) confirmed that the fragmentation number can be used to predict the mechanism of deagglomeration. Deagglomeration is possible for $Fa > 1$; for $Fa < 100$ erosion is observed, rupture is for $Fa > 100$ and shattering dominates for $Fa > 1000$.

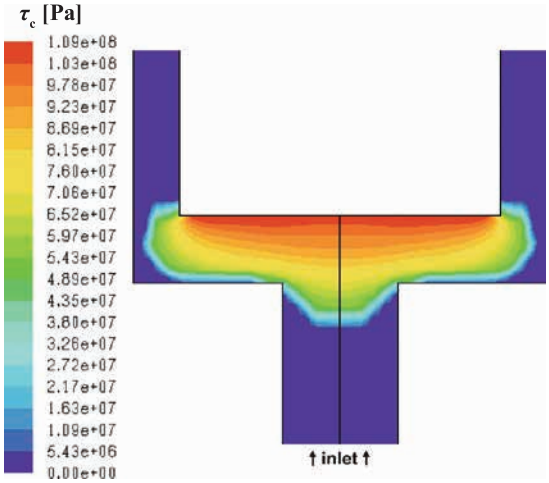

Fig. 25 Distribution of stresses generated by cavitation in the ultrasonic cell for 20 wt.% of Aerosil. (Bałdyga et al., 2008b, copyright 2008 The Institution of Chemical Engineers, reprinted with permission.)

6. Final discussion

There are many practical applications where the properties of precipitated particles are of key importance. The most important reason for this is that there is an increasing emphasis on high added value specialty chemicals such as pharmaceuticals, dyes, pigments, paints, and printing inks regarding the crystal size distribution, particle morphology and product purity. As presented by Karpinski (2006), many precipitated pharmaceutical organic products can form a range of polymorphs or solvatomorphs. There is also the effect of the precipitate properties on the downstream processes such as filtration or drying. This explains why attention is paid to "particle design".

The results presented in this paper show that particle size distribution (**Figs. 4**, **5**, **7**, **9** and **11**), particle morphology and many other properties depend on the spatial distribution of the supersaturation (**Fig. 6**) and the timing of its evolution. Important is also the evolution of fluid elements in the supersaturated zone which depends on the flow pattern (**Fig. 3**) and the rate of mixing (**Fig. 10**). Mixing controls both creation and dilution of supersaturation. However, not only the level but also the chemical structure of supersaturation is important, which can be shown using precipitation diagrams (Söhnel O., 1991); a simple example of such a diagram is shown in **Fig. 1**. One can plot on the precipitation diagram such important information on the type of precipitate that results from the solution composition represented by points on the diagram. The composition of the solution affects the chemical reaction and resulting properties of the solid phase. One can thus show those regions where a solid phase of uniform composition, morphology, color or crystal habit exists.

Another effect resulting from the solution composition is related to electrostatic interactions (**Fig. 13**) between colloidal particles that may control the stability of colloidal suspensions (**Fig. 12**) and particle aggregation (**Figs. 14**, **15** and **16**).

Another important distribution is the distribution of hydrodynamic properties such as the velocity gradients, deformation and rotation tensors, and resulting hydrodynamic stresses. The relation between fluid deformation and rotation affects the efficiency of micromixing, thus also affecting the creation rate of supersaturation. Very important is the distribution of stresses generated in the system, including hydrodynamic stresses (**Fig. 19**) and the stresses resulting from cavitation (**Fig. 25**). Direct interaction between the distribution of hydrodynamic properties, the distribution of supersaturation and the distribution of the particle populations results in the size distribution and morphology of agglomerates as shown in **Fig. 15** and **Fig. 16**. There is of course the direct effect of stress distribution on deagglomeration which is presented in **Fig. 20**, **Fig. 22** and **Fig. 24**.

Precipitation is a very complex process, which means that when designing and scaling up precipitation processes, complete similarity is impossible. In fact when scaling up, complete similarity is not necessary because as explained earlier, we want to obtain identical products from the systems differing in scale. As a first attempt to design the process, the time and length scale analysis is recommended in this paper, which is illustrated with examples. The comparison of time and length scales shows which of them are important for the process. This information can be used for scaling up and for formulating adequate models. The precipitation models have a multiscale character and are very complex. It is thus very important to choose an adequate model of mixing and to decide at which scale modeling is not necessary.

Nomenclature

CFD	Computational Fluid Dynamics
PDF	Probability Density Function
SEDS	Solution-Enhanced Dispersion by Supercritical Fluid
A, A^{n+}	reactant
a	activity of solute (–)
a	particle radius (m)
a_{eq}	equilibrium activity of solute (–)
a_p	particle surface area (m^2)
B, B^{n+}	reactant
B	constant in Eqn. (7)

$B(\vec{x},t)$ birth function

B_{fj} birth term for the moments of order j ($m^{j-3}s^{-1}$)

C product

C_D friction factor (–)

C_t Craya-Curtet number (–)

c velocity of compressional waves (ms^{-1})

c molar concentration (mol dm^{-3})

c_{eq} solubility (mol dm^{-3})

c_{i0} initial or feed concentration of i (mol dm^{-3})

c_{pair} pair probability function (–)

D molecular diffusion coefficient (m^2s^{-1})

D_{12}^{∞} mutual Brownian diffusivity (m^2s^{-1})

D_B^{∞} coefficient of Brownian diffusion (m^2s^{-1})

D_b crystalline bridge diameter (m)

D_{fj} death term for the moments of order j ($m^{j-3}s^{-1}$)

D_{pT} turbulent diffusivity of particles (m^2s^{-1})

D_S stirrer diameter (m)

D_t turbulent diffusion coefficient (m^2s^{-1})

D_v diameter of the precipitation vessel (s)

$D(\vec{x},t)$ death function

D_α molecular diffusivity of α (m^2s^{-1})

d molecular diameter (m)

d_{43} mean crystal size (μm)

d_f feed pipe diameter (m)

d_0 nozzle orifice diameter (m)

E engulfment parameter (s^{-1})

Fa fragmentation number (–)

F bonding force (N)

f mixture fraction (–)

$f(\vec{x}/d_0)$ dimensionless distribution of the rate of energy dissipation (–)

G rate of crystal growth (ms^{-1})

$G(r,\lambda)$ hydrodynamic function (–)

ΔG^* energy barrier for homogeneous nucleation (J)

ΔG_{het}^* energy barrier for heterogeneous nucleation (J)

H surface-to-surface distance (m)

Ha Hamaker constant (J)

I_S intensity of segregation (–)

J nucleation rate ($m^{-3}s^{-1}$)

K_a dissociation constant (mol dm^{-3})

K_{SP} thermodynamic solubility product (mol^2dm^{-6})

k_a surface shape factor (–)

k_B Boltzmann's constant (JK^{-1})

k_d mass transfer coefficient (ms^{-1})

k_R surface integration constant ($mdm^{3r}mol^{-r}s^{-1}$)

k_v volume shape factor (–)

L particle size (m)

L_e scale of large, energy-containing eddies (m)

M_C molecular mass of C (kg mol^{-1})

m number of particle properties (–)

m_j moment of order j (m^{j-3})

N stirrer speed (s^{-1})

N^* number of molecules or ions forming the critical embryo-nucleus (–)

n population number density

$\vec{n}$ normal to collision surface (–)

P_S efficiency of agglomeration (–)

Pe Péclet number (–)

p pressure (Pa)

Q feeding rate (m^3s^{-1})

R gas constant ($J\ mol^{-1}K^{-1}$)

Re Reynolds number (–)

R_D turbulent to Brownian diffusivity ratio (–)

Re_p particle Reynolds number (–)

r order of surface integration (–)

S supersaturation ratio based on x (–)

S_a supersaturation ratio based on a (–)

S_C entire collision surface (m^2)

Sc Schmidt number (–)

t time (s)

$\overline{t_c}$ time to build strong crystalline bridge (s)

$\overline{t_i}$ average interaction time (s)

T temperature (K)

T_L Lagrangian integral time scale (s)

u velocity (ms^{-1})

u' r.m.s. velocity fluctuation (ms^{-1})

$\vec{u}_f$ relative particle velocity resulting from the fluid flow (ms^{-1}) relative particle velocity resulting from colloidal interactions (ms^{-1})

$\vec{u}_{int}$ relative particle velocity resulting from colloidal interactions (ms^{-1})

u_{pi} component of particle velocity (m)

V interaction potential (J)

V_t tank volume (m^3)

V_j microjet velocity (ms^{-1})

v molecular volume (m^3)

v_p particle volume (m^3)

W stability ratio (–)

w relative velocity of particles (ms^{-1})

w_{pj} rate of change of particle property j (property j s^{-1})

x mol fraction of solute (–)

x_{eq} equilibrium mol fraction of solute (–)

$\vec{x}$ position vector (m)

x_i external coordinates (m)

β_c collision rate constant (m^3s^{-1})

β aggregation kernel (m^3s^{-1})

$\Gamma_h(L)$ hydrodynamic frequency (s^{-1})

$\Gamma_c(L)$ cavitation frequency (s^{-1})

$\dot{\gamma}$ rate of deformation (s^{-1})

γ_i activity coefficient of the ionic species i (–)

ε rate of energy dissipation (m^2s^{-3})

ε_a porosity of agglomerate (–)

Λ_C integral scale of concentration fluctuations (m)

λ particle size ratio (–)

Λ_f longitudinal integral scale of turbulence (m)

λ_K Kolmogorov length microscale (m)

μ molar chemical potential ($J\ mol^{-1}$)

μ fluid viscosity (Pas)

μ_{eq} molar chemical potential in saturated solution ($J\ mol^{-1}$)

ν kinematic viscosity (m^2s^{-1})

ν^+, ν^- stoichiometric coefficients for ions (–)

ρ liquid density ($kg\ m^{-3}$)

ρ_v vapour density ($kg\ m^{-3}$)

ρ_c molar density of solute ($mol\ m^{-3}$)

ρ_p density of solute ($kg\ m^{-3}$)

σ supersaturation (–)

σ surface energy ($J\ m^{-2}$)

σ_T tensile strength (Pa)

σ_S^2 variance of mixture fraction (–)

τ mean residence time (s)

τ in eqn. (49) stress τ_c or τ_h (Pa)

τ_B Brownian diffusion time (s)

τ_b blending time (s)

τ_C circulation time (s)

τ_c cavitation stress (Pa)

τ_D time constant for turbulent diffusion (s)

τ_E engulfment time constant (s)

τ_{Gcr} time constant for crystal growth (s)

τ_h hydrodynamic stress (Pa)

τ_{hydr} time constant for hydrodynamic stresses (s)

τ_{cav} time constant for cavitation stresses (s)

τ_K Kolmogorov time microscale (s)

τ_M time constant for mixing (s)

τ_N time constant for nucleation (s)

τ_p relaxation time (s)

τ_R time constant for chemical reaction (s)

τ_S time constant for inertial-convective mixing (s)

τ_{VCVD} time constant for viscous-convective and viscous-diffusive mixing (s)

Ω pre-exponential term in Eqn. (7) ($m^{-3}s^{-1}$)

$\Phi(f)$ PDF of mixture fraction (–)

References

Adler J.J., Rabinovich Y.I., Moudgil B.M., Origins of the non-DLVO force between glass surfaces in aqueous solution, Journal of Colloid and Interface Science, 237 (2001) 249–258.

Bałdyga J., Turbulent mixer model with application to homogeneous, instantaneous chemical reactions, Chemical Engineering Science, 44 (1989) 1175–1182.

Bałdyga J., Bourne J.R., Turbulent Mixing and Chemical Reactions, Wiley, Chichester, 1999.

Bałdyga J., Czarnocki R., Shekunov B.J., Smith K.B., Particle formation in supercritical fluids—Scale-up problem', Chemical Engineering Research & Design, 88 (2010) 331–341.

Bałdyga J., Henczka M., Shekunov B.Y., Fluid dynamics, mass transfer, and particle formation in supercritical fluids, in: York P., Kompella U.B., Shekunov B.Y. (Eds.), Supercritical Fluid Technology and Drug Product Development, Marcel Dekker, New York, 2004, pp. 91–157.

Bałdyga J., Jasińska M., Orciuch W., Barium Sulphate Agglomeration in a Pipe—An Experimental Study and CFD Modeling, Chemical Engineering & Technology, 26 (2003) 334–340.

Bałdyga J., Jasińska M., Jodko K., Petelski P., Precipitation of amorphous colloidal silica from aqueous solutions—Aggregation problem, Chem. Eng. Sci., 77 (2012) 207–216.

Bałdyga J., Krasiński A., Precipitation of benzoic acid in continuous stirred tank—effects of agglomeration, Proceedings of 16th International Symposium on Industrial Crystallization, in: Ulrich J. (Ed.), VDI-Verlag, Düsseldorf, 2005, pp. 411–416.

Bałdyga J., Kubicki D., Shekunov B.Y., Smith K.B., Mixing effects on particle formation in supercritical fluids, Proceedings of 17th International Symposium on Industrial Crystallization, in: Jansen J.P., Ulrich J. (Eds.), Maastricht, 2008a, pp. 141–148.

Bałdyga J., Makowski Ł., Orciuch W., Sauter C., Schuchmann H.P., Deagglomeration processes in high-shear devices, Chemical Engineering Research and Design, 86 (2008b) 1369–1381.

Bałdyga J., Makowski Ł., Orciuch W., Sauter C., Schuchmann H.P., Agglomerate dispersion in cavitating flows, Chemical Engineering Research and Design, 87 (2009) 474–484.

Bałdyga J., Orciuch W., Some hydrodynamic aspects of precipitation, Powder Technology, 121 (2001) 9–19.

Bałdyga J., Orciuch W., Makowski Ł., Malik K., Ozcan-Taskin G., Eagels W., Padron G., Dispersion on nanoparticle clusters in a rotor-stator mixer, Ind. Eng. Chem. Res., 47 (2008c) 3652–3663.

Bałdyga J., Podgórska W., Pohorecki R., Mixing-precipitation model with application to double feed semibatch precipitation, Chem. Eng. Sci., 50 (1995) 1281–1300.

Becker H.A., Hottel H.C., Williams G.C., Mixing and flow in ducted turbulent jets, Proceedings of 9th Int. Symp. on Combustion, Combustion Institute, New York, 1963, pp. 7–20.

Brennen C.E., Fundamentals of Multiphase Flow, Cambridge University Press, New York, USA, 2005.

Briesen H., Simulation of crystal size and shape by means of a reduced two-dimensional population balance model, Chem. Eng. Sci., 61 (2006) 104–122.

Bromley L.A., Thermodynamic properties of strong electrolytes in aqueous solutions, AIChE J., 19 (1973) 313–320.

Buyevich Yu. A. Kapbsov S.K., Segregation of a fine suspension in channel flow, Non-Newt. Fluid. Mech., 86 (1999) 157–184.

Craya A., Curtet R., On the spreading of a confined jet', Comptes Rendus. Acad. Des Sciences, 241 (1955) 611–622.

Crum L., Cavitation microjets as a contributory mechanism for renal disintegration in ESWL., J. Urol., 148 (1988) 1587–1590.

Davey R., Garside J., From molecules to Crystallizers. An Introduction to Crystallization, Oxford University Press, New York, 2000.

David R., Marchal P., Klein J.P., Villermaux J., Crystallization and precipitation engineering III. A discrete formulation of the agglomeration rate of crystals in a crystallization process, Chem. Eng. Sci., 46 (1991) 205–213.

Dirksen J.A., Ring T.A., Fundamentals of crystallization: kinetics effects on particle size distribution and morphology, Chem. Eng. Sci., 46 (1991) 2389–2427.

Di Veroli G., Rigopoulos S., Modeling of turbulent precipitation: A transported population balance-PDF method, AIChEJ, 56 (2010) 878–892.

Elimelech M., Gregory J., Jia X., Williams R.A., Particle Deposition and Aggregation: Measurement, Modelling and Simulation, Butterworth-Heinemann, Oxford, 1995.

Fissore D., Marchisio D.L., Barresi A.A., On the comparison between probability density function models for CFD applications, Can. J. Chem. Eng., 80 (2002) 1–11.

Fox R.O., The spectral relaxation model of the scalar dissipation rate in homogeneous turbulence, Phys. Fluids, 7 (1955) 1082–1094.

Gavi E., Marchisio D.L., Barresi A.A., CFD modeling and scale-up of confined impinging jet reactors, Chem. Eng. Sci., 62 (2007) 2228–2241.

Henczka M., Bałdyga J., Shekunov B.Y., Particle formation by turbulent mixing with supercritical antisolvent, Chem. Eng. Sci., 60 (2005) 2193–2201.

Hinze J.O., Turbulence, McGraw-Hill, New York, 1975.

Hulburt H.M., Katz S., Some problems in particle technology—A statistical mechanical formulation, Chem. Eng. Sci., 19 (1964) 555–574.

Karpinski P.H., Polymorphism of Active Pharmaceutical Ingredients, Chemical Engineering & Technology, 29 (2006) 233–237.

Kruis F.E., Kusters K.A., The Collision Rate of Particles in Turbulent Media, J. Aerosol Sci., 27 (1996) S263–S264

Launder B.E., Spalding D.B., Mathematical Models of Turbulence, Academic Press, London/New York, 1972.

Löbbus M., Vogelsberger W., Sonnefeld J., Seidel A., Current considerations for the dissolution kinetics of solid oxides with silica, Langmuir, 14 (1998) 4386–4396.

Marchisio D.L., Barresi A.A., Fox R.O., Simulation of turbulent precipitation in a semi-batch Taylor-Couette reactor using CFD, AIChE J., 47 (2001) 664–676.

Marchisio D.L., Rivautella L., Barresi A.A., Design and scale-up of chemical reactors for nanoparticle precipitation, AIChE J, 52 (2006) 1877–1887.

Marchisio D.L., Fox R.O., Computational Models for Polydisperse Particulate and Multiphase Systems, Cambridge University Press, Cambridge, 2013.

McGraw R., Description of aerosol dynamics by the quadrature method of moments, Aerosol Science and Technology, 27 (1997) 255–265.

Melis S., Verduyn M., Storti G., Morbidelli M., Bałdyga J., Effect of fluid motion on the aggregation of small particles subject to interaction forces, AIChE J., 45 (1999) 1383–1393.

Mersmann A. (Ed.), Crystallization Technology Handbook, 2nd ed., Marcel Dekker, New York, 2001.

Myerson A.S. (Ed.), Handbook of Industrial Crystallization, Elsevier, Amsterdam, 2002.

Nielsen A.E., Kinetics of Precipitation, Pergamon Press, Oxford: 1964.

Nývlt J., Industrial Crystallisation from Solutions, Butterworths, London, 1971.

Ochsenbein D.R., Schorsch S., Salvatori F., Vetter T., Morari M., Mazzotti M., Modeling the Facet Growth Rate Dispersion of β LGlutamic Acid—Combining Single Crystal Experiments with *n*D Particle Size Distribution Data., Chem. Eng. Sci., (2015a), DOI: 10.1016/j.ces.2015.02.026.

Ochsenbein D.R., Vetter T., Schorsch S., Morari M., Mazzotti M., Agglomeration of Needle-like Crystals in Suspension: I. Measurements., Cryst. Growth Des., 15 (2015b) 1923–1933.

Paul E.L., Atiemo-Obeng V., Kresta S.M., (Eds.), Handbook of Industrial Mixing: Science and Practice., Wiley-Interscience,

Hoboken, 2003.
Piton D., Fox R.O., Marcant B., Simulation of fine particle formation by precipitation using computational fluid dynamics, Can. J. Chem. Eng., 78 (2000) 983–993.
Pitzer K., Activity coefficients in electrolyte solutions, CRC Press, Boca Raton, 1991.
Qamar S., Seidel-Morgenstern A., An efficient numerical technique for solving multi-dimensional batch crystallization models with size independent growth rates, Computers and Chemical Engineering, 33 (2009) 1221–1226.
Randolph A.D., Larson M.A., Theory of Particulate Processes, 2nd ed., Academic Press, New York, 1988.
Ramkrishna D., Mahoney A.W., Population balance modeling. Promise for the future, Chemical Engineering Science, 57 (2002) 595–606.
Rowe J.M., Johnston K.P., Precipitation Technologies for Nanoparticle Production in Formulating Poorly Water Soluble Drugs, in: Williams III, R.O.O., Watts A.B., Miller D.A. (Eds.), AAPS Advances in the Pharmaceutical Sciences Series, 3 (2012) 501–568.
Rumpf H., The strength of granules and agglomerates, in Agglomeration, in: Knepper W.A. (ed.), Wiley, New York, USA, 1962, pp. 379–418.
Rwei S.P., Manas-Zloczower I., Feke D.L., Observation of carbon black agglomerate dispersion in simple shear flows, Polym. Eng. Sci., 30 (1990) 701–706.
Rwei S.P., Manas-Zloczower I., Feke D.L., Characterization of agglomerate dispersion by erosion in simple shear flows, Polym. Eng. Sci., 31 (1991) 558–562.
Saez V., Frias-Ferrer A., Iniesta J., Gonzalez-Garcia J., Aldoz A., Riera E., Characterization of a 20 kHz sonoreactor. Part I: analysis of mechanical effects by classical and numerical methods, Ultrasonics Sonochemistry, 12 (2005) 59–65.
Singhal A.K., Athavale M.M., Li H., Jiang Y., Mathematical Basis and Validation of the Full Cavitation Model, Journal Fluids Eng., 124 (2002) 617–624.
Shekunov B.Y., Bałdyga J., York P., Particle formation by mixing with supercritical antisolvent at high Reynolds numbers, Chem. Eng. Sci., 56 (2001) 2421–2433.
Smoluchowski M., Versuch einer matamatischen Theorie der Koagulationskinetik kolloider Lösungen, Z. Phys. Chem., 92 (1917) 129–168.
Söhnel O., Chemical design of precipitation processes in Advances in Industrial Crystallization. in: Garside J., Davey R.J., Jones A.G. (Eds.), Butterworth-Heinemann, Oxford (1991) 63–74.
Söhnel O., Garside J., Precipitation. Butterworth-Heinemann, Oxford:, 1992.
Tang S., Ma Y., Shiu C., Modeling of mechanical strength of fractal aggregates, Colloids Surf. A: Physical and Engineering Aspects, 180 (2001) 7–16.
Turnbull D., Vonnegut B., Nucleation catalysis, Ind. Eng. Chem., 44 (1992) 1292–1298.
Vicum L., Mazzotti M., Bałdyga J., Applying a thermodynamic model to the non-stoichiometric precipitation of barium sulphate, Chem. Eng. Technol., 26 (2003) 325–333.
Walton A.G., The Formation and Properties of Precipitates, Interscience Publishers, New York, 1967.
York P., Hanna M., Particle engineering by supercritical fluid technologies for powder inhalation drug delivery in Respiratory Drug Delivery V. Proceedings of the Conference on Respiratory Drug Delivery, Phoenix, Arizona, 1996, pp. 231–239.
Zauner R., Jones A.G., Scale-up of continuous and semi-batch precipitation processes, Industrial Engineering Chemistry, 39 (2000) 2392–2403.
Zlokarnik M., Scale-up in chemical engineering, Wiley-VCH, Weinheim, 2002.

Author's short biography

Jerzy Bałdyga

Jerzy Bałdyga, PhD; DSc, has been a professor of chemical engineering at the Warsaw University of Technology, Warsaw, Poland since 1997. He received his MSc in 1974, PhD in 1981, and DSc in 1989, all from the Warsaw University of Technology. In 1997, he was awarded the chair of mechanical engineering and process dynamics at the Chemical Engineering Faculty, Warsaw University of Technology. He chairs the working party on mixing of the European Federation of Chemical Engineering. The research of Professor Bałdyga can be characterized as the application of fluid mechanics to problems of chemical engineering and chemical reaction engineering.

KONA Powder and Particle Journal No. 33 (2016) 150–168/Doi:10.14356/kona.2016022 Review Paper

Granular Temperature and Segregation in Dense Sheared Particulate Mixtures †

Kimberly M. Hill [1]* and Yi Fan [2]

[1] *St. Anthony Falls Laboratory and the Department of Civil, Environmental, and Geo-Engineering, University of Minnesota, USA*
[2] *The Dow Chemical Company, USA*

Abstract

In gravity-driven flows of different-sized (same density) particles, it is well known that larger particles tend to segregate upward (toward the free surface), and the smaller particles downward in the direction of gravity. Alternatively, when the particles are of the same size but different density, lighter particles tend to segregate upward and heavier particles, downward. When particles differ in both size and density, true of most mixtures of interest in industry and nature, the details are complicated and no rule based on gravity alone has captured the segregation behaviours. Gradients of granular temperature and kinetic stress (i.e., energy and stress associated with velocity fluctuations) offer alternative segregation driving forces, but have, until recently, been discounted as these dynamics are relatively small in dense flows. Recently, gradients in kinetic stress have been shown to play a significant role in segregating densely sheared particle mixtures, even where the kinetic stress is a relatively small percentage of the total stress. We review recent modelling advances accounting for this effect and validation in computational experiments. We show how this framework may be useful in capturing the complicated segregation phenomenology that emerges for dense sheared flows of particles different in both size and density.

Keywords: segregation, mixing, DEM simulations, mixture model

1. Introduction

Sheared particulate mixtures of different sizes and/or densities segregate into a wide range of segregation patterns, important for a wide range of industrial processes (e.g., Mosby et al., 1996; Hogg, 2009), and complex even under simple boundary conditions. Examples include relatively simple experimental flows in a shear cell (Duffy and Puri, 2002; May et al., 2010a, 2010b), in an inclined plane flow (Savage and Lun, 1988; Gray and Thornton, 2005; Gray and Chugunov, 2006), and in a rotated drum (Hill et al., 1997; Khakhar et al., 1997; Hill et al., 1999b; Taberlet et al., 2004; Shinbrot and Muzzio, 2000), to relatively complex geophysical flows (e.g., Middleton, 1970), such as in a riverbed (Paola and Seal, 1995; Dietrich et al., 1989) and in a debris flow (Stock and Dietrich, 2006; Hsu et al., 2008; Yohannes et al., 2010).

The details of the segregation dynamics depend on several factors. Gravity has long been known to drive sorting of different types of particles (depending on relative size, density, etc) (Donald and Roseman, 1962; Bridgwater, 1976; Williams, 1976). For flow of very fine particles in air, the effect of air drag on particles likely is a cause of segregation (e.g., Williams, 1976; Schulze, 2008) just as in rivers, where drag from the moving water can lead to selective transport of smaller particles downstream, contributing to "downstream fining". Under many conditions, particularly in collisional flows, interparticle interactions play a dominant role. Through these interactions, gradients in granular temperature (i.e., the random kinetic energy of the particles, as in Jenkins and Mancini, 1987; Xu et al., 2003; Galvin et al., 2005), similar to gradients in kinetic stress (Fan and Hill, 2011b), and solid fraction gradients (Hill and Fan, 2008) drive segregation. We focus here on the dynamics associated with the unmixing of particles in high-concentration (high solids volume fraction) sheared flows, applicable to a wide range of systems of variable boundary conditions and advective flow patterns.

The focus of modeling efforts of segregation in high concentration gravity-driven flows has been largely associated with gravity as the driving force. In most cases, in mixtures of particles differing only in size, small particles sink in the direction of gravity, away from the free surface in gravity-driven flows, while large particles rise. In mixtures of particles differing only in density, the less

† Received 8 June 2015; Accepted 30 July 2015
J-STAGE online 28 February 2016
[1] Minneapolis, MN 55455, USA
[2] Midland, MI 48667, USA
* Corresponding author: Kimberly M. Hill;
E-mail: kmhill@umn.edu
TEL: +1-612-626-0311

dense particles rise, and the denser particles sink. While granular temperature has been shown to play a role in segregating sparse mixtures (e.g., Jenkins and Mancini, 1987; Xu et al., 2003; Galvin et al., 2005), stresses related to velocity fluctuations in dense flows are significantly less than stresses associated with gravity, so they have largely been neglected in modeling segregation in dense flows.

The gravity-driven flow models have taken a few different forms (e.g., Duffy and Puri, 2003). Savage, S. and Lun, C. (1988) developed a model for size-dependent segregation based on two simultaneous mechanisms: geometrically-associated, gravity-driven sorting they described as a 'random fluctuating sieve', and a mass-balancing 'squeeze expulsion' mechanism. Essentially gravity pushes all particles in one direction, but the structure associated with the high packing fraction prevents most particles from responding. Statistically, in a mixture of different-sized particles it is more likely that small particles will find holes sufficiently large for them to enter. As the mixture is excited and the particles shift, holes of different sizes open and close, giving the small particles opportunities to drop downward via what they refer to as a 'sieving' mechanism. A higher shear rate results in a more frequent availability of holes and thus a higher segregation rate. Mass balance is achieved when the downward migrating smaller particles squeeze the larger particles upward via the 'squeeze expulsion' mechanism. Savage, S. and Lun, C. (1988) developed a detailed statistical model to predict segregation trends based on this process. However, gravity is not explicitly included in the model so the direction of segregation has to be determined implicitly.

Another model framework that is particularly useful for predicting evolution of a mixture is based on mixture theory. Specifically, there is a family of these models that can predict local segregation flux and constituent concentration evolution based on other details of the flow such as local and instantaneous concentrations of each constituent. We review a few such models for systems in simple shear flows, where the system is uniform in all directions except one, and the average flow is normal to that direction. In all cases here, we will adjust the coordinate system so that the direction of non-uniformity and the direction of segregation is the y-direction, though the other details of the coordinate system vary a bit with boundary conditions.

Khakhar, D. et al. (1997) proposed a 'buoyancy' mechanism for gravity-driven segregation according to particle density that took a form similar to pressure on a submerged object by a surrounding fluid. For example, for flow of such a mixture down a plane inclined by ζ relative to the horizontal, where y is increasing away from the free surface (in the direction of gravity), the concentration flux of the less dense particles normal to the flow may be expressed according to:

$$\phi_\nabla^{\mathrm{ld}}\left(v^{\mathrm{ld}}-v\right)= -C_{\mathrm{K}}\left(1-\frac{\rho_{\mathrm{m}}^{\mathrm{ld}}}{\rho_{\mathrm{m}}^{\mathrm{d}}}\right)\phi_\nabla^{\mathrm{ld}}\left(1-\phi_\nabla^{\mathrm{ld}}\right)g\cos\zeta - D\frac{\partial\phi_\nabla^{\mathrm{ld}}}{\partial y} \tag{1.1}$$

In the original form of this theoretical framework, C_{K} was an empirically determined parameter with dimensions of time that is inversely related to the resistance to local motion, what might be called an inverse drag function; D is the diffusivity. v^i is the local average velocity of species i in the segregation direction (normal to the average flow), ρ_{m}^i is the material density of species i, and ϕ_∇^i is the local volume concentration of particles of species i. $\phi_\nabla^i = f^i / \Sigma f^i$, where f^i is the local solids fraction of constituent i. The subscripts $i = \mathrm{d}$, ld denote denser and less dense particles, respectively, and for the variables of the mixture no subscript is used (e.g., $\Sigma f^i = f^{\mathrm{ld}} + f^{\mathrm{d}}$, and $v = \Sigma f^i v^i / f$). g refers to gravitational acceleration.

Gray, N. and Thornton, A. (2005) and Gray, N. and Chugunov, V. (2006) developed a continuum framework for segregation according to particle size for equal density particles based in part on mixture theory. Similar to the segregation model of Khakhar, D. et al. (1997), the focus of the segregation mechanism is on the gradient in 'lithostatic pressure' induced by gravity, p. That is, for flow of a mixture down a plane inclined by ζ relative to the horizontal, and, again, where y is increasing away from the free surface (in the direction of gravity), $\partial p/\partial y = \rho g\cos\zeta$. The segregation mechanism is represented by the partitioning of that pressure among the different species. Specifically, each constituent i bears a fraction of the total pressure $p^i = \psi^{\mathrm{p},i} p$, where $\psi^{\mathrm{p},i}$ is a partial pressure coefficient, not necessarily equal to the local concentration of i in the mixture, ϕ_∇^i. The original argument posed by Gray, N. and Thornton, A. (2005) indicated that whichever constituent bears more of the stress relative to its local concentration moves to lower lithostatic pressures and the other constituent moves to higher pressures. For example, again, for y increasing away from the free surface (in the direction of gravity):

$$\phi_\nabla^i\left(v^i-v\right)=\frac{1}{c_{\mathrm{D}}}\left(\phi_\nabla^i-\psi^{\mathrm{p},i}\right)g\cos\zeta - D\frac{\partial\phi_\nabla^i}{\partial y} \tag{1.2}$$

In this Equation, c_{D} is a drag coefficient. They made some assumptions about the pressure partitioning coefficients, i.e., for the particles greater in size $i = b$, $\psi^{\mathrm{p},i} = \phi^b + B_{\mathrm{GT}}\phi^b(1 - \phi^b)$, where B_{GT} is the magnitude of a non-dimensional perturbation of the partial pressure coefficients away from the solid volume fractions for each species. Then, for a flowing bidisperse mixture, Eqn. (1.2) takes a form not dissimilar from that in Eqn. (1.1):

$$\phi_\nabla^b\left(v^b-v\right)=-\frac{B}{c_{\mathrm{D}}}\phi_\nabla^b\left(1-\phi_\nabla^b\right)g\cos\zeta - D\frac{\partial\phi_\nabla^b}{\partial y} \tag{1.3}$$

The function B/c_D in Eqn. (1.3) corresponds to the function $C_K \times (\rho_m^{ld} - \rho_m^d)$ in Eqn. (1.1).

For the purpose of the mathematical development in these original papers (Khakhar et al., 1997; Gray and Thornton, 2005; Gray and Chugunov, 2006), coefficients related to drag and diffusion (e.g., C_K, c_D, and D) were initially approximated as constant. These frameworks have been shown to be effective in reproducing segregation trends in a range of granular flows, e.g., in the case of the original model by Khakhar et al. (1997), segregation in cylindrical and spherical drums (e.g., Hill et al., 1999a, 1999b; Gilchrist and Ottino, 2003) and in the case of the Gray-Thornton-Chugunov framework in other simple and complex granular flows by, for example, Wiederseiner et al. (2011); Thornton et al. (2012); Weinhart et al. (2013); Fan et al. (2014). However, these studies have also provided evidence that some details are not fully captured by the model.

Subsequent work has suggested specific modifications to this general framework to better capture the discrepancies between model and experimental and computational data. For example, more recent work by Khakhar, and colleagues (Sarkar and Khakhar, 2008; Tripathi and Khakhar, 2011, 2013) derived a more physical form of the inverse drag function C_K by considering movement of particles differing in density through an effective medium and showed the drag increased with an effective temperature. May, L. et al. (2010a, 2010b) was the first who considered the effects of a non-constant shear rate on the Gray-Thornton-Chugunov model in the form of a shear-rate dependent maximal segregation rate, though a quantitative comparison between theory and experiments has not yet been performed. Weinhart, T. et al. (2013) demonstrated that the linear drag law contained within the original Gray-Thornton-Chugunov framework may not be sufficient for capturing the drag in the system, which appeared to vary with time in their system. Gray, J. and Ancey, C. (2011) expanded the framework into a theory incorporating multiple discrete particle sizes. Marks, B. et al. (2012) partitioned the stresses explicitly according to particle size ratio; they derived a shear-rate-dependent segregation velocity, and they extended the model for continuously varying particle size distributions. They demonstrated that their new model captured segregation dynamics in a simulated polydisperse mixture. Most recently, Fan, et al. (2014) considered both shear-rate-dependent coefficients of segregation, velocity, and diffusion in the framework and showed a more quantitative agreement with experiments and DEM simulations. Tunuguntla et al. (2014) extended this framework to mixtures of particles varying in density and size and, with a shear rate dependent drag coefficient, achieved good agreement with data from computational simulations of a broad range of mixtures.

As flexible as these frameworks are, they do not have the capacity to represent how shear rate gradients and associated effects such as granular temperature gradients might affect the direction and degree of segregation. Recent work has shown that dynamics associated with shear rate gradients not only may segregate particles in cases where gravity does not play a role in segregating the particles (Hill and Fan, 2008; Fan and Hill, 2010, 2011a, 2011b), as illustrated in **Fig. 1** but they also appear to play a significant role comparable to that of gravity (Hill and Tan, 2014).

A model developed by Fan, Y. and Hill, K. (2011b) showed how the basic development used for the original Gray-Thornton-Chugunov model (Gray and Thornton, 2005; Gray and Chugunov, 2006) for different sized particles could be expanded to include consideration of shear rate gradients, also in the context of a gravitational field (Hill and Tan, 2014) and for particles differing in density (Fan and Hill, 2015). As explained in more detail in the next section, the model considered the local stress to be the sum of contact and kinetic stresses, $\boldsymbol{\sigma}^c$ and $\boldsymbol{\sigma}^k$, respectively, so that $\boldsymbol{\sigma} = \boldsymbol{\sigma}^c + \boldsymbol{\sigma}^k$ (similar to others, such as Chikkadi, V. and Alam, M. 2009). The contact and kinetic stresses are separately partitioned between the mixture components according to partial stress coefficients $\psi^{c,i}$ and $\psi^{k,i}$, e.g., $\sigma_{yy}^{c,i} = \psi^{c,i}\sigma_{yy}^c$, and $\sigma_{yy}^{k,i} = \psi^{k,i}\sigma_{yy}^k$. For the flow of a mixture down a plane inclined by ζ, and y normal to the average flow direction as for Eqns. (1.1–1.3): $\Sigma_{j=c,k}(\partial\sigma_{yx}^j/\partial x + \sigma_{yy}^j/\partial y + \sigma_{yz}^j/\partial z) = \rho g cos\zeta$, for particles differing in size and density:

$$\rho^i(v^i - v) = \frac{(\psi^{c,i} - \psi^{k,i})}{c_D}\frac{\partial\sigma_{yy}^k}{\partial y} + \frac{(\phi_m^i - \psi^{c,i})}{c_D}\rho g\cos\zeta - D\frac{\partial\rho^i}{\partial y} \tag{1.4}$$

All variables are as previously defined, and ρ^i is the local bulk density of constituent i, related to the material density of constituent i and its local solids fraction f^i according to $\rho^i = f^i\rho_m^i$. While Equation (1.4) is of similar form to Eqns. (1.1–1.3), there are some key difference, most notably the new term dependent on the gradient in kinetic stress $\partial\sigma_{yy}^k/\partial y$.

In the following sections, we show how Eqn. (1.4) can be derived and the similarities to Eqns. (1.1–1.3) under analogous conditions where the gradient in kinetic stress is negligible. Then, we provide a few examples validating this framework for dense flows. We conclude with some discussion of both the potential generalizability and also limitations of this model in its current form and some next steps that are needed for further improving the model.

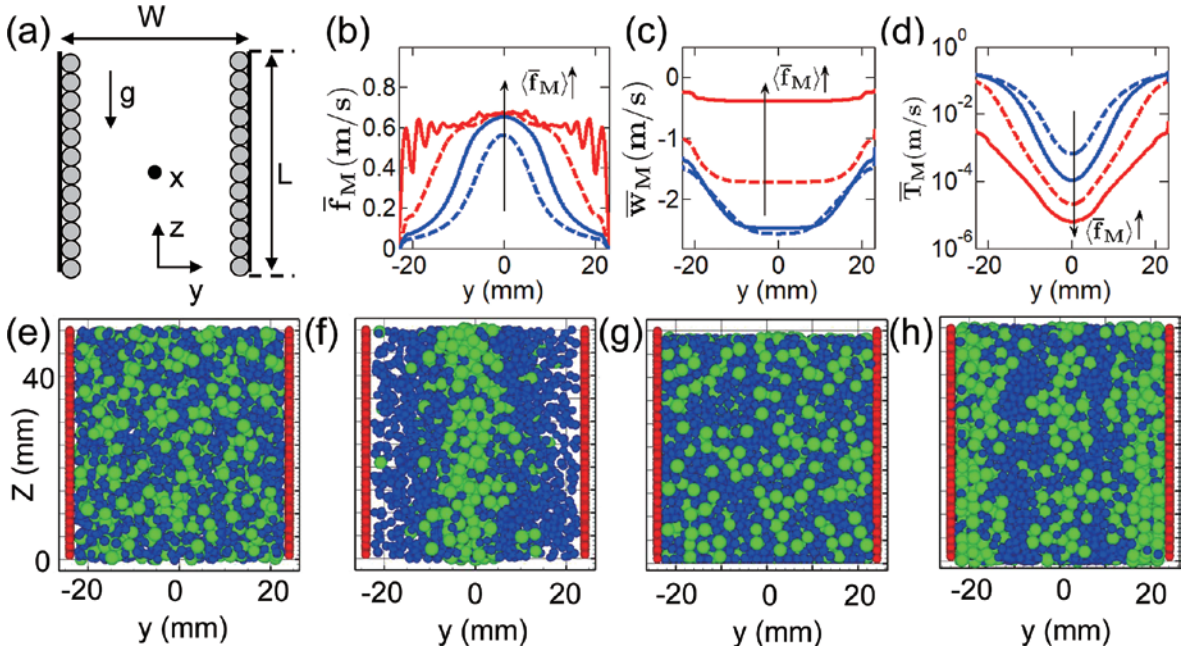

Fig. 1 Illustration of segregation driven by dynamics associated with shear rate gradients in a vertical chute, from Fan, Y. and Hill, K. (2011b). (a) Sketch of a vertical chute. (b)–(d) Time-averaged profiles of kinematic quantities for four mixtures at steady state, here $t = 5$–6 s for $\langle f \rangle = 0.2$ (red solid curve), $t = 20$–30 s for $\langle f \rangle = 0.4$ (blue dotted curve), $t = 30$–40 s for $\langle f \rangle = 0.5$ (red dotted curve), and $t = 300$–310 s for $\langle f \rangle = 0.6$ (blue solid curve): (b) streamwise velocity w of the mixture, (c) kinematic granular temperature $T = (u'u' + v'v' + w'w')/3$ of the mixture, (d) local solid fraction of the mixture f.

2. Mixture theory with effects of velocity fluctuations

Generalizing the work by Fan, Y. and Hill, K., (2011b, 2015) and Hill, K. and Tan, D. (2014) we consider a mixture of particles differing in size and/or density in high solids fraction sheared flows. For simplicity, we present the model in terms of binary mixtures of two constituents $i = 1, 2$ which may differ in material density ρ_{m}^{i} and diameter d^{i}, though the model is generalizable to multiple constituents. We denote bulk Eulerian properties of each species with superscripts and those of the mixture of both species together as variables without superscript.

As is true of standard mixture theory, the local bulk mixture density ρ is the sum of the densities of each of the constituents ρ^{i}, i.e., $\rho^{i} = f^{i}\rho_{\mathrm{m}}^{i}$, so $\rho = \Sigma_i \rho^{i} = \Sigma_i f^{i} \rho_{\mathrm{m}}^{i}$. We recall the volume concentration of species i is $\phi_{\forall}^{i} \equiv f^{i} / f$ and define the mass concentration of species i as $\phi_{\mathrm{m}}^{i} \equiv \rho^{i} / \rho$, both of which satisfy $\Sigma_i \phi^{i} = 1$. We approximate the solid fraction $f = \Sigma_i f^{i}$ as constant, but, if the particles of the two constituents differ in material density, ρ_{m}^{i}, the average local density $\rho = \Sigma_i \rho^{i}$ varies with the local concentrations of the constituents. The velocity of the constituents is allowed to differ from the average mixture velocity, and we define it in terms of the volume concentrations of the species: $u = \Sigma_i u^{i} \phi_{\forall}^{i}$.

2.1 Conservation equations for gravity-driven mixtures

We first consider conservation of mass and momentum for the mixture when subjected to gravity:

$$\frac{\partial \rho}{\partial t} + \nabla \cdot (\rho \boldsymbol{u}) = 0 \tag{2.1a}$$

$$\frac{\partial (\rho \boldsymbol{u})}{\partial t} + (\rho \boldsymbol{u} \otimes \boldsymbol{u}) = \nabla \cdot \boldsymbol{\sigma} + \boldsymbol{F} \tag{2.1b}$$

Here, $\boldsymbol{\sigma}$ represents the stress tensor, and $\boldsymbol{F}$ represents body forces per volume. Since our mixture is subjected to gravity, $\boldsymbol{F} = \rho \boldsymbol{g}$, where $\boldsymbol{g}$ is the gravitational acceleration vector.

The conservation equations are similar for the individual constituents:

$$\frac{\partial \rho^{i}}{\partial t} + \nabla \cdot (\rho^{i} \boldsymbol{u}^{i}) = 0 \tag{2.2a}$$

$$\frac{\partial (\rho^{i} \boldsymbol{u}^{i})}{\partial t} + \nabla \cdot (\rho^{i} \boldsymbol{u}^{i} \otimes \boldsymbol{u}^{i}) = \nabla \cdot \boldsymbol{\sigma}^{i} + \boldsymbol{F}^{i} + \boldsymbol{\beta}^{i} \tag{2.2b}$$

Here, all of the terms used for constituent i are identical in form to those used for the mixture in Equation (2.1b), with the exception of the new term $\boldsymbol{\beta}^{i}$. $\boldsymbol{\beta}^{i}$ represents the interaction force exerted on constituent i by the other species. $\boldsymbol{\sigma}^{i}$ is the total local stress borne by species i, where the total stress $\boldsymbol{\sigma} = \Sigma_i \boldsymbol{\sigma}^{i}$.

We consider these equations in the context of flows of relatively high concentration where the mixture kinematics reach steady state long before segregation reaches steady state, as demonstrated for simulations of flows of $f \approx 0.6$ in a vertical chute (Fan and Hill, 2011b, 2015) and in a rotated drum (Hill and Tan, 2014). Then, we can set $\partial\rho/\partial t$, $\partial(\rho \boldsymbol{u})/\partial t = 0$ in Eqns. (2.1a) and (2.1b). We then follow operations similar to Reynolds decomposition (Schlichting, 1979) and set each variable q at position r equal to a sum of the local temporal average $\overline{q}(\boldsymbol{r})$ and the difference between its instantaneous and average values $q'(\boldsymbol{r},t) = q(\boldsymbol{r},t) - \overline{q}(\boldsymbol{r})$. This mathematical manipulation allows for the explicit representation of the effect of fluctuating velocities on flow dynamics. In particular, the second term on the left side of Eqn. (2.1b) $\nabla \cdot (\rho \boldsymbol{u} \otimes \boldsymbol{u})$ may be written as $\nabla \cdot [(\overline{\rho} + \rho') \times (\overline{\boldsymbol{u}} + \boldsymbol{u}') \otimes (\overline{\boldsymbol{u}} + \boldsymbol{u}')]$. Taking the average of this expression, assuming temporal correlations between velocity fluctuations and densities are negligible (detailed in Fan and Hill, 2011b), yields terms like $\partial\left(\overline{\rho v v} + \overline{\rho v' v'}\right)/\partial y$. Assuming the simple flows that are non-uniform in only the y-direction and the average flow direction is in a direction normal to that direction, Eqn. (2.1b), the conservation of momentum equation normal to the flow for the mixture may be simply expressed according to:

$$\frac{\partial \overline{\sigma}^{\mathrm{c}}_{yy}}{\partial y} + \frac{\partial \overline{\sigma}^{\mathrm{k}}_{yy}}{\partial y} = \overline{\rho} g \cos\zeta \tag{2.3}$$

This indicates that the sum of the gradients in contact stresses and kinetic stresses balance the lithostatic pressure generated by the weight of the particles. Here, $\overline{\sigma}^{\mathrm{k}}_{yy} = \rho \overline{v' v'}$ is a normal component of the kinetic stress tensor (Chikkadi and Alam, 2009) and $\overline{\sigma}^{\mathrm{c}}_{yy}$ represents a component of the normal contact stresses generated by repulsive contacts between particles. We note that granular temperature scales as the trace of the kinetic stress tensor $T \sim \rho\left(\overline{v'_x v'_x} + \overline{v'_y v'_y} + \overline{v'_z v'_z}\right)$, and has a similar form to $\overline{\sigma}^{\mathrm{k}}_{yy}$ (e.g., Fan and Hill, 2011).

By performing Reynolds decomposition and then averaging the conservation of momentum equation for the constituents, Eqn. (2.2b), we may write:

$$\frac{\partial \overline{\sigma}^{\mathrm{c},i}_{yy}}{\partial y} + \frac{\partial \overline{\sigma}^{\mathrm{k},i}_{yy}}{\partial y} = \overline{\rho}^{i} g \cos\zeta + \overline{\beta}^{i}_{y} \tag{2.4}$$

Since all terms in Eqns. (2.3) and (2.4) are averaged, from this point on, we drop the overbar, so that unless noted for each variable q alone refers to the average $\overline{q}$.

2.2 Stress partitioning and interaction forces

To account for stress partitioning, this theory follows the suggestion of Gray, N. and Thornton, A. (2005) and Gray, N. and Chugunov, V. (2006) to allow for the partitioning of stresses between the constituents, but differs somewhat in the separate partitioning of the kinetic and contact. Specifically:

$$\sigma^{\mathrm{c},i}_{yy} = \psi^{\mathrm{c},i} \sigma^{\mathrm{c}}_{yy}, \text{ and } \sigma^{\mathrm{k},i}_{yy} = \psi^{\mathrm{k},i} \sigma^{\mathrm{k}}_{yy} \tag{2.5}$$

where we explicitly define the normal contact and kinetic stress partition coefficients for these stress components as $\psi^{\mathrm{c},i}$ and $\psi^{\mathrm{k},i}$, respectively. Neither stress partition coefficient is required to follow the concentrations of the constituents, for example, $\psi^{\mathrm{c},i}, \psi^{\mathrm{k},i} \neq \phi^{i}_{\forall}$. To assure that $\Sigma_i \sigma^{\mathrm{c},i}_{yy} = \sigma^{\mathrm{c}}_{yy}$, and $\Sigma_i \sigma^{\mathrm{k},i}_{yy} = \sigma^{\mathrm{k}}_{yy}$ two constraints must be satisfied: (1) that $\Sigma_i \psi^{\mathrm{c},i}$, $\Sigma_i \psi^{\mathrm{k},i} = 1$, and (2) wherever only one species is present (i.e., when $\phi^{i}_{\forall} = 1$) $\psi^{\mathrm{c},i}$, $\psi^{\mathrm{k},i} = \delta_{ij}$, where δ_{ij} is the Kronecker Delta function. Otherwise, no functional form is specified for either.

For the interaction term β^{i}_{y}, we can use a similar form to that proposed by Gray, N. and Chugunov, V. (2006) for granular mixtures and for flow through porous media provided by Morland, L. (1992):

$$\beta^{i}_{y} = \sigma^{\mathrm{c}}_{yy} \frac{\partial \psi^{\mathrm{c},i}}{\partial y} + \sigma^{\mathrm{k}}_{yy} \frac{\partial \psi^{\mathrm{k},i}}{\partial y} - \rho^{i} c_{\mathrm{D}} \left(v^{i} - v\right) - d \frac{\partial \rho^{i}}{\partial y} \tag{2.6}$$

The first two terms on the right side of the equation ensure that the segregation processes are driven by intrinsic rather than partial stress gradients. The third term is effectively a linear drag law, where c_{D} is the linear drag coefficient. The fourth term acts as a 'remixing force' along gradients in the concentration of each species, where the coefficient d is similar to a linear diffusion coefficient.

2.3 General segregation flux expression

Combining Eqn. (2.4)–(2.6) with Eqn. (2.3), we can express the theoretical net flux of species i, $\Phi^{i}_{\mathrm{T}} \equiv \left[\rho^{i}\left(v^{i} - v\right)\right]_{\mathrm{T}}$, as:

$$\Phi^{i}_{\mathrm{T}} \equiv \left[\rho^{i}\left(v^{i} - v\right)\right]_{\mathrm{T}} = \Phi^{i}_{\sigma\mathrm{k}} + \Phi^{i}_{\mathrm{g}} + \Phi^{i}_{\mathrm{d}} \tag{2.7}$$

where:

$$\Phi^{i}_{\sigma\mathrm{k}} = \frac{\left(\psi^{\mathrm{c},i} - \psi^{\mathrm{k},i}\right)}{c_{\mathrm{D}}} \frac{\partial \sigma^{\mathrm{k}}_{yy}}{\partial y} \tag{2.8a}$$

$$\Phi^{i}_{\mathrm{g}} = \frac{\left(\phi^{i}_{m} - \psi^{\mathrm{c},i}\right)}{c_{\mathrm{D}}} \rho g \cos\zeta \tag{2.8b}$$

$$\Phi^{i}_{\mathrm{d}} = -\frac{d}{c_{\mathrm{D}}} \frac{\partial \rho^{i}}{\partial y} \tag{2.8c}$$

This expression is identical to that in Eqn. 1.4, with the substitution $D = d/c_{\mathrm{D}}$, and suggests that there are three 'forces' dictating the segregation behavior. The first, $\Phi^{i}_{\sigma\mathrm{k}}$,

is controlled by the gradient in the kinetic stress of the mixture and the difference between the two stress partition coefficients. If a constituent bears a higher contact stress than kinetic stress then it moves in the direction of an increasing kinetic stress. The other two terms are similar to other models where the effects of kinetic stresses are not included. The second term in Eqn. (2.7), Φ_{g}^{i}, is the segregation associated with gravity, specifically, the pressure gradient induced by gravity. If a species supports a higher fraction of the contact stress than its local concentration, the species moves opposite the direction of gravity, toward the free surface. The third term in Eqn. (2.7), Φ_{d}^{i}, is akin to a diffusion force. Like normal Fickian diffusion with diffusion coefficient $D = d/c_{\mathrm{D}}$, this term results in a flux in the direction opposite to that of the concentration gradient of a particular species, and thus serves to limit the degree of local segregation.

In the next section, we show how the general flux expression in Eqn. (2.7) can be simplified to one of two scenarios: (1) where there is no kinetic stress or temperature gradient (as one would expect where fields such as the velocity and velocity fluctuations are uniform), and (2) to situations where there is a gradient in velocity fluctuations but no gravity. In these cases, the models are similar to those previously published. We demonstrate this in the next section.

3. Segregation flux in special cases

As noted above, Eqn. 2.7 is meant to be a general expression for high concentration sheared flows. For more insight about this expression, in this section we first investigate the implications of this expression for systems where the kinetic stress gradient is negligible and gravity dominates. Then we investigate this for systems where the effect of gravity on segregation is negligible, and kinetic stress gradients dominate.

3.1 Segregation flux for a negligible kinetic stress gradient

We mentioned in Section 1 that the general flux expression in Eqn. (2.7) is similar to those derived for mixtures of particles differing only in size or density (Eqn. (1.1) and (1.2), respectively) for cases where these is a negligible kinetic stress gradient. To demonstrate that, we first eliminate the kinetic stress gradient in Eqn. (1.4):

$$\rho^{i}\left(v^{i}-v\right)=\frac{\rho}{c_{\mathrm{D}}}\left(\phi_{\mathrm{m}}^{i}-\psi^{\mathrm{c},i}\right)g\cos\zeta-D\frac{\partial\rho^{i}}{\partial y} \tag{3.1}$$

In the case of particles of the same material density, if f is uniform, ρ is uniform and constant as well. Additionally, the mass and volumetric concentration of constituent i are the same, so one can substitute $\phi^{i}=\phi_{\mathrm{m}}^{i},\phi_{\forall}^{i}$. Then one may divide both sides of Eqn. (3.1) by ρ to get a segregation prediction similar to the one from Gray, N. and Chugunov, V. (2006) expressed by Eqn. (1.2):

$$\phi_{\forall}^{i}\left(v^{i}-v\right)=\frac{1}{c_{\mathrm{D}}}\left(\phi_{\forall}^{i}-\psi^{\mathrm{c},i}\right)g\cos\zeta-D\frac{\partial\phi_{\forall}^{i}}{\partial y} \tag{3.2}$$

For the expressions in Eqns. (1.2) and (3.2) to be identical, the contact stress must be partitioned between the constituents identically to the pressure and the kinetic stress. Then, for the large particles to rise to the top, the large particles must have more of the contact stress partitioned relative to their concentration (ϕ^{l}) than the small particles. In particular, for Eqns. (1.2) and (3.2) to be identical, we would require $\psi^{\mathrm{c},l}=\phi_{\forall}^{l}+B\phi_{\forall}^{s}\phi_{\forall}^{l}$. We explore this in the next section using computational simulations of sheared flows.

In the case of particles of the same size, different material density, we cannot simply divide by ρ. We recall that $\rho^{i}=f^{i}\rho_{\mathrm{m}}^{i}=f\phi_{\forall}^{i}\rho_{\mathrm{m}}^{i}$, and divide Eqn. (3.1) by $f\rho_{\mathrm{m}}^{i}$:

$$\phi_{\forall}^{i}\left(v^{i}-v\right)=\frac{\rho}{c_{\mathrm{D}}f\rho_{\mathrm{m}}^{i}}\left(\phi_{\mathrm{m}}^{i}-\psi^{\mathrm{c},i}\right)g\cos\zeta-D\frac{\partial\phi_{\forall}^{i}}{\partial y} \tag{3.3}$$

The model summarized by Eqn. (1.1) does not seem equivalent, at first glance. However, with a bit of algebra, one can show that if $\psi^{\mathrm{c},i}=\phi_{\forall}^{i}$, Eqns. (1.1) and (3.3) are actually equivalent. We will discuss this in more detail in Section 5 in the context of computational measurements of $\psi^{\mathrm{c},i}$ for special cases in Section 4.

3.2 Segregation flux for a negligible gravitational effect

There have also been situations where a gradient in velocity fluctuations have been shown capable of segregating particles without help from gravity. Examples include: microgravity experiments (Xu et al., 2003); experiments using thin layers (Conway et al., 2006) or internal shear bands (Hill and Fan, 2008), and simulations of vertical chutes (Fan and Hill, 2011a). These cases may be modeled using the general flux expression in Eqn. (2.7) by eliminating the term associated with gravity:

$$\rho^{i}\left(v^{i}-v\right)=\frac{\left(\psi^{\mathrm{c},i}-\psi^{\mathrm{k},i}\right)}{c_{\mathrm{D}}}\frac{\partial\sigma_{yy}^{\mathrm{k}}}{\partial y}-D\rho\frac{\partial\phi_{\forall}^{i}}{\partial y} \tag{3.4}$$

For a qualitative picture of the segregation process dictated by this term, we consider that the kinetic stress scales similarly to the granular temperature (e.g., Fan and Hill, 2011b). A constituent that bears more kinetic stress might be considered more mobile and more likely to find spaces or vacancies to move away from the high temperature region, somewhat like ‘kinetic sieving’ of the particles to the ‘cooler’ region. On the other hand, a constituent that bears more contact stress is physically pushed by in-

terparticle contacts to a region of lower contact stress and higher temperature, somewhat like 'squeeze expulsion' in the qualitative balance of movement induced by kinetic sieving suggested by Savage, S. and Lun, C. (1988). For mixtures of particles differing only in size, the mixture density ρ is nearly constant, so we can rewrite Eqn. (3.4) for a form identical to that originally proposed by Fan, Y. and Hill, K. (2011b):

$$\phi_\forall^i \left(v^i - v\right) = \frac{\left(\psi^{c,i} - \psi^{k,i}\right)}{c_D} \frac{1}{\rho} \frac{\partial \sigma_{yy}^k}{\partial y} - D \frac{\partial \phi_\forall^i}{\partial y} \tag{3.5}$$

While it is rare to have a situation where granular temperature works alone to segregate a particulate mixture, understanding its effect is important as in most cases gravity and granular temperature gradients coexist.

In the next section we review two examples of segregation associated with shear rate gradients and associated kinetic stress gradients in dense flows, one where gravitational effects do not contribute in the direction of segregation, and one where both kinetic stress gradients and gravity are both important.

4. Examples of shear-induced segregation

Examples supporting the framework described above have mainly been obtained from Discrete Element Method (DEM) Simulations first introduced by Cundall, P. and Strack, O. (1979). This simulation framework is powerful as it allows the user to input mechanistically representative interparticle forces and then essentially perform a computational experiment. The user may track all particles and associated forces throughout the simulations so all quantities in the model such as contact stresses and kinetic stresses can be calculated and used to test the theory. On the other hand, there can be significant limitations to the model. Even though contact forces can be represented reasonably well, they still have limitations in their representations for real dissipative materials. Additionally, variability of the surface such as roughness elements and asperities cannot be represented well. Ultimately, experiments are the best test of models. To this point, since we do not have access to experimental contact stresses, we limit our review to simulation results.

The simulations we review here use a nonlinear soft sphere contact force model. As is common, the particle deformations resulting from particle-particle contacts are represented by small overlaps between particles and related to interparticle forces. The model representing the relationship between deformations (overlaps) and interparticle forces follows Hertz-Mindlin contact theory with damping components related to the coefficient of restitution as developed by Tsuji et al. (1992) and Coulomb sliding friction:

$$F_n = -k_n \delta_n^{3/2} - \eta_n \delta_n^{1/4} \dot{\delta}_n \tag{4.1a}$$

$$F_t = \min\{-k_t \delta_n^{1/2} \delta_t - \eta_t \delta_n^{1/4} \dot{\delta}_t, \mu F_n\} \tag{4.1b}$$

where F_n and F_t are the contact forces in the directions normal and tangential to the contact plane between two contacting particles, δ_n and δ_t are the corresponding deformations, and $\dot{\delta}_n = \partial \delta_n / \partial t$ and $\dot{\delta}_t = \partial \delta_t / \partial t$ are the local time derivatives of these fluctuations. The coefficients in the force model (k_n, k_t, η_n, and η_n) are related to material properties of the two contacting particles such as elastic moduli, mass, and diameter as suggested in the original papers (e.g., Hertz, 1882; Mindlin and Deresiewicz, 1953; Johnson, 1985; Tsuji et al., 1992) and detailed in the relevant recent papers cited below (i.e., Fan and Hill, 2011; Hill and Tan, 2014).

4.1 Vertical chute flows

To isolate the effect of shear rate gradients from the effect of gravity, Fan, Y. and Hill, K. (2011a, 2011b; 2015) used DEM simulations of mixtures of particles differing only in size (Fan and Hill, 2011a) and only in density (Fan and Hill, 2015) sheared in a vertical chute [**Fig. 1(a)**]. The vertical chute is ideal for studying the effect of shear rate gradients and associated granular temperature gradients on segregation because of its simple geometry but inhomogeneous flow structure [**Fig. 1**].

Fig. 1 presents some kinematics and segregation snapshots for a mixture of 2 mm and 3 mm particles of different average system solids fractions, $\langle f \rangle = 0.2$ to 0.6. Here, we use angular brackets to indicate that these values represent the solid fraction of the whole mixture. For the high concentration system, $\langle f \rangle = 0.6$ Fan, Y. and Hill, K. (2011b) calculated partial stress coefficients throughout the simulations to test the applicability of the theory presented in Eqn. (3.4) for cases where the flow was dense and kinetic stress gradients dominated in the direction of segregation.

The results for the normalized coefficients $R^{c,i} = \psi^{c,i} / \phi_\forall^i$, and $R^{k,i} = \psi^{k,i} / \phi_\forall^i$ from the simulations for $\langle f \rangle = 0.6$ are plotted in **Fig. 2**. As shown, $R^{c,i} \approx 1$ everywhere except adjacent to solid boundaries, so that $\psi^{c,i} \approx \phi^i$ for these systems. In other words, the contact stress is partitioned between species exactly according to the volumetric concentration in the mixture. In contrast, $R^{k,s} > 1$ and $R^{k,l} < 1$ everywhere, so that $\psi^{k,s} > \phi_\forall^s$, and $\psi^{k,b} < \phi_\forall^b$, except where either $\phi^s = 1$ or $\phi^b = 1$. In other words, except in locations completely segregated where there are only large or small particles, the smaller particles carry a greater share of the kinetic stress than their concentration, while the larger particles carry less of the kinetic stress than their concentration. Considering this and the observation that the kinetic stress is greatest near the walls and

decreases inward, that is, $\partial\sigma^{\mathrm{k}}_{yy}/\partial y > 0$ for $y < 0$ and $\partial\sigma^{\mathrm{k}}_{yy}/\partial y < 0$ for $y > 0$ (similar to temperature in **Fig. 1(a)**), Eqn. (3.5) predicts that small particles segregate to the center of the chute, consistent with observation (**Fig. 1**).

For a more quantitative prediction, Fan, Y. and Hill, K., (2011b) adapted a simplifying form of the kinetic stress partition coefficient from the partial pressure coefficient from Gray, N. and Thornton, A. (2005). Specifically, they approximated $\psi^{\mathrm{k},s} \approx \phi^s + B_{\mathrm{FH},1}\phi^s_\forall\phi^b_\forall$, and $\psi^{\mathrm{k},b} \approx \phi^b_\forall - B_{\mathrm{FH},1}\phi^s_\forall\phi^b_\forall$, where $B_{\mathrm{FH},1}$ is the magnitude of a non-dimensional perturbation of the kinetic stress partition coefficients away from the solid volume fractions for each species. This form satisfies some basic restrictions on the partial pressure coefficients, namely, that they must sum to 1 so that that stresses of the constituents sum to the stress of the mixture, regardless of the concentration of the individual constituents. Using this form for the partial kinetic stress coefficients and the previously mentioned finding that $\psi^{\mathrm{c},i} \approx \phi^i_\forall$, we can write $\psi^{\mathrm{c},b} - \psi^{\mathrm{k},b} = B_{\mathrm{FH},1}\phi^s_\forall\phi^b_\forall$. Then, we can write Eqn. (3.5) for large particles as:

$$\phi^b_\forall\left(v^b - v\right) = \frac{B_{\mathrm{FH},1}\phi^s_\forall\phi^b_\forall}{c_{\mathrm{D}}}\frac{1}{\rho}\frac{\partial\sigma^{\mathrm{k}}_{yy}}{\partial y} - D\frac{\partial\phi^b_\forall}{\partial y} \tag{4.2}$$

Upon substituting Eqn. (4.2) into Eqn. (2.2a), we find the time dependence of the local concentration of larger particles:

$$0 = \frac{\partial\phi^b_\forall}{\partial t} + \frac{B_{\mathrm{FH},1}}{c_{\mathrm{D}}}\frac{\partial}{\partial y}\left(\phi^b_\forall\left(1-\phi^b_\forall\right)\frac{1}{\rho}\frac{\partial\sigma^{\mathrm{k}}_{yy}}{\partial y}\right) - \frac{\partial}{\partial y}\left(D\frac{\partial\phi^b_\forall}{\partial y}\right) \tag{4.3}$$

The tempo-spatial profiles of concentration of large particles can then be obtained by solving Eqn. (4.3) numerically provided that ρ, $\partial\sigma^{\mathrm{k}}_{yy}/\partial y$,, $D = d/c_{\mathrm{D}}$, and a segregation coefficient defined according to $q_s = B/c_{\mathrm{D}}$ can be obtained. Fan, Y. and Hill, K. (2011b) used empirically determined values: $q_s = 2.5 \times 10^{-3}$ s, and $D = 0.05$ mm^2/s. The comparison between simulation and theoretical prediction is shown in **Fig. 3**.

Figs. 3(a) and **(b)** show tempo-spatial profiles of concentration of large particles from simulation data and theoretical predictions, respectively. In both the simulation results and theoretical predictions, the large particles segregate to the side walls, and small particles segregate toward the center of the chute. For physical intuition about how this process is related to kinetic stresses, we can consider that particles tend to be pushed away from regions of high granular temperature associated with high collisional interactions. This is especially true for systems of lower solids fraction when all particles can move away from regions of high granular temperature (e.g., as in **Fig. 1(e)–(f)** and in other sheared systems, as those reported

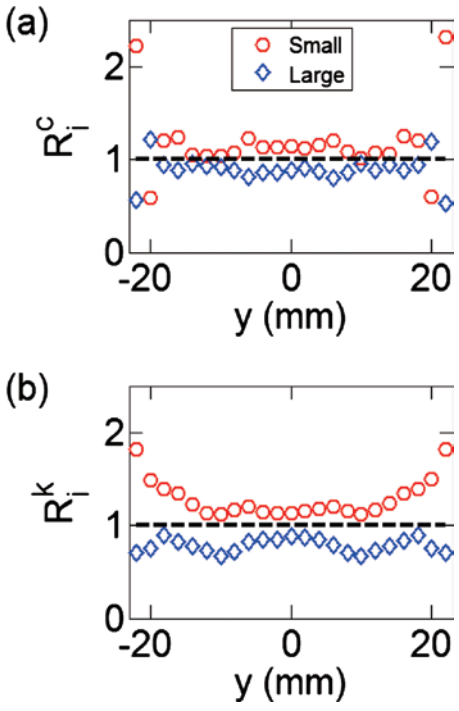

Fig. 2 Profiles of partial stress coefficients $R^{\mathrm{c},i} = \psi^{\mathrm{c},i}/\phi^i_\forall$, and $R^{\mathrm{k},i} = \psi^{\mathrm{k},i}/\phi^i_\forall$ from the first 50 s of chute flow simulations for 2 mm and 3 mm particles (e.g., **Fig. 1g–1h**) from Fan, Y. and Hill, K. (2011*b*). Data are typical of those throughout the simulation.

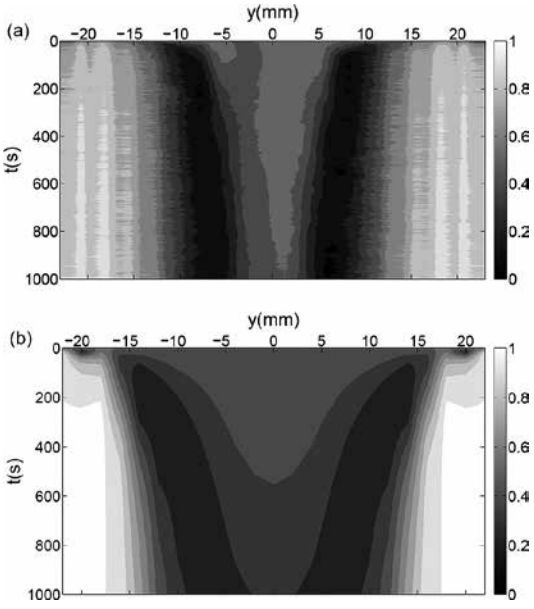

Fig. 3 Spatiotemporal profiles of the large-particle concentration $\phi^b_\forall$ from the first 1000 s of chute flow simulations for 2 mm and 3 mm particles (e.g., **Fig. 1g–1h**). (a) Simulation results. (b) Theoretical predictions. The legend indicates the shade of gray that corresponds to particular fraction of large particles. For example, $\phi^b_\forall = 1$ for white pixels and $\phi^b_\forall = 0$ for black pixels. From Fan, Y. and Hill, K. (2011b).

by Conway, S. et al., 2004). In high solid fraction sheared flows, where particles cannot "escape" en masse from the higher temperature regions, the smaller particles, with their higher kinetic stress or higher granular temperature but the same material density have more variability in their displacements (direction and magnitude). Thus have a higher likelihood of finding a way around other particles away from the region of higher granular temperature.

In the center of the chute, where the gradient of normal kinetic stress is very small, the segregation process is much slower than other regions. All of these indicate a good qualitative agreement between theoretical predictions and simulation results, though they do not reach a perfect quantitative agreement.

Hill, K. and Fan, Y. (2015) performed analogous chute flow simulations of mixtures of particles differing only in density (2mm particles of densities 2520 kg/m^3 and 7800 kg/m^3). In contrast with the mixtures of particles of different size, in this case, the heavier (denser) particles segregated to regions of low kinetic stress, low granular temperatures in the center of the chute.

The results for the normalized coefficients $R^{c,i} = \psi^{c,i} / \phi_\forall^i$, and $R^{k,i} = \psi^{k,i} / \phi_\forall^i$ from the simulations for $\langle f \rangle = 0.6$ are plotted in **Fig. 4**. As shown, $R^{c,i} \approx 1$ everywhere except adjacent to solid boundaries, so that $\psi^{c,i} \approx \phi_\forall^i$ for these systems. In other words, the contact stress is partitioned between species exactly according to the volumetric concentration in the mixture. In contrast, $R^{k,d} > 1$, and $R^{k,ld} < 1$ everywhere, so that $\psi^{k,d} > \phi_\forall^d$, and $\psi^{k,ld} < \phi_\forall^{ld}$, except where either $\phi_\forall^{ld} = 1$ or $\phi_\forall^d = 1$. In other words, except in locations completely segregated where there are only denser or less dense particles, the denser particles carry a greater share of the kinetic stress than their concentration, while the less dense particles carry less of the kinetic stress than their concentration. Considering this and the observation that the kinetic stress is greatest near the walls and decreases inward, that is, $\partial \sigma_{yy}^k / \partial y > 0$ for $y < 0$ and $\partial \sigma_{yy}^k / \partial y < 0$ for $y > 0$, Eqn. 3.4 predicts that denser particles segregate to the center of the chute, consistent with observation.

For a more quantitative prediction, similar to the case for different sized particles, Fan, Y. and Hill, K., (2015) approximated the variation of the kinetic stress partition functions as: $\psi^{k,d} \approx \phi_\forall^d + B_{FH,2} \phi_\forall^{ld} \phi_\forall^d$, and $\psi^{k,ld} \approx \phi_\forall^{ld} - B_{FH,2} \phi_\forall^{ld} \phi_\forall^d$, where $B_{FH,2}$ is the magnitude of a non-dimensional perturbation of the kinetic stress partition coefficients away from the solid volume fractions for each species. This form satisfies some basic restrictions on the partial pressure coefficients, namely, that they must sum to 1 so that that stresses of the constituents sum to the stress of the mixture, regardless of the concentration of the individual constituents. Using this form for the partial kinetic stress coefficients and the previously mentioned finding that $\psi^{c,i} \approx \phi^i$, we can write $\psi^{c,ld} - \psi^{k,ld} = B_{FH,2} \phi_\forall^{ld} \phi_\forall^d$. Then

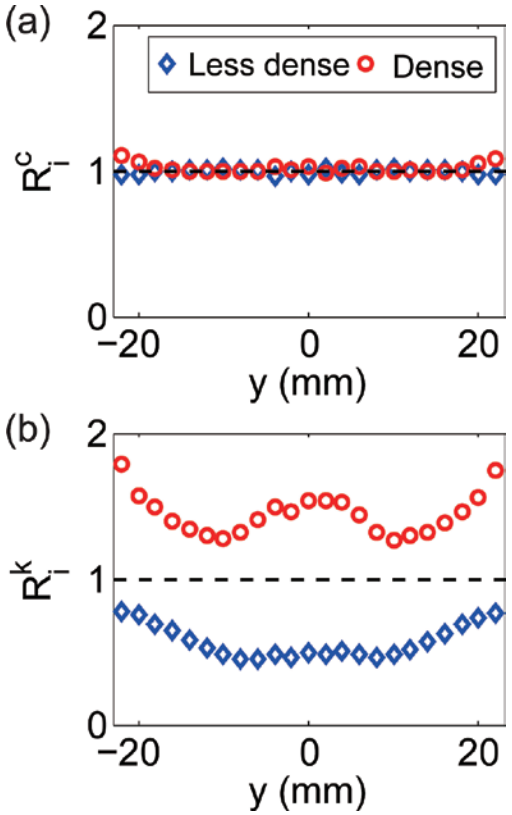

Fig. 4 Profiles of partial stress coefficients $R^{c,i} = \psi^{c,i} / \phi_\forall^i$, and $R^{k,i} = \psi^{k,i} / \phi_\forall^i$ at t = 50–100 s of chute flow simulations of 2 mm glass and steel particles from Fan & Hill (2015).

Eqn. 3.4 may be rewritten for less dense particles as:

$$\rho^{ld}(v^{ld} - v) = \frac{B_{FH,2} \phi_\forall^{ld} \phi_\forall^d}{c_D} \frac{\partial \sigma_{yy}^k}{\partial y} - D \frac{\partial \rho^{ld}}{\partial y} \tag{4.4}$$

Upon substituting Eqn. (4.4) into Eqn. (2.2a), we find the time dependence of the local concentration of less dense particles:

$$0 = \frac{\partial \rho^{ld}}{\partial t} + \frac{B_{FH,2}}{c_D} \frac{\partial}{\partial y} \left(\phi_\forall^{ld} (1 - \phi_\forall^{ld}) \frac{1}{\rho} \frac{\partial \sigma_{yy}^k}{\partial y} \right) - \frac{\partial}{\partial y} \left(D \frac{\partial \phi_\forall^{ld}}{\partial y} \right) \tag{4.5}$$

Again, noting that, $\rho^i = f^i \rho_m^i = f \phi_\forall^i \rho_m^i$, we divide by $f \rho_m^{ld}$ for the following expression for the evolution of the concentration:

$$\frac{\partial \phi_\forall^{ld}}{\partial t} = -\frac{B_{FH,2}}{c_D f \rho_m^{ld}} \frac{\partial}{\partial y} \left(\phi_\forall^{ld} (1 - \phi_\forall^{ld}) \frac{1}{\rho} \frac{\partial \sigma_{yy}^k}{\partial y} \right) + \frac{\partial}{\partial y} \left(D \frac{\partial \phi_\forall^{ld}}{\partial y} \right) \tag{4.6}$$

The tempo-spatial profiles of concentration of less dense particles can be obtained by solving Eqn. (4.6) numeri-

cally provided that ρ, $\partial\sigma^{k}_{yy}/\partial y$,, $D = d/c_D$, and a segregation coefficient defined according to $q_s = B/c_D$ can be obtained. For this case, Fan, Y. and Hill, K. (2015) found the best empirically determined values: $q_s = 1 \times 10^{-3}$ s, and $D = 0.2$ mm^2/s. q_s is approximately half that found for the mixture differing only in size, and D for this mixture is approximately four times that found for the mixture differing only in size. This is consistent with the observation that segregation is slower for these systems. However, it is not clear whether or not this difference is significant, particularly given that it is likely that both c_D and D vary spatially with shear rate or other quantity so the difference in these variables is only a qualitative indicator. The comparison between simulation and theoretical prediction for the mixture differing in density is in **Fig. 5**.

Fig. 5(a) and **(b)** show tempo-spatial profiles of concentration of denser particles from simulation data and theoretical predictions, respectively. In both the simulation results and theoretical predictions, the less dense particles segregate to the side walls, and denser particles segregate toward the center of the chute. For physical intuition about this process, we note first that, unlike the case of the different sized same density particles, for this case of the particle differing only in density, the particles have the same magnitude of velocity fluctuations. Thus the greater magnitude of the kinetic stresses in the dense particle constituent arises from the higher material density of particles alone. In this context, we can still consider that particles tend to be pushed away from regions of high granular temperature associated with high collisional interactions. In high solid fraction sheared flows, we posit that the denser particles are able to push through a relatively tight mass of particles toward the "cooler" regions, whereas the lighter particles cannot "escape" as easily. As is the case for the mixture of particles differing only in size, in the middle slow creeping region, where the gradient of normal kinetic stress is very small, the segregation process is much slower than other regions. There is evidence of the discrete nature of the particles in the segregation trends in **Fig. 5(a)** not realizable in the continuum model results shown in **Fig. 5(b)**. Nevertheless, the average trends are similar in both.

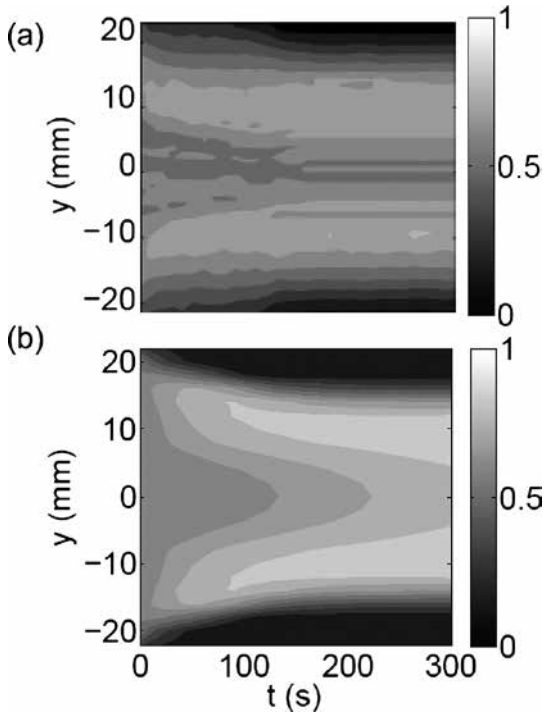

Fig. 5 Spatiotemporal profiles from the first 1000 s of chute flow simulations for binary mixtures of particles of two different densities. The gray scale indicates the solid fraction of higher material density particles $\phi^{d}_{\forall}$ from: (a) Simulation results. (b) Theoretical predictions. The legend indicates the shade of gray that corresponds to particular fraction of denser particles. For example, $\phi^{d}_{\forall} = 1$ for white pixels and $\phi^{ld}_{\forall} = 0$ for black pixels. From Fan & Hill (2015).

4.2 Rotating drum flows

In contrast with the simulations described in Section 4.1, in many sheared flows (such as inclined chute flows and rotated drums, e.g., **Fig. 6**), gravity, velocity gradients, and corresponding gradients in kinetic stress and temperature coexist in the direction of segregation. Hill, K. and Tan, D. (2014) investigated the effectiveness of the segregation expression in Eqn. (2.7) for the segregation in the thin flowing layer in a rotated drum (**Fig. 6**). In particular, they investigated whether the segregating effect of the kinetic stress gradient shown in vertical chute flows where the gravity had negligible segregating effect was significant in the presence of gravity.

Their simulated circular drum had periodic boundaries in the axial direction (e.g., no front and back walls in **Fig. 6(a)**) to eliminate side wall segregation effects (e.g. Hill and Zhang, 2008). The drum diameter is 72 mm; the thickness (periodic length in axial direction) is 30 mm. They 'filled' the drum partway with binary mixtures of particles of the same density and two different diameters, 2 mm and 3 mm, with a 10 % variability in particle size of each constituent. The particles were initially well-mixed when drum rotation was commenced at a speed of $\omega \approx 16$ rotations per minute (rpm). They studied the segregation dynamics for five different concentrations of large particles (by volume) in the mixture: $\langle \phi^{b}_{\forall} \rangle = 10$ %, 25 %, 50 %, 75 %, and 90 %. In all cases, the flow in the radial center of the drum (i.e., the center of the flowing layer) was nearly uniform in the streamwise (x-) and transverse (y-) directions, so the basic assumptions under which Eqn. (2.7) was developed hold, even though the entirety of the flow is relatively non-uniform.

The segregation dynamics vary somewhat from one

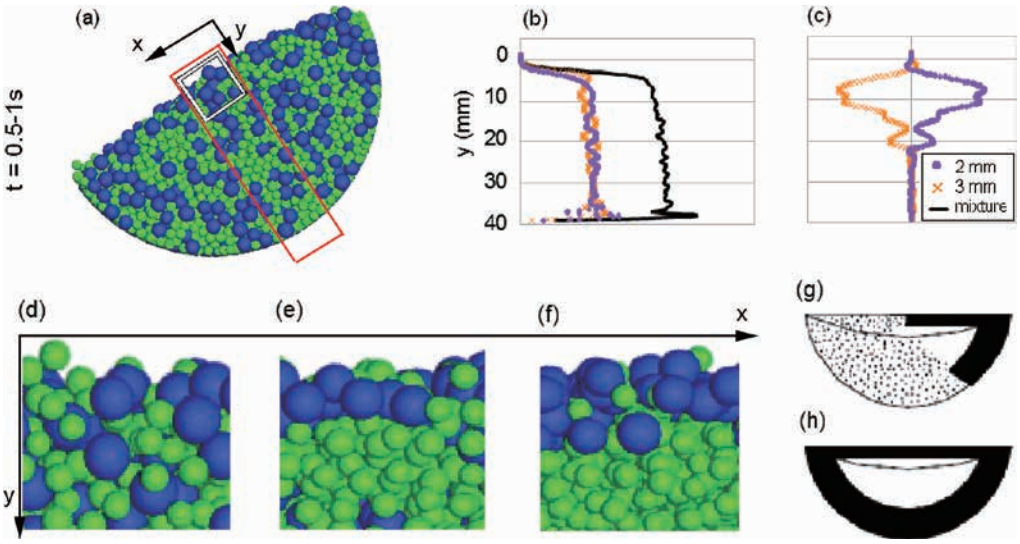

Fig. 6 The first row shows details of a 50/50 mixture of 2 mm and 3 mm diameter particles of the same material density in a drum near the beginning of the simulation when the constituents are well-mixed. (a) a snapshot (b) solid fraction f^i profile of each constituent i and (c) the vertical flux profile $f^i\Delta v^i = f^i(v^i - v)$ of each constituent. The second row shows (d)–(f) snapshots from the central part of the flowing layer in the simulations, denoted by the white box in (a). (The axes indicate the direction; all images were taken from the same location on the drum, indicated by the white box in (a).) (d) initial state (e) 5 s into the simulation (f) the steady segregated state of the system. (g)–(h) Sketches illustrating how the segregation in the top flowing layer is recorded into a radial segregation pattern in the solid-like granular materials in the majority of the drum (from Hill *et al.* (2004)). The plotted data were calculated from the middle 1/7 of the drum (as illustrated by the red box in (a)), and obtained by averaging over a 500 ms period and for three different equivalent runs differing only in the initial random configuration of the particles. (From Hill and Tan, 2014). The axes in (a) and (d)–(f) indicate the x- and y-directions. The z-direction is normal to the page.

mixture to the next, as shown in **Fig. 7**. Specifically, for each, **Fig. 7** row 1 shows snapshots of the near steady-state segregation patterns in the first row, the corresponding plot for the solid fractions f^i in the second row, and the early-time segregation fluxes $f^i\Delta v^i$ in the third row. In all cases, the large particles segregated upward in the flowing layer and toward the outside of the drum. However, the segregation flux magnitudes and steady state relative concentrations of the two constituents varied from one mixture to the next.

While the segregation dynamics varied from one system to the next, the stress partition coefficients did not. Similar to the vertical chute flows, $R^{c,i} \approx 1$ everywhere except adjacent to solid boundaries, so that $\psi^{c,i} \approx \phi^i_\forall$ for all mixtures. In other words, the contact stress is partitioned between species exactly according to the volumetric concentration in the mixture. That is, Eqn. (2.7) reduces to Eqn. (3.5) in this circumstance, as with the additional substitution that $\psi^{c,i} \approx \phi^i_\forall$, this yields:

$$\Phi^i_g = \frac{\left(\phi^i_\forall - \psi^{c,i}\right)}{c_D}\rho g\cos\zeta = 0 \tag{4.7a}$$

$$\phi^i_\forall\left(v^i - v\right) = \frac{\left(\phi^i_\forall - \psi^{k,i}\right)}{c_D}\frac{1}{\rho}\frac{\partial\sigma^k_{yy}}{\partial y} - D\frac{\partial\phi^i_\forall}{\partial y} \tag{4.7b}$$

In contrast, but, again, similar to the chute flows, $R^{k,s} > 1$ and $R^{k,b} < 1$ everywhere, so that $\psi^{k,s} > \phi^s_\forall$, and $\psi^{k,b} < \phi^b_\forall$, except where either $\phi^s_\forall = 1$ or $\phi^l = 1$. In other words, except in locations completely segregated where there are only large or small particles, the smaller particles carry a greater share of the kinetic stress than their concentration, while the larger particles carry less of the kinetic stress than their concentration. In fact, the relationship between $\psi^{k,b}$ and $\phi^b_\forall$ was essentially the same for all mixtures at all times (**Fig. 8**):

$$\psi^{k,b} = 0.39\times\left(\phi^b_\forall\right)^2 + 0.61\times\phi^b_\forall \tag{4.8}$$

These results are similar in form to the pressure coefficient suggested by Gray and colleagues note in Section 1, though here we would write:

$$\psi^{c,b} = \phi^b_\forall + B^c\phi^b_\forall\phi^s_\forall \tag{4.9a}$$

$$\psi^{k,b} = \phi^b_\forall + B^k\phi^b_\forall\phi^s_\forall \tag{4.9b}$$

where based on the simulations results, $B^c = 0$, and $B^k = -0.39$. Unlike the positive value of B for the analogous total pressure partition coefficient suggested by Gray and colleagues, these two values, B^c and B^k are distinct,

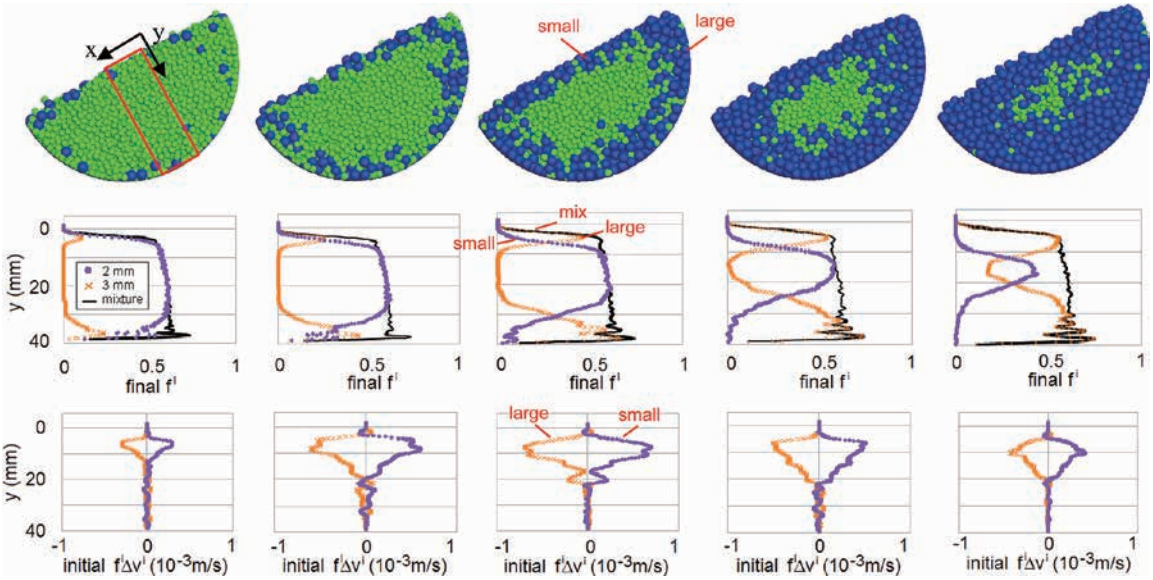

Fig. 7 Segregation of mixtures of different sized particles (2 mm and 3 mm) of equal material densities, where the system-averaged large (3 mm) particle concentration, $\langle \phi_\forall^b \rangle$, varies from one column to the next. Specifically, $\langle \phi_\forall^b \rangle$ increases from left to right from system-averaged large-particle concentrations $\langle \phi_\forall^b \rangle$ from 0.1 to 0.9 as noted above each column. Row 1: Snapshots of the segregated mixtures from the time at which mixtures were under statistically steady state conditions (after ≈ 30 s of rotation). Rows 2 and 3: Solid fraction and segregation flux data from the region of the drum indicated by the box in the first snapshot in row 1. In both rows, the *y-direction* is positive downward and normal to the free surface as indicated in the first snapshot in row 1. Row 2: Solid fraction profile for each species and for the mixture in the region corresponding to the simulation represented by each snapshot in the first row. The data are taken after ≈ 30 s of rotation once each system has reached a statistically steady segregated state. Row 3: The segregation flux at the beginning of the simulation for each mixture. In each case the mixture started relatively well-mixed, and the data shown in Row 3 was taken from ≈ 0.5 s after beginning rotation while the system was still relatively well-mixed. Negative values of the segregation flux indicate segregation upward toward the free surface, and positive values of the flux indicate segregation downward. The data shown in Rows 2 and 3 were obtained by averaging over a 500 ms period. From Hill, K. and Tan, D. (2014).

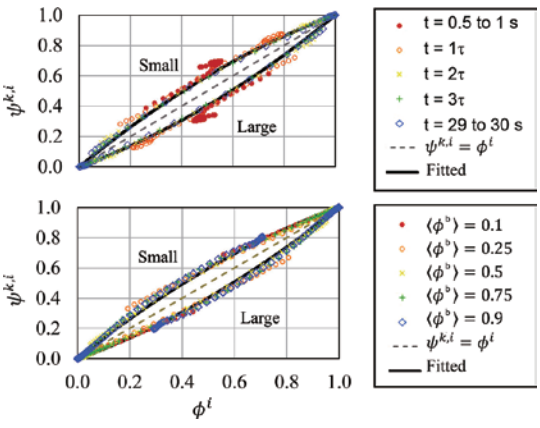

Fig. 8 Kinetic stress partition coefficient as a function of concentration in the flowing layer of the drum simulations: (a) For the mixture with 50 % large particles, at different times during segregation. (b) For mixtures of different global concentration, at steady state ($t \approx 29.5$ to 30 s). The fitted lines in both (a) and (b) are Eqns. 4.5a, 4.5b, $B^k = -0.39$.

and both less than or equal to zero because the large particles actually carry less than (or equal to) the portion of the stress compared to their concentration in the mixture. These results are not inconsistent with the results from the chute flows described in Section 4.1, for which Fan, Y. and Hill, K. (2011b, 2015) assumed, $\psi^{c,b} - \psi^{k,b} = B\phi_\forall^b \phi_\forall^s$. In these drum flows, $\psi^{c,b} - \psi^{k,b} = (B^c - B^k)\phi_\forall^b \phi_\forall^s$, so that $B = B^c - B^k = 0.39$.

Finally, a predictive form for these gravity-driven flows, including effects of kinetic stress gradients associated with the shear rate gradients, can be written:

$$\phi_\forall^b (v^b - v) = \frac{B^k \phi_\forall^b (1 - \phi_\forall^b)}{c_D \rho} \frac{\partial \sigma_{yy}^k}{\partial y} - D \frac{\partial \phi_\forall^b}{\partial y} \tag{4.10a}$$

$$\phi_\forall^s (v^s - v) = -\frac{B^k \phi_\forall^s (1 - \phi_\forall^s)}{c_D \rho} \frac{\partial \sigma_{yy}^k}{\partial y} - D \frac{\partial \phi_\forall^b}{\partial y} \tag{4.10b}$$

for the large or big (b) and small (s) particle constituents, respectively.

For any particular mixture, a reasonable functional form for the drag and diffusion coefficients c_D and D may be found empirically using simulations of the mixtures. At early times, c_D may be empirically derived by noting

the gradient in concentration $\partial\phi_\nabla^i/\partial y \approx 0$, so the total flux in Eqn. (4.8) reduces to that determined by the kinetic stress gradient alone:

$$\phi_\nabla^b\left(v^b - v\right) = \frac{B^{\mathrm{k}}\phi_\nabla^b\left(1-\phi_\nabla^b\right)}{c_{\mathrm{D}}\rho}\frac{\partial\sigma_{yy}^{\mathrm{k}}}{\partial y} \tag{4.11a}$$

$$\phi_\nabla^s\left(v^s - v\right) = -\frac{B^{\mathrm{k}}\phi_\nabla^s\left(1-\phi_\nabla^s\right)}{c_{\mathrm{D}}\rho}\frac{\partial\sigma_{yy}^{\mathrm{k}}}{\partial y} \tag{4.11b}$$

Once the functional form for B^{k} is determined as described above (e.g., Eqn. 4.8), all other variables in Eqns. (4.9a–4.9b) can be measured directly from the simulations, to determine the functional form for c_{D}. While it is likely that c_{D} is not constant, for a first order model, Hill and Tan (2014) first approximated c_{D} as constant for each mixture. Then they used the calculated values for each of the variables at early times to separately determine $\phi_\nabla^b\left(v^b - v\right)$ and $B^{\mathrm{k}}(\phi_\nabla^b\left(1-\phi_\nabla^b\right)/\rho)(\partial\sigma_{yy}^{\mathrm{k}}/\partial y)$ throughout the flowing layer. By using the method of least squares fitting, they determined the best value for c_D for each mixture. An example of these data for a 50/50 mixture is shown in **Fig. 9**, row 1.

The diffusion coefficient D can be similarly empirically determined. Hill and Tan (2014) used conditions at later times under steady segregated conditions, where the segregation flux $\phi_\nabla^i(v^i - v) \approx 0$. In this case, Eqns. (4.10a–4.10b) may be rewritten:

$$\frac{B^{\mathrm{k}}\phi_\nabla^b\left(1-\phi_\nabla^b\right)}{\rho}\frac{\partial\sigma_{yy}^{\mathrm{k}}}{\partial y} = c_{\mathrm{D}}D\frac{\partial\phi_\nabla^b}{\partial y} \tag{4.12a}$$

$$\frac{B^{\mathrm{k}}\phi_\nabla^s\left(1-\phi_\nabla^s\right)}{\rho}\frac{\partial\sigma_{yy}^{\mathrm{k}}}{\partial y} = -c_{\mathrm{D}}D\frac{\partial\phi_\nabla^b}{\partial y} \tag{4.12b}$$

Once B^{k} and c_{D} are determined as described above, all other variables can be determined for the simulations, except D. Again, Hill and Tan (2014) approximated D as constant for each mixture. Then, they used the values for each value computed from the simulations under later times at steady state conditions to independently determine $B^{\mathrm{k}}(\phi_\nabla^b\left(1-\phi_\nabla^b\right)/\rho)(\partial\sigma_{yy}^{\mathrm{k}}/\partial y)$ and $c_{\mathrm{D}}\partial\phi^b/\partial y$ throughout the flowing layer. Then they used the method of least squares fitting to determine the best value for D for each mixture. An example for a 50/50 mixture is shown in **Fig. 9**, row 2.

They found that there was some variability from one mixture to the next, but not a systematic variation of either c_{D} or D with ϕ_∇^b. While this is likely an artifact of performing these calculations assuming values for c_{D} and D this still provides a manner for validating the model more quantitatively and a first order estimate for these parameters. For a predictive form for all mixtures in their simulations they used the average value they obtained for each mixture: $c_{\mathrm{D}} = 6.3\ \mathrm{s}^{-1}$ and $D = 0.20\ \mathrm{mm}^2/\mathrm{s}$. When they used the results for different mixtures at different time steps (e.g., **Fig. 10**), they found reasonable agreement. While not a rigorous test, these data indicate that, indeed, the gradient kinetic stress is a dominant segregation driver, even in the presence of a gravitational field.

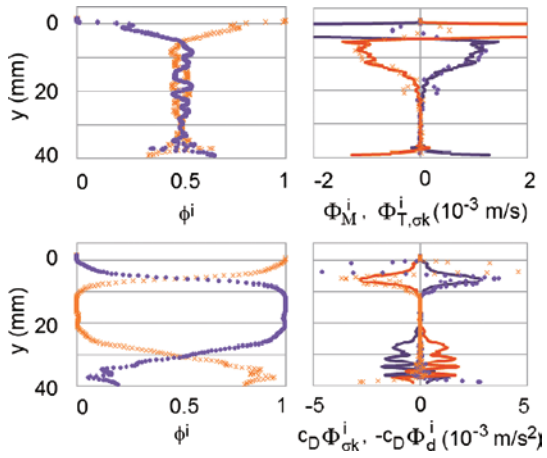

Fig. 9 Concentrations and calculations described in text to determine c_{D} and D, both sets shown for 50 % large particles. Row 1: early times where the mixture is relatively uniform. Row 2: late times when the segregation is nearly under steady state conditions. Column 1: Local concentration of each species. Column 2, top row: simulation (points) and model (lines) data from Eqns 4.11–4.12. Results shown for both large particles (purple) and small particles (orange). From Hill, K. and Tan, D. (2014).

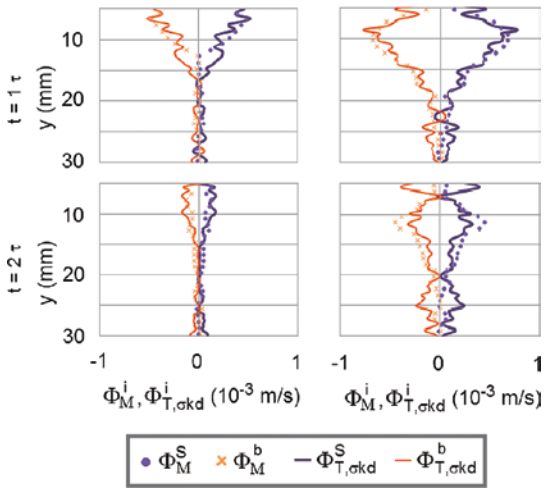

Fig. 10 Theoretical fluxes (Eqns 4.10(a)–(b)) using empirically-determined values for B^{k}, c_{D}, and D compared with simulated fluxes. Results for two different time steps for two different global concentrations of the bigger particles as noted at the top of each column. From Hill, K. and Tan, D. (2014).

5. Outlook for generalizability

For this model to be easily applicable to other systems, a mechanistic understanding and general expressions are needed for parameters such as the partition coefficients and the drag and diffusion coefficients. As mentioned in the introduction, there has been much work recently on developing these expressions for various types of particle mixtures. Additionally, some expressions are derivable from kinetic theory, e.g., Jenkins, J. and Mancini, F. (1987) and Larcher, M. and Jenkins, J. (2013). On the other hand, relatively little work has been done investigating how contact and kinetic stress are partitioned between the constituents. To investigate the generalizability of the simulation results for the stress partition coefficients described for certain mixtures in Section 4, we borrow insight from previous related work.

5.1 Contact stress partition coefficients—insight from density segregation model

The systems in Section 4 are relatively special in that the particles differ only in size or density. However, there are some considerations we can use to test the generalizability for other systems where the particles differ in both size and density.

First, we recall that the simulation data obtained by Fan, Y. and Hill, K. (2011b, 2015) and Hill, K. and Tan, D. (2014) indicate that for mixtures of particles differing modestly in density or size, the constituents bear a portion of the contact stress equal to their volumetric concentration in the mixture, i.e., $\psi^{c,i} \approx \phi_\forall^i$. For a working definition of "modest" for here and for the rest of the paper, we consider those where a different mechanism is not obviously in play, so we limit our immediate consideration to size differences in bimodal mixtures that do not exceed that for which the smaller particles can passively sieve through the larger particles and to density differences that range up to a factor of 7, approximately that of a mixture of steel and plastic particles. We revisit the general expression in Eqns. (2.7–2.8) and note this impacts the gravity flux. That is, based on the results that $\psi^{c,i} \approx \phi_\forall^i$ we can rewrite theoretical expression for the segregation flux associated with gravity in Eqn. (2.8b) as:

$$\left[\rho^i\left(v^i - v\right)\right]_{\mathrm{T,g}} = \frac{\left(\phi_{\mathrm{m}}^i - \phi_\forall^i\right)}{c_{\mathrm{D}}}\rho g\cos\zeta \tag{5.1}$$

If we substitute expressions for the definitions of $\phi_\forall^i = f^i / f$ and $\phi_{\mathrm{m}}^i = \rho^i / \rho$ in terms of the solid fractions and material densities of the constituents, e.g., $\phi_\forall^i = f^i / f$ and $\phi_{\mathrm{m}}^i = \rho^i / \rho = \rho_{\mathrm{m}}^i f^i / \Sigma_i(\rho_{\mathrm{m}}^i f^i)$, with a little algebra we can rewrite this as:

$$\left[\rho^i\left(v^i - v\right)\right]_{\mathrm{T,g}} = \frac{f^i f^j\left(\rho_{\mathrm{m}}^i - \rho_{\mathrm{m}}^j\right)}{f c_{\mathrm{D}}} g\cos\zeta \tag{5.2}$$

This is similar to what one might predict qualitatively from simple expectations that denser particles should sink relative to lighter particles, and the magnitude of the segregation flux associated with this should depend on their relative concentration in the mixture.

Moreover, we can compare by the model proposed by Khakhar, D. et al. (1997) by setting $i = \mathrm{ld}$ and recalling that $\rho^i = \rho_{\mathrm{m}}^i f^i = \rho_{\mathrm{m}}^i \phi_\forall^i f$. Then with a little rearranging of Eqn. (5.2), we can write:

$$\left[\phi_\forall^{\mathrm{ld}}\left(v^{\mathrm{ld}} - v\right)\right]_{\mathrm{T,g}} = -\frac{\rho_{\mathrm{m}}^{\mathrm{d}}}{\rho_{\mathrm{m}}^{\mathrm{ld}} c_{\mathrm{D}}}\phi_\forall^{\mathrm{ld}}\phi_\forall^{\mathrm{d}}\left(1 - \frac{\rho_{\mathrm{m}}^{\mathrm{ld}}}{\rho_{\mathrm{m}}^{\mathrm{d}}}\right) g\cos\zeta \tag{5.3}$$

This is nearly identical to the model originally proposed by Khakhar, D. et al. (1997) in Eqn. (1.1), with $C_{\mathrm{K}} = \rho_{\mathrm{m}}^{\mathrm{d}} / (\rho_{\mathrm{m}}^{\mathrm{ld}} c_{\mathrm{D}})$. This consistency between the general model predictions of Eqns. (2.7–2.8), with the more mechanistic derivation of the model in Eqn. (1.1) (e.g., Sarkar, S. and Khakhar, D., 2008; Tripathi A. and Khakhar, D., 2013) , lends credence to the results from the general theoretical framework and the further generalizability that $\psi^{c,i} \approx \phi_\forall^i$ for a wider range of mixtures. These results have not been tested extensively, but one might hypothesize that this is likely limited to cases where size and density are only modestly different.

5.2 Kinetic stress partition coefficients—insight from granular temperature

While similarly little work has been done investigating how kinetic stress is partitioned among constituents in a mixture, there has been some related work on granular temperatures, that is, kinetic energy associated with velocity fluctuations. In particular, Hill, K. and Zhang, J. (2008) investigated how granular temperature varies for particles in a mixture. We now consider the generalizability of the kinetic stress coefficient derived here based on their work. Then, we consider similar issues regarding the segregation flux associated with kinetic stress gradients.

Hill, K. and Zhang, J. (2008) investigated the variation of granular temperature of particle mixtures of different sizes and densities in the dense flows using experiments and simulations of drum flows similar to that in Section 4.2. In particular, they noted how the granular temperature and velocity fluctuations varied for different constituents in a mixture. While not exactly equal to the kinetic stress, they are related. In particular, Zhang, K. and Hill, J. (2008) reported on results for what they called a "kinematic temperature" (in 2d):

$$T^{\mathrm{k},i} \equiv \overline{u'u'}^b + \overline{v'v'}^b. \tag{5.4}$$

Here, u corresponds to the streamwise velocity, and $\overline{u'u'}^i$

is the variance of the velocity fluctuations of constituent i in the streamwise direction, analogous to $\overline{v'v'}^i$ in the direction normal to flow. Hill, K. and Zhang, J. (2008) noted that the fluctuations in the different directions scale similarly, that is, $\overline{u'u'}^i$ is roughly proportional to $\overline{v'v'}^i$ for mixtures of 2 mm and 3 mm particles differing in densities up to a factor of 3. While there are likely limits to this approximate relationship, we do not explore these limits here. Rather we use this as a method to explore the implication for how this theoretical framework may be further extended for similar systems. Based on this simplifying assumption, we can approximate:

$$T^{\mathrm{k},b} / T^{\mathrm{k},s} \approx \overline{v'v'}^b / \overline{v'v'}^s \tag{5.5}$$

We can compare this to the results for the mixtures described in Section 4 by noting

$$\frac{\psi^{\mathrm{k},b}}{\psi^{\mathrm{k},s}} = \frac{\rho^b \overline{v'v'}^b}{\rho^s \overline{v'v'}^s} \approx \frac{\rho^b}{\rho^s} \frac{T^{\mathrm{k},b}}{T^{\mathrm{k},s}}. \tag{5.6}$$

For a 50/50 mixture of equal density particles, $\rho^b = \rho^s$, and so for this special case $\psi^{\mathrm{k},b}/\psi^{\mathrm{k},s} \approx T^{\mathrm{k},b}/T^{\mathrm{k},s}$. We return to this analogy in a moment, but first explore these previous results for how relative kinematic temperature varies according to relative particle size and density in a mixture.

Hill, K. and Zhang, J. (2008) reported that in the dense region of the flowing layer in physical experiments, the velocity fluctuations scale primarily with relative size of particles in the mixture (increasing as relative particle size decreases) and have very little dependence on density. In other words, in mixtures of particles differing only in density the less dense particles have velocity fluctuations of similar magnitude to the dense particles, i.e., $T^{\mathrm{k},ld} \approx T^{\mathrm{k},d}$. In mixtures of particles differing only in size, small particles have higher average velocity fluctuations than large particles $T^{\mathrm{k},b} < T^{\mathrm{k},s}$. Moreover, they used simulations to investigate the effect of systematic variations of the relative particle density of particles of two different (fixed) sizes and found that $T^{\mathrm{k},b}/T^{\mathrm{k},s}$ did not change. In other words, they found that $T^{\mathrm{k},b}/T^{\mathrm{k},s}$ for particles differing in both size *and* density *only* depended on the relative sizes of particles in the mixture, not their relative densities.

To explain their results, Hill and Zhang reasoned that, in contrast with sparser regions of the flow, this scaling is associated with geometric considerations. They developed a simple model, the essence of which is as follows. Particle movement in sheared dense flow is primarily laminar in nature, where particles move in enduring contact over neighboring layers of particles. Velocity fluctuations are generated when beads must slide around neighbors below or when the neighbors below push them as they themselves slide around their neighbors. One can extend this qualitatively to particles of different properties by noting that smaller particles sliding over larger neighbors will be jostled more than larger particles sliding over smaller

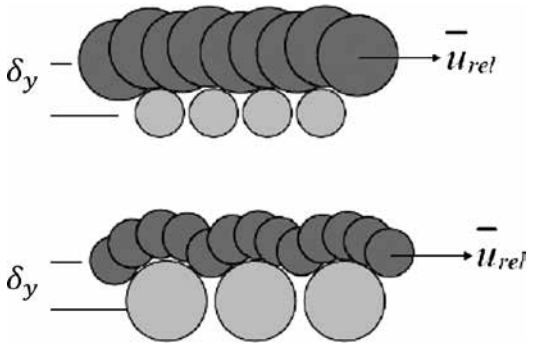

Fig. 11 Sketch illustrating how in dense sheared flows of similar shear rates ($\dot{\gamma} \sim \bar{u}_{rel} / \delta_y$ in the image above) geometric constraints could cause the smaller particles to have higher velocity fluctuations than the larger particles. From Hill, K. and Zhang, J. (2008).

neighbors (e.g., **Fig. 11**). On the other hand, density should have relatively little effect on this primarily geometric problem. The model, presented in more detail in the paper, fit the data well and the results are consistent with the kinetic stress partition coefficients described in Section 4.

The overlap between the measured temperature data from Hill, K. and Zhang, J. (2008) and the mixture results described in section 4 are in the 50/50 mixtures of particles of 2 mm and 3 mm. Hill, K. and Zhang, J. (2008) found the relative kinematic temperatures for a 50/50 mixture of 3 mm and 2 mm particles was approximately $(\overline{u'u'}^b + \overline{v'v'}^b) / (\overline{u'u'}^s + \overline{v'v'}^s) \approx 0.7$. Again, using the simplifying assumption that $\overline{u'u'}^i \sim \overline{v'v'}^i$ we use this to approximate $\overline{v'v'}^b / \overline{v'v'}^s \approx 0.7$. As noted above, for a 50/50 mixture of equal density particles, $\rho^b = \rho^s$. Thus, the results from Hill, K. and Zhang, J. (2008) indicate that for a 50/50 mixture of 2 mm and 3 mm particles $\psi^{\mathrm{k},b} / \psi^{\mathrm{k},s} = \overline{v'v'}^b / \overline{v'v'}^s \approx 0.7$. Using this with the requirement $\psi^{\mathrm{k},b} + \psi^{\mathrm{k},s} = 1$, these results imply $\psi^{\mathrm{k},b} \approx 0.41$, and $\psi^{\mathrm{k},s} \approx 0.59$. The results from Hill, K. and Tan, D. (2014) in Eqn. (4.9b) with $B^{\mathrm{k}} \approx -0.39$ and $\phi_\nabla^b = \phi_\nabla^s \approx 0.5$ indicate that $\psi^{\mathrm{k},b} \approx 0.40$, and $\psi^{\mathrm{k},s} \approx 0.60$, very similar.

Based on these results, Eqn. (5.6) and the results expressed by Eqn. (4.9b), we would suggest that for particles of modest size and density differences, the kinetic stress partition coefficients can be found using material densities of the two constituent particles, local volumetric concentrations, and one parameter B^{k}, according to:

$$\frac{\psi^{\mathrm{k},b}}{\psi^{\mathrm{k},s}} = \frac{\rho_{\mathrm{m}}^b}{\rho_{\mathrm{m}}^s} \times \frac{\phi_\nabla^b}{\phi_\nabla^s} \times \frac{\phi_\nabla^b + B^{\mathrm{k}} \phi_\nabla^b \phi_\nabla^s}{\phi_\nabla^s - B^{\mathrm{k}} \phi_\nabla^b \phi_\nabla^s} \tag{5.7}$$

Based on the results by Hill, K. and Zhang, J. (2008), the parameter B^{k} may likely be a function only of relative particle size in a mixture, but their theoretical expression for the relative temperatures is not easily expressed in this

form. While it is beyond the scope of this review, it provides some indication that the framework is generalizable to a range of mixtures modestly differing in both size and density.

6. Summary and outlook

In this paper, we reviewed recent developments indicating the importance of velocity fluctuations, such as that manifested in a "granular temperature" and "kinetic stress gradients" in segregating mixtures of particles of different sizes and densities. Simulations support recent model development. The model captures the segregation by considering two different types of stresses, the kinetic and contact stress, and allowing for independent partitioning of stresses between constituents that is different than their concentration in the mixture. In this way, the model illustrates that segregation can be driven solely by dynamics associated with gradients in kinetic stresses, or temperatures, such as those produced by a shear rate gradient.

Comparing predictions with computational experiments based on DEM simulations indicates that the model framework is reasonable for capturing shear-induced segregation in dense flows. Further, comparing with other model efforts and recent complimentary simulations, there is indication that the model is generalizable for a wide range of mixtures.

However, for a predictive model a deeper understanding of the rheology and other kinetics of dense sheared mixtures is needed. First, we need a predictive relationship between $\psi^{k,i}$ and flow properties such as particle concentrations, relative particle sizes and flow velocities to close the governing equations. Similarly, it is not clear that the drag force on the particles should be linear with relative velocity, or, even if it is linear, what the coefficient of drag should be. Further, it is unlikely that diffusivity D and the drag coefficient c_D are constant for any particular mixture. As mentioned by Wiederseiner, S. et al. (2011) and Natarajan, V. et al. (1995) and demonstrated by Hill et al. (2003) and others, D may depend on the local shear rate as well as other factors. A more mechanistic way to obtain relationships for D and c_D as they depend on kinematics on the flow is necessary for a predictive model for shear-induced segregation.

We conclude by briefly noting the potential importance of interstitial fluids in some segregating mixtures, not discussed in this review. Indeed, in many industrial and natural segregating systems, interstitial fluid (e.g., air in industrial powder or grains or water and mud in geophysical flows) is unavoidable and may alter or even drive (e.g., water over a riverbed) the system dynamics. For example, Burtally et al. (2002) demonstrated that the presence of an interstitial fluid can have a strong influence on a segregation pattern in a granular system, particularly for smaller particles. They showed that for mixtures composed of micron-sized glass and brass spheres, in the presence of air at atmospheric pressures, the segregation was markedly different compared to that where the air pressure was significantly reduced. On the other hand, in sediment transport in riverbeds, the particle transport itself is not only influenced by, but also, driven by fluid stresses; there is evidence that particle-particle dynamics can still play a significant role in driving segregation (e.g., Recking et al., 2009; Frey and Church, 2011). Thus, while the work reviewed in this paper takes a significant step toward a more complete representation of the importance of granular temperature in influencing segregation dynamics, for a more complete picture of segregation in a wide range of systems, the influence of fluid-particle interactions needs to be incorporated into this framework.

Acknowledgements

We gratefully acknowledge helpful discussions with Prof. Jenkins and funding that supported the original research described here from NSF Grant No. CBET-0932735 and Proctor & Gamble Co.

Nomenclature

B	$B^c - B^k$
B^c	magnitude of a non-dimensional perturbation of the contact stress partition coefficients away from the solid volume fractions for each species
B^k	magnitude of a non-dimensional perturbation of the kinetic stress partition coefficients away from the solid volume fractions for each species
C_K	a parameter in the model originally proposed by Khakhar, D. et al. (1997) related to an inverse drag coefficient (s)
c_D	a drag coefficient (1/s)
d	particle diameter (m)
D	the diffusivity (m^2/s)
B_{GT}	the magnitude of a non-dimensional perturbation of the partial pressure coefficients away from the solid volume fractions for each species in the model proposed by Gray, N. and Thornton, A. (2005). Specifically, for constituent i (consisting of larger or smaller particles) in a bimodal mixture of large and small particles of equal material density, $B_{GT} \equiv \lvert\psi^{p,i} - \phi^i\rvert/[\phi^i(1-\phi^i)]$
f^i	local solids fraction of constituent i
f	local solids fraction of the mixture
$\langle f \rangle$	system-averaged solid fraction of the mixture
F_n	interparticle normal force (N)

F_t interparticle tangential force (N)

g gravitational acceleration (m/s^2)

i indicative of the particles or constituent in the mixture; $i = b$, s, d, or ld if the constituent is comprised of bigger, smaller, denser, or less dense particles, respectively

k_n coefficient of stiffness associated with compressive deformation of a particle (N/m$^{3/2}$)

k_t coefficient of stiffness associated with shear deformation of a particle (N/m$^{3/2}$)

p lithostatic pressure, that is, the normal stress associated with the weight of a material (Pa).

$R^{c,i}$ contact stress partition coefficient for species i. $R^{c,i} = \psi^{c,i} / \phi^i_\forall$

$R^{k,i}$ kinetic stress partition coefficient for species i. $R^{k,i} = \psi^{k,i} / \phi^i_\forall$

t time (s)

T kinematic granular temperature $T = (u'u' + v'v' + w'w')/3$; (m^2/s^2)

u^i the local average velocity of species i in one of the two directions normal to the direction of segregation (m/s)

u the local average velocity of the mixture in one of the two directions normal to the direction of segregation ($u = \Sigma f^i u^i / f$) (m/s)

u' the local root mean square velocity of the mixture in one of the two directions normal to the direction of segregation (m/s)

v^i the local average velocity of species i in the direction normal to the average flow, and in the direction of segregation (m/s)

v the local average velocity of the mixture in the direction normal to the average flow and in the direction of segregation ($v = \Sigma f^i v^i / f$) (m/s)

v' the local root mean square velocity of the mixture in the direction of segregation (m/s)

w^i the local average velocity of species i in one of the two directions normal to the direction of segregation (m/s)

w the local average velocity of the mixture in one of the two directions normal to the direction of segregation ($w = \Sigma f^i w^i / f$) (m/s)

w' the local root mean square velocity of the mixture in one of the two directions normal to the direction of segregation (m/s)

x coordinate normal to the direction of segregation (m)

y coordinate normal to the average flow direction and in the direction of segregation (m)

z coordinate normal to the average direction of segregation (m)

$\dot{\gamma}$ shear rate (s^{-1})

δ_n interparticle overlap in normal direction (m)

δ_t interparticle overlap in tangential direction (m)

δ_y thickness of the flowing layer (m)

ζ the angle of inclination of a plane, above the horizontal down which a mixture flows

η_n damping coefficient associated with compressive deformation of a particle (Ns/m$^{5/4}$)

μ interparticle friction coefficent

ρ local bulk density of the mixture: $\rho = \Sigma \rho^i_m$ (kg/m^3)

ρ^i local bulk density of constituent i, related to the material density of constituent i and its local solids fraction f^i according to $\rho^i = f^i \rho^i_m$ (kg/m^3)

ρ^i_m the material density of the particles of which constituent i is comprised (kg/m^3)

$\boldsymbol{\sigma}^c$ local contact stress tensor of the mixture $\boldsymbol{\sigma}^c = \Sigma \psi^{c,i} \boldsymbol{\sigma}^{c,i}$ (N/m^2)

$\boldsymbol{\sigma}^k$ local contact stress tensor of the mixture $\boldsymbol{\sigma}^k = \Sigma \psi^{k,i} \boldsymbol{\sigma}^{k,i}$ (N/m^2)

$\boldsymbol{\sigma}^{c,i}$ local contact stress tensor of species i (N/m^2)

$\boldsymbol{\sigma}^{k,i}$ local kinetic stress tensor of species i, where the components are stresses associated with velocity fluctuation correlations, e.g., $\sigma^{k,i}_{xx} = \rho^i \overline{u'u'}^i$; $\sigma^{k,i}_{xy} = \rho^i \overline{u'v'}^i$; $\sigma^{k,i}_{yy} = \rho^i \overline{v'v'}^i$ (N/m^2)

ϕ^i_m the local mass concentration of particles of species i: $\phi^i_m = f^i \rho^i_m / \Sigma f^i \rho^i_m = \rho^i / \rho$

$\phi^i_\forall$ the local volume concentration of particles of species i: $\phi^i_\forall = f^i / \Sigma f^i$

Φ^i the segregation flux of species i: $\Phi^i = \rho^i (v^i - v)$

Φ^i_T the theoretical net segregation flux of species i derived in Section 2, according to Eqn. (2.7): $\Phi^i_T = \Phi^i_{\sigma k} + \Phi^i_g + \Phi^i_d$

$\Phi^i_{\sigma k}$ the kinetic stress segregation flux of species i; according to Eqn. 2.8a: $\Phi^i_{\sigma k} = \left(\partial \sigma^k_{yy} / \partial y\right) \times \left(\psi^{c,i} - \psi^{k,i}\right) / c_D$

Φ^i_g the gravity-driven segregation flux of species i; according to Eqn. 2.8b: $\Phi^i_g = \rho g \cos\zeta \times \left(\phi^i_m - \psi^{c,i}\right) / c_D$

Φ^i_d the diffusion flux of species i; according to Eqn. 2.8c: $\Phi^i_d = \left(\rho d / c_D\right) \times \left(\partial \rho^i / \partial y\right)$

$\psi^{c,i}$ the partial contact stress coefficient of species i

$\psi^{k,i}$ the partial kinetic stress coefficient of species i

$\psi^{p,i}$ the partial pressure coefficient of species i

References

Bridgwater J., Fundamental powder mixing mechanisms, Powder Technol., 15 (1976) 215–231.

Burtally N., King P.J., Swift M.R., Spontaneous air-driven separation in vertically vibrated fine granular mixtures, Science, 295 (2002) 1877–1879.

Chikkadi V., Alam M., Slip velocity and stresses in granular poiseuille flow via event driven simulation, Phys. Rev. E, 80 (2009) 021303.

Conway S.L., Liu X., Glasser B.J., Instability-induced clustering and segregation in high-shear couette flows of model granular materials, Chemical Engineering Science, 61 (2006) 6404.

Dietrich W.E., Kirchner J.W., Ikeda H., Iseya F., Sediment supply and the development of the coarse surface layer in gravel-bedded rivers, Nature, 340 (1989) 215.

Donald M.B., Roseman B., Mixing and de-mixing of solid par-

ticles: Part I. mechanisms in a horizontal drum mixer, Br. Chem. Eng., 7 (1962) 749–752.

Duffy S.P., Puri V.M., Primary Segregation Shear Cell for Size-Segregation Analysis of Binary Mixtures, KONA Powder and Particle Journal, 20 (2002) 196–207.

Duffy S.P., Puri V.M., Development and Validation of a Constitutive Model for Size-Segregation during Percolation, KONA Powder and Particle Journal, 21 (2003) 196–207.

Fan Y., Hill K.M., Shear-driven segregation of dense granular mixtures in a split-bottom cell, Phys. Rev. E, 81 (2010) 041303.

Fan Y., Hill K.M., Phase transitions in shear-induced segregation of granular materials, Phys. Rev. Lett., 106 (2011a) 218301.

Fan Y., Hill K.M., Theory for shear-induced segregation of dense granular mixtures, New Journal of Physics, 13 (2011b) 095009.

Fan Y., Hill K.M., Shear-induced segregation of particles by material density, Phys. Rev. E (2015) 022211.

Fan Y., Schlick C.P., Umbanhowar P.B., Ottino J.M., Lueptow R.M., Modelling size segregation of granular materials: the roles of segregation, advection and diffusion, J. Fluid Mech., 741 (2014) 252–279.

Frey P., Church M., Bedload: A granular phenomenon, Earth Surf. Process. Landforms, 36 (2011) 58–69.

Galvin J.E., Dahl S.R., Hrenya C.M., On the role of nonequipartition in the dynamics of rapidly flowing, granular mixtures, J. Fluid Mech., 528 (2005) 207.

Gilchrist J.F., Ottino, Competition between chaos and order: Mixing and segregation in a spherical tumbler, Phys. Rev. E, 68 (2003) 061303 .

Gray J.M.N.T., Ancey C., Multi-component particle-size segregation in shallow granular avalanches, J. Fluid Mech., 678 (2011) 535.

Gray J.M.N.T., Chugunov V.A., Particle-size segregation and diffusive remixing in shallow granular avalanches, J. Fluid Mech., 569 (2006) 365.

Gray J.M.N.T., Thornton A.R., A theory for particle size segregation in shallow granular free-surface flows, Proc. R. Soc. A, 461 (2005) 1447.

Hertz H.R., Ueber die Beruehrung elastischer Körper (On contact between elastic bodies), J. Reine Angew. Math., 92 (1882) 156–171.

Hill K.M., Gilchrist J.F., Ottino J.M., Khakhar D.V., McCarthy J.J., Mixing of granular materials: a test-bed dynamical system for pattern formation, International Journal of Bifurcation and Chaos, 9 (1999a) 1467–1484.

Hill K.M., Gioia G., Tota T., Structure and kinematics in dense free-surface granular flow, Phys. Rev. Lett., 91 (2003) 064302.

Hill K.M., Caprihan A., Kakalios J., Bulk segregation in rotated granular material measured by magnetic resonance imaging, Phys. Rev. Lett., 78 (1997) 50.

Hill K.M., Fan Y., Isolating segregation mechanisms in a split-bottom cell, Phys. Rev. Lett., 101 (2008) 088001.

Hill K.M., Khakhar D.V., Gilchrist J.F., McCarthy J.J., Ottino J.M., Segregation-driven organization in chaotic granular flows, Proc. Nat. Acad. Sci., 96 (1999b) 11701.

Hill K.M., Tan D.S., Segregation in dense sheared flows: gravity, temperature gradients, and stress partitioning, J. Fluid Mech., 756 (2014) 54–88.

Hogg R., Mixing and Segregation in Powders: Evaluation, Mechanisms and Processes, KONA Powder and Particle Journal, 27 (2009) 3–17.

Hsu L., Dietrich W.E., Sklar L.S., Experimental study of bedrock erosion by granular flows, J. Geophysical Research, 113 (2008) F02001.

Jenkins J.T., Mancini F., Balance laws and constitutive relations for plane flows of a dense, binary mixture of smooth, nearly elastic, circular disks, J. Appl. Mech., 54 (1987) 27.

Johnson K.L., Contact Mechanics, Cambridge Univ. Press, New York, 1985.

Khakhar D.V., McCarthy J.J., Ottino J.M., Radial segregation of granular mixtures in rotating cylinders, Phys. Fluids, 9 (1997) 3600.

Marks B., Rognon P., Einav I,. Grainsize dynamics of polydisperse granular segregation down inclined planes, J. Fluid Mech., 690 (2012) 499–511.

May L.B.H., Golick L.A., Phillips K.C., Shearer M., Daniels K.E., Shear-driven size segregation of granular materials: Modeling and experiment, Phys. Rev. E, 81 (2010a) 051301.

May L.B.H., Shearer M., Daniels K.E., Scalar Conservation Laws with Nonconstant Coefficients with Application to Particle Size Segregation in Granular Flows, J. Nonlinear Sci., 20 (2010b) 689–707.

Middleton G.V., Experimental studies related to problems of flysch sedimentation, in: Lajoie J. (Ed.), Flysch Sedimentology in North America, Business and Economics Science Ltd., Toronto, 1970, pp. 253–272.

Mindlin R.D., Deresiewicz H., Elastic spheres in contact under varying oblique forces, J. Appl. Mech., 20 (1953) 327–344.

Morland L.W., Flow of viscous fluids through a porous deformable matrix, Surv. Geophys., 13 (1992) 209.

Mosby J., de Silva S.R., Enstad G.G., Segregation of Particulate Materials—Mechanisms and Testers, KONA Powder and Particle Journal, 14 (1996) 31–43.

Natarajan V.V.R., Hunt M.L., Taylor E.D., Local measurements of velocity fluctuations and diffusion coefficients for a granular material flow, J. Fluid Mech., 304 (1995) 1.

Paola C., Seal R., Grain size patchiness as a cause of selective deposition and downstream fining, Water Resources Research, 31 (1995) 1395.

Recking A., Frey P., Paquier A., Belleudy P., An experimental investigation of mechanisms responsible for bedload sheet production and migration, J. Geophys. Res. Earth Surface, 114 (2009) F03010

Sarkar S., Khakhar D.V., Experimental evidence for a description of granular segregation in terms of the effective temperature. Europhys. Lett., 83 (2008) 54004.

Savage S.B., Lun C.K.K., Particle size segregation in inclined chute flow of dry cohesionless granular solids, J. Fluid Mech., 189 (1988) 311.

Schlichting H., Boundary-Layer Theory, McGraw-Hill, New York, 1979.

Schulze D., Powders and Bulk Solids: Behavior, Characterization, Storage, and Flow, Springer, Berlin, Germany, 2008.

Shinbrot T., Muzzio F., Nonequilibrium patterns in granular mixing and segregation, Physics Today, 53 (2000) 25.

Stock J.D., Dietrich W.E., Erosion of steepland valleys by debris flows, Geol. Soc. Am. Bull., 118 (2006) 1125.

Taberlet N., Losert W., Richard P., Understanding the dynamics of segregation bands of simulated granular material in a rotating drum, Europhys. Lett., 68 (2004) 552.

Thornton A., Weinhart T., Luding S., Bokhove O., Modeling of particle size segregation: calibration using the discrete particle method, International Journal of Modern Physics C, 23 (2012), 8.

Tripathi A., Khakhar D.V., Numerical simulation of the sedimentation of a sphere in a sheared granular fluid: a granular Stokes experiment, Phys. Rev. Lett., 107 (2011) 108001.

Tripathi A., Khakhar D.V., Density difference-driven segregation in a dense granular flow, J. Fluid Mech., 717 (2013) 643–669.

Tsuji Y., Tanaka T., Ishida T., Lagrangian numerical simulation of plug flow of cohesionless particles in a horizontal pipe, Powder Technol., 71 (1992) 239.

Tunuguntla D.R., Bokhove O., Thornton A.R., A mixture theory for size and density segregation in shallow granular free-surface flows, Journal of Fluid Mechanics, 749 (2014) 99-112. doi:10.1017/jfm.2014.223

Weinhart T., Luding S., Thornton A.R., From discrete particles to continuum fields in mixtures, Powders and Grains 2011, 1542 (2013) 1202–1205. American Institute of Physics.

Wiederseiner S.N., Andreini, Epely-Chauvin G., Moser G., Monnereau M., Gray J.M.N.T., Ancey C., Experimental investigation into segregating granular flows down chutes, Phys. Fluids, 23 (2011) 013301.

Williams J.C., The segregation of particulate materials, Powder Technol., 15 (1976) 245–256.

Xu H., Louge M., Reeves A., Solutions of the kinetic theory for bounded collisional granular flows, Continuum Mech. Thermodyn., 15 (2003) 321.

Yohannes B., Hsu L., Dietrich W.E., Hill K.M., Boundary stresses due to impacts from dry granular flows, J. Geophys. Res., 117 (2010) F02027.

Author's short biography

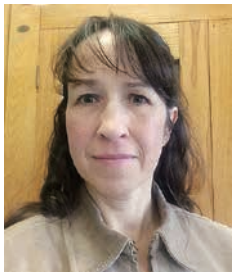

Kimberly Hill

Kimberly Hill is an Associate Professor in the Department of Civil, Environmental, and Geo- Engineering at the University of Minnesota, Twin Cities. Prior to this she held faculty positions in the Department of Theoretical and Applied Mechanics, University of Illinois, Champaign-Urbana and in the Department of Physics, University of Wisconsin, Whitewater and Postdoctoral Research positions in the Department of Chemical Engineering at Northwestern University and in Sandia National Laboratory, Albuquerque. Her research interests and experience are related to fundamental and applied particulate flows. They include segregation and rheology of granular mixtures including applications in geophysical and industrial flows.

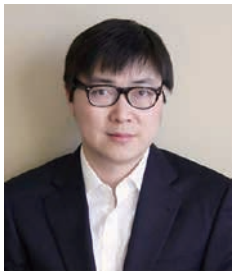

Yi Fan

Yi Fan is currently a senior R&D engineer at the Solids Processing group in the Corporate R&D of The Dow Chemical Company. Prior to this, he was a Postdoctoral Fellow in the Department of Mechanical Engineering at Northwestern University. He received his Bachelor (2003) and Mater (2006) degrees in Thermal and Power Engineering from Tsinghua University of China and received his PhD (2011) in Civil engineering from the University of Minnesota – Twin Cities. His research interests and experience focus on understanding the fundamental physics of particulate flows including granular flows and granular-fluid flows, as well as their applications in chemical industry.

KONA Powder and Particle Journal No. 33 (2016) 169–178/Doi:10.14356/kona.2016023 Review Paper

How Should the Discrete Element Method Be Applied in Industrial Systems?: A Review †

Mikio Sakai

[1] *Resilience Engineering Research Center, School of Engineering, The University of Tokyo, Japan*

Abstract

In this paper, we describe an industrial application of the discrete element method (DEM). The DEM has been applied to various powder systems thus far and therefore appears to be an established approach. However, it cannot be applied to many industrial systems because of several critical problems such as modeling of large-scale simulations, complexly shaped wall boundaries and free surface fluid flow. To solve these problems, novel models were developed by our group. A coarse-grain DEM model was developed for large-scale simulations, a signed distance function-based wall boundary model was developed for complexly shaped walls and a DEM-moving particle semi-implicit method was developed for solid-liquid flow involving a free surface. The adequacy of these models was demonstrated through verification and validation tests. Our approach shows promise in industrial applications.

Keywords: large-scale discrete element modeling, signed distance function-based wall boundary, multi-phase flow modeling, discrete element method, Lagrangian computational fluid dynamics, multi-physics modeling

1. Introduction

Granular flows usually differ from fluid flows. They are regarded as complex because constitutive equations are influenced by many parameters such as coefficient of restitution, coefficient of friction, particle size distribution, humidity, etc. Modeling of granular flow is extremely difficult. It may not be possible to model even simple phenomena in industries. Many requirements for numerical technologies should be applied in industrial design. The question arises as to how granular flow should be simulated in industrial systems. Granular flow could be simulated when individual particle behavior could be modeled. The discrete element method (DEM) (Cundall and Strack, 1979) was developed based on this idea and it became a successful model in the simulation of granular flow. The DEM is a Lagrangian approach and solid particle behavior is computed based on the Newton's second law of motion. The contact force acting on a solid particle is calculated using the Voigt model, namely, a spring-dashpot system. Recent improvements in computer hardware have allowed for an increase in number of solid particles and for complex phenomena such as solid-fluid coupling problems to be simulated. When solid-fluid coupling problems are computed, the DEM is coupled with computational fluid dynamics (CFD), where the local volume average technique (Anderson and Jackson, 1967) is used in the governing equations and semi-empirical momentum exchange coefficients (Wen and Yu, 1966; Ergun, 1952) are often used. This approach is referred to as the DEM-CFD method (Tsuji et al., 1993). Tsuji's contribution was significant to simulate solid-fluid coupling problems (Tsuji, 2007) and the DEM-CFD method became a standard global approach. Tsuji also investigated the application of a linear spring model, devised an efficient calculation setup (Tsuji et al., 1993) and proposed how physical properties should be set in a non-linear spring system (Tsuji et al., 1992). His research was exceptional and his proposal has become the standard approach.

At present, the DEM appears to be an established approach. It has been applied in various engineering fields and many DEM applications exist. With respect to single flow such as granular flow, the DEM has been applied to solid mixing (Radeke et al., 2010; Chandratilleke et al., 2012; Halidan et al., 2014; Eitzlmayr et al., 2014; Huang and Kuo, 2014), die filling (Guo et al., 2009; Wu, 2008; Mateo-Ortiz et al., 2014; Yue et al., 2014), powder transportation (Tsuji et al., 1992; Mio et al., 2009; Kuang et al., 2013), and granulation (Washino et al., 2013), among others. Since the DEM-CFD method was developed, the DEM

† Received 27 July 2015; Accepted 15 September 2015
J-STAGE online 28 February 2016
[1] 7-3-1 Hongo, Bunkyo-ku, Tokyo 113-8656, Japan
E-mail: mikio_sakai@n.t.u-tokyo.ac.jp
TEL: +81-3-5841-6977 FAX: +81-3-5841-6977

has been applied to new fields along with fluidized beds and cyclones. The DEM-CFD method was applied to simulations of coarse particles that belong to the Geldart B and D group (Kawaguchi et al., 1998; Wang et al., 2013; Hernández-Jiménez et al., 2014; Olaofe et al., 2014; Patil et al., 2014) and fine particles such as Geldart A (Pandit et al., 2006; Kobayashi et al., 2013; Hong et al., 2015). The DEM-CFD method has been validated in fluidized (Alobaid et al., 2013; Wu et al., 2013) or spouted (Jajcevic et al., 2013; Salikov et al., 2014) beds. The DEM-CFD method can be used in simulations of geometrically complex fluidized beds such as circulating fluidized beds (Xu et al., 2012; Lu et al., 2014). Hence, DEM technologies are regarded as a reliable approach.

Unfortunately, some critical problems exist for industrial application of the DEM. Although it has been applied to various engineering fields, the number of calculated particles is extremely small compared with the actual number in industrial processes. A maximum of one million calculated particles can be used on a single personal computer, whereas over one billion particles are required. Hence, the number of calculated particles becomes extremely small in industrial applications. In addition, modeling of solid-liquid flow involving a free surface is also a significant problems. Limited simulations of a wet ball mill and slurry transportation have been performed thus far because accurate simulation of free surface fluid flow is difficult, and this problem is common in a single flow. Recently, mesh-free Lagrangian CFD (Koshizuka et al., 1996; Monaghan, 1988) such as smoothed-particle hydrodynamics or the moving particle semi-implicit, volume-of-fluid (Yokoi, 2007; Xiao et al., 2011; Ohta et al., 2011) and front tracking methods (Vu et al., 2015) have been used extensively in simulations of free surface fluid flow. Indeed, solid-liquid flow could not be simulated in industrial systems. Perhaps coupling the DEM with these models for free surface fluid flow is a promising approach to simulate solid-liquid flow involving a free surface. Currently, models for solid-liquid flow that include a free surface are required. Finally, modeling of an arbitrary shaped wall is also important in industrial systems. In previous studies, a combination of simple surface equations (Mio et al., 2002; Liu et al., 2011; Sakai et al., 2005), the location of DEM particles and meshes (Shigeto and Sakai, 2011; Mateo-Ortiz et al., 2014) was used to create a wall boundary in the DEM. The combination of simple surface equations was difficult to create an arbitrarily shaped domain. In addition, the wall boundary model composed of the DEM particles exhibited difficulties in terms of accuracy for application to industrial systems. Although a mesh-based wall was often used to model a geometrically complex wall, collision detection may be difficult in programming the algorithm.

Hence, the DEM exhibits several problems when it was applied to industrial systems. To solve these problems, the authors have developed original models, namely, the coarse-grain DEM (Sakai and Koshizuka, 2009; Sakai et al., 2010; Sakai et al., 2012b; Sakai et al., 2014) for large-scale powder systems, the DEM-MPS method (Sakai et al., 2012a; Yamada and Sakai, 2013; Sun et al., 2014) for solid-liquid flow involving a free surface, and the signed distance function (SDF)-based wall boundary model (Shigeto and Sakai, 2013; Sakai et al., 2015) for granular flow in a geometrically complex device. These models are described in this paper.

2. Large-scale discrete element simulation

2.1 Existing problems

Although the DEM seems to be well established, it is problematic in that the number of calculated particles is restricted when the simulation needs to be completed in a reasonable time on a single personal computer. This is especially critical because a number of DEM simulations are performed without using a supercomputer and the calculation time increases significantly on a single personal computer when an excessive number of particles are used. This problem cannot be solved even with the latest multi-core processors (Liu et al., 2014; Yue et al., 2014). Many industries require application of the DEM to large-scale powder systems on a single personal computer.

2.2 Coarse-grain DEM model

In order to solve this problem, the authors have developed a physics model, which is termed the coarse-grain DEM model (Sakai and Koshizuka, 2009; Sakai et al., 2010; Sakai et al., 2012b; Sakai et al., 2014). The coarse-grain model was developed to model contact, drag, gravitational and cohesive forces as the scaling law model. As illustrated in **Fig. 1**, l^3 original particles exist in the coarse-grain particle whose size is l times larger than the original particle. Here, the coarse-grain ratio l was 2.0. In the coarse-grain model, the translational motion of the

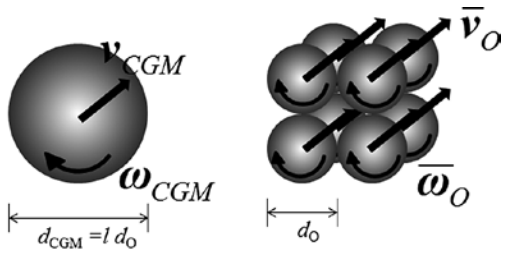

Fig. 1 Image of coarse-grain model (coarse-grain ratio $l = 2.0$). Reprinted with permission from Ref. (Sakai et al., Chem. Eng. J., 2014). Copyright: (2014) Elsevier B.V.

coarse-grain particle is assumed to be equivalent to be the average of that of the original particles. Hence, the velocity and displacement of the coarse-grain particle are assumed to be averages of the original particles, namely, $\bar{\boldsymbol{v}}_{\mathrm{O}} = \boldsymbol{v}_{\mathrm{CGM}}$ and $\bar{\boldsymbol{\delta}}_{\mathrm{O}} = \boldsymbol{\delta}_{\mathrm{CGM}}$, respectively. Besides, the original particles in the coarse-grain particle are assumed to rotate around each mass center with equal angular velocity, where the angular velocity is averaged as illustrated in **Fig. 1(b)**. The contact force acting on the coarse-grain particle was estimated assuming that the total energy of the coarse-grain particle is consistent with that of the original particles. When a binary collision of the coarse-grain particles occurs, binary collisions between each of the original particles (i.e., l^3 binary collisions due to the original particles) are assumed to occur simultaneously. The contact force acting on the coarse-grain particle is simulated using springs, dash-pots and a friction slider, as for the existing DEM. From the assumption of the translational motion of the coarse-grain model, the drag force and gravitational force acting on a coarse-grain particle become l^3 times larger than that of the original particle. Consequently, the following relationship is obtained between the coarse-grain and original particles:

$$\begin{aligned} m_{\mathrm{CGM}}\boldsymbol{v}_{\mathrm{CGM}} &= \boldsymbol{F}_{\mathrm{f_{CGM}}} - V_{\mathrm{CGM}}\nabla p + \sum \boldsymbol{F}_{\mathrm{C_{CGM}}} + \boldsymbol{F}_{\mathrm{g_{CGM}}} \\ &= l^3\bar{\boldsymbol{F}}_{\mathrm{f_O}} - l^3 V_{\mathrm{O}}\nabla p + l^3\sum \bar{\boldsymbol{F}}_{\mathrm{C_O}} + l^3\bar{\boldsymbol{F}}_{\mathrm{g_O}} \end{aligned} \tag{1}$$

where m, $\boldsymbol{v}$, l, $\boldsymbol{F}_{\mathrm{f}}$, V, p, $\boldsymbol{F}_{\mathrm{C}}$ and $\boldsymbol{F}_{\mathrm{g}}$ are the solid mass, solid velocity, coarse-grain ratio, drag force, particle volume, pressure, contact force and gravitational force, respectively. Subscripts CGM and O refer to the coarse-grain model and original particle, respectively. An important point of the coarse-grain model is that original physical properties such as density, coefficient of friction and coefficient of restitution can be applied directly.

Now, modeling of the contact force is described in the coarse-grain model. The contact force can be divided into a normal and tangential component. Both components are functions of relative particle position and velocity. The normal component of the contact force is given by:

$$\begin{aligned} \boldsymbol{F}_{\mathrm{C_{nCGM}}} &= l^3\left(-k\boldsymbol{\delta}_{\mathrm{nCGM}} - \eta\boldsymbol{v}_{\mathrm{nCGM}}\right) \\ &= l^3\left(-k\bar{\boldsymbol{\delta}}_{\mathrm{n_O}} - \eta\bar{\boldsymbol{v}}_{\mathrm{n_O}}\right) \end{aligned} \tag{2}$$

where k, $\boldsymbol{\delta}$ and η are the stiffness, the overlap and the damping coefficient, respectively. As described above, the translational motion of the coarse-grain particle is assumed to agree with that of the original particles. Hence, the CGM subscript can be replaced by O in Eq. (2). In the coarse-grain model, the normal component of the displacement is modeled by overlap as is the case with the existing DEM. Hence, the potential energy, i.e., elastic energy, is agreed between the coarse-grain particle and group of original particles by the modeling.

In the same manner as for the normal component, the tangential component of the contact force is given by:

$$\begin{aligned} \boldsymbol{F}_{\mathrm{C_{tCGM}}} &= \begin{cases} l^3\left(-k\boldsymbol{\delta}_{\mathrm{tCGM}} - \eta\boldsymbol{v}_{\mathrm{tCGM}}\right) \\ -l^3\mu\left|\boldsymbol{F}_{\mathrm{C_{nCGM}}}\right|\left|\boldsymbol{v}_{\mathrm{tCGM}}\right|/\left|\boldsymbol{v}_{\mathrm{tCGM}}\right| \end{cases} \\ &= \begin{cases} l^3\left(-k\bar{\boldsymbol{\delta}}_{\mathrm{t_O}} - \eta\bar{\boldsymbol{v}}_{\mathrm{t_O}}\right) \\ -l^3\mu\left|\bar{\boldsymbol{F}}_{\mathrm{C_{nO}}}\right|\left|\bar{\boldsymbol{v}}_{\mathrm{t_O}}\right|/\left|\bar{\boldsymbol{v}}_{\mathrm{t_O}}\right| \end{cases} \end{aligned} \tag{3}$$

where μ is the coefficient of friction. When the solid particle does not slip on the surface of solid particle or wall, upper equation is applied. The translational motion of the coarse-grain particle is assumed to agree with that of the original particles.

From the assumption of the translational motion of the coarse-grain model, namely, agreement of kinetic energy between the coarse-grain and original particles, the drag force acting on a coarse-grain particle becomes l^3 times larger than that of the original particle. The drag force $\boldsymbol{F}_{\mathrm{f}}$ acting on the coarse-grain particle is given by:

$$\begin{aligned} \boldsymbol{F}_{\mathrm{f_{CGM}}} &= \frac{\beta}{1-\varepsilon}(\boldsymbol{u} - \boldsymbol{v}_{\mathrm{CGM}})V_{\mathrm{CGM}} \\ &= l^3\frac{\beta}{1-\varepsilon}(\boldsymbol{u} - \bar{\boldsymbol{v}}_{\mathrm{O}})V_{\mathrm{O}} \end{aligned} \tag{4}$$

where ε, $\boldsymbol{u}$ and β are the void fraction, the fluid velocity and an interphase momentum transfer coefficient, respectively.

The following relationship is obtained for the rotational motion, namely, angular velocity and torque, in the original and coarse-grain particles:

$$\begin{aligned} \dot{\boldsymbol{\omega}}_{\mathrm{CGM}} &= \frac{\boldsymbol{T}_{\mathrm{CGM}}}{I_{\mathrm{CGM}}} = \frac{r_{\mathrm{CGM}} \times \boldsymbol{F}_{\mathrm{C_{CGM_t}}}}{I_{\mathrm{CGM}}} \\ &= \frac{l r_{\mathrm{O}} \times l^3\bar{\boldsymbol{F}}_{\mathrm{C_{O_t}}}}{l^5 I_{\mathrm{O}}} = \frac{l^4\bar{\boldsymbol{T}}_{\mathrm{O}}}{l^5 I_{\mathrm{O}}} = \frac{1}{l}\bar{\dot{\boldsymbol{\omega}}}_{\mathrm{O}} \end{aligned} \tag{5}$$

where $\boldsymbol{\omega}$, I and $\boldsymbol{T}$ are the angular velocity, the inertial momentum of the particle and the torque, respectively. Eq. (5) also ensures that the rotational energy between the coarse-grain particle and group of original particles agrees.

The governing equations of the gas phase, namely, the continuity and the Navier-Stokes equations are the same as those of the original DEM-CFD method even for the coarse-grain model.

The solid particle motion, namely, the velocity, position, angular velocity and angle, could be updated using time integration schemes (Fraige and Langston, 2004; Danby et al., 2013; Kruggel-Emden et al., 2008). A semi-implicit finite volume method that uses a staggered grid was used to discretize the incompressible fluid flow. A hybrid scheme (Patankar, 1980), which is a combina-

tion of a first-order upwind scheme and a second-order central scheme was used in the convection term. The pressure-velocity coupling was based on the fractional step method for incompressible fluid flows.

2.3 Numerical example of coarse-grain model

Adequacy of the coarse-grain model with high coarse-grain ratio is shown through the validation tests (Sakai et al., 2014). The validation results were described in this paper.

The calculation domain was 50 mm wide, 20 mm long and 200 mm high. The domain was discretized using 2.5 mm structural grids in the x, y and z directions. The grid size was chosen to be large relative to the solid particle diameter, where the fluid flow characteristics could be simulated accurately. The number of grids was 20, 80 and 8, in the x, y and z directions, respectively. The number of calculated particles was 230,400, which corresponded to the actual mass of powder used in the experiment. Initially, the spherical particles were packed randomly. Air was injected from the base, where the superficial velocity was 0.070 m/s. The density, stiffness, coefficient of restitution and coefficient of friction were 2,500 kg/m^3, 10 N/m, 0.9 and 0.3, respectively. The gas was air, where the density and the viscosity were 1.0 kg/m^3 and 1.8×10^{-5} Pa s, respectively.

Fig. 2 illustrates typical snapshots obtained from simulation and experimental results of the fluidized state at quasi-steady state. In the simulation and experiment, splashes and bubbles were observed in the quasi-steady state. From the appearance, macroscopic flow properties agreed qualitatively between the simulation and experiment.

The pressure drop and bed height were measured in the experiment and simulation for quantitative comparison. **Fig. 3** compares the pressure drop between the simulation and experiment, which agreed quantitatively. The bed height was measured by visual observation to compare the calculated and experimental results fairly. The simulated bed height had an error of 7.8 % against the experimental height, which is an allowable margin of error from an engineering perspective.

The coarse-grain model can therefore simulate the bulk bed state by setting a higher coarse-grain ratio. This implies that the particle-particle and particle-fluid interactions were modeled precisely in the coarse-grain model. We can easily predict that the coarse-grain model may simulate other phenomena related to bulk states, such as bubbling, channeling and slugging. The coarse-grain model has a sufficient potential to be used with much high coarse grain ratio. Hereafter, the possibility will be investigated by various validation tests.

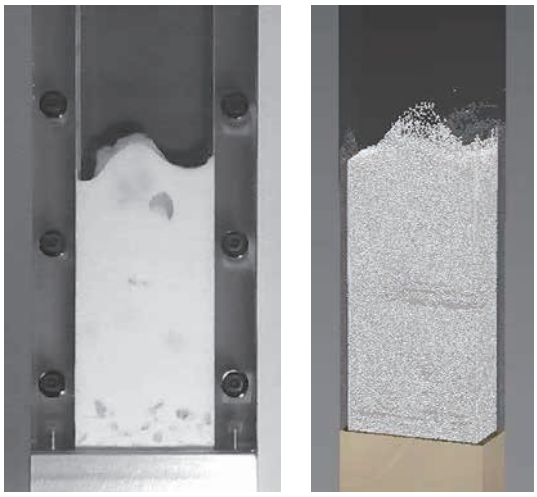

(a) Experiment (b) Simulation

Fig. 2 Particle spatial distribution at quasi-steady state in the validation test.
Reprinted with permission from Ref. (Sakai et al., Chem. Eng. J., 2014). Copyright: (2014) Elsevier B.V.

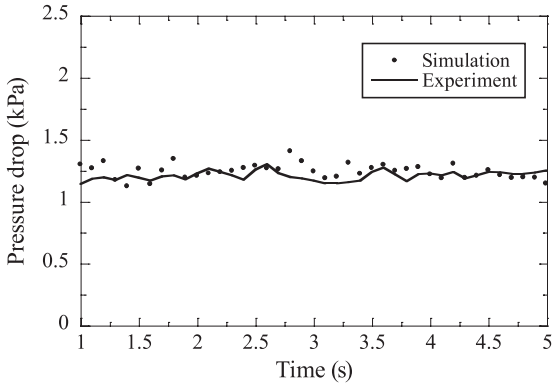

Fig. 3 Comparison of pressure drop between calculated and experimental results in a fluidized bed.
Reprinted with permission from Ref. (Sakai et al., Chem. Eng. J., 2014). Copyright: (2014) Elsevier B.V.

3. Modeling of solid-liquid flow involving a free surface

3.1 Existing problems

Solid-liquid flows involving a free surface occur in chemical engineering applications such as wet ball milling and slurry transport. Whereas numerical simulation of the process should be used for the design and optimization of operational conditions, such simulations have not yet been implemented extensively. This situation has arisen because of difficulties in modeling and computationally expensive calculations.

Currently, there is no broadly used numerical approach for modeling such solid-liquid flows, although some simulations have been reported previously. These approaches exhibit some problems, namely, some difficulties in mod-

eling large deformations of the fluid free surface, difficulties in modeling hydrodynamic forces and difficulties in modeling contact force. Therefore, the existing methodology cannot be used for many solid-liquid flow systems in chemical engineering applications. The development of a new method is desired to solve the above difficulties or problems. Many industrial solid-liquid flows involve large deformations and/or a high volume fraction of solid phase, where the contact force acting on a solid particle becomes important. Lagrangian method such as the SPH or MPS method makes it possible to simulate free surface fluid flow precisely. These methods have been applied to various engineering fields thus far. Lagrangian-Lagrangian approaches are applicable to these important industrial flows. Hence, the MPS method and the DEM are combined to simulate solid-liquid flow involving free surfaces (Sakai et al., 2012a; Yamada and Sakai, 2013; Sun et al., 2014). The DEM-MPS method whose algorithm was fully explicit is described in this paper.

3.2 DEM-MPS method

For a locally averaged description of continuous fluid motion, the mass and momentum conservation equations can be written as:

$$\frac{\mathrm{D}(\varepsilon\rho)}{\mathrm{D}t} + \varepsilon\rho\nabla\cdot\boldsymbol{u} = 0 \tag{6}$$

$$\frac{\mathrm{D}\boldsymbol{u}}{\mathrm{D}t} = -\frac{1}{\rho}\nabla p + \nu\nabla^2\boldsymbol{u} - \frac{1}{\varepsilon\rho}\boldsymbol{f} + \boldsymbol{g} \tag{7}$$

where ρ, p, ν, $\boldsymbol{f}$ and $\boldsymbol{g}$ are fluid density, pressure, kinematic viscosity, drag force and gravitational acceleration, respectively.

The governing equation for the solid particles is given by Newton's second law of motion:

$$m\frac{\mathrm{d}\boldsymbol{v}}{\mathrm{d}t} = \boldsymbol{F}_\mathrm{C} + \boldsymbol{F}_\mathrm{f} - V\nabla p + m\boldsymbol{g} \tag{8}$$

In a Lagrangian particle method such as the MPS method, the continuum phase is modeled as an assembly of fluid particles. In the MPS method, fluid particles are not connected and therefore so-called weight functions are used to define discretization schemes on the particle positions.

Weakly compressible and incompressible methods were developed in the MPS method. In the weakly compressible approach, fluid pressure is calculated by the modified Tait equation of state, which agrees well with the real behavior of water under typical circumstances.

$$p = \begin{cases} \dfrac{\rho_0 c^2}{\gamma}\left(\left(\dfrac{N}{n_0}\right)^\gamma - 1\right) & n \geq \varepsilon n_0 \\ 0 & n \geq \varepsilon n_0 \end{cases} \tag{9}$$

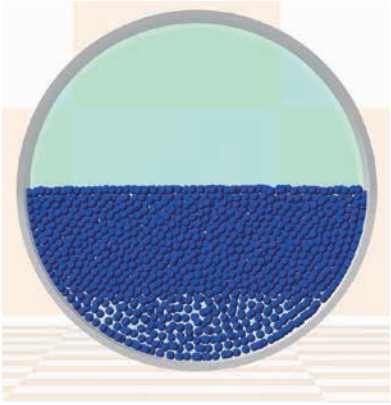

Fig. 4 Initial configuration of fluid particles. Reprinted with permission from Ref. (Sun et al., Chem. Eng. J., 2014). Copyright: (2014) Elsevier B.V.

where c is the speed of sound in a fluid at reference density and γ is a constant often set to 7.0 for water. For numerical purposes within a weakly compressible method, the speed of sound c can be tuned artificially to relax the restriction on time increments because of stability conditions. The c should be 10 times higher than the maximum main stream velocity to constrain density fluctuations up to 1 % and guarantee a nearly divergence-free velocity field.

The pressure gradient and viscous terms are discretized by the original MPS method.

3.3 Numerical example of DEM-MPS method

In order to illustrate the adequacy of the DEM-MPS method, a validation test was performed in our previous study (Sun et al., 2014). A cylindrical tank was used with inner diameter of 120 mm and depth of 100 mm. Water and glass beads were placed in the tank. The average diameter of the glass beads was ~2.7 mm, and their density was 2500 kg/m^3. In the laboratory experiment, the tank was revolved at 63 rpm and 1.25 kg of glass beads were inserted. Water was injected afterwards and adjusted to fill approximately half of the tank.

2D and 3D simulations were performed in this study. The diameter of the DEM particles was 2.7 mm and their density was 2,500 kg/m^3. The stiffness was set to be 10,000 N/m, coefficient of restitution was 0.9 and coefficient of friction was 0.3. For the liquid phase, the physical properties are equal to those of water, namely, the density was 1000 kg/m^3 and the kinematic viscosity was 0.89 mm^2/s. The fluid particle size, which was defined as the initial interval between two fluid particles, was chosen to be 2.7 mm.

Fig. 5(a) and **(b)** shows a snapshot of the 2D and 3D calculation results at quasi steady state. In this figure, liquid phase was visualized by using meshes. These observations have been confirmed by our experiment. The bed

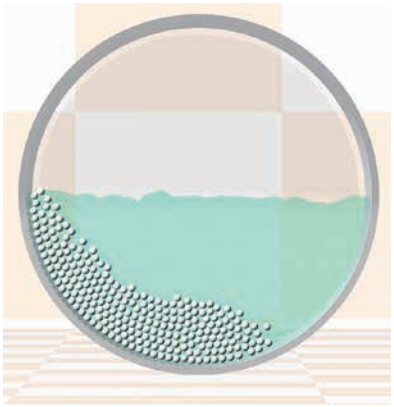

(a) 2D simulation.

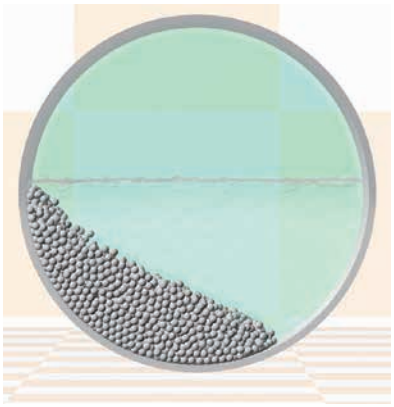

(b) 3D simulation.

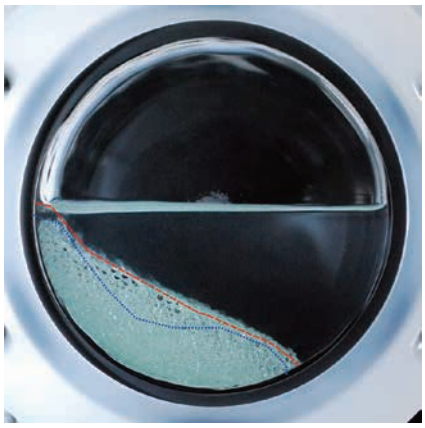

(c) Experiment.

Fig. 5 Quasi-steady solution of circulating flow by the DEM-MPS method.
Reprinted with permission from Ref. (Sun et al., Chem. Eng. J., 2014). Copyright: (2014) Elsevier B.V.

width and height were measured in the validation tests as shown in **Fig. 5(c)**, where 2D and simulation results are given by blue and red line respectively. The bed width and height obtained from the 2D and 3D simulation results agreed quantitatively with the experimental data, though bed shape obtained from the 3D simulation was more precise than the 2D simulation. Hence, adequacy of the DEM-MPS method was demonstrated through the validation tests.

4. Arbitrary shape boundary wall model

4.1 Existing problems

In the previous DEM simulations, the calculation domain, *i.e.*, the wall boundary, was modeled using surface equations (Sakai et al., 2005) or meshes (Shigeto and Sakai, 2011; Mateo-Ortiz et al., 2014). The use of surface equations is an easy approach to create simple regimes. Modeling of geometrically complex walls is often required in industrial systems. These domain shapes are substantially more difficult to express with combinations of the equations. Hence, arbitrary domain shapes were modeled using meshes. The meshes are more adaptable for arbitrary shapes than the equations, but there is a difficulty in introducing the algorithm of collision detection between particles and walls. To solve these problems, a simple boundary model was proposed, where the wall boundary is expressed by a scalar field, which is referred to as the SDF. The SDF model was based on the level set method (Osher and Fedkiw, 2002), which was originally proposed in the CFD. The uniqueness of the model is that collisions can be detected without complicated procedures. We developed the SDF model, which includes conservation of energy in non-dissipative systems. The DEM/SDF can also be applied to cohesive particle and rotating vessel systems (Shigeto and Sakai, 2013).

4.2 DEM/SDF model

As mentioned above, we developed the SDF model to retain energy conservation in a non-dissipative system. This idea is important to simulate cohesive and contact forces precisely in the DEM simulations. The contact force model based on the DEM/SDF is addressed now. The contact force is modeled based on elastic potential energy when the solid particles interact with walls. The energy is related to displacement by:

$$P_{\text{elastic}}^{\text{SDF}} = \frac{1}{2}k\left|\boldsymbol{\delta}_{\text{n}}^{\text{SDF}}\right|^2 = \frac{1}{2}k(r-\phi)^2 \tag{10}$$

where ϕ and r are the SDF and minimal distance between the wall and particle, respectively. The gradient of the energy P gives the elastic force between the particle and the SDF based wall boundary:

$$\begin{aligned}\boldsymbol{F}_{\text{elastic}}^{\text{SDF}} &= \nabla P_{\text{elastic}}^{\text{SDF}} \\ &= -k(r-\phi)\cdot\nabla\phi \\ &= -k\boldsymbol{\delta}^{\text{SDF}}\cdot|\nabla\phi|\end{aligned} \tag{11}$$

Hence, the normal component of the contact force is given by:

$$\boldsymbol{F}_{\text{C}_\text{n}}^{\text{SDF}} = -k\boldsymbol{\delta}_{\text{n}}^{\text{SDF}}|\nabla\phi| - \eta\boldsymbol{v}_{\text{n}} \tag{12}$$

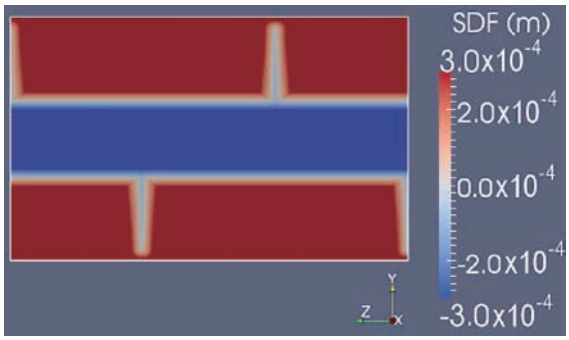

Fig. 6 Cross-sectional view of SDF in a screw conveyer.
Reprinted with permission from Ref. (Shigeto and Sakai, Chem. Eng. J., 2013). Copyright: (2013) Elsevier B.V.

which conserves the energy in non-dissipative systems because of the correction term $|\nabla\phi|$.

As a matter of course, our SDF model is applicable to cohesive particle systems that are affected by van der Waals force. In the same manner as for the elastic force, the van der Waals force is modeled based on the potential energy, namely:

$$P_{\mathrm{vdw}}^{\mathrm{SDF}} = -\frac{H_{\mathrm{A}} \cdot r}{6h^{\mathrm{SDF}}} \tag{13}$$

where $\boldsymbol{h}^{\mathrm{SDF}}$ is the intersurface distance.

$$h^{\mathrm{SDF}} = \phi - r \tag{14}$$

The gradient of Eq. (13) yields the van der Waals force between the particle and the SDF based wall boundary:

$$\boldsymbol{F}_{\mathrm{vdw}}^{\mathrm{SDF}} = \nabla P_{\mathrm{vdw}}^{\mathrm{SDF}} = -\frac{H_{\mathrm{A}} \cdot r}{6\left(h^{\mathrm{SDF}}\right)^2} \cdot \nabla\phi. \tag{15}$$

The conservation of energy is guaranteed theoretically in our SDF model. Hence, this scheme may stabilize the calculation. In addition, the algorithm is simpler the existing wall boundary composed of meshes.

We expected that the SDF will become a standard wall boundary model in the DEM simulations. Hereafter the DEM/SDF is going to be applied to investigate lots of phenomena in a geometrically complex boundary.

4.3 Numerical examples of DEM/SDF model

4.3.1 Screw conveying

In order to illustrate the adequacy of the DEM/SDF method, a verification test was performed in a screw conveyor (Shigeto and Sakai, 2013). In this test, simulations were carried out with the mesh- and new SDF-based models. Initially, 62,500 particles was located randomly at the bottom of the calculation domain. The particles have a uniform diameter of 200 μm and density of 2,500 kg/m^3. **Fig. 6** designates the scalar value distribution of the SDF model of the inner screw blade. The sign becomes positive inside the calculation domain and vice versa. The screw was rotated at 30 rpm. In the verification tests, cohesive particles were used, where the Hamaker constant was 5.0×10^{-20} J.

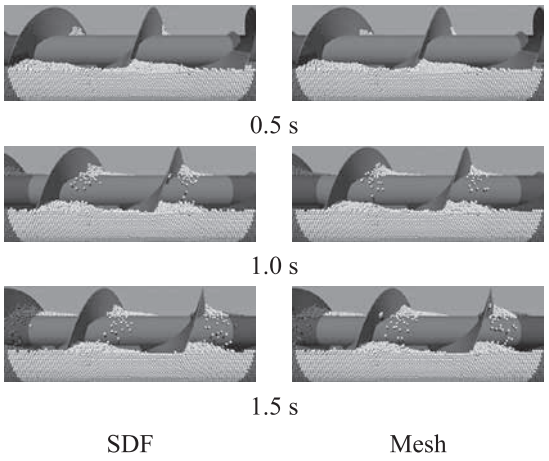

Fig. 7 Typical snapshots of granular flow in a screw conveying system.
Reprinted with permission from Ref. (Shigeto and Sakai, Chem. Eng. J., 2013). Copyright: (2013) Elsevier B.V.

Fig. 7 shows typical snapshots at 0.5, 1.0 and 1.5 s in the verification tests. Similar particle distributions, agreement of velocity distribution of the solid particles and agreement of transported mass were obtained in the SDF and mesh systems. Besides, the load torque on the screw agreed well between the SDF and mesh models. Consequently, these results illustrate that the accuracy of the SDF model is equivalent to the existing mesh model in the reproduction of granular flows in the screw conveying system.

4.3.2 Twin-screw kneader

Application of the DEM/SDF method to a twin-screw kneader is described according to past study (Sakai et al., 2015). In order to show the adequacy of the DEM/SDF method, a validation test was performed in a twin-screw kneader where the focus was on dry powder mixing. Simulation and experimental results were compared for the apparent solid particle location and particle bed height. For the validation system, the height, width and length were 106 mm, 186 mm and 46 mm, respectively. Four paddles were used in the depth direction. The paddles were rotated clockwise, and the paddle rotational velocity was 60 rpm in the validation tests. Glass beads (~1.0 mm) were used in the tests. The total amount of powder was 0.524 kg. Calculation conditions were set to compare the simulation and experimental results fairly. Mono-sized solid particles with 1.0 mm diameter were used in the calculations. A simple linear contact model was used in this study. The spring constant, coefficient of friction and coefficient of restitution were set at 1,000 N/m, 0.3 and 0.9,

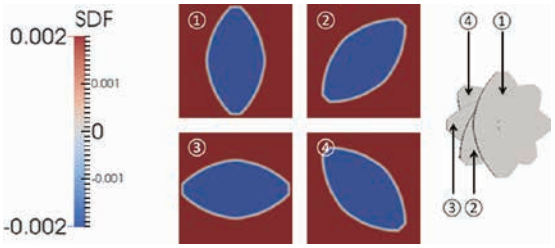

Fig. 8 Cross-sectional view of SDF in a twin-screw kneader in a twin-screw kneader.
Reprinted with permission from Ref. (Sakai et al., Chem. Eng. J., 2015). Copyright: (2015) Elsevier B.V.

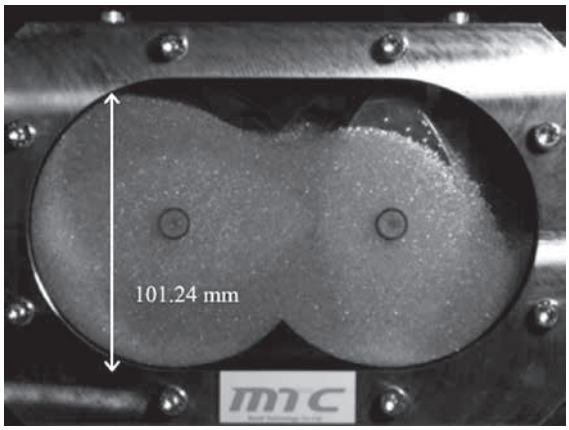

(a) Experiment

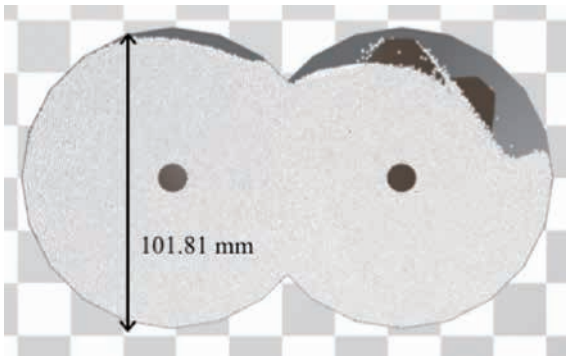

(b) Simulation

Fig. 9 Validation test result in a twin-screw kneader.
Reprinted with permission from Ref. (Sakai et al., Chem. Eng. J., 2015). Copyright: (2015) Elsevier B.V.

respectively. The number of solid particles in the calculation was 400,000 and their mass corresponded to that in the experiment. The time step was 1.0×10^{-5} s and the number of iterations was 1.6×10^{6}. The wall boundary was modeled by the SDF. **Fig. 8** shows the SDF for four cross-sectional views of the paddle. Once again, in the figure, positive and negative regions exist inside and outside the paddle, respectively. Distance and sign were given for the entire computational domain, i.e., the two paddles and the vessel. **Fig. 9** shows the validation test results. The simulation and experiment agreed qualitatively in terms of the spatial distribution of particles, namely, more particles were located on the left side. The quantitative bed height was compared between the simulations and the experiments. The bed heights were estimated to be 101.81 and 101.24 mm, respectively, in the simulation and experiment. Thus, differences between the simulation and experiment were quite small. The validation test result indicates that the DEM/SDF simulates the particle location precisely.

5. Conclusions

New modeling of the granular flow simulations were described for industrial applications. At first, problems of the existing DEM was designated from a view point of the industrial application such as modeling of large-scale simulations, complexly shaped wall boundaries and free surface fluid flow. In order to solve these problems, novel models were developed by our group. A coarse-grain DEM model was developed for large-scale simulations, a SDF-based wall boundary model was developed for complexly shaped walls and a DEM-MPS method was developed for solid-liquid flow involving a free surface. The adequacy of these models was demonstrated through verification and validation tests. Combination of these models becomes a key technology in applying the DEM to actual powder process.

Acknowledgments

My heartfelt gratitude and appreciation goes to Prof Seiichi Koshizuka whose enthusiastic tutelage was of inestimable value for my life. I'm sincerely grateful to Prof. Jusuke Hidaka and to Prof. Yutaka Tsuji for their encouragement and instructions. I would like to thank Dr. Yoshinori Yamada, Dr. Yusuke Shigeto and Dr. Xiaosong Sun for their insightful discussion on developing the numerical models.

Nomenclature

$\boldsymbol{\omega}$	angular velocity (rad/s)
CGM	coarse-grain model
l	coarse-grain ratio (–)
μ	coefficient of friction (–)
$\boldsymbol{F}_{\mathrm{C}}$	contact force (N)
η	damping coefficient (–)
$\boldsymbol{\delta}$	displacement (m)
$\boldsymbol{F}_{\mathrm{f}}$	drag force (N)
$\boldsymbol{f}$	drag force (N/m^3)
ρ	fluid density (kg/m^3)
$\boldsymbol{u}$	fluid velocity (m/s)
$\boldsymbol{g}$	gravitational acceleration (m/s^2)
$\boldsymbol{F}_{\mathrm{g}}$	gravity (N)
H_{A}	Hamaker constant (J)

I	inertia momentum of particle (kg m^2)
β	inter-phase momentum transfer coefficient (kg/m^{2}s)
$\boldsymbol{h}$	intersurface distance (m)
v	kinematic viscosity (m^2/s)
O	original
m	particle mass (kg)
PW	particle-to-wall
$\boldsymbol{v}$	particle velocity (m/s)
V	particle volume (m^3)
p	pressure (N/m^2)
SDF	signed distance function (–)
ϕ	signed distance function (–)
c	speed of sound (m/s)
k	stiffness (N/m)
$\boldsymbol{T}$	torque (N m)
ε	void fraction (–)

References

Alobaid F., Ströhle J., Epple B., Extended CFD/DEM model for the simulation of circulating fluidized bed, Adv. Powder Technol., 24 (2013) 403–415.

Anderson T.B., Jackson R., Fluid Mechanical Description of Fluidized Beds. Equations of Motion, luid Mech. Descr. Fluid. Beds. Equations Motion, 6 (1967) 527–539.

Chandratilleke G.R., Yu a.B., Bridgwater J., A DEM study of the mixing of particles induced by a flat blade, Chem. Eng. Sci., 79 (2012) 54–74.

Cundall P.A., Strack O.D.L., A discrete numerical model for granular assemblies, Geotechnique, 29 (1979) 47–65.

Danby M., Shrimpton J., Palmer M., On the optimal numerical time integration for DEM using Hertzian force models, Comput. Chem. Eng., 58 (2013) 211–222.

Eitzlmayr A., Koscher G., Reynolds G., Huang Z., Booth J., Shering P., Khinast J., Mechanistic Modeling of Modular Co-Rotating Twin-Screw Extruders, Int. J. Pharm., 474 (2014) 157–176.

Ergun S., Fluid flow through packed columns, Chem. Eng. Progr., 48 (1952) 89–94.

Fraige F.Y., Langston P.a, Integration schemes and damping algorithms in distinct element models, Adv. Powder Technol., 15 (2004) 227–245.

Guo Y., Kafui K.D., Wu C.Y., Thornton C., Seville J.P.K., A coupled DEM/CFD analysis of the effect of air on powder flow during die filling, AIChE J., 55 (2009) 49–62.

Halidan M., Chandratilleke G.R., Chan S.L.I., Yu A.B., Bridgwater J., Prediction of the mixing behaviour of binary mixtures of particles in a bladed mixer, Chem. Eng. Sci., 120 (2014) 37–48.

Hernández-Jiménez F., Li T., Cano-Pleite E., Rogers W., Acosta-Iborra A., Characterization of the particle-wall frictional forces in pseudo-2D fluidized beds using DEM, Chem. Eng. Sci., 116 (2014) 136–143.

Hong K., Chen S., Wang W., Li J., Fine-grid two-fluid modeling of fluidization of Geldart A particles, Powder Technol., 2015.

Huang A.N., Kuo H.P., Developments in the tools for the investigation of mixing in particulate systems—A review, Adv. Powder Technol., 25 (2014) 163–173.

Jajcevic D., Siegmann E., Radeke C., Khinast J.G., Large-scale CFD-DEM simulations of fluidized granular systems, Chem. Eng. Sci., 98 (2013) 298–310.

Kawaguchi T., Tanaka T., Tsuji Y., Numerical simulation of two-dimensional fluidized beds using the discrete element method (comparison between the two- and three-dimensional models), Powder Technol., 96 (1998) 129–138.

Kobayashi T., Tanaka T., Shimada N., Kawaguchi T., DEM-CFD analysis of fluidization behavior of Geldart Group A particles using a dynamic adhesion force model, Powder Technol., 248 (2013) 143–152.

Koshizuka S., Nobe A., Oka Y., Moving-particle semi-implicit method for fragmentation of incompressible fluid, Nucl. Sci. Eng., 123 (1996) 421–434.

Kruggel-Emden H., Sturm M., Wirtz S., Scherer V., Selection of an appropriate time integration scheme for the discrete element method (DEM), Comput. Chem. Eng., 32 (2008) 2263–2279.

Kuang S.B., Li K., Zou R.P., Pan R.H., Yu A.B., Application of periodic boundary conditions to CFD-DEM simulation of gas-solid flow in pneumatic conveying, Chem. Eng. Sci., 93 (2013) 214–228.

Liu H., Tafti D.K., Li T., Hybrid parallelism in MFIX CFD-DEM using OpenMP, Powder Technol., 259 (2014) 22–29.

Liu P.Y., Yang R.Y., Yu A.B., Dynamics of wet particles in rotating drums: Effect of liquid surface tension, Phys. Fluids, 23 (2011).

Lu L., Xu J., Ge W., Yue Y., Liu X., Li J., EMMS-based discrete particle method (EMMS-DPM) for simulation of gas-solid flows, Chem. Eng. Sci., 120 (2014) 67–87.

Mateo-Ortiz D., Muzzio F.J., Méndez R., Particle size segregation promoted by powder flow in confined space: The die filling process case, Powder Technol., 262 (2014) 215–222.

Mio H., Higuchi R., Ishimaru W., Shimosaka A., Shirakawa Y., Hidaka J., Effect of paddle rotational speed on particle mixing behavior in electrophotographic system by using parallel discrete element method, Adv. Powder Technol., 20 (2009) 406–415.

Mio H., Kano J., Saito F., Kaneko K., Effects of rotational direction and rotation-to-revolution speed ratio in planetary ball milling, Mater. Sci. Eng. A, 332 (2002) 75–80.

Monaghan J.J., An introduction to SPH, Comput. Phys. Comm., 48 (1988) 89–96.

Ohta M., Kikuchi D., Yoshida Y., Sussman M., Robust numerical analysis of the dynamic bubble formation process in a viscous liquid, Int. J. Multiph. Flow, 37 (2011) 1059–1071.

Olaofe O.O., Patil A.V., Deen N.G., van der Hoef M.A., Kuipers J.A.M., Simulation of particle mixing and segregation in bidisperse gas fluidized beds, Chem. Eng. Sci., 108 (2014) 258–269.

Osher S., Fedkiw R., Level Set Methods and Dynamic Implicit Surfaces, Springer, 2002.

Pandit J.K., Wang X.S., Rhodes M.J., On Geldart Group A behaviour in fluidized beds with and without cohesive interparticle forces: A DEM study, Powder Technol., 164 (2006) 130–138.

Patankar S.V., Numerical heat transfer and fluid flow, Routledge, 1980.

Patil A.V., Peters E.aJ.F., Kolkman T., Kuipers J.aM., Modeling bubble heat transfer in gas-solid fluidized beds using DEM, Chem. Eng. Sci., 105 (2014) 121–131.

Radeke C.A., Glasser B.J., Khinast J.G., Large-scale powder mixer simulations using massively parallel GPUarchitec-

tures, Chem. Eng. Sci., 65 (2010) 6435–6442.
Sakai M., Abe M., Shigeto Y., Mizutani S., Takahashi H., Viré A., Percival J.R., Xiang J., Pain C.C., Verification and validation of a coarse grain model of the DEM in a bubbling fluidized bed, Chem. Eng. J., 244 (2014) 33–43.
Sakai M., Koshizuka S., Large-scale discrete element modeling in pneumatic conveying, Chem. Eng. Sci., 64 (2009) 533–539.
Sakai M., Shibata K., Koshizuka S., Effect of Nuclear Fuel Particle Movement on Nuclear Criticality in a Rotating Cylindrical Vessel, J. Nucl. Sci. Technol., 42 (2005) 267–274.
Sakai M., Shigeto Y., Basinskas G., Hosokawa A., Fuji M., Discrete element simulation for the evaluation of solid mixing in an industrial blender, Chem. Eng. J., 279 (2015) 821–839.
Sakai M., Shigeto Y., Sun X., Aoki T., Saito T., Xiong J., Koshizuka S., Lagrangian-Lagrangian modeling for a solid-liquid flow in a cylindrical tank, Chem. Eng. J., 200-202 (2012a) 663–672.
Sakai M., Takahashi H., Pain C.C., Latham J.-P., Xiang J., Study on a large-scale discrete element model for fine particles in a fluidized bed, Adv. Powder Technol., 23 (2012b) 673–681.
Sakai M., Yamada Y., Shigeto Y., Shibata K., Kawasaki V.M., Koshizuka S., Large-scale discrete element modeling in a fluidized bed, Int. J. Numer. Meth. Fluids, 64 (2010) 1319–1335.
Salikov V., Antonyuk S., Heinrich S., Sutkar V.S., Deen N.G., Kuipers J.aM., Characterization and CFD-DEM modelling of a prismatic spouted bed, Powder Technol., 270 (2014) 622–636.
Shigeto Y., Sakai M., Arbitrary-shaped wall boundary modeling based on signed distance functions for granular flow simulations, Chem. Eng. J., 231 (2013) 464–476.
Shigeto Y., Sakai M., Parallel computing of discrete element method on multi-core processors, Particuology, 9 (2011) 398–405.
Sun X., Sakai M., Sakai M.-T., Yamada Y., A Lagrangian-Lagrangian coupled method for three-dimensional solid-liquid flows involving free surfaces in a rotating cylindrical tank, Chem. Eng. J., 246 (2014) 122–141.
Tsuji Y., Multi-scale modeling of dense phase gas-particle flow, Chem. Eng. Sci., 62 (2007) 3410–3418.
Tsuji Y., Kawaguchi T., Tanaka T., Discrete particle simulation of two dimensional fluidized bed, Powder Technol., 77 (1993) 79–87.
Tsuji Y., Tanaka T., Ishida T., Lagrangian numerical simulation of plug flow of cohesionless particles in a horizontal pipe, Powder Technol., 71 (1992) 239–250.
Vu T.V., Tryggason G., Homma S., Wells J., Takakura H., Front Tracking Computation of Trijunction Solidification with Volume Change, Procedia IUTAM, 15 (2015) 14–17.
Wang J., van der Hoef M.a., Kuipers J.aM., Particle granular temperature of Geldart A, A/B and B particles in dense gas-fluidized beds, Chem. Eng. Sci., 97 (2013) 264–271.
Washino K., Tan H.S., Hounslow M.J., Salman a.D., A new capillary force model implemented in micro-scale CFD-DEM coupling for wet granulation, Chem. Eng. Sci., 93 (2013) 197–205.
Wen C.Y., Yu Y.H., Mechanics of fluidization, Chem. Eng. Progr. Symp. Ser., 62 (1966) 100–111.
Wu C.Y., DEM simulations of die filling during pharmaceutical tabletting, Particuology, 6 (2008) 412–418.
Wu G., Ouyang J., Yang B., Li Q., Use of compromise-based local porosities for coarse grid DEM simulation of bubbling fluidized bed with large particles, Adv. Powder Technol., 24 (2013) 68–78.
Xiao F., Ii S., Chen C., Revisit to the THINC scheme: A simple algebraic VOF algorithm, J. Comput. Phys., 230 (2011) 7086–7092.
Xu M., Chen F., Liu X., Ge W., Li J., Discrete particle simulation of gas-solid two-phase flows with multi-scale CPU-GPU hybrid computation, Chem. Eng. J., 207-208 (2012) 746–757.
Yamada Y., Sakai M., Lagrangian-Lagrangian simulations of solid-liquid flows in a bead mill, Powder Technol, 239 (2013) 105–114.
Yokoi K., Efficient implementation of THINC scheme: A simple and practical smoothed VOF algorithm, J. Comput. Phys., 226 (2007) 1985–2002.
Yue X., Hao Z., Chunhai K., Congshu L., Shi S., Yuanqiang T., Chunsheng F., A GPU-based Discrete Element Modelling Code and its Application in Die Filling, Comput. Fluids, 110 (2014) 235–244.

Author's short biography

Mikio Sakai

Dr Mikio Sakai is an Associate Professor at The University of Tokyo. He earned his Ph.D. degree from The University of Tokyo in 2006 and became an Assistant Professor in 2007. He then became an Associate Professor in 2008. His interests include modeling of multi-phase flow such as gas-solid flows, solid-liquid flows and gas-liquid-solid flows, the arbitrary shaped wall boundary model for granular flows and parallel computing techniques. He is now an associate editor of Chemical Engineering Science.

KONA Powder and Particle Journal No. 33 (2016) 179–202/Doi:10.14356/kona.2016024 Review Paper

Developments of Blocking Filtration Model in Membrane Filtration †

Eiji Iritani* and Nobuyuki Katagiri

[1] *Department of Chemical Engineering, Nagoya University, Japan*

Abstract

Blocking filtration laws consist of four different filtration mechanisms: complete blocking, standard blocking, intermediate blocking, and cake filtration. Blocking filtration laws for describing both the pore blocking and cake formation have been extensively employed over the past several decades to evaluate the increase in filtration resistance with the progress of filtration in the field of classical particulate filtration. In recent years, blocking filtration laws become widely used also in membrane filtration such as microfiltration and ultrafiltration of colloids. This paper gives an overview of the developments of blocking filtration laws and equations under constant pressure and constant rate conditions reported for the filtrate flow of Newtonian and non-Newtonian fluids. The fouling index evaluating the degree of membrane fouling was examined on the basis of the blocking filtration equations. The blocking filtration laws were reexamined to extend the range of their application. Moreover, various combined models developed based on the blocking filtration laws were introduced for describing more rigorously the complicated filtration behaviors controlled by more than one mechanism which occurs successively or simultaneously.

Keywords: membrane fouling, pore blocking, blocking filtration law, cake filtration, membrane filtration, filtration rate

1. Introduction

Membrane filtration processes such as microfiltration and ultrafiltration of dilute colloids play an increasingly important and indispensable role in widely diversified fields ranging from industry to drinking water production, treatment of domestic and industrial effluents, and production of water suitable for reuse. While membrane filtration is a key process which has the widespread application, it is generally recognized that one of the major drawbacks to more widespread use of membrane filtration is a significant increase in the filtration resistance known as membrane fouling, resulting in a dramatic flux decline over time under constant pressure conditions or a remarkable pressure rise over time under constant rate conditions. The membrane fouling is affected by several factors, e.g., pore blocking and/or pore constriction (Hermans and Bredée, 1935, 1936; Grace, 1956; Shirato et al., 1979; Hermia, 1982; Iritani et al, 1992, 2009, 2013), cake formation (Reihanian et al., 1983; Chudacek and Fane, 1984; Iritani et al., 1991a, 2014a, b; Nakakura et al., 1997; Mohammadi et al., 2005; Thekkedath et al., 2007; Sarkar, 2013; Salinas-Rodriguez et al., 2015), solute adsorption (Fane et al., 1983; Iritani et al., 1994), and concentration polarization (Kimura and Sourirajan, 1967; Vilker et al., 1981). Initially, foulants smaller than the pore size of membrane deposit or adsorb onto the pore walls, thereby leading to the pore constriction. This induces a significant reduction in the cross-sectional area available to the filtrate flow. In contrast, larger foulants deposit or adsorb onto the pore entrances, resulting in a marked increase in the filtrate flow resistance. In either case, the pore constriction and pore plugging are followed by the formation of filter cake accumulating on the membrane surface, thus severely increasing the filtration resistance. Therefore, it is essential to elucidate the underlying mechanism controlling the membrane fouling such as the pore constriction, pore plugging, and cake formation during the course of membrane filtration.

So far, a number of models have been proposed to describe the fouling of filter medium during the classical liquid filtration. The theory of cake filtration in which the filter cake forms on the surface of filter medium was initially established by Ruth (1935, 1946) and then extended to deal with the case of the compressible filter cake, as referred to as the modern filtration theory (Grace, 1953;

† Received 27 August 2015; Accepted 25 September 2015
J-STAGE online 28 February 2016
[1] Furo-cho, Chikusa-ku, Nagoya 464-8603, Japan
* Corresponding author: Eiji Iritani;
E-mail: iritani@nuce.nagoya-u.ac.jp
TEL: +81-52-789-3374 FAX: +81-52-789-4531

Tiller, 1953; Okamura and Shirato, 1955; Tiller and Shirato, 1964; Shirato et al., 1969).

The classical blocking filtration laws describe three types of physical mechanisms controlling the blockage of membrane pores, in addition to the cake filtration model. The blocking filtration laws were originally presented by Hermans and Bredée (1935, 1936) and later systematized by Grace (1956), Shirato et al. (1979), and Hermia (1982). The model consists of four different filtration mechanisms: complete blocking, standard blocking, intermediate blocking, and cake formation. Among them, both complete and intermediate blocking laws describe the pore plugging due to foulants reaching the top surfaces of pores. In contrast, the standard blocking law deals with the pore constriction caused by the deposition of foulants onto the pore wall. Interestingly enough, these four filtration mechanisms reduce to a common differential equation with different values of power index. While blocking filtration laws are summarized in quite simple mechanisms, still present today they provide a powerful tool to reasonably evaluate the increasing behavior of filtration resistance in liquid filtration of relatively dilute suspension. Nowadays, blocking filtration laws have become widely used in the analysis of the flux decline behaviors observed not only in classical liquid filtration but also in membrane filtration such as microfiltration and ultrafiltration. Therefore, it is considered that there is a significant value to have an overview of the developments of blocking filtration laws and the related mechanisms.

This review paper initially describes the classical blocking filtration laws derived under constant pressure conditions. Then, the blocking filtration laws are extended to be applied to constant rate (flux) filtration and are generalized through the inclusion of filtrate (permeate) flow of non-Newtonian fluids. A common characteristic filtration form derived from the blocking filtration laws is revisited by considering the membrane pore fouling represented by Kozeny-Carman equation describing the flow through the granular bed. The paper explains that the blocking filtration laws are made available for evaluating the degree of membrane fouling, e.g., the maximum filtrate volume and the fouling index such as SDI and MFI. Finally, the combined models stemming from the blocking filtration laws are described to reasonably evaluate two fouling mechanisms occurring sequentially or simultaneously, which are frequently observed in the actual processes of membrane filtration of colloids. Specifically, much emphasis is placed on the combination of membrane pore blockage and cake formation on the membrane surface. These combined model can approximate highly complicated membrane fouling behaviors often encountered in membrane filtration.

2. Blocking filtration law

2.1 Mechanism of blocking filtration

Blocking filtration laws are applied to four different fouling patterns for describing the deposit of particles on filter media and membranes, as schematically illustrated in **Fig. 1**. The complete, intermediate, and standard blocking laws describe the blocking of membrane pores, while the cake filtration law is applied to the description of the growth of filter cake comprised of particles accumulating on the membrane. For simplicity, it is postulated that the membrane consists of parallel pores with constant diameter and length. Both the complete and intermediate blocking laws are applicable in case that the particle diameter is larger than the pore size. Thus, each particle reaching the membrane due to convection is inevitably trapped on the membrane surface in either case. However, pore blocking behaviors are substantially different from each other. In the complete blocking law, it is assumed that each particle blocks an open pore completely, as shown in **Fig. 1(a)**. When more appropriate, it is assumed that the probability that a particle blocks an open pore is constant during the course of filtration, considering the possibility that a particle deposits on the membrane surface other than pores. Therefore, the number of blocked pores is directly proportional to the filtrate volume v per unit effective membrane area. The variation of the number of open pores during the course of filtration is given by $(N_0' - xv)$, where N_0' is the total number of open pores per unit effective membrane area at start of filtration, x is the number of particles blocking pores per unit filtrate volume. Since

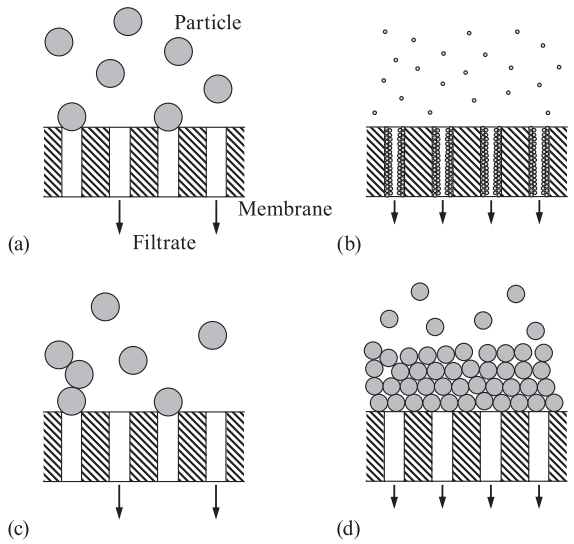

Fig. 1 Schematic view of four fouling patterns in blocking filtration laws: (a) complete blocking law, (b) standard blocking law, (c) intermediate blocking law, and (d) cake filtration law.

the filtration rate J is directly proportional to the number of open pores, it can be written as

$$J = \frac{dv}{dt} = k_c p (N_0' - xv) \tag{1}$$

where t is the filtration time, k_c is the proportional constant, and p is the applied filtration pressure. Differentiating Eq. (1) under the constant pressure condition ($p = p_0$ = const.), one obtains

$$\frac{d^2t}{dv^2} = k_c p_0 x \left(\frac{dt}{dv}\right)^2 = K_b \left(\frac{dt}{dv}\right)^2 \tag{2}$$

where K_b (= $k_c p_0 x$) is the blocking constant for complete blocking law.

However, in practice, the probability that a particle blocks an open pore varies with v during the course of filtration. As the number of open pores decreases due to the progress of filtration, particles newly reaching the membrane may deposit onto the particles that have already blocked the open pores, as shown in **Fig. 1(c)**. In the intermediate blocking law, it is assumed that the rate of pore blocking is proportional to the number of open pores, and thus dN'/dv may be written as

$$\frac{dN'}{dv} = -K_i N' \tag{3}$$

where N' is the number of open pores per unit effective membrane area at the filtrate volume v per unit effective membrane area, and K_i is the blocking constant for intermediate blocking law. Integrating Eq. (3), the number of open pores becomes $N_0' \exp(-K_i v)$. Consequently, the filtration rate is given by

$$J = \frac{dv}{dt} = k_c p N_0' \exp(-K_i v) \tag{4}$$

Differentiating Eq. (4) under the constant pressure condition, one obtains (Hermia, 1982)

$$\frac{d^2t}{dv^2} = K_i \left(\frac{dt}{dv}\right) \tag{5}$$

Although the intermediate blocking law had been considered to be empirical over the years (Grace, 1956), Hermia (1982) originally verified the theoretical background of the intermediate blocking law by considering the decrease in the probability blocking membrane pores with the progress of filtration. Around the same time, Hsu and Fan (1984) proposed the intermediate blocking equations applicable to constant rate filtration on the basis of the stochastic model (pure birth model) in order to use them in the analysis of sand filtration behaviors. Iritani et al. (1991b) derived the intermediate blocking equations for constant pressure filtration based on the stochastic model by considering the probabilistic event with the progress of the filtrate volume v per unit membrane area instead of the filtration time t because the number of particles reaching the membrane is proportional to v in the case of constant pressure filtration. Fan et al. (1985a, b) modified the intermediate blocking equations based on the birth-death model. In the model, scouring of particles blocking pores was also taken into consideration as the death process.

In the standard blocking law shown in **Fig. 1(b)**, the particle diameter is considerably smaller than the pore size. Therefore, solid-liquid separation proceeds by the deposition of particles on the pore wall and the pore gradually constricts with the progress of filtration. For simplicity, it is postulated that the pore volume decreases proportionally to the filtrate volume v per unit membrane area. Consequently, the filtration rate under the constant pressure condition gradually decreases with decreasing pore size. On the assumption that the pore radius decreases by dr by obtaining an infinitesimal amount of filtrate volume dv per unit membrane area, the mass balance produces (Grace, 1956)

$$-2\pi L N_0' r dr = \frac{c}{1-\varepsilon_p} dv \tag{6}$$

where L is the membrane thickness, c is the volume of particles trapped per unit filtrate volume v per unit membrane area, and ε_p is the packing porosity of the particle layer formed on the pore wall. Integrating Eq. (6) from $r = r_0$ at $v = 0$ to $r = r$ at $v = v$, one obtains

$$\frac{r}{r_0} = \left(1 - \frac{K_s v}{2}\right)^{0.5} \tag{7}$$

where K_s is the blocking constant for standard blocking law and defined by

$$K_s = \frac{2c}{N' L \pi (1-\varepsilon_p) {r_0}^2} \tag{8}$$

In general, the relation between the average flow rate u and pore radius r can be given by the Hagen-Poiseuille law applicable to the laminar flow in a capillary, and it is written as

$$u = \frac{r^2 p}{8\mu L} \tag{9}$$

where μ is the viscosity of the filtrate. Thus, the filtration rate through the membrane comprised of capillaries can be described by

$$J_0 = N' \pi {r_0}^2 \frac{{r_0}^2 p_0}{8\mu L} \tag{10}$$

at the start of filtration;

$$J = N' \pi r^2 \frac{r^2 p}{8\mu L} \tag{11}$$

at any time of filtration, where the subscript "0" indicates

the initial value. Substituting Eqs. (10) and (11) into Eq. (7) under the constant pressure condition ($p = p_0$ = const.), one obtains

$$J = J_0\left(1-\frac{K_s}{2}v\right)^2 \tag{12}$$

Differentiation of Eq. (12) yields

$$\frac{d^2t}{dv^2} = K_s {J_0}^{0.5}\left(\frac{dt}{dv}\right)^{1.5} \tag{13}$$

The filtration data of most dilute suspensions is described by the standard blocking law.

In contrast to the pore blocking, in cake filtration shown in **Fig. 1(d)**, the filter cake consisted of the particles deposited on the membrane surface gradually grows as filtration proceeds. The filter cake is viewed as a kind of granular bed which produces the increase in the thickness with the progress of filtration, thereby resulting in the increase in the additional resistance to flow. According to the Ruth theory, the filtration rate J is given by (Ruth, 1935, 1946)

$$\frac{1}{J} = \frac{dt}{dv} = \frac{\mu\alpha_{av}\rho s}{p(1-ms)}(v+v_m) \tag{14}$$

where α_{av} is the average specific cake resistance, ρ is the density of filtrate, s is the mass fraction of solids in colloids, m is the ratio of the mass of wet to the mass of dry cake, and v_m is the fictitious filtrate volume per unit membrane area required to obtain the cake with the flow resistance equivalent to that of the membrane. Since both α_{av} and m are considered to be constant throughout the period of filtration under the constant pressure condition, Eq. (14) becomes

$$\frac{1}{J} = \frac{dt}{dv} = \frac{2}{K_v}(v+v_m) \tag{15}$$

where K_v (= $2p(1 - ms)/(\mu\alpha_{av}\rho s)$) is the Ruth coefficient in constant pressure cake filtration and constant (Ruth, 1935, 1946). Although the filter cake generally exhibits compressible behavior in which α_{av} varies with the applied filtration pressure, it should be noted that Eq. (15) is applicable to not only the incompressible cake but also compressible cake (Tiller and Cooper, 1960; Tiller and Shirato, 1964). Differentiating Eq. (15) with respect to the time t, one gets

$$\frac{d^2t}{dv^2} = \frac{2}{K_v} = K_c \tag{16}$$

where K_c (= $2/K_v$) is the blocking constant for cake filtration law.

Interestingly enough, Eqs. (2), (5), (13), and (16) derived for four different filtration mechanisms reduce to the following common differential equation (Hermans and Bredée, 1935, 1936; Grace, 1956).

$$\frac{d^2t}{dv^2} = k\left(\frac{dt}{dv}\right)^n \tag{17}$$

where k and n are constants. The value of the blocking index n depends on the mode of filtration mechanisms, and indicates 2.0 for complete blocking, 1.5 for standard blocking, 1.0 for intermediate blocking, and 0 for cake filtration. The constant k is the resistance coefficient depending on the properties of suspension, membrane, and the operating conditions in filtration such as the applied filtration pressure. It is found from Eq. (17) that the changing rate in the filtration resistance is proportional to the filtration resistance raised to a power n. When the blocking filtration laws are represented by using the filtration rate J (= dv/dt), Eq. (17) reduces to (Sun et al., 2003)

$$\frac{dJ}{dt} = -kJ^{3-n} \tag{18}$$

A double logarithmic plot of d^2t/dv^2 vs. dt/dv is depicted based on the flux decline behaviors in order to understand the membrane fouling mechanism of constant pressure filtration with the aid of Eq. (17). The fouling mode can be easily determined from the slope of a linear regression fitting to the plot. However, since d^2t/dv^2 is the second order differential of the filtration time t with respect to the filtrate volume v per unit membrane area, the value of n determined from the direct use of Eq. (17) is likely to be influenced by the noise in the experimental data measured as the cumulative filtrate volume v per unit membrane area vs. the time t. Nevertheless, this plot provides important information on the fouling mechanism of membranes, as mentioned later (Bowen et al., 1995; Iritani et al., 1995, 2014c).

Table 1 systematically edits mathematical equations derived for each blocking filtration law under the constant pressure condition and represents v as functions of t and the filtration rate J as functions of t or v (Hermans and Bredée, 1935, 1936; Grace, 1956). These expressions can be used as a means for identifying the membrane fouling mechanism, just like the double logarithmic plot of d^2t/dv^2 vs. dt/dv. The fouling pattern of membranes can be judged from the plots shown in **Fig. 2** based on the linear expressions. For example, if the membrane fouling is controlled by the complete blocking filtration mechanism, the plot of J vs. v and the semi-logarithmic plot of J vs. t should show straight lines. Thus, the predominant blocking filtration law describing membrane fouling pattern can be determined from the graphical expression best fitted based on a linear regression analysis.

Integration of Eq. (18) with respect to the filtration time t produces the relation between the filtration rate J vs. the time t (Herrero et al., 1997; Ho and Zydney, 1999). It should be noted that the standard blocking (n = 1.5), intermediate blocking (n = 1.0), and cake filtration (n = 0)

Table 1 Blocking filtration equations for constant pressure filtration

Function	(a) Complete blocking	(b) Standard blocking	(c) Intermediate blocking	(d) Cake filtration
$\frac{d^2t}{dv^2}=k\left(\frac{dt}{dv}\right)^n$	$n=2.0$	$n=1.5$	$n=1.0$	$n=0$
$v=f(t)$	$v=\frac{J_0}{K_b}\{1-\exp(-K_bt)\}$ (19)	$\frac{t}{v}=\frac{K_s}{2}t+\frac{1}{J_0}$ (22)	$K_iv=\ln(1+K_iJ_0t)$ (25)	$\frac{t}{v}=\frac{K_c}{2}v+\frac{1}{J_0}$ (28)
$J=f(t)$	$J=J_0\exp(-K_bt)$ (20)	$J=\frac{J_0}{\left(\frac{K_sJ_0}{2}t+1\right)^2}$ (23)	$K_it=\frac{1}{J}-\frac{1}{J_0}$ (26)	$J=\frac{J_0}{(1+2K_cJ_0^2t)^{1/2}}$ (29)
$J=f(v)$	$K_bv=J_0-J$ (21)	$J=J_0\left(1-\frac{K_s}{2}v\right)^2$ (24)	$J=J_0\exp(-K_iv)$ (27)	$K_cv=\frac{1}{J}-\frac{1}{J_0}$ (30)

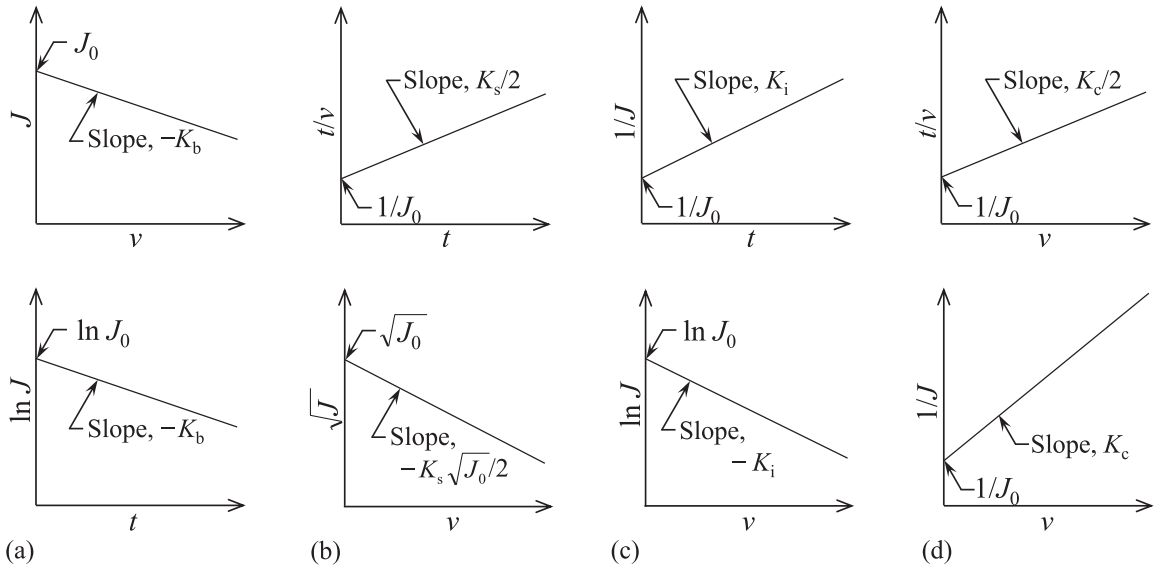

Fig. 2 Graphical identification of blocking filtration laws for constant pressure filtration: (a) complete blocking law, (b) standard blocking law, (c) intermediate blocking law, and (d) cake filtration law.

modes are represented as a common equation given by

$$J=\frac{J_0}{(1+k_jt)^{n_j}} \tag{31}$$

where k_j (= $k(2-n)J_0^{(2-n)}$) and n_j (= $1/(2-n)$) are constants. In contrast, in the case of the complete blocking law (n = 2), integrating Eq. (18), one obtains

$$J=J_0\exp(-kt) \tag{32}$$

Conventionally, the experimental data of the flux decline during the blocking filtration period have been analyzed by only one of above mentioned blocking filtration laws (Granger et al., 1985; Hodgson et al., 1993; Blanpain et al., 1993; Ruohomäki and Nyström, 2000; Gironès et al., 2006; Lee et al., 2008; de Lara and Benavente, 2009; Nandi et al., 2010; Li et al., 2012; Lim and Mohammad, 2012; Pan et al., 2012; Masoudnia et al., 2013, Palencia et al., 2014). Tettamanti (1982) proposed five blocking filtration laws by adding the adhesive filtration law in which the value of k in Eq. (17) is represented as zero. When a stepwise procedure is employed, the blocking filtration equation is derived in the form (Heertjes, 1957)

$$J=J_0\left(\frac{N'}{N'-axv}\right)^{-S_c} \tag{33}$$

where a and S_c are constants. In the case of complete blocking, a = 1.0 and S_c = 1.0. For partial blocking, a < 1.0 and S_c > 1.0. As the slurry concentration increases, a decreases and S_c increases, and both a and S_c depend on the form of pore and of the particle. In recent years, several problems are pointed out in applying the blocking filtra-

tion laws to the analysis of the experimental data of the flux decline during blocking filtration (Tien and Ramarao, 2011; Tien et al., 2014).

2.2 Blocking filtration equations for constant rate filtration

Although the membrane blocking research has been focused mostly on constant pressure filtration, which is easily tested on the laboratory scale, the membrane blocking in constant rate filtration is also crucially important from the viewpoint of the industrial level. While the flux decline behaviors are examined in constant pressure filtration, the pressure rising behaviors resulting from the increase in the filtration resistance are investigated in constant rate filtration in which the filtration rate is kept constant (Blankert et al., 2006; Liu and Kim, 2008; Sun et al., 2008; Mahdi and Holdich, 2013; Raspati et al., 2013).

The blocking filtration equations for constant rate filtration can be obtained in accordance with a procedure similar to that used in constant pressure filtration. For example, in complete blocking law, Eq. (1) is rewritten as

$$p = \frac{J}{k_c (N_0' - xv)} \tag{34}$$

Differentiating Eq. (34) with respect to v under constant rate condition ($J = J_0 = \text{const.}$), one gets

$$\frac{dp}{dv} = \frac{k_c x}{J_0} p^2 = \frac{K_b}{J_0 p_0} p^2 = K_{br} p^2 \tag{35}$$

where K_{br} ($= k_c x/J_0$) is the blocking constant for complete blocking law in constant rate filtration. Eventually, also in the case of constant rate filtration, four blocking filtration laws are represented by a common differential equation in the form (Grace, 1956)

$$\frac{dp}{dv} = k' p^{n'} \tag{36}$$

where k' and n' are constants. A power index n' is the blocking index which defines the filtration mechanism, and indicates the same value as constant pressure filtration for each blocking filtration law. **Table 2** lists the equations derived for constant rate filtration (Grace, 1956). Graphical indications are illustrated in **Fig. 3** and are employed in order to judge the blocking filtration law. The filtrate volume v per unit membrane area is directly proportional to the filtration time t in constant rate filtration, i.e., $v = J_0 t$. Consequently, it is also possible to identify the dominant blocking filtration law by plotting the data against t in place of v shown in **Fig. 3**.

The value of n' is 0 for cake filtration in which an incompressible filter cake forms during filtration. However, when the filter cake exhibits a compressible behavior, the use of Eq. (36) requires a considerable attention. Equation (14) is rewritten as

Table 2 Blocking filtration equations for constant rate filtration

Function	(a) Complete blocking	(b) Standard blocking	(c) Intermediate blocking	(d) Cake filtration
$\frac{dp}{dv} = k' p^{n'}$	$n' = 2.0$	$n' = 1.5$	$n' = 1.0$	$n' = 0$
$p = f(v)$	$\frac{p_0}{p} = 1 - \frac{K_b}{J_0} v$ (37)	$\left(\frac{p_0}{p}\right)^{1/2} = 1 - \frac{K_s}{2} v$ (38)	$\ln\left(\frac{p}{p_0}\right) = K_i v$ (39)	$\frac{p}{p_0} = 1 + K_c J_0 v$ (40)

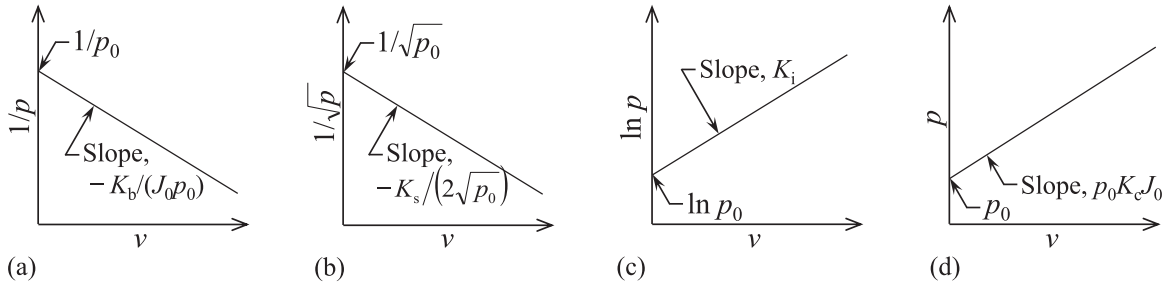

Fig. 3 Graphical identification of blocking filtration laws for constant rate filtration: (a) complete blocking law, (b) standard blocking law, (c) intermediate blocking law, and (d) cake filtration law.

$$p = \frac{\mu \alpha_{av} \rho s J}{1 - ms}(v + v_m) \tag{41}$$

The average specific cake resistance α_{av} in Eq. (41) is related to the applied filtration pressure p by (Sperry, 1921; Murase et al., 1987; Iritani et al., 2002; Zhou et al., 2015)

$$\alpha_{av} = \alpha_1 p^{n_1} \tag{42}$$

where α_1 and n_1 are constants, and n_1 is especially termed the compressibility coefficient of the filter cake. The higher the n_1-value, the more compressibility the cake is. Substituting Eq. (42) into Eq. (41), one obtains (Tiller, 1955; Shirato et al., 1968)

$$p^{1-n_1} = \frac{\mu \alpha_1 \rho s J}{1 - ms}(v + v_m) \tag{43}$$

Differentiation of Eq. (43) with respect to v under the constant rate conditions leads to

$$\frac{dp}{dv} = \frac{(1 - n_1)\mu \alpha_1 \rho s J}{1 - ms} p^{n_1} = k_1 p^{n_1} \tag{44}$$

where k_1 (= $(1 - n_1)\mu\alpha_1\rho sJ/(1 - ms)$) is a constant. Therefore, the value of n' in Eq. (36) is not 0 for constant rate cake filtration in which a compressible filter cake forms during filtration and increases as the compressible behaviors become more pronounced. If the compressibility coefficient n_1 is 1.0, as seen in highly compressible filter cake, the power index n' in the differential equation for cake filtration shows the same value as that derived for the intermediate blocking law, thereby leading to serious confusion.

Since v is directly proportional to the time t in constant rate filtration, Eq. (36) is rewritten as

$$\frac{dp}{dt} = k_2 p^{n'} \tag{45}$$

where k_2 is a constant. It should be noted that the characteristic differential equation can be represented also in the form (Hlavacek and Bouchet, 1993)

$$\frac{d^2 t}{dp^2} = k_1' \left(\frac{dt}{dp}\right)^{n_1'} \tag{46}$$

where k_1' and n_1' are constants. Equation (46) is similar to Eq. (17) in the form, by considering that p in Eq. (46) corresponds to v in Eq. (17). Alternatively, the characteristic form is represented by (Chellam and Xu, 2006; Chellam and Cogan, 2011)

$$\frac{d^2 p}{dv^2} = k_2' \left(\frac{dp}{dv}\right)^{n_2'} \tag{47}$$

where k_2' and n_2' are constants. Also in this case, the use of Eq. (47) requires a considerable attention in applying it to filtration forming compressible filter cakes. Chellam and Xu (2006) employed the expression of the average specific cake resistance α_{av} increasing with pressure p in the analysis of constant rate filtration behaviors, as described by

$$\alpha_{av} = \alpha_0 + \alpha_2 p \tag{48}$$

where α_0 and α_2 are constants, and α_0 is the average specific cake resistance at null stress. Eq. (48) has been applied to microbial suspensions, which exhibit highly compressible behaviors under relatively high pressure conditions. In this case, the value of exponent n_2' in Eq. (47) becomes 1.5, and thus is the same as the complete blocking law.

Blocking filtration equations applicable to variable pressure and variable rate filtration were proposed by Suarez and Veza (2000). For instance, in the complete blocking law, the relation among the filtration rate J, applied filtration pressure p, and filtrate volume v per unit membrane area can be obtained on the basis of Eq. (1) and thus is represented by

$$\frac{J}{p} = \frac{J_0}{p_0} - \frac{K_b}{p_0} v \tag{49}$$

The model adequately described the blocking filtration behaviors of effluent water from a municipal wastewater treatment plant.

2.3 Blocking filtration equations for filtrate of non-Newtonian fluids

When the filtrate flow presents with non-Newtonian behaviors, the analysis for blocking filtration law becomes even more complex than the filtrate flow of Newtonian fluids. In power-law non-Newtonian fluids, which are the simplest case, the rheological equation representing the relation between the shear stress τ and shear rate $\dot{\gamma}$ is written as

$$\tau = K \dot{\gamma}^N \tag{50}$$

where K is the fluid consistency index, and N is the fluid behavior index representing the intensity of non-Newtonian behaviors. When the fluid is characterized by Newtonian fluid, the value of N is equal to 1.0 and departs from 1.0 as non-Newtonian behaviors are more pronounced. The values of N less than 1.0 characterize pseudo-plastic or shear thinning fluids and melts. On the basis of Eq. (50), the relation between the average flow rate u and the tube radius r for power-law non-Newtonian fluids is given by (Kozicki et al., 1966)

$$u = \frac{N}{3N + 1}\left(\frac{p}{2KL}\right)^{1/N} r^{(N+1)/N} \tag{51}$$

When one puts N as 1.0 and K as the Newtonian viscosity μ, Eq. (51) reduces to the Hagen-Poiseuille equation applicable to Newtonian flow represented as Eq. (9).

While the number of open pores varies with the prog-

ress of filtration in both complete blocking and intermediate blocking laws, the radius of open pores remains constant since the start of filtration. Therefore, the forms of the blocking filtration equations for complete blocking and intermediate blocking laws are independent of the flow behaviors in pores, irrespective of the difference between Newtonian and non-Newtonian fluids. However, since the pore radius gradually decreases with the progress of filtration in the standard blocking law, the difference between Newtonian and non-Newtonian fluid is quite obvious, as inferred by Eq. (51). The filtration rates at the start and any time of filtration are, respectively, represented as

$$J_0 = N'\pi \frac{N}{3N+1}\left(\frac{p_0}{2KL}\right)^{1/N} r_0^{(3N+1)/N} \tag{52}$$

$$J = N'\pi \frac{N}{3N+1}\left(\frac{p}{2KL}\right)^{1/N} r^{(3N+1)/N} \tag{53}$$

Substituting Eqs. (52) and (53) into Eq. (7) under the constant pressure condition ($p = p_0 = \text{const.}$), one gets

$$J = J_0\left(1-\frac{K_s}{2}v\right)^{(3N+1)/2N} \tag{54}$$

Differentiating Eq. (54), one obtains (Shirato et al., 1979)

$$\frac{d^2t}{dv^2} = \frac{3N+1}{4N}K_s J_0^{2N/(3N+1)}\left(\frac{dt}{dv}\right)^{(5N+1)/(3N+1)} \tag{55}$$

The filtration rate in cake filtration is described by (Kozicki et al., 1968, 1972; Shirato et al., 1977, 1980; Murase et al., 1989)

$$\left(\frac{1}{J}\right)^N = \left(\frac{dt}{dv}\right)^N = \frac{K\gamma_{av}\rho s}{p(1-ms)}(v+v_m) \tag{56}$$

where γ_{av} is the average specific cake resistance for power-law non-Newtonian flow. Differentiating Eq. (56) with respect to v under the constant pressure condition ($p = p_0 = \text{cont.}$) where γ_{av} and m are treated as constant throughout the course of filtration, one obtains

$$\frac{d^2t}{dv^2} = \frac{K\gamma_{av}\rho s}{Np_0(1-ms)}\left(\frac{dt}{dv}\right)^{1-N} \tag{57}$$

Consequently, four blocking filtration laws for power-law non-Newtonian filtration under the constant pressure condition can be represented by a common differential equation with two constants k_N and n_N, as described by (Shirato et al., 1980; Hermia, 1982; Rushton, 1986)

$$\frac{d^2t}{dv^2} = k_N\left(\frac{dt}{dv}\right)^{n_N} \tag{58}$$

In the case of constant rate filtration, the characteristic form is represented as

$$\frac{dp}{dv} = k'_N p^{n'_N} \tag{59}$$

where k'_N and n'_N are constants. The blocking filtration equations are listed in **Table 3** for constant pressure and constant rate filtration processes for power-law non-Newtonian flow. In the case of constant pressure filtration, the complete and intermediate blocking filtration equations for the filtrate flow of non-Newtonian fluids are the same as those for the flow of Newtonian fluids and thus

Table 3 Blocking filtration equations for power-law non-Newtonian fluids-solids mixtures: (a) constant pressure filtration and (b) constant rate filtration

(a)

Function	Standard blocking	Cake filtration
$\frac{d^2t}{dv^2} = k_N\left(\frac{dt}{dv}\right)^{n_N}$	$n_N = \frac{5N+1}{3N+1}$	$n_N = 1-N$
$v = f(t)$	$v = \frac{2}{K_s}\left\{1-\left(\frac{N+1}{4N}K_sJ_0t+1\right)^{-2N/(N+1)}\right\}$ (60)	$\left\{K_cv+\left(\frac{1}{J_0}\right)^N\right\}^{(N+1)/N} - \left(\frac{1}{J_0}\right)^{N+1} = \frac{N+1}{N}K_ct$ (63)
$J = f(t)$	$J = J_0\left(\frac{N+1}{4N}K_sJ_0t+1\right)^{-(3N+1)/(N+1)}$ (61)	$\left(\frac{1}{J}\right)^{N+1} - \left(\frac{1}{J_0}\right)^{N+1} = \frac{N+1}{N}K_ct$ (64)
$J = f(v)$	$J = J_0\left(1-\frac{K_s}{2}v\right)^{(3N+1)/2N}$ (62)	$K_cv = \left(\frac{1}{J}\right)^N - \left(\frac{1}{J_0}\right)^N$ (65)

(b)

Function	Complete blocking	Standard blocking	Intermediate blocking	Cake filtration
$\frac{dp}{dv} = k_N' p^{n_N'}$	$n_N' = \frac{N+1}{N}$	$n_N' = \frac{3N+3}{3N+1}$	$n_N' = 1$	$n_N' = 0$
$p = f(v)$	$\left(\frac{p_0}{p}\right)^{1/N} = 1-\frac{K_b}{J_0}v$ (66)	$\left(\frac{p_0}{p}\right)^{2/(3N+1)} = 1-\frac{K_s}{2}v$ (67)	$\ln\left(\frac{p}{p_0}\right) = NK_iv$ (68)	$\frac{p}{p_0} = K_cJ_0^Nv+1$ (69)

they are omitted from the table. It should be stressed that the equations for Newtonian fluids is the special case of those for power-law non-Newtonian fluids.

Fig. 4 shows the experimental results of clarification filtration of dilute suspensions prepared by suspending diatomaceous earth in aqueous sodium polyacrylate exhibiting the behavior of power-law non-Newtonian fluid (Iritani et al., 1991b). The plots of $J^{2N/(3N+1)}$ vs. v yield linear relationships in accordance with Eq. (54) for the standard blocking law since the diameter d_p of the suspended solids is much smaller than the pore size d_m. As the solids mass fraction s in suspension decreases, the slope of straight line decreases and thus the filtrate volume obtained during clarification filtration increases.

2.4 Significance of blocking index *n* in blocking filtration laws

The unified characteristic form of blocking filtration laws is derived from four different filtration mechanisms. The blocking index n in Eq. (17) results in values of 2.0, 1.5, 1.0, and 0 for complete blocking, standard blocking, intermediate blocking, and cake filtration laws, respectively. However, in practice, the experimental data frequently exhibit the value other than these. Moreover, even though the pore size is much larger than the particle size, the blocking index n occasionally exhibits the value of 2.0. Therefore, from this point of view it is of significance to throw a new look at the underlying model of the characteristic form of blocking filtration laws.

In the blocking filtration model, for simplicity, it is assumed that the membrane consists of parallel cylindrical pores with constant diameter and length. However, in practice, the porous structure of most membranes is of a complex geometry with irregular pore morphology. The Kozeny-Carman equation can describe the flow through such a porous medium and is written as

$$J = \frac{\mathrm{d}v}{\mathrm{d}t} = \frac{\varepsilon^3}{k_0 S^2 (1-\varepsilon)^2} \cdot \frac{p}{\mu L} \tag{70}$$

where ε is the porosity, S is the specific surface area, and k_0 is the Kozeny constant. Iritani et al. (2007a) derived the characteristic form of blocking filtration laws on the basis of the Kozeny-Carman equation (70), by considering the variations of the porosity and the specific surface area of the membrane caused by the particle deposition within the porous membrane during filtration, as schematically illustrated in **Fig. 5**. The porosity ε in Eq. (70) decreases by particle deposition on the pore walls with the progress of filtration and is represented by

$$\varepsilon = \varepsilon_0 - K_p v = \left(1 - \frac{K_p v}{\varepsilon_0}\right)\varepsilon_0 \tag{71}$$

where ε_0 is the initial porosity of clean membrane, and K_p is a constant. The specific surface area S of the membrane in Eq. (70) also varies with the progress of filtration and it is assumed that S is described as

$$S^2(1-\varepsilon)^2 = \left(1 - \frac{K_p v}{\varepsilon_0}\right)^{\beta} S_0^2 (1-\varepsilon_0)^2 \tag{72}$$

where S_0 is the initial specific surface area of the clean membrane, and β is a constant which depends on the mode of the morphology of the deposit assemblages and defined as

$$\frac{D_s}{D_{s0}} = \left(\frac{D}{D_0}\right)^{\beta} \tag{73}$$

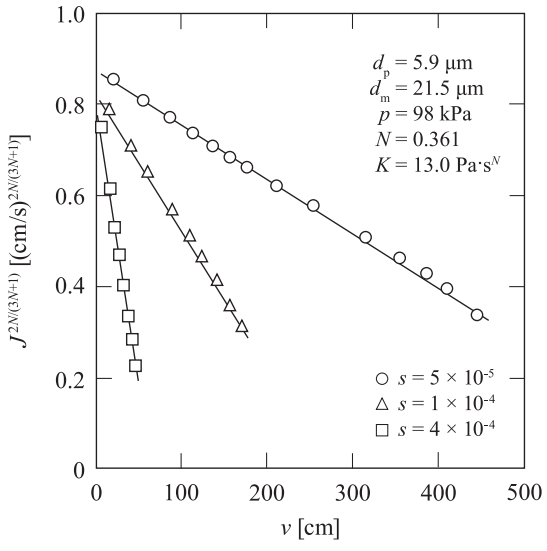

Fig. 4 Flux decline behaviors in clarification filtration of dilute suspensions prepared by suspending diatomaceous earth in aqueous sodium polyacrylate exhibiting behavior of power-law non-Newtonian fluid.

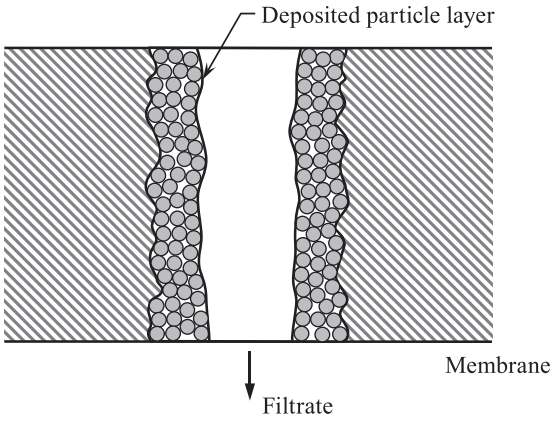

Fig. 5 Schematic view for illustrating the mechanism of membrane fouling in the model presented by Iritani et al. (2007a).

where D_s is the representative diameter of pores on a wetted perimeter basis, D is the representative diameter of pores on a flow cross-sectional area basis, and the subscript 0 indicates the clean membrane. The characteristic form represented by Eq. (17) can be obtained by substituting Eqs. (71) and (72) into Eq. (70) and then by differentiating the reciprocal filtration rate (dt/dv) with respect to v under constant pressure condition ($p = p_0 = \text{const.}$). It should be stressed that Eq. (17) derived in this way is no longer limited by the specific values of n. In this sense, it is concluded that the derivation of Eq. (17) based on the Kozeny-Carman equation is more universal than the classical blocking filtration laws. In a similar way, Eq. (36) applicable to constant rate filtration can be derived based on the Kozeny-Carman equation (Iritani et al., 2011). Some researches were conducted on pore fouling behaviors by employing the Kozeny-Carman equation (Broeckmann et al., 2006; Zhong et al., 2011; Wu et al., 2012). Cheng et al. (2011) derived the characteristic form described by Eq. (17) based on not the Kozeny-Carman equation but the Hagen-Poiseuille equation.

In the derivation of Eq. (17), it is implicitly assumed that the particles are in complete retention, or that the amount of particles deposited within the pores of the membrane increases linearly with v. However, in practice, there often exists some solid leakage through the membrane (Iritani et al., 1994; Rodgers et al., 1995; Hwang et al., 2006; Hwang and Sz, 2010; Polyakov, 2008; Polyakov and Zydney, 2013). As a result, the sieving coefficient of solids varies during the course of filtration. Therefore, the characteristic form represented by Eq. (17) can be generalized by accounting for the variation with time of the amount of the particle deposition within the pores of the membrane. By employing the mass σ of particles deposited on the pore wall per unit membrane area, referred to as the specific deposit (Maroudas and Eisenklam, 1965; Ives and Pienvichitr, 1965; Tien and Payatakes, 1979; Choo and Tien, 1995), the variations of ε and S with the progress of filtration can be, respectively, represented by

$$\varepsilon = \varepsilon_0 - K_m\sigma = \left(1 - \frac{K_m\sigma}{\varepsilon_0}\right)\varepsilon_0 \tag{74}$$

$$S^2(1-\varepsilon)^2 = \left(1 - \frac{K_m\sigma}{\varepsilon_0}\right)^{\beta} S_0^2(1-\varepsilon_0)^2 \tag{75}$$

where K_m is a constant. In a similar way to the derivation of Eq. (17), on the basis of Eq. (70), (74), and (75), the modified form of Eq. (17) can be derived as (Iritani et al., 2010)

$$\frac{d(dt/dv)}{d\sigma} = k\left(\frac{dt}{dv}\right)^n \tag{76}$$

Therefore, when the relation between σ and v is experimentally obtained, the left-hand side value of Eq. (76) may be calculated from the stepwise difference quotient using the experimental data of dt/dv vs. v with the aid of the relation between σ and v. Consequently, the values of n and k in Eq. (76) can be easily obtained from the double logarithmic plots of $d(dt/dv)/d\sigma$ vs. dt/dv.

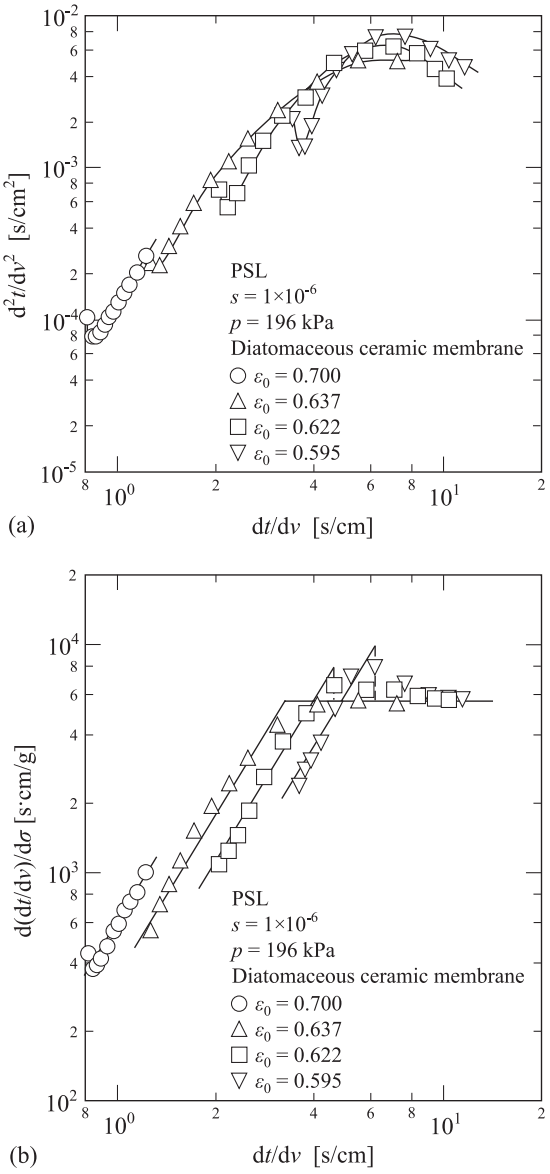

Fig. 6 Characteristic filtration curves for blocking filtration of dilute suspensions of PSL under constant pressure condition using diatomaceous ceramic membranes which are semi-permeable to PSL: (a) logarithmic plots of d^2t/dv^2 vs. dt/dv and (b) logarithmic plots of $d(dt/dv)/d\sigma$ vs. dt/dv.

Fig. 6 compares the logarithmic plots of d^2t/dv^2 vs. dt/dv with those of $d(dt/dv)/d\sigma$ vs. dt/dv for the experimental results in membrane filtration of dilute suspensions of monodisperse polystyrene latex (PSL) under the constant pressure condition using diatomaceous ceramic membranes which are semi-permeable to the PSL (Iritani et al., 2010). The plots for each run show a convex curve with the exception of the case when the initial porosity ε_0

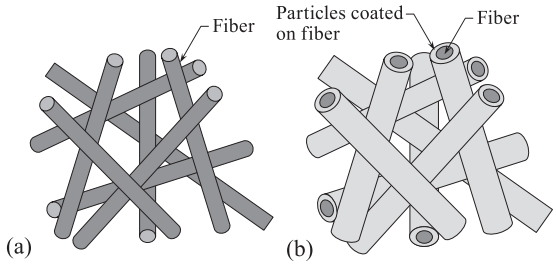

Fig. 7 Schematic view for illustrating the mechanism of membrane fouling in the fiber-coating model presented by Bolton et al. (2005): (a) clean fibers and (b) fouled fibers.

of the membrane is 0.7. The slope of curve gradually decreases with the increase in dt/dv in accordance with the progress of filtration. In contrast, the plots of d(dt/dv)/dσ vs. dt/dv show a linear relation with the same slope of 2.35 for each initial porosity except for the last part of filtration. Thus, Eq. (76) provides a much better description of blocking filtration behaviors obtained for semi-permeable membranes than Eq. (17).

On the basis of the Kozeny-Carman equation, Bolton et al. (2005) proposed a fiber-coating model in which the filter medium becomes plugged as solids coat the surface of cylindrical fibers that constitutes the filter medium. In the model, the fibers become thicker with the progress of filtration, as shown in **Fig. 7**. As a result, the effective radius of fibers increases with time, and correspondingly the porosity decreases, reducing the filter permeability. Therefore, with the aid of the Kozeny-Carman equation, the relation between the filtration rate J and v becomes

$$J = \frac{\mathrm{d}v}{\mathrm{d}t} = \frac{(1 - K_\mathrm{f} v)^3}{\left(1 + \dfrac{\varepsilon_0}{1-\varepsilon_0} K_\mathrm{f} v\right)} J_0 \tag{77}$$

where K_f is the fiber coating constant and equal to the inverse of the solution volume filtered until the filter void volume is completely filled with solids.

2.5 Evaluation of degree of membrane fouling

It is essential to evaluate the degree of membrane fouling during filtration on the basis of the theoretical background in the design of new filter equipment and optimization of commercial filtration operations. The maximum filtrate volume v_max per unit membrane area is defined as the value of v obtained by the time when the filtration rate drops to zero. If the flux decline behavior is controlled by the standard blocking law, on the basis of Eq. (24), v_max can be given as (Badmington et al., 1995; van Reis and Zydney, 2007)

$$v_\mathrm{max} = \frac{2}{K_\mathrm{s}} \tag{78}$$

Combining Eq. (78) with Eq. (24) yields

$$\frac{v}{v_\mathrm{max}} = 1 - \left(\frac{J}{J_0}\right)^{0.5} \tag{79}$$

Consequently, one can evaluate what percentage of v_max has been already obtained when the filtration rate ratio (J/J_0) is known. On the basis of Eqs. (10) and (11), the thickness Δr of the layer deposited on the pore wall is given by (Zeman, 1983; Bowen and Gan, 1991; Blanpain-Avet et al., 1999; Persson et al., 2003)

$$\frac{\Delta r}{r_0} = 1 - \left(\frac{J}{J_0}\right)^{0.25} \tag{80}$$

Similarly to the derivation of Eq. (78), v_max for complete blocking law is written as

$$v_\mathrm{max} = \frac{J_0}{K_\mathrm{b}} \tag{81}$$

Although infinite time is required until the filtration rate becomes zero for intermediate blocking and cake filtration laws, it is possible to calculate the filtrate volume per unit membrane area at an arbitrary ratio (J/J_0) of the flux decline. For instance, when the filtration rate J decreases to y percent of the initial filtration rate J_0, influenced by the intermediate blocking law, the filtrate volume v_y per unit membrane area can be obtained based on Eq. (27) and is represented as

$$v_y = \frac{\ln\left(\dfrac{y}{100}\right)}{K_\mathrm{i}} \tag{82}$$

For the cake filtration law, on the basis of Eq. (30), v_y can be written as

$$v_y = \frac{100 - y}{y K_\mathrm{c} J_0} \tag{83}$$

Fouling index (FI) such as the silt density index (SDI) has been employed to predict and evaluate the fouling potential of the feed water in membrane filtration. The SDI is the most widely applied method for many decades (Nagel, 1987; Yiantsios and Karabelas, 2003; Alhadidi et al., 2011a, 2011b; Koo et al., 2012). According to the ASTM standard (2007), the filtration test is performed under the constant pressure condition of 207 kPa (30 psi) using a microfiltration membrane with the pore size of 0.45 μm. Both the time t_1 required to collect the first 500 ml and the time t_2 required to collect the second 500 ml after 15 min are measured to obtain SDI. Based on the time ratio (t_1/t_2), SDI is calculated as

$$SDI = \frac{100}{15}\left(1 - \frac{t_1}{t_2}\right) \tag{84}$$

SDI values less than 1.0 and 4–5 are preferable for hollow fiber and spiral wound reverse osmosis membranes, respectively. In spite of the widespread application of SDI, it has been long thought that SDI lacks a theoretical basis and that it makes no distinction between different filtration mechanisms. In response to this criticism, White (1996) first clarified the theoretical background based on the cake filtration model. In this case, SDI is written by

$$SDI = \frac{50K_v}{{v_m}^2} \tag{85}$$

More recently, the relation between SDI and blocking filtration laws has been examined in detail for four types of blocking filtration laws consisted of complete blocking, intermediate blocking, standard blocking, and cake filtration (Matsumoto et al., 2009; Alhadidi et al., 2011a; Wei et al., 2012).

The modified fouling index (MFI) proposed by Schippers et al. (1981) was also developed to measure the fouling potential of feed water in membrane filtration. While the feed water is filtered under the constant pressure condition through a 0.45 μm microfiltration membrane in dead-end mode, as is the case in SDI, the filtrate volume is recorded every 30 seconds over the filtration period in the MFI measurement. On the basis of cake filtration model, integrating Eq. (15) under the initial condition that $v = 0$ at $t = 0$, one obtains

$$\frac{t}{v} = (MFI)v + \frac{2}{K_v}v_m \tag{86}$$

Consequently, MFI is the reciprocal of the Ruth coefficient K_v in constant pressure filtration appeared in Eq. (15). Thus, MFI is calculated from the slope obtained by the linear approximation to the plot of the reciprocal average filtration rate (t/v) vs. the filtrate volume v per unit membrane area (Keskinler et al., 2004; Srisukphun et al., 2009). This means that MFI is defined on the assumption that the separation mechanism is controlled by cake filtration. Since MFI includes the solid concentration s in feed water (Park et al., 2006), it is more convenient than the average specific filtration resistance α_{av} to evaluate the fouling potential of feed water in which the solid concentration is unknown. In order to evaluate the fouling potential of smaller colloidal particles or macromolecules, MFI was developed by using ultrafiltration membranes and nanofiltration membranes (referred to as MFI-UF (Boerlage et al., 2002, 2003, 2004) and MFI-NF (Khirani et al., 2006), respectively). Jin et al. (2015) proposed the cake fouling index (CFI) in which the true fouling cake layer resistance can be accurately evaluated by eliminating the effect of pore blocking.

3. Combined model based on blocking filtration law

3.1 Developments of consecutive combined model

Classical blocking filtration laws comprise of three pore blocking mechanisms and a cake formation mechanism. In the generality of cases, the membrane fouling proceeds in two steps: the initial membrane fouling caused by pore blockage and/or pore constriction followed by the long-term fouling arising from the filter cake gradually accumulating on the membrane surface (Kim et al., 1993; Tracey and Davis, 1994; Madaeni and Fane, 1996; Huang and Morrissey, 1998; Blanpain-Avet et al., 1999; Altman et al., 1999; Lim and Bai, 2003; Purkait et al., 2004, 2005; Wang and Tarabara, 2008; Juang et al., 2010; Mohd Amin et al., 2010; Ozdemir et al., 2012). The initial pore blocking frequently causes the irreversible fouling of membranes, resulting in the decrease in the efficiency of membrane cleaning. Once a sufficient fraction of the pores becomes clogged depending on the retentiveness of the membrane, an external cake begins to form on the fouled membrane.

In **Fig. 8**, the logarithmic plots of d^2t/dv^2 as a function of dt/dv are shown as the characteristic filtration curves for filtration of pond water in which the turbidity and concentration of suspended solids are 19.4 NTU and 18.0 mg/l, respectively (Iritani et al., 2007a). In the first stage of filtration (i.e., small dt/dv), the plots show a unique linear relationship, irrespective of the applied filtration pressure p. As filtration proceeds, the reciprocal filtration rate (dt/dv) increases and thus its derivative (d^2t/dv^2) increases. Once the value of d^2t/dv^2 reaches the limiting value, which depends on the filtration pressure, the second stage

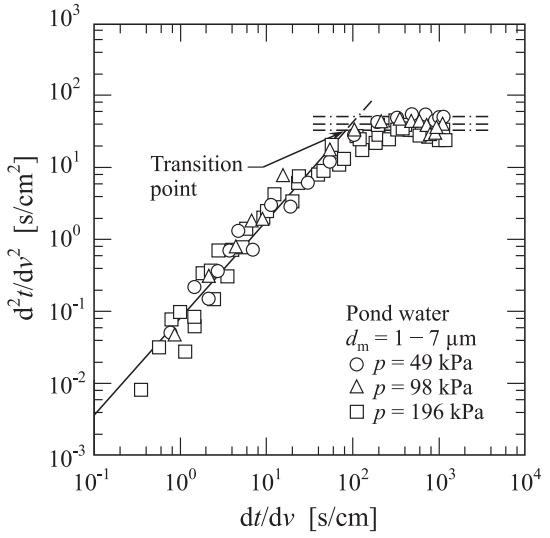

Fig. 8 Characteristic filtration curves for constant pressure filtration of pond water.

begins and the value of d^2t/dv^2 remains constant, as given by Eq. (16). Therefore, the transition point from the initial pore blocking to the following cake filtration during a filtration run can be determined from the change of the slope of the straight line in the double logarithmic plot of d^2t/dv^2 vs. dt/dv according to Eq. (17). It should be noted that the pore fouling is frequently represented by the pore constriction described by the standard blocking law followed by the pore plugging described by the complete or intermediate blocking law (Herrero et al., 1997; Griffiths et al., 2014).

The pore blockage and cake formation may be treated as two resistances in series. According to the resistance-in-series model based on Darcy's law, the filtration rate J is related to the filtration resistances in series as (Iritani et al., 2007b)

$$J = \frac{dv}{dt} = \frac{p}{\mu R} = \frac{p}{\mu(R_m + R_c)} \tag{87}$$

where R is the overall filtration resistance, and R_c is the filter cake resistance. It should be noted that R_m indicates not the resistance of clean membrane but the resistance of fouled membrane.

Bowen et al. (1995) and Iritani et al. (1995) found that the value of n in Eq. (17) gradually varied with the course of filtration in constant pressure dead-end microfiltration of bovine serum albumin (BSA) solution. Later, Hwang et al. (2007) reported a similar result in constant pressure dead-end microfiltration of particulate suspension. In their study, complete blocking ($n = 2$) initially occurred, then gradually changed to standard blocking ($n = 1.5$), and finally cake filtration ($n = 0$) started (Hwang and Chiu, 2008). Therefore, the values of n successively decreased with the progress of filtration.

It should be stressed that several researchers (Bowen et al., 1995; Iritani et al., 1995; Costa et al., 2006; Kim et al., 2007, Yukseler et al., 2007) reported the negative values of n in the later stages of filtration. **Fig. 9** shows the logarithmic plots of d^2t/dv^2 vs. dt/dv as the characteristic form of blocking filtration described by Eq. (17) for constant pressure microfiltration of BSA solution (Iritani et al., 1995). The curve shows a convex shape. The slope of the curve decreases with the increase in dt/dv due to the progress of filtration. Eventually, the slope of the curve has negative values after the slope reaches zero.

Strictly speaking, the blocking filtration laws can be applied only to unstirred dead-end filtration. It is impossible to apply the blocking filtration laws to crossflow filtration where the filter cake growth is restricted by external crossflow of the feed suspension. However, at the earlier stage of crossflow filtration where the solids deposited inside the pore structure, the blocking filtration laws are frequently employed to describe the progressive pore clogging. For instance, Murase and Ohn (1996) adopted

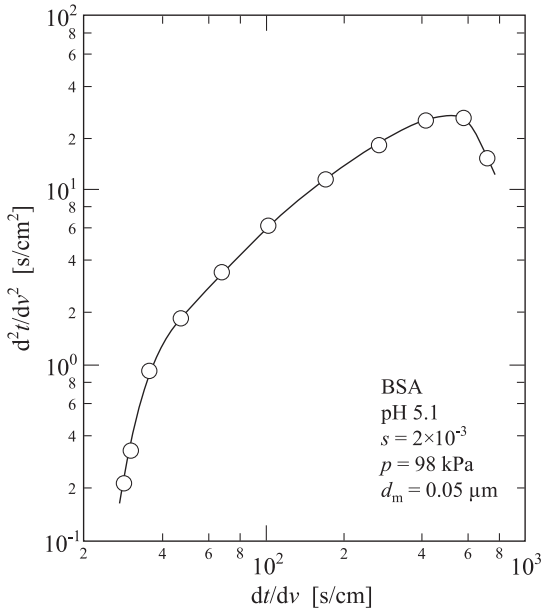

Fig. 9 Characteristic filtration curve for constant pressure microfiltration of BSA solution.

the intermediate blocking law to describe the membrane fouling behavior in the initial stage of crossflow microfiltration of polymethyl methacrylate (PMMA) suspension.

The blocking filtration law has been frequently employed in the analysis of the flux decline in crossflow filtration (Jonsson et al., 1996; Prádanos et al., 1996; Keskinler et al., 2004). In this case, the flux decline behaviors should be analyzed by introducing the term of a steady-state flux controlled by crossflow (Field et al., 1995; de Bruijn et al., 2005). Field et al. (1995) modified the blocking filtration equation (18) by accounting for the back-transport effect arising from crossflow as

$$\frac{dJ}{dt} = -k(J - J_{lim})J^{2-n} \tag{88}$$

where J_{lim} is the critical filtration rate under steady-state condition. Equation (88) has been widely employed in the analysis of the flux decline behaviors in crossflow membrane filtration of a variety of colloids (Todisco et al., 1996; Blanpain and Lalande, 1997; de Barros et al., 2003; Rai et al., 2006; Cassano et al., 2007; Mondal and De, 2009; Vera et al., 2009; Ma et al., 2010; Chang et al., 2011; Daniel et al., 2011; Field and Wu, 2011; Huang et al., 2014). Electric field-assisted membrane filtration in which the particle deposition was restricted due to an external electric field was also investigated on the basis of blocking filtration laws as well as crossflow membrane filtration (Sarkar and De, 2012).

3.2 Developments of concurrent combined model

While membrane fouling generally proceeds in two

steps consisted of pore blocking followed by cake formation, as mentioned above, pore blocking and cake formation may be frequently occurring simultaneously during the filtration process (Takahashi et al., 1991; Matsumoto et al., 1992; Katsoufidou et al., 2005; Fernández et al., 2011; Li et al., 2011; Nakamura et al., 2012). Bolton et al. (2006a) combined two blocking filtration laws occurring concurrently among four blocking filtration laws. On the basis of the Darcy's law, the volumetric flow rate Q through the membrane is related to the overall filtration resistance R and the effective filtration area A in the form

$$Q = \frac{A}{R} \cdot \frac{p}{\mu} \tag{89}$$

Since the apparent filtration area remains constant during the course of filtration, the filtration rate J (= dv/dt) is directly proportional to the volumetric flow rate Q in Eq. (89) as

$$\frac{J}{J_0} = \frac{Q}{Q_0} \tag{90}$$

where the subscript "0" indicates the value at the start of filtration. Substituting Eq. (89) into Eq. (90), one obtains

$$\frac{J}{J_0} = \frac{R_0 A}{R A_0} \tag{91}$$

Both complete and intermediate blocking mechanisms contribute the decrease in the effective filtration area A. In contrast, both standard blocking and cake filtration mechanisms increase the filtration resistance R. On the basis of Eqs. (21) and (27), the variations of the effective filtration area A in Eq. (91) for complete and intermediate blocking mechanisms are, respectively, represented as

$$\frac{A}{A_0} = 1 - \frac{K'_b}{J_0} V \tag{92}$$

$$\frac{A}{A_0} = \exp(-K'_i V) \tag{93}$$

where K'_b and K'_i are the blocking constants for complete and intermediate blocking laws, respectively, and V is the filtrate volume. On the basis of Eq. (24) and (30), the variations of the filtration resistance R in Eq. (91) for standard blocking and cake filtration models are, respectively, given in

$$R = R_0 \left(1 - \frac{K'_s V}{2}\right)^{-2} \tag{94}$$

$$R = R_0 (1 + K'_c J_0 V) \tag{95}$$

where K'_s and K'_c are the blocking constants for standard blocking and cake filtration laws, respectively. Consequently, for instance, the governing equation for the combined process in which both intermediate blocking and cake formation occur simultaneously is derived using Eqs. (91), (93), and (95) and is given by

$$\frac{J}{J_0} = (\exp(-K'_i V))(1 + K'_c J_0 V)^{-1} \tag{96}$$

Just around the same time, Duclos-Orsello et al. (2006) also proposed a very similar combined model for describing the membrane fouling. Rezaei et al. (2011) employed the combined model developed by Bolton et al. (2006a) to analyze the fouling mechanism in crossflow microfiltration of whey. Affandy et al. (2013) well described fouling behaviors in sterile microfiltration of large plasmids DNA with the use of the standard—intermediate model.

Bolton et al. (2006b) combined the adsorption model with the classical blocking filtration model by a method similar to that mentioned above. In the adsorption model, it is assumed that foulant adsorption occurs at the pore walls with zeroth-order kinetics, thereby reducing the pore size and thus increasing the filtration resistance. As a result, the increase in the resistance R with filtration time t is written as

$$\frac{R_0}{R} = (1 - K_a t)^4 \tag{97}$$

where K_a is the adsorption blocking constant. Consequently, for instant, in a combined intermediate blocking—adsorption model, substituting Eqs. (93) and (97) into Eq. (91), one gets

$$\frac{J}{J_0} = \exp(-K_i V)(1 - K_a t)^4 \tag{98}$$

Integration of Eq. (98) lead to the relation between V and t in the form:

$$V = \frac{1}{K_i} \ln\left(\frac{K_i J_0}{5K_a}\left\{1 - (1 - K_a t)^5\right\} + 1\right) \tag{99}$$

Giglia and Straeffer (2012) applied the combined intermediate blocking—adsorption model to the evaluation of filtration performance of microfiltration membranes operated in series. The combined cake—adsorption model can be described by adding the filtration resistances due to the adsorption and cake formation as

$$\frac{J}{J_0} = \left\{(1 - K_a t)^{-4} + K_c J_0 V\right\}^{-1} \tag{100}$$

In the initial stage of cake filtration, pore blocking of a membrane often occurs. As a result, the membrane resistance gradually increases with time and approaches to the saturated value, as indicated by Notebaert et al. (1975). On the assumption that the membrane resistance approaches a finite value due to the progress of filtration, the following equation was presented for describing the variation of the clogged membrane resistance R_m during the

course of filtration for cake filtration of liquefied coal (Tiller et al., 1981; Leu and Tiller, 1983).

$$\frac{R_m - R_{m0}}{R_{m\infty} - R_{m0}} = 1 - \exp(-\eta w) \tag{101}$$

where R_{m0} and $R_{m\infty}$ are the initial and infinite membrane resistances, respectively, η is the blocking rate constant, and w is the net solid mass in the filter cake per unit membrane area. Thereafter, Lee (1997) developed a more rigorous model by introducing the intermediate blocking law and derived the equation with two fitting parameters as

$$\frac{R_m - R_{m0}}{R_{m\infty} - R_{m0}} = \frac{1 - \exp(-\eta w)}{1 + \lambda \exp(-\eta w)} \tag{102}$$

where λ is a constant. Interestingly, Eq. (102) reduces to Eq. (101) found experimentally by Tiller et al. (1981) when the membrane clogging is quite-serious, i.e., at the limit $\lambda \to 0$.

By imposing the condition that some of pores of the membrane still remain open finally in the intermediate blocking law, Iritani et al. (2005) described the clogged membrane resistance R_m as

$$\frac{1 - \dfrac{R_{m0}}{R_m}}{1 - \dfrac{R_{m0}}{R_{m\infty}}} = 1 - \exp(-\eta w) \tag{103}$$

It should be noted that the variation of R_m with w can be represented by only one fitting parameter η in Eq. (103) while two fitting parameters η and λ are required in the analysis of pore clogging using Eq. (102). The cake resistance R_c is related to w as

$$R_c = \alpha_{av} w \tag{104}$$

Thus, the increasing behaviors of filtration resistance can be described by adding the cake resistance R_c represented by Eq. (104) to clogged membrane resistance R_m represented by Eq. (103) on the basis of Eq. (87) describing the resistance-in-series model. In this case, all the particles retained by the membrane contribute as the cake resistance R_c and a part of them also serve as the clogged membrane resistance R_m by clogging the membrane pores in accordance with the intermediate blocking law considering the limiting value of the clogging resistance on the basis of the concurrent combined model, as schematically shown in **Fig. 10**.

Fig. 11 shows the characteristic curves of blocking filtration laws, which is plotted in the form of d^2t/dv^2 vs. dt/dv, for different feed concentrations in constant pressure microfiltration of monodisperse PSL with a particle diameter d_p of 0.522 μm filtered under the applied pressure p of 196 kPa using the track-etched polycarbonate membrane with a nominal pore size d_m of 0.2 μm (Iritani et al., 2015). Each plot results in the distinct negative slope in

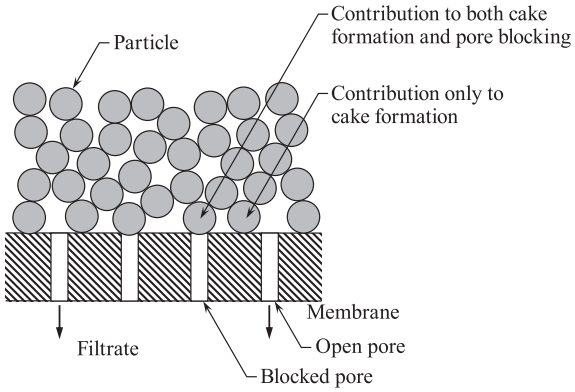

Fig. 10 Schematic view for illustrating the mechanism of membrane fouling comprised of both pore blocking and cake formation occurring simultaneously in the model presented by Iritani et al. (2005).

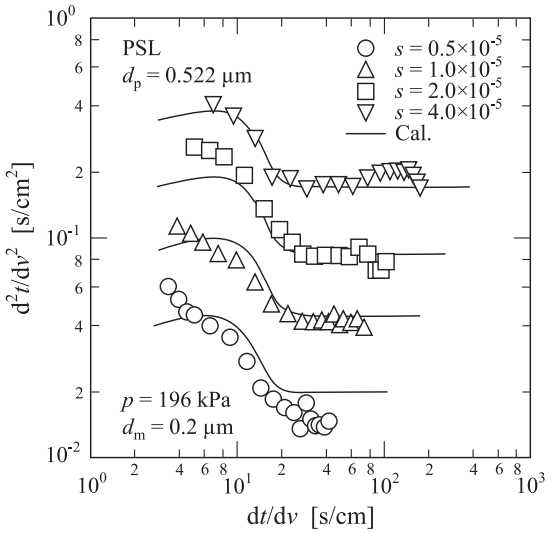

Fig. 11 Effect of solid mass fraction in suspension on characteristic filtration curves in constant pressure microfiltration.

the initial period of filtration since the filtration behaviors are influenced both by the pore blocking of membrane and by cake formation, as reported by several researchers (Bowen et al., 1995; Iritani et al., 1995; Ho and Zydney, 2000; Hwang et al., 2007; Yukseler et al., 2007). However, as filtration proceeds, cake filtration has a dominant influence on the filtration behaviors and thus the slope of the plot becomes equal to zero. Substituting Eqs. (103) and (104) into Eq. (87) and using the relation that $w = \rho s v$ on the assumption that suspension is very dilute, one obtains

$$\frac{dt}{dv} = \frac{\mu}{p}\left(\frac{R_{m\infty}}{1+F} + \alpha_{av}\rho s v\right) \tag{105}$$

where F is a function defined by

$$F = \frac{R_{m\infty} - R_{m0}}{R_{m0}} \exp(-\eta \rho s v) \tag{106}$$

Subsequently, differentiating Eq. (105) with respect to v under constant pressure condition, one gets

$$\frac{\mathrm{d}^2 t}{\mathrm{d}v^2} = \frac{\mu\rho s}{p}\left(\frac{\eta F}{(1+F)^2} + \alpha_{\mathrm{av}}\right) \tag{107}$$

Therefore, the curve of $\mathrm{d}^2t/\mathrm{d}v^2$ vs. $\mathrm{d}t/\mathrm{d}v$ can be evaluated from Eq. (107) with the aid of Eq. (105). The solid curves in **Fig. 11** are the calculations and it is of significance to note that the calculations roughly reflect the trends of experimental data, indicating the negative slope in the initial period followed by the straight line with the slope of zero.

Hwang et al. (2006) evaluated the protein capture into the interstices of filter cake in crossflow microfiltration of particle/protein binary mixtures on the basis of the deep-bed filtration mechanism. The apparent protein rejection R_{obs} is evaluated from

$$R_{\mathrm{obs}} = 1 - \frac{C_{\mathrm{p}}}{C_{\mathrm{b}}} = 1 - \exp(-\gamma L_{\mathrm{c}}) \tag{108}$$

where C_{p} and C_{b} are protein concentrations in the filtrate and in the bulk feed suspension, respectively, γ is a screening parameter which represents the protein fraction rejected by the filter cake per unit cake thickness, and L_{c} is the thickness of the filter cake.

Ho and Zydney (2000) presented a unique model describing pore blocking and cake formation occurring simultaneously in microfiltration processes. As schematically shown in **Fig. 12**, the filter cake only forms over the regions of the membrane which have already been blocked by the initial deposit in the membrane pores. This means that the pore blockage did not lead to complete loss of flow through the pore. As a result, according to Darcy's law, the flux J_{blocked} through the already blocked pores can be written as

$$J_{\mathrm{blocked}} = \frac{p}{\mu(R_{\mathrm{m0}} + R_{\mathrm{c}})} \tag{109}$$

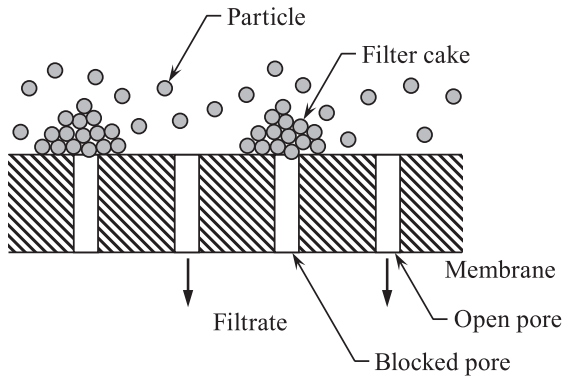

Fig. 12 Schematic view for illustrating the mechanism of membrane fouling comprised of both pore blocking and cake formation occurring simultaneously in the model presented by Ho and Zydney (2000).

The cake resistance R_{c} increases with time during the course of filtration as

$$\frac{\mathrm{d}R_{\mathrm{c}}}{\mathrm{d}t} = f'\alpha_{\mathrm{av}} J_{\mathrm{blocked}} C_{\mathrm{b}} \tag{110}$$

where f' is the fraction of solutes which contribute to the growth of filter cake. Integrating Eq. (110) with the aid of Eq. (109), one obtains

$$R_{\mathrm{c}} = (R_{\mathrm{m0}} + R_{\mathrm{c0}})\sqrt{1 + \frac{2f'\alpha_{\mathrm{av}} p C_{\mathrm{b}} t}{\mu(R_{\mathrm{m0}} + R_{\mathrm{c0}})^2}} - R_{\mathrm{m0}} \tag{111}$$

where R_{c0} is the flow resistance of the first cake layer. The filtration rate J can be given as the sum of the flow rate through open and blocked pores. Thus, with the use of Eq. (111), the variation of J with t can be approximately written as

$$\frac{J}{J_0} = \exp\left(-\frac{\alpha p C_{\mathrm{b}}}{\mu R_{\mathrm{m0}}} t\right) + \frac{R_{\mathrm{m0}}}{R_{\mathrm{m0}} + R_{\mathrm{c}}}\left\{1 - \exp\left(-\frac{\alpha p C_{\mathrm{b}}}{\mu R_{\mathrm{m0}}} t\right)\right\} \tag{112}$$

where α is the pore blocking constant in the complete blocking law. The first term in Eq. (112) represents a simple exponential decline in the flux through the open pores controlled by the classical complete blocking law. As filtration proceeds, the deposit continued to grow due to some fluid flow through pores partially blocked by the complete blocking mechanism, as illustrated by **Fig. 12**, and thus the filtration rate becomes governed by the classical cake filtration law represented by the second term in Eq. (112). The model has been extensively used to analyze the fouling behaviors in membrane filtration of a number of colloids under various operating conditions (Yuan et al., 2002; Ho and Zydney, 2002; Palacio et al., 2002, 2003; Taniguchi et al., 2003; Ye et al., 2005; Chandler and Zydney, 2006; Cogan and Chellam, 2009; Byun et al., 2011).

4. Conclusions and prospective view

The present article overviewed the blocking filtration laws comprised of the complete blocking, standard blocking, intermediate blocking, and cake filtration, which could describe the increase in the filtration resistance during the course of filtration in membrane filtration of colloids. The equations derived based on the blocking filtration laws were reported to describe the filtrate flow of Newtonian and non-Newtonian fluids through membranes for both constant pressure and constant rate filtration processes. The blocking filtration laws are quite useful due to the simplicity in use of the model to identify the prevailing fouling mechanism from the experimental data of the flux decline in constant pressure filtration or pressure rise in constant rate filtration. In order to evaluate more com-

plicate fouling behaviors in membrane filtration, several combined models have been developed based on the blocking filtration laws and well described the fouling phenomena in which more than one filtration mechanism occurred successively or simultaneously.

While the blocking filtration laws and their combinations largely contributed to the optimal choice of the membrane and membrane-cleaning strategy in industrial use, it is essential to develop more sophisticated models which can describe more accurately the complicated behaviors of membrane fouling actually encountered in industrial membrane filtration. In particular, there is a pressing need for developing the models which are applicable not only the simple model colloids but also to the actual colloids containing a wide variety of ingredients, as frequently encountered in water treatment.

In any case, the elucidation of mechanism predominating the membrane fouling in membrane filtration is ever lasting problems crying out for solutions. We believe that this article provides a valuable insight into the further developments of models which can reasonably describe the fouling behaviors in membrane filtration.

Acknowledgements

This work has been partially supported by Grant-in-Aid for Scientific Research from The Ministry of Education, Culture, Sports, Science and Technology, Japan. The authors wish to acknowledge with sincere gratitude the financial support leading to the publication of this article.

Nomenclature

A	effective filtration area (m^2)
A_0	initial effective filtration area (m^2)
a	constant in Eq. (33)
C_b	protein concentration in bulk feed suspension (kg/m^3)
C_p	protein concentration in filtrate (kg/m^3)
c	volume of particles trapped per unit filtrate volume v per unit membrane area (m)
D	representative diameter of pores on flow cross-sectional area basis (m)
D_s	representative diameter of pores on wetted perimeter basis (m)
d_m	pore size (m)
d_p	diameter of suspended solids (m)
F	function defined by Eq. (106)
f'	fraction of solutes which contribute to growth of filter cake
J	filtration rate (m/s)
J_0	initial filtration rate (m/s)
$J_{blocked}$	flux through already blocked pores (m/s)
J_{lim}	critical filtration rate under steady-state condition in crossflow filtration (m/s)
K	fluid consistency index for power-law non-Newtonian fluids ($kg\ m^{-1}\ s^{N-2}$)
K_a	adsorption blocking constant in Eq. (97) (s^{-1})
K_b	blocking constant in Eq. (2) for complete blocking law (s^{-1})
K'_b	blocking constant in Eq. (92) for complete blocking law ($m^{-2}\ s^{-1}$)
K_{br}	blocking constant in Eq. (35) for complete blocking law in constant rate filtation ($kg^{-1}\ s^2$)
K_c	blocking constant in Eq. (16) for cake filtration law (s/m^2)
K'_c	blocking constant in Eq. (95) for cake filtration law (s/m^4)
K_f	fiber coating constant in Eq. (77)
K_i	blocking constant in Eq. (3) for intermediate blocking law (m^{-1})
K'_i	blocking constant in Eq. (93) for intermediate blocking law (m^{-3})
K_m	constant in Eq. (74) (m^2/kg)
K_p	constant in Eq. (71) (m^{-1})
K_s	blocking constant in Eq. (7) for standard blocking law (m^{-1})
K'_s	blocking constant in Eq. (94) for standard blocking law (m^{-3})
K_v	Ruth coefficient in constant pressure cake filtration (m^2/s)
k	resistant coefficient in Eq.(17) ($m^{n-2}\ s^{1-n}$)
k'	resistant coefficient in Eq. (36) for constant rate filtration ($kg^{1-n'}\ m^{n'-2}\ s^{2n'-2}$)
k_0	Kozeny constant
k_1	constant in Eq. (44) ($kg^{1-n_1}\ m^{n_1-2}\ s^{2n_1-2}$)
k'_1	constant in Eq. (46) ($kg^{n'_1-2}\ m^{2-2n'_1}\ s^{5-5n'_1}$)
k_2	constant in Eq. (45) ($kg^{1-n'}\ m^{n'-1}\ s^{2n'-3}$)
k'_2	constant in Eq. (47) ($kg^{1-n'_2}\ m^{2n'_2-3}\ s^{2n'_2-2}$)
k_c	proportional constant in Eq. (1) ($kg^{-1}\ m^4\ s$)
k_j	constant in Eq. (31) (s^{-1})
k_N	constant in Eq. (58) ($m^{n_N-2}s^{1-n_N}$)
k'_N	constant in Eq. (59) ($kg^{1-n'_N}\ m^{n'_N-2}\ s^{2n'_N-2}$)
L	membrane thickness (m)
L_c	thickness of filter cake (m)
m	ratio of mass of wet to mass of dry cake
MFI	modified fouling index defined by Eq. (86) (s/m^2)

N fluid behavior index for power-law non-Newtonian fluids

N' number of open pores per unit effective membrane area at filtrate volume v per unit effective membrane area (m^{-2})

N'_0 total number of open pores per unit effective membrane area at start of filtration (m^{-2})

n blocking index in Eq. (17)

n' blocking index in Eq. (36) for constant rate filtration

n_1 compressibility coefficient in Eq. (42)

n'_1 constant in Eq. (46)

n'_2 constant in Eq. (47)

n_j constant in Eq. (31)

n_N constant in Eq. (58)

n'_N constant in Eq. (59)

p applied filtration pressure (Pa)

p_0 initial applied filtration pressure (Pa)

Q volumetric flow rate (m^3/s)

Q_0 initial volumetric flow rate (m^3/s)

R overall filtration resistance (m^{-1})

R_0 initial overall filtration resistance (m^{-1})

R_c filter cake resistance (m^{-1})

R_{c0} flow resistance of the first cake layer (m^{-1})

R_m clogged membrane resistance (m^{-1})

R_{m0} initial membrane resistance (m^{-1})

$R_{m\infty}$ infinite membrane resistance (m^{-1})

r pore radius (m)

r_0 initial pore radius (m)

S specific surface area of membrane (m^{-1})

S_0 initial specific surface area of clean membrane (m^{-1})

S_c constant in Eq. (33)

s mass fraction of solids in colloids

SDI silt density index defined by Eq. (84)

t filtration time (s)

t_1 time required to collect the first 500 ml of filtrate volume (s)

t_2 time required to collect the second 500 ml of filtrate volume after 15 min (s)

u average flow rate (m/s)

V filtrate volume (m^3)

v filtrate volume per unit effective membrane area (m)

v_m fictitious filtrate volume per unit membrane area required to obtain cake with flow resistance equivalent to that of membrane (m)

v_{max} maximum filtrate volume per unit membrane area (m)

v_y filtrate volume per unit membrane area obtained until filtration rate decreases to y percent of initial filtration rate (m)

w net solid mass in filter cake per unit membrane area (kg/m^2)

x number of particles blocking pores per unit filtrate volume (m^{-3})

y percentage of initial value of filtration rate

α pore blocking constant in Eq. (112) for complete blocking law (m^2/kg)

α_0 average specific cake resistance at null stress in Eq. (48) (m/kg)

α_1 constant in Eq. (42) ($kg^{-1-n_1} m^{1+n_1} s^{2n_1}$)

α_2 constant in Eq. (48) ($kg^{-2} m^2 s^2$)

α_{av} average specific cake resistance (m/kg)

β constant which depends on mode of morphology of deposit assemblages

γ screening parameter in Eq. (108) (m^{-1})

$\dot{\gamma}$ shear rate (s^{-1})

γ_{av} average specific cake resistance for power-law non-Newtonian flow (m^{2-N}/kg)

Δr thickness of layer deposited on pore wall (m)

ε porosity of membrane

ε_0 initial porosity of clean membrane

ε_p packing porosity of particle layer formed on pore wall

η blocking rate constant (m^2/kg)

λ constant in Eq. (102)

μ viscosity of filtrate (Pa s)

ρ density of filtrate (kg/m^3)

σ specific deposit, i.e., mass of particles deposited on pore wall per unit membrane area (kg/m^2)

τ shear stress (Pa)

References

Affandy A., Keshavarz-Moore E., Versteeg H.K., Application of filtration blocking models to describe fouling and transmission of large plasmids DNA in sterile filtration, Journal of Membrane Science, 437 (2013) 150–159.

Alhadidi A., Blankert B., Kemperman A.J.B., Schippers J.C., Wessling M., van der Meer W.G.J., Effect of testing conditions and filtration mechanisms on SDI, Journal of Membrane Science, 381 (2011a) 142–151.

Alhadidi A., Kemperman A.J.B., Schippers J.C., Wessling M., van der Meer W.G.J., The influence of membrane properties on the Silt Density Index, Journal of Membrane Science, 384 (2011b) 205–218.

Altman M., Semiat R., Hasson D., Removal of organic foulants from feed waters by dynamic membranes, Desalination, 125 (1999) 65–75.

ASTM Standard (D4189-07), Standard test method for silt density index (SDI) of water, D19.08 on membranes and ion exchange materials, 2007.

Badmington F., Wilkins R., Payne M., Honig E.S., Vmax testing for practical microfiltration train scale-up in biopharmaceutical processing, Pharmaceutical Technology, 19(Sep.) (1995) 64–76.

Blankert B., Betlem B.H.L., Roffel B., Dynamic optimization of a dead-end filtration trajectory: Blocking filtration laws, Journal of Membrane Science, 285 (2006) 90–95.

Blanpain P., Hermia J., Lenoël M., Mechanisms governing permeate flux and protein rejection in the microfiltration of beer with a cyclopore membrane, Journal of Membrane Science, 84 (1993) 37–51.

Blanpain P., Lalande M., Investigation of fouling mechanisms governing permeate flux in the crossflow microfiltration of beer, Filtration & Separation, 21 (1997) 1065–1069.

Blanpain-Avet P., Fillaudeau L., Lalande M., Investigation of mechanisms governing membrane fouling and protein rejection in the sterile microfiltration of beer with an organic membrane, Transactions of The Institution of Chemical Engineers, Part C, Food and Bioproducts Processing, 77 (1999) 75–89.

Boerlage S.F.E., Kennedy M.D., Dickson M.R., El-Hodali D.E.Y., Schippers J.C., The modified fouling index using ultrafiltration membranes (MFI-UF): Characterisation, filtration mechanism and proposed reference membrane, Journal of Membrane Science, 197 (2002) 1–21.

Boerlarge S.F.E., Kennedy M., Aniye M.P., Schippers J.C., Application of the MFI-UF to measure and predict particulate fouling in RO systems, Journal of Membrane Science, 220 (2003) 97–116.

Boerlage S.F.E., Kennedy M., Tarawneh Z., de Feber R., Shippers J.C., Development of the MFI-UF in constant flux filtration, Desalination, 161 (2004) 103–113.

Bolton G.R., LaCasse D., Lazzara M.J., Kuriyel R., The fiber-coating model of biopharmaceutical depth filtration, AIChE Journal, 51 (2005) 2978–2987.

Bolton G.R., Lacasse D., Kuriyel R., Combined models of membrane fouling: Development and application to microfiltration and ultrafiltration of biological fluids, Journal of Membrane Science, 277 (2006a) 75–84.

Bolton G.R., Boesch A.W., Lazzara M.J., The effects of flow rate on membrane capacity: Development and application of adsorptive membrane fouling models, Journal of Membrane Science, 279 (2006b) 625–634.

Bowen W.R., Gan Q., Properties of microfiltration membranes: Flux loss during constant pressure permeation of bovine serum albumin, Biotechnology and Bioengineering, 38 (1991) 687–696.

Bowen W.R., Calvo J.I., Hernández A., Steps of membrane blocking in flux decline during protein microfiltration, Journal of Membrane Science, 101 (1995) 153–165.

Broekmann A., Busch J., Wintgens T., Marquardt W., Modeling of pore blocking and cake layer formation in membrane filtration for wastewater treatment, Desalination, 189 (2006) 97–109.

Byun S., Taurozzi J.S., Alpatova A.L., Wang F., Tarabara V.V., Performance of polymeric membranes treating ozonated surface water: Effect of ozone dosage, Separation and Purification Technology, 81 (2011) 270–278.

Cassano A., Marchio M., Driori E., Clarification of blood orange juice by ultrafiltration: Analyses of operating parameters, membrane fouling and juice quality, Desalination, 212 (2007) 15–27.

Chandler M., Zydney A., Effects of membrane pore geometry on fouling behavior during yeast cell microfiltration, Journal of Membrane Science, 285 (2006) 334–342.

Chang E.E., Yang S.Y., Huang C.P., Liang C.H., Chiang P.C., Assessing the fouling mechanisms of high-pressure nanofiltration membrane using the modified Hermia model and the resistance-in-series model, Separation and Purification Technology, 79 (2011) 329–336.

Chellam S., Xu W., Blocking laws analysis of dead-end constant flux microfiltration of compressible cakes, Journal of Colloid and Interface Science, 301 (2006) 248–257.

Chellam S., Cogan N.G., Colloidal and bacterial fouling during constant flux microfiltration: Comparison of classical blocking laws with a unified model combining pore blocking and EPS secretion, Journal of Membrane Science, 382 (2011) 148–157.

Cheng Y.L., Lee D.J., Lai J.Y., Filtration blocking laws: Revisited, Journal of the Taiwan Institute of Chemical Engineers, 42 (2011) 506–508.

Choo C.U., Tien C., Simulation of hydrosol deposition in granular media, AIChE Journal, 41 (1995) 1426–1442.

Chudacek M.W., Fane A.G., The dynamics of polarization in unstirred and stirred ultrafiltration, Journal of Membrane Science, 21 (1984) 145–160.

Cogan N.G., Chellam S., Incorporating pore blocking, cake filtration, and EPS production in a model for constant pressure bacterial fouling during dead-end microfiltration, Journal of Membrane Science, 345 (2009) 81–89.

Costa A.R., Pinho M.N., Elimelech M., Mechanism of colloidal natural organic matter fouling in ultrafiltration, Journal of Membrane Science, 281 (2006) 716–725.

Daniel R.C., Billing J.M., Russell R.L., Shimskey R.W., Smith H.D., Peterson R.A., Integrated pore blockage – cake filtration model for crossflow filtration, Chemical Engineering Research and Design, 89 (2011) 1094–1103.

de Barros S.T.D., Andrade C.M.G., Mendes E.S., Peres L., Study of fouling mechanism in pineapple juice clarification by ultrafiltration, Journal of Membrane Science, 215 (2003) 213–224.

de Bruijn J.P.F., Salazar F.N., Bórquez R., Membrane blocking in ultrafiltration: A new approach to fouling, Transaction of The Institution of Chemical Engineers, Part C, Food and Bioproducts Processing, 83 (2005) 211–219.

de Lara R., Benavente J., Use of hydrodynamic and electrical measurements to determine protein fouling mechanisms for microfiltration membranes with different structures and materials, Separation and Purification Technology, 66 (2009) 517–524.

Duclos-Orsello C., Li W., Ho C.C., A three mechanism model to describe fouling of microfiltration membranes, Journal of Membrane Science, 280 (2006) 856–866.

Fan L.T., Hwang S.H., Chou S.T., Nassar R., Birth-death modeling of deep bed filtration: Sectional analysis, Chemical Engineering Communications, 35 (1985a) 101–121.

Fan L.T., Nassar R., Hwang S.H., Chou S.T., Analysis of deep bed filtration data: Modeling as a birth-death process, AIChE Journal, 31 (1985b) 1781–1790.

Fane A.G., Fell C.J.D., Suki A., The effect of pH and ionic environment on the ultrafiltration of protein solutions with retentive membranes, Journal of Membrane Science, 16 (1983) 195–210.

Fernández X.R., Rosenthal I., Anlauf H., Nirschl H., Experimental and analytical modeling of the filtration mechanisms of a paper stack candle filter, Chemical Engineering Research and Design, 89 (2011) 2776–2784.

Field R.W., Wu D., Howell J.A., Gupta B.B., Critical flux concept for microfiltration fouling, Journal of Membrane Science, 100 (1995) 259–272.

Field R.W., Wu J.J., Modeling of permeability loss in membrane filtration: Re-examination of fundamental fouling equations and their link to critical flux, Desalination, 283 (2011) 68–74.

Giglia S., Straeffer G., Combined mechanism fouling model and method for optimization of series microfiltration performance, Journal of Membrane Science, 417–418 (2012) 144–153.

Gironès M., Lammertink R.G.L., Wessling M., Protein aggregate deposition and fouling strategies with high-flux silicon nitride microsieves, Journal of Membrane Science, 273 (2006) 68–76.

Grace H.P., Resistance and compressibility of filter cake, Part I, Chemical Engineering Progress, 49 (1953) 303–318.

Grace H.P., Structure and performance of filter media. II. Performance of filter media in liquid service, AIChE Journal, 2 (1956) 316–336.

Granger J., Dodds J., Leclerc D., Filtration of low concentrations of latex particles on membrane filters, Filtration & Separation, 9 (1985) 58–60.

Griffiths I.M., Kumar A., Stewart P.S., A combined network model for membrane fouling, Journal of Colloid and Interface Science, 432 (2014) 10–18.

Heertjes P.M., Studies in filtration, Blocking filtration, Chemical Engineering Science, 6 (1957) 190–203.

Hermans P.H., Bredée H.L., Zur kenntnis der filtrationsgesetze, Recueil des Travaux Chimiques des Pays-Bas, 54 (1935) 680–700.

Hermans P.H., Bredée H.L., Principles of the mathematic treatment of constant-pressure filtration, Journal of The Society of Chemical Industry, 55T (1936) 1–4.

Hermia J., Constant pressure blocking filtration laws—Application to power-law non-Newtonian fluids, Transaction of The Institution of Chemical Engineers, 60 (1982) 183–187.

Herrero C., Prádanos P., Calvo J.I., Tejerina F., Hernández A., Flux decline in protein microfiltration: Influence of operative parameters, Journal of Colloid and Interface Science, 187 (1997) 344–351.

Hlavacek M., Bouchet F., Constant flowrate blocking laws and an example of their application to dead-end microfiltration of protein solutions, Journal of Membrane Science, 82 (1993) 285–295.

Ho C.C., Zydney A.L., Effect of membrane morphology on the initial rate of protein fouling during microfiltration, Journal of Membrane Science, 155 (1999) 261–275.

Ho C.C., Zydney A.L., A combined pore blockage and cake formation model for protein fouling during microfiltration, Journal of Colloid and Interface Science, 232 (2000) 389–399.

Ho C.C., Zydney A.L., Transmembrane pressure profiles during constant flux microfiltration of bovine serum albumin, Journal of Membrane Science, 209 (2002) 363–377.

Hodgson P.H., Leslie G.L., Schneider R.P., Fane A.G., Fell C.J.D., Marshall K.C., Cake resistance and solute rejection in bacterial microfiltration: The role of the extracellular matrix, Journal of Membrane Science, 79 (1993) 35–53.

Hsu E.H., Fan L.T., Experimental study of deep bed filtration: A stochastic treatment, AIChE Journal, 30 (1984) 267–273.

Huang L., Morrissey M.T., Fouling of membranes during microfiltration of surimi wash water: Roles of pore blocking and surface cake filtration, Journal of Membrane Science, 144 (1998) 113–123.

Huang Q., Gomaa H.G., Hashem N., Flux characteristics of oil separation from O/W emulsions using highly hydrophilic UF membrane in narrow channel, Separation Science and Technology, 49 (2014) 12–21.

Hwang K.J., Chou F.Y., Tung K.L., Effects of operating conditions on the performance of cross-flow microfiltration of fine particle/protein binary suspension, Journal of Membrane Science, 274 (2006) 183–191.

Hwang K.J., Liao C.Y., Tung K.L., Analysis of particle fouling during microfiltration by use of blocking models, Journal of Membrane Science, 287 (2007) 287–293.

Hwang K.J., Chiu H.S., Influence of membrane type on filtration characteristics and protein rejection in crossflow microfiltration, Filtration, 8 (2008) 317–322.

Hwang K.J., Sz P.Y., Filtration characteristics and membrane fouling in cross-flow microfiltration of BSA/dextran binary suspension, Journal of Membrane Science, 347 (2010) 75–82.

Iritani E., Nakatsuka S., Aoki H., Murase T., Effect of solution environment on unstirred dead-end ultrafiltration characteristics of proteinaceous solutions, Journal of Chemical Engineering of Japan, 24 (1991a) 177–183.

Iritani E., Sumi H., Murase T., Analysis of filtration rate in clarification filtration of power-law non-Newtonian fluids-solids mixtures under constant pressure by stochastic model, Journal of Chemical Engineering of Japan, 24 (1991b) 581–586.

Iritani E., Itano Y., Murase T., Ultrafiltration of proteinaceous solutions by use of dynamic membranes formed by body-feed method, Membrane, 17 (1992) 203–206.

Iritani E., Tachi S., Murase T., Influence of protein adsorption on flow resistance of microfiltration membrane, Colloids and Surfaces A: Physicochemical and Engineering Aspects, 89 (1994) 15–22.

Iritani E., Mukai Y., Tanaka Y., Murase T., Flux decline behavior in dead-end microfiltration of protein solutions, Journal of Membrane Science, 103 (1995) 181–191.

Iritani E., Mukai Y., Hagihara E., Measurements and evaluation of concentration distributions in filter cake formed in dead-end ultrafiltration of protein solutions, Chemical Engineer-

ing Science, 57 (2002) 53–62.
Iritani E., Mukai Y., Furuta M., Kawakami T., Katagiri N., Blocking resistance of membrane during cake filtration of dilute suspensions, AIChE Journal, 51 (2005) 2609–2614.
Iritani E., Katagiri N., Sugiyama Y., Yagishita K., Analysis of flux decline behaviors in filtration of very dilute suspensions, AIChE Journal, 53 (2007a) 2275–2283.
Iritani E., Katagiri N., Sengoku T., Yoo K.M., Kawasaki K., Matsuda A., Flux decline behaviors in dead-end microfiltration of activated sludge and its supernatant, Journal of Membrane Science, 300 (2007b) 36–44.
Iritani E., Modeling and evaluation of pore clogging of membrane in membrane filtration, Kagaku Kogaku Ronbunshu, 35 (2009) 1–11.
Iritani E., Katagiri N., Tadama T., Sumi H., Analysis of clogging behaviors of diatomaceous ceramic membranes during membrane filtration based upon specific deposit, AIChE Journal, 56 (2010) 1748–1758.
Iritani E., Katagiri N., Sugiyama Y., Clogging properties of membrane pores in constant-rate and constant-pressure microfiltration of dilute colloids, Kagaku Kogaku Ronbunshu, 37 (2011) 323–326.
Iritani E., A review on modeling of pore-blocking behaviors of membranes during pressurized membrane filtration, Drying Technology, 31 (2013) 146–162.
Iritani E., Katagiri N., Tsukamoto M., Hwang K.J., Determination of cake properties in ultrafiltration of nano-colloids based on single step-up pressure filtration test, AIChE Journal, 60 (2014a) 289–299.
Iritani E., Katagiri N., Nakajima R., Hwang K.J., Cheng T.W., Cake properties of nanocolloid evaluated by variable pressure filtration associated with reduction in cake surface area, AIChE Journal, 60 (2014b) 3869–3877.
Iritani E., Katagiri N., Ishikawa Y., Cao D.Q., Cake formation and particle rejection in microfiltration of binary mixtures of particles with two different sizes, Separation and Purification Technology, 123 (2014c) 214–220.
Iritani E., Katagiri N, Takenaka T., Yamashita Y., Membrane pore blocking during cake formation in constant pressure and constant flux dead-end microfiltration of very dilute colloids, Chemical Engineering Science, 122 (2015) 465–473.
Ives K.J., Pienvichitr V., Kinetics of the filtration of dilute suspension, Chemical Engineering Science, 20 (1965) 965–973.
Jin Y., Ju Y., Lee H., Hong S., Fouling potential evaluation by cake fouling index: Theoretical development, measurements, and its implications for fouling mechanisms, Journal of Membrane Science, 490 (2015) 57–64.
Jonsson G., Prádanos P., Hernández A., Fouling phenomena in microporous membranes: Flux decline kinetics and structural modification, Journal of Membrane Science, 112 (1996) 171–183.
Juang R.S., Lin S.H., Peng L.C., Flux decline analysis in micellar-enhanced ultrafiltration of synthetic waste solutions for metal removal, Chemical Engineering Journal, 161 (2010) 19–26.
Katsoufidou K., Yiantsios S.G., Karabelas A.J., A study of ultrafiltration membrane fouling by humic acids and flux recovery by backwashing: Experiments and modeling, Journal of Membrane Science, 266 (2005) 40–50.
Keskinler B., Yildiz E., Erhan E., Dogru M., Bayhan Y.K., Akay G., Crossflow microfiltration of low concentration-nonliving yeast suspensions, Journal of Membrane Science, 233 (2004) 59–69.
Khirani S., Ben Aim R., Manero M.H., Improving the measurement of the modified fouling index using nanofiltration membranes (NF-MFI), Desalination, 161 (2006) 1–7.
Kim K.J., Chen V., Fane A.G., Ultrafiltration of colloidal silver particles: Flux, rejection, and fouling, Journal of Colloid and Interface Science, 155 (1993) 347–359.
Kim J., Shi W., Yuan Y., Benjamin M.N., A serial filtration investigation of membrane fouling by natural organic matter, Journal of Membrane Science, 294 (2007) 115–126.
Kimura S., Sourirajan S., Analysis of data in reverse osmosis with porous cellulose acetate membranes used, AIChE Journal, 13 (1967) 497–503.
Koo C.H., Mohammad A.W., Suja F., Meor Talib M.Z., Review of the effect of selected physicochemical factors on membrane fouling propensity based on fouling indices, Desalination, 287 (2012) 167–177.
Kozicki W., Chou C.H., Tiu C., Non-Newtonian flow in ducts of arbitrary cross-sectional shape, Chemical Engineering Science, 21 (1966) 665–679.
Kozicki W., Tiu C., Rao A.R.K., Filtration of non-Newtonian fluids, The Canadian Journal of Chemical Engineering, 46 (1968) 313–321.
Kozicki W., Rao A.R.K., Tiu C., Filtration of polymer solutions, Chemical Engineering Science, 27 (1972) 615–626.
Lee D.J., Filter medium clogging during cake filtration, AIChE Journal, 43 (1997) 273–276.
Lee S., Park P.K., Kim J.H., Yeon K.M., Lee C.H., Analysis of filtration characteristics in submerged microfiltration for drinking water treatment, Water Research, 42 (2008) 3109–3121.
Leu W.A., Tiller F.M., Experimental study of mechanism of constant pressure cake filtration: Clogging of filter media, Separation Science and Technology, 18 (1983) 1351–1369.
Li W.W., Sheng G.P., Wang Y.K., Lie X.W., Xu J., Yu H.Q., Filtration behaviors and biocake formation mechanism of mesh filters used in membrane bioreactors, Separation and Purification Technology, 81 (2011) 472–479.
Li F., Tian Q., Yang B., Wu L., Deng C., Effect of polyvinyl alcohol to model Extracellular Polymeric Substances (EPS) on membrane filtration performance, Desalination, 286 (2012) 34–40.
Lim A.L., Bai R., Membrane fouling and cleaning in microfiltration of activated sludge wastewater, Journal of Membrane Science, 216 (2003) 279–290.
Lim Y.P., Mohammad A.W., Influence of pH and ionic strength during food protein ultrafiltration: Elucidation of permeate flux behaviors, fouling resistance, and mechanism, Separation Science and Technology, 47 (2012) 446–454.
Liu Q.F., Kim S.H., Evaluation of membrane fouling models based on bench-scale experiments: A comparison between constant flowrate blocking laws and artificial neural net-

work (ANNs) model, Journal of Membrane Science, 310 (2008) 393–401.

Ma N., Zhang Y., Quan X., Fan X., Zhao H., Performing a microfiltration integrated with photocatalysis using an Ag-TiO_2/HAP/Al_2O_3 composite membrane for water treatment: Evaluating effectiveness for humic acid removal and anti-fouling properties, Water Research, 44 (2010) 6104–6114.

Madaeni S.S., Fane A.G., Microfiltration of very dilute colloidal mixtures, Journal of Membrane Science, 113 (1996) 301–312.

Mahdi F.M., Holdich R.G., Laboratory cake filtration testing using constant rate, Chemical Engineering Research and Design, 91 (2013) 1145–1154.

Maroudas A., Eisenklam P., Clarification of suspensions: A study of particle deposition in granular media, Part II—A theory of clarification, Chemical Engineering Science, 20 (1965) 875–888.

Masoudnia K., Raisi A., Aroujalinan A., Fathizadeh M., Treatment of oily wastewaters using the microfiltration process: Effect of operating parameters and membrane fouling study, Separation Science and Technology, 48 (2013) 1544–1555.

Matsumoto K., Hirata S., Ohya H., Microfiltration model considering incomplete pore blocking and incomplete capture of particles by cake, Kagaku Kogaku Ronbunshu, 18 (1992) 455–462.

Matsumoto K., Furuichi M., Nakamura K., Nittami T., Evaluation of water quality by the modified SDI in the membrane filtration process, Membrane, 34 (2009) 94–103.

Mohammadi T., Kohpeyma A., Sadrzadeh M., Mathematical modeling of flux decline in ultrafiltration, Desalination, 184 (2005) 367–375.

Mohd Amin I.N.H., Mohammad A.W., Marcom M., Peng L.C., Hilal N., Analysis of deposition mechanism during ultrafiltration of glycerin-rich solutions, Desalination, 261 (2010) 313–320.

Mondal S., De S., Generalized criteria for identification of fouling mechanism under steady state membrane filtration, Journal of Membrane Science, 344 (2009) 6–13.

Murase T., Iritani E., Cho J.H., Nakanomori S., Shirato M., Determination of filtration characteristics due to sudden reduction in filtration area of filter cake surface, Journal of Chemical Engineering of Japan, 20 (1987) 246–251.

Murase T., Iritani E., Cho J.H., Shirato M., Determination of filtration characteristics of power-law non-Newtonian fluids-solids mixtures under constant-pressure conditions, Journal of Chemical Engineering of Japan, 22 (1989) 65–71.

Murase T., Ohn, T., New decline pattern of filtrate flux in cross-flow microfiltration of dilute suspension, AIChE Journal, 42 (1996) 1938–1944.

Nagel R., Seawater desalination with polyamide hollow fibre modules at DROP, Desalination, 63 (1987) 225–246.

Nakakura H., Yamashita A., Sambuichi M., Osasa K., Electrical conductivity measurement of filter cake in dead-end ultrafiltration of protein solution, Journal of Chemical Engineering of Japan, 30 (1997) 1020–1025.

Nakamura K., Orie T., Matsumoto K., Response of zeta potential to cake formation and pore blocking during the microfiltration of latex particles, Journal of Membrane Science, 401–402 (2012) 274–281.

Nandi B.K., Moparthi A., Uppaluri R., Purkait M.K., Treatment of oily wastewater using low cost ceramic membrane: Comparative assessment of pore blocking and artificial neural network models, Chemical Engineering Research and Design, 88 (2010) 881–892.

Notebaert F.F., Wilms D.A., van Haute A.A., A new deduction with a larger application of the specific resistance to filtration of sludges, Water Research, 9 (1975) 667–673.

Okamura S., Shirato M., Liquid pressure distribution within cakes in the constant pressure filtration, Kagaku Kogaku, 19 (1955) 104–110.

Ozdemir B., Saatci A., Yenigun O., Evaluation of cake filtration biological reactors (CFBR) vs. membrane biological reactor (MBR) in a pilot scale plant, Desalination, 288 (2012) 135–144.

Palacio L., Ho C.C., Zydney A.L., Application of a pore-blockage—cake-formation model to protein fouling during microfiltration, Biotechnology and Bioengineering, 79 (2002) 260–270.

Palacio L., Ho C.C., Prádanos P., Hernández A., Zydney A.L., Fouling with protein mixtures in microfiltration: BSA-lysozyme and BSA-pepsin, Journal of Membrane Science, 222 (2003) 41–51.

Palencia M., Rivas B.L., Valle H., Size separation of silver nanoparticles by dead-end ultrafiltration: Description of fouling mechanism by pore blocking model, Journal of Membrane Science, 455 (2014) 7–14.

Park C., Kim H., Hong S., Choi S.I., Variation and prediction of membrane fouling index under various feed water characteristics, Journal of Membrane Science, 284 (2006) 248–254.

Pan Y., Wang T., Sun H., Wang W., Preparation and application of titanium dioxide dynamic membranes in microfiltration of oil-in-water emulsions, Separation and Purification Technology, 89 (2012) 78–83.

Persson A., Jönsson A.S., Zacchi G., Transmission of BSA during cross-flow microfiltration: Influence of pH and salt concentration, Journal of Membrane Science, 223 (2003) 11–21.

Polyakov Y.S., Depth filtration approach to the theory of standard blocking: Prediction of membrane permeation rate and selectivity, Journal of Membrane Science, 322 (2008) 81–90.

Polyakov Y.S., Zydney A.L., Ultrafiltration membrane performance: Effects of pore blockage/constriction, Journal of Membrane Science, 434 (2013) 106–120.

Prádanos P., Hernández A., Calvo J.I., Tejerina F., Mechanisms of protein fouling in cross-flow UF through an asymmetric inorganic membrane, Journal of Membrane Science, 114 (1996) 115–126.

Purkait M.K., DasGupta S., De S., Resistance in series model for micellar enhanced ultrafiltration of eosin dye, Journal of Colloid and Interface Science, 270 (2004) 496–506.

Purkait M.K., Bhattacharya P.K., De S., Membrane filtration of leather plant effluent: Flux decline mechanism, Journal of

membrane Science, 258 (2005) 85–96.
Rai P., Majumdar G.C., Sharma G., DasGupta S., De S., Effect of various cutoff membranes on permeate flux and quality during filtration of Mosambi (*Citrus Sinensis* (L.) Osbeck) juice, Transactions of The Institution of Chemical Engineers, Part C, Food and Bioproducts Processing, 84 (2006) 213–219.
Raspati G.S., Meyn T., Leiknes T., Analysis of membrane and cake layer resistances in coagulation: Constant flux dead-end microfiltration of NOM, Separation Science and Technology, 48 (2013) 2252–2262.
Reihanian H., Robertson C.R., Michaels A.S., Mechanism of polarization and fouling of ultrafiltration membranes by proteins, Journal of Membrane Science, 16 (1983) 237–258.
Rezaei H., Ashtiani F.Z., Fouladitajar A., Effects of operating parameters on fouling mechanism and membrane flux in cross-flow microfiltration of whey, Desalination, 274 (2011) 262–271.
Rodgers V.G.J., Oppenheim S.F., Datta R., Correlation of permeability and solute uptake in membranes of arbitrary pore morphology, AIChE Journal, 41 (1995) 1826–1829.
Ruohomäki K., Nyström M., Fouling of ceramic capillary filters in vacuum filtration of humic acid, Filtration + Separation, 37(1) (2000) 51–57.
Rushton A., The flow and filtration of non-Newtonian fluids (Part A), Filtration & Separation, 10 (1986) 41–43.
Ruth B.F., Studies in filtration, III. Derivation of general filtration equations, Industrial & Engineering Chemistry, 27 (1935) 708–723.
Ruth B.F., Correlating filtration theory with industrial practice, Industrial & Engineering Chemistry, 38 (1946) 564–571.
Salinas-Rodriguez S.G., Amy G.L., Schippers J.C., Kennedy M.D., The Modified Fouling Index Ultrafiltration constant flux for assessing particulate/colloidal fouling of RO systems, Desalination, 365 (2015) 79–91.
Sarkar B., De S., A combined complete pore blocking and cake filtration model for steady-state electric field-assisted ultrafiltration, AIChE Journal, 58 (2012) 1435–1446.
Sarkar B., A combined complete pore blocking and cake filtration model during ultrafiltration of polysaccharide in a batch cell, Journal of Food Engineering, 116 (2013) 333–343.
Schippers J.C., Hanemaayer J.H., Smolders C.A., Kostense A., Predicting flux decline of reverse osmosis membranes, Desalination, 38 (1981) 339–348.
Shirato M., Aragaki T., Mori R., Sawamoto K., Predictions of constant pressure and constant rate filtrations based upon an approximate correction for side wall friction in compression permeability cell data, Journal of Chemical Engineering of Japan, 1 (1968) 86–90.
Shirato M., Sambuichi M., Kato H., Aragaki T., Internal flow mechanism in filter cakes, AIChE Journal, 15 (1969) 405–409.
Shirato M., Aragaki T., Iritani E., Wakimoto M., Fujiyoshi S., Nanda S., Constant pressure filtration of power-law non-Newtonian Fluids, Journal of Chemical Engineering of Japan, 10 (1977) 54–60.
Shirato M., Aragaki T., Iritani E., Blocking filtration laws for filtration of power-law non-Newtonian fluids, Journal of Chemical Engineering of Japan, 12 (1979) 162–164.
Shirato M., Aragaki T., Iritani E., Analysis of constant pressure filtration of power-law non-Newtonian fluids, Journal of Chemical Engineering of Japan, 13 (1980) 61–66.
Sperry D.R., Note and correspondence: A study of the fundamental laws of filtration using plant-scale equipment, Industrial & Engineering Chemistry, 13 (1921) 1163–1164.
Srisukphun T., Chiemchaisri C., Yamamoto K., Modeling of RO flux decline in textile wastewater reclamation plants using variable fouling index, Separation Science and Technology, 44 (2009) 1704–1721.
Suarez J.A., Veza J.M., Dead-end microfiltration as advanced treatment for wastewater, Desalination, 127 (2000) 47–58.
Sun S., Yue Y., Huang X., Meng D., Protein adsorption on blood contact membranes, Journal of Membrane Science, 222 (2003) 3–18.
Sun X., Kanani D.M., Ghosh R., Characterization and theoretical analysis of protein fouling of cellulose acetate membrane during constant flux dead-end microfiltration, Journal of Membrane Science, 320 (2008) 372–380.
Takahashi K., Ohmori N., Ishi K., Yokota T., Cake formation and spatial partitioning in batch microfiltration of yeast, Journal of Chemical Engineering of Japan, 24 (1991) 372–377.
Taniguchi M., Kilduff J.E., Belfort J., Modes of natural organic matter fouling during ultrafiltration, Environmental Science & Technology, 37 (2003) 1676–1683.
Tettamanti B., Modeling and scaling of filtration in industry, International Chemical Engineering, 22 (1982) 561–571.
Thekkedath A., Naceur W.M., Kecili K., Sbai M., Elane A., Auret L., Suty H., Machinal C., Pontié M., Macroscopic and microscopic characterization of a cellulosic ultrafiltration (UF) membrane fouled by a humic acid cake deposit: First step for intensification of reverse osmosis (RO) pre-treatments, Comptes Rendus Chimie, 10 (2007) 803–812.
Tien C., Payatakes A.C., Advances in deep bed filtration, AIChE Jornal, 25 (1979) 737–759.
Tien C., Ramarao B.V., Revisiting the laws of filtration: An assessment of their use in identifying particle retention mechanisms in filtration, Journal of Membrane Science, 383 (2011) 17–25.
Tien C., Ramarao B.V., Yasarla R., A blocking model of membrane filtration, Chemical Engineering Science, 111 (2014) 421–431.
Tiller F.M., The role of porosity in filtration, I. Numerical methods for constant rate and constant pressure filtration based on Kozeny's law, Chemical Engineering Progress, 49 (1953) 467–479.
Tiller F.M., The role of porosity in filtration, Part 2, Analytical equations for constant rate filtration, Chemical Engineering Progress, 51 (1955) 282–290.
Tiller F.M., Cooper H.R., The role of porosity in filtration: IV. Constant pressure filtration, AIChE Journal, 6 (1960) 595–601.
Tiller F.M., Shirato M., The role of porosity in filtration: VI. New definition of filtration resistance, AIChE Journal, 10

(1964) 61–67.
Tiller F.M., Weber W., Davies O., Clogging phenomena in the filtration of liquefied coal, Chemical Engineering Progress, 77(Dec.) (1981) 61–68.
Todisco S., Peña L., Drioli, E., Tallarico P., Analysis of the fouling mechanism in microfiltration of orange juice, Journal of Food Processing and Preservation, 20 (1996) 453–466.
Tracey E.M., Davis R.H., Protein fouling of track-etched polycarbonate microfiltration membranes, Journal of Colloid and Interface Science, 167 (1994) 104–116.
van Reis R., Zydney A., Bioprocess membrane technology, Journal of Membrane Science, 297 (2007) 16–50.
Vera M.C.V., Blanco S.Á., García J.L., Rodríguez E.B., Analysis of membrane pore blocking models adapted to crossflow ultrafiltration in the ultrafiltration of PEG, Chemical Engineering Journal, 149 (2009) 232–241.
Vilker V.L., Colton C.K., Smith K.A., Concentration polarization in protein ultrafiltration, AIChE Journal, 27 (1981) 632–645.
Wang F., Tarabara V.V., Pore blocking mechanisms during early stages of membrane fouling by colloids, Journal of Colloid and Interface Science, 328 (2008) 464–469.
Wei C.H., Laborie S., Ben Aim R., Amy G., Full utilization of silt density index (SDI) measurements for seawater pretreatment, Journal of Membrane Science, 405–406 (2012) 212–218.
White D.A., The interpretation of the SDI for water solids content using the filtration equation, Transactions of the Institution of Chemical Engineers, Part B, Process Safety and Environmental Protection, 74 (1996) 137–140.
Wu J., He C., Zhang Y., Modeling membrane fouling in a submerged membrane bioreactor by considering the role of solid, colloidal and soluble components, Journal of Membrane Science, 397–398 (2012) 102–111.
Ye Y., Clech P.L., Chen V., Fane A.G., Jefferson B., Fouling mechanisms of alginate solutions as model extracellular polymeric substances, Desalination, 175 (2005) 7–20.
Yiantsios S.G., Karabelas A.J., An assessment of the Silt Density Index based on RO membrane colloidal fouling experiments with iron oxide particles, Desalination, 151 (2003) 229–238.
Yukseler H., Tosun I., Yetis U., A new approach in assessing slurry filterability, Journal of Membrane Science, 303 (2007) 72–79.
Yuan W., Kocic A., Zydney A.L., Analysis of humic acid fouling during microfiltration using a pore blockage – cake filtration model, Journal of Membrane Science, 198 (2002) 51–62.
Zeman L.J., Adsorption effects in rejection of macromolecules by ultrafiltration membranes, Journal of Membrane Science, 15 (1983) 213–230.
Zhong Z., Li W., Zing W., Xu N., Crossflow filtration of nanosized catalysis suspension using ceramic membranes. Separation and Purification Technology, 76 (2011) 223–230.
Zhou J., Wandera D., Husson S.M., Mechanisms and control of fouling during ultrafiltration of high strength wastewater without pretreatment, Journal of Membrane Science, 488 (2015) 103–110.

Author's short biography

Eiji Iritani

Eiji Iritani is currently Professor of Department of Chemical Engineering at Nagoya University. He received his Docter degree of Engineering from Nagoya University in 1981. His research interests are in the area of cake filtration, membrane filtration, deliquoring due to expression, sedimentation, centrifugation, and water treatments based on solid-liquid separation technology.

Nobuyuki Katagiri

Nobuyuki Katagiri is currently Assistant Professor of Department of Chemical Engineering at Nagoya University. He received his Doctor degree of Agriculture from Gifu University in 1998. His research interests are in the area of filtration and expression of biologically-derived materials, and waste water treatments.

KONA Powder and Particle Journal No. 33 (2016) 203–218/Doi:10.14356/kona.2016001 Original Research Paper

Preparation of LaB_6 Powders via Calciothermic Reduction using Mechanochemistry and Acid Leaching †

Duygu Ağaoğulları *, Özge Balcı, M. Lütfi Öveçoğlu and İsmail Duman

[1] *Istanbul Technical University, Faculty of Chemical and Metallurgical Engineering, Department of Metallurgical and Materials Engineering, Particulate Materials Laboratories (PML), Turkey*

Abstract

This study reports a room temperature mechanochemical route for the synthesis of LaB_6 powders originated from related metal oxide powders as La_2O_3 and B_2O_3. Ca granules and B_2O_3 powders were respectively used as reducing agent and boron source in the experiments. This study is actually meaningful to create added value by using the native boron source of Turkey for the production of high-technology boron materials. Milling duration as the most important parameter of mechanochemistry was examined to reveal the ideal production conditions. Mechanochemically synthesized powders were subjected to selective HCl leaching in order to eliminate unwanted phases. Thermochemical software of HSC Chemistry™ program was utilized to determine the reaction probability and to estimate the predicted products. Characterization investigations were carried out by X-ray diffractometer (XRD), differential scanning calorimeter (DSC), particle size analyzer (PSA), stereomicroscope (SM), scanning electron microscope (SEM), transmission electron microscope/energy dispersive spectrometer (TEM/EDS) and atomic absorption spectrometer (AAS). Nanosized LaB_6 powders were achieved with/without an insignificant amount of $Ca_3(BO_3)_2$ phase via mechanochemistry in a high-energy ball mill for 3 h and via leaching with 4 M and 6 M HCl. Lastly, the experimental outputs obtained by a calciothermic reduction were compared with those of magnesiothermic reduction.

Keywords: lanthanum hexaboride powders, calciothermic reduction, mechanochemistry, room temperature process, lanthanum oxide, boron oxide

1. Introduction

Materials based on boron compounds have been explored since 1950s because of their superior properties in respect to chemical bonding, crystal structure and phonon and electron conduction. Especially, rare-earth metal hexaborides have numerous useful physical and chemical characteristics which make them important to investigate (Post et al., 1956; Futamoto et al., 1980; Otani and Ishizawa, 1996; Balakrishnan et al., 2004; Selvan et al., 2008; Wang et al., 2010; Ji et al., 2011; Brewer et al., 2011; Aprea et al., 2013).

Lanthanum hexaboride (LaB_6) has attracted significant interest in the last 60 years amongst transition metal borides and rare-earth metal borides (Samsonov et al., 1963; Paderno et al., 1979; Xu et al., 2012; Dou et al., 2012). LaB_6 is a refractory ceramic material characterized by high melting point, high strength, high chemical and thermal stability, low vapor pressure, low electronic work function, low resistivity, low thermal expansion coefficient, high transmission stability, high current and voltage capability and high neutron absorbability (Gao et al., 2005; Xu et al., 2006; Zhang et al., 2008; Selvan et al., 2008). LaB_6 is built from B_6 type crystal structure (octahedrons in cubic hexaboride) in which boron sublattice is electron-deficient and requires electron transfer from the metal atoms in order to be stabilized (Swanson and McNeely, 1979; Mitterer et al., 1996). Furthermore, these boron octahedrons are united by very strong covalent bonds giving the crystals their characteristic hardness (Ji et al., 2011). LaB_6 is defined as a dense Kondo material which show several interesting phases such as antiferro-quadrupolar ordered phase and antiferromagnetic ordered phase in the effect of magnetic field and temperature (Tanaka et al., 2004; Carlsson et al., 2005; Jha et al., 2012). According to the phase diagram of the La-B system, there is one congruently melting LaB_6 compound at 2715 °C, a peritectic LaB_4 phase at 1800 °C and an unstable LaB_9 phase at ~2007 °C (Massalski et al., 1990; Schlesinger et al., 1999).

All these superior properties make LaB_6 suitable to use as components of high-energy optical systems, sensors for high resolution detectors, electrical coatings for resis-

† Received 17 December 2014; Accepted 27 January 2015
J-STAGE Advance published online 10 April 2015
[1] Ayazağa Campus, 34469 Maslak, Istanbul, Turkey
* Corresponding author: Duygu Ağaoğulları;
E-mail: bozkurtdu@itu.edu.tr
TEL: +90-212-285-6893 FAX: +90-212-285-3427

tors, coatings for high-current hot cathodes, thermionic materials and to use in nuclear technology (Balakrishnan et al., 2004; Bao et al., 2011). It can also be used in wear and corrosion resistant hard coatings for decoration of consumer products such as eye-glass frames and wrist-watch casings (Mitterer et al., 1996; Selvan et al., 2008). Single crystalline LaB_6 nanowires are one of the most widely used electron emitter in electron gun, which can offer about 10 to 15 times higher brightness, higher emission stability, lower energy spread and longer service life than the tungsten cathodes utilized in a large variety of devices such as high-resolution electron microscopes, electron beam writing units, vacuum electron beam welding machines, microwave tubes, free electron lasers, X-ray tubes, electron beam surface reforming and electron beam lithography devices (Ahmed et al., 1975; Perkins et al., 1999; Chen et al., 2004; Wen et al., 2004; Zhang et al., 2006, 2007, 2008; Wang et al., 2009; Qin et al., 2010; Bao et al., 2011). Moreover, LaB_6 nanomaterials are candidates to motivate the new designs of nanoscale electronic devices operated at high temperatures with the need of enhanced electron collection and injection properties (Brewer et al., 2011). Also, LaB_6 has exceptional thermoelectric properties at low temperatures providing their usage in solid-state cryocooling, thermoelectric refrigerators, generators and single-photon detectors operating at temperatures near to the boiling point of liquid helium which serve in technical applications including quantum computing, quantum cryptography, homeland security, defect control in microchips, astronomy, chemical analysis and particle physics (Carlsson et al., 2005; Petrosyan et al., 2012; Jha et al., 2012). Recently, LaB_6 nanoparticles have been proved as effective materials in near-infrared absorption enabling application in reduction of solar heat gain (Yuan et al., 2011). Additionally, LaB_6 is considered as a potential grain refining agent in Al alloys due to its role as an effective, stable and reliable nucleation substrate for Al during the solidification process (Li et al., 2012).

Many production techniques have been applied in the preparation of lanthanum hexaboride (Baranovskiy et al., 2007; Loboda et al., 2009). Traditionally, LaB_6 has been synthesized by high temperature reaction processes such as direct solid-phase reaction of the corresponding elements or compounds, carbothermal reaction of the lanthanum oxide and B or boron carbide (B_4C) method (Post et al., 1956). In industry, carbothermal reduction and boron carbide method have been widely used due to their low cost and simple equipment (Dou et al., 2011; Hasan et al., 2013). However, disadvantages in these methods such as high content of carbon or high processing temperature limit the possibility of preparing LaB_6 powders with high purity and small particle sizes (Dou et al., 2012). Moreover, powders prepared by these conventional methods have generally poor sinterability (Dou et al., 2012). Floating zone method and electrosynthesis have been also developed conventionally in order to obtain LaB_6 crystals (Verhoeven et al., 1976). Essentially, floating zone method has been carried out to produce single crystals by using laser or RF heating (Otani and Ishizawa, 1996; Otani et al., 2000). Electrosynthesis of LaB_6 crystals has been applied by molten salt technique from an electrolyte consisting of La chlorides/oxides, boron sources (B_2O_3, $Li_2B_4O_7$, etc.) and chloride/fluoride agents (LiCl, LiF, etc.) (Amalajyothi et al., 2008, 2011). For a number of years, researchers have tried to obtain LaB_6 in different forms such as particles, whiskers, rods or cubes using various fabrication techniques. Recently, nanosized (nanocubes and nanorods) or submicron LaB_6 powders have been obtained by using low temperature synthesis in an autoclave and self-propagating high-temperature synthesis (SHS) methods (Ji et al., 2011; Dou et al., 2012). Autoclave systems provide an alternative route for synthesizing LaB_6 at lower temperatures than used in traditional methods (Wang et al., 2010). SHS methods have high reaction speed, simple equipment and low energy consumption but after ignition, the reaction process becomes uncontrolled which results in the occurrence of intermediate phases in the reaction products (Dou et al., 2011). LaB_6 whiskers, wires, tubes and obelisks in nano- or micro-scales have been produced by chemical vapor deposition technique (CVD) (Motojima et al., 1978; Zhang et al., 2006). CVD methods include self-catalyst or metal-catalyst (Au, Pt, etc.) growth of LaB_6 on a substrate based on the catalytic reaction of La element/compound containing powders and boron (BCl_3, $B_{10}H_{14}$, etc.), hydrogen and argon containing gas mixtures (Ji et al., 2011).

It is significant to develop an efficient method of preparing technologically important LaB_6 powders in high purity, small particle size and various morphologies. It has been attracting more attentions to find new synthesis strategies with low reaction temperature, easy to handle precursors, simple process control, less equipment requirements and low cost. Compared with the above-mentioned production techniques, mechanochemistry is a novel, simple and room temperature process which enables a great degree of controlling the product microstructure (content, shape, size, etc.) and obtaining highly pure materials (Suryanarayana, 2001). To the best of our knowledge, there is recently one report on the fabrication of LaB_6 powders via magnesiothermic reduction forced by ball milling process (Ağaoğulları et al., 2012b; Ağaoğulları, 2014).

In this study, LaB_6 powders originated from related metal oxide powders (as La_2O_3 and B_2O_3) were synthesized at room temperature, via calciothermic reduction using mechanochemistry. Consequently, this study will contribute the first results of the mechanochemically synthesized LaB_6 powders from La_2O_3-B_2O_3-Ca blends to the archival literature.

2. Experimental procedure

The experimental procedure of this study comprises the identification of raw materials, the step-by-step synthesis of LaB_6 powders, the purification treatments conducted on the synthesized powders and the characterization investigations carried out at each stage of the overall process.

2.1 Raw materials

The synthesis of LaB_6 was originated from its oxide powders such as La_2O_3 (ABCR™, in purity of 99.99 %). B_2O_3 (ETI Mine, in purity of 98 %) powders were used as a native boron source for the formation of boride phase. Ca (Alfa Aesar™, in purity of 99.5 %) granules were utilized as a reducing agent in order to examine their influence on the production of LaB_6. The images of all raw materials were captured by using a Zeiss™ Discovery.V12 stereomicroscope (SM) coupled with a Zeiss™ Axiocam ERc5s high resolution digital camera. SM images of the raw materials are represented in **Fig. 1(a)** through **Fig. 1(c)**. **Figs. 1(a)** and **(b)** more or less give an idea about the average particle sizes of La_2O_3 and B_2O_3 since their SM images respectively have the magnification scale (25X) of 200 and 500 µm. However, **Fig. 1(c)** whose magnification scale (8X) is 1000 µm obviously shows the average size of the Ca granules as 3 mm.

The crystalline phases of all raw materials were identified using a Bruker™ D8 Advanced Series X-ray diffractometer (XRD) with CuKα (1.54060 Å) radiation in the 2θ range of 10–90° incremented at a step size of 0.02° at a rate of 2°/min. International Center for Diffraction Data® (ICDD) powder diffraction files were utilized for the crystalline phase identification of the raw materials. The XRD patterns of La_2O_3, B_2O_3 and Ca granules are illustrated in **Fig. 2(a)** through **Fig. 2(c)**, respectively. Each figure shows diffraction peaks belonging only to the pure material with no trace of impurities. Although **Fig. 2(a)** exhibits intense crystalline peaks belonging to its content, **Fig. 2(b)** shows the characteristic peak structure of amorphous B_2O_3. The XRD peaks of Ca given in **Fig. 2(c)** have low intensities arising from its granule form which was very difficult to grind in an agate mortar applied for the proper analysis in the powder diffractometer.

Particle size measurements were conducted in a Malvern™ Mastersizer 2000 particle analyzer using distilled water as the aqueous media in order to determine the accurate particle sizes of the raw materials having powder forms. **Figs. 3(a)** and **(b)** represent the respective particle size distributions of the La_2O_3 [$d(0.1) = 7.5$ µm, $d(0.5) = 28.8$ µm, $d(0.9) = 67.9$ µm] and B_2O_3 [$d(0.1) = 268.5$ µm, $d(0.5) = 438.8$ µm, $d(0.9) = 708.2$ µm] powders. As seen in **Figs. 3(a)** and **(b)**, the average particle sizes of the La_2O_3 and B_2O_3 starting powders were measured as 33.6 µm and 466.9 µm, respectively.

Powder blends containing stoichiometric amounts of reactants for synthesizing LaB_6 powders were prepared according to the ideal reduction reaction given in Eq. (1).

$$La_2O_3 + 6B_2O_3 + 21Ca \rightarrow 2LaB_6 + 21CaO \quad (1)$$

Fig. 1 SM images of the raw materials: **a**, La_2O_3, **b**, B_2O_3 and **c**, Ca.

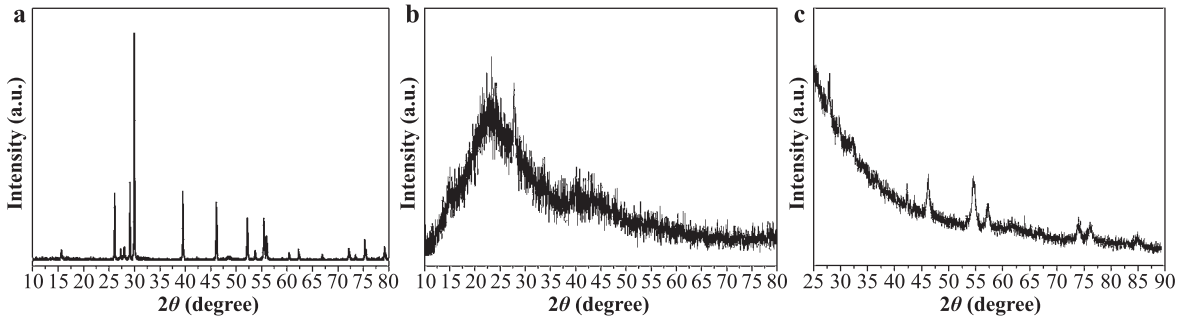

Fig. 2 XRD patterns of the raw materials: **a**, La_2O_3, **b**, B_2O_3 and **c**, Ca.

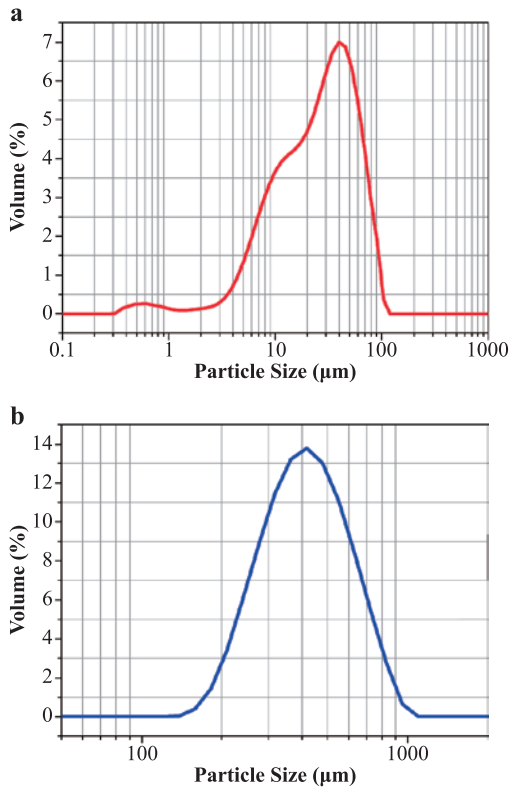

Fig. 3 Particle size distributions of the raw materials having powder forms: **a**, La_2O_3 and **b**, B_2O_3.

For each run, powder batches of 6 g were weighed in a Precisa^{TM} XB320M sensitive balance (precision: 0.001 g). Powder batches contained 1.233 g La_2O_3, 1.581 g B_2O_3 and 3.186 g Ca in regard of the 1.543 g LaB_6 formation reaction in Eq. (1). The prepared powder batches are hereafter referred to as La_2O_3-B_2O_3-Ca powder blends.

2.2 Mechanochemical synthesis

The prepared La_2O_3-B_2O_3-Ca powder blends were homogenized in a WAB^{TM} T2C Turbula blender for 1 h prior to mechanochemical synthesis experiments. The homogenized powder blends were mechanochemically synthesized by using a multi-axial and vibratory high-energy ball mill, Spex^{TM} 8000D Mixer/Mill, with a rotation speed of 1200 rpm. Non-milled powders, homogenized but not subjected to mechanochemical synthesis, were hereafter referred to as-blended (ab) powders and were used as references for the comparison with the milled ones.

In the mechanochemical synthesis experiments, ball-to-powder weight ratio (BPR) was chosen as 10:1. The milling container was a hardened steel vial with a capacity of 50 ml and the milling media was 50 pieces hardened steel balls with a diameter of 6 mm. Ar gas (Linde^{TM}, in purity of 99.999 %) was preferred as the milling atmosphere. The milling vials were evacuated to about 10^{-2} Pa and back filled with Ar gas in a Plaslabs^{TM} glove box to prevent surface oxidation and to prevent contamination of powder particles with oxide and nitride phases arising from the presence of air. After sealing the vials, milling was continually conducted at different durations up to 3 h. Preliminary experiments carried out intermittently and continuously up to a certain milling duration resulted in different products because the complete reaction took place by means of the internal heat generated from the repeated collisions of the reactant particles. The milled powders were unloaded again under Ar atmosphere in the glove-box. They are hereafter referred to as mechanochemically synthesized La_2O_3-B_2O_3-Ca powders.

2.3 Selective acid leaching

Mechanochemically synthesized La_2O_3-B_2O_3-Ca powders in which the reduction reaction completed contained LaB_6, CaO, etc. phases together as the intermediate products. Selective HCl (Merck^{TM}, in concentration of 37 %) leaching was applied on these products under the effect of ultrasonic stirring and heating using a Bandelin Sonorex^{TM} RK-100 H ultrasonic bath due to the fact that LaB_6 is insoluble in HCl. Leaching treatment enabled the removal of the unwanted phases and also Fe impurity which were worn off from the milling vial and milling balls. 4 M and 6 M HCl were used as the leaching solutions. This means that the intermediate products were leached using excess HCl molarity with the intention of obtaining pure LaB_6 powders. After a series of pre-experiments, leaching parameters such as solid-to-liquid ratio of the leaching solution, leaching duration and leaching temperature were fixed respectively to 1 g/10 cm^3, 30 min and 80 °C. During the first few seconds of the leaching treatments, the intermediate products violently reacted with the leaching solutions, arising from the high solubility of CaO in HCl solution as in the reactions given in Eqs. (2)–(4).

$$CaO + H_2O \rightarrow Ca(OH)_2 \quad (2)$$

$$CaO + 2HCl \rightarrow CaCl_2 + H_2O \quad (3)$$

$$Ca(OH)_2 + 2HCl \rightarrow CaCl_2 + 2H_2O \quad (4)$$

At the end of leaching treatment, the solutions containing insoluble solids were subjected to repeated centrifuging in a Hettich^{TM} Rotofix 32A centrifuge with a rotation speed of 3500 rpm for 30 min, repeated decanting and repeated washing with distilled water and lastly remained solids were dried under air in a FN 500 stove at 120 °C for 24 h. Supernatant liquids decanted from the solids after each centrifuging-decanting-washing treatment were collected into a volumetric flask and were equated to 150 ml with distilled water for the subsequent instrumental analysis. After each centrifuging-decanting-washing treatment, a few drop of leaching solution was added into

a 1 M $AgNO_3$ solution (Fluka™, in purity of 99.5 %) due to the detection of chlorine by precipitating AgCl and these treatments were repeated until any AgCl precipitation was not detected. Since the leaching process was carried out by using excess HCl molarity, the HCl adsorption on the boride powders can be also prevented by this detection method. Moreover, pH measurements were carried out on the supernatant liquids decanted from the solids after the last washing procedure, by using Thermo Scientific™ Orion Star A211 pH meter. The measured pH values varied between 5.5 and 6.5, indicating that there was not residual HCl in the media at the end of the repeated treatments. These findings conformed well to the results of AgCl precipitation method. So, the final products originated from the mechanochemically synthesized and leached La_2O_3-B_2O_3-Ca powders.

2.4 Characterization

XRD investigations of the as-blended, mechanochemically synthesized and leached powders were performed in a Bruker™ D8 Advanced Series powder diffractometer and in a PANalytical™ X'Pert³ powder diffractometer using the same conditions for the raw materials. As-blended and mechanochemically synthesized powders were imaged by the same stereomicroscope utilized for the raw materials. Particle size measurement was conducted on the leached powders using a Microtrac™ Nano-flex particle size analyzer (PSA) equipped with a Bandelin Sonopuls™ ultrasonic homogenizer. Thermal properties of the as-blended and mechanochemically synthesized powders were examined in a TA™ Instruments SDT Q600 differential scanning calorimeter (DSC): For each run, 15 mg of powders was placed in an alumina crucible and heated up to 1100 °C at a heating rate of 10 °C/min under Ar atmosphere. After DSC analyses, mechanochemically synthesized and heated powders were subjected to an additional XRD analysis for detecting the obtained phases. Microstructural characterizations and energy dispersive spectroscopy (EDS) analyses of the mechanochemically synthesized and leached powders were carried out using a Hitachi™ TM-1000 scanning electron microscope (SEM) operated at 15 kV and also using a Jeol™-JEM-2000EX transmission electron microscope (TEM) operated at 160 kV. For SEM analysis, the specimens were prepared by following the procedure of dissolving the powders in C_2H_5OH (Merck™, in purity of 99.9 %), syringing them onto a base plate, drying them in air and coating their surfaces with a thin layer of gold using a Polaron™ SC7620 Sputter Coater to enhance their conductivities. For TEM analysis, the particles were dispersed in the C_2H_5OH and a drop of it was taken on a porous carbon film supported on a copper grid and dried in a Jingke™ Scientific Instrument vacuum oven. EDS results were reported as the arithmetic mean of three different measurements taken from the same region in the sample. Furthermore, the amounts of elements (B, Ca and Fe) in the supernatant liquid after the purification by leaching process were analyzed in a Perkin Elmer™ 1100B atomic absorption spectrometer (AAS).

3. Results and discussion

HSC Chemistry™ Ver. 4.1 program was utilized for the reaction interpretations of the La_2O_3-B_2O_3-Ca system. The Gibbs free energy change and the enthalpy change versus temperature curves of the La_2O_3-B_2O_3-Ca system up to 2000 °C were graphed by using thermochemical software and they were illustrated in **Fig. 4**. The reaction has a large negative free energy change between −4100 and –2700 kJ in the temperature range of 0–2000 °C. It means that the reaction in Eq. (1) takes place spontaneously and therefore it is thermodynamically feasible at room temperature and above. Furthermore, a large negative enthalpy change between –4150 and –4510 kJ in the temperature range of 0–2000 °C implies that a large amount of heat is released during the occurrence of the reaction. It can be predicted that the vial temperature will significantly increase during milling due to these exothermic reactions. As seen in **Fig. 4**, the slope of the enthalpy change-temperature curve varies at some intervals. This is likely due to the melting of B_2O_3 at 450 °C, the formation of calcium borate phases in different compositions (CaB_2O_4, CaB_4O_7, CaB_6O_{10}, $Ca_2B_2O_5$, $Ca_2B_6O_{11}$ and $Ca_3B_2O_6$) at 600–1000 °C, the melting of Ca at 840 °C and the boiling of Ca at 1485 °C (Chen et al., 2008; Erfani et al., 2012).

It is already known from our previous study conducted on the La_2O_3-B_2O_3-Mg system that its related reaction has a large negative free energy change between –3300 and –1700 kJ and a large enthalpy change between –3440 and –3930 kJ, in the temperature range of 0–2000 °C (Ağaoğulları et al., 2012b). Besides, the slope of the enthalpy change-temperature curve for the La_2O_3-B_2O_3-Mg system arises from the melting of B_2O_3 at 450 °C, the melting of Mg at 650 °C, the formation of magnesium borate phases in different compositions (MgB_4O_7, $Mg_2B_2O_5$ and $Mg_3B_2O_6$) at 700–1000 °C and the boiling of Mg at 1095 °C (Ağaoğulları et al., 2012a; 2012b). On the basis of the enthalpy changes calculated by thermochemical software in case of using Ca or Mg as a reducing agent, it can be stated that calcium borate phases emerged at about 100 °C lower temperatures than those of magnesium borate phases. Furthermore, it is clearly understood that the calciothermic reduction of related oxides is more favorable than their magnesiothermic reduction since their free energy difference at the same temperature is about 800–

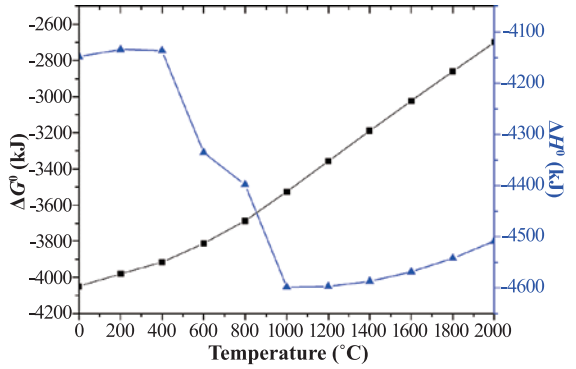

Fig. 4 The Gibbs free energy change (■) and enthalpy change (▲) versus temperature curves of the reaction given in Eq. (1).

1000 kJ. Thus, the use of Ca instead of Mg as a reductant seems to be more suitable in the synthesis of LaB_6 powders according to the thermodynamic calculations. However, the calcium borates regarded as unwanted phases in the boride synthesis form in several compositions at relatively lower temperatures than those of magnesium borates and hence their negative influence on the production step could be considered as a probability. It should be also noted that the results of the thermodynamic calculations show only the equilibrium phase composition at room and elevated temperatures without considering synthesis history and reaction kinetics. Actually, mechanochemical synthesis process is related to the repeated fracturing and repeated welding mechanism. Besides, the contact points between the particles provide favorable conditions for the formation of the products. Due to the fact that mechanochemical synthesis process is far from equilibrium, synthesized phases can not be expected to have complete consistence with the thermodynamically calculated phases.

Figs. 5(a) through **(g)** represents the XRD patterns of the as-blended and mechanochemically synthesized La_2O_3-B_2O_3-Ca powders using a 10:1 BPR in a Spex^{TM} 8000D Mixer/Mill up to a milling duration of 3 h.

Since Ca granules had an average size of 3 mm, they were milled for 30 min prior to the homogenization treatment, in the same conditions (BPR, media, atmosphere and container of milling, type and speed of mill, etc.) with those of mechanochemical synthesis experiments in order to obtain reduction in their sizes. According to **Fig. 5(a)**, as-blended powders contain La_2O_3 (ICDD Card No: 71-5408, Bravais lattice: primitive hexagonal, a = b = 0.393 nm, c = 0.614 nm), B_2O_3 (ICDD Card No: 76-1655, Bravais lattice: primitive hexagonal, a = b = 0.433 nm, c = 0.839 nm) and $Ca(OH)_2$ (ICDD Card No: 72-0156, Bravais lattice: primitive hexagonal, a = b = 0.358 nm, c = 0.489 nm) phases. Although B_2O_3 has a large characteristic amorphous peak in the 2θ range of 15–40° (**Fig. 2(b)**), it can be seen very slightly at the

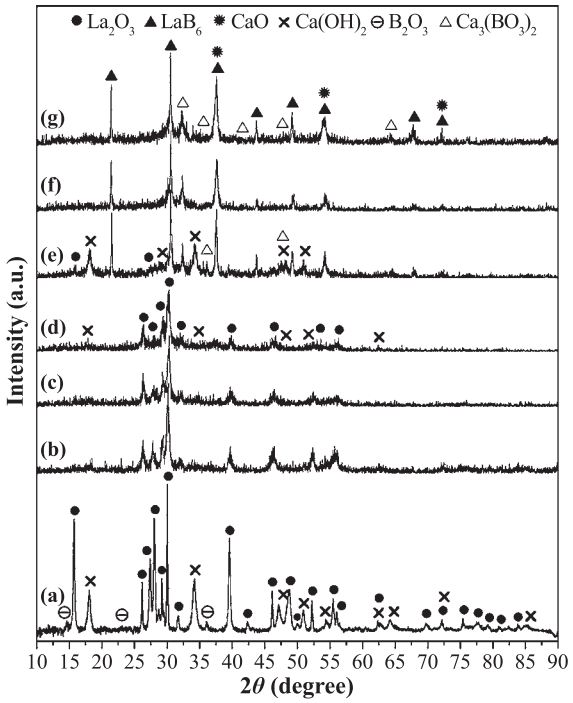

Fig. 5 XRD patterns of the as-blended La_2O_3-B_2O_3-Ca powders and those mechanochemically synthesized for different durations: **(a)** as-blended, **(b)** 30 min, **(c)** 45 min, **(d)** 1 h, **(e)** 1.5 h, **(f)** 2 h and **(g)** 3 h.

same range in the XRD pattern of the as-blended powders (**Fig. 5(a)**) with the peaks of other phases. It is well known that Ca powders easily absorb humidity and form calcium hydroxide at room temperature. Milled Ca powders reacted with humidity during handling in the laboratory atmosphere and hence $Ca(OH)_2$ phase was observed instead of Ca in the XRD pattern of the as-blended powders. As seen in **Figs. 5(b)**, **(c)** and **(d)**, mechanochemically synthesized La_2O_3-B_2O_3-Ca powders for 30 min, 45 min and 1 h durations have La_2O_3 and $Ca(OH)_2$ phases, indicating that there is still no reaction between the contacting particles. However, the intensities of these phases decrease as milling duration increases from 30 min to 1 h. This designates a gradual decrease in their crystallite sizes and an increase in their lattice deformations, which means that the reaction is getting closer step by step. Unlike **Fig. 5(a)**, no slight peaks belonging to the B_2O_3 phase can be detected in the XRD patterns of the 30 min, 45 min and 1 h milled powders (**Figs. 5(a)–(c)**), whose absence is attributed to its further amorphization during mechanochemical synthesis. Besides, there are very small incubations of LaB_6 (ICDD Card No: 34-0427, Bravais lattice: primitive cubic, a = b = c = 0.416 nm) and CaO (ICDD Card No: 70-5490, Bravais lattice: face-centered cubic, a = b = c = 0.482 nm) phases at about 37.5° at the end of 1 h milling (**Fig. 5(d)**). Further 30 min milling (**Fig. 5(e)**) results in LaB_6, CaO and $Ca_3(BO_3)_2$ (ICDD Card No: 70-0868, Bravais lattice: primitive rhombohedral, a = b = 0.864 nm, c = 1.185 nm)

phases in addition to very small amounts of unreacted La_2O_3 and $Ca(OH)_2$. X-ray reflections for the LaB_6 phase comprise eight peaks at values of 21.354°, 30.387°, 37.445°, 43.517°, 48.969°, 53.995°, 67.564° and 71.757° which are respectively indexed as (100), (110), (111), (200), (210), (211), (300) and (310) family of planes. After milling for 2 h, La_2O_3 and $Ca(OH)_2$ phases disappear and the composition of the mechanochemically synthesized powders includes only LaB_6, CaO and $Ca_3(BO_3)_2$ phases (**Fig. 5(f)**). The formation mechanism of $Ca_3(BO_3)_2$ phase can be explained with the reaction of B_2O_3 and CaO particles in regard of Eq. (5). However, the emergence of $Ca_3(BO_3)_2$ phase is unexpected considering the theoretical products of the ideal reduction reaction given in Eq. (1).

$$3CaO + B_2O_3 \rightarrow Ca_3(BO_3)_2 \quad (5)$$

As compared with the mechanochemical synthesis of La_2O_3-B_2O_3-Mg powder blends using the same milling conditions, it is obvious that calciothermic reduction provides a complete reaction 45 min earlier than that of magnesiothermic one in which LaB_6 and MgO phases occurred after milling for 2 h 45 min (Ağaoğulları et al., 2012b). Dissimilar to the magnesiothermic reduction of La_2O_3 and B_2O_3 powder blends, milled products of the calciothermic reduction contain a borate compound of the reducing agent since Ca is more favorable to form borate phase than Mg. **Fig. 5(g)** does not show any difference in the phase types of the 3 h milled powders in comparison with **Fig. 5(f)** because LaB_6, CaO and $Ca_3(BO_3)_2$ are still in the microstructure. However, there is a remarkable increase in the intensities of LaB_6 and CaO phases. On the basis of this intensity increment, extended milling durations up to 5 h were conducted on the La_2O_3-B_2O_3-Ca powder blends: Broadening of the LaB_6 and CaO peaks were observed instead of further intensity increment. It means that prolonged milling time does not contribute to the chemical reaction anymore after 3 h, but it contributes to the size reduction of the particles. Additionally, it should be stated that the actual mechanochemical reaction is different than the ideal reduction reaction in Eq. (1). So, the actual mechanochemical reaction in equilibrium amounts can be indicated as in Eq. (6) on the basis of the experimental results in **Fig. 5**.

$$La_2O_3 + 7B_2O_3 + 21Ca \rightarrow 2LaB_6 + 18CaO + Ca_3(BO_3)_2 \quad (6)$$

The ideal reduction reaction in Eq. (1) includes 6 moles of B_2O_3 whereas 7 moles of B_2O_3 is present in the actual reaction to represent the formation of $Ca_3(BO_3)_2$ phase. Due to the fact that the initial powder blends were prepared in regard of ideal reaction in Eq. (1) without considering the occurrence of borate phase, it should be also mentioned that the obtained LaB_6 phase can include an amount of sub-boride phases such as $La_{0.983}B_6$ (ICDD Card No: 70-8265, Bravais lattice: primitive cubic, a = b = c = 0.41561 nm), $LaB_{5.83}$ (ICDD Card No: 78-2381, Bravais lattice: primitive cubic, a = b = c = 0.41566 nm), $LaB_{5.832}$ (ICDD Card No: 75-1414, Bravais lattice: primitive cubic, a = b = c = 0.41566 nm), $LaB_{5.784}$ (ICDD Card No: 75-1402, Bravais lattice: primitive cubic, a = b = c = 0.41569 nm) and $LaB_{5.892}$ (ICDD Card No: 75-1415, Bravais lattice: primitive cubic, a = b = c = 0.41571 nm). The possibility of containing a sub-boride phase such as LaB_{6-x} is higher than that of $La_{1-x}B_6$. Because an amount of $Ca_3(BO_3)_2$ emergence and 1 mole lack of B_2O_3 according to the reaction in Eq. (5) could decrease the number of boron atoms for the boride formation. Although the use of Ca as a reductant provided shorter reaction duration than that of Mg, it could change the composition and hence the quality of the boride products, considering the formation probability of sub-borides.

Figs. 6(a) through **(g)** shows the SM images of the as-blended and mechanochemically synthesized La_2O_3-B_2O_3-Ca powders, for different durations up to 3 h. SM images can be helpful to control the reaction proceeding from the general appearance of the powders. The difference between as-blended and milled powders is clearly seen from **Figs. 6(a)–(g)**. As-blended powders contain white La_2O_3, B_2O_3 and $Ca(OH)_2$ clusters in the microstructure (**Fig. 6(a)**). After 30 min milling, white powders turned to gray with an indication of cluster disappearance and size reduction (**Fig. 6(b)**). The microstructures of the 30 min, 45 min and 1 h milled powders are very similar (**Figs. 6(b)–(d)**) in accordance with the XRD patterns in **Figs. 5(b)–(d)** exhibiting the same phases. The blurred SM images in **Figs. 6(b)–(d)** seem as $Ca(OH)_2$ having the highest weight ratio in the overall powder blend (~53 %) covered the La_2O_3 and B_2O_3 particles during milling process. As compatible with the XRD pattern in **Fig. 5(e)**, the microstructure changed after 1.5 h milling (**Fig. 6(e)**) in which the reaction took place but unreacted La_2O_3 and $Ca(OH)_2$ are still present. As the reaction completely took place at the 2 h milling duration without leaving unreacted La_2O_3 and $Ca(OH)_2$ behind (**Fig. 5(f)**), the color of the powders turned to dark and its morphology changes to a more stable agglomerated form (**Fig. 6(f)**) in which small LaB_6 particles are embedded in CaO and $Ca_3(BO_3)_2$.

The SM images in **Figs. 6(f)** and **(g)** are almost the same with each other since they only have LaB_6, CaO and $Ca_3(BO_3)_2$ phases after the complete reaction obtained at 2 h and after extended milling up to 3 h. It should be noted that the kinetics or the overall rate of the mechanochemical synthesis process depends on the kinetics of the milling in which newly fractured surfaces become active for the reaction initiated by the reducing agent. Mean-

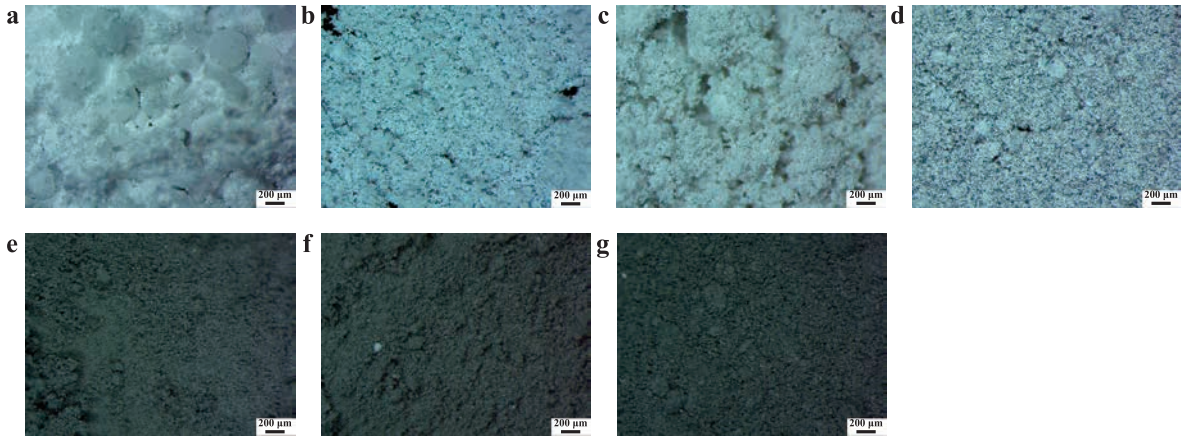

Fig. 6 SM images of the as-blended La_2O_3-B_2O_3-Ca powders and those mechanochemically synthesized for different durations: **a**, as-blended, **b**, 30 min, **c**, 45 min, **d**, 1 h, **e**, 1.5 h, **f**, 2 h and **g**, 3 h.

while, fresh surfaces of the particles have tendencies to agglomerate with each other. This phenomenon results in a morphological difference between **Figs. 6(b)–(d)** and **Figs. 6(e)–(g)**.

The DSC thermograms of the as-blended La_2O_3-B_2O_3-Ca powders and those mechanochemically synthesized for different durations up to 3 h are illustrated in **Figs. 7(a)–(g)**. DSC analyses conducted on the as-blended and milled powders suggest about the thermal behaviors of the samples and the reaction completion. As seen in **Fig. 7(a)**, the DSC curve of the as-blended powders have a small endotherm peaking at about 330 °C and a broad endotherm peaking at about 525 °C, which respectively correspond to the dehydration of small amount of H_3BO_3 in the structure of B_2O_3 and the decomposition of $Ca(OH)_2$ into CaO by releasing water. The broad endotherm emerged between the temperature range of 420 and 595 °C could include the partial melting of B_2O_3 ($T_{melting}$: 450 °C) and residual $Ca(OH)_2$ ($T_{melting}$: 580 °C). Furthermore, as-blended powders have three respective small exotherms with a maximum point at about 690, 820 and 1010 °C (**Fig. 7(a)**), indicating the formations of calcium borate phases in different compositions (Erfani et al., 2012) and the emergence of LaB_6 phase since there are La_2O_3, B_2O_3 and CaO phases in the structure of the sample after heating up to the end point of the broad endotherm. On the basis of **Figs. 7(b)**, **(c)** and **(d)**, 30 min, 45 min and 1 h milling cause shifts in the temperatures of the endothermic and exothermic peaks. In other words, milled powders up to 1 h have the same endothermic and exothermic peaks with those of as-blended one, corresponding to the dehydration of H_3BO_3 and $Ca(OH)_2$ and formation of calcium borate and lanthanum hexaboride phases, with a significant difference in their peaking temperatures. As compared with **Fig. 7(a)**, the temperature difference in the peaking points of the broad endotherm and three exotherms is respectively about 55, 110, 115 and 155 °C for the 1 h milled powders (**Fig. 7(b)**). However, the peaking points of the endotherm and consecutive exotherms change with a maximum value of 20 °C, as milling duration increases from 30 min to 1 h (**Figs. 7(b)–(d)**). It can be said that milling process incredibly changes the thermal behavior of the La_2O_3-B_2O_3-Ca powders, if DSC curve of the as-blended powders (**Fig. 7(a)**) are compared with those in **Figs. 7(b)–(d)**. Milling provides an homogeneous distribution of particles throughout the microstructure and hence the reactivity of the touching particles increases to form calcium borate and lanthanum hexaboride phases. Since as-blended, 30 min, 45 min and 1 h milled powders comprise La_2O_3, $Ca(OH)_2$ and B_2O_3 phases (**Figs. 5(a)–(d)**), general appearance of their DSC thermograms resemble each other, excluding the peaking temperatures. **Figs. 7(e)–(g)** only shows the broad endothermic peaks respectively at about 445, 440 and 410 °C, pertinent to the dehydration of $Ca(OH)_2$. Since 1.5 h milled powders contain LaB_6, CaO, $Ca_3(BO_3)_2$ and $Ca(OH)_2$ phases, its DSC curve only exhibits the dehydration endotherm, as compatible with the XRD pattern in **Fig. 5(e)**. The heat flow of the broad endotherm decreases as milling duration increases from 1.5 to 3 h, as seen in **Figs. 7(e)–(g)**. After the reaction took place at the end of 1.5 h, the DSC curves do not include any exotherms belonging to the formation of calcium borates and lanthanum hexaboride. Although 2 and 3 h milled powders had LaB_6, CaO and $Ca_3(BO_3)_2$ phases according to the XRD patterns in **Figs. 5(f)** and **(g)**, the presence of adsorbed $Ca(OH)_2$ was proved by its dehydration endotherms in **Figs. 7(f)** and **(g)**.

The contradiction between the outcomes of the XRD and DSC analyses arises from the amount of $Ca(OH)_2$ which is below the detection limit of XRD (< 2 wt.%). Similarly in the La_2O_3-B_2O_3-Mg system, DSC thermogram of the powders milled for 2 h 45 min, in which reaction was assumed to take place completely according to the XRD

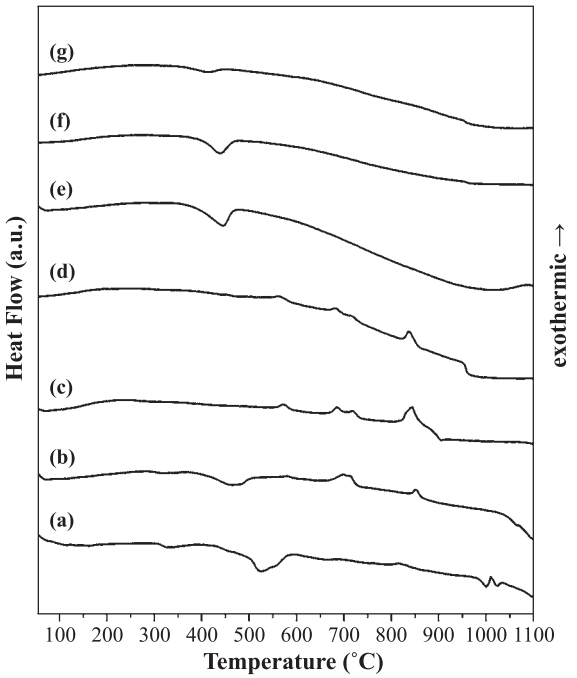

Fig. 7 DSC thermograms of the as-blended La_2O_3-B_2O_3-Ca powders and those mechanochemically synthesized for different durations: **(a)** as-blended, **(b)** 30 min, **(c)** 45 min, **(d)** 1 h, **(e)** 1.5 h, **(f)** 2 h and **(g)** 3 h.

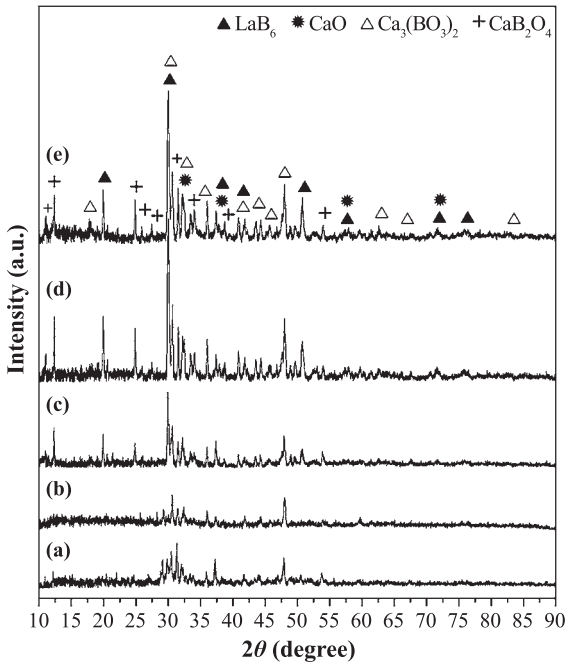

Fig. 8 XRD patterns of the La_2O_3-B_2O_3-Ca powders mechanochemically synthesized for different durations, after DSC analyses carried out up to 1100 °C: **(a)** 45 min, **(b)** 1 h, **(c)** 1.5 h, **(d)** 2 h and **(e)** 3 h.

analysis, shows a very small and narrow exotherm peaking at 651 °C corresponding to the oxidation of residual Mg in the powder blend (Ağaoğulları et al., 2012b).

The XRD patterns of the mechanochemically synthesized La_2O_3-B_2O_3-Ca powders after DSC analyses up to 1100 °C are given in **Figs. 8(a)–(e)**. The powders milled for 45 min, 1 h, 1.5 h, 2 h and 3 h were subjected to the subsequent XRD analyses in order to detect the existing phases after heating since as-blended powders and those milled for 30 min adhered into the alumina crucible during DSC experiments and hence they could not be discharged from the crucible. As seen in **Figs. 8(a)** and **(b)**, the powders contain CaO, $Ca_3(BO_3)_2$ and CaB_2O_4 (ICDD Card No: 72-1859, Bravais lattice: primitive orthorhombic, a = 0.838 nm, b = 1.382 nm, c = 0.501 nm) phases with a very small amount of LaB_6 phase after 45 min or 1 h milling and heating processes. Heating up to 1100 °C results in the formation of a new borate phase, CaB_2O_4, in addition to the $Ca_3(BO_3)_2$ which is already obtained after mechanochemical synthesis. Erfani et al. (2012) also obtained CaB_2O_4 phase after heating the reactants between 750 and 900 °C, which corresponds to the same temperature interval of borate formations in the DSC curves in **Figs. 7(a)–(d)**. After 1.5 h milling and heating, the intensities of the phases, especially that of LaB_6, get higher (**Fig. 8(c)**) and this increasing tendency continues as milling duration increases up to 3 h (**Figs. 8(d)** and **(e)**). These findings conform well to the results of the XRD analyses in **Figs. 5(c)–(g)** and DSC analyses in **Figs. 7(c)–(g)**. Since La_2O_3-B_2O_3-Ca powders milled for 45 min and 1 h contain La_2O_3, B_2O_3 and $Ca(OH)_2$ phases (**Figs. 5(c)** and **(d)**) after mechanochemical synthesis, they react to form LaB_6, CaO, $Ca_3(BO_3)_2$ and CaB_2O_4 phases by the effect of applied external heat. However, the desired LaB_6 phase is too few in the composition. Only heating up to 1100 °C without a holding time does not result in a complete conversion of the reactants even if short milling duration was conducted on the powders providing a homogeneous microstructure. Moreover, the powders mechanochemically synthesized for 1.5 h and for longer times as 2 and 3 h have already LaB_6, CaO and $Ca_3(BO_3)_2$ phases before heating (**Figs. 5(e)–(g)**) and it is expected to get increase in their intensities by the effect of heating which ensures grain growth. Although any exotherm indicating Ca borate formation were not detected in the DSC thermograms of the powders mechanochemically synthesized for 1.5, 2 and 3 h in **Figs. 7(e)–(g)**, an amount of CaB_2O_4 phase occurred in the powders after heating (**Figs. 8(c)–(e)**). The emergence of CaB_2O_4 phase can be attributed to the decomposition of $Ca_3(BO_3)_2$ with the applied heat, in regard of the reaction in Eq. (7).

$$Ca_3(BO_3)_2 \rightarrow CaB_2O_4 + 2CaO \quad (7)$$

Although the heating temperature is a little lower than the melting temperature of $Ca_3(BO_3)_2$ phase obtained after mechanochemical reaction for 1.5 h, an amount of it can decompose during heating by the effect of mechano-

chemistry which results in active surfaces in the reaction products. Furthermore, LaB_6 phase formed during milling (≥ 1.5 h) are thermally very stable because they have not any tendency to transform into an amount of lanthanum borate phases when exposed to high temperature. The results indicate that if milling are not carried out on the La_2O_3-B_2O_3-Ca powder blends, the heating process has only chance of LaB_6 incubation with additional borate compounds. The way of obtaining complete conversion of the reactants is to carry out milling process for longer durations than 2 h or to apply heating on these milled samples with a holding time. Therefore, the significance of the mechanochemical synthesis and its effect on the reduction mechanism of La_2O_3-B_2O_3-Ca powder system can be emphasized once more by means of the XRD patterns and DSC thermograms given in **Fig. 5** through **Fig. 8**. Similarly, an amount of $LaBO_3$, $Mg_3B_2O_6$ and MgO phases occurred in the as-blended La_2O_3-B_2O_3-Mg powders in addition to LaB_6, after heating up to 1200 °C (Ağaoğulları et al., 2012b). In magnesiothermic reduction, the formation of borate phases arose from both reducing agent and lanthanum source. However, the emergence of $LaBO_3$ phase were not detected in any step of the analyses. This can be evaluated as an advantage of the calciothermic reduction since its reaction does not consume the lanthanum oxide source to form borate, instead of that reducing agent participates in the generation of borates. The higher tendency of yielding Ca borates rather than that of La provides the generation of LaB_6 from all La_2O_3 reactant, after heating.

After the detailed characterizations of the as-blended and mechanochemically synthesized La_2O_3-B_2O_3-Ca powders, it can be stated that LaB_6 and CaO products are compatible with the reaction in Eq.(1). However, the presence of $Ca_3(BO_3)_2$ or CaB_2O_4 (after heating) conflicts with the theoretical reaction. Following the mechanochemical synthesis, reaction products should be purified to achieve fine-grained powders without any or with tolerable contaminations. Thus, leaching treatment was conducted on the powders mechanochemically synthesized for 3 h which contain LaB_6, CaO, $Ca_3(BO_3)_2$ and a very small amount of adsorbed $Ca(OH)_2$ according to the XRD (**Fig. 5(g)**) and DSC (**Fig. 7(g)**) analyses.

Fig. 9(a) is the XRD pattern of the La_2O_3-B_2O_3-Ca powders after mechanochemical synthesis for 3 h and leaching with 4 M HCl. As seen from the pattern, leached powders contain LaB_6 with a very slight and insignificant amount of $Ca_3(BO_3)_2$. Leaching with 4 M HCl solution provides the complete removal of CaO and $Ca(OH)_2$ in regard of reactions in Eqs. (2)–(4) and also results in the partial removal of $Ca_3(BO_3)_2$ phase. Due to the fact that some parameters of the leaching process such as solid-to-liquid ratio, leaching temperature and duration, centrifuging duration and speed, etc. were well-chosen,

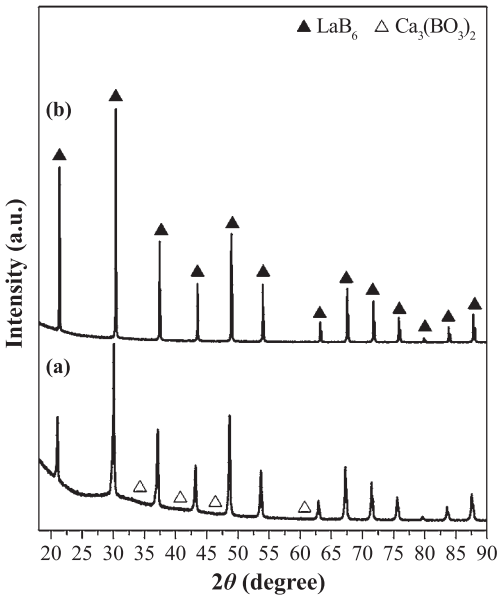

Fig. 9 XRD pattern of the **(a)** La_2O_3-B_2O_3-Ca powders after mechanochemical synthesis for 3 h and leaching with 4 M HCl, and **(b)** commercial LaB_6 powders, for comparison.

any $CaCl_2$, $CaCl_2.xH_2O$ and CaOHCl phases do not remain in the structure of the final powders as a leaching product. Furthermore, the AAS analysis of the supernatant liquid decanted from the leached powders gives the elemental results of 5710 ppm Ca, 309.3 ppm B and 3.76 ppm Fe. The Ca element in the supernatant liquid arises from the complete dissolution of CaO and the partial dissolution of $Ca_3(BO_3)_2$. So, the amount of Ca is lower than the expected amount since there is still remaining $Ca_3(BO_3)_2$ phase in the leached powders. It is believed that the presence of B element in the supernatant liquid can only arise from the slight dissolution of LaB_6 phase in the concentrated HCl solution since there is no unreacted B_2O_3 phase in the 3 h mechanochemically synthesized powders as verified by the DSC analysis in **Fig. 7(g)**.

Fig. 9(b) shows the XRD pattern of the commercial LaB_6 powders (Alfa Aesar™, in purity of 99.5 %, with an average particle size of 4 μm). It can be obviously seen that there is not any observable contamination in the commercial LaB_6 powders and their intensities are higher than those of laboratory-synthesized one, comparing the XRD patterns in **Figs. 9(a)** and **(b)**. Besides, the production method of commercial LaB_6 powders is not known. Due to obtain uncontaminated LaB_6 powders having an XRD pattern similar to that of commercial one, additional treatments should be carried out or concentration of HCl should be increased.

Fig. 10(a) is the SEM image of the La_2O_3-B_2O_3-Ca powders after mechanochemical synthesis for 3 h, in which rounded-shaped particles having sizes below 3 μm can be easily seen. Although the XRD pattern of the 3 h

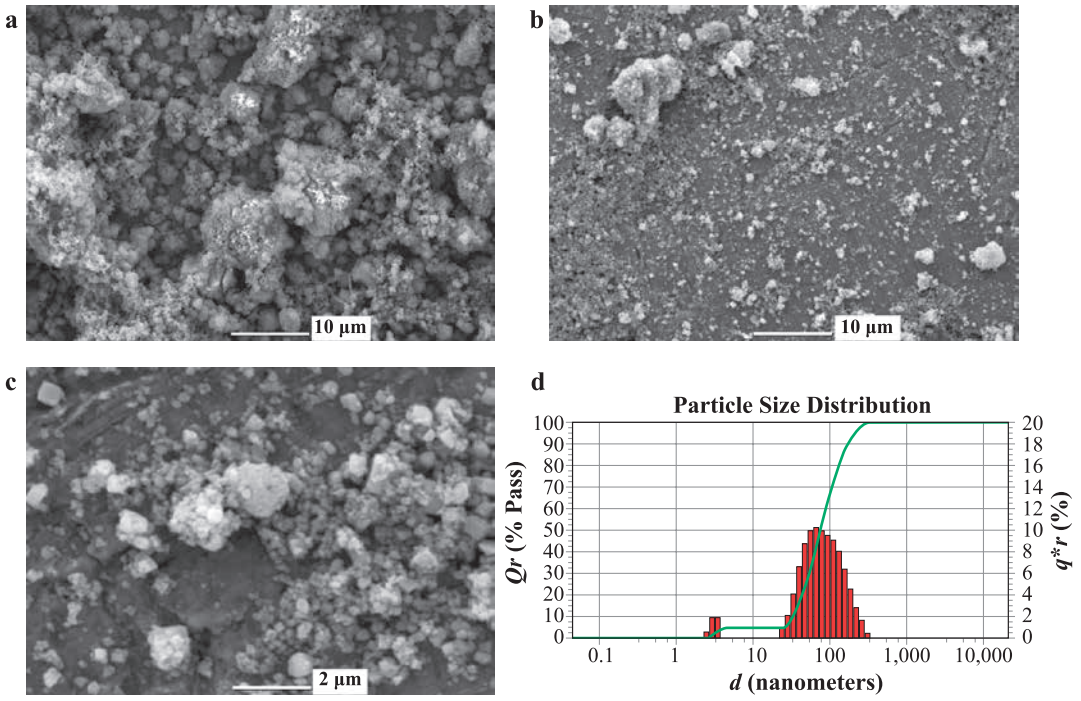

Fig. 10 SEM images of the La_2O_3-B_2O_3-Ca powders after: **a**, mechanochemical synthesis for 3 h, **b**, leaching with 4 M HCl, 2.000X, **c**, leaching with 4 M HCl, 10.000X, and **d**, its corresponding PSA analysis.

milled powders revealed the presence of LaB_6, CaO and $Ca_3(BO_3)_2$ phases (**Fig. 5(g)**), there are also white dendritic $Ca(OH)_2$ phases adsorbed on the small rounded-shaped particles, which agrees very well with the DSC analysis in **Fig. 7(g)**. The dendritic $Ca(OH)_2$ phase was also detected in a previous study related with the synthesis of CaB_6 powders via mechanochemical reaction of Ca-B_2O_3 blends (Balcı et al., 2012). **Figs. 10(b)** and **(c)** show the SEM images of the La_2O_3-B_2O_3-Ca powders after mechanochemical synthesis for 3 h and leaching with 4 M HCl, in different magnifications. SEM images illustrate the rounded-shaped LaB_6 particles together with the embedded $Ca_3(BO_3)_2$, ranging in sizes between 250 nm and 1 µm. Since **Figs. 10(a)** and **(b)** have the same magnification scale, it is evident to comprehend the effect of leaching on the 3 h milled powders. Before leaching treatment, Ca-based particles (CaO, $Ca_3(BO_3)_2$ and $Ca(OH)_2$) hold the LaB_6 particles together and it results in an agglomerated microstructure in which the presence of smaller particles can not be observed (**Fig. 10(a)**). Besides, leached powders do not consist of perfect spheroidal-shaped particles throughout the structure (**Figs. 10(b)** and **(c)**) because the repeated fracturing and repeated welding mechanism changed their morphologies during milling (Suryanarayana, 2001). After leaching, there is still agglomeration between the particles due to the existence of $Ca_3(BO_3)_2$ phase (**Figs. 10(b)** and **(c)**) and the measured size range of the particles monitored by SEM can result in misleading results. So, the average particle size of the leached powders was accurately determined under the effect of ultrasonic homogenizer. PSA graph in **Fig. 10(d)** displays the average size of the leached particles as about 80 nm.

As a result of analyses carried out after leaching treatment, it can be interpreted that Ca has an excessive tendency to form borate phases which can be completely eliminated by leaching with excess HCl in concentration above 4 M. Also, it is comprehensible that higher concentrations of HCl can cause the higher dissolution of synthesized LaB_6 phase at the same leaching conditions and so this can result in more decrease in the LaB_6 intensities. However, 6 M HCl was also used in order to remove undesirable $Ca_3(BO_3)_2$ phase for obtaining pure LaB_6 powders.

Fig. 11 represents the XRD pattern of the La_2O_3-B_2O_3-Ca powders after mechanochemical synthesis for 3 h and leaching with 6 M HCl. As seen from **Fig. 11**, 6 M leached powders have only LaB_6 phase without any detectable contamination. AAS analysis of the supernatant liquid decanted from these leached powders gives the amounts of the elements as 5820 ppm Ca, 356.4 ppm B and 3.78 ppm Fe. In comparison with the elemental results of 4 M leached powders, the amounts of Ca and B increase significantly, indicating the disappearance of $Ca_3(BO_3)_2$ phase in the powder composition and the dissolution of LaB_6 phase. Thus, the XRD pattern of the 6 M leached powders (**Fig. 11**) and also AAS analysis of the decanted supernatant liquid demonstrate that final LaB_6 powders are sufficiently pure and they do not contain any remnants of residual elements during HCl leaching. Dis-

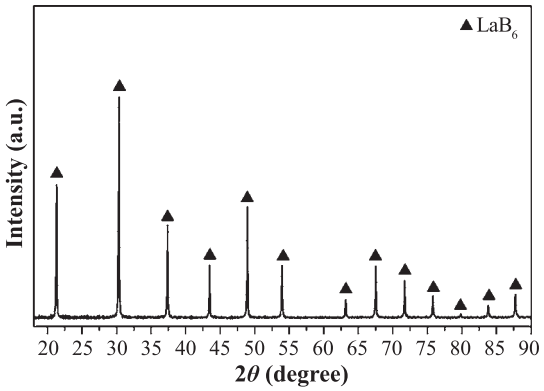

Fig. 11 XRD pattern of the La_2O_3-B_2O_3-Ca powders after mechanochemical synthesis for 3 h and leaching with 6 M HCl.

similarly, 3.6 M HCl is enough to remove all undesirable MgO in the milled La_2O_3-B_2O_3-Mg powders due to the absence of Mg borate phase in the microstructure (Ağaoğulları et al., 2012a).

Figs. 12(a) and **(b)** are the bright-field (BF) micrographs taken from the La_2O_3-B_2O_3-Ca powders after mechanochemical synthesis for 3 h and leaching with 6 M HCl. **Fig. 12(a)** shows both polygonal/spheroidal-shaped and equiaxed-shaped particles in sizes varying between 50 and 350 nm. Moreover, different morphologies of the particles arising from the milling mechanism can be distinctly observed from the BF image of the powders in higher magnification given in **Fig. 12(b)**. In comparison with **Fig. 12(a)**, the presence of smaller particles with an average size of 20 nm is proved in **Fig. 12(b)**. **Fig. 12(c)** displays the corresponding general EDS measurement taken from the particles in BF image (**Fig. 12(b)**).

EDS measurement reveals that there is 69.15 ± 1.60 wt.% La and 30.85 ± 0.75 wt.% B in the composition of the particles indicating the existence of LaB_6 phase, which is consistent with the amounts of elements in the stoichiometric phase. The detected Cu element arises from the copper grid on which the powders were supported. EDS results also prove that any contamination originating from the unwanted $Ca_3(BO_3)_2$ phase does not remain in the structure after 6 M leaching treatment, which is in good agreement with XRD analysis in **Fig. 11**. Consequently, pure LaB_6 powders were obtained from La_2O_3-B_2O_3-Ca powders after mechanochemical synthesis for 3 h and leaching with 6 M HCl, having particles in size between 20 and 350 nm.

Calciothermic reduction of La_2O_3 and B_2O_3 containing powder blends by mechanochemistry at room temperature can be an alternative method for the preparation of nanosized LaB_6 powders in high purity, rather than magnesiothermic reduction methods and other conventional production techniques.

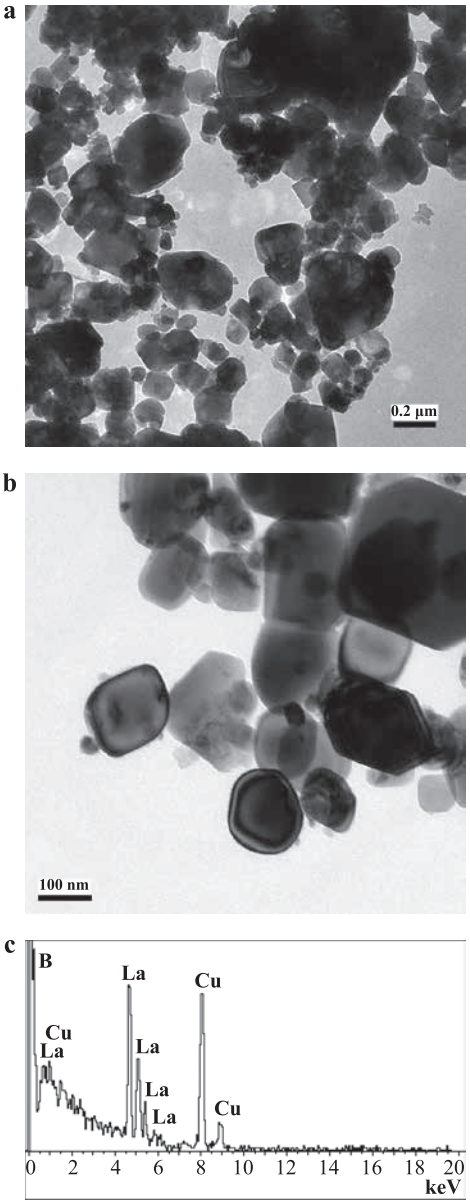

Fig. 12 TEM micrographs of the La_2O_3-B_2O_3-Ca powders after mechanochemical synthesis for 3 h and leaching with 6 M HCl: **a**, BF image (in 0.2 µm scale), **b**, BF image (in 100 nm scale), and **c**, its corresponding general EDS analysis.

4. Conclusions

In this study, nanosized LaB_6 powders were successfully synthesized from the related oxides of the elements, via calciothermic reduction by mechanochemistry performed at room temperature. Based on the results reported in the present study, the following conclusions can be drawn:

- After mechanochemical synthesis of the La_2O_3-B_2O_3-Ca powder blends in Spex^{TM} 8000D Mixer/Mill using a 10:1 BPR for 1.5 h, LaB_6, CaO and $Ca_3(BO_3)_2$ phases were obtained in addition to very small

amounts of unreacted La_2O_3 and $Ca(OH)_2$.

- XRD analyses showed that extending the milling duration to 2 h resulted in a complete reaction in which unreacted La_2O_3 and $Ca(OH)_2$ phases disappeared and the composition only contained LaB_6, CaO and $Ca_3(BO_3)_2$ phases. Besides, calciothermic reduction by mechanochemistry was achieved 45 min earlier than that of magnesiothermic one.
- All mechanochemically synthesized powders had the same LaB_6, CaO, $Ca_3(BO_3)_2$ and CaB_2O_4 phases after heating up to 1100 °C and there was an increasing tendency in the occurrence of the phases as the milling duration increased.
- LaB_6 phase synthesized during mechanochemical reactions (≥ 1.5 h) are thermally very stable since they have not any tendency to transform into an amount of lanthanum borate phases when exposed to high temperature.
- DSC results indicated that if longer milling durations were not applied on the La_2O_3-B_2O_3-Ca powder blends, the heating process of powders only yielded the incubation of LaB_6 with additional Ca borate compounds.
- DSC and SEM analyses exhibited that a dendritic $Ca(OH)_2$ phase adsorbed on the LaB_6, CaO and $Ca_3(BO_3)_2$ particles in the microstructure of the 2 and 3 h milled powders, which can be easily eliminated by HCl leaching.
- LaB_6 powders were obtained with an average particle size of 80 nm and in the presence of very small amount of $Ca_3(BO_3)_2$ phase from La_2O_3-B_2O_3-Ca powder blends after mechanochemical synthesis for 3 h and leaching with 4 M HCl.
- Pure LaB_6 powders were obtained from La_2O_3-B_2O_3-Ca powders after mechanochemical synthesis for 3 h and leaching with 6 M HCl, having particles in size between 20 and 350 nm.

Acknowledgements

This study was supported by “The Scientific and Technological Research Council of Turkey (TÜBİTAK)” with the project title of “Synthesis of Lanthanum, Cerium and Samarium Borides by Solid-State Reaction at Room Temperature” and with the project number of 109M364. It was also funded by “Istanbul Technical University Scientific Research Projects” with the project title of “Mechanochemical Synthesis and Characterization of Some Rare-Earth Metal Borides” and with the project number of 33549.

Nomenclature

AAS	Atomic Absorption Spectrometer
BF	Bright-Field
BPR	Ball-to-Powder Weight Ratio
CVD	Chemical Vapor Deposition
DSC	Differential Scanning Calorimeter
EDS	Energy Dispersive Spectrometer
ICDD	International Center for Diffraction Data
PSA	Particle Size Analyzer
RF	Radio Frequency
SEM	Scanning Electron Microscope
SHS	Self-propagating High-temperature Synthesis
SM	Stereomicroscope
XRD	X-ray Diffraction
TEM	Transmission Electron Microscope
TM	Trademark
a, b, c	lattice parameters
°C	degree Celsius
ab	as-blended
cm	centimeter
ΔG	Gibbs free energy change
ΔH	enthalpy change
g	gram
h	hour
kJ	kilojoule
kV	kilovolt
M	molarity
mg	miligram
min	minute
ml	mililiter
mm	milimeter
µm	micron
nm	nanometer
Pa	Pascal
rpm	rotation per minute
T	temperature
θ	diffraction angle
wt.%	weight percentage

References

Ağaoğulları D., Synthesis, Development and Characterization of Some Rare-Earth Hexaboride Powders and Their Sintered Products, Ph.D. Thesis, Advisor: Prof. Dr. İsmail Duman, Graduate School of Science, Engineering and Technology, Istanbul Technical University, 2014.

Ağaoğulları D., Balcı Ö., Gökçe H., Duman İ., Öveçoğlu M.L., Synthesis of magnesium borates by mechanically activated annealing, Metallurgical and Materials Transactions A, 43A (2012a) 2520–2533.

Ağaoğulları D., Duman İ., Öveçoğlu M.L., Synthesis of LaB_6 powders from La_2O_3, B_2O_3 and Mg blends via a mechanochemical route, Ceramics International, 38 (2012b) 6203–6214.

Ahmed H., Kanitkar P.L., Dharmadhikari C.V., Joag D.S., A new method for melting and recrystallization of lanthanum hexaboride (LaB_6) for preparing field emitters, Journal of Physics E: Scientific Instruments, 9 (1975) 4–5.

Amalajyothi K., Berchmans L.J., Angappan S., Visuvasam A., Electrosynthesis of cerium hexaboride by the molten salt technique, Journal of Crystal Growth, 310 (2008) 3376–3379.

Amalajyothi K., Berchmans L.J., Visuvasam A., Angappan S., Electrosynthesis of cerium hexaboride using lithium tetra borate melt, Materials and Manufacturing Processes, 26 (2011) 792–795.

Aprea A., Maspero A., Masciocchi N., Guagliardi A., Albisetti A.F., Giunchi G., Nanosized rare-earth hexaborides: low-temperature preparation and microstructural analysis, Solid State Sciences, 21 (2013) 32–36.

Balakrishnan G., Lees M.R., Paul D.M^{c}K., Rare earth hexaborides: large single crystals, Journal of Magnetism and Magnetic Materials, 272–276 (2004) 601–602.

Balcı Ö., Ağaoğulları D., Duman İ., Öveçoğlu M.L, Synthesis of CaB_6 powders via mechanochemical reaction of Ca/B_2O_3 blends, Powder Technology, 225 (2012) 136–142.

Bao L., Zhang J., Zhou S., Zhang N., Xu H., Floating zone growth and thermionic emission property of single crystal CeB_6, Chinese Physics Letters, 28 (2011) 088101-1-088101-4.

Baranovskiy A.E., Grechnev G.E., Fil V.D., Ignatova T.V., Logosha A.V., Panfilov A.S., Svechkarev I.V., Shitsevalova N.Y., Filippov V.B., Eriksson O., Electronic structure, bulk and magnetic properties of MB_6 and MB_{12} borides, Journal of Alloys and Compounds, 442 (2007) 228–230.

Brewer J.R., Jacobberger R.M., Diercks D.R., Cheung C.L., Rare earth hexaboride nanowires: general synthetic design and analysis using atom probe tomography, Chemistry of Materials, 23 (2011) 2606–2610.

Carlsson M., Garcia-Garcia F.J., Johnsson M., Gulian A., Synthesis of $La_xCe_{1-x}B_6$ whiskers, Journal of Materials Science, 40 (2005) 2991–2994.

Chen C., Aizawa T., Iyi N., Sato A., Otani S., Structural refinement and thermal expansion of hexaborides, Journal of Alloys and Compounds, 366 (2004) L6–L8.

Chen X., Li M., Chang X., Zhang H., Xiao W., Synthesis and crystal structure of a new calcium borate, CaB_6O_{10}, Journal of Alloys and Compounds, 464 (2008) 332–336.

Dou Z., Zhang T., Guo Y., Jicheng H., Research on preparation optimization of nano CeB_6 powder and its high temperature stability, Journal of Rare Earths, 30 (2012) 1129–1133.

Dou Z., Zhang T., Zhang Z., Zhang H., He, J., Preparation and characterization of LaB_6 ultra fine powder by combustion synthesis, Transactions of Nanoferrous Metals Society of China, 21 (2011) 1790–1794.

Erfani M., Saion E., Soltani N., Hashim M., Abdullah W.S.B.W., Navasery M., Facile synthesis of calcium borate nanoparticles and the annealing effect on their structure and size, International Journal of Molecular Sciences, 13 (2012) 14434–14445.

Futamoto M., Nakazawa M., Kawabe U., Thermionic emission properties of hexaborides, Surface Science, 100 (1980) 470–480.

Gao R., Min G., Yu H., Zheng S., Lu Q., Han J., Wang J., Fabrication and oxidation behavior of LaB_6-ZrB_2 composites, Ceramics International, 31 (2005) 15–19.

Hasan M., Sugo H., Kisi E., Low temperature carbothermal and boron carbide reduction synthesis of LaB_6, Journal of Alloys and Compounds, 578 (2013) 176–182.

Jha M., Patra R., Ghosh S., Ganguli A.K., Novel borothermal route for the synthesis of lanthanum cerium hexaborides and their field emission properties, Journal of Solid State Chemistry, 194 (2012) 173–178.

Ji X.H., Zhang Q.Y., Xu J.Q., Zhao Y.M., Rare-earth hexaborides nanostructures: recent advances in materials, characterization and investigations of physical properties, Progress in Solid State Chemistry, 39 (2011) 52–69.

Li P., Tian W., Wang D., Liu X., Grain refining potency of LaB_6 on aluminum alloy, Journal of Rare Earths, 30 (2012) 1172–1176.

Loboda P.I., Kysla H.P., Dub S.M., Karasevs'ka O.P., Mechanical properties of the monocrystals of lanthanum hexaboride, Materials Science, 45 (2009) 108–113.

Massalski T.B., Okamoto M., Subramanian P.R., Kacprzak L., Binary Alloy Phase Diagrams, ASM International, Materials Park, Ohio, 1990.

Mitterer C., Waldhauser W., Beck U., Reiners G., Structure and properties of decorative rare-earth hexaboride coatings, Surface and Coatings Technology, 86–87 (1996) 715–721.

Motojima S., Takahashi Y., Sugiyama K., Chemical vapor growth of LaB_6 whiskers and crystals having a sharp tip, Journal of Crystal Growth, 44 (1978) 106–109.

Otani S., Ishizawa Y., Thermionic emission properties of boron-rich LaB_6 and CeB_6 crystal cathodes, Journal of Alloys and Compounds, 245 (1996) L18–L20.

Otani S., Nakagawa H., Nishi Y., Kieda N., Floating zone growth and high temperature hardness of rare-earth hexaboride crystals: LaB_6, CeB_6, PrB_6, NdB_6, and SmB_6, Journal of Solid State Chemistry, 154 (2000) 238–241.

Paderno V.N., Paderno Yu.B., Pilyankevich A.N., Lazorenko V.I., Bulychev S.I., The micromechanical properties of melted borides of rare earth metals, Journal of the Less-Common Metals, 67 (1979) 431–436.

Perkins C.L., Trenary M., Tanaka T., Otani S., X-ray photoelectron spectroscopy investigation of the initial oxygen adsorption sites on the LaB_6 (100) surface, Surface Science Letters, 423 (1999) L222–L228.

Petrosyan V., Vardanyan V., Kuzanyan V., Konovalov M., Gurin V., Kuzanyan A., Thermoelectric properties and chemical composition of CeB_6 crystals obtained by various methods, Solid State Sciences, 14 (2012) 1653–1655.

Post B., Moskowitz D., Glaser F.W., Borides of rare earth metals, American Chemical Society, 78 (1956) 1800–1802.

Qin L., Zhang H., Zhang Q., Tang J., Single-crystalline, rare-earth metal hexaboride nanowires used as electron emitter for electron emission cathode used for electron gun, con-

tains rare-earth metals such as yttrium, lanthanum, cerium, samarium and gadolinium, US Patent, (2010) 2010028235-A1.

Samsonov G.V., Paderno Y.B., Fomenko V.S., Hexaborides of the rare-earth metals, Soviet Powder Metallurgy and Metal Ceramics, 2 (1963) 449–454.

Schlesinger M.E., Liao P.K., Spear K.E., The B-La (boron-lanthanum) system, Journal of Phase Equilibria, 20 (1999) 73–78.

Selvan R.K., Genish I., Perelshtein I., Moreno M.C., Gedanken A., Single step, low-temperature synthesis of submicron-sized rare earth hexaborides, Journal of Physical Chemistry C, 112 (2008) 1795–1802.

Suryanarayana C., Mechanical alloying and milling, Progress in Materials Science, 46 (2001) 1–184.

Swanson L.W., McNeely D.R., Work functions of the (001) face of the hexaborides of Ba, La, Ce and Sm, Surface Science, 83 (1979) 11–28.

Tanaka Y., Staub U., Narumi Y., Katsumata K., Scagnoli V., Shimomura S., Tabata Y., Onuki Y., Non-resonant X-ray Bragg diffraction by CeB_6, Physica B: Condensed Matter, 345 (2004) 78–81.

Verhoeven J.D., Gibson E.D, Noack M.A., Conzemius R.J., An arc floating zone technique for preparing single crystal lanthanum hexaboride, Journal of Crystal Growth, 36 (1976) 115–120.

Wang L., Xu L., Ju Z., Qian Y., A versatile route for the convenient synthesis of rare-earth and alkaline-earth hexaborides at mild temperatures, CrystEngComm, 12 (2010) 3923–3928.

Wang X., Jiang Y., Lin Z., Qi K., Wang B., Field emission characteristics of single crystal LaB_6 field emitters fabricated by electrochemical etching method, Journal of Physics D: Applied Physics, 42 (2009) 055409.

Wen C.H., Wu T.M., Wei W.J., Oxidation kinetics of LaB_6 in oxygen rich conditions, Journal of the European Ceramic Society, 24 (2004) 3235–3243.

Xu J.Q., Mori T., Bando Y., Golberg D., Berthebaud D., Prytuliak A., Synthesis of CeB_6 thin films by physical vapor deposition and their field emission investigations, Material Science and Engineering B, 177 (2012) 177–120.

Xu J.Q., Zhao Y.M., Zou C., Self-catalyst growth of LaB_6 nanowires and nanotubes, Chemical Physics Letters, 423 (2006) 138–142.

Yuan Y., Zhang L., Liang L., He K., Liu R., Min G., A solid-state reaction route to prepare LaB_6 nanocrystals in vacuum, Ceramics International, 37 (2011) 2891–2896.

Zhang H., Tang B., Zhu P.W., Zhang Q., Zhou O., Qin L.C., Fabrication of lanthanum hexaboride single nanowire field emitter and their field emission properties, Transactions of the Materials Research Society of Japan, 32 (2007) 747–750.

Zhang H., Tang J., Zhang L., An B., Qin L.C., Atomic force microscopy measurement of the Young's modulus and hardness of single LaB_6 nanowires, Applied Physics Letters, 92 (2008) 173121.

Zhang H., Tang J., Zhang Q., Zhao G., Yang G., Zhang J., Zhou O., Qin L.C., Field emission of electrons from single LaB_6 nanowires, Advanced Materials, 18 (2006) 87–91.

Author's short biography

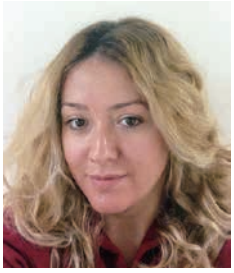

Duygu Ağaoğulları

Duygu Ağaoğulları received her M.Sc. degree in 2007 and Ph.D. degree in 2014 in Materials Science and Engineering Department from Istanbul Technical University. She worked as a research assistant between 2005 and 2013, and has been affiliated since 2013 in I.T.U. She has been assigned as researcher/scholar in 10 scientific projects. Now, she is working as a postdoctoral scholar in Materials Science and Engineering Department in Stanford University. Her main research activities are powder metallurgy, high-tech boron products and composite materials. She is author/co-author of 21 papers, 1 Patent cited in Web of Science and 75 international conference proceedings.

Özge Balcı

Özge Balcı received her M.Sc. degree in Metallurgical and Materials Engineering from Istanbul Technical University in 2010 and continues her Ph.D. in the same department. She has been assigned as researcher in 4 scientific projects and gained professional fellowships in 3 research projects. She has been as a visiting researcher at IFW Dresden for 6 months during her Ph.D studies. Her main research activities are powder metallurgy, high-tech boron products and composite materials. She is author/co-author of 11 papers and 1 Patent cited in Web of Science and 42 proceedings presented in international conferences.

M. Lütfi Öveçoğlu

Prof. Dr. M. Lütfi Öveçoğlu received his M.Sc. and Ph.D. degrees in Materials Science and Engineering from Stanford University in 1984 and 1987. He has been affiliated with the Department of Metallurgical and Materials Engineering at Istanbul Technical University since 1990. He is the founder and technical director of Particulate Materials Laboratories (PML), a cluster of 9 laboratories. His main research activities are mechanical alloying and mechanochemical synthesis of W-based, Al-based and boride-based materials. He is author/co-author of 145 papers and 1 patent cited in Web of Science, 2 book chapters and 3 edited conference proceedings having about 905 citations.

İsmail Duman

Prof.Dr. İsmail Duman received his M.Sc. degree from Istanbul Technical University in 1978 and Ph.D. degree from Berlin Technical University in 1985 in Metallurgical Engineering. He has been affiliated with Department of Metallurgical and Materials Engineering at Istanbul Technical University since 1980. His main research activities are extractive metallurgy, powder metallurgy, development of high-tech boron products and CVD technologies. He has been the supervisor of 17 M.Sc. and 8 Ph.D. dissertations and he has been assigned as project director or researcher in 23 industrial/scientific research projects. He is author/co-author of 49 papers and 7 Patents cited in Web of Science.

KONA Powder and Particle Journal No. 33 (2016) 219–227/Doi:10.14356/kona.2016002 Original Research Paper

Precipitation Process of Calcium Phosphate from Calcium Carbonate Suspension †

Nayane Macedo Portela da Silva, Fabienne Espitalier * and Ange Nzihou

[1] *Université de Toulouse, Centre RAPSODEE UMR CNRS 2392, France*

Abstract

The Ca-HA is synthesized by reacting calcium carbonate ($CaCO_3$) and ammonium dihydrogen orthophosphate ($NH_4H_2PO_4$) in stoichiometric proportions. In this precipitation process, the ratio of Ca/P by moles is 1.67. The experiments were performed in a batch reactor at 25 °C. From control parameters, the pH and the temperature were measured in line for all experiments. The tests were performed with two liquid-solid mass ratios (H_2O/$CaCO_3$) of 3 and 5. For each mass ratio, three stirring rates of 260, 400, and 600 rpm were tested. Samples of the synthesis were collected at different intervals and analysed by laser granulometry and by environmental scanning electron microscopy.

For the synthesis conducted at 260 rpm, synthesis monitoring was made using a contact probe in solution coupled to a Raman spectrometer in order to follow the formation of solid phase. This technique is valuable to follow the synthesis of Ca-HA in a concentrated solids suspension (around 20–30 wt%).

The results make it possible to propose a mechanism of the precipitation process of Ca-HA. It can be divided into four main stages: (i) dissolution of calcium carbonate ($CaCO_3$), (ii) precipitation of brushite ($CaHPO_4.2H_2O$), (iii) transformation of brushite into Ca-HA ($Ca_{10}(PO_4)_6(OH_2)$) and (iv) nucleation, growth and agglomeration of Ca-HA.

Keywords: precipitation, hydroxyapatite, brushite, Raman spectroscopy

1. Introduction

The exponential population growth has led to a similar increase in requirements for resources, energy, food, housing and land as well as an enormous increase in industrialization and urbanization. This rapid industrialization and urbanization have led to great demand for natural resources and created an increase in waste production. A continuing issue facing society today is the disposal of municipal and industrial wastes (Wey et al., 2006). Waste calcium carbonate ($CaCO_3$) from the paper, cosmetics, pharmaceuticals, catalyst, ceramics, rubber and paint industries often ends up in landfill (Wen et al., 2007). These $CaCO_3$ wastes can be used as the calcium compound in the synthesis of hydroxyapatite (Ca-HA). Ca-HA, $Ca_{10}(PO_4)_6(OH_2)$, is an insoluble calcium phosphate mineral. It is a main constituent of bones and teeth. Due to its excellent biocompatibility, slow biodegradation, good mechanical stability, great sorption properties and heterogeneous photocatalytic degradation under UV irradiation (Wang et al., 2003), it has been used extensively for bone repairs, bone implants, bioactive materials and for purification and separation of biological molecules and organic contaminants. It can accept a series of cationic and anionic substitution within its structure (Elliott, 1994). Similarly, it has been reported to be an efficient adsorbent to treat heavy metals (Chen et al., 1997) and to have a very high capacity for removing divalent heavy metal ions (Ma et al., 1993). Consequently, hydroxyapatite is used for the removal of heavy metals from contaminated soils, wastewater and fly ashes (Elliott, 1994). Several methods have been developed to prepare Ca-HA, including a dry process, precipitation, hydrolyzation of calcium phosphate and hydrothermal synthesis. Spray pyrolysis, freeze drying, gel diffusion, a sol-gel technique and electrochemical deposition have all also been used. Much work has been done on the synthesis of Ca-HA using different methods such as solid-solid reaction (Nakamura et al., 2001; Silva et al., 2003), ultrasonic spray freeze-drying (Itatani et al., 2000) or spray-drying techniques generating a Ca-HA powder of controlled morphology (Luo and Nieh, 1996), sol-gel technique (Anee et al., 2003; Bezzi et al., 2003; Salimi et al., 2012), precipitation in aqueous solution (Jarcho, and Bolen, 1976; Rodriguez-Lorenzo et al., 2001; Bailliez and Nzihou, 2004; Swain et al., 2012), emulsion

† Received 13 May 2014; Accepted 10 December 2014
J-STAGE Advance published online 28 April 2015
[1] Ecole des Mines d'Albi-Carmaux, Campus Jarlard F-81013 Albi Cedex 09, France
* Corresponding author: Fabienne Espitalier;
E-mail: fabienne.espitalier@mines-albi.fr
TEL: + 33-5-63493151 FAX: + 33-5-63493025

route (Saha et al., 2009; Okada et al., 2012), microwave-assisted synthesis (Ipekoglu and Altintas, 2010) and synthesis under hydrothermal conditions (Vasile et al., 2012; Murakami et al., 2012). Among all these methods, precipitation is characterized by the simplicity of the process, its low cost and its easy application in industrial production (Liu et al., 2001). The main objective of this work is to investigate this synthesis of calcium phosphate powders to be used as adsorbents for pollutants removal. To achieve this goal, the hydroxyapatite is synthesized by a crystallization reaction (precipitation) from solid calcium carbonate in a batch reactor in order to investigate systematically the effects of operating conditions such as the stirring speed and the liquid-solid mass ratios. These parameters determine the crystallization performance. Moreover in this study we show that the solid formations can be followed using Raman spectroscopy.

2. Experimental section

2.1 Materials and methods

In order to synthesize Ca-HA, laboratory-grade calcium carbonate ($CaCO_3$) powder (98 % pure) and ammonium dihydrogen orthophosphate powder ($NH_4H_2PO_4$) (94.4 % pure) were used. Both were obtained from Fisher Scientific U.K. and were used as received. The suspension of $CaCO_3$ was introduced into a 0.5 L glass vessel (diameter 10 cm) with double jacket equipped with a helicoidal stirrer (diameter 4.5 cm). Agitation was powered by a Eurostar IKA labortechnick 2000 motor. The reactor was equipped with four baffles (**Fig. 1**). The $NH_4H_2PO_4$ powder was dissolved for a minimum time of 30 min at ambient temperature. Then, this solution was gradually pumped into the reactor with a peristaltic pump (Master flex pump) at a flow rate of 11.11 cm^3/min in order to maintain the pH value higher than 7. The temperature was controlled by a water bath (Julabo VC F30). The pH value was monitored throughout the duration of the experiment using a pH meter (Meterlab PHM210). The reaction continued for 72 h at atmospheric pressure and temperature (25 ± 2 °C). The ratio of Ca/P by moles was 1.67. Two different liquid-solid mass ratios (water/$CaCO_3$ solid) of 3 and 5 and three stirring rates (260, 400 and 600 rpm) were tested. Addition times were equal to 18.6 min and 18.0 min, respectively, for a mass ratio of 3 and 5.

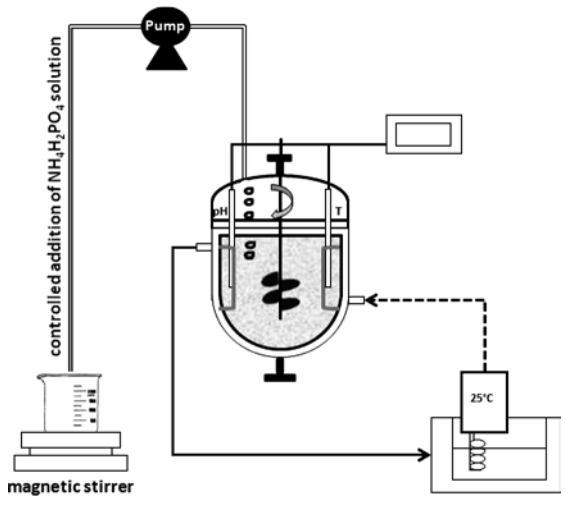

Fig. 1 Experimental set-up for precipitation.

2.2 Analytical methods

The reactor suspension, composed of calcium carbonate and calcium phosphates, was sampled at different intervals in order to characterize the solid and the solution.

Particle-size distributions: The particle size distributions were measured by laser diffraction with a Malvern Master Sizer 2000 instrument covering a size range of 0.1–2000 µm. Suspension samples were diluted and dispersed in water by ultrasonication for 4 min before measurement to disaggregate the solid. Direct sampling of the reactor suspension was used for these measurements.

For the other analysis, the collected samples were filtered. Solids were washed and dried in a vacuum oven (Heraeus Vacutherm—VT-6025) at 60 °C for 24 hours to yield a fine white powder. The dry solid was not very cohesive and it was simply broken up by manual grinding.

Ion chromatography was used to analyse the liquid, and TG-DSC and ESEM for the solids.

Ion phosphate concentration: The phosphate ion concentration was analysed using ion chromatographic separation and it is performed using a Dionex ICS-300 ion chromatograph system consisting of: a single pump (Dionex ICS-3000 SP), an eluent generator (Dionex ICS-3000 EG), a conductivity detector (Dionex Conductivity Detector P/N 061830), a precolumn (Dionex IonPac AG 19, 4 × 50 mm) and a column (Dionex IonPac AS 19 (4 × 250 mm). The eluent was the ultra-pure water with the pH value kept constant by using the KOH eluent generator. The eluent flow was 1 ml/min corresponding to a stable pressure in the column of about 120 bar. The results were analysed by using the software Chromelon.

Habitus: A scanning electron microscope (Philips XL30 ESEM FEG) equipped with EDAX fluorescence analysis following platinum sputtering of the sample, was used to study the morphology of the gold-coated intermediate and final products.

Weight losses: Thermal gravimetric analysis was performed using a Thermogravimetrical Analyser (TGA-DSC 111 Setaram). The experiment was performed with a heating rate of 2 °C/min using nitrogen flow (25 ml/min). The percentage weight loss of the samples (approximately

12 mg) was monitored from 20 to 800 °C.

Raman spectra: For the synthesis conducted at 260 rpm, the synthesis monitoring was conducted using a contact probe in solution coupled to a Raman spectrometer RXN2C785, Mettler-Toledo/Kaiser analysers (Kaiser Optical Systems, Ann Arbor, Michigan, USA). A 400 mW external cavity stabilized by an Invictus NIR diode laser at 785 nm was used for sample illumination. All the spectra were recorded at a resolution of 4 cm^{-1}.

XR diffraction: For the synthesis conducted at 260 rpm, the phase identification of some samples was carried out using XR diffractometry (Phillips PanAlytical X'Pert Pro MPD diffractometer), which had a Cu Ka radiation (l = 1.54 A) at 45 kV and 40 mA. The reflections were collected in the 2θ ranges from 10 to 75° with a step size of 0.17° and a time of 13.02 s per step. The phase identification was carried out with the JCPDS database.

3. Results

During the process for the formation of hydroxyapatite, it was possible to form other calcium phosphates. Their solubilities decrease with the pH value (Ferreira et al., 2003). The comparisons of the solubility of the $CaHPO_4.2H_2O$ named brushite and the solubility of hydroxyapatite Ca-HA for a pH value lower than 4, show that brushite is a stable compound and for a pH value higher than 4, the Ca-HA is prominent. **Fig. 2** shows the evolution of the pH value during the synthesis for the two liquid-solid mass ratios (3 and 5) at 400 rpm. It can be observed that the pH value readily decreases from 10.2 to 6.9 during the first 15 minutes of reaction. Then it gradually increases to 8.5 and after 40 hours, the pH value stabilizes at about 9. The liquid-solid mass ratio does not influence the pH value.

At 25 °C in the pH range [8-9] (**Fig. 2**), it was possible to form three solids: the monetite ($CaHPO_4$), the brushite ($CaHPO_4.2H_2O$) and the hydroxyapaptite ($Ca_{10}(PO_4)_6(OH_2)$).

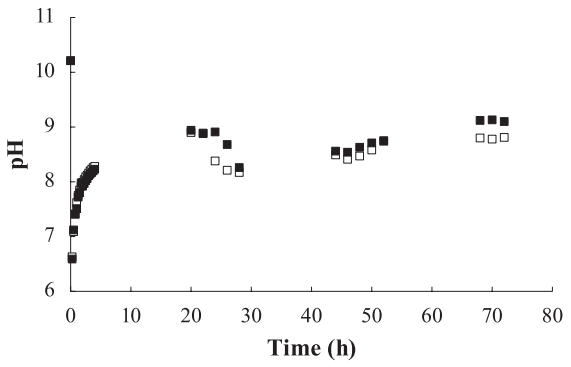

Fig. 2 Evolution of the pH value during synthesis at 400 rpm for two mass ratios (3 □ and 5 ■).

Their formation follows these three reactions respectively (Chkir, 2011; Verwilghen, 2009):

(1) Monetite (metastable phase):

$$CaCO_3 + NH_4H_2PO_4 \rightarrow CaHPO_4 + CO_2 + H_2O + NH_3$$

(2) Brushite:

$$CaCO_3 + NH_4H_2PO_4 + H_2O \rightarrow CaHPO_4.2H_2O + CO_2 + NH_4OH$$

(3) Hydroxyapatite:

$$10CaCO_3 + 6NH_4H_2PO_4 \rightarrow Ca_{10}(PO_4)6(OH_2) + 10CO_2 + 2H_2O + 6NH_4OH$$

(4) Transformation of brushite into hydroxyapatite

$$10CaHPO_4.2H_2O + 4NH_4OH \rightarrow Ca_{10}(PO_4)_6(OH_2) + 4NH_4H_2PO_4 + 18H_2O$$

The analysis did not detect monetite.

When any amount of ammonium dihydrogen phosphate is introduced into the reactor containing the calcium carbonate suspension, gas bubbles with an ammonium odor are observed. This confirms the formation of carbon dioxide and ammonium during the reaction.

As the pH showed low values at the beginning of the synthesis, this may have favored the formation of brushite. The end of synthesis, which sees the stabilization of the pH value at around 9, favors the formation of hydroxyapatite.

3.1 Influence of mass ratio

Two syntheses with two liquid-solid mass ratios of 3 and 5, respectively, carried out at a low stirring rate of 260 rpm in the presence of a RAMAN probe to study the influence of this ratio on the synthesis of Ca-HA.

Tsuda and Arends (1993) give the Raman bands observed for three pure minerals (brushite, octacalcium phosphate OCP and Ca-HA). The spectral features of solids can be characterized as Raman bands due to phosphate (PO_3^{4-}) vibrational modes of v_4, v_2, v_1 and v_3. The intensity of the v_1, band is the strongest, and can be used for the identification of minerals.

Figs. 3, **4** and **5** show the Raman spectra during the synthesis made with a mass liquid-solid ratio of 5 and a stirring rate of 260 rpm. In **Fig. 3**, we observe the appearance of a peak at 983 cm^{-1} after 20 min of synthesis. This peak is relatively wide. Its intensity increases with time. This peak noted on **Fig. 4** corresponds to the brushite, a compound observed in previous studies (Chkir, 2011).

The presence of brushite is confirmed by XR diffraction analysis (**Fig. 6**).

After 19 h, a second peak close to the brushite peak appears at 962 cm^{-1}; this corresponds to the Ca-HA. While the peak intensity of brushite decreases, the peak inten-

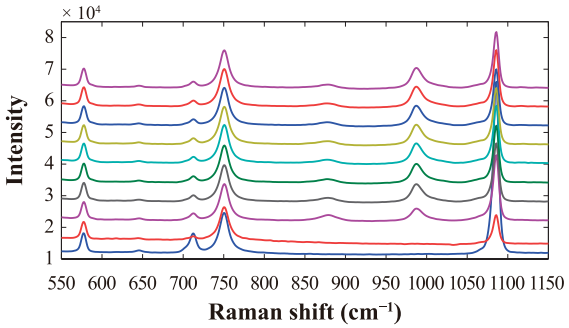

Fig. 3 Raman spectra measured every 19 min between 0 and 3 h, (liquid-solid mass ratio = 5 and N = 260 rpm). Times from the bottom to the top.

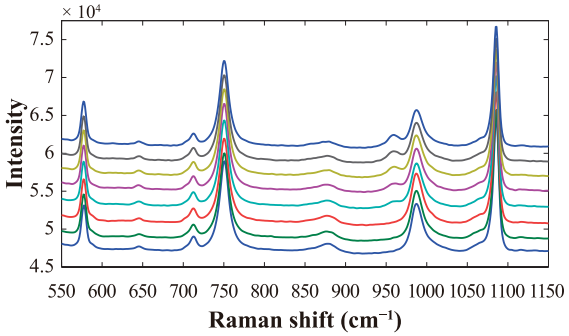

Fig. 4 Raman spectra measured every 4 h between 3 h 10 min and 24 h 19 min, (liquid-solid mass ratio = 5 and N = 260 rpm). Times from the bottom to the top.

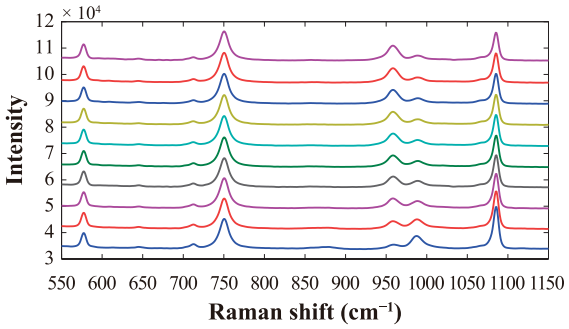

Fig. 5 Raman spectra measured every 8 h between 19 h 20 min and 91 h 20 min, (liquid-solid mass ratio = 5 and N = 260 rpm). Times from the bottom to the top.

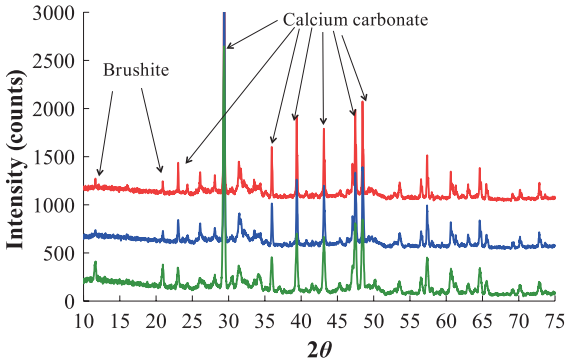

Fig. 6 XR diffraction spectra at 0.75, 2 and 4 hours (liquid-solid mass ratio = 5 and N = 260 rpm). Times from the bottom to the top.

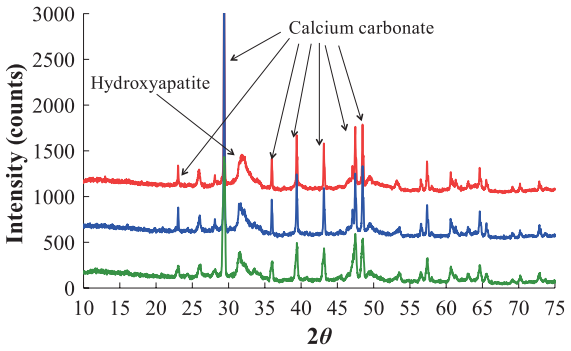

Fig. 7 XR diffraction spectra at 44, 50 and 68 hours (liquid-solid mass ratio = 5 and N = 260 rpm). Times from the bottom to the top.

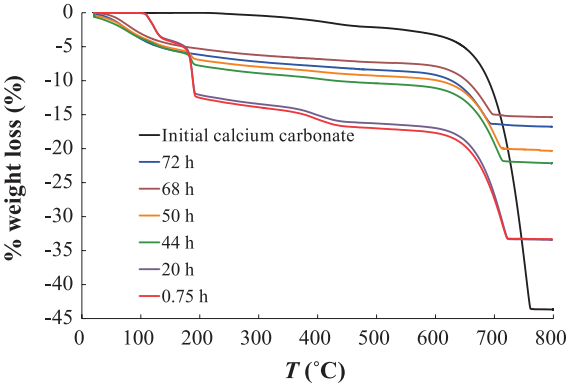

Fig. 8 Weight losses between 20 and 800 °C at 0, 0.75, 4, 20, 44, 50, 68 and 72 h (liquid-solid mass ratio = 5 and N = 260 rpm).

sity of Ca-HA increases (**Figs. 4** and **5**). After 30 h, the intensities of all peaks are stable. This assumption has been verified qualitatively by XR diffraction analysis (**Fig. 7**). At 44 h, the brushite is no longer visible by this technique. The large peak observed at 30–33° corresponds to Ca-HA.

Fig. 8 shows the weight losses of the different samples measured between 20 and 800 °C by TG analysis for dry solids obtained during the synthesis made with a mass ratio of 5 and a stirring rate of 260 rpm. For the pure calcium carbonate, two weight losses are observed: one between 350 and 400 °C and another after 600 °C. The first loss is due to the degradation of impurities contained in $CaCO_3$. The decomposition of calcium carbonate ($CaCO_3$) in calcium oxide (CaO) and carbon dioxide (CO_2) (decarbonation) induces the second loss.

For the other samples, three weight losses are observed.

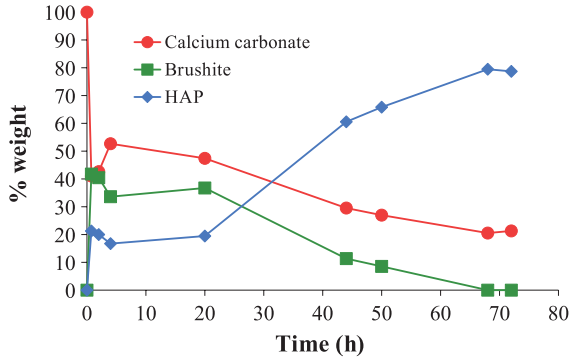

Fig. 9 Mass percentages of brushite, calcium carbonate and Ca-HA during the synthesis.

The first is between 180 and 200 °C, the second between 350 and 400 °C and the third after 600 °C. This first is attributed to loss of the hydration water of brushite (detected by RAMAN spectra analysis), the second to impurities and the third to the decarbonation of unreacted $CaCO_3$. The weight loss observed between 50 and 120 °C is due to insufficient drying of these samples. From these mass losses, by assuming that only three solids are present in the reactor ($CaCO_3$, $CaHPO_4.2H_2O$ and $Ca_{10}(PO4)_6(OH_2)$), the mass percentage of these three components in the solid can be calculated (**Fig. 9**).

Four steps can be observed. The first step (I) corresponds to the dissolution of calcium carbonate and formation of apatite: a sharp decrease in calcium carbonate (around 40 %) during the first hour, and a sharp increase in brushite (around 40 %) and Ca-HA (around 20 %).

During the second step (II) between 4 and 20 h, the weight percentage of solids seems to be constant. After 20 h, we can observe an increase in the weight percentage of Ca-HA up to 80 wt% and a decrease in the $CaCO_3$ and brushite weight percentages. This step (III) corresponds to the transformation of brushite into Ca-HA by dissolution-crystallization or by solid-solid transformation. However, the reaction is not complete and 20 wt% of the solid remaining is composed of calcium carbonate. After 68 h, two solids are in suspension: $CaCO_3$ and Ca-HA. The mass balance on calcium leads to the total weight as a function of time from mass fractions and initial weight of $CaCO_3$:

$$m_T(t) = \frac{m^i_{CaCO_3}}{M_{CaCO_3}} \frac{1}{\left(\frac{w_{brushite}}{M_{brushite}} + 10\frac{w_{HAP}}{M_{HAP}} + \frac{w_{CaCO_3}}{M_{CaCO_3}} \right)} \quad (1)$$

where $m^i_{CaCO_3}$ is the initial weight of $CaCO_3$, M_j the molar weight and w_j the mass fraction of the component j in the solids mixture.

Fig. 10 presents the evolution of weight of each solid during a synthesis for both liquid-solid mass ratios, 3 and 5.

Furthermore, by coupling the results of the loss of mass

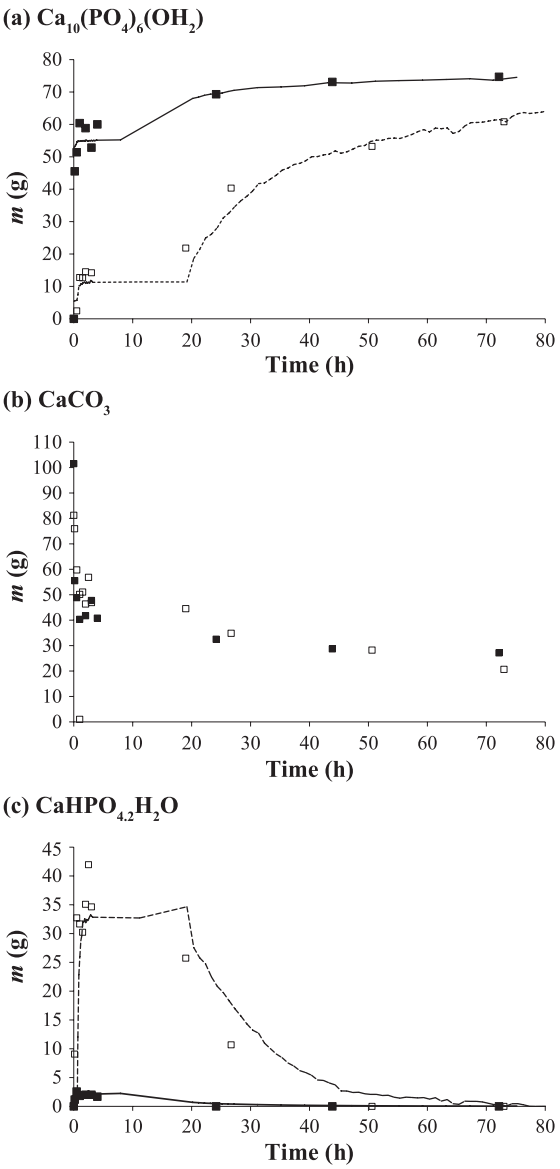

Fig. 10 Masses during the synthesis (N = 260 rpm) for liquid-solid mass ratio = 5, symbols: hollow square and - -; and liquid-solid mass ratio = 3, symbols: black square and - .

and the RAMAN spectra, it is possible to calibrate the area of RAMAN peaks observed in 983 and 962 cm^{-1}, respectively, for the brushite and the Ca-HA according to the mass fractions obtained by TGA. This calibration leads to the continuous curves given in **Fig. 10**. Both weight ratios lead to final masses that are close to $CaCO_3$ initial masses.

The conversion does not seem to depend on the initial weight ratio. This conversion is not total, but is of the order of 73–74 wt%. We also note that the maximum mass of brushite formed for a liquid-solid mass ratio equal to 3 is 13 times weaker than that formed for a liquid-solid mass ratio of 5 (**Fig. 10 (c)**).

Beyond 20 h for a liquid-solid ratio of 3 and 40 h for a

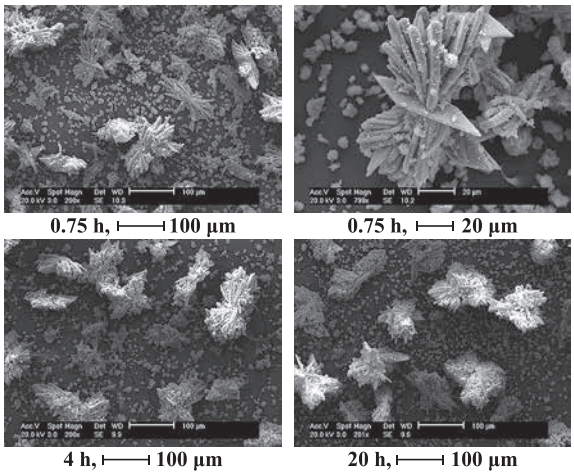

Fig. 11 Morphology of brushite at 0.75, 4 and 20 h (liquid-solid mass ratio = 5 and N = 260 rpm).

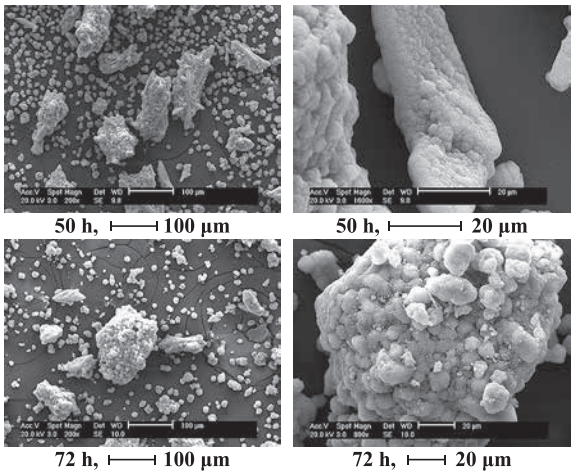

Fig. 13 Morphology of Ca-HA 50 and 72 h (liquid-solid mass ratio = 5 and N = 260 rpm).

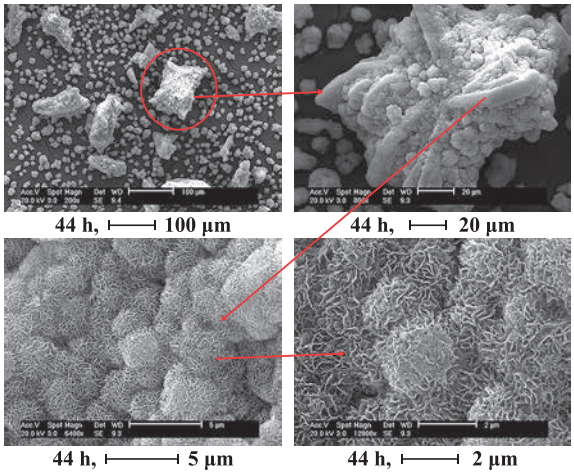

Fig. 12 Morphology of Ca-HA at 44 h (liquid-solid mass ratio = 5 and N = 260 rpm).

liquid-solid ratio of 5, the brushite seems to have totally disappeared. In parallel, the formation of Ca-HA is much faster for an *L/S* ratio of 3 within the first hours (77 wt% of the final mass is reached (**Fig. 10 (a)**). After 10 h of synthesis, a slowing down is observed.

The particles of brushite are formed preferably in the solution (**Fig. 11**), while the particles of Ca-HA are created on the surface of the brushite particles (**Fig. 12**) or (**Fig. 11**). The particles of $CaCO_3$ are attacked by orthophosphate ions. Therefore, $CaCO_3$ is used to form monetite. This compound is transformed into brushite which evolves to the hydroxyapatite (calcium phosphate thermodynamically more stable). When the liquid-solid mass ratio decreases, the available surface of $CaCO_3$ is larger, allowing the reaction (3) to occur on the surface of $CaCO_3$. This behavior limits the brushite formation by reaction (2). The mass growth rate of Ca-HA at the initial time can be written as:

$$\left.\frac{dm_{Ca\text{-}HA}}{dt}\right|_{t=0} = K\, S^{j}\, \Delta C^{g} \qquad (2)$$

where K is a kinetic constant, ΔC is the absolute supersaturation of Ca-HA, and S is the $CaCO_3$ disposable surface at the time at which Ca-HA is detectable.

As the initial size distribution of calcium carbonate is identical, the surface (S) is assumed proportional to mass.

The ratio of these initial rates for liquid-solid mass ratios of 3 and 5 leads to a coefficient j of the order of 12.5, thereby showing a strong influence of the available surface of calcium carbonate on the Ca-HA formation. As the Ca-HA layer forms on the surface of $CaCO_3$, the diffusion of orthophosphate and calcium ions is limited thus reducing the mass growth formation of Ca-HA observed beyond 10 h for a liquid-solid mass ratio of 3. In the case of a higher ratio, it can be assumed that reactions (2) and (4), which represent the $CaCO_3$ and brushite formations, respectively, occur in parallel.

Fig. 14 shows the evolution of the mass mean diameter as a function of the time based on both mass ratios (liquid-solid mass ratios of 3 and 5) for a stirring speed of 260 rpm. For a liquid-solid mass ratio of 5, the increase in average diameter (7–22 microns) between 0 and 3 is due to the brushite formation (**Fig. 14 (a)**). After 3 h, the mean diameter decreases assumed by brushite dissolution. Beyond 20 h, the mean diameter increases following the same trend as Ca-HA mass (**Fig. 14 (b)**).

Brushite dissolution allows Ca-HA formation. This compound is thermodynamically more stable than brushite (Ferreira et al. 2003) and it forms on the surface of $CaCO_3$ causing the increase in diameter. For a liquid-solid mass ratio of 3 (**Figs. 15 (a)** and **(b)**), the same behavior is observed, meaning that the mass mean diameter increases, then decreases and finally increases again. However, beyond 20 h, the mean diameter does not change (about 20 µm) because the Ca-HA mass stabilizes.

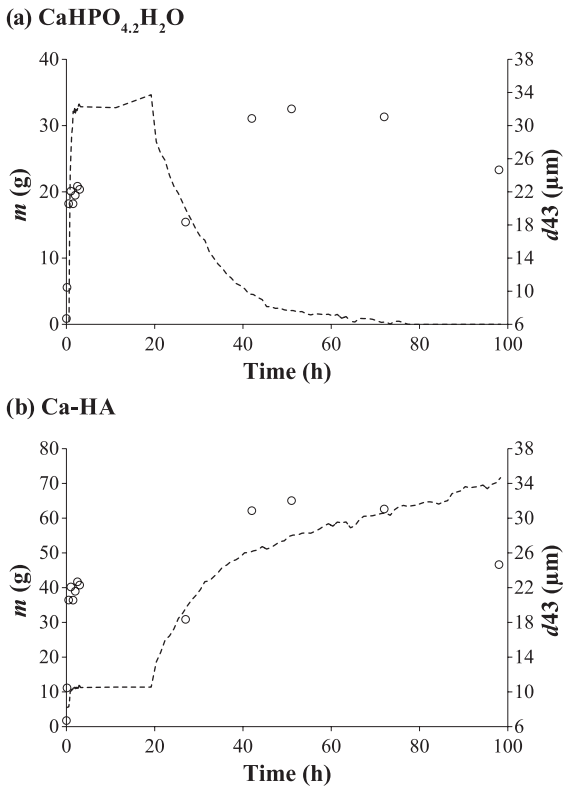

Fig. 14 CaHPO4.2H2O and Ca-HA masses calculated from RAMAN spectra and mean volume diameter during synthesis (N = 260 rpm and liquid-solid mass ratio = 5), symbols: hollow circle ($d43$) and -- (compound masses).

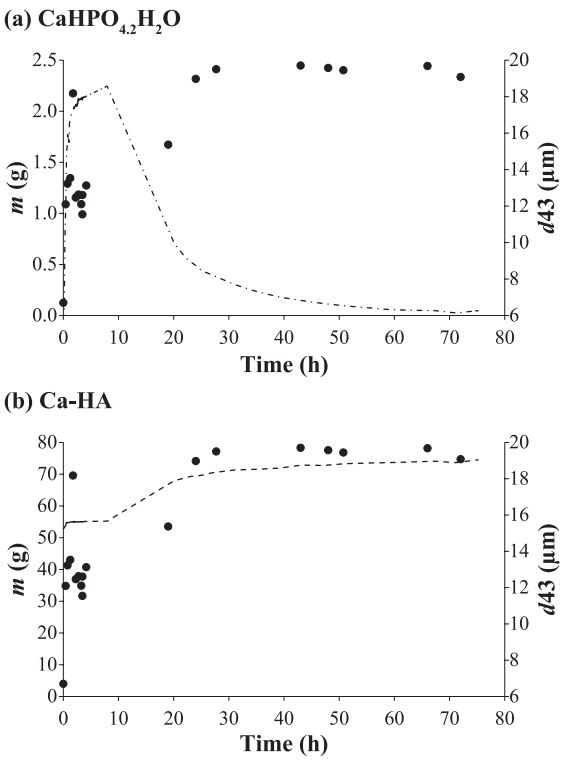

Fig. 15 CaHPO4.2H2O and Ca-HA masses calculated from RAMAN spectra and mean volume diameter during synthesis (N = 260 rpm and liquid-solid mass ratio = 3), symbols: black circle ($d43$) and -- (compound masses).

Fig. 16 presents the mean diameters of the particles during synthesis for different stirring speeds (400 and 600 rpm) for both mass ratios (L/S = 3 and 5). The results obtained at 400 and 600 rpm show the same behavior obtained at 260 rpm (increase, decrease, re-increase and stabilization of mean diameter). After 40 h of synthesis, the measured diameters are identical (23 ± 1 µm) for a stirring speed equal to 400 rpm (**Fig. 16 (a)**). Larger agglomerates are observed at a low stirring speed after 72 h of synthesis. The stabilization of the mean diameter is observed after 40 h for all the syntheses except for the synthesis performed at 600 rpm. In this case after 20 h of synthesis, the mass mean diameter is stable and equals 16 ± 1 µm (**Fig. 16 (b)**).

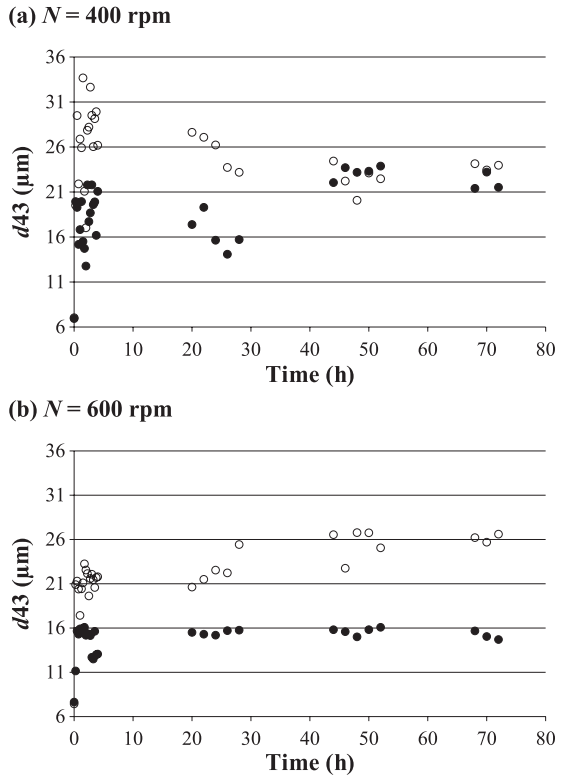

Fig. 16 Mean volume diameter during the synthesis, symbols: black circle (liquid-solid mass ratio = 3) and hollow circle (liquid-solid mass ratio = 5).

4. Conclusions

In this study, we show that Raman spectroscopy is a valuable technique to follow the synthesis of Ca-HA in a concentrated solids suspension (around 20–30 wt%). This technique makes it possible to follow the formation of Ca-HA and brushite and to deduce from complementary measurements a formation mechanism described as fol-

lows:

- The dissolution of calcium carbonate is observed in the first minutes of synthesis.
- The precipitation of brushite and Ca-HA particles is observed in the first four hours of synthesis.
- The transformation of brushite into hydroxyapatite begins after one day. It seems to be the limiting step.

In terms of morphology, agglomerates of hollow ellipsoidal particles were obtained corresponding to the calcium carbonate, while platelets agglomerated like stars corresponded to the brushite and agglomerated spongy spheres or round stick-like compounds of spongy spheres corresponded to the hydroxyapatite.

Through the mass balance obtained from thermogravimetric analysis and from the phosphate ions, it was also verified that at the end of the synthesis, the calcium carbonate was not completely consumed.

Therefore, the reaction is not complete at the end of the synthesis (72 h).

From the analysis performed by laser granulometry during the synthesis with a mass equal to five and three at 260, 400 and 600 rpm, there was a strong influence of the stirring speed on the process. The two effects (positive and negative) that explain the agglomeration process have been presented. For the synthesis with a mass ratio equal to five, the first effect called the size-enlargement phenomenon predominated. In contrast, for the synthesis with a mass ratio equal to three, a predominance of the second effect called the breakage phenomenon was observed. These phenomena were confirmed by the observations made using the environmental electron microscopy of the synthesized solids.

5. Acknowledgements

The authors would like to thank M. H. Lucas for support in the data analysis of RAMAN spectra. They also thank Ms S. Del Confetto, Ms C. Rolland, Ms N. Lyczko and M.P. Accart, respectively, for TG measurements, microscopy analysis and X-Ray, and particle size analysis.

References

Anee T.K., Ashok M., Palanichamy M., Kalkura S.N., A novel technique to synthesize hydroxyapatite at low temperature, Materials Chemistry and Physics, 80 (2003) 725–730.

Bailliez S., Nzihou A., The kinetics of surface area reduction during isothermal sintering of hydroxyapatite adsorbent. Chemical Engineering Journal, 98 (2004) 141–152.

Bezzi G., Celotti G., Landi E., La Torretta T.M.G., Sopyan I., Tampieri A., A novel sol−gel technique for hydroxyapatite preparation. Materials Chemistry and Physics, 78 (2003) 816–824.

Chen X., Wright J.V., Conca, L.M., Peurrung J.L., Effects of ph on heavy metal sorption on mineral apatite. Environmental Science and Technology, 31 (1997) 624–631.

Chkir M., Synthèse de gels phosphocalciques issus de déchets industriels carbonates. Caractérisation physico-chimique, thermique et rhéologique. PhD thesis, Thèse de l'Université de Toulouse Institut National Polytechnique de Toulouse, 2011.

Elliott J.C., Structure and Chemistry of the Apatites and Other Calcium Orthophosphates, Elsevier, Amsterdam, 1994.

Ferreira A., Oliveira C., Rocha F., The different phases in the precipitation of dicalcium phosphate dihydrate, Journal of Crystal Growth, 253 (2003) 599–611.

Itatani K., Iwafune K., Howell F.S., Aizawa M., Preparation of various calcium-phosphate powders by ultrasonic spray freeze-drying technique. Materials Research Bulletin, 35 (2000) 575–585.

Ipekoglu M., Altintas S., Silver substituted nanosized calcium deficient hydroxyapatite. Materials Technology: Advanced Performance Materials, 25 (2010) 295–301.

Jarcho M., Bolen C.H., Hydroxylapatite synthesis and characterization in dense polycrystalline form, Journal of Materials Science, 11 (1976) 2027–2035.

Liu C., Huang Y., Shen W., Cui J., Kinetics of hydroxyapatie precipitation at pH 10 to 11, Biomaterials, 22 (2001) 301–306.

Luo P., Nieh T.G., Preparing hydroxyapatite powders withcontrolled morphology, Biomaterials, 17 (1996) 1959–1964.

Ma Q.Y., Traina S.J., Logan T.J., Ryan J.A., In situ lead immobilisation by apatite, Environnental Science and Technology, 27 (1993) 1803–1810.

Murakami S., Kato K., Enari Y., Kamitakahara M., Watanabe N., Ioku K., Hydrothermal synthesis of porous hydroxyapatite ceramics composed of rod-shaped particles and evaluation of their fracture behaviour. Ceramics International, 38 (2012) 1649–1654.

Nakamura S., Isobe T., Senna M., Hydroxyapatite nano sol prepared via a mechanochemical route. Journal of Nanoparticle Research, 3 (2001) 57–61.

Okada M., Fujii S., Nishimura T., Nakamura Y., Takeda S., Furuzono T., Solvent-free formation of hydroxyapatite coated biodegradable particles via nanoparticle-stabilized emulsion route, Applied Surface Science, 262 (2012) 39–44.

Rodriguez-Lorenzo L.M., Vallet-Regi M., Ferreira J.M.F., Fabrication of hydroxyapatite bodies by uniaxial pressing from a precipitated powder, Biomaterials, 22 (2001) 583–588.

Saha S.K., Banerjee A., Banerjee S., Bose S., Synthesis of nanocrystalline hydroxyapatite using surfactant template systems: Role of templates in controlling morphology. Materials Science and Engineering: C, 29 (2009) 2294–2301.

Silva C.C., Pinheiro A.G., Miranda M.A.R., Góes J.C., Sombra, A.S.B., Structural properties of hydroxyapatite obtained by mechanosynthesis, Solid State Science, 5 (2003) 553–558.

Swain S.K., Dorozhkin S.V., Sarkar D., Synthesis and dispersion of hydroxyapatite nanopowders, Materials Science and Engineering: C, 32 (2012) 1237–1240.

Tsuda H., Arends J., Raman spectra of human dental calculus, Journal of Dental Research, 72 (1993) 1609–1613.
Vasile E., Popescu L.M., Piticescu R.M., Burlacu A., Buruiana T., Physico-chemical and biocompatible properties of hydroxyapatite based composites prepared by an innovative synthesis route, Materials Letters, 79 (2012) 85–88.
Verwilghen C., Chkir M., Rio S., Nzihou A., Sharrock P., Depelsenaire G., Convenient conversion of calcium carbonate to hydroxyapatite at ambient temperature, Materials Science and Engineering: C, 29(3) (2009) 771–773.
Wang C.X., Wang M., Zhou X., Nucleation and growth of apatite on chemically treated titanium alloy: an electrochemical impedance spectroscopy study, Biomaterials, 24 (2003) 3069–3077.
Wen C.F., Zhao Y.L., Liang R.Z., Recycle of low chemical potencial substance resources, Conservation and Recycling, 51 (2007) 475–486.
Wey M.Y., Liu K.Y., Tsai T.H, Chou J.T., Thermal treatment of the y ash from municipal solid waste incinerator with rotary kiln, Journal of Hazardous Material, 137 (2006) 981–989.

Author's short biography

Nayane Macedo Portela da Silva

Dr Nayane Macedo Portela da Silva was born in 1986. She completed her graduate studies at UFRN university of Natal, Brazil. Before her diploma, she joined the EMAC school at Albi, France, to do an internship concentrating on hydroxyapatite synthesis by reaction crystallization (precipitation). She prepared a PhD thesis on microfluidic systems under high pressure in the Laboratory Rapsodee of EMAC school and received her PhD from Toulouse University in 2014.

Fabienne Espitalier

Professor Fabienne ESpitalier is the head of the research group "Powder and Processes" at the Research Centre in Albi for Particulate Solids, Energy and Environment (Rapsodee research centre)-CNRS UMR 5302 at Ecole des Mines Albi in France. Her major research interests concern crystallization assisted or not by ultrasound, non-standard solvents such as ionic liquids, population balance simulation, characterization and particle technology.

Ange Nzihou

Professor Ange Nzihou is the Director of the Research Centre in Albi for Particulate Solids, Energy and Environment (Rapsodee research centre)-CNRS UMR 5302 at Ecole des Mines Albi in France. He is also editor in chief of the international peer-reviewed journal Waste and Biomass Valorization (Springer), and chair of the WasteEng conference series. He has developed outstanding research in the field of the engineering of phosphate-based materials for sorbents and catalysts, and heavy metals contaminants remediation. He has published about 87 papers in peer-reviewed journals.

KONA Powder and Particle Journal No. 33 (2016) 228–238/Doi:10.14356/kona.2016003 Original Research Paper

A Novel Fluorescent Chemosensor Based on β-(2-Pyridyl)acrolein-Rhodamine B Derivative: Polymer Particle Interaction with an Enhanced Sensing Performance †

Kyo-Sun Ku, Ji-Yong Hwang, Palanisamy Muthukumar and Young-A Son *

[1] *Department of Advanced Organic Materials Engineering, Chungnam National University, South Korea*

Abstract

A novel, fluorescent chemosensor based on β-(2-pyridyl)acrolein-rhodamine B (RB-AC) derivative was synthesized and its sensing performance with poly(ethylene glycol) dimethacrylate (PEGDMA) polymer particle was investigated. The prepared β-(2-pyridyl)acrolein-rhodamine B/poly(ethylene glycol)dimethacrylate (PEGDMA/RB-AC) particle was used for sensing of Al^{3+}. The PEGDMA/RB-AC particles showed immediate "off–on" fluorescent responses toward Al^{3+}. The fluorescent response was attributed to the spirolactam ring opening of RB-AC. This sensor particle showed high selectivity towards Al^{3+} in the presence of other competing metal ions. The sensitivity of PEGDMA/RB-AC particle was demonstrated by confocal laser scanning microscopy (CLSM) and scanning electron microscopy (SEM). The binding stoichiometry and binding mode of the metal complex was established by Job's plot and FT-IR spectroscopy.

Keywords: β-(2-pyridyl)acrolein-rhodamine B derivative, rhodamine/polymer particles, aluminium sensing, fluorescent sensor

1. Introduction

The development of selective and sensitive probe for the detection of biologically and environmentally important species has emerged as a significant goal in the field of chemical sensors (Zhou et al., 2014; Xu et al., 2010; Wang et al., 2014). So far, a number of fluorescent probes with different excitation and emission wave lengths have been used as signal receptors of chemosensors such as coumarin (Chen et al., 2014), pyrene (Wang et al., 2013), 1,8-naphthalimide (Dai and Xu, 2011), xanthenes (Chen et al., 2012), squaraine (Akkaya, 1997), cyanine (Zheng et al., 2012) and boron dipyrromethene difluoride (BODIPY) (Li et al., 2012). Among these, xanthene derivatives are of great interest due to their excellent photophysical properties such as long absorption and emission wavelengths, large absorption co-efficient and high fluorescence quantum yield (Beaumont et al., 1993). Rhodamine is a well known dye of xanthenes derivative having spirolactam ring which is color less and non-fluorescent, whereas its ring opened amide form gives strong color and fluorescent emission. Based on this, many rhodamine derivatives have been used as a fluorescent probe for the detection of various metal ions (Kim et al., 2008). The sensing behavior of most of the rhodamine based fluorescent probes was studied in the solution (Zhang et al., 2012; Lee et al., 2015; Lee et al., 2010; Weerasinghe et al., 2009; Ju et al., 2011). In order to use these probes in the fields, it should be materialized. In recent years, the preparation of rhodamine functionalized fluorescent particles for the removal of metal ions received much interest (Jung et al., 2011).

Molecular imprinting polymerization (MIP) is also known as template polymerization and widely used method for synthesizing host polymer which has been recognizing target species. Due to their chemical and mechanical stability, simple preparation, low cost and high selectivity, MIP has been used in wide range of fields such as chromatographic separation, solid-phase extraction, catalysts and sensors (Yang et al., 2009; Andersson, 2000; Li and Husson, 2006). The imprinting mechanism is explained as the trapping of template molecule into the polymer matrix during polymerization as a result the molecular information of the template is retained in the polymeric material in the cross linked powders after complete extraction of the template from the matrix membranes. Two types of interactions between the template

† Received 14 April 2015; Accepted 18 May 2015
J-STAGE Advance published online 30 June 2015
[1] 99 Daehak-ro, Yuseong-gu, Daejeon 305-764, South Korea
* Corresponding author: Young-A Son;
E-mail: yason@cnu.ac.kr
TEL: +82-42-821-6620 FAX: +82-42-821-8870

molecule and functional monomers have been explained such as covalent and non-covalent interactions. The covalent interaction (Wulff and Sarhan, 1972) creates bonds between the template and polymer whereas non-covalent interaction (Haupt and Mosbach, 2000) creates electrostatic interactions such as π-π interaction and hydrogen bonds. The non-covalent technique has been preferentially used for different reasons such as easily conducted, the removal of the template is achieved through continuous extraction and a substantial number of functionalities can be introduced into the binding sites (Yan and Row, 2006). Immobilization of the indicators in matrices has substantial effects on the performance of the optical sensors in terms of selectivity, sensitivity, and stability. Keeping these factors in mind, in this study, we have retained the template in polymer matrices as a recognizing unit instead of extraction of template from polymer matrices.

Recently, our research group involves the development of colorimetric/fluorogenic chemosensors for selective detection of different types of analytes (So et al., 2014; Jeong et al., 2015). It is well documented that the spirolactam ring of the rhodamine derivative is open when it interacts with the metal ions and in turn it shows the fluorescence. Thus, in this article we have made an attempt to synthesis a simple new rhodamine derivative and used this as a template for the preparation of PEGDMA/rhodamine solid sensory particles. The prepared PEGDMA-rhodamine particles have been used for the sensing of Al^{3+}. The particle shows fluorescent turn on when it interact with Al^{3+}. The prepared rhodamine template was characterized using ^{1}H NMR and mass spectroscopy and the PEGDMA/rhodamine solid sensory particles were characterized confocal image and scanning electron microscopy.

2. Experimental section

2.1. Materials

The chemicals for the synthesis of β-(2-pyridyl)acrolein-rhodamine B derivative (RB-AC) were purchased from Aldrich and Kanto Chemicals Japan and were used without further purification. All reagents and solvents are of analytical grade and used without further purification. The metal ions such as Li^+, Na^+, K^+, Cs^+, Mg^{2+}, Ca^{2+}, Fe^{2+}, Co^{2+}, Ni^{2+}, Cu^{2+}, Zn^{2+}, Ag^+, Cd^{2+}, Hg^{2+}, Pb^{2+}, Al^{3+} as perchlorate salts were purchased from commercial suppliers and used without further purification. Ethylene glycol dimethacrylate (EGDMA) was obtained from the Sigma Chemical Company, USA, and was used as received without purification. Azobisisobutyronitrile (AIBN) and poly(vinylpyrrolidone) (PVP) were obtained from Acros Organics, New Jersey, USA. Ethylene glycol dimethacrylate (EGDMA) was used as the monomer. 2,2-Azobisisobutyronitrile (AIBN) and poly(vinyl pyrrolidone) (PVPK-85-95, Mw = 1,300,000) were used as the initiator and stabilizer, respectively.

2.2. Instrumentation

Nuclear magnetic resonance (NMR) spectra were recorded in $CDCl_3$ unless otherwise stated, with tetramethylsilane (TMS) as internal reference at ambient temperature, mainly on a BRUKER AVANCE III 300 Magnet: Ascend TM series, 14.1 Tesla, ^{1}H resonance frequency 300 MHz, Top Spin 3.1 (software) spectrometer Germany spectrometers. HR-MS spectrum was recorded with Bruker autoflex III mass spectrometer. FT-IR spectra were recorded with an FTS-175C spectrometer. UV-Visible absorption spectra were recorded on an Agilent 8453 spectrophotometer. Fluorescence emission spectra were recorded on a Shimadzu RF-5301PC spectroflurophotometer. The slit width was 1.5 nm for both excitation and emission. Samples were contained in 10.0 nm path length quartz cuvettes (3.5 mL volume). Fluorescence imaging was performed by confocal fluorescence microscopy on LSM5Live, (Germany) with Zeiss LSM5 Live Release version 4.2.SP1 Image Browser software were used. The scanning electron microscope (SEM) images were obtained by JEOL, JSM-7000F.

2.3. Synthesis of RB-AC

Rhodamine B hydrazide and β-(2-pyridyl)acrolein were prepared following the literature method (Zhang et al., 2011; Krasnaya et al., 1997). The synthesis of RB-AC is shown in **Scheme 1**. In a 100 mL three necked round bottom flask, rhodamine B hydrazide (1.23 g, 2.6 mmol) was dissolved in hot ethanol (30 mL). Then, a solution of 0.5 g (3 mmol) of β-(2-pyridyl)acrolein in 20 ml of ethanol was added drop wise to the flask in 1 h. After the addition of β-(2-Pyridyl)acrolein, 1 ml of acetic acid was added to the reaction mixture. Under stirring, the reaction mixture was refluxed for 5 h. After 5 h, the reaction mixture was cool to room temperature and the formed precipitate was filtered and washed with cold ethanol. The crude product was purified by column chromatography using hexane-ethyl acetate (60:40) as eluent to get pure product (1.01 g, yield = 69.1 %). The Product was confirmed by ^{1}H NMR and mass spectroscopy (**Fig. S1 and S2**).

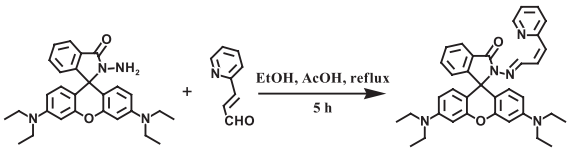

Scheme 1 Synthesis of RB-AC.

2.4. Synthesis of PEGDMA/RB-AC particles

The dispersion medium (stabilizer) was prepared by dissolving 1.5 g of poly(vinyl pyrrolidone) (PVP) in de-ionized water (150 mL). The synthesis was performed in a three-necked flask equipped with a stirrer, water condenser and thermometer. A mixture containing 17 g of ethylene glycol dimethacrylate (EGDMA), initiator, 0.255 g of azobisisobutyronitrile (AIBN) and 0.0017 g of RB-AC was diluted with a mixed solvent (toluene (8 mL)/ butanol (8 mL)).The reaction mixture transferred to the PVP dispersion medium and this reaction mixture was purged with N_2 gas for 10 min after that the reaction mixture was sealed under this nitrogen atmosphere and heated at 80 °C for overnight. The produced polymer was filtered using a Whatman filter number 1 and washed with acetone and methanol to get the RB-AC encapsulated PEGDMA (PEGDMA/RB-AC) as white powder.

3. Results and discussion

3.1. Preliminary studies

In order to evaluate the sensing behavior of PEGDMA/RB-AC, we have examined the absorbance, fluorescence and visible color change of the RB-AC in solution in the presence of various metal ions including alkali, alkaline-earth and transition-metal ions such as Li^+, Na^+, K^+, Cs^+, Mg^{2+}, Ca^{2+}, Fe^{2+}, Co^{2+}, Ni^{2+}, Cu^{2+}, Zn^{2+}, Ag^+, Cd^{2+}, Hg^{2+}, Pb^{2+} and Al^{3+}, in ethanol/DMF (v/v = 9/1). The absorbance spectrum of RB-AC doesn't show any peaks longer than 500 nm which was attributed to the ring closed spirolactam form of RB-AC (**Fig. 1**) (Chen et al., 2012). As shown in **Fig. 1**, the absorbance intensity of RB-AC was significantly increased at 560 nm upon the addition of Al^{3+} whereas no changes in absorbance intensity of RB-AC were observed upon the addition of other competitive metal ions. **Fig. 2** shows the fluorescence changes of RB-AC in the presence of different metal ions. The RB-AC alone doesn't show any fluorescence peak around 580 nm. The addition of Al^{3+} into RB-AC showed the considerable enhancement in fluorescence intensity at 580 nm. Further the addition of other competitive metal ions doesn't lead the fluorescence enhancement of the RB-AC.

Furthermore, the sensing behavior of RB-AC with different significant metal ions was checked by 'naked eye' detection methods. As shown in **Fig. 3**, the synthesized RB-AC displays a 'naked-eye' color change from color less to pink (**Fig. 3, top**) after the addition of 10 μM of Al^{3+} in ethanol/DMF (9:1) mixture. While in the case of other cations such as Li^+, Na^+, K^+, Cs^+, Mg^{2+}, Ca^{2+}, Fe^{2+}, Co^{2+}, Ni^{2+}, Cu^{2+}, Zn^{2+}, Ag^+, Cd^{2+}, Hg^{2+} and Pb^{2+} does not produce any significant color changes. Further, the addition of Al^{3+} exhibits intense yellow fluorescence under illumination of UV-light (**Fig. 3, bottom**). Thus, the sensing of Al^{3+} by RB-AC can be detected by the naked eye without the assistance of any instrument.

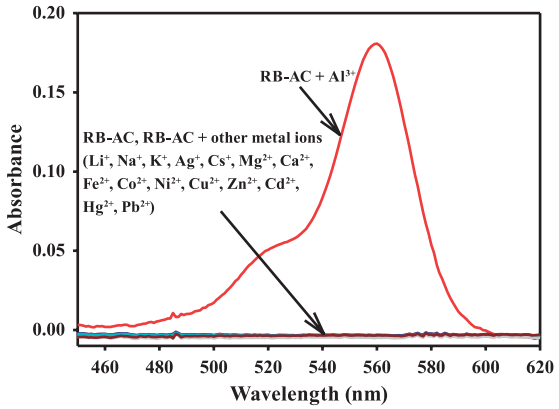

Fig. 1 Absorbance spectra of 10 μM of RB-AC in ethanol/DMF (9:1) in the presence of 10 μM of different metal ions.

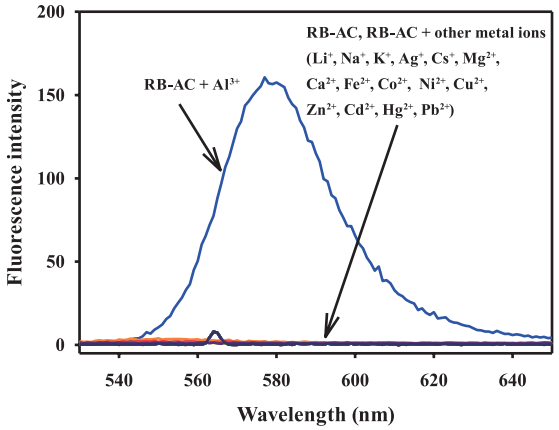

Fig. 2 Fluorescence spectra of 10 μM of RB-AC in ethanol/DMF (9:1) in the presence of 10 μM of different metal ions.

3.2. Spectroscopic recognition of RB-AC towards Al^{3+}

UV-Vis and fluorescence spectral methods were used to study the recognition of RB-AC towards Al^{3+}. UV-vis spectra of RB-AC in ethanol/DMF (9:1) mixture in the presence of different concentrations of Al^{3+} are shown in **Fig. S3**. In the absence of Al^{3+}, the absorption spectrum of RB-AC doesn't exhibit any characteristic absorption of rhodamine moiety whereas upon the addition of Al^{3+}, a new absorption band centered at 560 nm was observed. Further addition of Al^{3+} into RB-AC leads to the increase in absorbance at 560 nm. This indicated a clear and gradually color change from colorless to pink due to the opening of the closed rhodamine spirolactam ring.

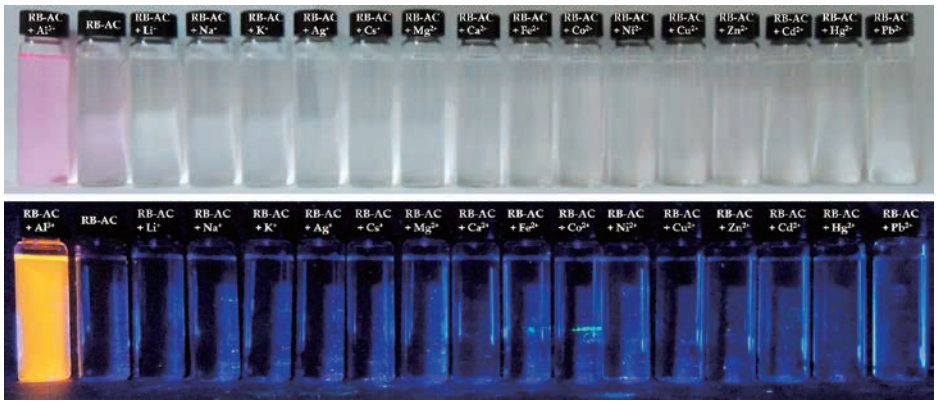

Fig. 3 Photographs of color changes of RB-AC (10 μM) in ethanol/DMF (9:1) in the presence of various metal ions detected by naked eye (top) and by UV-lamp (bottom).

Due to its high sensitivity, fluorescence spectroscopy has been widely used in the study of molecular interactions between rhodamine and metal ions (Chen et al., 2009). **Fig. S4** shows the fluorescence spectra of RB-AC in ethanol/DMF (9:1) mixture was recorded against the different concentrations of Al^{3+}. As shown in **Fig. S4**, while increasing the concentration of Al^{3+} the fluorescence intensity at 580 nm was gradually increased. The binding constant of RG-HN with Al^{3+} was determined using Benesi-Hildebrand equation (**Fig. S5**). It was found to be 4.70×10^4 which was within the range of reported Al^{3+} chemosensors (Kim et al., 2014).

The detection limit of the receptor RB-AC towards Al^{3+} was calculated based on 3δ/k (Lohani et al., 2010). Where, δ is the standard deviation of the blank solution and k is the slope of the calibration plot. A linear response was observed when the concentration of Al^{3+} is plotted against fluorescence intensity with a correlation coefficient of 0.982 (**Fig. S6**). The detection limit was calculated from slope and it was found to be 5.4×10^{-8} M.

3.3. Sensing property of PEGDMA/RB-AC particles towards Al^{3+}

The results discussed in previous sections indicated that the synthesized RB-AC has good recognition towards Al^{3+} and it can be used for the preparation of sensing probe for Al^{3+}. In order to improve the sensing performance of RB-AC, we have addressed the task of designing of RB-AC encapsulated PEGDMA particles. To demonstrate the encapsulation of RB-AC by PEGDMA, we have studied the color change of PEGDMA/RB-AC particles in ethanol/DMF (9:1) mixture with and without Al^{3+}. In the absence of Al^{3+}, PEGDMA/RB-AC particles in ethanol/DMF (9:1) mixture doesn't show any color. After the addition of Al^{3+} to the PEGDMA/RB-AC particles in ethanol/DMF mixture (9:1), the color of the particles was changed colorless to pink and the particle

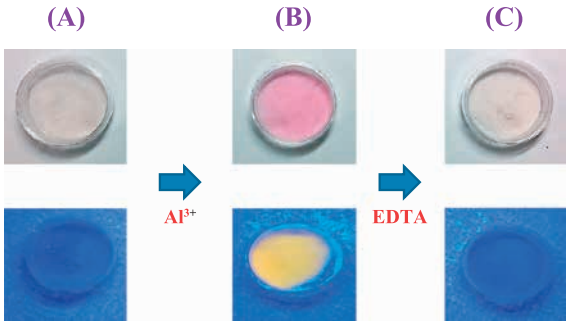

Fig. 4 Photographs of PEGDMA/RB-AC in absence (A), presence (B) of 10 μM of Al^{3+} and reversibility with 10 μM of EDTA (C) detected by naked eye (top) and UV-lamp (bottom).

showed yellow fluorescence under the illumination of UV-light as shown in the **Fig. S7**. Further, the sensing performance was examined by the addition of 1 mL of 10 μM of Al^{3+} in ethanol/DMF (9:1) mixture into the 1.0 g of synthesized PEGDMA/RB-AC particles. Besides that the mixture was stirred for 5 min up to attain the pink solid and filtered through the filter paper. As shown in **Fig. 4**, after the addition of Al^{3+}, the color of the PEGDMA/RB-AC was turned from colorless to pink and it showed yellow emission under illumination of UV light, which is sensible via naked eye. The reversibility of PEGDMA/RB-AC was checked by the addition of 1 mL of 10 μM of EDTA extraction. Upon addition of EDTA in to Al^{3+} bounded PEGDMA/RB-AC, the color of the particle was turned from pink to color less and the yellow fluorescent emission was also turned off (**Fig. 4**). Further, the selectivity of PEGDMA/RB-AC particles towards Al^{3+} in the presence of 10 μM of other competitive metal ions was checked. As depicted in **Fig. 5**, Al^{3+} only changes the color of PEGDMA/RB-AC particles from color less to pink in visible light and yellow fluorescence under UV light whereas other competitive metal ions did not showed any changes. This indicates that the

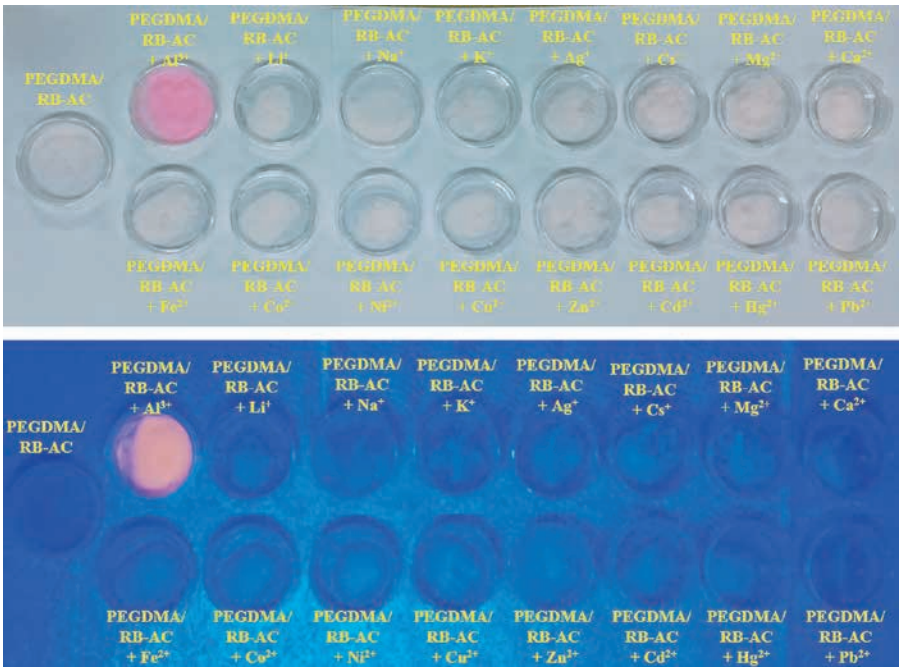

Fig. 5 Photographs of PEGDMA/RB-AC in the presence of 10 μM of various metal ions detected by naked eye (top) and by UV-lamp (bottom).

PEGDMA/RB-AC particles show the fluorescence turn on by sensing of Al^{3+} with good selectivity and reversibility.

3.4. Depicting the sensing property of PEGDMA/RB-AC by confocal laser scanning microscopy (CLSM)

Consequently, it was of great interest to investigate the sensory property by CLSM (Tao et al., 2011). The 1 mL of 1×10^{-6} M Al^{3+} (ethanol/DMF (9:1)) was dropped on the surface of a dry PEGDMA/RB-AC particles and allowed to stand for 1 min, resulting in the immediate adsorption of the Al^{3+} by particles, after drying the particles in an oven at 150 °C, the CLSM was performed. As shown in **Fig. 6A**, PEGDMA/RB-AC particles did not show any fluorescence under the selective excitation whereas after the dropping of Al^{3+} (1 mL) in to the PEGDMA/RB-AC particles, a significant increase in the fluorescence was observed from the selective excitation area (**Fig. 6B**).

3.5. Al^{3+} binding on PEGDMA/RB-AC by SEM analysis

The CLSM results confirmed that the sensing property of PEGDMA/RB-AC towards Al^{3+}, to get further insight, SEM analysis was carried out. **Fig. 7** showed the SEM images of prepared PEGDMA polymer encapsulated RB-AC in the absence and presence of Al^{3+}. The morphology of prepared PEGDMA/RB-AC particles is spherical in shape, and was arranged in an orderly three-dimensional shape and the particle size distribution is given in **Fig. S8**. There is only a little bonding between the particles (**Fig. 7A**). While in the presence of 1×10^{-5} M of Al^{3+}, the PEGDMA/RB-AC particles were aggregated together (**Fig. 7B**). The difference in the surface morphology of these samples may be due to the formation of complex between RB-AC and Al^{3+} followed by ring opening. Energy-dispersive analysis of X-rays (EDAX) was used to analyze the elemental constituents of prepared PEGDMA/RB-AC particles in the presence of Al^{3+}. **Fig. 8** illustrates the EDAX spectra of PEGDMA/RB-AC particles after the sensing of Al^{3+}. The presence of aluminum in elemental analysis confirmed that the Al^{3+} has been entrapped into PEGDMA/RB-AC by formation of complex with RB-AC.

3.6. Mechanism for the sensing of Al^{3+} by PEGDMA/RB-AC

Since the sensing part of PEGDMA/RB-AC is RB-AC, to investigate the recognition of PEGDMA/RB-AC towards Al^{3+}, the stoichiometry and complex formation of RB-AC to Al^{3+} were studied. The stoichiometry of RB-AC to Al^{3+} was calculated by Job's plot analysis and the complex formation was explained by FT-IR binding study. Total concentration of RB-AC and Al^{3+} was kept constant at 10 μM according to the continuous variations changing the mole fraction of RB-AC from 0.1 to 0.9 (**Fig. S9**). The stoichiometry ratio of RB-AC with Al^{3+} was analyzed by absorbance method. The maximum of curve

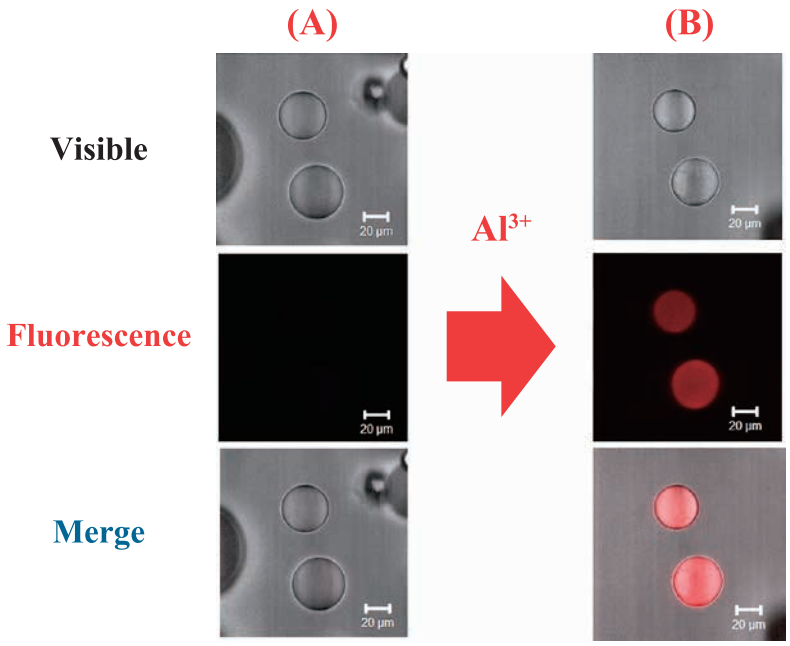

Fig. 6 CLSM images of PEGDMA/RB-AC in absence (A) and presence (B) of Al^{3+}.

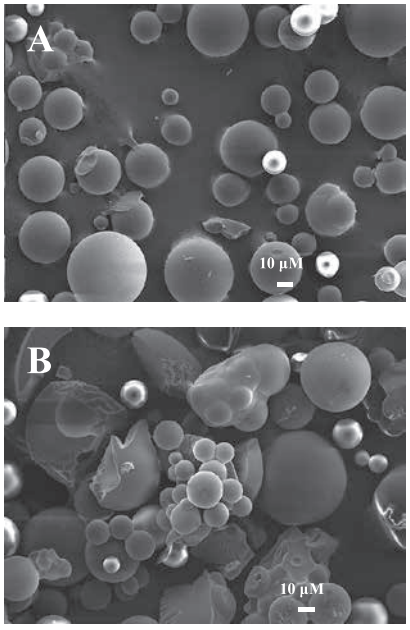

Fig. 7 SEM images of PEGDMA/RB-AC in absence (A) and presence (B) of Al^{3+}.

was showed at 0.5 mole fraction, indicating that the formation of 1:1 complex between RB-AC and Al^{3+}. **Fig. 9** shows the FT-IR spectra of RB-AC before and after binding with Al^{3+}. The FT-IR spectrum of RB-AC alone shows the peaks at 1678, 1610 and 1550 cm^{-1} corresponding to spirolactam amide carbonyl, imine (C = N) and pyridine (C = N) stretching vibrations, respectively. While the addition of 1 eq of Al^{3+}, the stretching frequency of these peaks was changed. Upon the addition of 1 eq Al^{3+} the characteristic stretching frequency of spirolactam rings amide carbonyl at 1698 cm^{-1} was completely disappeared and the imine (C = N) and pyridine (C = N) stretching vibrations are shifted to 1643 and 1580 cm^{-1}, respectively. Which confirms the Al^{3+} was opened the spirolactam ring, formed the complex with oxygen and imine and pyridine nitrogen. It has been well established that Al^{3+} forms complex with oxygen and nitrogen rich ligands (Dhara et al., 2014; Ghosh et al., 2014). Based on this, we have proposed the complex formation of Al^{3+} with RB-AC (**Scheme 2**).

4. Conclusion

In conclusion, we have developed a novel fluorescent probe β-(2-pyridyl)acrolein-rhodamine B/poly(ethylene glycol) dimethacrylate (PEGDMA/RB-AC). The PEGDMA/RB-AC particles showed good selectivity and sensitivity towards Al^{3+}. Fluorescence enhance mechanism is presumably due to the chelation of Al^{3+} with the oxygen atoms of the amide groups of RB-AC results in the formation of the open-ring form, which leads to the enhancement of fluorescence of PEGDMA/RB-AC particles. The selectivity for Al^{3+} can be attributed to the rigid hydrazone binding site as well as the affinity of the pyridine group toward Al^{3+}.

Acknowledgements

This work was supported by research fund of Chungnam National University.

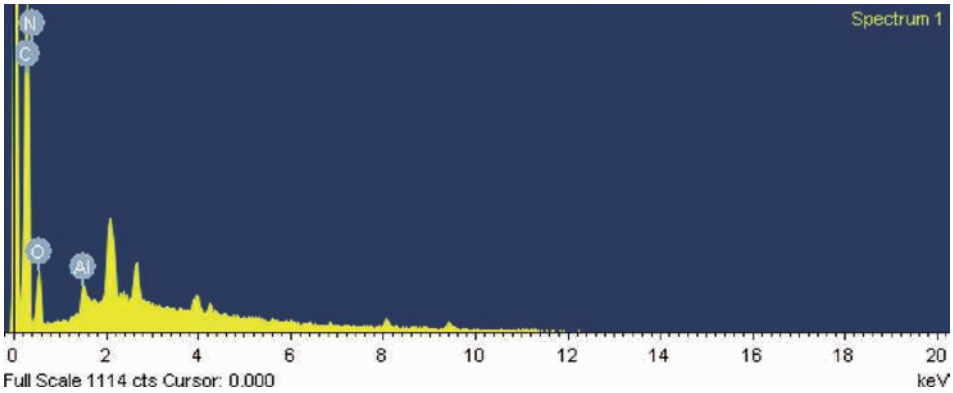

Fig. 8 EDAX spectra of PEGDMA/RB-AC in the presence of Al^{3+}.

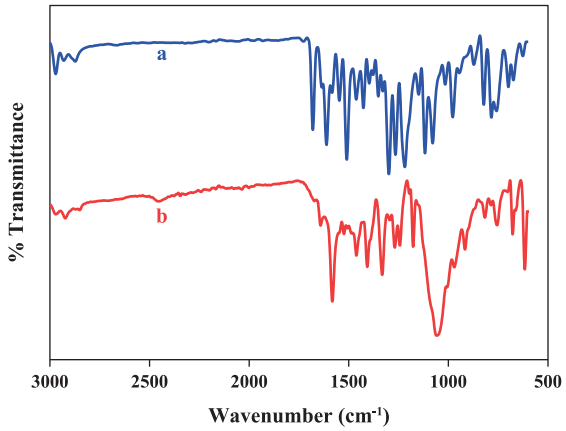

Fig. 9 FT-IR spectra of RB-AC before (a) and after (b) binding with Al^{3+}.

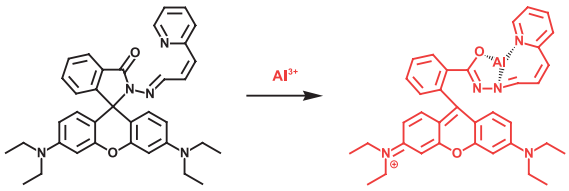

Scheme 2 Plausible binding mode of RB-AC with Al^{3+}.

References

Akkaya E.U., Squaraine-based long wavelength fluorescent chemosensors for ions, Chemosensors of Ion and Molecule Recognition, 492 (1997) 177–188.

Andersson L.I., Molecular imprinting for drug bioanalysis: A review on the application of imprinted polymers to solid-phase extraction and binding assay, J. Chromatogr. B., 739 (2000) 163–173.

Beaumont P.C., Johnson D.G., Parsons B.J., Photophysical properties of laser dyes: picosecond laser flash photolysis studies of rhodamine 6G, rhodamine B and rhodamine 101, J. Chem. Soc., Faraday Trans., 89 (1993) 4185–4191.

Chen F., Liu .G., Shi Y., Xi P., Cheng J., Hong J., Shen R., Yao X., Bai D., Zeng Z., A coumarin-derived fluorescent chemosensor for selectively detecting Cu^{2+}: Synthesis, DFT calculations and cell imaging applications, Talanta, 124 (2014) 139–145.

Chen X., Jou M.J., Lee H., Kou S., Lima J., Nam S-W., Park S., Kim K.W., Yoon J., New fluorescent and colorimetric chemosensors bearing rhodamine and binaphthyl groups for the detection of Cu^{2+}, Sen. Actuators B, 137 (2009) 597–602.

Chen X., Pradhan T., Wang F., Kim J.S., Yoon J., Fluorescent chemosensors based on spiroring-opening of xanthenes and related derivatives, Chem. Rev., 112 (2012) 1910–1956.

Dai H., Xu H., A water-soluble 1,8-naphthalimide-based 'turn on' fluorescent chemosensor for selective and sensitive recognition of mercury ion in water, Bioorg. Med. Chem. Lett., 21 (2011) 5141–5144.

Dhara A., Jana A., Guchhait N., Ghosh P., Kar S.K., Rhodamine-based molecular clips for highly selective recognition of Al^{3+} ions: synthesis, crystal structure and spectroscopic properties, New. J. Chem., 38 (2014) 1627–1634.

Ghosh K., Majumdar A., Sarkar T., Selective sensing of Al^{3+} by naphthyridine coupled rhodamine chemosensors, RSC Adv., 4 (2014) 23428–23432.

Haupt K., Mosbach K., Molecularly imprinted polymers and their use in biomimetic sensors, Chem. Rev., 100 (2000) 2495–2504.

Jeong J.W., Rao B.A., Son Y-A., Rhodamine-chloronicotinaldehyde-based "OFF–ON" chemosensor for the colorimetric and fluorescent determination of Al^{3+} ions, Sens. Actuator B, 208 (2015) 75–84.

Ju H., Lee M.H., Kim J., Kim J.S., Kim J., Rhodamine-based chemosensing monolayers on glass as a facile fluorescent "turn-on" sensing film for selective detection of Pb^{2+}, Talanta, 83 (2011) 1359–1363.

Jung J.H., Lee J.H., Shinkai S., Functionalized magnetic

nanoparticles as chemosensors and adsorbents for toxic metal ions in environmental and biological fields, Chem. Soc. Rev., 40 (2011) 4464–4474.

Kim H.N., Lee M.H., Kim H.J., Kim J.S., Yoon J., A new trend in rhodamine-based chemosensors: application of spirolactam ring-opening to sensing ions, Chem. Soc. Rev., 37 (2008) 1465–1472.

Kim K.B., You D.M., Jeon J.H., Yeon Y.H., Kim J.H., Kim C., A fluorescent and colorimetric chemosensor for selective detection of aluminum in aqueous solution., Tetrahedron Lett., 55 (2014) 1347–1352.

Krasnaya Zh.A., Burova S.A., Bogdanov., Smirnova Yu.V., Synthesis of δ-Hetraryl-α,α-dicarbonylalkadines and a study of their isomerization, Chem. Hetrocycl. Compd., 33 (1997) 410–422.

Lee Y.H., Lee M.H., Zhang J.F., Kim J.S., Pyrene excimer-based calix[4]arene FRET chemosensor for mercury(II), J. Org. Chem., 75 (2010) 7159–7165.

Lee S., Rao B.A., Y-A Son, A highly selective fluorescent chemosensor for Hg^{2+} based on asquaraine–bis(rhodamine-B) derivative: Part II, Sens. Actuators B., 210 (2015) 519–532.

Li Q., Guo Y., Shao S., A BODIPY based fluorescent chemosensor for Cu(II) ions and homocysteine/cysteine, Sens. Actuators B., 171–172 (2012) 872–877.

Li X., Husson S.M., Two-dimensional molecular imprinting approach to produce optical biosensor recognition elements, Langmuir, 22 (2006) 9658–9663.

Lohani C.R., Kim J.-M., Chung S.-Y., Yoon J., Lee K.-H., Colorimetric and fluorescent sensing of pyrophosphate in 100 % aqueous solution by a system comprised of rhodamine B compound and Al^{3+} complex, Analyst, 135 (2010) 2079–2084.

So H-S., Rao B.A., Hwang J., Yesudas K., Son Y-A., Synthesis of novel squaraine-bis(rhodamine-6G): A fluorescent chemosensor for the selective detection of Hg^{2+}, Sens. Actuators B, 202 (2014) 779–787.

Tao X., Fernandez B., Azucena O., Fu M., Garcia D., Zuo Y., Chen D.C., Kubby J., Adaptive optics confocal microscopy using direct wavefront sensing, Optics Letters, 36 (2011) 1062–1064.

Wang F., Wang L., Chen X., Yoon J., Recent progress in the development of fluorometric and colorimetric chemosensors for detection of cyanide ions, Chem. Soc. Rev., 43 (2014) 4312–4324.

Wang M., Xu J., Liu X., Wang H., A highly selective pyrene based "off–on" fluorescent chemosensor for cyanide, New. J. Chem., 37 (2013) 3869–3872.

Weerasinghe A.J., Schmiesing C., Sinn E., Highly sensitive and selective reversible sensor for the detection of Cr^{3+}, Tetrahedron Lett., 50 (2009) 6407–6410.

Wulff G., Sarhan A., Über die Anwendung von enzymanalog gebauten Polymeren zur Racemattrennung, Angew. Chem. 84 (1972) 364–365.

Xu Z., Yoon J., Spring D.R., Fluorescent chemosensors for Zn^{2+}, Chem. Soc. Rev., 39 (2010) 1996–2006.

Yan H., Row K.H., Characteristic and synthetic approach of molecularly imprinted polymer, Int. J. Mol. Sci. 7 (2006) 155–178.

Yang Q.Y., Sun Q., Zhou T.S., Shi G.Y., Jin L.T., Determination of parathion in vegetables by electrochemical sensor based on molecularly imprinted polyethyleneimine/silica gel films, J. Agric. Food Chem., 57 (2009) 6558–6563.

Zhang J., Yu C., Qian S., Lu G., Chen J., A selective fluorescent chemosensor with 1, 2, 4-triazole as subunit for Cu (II)and its application in imaging Cu (II) in living cells, Dyes Pigm., 92 (2012) 1370–1375.

Zhang Z., Zheng Y., Hang W., Yan X., Zhao Y., Sensitive and selective off–on rhodamine hydrazide fluorescent chemosensor for hypochlorous acid detection and bioimaging, Talanta, 85 (2011) 779–786.

Zheng H., Yan M., Fan X-X., Sun D., Yang S-Y., Yang L-J., Li J-D., Jiang Y-B., A heptamethine cyanine-based colorimetric and ratiometric fluorescent chemosensor for the selective detection of Ag^{+} in an aqueous medium, Chem. Commun., 48 (2012) 2243–2245.

Zhou Y., Zhang J.F., Juyoung Yoon J., Fluorescence and colorimetric chemosensors for fluoride-ion detection, Chem. Rev., 114 (2014) 5511–5571.

Appendix: Supporting information

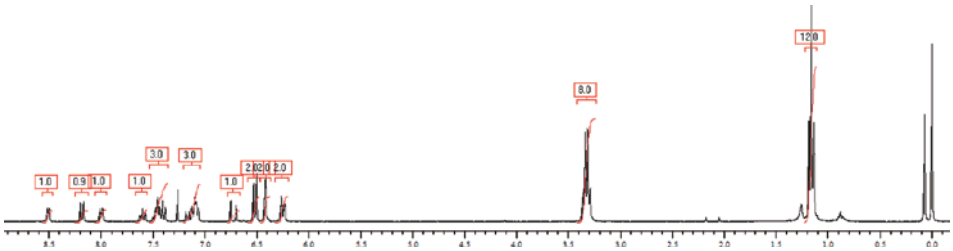

Fig. S1 ^{1}H NMR spectrum of RB-AC.

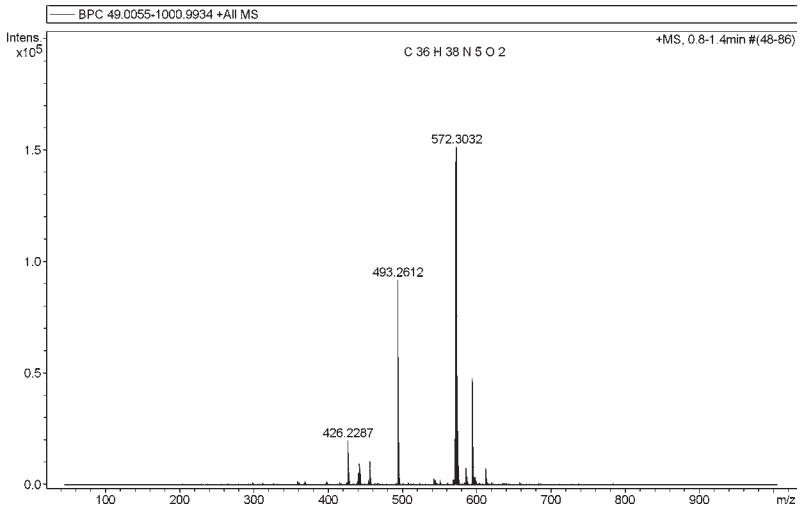

Fig. S2 HR-MS spectrum of RB-AC.

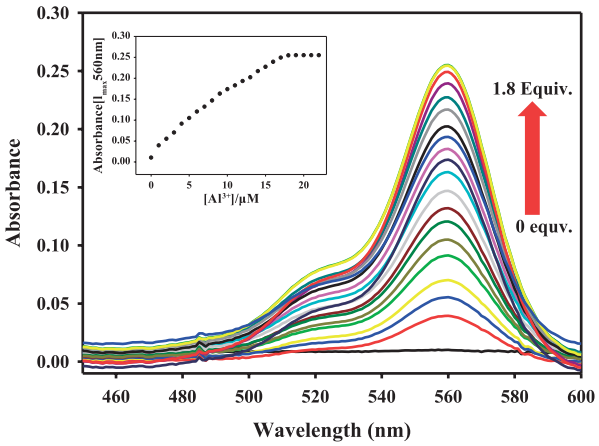

Fig. S3 UV-Vis spectra of 10 μM of RB-AC in ethanol/DMF (9:1) in the presence of different concentrations of Al^{3+}. Inset: Absorbance at 560 nm as a function of the concentration of Al^{3+}.

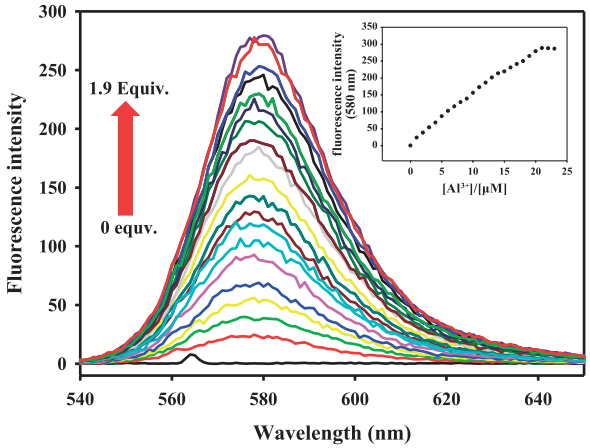

Fig. S4 Fluorescence spectra of 10 μM of RB-AC in ethanol/DMF (9:1) in the presence of different concentrations of Al^{3+}. Inset: Fluorescence at 580 nm as a function of the concentration of Al^{3+}.

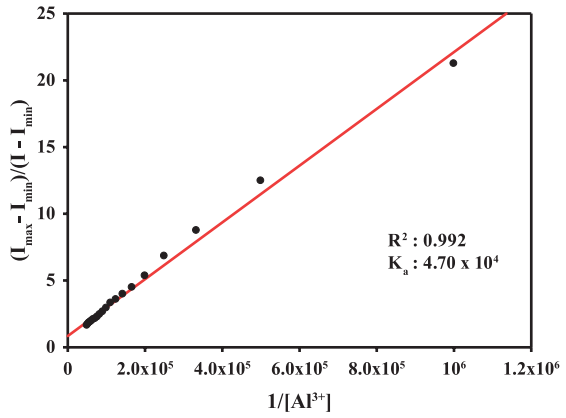

$$\frac{1}{I - I_{max}} = \frac{1}{I_{max} - I_{min}} + \frac{1}{K_{[Metal]}} \frac{1}{I_{max} - I_{min}}$$

Fig. S5 Benesi-Hildebrand plot and equation for binding of Al^{3+}.

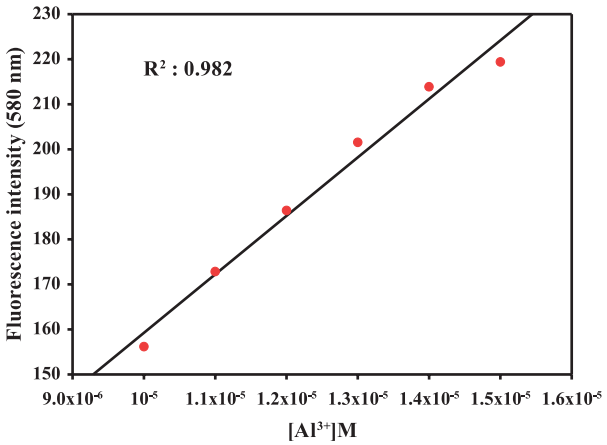

Fig. S6 Calibration plot for fluorescence intensity against concentration of Al^{3+}.

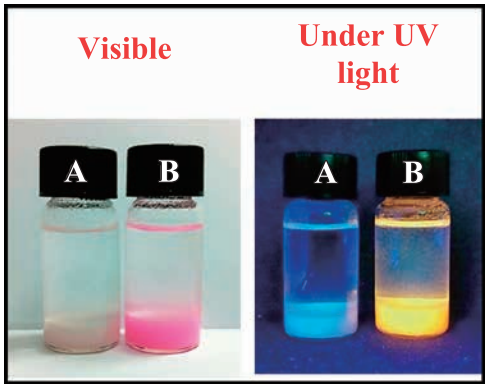

Fig. S7 Photographs of PEGDMA/RB-AC particles in ethanol/DMF mixture (9:1) (A) absence and (B) presence of Al^{3+}.

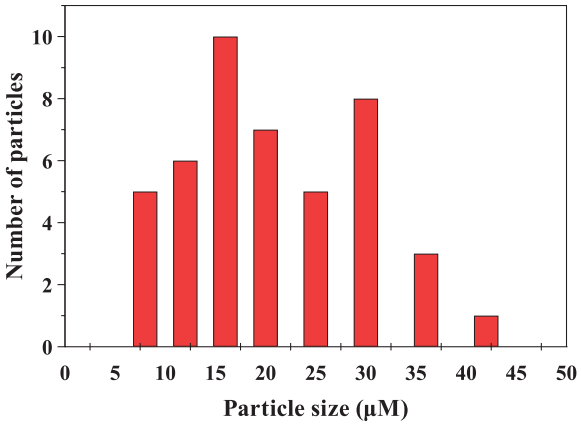

Fig. S8 Size histogram of PEGDMA/RB-AC particles.

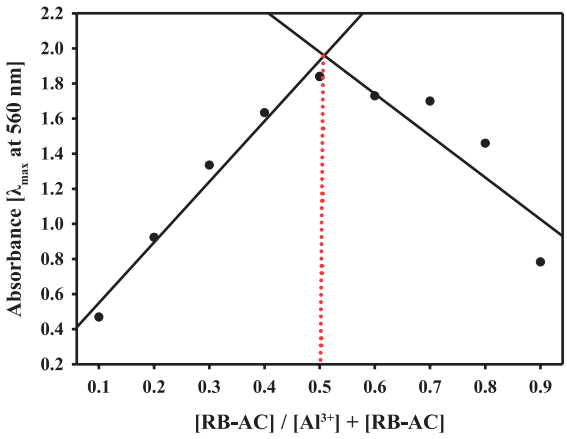

Fig. S9 Job's plot for RB-AC with Al^{3+} ion.

Author's short biography

Kyo-Sun Ku

Kyo-Sun Ku received his B.Sc. (Advanced Organic Materials Engineering) in 2015 at Chungnam National University, Daejeon, South Korea, under the supervision of Prof. Dr. Young-A Son. He is currently a master candidate in the Department of Advanced Organic Materials and Textile System Engineering, Chungnam National University. His research interests lie in the synthesis of rhodamine, pyridine derivatives and their sensing applications towards cation and anion.

Ji-Yong Hwang

Ji-Yong Hwang is currently a master candidate in the Department of Advanced Organic Materials and Textile System Engineering, Chungnam National University, South Korea. His main research fields are rhodamine based fluorescent chemosensors.

Palanisamy Muthukumar

Palanisamy Muthukumar received his Ph.D. degree in chemistry under the supervision of Prof. Dr. S. Abraham John, from Gandhigram Rural Institute (Deemed University), Gandhigram, India. Currently, he is working as a Post-Doctoral Fellow in Prof. Young-A. Son's group, Chungnam National University, Daejeon, South Korea. His current interests are rhodamine based fluorescent probes design and chemical sensors for cations and anions.

Young-A Son

Young-A Son is a professor in the Department of Advanced Organic Materials Engineering, Chungnam National University. He received his doctoral degree in color chemistry from the Department of Color Chemistry, University of Leeds, United Kingdom in 2001. His current research interests include luminescent organic materials, chemosensors, thermochromic dyes, color filter, functional dye materials and biosensors.

KONA Powder and Particle Journal No. 33 (2016) 239–248/Doi:10.14356/kona.2016004 Original Research Paper

Controlling of Segregation in Rotating Drums by Independent End Wall Rotations †

Hsiu-Po Kuo *, Wei-Ting Tseng and An-Ni Huang

[1] *Department of Chemical and Materials Engineering, Chang Gung University, Taiwan*

Abstract

We present in this study that particle segregation in rotating drums can be controlled by end wall rotations. While the end wall rotational speed dominates the time required for reaching the steady state, the rotational direction of the end walls determines the segregation patterns and the shearing zone size. New segregation patterns with two well-mixed regions close to the end walls are observed in the drums with the end wall rotates in the direction opposite to the cylindrical wall. The end wall rotation causes the formation of the local valley and hill next to the wall. Particles flow into the valley and down the hill causing the formation of the convective flow cell at bed surface. It is the difference of the axial velocities between the large particles and small particles close to the end walls separating the particles of difference sizes in the axial direction. The controlling of the end wall roughness and rotating directions effectively enlarge the size of the end wall shearing zone; resulting segregation patterns which are different from the previous simple segregation band patterns.

Keywords: rotating drum, segregation, mixing, end wall rotation, spatio-tempral diagram

1. Introduction

Particulate systems in most processes usually consist of components of different physical properties. These properties include sizes, densities, shapes, surface roughness, elasticity and etc. During the particle processing, differences in the particle physical properties may cause segregation, the phenomenon by which particles of similar properties separate into their individual components (Huang and Kuo, 2014). Although size-induced segregation (Klisiewicz et al., 2015), density-induced segregation (Oshitani et al., 2013), elasticity-induced segregation (Kuo et al., 2006a) and surface stickiness-induced segregation (Troiano et al., 2014) have been studied, the underlying physics of such a unique granular segregation phenomenon remains incompletely understood still now (Windows-Yule and Parker, 2015).

Rotating drums, showing rich granular behavior, widely used in industry for mixing, drying, agglomeration, calcinations, cooling and roasting are commonly used to study granular flows and/or particle segregation (Abouzeid and Fuerstenau, 2010; Grajales et al., 2012; Dhawan et al., 2014). Studies of particles segregation in rotating drums have long history since 1939 (Oyama, 1939). Researchers used particles of different sizes, masses, densities, shapes and elasticities to experimentally investigate segregation in dry rotating drums (Kuo et al., 2006a; Arntz et al., 2014) or in drums with different interstitial fluids (Chou et al., 2010). Numerically studies of particle flows/segregation in rotating drums are also conducted by a number of groups using DEM and CFD (Marigo et al., 2012; Huang et al., 2013a; Alizadeh et al., 2014; Marigo and Stitt, 2015). Segregation structures have been reported three-dimensionally using MRI and the freeze-slicing method (Kawaguchi et al., 2006; Sederman et al., 2007; Huang and Kuo, 2012). Although other complex segregation patterns have been reported in high fill level drums (Kuo et al., 2006b), particle segregation in rotating drums generally consist of a radial segregation core and segregation bands in the axial direction. The intensity of segregation is affected by the physical properties of the materials and by the drum operating parameters (Huang and Kuo, 2011).

A reasonable level of understanding of the segregation processes within a bidisperse rotating drum system has been achieved. Small particles are wrapped by large particles in the radial direction after several revolutions by the particle percolation mechanism and balancing between the centrifugal and the gravitational forces. Alternative small-particle-rich and large-particle-rich bands in the axial direction are then observed later at the bed

† Received 29 May 2015; Accepted 8 June 2015
J-STAGE Advance published online 30 June 2015
[1] No. 259, Wenhua 1st Road, Guishan District, Taoyuan City 33302, Taiwan
* Corresponding author: Hsiu-Po Kuo;
E-mail: hpkuo@mail.cgu.edu.tw
TEL: +886-3-2118800 ext 5488 FAX: +886-3-2118668

surface (Turner and Nakagawa, 2000; Maneval et al., 2005; Alizadeh et al., 2013). Comparing to the level of comprehension of the radial segregation cores, our knowledge to the axial segregation bands is poor. Controversially formation mechanisms of the axial segregation bands in the rotating drums have been reported, including the Stochastic diffusion model (Fan and Shin, 1979), the difference of the static/dynamic angle of repose induced diffusional model (Hill and Kakalios, 1994, 1995), the core–thickening model (Khan et al., 2004), and the end wall shearing induced local percolation theory (Kuo et al., 2005). Although most of these models reasonably explain the evolution of the axial segregation bands, the fact that the segregation bands originating close to the two end walls is not satisfactory explained.

Nakagawa is probably the first person who pointed out the importance of the end walls in axial segregation band formation (Nakagawa, 1994). The angle of repose of the particles next to the end wall is different to that in the bulk and particle motion in the axial direction accelerates, causing the formation of the segregation bands. Related reports focused on the influences of the end wall roughness on particle flow/segregation in rotating drums (Maneval et al., 2005; Arntz et al., 2013; Chand et al., 2012). End wall roughening increases the rate of axial segregation and reduces the particle near-wall transverse speed. The change of the frictional force between the end walls and the particles by end wall roughness alters the numbers of the axial segregation bands. A specially designed rotating drum with two independent rotating end walls has been used to improve the comprehension of the role of end wall on the segregation dynamics (Huang et al., 2013b). The central segregation bands were initiated where the end wall shearing was higher.

Understanding and controlling of particle segregation by the end walls has not yet been successful. In this work, the rotating drum with two end walls rotating in the same direction or in the opposite direction to that of the cylindrical wall is used to improve our understanding and to control segregation in rotating drums. The design of the drum and the operating conditions are shown in section 2. The influence of the end wall rotation on particle segregation and the controlling of particle segregation by end wall rotation are in section 3. Finally, we summarize our major findings and conclusions arising from this study in section 4.

2. Experimental details

The experimental set-up is a rotating drum of 98 mm inner diameter and 138 mm length. The drum consists of a Perspex cylindrical wall and the two end walls which rotate independently to the cylindrical wall. Two end wall roughness are investigated: PSS, in which end wall surface is polish stainless steel, and #220, in which #220 sand paper (i.e., 220 mm × 220 mm, 68 μm diameter sand particles per square inch) is glued on the surface of the end walls. The frictional angles of the end walls with different roughness are measured. The frictional coefficients between the particles used in this study and PSS end wall, and the #220 end wall are 0.47 and 0.57, respectively. While the cylindrical column rotational speed is set as 10 rpm, which corresponds to a tip speed of 0.05 m/s, the rotational speed of the end wall is 5 rpm, 10 rpm, 15 rpm, 30 rpm, 50 rpm, 70 rpm, or 90 rpm. In our experiments, two end wall rotational directions are studied: S, in which the rotational direction of the end wall is the same as that of the cylindrical wall, and O, in which the rotational direction of the end wall is opposite to that of the cylindrical wall. The schematic drawing of the experimental set-up is shown in **Fig. 1**.

Particle segregation is investigated in a bidisperse system using two species of glass particles (density = 2510 kg m^{-3}), each of equal physical properties but differing in their sizes and colors. The large particles are black and within the sieving size range of 1.19 mm–1.41 mm. The small particles are white and within the sieving size range of 0.81 mm–1.00 mm. The large and small particles are only different in colors and sizes. The dynamic angles of repose of small and large particles in the 10 rpm PSS rotating drum are 24° and 27°, respectively. The relatively large size of the particles and the materials used in this study allow us to neglect the triboelectric effects within the system.

In a typical segregation experiment, 20 % of the drum volume is firstly filled by large particles. Small particles are then placed on top of the large particles and the total

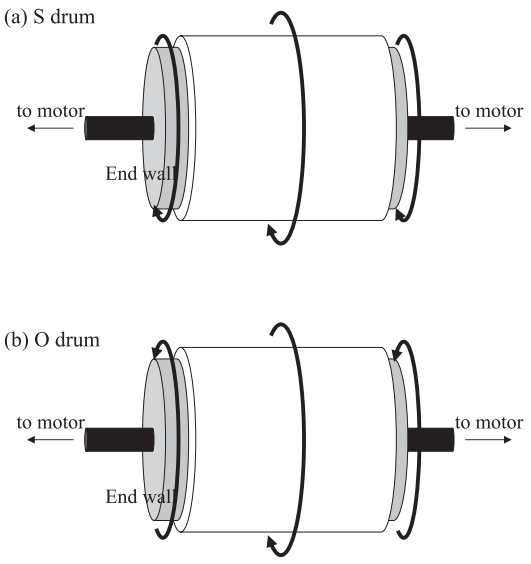

Fig. 1 Schematic drawings of the (a) S drum and (b) O drum.

level is set as 40 %. Two motors independently control the rotational speeds/directions of the cylindrical wall and the end walls. Two motors start at the same time and the bed surface is simultaneously recorded by a video camera (1 fps, HDR XR-520, Sony, Japan) for 60 min and by a high speed camera (300 fps, MotionPro-Y3, Nikon, Japan) for 5 s. The lightings are adjusted to show the best color contrast between the two species.

The trajectories of the tracer particles are recorded by the MotionPro-Y3 high speed camera and the Particle Imaging Velocimetry (PIV) technique is used to visualize the flow patterns at the bed surface (Chung et al., 2010). The tracer particles are identical to the particles used in the segregation experiments but differing in their colors. The cell size for flow pattern visualization is 2.4 mm × 2.4 mm.

The development and long lasting instabilities of the bed surface segregation patterns are studied by the spatio-tempral diagrams (Caps et al., 2003). Here, the spatio-tempral diagrams are prepared by stacking 3600 300 pixel (W) × 1 pixel (H) video camera images. The colors of the spatio-tempral diagrams are in gray-scale. The color calibration confirms that the large black particle show a gray-scale color less than 80. The large black particle concentrations in the near-wall region (i.e., within 2 cm next to the end walls) is approximated by the fractions of the black pixels in the left-most 43 pixel (W) × 3600 pixel (H) area and in the right-most 43 pixel (W) × 3600 pixel (H) area in the spatio-tempral diagrams.

3. Results and discussion

The bed surface spatio-tempral diagrams of the drums operating at different conditions are shown in **Fig. 2**. The end walls of the drums in **Fig. 2(a)** and **Fig. 2(b)** are PSS and #220, respectively.

Symmetric segregation patterns are observed after a relatively long operation time since the two end walls rotate in the same direction and at the same speed. The spatio-tempral diagrams represent the development of the segregation patterns. While the end wall rotational speed dominates the time required for reaching the steady state, the rotational direction of the end walls determines the segregation patterns. In S drums, the segregation pattern is characterized by two separating small-particle-rich white bands at two sides of the drum. In O drums, the segregation pattern is characterized by one small-particle-rich white band at the central of the drum. At the same rotational time, the color of the small-particle-rich white band turns grayer when the rotational speed of the end wall increases, indicating the increasing of the amount of the black large particles onto the small-particle-rich white bands.

In O drums, the local mixing at steady state is good

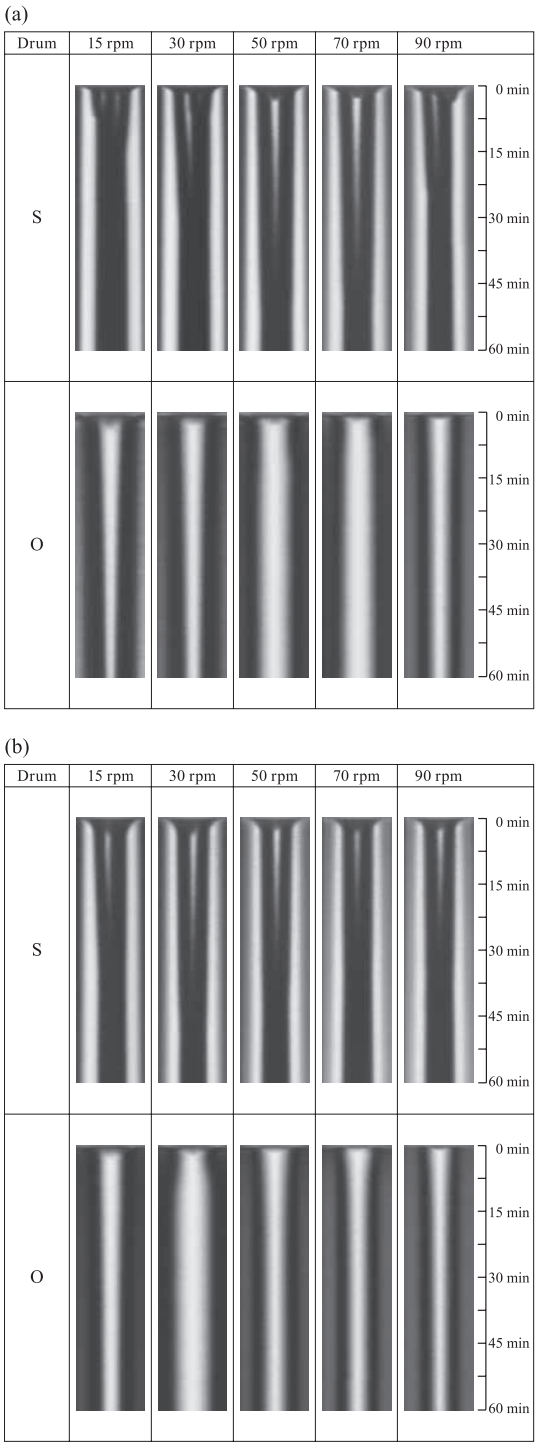

Fig. 2 The spatio-tempral diagrams of the segregation patterns in the drums rotating at different end wall speeds: (a) PSS and (b) #220 end walls.

and the comparisons between different rotational speeds are neglected. The local mixing in the near end wall region (say 2 cm next to the end wall) as a function of the end wall rotational speed is analyzed in S drums. The fractions of the large black particle pixels at steady state (i.e., the last 200 s in **Fig. 2**) are calculated and the results are shown in **Fig. 3**. As the rotational speed of the end

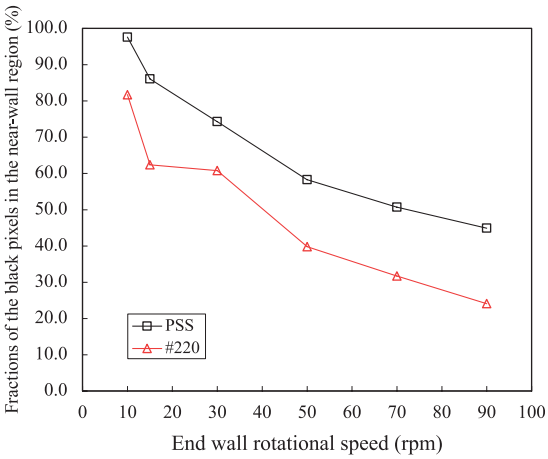

Fig. 3 The fractions of the black pixels in the next to wall region at steady state as a function of the end wall rotational speed in S drums.

walls increases, the number of the small white particles in the near end wall large-black-particle-rich band increases, causing the decreasing of the fraction of the black pixels in the next to wall region. The fraction of the black pixels in the next to the end wall region at steady state is lower when the end wall surface is rougher #220. The end wall roughness enhances local mixing in the region next to the end walls in S drums.

The small white particles migrate from the center of the drum to two end walls in S drums in **Fig. 2**, causing the disappearance of the (central) small-white-particle-rich segregation band and an increasing of the width of the white-particle-rich segregation bands at two sides. While the widths of the steady state white-particle-rich segregation bands at two sides are similar in all cases in S drums, the width of the steady state central white-particle-rich

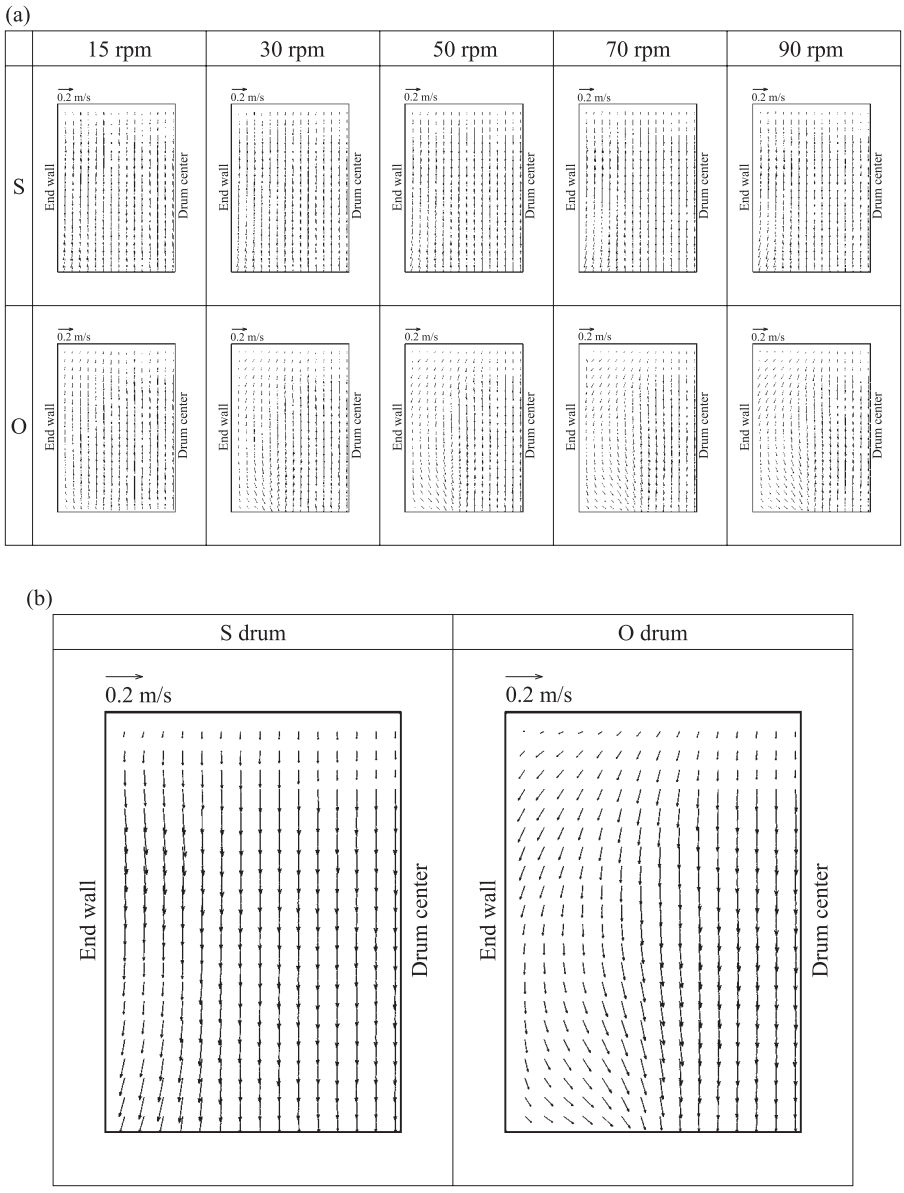

Fig. 4 (a) Large particle PIV flow patterns in the left-hand side of the drum fitted with PSS end walls. (b) The enlargement of 90 rpm cases.

segregation band in O drums is a function of the end wall rotational speed. It is interesting to note that the largest central band width at steady state occurs at 70 rpm in O drums with PSS end walls and at 30 rpm in O drums with #220 end walls. Although the existence of the maximum steady state central band width has been reported (Huang et al., 2013b), its dependence on the end wall rotational speed and roughness is initially reported.

The large particle PIV velocity profiles at the bed surface in the left-hand side of the drum with PSS end walls are shown in **Fig. 4(a)** and the enlargements of 90 rpm cases are shown in **Fig. 4(b)**. The motion of the particles close to the end walls is affected by the end wall rotation. Depending on their positions, the particles may be pushed inside the bed by the end wall rotation, forming a local valley next to the wall, or they may be pushed outside the bed by the end wall rotation, forming a local hill next to the wall.

The direction of the end wall rotation determines positions of the local valley and the local hill and hence the direction of the convective flow cell. The flows of the particles into the valley and down the hill cause the axial motion of the particles and the formation of the convective flow cell observed in **Fig. 4**. In O drums, while the particles at the upper half of the bed surface fall into the valley and move towards the end walls, the particles at the lower half of the bed surface flow down the hill and move towards to the center of the drum.

Axial velocities of the large and small particles in S drums with PSS end walls and in O drum with PSS end walls are shown in **Fig. 5** and **Fig. 6**, respectively. The values of the particle axial velocity just next to the end walls are not shown here due to the limitations of the resolution of the camera. The influence of the end wall rotational speed on the particle axial velocity is more pronounced in O drums. The large and small particles located to the region next to the end walls are both dragged up to the local hill by the rotation of the end walls to about the same height. The local hills are in the upper 1/3 of the bed surface close to the end walls in S drums and in the lower 1/3 of the bed surface close to the end walls in O drums. Since the large particles experienced greater inertia than the small particles, when the particles fall down from the local hills, the large particles show greater downslope axial velocities than the small particles in **Fig. 5(a)** and **Fig. 5(b)** and in **Fig. 6(c)** and **Fig. 6(d)**.

The differences between the axial velocities of the small and large particles in rotating drums with PSS end walls are shown in **Fig. 7**. The differences between the axial velocities of the small and large particles are greater in O drums than those in S drums. We show direct evidence that it is the difference of the axial velocities between the large particles and small particles close to the end walls causing the separation of the particles in the

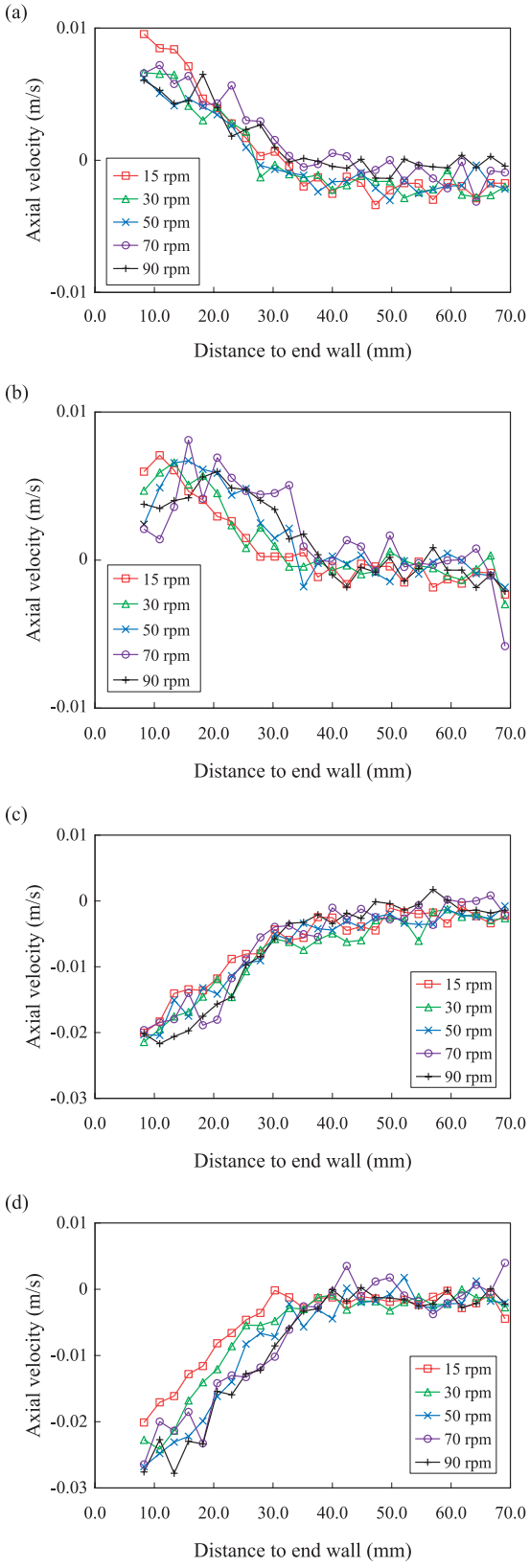

Fig. 5 Axial velocities of (a) large particles in the upper 1/3 of bed surface, (b) small particles in the upper 1/3 of bed surface, (c) large particles in the lower 1/3 of bed surface, and (d) small particles in the lower 1/3 of bed surface in S drums with PSS end walls.

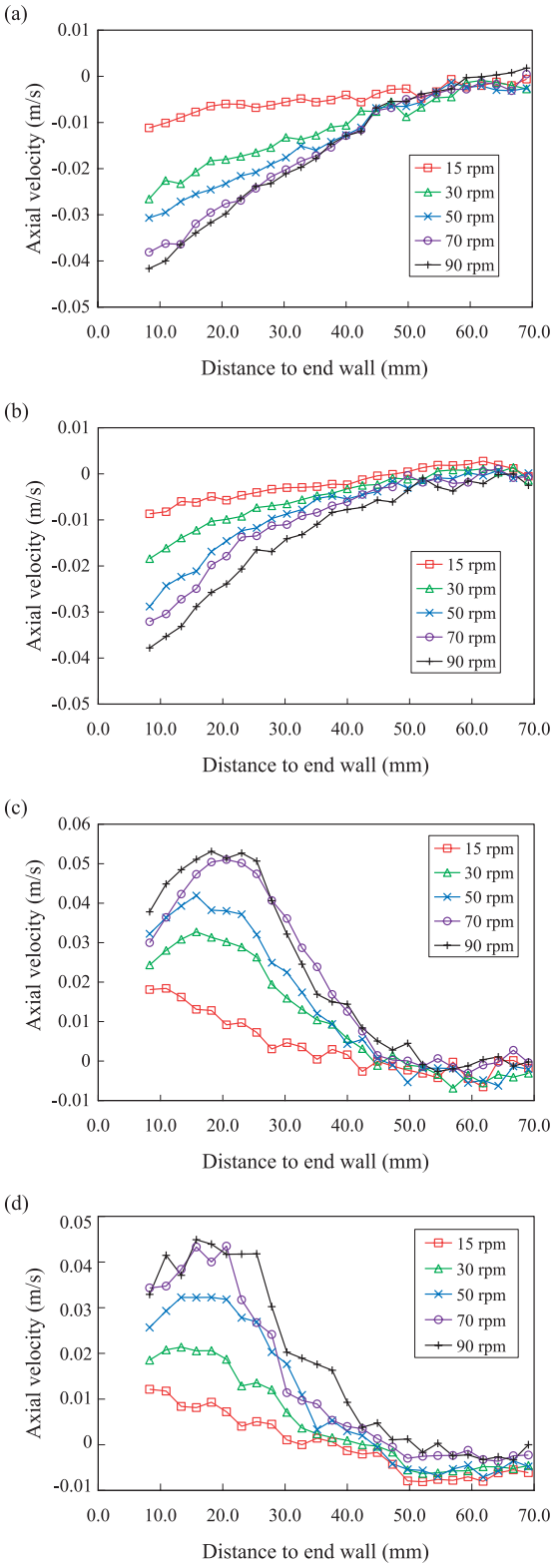

Fig. 6 Axial velocities of (a) large particles in the upper 1/3 of bed surface, (b) small particles in the upper 1/3 of bed surface, (c) large particles in the lower 1/3 of bed surface, and (d) small particles in the lower 1/3 of bed surface in O drums with PSS end walls.

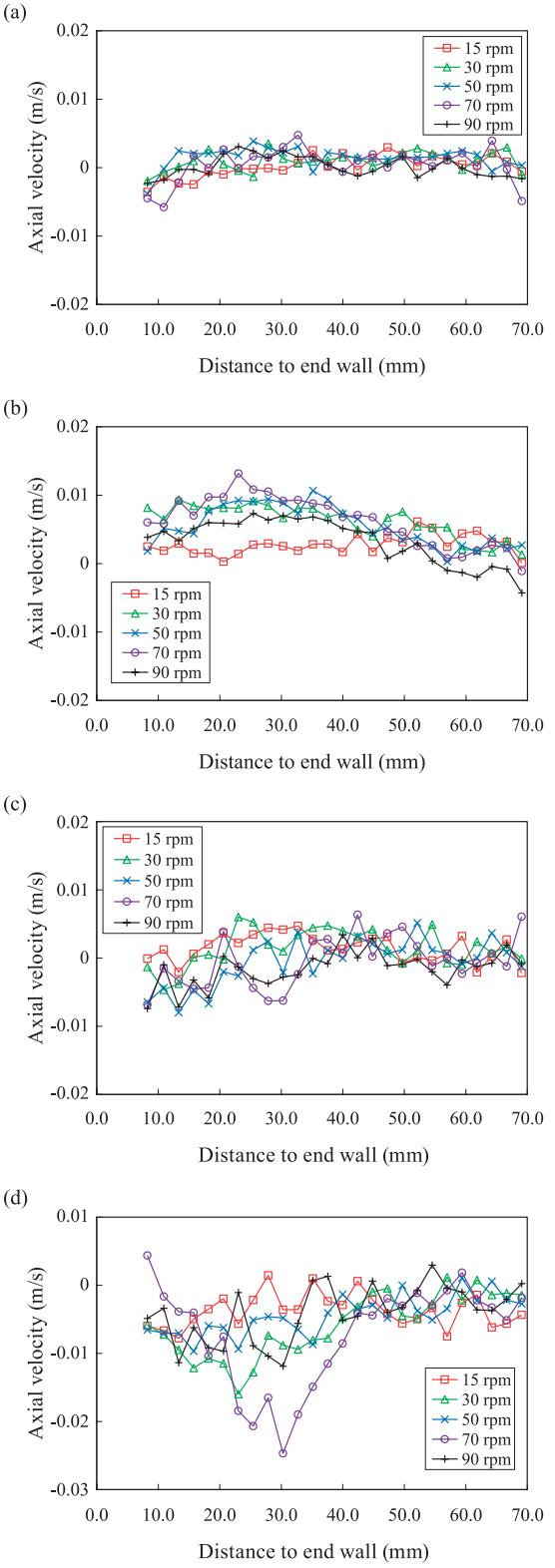

Fig. 7 The difference of the particle axial velocities between small particles and large particles in the (a) upper 1/3 of the bed surface in S drums, (b) upper 1/3 of the bed surface in O drums, (c) lower 1/3 of the bed surface in S drums, and (d) lower 1/3 of the bed surface in O drums with PSS end walls.

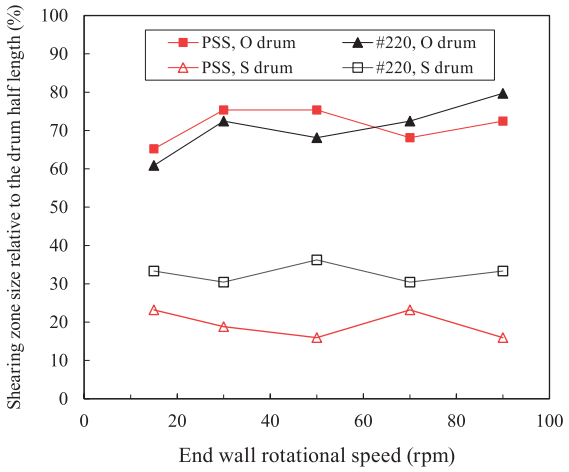

Fig. 8 The comparison of the sizes of the shearing zones at different operation conditions.

axial direction. The region far away from the end walls is less affected by the end wall rotation and the particle axial velocity shows a near zero value. The shearing zone affected by the end wall rotation is determined and the sizes of the shearing zone are compared at different operating conditions.

To avoid the errors in the measurement, the shearing zone is defined as the large particles therein a cell (2.4 mm × 2.4 mm) have an absolute average cell axial velocity greater than 0.005 m/s for at least 2 successive cells in the axial direction. The sizes of the shearing zone determined in the upper 1/3 of the bed surface are shown in **Fig. 8**. While the surface roughness increases the size of the shearing zone in S drums, it has little effects on the shearing zone size in O drums.

The size of the shearing zone is about 60 %–80 % of the half drum length in O drums and about 15 %–35 % of the half drum length in S drums. In previous reports, the blade shearing zone is only about 5–10 particle diameter (Nedderman and Laohakul, 1980; Kuo et al., 2003), which corresponds to about 10 %–20 % of the half drum length in this work. The shearing zone in O drums is apparently much larger than the previous findings.

Although the rougher surface contributes to end wall shearing and slightly increases the shearing zone sizes, it is the direction of the end wall rotation dominating the magnitude of end wall shearing and hence the size of the shearing zone. It is probably the relatively large shearing zone causing the fast evolution of the segregation bands in O drums in **Fig. 2**. The controlling of the end wall roughness in S drums and the end wall rotational directions effectively enlarge the size of the end wall shearing zone, and the resulting segregation patterns are different from the previous simple alternative small-white-particle-very-rich and large-black-particle-very -rich bands.

The comparisons of the axial velocities of the large

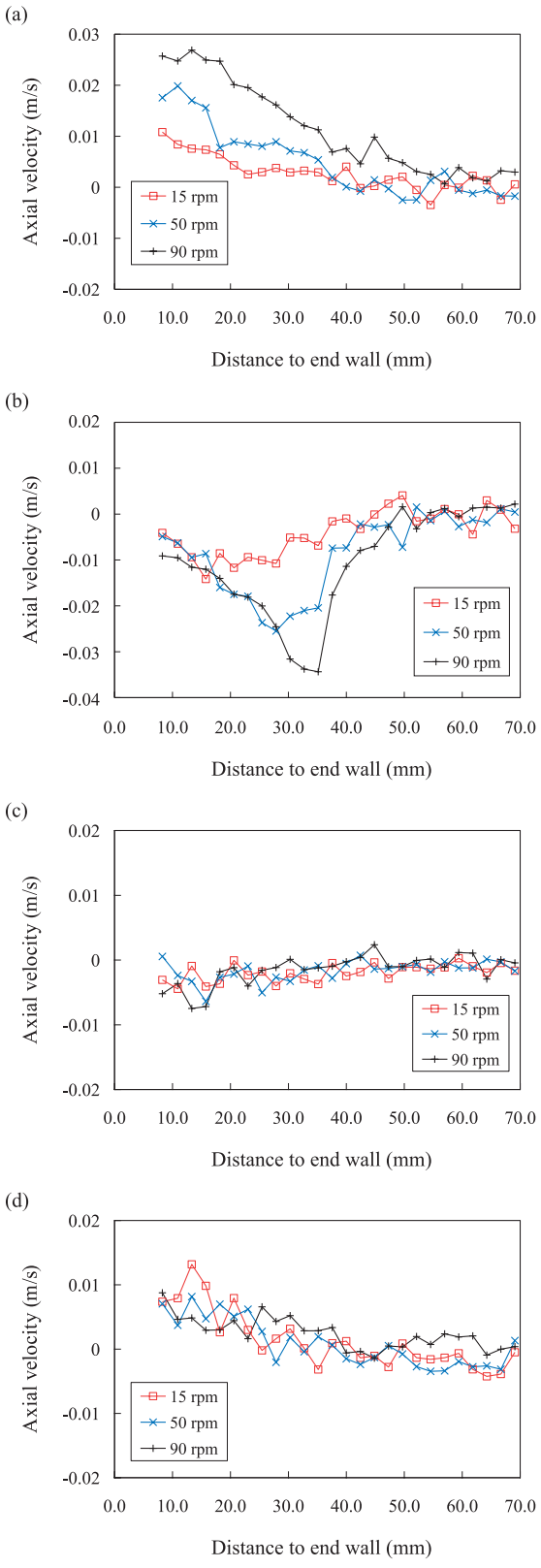

Fig. 9 The differences of the large particle axial velocities in the drums with PSS end walls and those in the drums with #220 end walls: (a) in the upper 1/3 of bed surface in O drums, (b) in the lower 1/3 of bed surface in O drums, (c) in the upper 1/3 of bed surface in S drums, and (d) in the lower 1/3 of bed surface in S drums.

particles in drums with different end wall roughnesses are shown in **Fig. 9**. Only three rotational speeds are presented here to ease the comparisons.

The differences are observed in the shearing zones only and are greater in O drums than in S drums. Since the influence of the end wall surface roughness on particle axial motion is not significant in S rums, previous researchers who studied the influence of the end wall roughness on segregation patterns in rotating drums did not observed new segregation patterns as those shown in **Fig. 2**. The dual effects of the end wall roughness and rotational speeds in O drums noticeably change the particle axial velocities. New segregation patterns with two quite well mixed regions close to the end walls shown in O drums are thus observed in **Fig. 2**.

4. Conclusions

An original rotating drum is used to study the effects of the end wall rotation/shearing on particle segregation in rotating drums. The rotational direction of the end walls determines the segregation patterns and new segregation patterns with two well-mixed regions close to the end walls are initially observed in O drums. The end wall roughness enhances local mixing in the region next to the end walls in S drums. There exists a maximum central band width at steady state in O drums: at 70 rpm while using polished stainless steel end walls and at 30 rpm while using #220 sand paper end walls. The end wall rotation causes the formation of the local valley and hill next to the wall. Particles flow into the valley and down the hill cause the formation of the convective flow cell at bed surface. The influence of the end wall rotational speed on the particle axial velocity is more pronounced in O drums. The difference of the axial velocities between the large particles and small particles close to the end walls causing the separation of the particles in the axial direction. The dual effects of the end wall roughness and rotational speeds in O drums noticeably change the particle axial velocities. The controlling of the end wall rotational speed and direction effectively enlarge the size of the end wall shearing zone.

Acknowledgements

The authors are grateful for the financial support from Ministry of Science and Technology, Taiwan (MOST 103-2221-E-182-068) and Chang Gung Memorial Hospital (BMRP 634). We would also like to gratefully acknowledge Professor S.S. Hsiau at National Central University, Taiwan for his help in the PIV measurements.

References

Abouzeid A.-Z.M., Fuerstenau D.W., Flow of non-homogeneous particulates in rotating drums, KONA Powder and Particle Journal, 28 (2010) 155–166.

Alizadeh E., Bertrand F., Chaouki J., Comparison of DEM results and lagrangian experimental data for the flow and mixing of granules in a rotating drum, AIChE Journal, 60 (2014) 60–75.

Alizadeh E., Dubé O., Bertrand F., Chaouki J., Characterization of mixing and size segregation in a rotating drum by a particle tracking method, AIChE Journal, 59 (2013) 1894–1905.

Arntz M.M.H.D., Beeftink H.H., den Otter W.K., Briels W.J., Boom R.M., Segregation of granular particles by mass, radius, and density in a horizontal rotating drum, AIChE Journal, 60 (2014) 50–59.

Arntz M.M.H.D., Den Otter W.K., Beeftink H.H., Boom R.M., Briels W.J., The influence of end walls on the segregation pattern in a horizontal rotating drum, Granular Matter, 15 (2013) 25–38.

Caps H., Michel R., Lecocq N., Vandewalle N., Long lasting instabilities in granular mixtures, Physica A, 326 (2003) 313–321.

Chand R., Khaskheli M.A., Qadir A., Ge B., Shi Q., Discrete particle simulation of radial segregation in horizontally rotating drum: Effects of drum-length and non-rotating end-plates, Physica A: Statistical Mechanics and its Applications, 391 (2012) 4590–4596.

Chou S.H., Liao C.C., Hsiau S.S., An experimental study on the effect of liquid content and viscosity on particle segregation in a rotating drum, Powder Technology, 201 (2010) 266–272.

Chung Y.C., Hsiau S.S., Liao H.H., Ooi J.Y., An improved PTV technique to evaluate the velocity field of non-spherical particles, Powder Technology, 202 (2010) 151–161.

Dhawan N., Rashidi S., Rajamani R.K., Population balance model for crushed ore agglomeration for heap leach operations, KONA Powder and Particle Journal, 31 (2014) 200–213.

Fan L.T., Shin S.H., Stochastic diffusion model of non-ideal mixing in a horizontal drum mixer, Chemical Engineering Science, 34 (1979) 811–820.

Grajales L.M., Xavier N.M., Henrique J.P., Thoméo J.C., Mixing and motion of rice particles in a rotating drum, Powder Technology, 222 (2012) 167–175.

Hill K.M., Kakalios J., Reversible axial segregation of binary mixtures of granular materials, Physical Review E, 49 (1994), R3610–R3613.

Hill K.M., Kakalios J., Reversible axial segregation of rotating granular media, Physical Review E, 52 (1995) 4393–4400.

Huang A.N., Kao W.C., Kuo H.P., Numerical studies of particle segregation in a rotating drum based on Eulerian continuum approach, Advanced Powder Technology, 24 (2013a) 364–372.

Huang A.N., Kuo H.P., A study on the transition between neighbouring drum segregated bands and its application to functionally graded material production, Powder Technology,

212 (2011) 348–353.

Huang A.N., Kuo H.P., A study of the three-dimensional particle size segregation structure in a rotating drum, AIChE Journal, 58 (2012) 1076–1083.

Huang A.N., Kuo H.P., Developments in the tools for the investigation of mixing in particulate systems—A review, Advanced Powder Technology, 25 (2014) 163–173.

Huang A.N., Liu L.C., Kuo H.P., The role of end wall shearing in the drum segregation band formation, Powder Technology, 239 (2013b) 98–104.

Kawaguchi T., Tsutsumi K., Tsuji Y., MRI measurement of granular motion in a rotating drum, Particle and Particle Systems Characterization, 23 (2006) 266–271.

Khan Z.S., Tokaruk W.A., Morris S.W., Oscillatory granular segregation in a long drum mixer, Europhysics Letters, 66 (2004) 212–218.

Klisiewicz P., Roberts J.A., Pohlman N.A., Segregation of titanium powder with polydisperse size distribution: Spectral and correlation analyses, Powder Technology, 272 (2015) 204–210.

Kuo H.P., Burbidge A.S., Knight P.C., Parker D.J., Adams M.J., Seville J.P.K., Non-equilibrium particle motion in the vicinity of a single blade, Powder Technology, 132 (2003) 1–9.

Kuo H.P., Hsiao Y.C., Shih P.Y., A study of the axial segregation in a rotating drum using deformable particles, Powder Technology, 166 (2006a) 161–166.

Kuo H.P., Hsu R.C., Hsiao Y.C., Investigation of axial segregation in a rotating drum, Powder Technology, 153 (2005) 196–203.

Kuo H.P., Shih P.Y., Hsu R.C., Coupled axial-radial segregation in rotating drums with high fill levels, AIChE Journal, 52 (2006b) 2422–2427.

Maneval J.E., Hill K.M., Smith B.E, Caprihan A., Fukushima E., Effects of end wall friction in rotating cylinder granular flow experiments, Granular Matter, 7 (2005) 199–202.

Marigo M., Cairns D.L., Davies M., Ingram A., Stitt E.H., A numerical comparison of mixing efficiencies of solids in a cylindrical vessel subject to a range of motions, Powder Technology, 217 (2012) 540–547.

Marigo M., Stitt E.H., Discrete element method (DEM) for industrial applications: Comments on calibration and validation for the modelling of cylindrical pellets, KONA Powder and Particle Journal, 32 (2015) 236–252.

Nakagawa M., Axial segregation of granular flows in a horizontal rotating cylinder, Chemical Engineering Science, 49 (1994) 2540–2544.

Nedderman R.M., Laohakul C., The thickness of the shear zone of flowing granular materials, Powder Technology 25 (1980) 91–100.

Oshitani J., Ohnishi M., Yoshida M., Franks G.V., Kubo Y., Nakatsukasa S., Dry separation of particulate iron ore using density-segregation in a gas-solid fluidized bed, Advanced Powder Technology, 24 (2013) 554–559.

Oyama Y., Bull. Inst. Phys. Chem Res. (Tokyo), Rep. 5. 1939;18:600. (Oyama's work was reported by Weidenbaum SS in Advances in Chemical Engineering, Vol. 2, p.211, edited by Drew TB and Hoopes JW. New York: Academic, 1958.)

Sederman A.J., Gladden L.F., Mantle M.D., Application of magnetic resonance imaging techniques to particulate systems, Advanced Powder Technology, 18 (2007) 23–38.

Troiano M., Salatino P., Solimene R., Montagnaro F., Wall effects in entrained particle-laden flows: The role of particle stickiness on solid segregation and build-up of wall deposits, Powder Technology, 266 (2014) 282–291.

Turner J.L., Nakagawa M., Particle mixing in a nearly filled horizontal cylinder through phase inversion, Powder Technology, 113 (2000) 119–123.

Windows-Yule K., Parker D., Density-driven segregation in binary and ternary granular systems, KONA Powder and Particle Journal, 32 (2015) 163–175.

Author's short biography

Hsiu-Po Kuo

Hsiu-Po Kuo received his B.Sc. degree and Ph.D. degree in Chemical Engineering from National Taiwan University, Taiwan in 1995 and from the University of Birmingham, UK in 2001, respectively. He joined Chang Gung University in 2002 and promoted as full Professor in 2012. He won the most-contributed editor title of Advanced Powder Technology journal from 2010 to 2013. He works closely with the Formosa Plastic Groups in Taiwan. He is interested in all particle technology related studies.

Wei-Ting Tseng

Mr. Wei-Ting Tseng received his bachelor in Department of Chemical and Materials Engineering, Chang Gung University, Taiwan in 2013. He is currently in his master program in Department of Chemical and Materials Engineering, Chang Gung University, Taiwan.

An-Ni Huang

Dr. An-Ni Huang received her bachelor degree from Yuan-Ze University, Taiwan in 2006 and doctor degree in Chemical and Materials Engineering from Chang Gung University, Taiwan in 2012. She is currently a post-doctoral researcher at Chang Gung University, Taiwan. Her research interests include CFD-DEM modeling of multiphase flows, mixing and ash management.

KONA Powder and Particle Journal No. 33 (2016) 249–263/Doi:10.14356/kona.2016006 Original Research Paper

Consolidation of Non-Colloidal Spherical Particles at Low Particle Reynolds Numbers †

Kevin P. Galvin, Marveh Forghani, Elham Doroodchi and Simon M. Iveson *

[1] *Centre for Advanced Particle Processing and Transport, Newcastle Institute for Energy and Resources, The University of Newcastle, Australia*

Abstract

When a system of identical spheres settles under conditions of negligible surface and inertial forces an idealised form of sediment consolidation unfolds amenable to a universal description. We have described this complex process using a simple constitutive model expressed as an elementary scaling law in time, t, applied at the local particle level. The free-volume surrounding a particle consists of two volume contributions occupied by fluid, one portion fixed and the other portion variable, the latter of which declines with t^{-2}. A comprehensive system of analytical equations was derived using this one idea, and associated boundary conditions, to describe all aspects of the batch settling process. An experimental system exhibiting negligible surface and inertial forces was used to validate the model and hence assess the merits of the scaling law. Excellent agreement was achieved. The precise physics responsible for this scaling law, and the applicable boundary conditions, remain unclear at this stage. Hence this work is likely to motivate further work in this area, concerned with the dynamics of random consolidation of settling spheres.

Keywords: sedimentation, consolidation, scaling laws, non-colloidal spheres, low Reynolds number

1. Introduction

Concha F. and Bürger R. (2002) have provided a useful historical review of batch settling, evolving from a mere "art" into one of the most studied problems in solid-liquid separation. Batch settling has been used to provide the data needed to design industrial thickeners (Fitch B., 1979), and to examine the effectiveness of settling aids such as flocculants. Coe H. and Clevenger G. (1916) are credited with providing the first insights into the flux limits of continuous thickening, basing their approach on multiple batch settling tests conducted at different initial concentrations.

A batch settling test is generally used to develop an understanding of the sedimentation of a given feed, and its expected response to the thickening process. This test is illustrated in **Fig. 1** and the batch settling test curve is presented in **Fig. 2**. Given most industrial feeds are subjected to flocculation or coagulation, the ultrafine particles form larger entities called flocs. These can be considered to be effectively of the same size and density, and to therefore act as distinct particles during the sedimentation. Thus, in general, batch settling is often examined in terms of the settling of particles of one size and density.

Consider an initially uniform suspension of mono-sized particles of one density (**Fig. 1**). The subsequent process of sedimentation can be divided into two stages. The first, termed "free-settling", involves minimal inter-particle contact, hence the net particle gravitational force in the fluid (taking into account gravity and buoyancy) is balanced entirely by the fluid drag force. The initial suspension height is H_i and volume fraction of the particles ϕ_i. The bulk of the particles will start to settle with a constant settling velocity, forming a supernatant or clear water layer as the suspension interface moves downwards. Meanwhile particles start to form sediment at the base of the container, producing a settled bed that rises upwards (**Fig. 1**). Ultimately the rising bed meets the falling suspension interface at time t_o and height H_o. The process of bed consolidation continues, causing the surface of the settled bed to decline gradually until the bed reaches its final bed height, H_f.

Kynch G. (1952) developed the first complete description of sedimentation linking the free-settling and consolidation zones to achieve a unified theory. His fundamental assumption was that the settling velocity of the particles is governed by the local volume fraction of solids only.

† Received 2 June 2015; Accepted 25 June 2015
J-STAGE Advance published online 11 July 2015
[1] University Drive, Callaghan NSW 2308, Australia
* Corresponding author: Simon M. Iveson;
E-mail: simon.iveson@newcastle.edu.au
TEL: +61-2-4033-9079 FAX: +61-2-4033-9095

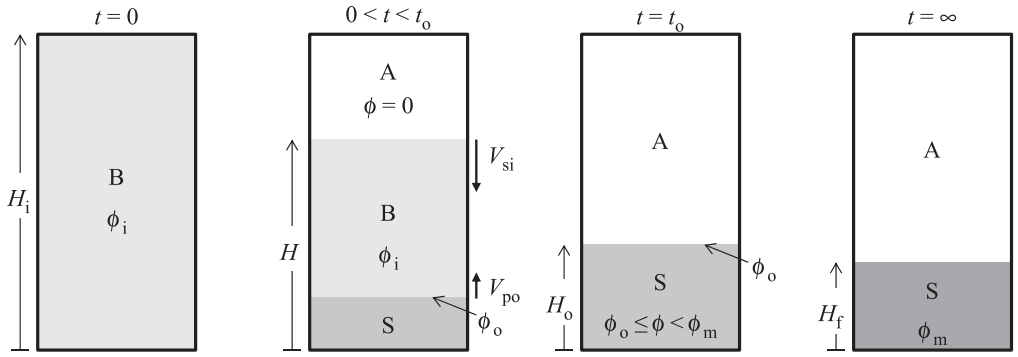

Fig. 1 Diagram of the zones formed during batch settling illustrating some of the key variables. B = free settling zone of initial uniform suspension of concentration ϕ_i and settling velocity V_{si}. A = clear supernatant. S = sediment bed which propagates upwards at a velocity V_{po} with a constant volume fraction of solids ϕ_o at its upper surface until time t_o, the critical settling point, when the rising bed meets the falling interface between the free-settling and supernatant. The maximum volume fraction of the solids is ϕ_m.

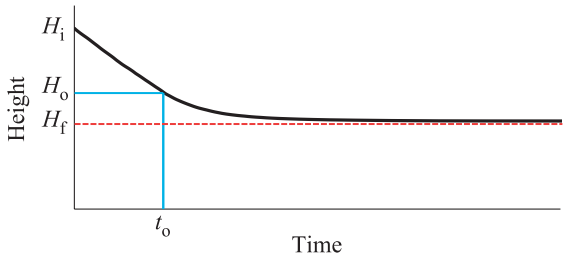

Fig. 2 A typical batch settling curve. H_i is the height of the upper free-settling interface at time $t = 0$. H_o and t_o are the height and time when the upper interface meets the rising sediment bed interface. H_f is the final sediment height. These quantities are also explained in the text.

His model, which was based on the continuity equation, provided a basis for calculating the concentration of the particles at the upper interface of the sediment, allowing a thickener to be sized for the first time on the basis of a single batch settling test.

The analysis of Kynch neglected the compressive state of the sediment. A given particle within the sediment rests, at least in part, on the particles below, which rest at least in part on those even further below, which in turn rest on the bottom of the container. Thus, a particle within the sediment experiences a state of compression, and is not entirely free to settle. Rather, its movement is constrained by the presence of those particles below, and the subsidence of those particles. Therefore, the perceived settling velocity of the particles in the sediment at a given volume fraction of solids cannot be the same as the settling velocity observed when a uniform suspension is prepared at the same volume fraction of solids.

Since then many more complex models of the process of sedimentation and consolidation have been proposed. Buscall R. and White L. (1987) and later Howells I. et al. (1990) assumed that a complex, irreversible, network structure evolved within the consolidation zone, exhibiting a compressive yield stress condition. Bürger R. and Concha F. (1998) developed a one-dimensional transient model of an operating thickener incorporating the effects of compression while Usher S. et al. (2006) focused on the effects of compression over long time-scales.

Dimitrova T. et al. (2000) applied the ideas of Buscall R. and White L. (1987) to describe the process of creaming, during which the particles settle in the upwards direction to form the cream, leaving clear serum below. Again, inter-particle forces result in a complex network structure that yields under the influence of a compressive load. They presented the following governing equation for describing the process of sedimentation and consolidation. That is,

$$\frac{\partial \phi}{\partial t} - \frac{v}{\zeta}\frac{\partial}{\partial z}\left(K(\phi)\frac{\mathrm{d}p}{\mathrm{d}\phi}\frac{\partial \phi}{\partial z}\right) - \frac{\Delta\rho g v}{\zeta}\frac{\partial}{\partial z}(\phi K(\phi)) = 0 \tag{1}$$

where $K(\phi)$ is the hindered settling factor, ζ the friction coefficient of an isolated particle in an infinite medium, $\Delta\rho$ the particle-liquid density difference, g the acceleration due to gravity and v the volume of one particle. The dimensionless particle pressure developed by the network structure is usually assumed to be a function of the volume fraction only,

$$p = p_o\left(\frac{\phi}{\phi_o}\right)^4 \tag{2}$$

with $p_o \sim 0.002$. We have solved their equation, setting $p_o = 0.0003$, the smallest possible value for a stable solution, with the aim being to minimize the critical yield stress. That solution is compared later with the solution obtained using our new theoretical model.

1.1 Outline of the problem

In this paper we examine an idealised system consisting of smooth, incompressible, mono-sized, spherical particles settling within a Newtonian fluid. Both inertial forces and surface forces are assumed to be negligible, while viscous forces dominate. All particles exhibit some scale of surface roughness that places limits on the magnitude of the viscous lubrication force, hence even for "smooth" spheres some level of inter-particle friction will also play a role (Galvin K. et al., 2001). The system undergoes a complex, well defined, process of gradual particle packing, driven towards a state of minimum potential energy. The movement of a given particle is invariably constrained by the extent of the cumulative movement of the particles below, while occasionally promoted by the *ad hoc* presentation of local vacancies.

This paper seeks to reduce this problem of sediment consolidation to the most elementary description that is possible, recognising the existence of two volume contributions to the space surrounding a given spherical particle, one portion fixed and the other variable. The variable portion declines with time according to a simple, constitutive, scaling law due to the consolidation. This idea was first presented in a conference forum by Forghani M. et al. (2013), and has been built upon here into a more complete theory, sufficient for experimental validation. Their simple scaling law, inferred from the experimental findings of Galvin K. (1996), is used here to derive a comprehensive system of equations to describe the fall of the upper interface with time, the consolidation velocity of the particles versus time at any fixed elevation, and the changing concentration profile of the sediment. This description should be universal, within the constraints of the assumptions, and in the absence of surface asperities. An experimental system, reasonably consistent with the above assumptions, was used to validate the model.

Galvin K. (1996) undertook an experimental study investigating the sediment consolidation of a model particle system. The particles, known as Sephadex, swelled in water to form spheres with a mean diameter of 220 μm and low density of 1018 kg m^{-3}. The relatively large particle size and hence gravitational force minimized the significance of surface forces, while the very low particle density minimized the particle Reynolds number. According to Evans I. and Lipps A. (1990), these particles settle to form a sediment with a volume fraction of 0.64. Within the limits of the experimental conditions, the particles can be considered incompressible hence the final volume fraction of the particles is not governed *per se* by the compressive load that arises from the gravitational force minus that of the buoyancy force of the sediment bed.

Galvin measured the velocity of individual particles at a fixed elevation during the process of consolidation, and repeated the approach at other fixed elevations. Within the field of view the particles appeared to move, largely *en masse*, in a downwards direction, while sometimes individual particles would momentarily free themselves from others and settle before re-contacting other particles. At each elevation the velocity of the particles decreased gradually, until there was virtually no movement at that elevation. He found that the particle velocities, V_s, at each level scaled with time, t, as $V_s \propto t^{-3}$. This scaling law forms the basis of a simple constitutive relationship used in this study. Integration suggests that changes in height due to consolidation should scale with t^{-2}.

Our work is motivated by the curious proposition that a simple constitutive scaling law may underpin much of what is observed in this idealised form of batch settling. Thus our work is not motivated by the need to develop yet another method for sizing thickeners. Rather the findings should motivate new lines of enquiry, in particular the dynamics of random particle packing and consolidation using discrete element modelling, which should help explain the physical underpinnings of the assumed scaling law. Further, the transition to systems influenced by inertial and surface forces, and to systems with different particle sizes, should then follow.

2. Consolidation model

This study is concerned with the batch settling of initially uniform suspensions of particles of the same size and density. The settling commences via a process of free settling at the initial concentration, ϕ_i, resulting in an upper interface H which falls at constant velocity V_{si} (**Fig. 1**). The gravitational force on the particles during this free-settling stage is balanced entirely by the buoyancy and drag force. When the particles deposit onto the base of the container, evolving a bed of particles, much of the particle gravitational force minus that of the buoyancy force, become supported by the reaction force from off the base of the container. The system is then in a state of compression.

It is assumed that when material deposits onto the surface of the rising sediment there are three distinct components. These components may be described as the solids portion, ΔS, the fixed free-volume portion corresponding to the retained fluid, ΔR, and the variable free-volume portion corresponding to the expressible fluid, ΔW, all taken as a volume per unit bed cross-sectional area. This distinction between these three components is made in the knowledge that ultimately the quantum of solids, ΔS, will be associated in the end with a quantum of fluid, ΔR, corresponding to the maximum volume fraction of solids, $\phi_m = \Delta S/(\Delta S + \Delta R)$ at the completion of the consolidation. Thus the remaining portion, ΔW, decreases with time due

to the consolidation. Clearly, during the consolidation of the bed, the fluid associated with the solids below is expressed through the void spaces surrounding the particles and hence in physical terms the fluid does not have an intimate association with the particles. Thus the portion of the so-called retained fluid, ΔR, reflects a portion of the void space around the particles that will always retain some fluid. The remainder of the void space, referred to as the expressible portion, ΔW, gradually decreases with time.

Galvin K. (1996) examined in detail the consolidation of a model sediment at a fixed elevation, showing that the observed consolidation velocity, V_s, scaled with the time, t, as $V_s \propto t^{-3}$. Thus, we hypothesize that the volume of expressible fluid, ΔW, decreases with time t according to the simple scaling law,

$$\Delta W \propto t^{-2} \tag{3}$$

Equation 3 is effectively a guess, which is hereby used to derive a system of equations to describe the consolidation. It is shown later by Equation 38 that the resulting system of equations is in fact consistent with the scaling law identified by Galvin K. (1996).

A key objective of this paper is to show how this simple scaling law can be used to derive other properties of the consolidating system, such as the particle velocity and volume fraction as a function of time and height, and to test these predictions against experimental data.

2.1 Variation of concentration with time

When the particles first join the bed surface, the initial sediment volume fraction of solids is,

$$\phi_o = \frac{\Delta S}{\Delta S + \Delta R + \Delta W_o} \tag{4}$$

where ΔW_o is the initial value of the variable fluid volume observed at the top of the sediment. In general, the volume fraction of solids at any other bed location k and time t is,

$$\phi_k = \frac{\Delta S}{\Delta S + \Delta R + \Delta W_k} \tag{5}$$

where ΔW_k is the value of the variable fluid volume at a time $t = n\Delta t$, directly associated with the particles that arrived at the surface of the rising sediment at time $t_k = k\Delta t$. These time values are defined in **Fig. 3**. Introducing our fundamental constitutive scaling relationship, it follows that,

$$\Delta W_k = \Delta W_o \left(\frac{t}{t_k}\right)^{-2} = \Delta W_o \left(\frac{k}{n}\right)^2 \tag{6}$$

The maximum volume fraction of the solids, ϕ_m, is reached once all of the expressible fluid has left the portion of solids. Thus,

$$\phi_m = \frac{\Delta S}{\Delta S + \Delta R} \tag{7}$$

We have used $\phi_m \approx 0.64$, the accepted value for the non-interacting random packing of mono-sized spheres, as obtained by Shannon P. et al. (1964). It should be noted that for other systems the final volume fraction of the bed can be considerably lower due to specific attraction between the particles comprising the particle network (Franks G. et al., 1999).

A useful identity derived from (4) and (7) is,

$$\left(\frac{1}{\phi_o} - \frac{1}{\phi_m}\right) = \frac{\Delta W_o}{\Delta S} \tag{8}$$

Substituting Eqn. 6 into Eqn. 5 gives,

$$\phi_k = \frac{\Delta S}{\Delta S + \Delta R + \Delta W_o \left(\frac{t_k}{t}\right)^2} \tag{9}$$

As already noted, t_k, is the time of arrival of the particles at the surface of the rising sediment, and t is the time since the commencement of the batch settling test. Again we refer the reader to **Fig. 3**. Rearranging Eqn. 9 while incorporating Eqn. 8 gives a relationship for the volume fraction of the particles as a function of the time spent in the sediment, defined by t_k and t,

$$\frac{t_k}{t} = \left(\frac{1}{\phi_k} - \frac{1}{\phi_m}\right)^{1/2} \Big/ \left(\frac{1}{\phi_o} - \frac{1}{\phi_m}\right)^{1/2} \tag{10}$$

Eqn. 10 is combined later with the integrated sum of the sediment height, relevant to the time values defined by t_k and t, to produce a description of the concentration profile at time t. It is noted that the time, t_k, is linked intimately with the particles that arrive at the sediment at that time. For instance, the time t_k can be replaced with the time, t_o, that the rising sediment meets the falling interface of the suspension. Eqn. 10 then provides a measure of the volume fraction of the particles, ϕ_k, at the surface of the suspension as a function of time.

2.2 Variation of sediment height with time

Fig. 3 shows the deposition of particles onto the rising sediment. The sediment is discretised into the elements of material that are added to the sediment as a function of time, providing the framework for describing the accounting system. These elements arrive at a time $t_1 = \Delta t$, then $t_2 = 2\Delta t$, $t_3 = 3\Delta t$, and so on. Thus in general the kth layer of material joins the surface of the bed at a time, $t_k = k\Delta t$. Each element carries the portions, ΔS solids, ΔR retained fluid, and ΔW_o expressible fluid. Eqn. 6 describes the variation in the expressible fluid with time. For example, at time interval $n = 4$ the expressible fluid in elements $k = 1$,

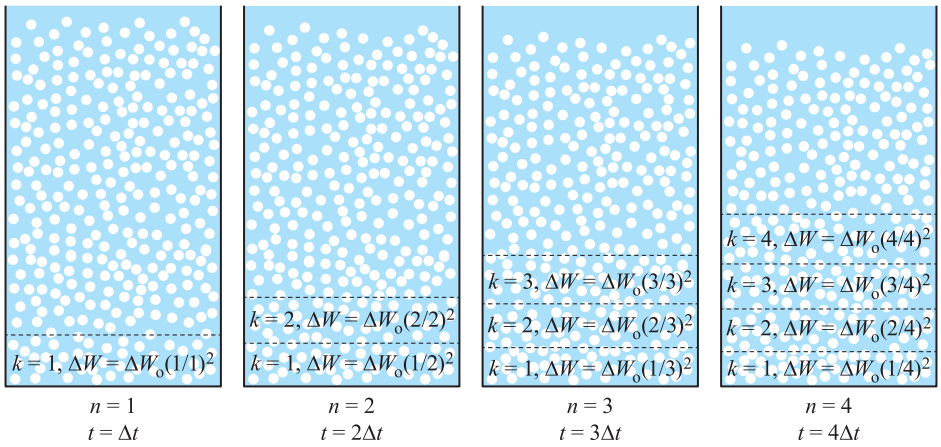

Fig. 3 Schematic of the proposed discretised model for the bed formation and consolidation process up to time $t = 4\Delta t$ when four layers identified $k = 1$ to 4 have settled to form a consolidating bed. Each layer has a varying volume of expressible fluid ΔW (given by Eqn. 6) which results in each layer having a variable thickness Δh.

2, 3 and 4 are,

$$\Delta W_1 = \Delta W_o\left(\frac{1}{4}\right)^2;\Delta W_2 = \Delta W_o\left(\frac{2}{4}\right)^2;$$

$$\Delta W_3 = \Delta W_o\left(\frac{3}{4}\right)^2;\Delta W_4 = \Delta W_o\left(\frac{4}{4}\right)^2 \tag{11}$$

Hence the height h_k to the top of sediment layer k at a time $t = n\Delta t$ (where $n \geq k$) is,

$$h_k = \sum_{i=1}^{k}\Delta h_i = k(\Delta S + \Delta R) + \frac{\Delta W_o}{n^2}\sum_{i=1}^{k} i^2 \tag{12}$$

Incorporating the series summation, the height becomes,

$$h_k = k(\Delta S + \Delta R) + \frac{\Delta W_o k(k+1)(2k+1)}{6n^2} \tag{13}$$

Noting that for large k the term $k(k + 1)(2k + 1) \rightarrow 2k^3$, Eqn. 13 becomes,

$$h_k = k(\Delta S + \Delta R) + \frac{\Delta W_o k^3}{3n^2} \tag{14}$$

Introducing the times $t_k = k\Delta t$ and $t = n\Delta t$, and incorporating Eqns. 7 and 8 gives,

$$\frac{h_k}{t_k} = \frac{\Delta S}{3\Delta t}\left[\frac{3}{\phi_m} + \left(\frac{1}{\phi_o} - \frac{1}{\phi_m}\right)\left(\frac{t_k}{t}\right)^2\right] \tag{15}$$

Let H_o be the total height of the sediment layer at the moment t_o when the rising sediment meets the interface of the falling suspension. Invoking the boundary condition, $t = t_k = t_o$, gives,

$$\frac{H_o}{t_o} = V_{po} = \frac{\Delta S}{3\Delta t}\left[\frac{1}{\phi_o} + \frac{2}{\phi_m}\right] \tag{16}$$

Thus the effective solids feed flux, G_F, of the batch settling test is,

$$G_F = \frac{\Delta S}{\Delta t} = \frac{3V_{po}}{\left(\frac{1}{\phi_o} + \frac{2}{\phi_m}\right)} \tag{17}$$

At relatively high initial concentrations, ϕ_i, there should be no discontinuity with the concentration just below the surface of the rising bed and hence $\phi_o = \phi_i$. In this case the feed flux is given by $G_F = (-V_{si} + V_{po})\phi_i$. Thus, in this case we can calculate V_{po} and in turn locate the boundary of the rising sediment. This boundary condition is used later in the analysis of the batch settling tests.

Incorporating Eqn. 17 into Eqn. 15 gives the height h_k of particles that arrived at the sediment surface at time t_k, at any given later time, t. That is,

$$\frac{h_k}{t_k} = \frac{V_{po}}{\left(\frac{1}{\phi_o} + \frac{2}{\phi_m}\right)}\left[\frac{3}{\phi_m} + \left(\frac{1}{\phi_o} - \frac{1}{\phi_m}\right)\left(\frac{t_k}{t}\right)^2\right] \tag{18}$$

In batch settling, the last particles arrive at the sediment surface at the time, $t_k = t_o$. Hence the observed consolidation, defined in terms of the falling upper interface, proceeds according to,

$$H = \frac{t_o V_{po}}{\left(\frac{1}{\phi_o} + \frac{2}{\phi_m}\right)}\left[\frac{3}{\phi_m} + \left(\frac{1}{\phi_o} - \frac{1}{\phi_m}\right)\left(\frac{t_o}{t}\right)^2\right] \tag{19}$$

where H is the total height of the sediment bed at time $t \geq t_o$.

It is evident from Eqn. 19 that at time $t = t_o$,

$$H = H_o = t_o V_{po} \tag{20}$$

and that at time $t = \infty$ the final sediment height is,

$$H_f = \frac{3H_o}{\left(2 + \frac{\phi_m}{\phi_o}\right)} \tag{21}$$

Substituting these conditions into Eqn. 19 gives a simple dimensionless description for the height of the falling interface, applicable for $t \geq t_o$ and $H \leq H_o$. That is,

$$\frac{H - H_f}{H_o - H_f} = \left(\frac{t_o}{t}\right)^2 \tag{22}$$

This equation is used formally to validate this model against a series of batch settling test results.

2.3 Description of the concentration profile

Sections 2.1 and 2.2 provided expressions for the concentration of the particles ϕ_k and height of the particles h_k as a function of time t, in terms of the time, t_k, that these particles first reached the rising sediment. Combining Eqns. 10 and 18 gives,

$$h_k \frac{t}{t_k} = \frac{tV_{po}}{\left(\frac{1}{\phi_o} + \frac{2}{\phi_m}\right)}\left[\frac{3}{\phi_m} + \left(\frac{1}{\phi_o} - \frac{1}{\phi_m}\right)\frac{\left(\frac{1}{\phi_k} - \frac{1}{\phi_m}\right)}{\left(\frac{1}{\phi_o} - \frac{1}{\phi_m}\right)}\right] \tag{23}$$

Simplifying Eqn. 23 leads to,

$$h_k \frac{t}{t_k} = \frac{tV_{po}}{\left(\frac{1}{\phi_o} + \frac{2}{\phi_m}\right)}\left[\frac{3}{\phi_m} + \left(\frac{1}{\phi_k} - \frac{1}{\phi_m}\right)\right] \tag{24}$$

Incorporating Eqn. 10 again eliminates t_k and gives the concentration profile of the sediment as a function of time. Here we drop the subscript k, noting that $h = h(\phi, t)$. That is,

$$h = tV_{po}\frac{\left(\frac{1}{\phi} + \frac{2}{\phi_m}\right)\left(\frac{1}{\phi} - \frac{1}{\phi_m}\right)^{1/2}}{\left(\frac{1}{\phi_o} + \frac{2}{\phi_m}\right)\left(\frac{1}{\phi_o} - \frac{1}{\phi_m}\right)^{1/2}} \tag{25}$$

Eqn. 25 shows that the concentrations propagate from the origin as a fan (Lester D. et al., 2005) over the full range from ϕ_o to ϕ_m, reflecting the absence of a traditional network structure.

Fig. 4a shows the concentration profile of the system as a function of time, obtained using the model of Dimitrova T. et al. (2000) with the parameter defining the strength of the particle pressure, $p_o = 0.0003$, set at the lowest possible value for a stable numerical solution. The objective was to obtain the solution for a system with a very low critical yield stress. The profiles are reported for different dimensionless time values. It is evident that the bed concentration evolves towards the maximum possible volume fraction of particles, set equal to 0.64. **Fig. 4b** shows the solution given by Eqn. 25, and Eqn. 22, obtained using the new theoretical model developed in this Section. Good agreement is evident.

Defining the propagation velocity of a wave of concentration ϕ as,

$$V_{p\phi} = \left.\frac{dh}{dt}\right|_{\phi} \tag{26}$$

it follows that the propagation velocity is a function of the solids concentration, ϕ, and is influenced strongly by the boundary conditions, V_{po}, ϕ_o, and ϕ_m.

$$V_{p\phi} = V_{po}\frac{\left(\frac{1}{\phi} + \frac{2}{\phi_m}\right)\left(\frac{1}{\phi} - \frac{1}{\phi_m}\right)^{1/2}}{\left(\frac{1}{\phi_o} + \frac{2}{\phi_m}\right)\left(\frac{1}{\phi_o} - \frac{1}{\phi_m}\right)^{1/2}} \tag{27}$$

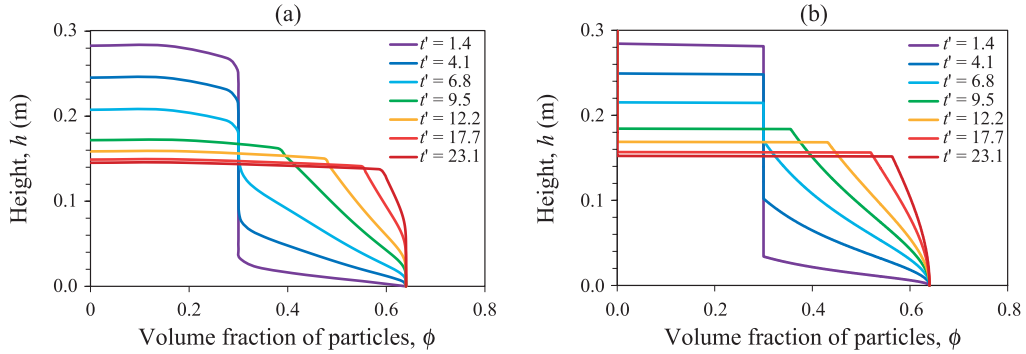

Fig. 4 Comparison of predicted concentration profiles as a function of time from (a) the model of Dimitrova T. et al. (2000) with $p_o = 0.0003$, and (b) the model developed in this work. The profile curves are given by dimensionless time values, based on common initial values of the suspension height, concentration, settling velocity, and maximum concentration.

2.4 Consolidation velocity of bed particles

The consolidation velocity of the particles within the sediment, relative to the vessel, is governed by the reorganisation of the sediment, and hence the gradual release of expressible fluid from below. This particle velocity, defined as negative in the downwards direction, is obtained by differentiating the height, h_k, in Eqn. 18 with respect to time, t, with the value of t_k held constant. Therefore,

$$V_{sk} = \frac{\mathrm{d}h_k}{\mathrm{d}t} \tag{28}$$

and

$$V_{sk} = \frac{-2V_{po}}{\left(\frac{1}{\phi_o} + \frac{2}{\phi_m}\right)}\left(\frac{1}{\phi_o} - \frac{1}{\phi_m}\right)\left(\frac{t_k}{t}\right)^3 \tag{29}$$

Incorporating Eqn. 10 which describes the concentration as a function of time, and again dropping the subscript k and noting that $V_s = V_s(\phi)$, gives,

$$V_s = \frac{-2V_{po}\left(\frac{1}{\phi} - \frac{1}{\phi_m}\right)^{3/2}}{\left(\frac{1}{\phi_o} + \frac{2}{\phi_m}\right)\left(\frac{1}{\phi_o} - \frac{1}{\phi_m}\right)^{1/2}} \tag{30}$$

While Eqn. 30 is a function of the local volume fraction of the particles, it is emphasized that this dependence is fundamentally different to that in the free settling zone, as it reflects the constrained nature of the consolidation. Indeed the consolidation velocity is always less than the free settling velocity. Eqns. 27 and 30 conform to the requirements of continuity. That is,

$$V_p = -\frac{\mathrm{d}(V_s\phi)}{\mathrm{d}\phi} \tag{31}$$

2.5 Settling velocity at constant elevation

Galvin K. (1996) examined the settling of the individual particles within the sediment at a fixed elevation. Particles passed downwards into and out of the field of view, and hence the data collected involved different particles. Firstly we set

$$\beta_k = \left(\frac{t_k}{t}\right)^3 \tag{32}$$

Then, combining Eqns. 17, 29 and 32 gives,

$$V_s = \frac{-2G_F\beta_k}{3}\left(\frac{1}{\phi_o} - \frac{1}{\phi_m}\right) \tag{33}$$

Returning to Eqn. 18, and incorporating Eqns. 17, and 32 gives,

$$\frac{h_k}{t} = \frac{G_F\beta_k^{1/3}}{\phi_m} + \frac{G_F\beta_k}{3}\left(\frac{1}{\phi_o} - \frac{1}{\phi_m}\right) \tag{34}$$

Setting the height, h_k, to be equal to the constant elevation, h_c, provides the corresponding time, t.

$$t = \frac{h_c}{\frac{G_F\beta_k^{1/3}}{\phi_m} + \frac{G_F\beta_k}{3}\left(\frac{1}{\phi_o} - \frac{1}{\phi_m}\right)} \tag{35}$$

A series of values of β_k provide a common independent variable for calculating the consolidation velocity, V_s, from Eqn. 33, and the value of the time, t, from Eqn. 35, revealing the scaling law, $V_s \propto t^{-3}$. Alternatively, Eqn. 33 can be inserted into Eqn. 35, giving

$$\frac{h_c}{t} = \frac{G_F}{\phi_m}\left(\frac{-3V_s}{2G_F\left(\frac{1}{\phi_o} - \frac{1}{\phi_m}\right)}\right)^{1/3} - \frac{V_s}{2} \tag{36}$$

Note that the consolidation velocity, V_s, is numerically negative. During consolidation the value of $(-V_s)^{1/3}$ eventually dominates over the value of $-V_s$, and hence the second term on the right hand-side of Eqn. 36 can be neglected. It then follows that at fixed elevation,

$$-V_s \approx \frac{2\phi_m^3}{27V_{po}^2}\left(\frac{1}{\phi_o} + \frac{2}{\phi_m}\right)^2\left(\frac{1}{\phi_o} - \frac{1}{\phi_m}\right)\left(\frac{h_c}{t}\right)^3 \tag{37}$$

Eqn. 37 provides the asymptotic behaviour of the consolidation process within the sediment at fixed elevation, as observed by Galvin (1996). That is,

$$-V_s \propto \left(\frac{h_c}{t}\right)^3 \tag{38}$$

Galvin K. (1996) obtained data on the settling velocity at various fixed elevations. The data sets collapsed to produce a single curve in accordance with Eqn. 38.

3. Experimental method

Sephadex G-200 grade granules, made by cross-linking dextran with epichlorohydrin under alkaline conditions, were sourced from Pharmacia. The dry particles, with density of 1538 kg m^{-3}, were sieved to obtain the –75 +63 μm size fraction. These particles were added to a beaker of distilled water and allowed to swell. Evans I. and Lips A. (1990) studied a number of different grades of Sephadex particles and found that the settled bed packing fraction was always close to 0.64, as expected for random tight packing of spheres (Shannon P. et al., 1964). Galvin K. (1996), who used the same system of particles,

reported the particles swelled over a 24 h period to a diameter of 220 μm, forming a settled bed of 30 cm^3 per 1 g of dry Sephadex. Assuming the settled bed volume fraction was 0.64 and that the volumes of Sephadex and water were additive, this implies that the swollen particles had a density of 1018 kg m^{-3}.

In the present work, the same batch of Sephadex particles was re-used multiple times over a prolonged period. **Fig. 5** shows that whilst much of the swelling was complete within the first 24 h, there was clear evidence of additional swelling over the following months as the final settled bed height was observed to increase from around 2.0 cm/g (volume of 39 cm^3/g) to over 2.4 cm/g (47 cm^3/g). Again, assuming a constant final settled bed volume fraction of 0.64, this suggests the density of the swollen particles decreased from 1014 kg m^{-3} down to 1012 kg m^{-3}. Thus, for internal consistency, it was necessary to limit comparisons between experiments to insure that the degrees of swelling were similar.

Eventually, the observed diameter of the spheres was around 250 μm, with a density of about 1013 kg m^{-3}. Hence these particles settled in water according to Stokes' law (Stokes, 1901) with a very low particle Reynolds number of ~ 0.1. Although the final particles were in principle deformable, within the limits of the experimental conditions, the particles did not compress or deform. Evans I. and Lips A. (1990) formed the same conclusions while also noting that surface forces were also negligible. Thus this experimental system is a very close approximation to the ideal system of non-deformable, mono-sized spherical particles settling at low Reynolds numbers with negligible surface forces.

A set of batch settling tests was conducted, focused initially on the fall of the upper interface versus time. A given series of experiments involved the same mass of the Sephadex granules. In the first series the mass was 12 g.

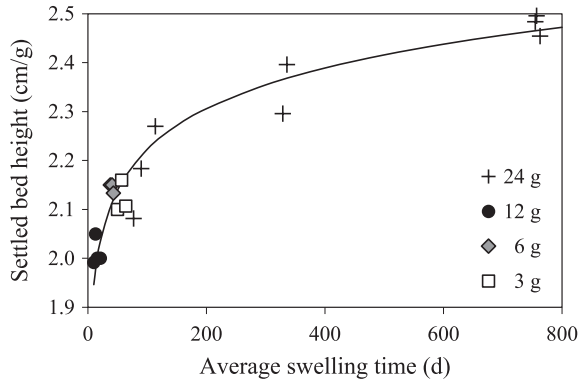

Fig. 5 Extent of swelling of the Sephadex particles over 24 months, accounting for different bed volumes in experiments conducted at different times. Legend shows the mass of dry Sephadex in the system. Line is drawn to guide the eye.

Then this batch of material was halved to perform a series of tests using 6 g of Sephadex, and then halved again to test 3 g of Sephadex. Then all this material was recombined and an additional 12 g of Sephadex added in order to perform a series of tests using 24 g. Within each series, different initial suspension concentrations were obtained by adding or removing different quantities of distilled water.

At the start of an experiment the Sephadex spheres were suspended within a 1.25 m high Perspex cylinder of internal diameter 50 mm using a perforated plunger, and the initial height, H_i, noted. A quiescent state was formed within seconds. A ruler located down the wall of the cylinder provided elevations accurate to within 1 mm. During the experiment the height of the upper interface, H, was recorded versus the time, t. The final height of the sediment, H_f, was recorded after the material had been left to consolidate for at least 24 h. Based on the findings of Evans and Lips (1990), it was assumed the final volume fraction of the spheres was $\phi_m = 0.64$. Hence the initial volume fraction was calculated to be $\phi_i = (H_f/H_i)\phi_m$. Experiments were conducted using initial volume fractions in the range 0.28 to 0.55.

Following the initial set of experiments, approximately 12 months later additional experiments were conducted using the same batch of Sephadex in order to study the consolidation velocity of spherical particles at fixed elevations. A CCD video camera was positioned at a specific elevation during the experiment. The movement of different particles within a height range of about 1 mm was recorded over an extended time period. Experiments were repeated in order to observe the internal consolidation at different elevations. In addition, the height of the upper interface versus time was recorded during each of these experiments in order to properly characterise the settling process.

Finally, about 24 months after the first set of experiments, additional experiments were conducted in order to examine the evolution of the concentration profile versus time. Suspension concentration was measured using the light extinction method (Hinds W., 1982). The experimental system shown in **Fig. 6** was located in a dark room, free of spurious light sources. A 5 mW 532 nm laser beam was directed horizontally into the suspension at a given elevation and the light exiting the opposite side recorded using a CCD camera. The laser and camera were then moved in unison to a new elevation in order to record the transmitted light at that point. A set of these measurements at different elevations was recorded within a relatively brief time period, allowing a single time value to be assigned to a given concentration profile data set. This process was repeated at multiple nominal time values during the batch settling.

Each image was later analysed to measure the average

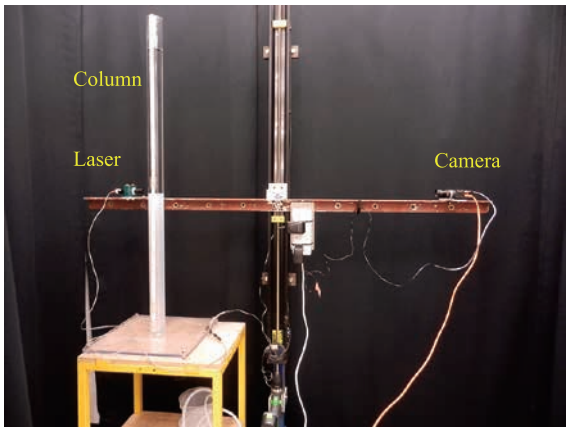

Fig. 6 Photograph of the experimental set up which consisted of a vertical 1.25 m high Perspex column with internal diameter of 50 mm. A 5 mW 532 nm laser was mounted on one side and a camera mounted on the opposite side on a frame with adjustable height.

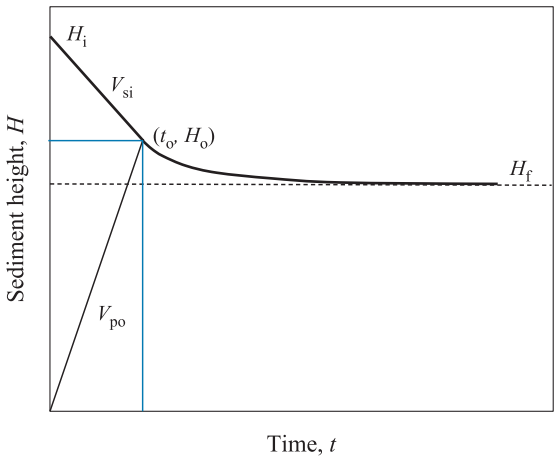

Fig. 7 Representation of the batch settling test showing the initial constant settling rate followed by the consolidation phase. The rise velocity of the sediment is $V_{po} = H_o/t_o$.

intensity of the transmitted light. The signal obtained at the start of the batch settling test corresponded to the initial volume fraction, ϕ_i, while the signal obtained after one week near the base of the sediment, corresponded to ϕ_m. Tests showed that the transmission for intermediate concentrations could be obtained by linear interpolation between these two extremes. Thus it was possible to obtain the volume fraction value corresponding to a given signal.

4. Results and discussion

4.1 Boundary condition between free-settling and consolidating bed

The initial suspension exists in a state of uniform concentration hence the particle gravitational force, less that of the buoyancy force is fully supported by the hydrodynamic drag force. Thus, the initial settling velocity of the particles is a well-defined function of the volume fraction of the particles, referred to as the hindered settling function. **Fig. 7** shows a typical batch settling test curve ranging in height from the initial value, H_i through to the final height, H_f. The suspension settles at the initial velocity, V_{si}, while the sediment rises at the velocity V_{po}, producing an initial sediment height, H_o, in a time period t_o.

The analysis of the batch settling test commences with the identification of the boundary condition (t_o, H_o), something that can be difficult to achieve objectively. The approach adopted in this study was to locate this point using the experimental data in conjunction with the consolidation model. The feed flux, G_F, given by Eqn. 17, can be equated with the magnitude of the initial settling flux, relative to the velocity of the rising sediment. That is,

$$G_F = \frac{3V_{po}}{\left(\frac{1}{\phi_o} + \frac{2}{\phi_m}\right)} = \phi_i\left(-V_{si} + V_{po}\right) \tag{39}$$

where the initial settling velocity, V_{si}, has a negative value indicating its downwards direction. Rearranging and setting $V_{po} = H_o/t_o$ gives,

$$V_{po} = \frac{H_o}{t_o} = \frac{-V_{si}\left(\frac{\phi_i}{\phi_o} + 2\frac{\phi_i}{\phi_m}\right)}{\left(3 - \frac{\phi_i}{\phi_o} - \frac{2\phi_i}{\phi_m}\right)} \tag{40}$$

With reference to **Fig. 7**, it follows that

$$-V_{si} = \frac{H_i - H_o}{t_o} \tag{41}$$

It is tacitly assumed that the concentration at the surface of the rising sediment is equal to the initial concentration, $\phi_o = \phi_i$. This assumption appears to be valid when the initial volume fraction is sufficiently high, and inertial forces are negligible. Thus the condition appears to apply in this study. Eqn. 40 then becomes,

$$V_{po} = \frac{H_o}{t_o} = \frac{-V_{si}(\phi_m + 2\phi_i)}{2(\phi_m - \phi_i)} \tag{42}$$

It is noted that this equation potentially approaches a singularity when $\phi_i \to \phi_m$. This singularity can only be avoided if V_{si} approaches 0 as $\phi_i \to \phi_m$. Hence the Richardson-Zaki equation (given later by Eqn. 45) cannot be used near $\phi_i = 0.64$ because it incorrectly predicts that V_{si} still has finite values up to the limit $\phi_i = 1.0$. However, as the highest ϕ_i value used in this work was 0.55, this limitation was not an issue here.

Substituting Eqn. 41 into Eqn. 42 to eliminate V_{si} gives,

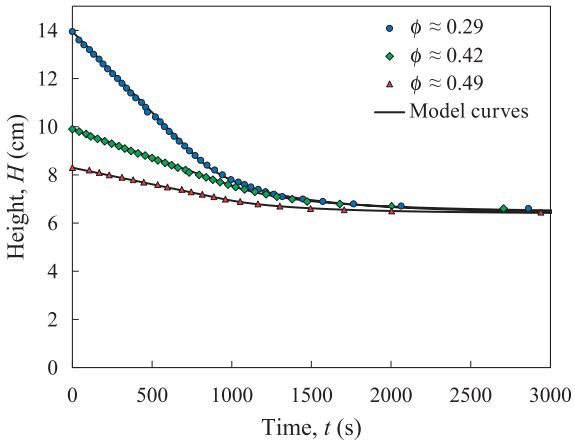

Fig. 8 Batch settling test results obtained using 3 g of Sephadex, with different initial concentrations. The curves through the data are based on the model developed in this paper.

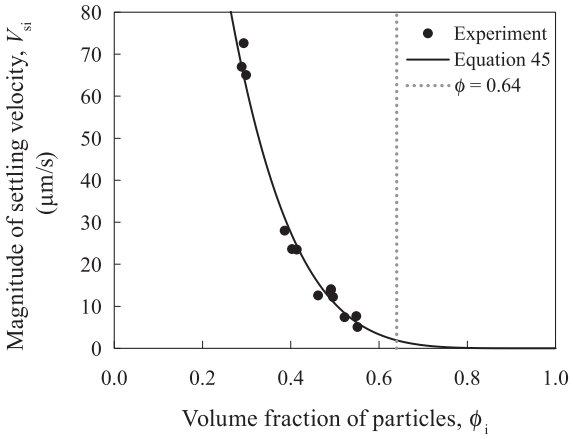

Fig. 9 Initial free-settling velocity of the particles versus the initial volume fraction of the particles. The curve denotes the best fit of Eqn. 45 to the experimental data with $V_t = -399$ μm/s and $n = 5.23$.

$$H_o = \frac{H_i}{3}\left(1+\frac{2\phi_i}{\phi_m}\right) \tag{43}$$

and hence the value of t_o is,

$$t_o = \frac{2H_i}{-3V_{si}}\left(1-\frac{\phi_i}{\phi_m}\right) \tag{44}$$

The boundary condition defining the point at which the rising sediment meets the falling interface of the suspension can be obtained through trial and error. The first few data points can be used to estimate the initial settling velocity, V_{si}, which in turn can be used to obtain t_o via Eqn. 44. Then the initial settling velocity can be based on a linear best-fit to all of the data covering the range of time values up to t_o. The resultant value, V_{si}, can then be used to update the value of t_o, leading to confirmation of the boundary condition, (t_o, H_o), and the value of V_{po}. This objective approach insures the boundary condition is consistent with the consolidation model.

4.2 Free-settling velocity—The hindered settling function

In order to properly describe the velocity of propagation of the rising sediment, given by Eqn. 42, we need to firstly describe the initial free-settling velocity, V_{si}. The empirical hindered settling function of Richardson J. and Zaki W. (1954),

$$V_{si} = V_t(1-\phi_i)^n \tag{45}$$

provides an accurate description. The exponent, n, varies with the particle Reynolds number while the terminal velocity, V_t, of an isolated spherical particle settling according to Stokes' law is:

$$V_t = -\frac{d^2(\rho_s-\rho)}{18\mu} \tag{46}$$

Here, d is the particle diameter, ρ_s the particle density, ρ the fluid density, g the acceleration due to gravity, and μ the fluid viscosity.

Fig. 8 shows batch settling test results for experiments conducted using 3 g of Sephadex particles, using different initial concentrations. Additional results are shown in Forghani M. (2015). **Fig. 9** shows the initial settling velocities of the particles used in the batch settling tests versus the initial volume fractions of the particles. These data can be described very well using Eqn. 45 with $V_t = -399$ μm/s and $n = 5.23$. As mentioned above, Eqn. 45 incorrectly predicts finite values of V_{si} for $\phi > 0.64$. However, within the range of the experimental conditions up to $\phi_i = 0.55$, the prediction is sufficiently accurate.

Fig. 10 shows the data for velocity of propagation, V_{po}, versus the initial volume fraction of the particles, sourced directly from the batch settling tests. The solid curve passing through the data was formed by substituting the expression for V_{si} (Eqn. 45) into Eqn. 42. The singularity as ϕ_i approaches 0.64 is clearly evident. However, within the range of experimental conditions the data are reasonably consistent with the curve, given the inherent scatter. By comparison, Kynch theory predicts a propagation velocity:

$$V_p = -\frac{\partial(V_s\phi)}{\partial\phi} \tag{47}$$

which combined with Eqn. 45 gives,

$$V_p = V_s - V_s\frac{n\phi}{(1-\phi)} \tag{48}$$

The result obtained using Eqn. 48 is also shown in **Fig.**

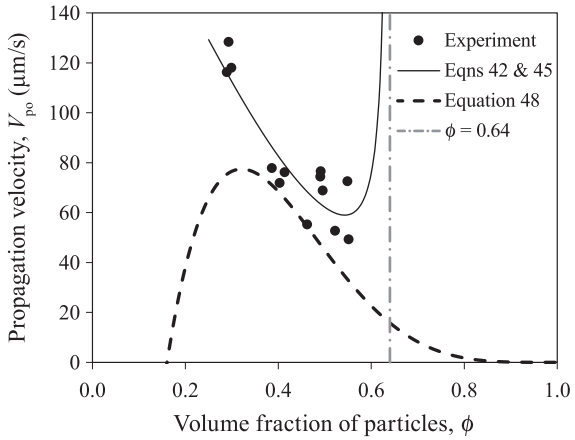

Fig. 10 Propagation velocity of the rising sediment versus the suspension initial volume fraction. The solid curve is based on the theoretical consolidation model (Eqn. 42) and the dashed curve is based on the theory of Kynch (Eqn. 48).

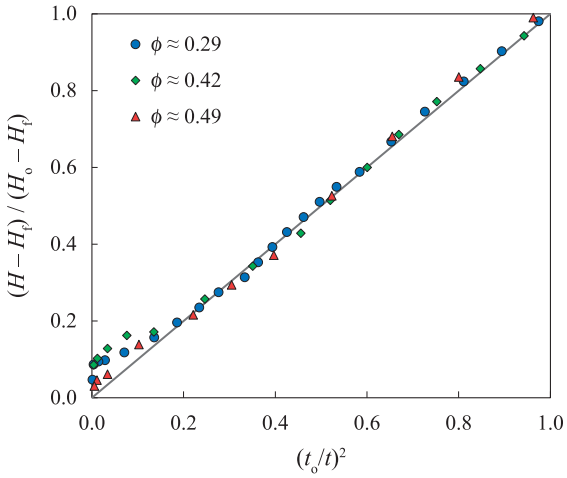

Fig. 11 Normalized plots of the batch settling data shown in **Fig. 8** based on 3 g of Sephadex and different initial volume fractions. The linearity between (0,0) and (1,1) provides strong support for the consolidation model, and hence the underlying scaling law.

10. It is evident the actual propagation velocities were higher than those predicted using Kynch theory, reflecting the constrained nature of the consolidation process compared to free-settling.

4.3 Consolidation

According to the theoretical model, the consolidation process within the bed is characterised by the normalised function given by Eqn. 22. That is,

$$\frac{H - H_f}{H_o - H_f} = \left(\frac{t_o}{t}\right)^2 \tag{22}$$

where H_f is the final sediment height after infinite time. It is noted that the pair of starting values required in Eqn. 22, H_o and t_o, were set equal to the values at the end of the free-settling period as described in Section 4.1. **Fig. 11**, which is based on the experimental data shown in **Fig. 8**, shows the full collapse of the data sets along the diagonal from the upper coordinate (1, 1) to the lower coordinate (0, 0). These data provide strong evidence to support the proposed scaling law in this study. Additional data sets are provided in Forghani M (2015) for different initial quantities of Sephadex.

4.4 Analysis of the internal consolidation

The analysis in the previous section was focused on the falling height of the upper interface versus time. While this work provided support for the consolidation model, the strength of the validation is limited given the relatively small changes in the measured height versus time, especially towards the end of the consolidation.

Thus, in this section a much more thorough validation of the model is presented. Two approaches are taken. The first is based on the original approach of Galvin K. (1996). In this work the vertical motion of the actual Sephadex particles during the consolidation was examined versus time at a fixed elevation. Initially the particles consolidated at a relatively high velocity. But over time, the consolidation velocity decreased by a significant factor. Eqns. 33 and 35 describe the consolidation velocity versus time, at fixed elevation h_c.

This second phase of the study occurred some 12 months after the previous work using the same particles of Sephadex. It is noted that the particles underwent additional swelling during this period resulting in larger particles of marginally lower density and hence a final sediment height greater than obtained previously. The increase in the final sediment height was consistent with the increase in the observed size of the particles. Thus we are satisfied the final sediment volume fraction of the particles remained at the standard random packing value of 0.64.

Fig. 12 shows the batch settling test curve obtained using 24 g of Sephadex, with an initial volume fraction of 0.40. The smooth curve through the data was based on the theoretical consolidation model, with $V_{si} = 20.7$ μm/s and $V_{po} = 59.5$ μm/s.

Fig. 13 shows log-log plots of the observed particle velocity within the system at fixed elevation. The velocities were obtained by observing the movement of specific particles present at that moment in the field of view. The quality of the images was not high, but was sufficient for identifying the boundaries of the particles, and hence sufficient for measuring the consolidation velocity. In general, movement occurred *en masse* and therefore the velocity of a given particle was representative of the rest.

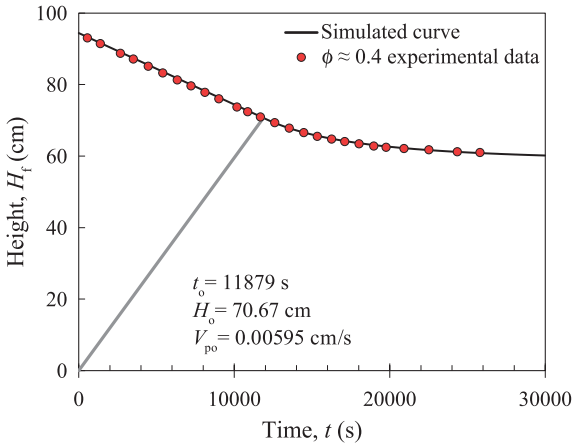

Fig. 12 Batch settling test with 24 g of Sephadex used to validate the model for describing the internal consolidation within the sediment.

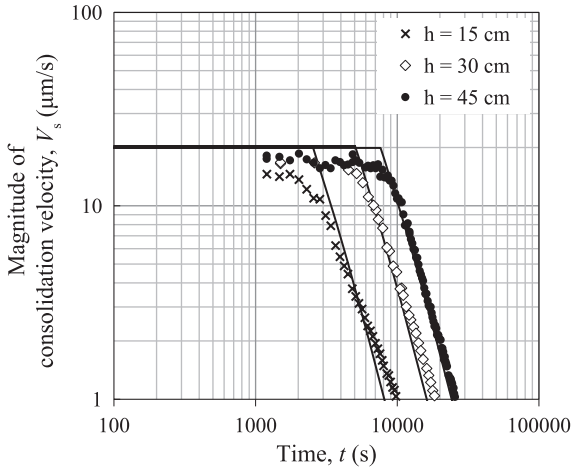

Fig. 13 Consolidation velocity versus time based on observations at elevations of h_c = 15 cm, 30 cm, and 45 cm for experiments with 24 g of Sephadex and ϕ_i = 0.40. Line shows prediction of Eqns. 33 and 35.

The data sets correspond to observations at elevations of 15, 30, and 45 cm above the base of the vessel, well below the final sediment height of approximately 58 cm.

The results in **Fig. 13** are very significant. Effectively they describe the actual consolidation velocity as a function of both time and position. Moreover, it is evident that initially the velocity is constant, approximately 20 μm/s, reflecting the corresponding free-settling of the particles. The velocity then decreases to lower and lower values as the consolidation proceeds. The exact predictions of the theoretical consolidation model are given by the three solid curves. These curves show the formal scaling according to $V_s \propto t^{-3}$, consistent with the original finding of Galvin (1996). While the agreement between the model and the experimental data is weakest at 15 cm, the agreement appears to strengthen at the higher elevation of 30 cm, and become very strong at 45 cm. The improvement in the scaling with distance above the base is a reasonable expectation, given that the scaling should fail at the fixed base of the system. These results are remarkable, predicting the consolidation velocity to within 1 μm/s after a period of 20000 s at a significant elevation in the bed of 45 cm.

The knowledge of the consolidation velocity as a function of time and position provides arguably the most definitive description that is possible. Correct prediction of the consolidation velocities should lead to the correct prediction of the liquid expression and thus the volume fractions of the particles as a function of time and position.

Fig. 14 shows the concentration profiles of the consolidation zone versus time, measured using the experimental method outlined in Section 3. The theoretical predictions based on Eqn. 25 show excellent overall agreement, though there is some discrepancy again near the base. These findings provide comprehensive validation of the

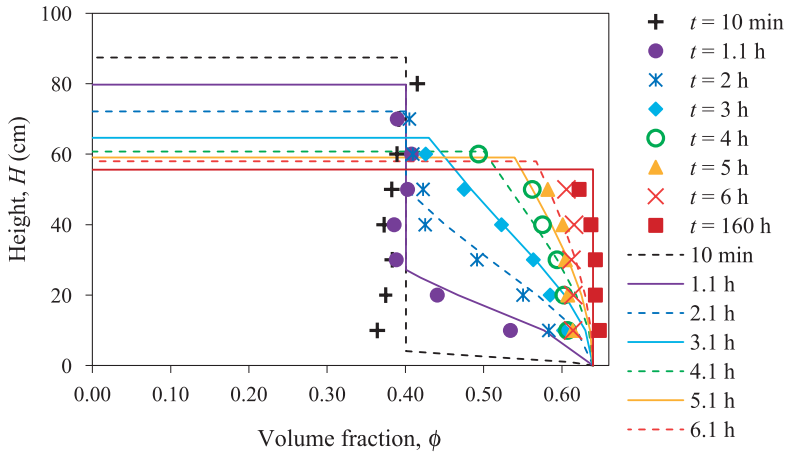

Fig. 14 Concentration profiles at different times, showing the height versus the volume fraction of the particles. The experimental data is for 24 g of Sephadex at an initial concentration ϕ_i = 0.40. Lines show theoretical predictions of Eqn. 25 which uses the V_{po} value obtained from **Fig. 12** and the assumption that $\phi_o = \phi_i$.

model describing sediment consolidation of an ideal system consisting of mono-sized, non-deformable spheres at low Reynolds number and with negligible inter-particle forces.

In the above analysis we have assumed that there is full continuity between the free settling and consolidation zones. Thus the volume fraction of solids just below the surface of the rising sediment, ϕ_o, is equated with the initial volume fraction, ϕ_i, used in the batch settling. In turn the model requires that the particles at the surface of the sediment consolidate at the free settling velocity, even though the particles at the surface of the rising sediment have achieved formal contact with the structure below. It should be noted, however, that the consolidation velocity of the particles within the sediment varies with the volume fraction according to the consolidation model, and not according to the free settling function. Thus, the agreement between the consolidation and free settling velocities only exists at the interface.

This paper requires further discussion concerning the boundary condition at the surface of the rising sediment. In most studies, the minimum sediment concentration is defined by the so-called gel concentration, an input into the model. The theory presented in this paper does not offer a general solution for determining the relevant volume fraction just below the surface of the sediment. In the context of the present problem there is scope for developing a Discrete Element Model (DEM) to improve our understanding of the boundary condition. We have recently established, using a Monte Carlo approach, that a network formed through a simple random deposition model, with fixed attachment between the particles, produces a bed with a volume fraction of approximately 0.194. Clearly a higher concentration is expected in the absence of particle-particle attachment.

Although Kynch theory has its limitations, the approach offers some insight here into the effects of an increase in the particle Reynolds number. According to drift flux theory (Wallis G., 1962) there is an inflection in the flux curve at the volume fraction, $\phi_I = 2/(n + 1)$, where n is the exponent defined by the Richardson and Zaki equation. When the initial volume fraction of the particles, ϕ_i, is higher than the inflection value, ϕ_I, there is, in principle, no discontinuity in the concentration between the free settling particles and the surface of the rising sediment. This study has focused on such a concentration regime, $\phi_i > \phi_I$. The nature of the problem becomes a strong function of the particle Reynolds number, Re_t, with $n \approx 2.4$ applicable for large Re_t and $n = 5.2$ applicable for the very low Re_t used in this study. The corresponding concentrations at the flux curve inflexions are $\phi_I = 2/(1 + 2.4) = 0.59$ for large Re_t with $n = 2.4$, and $\phi_I = 2/(1 + 5.2) = 0.32$ for small Re_t with $n = 5.2$. Thus large spherical glass marbles settling in water at a high Re_t should form densely packed sediment, with the volume fraction of the particles ranging from at least $\phi_I = 0.59$ just below the surface of the sediment. Thus, for large glass spheres, the sediment forms with a bed concentration ranging from at least 0.59 through to 0.64. Here there is little prospect for particle re-ordering and hence consolidation, as the high inertial forces drive the particles rapidly towards the lowest potential energy state, and a high volume fraction. For highly viscous systems, however, the volume fraction of the particles just below the surface of the sediment should range from at least 0.32. Thus viscous systems present the most interesting problem of sediment consolidation, with the potential for significant particle re-ordering towards the lowest potential energy state, slowed by significant viscous forces.

Further work is needed to account for (i) the boundary condition at the interface between the free settling and consolidating sediment bed and (ii) the scaling law that underpins the model developed in this study. Why does the volume of expressible fluid associated with the particles decay proportional to t^{-2}? A discrete element model could be used to investigate both of these issues.

5. Conclusions

This work commenced with a simple idea, which in turn led to the development of a comprehensive theoretical model of the consolidation that occurs during batch settling. This model provided a description of the fall in the height of the upper interface with time, a description of the internal consolidation velocity as a function of time and position, and a description of the evolving concentration profile. An experimental study then followed, providing validation of the new model.

In this model a given portion of solids is associated with a void space that is occupied by a fixed portion of retained fluid and a further portion of expressible fluid. The space occupied by the expressible fluid decays according to a scaling law proportional to t^{-2}. As noted, further work is recommended based on a discrete element modelling approach to further understand the physical processes that result in this scaling law.

Nomenclature

d	particle diameter (m)
G_F	solids feed flux ($m^3\ m^{-2}\ s^{-1}$)
g	acceleration due to gravity ($m\ s^{-2}$)
H	height of suspension upper interface (m)
H_i	initial suspension height (m)
H_f	final height of sediment (m)

H_o	height where upper interface of settling suspension meets rising sediment bed (m)
h_c	a constant elevation within the bed (m)
h_k	height of layer k within the sediment bed (m)
k	bed layer increment number (-)
n	time increment number (-)
n	coefficient in Richardson-Zaki equation (-)
t	time (s)
t_k	time material reached sediment surface (s)
t_o	time when falling suspension interface meets rising sediment bed (s)
Δt	time step size (s)
ΔS	volume of solids ($m^3\ m^{-2}$)
ΔR	volume of retained fluid ($m^3\ m^{-2}$)
Re_t	particle Reynolds number at its terminal settling velocity (-)
V_{po}	upwards propagation velocity of initial sediment surface concentration ($m\ s^{-1}$)
$V_{p\phi}$	upwards propagation velocity of layer of concentration ϕ ($m\ s^{-1}$)
V_s	consolidation velocity of particles ($m\ s^{-1}$)
V_{si}	initial settling velocity of particles ($m\ s^{-1}$)
V_t	terminal free settling velocity ($m\ s^{-1}$)
ΔW	volume of expressible fluid ($m^3\ m^{-2}$)
ΔW_o	initial volume of expressible fluid ($m^3\ m^{-2}$)
β_k	defined by Eqn. 32 as $(t_k/t)^3$ (-)
ϕ	solids volume fraction (-)
ϕ_I	solids volume fraction at inflection point (-)
ϕ_i	initial suspension solids volume fraction (-)
ϕ_m	maximum solids volume fraction (-)
ϕ_o	volume fraction of solids at upper surface of rising sediment bed for $t < t_o$ (-)
μ	fluid viscosity (Pa s)
ρ	fluid density ($kg\ m^{-3}$)
ρ_s	solid density ($kg\ m^{-3}$)

References

Bürger R., Concha F., Mathematical model and numerical simulation of the settling of flocculated suspensions, Int. J. of Multiphase Flow, 24 (1998) 1005–1023.

Buscall R., White, L.R., The Consolidation of Concentrated Suspensions, Part I. The Theory of Sedimentation, J. Chem. Soc. Faraday Trans. 1, 83 (1987) 873–891.

Coe H.S., Clevenger G.H., Methods for Determining the Capacities of Slime-Settling Tanks, Trans. Am. Inst. Min. Eng., 60 (1916) 356–384.

Concha F., Bürger R., A century of research in sedimentation and thickening, KONA Powder and Particle, 20 (2002) 38–70.

Dimitrova T.D., Gurkov T.D., Vassileva N., Campbell B., Borwankar R.P., Kinetics of Cream Formation by the Mechanism of Consolidation in Flocculating Emulsions, Journal of Colloid and Interface Science, 230 (2000) 254–267.

Evans I.D., Lips A., Concentration dependence of the linear elastic behaviour of model microgel dispersions, Journal of the Chemical Society, Faraday Transactions, 86 (1990) 3413–3417.

Fitch B., Sedimentation of Flocculent Suspensions: State of the Art, AIChE Journal, 25 (1979) 913–930.

Forghani M., Doroodchi E., Galvin K.P. Universal Scaling of Consolidation in Batch Settling, in: Chemeca 2013: Challenging Tomorrow. Barton, ACT: Engineers Australia, (2013) 376–382.

Forghani M. (2015). Consolidation of Large Spherical Particles at Low Reynolds Numbers, MPhil Thesis, University of Newcastle, Australia (*submitted*).

Franks G.V., Johnson S.B., Scales P.J., Boger D.V., Healy T.W., Ion Specific Strength of Attractive Particle Networks, Langmuir, 15 (1999) 4411–4420.

Galvin K.P., Measurement of particle velocity during sediment consolidation, Chemical Engineering Science, 51 (1996) 3241–3246.

Galvin K.P., Zhao Y., Davis R.H., Time-averaged hydrodynamic roughness of a non-colloidal sphere in low Reynolds number Motion Down an Inclined Plane, Physics of Fluids, 13 (2001) 3108–3119, DOI: 10.1063/1.1409368

Hinds W.C., Aerosol Technology, Wiley-Interscience, New York (1982).

Howells I., Landman K.A., Panjkov A., Sirakoff C., White L.R., Time-dependent batch settling of flocculated suspensions, Appl. Math. Modelling, 14 (1990) 77–86.

Richardson J.F., Zaki W.N., Sedimentation and Fluidisation: Part I., Trans. Instn. Chem. Engrs. 32 (1954) 82–100.

Kynch G.J., A Theory of Sedimentation, Trans. Farady Soc., 48 (1952) 166–176.

Lester D.R., Usher S.P. Scales P.J., Estimation of the Hindered Settling Function $R(\phi)$ from Batch-Settling Tests, AIChE J., 51 (2005) 1158-1168. DOI: 10.1002/aic.10333

Shannon P.T., DeHaas R.D., Stroupe E.P., Tory E.M., Batch and Continuous Thickening. Prediction of Batch Settling Behavior from Initial Rate Data with Results for Rigid Spheres, Ind. Eng. Chem. Fundamen., 3 (1964) 250–260.

Stokes G.G., Mathematical and Physical Papers, Cambridge University Press, 3 (1901).

Usher S.P., Scales P.J., White L.R., Prediction of Transient Bed Height in Batch Sedimentation at Large Times, AIChE J., 52 (2006) 986–993, DOI: 10.1002/aic.10709

Wallis G.B., A simplified one-dimensional representation of two-component vertical flow and its application to batch sedimentation, in: Proc. of the Symposium on the Interaction between Fluids and Particles, London, Instn. Chem. Engrs. (1962) 9–16.

Author's short biography

Kevin P. Galvin

Kevin Galvin obtained his BE (Chemical Engineering) with 1st Class Honours and the University Medal from the University of Newcastle in 1987 while working full-time for BHP Central Research Laboratory. He then obtained his PhD (1990) from Imperial College, London, returning to BHP for 3 years, prior to joining the University of Newcastle. His research interests are concerned with bubbles, drops, and particles in process systems. He is the inventor of the Reflux Classifier, a novel fluidized bed device, deployed around the world in coal and mineral processing. He is the Director of the ARC Research Hub for Advanced Technologies for Australian Iron Ore and a Fellow of the Australian Academy of Technological Sciences and Engineering.

Marveh Forghani

Marveh Forghani completed her undergraduate degree in Civil Engineering-Building at the Shomal University of Amol, Iran in 2007. She graduated with a Master of Engineering Science (Specialisation in Energy) at the University of Newcastle, Australia, in 2011. She is in the process of completing her MPhil in Chemical Engineering at the University of Newcastle, Australia.

Elham Doroodchi

Elham Doroodchi obtained her PhD from The University of Newcastle in 2005 after completing her undergraduate studies in Chemical Engineering at the same university with 1st Class Honours and The University Medal. Her research interests are in the area of particle technology and fluidization with a focus on developing energy efficient processes. She is the inventor of GRANEX, an emission-free engine that turns heat from low-grade sources such as geothermal and industrial waste heat into electricity.

Simon M. Iveson

Simon Iveson completed his BE (Chemical Engineering) with university medal (1992) and PhD (1997) at the University of Queensland, Australia. His research was on granule consolidation, deformation and growth. In 1997 he moved to the Centre for Multiphase Processes at the University of Newcastle, Australia, where he continued his research on particle agglomeration until 2002. From 2003 to 2006 he lectured at the *Universitas Pembangunan Nasional*, Yogyakarta, Indonesia. In 2007 he returned to the University of Newcastle where he has since been lecturing and researching in the field of coal and mineral processing.

KONA Powder and Particle Journal No. 33 (2016) 264–277/Doi:10.14356/kona.2016008 Original Research Paper

Effect of Drag Models on Residence Time Distributions of Particles in a Wurster Fluidized Bed: a DEM-CFD Study †

Liang Li [1,2], Johan Remmelgas [2], Berend G.M. van Wachem [3], Christian von Corswant [2], Staffan Folestad [2], Mats Johansson [2] and Anders Rasmuson [1]*

[1] *Department of Chemistry and Chemical Engineering, Chalmers University of Technology, Sweden*
[2] *Pharmaceutical Development, AstraZeneca R&D, Sweden*
[3] *Division of Thermofluids, Department of Mechanical Engineering, Imperial College London, United Kingdom*

Abstract

Fluidized bed coating has been used to coat pellets or tablets with functional substances for a number of purposes. In this coating process, particle wetting, drying and film formation are coupled to particle motion. It is therefore of interest to study particle motion in such fluidized beds and to use the results to develop a model for predicting the quality of the final product. In this paper, we present results from DEM-CFD simulations, i.e. discrete element method and computational fluid dynamics simulations of particle motion in a laboratory-scale Wurster fluidized bed that was also employed in positron emission particle tracking (PEPT) experiments. As the drag force is the dominant interaction between the gas flow and the particle motion in this type of fluidized bed, the effect of drag models on the particle motion is investigated. More specifically, the particle velocity and residence time distributions of particles in different regions calculated from five different drag models are presented. It is found that the Gidaspow and Tang drag models predict both particle cycle and residence times well. The HKL and Beetstra drag models somewhat overestimate the particle velocity in the Wurster tube and therefore predict a reduced number of recirculations and a significantly shorter cycle time.

Keywords: fluidized bed, particles, residence time distributions, drag, DEM, CFD

1. Introduction

The Wurster coating process (Wurster D.E., 1959), which takes place in a fluidized bed, has been utilized for pellet coating for several decades. In this process, particles are circulated in the fluidized bed and are coated in a spray zone for different functional needs (Teunou E. and Poncelet D., 2002; Ström D. et al., 2005). At the bottom of the fluidized bed, a fluidization air flow is supplied through a distributor plate. The distributor plate usually consists of a number of orifices that have been distributed so as to provide a specific flow distribution. An atomization air flow and a liquid solution in the form of droplets are introduced by one or more two-fluid nozzles at the bottom of the fluidized bed.

This type of fluidized bed can be divided into different regions (Christensen F.N. and Bertelsen P., 1997; Karlsson S. et al., 2009), as illustrated in **Fig. 1**. In an ideal coating cycle, a particle begins to receive coating in the spray zone, is then dried in the Wurster tube and the fountain region, and moves back towards the horizontal transport region through the downbed region. After travelling through these different regions, the particle is ready to begin the next coating cycle when it moves into the spray zone again. The sequence of coating and drying that occurs as the particles travel through these different regions is usually regarded as a particle coating cycle (Li L. et al., 2015a). It has been pointed out that the cycle time distribution (CTD) and the residence time distribution (RTD) in different regions are critical factors in determining the quality of the final product such as the film thickness and the film thickness variability (Cheng X.X. and Turton R., 2000; Shelukar S. et al., 2000; Li L. et al., 2015a). For example, the particles must spend sufficient time in the regions for drying before returning to the horizontal transport region; otherwise, the risk of agglomeration increases due to collisions between wet particles.

The CTD and RTD of particles in similar fluidized

† Received 14 May 2015; Accepted 24 June 2015
J-STAGE Advance published online 31 July 2015
1 SE-412 96 Gothenburg, Sweden
2 SE-414 83 Mölndal, Sweden
3 Exhibition Road, London SW7 2AZ, United Kingdom
* Corresponding author: Anders Rasmuson;
E-mail: rasmuson@chalmers.se
TEL: +46 31 772 2940 FAX: +46 31 81 46 20

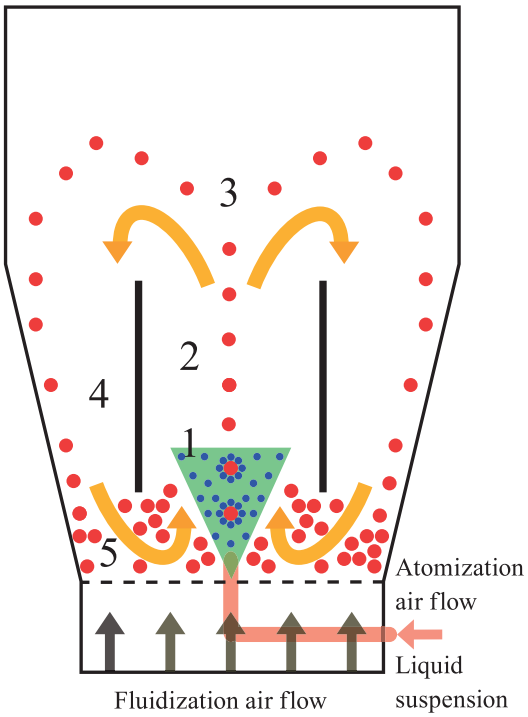

Fig. 1 A schematic of the Wurster process: (1) spray zone, (2) Wurster tube, (3) fountain region, (4) downbed region, and (5) horizontal transport region.

beds have been studied using both experimental (Mann V. and Crosby E., 1975; Shelukar S. et al., 2000; San José M.J. et al., 2013; Li L. et al., 2015a) and modeling (Fries L. et al., 2011; Yang S. et al., 2014; Li L. et al., 2015b) methods. It was found that particles spend most of the cycle time in the horizontal transport region and that different residence times in this region can cause a large variability in the cycle time, and therefore a large variability in the film thickness. Due to limitations of experimental techniques, it is difficult to measure how particles behave in detail in the spray zone. For example, in the positron emission particle tracking (PEPT) measurements (Parker D.J. et al., 1993), the γ-rays tend to be absorbed by the metal in the lower region of the fluidized bed, which results in poor data quality in the spray region (Li L. et al., 2015a). However, the particle behavior in the spray zone is important for coating. Thus advanced modeling methods, such as the discrete element method (DEM), in combination with computational fluid dynamics (CFD), offer an attractive way of addressing this kind of issue that cannot be handled experimentally.

The discrete element method was initially proposed for granular assemblies by Cundall P.A. and Strack O.D. (1979), and was introduced into particle flow in fluidized beds by Tsuji Y. et al. (1993). In this approach, every particle is modeled as an individual element and the gas phase is treated as a continuum. Particle-particle and particle-wall interactions can be accounted for in a straightforward fashion and it is also simple to include particles of different sizes. Owing to this benefit, a number of reviews and applications of this method have been presented in the literature (Kafui K.D. et al., 2002; Deen N.G. et al., 2007; Van der Hoef M.A. et al., 2008; Link J.M. et al., 2008; Zhu H.P. et al., 2008; Ketterhagen W.R. et al., 2009; Turton R., 2010; Darabi P. et al., 2011; Fries L. et al., 2013).

On the other hand, since every particle is modeled, the discrete element method is not practical for systems involving a considerable number of particles. For many particle coating processes in pharmaceutical development, the systems often have a batch size ranging from a few grams to a few hundred grams, which corresponds to from tens of thousands to a few million particles. Nowadays, simulating tens of thousands particles can be done at a reasonable computational cost, while modeling systems with a few million particles is challenging, though still feasible (Jajcevic D. et al., 2013). Hence, DEM-CFD modeling offers a great opportunity to assist process and product development.

In DEM-CFD simulations, particles and gas flow are coupled through an interphase momentum transfer term via a suitable drag model. It is well known that in fluidized beds, particles interact strongly with the gas flow, and consequently the drag model implemented affects the predicted particle motion, as well as the CTD and RTD. In the assessment of drag models by Du W. et al. (2006) based on the two-fluid model (TFM), the Gidaspow drag model (Gidaspow D., 1994) gave the best agreement with experimental observations in modeling of spouted beds. With the recent increase in computational power, it has become feasible to derive the drag model by fully solving the flow between particles (Kriebitzsch S.H.L. et al., 2013). New drag models have been proposed and developed in recent years based upon simulations using the Lattice-Boltzmann method (LBM) or immersed boundary method (IBM) (Hill R.J. et al., 2001a; 2001b; Van der Hoef M.A. et al., 2005; Benyahia S. et al., 2006; Beetstra R. et al., 2007; Tang Y. et al., 2015). In a combined experimental and simulation study, Link J.M. et al. (2005) evaluated the Gidaspow and Hill drag models and found that they could reproduce several important regimes in spout-fluid beds. At this moment, however, it is still unclear how the drag model affects the residence time distributions of particles in different regions of fluidized beds.

In the present study, the objective is to investigate the effect of drag models on the residence time distributions of particles in different regions of a Wurster fluidized bed. The CTD and RTD are obtained using DEM-CFD simulations with different drag models and are compared to recent PEPT experimental data (Li L. et al., 2015a). The performance of the selected drag models for fluidized bed coating applications is discussed.

2. Mathematical model

2.1 Equations of particle motion

For every particle, the particle motion is described using Newton's second law

$$m_i \frac{\mathrm{d}\vec{v}_i}{\mathrm{d}t} = \beta \frac{V_i}{\varepsilon_s}\left(\vec{u}_g - \vec{v}_i\right) + m_i\,\vec{g} - V_i \nabla P + \vec{F}_{c,i} \tag{1}$$

where m_i is the particle mass, $\vec{v}_i$ is the particle velocity, $\vec{u}_g$ is the gas velocity, $\vec{g}$ is the gravitational acceleration, V_i is the particle volume, ∇P is the gas pressure gradient, ε_s is the particle volume fraction, $\vec{F}_{c,i}$ is the contact force during particle-particle and particle-wall collisions and β is the interphase momentum transfer coefficient. It is noted that other forces such as a cohesion force (Thornton C. and Yin K.K., 1991) can be incorporated into Eqn. (1) in a straightforward manner.

The angular momentum of each particle is described using

$$I_i \frac{\mathrm{d}\vec{\omega}_i}{\mathrm{d}t} = \sum \vec{T}_i \tag{2}$$

where I_i is the moment of inertia of the particle, $\vec{\omega}_i$ is the rotational velocity and $\vec{T}_i$ is the total torque acting on the particle.

2.2 Equations of gas flow

As discussed by Li L. et al. (2015b), turbulence can be neglected in this study. Hence, the continuity and momentum equations are written as follows

$$\frac{\partial}{\partial t}\left(\varepsilon_g \rho_g\right) + \nabla \cdot \left(\varepsilon_g \rho_g \vec{u}_g\right) = 0 \tag{3}$$

$$\begin{aligned} &\frac{\partial}{\partial t}\left(\varepsilon_g \rho_g \vec{u}_g\right) + \nabla \cdot \left(\varepsilon_g \rho_g \vec{u}_g \vec{u}_g\right) = -\varepsilon_g \nabla P \\ &-\nabla \cdot \left(\varepsilon_g \rho_g \mu_g \left(\nabla \vec{u}_g + \left(\nabla \vec{u}_g\right)^T\right)\right) - \sum_{i=1}^{n} \beta\left(\vec{u}_g - \vec{v}_i\right) \end{aligned} \tag{4}$$

where $\varepsilon_g = 1 - \varepsilon_s$ is the gas volume fraction, ρ_g is the density of air and μ_g is the dynamic viscosity of air, respectively.

2.3 Soft sphere model

In accounting for interparticle forces, i.e. $\vec{F}_{c,i}$ (see Eqn. (1)), there are two common models available (Crowe C.T. et al., 2012), the hard sphere model and the soft sphere model. In the current study, the latter is selected since it is more appropriate for describing the behavior in a dense fluidized bed where particles can remain in contact for a long time. In this model, particle-particle collisions are described via a spring-dashpot system (Tsuji Y., 1993), as

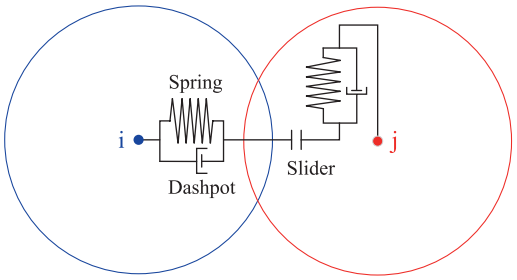

Fig. 2 A schematic of the soft sphere model.

sketched in **Fig. 2**. In the present work, the contact forces in the normal and tangential directions are calculated using the Hertz-Mindlin theory (Hertz H., 1882).

2.4 Drag models

In Eqn. (1), the interphase momentum transfer coefficient can be specified using different drag models. In this study, five drag models are examined: the Gidaspow, Min, HKL, Beetstra and Tang drag models. Their respective expressions are presented in **Table 1** and a brief summary is given below.

As mentioned in the introduction, Ergun S. (1952) obtained an expression for the average fluid particle force based on a classic study of pressure drop through packed beds. Wen C. and Yu Y. (1966) also conducted a series of fluidization experiments and presented their correlation. Later, Gidaspow D. (1994) suggested a model based on the Ergun equation for the dense regime and the Wen-Yu correlation for the dilute regime. The modification made by Gidaspow D. was found to be the best in modeling of spouted beds (Du W. et al., 2006) and has been widely used in engineering practice (Deen N.G. et al., 2007).

In other cases, the minimum value given by the Ergun equation and the Wen-Yu correlation is adopted (the Min drag model), for example, in the work of Link J.M. et al. (2005).

Using accurate numerical data from LBM simulations, Hill R.J. et al. (2001b) derived a new drag model for moderate Reynolds-number flows in ordered and random arrays of spheres. In this model, a dimensionless drag force, $F(\varepsilon_s, Re_p)$, is defined and solved via a force balance. That is, the total force exerted on a particle by the gas flow, $\vec{F}_{g\to s}$, is the sum of the drag force, $\vec{F}_d$, and the buoyancy-type force due to the gas pressure gradient, $\vec{F}_b$. Van der Hoef M.A. et al. (2005) pointed out that the drag force and the total force differ by a factor of ε_g, i.e. $\vec{F}_d = \varepsilon_g \vec{F}_{g\to s}$, and that the dimensionless drag force can be converted to the interphase momentum transfer coefficient in Eqn. (1) via the following expression:

$$\beta = \frac{18 \mu_g \varepsilon_s \varepsilon_g}{{d_p}^2} F\left(\varepsilon_s, Re_p\right) \tag{5}$$

Table 1 Drag models

Drag model	Expression
Gidaspow	$\beta_{\text{Gidaspow}} = \begin{cases} \beta_{\text{Ergun}} = \left(150\dfrac{\varepsilon_s^2}{\varepsilon_g} + 1.75\varepsilon_s Re_p\right)\dfrac{\mu_g}{d_p^2} & \varepsilon_s > 0.2 \\ \beta_{\text{Wen-Yu}} = \dfrac{3}{4} Re_p C_D \dfrac{\mu_g \varepsilon_s}{d_p^2}\varepsilon_g^{-2.65} & \varepsilon_s \le 0.2 \end{cases}$ $Re_p = \varepsilon_g \rho_g \lvert \vec{u}_g - \vec{v}_i \rvert \dfrac{d_p}{\mu_g}$ $C_D = \begin{cases} 24\left(\dfrac{1 + 0.15 Re_p^{0.687}}{Re_p}\right) & Re_p < 1000 \\ 0.44 & Re_p \ge 1000 \end{cases}$
Min	$\min\left(\beta_{\text{Ergun}}, \beta_{\text{Wen-Yu}}\right)$
HKL	$\beta_{\text{HKL}} = \dfrac{18\mu_g \varepsilon_g \varepsilon_g^2}{d_p^2} F\left(\varepsilon_s, Re_p\right)$ $F\left(\varepsilon_s, Re_p\right) = F_2 + 0.5 F_3 Re_p$ $F_2 = \begin{cases} \omega\left[10\dfrac{\varepsilon_s}{\varepsilon_g^3}\right] + (1-\omega)\left[\dfrac{1 + \dfrac{3}{\sqrt{2}}\sqrt{\varepsilon_s} + \dfrac{135}{64}\varepsilon_s \ln(\varepsilon_s) + 17.89\varepsilon_s}{1 + 0.681\varepsilon_s - 11.03\varepsilon_s^2 + 15.41\varepsilon_s^3}\right] & \varepsilon_s < 0.4 \\ 10\dfrac{\varepsilon_s}{\varepsilon_g^3} & \varepsilon_s \ge 0.4 \end{cases}$ $F_3 = \begin{cases} 0.9351\ \varepsilon_s + 0.03667 & \varepsilon_s < 0.0953 \\ 0.0673 + 0.212\ \varepsilon_s + 0.0232\ \varepsilon_g^{-5} & \varepsilon_s \ge 0.0953 \end{cases}$ $w = \exp\left(\dfrac{-10(0.4 - \varepsilon_s)}{\varepsilon_s}\right)$
Beetstra	$\beta_{\text{Beetstra}} = \dfrac{18\mu_g \varepsilon_s \varepsilon_g}{d_p^2} F\left(\varepsilon_s, Re_p\right)$ $F\left(\varepsilon_s, Re_p\right) = \dfrac{10\ \varepsilon_s}{\varepsilon_g^2} + \varepsilon_g^2\left(1 + 1.5\sqrt{\varepsilon_s}\right) + \dfrac{0.413 Re_p}{24\varepsilon_g^2}\left[\dfrac{\varepsilon_g^{-1} + 3\ \varepsilon_s\varepsilon_g + 8.4 Re_p^{-0.343}}{1 + 10^{3\ \varepsilon_s} Re_p^{-(1+4\varepsilon_s/2)}}\right]$
Tang	$\beta_{\text{Tang}} = \dfrac{18\mu_g \varepsilon_s \varepsilon_g}{d_p^2} F\left(\varepsilon_s, Re_p\right)$ $F\left(\varepsilon_s, Re_p\right) = \dfrac{10\ \varepsilon_s}{\varepsilon_g^2} + \varepsilon_g^2\left(1 + 1.5\sqrt{\varepsilon_s}\right) + \left[0.11\ \varepsilon_s(1 + \varepsilon_s) - \dfrac{0.00456}{\varepsilon_g^4} + \left(0.169\ \varepsilon_g + \dfrac{0.0644}{\varepsilon_g^4}\right) Re_p^{-0.343}\right] Re_p$

Later on, this drag model was extended by Benyahia S. et al. (2006) to cover a wider range of Reynolds numbers and particle volume fraction. The model proposed is complicated and in **Table 1**, a simplification suggested by Benyahia S. et al. (2006) is provided[1].

Beetstra R. et al. (2007) used the same method to derive a drag model where a more complex functional form was proposed instead of a linear scaling with *Re* to describe the inertial effects. Moreover, their extensive LBM simulations covered a wider range of parameters and were performed for Reynolds numbers up to 1000.

Quite recently, Tang Y. et al. (2015) proposed a new drag model based on simulation results obtained using fully resolved IBM simulations. In order to obtain highly accurate (essentially grid-independent) results, they resolved the flow past fixed assemblies of monodisperse spheres. It was stated that the grid resolution effects are consistently better resolved compared to the previous LBM simulations (Hill R.J. et al., 2001b; Beetstra R. et al., 2007).

For these different drag models, the interphase momentum transfer coefficient, β, is plotted in **Fig. 3** as a function of the particle volume fraction, ε_s. Since the characteristic slip velocity and the particle volume fraction are to a large extent different in different regions of the present fluidized bed, β is calculated for a slip velocity of 5 m/s and a particle volume fraction up to 0.2 for the dilute region, e.g. the Wurster tube. For the dense region, e.g. the horizontal transport region, β is calculated for a slip velocity of 1 m/s and a particle volume fraction ranging from 0.2 to 0.6. It can be seen that in the dilute region, β decreases in the following order: the HKL, Beetstra, Tang, Gidaspow and Min drag models. More specifically, β for $\varepsilon_s < 0.2$ due to the HKL and Beetstra drag models is nearly twice that for the other three. For the moderately dense region with $0.2 \le \varepsilon_s < 0.4$, there is only a slight difference in the interphase momentum transfer coefficient between the different drag models. For the very dense region with $\varepsilon_s \ge 0.4$, the Beetstra, Tang and HKL drag models give a significantly larger interphase momentum transfer coefficient than the Gidaspow and Min drag models.

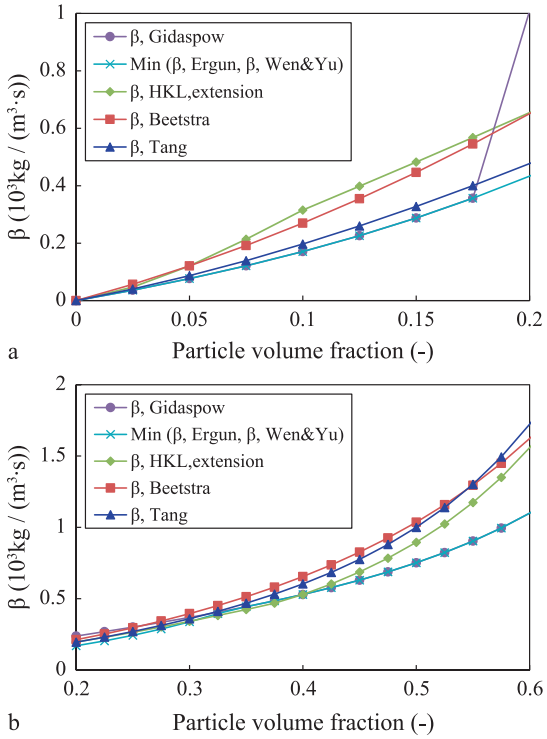

Fig. 3 Comparison of drag models, the relative velocity between gas flow and particles is (a) 5 m/s and (b) 1 m/s, respectively.

[1] It must be noted that this extension was developed following the original derivation by Hill R. J. et al, where the total force exerted on the particle was referred to as the drag force. Thus another factor of the gas volume fraction is required when converting the dimensionless drag force to the interphase momentum transfer coefficient using Eqn. (5).

3. Method

3.1 Experimental

Recent PEPT experimental data presented by Li L. et al. (2015a) are used in this study to evaluate different drag models by comparing the calculated particle velocity, cycle and residence time distributions with the measured values.

In the PEPT experiments, a tracer particle labeled with Fluorine-18 is incorporated into the fluidized bed. As the tracer particle moves around in the vessel, the radioisotope decays and releases back-to-back γ-rays. These γ-rays are detected via two large position-sensitive detectors located on both sides of the fluidized bed. Each pair of γ-rays can be used to calculate the location of the tracer particle by means of three-dimensional triangulation. More details about the technique and the algorithms for data processing can be found in the literature (Parker D.J. et al., 1993; 1997; 2002; Forster R. et al., 2000).

The fluidized bed used in the PEPT experiments was based on the STREA-1^{TM} laboratory fluidized bed from Aeromatic-Fielder. The fluidized bed is 380 mm high, with top and bottom diameters of 250 mm and 114 mm, respectively; detailed dimensions are provided elsewhere (Li L. et al., 2015a). A nozzle with a diameter of 5 mm was employed in order to avoid the numerical difficulties in simulating sonic or even supersonic flow while retaining the feature of high jet velocity due to the atomization air flow. The nozzle was only a big circular orifice and no liquid solution was introduced. The fluidization air flow was supplied through a bowl-shaped distributor, consist-

ing of a central base and an outer annular region. The central base of the distributor is fully open, while the outer annular region of the distributor has a number of orifices that correspond to approximately 4 % of the area of the outer annulus region. A wire mesh screen was put over the distributor to prevent particles from falling down below the distributor.

Microcrystalline cellulose (MCC) pellets, a common material in the pharmaceutical industry, were employed in the PEPT experiments. The particle size was measured using QICPIC Particle Size Analysis (Sympatec GmbH), and the particle density was determined using mercury intrusion porosimetry (Micromeritics AutoPore III 9410). The material parameters are given in **Table 2**; they were selected to match those of MCC. A photograph of a sample of the MCC pellets is provided in **Fig. 4**.

Table 2 The material parameters used in the numerical simulations (Roberts R. et al., 1994; Bharadwaj R. et al., 2010; Darelius A. et al., 2007; Li L. et al., 2015b)

Variable	Unit	Value
Air density	kg/m^3	1.204
Air viscosity	Pa·s	1.837×10^{-5}
Particle diameter	μm	1749
Particle density	kg/m^3	1420
Particle sphericity	—	0.85–0.95
Poisson's ratio of particles	—	0.30
Young's modulus	Pa	1.0×10^6
Particle-particle friction coefficient	—	0.53
Particle-particle restitution coefficient	—	0.83
Poisson's ratio of walls	—	0.33
Particle-wall friction coefficient	—	0.20
Particle-wall restitution coefficient	—	0.80
Fluid time step	s	5.0×10^{-5}
Particle time step	s	5.0×10^{-6}

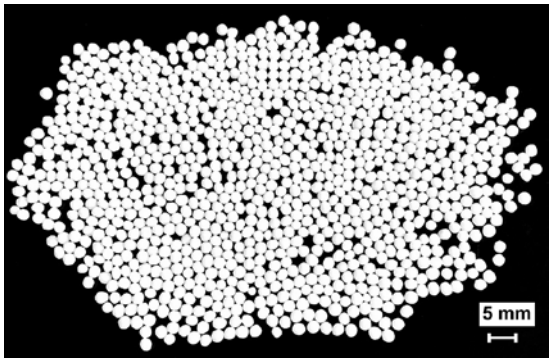

Fig. 4 A photograph of a sample of the MCC pellets.

The shape of particles may affect the drag force acting on the particles. In this case, the so-called sphericity factor can be used to account for the effect of the shape of particles (see, e.g. (Zastawny M. et al., 2012)). In order to evaluate the drag force more accurately, correlations are required according to, e.g. Crowe C.T. (2006), using the sphericity of particles provided in **Table 2**. In addition, the shape of particles may affect the porosity in the dense downbed region and therefore the air flow passing through this region. However, this is beyond the scope of the current study.

3.2 Numerical

3.2.1. General

A fully coupled multi-phase flow solver, MultiFlow (www.multiflow.org), was employed in this study to solve the equations of particle motion and gas flow. The fluid mesh, which is refined near the nozzle and in the Wurster tube, contains approximately 65000 hexahedral cells. Simulations of single-phase gas flow were performed to ensure grid independence.

In order to specify the boundary conditions in the DEM-CFD simulations, the flow rates of the atomization and fluidization air flow, as well as the flow distribution at the distributor are required. The global flow rates were measured using a rotameter in the PEPT experiments (Li L. et al., 2015a). However, it was not possible to measure the flow distribution in the experiments. Instead, a single-phase CFD model including the air supplying chamber, the distributor, the wire mesh screen, and the fluidized bed was developed in Ansys Fluent to determine the flow distribution at the distributor. The results (not shown) obtained using this single-phase CFD model show that the air flow passing through the central base of the distributor is between 53 % and 64 % of the total fluidization air flow. Since the particle velocity profile is an indication of the flow distribution, DEM-CFD simulations with different flow distributions at the distributor were performed to compare the particle velocity at different heights above the distributor with the corresponding experimental data. These additional simulations were used to verify that a flow distribution for which approximately 55 % of the fluidization flow enters normal to the boundary in the central base of the distributor and 45 % enters normal to the boundary in the outer annular region (Li L. et al., 2015b) gave adequate agreement with the experimental data.

The atomization nozzle is modeled as a flow normal to the inlet boundary, while the outlet of the domain is considered to be a pressure outlet. The walls of the fluidized bed and the Wurster tube are set to be no-slip for the gas flow.

In order to obtain a reasonable compromise between

data quality and computational cost, the CTD and RTD in different regions were evaluated for different simulation times. It was found that the CTD becomes fairly steady after a simulation time of 25 s. It was also found that a simulation time of 10 s was appropriate to determine the RTD in different regions, except in the horizontal transport region.

3.2.2. Simulation parameters

The numerical parameters and the operating conditions are presented in **Tables 2** and **3**, respectively. The partition gap is set to 15 mm and the Wurster tube length is 150 mm. The fluidization and atomization air flow rates are 73.3 m^3/h and 3.50 m^3/h, respectively. A base case with a batch size of 200 g was selected in this study to investigate the drag models. In addition to the base case, which uses the Gidaspow drag model (Run #1), DEM-CFD simulations with the same operating conditions are performed for the other drag models in Runs #2–5 and for larger batch sizes in Runs #6–9. A typical simulation was run in parallel using 32–40 CPU cores and took about 12 hours wall clock time per simulated second.

3.2.3. Post-processing

From the point of view of a typical coating cycle, we define the start of a particle coating cycle as the point when a particle enters the spray zone from the horizontal transport region or the lower region in the Wurster tube. The particle coating cycle then ends when the particle reappears in the spray zone after having subsequently traveled through the Wurster tube, the fountain, downbed, and horizontal transport regions. When one particle coating cycle ends, the next one begins. The particle cycle time is thus defined to be the time it takes for a particle to complete one cycle.

In the PEPT experiments, it was difficult to detect the tracer particle in the lower region of the fluidized bed. In the experiments, it was therefore not possible to identify a spray region and the particle cycle was defined so that it begins and ends in the Wurster tube. A spray zone is therefore not defined in the simulations either, and the particle cycle is defined in the same way as in the experiments.

It is noted that in the PEPT experiments, only one tracer particle was incorporated into each run and continuously followed for 1.5 hours. In the simulations, on the other hand, different particle trajectories are followed for 25 s. As a result, the cycle and residence time distributions were calculated from different cycles for the same tracer particle in the experiments, while they are obtained from many different particles in the DEM-CFD simulations. For the pseudo-steady particle dynamics in this fluidized bed, it is thus assumed that the information obtained (such as the particle velocity or the cycle time distribution) by following one particle for a long time is equivalent to the information obtained by following all particles for a short period of time (Li L. et al., 2015b).

Table 3 Set-up of simulations

Simulation #	Drag model	Batch size (g)
1	Gidaspow	200
2	Min	200
3	HKL	200
4	Beetstra	200
5	Tang	200
6	HKL	400
7	Tang	400
8	HKL	600
9	Tang	600

4. Results and discussion

In **Table 4**, the mean cycle time and mean residence times of particles in different regions are summarized for the batch size of 200 g; the corresponding experimental data is also provided. **Figs. 5** and **6** show the cycle time distributions and mean residence times of particles in different regions, respectively, including values both measured in the PEPT experiment and calculated from the DEM-CFD simulations for different drag models. For all selected drag models, the general feature of the particle residence times in different regions is captured. As can be seen in **Table 4**, the fraction of the cycle time that particles spend in different regions corresponds closely to PEPT measured values for the different drag models.

However, the cycle time and the residence time in the different regions, particularly in the Wurster tube and in the horizontal transport region, exhibit distinct differences for the different drag models. It can be seen that both the mean cycle time in **Table 4** and the CTD in **Fig. 5** calculated with the Gidaspow and Tang drag models agree quantitatively with the experimental data. For the Min drag model, there is a greater fraction of particles with a longer cycle time, which can be attributed to a somewhat slower acceleration in the Wurster tube and a longer residence time in the Wurster tube (see in **Table 4**). Interestingly, the CTDs predicted using the HKL and Beetstra drag models peak at a shorter cycle time and are narrower than the others. These two effects result in a much shorter mean cycle time for these two drag models.

In order to understand the cause of these differences, the vertical particle velocity at selected heights above the

Table 4 Summary of particle cycle and residence time distributions for the batch size of 200 g

	Cycle time (s)	Residence time in				Fraction of cycle time in			
		the Wurster tube (s)	the fountain region (s)	the downbed region (s)	the horizontal transport region (s)	the Wurster tube (–)	the fountain region (–)	the downbed region (–)	the horizontal transport region (–)
PEPT	8.5	1.33	0.27	0.30	6.61	0.19	0.05	0.04	0.72
Gidaspow	7.4	1.27	0.27	0.25	5.61	0.19	0.05	0.04	0.73
Min	7.7	1.50	0.27	0.30	5.68	0.21	0.04	0.04	0.71
HKL	3.6	0.46	0.30	0.14	2.72	0.14	0.09	0.04	0.72
Beetstra	4.9	0.73	0.28	0.25	3.67	0.16	0.07	0.05	0.71
Tang	7.1	1.27	0.27	0.22	5.36	0.19	0.05	0.04	0.73

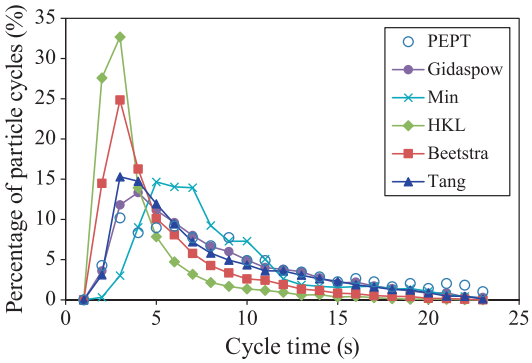

Fig. 5 The cycle time distribution of particle cycles shorter than 25 s for the base case.

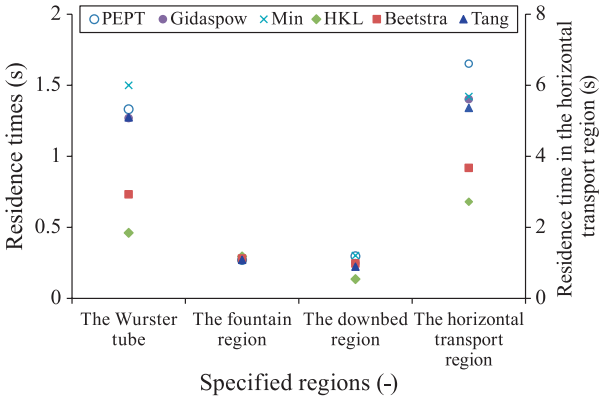

Fig. 6 The residence times of particles in different regions for the base case (the secondary y-axis is used for the residence time in the horizontal transport region due to the higher values).

bottom of the fluidized bed, i.e. 45 mm, 75 mm and 105 mm, is plotted in **Fig. 7**. At 45 mm, which is the lowest location where reliable PEPT data could be obtained, the particle velocity is close to the PEPT measured velocity in the Wurster tube for all drag models studied, while the HKL drag model shows better agreement with the PEPT data in the downbed region. At 75 mm, all the drag models give very similar results. At 105 mm, only the particle velocity in the Wurster tube is shown, and it can be seen that all the drag models overpredict the particle velocity to a great extent in a central region corresponding to a radial location smaller than approximately 5 mm. This latter difference is probably due to the fact that in the experiments, there is turbulence in this central region induced by the atomization air flow, while the simulations employ a laminar model to predict the air flow.

Nevertheless, since this central region contains only a few particles, it is not expected to affect the general particle motion in the fluidized bed and the predicted CTD and RTD. It can also be seen that the HKL and Beetstra drag models give a distinctly higher velocity than the other drag models in this central region. Outside of this central region, the particle velocity for all of these drag models shows better agreement with the PEPT measured velocity. But a larger overprediction of the particle velocity compared to the PEPT measurement—though smaller than that in the central region—can be found for the HKL drag model than for the other drag models. This is similar to the results presented by Link J.M. et al. (2005) for a pseudo-two-dimensional spout-fluid bed, where it was concluded that the HKL drag model has the best predictive capabilities.

Fig. 8 shows the particle volume fraction examined at two heights above the bottom of the fluidized bed, corresponding to the inlet (15 mm) and outlet (165 mm) of the Wurster tube, respectively. It can be seen that the particle volume fraction is lower for the HKL and Beetstra drag models at the inlet of the tube and vice versa at the outlet of the tube. Since the Beetstra, Tang and HKL drag models give a larger interphase momentum exchange coefficient in the dense downbed region (cf. **Fig. 3**), there is a larger pressure drop in the downbed region for these models. As a result of the larger pressure drop in the

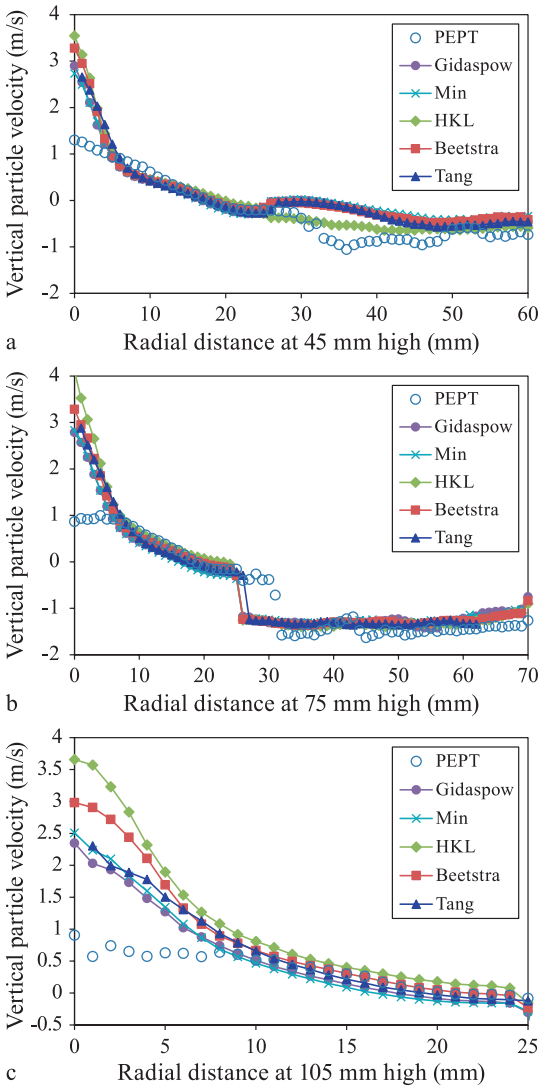

Fig. 7 The time-averaged vertical particle velocity at 45 mm, 75 mm and 105 mm, for the base case.

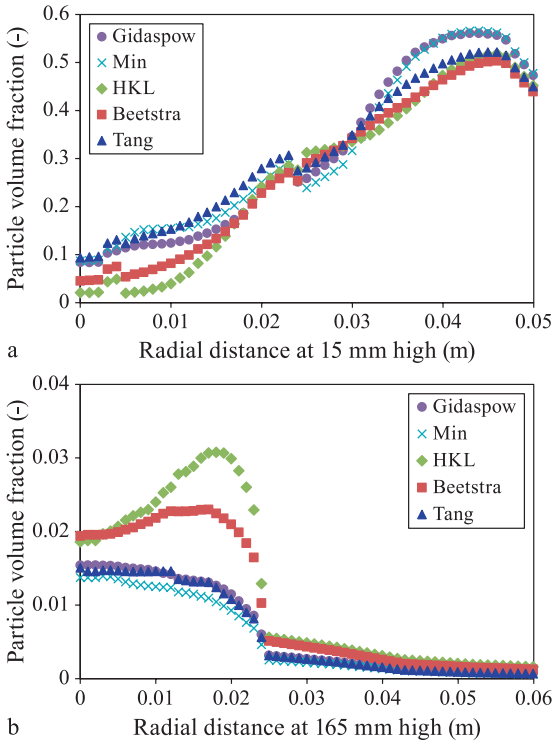

Fig. 8 The time-averaged particle volume fraction at 15 mm (the tube inlet) and 165 mm (the tube outlet) for the base case.

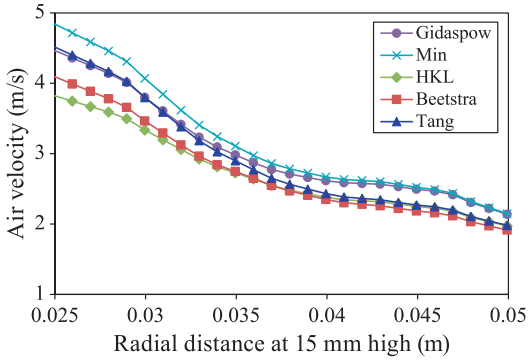

Fig. 9 The time-averaged air velocity in the downbed region at 15 mm (the tube inlet) for the base case.

downbed region, a certain amount of fluidization air flow is diverted from this region into the Wurster tube. This is supported by a lower air velocity at 15 mm in the downbed region for these models, as shown in **Fig. 9**. Since the particles are accelerated by the air flow through the Wurster tube, the particle volume fraction at the outlet of the tube decreases compared to that at the inlet for each drag model. For the HKL and Beetstra drag models, the larger interphase momentum exchange coefficient in the dilute Wurster tube (cf. **Fig. 3**) results in a higher particle velocity in the tube compared to other drag models. Correspondingly, a larger mass flow rate through the Wurster tube is expected and a higher particle volume fraction at the outlet of the tube is obtained for the HKL and Beetstra models than for the other drag models.

The higher particle volume fraction at the inlet of the Wurster tube for the Tang, Gidaspow and Min drag models can be attributed to a lower air flow rate in the Wurster tube and a lower interphase momentum transfer coefficient. The resulting slower acceleration of particles in the Wurster tube leads to particles having a greater risk of recirculating in the Wurster tube and moving back towards the horizontal transport region from the lower edge of the Wurster tube. This type of behavior was also observed in the PEPT experiments (Li L. et al., 2015a) and is sketched in **Fig. 10**. Thus, it is of interest to examine the number of particle recirculations in the Wurster tube, as shown in **Fig. 11**. It is significant in **Fig. 11** that for the HKL and Beetstra drag models, the fraction of ideal cycles, i.e. the fraction of particle cycles without any recirculation, is approximately 63 % and 43 %, which is much higher than

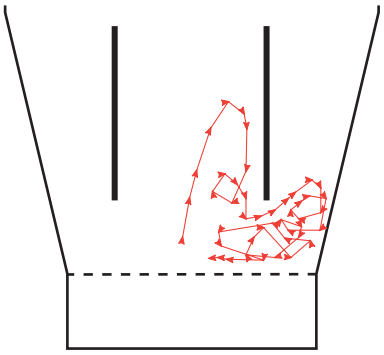

Fig. 10 An illustration showing particle recirculation. The particle moves back towards the horizontal transport region from the lower edge of the Wurster tube.

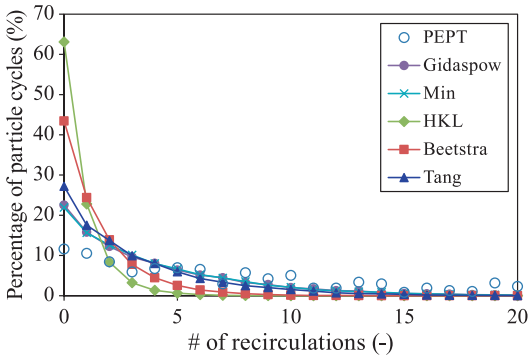

Fig. 11 The fraction distribution of particle recirculations in the Wurster tube for the base case.

the PEPT measured value of 12 %. The reduced number of particle recirculations for the HKL and Beetstra drag models can thus decrease the residence time in the Wurster tube and prevent a very long residence time in the horizontal transport region. This again emphasizes how important the detailed particle motion in the Wurster tube is to the operation of this type of fluidized bed.

In order to explore a scenario where the dense region is likely to have a greater effect, simulations of larger batch sizes of 400 g and 600 g were performed for the HKL and Tang drag models. The results obtained for the mean particle cycle times are presented in **Fig. 12** for different batch sizes. In agreement with the recent PEPT experiments, all selected drag models predict a shorter cycle time for a larger batch size. Notably, the Tang drag model shows the closest agreement for the increased batch size of 400 g. The results also indicate that, as the batch size increases, the deviation from the experiments is reduced for the HKL drag model, since the effect due to particle recirculations in the Wurster tube is reduced.

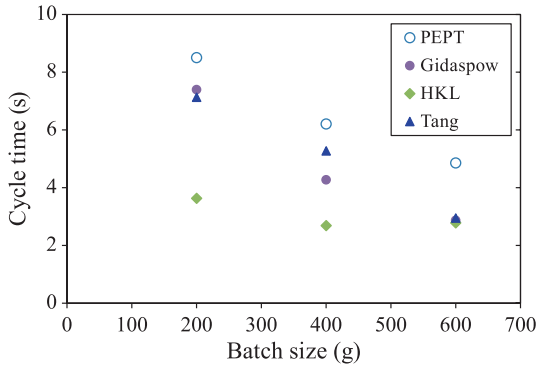

Fig. 12 The mean particle cycle times for different batch sizes.

5. Conclusions

In this study, DEM-CFD simulations of particle motion in a Wurster fluidized bed have been performed in order to study the effect of drag models on particle cycle and residence times. A comparison between the calculated particle cycle and residence time distributions from the simulations and recent PEPT experimental data was made. It was found that the Gidaspow, Min and Tang drag models predict the particle cycle time, the CTD and the RTDs qualitatively and quantitatively. The Tang drag model also demonstrates better agreement with experimental data for a larger batch size. The HKL and Beetstra drag models slightly overestimate the particle velocity in the Wurster tube. This overestimation of the particle velocity in the Wurster tube results in a much smaller number of recirculations, and therefore a much shorter residence time in the horizontal transport region and a much shorter cycle time. For the larger batch sizes, where the effect of particle recirculations is less pronounced and the dense region becomes more dominant, the agreement between the experimental data and the predictions of the HKL drag model improves. The present results thus suggest that the drag model must be selected carefully for the purpose of studying residence time distributions and, hence, coating processes in fluidized beds.

Acknowledgements

This work was undertaken within the EU seventh framework program, the PowTech Marie Curie Initial Training Network (Project no. EU FP7-PEOPLE-2010-ITN-264722). Dr. Andy Ingram at the University of Birmingham is gratefully acknowledged for his contribution to the PEPT experiments. The authors would also like to thank the high-performance computing (HPC) team at AstraZeneca R&D for their kind support during computations.

Nomenclature

DEM	Discrete Element Method
CFD	Computational Fluid Dynamics
TFM	Two Fluid Model
PEPT	Positron Emission Particle Tracking
CTD	Cycle Time Distribution
RTD	Residence Time Distribution
LBM	Lattice Boltzmann Method
IBM	Immersed Boundary Method
C_D	drag coefficient (–)
d_p	particle diameter (m)
$\vec{F}_{c,i}$	contact force (N)
$\vec{g}$	gravity vector (m/s^2)
m_i	particle mass (kg)
I_i	moment of inertia (kg·m^2)
P	pressure (N/m^2)
Re_p	particle Reynolds number (–)
$\vec{T}_i$	torque (N·m)
t	time (s)
$\vec{u}_g$	gas velocity (m/s)
$\vec{v}_i$	particle velocity (m/s)
V_i	particle volume (m^3)
$\vec{\omega}_i$	rotational velocity of the particle (rad/s)
ε_g	gas volume fraction (–)
ε_s	particle volume fraction (–)
β	interphase momentum transfer coefficient (kg/(m^3·s))
μ_g	dynamic viscosity (Pa·s)
ρ_g	air density (kg/m^3)

References

Beetstra R., van der Hoef M.A., Kuipers J.A.M., Drag force of intermediate Reynolds number flow past mono- and bidisperse arrays of spheres, AIChE Journal, 53 (2007) 489–501.

Benyahia S., Syamlal M., O'brien T.J., Extension of Hill–Koch–Ladd drag correlation over all ranges of Reynolds number and solids volume fraction, Powder Technology, 162 (2006) 166–174.

Bharadwaj R., Smith C., Hancock B.C., The coefficient of restitution of some pharmaceutical tablets/compacts, International journal of pharmaceutics, 402 (2010) 50–56.

Cheng X.X., Turton R., The prediction of variability occurring in fluidized bed coating equipment. I. The measurement of particle circulation rates in a bottom-spray fluidized bed coater, Pharmaceutical Development and Technology, 5 (2000) 311–322.

Christensen F.N., Bertelsen P., Qualitative description of the Wurster-based fluid-bed coating process, Drug Development and Industrial Pharmacy, 23 (1997) 451–463.

Crowe C.T., Multiphase flow handbook, CRC, Boca Raton, FL, 2006.

Crowe C.T., Schwarzkopf J.D., Sommerfeld M., Tsuji Y., Multiphase Flows with Droplets and Particles, Second Edition, CRC Press Inc, GB, 2012.

Cundall P.A., Strack O.D., A discrete numerical model for granular assemblies, Geotechnique, 29 (1979) 47–65.

Darabi P., Pougatch K., Salcudean M., Grecov D., DEM investigations of fluidized beds in the presence of liquid coating, Powder Technology, 214 (2011) 365–374.

Darelius A., Lennartsson E., Rasmuson A., Niklasson Björn I., Folestad S., Measurement of the velocity field and frictional properties of wet masses in a high shear mixer, Chemical Engineering Science, 62 (2007) 2366–2374.

Deen N.G., Annaland M.V., van der Hoef M.A., Kuipers J.A.M., Review of discrete particle modeling of fluidized beds, Chemical Engineering Science, 62 (2007) 28–44.

Du W., Bao X., Xu J., Wei W., Computational fluid dynamics (CFD) modeling of spouted bed: Assessment of drag coefficient correlations, Chemical Engineering Science, 61 (2006) 1401–1420.

Ergun S., Fluid flow through packed columns, Chemical Engineering Progress, 48 (1952) 89–94.

Forster R., Seville J., Parker D., Ding Y., Tracking Single Particles in Process Equipment or Probing Processes Using Positrons, KONA Powder and Particle Journal, 18 (2000) 139–148.

Fries L., Antonyuk S., Heinrich S., Dopfer D., Palzer S., Collision dynamics in fluidised bed granulators: A DEM-CFD study, Chemical Engineering Science, 86 (2013) 108–123.

Fries L., Antonyuk S., Heinrich S., Palzer S., DEM–CFD modeling of a fluidized bed spray granulator, Chemical Engineering Science, 66 (2011) 2340–2355.

Gidaspow D., Multiphase flow and fluidization: continuum and kinetic theory description, Academic, Boston, 1994.

Hertz H., Ueber die Berührung fester elastischer Körper, Journal für die reine und angewandte Mathematik, 92 (1882) 156–171.

Hill R.J., Koch D.L., Ladd A.J.C., The first effects of fluid inertia on flows in ordered and random arrays of spheres, Journal of Fluid Mechanics, 448 (2001a) 213–241.

Hill R.J., Koch D.L., Ladd A.J.C., Moderate-Reynolds-number flows in ordered and random arrays of spheres, Journal of Fluid Mechanics, 448 (2001b) 243–278.

Jajcevic D., Siegmann E., Radeke C., Khinast J.G., Large-scale CFD–DEM simulations of fluidized granular systems, Chemical Engineering Science, 98 (2013) 298–310.

Kafui K.D., Thornton C., Adams M.J., Discrete particle-continuum fluid modelling of gas–solid fluidised beds, Chemical Engineering Science, 57 (2002) 2395–2410.

Karlsson S., Rasmuson A., van Wachem B., Björn I.N., CFD modeling of the Wurster bed coater, AIChE Journal, 55 (2009) 2578–2590.

Ketterhagen W.R., Am Ende M.T., Hancock B.C., Process modeling in the pharmaceutical industry using the discrete element method, Journal of Pharmaceutical Sciences, 98

(2009) 442–470.

Kriebitzsch S.H.L., van der Hoef M.A., Kuipers J.A.M., Drag force in discrete particle models—Continuum scale or single particle scale?, AIChE Journal, 59 (2013) 316–324.

Li L., Rasmuson A., Ingram A., Johansson M., Remmelgas J., Von Corswant C., Folestad S., PEPT study of particle cycle and residence time distributions in a Wurster fluid bed, AIChE Journal, 61 (2015a) 756–768.

Li, L., Remmelgas, J., van Wachem, B.G.M., von Corswant, C., Johansson, M., Folestad, S., Rasmuson, A., Residence time distributions of different size particles in the spray zone of a Wurster fluid bed studied using DEM-CFD, Powder Technology, 280 (2015b) 124–134.

Link J.M., Cuypers L.A., Deen N.G., Kuipers J.A.M., Flow regimes in a spout–fluid bed: A combined experimental and simulation study, Chemical Engineering Science, 60 (2005) 3425–3442.

Link J.M., Deen N.G., Kuipers J.A.M., Fan X., Ingram A., Parker D.J., Wood J., Seville J.P.K., PEPT and discrete particle simulation study of spout-fluid bed regimes, AIChE Journal, 54 (2008) 1189–1202.

Mann V., Crosby E., Cycle time distribution measurements in spouted beds, Canadian Journal of Chemical Engineering, 53 (1975) 579–581.

Parker D.J., Allen D.A., Benton D.M., Fowles P., Mcneil P.A., Tan M., Beynon T.D., Developments in particle tracking using the Birmingham Positron Camera, Nuclear Instruments and Methods in Physics Research Section A: Accelerators, Spectrometers, Detectors and Associated Equipment, 392 (1997) 421–426.

Parker D.J., Broadbent C.J., Fowles P., Hawkesworth M.R., Mcneil P., Positron emission particle tracking—a technique for studying flow within engineering equipment, Nuclear Instruments and Methods in Physics Research Section A: Accelerators, Spectrometers, Detectors and Associated Equipment, 326 (1993) 592–607.

Parker D.J., Forster R.N., Fowles P., Takhar P.S., Positron emission particle tracking using the new Birmingham positron camera, Nuclear Instruments and Methods in Physics Research Section A: Accelerators, Spectrometers, Detectors and Associated Equipment, 477 (2002) 540–545.

Roberts R., Rowe R., York P., The Poisson's ratio of microcrystalline cellulose, International journal of pharmaceutics, 105 (1994) 177–180.

San José M.J., Alvarez S., Peñas F.J., García I., Cycle time in draft tube conical spouted bed dryer for sludge from paper industry, Chemical Engineering Science, 100 (2013) 413–420.

Shelukar S., Ho J., Zega J., Roland E., Yeh N., Quiram D., Nole A., Katdare A., Reynolds S., Identification and characterization of factors controlling tablet coating uniformity in a Wurster coating process, Powder Technology, 110 (2000) 29–36.

Ström D., Karlsson S., Folestad S., Niklasson Björn I., Laurell T., Nilsson J., Rasmuson A., A new device for coating single particles under controlled conditions, Chemical Engineering Science, 60 (2005) 4647–4653.

Tang Y., Peters E.A.J.F., Kuipers J.A.M., Kriebitzsch S.H.L., van der Hoef M.A., A new drag correlation from fully resolved simulations of flow past monodisperse static arrays of spheres, AIChE Journal, 61 (2015) 688–698.

Teunou E., Poncelet D., Batch and continuous fluid bed coating—review and state of the art, Journal of Food Engineering, 53 (2002) 325–340.

Thornton C., Yin K.K., Impact of elastic spheres with and without adhesion, Powder Technology, 65 (1991) 153–166.

Tsuji Y., Discrete particle simulation of gas-solid flows (From dilute to dense flows), KONA Powder and Particle Journal, 11 (1993) 57–68.

Tsuji Y., Kawaguchi T., Tanaka T., Discrete particle simulation of two-dimensional fluidized bed, Powder Technology, 77 (1993) 79–87.

Turton R., The application of modeling techniques to film-coating processes, Drug Development and Industrial Pharmacy, 36 (2010) 143–151.

Van der Hoef M.A., Beetstra R., Kuipers J.A.M., Lattice-Boltzmann simulations of low-Reynolds-number flow past mono- and bidisperse arrays of spheres: results for the permeability and drag force, Journal of Fluid Mechanics, 528 (2005) 233–254.

Van der Hoef M.A., van Sint Annaland M., Deen N.G., Kuipers J.A.M., Numerical simulation of dense gas-solid fluidized beds: A multiscale modeling strategy, 40 (2008) 47–70.

Wen C., Yu Y., Mechanics of Fluidization, Fluidization, Chemical Engineering Progress Symposium Series 62, (1966) 100–111.

Wurster D.E., Air-suspension technique of coating drug particles. A preliminary report, Journal of the American Pharmaceutical Association, 48 (1959) 451–454.

Yang S., Luo K., Fan J., Cen K., Particle-scale investigation of the solid dispersion and residence properties in a 3-D spout-fluid bed, AIChE Journal, 60 (2014) 2788–2804.

Zastawny M., Mallouppas G., Zhao F., van Wachem B., Derivation of drag and lift force and torque coefficients for non-spherical particles in flows, International Journal of Multiphase Flow, 39 (2012) 227–239.

Zhu H.P., Zhou Z.Y., Yang R.Y., Yu A.B., Discrete particle simulation of particulate systems: A review of major applications and findings, Chemical Engineering Science, 63 (2008) 5728–5770.

Author's short biography

Liang Li

Liang Li obtained a B.Eng. from Sichuan University and a M.Sc. in fluid mechanics from Chongqing University, China. Since Sept. 2011, he has received a Marie Curie fellowship within EU 7th framework program and has worked as a Ph.D. candidate, under the supervision of Professor Anders Rasmuson, in chemical engineering at the Chalmers University of Technology, Sweden. His current research is focused on developing an advanced modeling tool for fluidized bed coating. In order to understand the link between process conditions and film formation at the level of a single pellet, the discrete element method (DEM), together with computational fluid dynamics (CFD), is selected.

Johan Remmelgas

Johan Remmelgas is an associate principal scientist in pharmaceutical development at AstraZeneca R&D, Mölndal, Sweden. He is currently working on developing and applying mechanistic models to predict product and process performance. He holds degrees in chemical engineering from Stanford University and the University of California, Santa Barbara, where he worked on developing and evaluating constitutive equations for polymer solutions. Before joining AstraZeneca, Johan worked on the development of heavy-duty diesel engines at Volvo Powertrain, Gothenburg, Sweden. He is the author or co-author of patents for applications ranging from diesel engines to inhalation devices.

Berend van Wachem

Berend van Wachem is a professor of fluid mechanics at the Department of Mechanical Engineering of the Imperial College London. He has been active in developing, employing and validating advanced computational and modelling methods to predict the behaviour of complex flows. The ultimate aim of his research is understanding the underlying physics at the various length and time scales involved. He has presented comprehensive reviews on computational techniques for the modelling of multiphase flows, including droplets, interfaces and particles in fluids. He is co-editor and co-author of two handbooks on multiphase flow computations. He has also written highly cited papers on gas-liquid interface modelling. He is also the author of computational codes, such as www.multiflow.org.

Christian von Corswant

Dr. Christian von Corswant studied to be a chemical engineer at the Chalmers University of Technology and wrote his thesis at the Lund University of Technology. The title of the thesis is "Lecithin-based microemulsions for pharmaceutical use". He has worked at AstraZeneca R&D for more than 20 years in different positions within the pharmaceutical development unit and since 2008, has a specialist role as principal scientist for advanced drug delivery systems with a special focus on orally controlled release formulations. Christian has authored/co-authored about 20 publications to date.

Author's short biography

Staffan Folestad

Dr Staffan Folestad is a senior principal scientist in AstraZeneca with global responsibilities in manufacturing sciences and pharmaceutical innovation. On a part-time basis, he was adjunct prof at Uppsala University (from 1999), and is currently affiliated to the Chalmers University of Technology. His research focus is in advanced in-situ process sensors and in-silico process modeling for powder processes. He is the author of > 85 scientific papers, 5 book chapters, and > 20 patents and is a member of the Royal Swedish Academy of Engineering Sciences, on the board of the Chalmers Center for Chemical Process Engineering, and initiator of the pan-European science conference series EuPAT. He received the "New Safe Medicines Faster Award 2007" from the European Federation of Pharmaceutical Sciences.

Mats O. Johansson

Mats Johansson is a senior scientist in the pharmaceutical development unit at AstraZeneca R&D, Mölndal, Sweden. Mats has a background in chemical engineering. Mats has played a major role in establishing fluidized bed technology for orally controlled release products at AstraZeneca over the past decades. He is currently leading a network on developing and further optimizing fluidized bed equipment and processes for modified release coatings for high-performance pharmaceutical products. He is the author or co-author of several patents for pharmaceutical applications.

Anders Rasmuson

Anders Rasmuson has been a professor in chemical engineering at the Chalmers University of Technology in Gothenburg since 1990. He has published approximately 150 papers in international scientific journals with nearly 2000 citations in the areas of particulate processes, multi-phase flows and transport phenomena, mixing and separation processes. He is a member of the Royal Swedish Academy of Engineering Sciences, a member of the EFCE working party of mixing, and a member of the board of the Chalmers Centre of Chemical Process Engineering. He has recently participated in the EU Marie Curie project POWTECH as an examiner/supervisor for three PhD candidates.

KONA Powder and Particle Journal No. 33 (2016) 278–286/Doi:10.14356/kona.2016009 Original Research Paper

Reduction Kinetics of Zinc Powder from Brass Converter Slag by Pyrometallurgical Method Using Hydrogen Gas †

Tae-Hyuk Lee [1], Sin-Hyeong Joo [1], Hayk H. Nersisyan [1,2], Man-Sik Kong [3], Jae-Woo Lee [4], Ki-Won Park [4] and Jong-Hyeon Lee [1,2]*

[1] *Department of Materials Science & Engineering, Chungnam National University, Republic of Korea*
[2] *Rapidly solidified Materials Research Center, Republic of Korea*
[3] *Advanced Materials & Processing Center, Institute for Advanced Engineering, Republic of Korea*
[4] *Seowon Co., LTD, Republic of Korea*

Abstract

A pyrometallurgical reduction process for the recovery of copper and zinc from brass secondary slag (BSS) was studied. Specifically, the effect of reduction temperature and time on the conversion to metallic phases was investigated. The brass secondary slag was characterized by X-ray diffraction, inductively coupled plasma-atomic emission spectrometry, automatic elemental analysis, thermogravimetric analysis, and field emission scanning electron microscopy. A two-step reduction of BSS was identified. The step 1 comprised the reduction of ZnO, while the step 2 featured the reduction of $ZnO{\cdot}Al_2O_3$. Furthermore, the application of a first-order reaction model with Arrhenius analysis, indicated a conversion of ZnO to Zn(g) that had a rate constant increasing from $1.4 \pm 0.13 \times 10^{-3}$ s^{-1} at 900 °C to $2.18 \pm 0.15 \times 10^{-2}$ s^{-1} at 1050 °C. This reaction had an activation energy of 233.2 ± 26.1 kJ/mol. Secondly, the conversion of $ZnO{\cdot}Al_2O_3$ to Zn(g) and Al_2O_3 increased from $1.54 \pm 0.21 \times 10^{-5}$ s^{-1} at 900 °C to $1.09 \pm 0.19 \times 10^{-3}$ s^{-1} at 1050 °C, and the activation energy was 376.7 ± 22.4 kJ/mol. This reaction mechanism and its associated kinetic data can be applied to optimize the operation conditions of recycling processes for Cu-containing wastes.

Keywords: pyrometallurgy, copper converter slag, kinetic analysis, zinc powder

1. Introduction

Copper and zinc are important base metals required for various applications in metallurgical and chemical industries. The annual global output of copper and alloy products represents around 16.1 million tons, of which about 15.3 million tons (75–80 %) originate from refined copper, while about 4.2 million tons (20–25 %) are derived from direct melt scrap (Moskalyk P.R. and Alfantazi A.M., 2003).

However, the increasing worldwide demand for zinc and copper has necessitated intensive studies into the recovery and extraction of these metals from different sources (Rudnik E. et al., 2009). Some of these metals are recovered from different secondary slags, e.g., brass dross, brass ash, and flue dusts in electric furnaces. These brass secondary slags (BSS) are by-products obtained during brass scrap smelting and crushing of brass slag. It has been estimated that for every tons of copper production about 2.2 tons of slag are generated, so that 24.6 million tons of slag result from world copper production every year (Gorai B. et al., 2003).

BSS usually contains Cu, Zn, and other minor elements such as Pb, Fe, Ni, Si, and Sb (Jha M.K. et al., 2001). However, these slags contain different level of impurities depending on source. Recovery and extraction of these metals is necessary and important from both economic and environmental viewpoints.

In industries, various methods are used to extract metals from BSS. One of these, the hydrometallurgical process, is used to recover and recycle metals from BSS using different leaching agents, including sulfuric acid (Anand S. et al., 1983), hydrochloric acid (Sharma K.D. and Row B.R.L., 1985), cyanide (Anand S. et al., 1980) acetic acid (Altundogan H.S. and Tumen F., 1997), and ammonia (Sukla L.B. et al., 1986). However, the use of leaching agents is harmful to the human body and can cause environmental pollution.

† Received 27 May 2015 Accepted 14 July 2015
J-STAGE Advance published online 5 August 2015
[1,2] 99 Daehak-ro, Yuseong-gu, Daejeon, Republic of Korea
[3] 51 Goan-ro, Baekam-myeon, Cheoan-gu, Yongin, Republic of Korea
[4] 6B-15 Banwol Ind. #402-1 Moknae-dong, Danwon-gu, Ansan, Kyunggi-do, Republic of Korea
* Corresponding author: Jong-Hyeon Lee;
E-mail: jonglee@cnu.ac.kr
TEL: +82-42-821-6596 FAX: +82-42-822-5850

These drawbacks can be overcome using pyro-metallurgical smelting to recover Cu and Zn from BSS. The top submerged lance (TSL) process is a typical pyro-metallurgy method that was commercialized and researched to improve recovery efficiency. The TSL process provides highly efficient mixing and a heat source for reaction, due to combustion of the fuel and oxygen-mixed gas with the BSS. Moreover, TSL process can easily remove the impurities that are generated through the formation of slag in the upper furnace (Bakker M.L. et al., 2011).

However, it is difficult to directly feed certain raw materials that are fine dusts to a TSL furnace because of dust-scattering during the injection step. To solve this problem, the density of the BSS can be increased during the reduction process using a fluidized bed reactor. This is done in a stage prior to the TSL furnace, and can be effective for increasing process throughput. The reduction rate and reaction mechanism of BSS are very complex to determine because such slags can contain mixtures of copper, zinc, and various elements. Therefore, further research into the thermodynamics and reaction kinetics of BSS recovery processes is necessary to optimize process conditions in fluidized bed reactors.

The aim of this work is to determine the activation energy and reaction mechanism of BSS reduction by applying a pyro-metallurgical method using different reduction gas. Firstly, different parameters affecting the reduction ratio, such as reduction temperature and reduction time, were investigated. Then, based on the results of the reduction, the activation energy and reaction mechanism of BSS were determined using the Arrhenius equation (Igor I. K., 2008).

2. Experimental

The BSS that was used in this experimental was taken from the brass smelter of SEOWON CO. LTD in South Korea. The BSS sample was analyzed by inductively coupled plasma-atomic emission spectrometry (ICP-AES, ARL 3410, Switzerland) and X-ray diffraction (XRD, Siemens D-5000, Germany). The carbon concentration of the BSS sample was determined by an automatic elemental analyzer (AEA, Flash EA 1112 series, Thermo Fisher Scientific, U.S.A.). The extent of reduction of the BSS sample was estimated by a simultaneous thermogravimetric analyzer (TGA, TA SDT model 2060, TA Instruments, U.S.A.), under a flow of 5 % H_2 + 95 % N_2, at a flow rate 100 cm^3/min. The sample was heated to 850 °C at a heating rate of 5 °C/min.

The reduction of the BSS sample was carried out under a hydrogen atmosphere in a horizontal alumina tube furnace. The hydrogen flow rate was fixed at 100 cm^3/min in all experiments. The respective effects of reduction temperature and time on the reaction rates of the brass secondary slags were investigated. Specifically, the reduction temperature was varied from 900 to 1050 °C, and the reduction time was varied from 10 to 480 min. Each sample of BSS, weighing 15 g, was placed in an alumina crucible and then put in the tube furnace. Then, the samples were heated to the desired reduction temperature at a heating rate of 5 °C/min. Finally, the samples were cooled in the furnace.

After reduction, phase analysis of the reduction products was performed by X-ray diffraction, using Cu *Kα* radiation (40 kV, 30 mA) at step size increments of 0.1°. The microstructures of the reduction samples were observed using a field emission scanning electron microscopy (FE-SEM, JSM 6330F, Jeol, Japan). The respective chemical compositions of copper and zinc were analyzed using energy-dispersive X-ray spectroscopy (EDS, INCA, Oxford, U.K.).

3. Results and discussion

3.1 Characteristic of BSS

The chemical composition of the BSS sample used in this study is presented in **Table 1**, as determined by ICP-AES and AEA. ZnO and CuO were identified by X-ray diffraction analysis as major components in the BSS, whereas Zn-spinel ($ZnO{\cdot}Al_2O_3$) and Al_2SiO_4 were detected as a minor component, as shown in **Fig. 1**. **Fig. 2a** shows all the morphological features of the initial BSS sample. The latter consisted mainly of well-distinguishable, submicron-sized ZnO particles (**Fig. 2b**). The BSS samples were also leached with HNO_3 + HCl (3M: 1M) to measure the other impurities. Bright particles indicate aluminum and silicon compounds, whereas other particles indicate silicon dioxide (**Figs. 2c, d**).

The thermogravimetric curve of the reduction process, which was recorded during a linear program at a constant heating rate, is shown in **Fig. 3**. As shown in **Fig. 3**, the TGA curve of the initial sample reveals two major weight losses: one has a monotonous weight decrease of 1.3 % in the range of 50–760 °C, and the other is very rapid and occurs at 760 °C with approximately 1.4 % weight loss. The first weight loss is possibly related to the combustion of impurities, evaporation of water, and a chemical reaction between carbon in the BSS sample (2.2 mass% in

Table 1 Chemical composition of the initial brass secondary slags (mass%)

Cu	Zn	Si	Al	Pb	Fe	Mn	C	Other
14.74	70.54	3.92	5.7	1.01	0.74	0.32	2.2	0.83

Table 1) and hydrogen gas. The other weight loss (1.4 %) is due to the reduction of zinc oxide in the BSS sample to zinc gas phase, by hydrogen gas (Gioia F. et al., 1977).

3.2 Reduction mechanism of BSS

Fig. 4 shows the XRD patterns of BSS samples prior to and after reduction at various temperatures (900–1050 °C) for varying reaction times (10–480 min). Generally, XRD patterns for reductions at the four temperatures are similar, with the exception of time-scale, indicating that the same reduction mechanism prevails in the range of 900–1050 °C. These results suggest a stepwise reduction mechanism of BSS with hydrogen gas. Thus, based on these XRD results, a two-step reaction was identified. The main reactions at each step are as follows: Step 1 is the ZnO reduction (Eqn. 1), and step 2 is the $ZnO{\cdot}Al_2O_3$ reduction (Eqn.2).

$$ZnO(s) + H_2(g) \rightarrow Zn(g) + H_2O(g) \quad (1)$$

$$ZnO{\cdot}Al_2O_3(s) + H_2(g) \rightarrow Zn(g) + Al_2O_3(s) + H_2O(g) \quad (2)$$

The morphology changes in the BSS samples versus the reduction times at 1050 °C are shown in **Fig. 5**. It is seen that the initial fine ZnO powder is aggregated at the

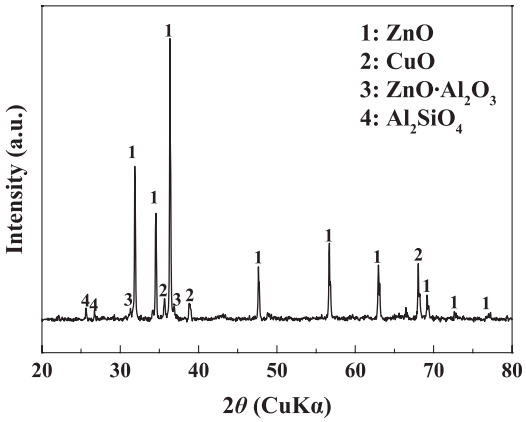

Fig. 1 X-ray diffraction pattern of initial BSS sample.

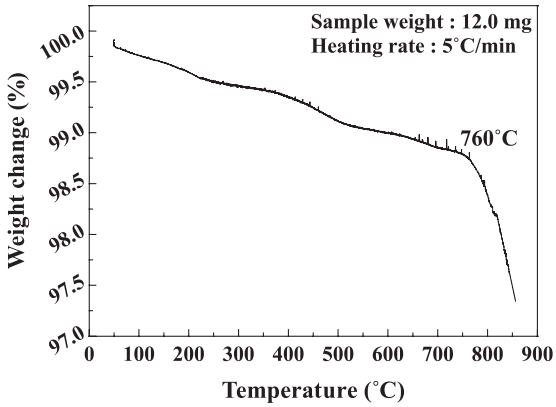

Fig. 3 TGA analysis of the BSS sample in mixed gas (5 % H_2 + 95 % N_2).

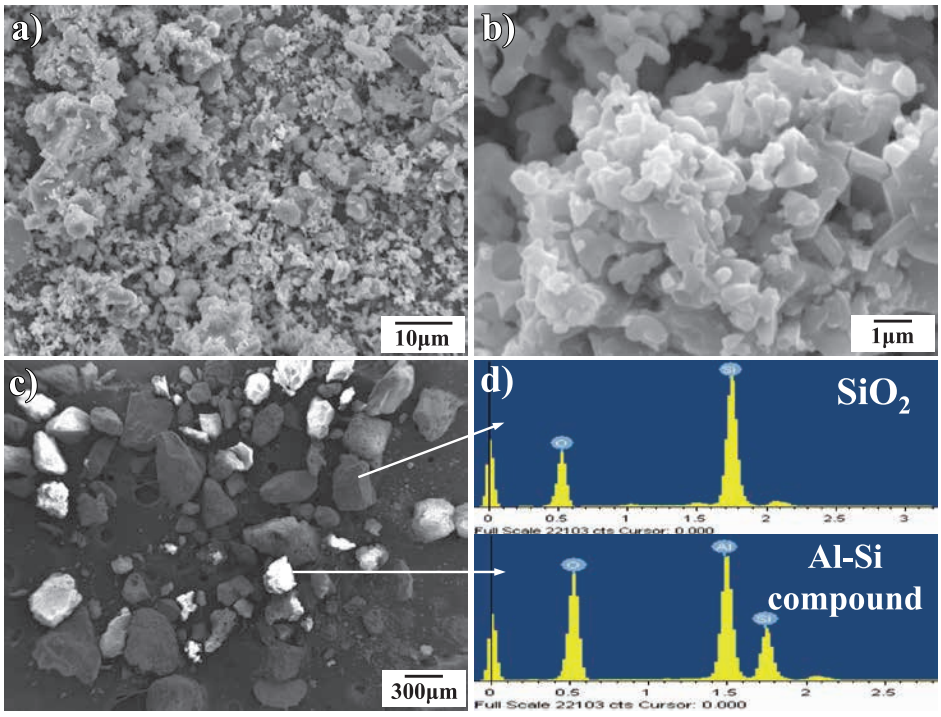

Fig. 2 SEM morphologies of BSS samples: a) whole morphological features of the initial samples, b) the submicron-size ZnO, c) after ZnO leaching with HCl + HNO_3, and d) EDS analysis results.

initial stage of the reaction, after which the [$ZnO{\cdot}Al_2O_3$/Cu] mixture forms a more dense structure as shown in **Figs. 5a, b**, respectively. The amount of ZnO powder decreased with increasing reduction time because Zn evaporated after reduction by hydrogen gas according to Eqn. 1. Also, it should be noted that Cu powder, having spherical particles of ~1 μm, appeared after removal of the ZnO at 120 min of the reaction time. Furthermore, there was no significant change in the shape or particle size of the Cu particles, even after 480 min.

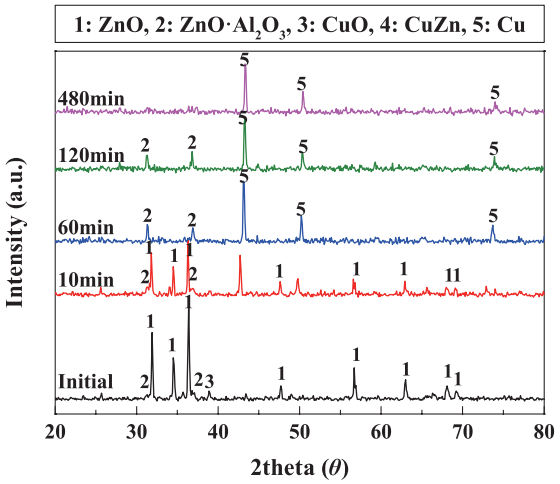

Fig. 4 XRD patterns of BSS, prior to, and after, hydrogen reduction at 1000 °C for various times.

The distilled Zn was recovered as metallic Zn in the cold zone of the alumina tube, as shown in the inset of **Fig. 6a**. In the cold zone, it was condensed and formed Zn powder immediately. The latter had spherical particles with a size range of approximately 1–6 μm. The XRD pattern confirms that the recovered powder is composed of pure Zn, without any other components. This is due to much difference in evaporation temperature between Zn (907 °C) and Cu (2562 °C), SiO_2 (2950 °C), Al_2O_3 (2977 °C) and CuO (2000 °C), respectively.

From the XRD and SEM data, the process of Cu reduction from BSS comprises several stages. The first step is the conversion of brass to Cu with distilled Zn. According to previous research, the brass is generated by the reaction of CuO and ZnO with hydrogen gas at above 600 °C (Kappenstein C. et al., 1996). The concentration of Zn in brass decreased with increasing reduction temperature and times. This was due to loss of Zn by distillation from the brass during the first step. **Fig. 7** shows the respective concentrations of Cu and Zn in brass as a function of reduction temperature and reaction time. Here, Cu concentration increases with reduction time; moreover, the rate of increase of Cu concentration is reduced with decreasing reduction temperature as shown in **Fig. 7a**.

The Cu concentration increase is attributed to not only reduction of CuO but also evaporation of reduced Zn. The contribution of Zn is presented in **Fig. 7b**, where Zn concentration linearly decreases in the early of the reaction time at most of the reduction temperature. In the case of

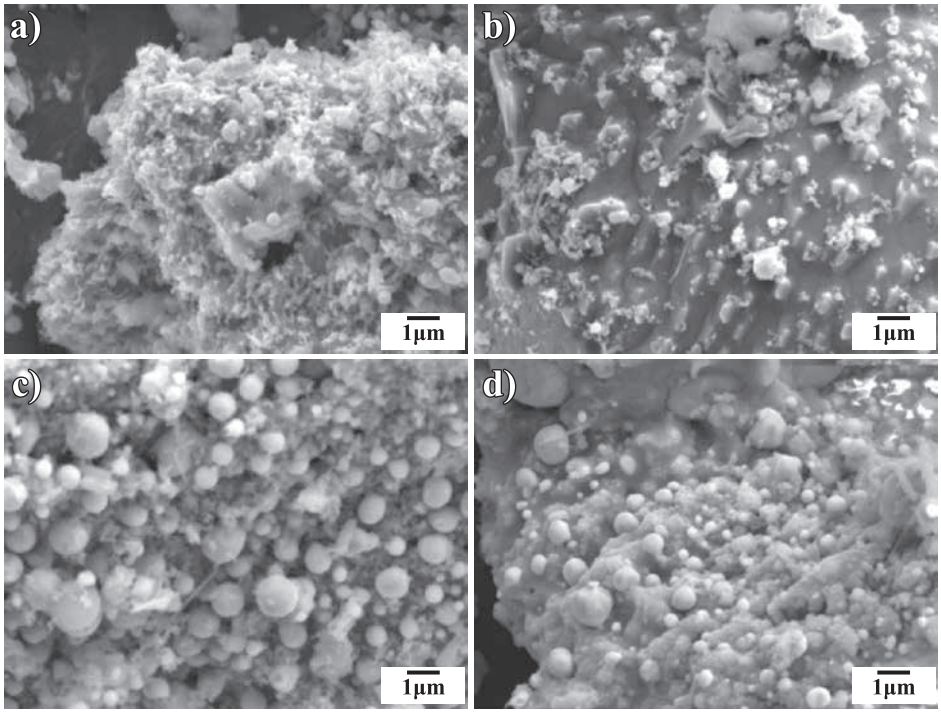

Fig. 5 The morphology change in BSS versus hydrogen reduction times at 1050 °C: a) 10, b) 60, c) 120, and d) 480 min.

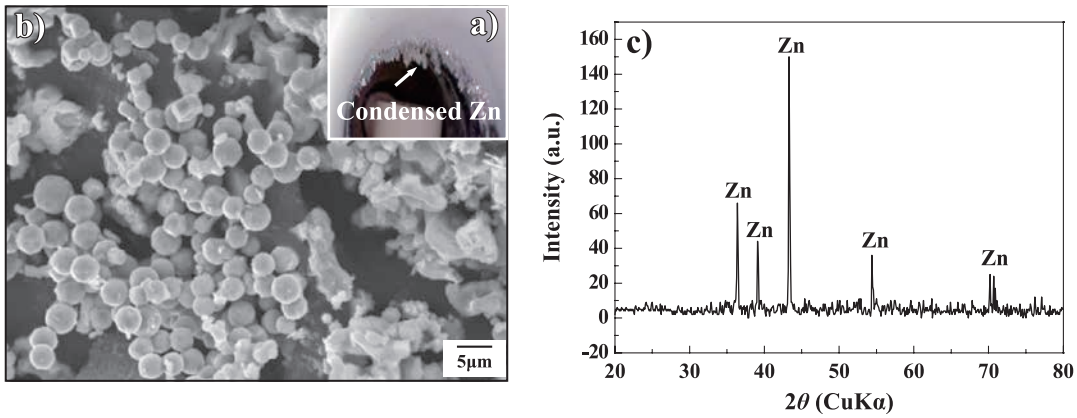

Fig. 6 a) Metal zinc powders recovered from ZnO in BSS at the cold zone of furnace, b) morphology of metal Zn powder, and c) XRD pattern of metal Zn powder.

reactions performed at 1000 °C and 1050 °C, all Zn is eliminated by 480 min and 360 min, respectively. Lastly, a significant amount of Zn remained in the Cu phase at 900 °C for all reduction times.

3.3 The kinetics analysis of BSS

In order to understand the reduction mechanism for BSS, a series of kinetic analyses were performed. For this, the extent of BSS reduction was integrated with respect to time and plotted cumulatively as a reaction ratio (α). The reaction ratio was defined as 0 before the reaction and 1 when it was completed. The rate of each reaction was expressed as a function of Arrhenius parameters with reaction model in Eqn. 3:

$$d\alpha/dt = k(T)\, f(\alpha) \tag{3}$$

where $d\alpha/dt$ is the reaction rate, α the reaction ratio, $k(T)$ *is* the temperature-dependent rate constant, t *is* the time, T *is* temperature, and $f(\alpha)$ *is* the differential form of the reaction model (Santosh K.U., 2006). We used the first-order reaction model $f(\alpha) = 1 - \alpha$ for this reaction. This model is applicable to a wide range of solid-state reactions: Reactant(s) → Product(s) + Gas (g) (James E.H., 2007). For the purpose of this kinetic analysis, the residual mass at various reduction times was expressed as the reaction ratio (α), by means of Eqn. 4:

$$\alpha = (M_0 - M_t)/M_0 \tag{4}$$

where M_t represents the mass of the sample at a reduction time t and M_0 is the initial mass of the sample. Therefore, a more general form of the first-order reaction equation can be written as follows:

$$-\ln(1 - \alpha) = k(T)\, t \tag{5}$$

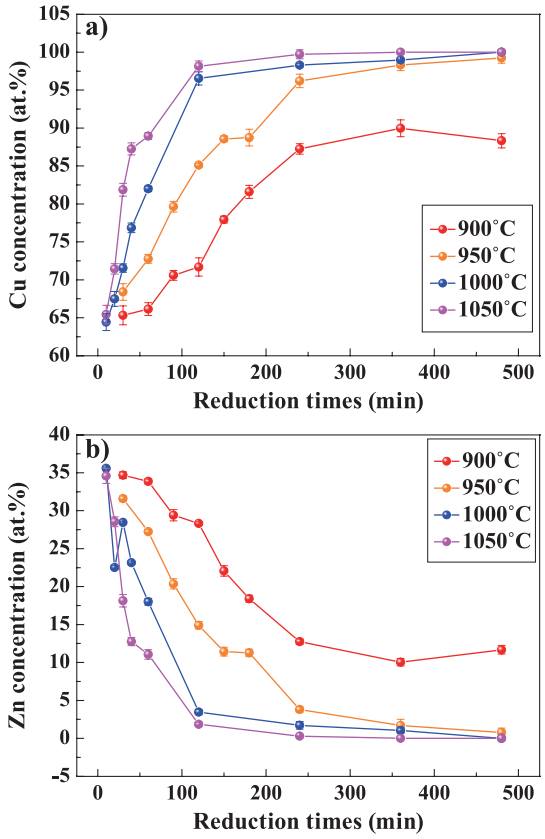

Fig. 7 Concentration change of Cu and Zn in brass by Zn vaporization according to reduction times and temperature: a) Cu, and b) Zn.

Thus, by plotting $-\ln(1 - \alpha)$ versus t, the rate constant (k) can be determined from the slope and intercept of the fitted straight line. Values for the rate constant (k) calculated for α, in the range 0.2–1, are given in **Table 2**. The transformation step 2 is not as rapid as step 1, although the amount of $ZnO{\cdot}Al_2O_3$ is relative small. Specifically, the rate constant of step 1 increases from $1.4 \pm 0.13 \times 10^{-3}$ s^{-1} at 900 °C to $2.18 \pm 0.15 \times 10^{-2}$ s^{-1} at 1050 °C. Meanwhile, the rate constant of step 2 increases from $1.54 \pm 0.21 \times 10^{-5}$ s^{-1} at

Table 2 Summary of rate constants k of BSS sample reduction at different temperature and step

	STEP 1 (s^{-1})	STEP 2 (s^{-1})
900 °C	$1.4 \pm 0.13 \times 10^{-3}$	$1.54 \pm 0.21 \times 10^{-5}$
950 °C	$5.52 \pm 0.72 \times 10^{-3}$	$5.61 \pm 0.68 \times 10^{-5}$
1000 °C	$1.16 \pm 0.24 \times 10^{-2}$	$3.45 \pm 0.52 \times 10^{-4}$
1050 °C	$2.18 \pm 0.15 \times 10^{-2}$	$1.09 \pm 0.19 \times 10^{-3}$

900 °C to $1.09 \pm 0.19 \times 10^{-3}$ s^{-1} at 1050 °C. The temperature-dependence of the rate constant is traditionally described by the Arrhenius law:

$$k(T) = A \exp - (E_a/RT) \quad (6)$$

In Eqn. 6, A is the pre-exponential factor, E is the activation energy, and R is the universal gas constant. Rewriting Eqn. 6 (Jelic D. et al. 2011),

$$\ln k = \ln k - (E_a/RT) \quad (7)$$

The activation energies (E_a) calculated for steps 1 and 2 are 233.2 ± 26.1 and 376.7 ± 22.4 kJ/mol, respectively, as shown in **Fig. 8**. The significant coefficients of determination (R^2) of the activation energy indicated 0.963 and 0.989 as confidence level, respectively. The reaction mechanism, deduced from the kinetic data, is depicted graphically as shown in **Fig. 9**. In step 1, the reductions of CuO and ZnO begin at 500 °C and 600 °C, respectively. ZnO starts to evaporate as soon as it is reduced to the metallic phase, due to its high vapor pressure, and this evaporation is the main cause of the weight loss in this reaction system. In the temperature up to 600 °C, Cu forms a brass phase with Zn, whereas the brass phase decomposes into solid Cu and Zn vapor at 900 °C, which is step 2. It should be noted that ZnO in the $ZnO{\cdot}Al_2O_3$ spinel phase is also reduced in this step; hence, Cu, SiO_2, and Al_2O_3 are the final phase formed in this BSS reduction system. It is supposed that the ceramic impurities are removed by the succeeding smelting process.

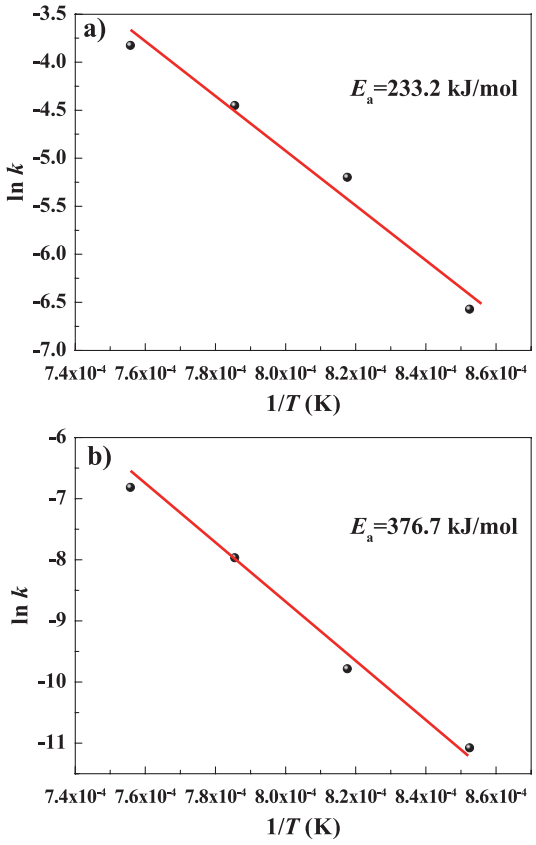

Fig. 8 Arrhenius plot for the dominant reaction in the range of 900–1050 °C with hydrogen gas: a) step 1 (ZnO reduction); and b) step 2 ($ZnO{\cdot}Al_2O_3$ reduction).

4. Conclusion

The reduction kinetics of BSS in a hydrogen atmosphere has been studied at 900 °C to 1050 °C, and for the reduction times between 10 min and 480 min. The characterization of the samples was done by means of SEM and XRD analysis. The results indicated that the reduction of BSS samples was found to occur in a two-step process, with recovery of Zn powder (spherical particles, size: approximately 1~6 μm). The first step involved a rapid transformation of ZnO to Zn (g), whereas the second step involved the slow conversion from $ZnO{\cdot}Al_2O_3$ to Zn (g).

A first-order function and Arrhenius analysis were utilized to calculate the rate constants and activation energies for the BSS reduction. In particular, the rate constant for the transformation from ZnO to Zn (g) increased from $1.4 \pm 0.13 \times 10^{-3}$ s^{-1} at 900 °C to $2.18 \pm 0.15 \times 10^{-2}$ s^{-1} at 1050 °C with an activation energy of 233.2 ± 26.1 kJ/mol in step 1. In step 2, the corresponding rate constant for the transformation from $ZnO{\cdot}Al_2O_3$ to Zn (g) increased from $1.54 \pm 0.21 \times 10^{-5}$ s^{-1} at 900 °C to $1.09 \pm 0.19 \times 10^{-3}$ s^{-1} at 1050 °C with an activation energy of 376.7 ± 22.4 kJ/mol. It is believed that further understanding of the reaction mechanism observed in this study can contribute to the further optimization of process conditions in fluidized bed reactors.

Acknowledgements

This research was supported by a grant from the Fundamental R & D Program for Energy (No. 2012T100100092, ("Development of pyrometallurgical technology for low quality urban mining by-products") funded by the Ministry of Knowledge Economy, Republic of Korea.

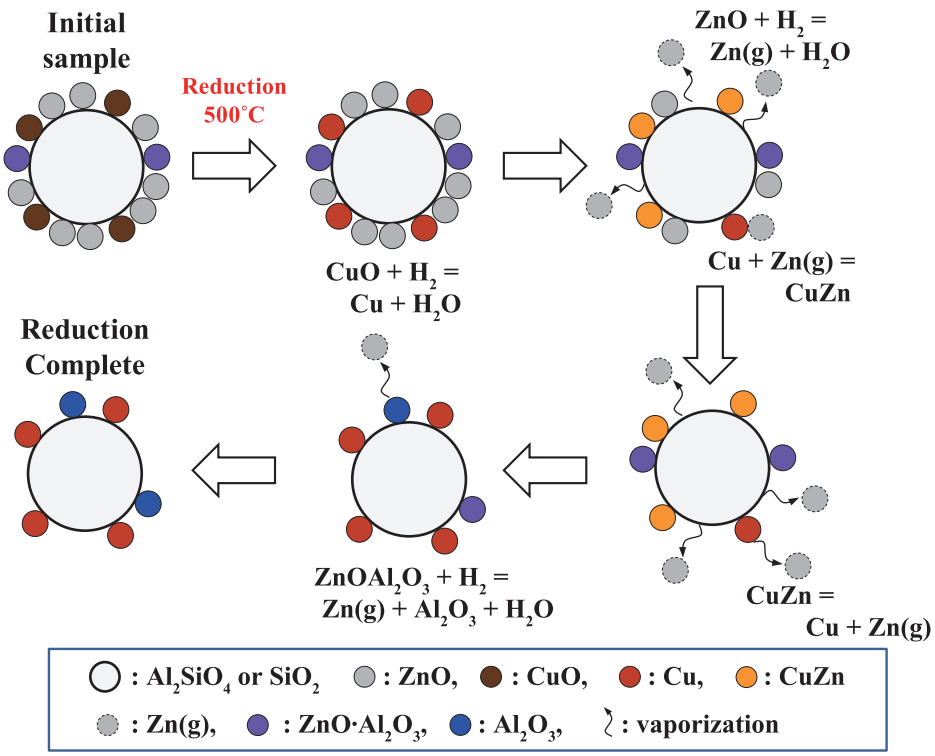

Fig. 9 Schematic diagram of BSS samples reduction mechanism between room temperature and 1050 °C with hydrogen gas.

References

Altundogan H.S., Tumen F., Metal recovery from copper converter slag by roasting with ferric sulphate, Hydrometallurgy, 44 (1997) 261–267.

Anand S., Kanta R.P., Jena P.K., Recovery of metal values from copper converter and smelter slags by ferric chloride leaching, Hydrometallurgy, 5 (1980) 355–365.

Anand S., Sarveswara R.K., Jena P.K., Pressure leaching of copper converter slags using dilute sulphuric acid for the extraction of cobalt, nickel and copper values, Hydrometallurgy, 67 (1983) 1–7.

Bakker M.L., Nikolic S., Mackey P.J., ISASMELT^{TM}-Application for nickel, Minerals Engineering, 24 (2011) 610–619.

Gioia F., Mura G., Viola A., Experimental study of the direct reduction of sinterized zinc oxide by hydrogen, Chemical Engineering Science, 33 (1977) 1401–1409.

Gorai B., Jana R.K. Premchand, Characteristics and utilisation of copper slag—a review, Resources conservation and recycling, 39 (2003) 299–313.

Igor I. Katkov, Challenge from the simple: Some caveats in linearization of the Boyle-van't Hoff and Arrhenius plots, Cryobiology, 57 (2008) 142–149.

James E.H., Principles of chemical kinetics 2nd eds., Academic Press, New York, 2007.

Jelic D., Tomic-Tucakovic B., Mentus S., A kinetic study of copper oxide powder reduction with hydrogen, based on thermogravimetry, Thermochimica Acta, 521 (2011) 211–217.

Jha M.K., Kumar V., Singh R.J., Review of hydro-metallurgical recovery of zinc from industrial wastes, Resources conservation and recycling, 33 (2001) 1–22.

Kappenstein C., Cernak H., Brahmi R., Duprez D., Chomic J., Copper-zinc oxide catalysts. Part IV. Thermal treatment in air, argon and hydrogen and XRD study of new bimetallic precursors-direct formation of alloys, Thermochimica Acta, 279 (1996) 65–76.

Moskalyk P.R., Alfantazi A.M., Review of copper pyrometallurgical practice: today and tomorrow, Minerals Engineering, 16 (2003) 893–919.

Rudnik E., Burzynska L., Gumoska W., Hydrometallurgical recovery of copper and cobalt from reduction-roasted copper converter slag, Minerals Engineering, 22 (2009) 88–95.

Santosh K.U., Chemical kinetics and reaction dynamics, Springer, New Delhi, 2006.

Sharma K.D. and Row B.R.K., An electrolytic process for recovery of zinc dust from melting furnace slag, Hydrometallurgy, 13 (1985) 377–383.

Sukla L.B., Panda S.C., Jena P.K., Recovery of cobalt, nickel and copper from converter slag through roasting with ammonium sulphate and sulphuric acid, Hydrometallurgy, 16 (1986) 153–165.

Author's short biography

Tae-Hyuk Lee

Tae-Hyuk Lee is a doctor candidate for Materials Engineering, Chungnam National University, South Korea. He received his M.D. from Chungnam National University, South Korea in 2012. He is now pursuing his Ph.D. in Chungnam National University focusing on stress corrosion cracking of Inconel 690 for steam generator tubes. His research interests include stress corrosion cracking, recycling of metals, and metal matrix composites.

Sin-Hyeong Joo

Sin-Hyeong Lee is a master's course for Materials Engineering, Chungnam National University, South Korea. He received his B.S. from Chungnam National University, South Korea. His research interests include powder metallurgy materials and processing, in particular non-ferrous materials, such as boron, boron composite, silver and silicon.

Hayk H Nersisyan

Hayk Nersisyan is research professor of Materials Science & Engineering at Chungnam National University in South Korea and Rapidly Solidified Materials Research Center. He received his B.S., M.S. and Ph D degrees from Yerevan State University in Armenia. His major research field is powder metallurgy materials and processing, in particular non-ferrous materials and their composites such as magnesium, titanium, aluminium and copper.

Man-Sik Kong

Man-Sik Kong is senior researcher of Plant Engineering Center, Institute for Advanced Engineering, South Korea. He received his B.S., and M.S degree from Gyeongsang National University and Ph D. degree from Ajou University in South Korea. Dr. Kong's research interests include powder metallurgy materials, processing and recycling of rare metals.

Author's short biography

Jae-Woo Lee

Jae-Woo Lee is director of SEWON CO., LTD, South Korea. He received his B.S. degree from Hanyang University in South Korea. His research interests include recycling process of copper and copper alloy, recovery of metals from urban mine.

Ki-Won Park

Ki-Won Park is head of research center of SEWON CO., LTD, South Korea. He received his B.S. degree from Inha University in South Korea. His research interests include recycling process of copper and copper alloy, recovery of metals from urban mine.

Jong-Hyeon Lee

Jong-Hyeon Lee is Professor in Department of Materials Science & Engineering at Chungnam National University in South Korea and head of Rapidly Solidified Materials Research Center. He received his B.S., M.S, and Ph D degrees from Chungnam National University. His major research field is electro refining, winning, and coating of rare metals. He also studies on powder synthesis by self-propagating high temperature synthesis. He published more than 100 articles and 30 patents.

KONA Powder and Particle Journal No. 33 (2016) 287–295/Doi:10.14356/kona.2016011 Original Research Paper

Mechanical Properties of Agglomerates Produced by the Mechanical Vibration of Cohesive Powders †

Hamid Salehi Kahrizsangi, Diego Barletta and Massimo Poletto *

[1] *Department of Industrial Engineering, University of Salerno, Italy*

Abstract

The process of granule formation from aggregative cohesive powders under the action of mechanical vibration is studied. Vibration frequency and acceleration levels were set independently in the experiments. The process of agglomerate formation is examined by measuring the size distributions of the agglomerates and their resistance under uniaxial compression. The results indicate the formation of wide particle size distributions and hard and compact agglomerates. The experimental results and the interpretation of data suggest that, in order to produce agglomerates by mechanical vibration, powders should have flow functions with a flow factor value smaller than 3. In agreement with the theoretical framework proposed, agglomerate consolidation pressures and deformation at breakage seem to be almost independent of the agglomerate diameter and the vibration conditions.

Keywords: cohesive powders, mechanical vibration agglomerates, compression test

1. Introduction

Powder granulation is used in many different industrial applications such as the production of pesticides, fertilizers and ceramics. The general purpose is to improve the handling and the storage behavior of these solid materials. On the one hand, with fine and cohesive powders, mechanical vibrations can be used to produce stable agglomerates (Kua N. et al., 2014; Mawatari Y. et al., 2007). On the other hand, the self-agglomeration of cohesive powders may happen in processes involving mechanical vibrations, leading to undesired problems. Among these, we mention solids segregation in processes involving powder flow and also gas-solids segregation in industrial applications which require an intimate gas-solids contact. The aggregative behavior of fine cohesive powders under the action of vibrations was described by Barletta D. and Poletto M. (2012) following the analysis introduced previously (Barletta D. et al., 2007). Nano-powders also produce self-aggregation phenomena in vibrated beds (Van Ommen J.R. et al., 2012). Mechanical vibrations have also been applied together with powder drying processes to control and promote powder agglomeration (Cruz M.A.A. et al., 2005). The objective of this paper, however, will be the agglomeration of cohesive powders due to compaction in vibrated beds without the use of a fluidizing gas or at least under application of a minimum gas rate with the purpose of system conditioning, but not the ability to sustain the bed.

One of the most significant characteristics of a granulation process is the granules' mechanical resistance. In fact, the produced granules should be able to resist the external forces during storage and transportation in order to avoid dust formation and changes to the granules' size distribution. A recent study on the resistance of agglomerates under the action of compression and their mechanical behavior was given by Antonyuk S. et al. (2005). They provided a significant insight into the rupture mechanism and into the mechanical response of agglomerates for elastic, elastic-plastic and plastic agglomerate deformation regimes. The resistance of agglomerates in dynamic conditions was studied by Antonyuk S. et al. (2006).

In this paper, the process of granule formation from aggregative cohesive powders under the action of mechanical vibration is studied. The equipment used allows the vibration frequency and acceleration levels to be set independently. The process of agglomerate formation is examined by measuring the agglomerate's size distributions and also by the agglomerate's resistance under uniaxial compression.

2. Experimental

2.1 Apparatus

The apparatus used is described by Barletta D. et al.

† Received 16 May 2015; Accepted 6 July 2015
J-STAGE Advance published online 21 August 2015
[1] Via Giovanni Paolo II, 132, 84084 Fisciano (SA), Italy
* Corresponding author: Massimo Poletto;
E-mail: mpoletto@unisa.it
TEL: +39-089-96-4132 FAX: +39-089-96-8781

(2013). A sketch of the apparatus, a vibrated fluidization column, is shown in **Fig. 1**. The fluidization column was made of Perspex with an 85-mm ID and a height of 400 mm (1). At the bottom, the air was distributed by a 10-mm thick porous plate of sintered brass particles. The porous plate was clamped in the flange connecting the wind box and the fluidization column. In the column flange, a pressure port was connected to a U-tube manometer (6) filled with water. Desiccated air from the laboratory line was fed to the wind box by a thermal mass flow controller (Tylan FC2900V) with a maximum flow rate of 5 10^{-5} Nm^3 s^{-1} (4). The column was fixed to the vibrating plane of the actuator by means of a rigid steel and aluminum structure (3). The actuator (2) was an electric inductance vibrator (V100 Gearing and Watson, USA) that was able to produce a sinusoidal vertical movement in the range between 2 and 6500 Hz with displacement amplitudes of up to 12.7 mm, exerting a maximum force of 26.7 kN. The vibrator amplifier was connected to a vibration controller Sc-121 (Labworks inc., USA) (7). The controller measured the effective vibrations by means of a piezoelectric accelerometer (8636B60M05 Kistler, USA) (5) fixed on the metal structure supporting the fluidization column. The system was able to control vibrations by fixing, within the operating range, any of the two possible pairs of vibration parameters, *i.e.* acceleration, amplitude or frequency. In fact, the maximum acceleration, a, is related to the oscillation amplitude, A, and the oscillation frequency, f, or the pulsation value, ω by means of the following relationship:

$$a = A\omega^2 = A(2\pi f) \tag{1}$$

In our experiments, we chose to define the vibration acceleration and the frequency.

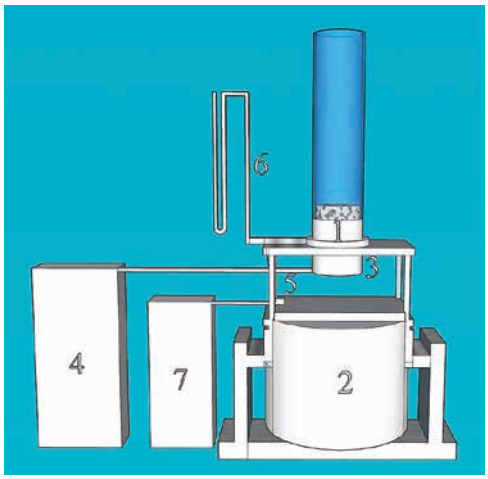

Fig. 1 Schematic of a mechanically vibrated bed. Legend: 1. fluidization column; 2. electro-dynamic vibrator; 3. metallic frame; 4. mass flow controller and air feed unit; 5. accelerometer; 6. water manometer; 7. vibration control block.

2.2 Materials

Two different powders were used in the experiments, a calcium carbonate ($CaCO_3$) powder and a titanium dioxide (TiO_2) powder. The properties of these two powders are reported in **Table 1**. The rheological properties were measured with a Schulze ring shear tester (Schulze D., 1994). The flow functions (unconfined yield strength as a function of the major principal stress) at high consolidation values, namely between 10 kPa and 170 kPa, were measured with a uniaxial testing procedure carried out on an Instron tester (Series 5860) equipped with a 1-kN load cell. The mold was a steel cylinder made of two detachable halves as described by Parrella L. et al. (2008). It allowed the production of cylindrical samples of compacted powder of 50 mm in diameter and about the same height. In order to compensate for wall friction in the consolidation phase, a Janssen (Janssen H.A., 1895) correction was used to determine the vertical consolidation stress during the uniaxial compression tests

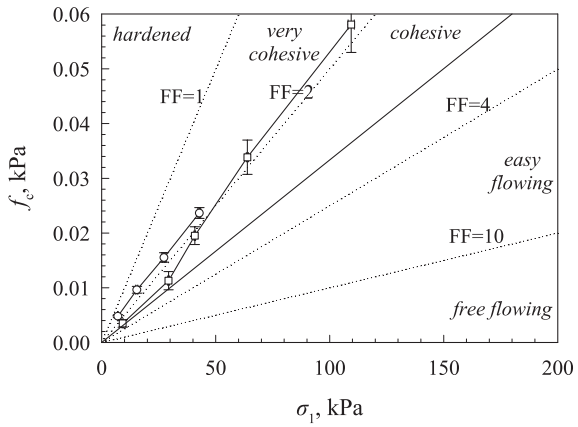

Fig. 2 Flow functions of calcium carbonate (○) and of titanium dioxide (□) measured with a uniaxial testing procedure.

Table 1 Material properties

Material	d_p µm	ρ_p kg m^{-3}	σ_1 Pa	f_c Pa	ρ_b kg m^{-3}	ϕ deg	ϕ_e deg	ϕ_w deg	S_c^*/d_a Eqn. (15)
$CaCO_3$	4.1	2540	471	410	350	35	50	30	0.039
TiO_2	0.2	4500	345	300	785	40	50	39	0.019

$$\sigma = \sigma_0 \exp\left(-\frac{4\mu_w K z}{D}\right) \quad (2)$$

where D is the mold diameter, z is the final sample height after consolidation, σ_0 is the applied stress on the sample surface, $\mu_w = \tan \phi_w$ is the mold wall friction, ϕ_w is the wall friction angle, K is the vertical to horizontal stress ratio that, for lack of a better evaluation (Barletta D. and Poletto M., 2013), it is calculated as suggested by Kwade A. et al. (1994):

$$K = 1.2(1 - \sin \phi_e) \quad (3)$$

where ϕ_e is the effective angle of internal friction. The wall friction tests of the powders were measured by a Brookfield Powder Flow tester by using a stainless steel coupon.

2.3 Procedure

Beds of cohesive calcium carbonate and titanium dioxide powders were vibrated vertically at frequencies of 25 or 50 Hz and at acceleration levels, *a/g,* of 6 or 9. A desiccated air flow was used to keep the powder humidity constant during the experiments. The experimental conditions for both materials are reported in **Table 2**. For calcium carbonate, if we assume test C3 as a reference case, then the other test conditions change for one or maximum two variables. Namely, in Test C1, half of the process time is considered; in Test C2, the frequency is doubled and the processing time is tripled; in test C4, the acceleration is reduced by 1/3. Similarly, for titanium dioxide, we can assume test T2 as a reference case, then in Test T1, half of the bed mass is considered; in Test T3, the processing time is tripled; in tests T4 to T6, the frequency is doubled; double process time is used in T5 and 4 times the process time in T6.

The resulting granules were classified by coarse sieving using a stack of three sieves of 400 μm, 1 mm and 2 mm aperture size, respectively. For some of the test conditions, the portion of granules bigger than 2 mm was collected to measure the granules' mechanical resistance. For this purpose, a uniaxial compression test was adopted by using an Instron machine (Series 5860) equipped with a 1-N load cell.

3. Results

3.1 Agglomerates' size distribution

Sieve analysis was applied to the processed powders including agglomerates. Significant losses of fines were recorded due to adhesion to the column wall and to elutriation of dust. **Fig. 3a** shows the 2-mm oversize fraction for calcium carbonate. Besides the weight distribution in the different classes identified by the sieving process in **Table 3**, **Fig. 4** also reports an estimate of the median-mass-weighted agglomerate size and the error bars are the diameter range covering the 80 %-by-weight of the distribution of agglomerate size. This latter size range was estimated by fitting the weight distribution by means of a power law. By comparing results, it is possible to observe a limited effect of the operating parameters. In general, the median agglomerate size is between 0.5 and 1.6 mm and the largest agglomerates are above 3–4 mm.

Table 2 Operating conditions in the vibration experiments

Test code	Material	Frequency Hz	Acceleration a/g	Displacement mm	Air rate NL h-1	Bed mass g	Test time min	Description
C1	$CaCO_3$	25	9	6.8	1200	100	**10**	half time
C2	$CaCO_3$	**50**	9	1.5	1200	100	**30**	double freq., long time
C3	***$CaCO_3$***	***25***	***9***	***6.8***	***1200***	***100***	***20***	***reference***
C4	$CaCO_3$	25	**6**	4.6	1200	100	20	reduced accel.
T1	TiO_2	25	9	6.8	1200	**100**	5	half mass
T2	***TiO_2***	***25***	***9***	***6.8***	***1200***	***200***	***5***	***reference***
T3	TiO_2	25	9	6.8	1200	200	**10**	double time
T4	TiO_2	**50**	9	1.5	1200	200	5	double freq.
T5	TiO_2	**50**	9	1.5	1200	200	**10**	double freq., double time
T6	TiO_2	**50**	9	1.5	1200	200	**20**	double freq., long time

Fig. 3 Examples of agglomerates formed: a) 2-mm oversize fraction for $CaCO_3$; b) $CaCO_3$; c) TiO_2.

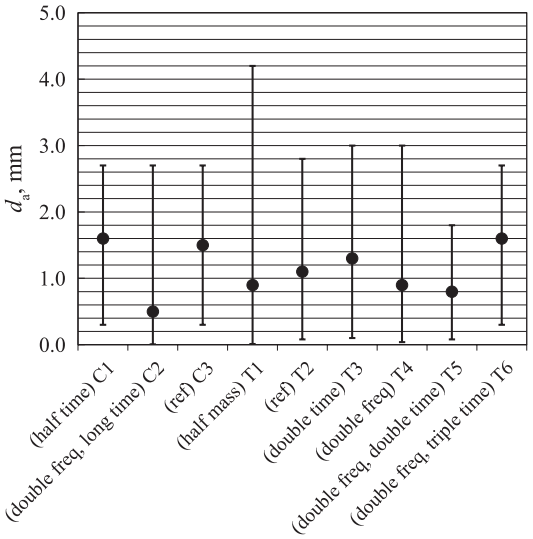

Fig. 4 Agglomerate size distributions for different test conditions obtained from a fitting regression of a power law distribution on the experimental data of **Table 3**. Dots are the median values and bars cover the 80 % range of distributions between the 10th and 90th percentiles.

Table 3 Experimental agglomerate size distributions

Test code	sampled weight fractions in d_a ranges, %			
	< 0.4 mm	0.4–1 mm	1–2 mm	> 2 mm
C1	11.2	22.6	27.6	38.6
C2	43.4	24.4	9.8	22.4
C3	13.6	27.4	21.1	37.9
T1	35.8	19.4	10.5	34.3
T2	26.7	24.8	19.0	29.6
T3	21.2	25.1	18.5	35.2
T4	31.7	23.5	15.3	29.4
T5	29.4	37.5	25.5	35.6
T6	26.5	22.3	22.2	29.0

Increasing the frequency from 25 to 50 Hz has negligible effects on the size of the titanium dioxide agglomerates, while it seems to produce smaller agglomerates of calcium carbonate. Increasing the vibration times results in larger titanium dioxide agglomerates.

3.2 Mechanical resistance of agglomerates

Fig. 5a shows a schematic of the uniaxial compression test carried out on the largest agglomerates with the main geometrical variables of the deformed agglomerate during the test as defined in the following text. An example of the trace of the mechanical response of the agglomerates is reported in **Fig. 6**. The size of the agglomerates, d_a can be determined from the first contact position at which the forces ramp, corresponding to the start of agglomerate deformation. The force vs. displacement curve is always well represented by a line segment indicating, as it will be discussed later, a plastic deformation regime of the agglomerate.

The agglomerate rupture is well identified by the peak force. Within the agglomerate deformation regime, the contact deformation, s_c, will be assumed to be half of the agglomerate deformation, s_a, that is the distance travelled by the compression piston starting from the first contact position. Given the contact deformation at breakage, s_{cb}, and the agglomerate deformation at breakage, s_{ab}, it is $s_{cb} = 1/2 s_{ab}$, and assuming a spherical agglomerate shape, it is possible to estimate the contact area A_{cb} at breakage

$$A_{cb} = \pi d_a s_{cb} \tag{4}$$

Consequently, the average pressure at the contact at breakage can be easily calculated from the force measured at breakage, F_b:

$$p_b = \frac{F_b}{\pi d_a s_{cb}} \tag{5}$$

The force F_b, the relative deformation of the contact, s_{cb}/d_a, the contact area, A_c, and the pressure p_{fb} measured at breakage in the agglomerate breakage tests are reported as a function of the agglomerate diameter in **Fig. 7** and **Fig. 8** for both calcium carbonate and titanium dioxide, respectively. Data are separated for each of the examined conditions and, correspondingly, a best-fit linear approximation is drawn to highlight possible trends. These figures indicate a clear dependence of both the breakage force (for calcium carbonate only) and also of the contact

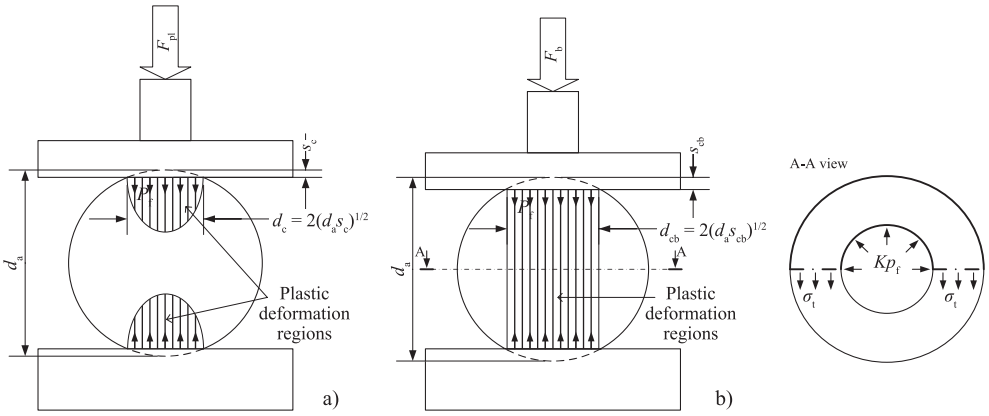

Fig. 5 Uniaxial compression test for agglomerates and contact deformation parameters: a) plastic deformation; b) breakage conditions.

area at breakage on the agglomerate diameter. If any, only a slight dependence on the agglomerate diameter is evident for the relative deformation and the contact pressure at breakage. Furthermore, it is not possible to identify a clear trend of the vibrations and other aggregation process parameters on the observed results. Some differences can be observed comparing two different materials, in fact, with respect to calcium carbonate, the population of agglomerate tested for titanium dioxide is a bit smaller and, in any case, tends to show a slightly higher breakage force (averages around 0.2 N for $CaCO_3$ and about 0.3 N for TiO_2), a slightly smaller relative deformation at breakage (averages around 0.025 for $CaCO_3$ and less than 0.020 for TiO_2), correspondingly a slightly lower contact area at breakage (averages around 0.4 mm^2 for $CaCO_3$ and 0.2 mm^2 for TiO_2) and significantly higher pressures at breakage (averages less than 40 kPa for $CaCO_3$ and around 100 kPa for TiO_2).

According to Antonyuk S. et al. (2006), a spherical agglomerate compressed against a flat surface will deform and a force will set in between the agglomerate and the surface. This force expression will depend upon the regime of deformation which might be elastic, elastic-plastic or completely plastic. In the presence of an elastic component, the agglomerate deformation will follow a Hertzian law of deformation that reveals an upward concavity in the force-displacement curve. Instead, a purely plastic deformation can be hypothesized in the case of a perfectly linear plastic relationship between the contact deformation and the force. In fact, this is the case in almost all our tests, as is shown in the force vs. displacement curve of **Fig. 6**. The simple Eqn. 6 is used in this case:

$$F_{pl} = \pi p_f d_a s_c \tag{6}$$

where d_a is the agglomerate diameter, s_c is the contact deformation and p_f is the material strength at deformation on the contact point. Eqn. 6 is very simple since it is the

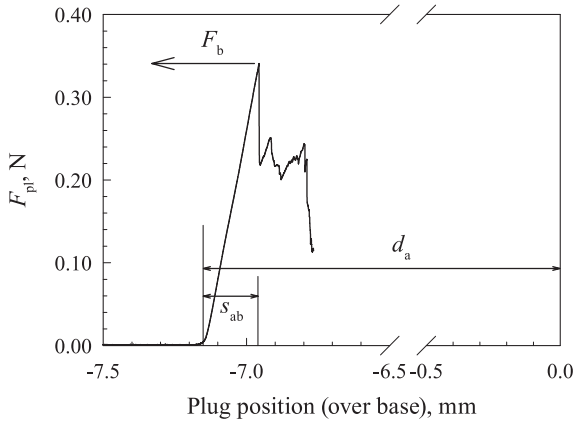

Fig. 6 Force vs displacement curve for agglomerate breakage experiments.

combination of the area of the flattened surface contact point:

$$A_c = \pi d_a s_c \tag{7}$$

and of the pressure exerted by the material p_f.

According to the theoretical works of Hencky H. (1923) and Ishlinsky A.J. (1944) as reported by Molerus O. (1975), p_f can be approximated to three times the material unconfined yield strength. In the present case of agglomerates we have:

$$p_f = 3 f_c \tag{8}$$

We assumed that the agglomerate grows by hitting some powder laying on other agglomerates or on the vibrating column surface. Accordingly, the material will consolidate on the agglomerate with subsequent hits in which the consolidation stress σ_1 is equal or smaller than the material strength p_f. The resulting consequence of this assumption and Eqn. 8 is that the flow factor at which the

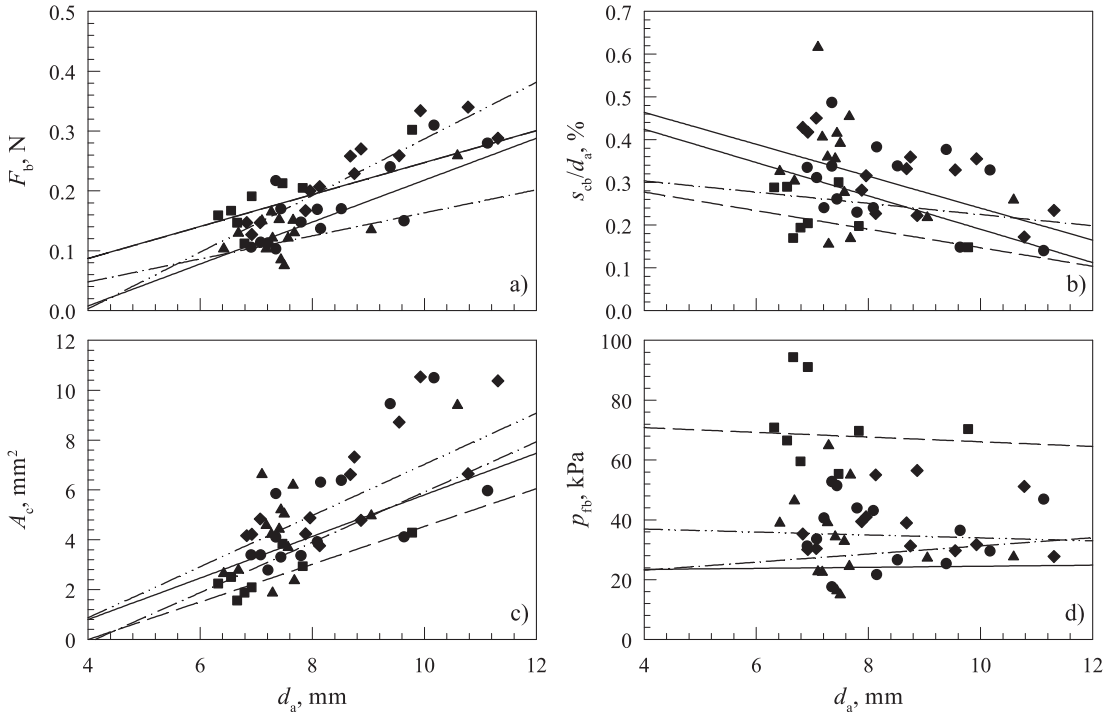

Fig. 7 Force (a), relative deformation of the contact (b), contact area (c) and pressure (d) measured at breakage test for the aggregates as a function of the aggregate diameter for Calcium Carbonate. Test conditions for data points: ●, C1; ■, C2; ▲, C3; ◆, C4. Test conditions for regression lines: ——, C1; — —, C2; –·–, C3; –··–, C4.

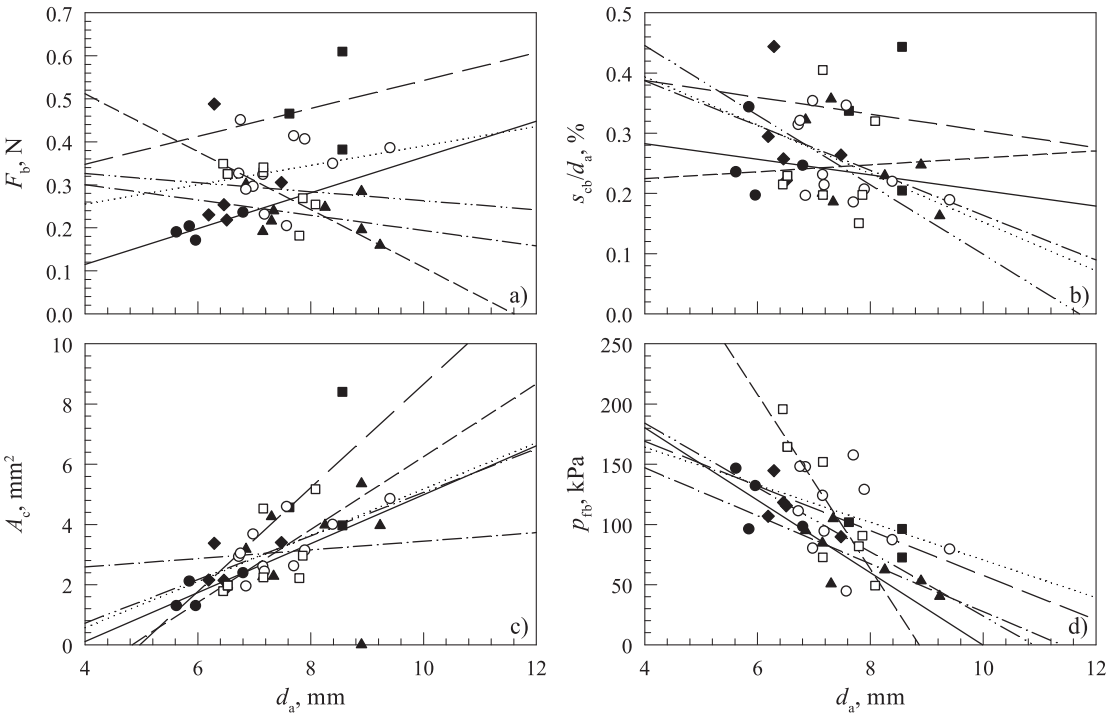

Fig. 8 Force (a), relative deformation of the contact (b), contact area (c) and pressure (d) measured at breakage test for the aggregates as a function of the aggregate diameter for Titanium dioxide. Test conditions for data points: ●, T1; ■, T2; ▲, T3; ◆, T4; ○, T5; □, T6. Test conditions for regression lines: ——, T1; — —, T2; –·–, T3; –··–, T4; ·····, T5; – – –, T6.

material consolidates is:

$$\mathrm{FF} = \frac{\sigma_1}{f_c} = \frac{\sigma_1}{p_f} 3 \le 3 \tag{9}$$

The flow factor line FF = 3 is reported in **Fig. 2**. According to the reasoning above, flow functions with flow factors values close to 3, suggest an equilibrium in the agglomerate growth process. Materials with flow functions showing flow factors values smaller than 3 should not be able to produce agglomerated with vibrations. Instead, the agglomeration process by vibration should be largely favored in materials with flow functions characterized by flow factors values larger than 3. This is the case of the tested powders, for which it is verified that both materials have a flow factor smaller than 3. In general, it should be said that according to the mechanism hypothesized to derive Eqn. 9, the agglomerate strength should be largely independent of the vibration parameters and of the agglomerate diameter. This seems to be confirmed by findings in **Fig. 7d**. **Fig. 8d**, instead, may suggest some dependence of the material strength on the agglomerate diameter which, however, should be confirmed by a larger number of samples.

The agglomerate breakage phenomenon has been widely discussed by Antonyuk S. et al. (2005). In particular, it has been highlighted that the agglomerate under plastic deformation breaks because the plasticized nucleus radially expands to the yield of the equatorial band of the particles. **Fig. 3b** shows the mechanism. A rough evaluation of the breakage conditions can be carried out as follows. According to **Fig. 5b**, we assume an inner cylinder of material completely plasticized and characterized by a diameter of $2(d_a s_c)^{0.5}$ and a height of d_a-$2s_c \approx d_a$. The material in this cylinder pushes radially outwards with a pressure Kp_f, where K is the material vertical to the horizontal stress ratio. Eqn. 2 is valid within the Mohr-Coulomb assumption. The outward pressure of the inner material is balanced by the strength of the material in the unplasticized external toroid. A force balance allows calculation of the collapse condition of this band that occurs when the tangential stress equals the material's unconfined yield strength:

$$p_f K 2\sqrt{d_a s_c}\, d_a = \sigma_t 2A_t \tag{10}$$

where A_t is the cross-section of the unplasticized toroid. The fact that, in general, it is $s_c \ll d_a$, allows second-order terms to be neglected and therefore:

$$2A_t = \frac{\pi d_a^2}{4} - 2d_a\sqrt{d_a s_c} \tag{11}$$

Furthermore, within the Mohr-Coulomb hypotheses we have:

$$f_c = \frac{2C\cos\phi}{1-\sin\phi} \tag{12}$$

and

$$\sigma_t = \frac{2C\cos\phi}{1+\sin\phi} \tag{13}$$

Combining Eqns. 7 and 9 to 12, it is

$$\frac{6C\cos\phi}{1-\sin\phi} 2K\sqrt{d_a s_c}\, d_a = \frac{2C\cos\phi}{1+\sin\phi}\left(\frac{\pi d_a^2}{4} - 2d_a\sqrt{d_a s_c}\right) \tag{14}$$

That is

$$\frac{s_c}{d_a}^* = \left\{\frac{\pi}{8} \Big/ \left[\left(\frac{1+\sin\phi}{1-\sin\phi}\right)3K - 1\right]\right\}^2 \tag{15}$$

It appears that the agglomerate deformation at breakage expressed by Eqn. 14 should be a function only of the material properties. The values predicted for the deformation at breakage for the two materials are reported in **Table 2**. It can be verified that also the theory predicts a result that is independent of the vibration parameters and of the agglomerate diameter as roughly suggested by **Figs. 7b** and **8b**. Furthermore, in agreement with the experiments, the theory predicts a smaller deformation at breakage for titanium dioxide than for calcium carbonate.

4. Conclusion

The process of agglomerate formation by means of mechanical vibrations was studied by means of agglomerate size distributions and uniaxial compression tests on agglomerate deformation and resistance. Results indicate the formation of wide agglomerates' size distributions and hard and compact agglomerates.

Considering the experimental results and the interpretation of data, it is suggested that in order to produce agglomerates with this mechanism, powders should have flow functions close or smaller than a flow factor value of 3. The same analysis suggests that agglomerates' consolidation pressures and deformation at breakage is almost independent of the agglomerate diameter and of the vibration conditions.

Nomenclature

a	acceleration due to vibration (m s^{-2})
A	vibration amplitude (m)
A_c	contact area (mm^2)

A_{cb} contact area at breakage (mm^2)

A_t cross-section of the unplasticized toroid (mm^2)

D mold diameter (mm)

d_a agglomerate diameter (mm)

d_p particle diameter (μm)

f oscillation frequency (s^{-1})

F_b force measured at breakage (N)

F_{pl} force measured in the agglomerate plastic deformation range (N)

f_c unconfined yield strength (Pa)

FF flow factor (–)

g acceleration due to gravity ($m\ s^{-2}$)

ID internal diameter (mm)

K vertical to horizontal stress ratio (–)

p_b average pressure at the contact at agglomerate breakage (kPa)

p_f the material strength at the agglomerate contact point (kPa)

p_{fb} pressure measured at breakage at the agglomerate contact point (kPa)

s_a agglomerate deformation (mm)

s_{ab} agglomerate deformation at breakage (mm)

s_c contact deformation (mm)

s_{cb} contact deformation at breakage (mm)

Z final sample height after consolidation (mm)

ρ_b average bed density ($kg\ m^{-3}$)

ρ_p particle density ($kg\ m^{-3}$)

σ normal stress (Pa)

σ_0 applied normal stress on the sample surface in the uniaxial tester (Pa)

σ_1 major principal stress at consolidation (Pa)

σ_t tensile strength, Pa

ϕ angle of internal friction (Deg)

ϕ_e effective angle of internal friction (Deg)

ϕ_w angle of wall friction (Deg)

μ_w mold wall friction (–)

ω vibration pulsation (s^{-1})

References

Antonyuk S., Tomas J., Heinrich S., Mörl L., Breakage behaviour of spherical granulates by compression, Chemical Engineering Science, 60 (2005) 4031–4044, DOI: 10.1016/j.ces.2005.02.038.

Antonyuk S., Khanal M., Tomas J., Heinrich S., Mörl L., Impact breakage of spherical granules: experimental study and DEM simulation, Chemical Engineering and Processing: Process Intensification, 45 (2006) 838–856, DOI: 10.1016/j.cep.2005.12.005.

Barletta D., Donsì G., Ferrari G., Poletto M., Russo P., Solid flow rate prediction in silo discharge of aerated cohesive powders, AIChE Journal, 53 (2007) 2240–2253, DOI:10.1002/aic.11212.

Barletta D., Poletto M., Aggregation phenomena in fluidization of cohesive powders assisted by mechanical vibrations, Powder Technology, 225 (2012) 93–100, DOI: 10.1016/j.powtec.2012.03.038.

Barletta D., Poletto M., A device for the measurement of the horizontal to vertical stress ratio in powders, Granular Matter, 15 (2013) 487–497, DOI: 10.1007/s10035-013-0427-7.

Barletta D., Russo P., Poletto M. Dynamic response of a vibrated fluidized bed of fine and cohesive powders, Powder Technology, 237 (2013) 276–285, DOI: /10.1016/j.powtec.2012.12.004

Cruz M.A.A., Passos M.L., Ferreira W.R., Final drying of whole milk powder in vibrated-fluidized beds, Drying technology, 23 (2005) 2021–2037, DOI: 10.1080/07373930500210473.

Janssen H.A., Versuche über Getreidedruck in Silozellen, Zeitschrift des Vereins Deutscher Ingenieure, 39 (1895) 1045–1049.

Kua N., Hare C., Ghadiri M., Murtagh M., Oram P., Haber R., Auto-granulation of fine cohesive powder by mechanical vibration, Procedia Engineering, 102 (2015) 72–80, DOI: 10.1016/j.proeng.2015.01.108.

Kwade A., Schulze D., Shwedes J. Determination of the Stress Ratio in Uniaxial Compression Tests—Part2, Powder Handling and Processing, 6 (1994) 199–203.

Hencky H., Über Einige Statisch Bestimmte Fälle Des Gleichgewichts In Plastischen Körpern, Zeitschrift für Angewandte Mathematik und Mechanik, 3 (1923) 241–251, DOI: 10.1002/zamm.19230030401.

Ishlinsky A.J., The axi-symmetrical problem in plasticity and Brinell test, Journal of Applied Mathematics and Mechanics (USSR), 8 (1944) 201–224.

Mawatari Y., Tatemoto Y., Noda K., Yamamura M., Kageyy H., Vibro-fluidization characteristics for size arranged agglomerates, Proc. of The 12th Int. Conf. on Fluidization—New Horizons in Fluidization Engineering Vancouver, Canada, May 13–18, (2007) 424–432.

Molerus O., Theory of yield of cohesive powders, Powder Technology, 12 (1975) 259–275, DOI: 10.1016/0032- 5910(75)85025-X.

Schulze D., Development and application of a novel ring shear tester, Aufbereitungstechnik, 35 (1994) 524–535.

Parrella L., Barletta D., Boerefijn R., Poletto M., Comparison of uniaxial compaction tester and shear tester for characterization of powder flowability, Kona Journal, 26 (2008) 178–189, DOI: 10.14356/kona.2008016.

Van Ommen J.R., Valverde J.M., Pfeffer R., Fluidization of nanopowders: a review, Journal of Nanoparticle Research, 14 (2012) 1–29, DOI: 10.1007/s11051-012-0737-4.

Author's short biography

Hamid Salehi Kahrizsangi

Hamid Salehi Kahrizsangi is a PhD student at the Department of Industrial Engineering, University of Salerno, Italy. He graduated from Lund University, Lund, Sweden, as a food engineer specialized in powder technology in 2012.

Diego Barletta

Diego Barletta is assistant professor of chemical engineering at the Faculty of Engineering of the University of Salerno. His research interests include powder flow from storage units, rheology of powders and biomass particulate solids, fluidization of cohesive powders assisted by vibrations and process systems engineering for renewable energy. He is the author of more 30 papers on refereed international journals and books on chemical engineering and of more than 50 papers for international conferences. He reviews papers for international journals and conferences on chemical engineering and powder technology.

Massimo Poletto

Massimo Poletto is professor of chemical engineering since December 2012 at the Department of Industrial Engineering. Since January 2011, he has served as the chairman of the degree programme board of chemical and food engineering. In the period 2008–2013, he served as the chairman of a working party of the European Federation of Chemical Engineering (EFCE) on "Mechanics of Particulate Solids" that he joined in 2004 as a delegate from the Italian Association of Chemical Engineering (AIDIC). He is a member of the editorial board of Chemical Engineering Research and Design, the official journal of IChemE and of EFCE. (ChERD, www.icheme.org/journals).

KONA Powder and Particle Journal No. 33 (2016) 296–303/Doi:10.14356/kona.2016013 Original Research Paper

Effects of Mixing Ratio of Binary Fine Particles on the Packing Density and Filtration Characteristics †

Kuo-Jen Hwang * and Iou-Liang Lin

[1] *Department of Chemical and Materials Engineering, Tamkang University, Taiwan*

Abstract

Binary fine particles were dispersed in glycerol aqueous solutions with different mixing ratios to study the effects of particle size distribution and fluid viscosity on the cake properties in dead-end filtration, such as average porosity, average specific filtration resistance and compressibility of cake. The average specific cake filtration resistance increases with increasing the fraction of small particles. However, the lowest cake porosity occurs under the volume fraction of large particles of 0.75. Comparing different methods for porosity estimations, model estimation is more accurate for those particles near pure composition, while simulation method is more suitable for moderate composition of particle mixtures. Furthermore, the cake porosity increases but the average specific cake filtration resistance decreases with increasing fluid viscosity. An 18 % porosity increase and a 30 % filtration resistance decrease are obtained when fluid viscosity increases from 1 to 10×10^{-3} Pa·s. The cake properties, such as the particle packing structure in the cake and the resulting filtration resistance, are affected not only by the particle size distribution but also by the fluid viscosity. The particle size distribution plays a much more important role on the cake compressibility than the fluid viscosity does.

Keywords: particle size distribution, microfiltration, cake properties, fluid viscosity, packing porosity, filtration.

1. Introduction

Microfiltration has been widely used for separating fine particles from liquids in various industrial processes. In such a filtration, how to enhance filtration rate and separation efficiency are the most important issues on process engineers concern. In general, the cake properties, such as porosity and specific filtration resistance, are the most important parameters affecting filtration performance. The cake properties are determined mainly by many factors, for instance, the particle size distribution, fluid rheology and operating conditions. Therefore, understanding the effects of particle size distribution and fluid viscosity on the cake properties is an essential step in grasping a filtration problem.

Tiller F.M. et al. (1972) proposed power-type empirical equations to correlate cake porosity or specific filtration resistance with solid compressive pressure. The cake compressibility could be indicated by the exponent of those empirical equations. Lu W.M. and Hwang K.J. (1993) employed a force balance model to discuss the critical friction angle for particle deposition on the cake surface in constant pressure filtration. The packing structure in cake could then be simulated using the friction angle under various conditions. When the critical friction angle was larger, the particles were more stable on the cake surface, the packing structure would be looser, and the cake porosity increased but the specific filtration resistance decreased. To discuss how the properties of cakes formed by dual-sized submicron particles affect the performance of cross-flow microfiltration, Hwang K.J. and Lin K.P. (2002) used packing theories of cavern and displacement effects to estimate the cake porosities with different particle compositions. Although the fluid flow effect in the tangential direction was ignored, the theoretical results agreed with the experimental data in the region near uniform sized particles.

The basic filtration equation was frequently used for estimating filtration flux based on the well-known Darcy's law, that is,

$$q = \frac{\Delta P}{\mu(\mathrm{R_c} + R_\mathrm{m})} = \frac{\Delta P}{\mu(w_\mathrm{c} \cdot \alpha_\mathrm{av} + R_\mathrm{m})} \tag{1}$$

where q is the filtration flux, ΔP is the filtration pressure, μ is the fluid viscosity, w_c is the cake mass, α_av is the average specific cake filtration resistance, and R_c and R_m are the filtration resistances of filter cake and medium,

† Received 7 June 2015; Accepted 4 August 2015
J-STAGE Advance published online 12 September 2015
[1] No.151, Yingzhuan Rd., Tamsui Dist., New Taipei City 25137, Taiwan
* Corresponding author: Kuo-Jen Hwang;
E-mail: kjhwang@mail.tku.edu.tw
TEL: +886-2-2621-5656 ext.2726 FAX: +886-2-2620-9887

respectively. According to this equation, the fluid viscosity is separated from cake filtration resistance. It implies that the cake properties are independent on the fluid flow behavior. The hypothesis is questionable because the particle packing is possible to be affected by the drag force exerted on the particles. This point will be discussed in this study.

Although the particle size distribution is believed an important factor affecting cake properties, few researchers devoted their efforts on the theoretical study of this issue. In this study, the effects of particle size distribution and fluid viscosity on the cake porosity and specific filtration resistance in dead-end microfiltration were studied. The cake properties under various conditions were estimated using theoretical models and simulation method, and were compared with experimental data.

2. Estimation of cake properties

2.1 Models

2.1.1 Cake porosity

Many models were derived for estimating the packing density of binary particles in the past 30 years (German, R.M., 1989), in which to consider the cavern and displacement effects are the simplest models for random packing. Cavern effect is used for the condition that few small particles are filled into the vacant space in a packed bed constructed by large particles. The packing porosity can then be estimated by a material balance (German R.M., 1989)

$$\varepsilon_{av} = \frac{\phi_L - 1 + \varepsilon_L}{\phi_L} \tag{2}$$

where ϕ is the volume fraction of particles, and the subscript L represents large particles. Another effect is considered that some small particles are replaced by few large particles in a packed bed constructed by most of small particles. The packing porosity in such a condition can also be estimated by a material balance (German R.M., 1989)

$$\varepsilon_{av} = 1 - \frac{1-\varepsilon_S}{1-\varepsilon_S \phi_L} \tag{3}$$

where the subscripts S represent small particles. Because both cake porosity and particle volume fraction are smaller than 1, the cakes formed by dual-sized particles have smaller porosity than that by uniform-sized, and the difference becomes more obvious when the composition is far distant from uniform. The lowest porosity can then be given from the intersection point of the curves plotted using Eqs. (2) and (3), that is,

$$\varepsilon_{av} = \varepsilon_s \cdot \varepsilon_L \tag{4}$$

2.1.2 Specific cake filtration resistance

According to Kozeny equation, the average specific filtration resistance of cake can be estimated using the following equation:

$$\alpha_{av} = \frac{kS_o^2 \cdot (1-\varepsilon_{av})}{\rho_s \cdot {\varepsilon_{av}}^3} \tag{5}$$

where k is the Kozeny constant, and S_o is the specific surface area of particles. The theoretical Kozeny constant is 5.0 for a compact packed bed constructed by smooth spheres. For a random packing, the relationship between Kozeny constant and packing porosity can be derived theoretically using the free cell model (Happel J. and Brenner H., 1965) as:

$$k = \frac{2\varepsilon^3}{(1-\varepsilon)\cdot\left\{\ln\left[\frac{1}{(1-\varepsilon)}\right] - \frac{\left[1-(1-\varepsilon)^2\right]}{\left[1+(1-\varepsilon)^2\right]}\right\}} \tag{6}$$

The mean particle diameter, $d_{p,av}$ for dual-sized particles can be calculated by the primary sizes and the volume fractions of particles, that is,

$$\frac{1}{d_{p,av}} = \frac{\phi_L}{d_{p,L}} + \frac{\phi_S}{d_{p,S}} \tag{7}$$

Because the specific surface area exactly equals $6/d_p$ for a spherical particle, the value of S_o for a particle mixture can be estimated using the mean particle diameter as following:

$$S_o = \frac{6}{d_{p,av}} \tag{8}$$

Once the variables in Eq.(5), such as k, S_o and ε_{av}, are known, the average specific filtration resistance of cake can be calculated.

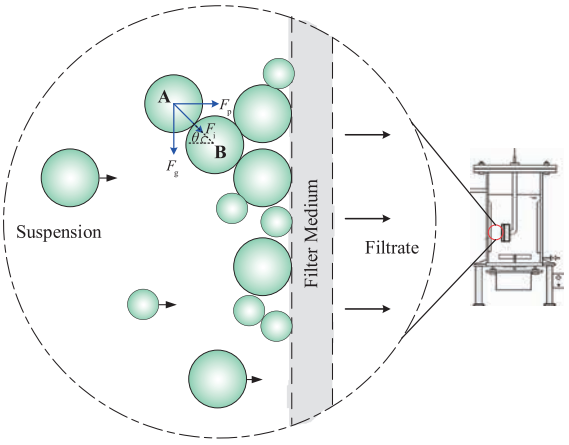

Fig. 1 Forces exerted on a depositing particle in microfiltration.

2.2 Numerical simulation

A numerical method for simulating the particle packing structure and cake porosity in dead-end filtration was proposed by Lu W.M. and Hwang K.J. (1993). It was modified to be used for the system of this study. Refer to **Fig. 1**, the external forces exerted on a depositing particle, Particle A, include the drag force due to permeate flow, F_p, the net inter-particle force, F_i, and the net gravitational force, F_g. The drag force can be estimated using the modified Stokes law (Lu W.M. and Hwang K.J., 1993). The inter-particle force can be estimated using the DLVO theory based on a pair-wise assumption. According to this theory, the net inter-particle force is a summation of van der Waals force and electrostatic force (Hwang K.J. et al., 1997).

The Newton's second law of motion is integrated to estimate the velocity and the displacement of particle migration during filtration. Particle migrations are simulated until they can deposit stably. The details can be referred to Lu W.M. and Hwang K.J. (1993, 1995).

3. Materials and methods

Two uniform-sized polymethyl methacrylate (PMMA) spherical particles with a density of 1210 kg/m^3 were used in experiments. The particles were purchased from Soken Co., Japan. Their density was 1210 kg/m^3, and their mean diameters were 0.45 μm (Ca.#: MP-1000) and 5.0 μm (Ca.#: MX-500), respectively. Their particle size distributions were measured using a HORIBA LA-300 laser particle size analyzer and are shown in **Fig. 2**. Propane-1,2,3-triol (glycerol) with a density of 1255 kg/m^3 and purity of 99.5 % in volume was purchased from Fisher Scientific Co. in USA (Ca.#: G33-4). Different amounts of glycerol were added into de-ionized water to prepare aqueous solutions with different viscosities. The fluid viscosity was measured using a viscometer (Brookfield LVDV-II CP, USA). The particle suspensions with a concentration of 3 kg/m^3 were prepared by dispersing particles into those aqueous solutions under different particle mixing ratios. The particle size distributions were then adjusted by different mixing ratios of the dual-sized particulate samples. The pH and temperature of the suspension were kept at 7.0 and 20 °C, respectively. The zeta potential of particles under such a condition was measured as –25 mV. A membrane manufactured by ADVANTEC Co. in Japan (Ca.#: A010A142C) was used in filtration as filter medium. The membrane was made of mixed cellulose ester, its mean pore size was 0.1 μm, and its filtration resistance was 2.26×10^{11} m^{-1} under a filtration pressure of 2×10^4 N/m^2.

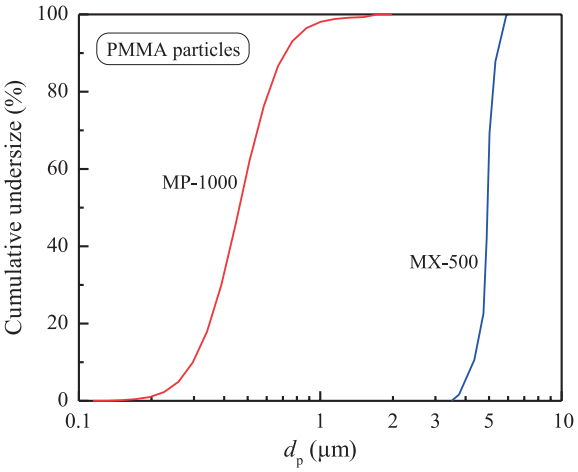

Fig. 2 Size distributions of particles used in this study.

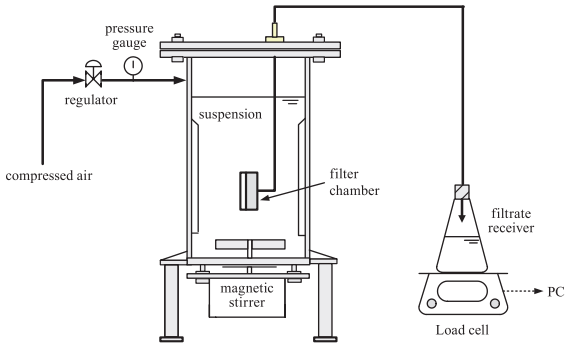

Fig. 3 Schematic diagram of the dead-end microfiltration system.

Dead-end microfiltration experiments were performed using a bomb filter shown in **Fig. 3**. The filtration area in the filter chamber was 8.04×10^{-4} m^2. Suspension was prepared in the filter and prevented particle settling using a magnetic stirrer. The filter chamber was installed to orient to the filter wall, as shown in **Fig. 3**, to prevent the obstruction or destruction of cake formation by stirring. The filtration pressure was supplied by a compressed air, adjusted using a regulator, and indicated by a pressure gauge. The filtrate was received into a flask and weighed using a load cell. The data of filtrate weight was transferred to volume and recorded on a personal computer during the whole course of filtration. An orifice plate was installed in the filter chamber to indicate the cake growth. When the growing cake surface reached the orifice plate, the filtration area decreased suddenly, and the tangent slope of the filtration curve of dt/dv vs. v increased drastically. Therefore, the average cake porosity could be calculated using the received filtrate volume based on a mass balance, and the average specific cake filtration resistance was determined by the tangent slope of the filtration curve before the sudden change.

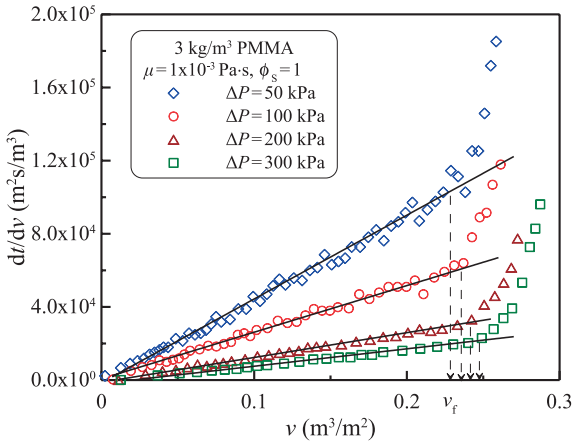

Fig. 4 Filtration curves of d*t*/d*v* vs. *v* under various filtration pressures.

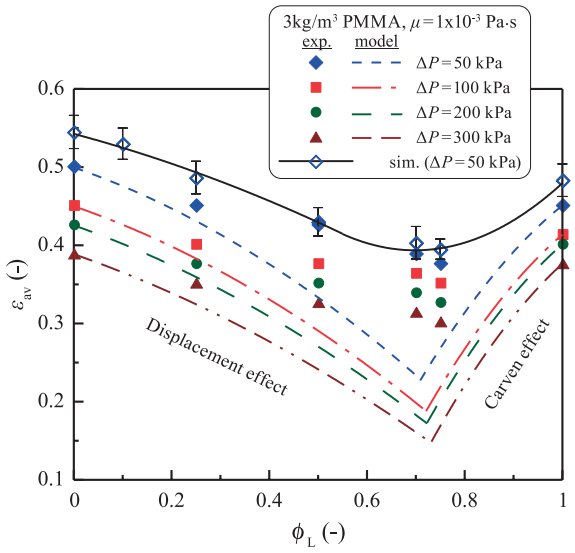

Fig. 5 Comparisons of cake porosity among model estimations, simulated results, and experimental data for various mixing fractions of large particles.

4. Results and discussion

Fig. 4 shows the filtration curves of d*t*/d*v* versus *v* under various filtration pressures for uniform PMMA particle with a mean size of 0.4 μm. The dispersion medium was de–ionized water with a viscosity of 1×10^{-3} Pa·s. The filtration curves have the same trend; each of them can be divided into two parts. The first part is a straight line. This implies that the average specific cake filtration resistance is constant during filtration. When the filter chamber is filled with cake, the received filtrate volume reaches v_f, and the tangent slope of the filtration curve suddenly increases due to the decrease in filtration area. The average specific cake filtration resistance is then calculated by the slope of the straight line before the transition point, as those shown in the figure. The average cake porosity can be obtained using the mass balance at the transition point because the cake volume is known. Comparing the values of v_f under various pressures, a smaller v_f value under lower pressure indicates a higher cake porosity in such condition. Furthermore, because the value of d*t*/d*v* is the reciprocal of filtration flux, the curves shown in **Fig. 4** also reveal that a lower filtration pressure results in a lower filtration flux.

Fig. 5 shows the comparisons of cake porosity among the experimental data, simulated results and model calculated results under various large particle fractions and various filtration pressures. The dispersed medium was de-ionized water with a viscosity of 1×10^{-3} Pa·s. The values of cake porosity of dual-sized particles are lower than those of mono-sized under a given filtration pressure, and the lowest cake porosity occurs around the large particle fraction $\phi_L = 0.75$. When a few large particles exist in a small particle packing, some original packing positions of small particles are replaced by large particles, and the cake porosity due to this "displacement effect" can be estimated using Eq. (3). The cake porosity decreases with increasing the volume fraction of larger particles. On the other hand, when a small portion of small particles packs into a cake constructed by large particles, small particles may pack into the void space among large particles, and the cake porosity due to the "carven effect" can be estimated using Eq. (2). This effect causes the cake porosity decreases with increasing the fraction of small particles. The curves calculated using Eqs. (2) and (3) show that the lowest cake porosities occurring at $\varepsilon_L\varepsilon_S$ where is the intersection point of those two curves, i.e, Eq. (4). These results agree qualitatively with the experimental data. However, the estimated results are always lower than experimental data, and obvious deviations between them can be found under moderate fractions of large (or small) particles. The maximum deviation is as high as 30 % occurring at the lowest cake porosity. This demonstrates that the models of cavern and displacement effects can be used properly only when a few different-sized particles are added into a cake formed by uniform-sized particles. Those models were originally used for estimating the random packing of particles under gravity. All particles have opportunities to migrate to reach stable positions. This is similar to the conditions under high filtration rates. However, when filtration rate is not high enough, the depositing particles may have no enough drag force to push them to form a compact cake. Thus, the packing porosity increases with decreasing filtration rate. This is therefore another reason why the deviation between the model estimations and experimental data becomes larger for a more compact cake. Furthermore, comparing the cake porosities under various filtration pressures at a fixed volume fraction of large particles, an increase in filtration pressure leads to lower cake porosity. It is attributed to more

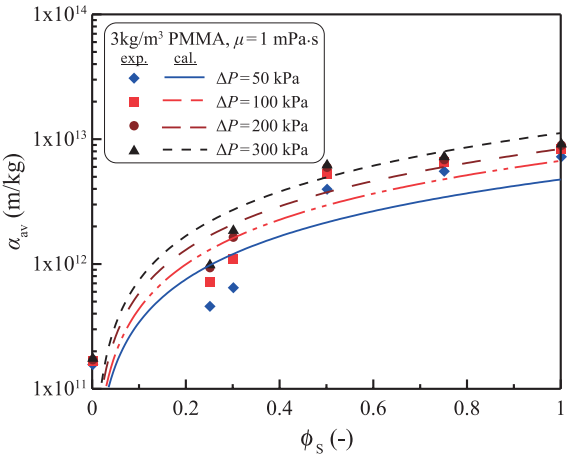

Fig. 6 Comparisons of average specific cake filtration resistance between calculated results and experimental data for various mixing fractions of small particles.

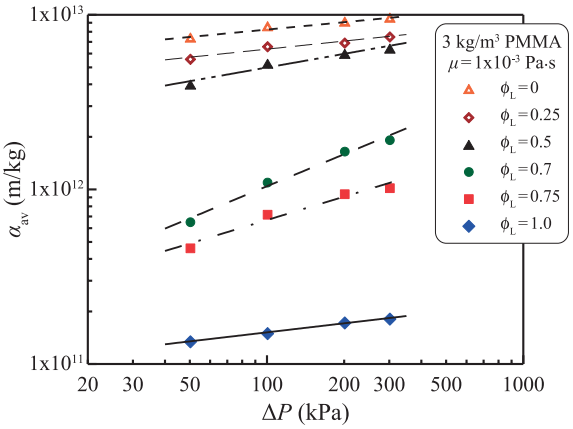

Fig. 7 Plots of α_{av} versus ΔP under various mixing fractions of large particles.

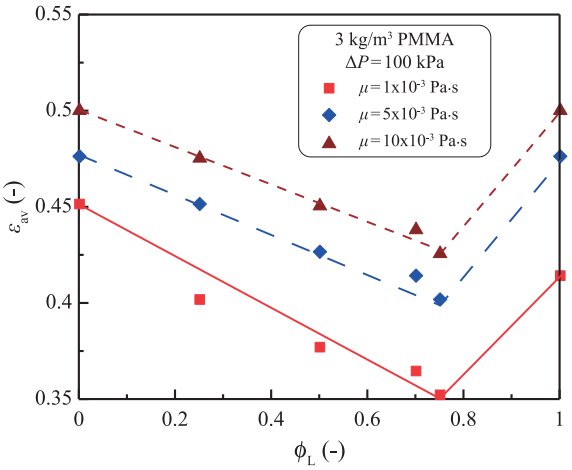

Fig. 8 Effects of fluid viscosity and particle mixing fraction on the average cake porosity.

severe cake compression under a higher pressure. Another method for cake porosity estimation is computer simulation. Although the simulation results are scattered, the trend of the simulated curve is much closer to that of experimental data. Comparing those estimations obtained by different methods, model estimation is more accurate for those particles near pure composition, while simulation method is more suitable for moderate composition of particle mixtures, especially for the compositions to result in the lowest cake porosity.

Fig. 6 shows the effects of small particle fraction, ϕ_S, and filtration pressure, ΔP, on the average specific cake filtration resistance, α_{av}. The theoretical curves were calculated by substituting the calculated average cake porosity into Eq. (5), in which the values of Kozeny constant and specific surface area of particles were estimated using Eqs. (6)–(8), respectively. Comparing those factors affecting specific filtration resistance, specific surface area and particle size play the most important roles. The mean particle size decreases from 5 to 1 μm as ϕ_S value increases from 0 to 0.3. However, there has only a 50 % decrease in the mean particle size when ϕ_S increases from 0.3 to 1.0. Therefore, the value of α_{av} increases very rapidly with increasing ϕ_S when ϕ_S value is smaller than 0.3. The slight increase in cake porosity and decrease in mean particle size with ϕ_S cause the α_{av} values to become nearly invariant when $\phi_S > 0.5$. The calculated results agree with experimental data except for the overestimations occurring around $\phi_S = 0.3$. This is attributed to the marked underestimations of cake porosity at that particle mixing fraction, as shown in **Fig. 5**.

The experimental data of average specific cake filtration resistance are plotted against filtration pressure for different large particle fractions in logarithm scales in **Fig. 7**. The data can be regressed to a straight line for a given particle mixing fraction. This reveals that the relationship between α_{av} and ΔP follows a power function proposed by Tiller et al. (1980). The α_{av} value increases with increasing pressure and decreasing the fraction of large particles. The α_{av} value of pure small particles is *ca* two order-of-magnitudes higher than that of pure large particles under a given pressure. This is because the α_{av} value is proportional to the inverse square of particle size. According to the Tiller's empirical equation, the slope of a curve represents the cake compressibility. Comparing the slopes of the curves shown in the figure, the cake compressibility is very low (around 0.07) for uniform-sized particles and shows the highest value around 0.55 occurring at the fraction of large particles of 0.7. This result indicates that the cake compressibility is sensitive to particle size distribution and will be discussed in more detail later.

The viscosity of dispersed fluid was adjusted by adding different amounts of glycerol into de-ionized water. The aqueous solutions were measured as Newtonian fluids, and the values of viscosity were 10 and 5×10^{-3} Pa·s for

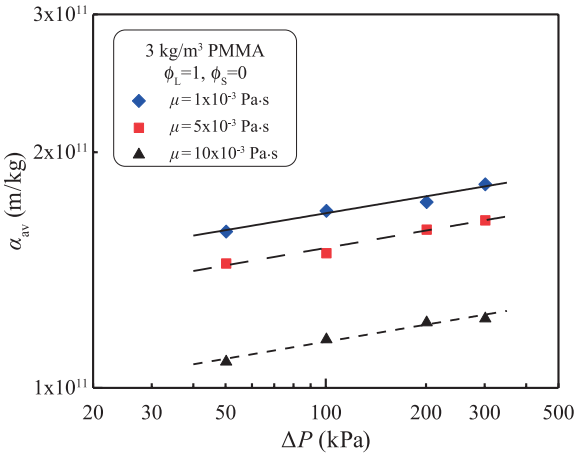

Fig. 9 Plots of α_{av} versus ΔP under various fluid viscosities.

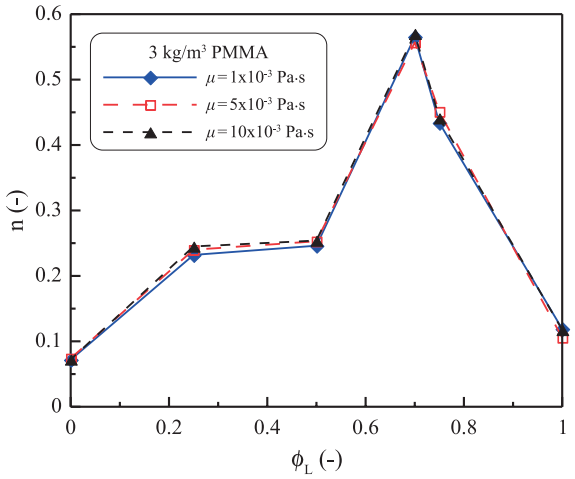

Fig. 10 Effects of particle mixing fraction and fluid viscosity on the cake compressibility.

53 and 45 vol% glycerol solutions, respectively. The same viscosity values measured before and after filtration experiments demonstrate that no glycerol molecule was retained on or adsorbed onto the particles, cake or filter media during filtration. **Fig. 8** shows the effects of fluid viscosity and volume fraction of large particles on the average cake porosity. The curve trend for each fluid viscosity is similar to that in **Fig. 5**. The values of cake porosity are higher for uniform-sized particles, and a minimum cake porosity occurs at $\phi_L = 0.75$. An increase in fluid viscosity leads to higher cake porosity. An 18 % porosity increase is obtained as fluid viscosity increases from 1 to 10×10^{-3} Pa·s. This is because a higher fluid viscosity causes a larger drag force exerted on the depositing particles as well as larger surface friction between particles. As a result, the particle packing structure in a filter cake is looser.

Fig. 9 shows the effects of fluid viscosity and filtration pressure on the average specific cake filtration resistance for pure large particles. The relationship between α_{av} and ΔP can be regressed to straight lines, *i.e.*, power-type Tiller's empirical equations, the same as those mentioned in **Fig. 7**. Because the cake porosity is lower (a more compact cake) for a dispersed fluid with lower viscosity, the α_{av} value is therefore higher. A 30 % filtration resistance decrease is obtained when fluid viscosity increases from 1 to 10×10^{-3} Pa·s. This magnitude variation in α_{av} can be reasonably explained by the particle packing structure for a given particle size distribution. Thus, the α_{av} value is not a sole function of particles themselves; but it is also affected by the physical properties of dispersed fluid, e.g., fluid viscosity. This result is different from those previous inferences in which the resistance caused by dispersed medium, fluid viscosity, is separated from cake resistance term, e.g., α_{av}. In conclusion, the influence of fluid properties on the overall filtration resistance cannot be separated to a single term of fluid viscosity. The cake properties, at least the particle packing structure in the cake and the resulting filtration resistance, are also affected by fluid viscosity. However, the similar slopes of the curves shown in the figure indicate that the cake compressibility is similar and independent of fluid viscosity.

The cake compressibility can be obtained from the line slope plotted by α_{av} vs. ΔP in logarithm scales, as those shown in **Figs. 7** and **9**. The effects of particle mixing fraction and fluid viscosity on the cake compressibility are shown in **Fig. 10**. The particle size (distribution) plays a much more important role on the cake compressibility than the fluid viscosity does. Although the average specific cake filtration resistance was affected obviously by the fluid viscosity, the cake compressibility was nearly constant for a given particle mixing fraction. For those uniform-sized conditions, the values of cake compressibility are as low as 0.1; and the cakes are only slightly compressible. The cake compressibility becomes higher in the conditions of particles with size distributions. This is because particles have more opportunity to pack into the voids to form more compact structure during filtration. The highest cake compressibility is *ca* 0.56 occurring at the mixing fraction of large particles of 0.70. This particle mixing fraction is a little different from that resulting in the lowest cake porosity ($\phi_L = 0.75$, as those shown in **Fig. 8**). It is because the factors affecting the specific cake filtration resistance is not only the cake porosity but also the particle size distribution.

5. Conclusions

The effects of particle size distribution, fluid viscosity and filtration pressure on the average cake porosity, average specific cake filtration resistance, and cake compressibility in dead-end constant pressure microfiltration were

studied. An increase in filtration pressure led to lower average cake porosity and higher specific cake filtration resistance. The effect of particle mixing fraction on the cake porosity was explained using packing models, such as cavern and displacement effects. The lowest cake porosity occurred under the volume fraction of large particles of 0.75. Model estimation for cake porosity was more accurate for those particles near pure composition, while simulation method was more suitable for moderate composition of particle mixtures, especially for the compositions resulting in the lowest cake porosity. The average specific cake filtration resistance increased with increasing the fraction of small particles, especially for low fraction of small particles. Furthermore, the cake properties were affected by fluid viscosity. The cake porosity increased but the average specific cake filtration resistance decreased with increasing fluid viscosity. An 18 % porosity increase and a 30 % filtration resistance decrease were obtained when fluid viscosity increases from 1 to 10×10^{-3} Pa·s. This was attributed to the larger surface friction causing by higher viscous flow. The cake properties, such as the particle packing structure in the cake and the resulting filtration resistance, were indeed affected not only by particle size distribution but also by fluid viscosity. The particle size distribution played a much more important role on the cake compressibility than the fluid viscosity does, and the highest cake compressibility occurred approximately at the particle mixing fraction resulting in the lowest cake porosity.

Acknowledgements

The authors wish to express their sincere gratitude to the Ministry of Science and Technology of the Republic of China for its financial support (Grant number: MOST 103-2221-E-032-057-MY3).

Nomenclature

d_p particle diameter (μm)

F_g net gravitational force (N)

F_i net inter-particle force (N)

F_p drag force due to permeate flow (N)

k Kozeny constant (–)

ΔP filtration pressure (Pa)

q filtration flux (m^3/m^2 s)

R_c filtration resistance of cake (m^{-1})

R_m filtration resistance of medium (m^{-1})

S_o specific surface area of particles (m^2/m^3)

t filtration time (s)

v filtrate volume per unit filtration area (m^3/m^2)

v_f filtrate volume per unit filtration area at which the growing cake surface reached the orifice plate (m^3/m^2)

w_c cake mass (kg/m^2)

α specific filtration resistance of cake (m/kg)

ε cake porosity (–)

ϕ volume fraction of particles (–)

μ fluid viscosity (Pa·s)

Subscripts

av average cake property

L large particle

S small particle

References

German R.M., Particle Packing Characteristics, Chap. 6, Metal Powder Industries Federation, Princeton, New Jersey, USA, 1989.

Happel J., Brenner H., Low Reynolds Number Hydrodynamics, Englewood Cliffs, NJ, Prentice Hall, 1965.

Hwang K.J., Yu M.C., Lu W.M., Migration and deposition of submicron particles in crossflow microfiltration, Separation Science and Technology, 32 (1997) 2723–2747.

Hwang, K.J., Lin, K.P., Cross-Flow Microfiltration of dual-sized submicron particles, Separation Science and Technology, 37 (2002) 2231–2249.

Lu W.M., Hwang K.J., Mechanism of cake formation in constant pressure filtrations, Separation Technology, 3 (1993) 122–132.

Lu W.M., Hwang K.J., Cake formation in 2-D cross-flow filtration, A.I.Ch.E. Journal, 41 (1995) 1443–1455.

Tiller F.M., Haynes S., Lu W.M., The role of porosity in filtration VII Effect of side-wall friction in compression-permeability cells, A.I.Ch.E. Journal, 18 (1972) 13–20.

Author's short biography

Kuo-Jen Hwang

Dr. Kuo-Jen Hwang is now a Professor at Tamkang University, Taiwan. After getting his PhD degree in National Taiwan University in 1992, he moved to the Department of Chemical Engineering at Tamkang University, as an Associate Professor. He became a full professor at Tamkang University in 1997. He was appointed as the Chairman of the Department of Chemical Engineering, Tamkang University from 1997 to 2001.

His research interests focus on solid-liquid separation and powder technology, especially for microfiltration of fine and soft particles, and hydrocyclone for separation and classification of fine particles. He has published over 100 papers in peer reviewed journals and 150 conference papers. He is also the Chairmen of the Taiwan Filtration and Separations Society and the International Delegates on Filtration since 2012.

Iou-Liang Lin

Mr. Iou-Liang Lin received his MS degree at the Department of Chemical and Materials Engineering, Tamkang University in 2009. He is a System Engineer in INNOLUX Corporation, Taiwan now.

KONA Powder and Particle Journal No. 33 (2016) 304–309/Doi:10.14356/kona.2016015 Original Research Paper

Improving Dispersion of Bacterial Endospores for Enumeration †

Vijay B. Krishna [1a], Jue Zhao [2b], Smithi Pumprueg [2c], Ben L. Koopman [2] and Brij M. Moudgil [1*]

[1] *Particle Engineering Research Center, Department of Materials Science and Engineering, University of Florida, USA*
[2] *Particle Engineering Research Center, Department of Environmental Engineering Sciences, University of Florida, USA*

Abstract

Precise enumeration of spores is crucial for accurate evaluation of spore survival in the presence of inactivating agents or extreme environmental conditions. Bacterial endospores tend to agglomerate, leading to low estimates of spore numbers. We have shown that addition of SDS to diluent used in counting bacterial endospores better disperses spores, leading to a ten-fold increase in counts. We attribute this effect to steric hindrance and electrostatic repulsion between micellar structures of SDS adsorbed at spore surfaces. We have also demonstrated that use of a low surface energy material (Teflon) improves spread-plate counts, an effect we attribute to lesser hold-up of liquid on Teflon versus glass.

Keywords: spore, enumeration, plating, agglomeration, surfactant, teflon

1. Introduction

Bacterial endospores have received considerable attention in the last few years. As a result of the anthrax attacks in 2001 (CDC, 2006), researchers are designing more potent and faster acting sporicidal agents. Survival of bacterial endospores is being investigated under extreme conditions of pressure, temperature and radiation, such as those encountered in outer space (Mastrapa et al., 2001; Moeller et al., 2008; Moeller et al., 2007; Nicholson et al., 2000). Precise enumeration of spores in a given sample is crucial for accurate evaluation of spore survival in the presence of inactivating agents or extreme environmental conditions. *Bacillus subtilis* and *Bacillus cereus* are common bacterial species employed for such investigations. Although *B. cereus* spores have an outer coat called exosporium, similar to *B. anthracis*, both *B. cereus* and *B. subtilis* (lacking exosporium) are employed as surrogates for *Bacillus anthracis* (Ivanova et al., 2003; Krishna V. et al., 2005; Krishna Vijay B., 2007; Nicholson et al., 2003; Read et al., 2003; Vohra et al., 2005; Vohra et al., 2006).

Plate counts are the primary means (gold standard) of enumerating viable spores and other techniques, such as optical microscopy or particle counting method, utilize the plate count method to verify the concentration of viable spores. Spores must be maintained in a dispersed state prior to plating in order to achieve accurate and reproducible counts. Bacterial endospores, particularly spores of *B. cereus*, are hydrophobic and thus tend to agglomerate (Peng et al., 2001; Ronner et al., 1990), leading to low estimates of spore numbers. Inaccurate counting can lead to misleading conclusions, particularly in spore inactivation studies. Agglomeration as a potential cause of inaccurate spore enumeration has been largely ignored. In the last ten years, more than 1000 papers have been published on inactivation of bacterial spores, however, only ten studies have considered agglomeration of spores during inactivation, and none has taken into account the agglomeration of spores during the enumeration step.

In the spread-plating method, which is one of the most widely used plate counting approaches, the spore suspension must be spread uniformly over the surface of the agar plates. The spreader material employed for spread-plating of spores is crucial in achieving uniform and reproducible counts (Koch, 1981). Use of a Teflon coating for the spreader was recommended by Koch because of its low affinity for bacterial cells (Koch, 1981). None of the literature reviewed mentions the type of spreader material

† Received 21 August 2015; Accepted 27 August 2015
J-STAGE Advance published online 30 September 2015
[1,2] University of Florida, P.O. Box 116135, Gainesville, Florida 32611, USA
Present address:
[a] Department of Biomedical Engineering, Lerner Research Institute, Cleveland Clinic, USA, Cleveland, Ohio 44195, USA
[b] City of Grand Island Wastewater Treatment Plant, USA, Grand Island, Nebraska 68801, USA
[c] Vigo Engineering Co. Ltd., Rayong, 21150, Thailand
* Corresponding author: Brij M. Moudgil;
E-mail: bmoudgil@perc.ufl.edu
TEL: +1-352-846-1194 FAX: +1-352-846-1194

employed for spread-plating.

We hypothesize that addition of surfactant to enhance dispersion of spores in suspension will significantly improve spore enumeration. Non-ionic surfactants, such as Tween80 are sometimes used for dispersion of bacteria. However, these are not suitable as dispersion aids for spores in inactivation studies as Tween80 can induce germination of spores thereby exposing the susceptible germinating spores to inactivating agents present along with spores (Parker et al., 1968). Similarly, cationic surfactants can induce germination and inactivate spores, and, thus, are not suitable as dispersion aids for spore enumeration (Pinzon-Arango et al., 2009). Anionic surfactants at lower concentrations are not known to induce germination or inactivate spores (Grund et al., 1982). Sodium dodecyl sulfate (SDS), an anionic surfactant used in washing of spores treated with lysozyme during purification, was employed as a model surfactant in the present study. Because of its anionic nature, SDS can reduce aggregation by enhancing electrostatic repulsion between spores. The presence of surfactant structures (e.g., micelles) on spore surfaces can act as a barrier to close approach of other particles, further limiting agglomeration. Teflon and glass spreaders were employed to investigate the effect of spreader material. Deionized water and phosphate buffered solution (PBS) were employed for spore storage and serial-dilution.

2. Materials and methods

2.1 Chemicals

Chemicals were obtained from Fisher Scientific (Hampton, NH), except as noted. Solutions and deionized water for washing bacterial suspensions were autoclaved before use. Lysozyme and phenylmethylsulfonyl fluoride (PMSF) solutions were prepared using autoclaved buffers. Lysozyme powder was stored at 4 °C and lysozyme solution was prepared from powder for each use. The PMSF powder was stored at 4 °C. PMSF solution was prepared by dissolving the powder in 2 to 3 mL (the minimum possible) ethanol. TEP buffer containing 50 mM Tris.Cl at pH 7.2, 10 mM EDTA, and 2 mM PMSF was prepared fresh for each use. Phosphate buffered saline (PBS) was prepared by combining 10.9 g of Na_2HPO_4, 3.2 g of NaH_2PO_4, 90 g of NaCl and deionized water to prepare 1 L of solution. The solution was autoclaved and diluted ten times prior to use.

2.2 Culturing of *B. cereus* spores

Culture media was prepared according to the American Society for Testing and Materials ASTM E2111-00 standard (ASTM, 2001) using Difco Columbia broth powder. *Bacillus cereus* (ATCC 2) colonies from Difco Tryptic soy agar plates were inoculated in 500 mL Erlenmeyer flasks containing 100 mL of $1/10^{th}$ strength culture media fortified with 0.1 mM $MnSO_4.2H_2O$. The flasks were capped with foam plugs and wrapped in aluminum foil. The inoculated growth media was incubated for 72 h at 35 ± 2 °C on an orbital incubator-shaker (Model C24, New Brunswick Scientific, Edison, NJ) with a speed of 200 rev/min.

2.3 Purification of *B. cereus* spores

The *B. cereus* spores were purified by lysozyme method according to Xue and Nicholson (1996). Culture was centrifuged at 10,000 × g for 10 min at 4 °C and the pellet was resuspended in 20 mL of 1 M KCl/0.5 M NaCl. This suspension was centrifuged and the pellet was resuspended in 20 mL of 50 mM Tris.Cl (pH 7.2) containing 50 μg/mL lysozyme and incubated at 37 °C for 60 minutes. The suspension was then washed with, respectively, 1 M NaCl, deionized water, 0.05 % (w/v) SDS, TEP buffer, and deionized water (three times). The washed suspension was heat shocked at 80 ± 2 °C for 15 min, followed immediately by cooling to 4 °C. Spores were stored at 4 °C in deionized water for no more than one week. The purity (proportion of spores relative to the total number of spores and cells) of the final suspension was 99 %.

2.4 Counting

The spore suspension was serially diluted (ten-fold) and aliquots of the three highest dilutions (either dilution numbers 2, 3 and 4 or 3, 4 and 5) were plated in triplicate on Tryptic soy agar in 100 × 25 mm Petri dishes by the spread-plate technique. The plates were then incubated at 37 °C for 12–16 hours and then the colonies were counted. Counts between 30 and 300 were used for data analysis (Koch, 1981).

2.5 Statistical tests

Hypothesis testing for the significance of differences between two means was based on two-tailed Student's *t* test (Sokal et al., 1997). Post-hoc testing of the significance of the differences between three or more means was carried out by Tukey's test (Berthouex et al., 1994).

2.6 Surface tension measurements

Surface tension was used to estimate the critical micelle concentration of SDS in phosphate buffered saline. Surface tension was determined by the Wilhelmy plate technique,

which measures the maximum force required to pull a vertical platinum plate from solution at the liquid-air interface. Measurements were made at SDS concentrations of 0, 0.25, 0.50, 0.75, 1.00, 1.25, 1.50, 5.00 and 10.00 mM in PBS at 24 ± 2 °C.

2.7 Particle counting

Spores suspended in PBS with and without SDS were counted with a Multisizer™ 3 Coulter Counter® (Beckman Coulter, Inc., Fullerton, CA) using a 5 µm orifice. The spores were serially diluted to obtain a final concentration of 10^3 CFU ml^{-1} in the sample holder.

2.8 Zeta potential

Zeta potential of *B. cereus* spores in deionized water (pH = 5.8) was determined with a Brookhaven ZetaPlus (Brookhaven Instruments Corporation, Holtsville, NY).

3. Results and discussion

3.1 Effect of suspending media and surfactant

Average colony counts of *Bacillus cereus* spores plated in triplicate, with DI water and PBS as diluents, are given in **Fig. 1**. The colony counts with DI water were two times higher than the counts obtained with PBS. Since the starting material (bacterial spore suspension) was the same in the various trials, an increase in spore counts is indicative of a lesser degree of agglomeration. Thus the lower counts obtained with PBS versus distilled water suggest a higher extent of spore agglomeration in the PBS. *B. cereus* spores have very low zeta potential (–11 mV in DI water) compared to bacteria (–40 mV) (Li et al., 2004; Peng, Tsai and Chou, 2001) and, thus, are more susceptible to changes in ionic strength of diluent. The high ionic strength (0.2 M) of PBS can effectively screen the net negative charge and aid in agglomeration of spores.

Sodium dodecyl sulfate (SDS) was added to PBS for the purpose of improving the dispersion of spores. **Fig. 2** shows the plot of surface tension as a function of SDS concentration. The critical micelle concentration (the concentration at which surfactant molecules self-assemble into micelles) for SDS in phosphate buffered saline was found to be 1 mM, which is close to the reported value of 0.83 mM at 0.2 M NaCl (Rosen, 2004). The CMC for SDS in DI water is 8 mM (Rosen, 2004). Thus, the beneficial effect of SDS is achieved in PBS with a much lower concentration of SDS (e.g., 1 mM) than would be required for DI water. The effect of SDS concentration on colony counts with PBS as diluent is shown in **Fig. 3**. Significant improvement is obtained at one-half the critical micelle concentration (CMC). Further improvement was observed at a concentration equal to twice the CMC. Counts achieved in PBS with 2 mM SDS were much higher than

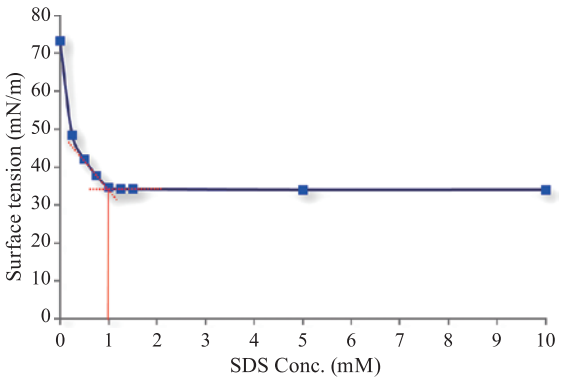

Fig. 2 Estimation of critical micelle concentration for sodium dodecyl sulfate in phosphate buffered saline. The error bars are too small to be seen.

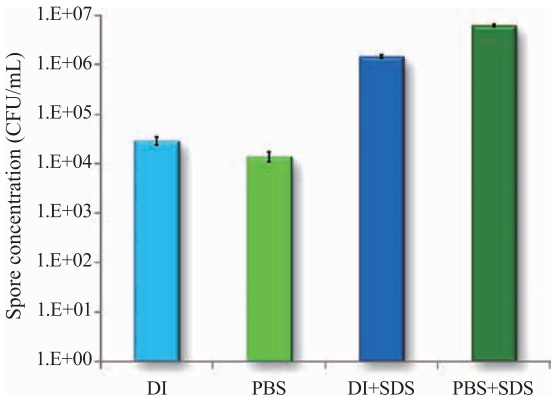

Fig. 1 Mean colony counts obtained with deionized water (DI) and phosphate buffered saline (PBS) without and with 2 mM sodium dodecyl sulfate (SDS) as diluents. (Means are significantly different at alpha = 0.01)

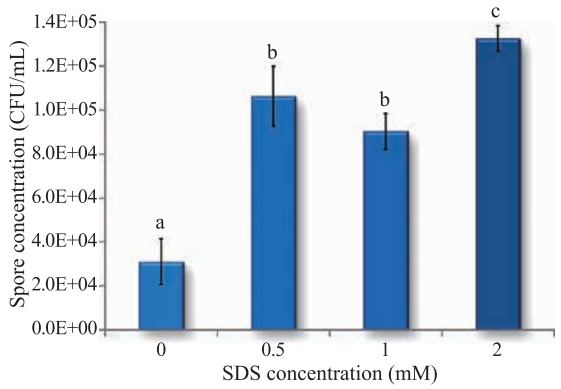

Fig. 3 Effect of sodium dodecyl sulfate concentration on colony counts with phosphate buffered saline as diluent. Means with different letters are significantly different at alpha = 0.05.

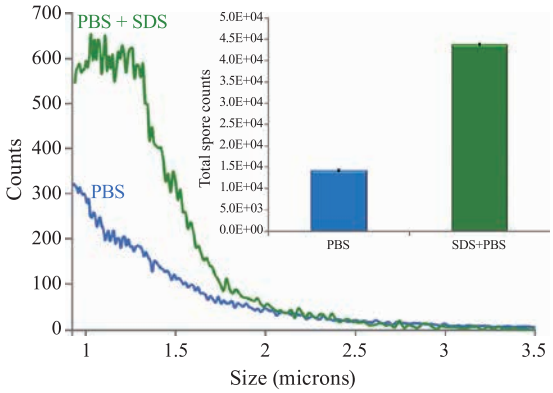

Fig. 4 Effect on particle counts of sodium dodecyl sulfate (SDS) addition (2 mM final concentration) to phosphate buffered saline (PBS). The inset figure shows the total spore counts for SDS and SDS + PBS diluents. The error bars are too small to be seen.

counts achieved in DI water with 2 mM SDS (**Fig. 1**).

Enhanced dispersion with SDS addition was verified by particle counts (**Fig. 4**). In the presence of SDS, a peak in the concentration of *B. cereus* spores, as indicated by the measured count frequency, occurred in the range of 1–1.5 μm. Without SDS, counts were generally lower and no peak was observed. Since the length of *B. cereus* spores is in the range of 0.95–1.5 μm, it is apparent that much higher numbers of individual spores are found in the presence of SDS. Since the outer protein coats of spores have positively and negatively charged sites as well as hydrophobic sites, it is possible that micelles or hemi-micelles of an anionic surfactant such as SDS can adsorb on spore surfaces and inhibit agglomeration by steric hindrance and electrostatic repulsion. The observation of higher spore counts in the presence of SDS supports this conjecture.

3.2 Effect of spreader material

Compounding errors in counting due to incomplete spore dispersion is the potential for liquid hold-up by the spreader. A thinner film of spore suspension will adhere to Teflon than to glass because of Teflon's lower surface energy (20 vs. 47 mN m^{-1}). Thus, with Teflon, there will be a smaller hold-up volume of spore suspension remaining on the spreader when it is removed from the agar surface. Indeed, significantly higher counts and more consistent counts were obtained with a Teflon spreader compared to a glass spreader, with or without SDS present (**Table 1**). However, addition of SDS to the diluent increased the spore counts ten-fold with either spreader material. The combination of a Teflon spreader and SDS amended diluent provided the highest counts.

Table 1 Effect of spreader material on spore counts

Spreader Material	PBS		PBS + 2 mM SDS	
	Mean* (CFU)	CV	Mean* (CFU)	CV
Glass	2.4×10^5	18 %	5.2×10^6	20 %
Teflon	5.0×10^5	17 %	7.5×10^6	5 %

* Means were significantly different at $\alpha = 0.05$; one-tailed *t*-test.

4. Conclusions

We have shown that agglomeration is a significant problem in enumeration of *B. cereus* spores. An anionic surfactant was successful in dispersing spores and increasing the spore counts. The adherence of liquid to the spreader is another source of error in spread-plate counting. This problem can be ameliorated by use of a low surface energy material, such as Teflon, for the spreader.

Acknowledgments

The authors acknowledge the financial support of the Particle Engineering Research Center (PERC) at the University of Florida, the National Science Foundation (NSF Grant EEC-94-02989), and the Industrial Partners of the PERC for support of this research. Any opinions, findings and conclusions or recommendations expressed in this material are those of the author(s) and do not necessarily reflect those of the National Science Foundation. Experiments were carried out at the University of Florida's Water Reclamation and Reuse Laboratory. The second author was supported by a University of Florida Alumni Fellowship.

References

ASTM, Standard quantitative carrier test method to evaluate the bactericidal, fungicidal, mycobactericidal and sporicidal potencies of liquid chemical germicides., ASTM Designation: E2111-00 (2001).

CDC, Questions and answers about anthrax, http://www.bt.cdc.gov/agent/anthrax/faq (2006).

Grund A.D., Ensign J.C., Activation of *Streptomyces viridochromogenes* spores by detergents, Current Microbiology, 7 (1982) 223–227.

Ivanova N., Sorokin A., Anderson I., Galleron N., Candelon B., Kapatral V., Bhattacharyya A., Reznik G., Mikhailova N., Lapidus A., Chu L., Mazur M., Goltsman E., Larsen N., D'Souza M., Walunas T., Grechkin Y., Pusch G., Haselkorn R., Fonstein M., Ehrlich S.D., Overbeek R., Kyrpides N., Genome sequence of *Bacillus cereus* and comparative anal-

ysis with *Bacillus anthracis*, Nature, 423 (2003) 87–91.
Krishna V., Pumprueg S., Lee S.H., Zhao J., Sigmund W., Koopman B., Moudgil B.M., Photocatalytic disinfection with titanium dioxide coated multi-wall carbon nanotubes, Process Safety and Environmental Protection, 83 (2005) 393–397.
Li B., Logan B.E., Bacterial adhesion to glass and metal-oxide surfaces, Colloids Surf B Biointerfaces, 36 (2004) 81–90.
Mastrapa R.M.E., Glanzberg H., Head J.N., Melosh H.J., Nicholson W.L., Survival of bacteria exposed to extreme acceleration: implications for panspermia, Earth and Planetary Science Letters, 189 (2001) 1–8.
Moeller R., Horneck G., Rabbow E., Reitz G., Meyer C., Hornemann U., Stoffler D., Role of DNA protection and repair in resistance of *Bacillus subtilis* spores to ultrahigh shock pressures simulating hypervelocity impacts, Appl Environ Microbiol, 74 (2008) 6682–6689.
Moeller R., Stackebrandt E., Reitz G., Berger T., Rettberg P., Doherty A.J., Horneck G., Nicholson W.L., Role of DNA repair by nonhomologous-end joining in *Bacillus subtilis* spore resistance to extreme dryness, mono- and polychromatic UV, and ionizing radiation, J Bacteriol, 189 (2007) 3306–3311.
Nicholson W.L., Galeano B., UV resistance of *Bacillus anthracis* spores revisited: Validation of *Bacillus subtilis* spores as UV surrogates for spores of *B. anthracis* Sterne, Applied and Environmental Microbiology, 69 (2003) 1327–1330.
Nicholson W.L., Munakata N., Horneck G., Melosh H.J., Setlow P., Resistance of *Bacillus* endospores to extreme terrestrial and extraterrestrial environments, Microbiology and Molecular Biology Reviews, 64 (2000) 548–572.
Parker M.S., Bradley T.J., A reversible inhibition of the germination of bacterial spores, Can J Microbiol, 14 (1968) 745–746.
Peng J.S., Tsai W.C., Chou C.C., Surface characteristics of *Bacillus cereus* and its adhesion to stainless steel, International Journal of Food Microbiology, 65 (2001) 105–111.
Pinzon-Arango P.A., Scholl G., Nagarajan R., Mello C.M., Camesano T.A., Atomic force microscopy study of germination and killing of Bacillus atrophaeus spores, J Mol Recognit, 22 (2009) 373–379.
Read T.D., Peterson S.N., Tourasse N., Baillie L.W., Paulsen I.T., Nelson K.E., Tettelin H., Fouts D.E., Eisen J.A., Gill S.R., Holtzapple E.K., Okstad O.A., Helgason E., Rilstone J., Wu M., Kolonay J.F., Beanan M.J., Dodson R.J., Brinkac L.M., Gwinn M., DeBoy R.T., Madpu R., Daugherty S.C., Durkin A.S., Haft D.H., Nelson W.C., Peterson J.D., Pop M., Khouri H.M., Radune D., Benton J.L., Mahamoud Y., Jiang L.X., Hance I.R., Weidman J.F., Berry K.J., Plaut R.D., Wolf A.M., Watkins K.L., Nierman W.C., Hazen A., Cline R., Redmond C., Thwaite J.E., White O., Salzberg S.L., Thomason B., Friedlander A.M., Koehler T.M., Hanna P.C., Kolsto A.B., Fraser C.M., The genome sequence of *Bacillus anthracis Ames* and comparison to closely related bacteria, Nature, 423 (2003) 81–86.
Ronner U., Husmark U., Henriksson A., Adhesion of bacillus spores in relation to hydrophobicity, J Appl Bacteriol, 69 (1990) 550–556.
Vohra A., Goswami D.Y., Deshpande D.A., Block S.S., Enhanced photocatalytic inactivation of bacterial spores on surfaces in air, Journal of Industrial Microbiology and Biotechnology, 32 (2005) 364–370.
Vohra A., Goswami D.Y., Deshpande D.A., Block S.S., Enhanced photocatalytic disinfection of indoor air, Applied Catalysis B-Environmental, 64 (2006) 57–65.
Xue Y.M., Nicholson W.L., The two major spore DNA repair pathways, nucleotide excision repair and spore photoproduct lyase, are sufficient for the resistance of *Bacillus subtilis* spores to artificial UV-C and UV-B but not to solar radiation, Applied and Environmental Microbiology, 62 (1996) 2221–2227.

Author's short biography

Vijay B. Krishna

Dr. Vijay Krishna is an Assistant Professor of Molecular Medicine in the Department of Biomedical Engineering at the Lerner Research Institute, Cleveland Clinic. His current research interests include carbon nanostructures, nanomedicine and light-nanomaterial interactions for biomedical applications. Dr. Krishna received his B.E. in Chemical Engineering from Bangalore University and Ph.D. in Materials Science and Engineering from University of Florida. He continued as a Postdoctoral Associate at the Particle Engineering Research Center at the University of Florida. Dr. Krishna has 19 peer-reviewed publications and 11 patents.

Author's short biography

Jue Zhao

Dr. Jue Zhao is a Plant Operations Engineer at the City of Grand Island Wastewater Treatment Plant. Her expertise includes hydraulic and biological modeling of wastewater treatment, process design and pilot to scale development of water and wastewater treatment, and biological nutrient removal operations. Dr. Zhao received her Ph.D. in Environmental Engineering Sciences from University of Florida. Her research interest is photocatalytic disinfection using nanoparticles. She is registered as a Professional Engineer in the State of Florida and State of Nebraska.

Smithi Pumprueg

Mr. Smithi Pumprueg is the founder of Vigo Engineering Co. Ltd., a company focusing on engineering projects based in Rayong, Thailand. He received his M.E. in Environmental Engineering Sciences from University of Florida.

Ben L. Koopman

Dr. Ben Koopman is a Professor and Undergraduate Coordinator in the Department of Environmental Engineering Sciences at the University of Florida. His research interests include removal of microorganisms by surface-modified filter media and bio films, photocatalytic antimicrobial coatings, microbial water-treatment, one-dimensional modeling of activated sludge secondary settling tanks, and biological nutrient removal. Dr. Koopman received his B.S. in Civil Engineering from Oregon State University and Ph.D. in the same field from the University of California, Berkeley.

Brij M.Moudgil

Dr. Brij M. Moudgil is a Distinguished Professor of Materials Science and Engineering at the University of Florida. His current research interests are in particulate materials based systems for enhanced performance in bioimaging, nanomedicine, photocatalytic degradation of hazardous microbes, polymer and surfactant adsorption, dispersion and aggregation of fine particles and nanotoxicity. Dr. Moudgil received his B.E from the Indian Institute of Science, Bangalore, India and his M.S and Eng.Sc.D degrees from Columbia University, New York. He has published more than 400 technical papers and has been awarded 14 patents. He is a member of the U.S National Academy of Engineering.

KONA Powder and Particle Journal No. 33 (2016) 310–321/Doi:10.14356/kona.2016016 Original Research Paper

Optical Characterization of Industrial Slurries †

Marco Potenza [1,2,3]*, Tiziano Sanvito [2,3] and Giuseppe Fazio [4]

[1] *Department of Physics, University of Milan, Italy*
[2] *CIMAINA, Italy*
[3] *EOS Srl, Italy*
[4] *ST Microelectronics, Italy*

Abstract

In this work we focus on the characterization of micro- and nano-powders typically adopted for chemical mechanical polishing, extensively used whenever the global and local planarization of surfaces is required as in nanoelectronic fabs. We present an innovative method for the accurate characterization of water suspensions of nanoparticles. It relies upon the combination of a new approach to extract light-scattering information from single particles and the recently developed diagnostic tool named Single Particle Extinction and Scattering. It can be used in line. Data interpretation becomes independent of any a-priori assumptions about the samples. The results of accurate measurements performed on ceria as well as aluminium oxide slurries are reported. We show the strong advantages of this method compared with traditional ones by explicitly reporting experimental results on calibrated spheres made of different materials. We discuss possible applications for in-line characterization of ultrapure water, chemicals, slurries for abrasive processes, for example, as well as the detection of any undesired particles – which could be the key for future improvements to advanced process control systems.

Keywords: particle sizing, slurries, ceria, CMP, light scattering

1. Introduction

The worldwide nanoelectronic industrial environment is currently under pressure to achieve better goals in terms of cost reduction and manufacturing efficiency, while the rate of technological advancement must be preserved. The improvement of fab productivity through novel methods or the introduction of in-line monitoring of processes, equipment, facilities (e.g. power, gas, chemicals ...), which will make the manufacturing efficiency higher is an increasing need in this field.

1.1 Chemical mechanical polishing

One of these applications has been recognized to be monitoring the Particle Size Distribution (PSD) of the slurries used for the Chemical Mechanical Polishing (CMP) processes, required by the most advanced technology applied to the production of silicon-based technologies (Li, 2008), as well as a number of industrial processes such as, for example, compact disks, hard disks and optical surface polishing. It is generally known that CMP involves both chemical and mechanical mechanisms where the abrasive slurries are one of the main actors. Slurries are aqueous dispersions of nanoparticles where the characteristics of the abrasive material and PSD typically play an important role in determining the removal behaviour (Pate, 2011). Modern slurries are characterized by two main drawbacks that make them difficult to handle: 1) they rapidly undergo sedimentation; 2) they are affected by aggregation phenomena (Basim, 2000; Basim, 2002). Moreover, slurries are typically handled within closed-loop circuits, so that guaranteeing the stability of the suspension is a particularly demanding issue. Finally, aging effects occur during the process which affect the process performance (Cumbo, 1995; De Nardis, 2005; Remsenz, 2006).

1.2 Common slurries

The common materials available on the market are silica (SiO_2) and ceria (CeO_2) particle suspensions for the most demanding nanoelectronic applications, and aluminium, copper and other oxides for other cases (e.g. optical polishing). Ceria slurries represent the most innovative application for silicon insulation definition, and are the

† Received 8 May 2015; Accepted 17 July 2015
J-STAGE Advance published online 30 September 2015
[1,2] via Celoria, 16 – I-20133 Milan, Italy
[3] Viale Ortles 22/4, I-20139, Milan, Italy
[4] via Olivetti 2, I-20864 Agrate Brianza, Italy
* Corresponding author: Marco Potenza;
E-mail: marco.potenza@unimi.it
TEL: +39-02-50317209 FAX: +39-02-50317712

most demanding in terms of characterization due to the tight requirements and the high costs. Notwithstanding the complicated transformation method of the ceria raw material into the final slurry product and the fact that it belongs to the rare earths, with consequently increased costs and availability problems, ceria slurries are quite diffuse thanks to their improved local planarization performance with respect to silica. Moreover, they are typically used in addition to chemical additives, thus leading the high selectivity between oxides and nitrides (Merriks, 2008). Because of the natural sedimentation and aggregation behaviour of ceria particles, several studies have been performed to correlate the PSD with the features of handling and distribution systems, as well as correlation of the CMP with the material removal rate in order to guarantee the proper process control and quality level in the semiconductor manufacturing environment.

1.3 Slurry characterization

The particle size specifications in the semiconductor industry of ceria slurries are based on supplier methodology, generally based on laser diffraction. The Mastersize laser diffraction tool (Malvern TM) is a reference here.

As already mentioned, one of the most critical drawbacks of ceria slurries is the stratification and sedimentation behaviour that must be taken into account prior to and during use. This is simply caused by the high specific weight of the material. Thus, strong shaking is needed to re-disperse the solids content over the entire drum and a minimum flow speed in piping is required to avoid sedimentation. These are the main topics for the design of the Chemical Distribution System (CDS). Along the CDS, continuous shaking is still necessary to avoid sedimentation. As it appears clear from this analysis, the most important parameter to be monitored is the PSD, *D*99 percentile in particular, and NVC%. In **Figs. 1.1** and **1.2**, the effect of the NVC% and *D*99 particle class on the CMP process performance is shown in terms of the material removal rate. Since the *D*99 classification is extremely dependent on the particle size analysis technique, the monitor is typically performed indirectly on the basis of the NVC% only, since a correlation between D99 and NVC% has been determined. No direct measurement of the PSD is usually performed.

The state of the art for slurries in the semiconductor industry is clearly stated in the ITRS guidelines (ITRS and ITRS, 2009), which are briefly summarized and discussed below.

At present, the characterization of free nanoparticles in general does not meet the criteria for a wide class of applications due to lack of accuracy, high throughput, ease of operation and the actual possibility of operation for routine, in-line characterization (Zelenyuk, 2006; Ghosal,

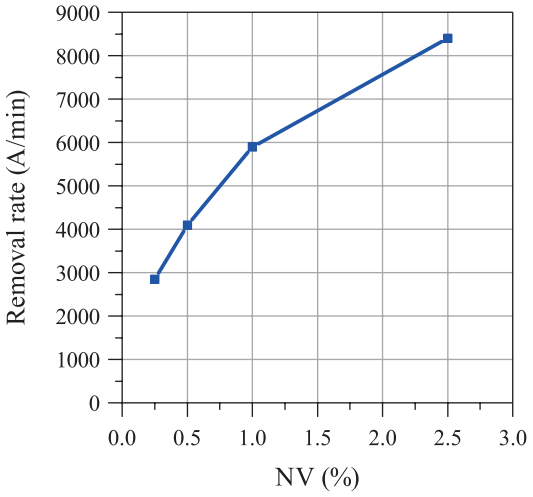

Fig. 1.1 Non-volatile content (NVC%) vs CMP removal rate.

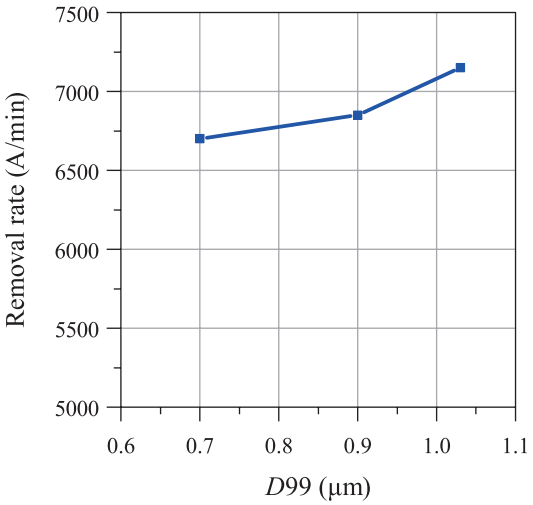

Fig. 1.2 *D*99 concentration vs CMP removal rate.

2014). Optical methods are among the most popular ones due to the non-invasiveness of the measurement, reliability, flexibility, robustness, but nevertheless they suffer from fundamental limitations which make them inapplicable for the case in point here. The main limitation is that most of these methods operate on collections of highly polydisperse particles, making it necessary to apply data analysis with inversion algorithms for extracting the PSD from the superposition of the signals given by a number of different particles. This often involves ill-posed problems like in DLS or SALS, and limits the reliability of the methods for the specific applications, especially at nanoelectronic fabs. Alternatively, non-optical methods exist which can be adopted for characterizing the PSD of dense materials such as ultrasonic spectroscopy (Hipp, 1999). This method can be considered a valid alternative to optical methods, with the advantage of operation without need of any dilution.

As a matter of fact, no in-line monitoring is currently performed on the slurries at nanoelectronic fabs. Samples are picked up and sent to the producer for size characterization. This process is extremely far from what would be needed in terms of an efficient, immediate responsive tool for deciding within a short time the actions to be taken (Budge, 2009; Budge, 2013).

1.4 Future needs

A clear breakthrough here could be made by means of an in-line Particle Monitoring (PM) tool that continuously determines the PSD and generates the inputs for a Decision-Making (DM) tool capable of performing the following actions: 1) foreseeing the requisite actions to be taken during the maintenance stops, based on an effective, rational and sustainable basis; 2) adapting the CMP to maintain the required specification of the product despite the modified characteristics of the slurries that are currently present inside the machinery.

To present things in a more schematic way, the current status and the progress beyond the state of the art which would dramatically change the fab performance are compared below, referring to the main issues and needs of industry.

1) At present, no PM tool is available for in-line monitoring. A new sensor and the relevant tool with the specifications needed to fulfil the objective must therefore still be developed, tested and implemented in-line.
2) No DM protocol is available. A PM tool with the specified requirements would enable development of such a protocol.
3) The common way to employ sensor integration is by adapting the FDC system to match the sensor requirements in terms of physical and logical connection. It is necessary to develop a sensor interface capable of making the interfacing of the new sensors easy and intelligent.
4) The scattering parameters of nanoparticles can be measured with methods that estimate only the size based upon reasonable hypotheses about the composition. A possibility is to develop an extended database of both size and absorption coefficients, independent of the calibration of numerical methods.

Development of a new instrument in view of the PM tool with the requirements above is challenging simply because of the intrinsic limitations imposed by both industrial requirements and by basic physics arguments. In the following text, we report a list of the ITRS target technology issues for particle counter performance (ITRS and ITRS, 2009).

- Particle counter performance is strongly dependent on the number of particles counted per unit of time.
- The number of particles counted per unit of time determines the precision of the measurement. The precision is predictable based on particle counting statistics.
- The number of particles counted per unit of time is dependent on the sensitivity of the particle counter and the volume of the chemical measured.
- Particle measurements (with reasonable precision) at a specific particle size combined with the knowledge of particle distributions in liquid chemicals can be used in predicting particle concentrations at another size.
- PSD in continuously filtered liquid chemical systems are usually between $1/D^{2.5}$ and $1/D^{3.5}$, with $1/D^{3}$ being typical. While a PSD can be estimated from any sample, it is more accurate to use a large number of samples and a large number of instruments in making this determination.
- Elimination or minimization of background counts due to cosmic rays is necessary to ensure that the measured particle counts represent real particle events.

In the following section, we introduce a completely novel approach to the characterization of particles suspended in a liquid, and show experimental evidence that this is able to overcome the main issues listed above. We think this method is one of the best candidates to achieve the PM tool described above.

2. Analysis of the field scattered by single particles

In this section, we recall the fundamentals of the traditional methods for the sizing of single particles, and introduce the approach we will adopt here based upon measurement of the scattered field. As it has been recently discussed (Potenza, 2014), the knowledge of the complex field scattered by single particles, meaning either amplitude and phase, or real and imaginary parts, is hugely advantageous in assessing information about the samples. The knowledge of the whole field is the key ingredient which enables information that is otherwise not available with traditional methods to be assessed.

Traditional optical methods for measuring the size of single particles are based on the fundamentals of light scattering, typically the dependence of the scattering cross-section C_{sca} upon the particle radius a and the wavelength λ. A tightly focused light beam is usually exploited to maximize the intensity falling onto a single particle, and the scattered intensity (almost isotropic for $a<<\lambda$) is collected over a wide solid angle (Chylek, 1976; Sachweh, 1998; Terrel, 2006; Heim, 2008). The ratio of the total scattered power and the incident intensity gives C_{sca}. In order to reduce the uncertainties introduced by the unavoidable shape effects, which can be particularly import-

ant at high scattering angles, low angle detection has been alternatively adopted. A colloidal suspension is hydrodynamically focused into a narrow stream illuminated by a perpendicular laser beam with constant intensity and an elliptical focus. The case of highly concentrated suspensions has also been addressed successfully (Mavliev, 2004). As the particles pass one by one through the laser beam spot, the scattered light is collected under a scattering angle of 5°. The signals are processed by a multichannel analyser and delivered to an electronic processing unit. The particle size is more accurately determined, also for systems subject to aggregation phenomena (Pelssers, 1990).

An alternative approach has been recently introduced based upon direct measurement of the transmitted beam intensity. By definition, this provides the extinction cross-section C_{ext}. The method was commercialized by Klotz GmbH, and has been extensively compared to the scattering-based methods in some cases of interest for basic science (Ruth, 2002).

In some cases, the two principles mentioned above have been adopted in a measurement of both the extinction and the scattering cross-sections of single particles in order to extend the accessible size range (Wells, 1996).

In any of the previous cases, the size is recovered from just one parameter, which is the measured power: the amount of light scattered or removed by the impinging light beam gives the particle size through the proper cross-section (either scattering or extinction). Any other features affecting the scattering of light remain out of control. Even if size by far determines the amount of extinguished and scattered light, other parameters are also involved, thus limiting the accuracy of the size recovery (Gebhart, 1991; Liu, 2000; Whitby, 1967). The composition, shape and internal structure of a particle also participate in determining the scattered field and intensity, and recovering the size from the measured intensity ideally requires the knowledge of this information which is usually unknown (see, for example, Bohren, 1983; Mischenko, 1999; Borghese, 2003). Moreover, especially when working at high scattering angles, the specific orientation of a given non-spherical particle represents an additional parameter that determines the scattered field and intensity, thus making the data intrinsically affected by the uncertainties introduced by the random orientations the particles have in the sensible region (Tinkea, 2008).

The new approach we adopt here (Potenza, 2014) has been shown to give strong advantages in the characterization of free particles. This approach was first used to characterize ceria slurries (Potenza, 2015) in the submicron range. Here, we report the experimental results obtained, adopting the same approach for a more general class of slurries, including CeO_2 and Al_2O_3 slurries, with the aim of proving the feasibility of easy and reliable characterization for these kinds of suspensions.

For the basics of this approach we refer to the literature (see Potenza, 2014). Here, we just recall that for liquid suspensions of particles with a given composition, even if unknown, several drawbacks of the traditional methods have been overcome. Moreover, the presence of any polydispersity is of advantage here, since a statistical approach can be applied to the data as shown below. Therefore, the typical industrial problem of analysing samples containing particles of homogeneous composition is particularly promising to facilitate going beyond the state of the art (Potenza, 2015). Other advantages will be further discussed. The only drawback of the present approach, which is due to and in common with any other single particle detection method, is the need of highly dilute suspensions. This requires strong dilutions, and in principle could affect the physico-chemical properties of the suspension. This is the requirement also for other optical methods commonly adopted for the off-line characterization of slurries for industries, so that our results are comparable to those obtained with such methods. As discussed in the introduction, in those cases when just the properties of the concentrated sample are of interest, different approaches shall be adopted to avoid dilution (for example, the ultrasonic spectroscopy mentioned above; Hipp, 1999).

3. Single particle extinction and scattering

Simultaneous measurements of the complex scattered field have been attempted with several methods by different groups (Batchelder, 1991; Bassini, 1992; Giglio, 2004; Giglio, 2005; Potenza, 2010). Here we adopt a new method recently developed (Giglio, 2005; Potenza, 2015), which overcomes the main issues encountered by any other method. Actually, the only method which is really viable for characterizing single particles in a flux is the one described in Batchelder 1991, which was previously patented (Batchelder, 1990). Nevertheless, the method we adopt here is simpler, cheaper and more robust such that we believe it really can be adopted for in-line measurements of nanoparticles suspended in a fluid of industrial interest. For this reason, in the following text we will not compare the new method with those mentioned above to measure the complex field.

The method we use here has been developed by the optics group at the University of Milan. It is named Single Particle Extinction and Scattering (SPES) because of its ability to access simultaneous measurements of the extinction cross-section and the amplitude of the forward scattered field for each particle. These parameters are ultimately related to the real and imaginary parts of it. The SPES method is described elsewhere (Potenza, 2015). It

relies upon a self-reference interferometric scheme in which particles are driven through the focal region of a light beam, and the transmitted light is collected on a sensor placed in the far field. Particles are delivered into the beam through a flow cell (Hellma 137 series), the dilution being properly chosen so that just one particle is present in the beam at a time. The superposition of the intense transmitted beam and the faint scattered wave gives time-dependent interference patterns which deliver the information of both the extinction (power reduction of the main beam) and scattering (intensity modulations due to interference). Collecting data at high speed with a time base much smaller than the particle transit time through the beam and adopting a segmented sensor allow recovery of the information on both. The advantages with respect to current methods for measuring single particles are: high size resolution; simultaneous measurement of size and refractive index of single particles; calibration-free; very simple optical layout; minimum fake events. More specifically, working with slurries, one can rely on 1) the knowledge of the composition, and 2) the almost isometric shape of the grains (Potenza, 2015). The former is of paramount importance since the refractive index of compact grains is well known, which allows recognition of spurious grains and aggregates of grains. The latter is important since data are not affected by any uncertainty coming from the shape and orientation of the grains in the scattering volume (see, the simulations in Potenza, 2014). As a result, a precise measurement of the single particle sizes is possible that is free from any contribution of spurious events. A precise PSD can then be obtained and followed with time, which is one of the basic requirements for a routine, in-line process control.

The almost complete absence of fake events warrants a specific discussion here. It is mainly due to 1) the continuous measurement of the transmitted beam, so that the system does not produce any signal at the detection limit when measuring very small particles, and 2) the fast signal detection, which makes an accurate pulse shape analysis of the signals possible. In both cases fake events such as cosmic rays, electronic noise, as well as double transits through the beam can be accurately rejected. Moreover, air bubbles can be easily recognized from the pulse shape analysis, thanks to the unique, known relative refractive index of air with respect to the liquid.

In order to show the specific properties of the SPES method and the way we show data in the following sections, we report some experimental results obtained with calibrated polystyrene (PS) spheres suspended in water. In **Fig. 3.1** we report the raw data in the complex field (abscissas and ordinates represent the real and imaginary parts, respectively). Data are represented in the complex field by a two-dimensional histogram where the number of events detected within a given two-dimensional bin is represented in grey tones (white corresponds to zero particles, black to the maximum number in the plot). Disturbances in the signals give rise to the spread in the complex plane around the centroid of the distribution, which is more extended towards the lower real and imaginary parts. Bin size was chosen in such a way to be close to the ultimate sensibility of the method in the intermediate region of the accessible range. Spheres of 290, 430 and 600 nm in diameter, refractive index (in air) $n = 1.59$ for the laser source adopted here were measured. The data show a trend identified by the black continuous line, the size increasing for larger complex amplitudes. For the sake of clarity we report the expected complex values for ceria, n = 2.1 (dotted line). Moreover, we stress here that for non-spherical particles, the population is expected to be characterized by a spread in the vertical direction which is larger for higher aspect ratios (Potenza, 2014). By contrast, isometric particles show a distribution that is much narrower close to the expected lines in the figure.

In **Fig. 3.2** we report the PSD as obtained by the same data in **Fig. 3.1**. The size has been recovered by simply associating the measured field of each particle to the corresponding size, on the basis of the exact Mie theory. Notice that no true inversion is needed here, thanks to the single particle measurement. The histogram represents the distribution, expressed as the fractional abundance (%) of particles within each bin. Each bin was chosen to be close to the sensibility of the method in the intermediate size range (where noise affects the data at minimum). The red line is the cumulant distribution, while the blue triangles show the expected sizes on the basis of the calibration of the samples.

In order to show the specific ability of the SPES method to give two independent parameters, we show in **Fig. 3.3** the results obtained from measurement of a suspension

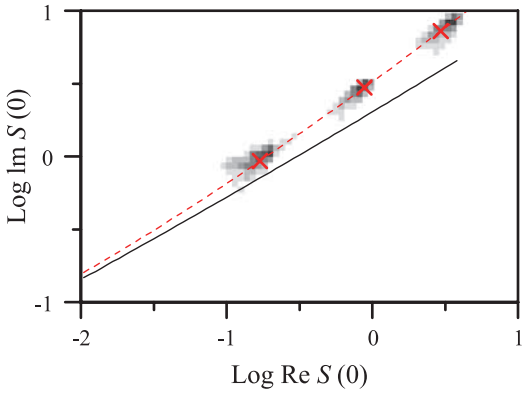

Fig. 3.1 An example of the complex field data obtained with calibrated PS spheres. The 2D histogram represents the number of particles detected within each 2D bin. The continuous line represents the expected complex fields for PS spheres. The dotted line represents the expected fields for n = 2.1, respectively.

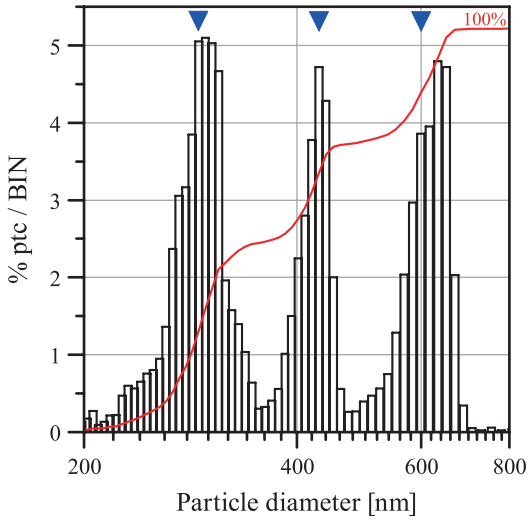

Fig. 3.2 PSD obtained from the data reported in **Fig. 1.1**. The histogram reports the experimental data, the red line the cumulant curve, the blue triangles are the expected median values.

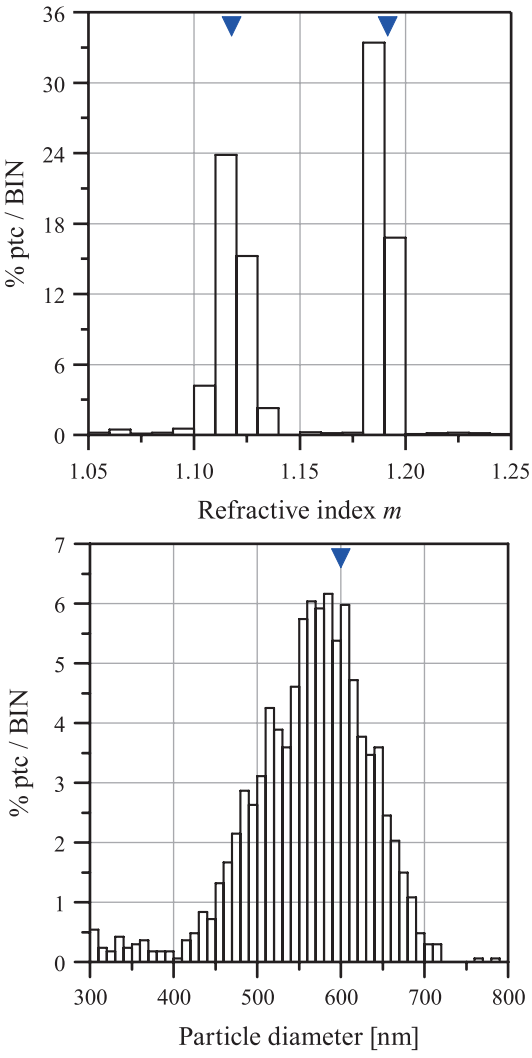

Fig. 3.3 Results obtained with PMMA and PS spheres 600 nm in diameter. a) The index distribution is as expected (see text for details). b) The size distribution is not influenced by different scattering properties due to the different materials. For comparison, see **Fig. 3.2**.

containing spheres of 600 nm in diameter, made of PS and PMMA. The two materials present different refractive indexes so that we can distinguish them in the complex field and recover the corresponding refractive index distribution. Moreover, when inverting data to recover the size, we still obtain a single distribution cantered at 600 nm. Both results cannot be obtained with any traditional single particle method. The refractive index can be accurately measured by capitalizing on the statistical parameters of the bimodal distribution, turning out with relative refractive indexes (in water) $m = 1.12$ and $m = 1.19$. The expected values for the wavelength $\lambda = 635$ nm are $m = 1.118$ for PMMA (Szczurowski, 2014) and $m = 1.192$ for PS (Sultanova, 2009).

In the following sections we report results obtained with ceria slurries under different conditions of interest for industries, and we also show an analysis of Al_2O_3 slurries to extend the analysis to perhaps the most diffuse abrasive materials in the industry worldwide.

4. Ceria slurries

We first consider the case of ceria slurries. We have considered a sample of slurry commonly adopted for a CMP process for global planarization of metal or dielectric layer of semiconductor production. Samples of ceria have been carefully analysed through the SPES method, operating in the size range from some 100 nm to approximately 1 micron.

In the first series of measurements, the samples were prepared by accurately shaking the high-concentration slurries (carefully preventing the sample from forming air bubbles), and a small amount of slurry was strongly diluted in ultrapure water. A series of samples was prepared by passing the dilute suspensions through an ultrasonic bath for different time intervals. The aim was to check whether any differences arise in the size distribution of samples treated for different times due to some kind of aggregation process occurring in the original slurry, which would be broken by sonication. Notice that after dilution, the characteristic time for aggregation is large enough to allow measuring for hours without suffering any aggregation process. Data collected at different times after the sample preparation confirm this assumption. Moreover, data from samples sonicated for different times (including no sonication) did not bring any appreciable difference.

A number of measurements were performed in such a way to test the reliability of the method, both experimentally and from the point of view of data analysis. We show here typical examples of the measurements, focusing on assessing the PSD. Finally, in order to focus on one of the main issues which is the stability of suspensions and the

presence of unwanted large grains, we show results obtained with slurries which suffered aggregation processes due to instabilities induced by chemical additives.

The results are shown in the complex plane in **Fig. 4.1**. One population is evident here, polydispersity determining the extension over the complex plane. The complex fields scattered by a polydisperse suspension of spheres with the typical refractive index of ceria is drawn as the dashed line. Notice that the spread around the line is compatible with the presence of grains of homogeneous composition and almost isometric shape, which is in accordance with the expected case for ceria. The red continuous line was obtained as the line joining the median values of the distributions obtained as the vertical sections of the raw data results. In **Fig. 4.2** we show the PSD obtained as described above from the same data shown in **Fig. 4.1**. Abscissas are expressed in nm, ordinates represent the fraction of the whole population contained in each bin. A total amount of several 10^4 events is represented in the figure which allows channelling the diameters in narrow bins with an appreciable number of counts each. This makes the Poisson's errors associated to the number of counts for each bin reasonably small, as indicated by the error bars (which indicate one standard deviation error).

Here we present results obtained with the same slurry as above, mixed with a chemical (MBIT) adopted for HSS applications. The same preparation procedure was adopted to ensure full consistency with the previous measurements. **Fig. 4.3** represents the results for this sample. Although the amount of detected particles is much less compared to **Fig. 4.1**, the relative population shows important contributions for the largest sizes (upper right region of the plot). These can be attributed to the presence of aggregates composed of several particles. In **Fig. 4.4** we present the results of measurements performed on the same sample of **Fig. 4.3** after passing through strong sonication. The population in this case shows 1) an evident depression of the upper size population, and 2) a population which is compatible with the results shown in **Fig. 4.1**. In this case, the presence of aggregates is evidenced solely by the PSD. More generally, aggregates can be better recognized if they grew in size to acquire the typical fractal structure. In such a case, the response of the SPES measurements permit a clear assessment of the fractal nature of the objects (Potenza, 2014).

Notice that the identification of aggregates is one of the key issues for the exploitation of slurries for high-quality applications, as for example in semiconductor fabs. We then consider this series of measurements as the bench-

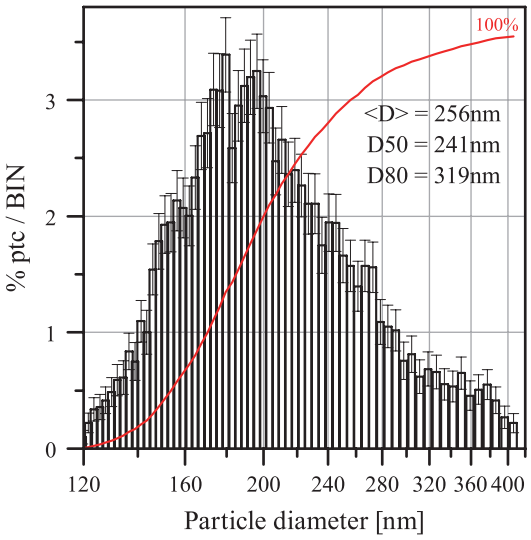

Fig. 4.2 The PSD as obtained from the raw data in **Fig. 4.1**, as described in the text. Error bars represent the Poisson's standard deviations for the number of particles within each bin.

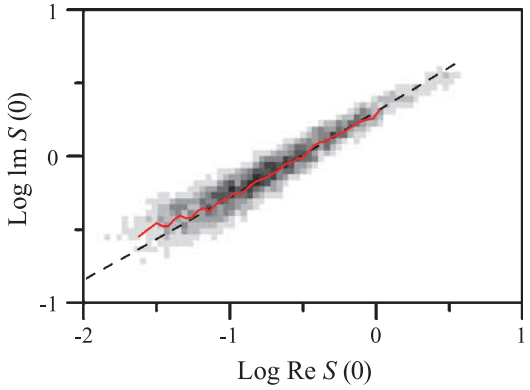

Fig. 4.1 Raw data obtained with ceria slurry, expressed as the histogram in the complex plane. The dashed line is the expected field distribution for spheres with the refractive index of ceria. The red continuous line describes the median of the distribution obtained by selecting bins along the vertical direction.

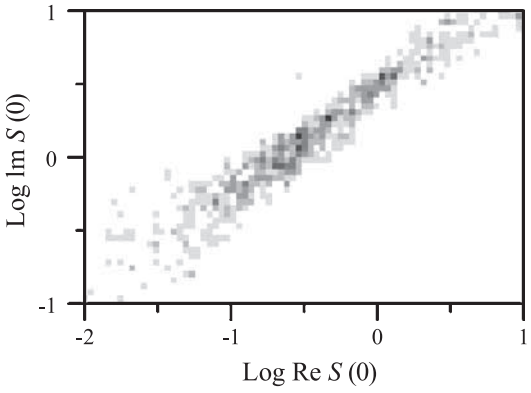

Fig. 4.3 Experimental results obtained with ceria slurry mixed with chemicals (see text). The measurement was performed just after the sample preparation. The difference to **Fig. 4.1** is evident in the upper part of the diagram, corresponding to the larger particles.

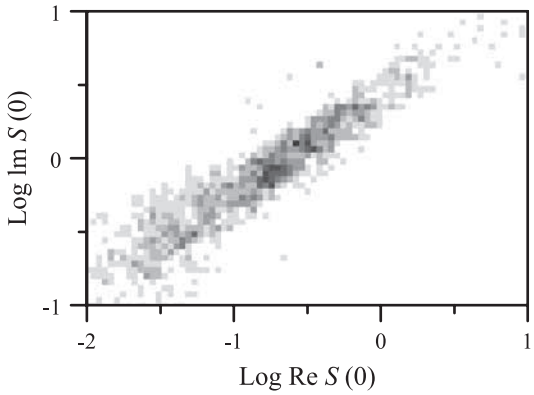

Fig. 4.4 Experimental results obtained with the same sample as in **Fig. 4.3** put in an ultrasonic bath. The additional population evidenced in **Fig. 4.3** is drastically depressed, indicating the aggregate nature of the objects which are broken into their original components.

mark to validate the present approach as a candidate for the most demanding characterization of slurries.

5. Aluminium oxide slurries

In this section we present an example of the results obtained with exhaust AlO_3 slurries for polishing plastic ophthalmic lenses. The expected sizes are appreciably larger than for ceria slurries, so that the accessible range of fields with the instrument exploited for ceria is not suitable for these particles. We then adopted a different realization of the SPES method, an instrument capable of measuring real and imaginary parts more than 10 times larger. Measurements performed with the SPES instrument adopted for ceria confirmed this choice. In **Fig. 5.1** we show the raw data in the complex plane. Notice that the real and imaginary parts are 10 times larger than in the previous figures. The fields of about 20,000 particles are represented, accurately selected on the basis of stringent validation procedures mentioned above. The continuous blue line is the expected field distribution for spheres with the expected refractive index ($n = 1.75$ in vacuum), obtained through a simplified model (Van de Hulst, 1957). No free parameters are present in this plot. The data are in good accordance with the expected values for spheres in the small size range (left-hand bottom part of the plot; we stress that the plot is represented on a logarithmic scale), while the larger sizes present an evident discrepancy. Here we give evidence that this is in accordance with what was expected in the case that fractal aggregates are present in the suspension. The black, dashed line is the field distribution obtained on the basis of the model describing the scattered fields from fractal aggregates, obtained following a simplified model (Van de Hulst, 1957) for the Rayleigh-Gans approximation of the Mie theory

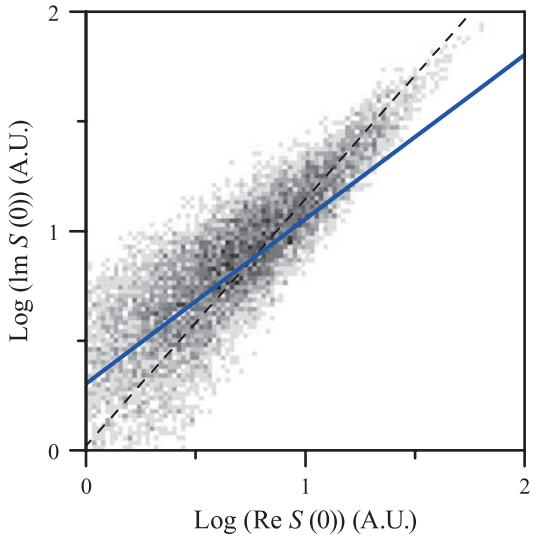

Fig. 5.1 Experimental results obtained with more than 20,000 particles detected by the SPES instrument. The histogram represents the raw data in the complex plane. The blue, thick, continuous line is the expected distribution of fields scattered by spherical particles with the expected refractive index ($n = 1.75$ in vacuum), based upon a simplified Van-de-Hulst model calculated for a fractal dimension $d = 1.8$. The black, dashed line represents the expected values for aggregates (see text for details).

adapted to the case of fractal aggregates (Potenza, 2014). It considers the effect of the reduced amount of matter within an aggregate with a given fractal dimension which determines an increase of the imaginary parts with respect to the values for compact particles. Here the smallest particles have been considered to form aggregates with a fractal dimension d = 1.8, a typical value for aggregates formed by instabilities due to electric activity between small grains. This is the case for small mineral grains like those studied here. Notice that a precise value of the fractal dimension does not overly affect the behaviour of the field distribution. Irrespective of the specific values for the parameters in this model (monomer size, fractal dimension), we stress that in the complex plane, a behaviour like that is only compatible with the presence of aggregates. In fact, imaginary parts larger than those for spheres of a given index solely indicate particles with a smaller index, which can only be obtained for non-compact objects.

By exploiting again the simplified model for the forward scattered field (Van de Hulst, 1957), expanding at the second order the real and imaginary parts, and by inverting the outcoming relations in terms of the reduced particle radii, we can give an estimate of the PSD of the particles represented in **Fig. 5.1**. In **Fig. 5.2** the diameter distribution is represented for the same 20,000 particles as above. We stress that this approach to the inversion, al-

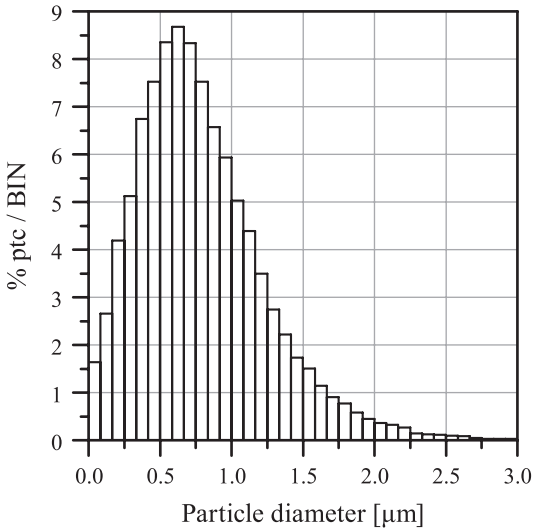

Fig. 5.2 PSD obtained from the raw data in **Fig. 5.1**. The particles in the upper part of the distribution are mainly composed of aggregates, while the smallest ones are compact objects.

though roughly describing the particles as spheres, takes advantage of the complete independence of the result on the knowledge of the particle refractive index. It is therefore particularly suitable for analysing heterogeneous data as the one of interest here, which contains both compact particles and aggregates. Within the simplified model adopted here, each particle is associated to its diameter without any free parameter.

From the statistical analysis of this distribution we obtain an average size of 780 nm and a median of 711 nm. The 10th, 25th, 75th, 90th percentiles are 250 nm, 547 nm, 1021 nm, 1363 nm, respectively.

6. Discussion and conclusions

The data presented so far clearly show the superior ability of the complex field approach to give insights into the details of real, polydisperse suspensions of small particles like those in slurries. In connection with the SPES technology, several advantages are introduced, and their effectiveness makes this approach capable of overcoming the present status and the most important ITRS target technology issues for particle counters listed above. We can sum up the progress beyond the state of the art which is achievable through the SPES method by discussing each item mentioned above, taken from the ITRS target technology issues.

- Capable of operating in-line, and integrated into a DM tool as described above
- Suitable for specific applications in nanoelectronic fabs
- The scattering parameters give access to precise sizing and classifies the composition
- The scattering parameters give access to information about the presence of aggregates
- Performance is not dependent on the number of particles counted per unit of time
- The results and the quality of the results are not obtained on the basis of any statistical approach
- Background counts due to cosmic rays and electronic noise do not affect the measurements
- Air bubbles are rigorously got rid of on the basis of a deterministic algorithm

We stress that thanks to the given composition and very simple structures of the single grains, the ceria slurries are well described solely on the basis of the PSD. This is strongly supported by the 2D histograms, which show the correctness of the choice of one refractive index to recover the PSD. Differences like that shown above can then be fully understood in terms of the PSD and properly determined thanks to our approach. Nevertheless, in the case of Al_2O_3, the presence of aggregates can be clearly recognized in the complex plane.

An additional advantage of the complex field approach is to recognize events clearly attributable to spurious particles such as water impurities (Potenza, 2015). This is typically not the case of very dense slurries such as those measured here, where proper handling protects them from the presence of impurities, but could be of importance in connection with stringent requirements in process control such as the presence of unwanted grains suspended in the slurry.

Moreover, the opportunity to monitor slurries easily and in-line will enable industries to better decide about the use of these materials. Increasing interest is given to the possibility of reusing exhaust slurries, which is currently difficult simply due to the impossibility of adequately characterizing these materials. The slurry market for applications less demanding than nanoelectronic fabs could be fruitfully integrated by introducing reused slurries, once properly characterized (Seo, 2007; Testa, 2011; Testa, 2014).

Acknowledgements

This scientific work was partially financed from the ENIAC Joint Undertaking IMPROVE project JU Grant Agreement No. 120005. Ceria slurries were supported by ST Microelectronics. The devices used in this work were built with the collaboration of F. Cavaliere and D. Viganò of the Mechanical Workshop of the Department of Physics. We acknowledge the anonymous referee for useful comments.

Nomenclature

2D	Two-dimensional
CMP	Chemical Mechanical Polishing
CDS	Chemical Distribution System
DM	Decision Making
HSS	High Selective Slurry
FDC	Fault Detection System
IC	Integrated Circuit
ITRS	International Technology Roadmap for Semiconductors
NVC%	Non-Volatile Content
PM	Particle Monitoring
PMMA	Polymethilmetacrylate
PS	Polystyrene
PSD	Particle Size Distribution
SPES	Single Particle Extinction and Scattering
STI	Shallow Trench Isolation
ULSI	Ultra-Large-Scale Integration
a	Particle radius
C_{ext}	Extinction cross-section
C_{sca}	Scattering cross-section
d	Fractal dimension
D	Particle diameter
m	Relative refractive index (with respect to the surrounding medium)
n	Refractive index (with respect to the vacuum)
$S(0)$	Complex amplitude of the forward scattered field
λ	Light wavelength

References

Basim G.B., Adler J.J., Mahajan U., Singh R.K., Moudgil B.M., Effect of particle size of chemical mechanical polishing slurries for enhanced polishing with minimal defects, Journal of The Electrochemical Society, 147 (2000) 3523–3528. doi:10.1149/1.1393931

Basim G.B., Moudgil B.M., Effect of Soft Agglomerates on CMP Slurry Performance, Journal of Colloid and Interface Science, 256 (2002) 137–142.

Bassini A., Musazzi S., Paganini E., Perini U.U., Ferri F., Giglio M., Optical particle sizer based on the Chahine inversion scheme, Optical Engineering, 31 (1992) 1112–1117. doi: 10.1117/12.56158

Batchelder J.S., Taubenblatt M.A., Measurement of the size and refractive index of a small particle using the complex forward-scattered electromagnetic field, Appl. Opt., 30 (1991) 4972–4979.

Batchelder J.S., Taubenblatt M.A., Measurement of the size and refractive index of particles using the complex forward-scattered electromagnetic field, US Patent (1990) 547735.

Bohren C.F., Huffmann D.R., Absorption and Scattering by Small Particles, Wiley, N.Y., 1983.

Borghese F., Denti P., Saija R., Scattering from Model Non-spherical Particles, Springer-Verlag Berlin-Heidelberg, 2003.

Budge J., Benefits and Limitations of Slurry Particle Analysis and the Need for Next Generation Capabilities, 5th Annual Levitronix CMPUG Symposium, 2009.

Budge J., Challenges of Large Particle Size Analysis in CMP Slurries, and Opportunities for Improved Reliability, 29th European CMP Users Symposium Spring, 2013.

Chylek P., Grams G.W., Pinninck R.G., Light Scattering by Irregular Randomly Oriented Particles, Science, 193 (1976) 480–482

Cumbo M.J., Fairhurst D., Jacobs S.D., Puchebner B.E., Slurry particle size evolution during the polishing of optical glass, Applied Optics, 34 (1995) 3743–3755. doi: 10.1364/AO.34.003743

Denardis D., Choi H., Kim A., Moinpour M., Oehler A., Investigating the effects of diluting solutions and trace metal contamination on aggregation characteristics of silica-based ILD CMP slurries, MRS Online Proceedings Library, 867 (2005) W7.9. doi:10.1557/PROC-867-W7.9.

Gebhart J., Response of Single-Particle Optical Counters to Particles of irregular shape, Particle & Particle System Characterization, 8 (1991) 40–47.

Ghosal S., Weber P.K., Laskin A., Spatially resolved chemical imaging of individual atmospheric particles using nanoscale imaging mass spectrometry: Insighs into particle origin and chemistry, Analytical Methods, 6 (2014) 2413–2792.

Giglio M., Potenza M.A.C., A method for measuring properties of particles by means of interference fringe analysis and corresponding apparatus, Patent IT (2004) TO20040100; PCT/IB2005/000411

Giglio M., Potenza M.A.C., A method for measuring properties of particles and corresponding apparatus, PCT Patent (2005) PCT/IT2005/00362

Heim M., Mullins B.J., Umhauer H., Kasper G., Performance evaluation of three optical particle counters with an efficient “multimodal” calibration method, Journal of Aerosol Science, 39 (2008) 1019–1031. doi:10.1016/j.jaerosci.2008.07.006

Hipp A.K, Storti G., Morbidelli M., Particle Sizing in Colloidal Dispersions by Ultrasound. Model Calibration and Sensitivity Analysis, Langmuir, 15 (1999) 2338–2345.

ITRS (International Technology Roadmap for Semiconductors), ITRS Industry Goals for Particle Measurements in UPW and Liquid Chemicals, <www.itrs.net> accessed 2.09.2015

ITRS (International Technology Roadmap for Semiconductors), ITRS Yield Enhancement 2009 Edition, <www.itrs.net> accessed 2.09.2015

Li Y., Microelectronic Applications of Chemical Mechanical Planarization, Wiley and Sons, 2008.

Liu Y., Daum P.H., The effect of refractive index on size distri-

butions and light scattering coefficients derived from optical particle counters, J. Aerosol Sci., 31 (2000) 945–957.

Mavliev R., Method and apparatus for detecting individual particles in a flowable sample, US Patent (2004) 6710874 B2

Merricks D., Santora B., Her B., Zedwick C., Evolution and Revolution of Cerium Oxide Slurries in CMP (2008) doi: http://www.ferro.com/nr/rdonlyres/b92195ab-8d53-4bb4-8f49-078c6763f859/0/istc2008.pdf

Mishchenko M.I., Hovenier J.W., Travis L.D., Light Scattering by Nonspherical Particles: Theory, Measurements, and Applications, Academic Press, San Diego, 1999.

Pate K., Tregub A., Characterization of abrasive particle distribution in CMP slurries, ICPT2011 Conference, 2011.

Potenza M.A.C., Sabareesh K.P.V., Carpineti M., Alaimo M.D., Giglio M., How to measure the optical thickness of scattering particles from the phase delay of scattered waves: Application to turbid samples, Physical Review Letters, 105 (2010) 193901.doi: 10.1103/PhysRevLett.105.193901

Potenza M.A.C., Milani P., Free nanoparticle characterization by optical scattering field analysis: opportunities and perspectives, JNR, 16 (2014) 2680.

Potenza M.A.C., Sanvito T., Pullia A., Accurate Sizing of Ceria Oxide Nanoparticles in Slurries by the Analysis of the Optical Forward Scattered Field, JNR, 17 (2015) 110.

Potenza M.A.C., Sanvito T., Pullia A., Measuring the Complex Field Scattered by Single Submicron Particles, submitted to Applied Physics Letters (2015b)

Pelssers E.G.M., Cohen M.A., Fleer G.J., Single Particle Optical Sizing (SPOS): I. Design and improved SPOS instrument and application to stable dispersions, Journal of Colloid and Interface Science, 137 (1990) 350–361.

Remsen E.E., Anjur S., Boldridge D., Kamiti M., Li S., Johns T., Dowell C., Kasthurirangan J., Feeney P., Analysis of large particle count in fumed silica slurries and its correlation with scratch defects generated by CMP, Journal of The Electrochemical Society, 153 (2006) G453–G461. doi: 10.1149/1.2184036

Ruth U., Concentration and size distribution of microparticles in the NGRIP Ice Core (Central Greenland) during the last glacial period. PhD Dissertation at Department of Geosciences of the University of Bremen. Published as Report n. 428 of the Berichte zur Polar- und Meeresforschung (2002) (ISSN 1618-3193). Available at: http://www.ub.uni-heidelberg.de/archiv/2291

Sachweh B., et al., In situ optical particle counter with improved coincidence error correction for number concentrations up to 10^7 particles cm^{-3}, Aerosol Science, 29 (1998) 1075–1086.

Seo Y.J., Methodological Study on the Recycle of Oxide-Chemical Mechanical Polishing Slurry, Journal of the Korean Physical Society, 50 (2007) 700–707.

Sultanova N., Kasarova S., Nikolov I., Dispersion properties of optical polymers, Acta Physica Polonica A, 116 (2009) 585–587.

Szczurowski M., (2014) private communication.

Terrell E., Beal D., Gromala J., Understanding Liquid Particle Counters. PMS Inc. Boulder, Colorado, 2006.

Testa F., Coetsier C., Carretier E., Ennahali M., Laborie B., Serafino C., Bulgarelli F., Moulin P., Retreatment of silicon slurry by membrane processes, Journal of Hazardous Materials, 192 (2011) 440–450. doi: 10.1016/j.jhazmat.2011.05.016

Testa F., Coetsier C., Carretier E., Ennahali M., Laborie B., Moulin P., Recycling a slurry for reuse in chemical mechanical planarization of tungsten wafer: Effect of chemical adjustments and comparison between static and dynamic experiments, Microelectronic Engineering, 113 (2014) 114–122. doi: 10.1016/j.mee.2013.07.022

Tinke A.P., Carnicer A., Govoreanu R., Scheltjens G., Lauwerysen L., Mertens N., Vanhoutte K., Brewster M.E., Particle shape and orientation in laser diffraction and static image analysis size distribution analysis of micrometer sized rectangular particles, Powder Technology, 186 (2008) 154–167. doi: 10.1016/j.powtec.2007.11.017

Van de Hulst H.C., Light Scattering by Small Particles, Dover N.Y, 1957.

Wells D., Nicoli D., Single-particle optical sensor with improved sensitivity and dynamic size range, US Patent (1996) 5835211 A

Whitby K.T., Vomela R.A., Response of Single Particle Optical Counters to Nonideal Particles, Environmental Science and Technology, 10 (1967) 801–814.

Zelenyuk A., Cai L., Imre D., From agglomerates of spheres to irregularly shaped particles: Determination of dynamic shape factors from measurements of mobility and vacuum aerodynamic diameters, Aerosol Sci Technol, 40 (2006) 197–217.

Author's short biography

Marco Potenza

Marco Potenza obtained his PhD in physics at the University of Milan with a thesis about the applications of nonlinear optics. Since 2002, he has been a permanent researcher at the University of Milan, where he now leads the Optics Group, developing novel instrumentation with scientific and technological applications. Since 2004, he has been working for the European Space Agency developing optical instrumentation for space, and he was the instrument scientist for the COLLOID experiment aboard the space station in 2010. He is the author of more than 50 papers and 5 patents.

Tiziano Sanvito

Tiziano Sanvito obtained his PhD in physics in 2013 within the Optics Group at the University of Milan with a thesis on the development of a novel technique for depolarized dynamic light scattering. He has been working on development of the SPES method and its applications in different fields of physics and science in general. He is the author of several research papers and a patent.

Giuseppe Fazio

Giuseppe Fazio is a physics graduate (application bearing, electronic branch) from Milan University. He has significant experience in industrial electronic devices and since 2000, he has been working in the semiconductor industry. In the semiconductor field, Giuseppe has significant experiences in advanced process and equipment control. He was the APC/AEC group leader in ST Microelectronics. He is the author and co-author of several publications and patents.

KONA Powder and Particle Journal No. 33 (2016) 322–332/Doi:10.14356/kona.2016018 Original Research Paper

Decoration of Carbon Nanotubes by Semiconducting or Metallic Nanoparticles using Fluidized Bed Chemical Vapour Deposition †

Pierre Lassègue [1], Nicolas Coppey [1], Laure Noé [2], Marc Monthioux [2] and Brigitte Caussat [1]*

[1] *Université de Toulouse, Laboratoire de Génie Chimique, France*
[2] *Centre d'Élaboration de Matériaux et d'Etudes Structurales (CEMES), UPR-8011 CNRS, France*

Abstract

Multi-Walled Carbon Nanotubes (MWCNTs) have promising properties that make them potentially useful in a wide variety of applications. The decoration of MWCNTs by metallic or semiconducting nanoparticles aims to intensify some of their properties, in particular thermal and electrical conductivity. Fluidized Bed Chemical Vapour Deposition (FBCVD) is an efficient process to uniformly coat powders by various materials. The coating by SnO_2, Fe and Si nanoparticles of MWCNTs (Graphistrength®) tangled in balls of 360 microns in mean diameter using the FBCVD process has been studied. The influence of some deposition parameters with and without oxidative pre-treatment is analysed on the nucleation and growth of nanoparticles. The various results obtained indicate that the intrinsic surface reactivity of MWCNTs is high enough for CVD precursors involving the formation of highly reactive unsaturated species such as silylene SiH_2 formed from silane SiH_4 pyrolysis in the case of Si deposition. But it must be enhanced for less reactive CVD precursors such as tin tetrachloride $SnCl_4$ which needs the presence of oxygen-containing groups at the nanotube surface to allow Sn nucleation. So, provided the reactivity of the powder surface and that of the CVD precursors are well tuned, the FBCVD process can uniformly coat the outer surface of MWCNTs by metallic or semiconducting nanoparticles.

Keywords: fluidized bed, chemical vapour deposition, multi-walled carbon nanotubes, nanoparticle deposition, silicon, tin oxide, iron

1. Introduction

Multi-Walled Carbon Nanotubes (MWCNTs) are nowadays a popular nanoform of graphenic carbon in which graphenes are arranged more or less parallel to the nanofilament axis. They have promising properties that make them potentially useful in a wide variety of applications such as electronics, renewable energy and composite materials. They exhibit a large surface area, high mechanical strength, and unique electrical properties, and are efficient thermal conductors (Monthioux et al., 2007). The decoration of MWCNTs by semiconducting or metallic nanoparticles (NPs) aims to intensify some of their physical properties. For instance, the deposition of silicon NPs on MWCNT networks allows the formation of anodes of Li-ion batteries with improved electrochemical performance due to the high specific capacity of silicon and good mechanical strength and structural flexibility of MWCNTs (Cui et al., 2010). Composites made of SnO_2 NPs deposited on MWCNTs present excellent sensing responses for gas detection at room temperature (Mendoza et al., 2014). Metal-coated MWCNTs can be used as reinforcing and conductive fillers for high-performance polymer composites by combining the electrical conductivity of the metal and the mechanical properties of the nanotubes (Babal et al., 2014).

There are many methods of depositing nanoparticles onto MWCNTs, each offering various degrees of control of particle size and distribution along the MWCNTs (Wildgoose et al., 2006; Bacsa and Serp, 2012). They are generally classified in two groups: the wet methods including the electrochemical, sol-gel and impregnation methods, and the gas processes such as Physical Vapour Deposition (PVD), Atomic Layer Deposition (ALD) and Chemical Vapour Deposition (CVD) (Kuang et al., 2006; Bacsa and Serp, 2012; Goulas et al., 2014). The wet im-

† Received 13 May 2015; Accepted 17 July 2015
J-STAGE Advance published online 10 October 2015
[1] ENSIACET/INP Toulouse/UMR CNRS 5503, 4 allée Émile Monso, BP84234, 31432 Toulouse Cedex 4, France
[2] 29 rue Jeanne Marvig, BP94347, 31055 Toulouse Cedex 4, France
* Corresponding author: Brigitte Caussat;
E-mail: brigitte.caussat@ensiacet.fr
TEL: +33-53-432-3632 FAX: +33-53-432-3697

pregnation method is the most widely used technique even if a multi-step method, because of its simplicity (Bacsa and Serp, 2012). However, the size of the coated particles is difficult to control precisely (Kuang et al., 2006). The gas processes yield products purer than the wet methods. They are single-step methods and generally involve high coating rates (Bacsa and Serp, 2012). CVD on MWCNTs has often been used to deposit metallic (Pt, Pd, Ru, Rh) or semiconducting (InP, CdSe) nanoparticles (Bacsa and Serp, 2012), but most often at the milligram scale, on nanotubes either deposited or supported on a planar substrate or put into a crucible as a fixed powder bed.

CVD can be adapted to the large-scale production of coated MWCNTs provided a good gas-solids contact can be achieved. Gas-solids fluidisation consists in flowing a gas upwards through a vertical bed of particles, thus generating an intense gas-solids mixing and subsequently high thermal and mass transfer rates between the gas and the powders (Kunii and Levenspiel, 1991). Fluidisation can be combined with the CVD technology, giving rise to the Fluidized Bed Chemical Vapour Deposition (FBCVD) process. If the MWCNTs can be fluidized, this technology allows multi-gram-scale beds of nanotubes to be uniformly coated with a high conversion rate of the gaseous precursor into solids, high versatility, good homogeneity of products and the possibility of continuous operations (Vahlas et al., 2006). This technology is also easy to use and to rescale, and requires low equipment costs (Vahlas et al., 2006).

Whatever the process used, a bottleneck in the coating of MWCNTs by metallic or semiconducting materials often concerns their surface reactivity. Nanotubes are formed of graphenes often arranged in a concentric manner with both ends ideally capped by fullerene-like structures. Due to the seamless arrangement of hexagon rings without any dangling bonds, carbon nanotube walls are rather unreactive (Lin et al., 2003). Experimental observations have clearly shown that surface defects which are inherently present play an important role in the adsorption of atoms on MWCNTs. But as the density in defects is generally low, a surface activation in the form of functionalization or creation of defects at the carbon nanotube surface is essential to achieve a high coating density (Feng and Puddephatt, 2007; Bacsa and Serp, 2012). The most common method at the lab scale is the oxidative acid reflux that purifies and functionalizes the nanotubes in one step by grafting hydroxyl (C-OH), carbonyl (C = O) and carboxyl (O = C-OH) groups on the nanotube surface (Bacsa and Serp, 2012; Vennerberg et al., 2014). However, the liquid wastes generated by these wet oxidation methods are not suited to industrial use (Kim and Min, 2010). Some works about gas-phase oxidation of CNTs using either air (Ajayan et al., 1993; Behler et al., 2006) or nitric acid vapours (Xia et al., 2009; Li et al., 2012; Rong et al., 2010) at high temperatures have led to mixed results: the CNTs were structurally damaged or far worse, even partially burnt. Gas-phase oxidation from ozone (O_3) is an environmentally friendly and low-cost route to form oxygen-containing groups on the CNT surface, even for mass production (Vennerberg et al., 2014). This route will be tested in the present work. By a pre-deposition of a titanium carbide (TiC) layer by CVD acting as a surface functionalization, Feng and Puddephatt (2007) have successfully increased the surface coverage of CNTs by Ni, Pd and Pt films deposited by CVD.

The present article aims to detail some examples of MWCNT coating by FBCVD in order to provide new insights concerning the interaction between a reactive gaseous phase leading to nanoparticle deposition and the nanotube surface. Three deposits were selected involving CVD precursors of very different reactivity and decomposition pathways. Tin oxide deposition from tin tetrachloride $SnCl_4$ and water vapour will be first presented, and then silicon deposition from silane SiH_4, and finally iron deposition from ferrocene $Fe(C_5H_5)_2$. In particular, it will be shown that surface activation is not always necessary to coat MWCNTs by metallic or semiconducting particles.

2. Experimental set-up

The experimental set-up (**Fig. 1**) is composed of a vertical stainless steel FBCVD reactor (internal diameter of 8.3 cm and 1 m in height) heated by a two-zone external furnace. The top of the reactor is water-cooled to ensure gas tightness. A high-performance HEPA13 filtration cartridge is placed at the exhaust of the reactor to collect any elutriated particles.

At the bottom, a perforated steel plate provides a homogeneous gas distribution and the conical zone of the gas inlet is pre-heated by either an oil bath or heating ribbons. A differential pressure sensor (Unik5000; Druck Ltd.) with taps under the distributor and at the top of the reactor measures the pressure drop across the MWCNT bed. An absolute pressure sensor (PR21; Keller) allows monitoring the total pressure below the distributor. Temperature is measured by several K-type thermocouples: three in a small tube along the vertical axis of the reactor to check the MWCNT bed isothermicity (T1 at 6 cm above the distributor, T2 at 21 cm and T3 at 28 cm for the SnO_2 and Si depositions, T1 at 6 cm, T2 at 12 cm and T3 at 21 cm for the Fe deposition), two on the outer reactor walls to control the temperature furnace and one in the bubblers when used.

Ferrocene $Fe(C_5H_5)_2$ (98 %, Strem Chemicals) and tin chloride $SnCl_4$ (anhydrous, 98 %, Strem Chemicals) are used as received. Deionised water is mixed to $SnCl_4$ to

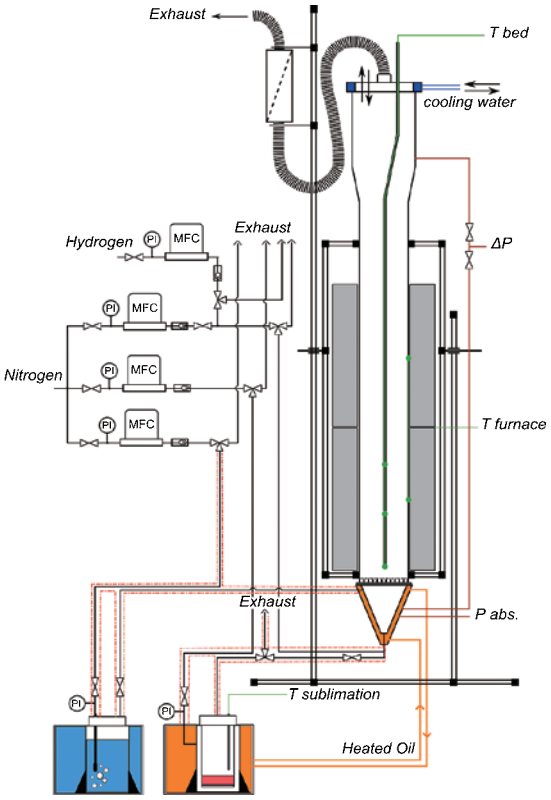

Fig. 1 FBCVD reactor.

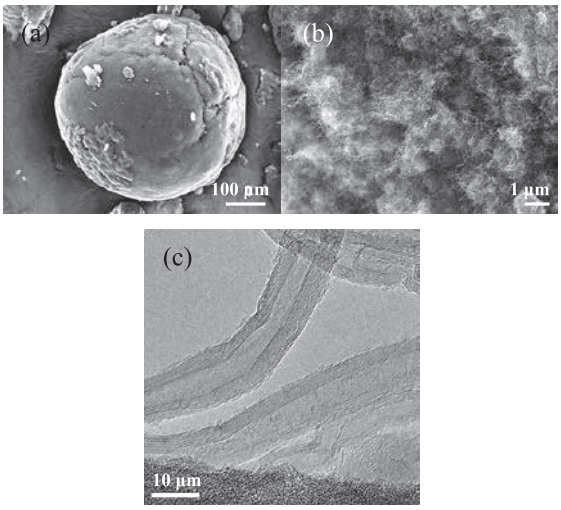

Fig. 2 **(a, b)** SEM and **(c)** TEM views of the raw MWCNTs.

deposit SnO_2. Each is loaded into a specific bubbler placed in a thermostatically controlled oil bath and connected to the reactor entrance by thermostated controlled gas lines. The bath temperature is fixed at 50 °C for $SnCl_4$ and H_2O and at 155 °C for ferrocene. All the gas lines are heated by heating ribbons to the same temperature as the precursor bubblers to avoid any premature condensation. Gas flows (N50 N_2 and H_2, Air Liquide) are regulated by mass flow controllers (MFC-7700 type; Aera), except silane (Electronic grade SiH_4, Air Liquide) whose flow rate is regulated by a ball rotameter (GT1355, Brooks Instrument). The ozone generator (Lab2B, Ozonia) is connected to the bottom of the FBCVD reactor and is fed with oxygen (Alphagaz oxygen, Air Liquide), ensuring an ozone concentration of 10 $g.h^{-1}$. All the experiments are performed at atmospheric pressure.

Multi-walled carbon nanotubes (Graphistrength® C100; Arkema) were used without any purification treatment. As can be seen in **Fig. 2a** and **2b**, they are entangled in the form of coarsely spherical balls of 388 µm in Sauter diameter.

Nanotube walls are made of 10–15 concentric graphenes with a mean external diameter of 12 nm. Some amorphous carbon is present on the walls and internal defects are visible (**Fig. 2c**). Their intrinsic iron content is 1.35 wt%. Their skeleton density is 1.984 kg/m^3, whereas the grain density of the MWCNT balls was estimated at ~180 kg/m^3 and their untapped density is equal to 90 kg/m^3 (Coppey, 2013) As found by other authors in the case of nanotubes (Yu et al., 2006; Dasgupta et al., 2011), these MWCNT balls display very good fluidization performance. They exhibit agglomerate particulate fluidization (APF) characteristics between 0 and 3.3 U_{mf} (minimum fluidization velocity) and agglomerate bubbling fluidization (ABF) features beyond 3.3 U_{mf} with high bed expansion (Coppey, 2013). This behaviour is characteristic of the fluidization of nanoparticle agglomerates (Zhu et al., 2005; Wang et al., 2007). It should favour excellent gas-solid contact and then high conversion rate of the CVD precursors and also uniform deposition. The minimum fluidization velocity U_{mf} of the MWCNT balls measured at ambient temperature under N_2 is equal to 1.2 $cm.s^{-1}$ (Coppey, 2013).

MWCNTs were analysed before and after ozone pre-treatment and CVD by several characterization techniques. The powder morphology was observed by Field Emission Gun Scanning Electron Microscopy (FEG-SEM) on a Jeol JSM-7100F linked to an Energy Dispersive X-ray (EDX) detector (X-MAX^N Oxford Instrument) and High-Resolution Transmission Electron Microscopy (HRTEM) using a CM30 (Philips) with LaB_6 gun and operated at 150 kV to minimise damaging irradiation effects. The SEM and TEM images presented in the article were selected from many as the most representative ones of each sample. X-ray Diffraction (XRD) results were obtained using a D8-2 (Drucker) with a monochromatic Kα copper (Cu) source (λ = 1.5418 Å). The iron weight percentage deposited on MWCNTs was measured by ICP-MS (XSeries2 Thermo Scientific).

A dimensionless bed pressure drop ΔP* was calculated as the ratio between the bed pressure drop and the theoretical one (the latter being equal to the bed weight per unit section area). The bed pressure drop was obtained by subtracting the pressure drop of the distributor from the

differential pressure measured.

The operating conditions tested are detailed in **Table 1**. 100 g of MWCNTs were used for each experiment, corresponding to a ratio between the fixed bed height and the reactor diameter of 2.3. Such a ratio is necessary to ensure good thermal transfer between the reactor walls and the FB and isothermal bed conditions, which are both well-suited to thermal CVD. The fluidization ratio U/U_{mf} was fixed to 4 to ensure a good compromise between the gas-particle mixing and the residence time of the gas in the bed. For liquid and solid precursors, the gaseous precursor molar fractions entering into the reactor were estimated by assuming the equilibrium in the bubblers and using the vapour pressure laws of Yaws (1999) for $SnCl_4$ and of Emel'yanenko et al. (2007) for ferrocene.

3. Results

3.1 Process behaviour

Fig. 3 presents the dimensionless bed pressure drop and thermal profile measured during run nCNT3. They are characteristic of the overall results obtained. The thermocouples T1 and T2 are located in the fluidized bed whereas T3 is just above the FB. Indeed, in a preliminary study conducted in a glass column, the fluidized bed height was measured at $U/U_{mf} = 4$ as varying between 25 and 27 cm (Coppey, 2013).

This explains that the temperatures measured by T1 and T2 are very close to each other, thanks to the good gas-solids mixing and particle-wall contact existing in the fluidized bed. The bed thermal gradient did not exceed 5 °C for all the CVD experiments. The temperature measured by T3 is lower because the thermocouple is located in a region where the fluidized particles are more diluted in the gas and then it is directly in sight of the reactor walls.

The T1 and T2 temperatures were not adversely affected by the deposit, probably due to the quite low inlet molar fractions of the precursors tested. The T3 temperature decreases with run duration because the fluidized bed height tends to decrease due to the grain density increase induced by the deposit.

The dimensionless bed pressure drop ΔP* progressively increased during deposition, which is indicative of the good fluidization of the bed. This allows the increase of the bed weight due to deposition to be followed in real time. The agreement between the deposited masses deduced from the bed pressure drop and those obtained by weighing the bed before and after deposition is good on average, confirming that the bed of MWCNTs remained fluidized during the whole experiment.

The elutriation of the powder was low, on average less than 1 wt% of the bed after the CVD experiments. This is due to the fact that the MWCNT balls were not broken by the FBCVD treatment: the Sauter diameter of the powders after CVD remained very close to that before treatment, as measured by laser size scattering analysis (not shown).

3.2 SnO_2 deposition

Possible CVD precursors of SnO_2 are $SnCl_4$, $Sn(CH_3)_4$, $(CH_3)_2SnCl_2$ and SnH_4 (VanMol, 2003; Coppey, 2013). By oxidation with O_2 or hydrolysis with H_2O, these precursors form a SnO_2 layer. The most commonly used precursor is tin tetrachloride $SnCl_4$ mixed with water, for which the deposition conditions are quite well established (Li

Table 1 Operating conditions tested and experimental results obtained

Run	Substrate	Target deposit	Average bed temperature (°C)	Run duration (min)	Precursor and inlet molar %	Deposited mass deduced from bed weighing (g)	Conversion rate of the main precursor (%)
T02	Raw CNTs	SnO_2	500	90	$SnCl_4$—0.9 H_2O—1.8	27	78
T05	Raw CNTs	SnO_2	550	125	$SnCl_4$—0.5 H_2O—1.9	17	90
T06	H_2O-CNTs	SnO_2	550	120	$SnCl_4$—0.5 H_2O—1.9	15	79
S30	Raw CNTs	Si	500	60	SiH_4—7	40	100
W6	H_2O-CNTs	Si	500	60	SiH_4—7	38.6	100
nCNT3	Raw CNTs	Fe	650	180	$Fe(C_5H_5)_2$—2.3	57	87
nCNT9	O_3-CNTs	Fe	650	180	$Fe(C_5H_5)_2$—2.3	52.5	100
nCNT10	O_3-CNTs	Fe	550	180	$Fe(C_5H_5)_2$—2.3	37.8	90
nCNT13	Raw CNTs	Fe	650	180	$Fe(C_5H_5)_2$—2.3	40	84

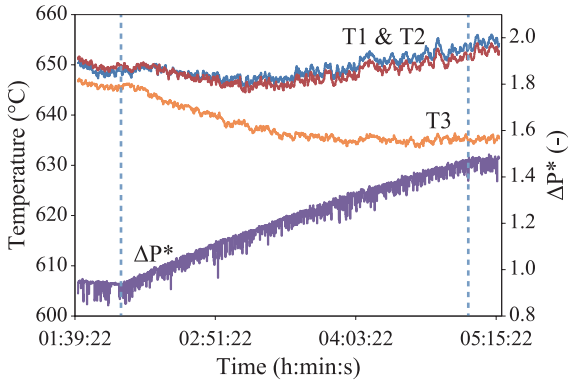

Fig. 3 Bed thermal profile and dimensionless pressure drop during run nCNT3 (the dotted lines indicate the beginning and the end of the deposit).

and Hua, 1997; VanMol, 2003; Coppey, 2013). This route has been used here.

Fig. 4a presents SEM images of the MWCNT balls after run T02 was performed at 500 °C as detailed in **Table 1**. The deposit appears as micron-size particles at the ball surface, predominantly in the interstices and cracks within the balls. At higher magnification (**Fig. 4b**), some particles of the deposit can be distinguished. They present a pyramidal form, characteristic of crystalline materials. Their size ranges from a few hundred nanometres to several microns. The largest ones might be made up of aggregates of primary particles of the deposit. So, the surface coverage of the MWCNTs is low.

Some SEM-EDX analyses on MWCNT balls which had been opened along their hemisphere (**Fig. 5**) reveal that the SnO_2 particles are present everywhere inside the balls. This means that the mass transfer rate inside the porous MWCNT balls is higher than or equal to the heterogeneous reaction rate, probably thanks to the quite low reactivity of the $SnCl_4$ precursor on the nanotube walls. **Table 2** summarizes the chemical reactions and pathways available in the literature about SnO_2 CVD from $SnCl_4/H_2O$. It appears that at our deposition temperature (500 °C), seeds can be formed in the gas phase and can then be captured by the particles of the bed to act as nuclei for the deposit (Li and Hua, 1997). A direct heterogeneous deposition pathway also exists. The two pathways could co-exist in our conditions.

In order to increase the reactivity of the precursors and then the direct nucleation on the MWCNT surface, a higher temperature was imposed for run T05. The $H_2O/SnCl_4$ ratio was also increased in order to favour the water adsorption on the MWCNTs and then to intensify the MWCNT surface reactivity. H_2O adsorption on the substrate is also necessary to allow Sn (Wartenberg et Ackermann, 1988) to be deposited.

Fig. 4c shows that the number of deposited particles seems to have decreased in comparison with run T02.

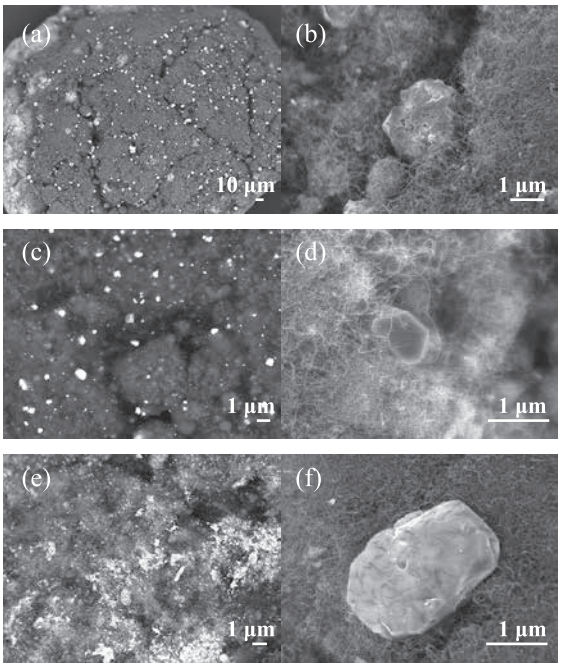

Fig. 4 SEM images of MWCNTs after **(a, b)** run T02, **(c, d)** run T05, **(e, f)** run T06 (SnO_2 deposition).

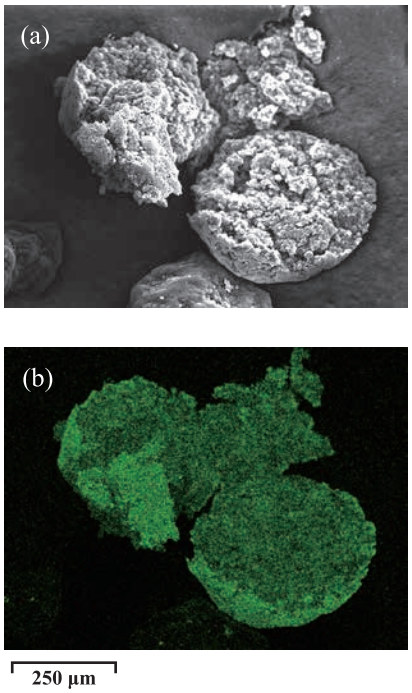

Fig. 5 **(a)** SEM image of a cut MWCNT ball after SnO_2 deposition, **(b)** corresponding EDX cartography of Sn (run T02).

This has been confirmed by the entire SEM analyses performed for these runs. Their formation still occurs predominantly in the interstices of the MWCNT balls. At higher magnification (**Fig. 4d**), the size of the particles seems larger than for run T02. As detailed in **Table 1**, the conversion rate of $SnCl_4$ is higher than for run T02 (90 %

Table 2 Chemical reactions and pathways involved in the CVD of SnO_2, Si and Fe

Deposit	Homogeneous chemical reactions	Heterogeneous chemical reactions	References
SnO_2	Unknown reaction pathway leading to SnO_2 fines formation above 400 °C at sufficiently high $SnCl_4$ and H_2O concentrations	From 200 °C: $SnCl_4 + 2\ H_2O \rightarrow SnO_2 + 4\ HCl$ Necessity of H_2O adsorption on the substrate to deposit Sn	Li and Hua (1997)–Van Mol (2003)–Wartenberg and Ackermann (1988)
Si	$SiH_4 \leftrightarrow SiH_2 + H_2$ $SiH_2 + SiH_4 \leftrightarrow Si_2H_6$ $SiH_2 + Si_nH_{2n+2} \leftrightarrow Si_{n+1}H_{2n+4}$	$SiH_4 \rightarrow Si + 2\ H_2$ $SiH_2 \rightarrow Si + H_2$ $Si_nH_{2n+2} \rightarrow n\ Si + (n+1)\ H_2$	Reuge et al. (2009)–Liu and Xiao (2015)
Fe	Possible homogeneous formation of Fe_3C particles and of CNT at temperatures higher than 500 °C	Under N_2: $Fe(C_5H_5)_2 \rightarrow Fe + 2\ C_5H_5$ Under H_2: $Fe(C_5H_5)_2 + H_2 \rightarrow Fe + 2\ C_5H_6$ Under H_2O: $4\ Fe(C_5H_5)_2 + 45\ H_2O \rightarrow 4\ Fe + 35\ CO + 65\ H_2 + 5\ CO_2$	Lubej and Plazl (2014)–Wasel et al. (2007)–Senocq et al. (2006)

instead of 78 %), meaning that the reactivity of the $SnCl_4/H_2O$ mixture was increased but the surface reactivity of the MWCNTs still remained too low. It can be concluded that the concomitant increase of the temperature and of the $H_2O/SnCl_4$ ratio was adequate to increase the precursor reactivity on already formed nuclei since growth was intensified, as found by Li and Hua (1997). However, this increase of precursor reactivity was not high enough to enhance SnO_2 heterogeneous nucleation on the graphenic surface of the MWCNTs, which is clearly the limiting step of the deposit, as found by Feng and Puddephatt (2007) for Ni deposition on CNTs.

In order to increase the MWCNT surface reactivity, a pre-treatment of the nanotube bed using water vapour was finally applied during 60 min at 650 °C at a fluidization ratio U/U_{mf} of 4, just before proceeding with the deposition using conditions close to those of run T05. **Fig. 4e** shows that after run T06, the deposit is mainly formed of nanosized particles even if some larger particles are present in which MWCNTs seem to be embedded, as shown on **Fig. 4f**.

So, the surface reactivity of the MWCNTs towards the $SnCl_4/H_2O$ precursors has been intensified by the water pre-treatment since the nucleation is clearly higher than for the previous runs. The fact that some MWCNTs have been trapped by the deposit in the largest deposited particles confirms the higher wettability of the MWCNT surface by the deposit.

The conversion rate of $SnCl_4$ is lower than for run T05, in fact quite close to that of run T02. This could mean that the nucleation rate on the graphenic surface remained lower than the growth rate on the already formed nuclei. An autocatalytic behaviour could exist, as it is often the case in the CVD of metals (Feng and Puddephatt, 2007).

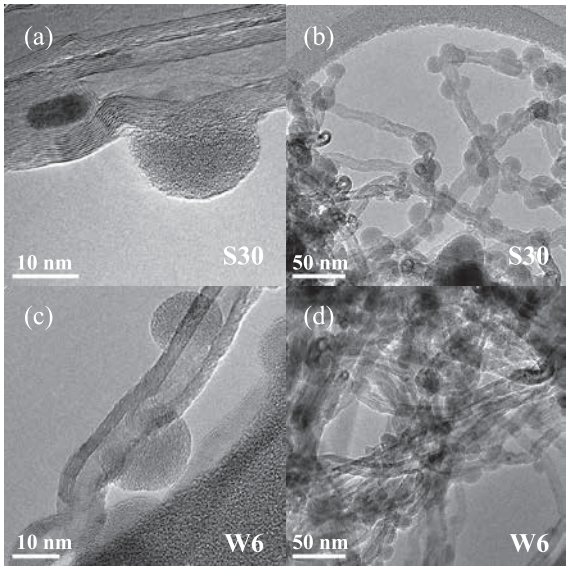

Fig. 6 TEM images of MWCNTs after **(a, b)** run S30, **(c, d)** run W6 (silicon deposition).

3.3 Si deposition

Silicon CVD precursors are most often chosen among the silanes (silane SiH_4, disilane Si_2H_6), the silicon chlorides ($SiHCl_3$, SiH_2Cl_2) or the organosilanes (in particular trimethyl silane $SiH(CH_3)_3$) (McEvoy et al., 2013). Even if pyrophoric, silane presents the advantages of producing pure silicon deposits at temperatures lower than 700 °C without any corrosive by-products, which explains its massive use in the microelectronic and photovoltaic industry (Braga et al., 2008; Reuge et al., 2009; McEvoy et al., 2013).

Figs. 6a and **6b** present TEM views of the MWCNTs after run S30 performed at 500 °C, as detailed in **Table 1**.

Silicon is present everywhere in the MWCNT balls, taking the form of nanoparticles of 20 nm in average diameter. This indicates that the mass transfer into the porous balls is not a limiting step of the process, as for the SnO_2 deposition. The nanoparticles are predominantly present on structural defects of the MWCNT surface.

The conversion rate of silane was 100 %, probably due to the high surface area of the MWCNT powder and to the quite high reactivity of silane.

The silicon nanoparticles are clearly more numerous and smaller than the SnO_2 particles. These results mean that the reactivity of silane is higher than that of the $SnCl_4/H_2O$ mixture. However, a nucleation limitation still exists for Si deposition since the surface coverage of the MWCNT surface is not 100 %. It is well-known that, as detailed in **Table 2**, when silane is heated to temperatures higher than 370 °C, pyrolysis reactions occur in the gas phase leading to the formation of very reactive unsaturated molecules such as silylene SiH_2. It is likely that these unsaturated molecules are the origin of the first formation of nuclei on the MWCNT surface.

They are probably much more reactive than the species formed during the depositions from $SnCl_4/H_2O$. However, they are not reactive enough to chemisorb and form nuclei everywhere on the inert MWCNT surface. Once the first Si nuclei are formed on the nanotube surface, the growth is probably easier as shown by Zahi et al. (2011) on SiO_2 planar substrates, explaining the 100 % conversion of silane.

In order to intensify the surface reactivity of the MWCNTs, a pre-treatment using water vapour at 650 °C was applied during 60 min at a fluidization ratio of 4 just before the deposition using the conditions of run S30, as detailed in **Table 1**. The conversion rate of silane for run W6 was still 100 %. As can be seen in **Figs. 6c** and **6d**, no significant difference can be seen regarding the morphology of the deposit between this run and run S30. The size, localisation and surface density of the Si nanoparticles are unchanged. It can be concluded that for the conditions tested, the water pre-treatment has not modified the surface reactivity of the MWCNTs for the silicon deposition from silane.

If we compare with the SnO_2 deposition results, the same pre-treatment was applied to the MWCNTs. In the case of $SnCl_4/H_2O$, an increase of the deposit nucleation had occurred, whereas this was not the case for silane. As previously explained, $SnCl_4$ needs a preliminary H_2O adsorption step for allowing the chemisorption of Sn to occur. It is then logical that the SnO_2 deposition is intensified by an H_2O pre-treatment. On the contrary, the surface reactivity of the chemical species responsible for silicon deposition is not intensified by the H_2O pre-treatment. Previous works (Zahi et al., 2011) about the first steps of nucleation and growth during silicon CVD from silane on planar substrates have shown that substrates covered by hydroxyl (OH) groups involve a quite low surface reactivity of unsaturated species such as SiH_2 due to the high electronegativity of the oxygen atom. For the Si FBCVD process, the creation of more defects on the MWCNT surface would probably have been more efficient to increase Si nucleation.

3.4 Fe deposition

Among the possible CVD precursors of iron, ferrocene ($Fe(C_5H_5)_2$) is an organometallic compound stable in air and non-toxic, quite cheap and easy to sublimate, forming stable vapour to feed the CVD reactor (Philippe, 2006; Senocq et al., 2006) and able to deposit pure iron (Stauf et al., 1987; Dormans, 1991).

As detailed in **Table 1**, the deposition temperature was fixed at 650 °C, except for nCNT10 (550 °C) because of the reactivity increase of ferrocene induced by the presence of hydrogen (Wasel et al., 2007; Qian et al., 2001).

Under an inert atmosphere (N_2), **Figs. 7** and **8a** show that the deposit occurs in the form of discrete iron-based nanoparticles of 50–500 nm in diameter confined in a graphenic carbon shell and present everywhere in the MWCNT balls. This has been confirmed by SEM-EDX analyses (not shown) at the ball scale.

This uniform distribution indicates that the mass transfer into the porous balls is not a limiting step of the process, as for the previous deposits. But the surface coverage of the MWCNTs is low. So, a nucleation limitation also exists for this deposit. X-Ray Diffraction (XRD) analyses (**Fig. 9**) indicate that the nanoparticles are composed of iron and iron carbide Fe_3C for all runs. A possible explanation is that the homogeneous decomposition of ferrocene under N_2 is auto-catalytic beyond 500 °C (Senocq et al., 2006) and forms Fe_3C particles (cementite) which can then be captured by the nanotubes of the bed. Some nanoparticles could also directly nucleate on the MWCNT surface, probably on surface defects like for silicon. Some

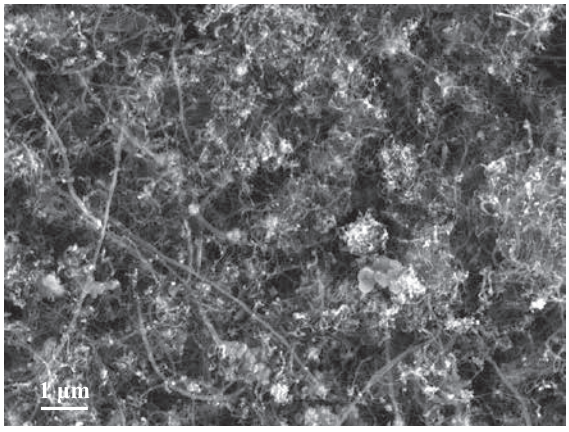

Fig. 7 SEM image of MWCNTs after run nCNT3 (deposition from ferrocene).

of the nanoparticles seem to catalyse the formation of nanofibres (CNFs) or of large CNTs.

Ferrocene is indeed known to be a precursor of both iron and carbon nanomaterials (Bhatia and Prasad, 2010). Carbon coming from the ligands lost by ferrocene during its decomposition could saturate iron nanoparticles to form Fe_3C and then CNTs and/or carbon nanofibres (CNFs).

The conversion rate of ferrocene into iron deposited within the MWCNT balls was deduced from ICP-MS measurements and bed weighing. It is 87 %, as detailed in **Table 1**. ICP-MS measurements indicate that the powder after run nCNT3 is composed of 11.8 wt% of iron (without removing the initial iron content).

The same deposition conditions were tested after an O_3 pre-treatment (nCNT9) in order to increase the surface reactivity of MWCNTs and then the nucleation of iron. TEM images (**Fig. 8b**) indicate that the deposit produces 10–100-nm-size iron-based particles more uniformly distributed at the TEM scale than previously. The deposited particles are then more numerous and smaller than previously. These two effects and the more uniform presence of nanoparticles on the nanotube surface could be a consequence of ozonation. By grafting oxygen-containing groups (hydroxyl or carboxyl) onto the nanotube surface, ozonation increases the nucleation of iron-based nanoparticles and then the surface reactivity of MWCNTs towards ferrocene and its gaseous products of decomposition. This is confirmed by the ICP-MS iron content of 17.6 wt% in the powder and by the higher ferrocene conversion rate (close to 100 %), as detailed in **Table 1**. However, the deposited nanoparticles are still covered by graphenic shells, CNFs/CNTs are still formed and the deposit is still composed of Fe and Fe_3C (**Fig. 9**). Moreover, a large amount of amorphous carbon was deposited everywhere.

The addition of H_2 at a volume percentage higher than 25 % is known to limit CNF/CNT growth and amorphous carbon formation (Wasel et al., 2007; Qian et al., 2001). Consequently, H_2 was added with a H_2/N_2 ratio of 67/33 vol.% during run nCNT10. TEM images (**Fig. 8c**) reveal less numerous iron-based nanoparticles which are less uniformly distributed at the TEM scale. These Fe/Fe_3C particles are smaller (20–50 nm) and still covered by graphenic shells but no CNFs/CNTs were observed and the large amount of amorphous carbon previously reported is absent. So, the addition of H_2 seems to have inhibited the formation of both the amorphous carbon and the CNT/CNFs, but seems also to reduce the nanoparticle nucleation and growth, as confirmed by the ICP-MS iron content of 13.7 wt% and by the ferrocene lower conversion rate (90 %).

According to Senocq et al. (2006), the addition of water

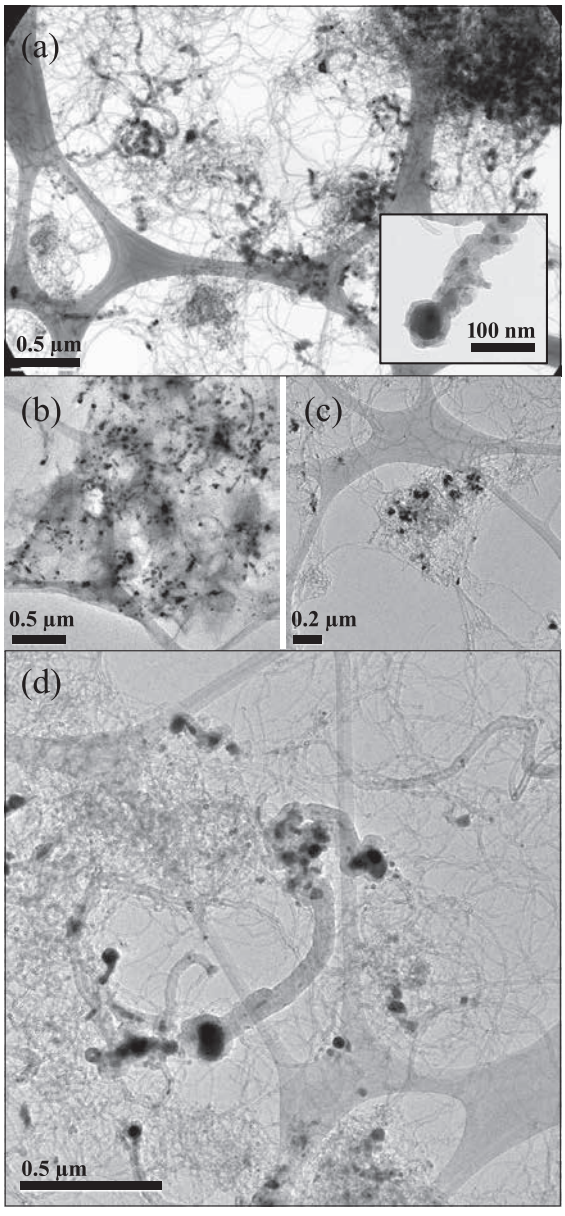

Fig. 8 TEM images of MWCNTs (a) run nCNT3—insert: view of a Fe nanoparticle forming **(a)** CNF, **(b)** run nCNT9, **(c)** run nCNT10, **(d)** run nCNT13 (deposition from ferrocene).

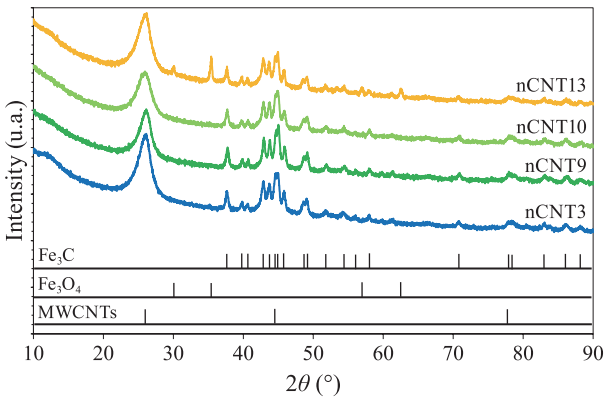

Fig. 9 XRD spectra of MWCNTs after deposition from ferrocene.

vapour to ferrocene could favour the formation of pure iron films under conditions close to ours. The run nCNT13 was then performed in the presence of water vapour. TEM images are shown in **Fig. 8d**. Less numerous and less uniformly distributed Fe_3O_4/Fe_3C nanoparticles are covered by graphenic shells and have catalysed the formation of large CNFs/CNTs. Their diameter is related to the nanoparticle size, ranging between 10 and 100 nm. The ICP-MS iron content is 12.3 wt%, which is similar to that of run nCNT3. This means that under the conditions tested, the addition of water vapour does not favour the deposition of pure iron nanoparticles as expected. It even seems to lower the ferrocene reactivity in proportion close to that observed in the presence of hydrogen, as indicated by the ferrocene conversion rate of 84 % given in **Table 1**.

When compared with the two previous deposition experiments (SnO_2 and Si), the use of ferrocene involves not only a nucleation limitation on the nanotube surface as strong as for the $SnCl_4/H_2O$ system, but also a difficulty to form pure iron deposits, which was not the case of the two previous deposits studied. When compared with other works performed on steel, quartz or Si planar substrates (Stauf et al., 1987; Dormans, 1991; Senocq et al., 2006), this difficulty to deposit pure iron is clearly reinforced by the chemical nature of the MWCNT surface. A pre-deposit of TiC as done by Feng and Puddephatt (2007) could improve both the surface reactivity of the MWCNTs and the selectivity of ferrocene decomposition to produce pure iron deposits.

4. Conclusion

Multi-walled carbon nanotubes were decorated by three kinds of nanoparticles from precursors of very different reactivity using the fluidized bed chemical vapour deposition process.

When comparing the results obtained in terms of nucleation of nanoparticles on the nanotube surface, it clearly appears that the intrinsic reactivity of the CVD precursors is a key factor. The most reactive precursor we studied, silane SiH_4, forms many silicon nanoparticles of several tens of nanometres on the nanotube surface, without any nanotube pre-treatment. This is not the case with the less reactive $SnCl_4/H_2O$ system for which the nucleation of SnO_2 nanoparticles was favoured by an H_2O pre-treatment. A third situation was observed using ferrocene, for which not only a nucleation limitation on the nanotube surface exists, but also a difficulty to obtain pure iron deposits which seems reinforced by the chemical nature of the nanotube surface. However, an ozone pre-treatment of the nanotubes made it possible to increase the iron deposition.

So, the FB-CVD process can successfully decorate carbon nanotubes by metallic or semi-conducting nanoparticles provided that the reactivity of the precursors towards the nanotube surface is high enough. If this is not the case, a dry mode pre-treatment of the nanotubes by ozone or water vapour can be efficient if the surface modification involved is well-suited to the precursor reactivity. The reactive pathways of the precursor must then be analysed accurately before deciding whether to apply a pre-treatment and what kind of pre-treatment.

In comparison with the wet methods, a main advantage of the dry mode pre-treatments in fluidized beds and of the FB-CVD process is that they can treat large amounts of carbon nanotubes, i.e. 100 g at lab-scale and tons at the industrial scale, opening the way for a mass production of decorated MWCNTs for applications such as nano-fillers of innovative multi-functional composite materials or high-capacity anodes for Li-ion batteries.

Acknowledgements

The part of work concerning iron deposition was supported by the French Midi-Pyrénées region and by the Waspe FUI project. The authors thank M. Molinier and E. Prévot from LGC for technical help and ARKEMA for providing the carbon nanotubes.

References

Ajayan P.M., Ebbesen T.W., Ichihashi T., Iijima S., Tanagaki K., Hiura H., Opening carbon nanotubes with oxygen and implications for filling, Nature, 362 (1993) 522–525.

Babal A.S., Gupta R., Singh B.P., Singh V.N., Dhakate S.R., Mathur R.B., Mechanical and electrical properties of high performance MWCNT/polycarbonate composites prepared by an industrial viable twin screw extruder with back flow channel, RSCAdv., 4 (2014) 64649–64650.

Bacsa R., Serp P., Decorated (coated) carbon nanotubes, in: Monthioux M. (Ed.), Carbon meta-nanotubes, synthesis, properties and applications, Wiley, 2012, pp. 163–207.

Behler K., Osswald S., Ye H., Dimovski S., Gogotsi Y., Effect of thermal treatment on the structure of multiwall carbon nanotubes, J. Nanopart. Res., 8 (2006) 615–625.

Bhatia R., Prasad V., Synthesis of multiwall carbon nanotubes by chemical vapour deposition of ferrocene alone, Solid State Commun., 150 (2010) 311–315.

Braga A.F., Moreira S.P., Zampieri P.R., Bacchin J.M.G., Mei P.R., New processes for the production of solar-grade polycrystalline silicon: a review, Solar En. Mat. Solar Cells, 92 (2008) 418–424.

Coppey N., Nanotubes de carbone décorés par CVD en lit fluidisé: application en batterie lithium-ion, PhD thesis, INP Toulouse, France, 2013.

Cui L.F., Hu L., Choi J.W., Cui Y., Light-weight free-standing carbon nanotube-silicon films for anodes of lithium ion

batteries, ACSNano, 4 (2010) 3671–3678.
Dasgupta K., Joshi J.B., Banerjee S., Fluidized bed synthesis of carbon nanotubes—A review, Chem. Eng. J., 171 (2011) 841–869.
Dormans G.J.M., OMCVD of transition metals and their silicides using metallocenes and (di)silane or silicon tetra-bromide, J. Cryst. Growth, 5 (1991) 806–816.
Emel'yanenko V.N., Verevkin S.P., Krol O.V., Varushchenko R.M., Chelovskaya N.V., Vapour pressures and enthalpies of vapourization of a series of the ferrocene derivatives, J. Chem. Thermodyn., 39 (2007) 594–601.
Feng M., Puddephatt R.J., Chemical Vapour Deposition of nickel-group metals on multiwall carbon nanotubes, Can. J. Chem., 85 (2007) 645–650.
Geldart D., Types of gas fluidization, Powder Techn., 7 (1973) 285–292.
Goulas A., Ruud van Ommen J., Scalable production of nanostructured particles using atomic layer deposition, Kona Powder and Particle Journal, 31 (2014) 234–246.
Kim J.H., Min B.G., Functionalization of multi-walled carbon nanotube by treatment with dry ozone gas for the enhanced dispersion and adhesion in polymeric composites, Carbon Lett., 11 (2010) 298–303.
Kuang Q., Li S.F., Xie Z.X., Lin S.C., Zhang X.H., Xie S.Y., Huang R.B., Zheng L.S., Controllable fabrication of SnO_2-coated multiwalled cabon nanotubes by Chemical Vapour Deposition, Carbon, 44 (2006) 1166–1172.
Kunii D., Levenspiel O., Fluidization engineering, second edition, John Wiley & sons Inc., New York, 1991.
Li C., Hua B., Preparation of nanocrystalline SnO_2 thin film coated Al_2O_3 ultrafine particles by fluidized chemical vapour deposition, Thin Solid Films, 310 (1997) 238–243.
Li C., Zhao A., Xia W., Liang C., Muhler M., Quantitative studies on the oxygen and nitrogen functionalization of carbon nanotubes performed in the gas phase, J. Phys. Chem. C, 116 (2012) 20930–20936.
Lin T., Bajpai V., Ji T., Dai L., Chemistry of carbon nanotubes, Aust. J. Chem., 56 (2003) 635–651.
Liu S.S., Xiao W.D., CFD-PBM coupled simulation of silicon CVD growth in a fluidized bed reactor: Effect of silane pyrolysis kinetic models, Chem. Eng. Sci., 127 (2015) 84–94.
Lubej M., Plazl I., Theoretical and experimental study of iron catalyst preparation by chemical vapour deposition of ferrocene in air, Chem. Eng. J., 242 (2014) 306–312.
McEvoy A., Markvart T., Castaner L., Solar Cells: Materials, Manufacture and Operation, Elsevier, second edition, 2013.
Mendoza F., Hernandez D.M., Makarov V., Febus E., Weiner B.R., Morell G., Room temperature gas sensor based on tin dioxide-carbon nanotubes composite films, Sensors Actuat. B, 190 (2014) 227–233.
Monthioux M., Serp P., Flahaut E., Laurent C., Peigney A., Razafinimanana M., Bacsa W., Broto J.M., Introduction to carbon nanotubes, in: Brushan B. (Ed.), Springer Handbook of Nanotechnology, Second revised and extended edition, Springer-Verlag, Heidelberg, 2007.
Philippe R., Synthèse de nanotubes de carbone multi-parois par dépôt chimique en phase vapeur catalytique en lit fluidisé. Nouvelle classe de catalyseurs, étude cinétique et modélisation, PhD thesis, INP Toulouse, France, 2006.
Qian D., Dickey E.C., Andrews R., Jacques D., Kinetics of carbon nanotube growth by pyrolysis of ferrocene/xylene, Carbon, 1 (2001) 1117–1119.
Reuge N., Cadoret L., Caussat B., Multifluid eulerian modelling of a silicon fluidized bed Chemical Vapour Deposition process: analysis of various kinetic models, Chem. Eng. J., 148 (2009) 506–516.
Rong H., Liu Z., Wu Q., Lee Y.H., A facile and efficient gas phase process for purifying single-walled carbon nanotubes, Curr. Appl. Phys., 10 (2010) 1231–1235.
Ruan S.L., Gao P., Yang X.G., Yua T.X., Toughening high performance ultrahigh molecular weight polyethylene using multiwalled carbon nanotubes, Polymer, 44 (2003) 5643–5654.
Senocq F., Duminica D., Maury F., Delsol T., Vahlas C., Iron thin films from $Fe(CO)_5$ and $FeCp_2/H_2O$ under atmospheric pressure, J. Electrochem. Soc., 153 (2006) G1025–G1031.
Stauf G.T., Driscoll D.C., Dowben P.A., Barfuss S., Grade M., Iron and nickel thin film deposition via metallocene decomposition, Thin Solid Films, 153 (1987) 421–430.
Vahlas C., Caussat B., Serp P., Angelopoulos G., Principles and applications of CVD powder technology, Mat. Sci. Eng.: Reports, 53 (2006) 1–72.
Van Mol A.M.B., Chemical Vapour Deposition of tin oxide thin films, Technische Universiteit Eindhoven, 2003, ISBN 90-386-2715-7.
Vennerberg D.C., Quirino R.L., Jang Y., Kessler M.R., Oxidation behaviour of multi walled carbon nanotubes fluidized with ozone, Appl. Mater. Interfaces, 6 (2014) 1835–1842.
Wang X.S., Rahman F., Rhodes M.J., Nanoparticle fluidization and Geldart's classification, Chem. Eng. Sci., 62 (2007) 3455–3461.
Wartenberg E.W., Ackermann P.W., Electrical and mechanical properties of quenched SnO_2 films on glass substrates, Glastechnische Berichte, 61 (1988) 256–262.
Wasel W., Kuwana K., Reilly P.T.A., Saito K., Experimental characterization of the role of hydrogen in CVD synthesis of MWCNTs, Carbon, 45 (2007) 833–838.
Wildgoose G.G., Banks C.E., Compton R.G., Metal nanoparticles and related materials supported on carbon nanotubes: methods and applications, Small, 2 (2006) 182–193.
Xia W., Jin C., Kundu S., Muhler M., A highly efficient gas-phase route for the oxygen functionalization of carbon nanotubes based on nitric acid vapour, Carbon, 47 (2009) 919–922.
Yaws C.L., Chemical Properties Handbook, McGrawHill, 1999.
Yu H., Zhang Q., Gu G., Wang Y., Luo G., Wei F., Hydrodynamics and gas mixing in a carbon nanotube agglomerate fluidized bed, A.I.Ch.E. Journal, 52 (2006) 4110–4123.
Zahi I., Mur P., Blaise Ph., Esteve A., Djafari Rouhani M., Vergnes H., Caussat B., Multi scale modelling of silicon nanocrystals synthesis by Low Pressure Chemical Vapour Deposition, Thin Solid Films, 519 (2011) 7650–7658.
Zhu C., Yu Q., Dave R.N., Gas fluidization characteristics of nanoparticle agglomerates, A.I.Ch.E. Journal, 51 (2005) 426–437.

Author's short biography

Pierre Lassègue

Pierre Lassègue is a PhD student in the Innovative Multiphase Reactor Engineering Department of the Laboratory of Chemical Engineering at the National Polytechnic Institute of Toulouse. He received his BSc degree in chemistry and physico-chemical processes in 2011 and his two MSc degrees in process engineering and in environment and processes in 2013 from Toulouse University. His research interests concern carbon nanotubes and fluidized bed chemical vapour deposition.

Nicolas Coppey

Dr. Nicolas Coppey is currently working as a laboratory manager at SNAM, a European player collecting and recycling metals from batteries. He is taking part in the development of hydrometallurgy treatment units to optimise recycling performance. He received his PhD. in process engineering and environment from the University of Toulouse in 2013 under the supervision of Prof. Brigitte Caussat. He studied the decoration of carbon nanotubes by silicon nanoparticles and the application as an electrode material in lithium-ion batteries.

Laure Noé

Mrs Laure Noé has been tenured at the French National Research Institute (CNRS) since 1991, where she is currently working as an assistant engineer. She is dedicated to the synthesis and/or characterization of materials (mostly carbon nanoforms, but other nanomaterials as well, and more recently archaeological crafts), formerly regarding their chemical composition by means of chemical analytical routes, nowadays regarding their structural, textural, and chemical features by means of TEM-related methods (HRTEM, electron diffraction, X-EDS). She has co-authored 22 publications in international journals and 37 papers in colloquia and conferences.

Marc Monthioux

Dr. Marc Monthioux is currently working as a research director at the French National Research Institute (CNRS). He has been working on the synthesis and/or structural characterisation of carbon and carbon-containing materials of any kind since 1979. He is currently co-editor of CARBON journal (Elsevier), former chairman of the French Carbon Group (GFEC) and former chairman of the European Carbon Association (ECA). He has (co)authored 18 book chapters, more than 340 papers in conferences, and more than 130 papers in international journals cited more than 5000 times (h = 30).

Brigitte Caussat

Brigitte Caussat is a professor of chemical engineering in the Innovative Multiphase Reactor Engineering Department of the Laboratory of Chemical Engineering at the National Polytechnic Institute of Toulouse. She is an engineer in chemical engineering and received her PhD in 1994. Her research interests concern the chemical vapour deposition processes either on planar substrates to form graphene and thin films, or in fluidized bed to decorate carbon nanotube balls and to coat powders. She is co-author of more than 80 publications, 6 patents and 90 papers.

KONA Powder and Particle Journal No. 33 (2016) 333–339/Doi:10.14356/kona.2016019 Original Research Paper

Nanostructure Design on Porous Carbon Powders under Chemical Process and Their Physical Properties †

Tomoya Nakazono* and Takahiro Morishita

[1] *Performance chemicals Div., Advanced Carbon Technology Center, ToyoTanso Co. Ltd, Japan*

Abstract

The carbon pore-structure formed by MgO-templated method consists of nano-carbon wall and mesopore made with MgO. From MgO and its mixtures with resin that have high yield of carbon, micro-mesoporous carbons were obtained through their carbonization at 900 °C, followed by the dissolution of MgO. The carbon powder prepared by this method possesses high surface area without any activation process. The mesopore size of carbon powders is controlled by the crystallite size of MgO, and micropore amount depends on resin structure. Crystallinities of their carbon powders with heat-treatment up to 2500 °C were very uniform.

Keywords: MgO-templated carbon coating process, mesoporous carbon, crystallinity, nano structure

1. Introduction

Various kinds of porous carbon materials are produced, which can be used as adsorbents, energy storage electrodes, and catalyst supports, etc. (Derbyshire F. et al., 1995). In order to get a high surface area, the oxidation and vapor activation process of carbon are usually employed. Through this process various activated carbons are prepared and applications developed (Derbyshire F. et al., 1995; Sanada Y. et al., 1992; Inagaki M, 2000).

On the other hand, there have been reported various precursors and processes to prepare porous carbons without any activation process. Pore size controlled carbons were prepared by using hard templates, such as zeolites and silicates (Kyotani T. et al., 2003; Shi Z-G. et al., 2003). For these template processes, however, it was pointed out that the template had to be dissolved out by strong acids after carbonization and that large amount of production was not easy, although the pores with a specific size were easily obtained. On the other hand, without template use, carbonization of organic aerogels was also reported to give mesoporous carbons (Hanzawa Y. et al., 1998; Tamon H. et al., 1997; Yamamoto T. et al., 2001).

We have developed easy process to coat metal-oxide ceramic particles by carbon; the powder mixtures of thermoplastic resin, such as poly(vinyl alcohol) and phenol resin dispersion, etc., and ceramics were heat-treated at a high temperature in an inert atmosphere. The carbon layer coated on the surface of a ceramic particle was found to be porous, and 3D-nano dimensions when using MgO as substrate metal oxide and dissolving it out by sulfuric acid (Inagaki M. et al., 2004). This result suggested us a new preparation process of porous carbons without any stabilization and activation processes even starting from thermoplastic precursors.

Following this idea, MgO-templated carbonization process was developed for preparing mesoporous carbons by heat-treatment of mixtures of carbon precursor and MgO powder or through the thermal decomposition of magnesium citrate (Morishita T. et al., 2006). Characterization of heat-treated MgO-templated carbons derived from magnesium citrate was reported. The obtained carbons show high BET surface area and superior electric conductivity even after the heat-treatment at around 2000 °C (Orikasa H. et al., 2012). These carbons also show high performance as negative electrode of a Li-ion capacitor (Soneda Y. et al., 2013).

In this study, we prepared the porous carbons derived from three different carbon precursors and MgO powders, and characterized them. Each carbon precursor's difference is reported.

2. Experimental

2.1 Non-crystalline mesoporous carbon

Magnesium oxide (MgO) was used as a template because of its chemical and thermal stability, no structural and compositional changes, no reduction with carbon, and

† Received 1 July 2015; Accepted 17 September 2015
J-STAGE Advance published online 10 October 2015
[1] 5-7-12 Takeshima, Nishiyodogawa-ku, Osaka 555-0011, Japan
* Corresponding author: Tomoya Nakazono;
E-mail: t_nakazono@toyotanso.co.jp
TEL: +81-6-6472-5914 FAX: +81-6-6471-0617

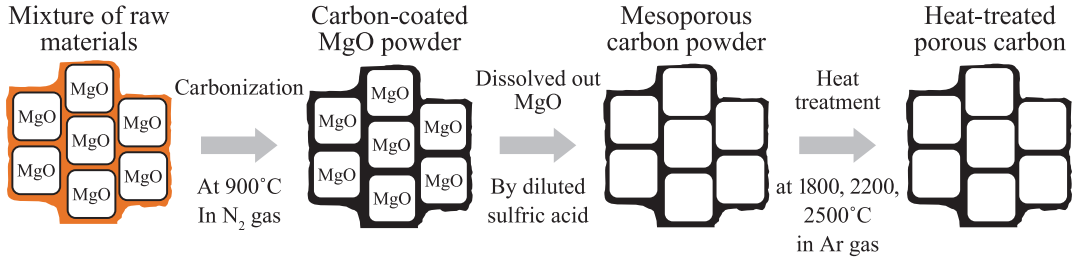

Fig. 1 Illustration of preparation method of porous carbons.

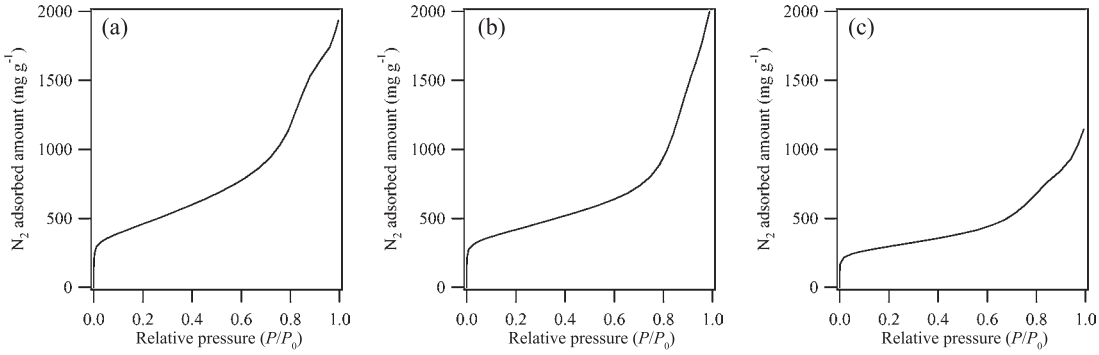

Fig. 2 N_2 adsorption isotherms of the carbons derived from (a), PVA (b) phenol and (c) imide.

easy dissolving to dilute acidic aqueous solutions. MgO powders were analyzed by XRD and these crystallite sizes were calculated by a Scherrer equation. In this study, MgO powders with an average crystallite size of 11 nm were used. Carbon precursors were poly(vinyl alcohol) (PVA), Kapton-type polyimide (Imide), and phenol resin dispersion (Phenol). MgO powders/carbon precursors were mixed 4/6 by weight. Its mixtures of Phenol or Imide were cured in inert atmosphere and then ground to powders. Its mixtures thus prepared were heated at a temperature of 900 °C for 1 h in a flow of N_2. Heating rate was 5 °C/min. After carbonization, the mixture was stirred in diluted sulfuric acid (3.5 mol/L) to dissolve out MgO. Its slurry was repeated suction filtration and water rinse until the pH of its filtrate showed 5 to 7. Finally carbons were recovered as powders after drying at 150 °C for 96 h in a flow of air. Illustration of the preparation method is shown in **Fig. 1**.

2.2 Highly crystalline mesoporous carbon

As-prepared carbon powders were heat-treated at 1800, 2200, 2500 °C for 1 h in Ar atmosphere for graphitization.

The obtained carbons were characterized by XRD, TEM, Thermogravimetry, and N_2 adsorption analysis. BET surface area was determined from the adsorption isotherms of N_2 gas measured at 77 K. Pore size distribution was evaluated by BJH method and HK method. Oxidation loss temperature was estimated by thermogravimetry in air up to 900 °C.

Table 1 BET surface areas and pore volumes

	BET surface area (m^2/g)	Vtotal (ml/g)	Vmeso (ml/g)	Vmicro (ml/g)
PVA	1315	2.12	1.64	0.48
Phenol	1189	2.15	1.70	0.45
Imide	837	1.20	0.88	0.32

3. Results and discussion

3.1 Non-crystalline mesoporous carbon

The carbons derived from PVA and Phenol had similar N_2 adsorption isotherms as seen in **Fig. 2**. BET surface areas and pore volumes are listed in **Table 1**. The pore size distributions by BJH method are shown in **Fig. 3**. The as-prepared carbons have high mesopore volume of 0.88–1.70 ml/g, with micropore volume of 0.32–0.48 ml/g slightly depending on the carbon precursor. The pore size at the peak distribution is about 11 nm on each carbon precursor. It's the same about crystallite size of MgO. This result suggests that carbons were coated along crystallite of MgO. TEM images of carbons derived from phenol and imide are shown in **Fig. 4(a)** and **(b)**. Pores are formed with amorphous carbon layers. The porous structure seemed like inter-connected three dimensionally. Thus, pore volume parameters depend slightly on three different carbon precursors, but the pore size at the peak distribution depends on crystallite size of MgO, not carbon precursors.

3.2 Highly crystalline mesoporous carbon

BET surface area and pore volumes of mesoporous carbons are shown in **Fig. 5** and **Table 2**. Pore size distributions measured by BJH method are shown in **Fig. 6**. The heat-treatment at 1800 °C gave only a small change in pore structure; no change in mesopore volume, a slight decrease in micropore volume, and consequently small decreases in total pore volume and BET surface area. Pore size profiles also nearly unchanged after heat-treatment at 1800 °C. However, it has to be pointed out that these changes show a sharp contrast to some commercially available activated carbons, where marked collapsing of micropores has been observed (Inagaki M. et al., 2014). After the heat-treatment above 1800 °C, all pore parameters decreased markedly. But the peak positions at around 11 nm didn't shift even after pore volume decreased relatively. These results suggest that mesopore structures didn't collapse by heat-treatment despite decreasing mesopore volumes for some reasons such as forming closed pore by shrinking of micropores. Thus their heat-treatment temperature dependences are very similar.

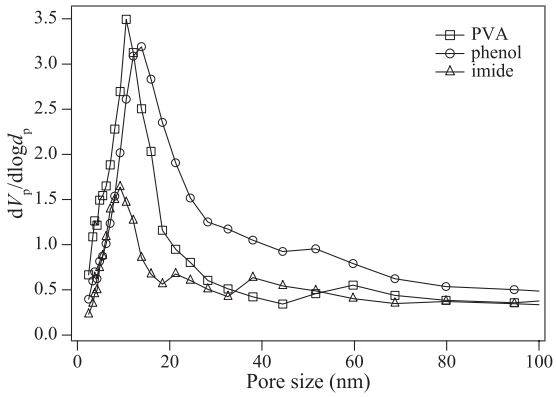

Fig. 3 Pore size distribution profiles by BJH method.

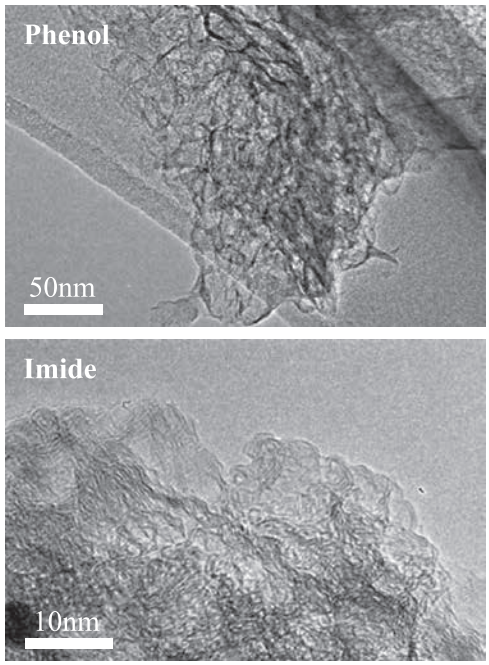

Fig. 4 TEM images of carbons derived from (a) phenol and (b) imide.

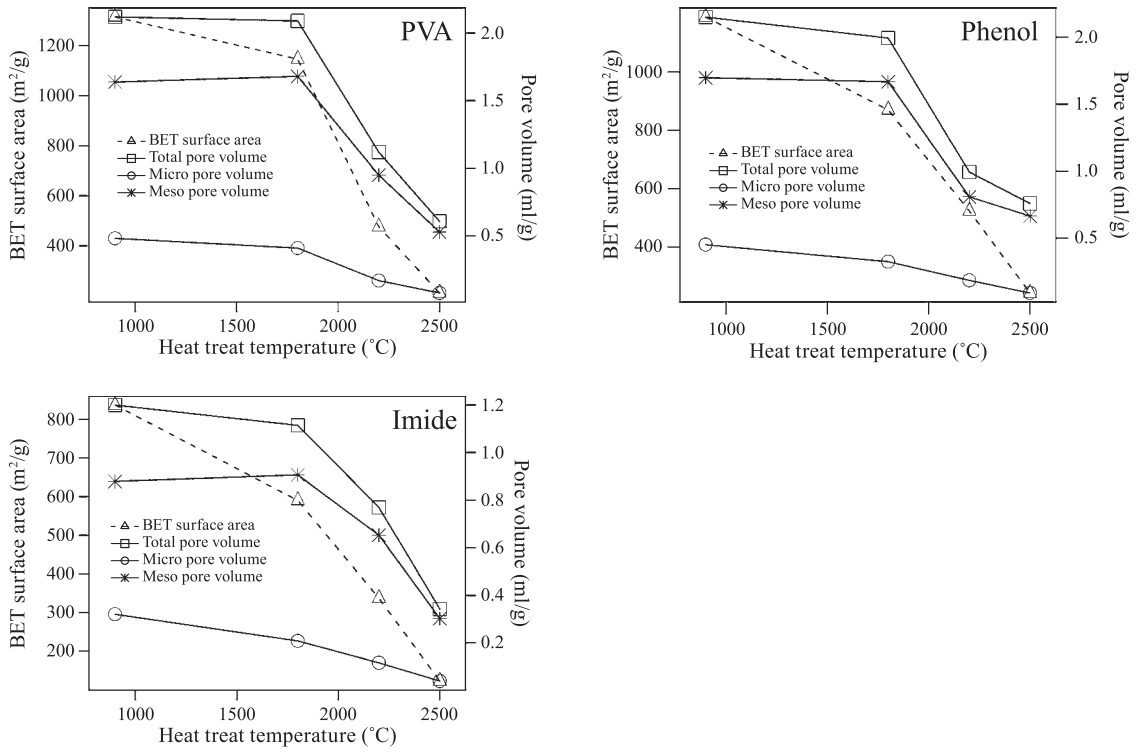

Fig. 5 BET surface areas and pore volumes on each carbon precursor.

(002) X-ray peak profiles of carbons derived from PVA are shown depending on each heat-treatment temperatures in **Fig. 7**. Obvious (002) peak was observed only the carbons heat-treated at 2500 °C. This peak profile can be separated into several peaks. These peak profiles suggest the formation of structural components having different crystallinity. The similar peak profile was also observed on the carbons derived from magnesium citrate(Orikasa H. et al., 2012). (002) peak profiles of carbons heat-treated at 2200 °C and 2500 °C are shown in **Fig. 8(a)** and **(b)**.

Table 2 BET surface areas and pore volumes on each carbon precursor and heat-treatment temperatures

		BET surface area (m^2/g)	Vtotal (ml/g)	Vmeso (ml/g)	Vmicro (ml/g)
PVA	as-prepared	1315	2.12	1.64	0.48
	1800 °C	1146	2.09	1.68	0.41
	2200 °C	476	1.12	0.95	0.17
	2500 °C	212	0.61	0.53	0.08
Phenol	as-prepared	1189	2.15	1.70	0.45
	1800 °C	870	1.99	1.67	0.33
	2200 °C	523	0.99	0.81	0.19
	2500 °C	242	0.76	0.67	0.09
Imide	as-prepared	837	1.20	0.88	0.32
	1800 °C	590	1.11	0.91	0.21
	2200 °C	337	0.77	0.65	0.12
	2500 °C	123	0.34	0.30	0.04

On the same heat-treatment temperature, (002) peak profiles depend on carbon precursors.

Thermogravimetry profiles in air are shown in **Fig. 9**. The beginning temperatures of oxidation of as-prepared carbons depended on carbon precursors. When reaching at about 600 °C, as-prepared carbons were almost entirely oxidized. But the carbons heat-treated at 1800 °C didn't start oxidation at about 600 °C. In addition, the TG profiles were almost the same on each carbon precursor. The starting temperatures of oxidation of carbons heat-treated above 2200 °C almost didn't shift to high temperatures despite the crystalline growth as shown in **Fig. 5**.

TEM images of carbons derived from polyimide and phenol resin are shown in **Fig. 10** and **Fig. 11**, respectively. As seen in these images, before the heat-treatment, amorphous layers were observed. And pores were seemed like inter-connected in three-dimensionally. After the heat-treatment at 1800 °C, stacked layers were observed.

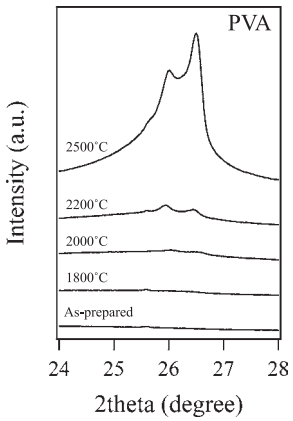

Fig. 7 (002) peak profiles of the carbons derived from PVA.

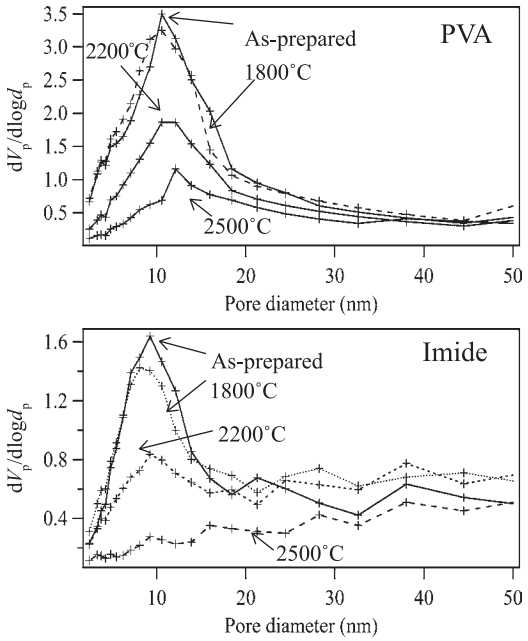

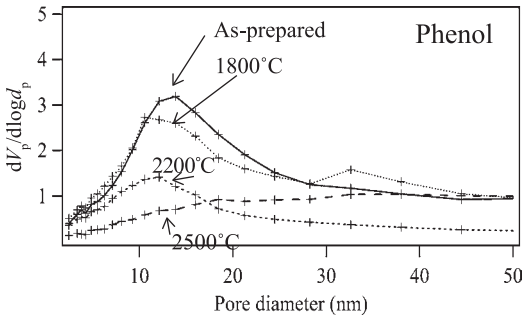

Fig. 6 Pore size distribution by BJH method on each carbon precursor.

On the other hand, pore structures were just a little changed. The carbons heat-treated above 2200 °C were more graphitized and pores were still inter-connected. Thus, the inter-connected pore structures still existed continuously after heat-treatment despite carbon walls was crystallized.

Pore volumes of carbons derived from MgO-templated carbonization process didn't change after the heat-treatment at 1800 °C. Crystal growth of carbons wasn't observed by XRD analysis. But the results of TEM and TG analysis suggest that carbon wall was crystallized. These results suggest that both the high porosity and good characteristics by crystallization of carbon walls can be obtained by heat-treatment at 1800 °C.

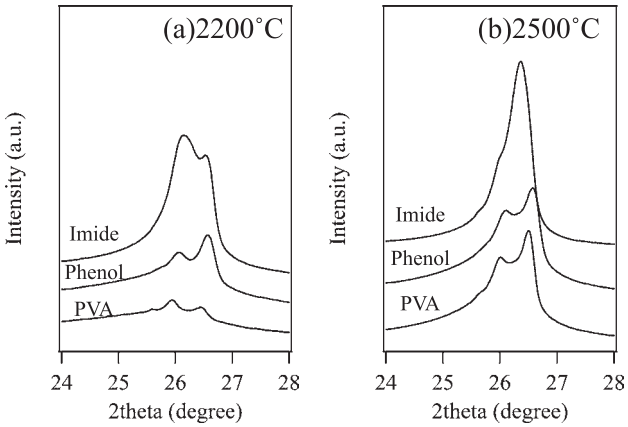

Fig. 8 (002) peak profiles of the carbons heat-treated at (a) 2200 °C and (b) 2500 °C.

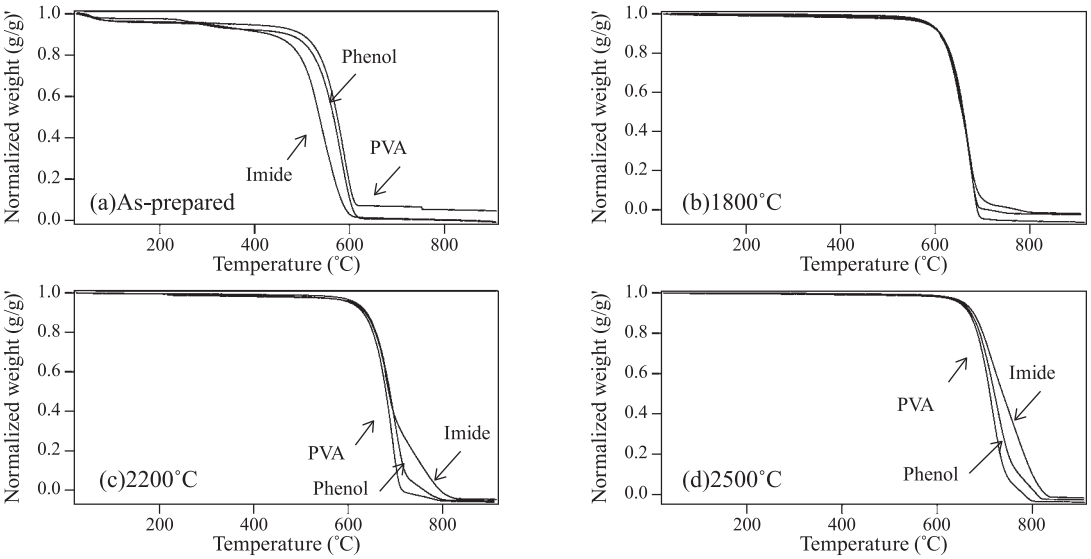

Fig. 9 (002) peak profiles of the carbons heat-treated at (a) 2200 °C and (b) 2500 °C.

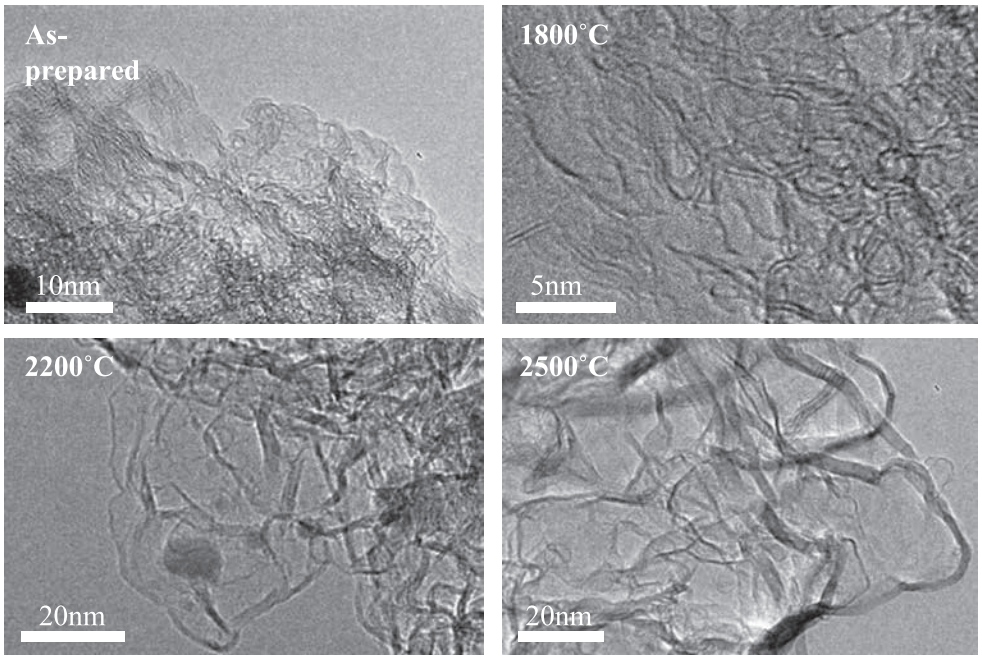

Fig. 10 TEM images of carbons derived from imide.

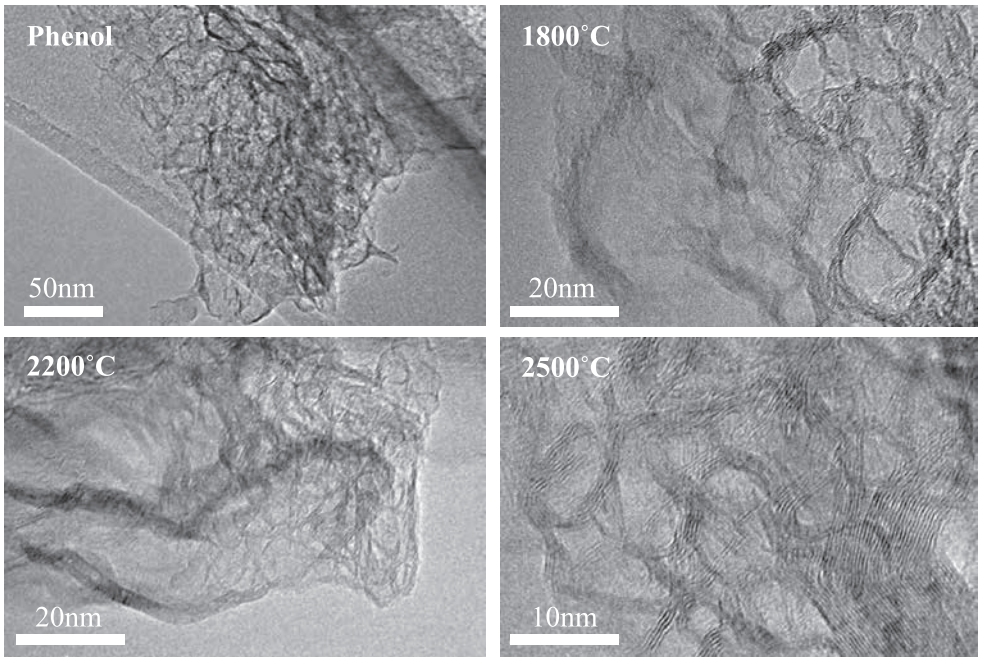

Fig. 11 TEM images of carbons derived from phenol.

4. Conclusions

Carbon coating on MgO was successfully processed using the mixtures of carbon precursors with MgO precursors prepared by physical mixing. BET surface area of the carbons isolated from MgO by dissolving out was very high, such as over 1000 m^2/g, even though activation processes were not applied. The carbons obtained through ten-odd crystallite size MgO were rich in mesopores, of which sizes were almost the same as MgO particles.

Furthermore, we found that pore structure of as-prepared MgO-templated carbon depends slightly on the carbon precursor, but their heat-treatment temperature dependences are very similar. And MgO-templated carbons heat-treated at 1800 °C satisfy both high porosity and oxidation resistance on each carbon precursor. The surface area was kept to 70–80 % even by the 1800 °C treatment. This would be due to the characteristic morphology and structure of the MgO-template carbon.

These results will be useful to pursue the method of preparation for highly porous carbon materials with a high thermal stability. The porous carbon having huge mesopores will also provide an unprecedented new function to various applications.

References

Derbyshire F., Jagtoven M., Thwaiter M., Activated Carbons-Production and Application, in Porosity in Carbons, Patrick J.W. (Ed.), Edward Arnold. 1995.

Hanzawa Y., Kaneko K., Yoshizawa N., Pekara R.W., Dresselhaus M.S., The Pore Structure Determination of Carbon Aerogels, Adsorption, 4 (1998) 187–195.

Inagaki M., Porous carbons, in New Carbons, -Control of Structure and Functions, Elsevier, 2000.

Inagaki M., Kobayashi S., Kojin F., Tanaka N., Morishita T., Tryba B., Pore structure of carbons coated on ceramic particles, Carbon, 42 (2004) 3153–3158.

Inagaki M., Toyoda M., Tsumura T., Control of crystalline structure of porous carbons, RSC Adv., 4 (2014) 41411–41424.

Matsuoka K., Yamagishi Y., Yamazaki T., Setoyama N., Tomita A., Kyotani T., Extremely high microporosity and sharp pore size distribution of a large surface area carbon prepared in the nanochannels of zeolite Y, Carbon, 43 (2005) 876–879.

Morishita T., Soneda Y., Tsumura T., Inagaki M., Preparation of porous carbons from thermoplastic precursors and their performance for electric double layer capacitors, Carbon, 44 (2006) 2360–2367.

Orikasa H., Morishita T., Nano structure of MgO-templated carbon and its change induced by heat-treatment, TANSO, 254 (2012) 153–159.

Shi Z-G., Feng Y-Q., Xu L., Da S-L., Preparation of porous carbon-silica composite monoliths, Carbon, 41 (2003) 2653–2689.

Soneda Y., Suzuki M., Fujimoto K., Activated Carbons, Fundamentals and Applications, Koudannsha, 1992.

Soneda Y., Yamaguchi T., Imoto K., Kodama M., Morishita T., Orikasa H., Performance of MgO-templated mesoporous carbons as electrode materials in lithium-ion capacitor, TANSO, 256 (2013) 57–59.

Tamon H., Ishizaki H., Mikami M., Okazaki M., Porous structure of organic and carbon aerogels synthesized by sol-gel polycondensation of resorcinol with formaldehyde, Carbon, 35 (1997) 791–796.

Author's short biography

Tomoya Nakazono

Mr. Tomoya Nakazono is a researcher of Performance chemicals Div. in ToyoTanso Co., Ltd. in Japan. He received his master's degree from Kyoto Institute of Technology in 2012. His research focuses on the crystallinities and the nanostructure of MgO-templated porous carbons.

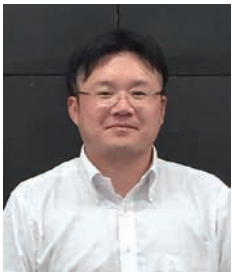

Takahiro Morishita

Dr. Takahiro Morishita is performance chemicals division manager at ToyoTanso Co., Ltd. in Japan. He received his Ph.D. degree from Aichi Institute of Technology in 2006. His research field is a synthesis of fine carbon particles and application of the energy device. His research interest process of fully nano-pore size controlled on carbons and its three-dimensional microstructure.

KONA Powder and Particle Journal No. 33 (2016) 340–353/Doi:10.14356/kona.2016025 Original Research Paper

Preparation of Monodispersed Nanoparticles of Transparent Conductive Oxides †

Atsushi Muramatsu [1]*, Kiyoshi Kanie [1], Takafumi Sasaki [2] and Masafumi Nakaya [1]

[1] *Institute of Multidisciplinary Research for Advanced Materials (IMRAM), Tohoku University, Japan*
[2] *Mitsui Mining & Smelting Co., Ltd., Japan*

Abstract

Generally, indium-tin-oxides (ITO) thin film is prepared by the sputtering process with ITO target, but only 20 % of ITO yielded from the target is deposited on the substrate. Namely, about 80 % ITO is exhausted by the deposition elsewhere far from the substrate. The recycling process of indium is limited so that ca. 20 % ITO of the starting material is lost without any recovery. Even if the recycling of ITO has been carried out in this process, we should prepare ITO target of 5 times more than apparent use of ITO on film. If we change it to printing process from the sputtering, the reduction in ITO use is expected as ca. 50 %, considering the increase in film thickness by printing. Our target technology also includes ITO nanoink for the project. As a result, monodispersed ITO nanoparticles (NPs) with a cubic shape were fabricated by using quaternary ammonium hydroxide-assisted metal hydroxide organogels. These NPs have perfect uniformity in size with beautiful shape, and perfect single crystalline structure including Sn. As we were attempted to make thin film with ITO nanoink, it was successfully fabricated below 200 nm in thickness and the resistivity was drastically decreased below 1.0×10^{-3} Ω cm after heat treatments. GZO nanoink as substitute of ITO has also been developed.

Keywords: uniform nanoparticles, transparent conductive oxides, indium tin oxide, shape control.

1. Introduction

Indium is well known to use as indium-tin-oxides (ITO) materials for transparent conductive oxides (TCO), which is often used in devices such as a flat panel display, touch-panel, solar cell, etc. Japan has an excellent advantage to produce ITO-relating devices, since Toyoha Mine in Sapporo, Japan, had supplied Indium as a top of world. But it was closed on March 31, 2006 mainly due to the economical reason. Before that, METI (Ministry of Economy, Trade and Industry, Japan) and Tohoku Univ. had started to discuss the project on substitute materials development of indium from 2004.

ITO thin film for devices is prepared by the sputtering process with ITO target, but only 20 % of ITO yielded from the target is deposited on the substrate. Namely, about 80 % ITO is exhausted by the deposition elsewhere far from the substrate as shown in **Fig. 1**. The recycling process is limited to be recovered so that only ca 80 % ITO of the starting materials can be recycled but 20 % is lost without any recovery. Even if the recycling of ITO has been carried out in this process, we should prepare ITO target of 5 times more than apparent use of ITO on film. If we change it to printing process from the sputtering, the reduction in ITO use is expected as ca. 50 %, considering the increase in film thickness by printing. Principally, the printing process results in the approximately 100 % yield of film production from ITO nanoink, as shown in **Fig. 2**. As a result, our target technology included the development of ITO nanoink for this project. ITO nanoink was the next important technology for Japan, since the concept of printed electronics by use of nanoink has recently accepted as a novel engineering to make a functional thin film and/or advanced electronic circuits. Moreover, ITO film prepared by ink-jet of its

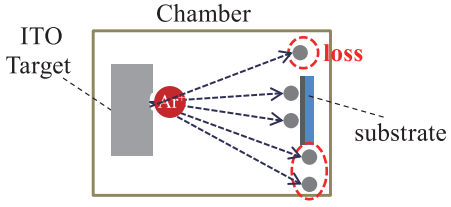

Fig. 1 ITO loss in sputtering process.

† Received 16 May 2015; Accepted 10 August 2015
J-STAGE online 28 February 2016
[1] Katahira 2-1-1, Aoba-ku, Sendai 980-8577, Japan
[2] 1-1-1 Hikoshimanishiyamacho, Shimonoseki-shi, Yamagachi, 750-0093 Japan
* Corresponding author: Atsushi Muramatsu;
E-mail: mura@tagen.tohoku.ac.jp
TEL: +81-22-217-5163 FAX: +81-22-217-5165

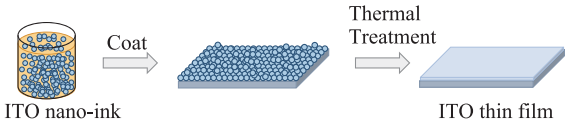

Fig. 2 Printing process of ITO nanoink.

nanoink has been expected as the transparent electrode of the next-generation solar cell. Namely, indium is well recognized as one of the most important resources for the future devices in Japan.

METI has started "Japan Rare Metal Substitute Materials Development Project" from the financial year of 2007, where Tohoku Univ. is the main university for research so that our project was also included as "Reduction of Indium use in transparent conducting electrodes." The sub-project, "Development of high performance ITO nanoparticles (NPs) for nano-ink," was composed of Tohoku University, ULVAC, Inc., Mitsui Mining & Smelting Co., Ltd., DOWA Electronics Materials Co., Ltd., and Sharp Co., Ltd. This project has been carried out until FY2011. During it, several patents on ITO nanoink has been submitted. Besides, U.S.—Japan Roundtable on Rare Earth Elements Research and Development for Clean Energy Technologies, was held on November 18–19, 2010 on U.S. Department of Energy Lawrence Livermore National Laboratory so that we reported the investigation of ITO nanoink as a reduction technology of indium use.

The key technology of ITO nanoink is the production of ITO NPs precisely controlled in size, shape, and crystalline properties. However, ITO particles could not be prepared by hydrothermal synthesis because Sn-containing InOOH or $In(OH)_3$ crystalline particles were once formed during aging even at higher temperature and at rather higher pressure but they could not be converted into ITO phase anymore. Considering the fact that alumina cannot be also prepared by the hydrothermal synthesis method, InOOH and $In(OH)_3$ must be too stable to convert into ITO in aqueous media. Namely, we have reported the size and shape control of $In(OH)_3$ nanoparticles by amino-acid assisted hydrothermal method. (Sasaki et al., 2009). Cubic-shaped $In(OH)_3$ nanoparticles with the size of 50 nm were formed by addition of aspartic acid in the reaction solution. Hence, size- and shape-controlled $In(OH)_3$ nanoparticles has been successfully prepared; however, the further thermal treatment is inescapable to obtain ITO nanoparticles.

We have found a novel solvothermal method to directly obtain ITO NPs with cubic morphology on 2008. (Endo et al., 2008). Remarkably, only by use of this procedure, highly crystalline cubic-shaped ITO NPs with narrow size distribution were successfully prepared, for the first time, through one-step process from a mixed ethylene glycol solution of indium and tin salts. (Sasaki et al., 2010) In order to enhance the uniformity of as-prepared ITO, quaternary ammonium hydroxides were first applied for the solvothermal synthesis of monodispersed ITO NPs controlled in cubic morphology. Formation of a gel-like intermediate was a decisive factor for the precise control in size and shape. (Kanie et al., 2013) We also will show that their blue-colored compacts exhibits low resistivity as a transparent conductive oxide.

2. Concept

The unique properties of highly optical transparency of ITO in the visible region and controllable low resistivity have been utilized (Hartnagel, 1995) (Hamberg and Granqvist, 1986) so that ITO electrode is industrially prepared by sputtering or laser deposition method followed by chemical etching process. (Chiou et al., 1993) (Lin et al., 2008) (Gessert et al., 2009) On the other hand, since ITO is used in tandem with the penetration of a flat panel display, the world-wide demand for In as a TCO has been remarkably increased so that the saving and utilization of indium becomes task of pressing urgency. Furthermore, from the environmental point of view, such an energy-consumed system, including high-temperature and gas-phase deposition manufacturing process, fundamentally deserves a new look for the preparation of ITO electrode with low resistivity. In this regard, ITO nanoink, obtained by extremely stable dispersion of ITO NPs into medium, has been paid attention as an alternative to the conventional processes (Hong and Han, 2006) (Hong et al., 2008) (Bühler et al., 2007) However, TCO manufacture based on ITO nanoink contains many problems toward its practical use, as shown in **Fig. 3**. One of the most serious problems is the high resistivity of TCO electrodes from the nanoink, mainly because of the interfacial resistance between the particles, even if highly conductive ITO NPs are synthesized. As mentioned in **Fig. 3**, in order to reduce this resistance, the shape of the ITO particles can be designed as a cubic so that the face-to-face contact, 2-dimensional one, between particles is expected to decrease the resistance, compared with the point-to-point one between uncontrolled particles. In addition, for the high transparency and low haze, the particle size of ITO is to be below 100 nm.

However, single-nanometer particles are not target materials in this study, as shown in **Fig. 4**. Even if monodispersed single-nanometer ITO particles are succeeded to produce, they are tremendously aggregated to form aggregates. Since the particle characteristics obey the apparent particle size, the size and shape of aggregates determines the quality and property. The control of size and shape of aggregates is theoretically impossible. Because of the higher surface reactibility, the corner become rounded

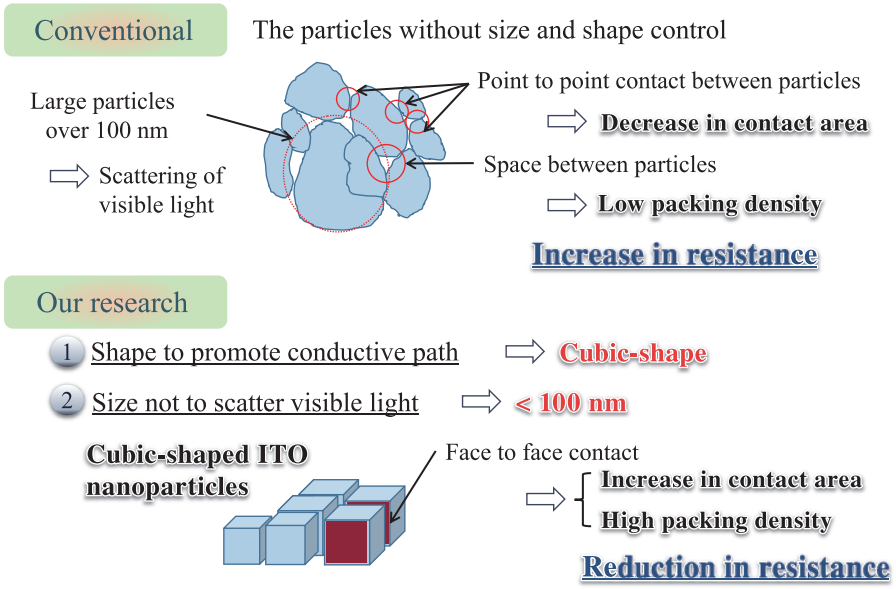

Fig. 3 Concept and design to synthesize ITO nanoparticles to be applied to the transparent conductive oxide electrodes.

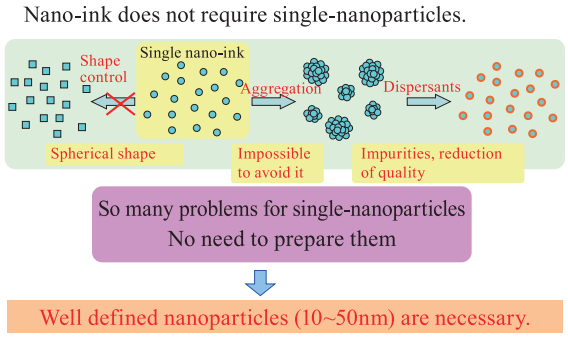

Fig. 4 Basic concept for uniform ITO particles synthesis.

off, even if cubic nanoparticles are initially formed. In addition, since the particle size is nearly equal to nuclei size, they are not well grown. The precise control in shape for single-nanoparticles are basically impossible. Since the dispersant is strongly and chemically adsorbed on the surface, the TCO properties get worse after calcination treatment. However, the dispersant is indispensable for well-dispersion of single-nanoparticles.

As a result, in order to achieve both the requirement of shape and size with higher cubic surface as well as less than 100 nm over 10 nm, the preparation method of ITO NPs with high crystallinity, uniform composition, and well-defined particle morphology with monodispersed size distribution should be established.

3. Gel-Sol method: Synthesis of uniform anatase-type TiO_2 Nanoparticles

The liquid-phase synthesis has much more advantages for the precise shape and size control of NPs, where the shape can be controlled by the addition of shape controller adsorbing selectively onto the specific surface and the size be by the strict separation of nucleation step, determining nuclei number, that is, the final particle size, from the particle growth, compared with other methods such as gas or solid-phase synthesis. (Sugimoto et al., 1998) (Kanie and Sugimoto, 2004) (Niederberger, 2007)

Owing to DLVO theory (Derjaguin and Landau, 1941) (Verwey and Overbeek, 1948), the dispersion and aggregation of fine particles have been estimated in rather diluted solution system. The concentrated solution leads to the tremendous aggregation between particles because of the compression of electrical double-layer, which contributes the dispersion of the particles through the electrostatic repulsion. In this regard, the dilute solution system is required for the monodispersed particle synthesis until our discovery of Gel-Sol method in the concentrated solution. The features of Gel-Sol method can be listed as follows. (Sugimoto et al., 2003) 1) Gel is a reservoir of metal ion so as to gradually supply it to the system under the rather low concentration of metal ions in solution phase. 2) Gel makes condensed viscous network in order to prevent the motion of particles to be aggregated each other by the anchoring particles in it. 3) Particles grow at the expense of the Gel until its complete consumption.

Here, as we illustrate a typical example of the Gel-Sol method in **Fig. 5**, the preparation method of monodispersed anatase-type TiO_2 nanoparticles will be introduced as follows, since it is well-established procedure, based on the Gel-Sol transformation as above mentioned. This outstanding technology for the preparation of anatase nanoparticles precisely controlled in size and shape in-

cludes 3 steps in the most important procedure. Namely, they are 1) the formation of rather stable Ti complex from Ti iso-propoxide with triethanol amine to inhibit the uncontrolled hydrolysis after the addition of water, 2) the fabrication of well stable gel network to avoid the tremendous aggregation between growing particles, 3) the strict control in the process temperature to strictly separate the nucleation stage from the particle growth one.

Established procedure will be shown in **Fig. 5** in detail. The Ti stable complex composed of Ti and triethanol amine with 1/2 in molar ratio. Since the formation rate of this complex is too slow to complete, it takes at least a whole day after Ti mixing with triethanol amine. If the complexation reaction is incomplete, the uncontrolled hydrolysis is promoted in the addition of water to the system. In that case, both the structure and composition must be inhomogeneous so that the monodispersed particles cannot be obtained.

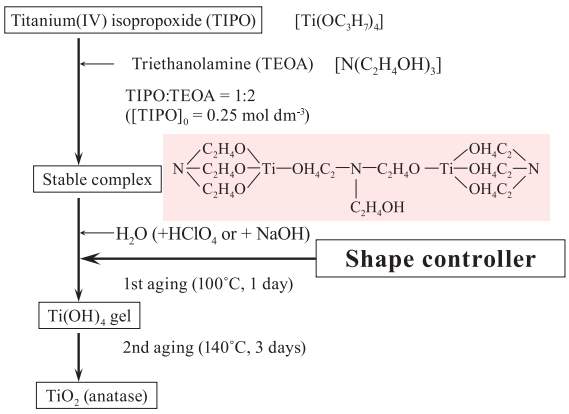

Fig. 5 Synthesis procedure of uniform TiO_2 particles.

In order to apply them to a photocatalyst, the precise control of shape is the most important, because photocatalytic activities strongly depends on crystal facets (Kimijima et al., 2010),. In Gel-Sol methods, the shape control can be also carried out simultaneously as the particle formation in their growth stage. Namely, the shape controller is added in the particle synthesis system. It is strongly adsorbed on the specific plane to disturb the crystal growth normal to the plane. As a result, the particles are formed, bounded by the plane adsorbed by the shape controller. **Fig. 6** illustrates TEM photos of shape-controlled TiO_2 nanoparticles. Basic reagents such as amines and amides were found effective to the shape control for anatase-type TiO_2 nanoparticles, in comparison with oleic acid to shaping as cube. This synthesis procedure has been applied to the Ti-perovskite particles, such as $SrTiO_3$ and $BaTiO_3$, which showed characteristics unique in photocatalytic activities. (Kimijima et al., 2014)

The development of the synthesis method for monodispersed Ti-based oxide nanoparticles precisely controlled in size and shape directly led to the success in the production of uniform $Na_xK_yNbO_3$ fine particles as a precursor of lead-free piezo materials for industrial use. (Kanie et al 2011) The niobate particle synthesis is basically the same as TiO_2 preparation. In addition, it finally affects the development research for TCO nanoparticles, as described below.

4. Application to direct ITO Synthesis

Preparation methods of In_2O_3 or ITO NPs have been reported based on the combination of coprecipitation of

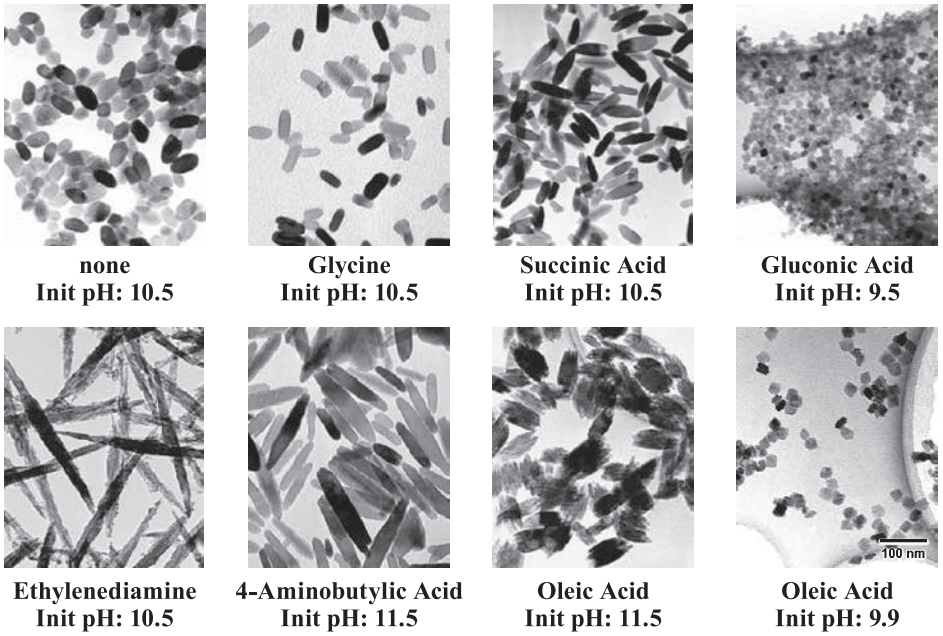

Fig. 6 TEM photos of as-prepared uniform TiO_2 particles.

metal precursors and successive thermal treatment (Song et al., 2005) (Kim and Park, 2004), laser-induced fragmentation (Usui et al., 2006), solvothermal synthesis (Lee et al., 2005) (Yang et al., 2008a)), microwave-assisted synthesis (Okuya et al., 2007), emulsion techniques (Sujatha Devi et al., 2002), sol-gel synthesis (Aoki et al., 2006), and one-pot preparation of colloids (Seo et al., 2003) (Liu et al., 2005 (Lee et al., 2006) (Zhang et al., 2005) (Kanehara et al., 2009) (Gilstrap Jr. et al., 2008) (Gilstrap Jr. and Summers, 2009) However, the precise control of ITO NPs in size, shape, and structure simultaneously has never been reported, in particular, for monodispersed particle synthesis system. Namely, there is the technological difficulty for tin-doped indium oxide in the strict separation of nucleation and growth, and crystallization at rather low temperature below 300 °C. Recently, we have reported size and shape control of $In(OH)_3$ NPs by amino-acid assisted hydrothermal method(Sasaki et al., 2010). In this report, cubic-shaped $In(OH)_3$ NPs with the size of 50 nm were formed by addition of aspartic acid in reaction solution. Since the thermal treatment is indispensable so as to obtain ITO particles at rather higher temperature, as-prepared ITO is aggregated and/or sintered so that the size and shape is changed. Even though monodispersed $In(OH)_3$ NPs are obtained, finally formed ITO NPs is not uniform. As a result, the monodispersed ITO NPs should be obtained by one-step synthesis.

ITO particles cannot be prepared directly by the hydrothermal synthesis, because $In(OH)_3$ is not converted into ITO phase by solution-reprecipitation mechanism due to the extremely stable state of $In(OH)_3$ phase. In this regard, the solvothermal system with use of an organic solvent, such as methanol, ethanol, and polyols, is applicable to the ITO synthesis by place of hydrothermal one, where water content can be reduced into the stoichiometric one for ITO formation. In the present paper, the direct synthesis of ITO NPs will be described by the combination of gel-sol and solvothermal method. Also, the present method will be applicable to the preparation of GZO, an alternative TCO for ITO.

5. Experimental

5.1 First trial

The first trial is unique in use of NaOH as a base as follows (Muramatsu, 2010). The reagent-grade indium (III) chloride tetrahydrate ($InCl_3 \cdot 4H_2O$), tin (IV) chloride pentahydrate ($SnCl_4 \cdot 5H_2O$), sodium hydroxide (NaOH), ethylene glycol (EG), diethylene glycol (DEG), and 1-butanol (BuOH) were used as received. The established procedure is as follows: $InCl_3$ and $SnCl_4$ were dissolved in EG with 0.50 and 0.050 mol L^{-1}, respectively. In order to clarify the effect of Sn concentration on the electric resistivity, $SnCl_4$ concentration was varied in the range of 0–0.050 mol L^{-1} under the same $InCl_3$ concentration at 0.50 mol L^{-1}. An ethylene glycol solution of NaOH was also prepared and added to the same volume of $InCl_3$ and $SnCl_4$ ethylene glycol solution at 0 °C under agitation. The concentration of NaOH was adjusted to 1.0, 1.5, and 2.0 mol L^{-1}. After 15 min stirring, the 10 mL suspension was transferred into a Teflon-lined autoclave (Parr Instrument, volume: 23 mL) and aged at 250 °C for 4 days. The standard conditions are molar ratio $[In^{3+}]/[Sn^{4+}] = 10/1$, $[In^{3+}]/[OH^-] = 1/3$, and 250 °C for 12 h. As-obtained product was purified by centrifugation (18,000 rpm, 10 min), washed 3 times with ethanol, and dried at 60 °C in an oven. **Fig. 7** illustrates the standard procedure with use of NaOH as an alkaline reagent, we have developed first, to obtain ITO NPs by the present method.

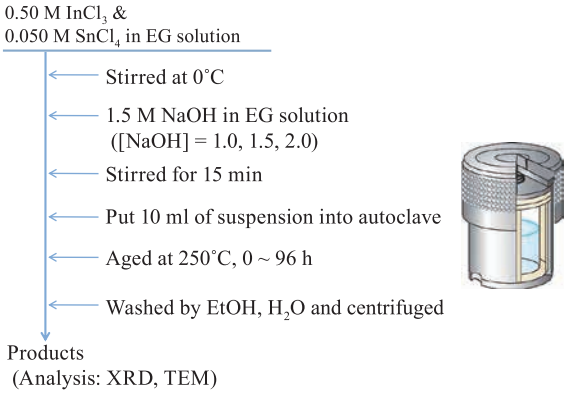

Fig. 7 Schematic drawing of the direct preparation of ITO nanoparticles by the solvothermal method with using ethylene glycol (EG) as a solvent.

5.2 Established procedure

As a result of all our attempts to prepare ITO, the established procedure is composed of the solvothermal synthesis and the Gel-Sol method as shown in **Fig. 8** (Kanie et al., 2013). Namely, an EG solution of tetramethylammonium hydroxide (TMAH) in place of NaOH was prepared by using a 10 wt% TMAH methanol solution as follows. Initially, 100 mL of the TMAH solution was mixed with 25 mL of EG. Then, methanol was roughly removed by a rotary evaporator at 40 °C under 4 kPa, and the residue was evacuated at room temperature with stirring. Removal of methanol was confirmed by ^{1}H-NMR measurement. Then, the TMAH concentration was determined by acid-base titration, and the concentration was adjusted from 1.0 to 2.5 M by the dilution with EG. The synthesis procedure of ITO NPs with a cubic shape will be shown as follows. Initially, indium chloride tetrahydrate ($InCl_3 \cdot 4H_2O$, 0.50 M) and tin chloride pentahydrate ($SnCl_4 \cdot 5H_2O$, 0.050 M) were dissolved in EG at room

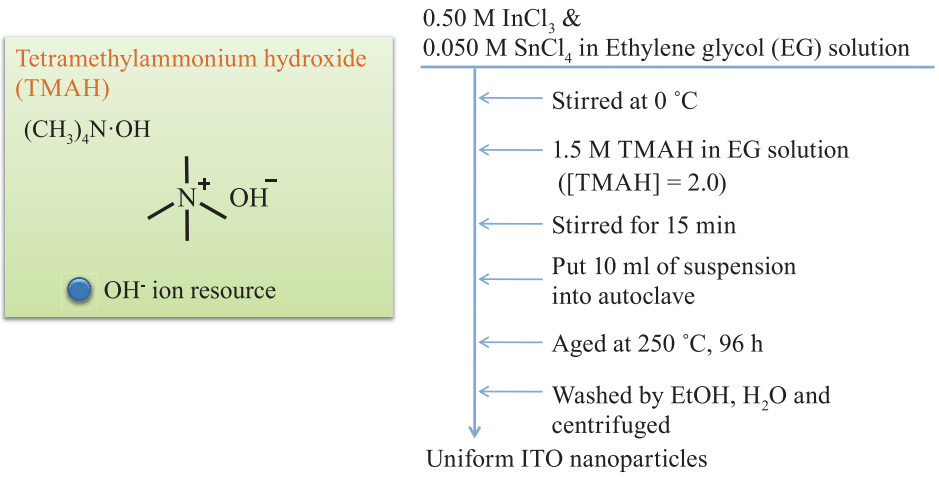

Fig. 8 Schematic drawing of the direct preparation of ITO nanoparticles by the combination of the solvothermal and Gel-Sol method with use of ethylene glycol (EG) as a solvent and TMAH as an alkaline reagent.

temperature. Then, 5.0 ml of 2.5 M TMAH solution in EG was poured into the same volume of as-prepared solution mixture of indium and tin under agitation at 0 °C. The resultant solution was stirred at the temperature for 15 min, transferred into a Teflon-lined autoclave (Parr Instrument Company, Model 4749) and aged in an oven at 250 °C for 96 h. As-obtained blue-coloured precipitates were collected by centrifugation (18,000 rpm, 10 min) and washed three times with ethanol and one time with ion-exchanged water.

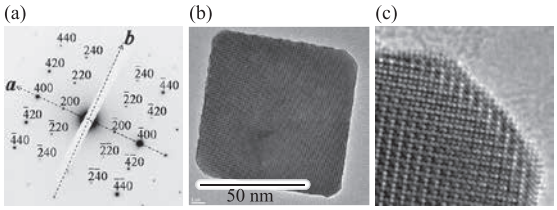

Fig. 9 Selected-area electron diffraction (a), respective TEM images (b), and HRTEM (c), of ITO nanoparticles shown in Fig. 10 (a).

5.3 Characterization

The crystallographic structures of the dried powders were identified by a Rigaku Ultima-IV X-ray diffraction (XRD) measurement system using Cu Kα radiation (40 kV, 40 mA) equipped with a D/teX Ultra detector. As-prepared particles were observed by a transmission electron microscope (TEM) using a Hitachi H7650 system with an acceleration voltage of 100 kV. High resolution TEM (HRTEM) analysis was carried out on a FEI TITAN 80–300. The particle surface was characterized by X-ray photoelectron spectroscopy using an ESCA-3400 (SHIMADZU Corporation).

6. Results and Discussion

6.1 First trial with use of NaOH

In our first trial to prepare ITO directly by the solvothermal procedure, (Muramatsu et al., 2010) initially, the effect of NaOH concentration on the particle morphology and size in this system was investigated. The particle size was successfully controlled in the range from 10 to 50 nm, as the initial NaOH concentration was decreased, possibly due to the increase in number of nucleus formed. Generally speaking, the rather higher alkaline condition is advantageous to the formation of the monomer, precursor complex, of metal oxide. ITO NPs were also prepared with different initial molar ratios of Sn/In from 0 to 0.15. In all cases, In_2O_3 and ITO NPs with cubic crystal structures were obtained. Trace amount of SnO_2 was also formed only in the case with Sn/In = 0.15, confirmed by XRD measurement. On the other hand, for Sn/In = 0.10, Sn/In molar ratio in as-prepared one ITO particle was found to keep in the same as the initial feed one, estimated by the energy dispersive X-ray (EDX) analysis.

Fig. 9 shows conventional TEM and high-resolution TEM (HRTEM) images with the electron diffraction (ED) spots. The ED spots as well as HRTEM analyses of the one particle shown in **Fig. 9** (a) revealed that the crystal structure of the cubic shaped ITO NPs is basically single crystalline with the lattice parameter of the a-axis as 1.014 nm, which is consistent with the a-axis of In_2O_3 with a cubic crystal structure (JCPDS No 06-0416) of 1.012 nm. Thus, the incorporation of Sn ions into the crystal structure of In_2O_3 is not influenced to the change in the lattice parameter.

As a result of the effect of solvents, **Figs. 10** and **11** show the TEM images and XRD patterns of the particles

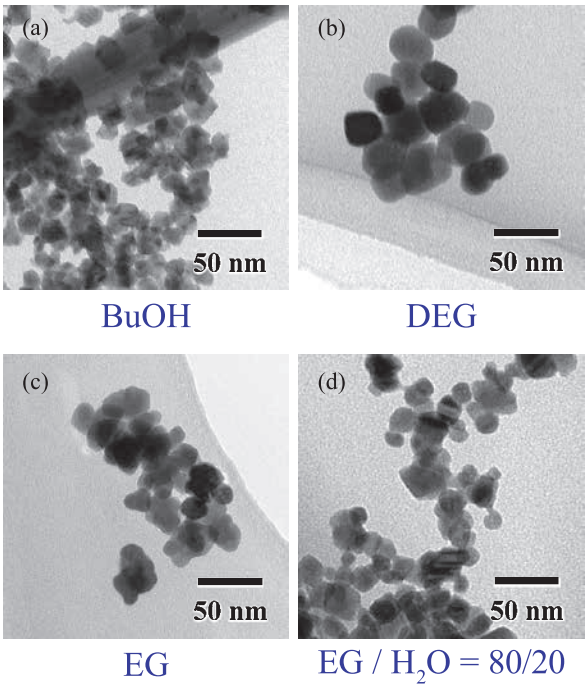

Fig. 10 TEM images of particles obtained in (a): BuOH; (b): DEG; (c): EG; (d): 80 wt% EG aqueous solution.

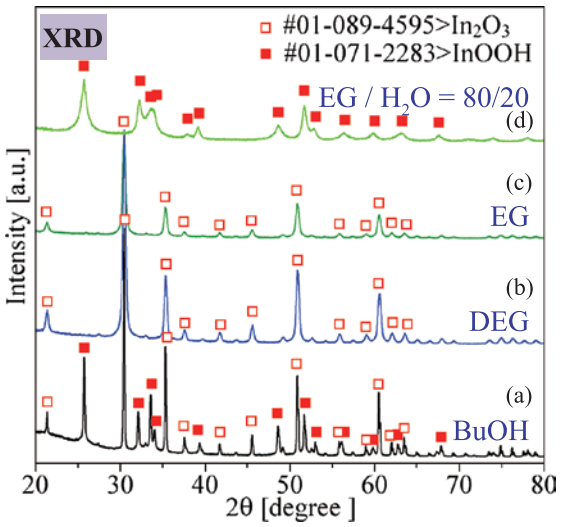

Fig. 11 XRD patterns of particles obtained in (a): BuOH; (b): DEG; (c): EG; (d): 80 wt% EG aqueous solution.

obtained in (a): EG; (b): diethylene glycol (DEG); (c): 80 % EG aqueous solution; (d): butanol (BuOH), respectively. Here, the molar ratios of In^{3+}/OH^{-} and Sn/In were fixed as 1/3 and 0.10, respectively, with otherwise the standard condition, but aging time was 12 h. As shown in **Fig. 10** (a), irregular-shaped ITO NPs are obtained in EG aged for 12 h, and the particle size is ca. 10 nm. In the case of DEG, ITO NPs are also formed as a single phase, and the particle shape is basically cubic and the size is about 20 nm. In contrast, the diffraction peaks of colorless powder obtained in an 80 wt% EG aqueous solution system (**Fig. 11** (c)) are indexed to be an indium oxyhydrate (InOOH).

As a result of the comparison of EG-water and EG alone system, the addition of water seems inhibitory to the formation of ITO crystal. In the aqueous solution system of In salts, the formation of InOOH was strongly enhanced. One might consider that InOOH once formed during the reaction is hardly converted into In_2O_3 phase, because of the extremely low solubility of InOOH. In other word, InOOH cannot play a role in an intermediate for In_2O_3 formation. In contrast, as has been reported elsewhere (Sugimoto et al., 1993) (Sugimoto et al., 2001), monodispersed hematite, α-Fe_2O_3, particles in the concentrated Gel-Sol system, are formed through the 2-step phase transformation, namely, $Fe(OH)_3$ to akaganeite, β-FeOOH, and β-FeOOH to α-Fe_2O_3, via a solution phase in the dissolution-reprecipitation process. In this case, β-FeOOH plays a role in the intermediate for α-Fe_2O_3, because of the higher solubility.

The solid particles obtained by using BuOH as a solvent consist of In_2O_3 and InOOH. It shows stepwise phase transition from metal hydroxides to give oxides by way of oxyhydroxides by the dissolution-precipitation is seen in the BuOH system. This behavior is commonly observed in aqueous systems to form metal oxides. In contrast, in the solvothermal system as shown here, direct formation of ITO solid particles is observed starting from amorphous-like indium hydroxides, $In(OH)_3$ and InOOH phases are not detected as intermediates.

The temperature at aging in the autoclave was changed from 200 to 250 °C in ethylene glycol as a solvent, where aging period was fixed at 96 h. **Fig. 12** shows the effect of aging temperature on the ITO formation. Left-side of **Fig. 12** illustrates TEM observation while right-side XRD. Judging from the TEM images, only an amorphous like product was formed at 200 °C, but the shape-distinct solid particles were clearly observed over 220 °C. XRD patterns of the products also indicate not crystalline structure for 200 °C aging sample, in contrast to crystalline ITO phase over 220 °C. Thus, the crystallinity was obviously improved with increase in the aging temperature. Taking this remarkable temperature effect into consideration, the activation energy of the particle formation may be rather large so that the promoted formation rate can lead to the brisk nucleation and then the growth.

6.2 Established synthesis method of ITO nanoparticles

As has been reported (Kanie et al., 2013), **Fig. 13** shows TEM images of the NPs obtained with different concentration of TMAH, (a) 0.50 M, (b) 0.75 M, (c) 1.0 M, and (d) 1.25 M under 0.25 M $[In^{3+}]$ 0.025 M $[Sn^{4+}]$. XRD measurements revealed that all products could be assigned as an In_2O_3 with a cubic system of *Ia3* (unit cell parameter:

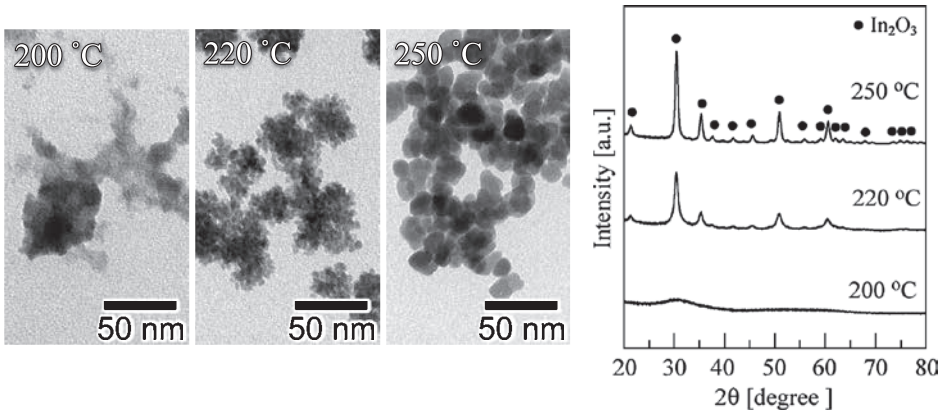

Fig. 12 Effect of the aging temperature of ITO particle synthesis under otherwise the standard condition. The temperature was varied in the range from 200 to 250 °C. (a) TEM observation, (b) XRD patterns.

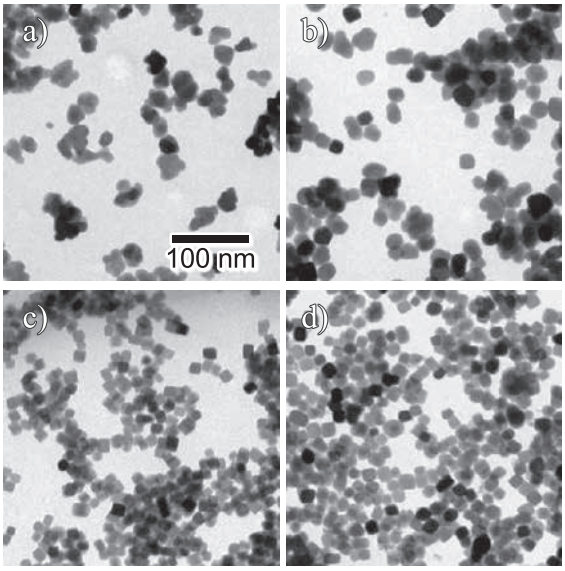

Fig. 13 TEM images of ITO NPs synthesized at 250 °C for 96 h. The TMAH concentrations are (a) 0.50 M; (b) 0.75 M; (c) 1.0 M; (d) 1.25 M. The scale bar in (d) is common for all images.

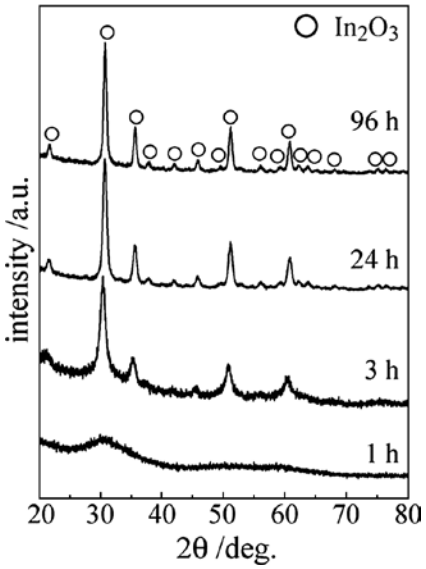

Fig. 14 XRD patterns of the precipitates formed by aging for (a) 1 h; (b) 3 h; (c) 24 h; (d) 96 h at TMAH concentration of 1.0 M in the solution.

a = 1.012 nm) as a single-phase. As shown in **Figs. 13** (a) and (b), inhomogeneous- and pseudocubic-shaped ITO NPs with round edges are formed at TMAH concentration of 0.50 and 0.75 M in the solutions. In contrast, ITO NPs with a cubic shape with sharp edges are obtained for the TMAH concentration of more than 1.0 M (**Figs. 13** (c) and (d)). The average sizes of ITO NPs at different TMAH concentration are 26.1 ± 6.5 nm (0.50 M), 20.9 ± 3.4 nm (0.75 M), 15.0 ± 1.6 nm (1.0 M), and 17.3 ± 1.9 nm (1.25 M). Nucleation for metal oxide particle formation is generally promoted at higher alkaline condition in hydrothermal systems; since the formation of the metal hydroxide monomers precursory to oxide particles is accelerated. In the present solvothermal system, the initial mixing molar ratio of [TMAH]/[In^{3+}] was fixed to 2/1, 3/1, 4/1, and 5/1. In this regard, the decrease in the particle size by increase in the TMAH concentration might be due to the promotion of metal hydroxides monomers in the initial reaction solution. The size distribution of particles obtained at 1.0 and 1.25 M TMAH was found extremely narrow; actually, the standard deviation of the average size divided by the average size is calculated as 11.0 %. As a result, monodispersed ITO NPs were prepared with precise control in size and shape only by the present method.

Time evolution of the products at 250 °C under TMAH concentration of 1.0 M was investigated. As shown in **Fig. 14**, only broad halo-peaks in XRD analyses indicated the formation of an amorphous matter until 1 h aging. After 3 h aging, crystalline ITO phase was confirmed as a single phase, in contrast to no peak of crystalline $In(OH)_3$ and InOOH phases. The diffraction peaks of ITO became sharpen with aging time so that crystallite size of the NPs

was increased. TEM images of the products obtained at different aging time with 1.0 M TMAH are shown in **Fig. 15**, of which **Fig. 15** (a) indicates an amorphous-like gel for the products obtained at 1 h aging. Judging from **Fig. 15** (b), irregular-shaped ITO NPs are seemed to be formed in the amorphous-like gel matrix after 3 h aging. The particles grow at the expense of the amorphous gel, as shown in **Fig. 15** (c). After 96 h aging, monodispersed ITO NPs with the cubic shape are finally formed as shown in **Fig. 15** (d).

Fig. 16 illustrates a macroscopic change of the reactant mixture with aging time, including TEM images of the products obtained at each step. The reaction solution just after mixing both EG solutions of In/Sn and TMAH seemed homogeneous without any precipitates (**Fig. 16** (a)). A viscous gel with pale yellow color was formed after 1 h aging at 250 °C (**Fig. 16** (b)). As increasing aging time, the gel was gradually converted into a blue colored sol (**Fig. 16** (c)), which suggests the formation of ITO NPs. The gel formed 1 h aging was further characterized by ICP, IR, and NMR analyses, after the gel was separated from solid and liquid parts by centrifugation. As a result of ICP measurement of the dried gel, the molar ratio of the Sn/In was estimated as 0.038, while indium ion concentration of the supernatant solution was 0.060 M. Namely, 75 mol% of indium was used in the gel-intermediate transformed from the initial solution mixture. The actual concentration of the indium ions in the solution was kept at low state under aging. In this period, only particle growth became a predominant process to form monodispersed ITO NPs. FTIR analysis resulted in the distinct adsorption bands assigned to TMAH and EG. Since the amounts of TMAH and EG in the xerogels were quantitatively analyzed by ^{1}H-NMR, 2.2 wt% of TMAH and 22.8 wt% of EG was included. As a result, the molar ratio of In:EG:TMAH was estimated as 1.0:0.8:0.05, respectively. The gel must be formed via the complex formation of indium hydroxides with EG and TMAH with hydrogen bonding network, confirmed by IR measurement of the xerogel. Yang *et al* also mentioned such chelation behavior of indium ions with polyols (Yang J. et al., 2008b). Thus, it is to be noted that TMAH may play a critical factor for the formation of the gel because such gel was not obtained by using NaOH as a basic agent (Sasaki et al., 2010). ITO NPs were formed, obeying the following gel-sol transformation mechanism, as a principle of the Gel-Sol method established in our laboratory. Initially, mixed solution of indium and tin salts dissolved in

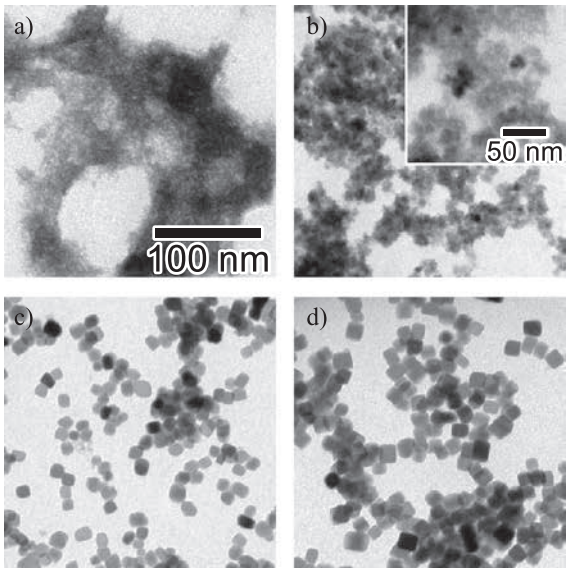

Fig. 15 TEM images of the precipitates formed by aging for (a) 1 h; (b) 3 h; (c) 24 h; (d) 96 h at TMAH concentration of 1.0 M in the solution. The scale bar in (a) is common for all images.

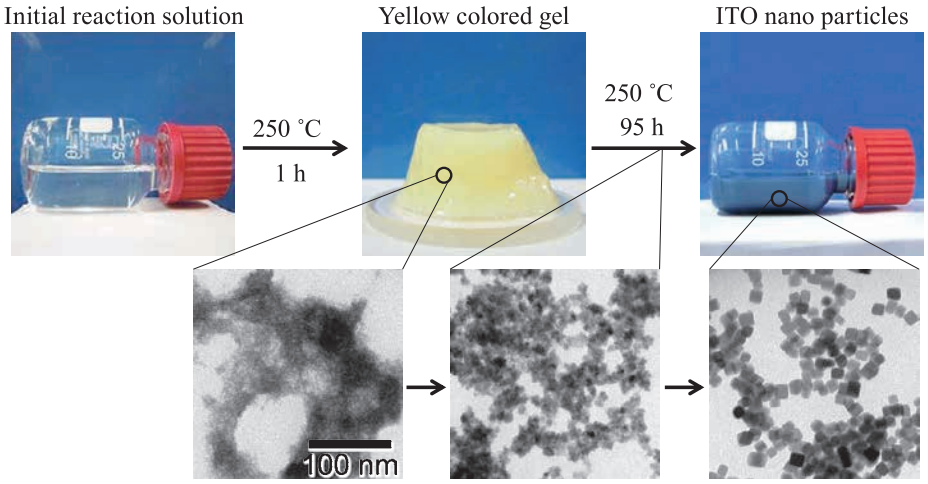

Fig. 16 A schematic illustration of time change of reaction solution at 250 °C in 1.0 M TMAH. (a) A transparent precursor solution of the ITO NP synthesis. (b) A pale yellow viscous gel formed by aging for 1 h at 250 °C. (c) A blue-colored ITO NP sol obtained by the present method.

the EG solution with TMAH was transformed into metal hydroxides at the early stage in aging time at 250 °C. During aging, the viscous gel network was shaped via hydrogen bonding, as shown in **Fig. 16** (b). Maybe, the nucleation of ITO were processed in the period of the gel matrixes formation. The growing particles were very tightly held on the gel matrixes so that NPs were grown through dissolution and recrystallization process at the expense of the gel. Such a gel-sol transformation of reaction solution was only observed at TMAH of 1.0 and 1.25 M, while the gel was not formed at lower TMAH concentration. Thus, the gel-sol transformation must be a key factor for synthesis of monodispersed ITO NPs.

The effect of Sn/In ratio on the resultant particle size and shape was investigated so that cubic-shaped ITO NPs were also formed in the Sn/In range from 0 to 0.20. Predominant In_2O_3 and ITO NPs with the cubic crystal structures were obtained at Sn/In from 0 to 0.15 without the formation of tin oxides such as SnO and SnO_2. However, for Sn/In = 0.20, a trace amount of SnO_2 was identified. In this investigation, the average sizes with size distributions were 26.1 ± 2.7 nm (Sn/In = 0) and 23.9 ± 2.8 nm (Sn/In = 0.020). The particle size was decreased with increase in Sn/In ratio, possibly due to the acceleration of nucleation by tin. Such the size change with increase in Sn content was good agreement with the literature (Ba et al., 2006). The influence of species of the quaternary ammonium hydroxides on the ITO synthesis. Tetrabutylammonium (TBA) and tetrahexyl-ammonium (THA) hydroxides was also investigated. They also played the same role of promoting the formation of the cubic-shaped ITO NPs with sharp edges by way of gel-intermediates. The particle mean size and the distribution of the ITO NPs obtained by using 1.0 M TBAH and THAH were 24.0 ± 3.3 and 25.5 ± 4.6 nm, respectively.

HRTEM and Fourier transform (FT) image of the cubic-shaped ITO NP (**Fig. 15** (c)) are illustrated in **Fig. 17**. They clearly show the single-crystalline structure for the cubic-ITO NP. The lattice spacing parallel to exposing crystal plane calculated from **Fig. 17** (b) is 0.50 nm, corresponding to an interplanar distance of (200) planes of ITO with the cubic crystal system of *Ia3*. The FT pattern of **Fig. 17** (b) means the particle growth perpendicular to {200} plane. In general, particle morphology is controlled by the specific adsorption of additives, which regulates the growth rate of the particle in this direction. Thus, the reduction in the growth rate perpendicular to {200} plane by specific adsorption of EG and TMAH leads to form the cubic-shaped ITO NPs in this system. The streaks, observed among each spots in the FT in the inset of **Fig. 17** (b), suggested homogeneous substitutional doping of tin ions in the In_2O_3 crystal structure. Resistivity measurements of compacts prepared with ITO NPs with different Sn/In molar ratio of 0, 0.04, 0.10, and 0.15 were 17.34, 1.06, 1.93, and 2.67 Ω cm, respectively. Thus, the optimized range in the tin doping amount was found about 0.04–0.10 mol%, and the minimal value of the powder resistivity was reached at 1.06 Ω cm. It should be noted that the resistivity of the particles with the Sn/In ratio of 0.10 was drastically decreased to 8.4×10^{-2} Ω cm after the heat treatment at 300 °C for 30 min under air followed by 300 °C for 30 min under a 1 % H_2 in N_2 atmosphere. As a result, the cubic-shaped monodispersed ITO NPs with low resistivity synthesized in the present method, have large potential for the development of printable TCO nano-inks.

Finally, we were attempted to make thin film with ITO nanoink. As a result, ITO film below 200 nm in thickness was successfully fabricated and the resistivity of the particles (Sn/In ratio of 0.10) drastically decreased to below 1.0×10^{-3} Ω cm by various heat treatments 1 % H_2/N_2 atmosphere. The value seems enough to apply to some specific region. Now, some companies are preparing commercial ITO nanoink after so many examinations for inkjet as shown in **Fig. 18**.

6.3 GZO as a substitute ITO

The substitute materials synthesis of ITO has been studied. Antimony-doped tin oxide (ATO), aluminum-doped zinc oxide (AZO), and gallium-doped zinc oxide (GZO) has been focused on in our laboratory. Gallium doped zinc oxide (GZO) has been expected as a substitute material of ITO for TCO. We also have been developed the synthesis method of GZO based on the similar one to ITO. For established procedure, 50 mL of 0.30 M $Zn(NO_3)_2 \cdot 6H_2O$ and x mol% $Ga(NO_3)_3 \cdot 5.8H_2O$ solution (x = Ga/Zn = 0–30) in methanol was mixed well with the same volume of 0.60–1.8 M NaOH. The mixed solution was aged at 200 °C for 1–48 hours. For ATO, mixed solution of SbCl5 and SnCl4 After washing process with ethanol and distilled water, dried sample was evaluated with TEM.

Fig. 19 shows TEM photos GZO formed with 1,8 M NaOH after aging at 200 °C for 48 hours. GZO NPs were

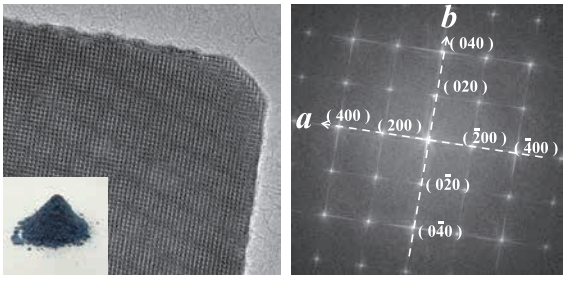

Fig. 17 (a) A HRTEM image of an ITO NP shown in Fig.15 (c); (b) A magnified and a FT images (inset) of the ITO NP exhibited in Fig. 15 (c).

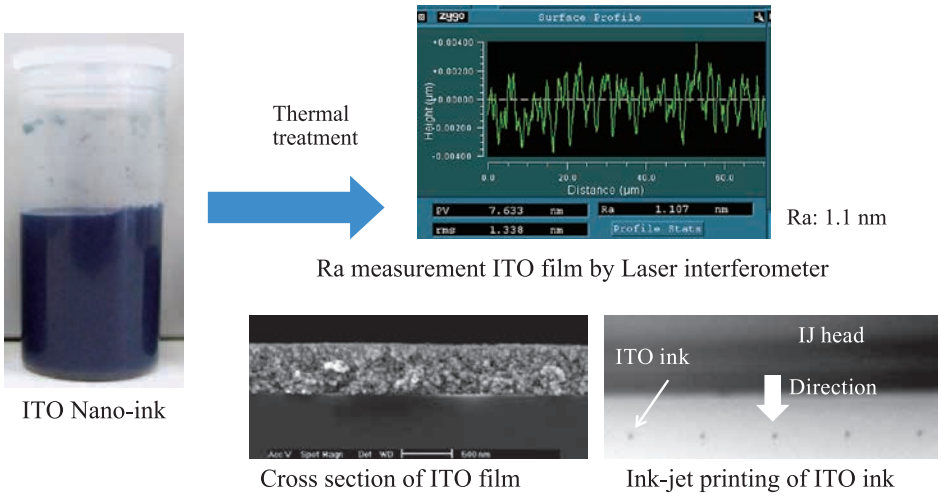

Fig. 18 ITO nanoink for industrial use.

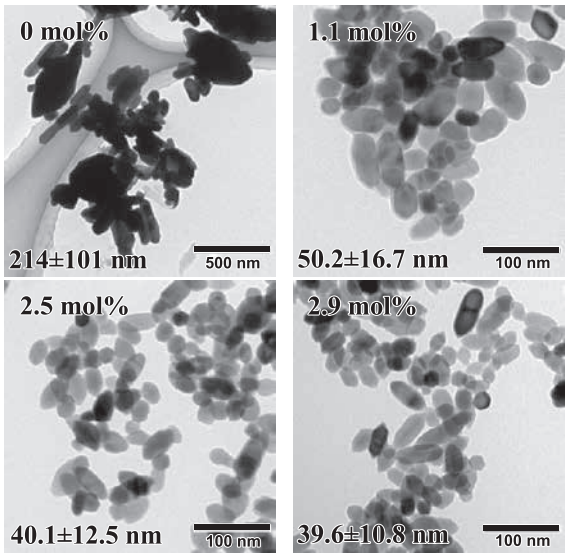

Fig. 19 GZO formed with 1.8M NaOH, aging time 24 h.

successfully synthesized with narrow size distribution and precise control in Ga content. Judging from transmittance and resistivity of GZO thin film prepared by inkjet of GZO nanoink and then the thermal treatment with different temperature under air and then H_2 for 1 h each, it is concluded that resistivity was monotonously decreased with increase in temperature, but the transmittance and haze was independent from it. As a result, our GZO nanoink can be applied for TCO as a substitute ITO.

7. Conclusions

Highly-crystalline monodispersed ITO NPs with a cubic shape were successfully synthesized by way of the combination of Gel-sol and solvothermal method by use of TMAH as a basic agent and EG as a solvent. The monodispersed ITO NPs were formed through dissolution and recrystallization process of the gel formed at early stage of aging. The initially formed gel consisted of indium hydroxide, EG, and TMAH played an important role for formation of monodispersed NPs. The HRTEM and FT analyses showed that the single crystalline cubic-shaped NP was formed by the reduction in the growth normal to {200} plane. The FT analysis indicated Sn ions were substituted homogeneously in the ITO NP lattice. ITO nanoink was also prepared by the dispersion of ITO NPs into EG solution. Also, this combined method was applied to the synthesis of the other TCO NPs so that uniform GZO nanoparticles and their nanoink have been successfully prepared.

Acknowledgements

This work was financially supported by METI & NEDO Rare Metal Substitute Materials Development Project and Industrial Technology Research Grant Program in 2011 (No. 11b15004d) from NEDO.

References

Aoki Y., Huang J., Kunitake T., Electro-conductive nanotubular sheet of indium tin oxide as fabricated from the cellulose template, Journal of Materials Chemistry, 16 (2006) 292–297.

Ba J., Fattakhova Rohlfing D., Feldhoff A., Brezesinski T., Djerdj I., Wark M., Niederberger M., Nonaqueous synthesis of uniform indium tin oxide nanocrystals and their electrical conductivity in dependence of the tin oxide concentration, Chemistry of Materials, 18 (2006) 2848–2854.

Bühler G., Thölmann D., Feldmann C., One-pot synthesis of highly conductive indium tin oxide nanocrystals, Advanced Materials, 19 (2007) 2224–2227.

Chiou B.-S., Hsieh S.-T., R.F. Magnetron-sputtered indium tin

oxide film on a reactively ion-etched acrylic substrate, Thin Solid Films, 229 (1993) 146–155.

Derjaguin B.V., Landau L., Theory of the stability of strongly charged lyophobic sols and of the adhesion of strongly charged particles in solutions of electrolytes, Acta Phys. Chim. URSS, 14 (1941) 633–662.

Endo Y., Sasaki T., Kanie K., Muramatsu A., Direct preparation and size control of highly crystalline cubic ITO nanoparticles in a concentrated solution system, Chemistry Letters, 37 (2008) 1278–1279.

Gessert T.A., Yoshida Y., Fesenmaier C.C., Coutts T.J., Sputtered In_2O_3 and ITO thin films containing zirconium, Journal of Applied Physics, 105 (2009) 083547.

Gilstrap Jr R.A., Summers C.J., Synthesis and analysis of an indium tin oxide nanoparticle dispersion, Thin Solid Films, 518 (2009) 1136–1139.

Gilstrap Jr R.A., Capozzi C.J., Carson C.G., Gerhardt R.A., Summers C.J., Synthesis of a nonagglomerated indium tin oxide nanoparticle dispersion, Advanced Materials, 20 (2008) 4163–4166.

Hamberg I., Granqvist C.G., Evaporated Sn—doped In_2O_3 films: Basic optical properties and applications to energy—efficient windows, Journal of Applied Physics, 60 (1986) R123–R160.

Hartnagel H., Semiconducting transparent thin films, Institute of Physics Pub., Bristol [England]; Philadelphia, PA, 1995.

Hong S.-J., Han J.-I., Indium tin oxide (ITO) thin film fabricated by indium–tin–organic sol including ITO nanoparticle, Current Applied Physics, 6, Supplement 1 (2006) e206–e210.

Hong S.-J., Kim Y.-H., Han J.-I., Development of ultrafine indium tin oxide (ITO) nanoparticle for ink-jet printing by low-temperature synthetic method, Nanotechnology, IEEE Transactions on, 7 (2008) 172–176.

Kanehara M., Koike H., Yoshinaga T., Teranishi T., Indium tin oxide nanoparticles with compositionally tunable surface plasmon resonance frequencies in the near-IR region, Journal of the American Chemical Society, 131 (2009) 17736–17737.

Kanie K., Numamoto Y., Tsukamoto S., Takahashi H., Mizutani H., Terabe A., Nakaya M., Tani J., Muramatsu A., Hydrothermal synthesis of sodium and potassium niobates fine particles and their application to lead-free piezoelectric material, MATERIALS TRANSACTIONS, 52 (2011) 2119–2125.

Kanie K., Sasaki T., Nakaya M., Muramatsu A., Quaternary ammonium hydroxide-assisted solvothermal synthesis of monodispersed ITO nanoparticles with a cubic shape, Chemistry Letters, 42 (2013) 738–740.

Kanie K., Sugimoto T., Shape control of anatase TiO_2 nanoparticles by amino acids in a gel-sol system, Chemical Communications, 14 (2004) 1584–1585.

Kim K.Y., Park S.B., Preparation and property control of nano-sized indium tin oxide particle, Materials Chemistry and Physics, 86 (2004) 210–221.

Kimijima T., Kanie K., Nakaya M., Muramatsu A., Solvothermal synthesis of $SrTiO_3$ nanoparticles precisely controlled in surface crystal planes and their photocatalytic activity, Applied Catalysis B: Environmental, 144 (2014) 462–467.

Kimijima T., Sasaki T., Nakaya M., Kanie K., Muramatsu A., Photocatalytic activity of Ni-loaded TiO_2 nanoparticles precisely controlled in size and shape, Chemistry Letters, 39 (2010) 1080–1081.

Lee C.H., Kim M., Kim T., Kim A., Paek J., Lee J.W., Choi S.-Y., Kim K., Park J.-B., Lee K., Ambient pressure syntheses of size-controlled corundum-type In_2O_3 nanocubes, Journal of the American Chemical Society, 128 (2006) 9326–9327.

Lee J.-S., Choi S.-C., Solvent effect on synthesis of indium tin oxide nano-powders by a solvothermal process, Journal of the European Ceramic Society, 25 (2005) 3307–3314.

Lin Y.C., Li J.Y., Yen W.T., Low temperature ITO thin film deposition on PES substrate using pulse magnetron sputtering, Applied Surface Science, 254 (2008) 3262–3268.

Liu Q., Lu W., Ma A., Tang J., Lin J., Fang J., Study of quasi-monodisperse In_2O_3 nanocrystals: Synthesis and optical determination, Journal of the American Chemical Society, 127 (2005) 5276–5277.

Muramatsu A., Sasaki T., Endo Y., Doi Y., Kanie K., Solvothermal Synthesis of ITO Nanoparticles Precisely Controlled in Size and Shape, Advances in Science and Technology, 62 (2010) 50–55.

Niederberger M., Nonaqueous sol–gel routes to metal oxide nanoparticles, Accounts of Chemical Research, 40 (2007) 793–800.

Okuya M., Ito N., Shiozaki K., ITO thin films prepared by a microwave heating, Thin Solid Films, 515 (2007) 8656–8659.

Sasaki T., Endo Y., Nakaya M., Kanie K., Nagatomi A., Tanoue K., Nakamura R., Muramatsu A., One-step solvothermal synthesis of cubic-shaped ITO nanoparticles precisely controlled in size and shape and their electrical resistivity, Journal of Materials Chemistry, 20 (2010) 8153–8157.

Sasaki T., Nakaya M., Kanie K., Muramatsu A., Amino acid assisted hydrothermal synthesis of $In(OH)_3$ nanoparticles controlled in size and shape, MATERIALS TRANSACTIONS, 50 (2009) 2808–2812.

Seo W.S., Jo H.H., Lee K., Park J.T., Preparation and optical properties of highly crystalline, colloidal, and size-controlled indium oxide nanoparticles, Advanced Materials, 15 (2003) 795–797.

Song J.E., Lee D.K., Kim H.W., Kim Y.I., Kang Y.S., Preparation and characterization of monodispersed indium–tin oxide nanoparticles, Colloids and Surfaces A: Physicochemical and Engineering Aspects, 257–258 (2005) 539–542.

Sugimoto T., Chapter 8—control of particle characteristics, in: Sugimoto T. (Ed), Monodispersed particles, Elsevier, Amsterdam, 2001, pp. 376–388.

Sugimoto T., Khan M.M., Muramatsu A., Itoh H., Formation mechanism of monodisperse peanut-type α-Fe_2O_3 particles from condensed ferric hydroxide gel, Colloids and Surfaces A: Physicochemical and Engineering Aspects, 79 (1993) 233–247.

Sugimoto T., Wang Y., Itoh H., Muramatsu A., Systematic control of size, shape and internal structure of monodisperse

α-Fe_2O_3 particles, Colloids and Surfaces A: Physicochemical and Engineering Aspects, 134 (1998) 265–279.

Sugimoto T., Zhou X., Muramatsu A., Synthesis of uniform anatase TiO_2 nanoparticles by gel–sol method: 4. Shape control, Journal of Colloid and Interface Science, 259 (2003) 53–61.

Sujatha Devi P., Chatterjee M., Ganguli D., Indium tin oxide nano-particles through an emulsion technique, Materials Letters, 55 (2002) 205–210.

Usui H., Sasaki T., Koshizaki N., Optical transmittance of indium tin oxide nanoparticles prepared by laser-induced fragmentation in water, The Journal of Physical Chemistry B, 110 (2006) 12890–12895.

Verwey E.J.W., Overbeek J.T.G, Theory of the stability of lyophobic colloids. The interaction of particles having an electric double layer. Elsevier, New York-Amsterdam, 1948.

Yang J., Li C., Quan Z., Kong D., Zhang X., Yang P., Lin J., One-step aqueous solvothermal synthesis of In_2O_3 nanocrystals, Crystal Growth & Design, 8 (2008a) 695–699.

Yang J., Li C., Quan Z., Zhang C., Yang P., Li Y., Yu C., Lin J., Self-assembled 3D flowerlike Lu_2O_3 and Lu_2O_3:Ln^{3+} (Ln = Eu, Tb, Dy, Pr, Sm, Er, Ho, Tm) microarchitectures: Ethylene glycol-mediated hydrothermal synthesis and luminescent properties, The Journal of Physical Chemistry C, 112 (2008b) 12777–12785.

Zhang W., Huang Z., Li T., Tang Q., Ma D., Qian Y., A novel route to octahedral In_2O_3 particles exhibiting near band emission, Chemistry Letters, 34 (2005) 118–119.

Author's short biography

Atsushi Muramatsu

Dr.Atsushi Muramatsu is the Director and Professor of the Institute of Multidisciplinary Research for Advanced Materials, Tohoku University. The strategy of his laboratory, named as the Hybrid-Nanoparticle Lab., is to develop the novel synthesis method of highly functional nano-materials.

He graduated from the University of Tokyo in 1984 and then took the degree of Doctor of Engineering at the same university in 1988. He had a post of Research Associate at Tohoku University in 1988 and then Professor in 2001.

He was given the present position of the Director last spring.

Kiyoshi Kanie

Dr. Kiyoshi Kanie, born in 1971, received his Bachelor's deg. from Nagoya Inst. of Tech. in 1994 and Master's deg. from Tokyo Inst. of Tech., 1996.

Then, he was appointed to an Assistant Prof. at the Univ. of Tokyo in 1998.

His research was exploration of materials with novel organic functionality through self-organization. In 2000, he received his Ph.D. degree from Kyoto Univ. He moved to the present institution as an Assistant Prof.in 2002 and promoted to an Associate Prof. in 2008. His current research includes the development of liquid-phase synthetic methods of functional inorganic nanoparticles preciously controlled in size and shape. He also focus on design and synthesis of functional organic materials.

Author's short biography

Takafumi Sasaki

Dr. Takafumi Sasaki, born in 1979 in Sendai, received his Ph.D. degree from Tohoku Univ. in 2008. Then, he worked in the Univ. as a post-doc researcher for 3 years. His main research subject was synthesis of functional inorganic nanoparticles and development in size control of the particles. In 2011, He moved his occupation to MITSUI MINING & SMELTING CO., LTD.. He's engaged in work in Shimonoseki at present. His hobby is tour of hot springs in western Japan.

Masafumi Nakaya

Dr. Masafumi Nakaya, born in 1978, received his Bachelor's deg. from Kanazawa University, in 2002, Master's deg. from Japan Advanced Institute of Science and Technology, 2004, and Ph.D. degree from University of Tsukuba, 2007. Then, he worked in University of Tsukuba as a post-doc researcher for a year. He has worked in Tohoku University as an Assistant Professor since 2008. His main research theme is "Preparation of iron-based magnetic nanoparticles with tunable size and shape and control of their magnetic properties".

The 49th Symposium on Powder Technology

The 49th Symposium on Powder Technology was held at Senri Hankyu Hotel, Japan on Monday, September 7, 2015. It was organized by Hosokawa Powder Technology Foundation with the sponsorship of Hosokawa Micron Corporation. More than 160 people from the industries and universities attended this symposium. The theme of the symposium this year was "Powder Technology, advancing in response to the requirements of the era". There were six lectures with questions and answers followed by a get-acquainted party for further free discussions.

The first lecture was given by Prof.Otani, who was presented the KONA Award last year, on his lifework research in the field of air filters including the recent trends of new advanced filters. Four lectures were carried out by the professors with the diversity of the fields including the electrode/solid electrolyte composite of secondary batteries, the functional devices using 3D micro/nano stereolithograph and the tailored composite particles as well as its processing. The other two lectures were from the industrial fields introducing the casting technology, which has been developed since the ancient days supporting the manufacturing industry, and the new-type vacuum dryer with the agitating mechanism which is capable of handling heat-sensitive materials like pharmaceuticals and food staff.

The contents of the symposium are shown in the followings.

The 49th Symposium on Powder Technology

Theme: Powder Technology, advancing in response to the requirements of the era

Opening address Prof. emeritus Minoru Takahashi (Nagoya Institute of Technology)

Session 1 Chaired by Prof. emeritus Fumio Saito (Tohoku University)

- Lecture 1
  "Present Status of Air Filters and Exploration of Their New Applications"
  Prof. Yoshio Otani (Kanazawa University)
- Lecture 2
  "Room Temperature Fabrication of Electrode-Solid Electrolyte Composite for All-Solid-State Rechargeable Lithium Batteries"
  Prof. Yasutoshi Iriyama (Nagoya University)

Session 2 Chaired by Prof. Hirofumi Takeuchi (Gifu Pharmaceutical University)

- Lecture 3
  "Development of Functional Devices Using Three-Dimensional Micro/Nano Stereolithography"
  Prof. Shoji Maruo (Yokohama National University)
- Lecture 4
  "Design of Tailored Composite Fine Particles and Its Processing"
  Prof. Satoru Watano (Osaka Prefecture University)

Session 3 Chaired by Prof. Makio Naito (Osaka University)

- Lecture 5
  "Casting Technology, Supporting Manufacturing Industry over 5,000 Years"
  Dr. Haruyoshi Hirano (Takeyama Foundry Co., Ltd.)
- Lecture 6
  "New Dyer for the Efficient Drying of Heat-Sensitive Materials"
  Mr. Takashi Ochiai (Hosokawa Micron Corporation)

Closing address Mr. Yoshio Hosokawa (President of Hosokawa Powder Technology Foundation)

The 49th Symposium on Powder Technology

Get-acquainted Party

The 22nd KONA Award

Dr. Yoshio Otani, Professor of Kanazawa University, was selected as the winner of the 22nd KONA Award. The KONA Award is sponsored by Hosokawa Powder Technology Foundation and presented to scientists or groups who have achieved distinguished research work in the field of particle science and technology.

Dr. Otani received his B.E. in 1977, M.E. in 1979, from Kanazawa University, and Ph.D. in 1982 from Syracuse University, New York. After completion of his Ph.D., he joined Kanazawa University as a research associate in 1982. He became a professor of the Faculty of Engineering in 1998. Since then, he has steered the particle technology lab to be the one of the leading labs in the field of particle technology and aerosol science in Japan. In 1999–2000, he took a sabbatical leave to the School of Public Health, Harvard University, where he worked on the irreversibility of inhaled air in the periphery of the lung.

He has served on the executive board of the Society of Powder Technology, Japan, the Japan Association of Aerosol Science and Technology, and Japan Air Cleaning Association. He hosted the 2015 Asian Aerosol Conference (AAC2015) in June, 2015, inviting more than 500 attendees from abroad and Japan. At the AAC2015 he was appointed as President of Asian Aerosol Research Assembly to lead in the collaboration of Asian aerosol societies.

In over thirty years of his career at Kanazawa University, Dr. Otani has made outstanding contributions to aerosol science and technology through research on aerosol generation, measurement and collection. He is one of the research authorities making substantial achievements in the development of air cleaning technology with air filters. He has supervised over ten Ph.D. students and more than 200 master course students. Most of his students now work actively in companies related to particle technology. His contribution is not limited to academics. He has served as the chairmen of ISO/TC24/SC4 and ISO/TC142 Japanese mirror committees and contributed to the international standardization of particle measurement instruments and air cleaning equipment.

He has over 150 published research papers and more than 50 review articles, book chapters and textbooks. In recent five years, he has been an invited lecturer of six Asian and international conferences. His research field covers (i) influence of filter structure on the collection performance, (ii) evaluation method of air filter performance, (iii) generation of test aerosol, (iv) charging of aerosol particles, and (v) aerosol instrumentation. He was the first to apply an air filter to classify aerosol nanoparticles by passing aerosol particles through an air filter at an extremely high filtration velocity, which is now commercialized as “Nanosampler” for the measurement of atmospheric nanoparticles.

He has conducted much collaborative research work with companies dealing with powder products, industrial hygiene, air filter and aerosol measuring instruments, since air filtration is an immediate research topic closely related to the problems which many manufacturing companies are now confronted with.

In summary, his contributions to academics and societies are outstanding and his progress in networking the international research collaboration is making great strides forward.

On March 9, 2015, Mr. Kiyomi Miyata, Vice-President of the Foundation, presented the 22nd KONA Award to Dr. Yoshio Otani at the presentation ceremony held at Hosokawa Micron Corporation in Hirakata.

General Information

History of the Journal

In the history of KONA Powder and Particle Journal, two organizations have been playing an important role. The one is the Council of Powder Technology, Japan (CPT) and the other is the Hosokawa Powder Technology Foundation (Hosokawa Foundation). The CPT was established in 1969 by Hosokawa Micron Corporation as a nonprofit organization to enhance the activities of research and development on powder science and technology. The Hosokawa Foundation was established in 1991 as a public-service corporation approved by the Ministry of Education, Culture, Sport, Science and Technology of Japan. The issues from No.1 (1983) to No.12 (1994) of KONA were published by CPT and the issues from No.13 (1995) by the Hosokawa Foundation.

The aim of KONA in the early days was to introduce excellent Japanese papers to the world and thus KONA consisted of papers recommended by some Japanese academic societies and translated from Japanese to English. From the issue of No.8, the CPT changed its editorial policy to internationalize the KONA and to incorporate papers by authors throughout the world in addition to translated papers. In response to this change, three editorial blocks have been organized in the world; Asian-Oceanian, American and European. The policy and system have not changed even after the Hosokawa Foundation has taken over from the CPT. From the issue of No.27 (2009), publication of translated papers has been terminated and only original papers have been published. The CPT is active still today and collaborates with the Hosokawa Foundation.

Aims and Scope

KONA publishes papers in a broad field of powder science and technology, ranging from fundamental principles to practical applications. The papers describing technological experiences and critical reviews of existing knowledge in special areas are also welcome.

The submitted papers are published only when they are judged by the Editor to contribute to the progress of powder science and technology, and approved by any of the three Editorial Committees.

The paper submitted to the Editorial Secretariat should not have been previously published.

Category of Papers

- Invited articles
  Review papers and special articles invited by the KONA Editorial Committees.
- Contributed papers
  Original research and review papers submitted to the KONA Editorial Committees, and refereed by the reviewers and editors.

Submission of Contributed Papers

"Inquiry Letter" for submission on the KONA website (http://www.kona.or.jp) needs to be sent to the Editor-in-Chief (mail to:contact_zasubmit@hmc.hosokawa.com) prior to the submission of the manuscript. After then, papers will be guided to each KONA Editorial Secretariat as follows.

- Asian/Oceanian Editorial Secretariat
  Dr. T. Yokoyama or Dr. L. Cui
  Hosokawa Powder Technology Foundation
  1-9, Shodaitajika, Hirakata-shi, Osaka, 573-1132 Japan
- European / African Editorial Secretariat
  Dr. S. Sander or Ms. L. Kneisl
  Hosokawa Alpine AG
  Peter-Dörfler-Straße 13-25, D - 86199 Augsburg, Germany
- American Editorial Secretariat
  Dr. C. C. Huang
  Hosokawa Micron Powder Systems
  10 Chatham Road, Summit NJ 07901 USA

Publication in KONA is free of charge.

Publication Schedule

KONA is published annually. The publication date is around January 10th.

Subscription

KONA is distributed free of charge to senior researchers at universities and laboratories as well as to institutions and libraries in the field throughout the world. The publisher is always glad to consider the addition of names of those, who want to obtain this journal regularly, to the mailing list.

Instructions to Authors

(1) **Manuscript format**

- Electric files should be submitted to the Editorial Secretariat by online. Authors' short biography with less than 100 words per person and color photographs of all the authors should be attached to the final version.
- The structure of manuscripts should follow the following order; title, authors, affiliations, abstract, graphical abstract, keywords, main text, (acknowledgement), (appendix), (nomenclature), references. The items with parentheses are not mandatory.
- Full postal addresses must be given for all the authors. Indicate the corresponding author by the mark"*" after the name. Telephone and fax numbers and e-mail address should be provided for the corresponding author.
- Abstract should not exceed 200 words.
- Graphical abstract should be a concise, visual summary of the article which will be displayed in the contents list both online and print.
- The appropriate number of keywords is 5 or 6.
- The maximum pages printed in KONA are supposed to be: 15 for an original paper and 25 for a review paper.
- Symbols and units should be listed in alphabetical order with their definition and dimensions in SI units.
- The color figures will appear in color both on the KONA Website (http://www.kona.or.jp) and also in the paper version.
- Concerning references, the alphabetical system should be adopted. Please use reference management software such as Endnote to manage references as far as possible.
  List: References should be arranged first alphabetically and then further sorted chronologically if necessary. More than one reference from the same author(s) in the same year must be identified by the letters "a", "b", "c", etc., placed after the year of publication.
  Examples:
  - Reference to a book:
  Strunk Jr. W., White E.B., The Elements of Style, fourth ed., Longman, New York, 2000.
  - Reference to a chapter in an edited book:
  Mettam G.R., Adams L.B., How to prepare an electronic version of your article, in: Jones B.S., Smith R.Z. (Eds.), Introduction to the Electronic Age, E-Publishing Inc., New York, 2009, pp.281–304.
  - Reference to a journal publication:
  Tsuji Y., Tanaka T., Ishida T., Lagrangian numerical simulation of plug flow of cohesionless particles in a horizontal pipe, Powder Technology, 71 (1992) 239–250.
  Text: All citations in the text should refer to:
  1. Single author: the author's name (without initials, unless there is ambiguity) and the year of publication;
  2. Two authors: both authors' names and the year of publication;
  3. Three or more authors: first author's name followed by "et al." and the year of publication.
  Citations may be made directly (or parenthetically). Groups of references should be listed first alphabetically, then chronologically.
  Examples: "as demonstrated (Hidaka J. et al., 1995; Tsuji Y., 1992a, 1992b, 1993). Mori Y. and Fukumoto Y. (2002) have recently shown ...."

(2) **Copyright and permission**

- The original paper to be submitted to KONA has not been published before in any language or in any journal or media; it is not submitted and not under consideration for publication in whole or in part elsewhere.
- Authors are responsible for obtaining permission from the copyright holders to reproduce any figures, tables and photos for which copyright exists.
- The KONA Journal applies the **Creative Commons Attribution License** to all works published by the Journal. Copyright stays with the agreed copyright owner, and the Hosokawa Powder Technology Foundation is granted the exclusive right to publish and distribute the work, and to provide the work in all forms and media.
- Users of the journal will be able to reuse the contents in any way they like, provided they are accurately attributed. No permission is required from either the authors or the publisher.

Free electronic publication of KONA is available at http://www.kona.or.jp

Table top lab equipments

Pin mills, Impact mill, Jet mills, Wet beads mill,

Classifier, Mixer, Particle composers

picoline
HOSOKAWA ALPINE

www.hosokawa-alpine.com

Laboratory by HOSOKAWA

Lypholizer

Active Freeze Dryer AFD

www.hosokawamicron.nl

Containment

Isolator

www.hosokawa.co.uk

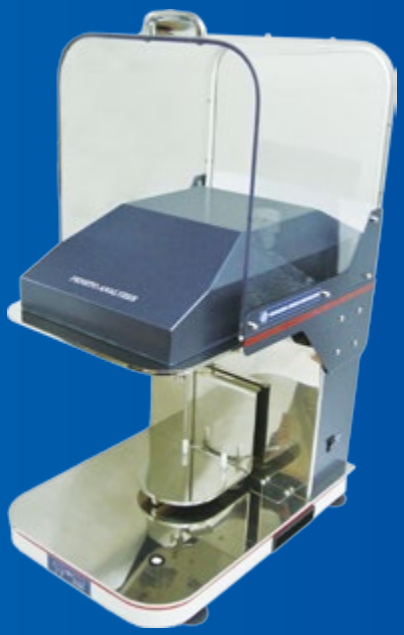

Measuring instruments

Powder characteristics tester : PT-X

Penetration speed : Peneto Analyzer PNT-N

Wet sieving : Viblette VBL

www.hosokawamicron.co.jp

Technology

MICRON GROUP

Sieving

Air jet sieve MAJS

www.hmicronpowder.com

HOSOKAWA MICRON GROUP

The Hosokawa Micron Group will always be the leading global company covering the mountain range of Powder Technologies. The Group has been a pioneer in the filed of powder and particle processing and blown film processing. We provide R&D, engineering, manufacturing and services in various fields of the world's major industrial markets.

Process Technologies for Tomorrow

HOSOKAWA MICRON

Headquaters Location :

HOSOKAWA MICRON CORPORATION

http://www.hosokawamicron.co.jp